

UNCLASSIFIED

AD NUMBER

AD869018

LIMITATION CHANGES

TO:

Approved for public release; distribution is unlimited.

FROM:

Distribution authorized to U.S. Gov't. agencies and their contractors; Critical Technology; FEB 1970. Other requests shall be referred to Air Force Materials Laboratory, Wright-Patterson AFB, OH 45433. This document contains export-controlled technical data.

AUTHORITY

AFML ltr dtd 7 Dec 1972

THIS PAGE IS UNCLASSIFIED



AFML-TR-69-204, Part II

A STRENGTH ANALYSIS OF A POLYGRAPHITE

C. D. Pears  
H. G. Sanders

Southern Research Institute

Technical Report No. AFML-TR-69-204, Part II  
February 1970

Air Force Materials Laboratory  
Air Force Systems Command  
Wright-Patterson Air Force Base, Ohio

## NOTICE

When Government drawings, specifications, or other data are used for any purpose other than in connection with a definitely related Government procurement operation, the United States Government thereby incurs no responsibility nor any obligation whatsoever; and the fact that the Government may have formulated, furnished, or in any way supplied the said drawings, specifications, or other data, is not to be regarded by implication or otherwise as in any manner licensing the holder or any other person or corporation, or conveying any rights or permission to manufacture, use, or sell any patented invention that may in any way be related thereto.

This document is subject to special export controls and each transmittal to foreign governments or foreign nationals may be made only with prior approval of Air Force Materials Laboratory (MAAS), WPAFB, Ohio.

~~The distribution of this report is limited because it contains technology related to materials restricted by the Export Control Act.~~

Copies of this report should not be returned unless return is required by security considerations, contractual obligations, or notice on a specific document.

AFML-TR-69-204, Part II

A STRENGTH ANALYSIS OF A POLYGRAPHITE

C. D. Pears  
H. G. Sanders

Southern Research Institute

Technical Report No. AFML-TR-69-204, Part II

February 1970

This document is subject to special export controls and each transmittal to foreign governments or foreign nationals may be made only with prior approval of Air Force Materials Laboratory (MAAS), WPAFB, Ohio

Air Force Materials Laboratory  
Air Force Systems Command  
Wright-Patterson Air Force Base, Ohio

## FOREWORD

This is the final report to the Air Force under Contract Number F33615-67-C-1523, Subcontract No. 750464 from the Avco Applied Technology Division to perform destructive tests on polygraphites and to relate flaws to their ability to act as strength reducers in tension. This contract was initiated under Project No. 7381, "Materials Application", Task No. 738102, "Space, Missile and Propulsion Systems Material and Component Evaluation" and supported by the Director's Laboratory Discretionary Fund. This report covers work conducted from 1 April 1968 to 15 September 1969. This program was organized through joint interests by the Air Force Materials Laboratory, Lockheed Missiles and Space Company, Avco Applied Technology Division, Union Carbide, and Southern to develop better understanding of structural polygraphite. Specifically, the program was aimed toward detecting and characterizing the different types of flaws which are found in polygraphites and defining their effects on strength. The particular point was to find the point at which a flaw became a strength reducer or property change. That is, what is a threshold flaw? The grade of polygraphite which received particular attention was Union Carbide Grade ATJ-S.

As a result of losing the project leader about midway through the program, C. D. Pears, Head of the Mechanical Engineering Division, assumed the responsibility of organizing the report, searching the data for first order relations, conducting confirming experiments, and writing the sections on Analysis and Discussion and Conclusions. H. G. Sanders provided invaluable assistance, particularly in assembling the Experimental Results and searching all data to be sure that significant data were not omitted. He also conducted a detailed search for relations of NDT signals to particular specimens. Dr. R. E. Bicklehaupt assisted in establishing proper techniques for some of the monitors and making judgments in their indications, particularly as related to microstructure. H. S. Starrett and J. R. Brown, Jr. were quite helpful in the statistical analysis of the data and in providing useful comments on the influence of monitors.

Special thanks are offered to A. W. Schultz who was our technical contact at Avco who administered the contract, and to C. H. Hastings and S. W. Carter of Avco who helped us gain some initial insight in NDT methods. Finally, we are equally grateful to Dean Temple of Lockheed, Bud Townsend of Union Carbide, and Clarence Pratt of AFML.

This technical documentary report has been reviewed and is approved.



L. N. HJEIM, Chief  
Space & Missiles Systems Support Branch  
Materials Support Division  
AF Materials Laboratory

## ABSTRACT

A strength analysis was conducted on ATJ-S graphite to relate flaws in a specimen to (1) their ability to act as strength reducers in tension, and (2) to various monitors such as porosity, sonic velocity, and others that relate to the macro and microstructure. Various methods of non-destructive inspection, such as ultrasonics and radiography, were applied to the billets, blanks and specimens in an attempt to relate existing inspection techniques to ultimate performance of a specimen. The major strength reducers in ATJ-S were found to be disparate voids, void clusters, and large porous zones. Further, the strength was found to be a smooth function of open porosity ranging from the precursor to the fully densified form. Velocity and electrical resistivity were good monitors of open porosity, but not of disparate flaws. A satisfying method of preselecting disparate flaws in all cases was not found. Except for the disparate specimens with unique flaws, this graphite did respond in a way suggesting an orderly relation to some parametric analyses, and fracture seemed to be described by uniform distributions. A failure mode and criteria are discussed.

70 pp) (28 fig.) (24 tabs.) (0 ref.)

## TABLE OF CONTENTS

	Page
INTRODUCTION . . . . .	1
MATERIALS . . . . .	3
THE DESIGN PROCESS AND MATERIAL VARIABILITY . . . . .	4
Background Flaws . . . . .	5
Disparate Voids . . . . .	5
Disparate Inclusion . . . . .	6
Disparate Macrocracks . . . . .	7
Striations . . . . .	7
Void Cluster . . . . .	8
Structure Nuances . . . . .	8
Nonuniformity . . . . .	8
Nonreproducibility . . . . .	9
SUMMARY ON DESIGN AND VARIABILITY . . . . .	9
TEST METHODS . . . . .	10
Tensile Apparatus . . . . .	10
Ultrasonics . . . . .	14
Radiography . . . . .	15
Electrical Resistivity . . . . .	16
Open and Closed Porosity by Liquid Absorption . . . . .	18
Porosity by Point Count . . . . .	20
Inspection of Fracture Faces by Flicks . . . . .	22
Weight/Volume Bulk Density . . . . .	24
Application of Alcohol Penetrant for Evaluation of Surface Porosity . . . . .	24
Other Methods of Inspection . . . . .	24
EXPERIMENTAL RESULTS . . . . .	25
ATJ-S Billet L-16-7 . . . . .	25
ATJ-S Billet L-7-1 . . . . .	28
ATJ-S Billet L-1-4 . . . . .	28
ATJ-S Billet L-1-8 . . . . .	31

# TABLE OF CONTENTS - Continued

	Page
ATJ-S Billet L-4-6 . . . . .	34
ATJ-S Billet L-6-3 . . . . .	38
ATJ-S Billet L-9-10 . . . . .	39
ATJ-S Billet L-10-6 . . . . .	42
ATJ-S Billet L-11-4 . . . . .	43
ANALYSIS AND DISCUSSION OF RESULTS . . . . .	45
ATJ-S Billet L-16-7 . . . . .	46
ATJ-S Billet L-7-1, With Grain . . . . .	61
ATJ-S Billet L-1-4, With Grain . . . . .	62
ATJ-S Billet L-1-4, Across Grain . . . . .	66
ATJ-S Billet L-1-8, With Grain . . . . .	70
ATJ-S Billet L-1-8, Across Grain . . . . .	75
ATJ-S Billet L-4-6, With Grain . . . . .	78
ATJ-S Billet L-6-3, With Grain . . . . .	84
ATJ-S Billet L-6-3, Across Grain . . . . .	85
ATJ-S Billet L-9-10, With Grain . . . . .	85
ATJ-S Billet L-10-6, With Grain and Across Grain . . . . .	89
ATJ-S Billet L-11-4, With Grain and Across Grain . . . . .	90
Comparison of Different Billets, With Grain . . . . .	90
CONCLUSIONS . . . . .	97
APPENDICES . . . . .	416





## LIST OF ILLUSTRATIONS

Figure		Page
1	Picture of a Tensile Stress-Strain Facility . . . . .	100
2	Schematic of the Gas Bearings and Load Train for the Tensile Apparatus . . . . .	101
3	Location of the Flag Attachments on the Tensile Specimens .	102
4	Precision Collet Grip for Tensile Specimens 2:1 Scale . . .	103
5	Small 5500°F Graphite Resistance Furnace . . . . .	104
6	Arrangement of Optical Strain Analyzer . . . . .	105
7	Potentiometer Method for Measuring Electrical Resistivity .	106
8	Setup for Determining Suspended Weight of Saturated Specimen for Liquid Absorption Evaluation . . . . .	107
9	Composite Curve for Tensile Strength versus Open Porosity for Various ATJ-S Billets, ATJ Weak/Strong Data, and NS-4 Data Showing Least Squares Fit, 95% Probability Limits, and Weak and Disparate Specimens, With Grain at 70°F . . . . .	108
10	Composite Curve for Tensile Strength versus Section Bulk Density for Various ATJ-S Billets, ATJ Weak/Strong Data, and NS-4 Data Showing Least Squares Fit, 95% Probability Limits, and Weak and Disparate Specimens, With Grain at 70°F . . . . .	109
11	Composite Curve for Tensile Strength versus Closed Porosity for Various ATJ-S Billets, ATJ Data, and NS-4 Data Showing Least Squares Fit, 95% Probability Limits, and Weak and Disparate Specimens, With Grain at 70°F . . .	110

# LIST OF ILLUSTRATIONS - Continued

Figure		Page
12	Composite Curve for Tensile Strength versus Velocity for Various ATJ-S Billets and NS-4 Data Showing Least Squares Fit, 95% Probability Limits, and Weak and Disparate Specimens, With Grain at 70°F . . . . .	111
13	Composite Curve for Tensile Strength versus Gage Electrical Resistivity for the Various ATJ-S Billets Showing Least Squares Fit, 95% Probability Limits, and Weak and Disparate Specimens With Grain at 70°F . . . . .	112
14	Composite Curve for Gage Electrical Resistivity versus Open Porosity for Various ATJ-S Billets Showing Least Squares Fit, 95% Probability Limits, and Weak and Disparate Specimens, With Grain at 70°F . . . . .	113
15	Cutting Plan for Billet L-16-7 . . . . .	114
16	Cutting Plan for Even Numbered Slabs from Billet L-16-7 . . . . .	115
17	Sketch of Slab Number 2 Showing Porous Region as Determined by Avco, ATJ-S Billet L-16-7 . . . . .	116
18	Sketch of Slab Number 4 Showing Porous Region as Determined by Avco, ATJ-S Billet L-16-7 . . . . .	117
19	Sketch of Slab Number 6 Showing Porous Region as Determined by Avco, ATJ-S Billet L-16-7 . . . . .	118
20	Sketch of Slab Number 8 Showing Porous Region as Determined by Avco, ATJ-S Billet L-16-7 . . . . .	119
21	Sketch of Slab Number 10 Showing Porous Region as Determined by Avco, ATJ-S Billet L-16-7 . . . . .	120

# LIST OF ILLUSTRATIONS - Continued

Figure		Page
22	Original Avco Cutting Plan for Slab Number 2 Showing Radiometric Density, ATJ-S Billet L-16-7 . . . . .	121
23	Original Avco Cutting Plan for Slab Number 4 Showing Radiometric Density, ATJ-S Billet L-16-7 . . . . .	122
24	Original Avco Cutting Plan for Slab Number 6 Showing Radiometric Density, ATJ-S Billet L-16-7 . . . . .	123
25	Original Avco Cutting Plan for Slab Number 8 Showing Radiometric Density, ATJ-S Billet L-16-7 . . . . .	124
26	Original Avco Cutting Plan for Slab Number 10 Showing Radiometric Density, ATJ-S Billet L-16-7 . . . . .	125
27	Avco Ultrasonic Flaw Detection, Slab Number 2, ATJ-S Billet L-16-7 . . . . .	126
28	Avco Ultrasonic Flaw Detection, Slab Number 4, ATJ-S Billet L-16-7 . . . . .	127
29	Avco Ultrasonic Flaw Detection, Slab Number 6, ATJ-S Billet L-16-7 . . . . .	128
30	Avco Ultrasonic Flaw Detection, Slab Number 8, ATJ-S Billet L-16-7 . . . . .	129
31	Avco Ultrasonic Flaw Detection, Slab Number 10, ATJ-S Billet L-16-7 . . . . .	130

# LIST OF ILLUSTRATIONS - Continued

Figure		Page
32	Cutting Plan Showing Results of Avco Ultrasonic Inspection of Specimen Blanks for Slab Number 2, ATJ-S Billet L-16-7 . . . . .	131
33	Cutting Plan Showing Results of Avco Ultrasonic Inspection of Specimen Blanks for Slab Number 4, ATJ-S Billet L-16-7 . . . . .	132
34	Cutting Plan Showing Results of Avco Ultrasonic Inspection of Specimen Blanks for Slab Number 6, ATJ-S Billet L-16-7 . . . . .	133
35	Cutting Plan Showing Results of Avco Ultrasonic Inspection of Specimen Blanks for Slab Number 8, ATJ-S Billet L-16-7 . . . . .	134
36	Cutting Plan Showing Results of Avco Ultrasonic Inspection of Specimen Blanks for Slab Number 10, ATJ-S Billet L-16-7 . . . . .	135
37	Tensile Test Specimen Blank Configuration Used for ATJ-S Billet L-16-7 . . . . .	136
38	Tensile Test Specimen Configuration Used for ATJ-S Billet L-16-7 . . . . .	137
39	Tensile Stress-Strain Curve Envelope for ATJ-S Billet L-16-7 With Grain at 70° F . . . . .	138
40	Average Blank Ultrasonic Velocity, Blank Density, and Tensile Strength versus Slab Position for ATJ-S Billet L-16-7 . . . . .	139
41	Tensile Strength versus Section Bulk Density for ATJ-S Billet L-16-7 . . . . .	140
42	Tensile Strength versus Percent Absorption for ATJ-S Billet L-16-7 With Grain at 70° F . . . . .	141

# LIST OF ILLUSTRATIONS - Continued

Figure		Page
43	Tensile Strength versus Total Porosity for ATJ-S Billet L-16-7 (including L-7-1 Scrap), With Grain at 70°F . . . . .	142
44	Tensile Strength versus Open Porosity for ATJ-S Graphite Billet L-16-7 (including L-7-1 Scrap), With Grain at 70°F . . . . .	143
45	Tensile Strength versus Percent Open Porosity for ATJ-S Billet L-16-7, With Grain at 70°F . . . . .	144
46	Tensile Strength versus Section Ultrasonic Velocity for ATJ-S Billet L-16-7, With Grain at 70°F . . . . .	145
47	Tensile Strength versus Gage Section Electrical Resistivity for ATJ-S Billet L-16-7 With Grain at 70°F . . . . .	146
48	Pulse-Echo Smear on Disparates S6-5 and S8-6, ATJ-S Billet L-16-7 . . . . .	147
49	Radiograph of Short End of Specimen Having Highest Open Porosity (S2-2 at 14.7%) of ATJ-S Billet L-16-7 . . . . .	148
50	Avco Sectioning of Billets L-1-4 and L-1-8 and Specimen Designations . . . . .	149
51	Tensile Test Specimen Configuration Used on ATJ-S Billet L-1-4 . . . . .	150
52	Photograph of Void Found in Disparate A12W during Machining, ATJ-S Billet L-1-4 . . . . .	151
53	Tensile Stress-Strain Curve Envelope for ATJ-S Billet L-1-4, With Grain at 70°F . . . . .	152

# LIST OF ILLUSTRATIONS - Continued

Figure		Page
54	Tensile Stress-Strain Curve Envelope for ATJ-S Billet L-1-4 With Grain at 70°F . . . . .	153
55	Tensile Strength versus Section Bulk Density for ATJ-S Billet L-1-4 With Grain at 70°F . . . . .	154
56	Tensile Strength versus Percent Absorption for ATJ-S Billet L-1-4 With Grain at 70°F . . . . .	155
57	Tensile Strength versus Percent Total Porosity for ATJ-S Billet L-1-4 With Grain at 70°F . . . . .	156
58	Tensile Strength versus Percent Open Porosity for ATJ-S Billet L-1-4 With Grain at 70°F . . . . .	157
59	Tensile Strength versus Percent Closed Porosity for ATJ-S Billet L-1-4 With Grain at 70°F . . . . .	158
60	Tensile Strength versus Section Ultrasonic Velocity for ATJ-S Billet L-1-4 With Grain at 70°F . . . . .	159
61	Tensile Strength versus Section Bulk Density for ATJ-S Billet L-1-4 With Grain at 70°F . . . . .	160
62	Tensile Strength versus Section Bulk Density for ATJ-S Billet L-1-4 Across Grain at 70°F . . . . .	161
63	Tensile Strength versus Percent Absorption for ATJ-S Billet L-1-4 Across Grain at 70°F . . . . .	162
64	Tensile Strength versus Percent Total Porosity for ATJ-S Billet L-1-4 Across Grain at 70°F . . . . .	163

# LIST OF ILLUSTRATIONS - Continued

Figure		Page
65	Tensile Strength versus Percent Open Porosity for ATJ-S Billet L-1-4 Across Grain at 70°F . . . . .	164
66	Tensile Strength versus Percent Closed Porosity for ATJ-S Billet L-1-4 Across Grain at 70°F . . . . .	165
67	Tensile Strength versus Section Ultrasonic Velocity for ATJ-S Billet L-1-4 Across Grain at 70°F . . . . .	166
68	Tensile Strength versus Gage Electrical Resistivity for ATJ-S Billet L-1-4 Across Grain at 70°F . . . . .	167
69	Pulse-Echo Smears on Weak Specimens A12W and B14A from ATJ-S Billet L-1-4 . . . . .	168
70	Radiograph of Typical Material from ATJ-S Billet L-1-4 (Gage Section of Specimen A24W) . . . . .	169
71	Tensile Test Specimen Configuration Used for ATJ-S Billet L-1-8 . . . . .	170
72	Tensile Stress-Strain Curve Envelope for ATJ-S Billet L-1-8 With Grain at 70°F . . . . .	171
73	Tensile Stress-Strain Curve Envelope for ATJ-S Billet L-1-8 Across Grain at 70°F . . . . .	172
74	Tensile Strength versus Section Bulk Density for ATJ-S Billet L-1-8 With Grain at 70°F . . . . .	173
75	Tensile Strength versus Percent Absorption for ATJ-S Billet L-1-8 With Grain at 70°F . . . . .	174
76	Tensile Strength versus Percent Total Porosity for ATJ-S Billet L-1-8 With Grain at 70°F . . . . .	175

# LIST OF ILLUSTRATIONS - Continued

Figure		Page
77	Tensile Strength versus Percent Open Porosity for ATJ-S Billet L-1-8 With Grain at 70°F . . . . .	176
78	Tensile Strength versus Percent Closed Porosity for ATJ-S Billet L-1-8 With Grain at 70°F . . . . .	177
79	Tensile Strength versus Section Ultrasonic Velocity for ATJ-S Billet L-1-8 With Grain at 70°F . . . . .	178
80	Tensile Strength versus Gage Electrical Resistivity for ATJ-S Billet L-1-8 With Grain at 70°F . . . . .	179
81	Tensile Strength versus Section Bulk Density for ATJ-S Billet L-1-8 Across Grain at 70°F . . . . .	180
82	Tensile Strength versus Percent Absorption for ATJ-S Billet L-1-8 Across Grain at 70°F . . . . .	181
83	Tensile Strength versus Percent Total Porosity for ATJ-S Billet L-1-8 Across Grain at 70°F . . . . .	182
84	Tensile Strength versus Percent Open Porosity for ATJ-S Billet L-1-8 Across Grain at 70°F . . . . .	183
85	Tensile Strength versus Percent Closed Porosity for ATJ-S Billet L-1-8 Across Grain at 70°F . . . . .	184
86	Tensile Strength versus Section Ultrasonic Velocity for ATJ-S Billet L-1-8 Across Grain at 70°F . . . . .	185
87	Tensile Strength versus Blank Electrical Resistivity for ATJ-S Billet L-1-8 Across Grain at 70°F . . . . .	186
88	Pulse-Echo Smears on Weak Specimens A18W, A30W, and A32W from ATJ-S Billet L-1-8 . . . . .	187
89	Radiograph of Weak Specimens A18W, A30W, and A32W of ATJ-S Billet L-1-8 . . . . .	188



# LIST OF ILLUSTRATIONS - Continued

Figure		Page
90	Pulse-Echo Smears on Selected Weak Specimens A5W and A10W from ATJ-S Billet L-1-8 . . . . .	189
91	Pulse-Echo Smears on Selected Weak Specimens A11W and A14W from ATJ-S Billet L-1-8 . . . . .	190
92	Pulse-Echo Smears on Selected Weak Specimens A21W and A28W from ATJ-S Billet L-1-8 . . . . .	191
93	Pulse-Echo Smears on Selected Weak Specimens A29W and B27W from ATJ-S Billet L-1-8 . . . . .	192
94	Pulse-Echo Smears on Selected Weak Specimens B36W and B38W from ATJ-S Billet L-1-8 . . . . .	193
95	Pulse-Echo Smears on Selected Weak Specimen B43W from ATJ-S Billet L-1-8 . . . . .	194
96	Slab Cutting Plan for ATJ-S Billet L-4-6 . . . . .	195
97	Tensile Specimen Cutting Plan for ATJ-S Billet L-4-6 . . .	196
98	Specimen Blank Layout for Slab 1 of ATJ-S Billet L-4-6 . .	197
99	Specimen Blank Layout for Slab 2 of ATJ-S Billet L-4-6 . .	198
100	Specimen Blank Layout for Slab 3 of ATJ-S Billet L-4-6 . .	199
101	Specimen Blank Layout for Slab 4 of ATJ-S Billet L-4-6 . .	200
102	Specimen Blank Layout for Slab 5 of ATJ-S Billet L-4-6 . .	201

# LIST OF ILLUSTRATIONS - Continued

Figure		Page
103	Specimen Blank Layout for Slab 6 of ATJ-S Billet L-4-6 . .	202
104	Specimen Blank Layout for Slab 7 of ATJ-S Billet L-4-6 . .	203
105	Specimen Blank Layout for Slab 8 of ATJ-S Billet L-4-6 . .	204
106	Tensile Test Specimen Configuration Used for Round Robin on ATJ-S Billet L-4-6 . . . . .	205
107	Tensile Stress-Strain Curve Envelope for 70°F Evaluations (Slabs 4 and 8) from ATJ-S Billet L-4-6 . . . . .	206
108	Tensile Strength versus Section Bulk Density ( $\frac{1}{4}$ -inch Fracture Section) for ATJ-S Billet L-4-6 With Grain at 70°F and 3000°F . . . . .	207
109	Tensile Strength versus Percent Absorption ( $\frac{1}{4}$ -inch Fracture Section) for ATJ-S Billet L-4-6 With Grain at 70°F and 3000°F . . . . .	208
110	Specimen Position versus Section Bulk Density, Open Porosity, Total Porosity, and 0.02 Percent Offset Tensile Strength for Slab 4 of ATJ-S Billet L-4-6 With Grain at 70°F . . . . .	209
111	Specimen Position versus Blank Ultrasonic Velocity, Blank Density, and Tensile Strength for Slab 4 of ATJ-S Billet L-4-6 With Grain at 70°F . . . . .	210
112	Specimen Position versus Section Bulk Density, Open Porosity, Total Porosity, and 0.02 Percent Offset Tensile Strength for Slab 8 of ATJ-S Billet L-4-6 With Grain at 70°F . . . . .	211

# LIST OF ILLUSTRATIONS - Continued

Figure		Page
113	Specimen Position versus Blank Ultrasonic Velocity, Blank Density, and Tensile Strength of Slab 8 of ATJ-S Billet L-4-6 With Grain at 70°F . . . . .	212
114	Tensile Strength versus Blank Ultrasonic Velocity From ATJ-S Billet L-4-6 With Grain at 70°F and 3000°F . . . . .	213
115	Radiograph of Weak Specimen T91 W of ATJ-S Billet L-4-6 . . . . .	214
116	Slab Cutting Plan for ATJ-S Billet L-6-3 . . . . .	215
117	Cutting Plan for Slab 1 of Billet ATJ-S L-6-3 . . . . .	216
118	Cutting Plan for Slab 2 of ATJ-S Billet L-6-3 . . . . .	217
119	Tensile Test Specimen Configuration Used for ATJ-S Billet L-6-3 . . . . .	218
120	Tensile Stress-Strain Curves for ATJ-S Billet L-6-3 With Grain at 70°F . . . . .	219
121	Tensile Stress-Strain Curves for ATJ-S Billet L-6-3 With Grain at 3000°F . . . . .	220
122	Tensile Stress-Strain Curves for ATJ-S Billet L-6-3 With Grain at 4500°F . . . . .	221
123	Tensile Stress-Strain Curves for ATJ-S Billet L-6-3 With Grain at 5500°F . . . . .	222
124	Tensile Stress-Strain Curves for ATJ-S Billet L-6-3 Across Grain at 70°F . . . . .	223

# LIST OF ILLUSTRATIONS - Continued

Figure		Page
125	Tensile Stress-Strain Curves for ATJ-S Billet L-6-3 Across Grain at 3000°F . . . . .	224
126	Tensile Stress-Strain Curves for ATJ-S Billet L-6-3 Across Grain at 4500°F . . . . .	225
127	Tensile Stress-Strain Curves for ATJ-S Billet L-6-3 Across Grain at 5500°F . . . . .	226
128	Tensile Strength versus Section Bulk Density for ATJ-S Billet L-6-3 With Grain at 70°F, 3000°F, and 4500°F . . . . .	227
129	Tensile Strength versus Percent Absorption for ATJ-S Billet L-6-3 With Grain at 70°F, 3000°F, and 4500°F . . . . .	228
130	Tensile Strength versus Percent Total Porosity for ATJ-S Billet L-6-3 With Grain at 70°F, 3000°F, and 4500°F . . . . .	229
131	Tensile Strength versus Percent Open Porosity for ATJ-S Billet L-6-3 With Grain at 70°F, 3000°F, and 4500°F . . . . .	230
132	Tensile Strength versus Closed Porosity for ATJ-S Billet L-6-3 With Grain at 70°F, 3000°F, and 4500°F . . . . .	231
133	Tensile Strength versus Section Ultrasonic Velocity for ATJ-S Billet L-6-3 With Grain at 70°F, 3000°F, and 4500°F . . . . .	232
134	Tensile Strength versus Section Bulk Density for ATJ-S Billet L-6-3 Across Grain at 70°F, 3000°F, and 4500°F . . . . .	233

# LIST OF ILLUSTRATIONS - Continued

Figure		Page
135	Tensile Strength versus Percent Absorption for ATJ-S Billet L-6-3 Across Grain at 70°F, 300°F, and 4500°F . . . . .	234
136	Tensile Strength versus Percent Total Porosity for ATJ-S Billet L-6-3 Across Grain at 70°F, 3000°F, and 4500°F . . . . .	235
137	Tensile Strength versus Percent Open Porosity for ATJ-S Billet L-6-3 Across Grain at 70°F, 3000°F, and 4500°F . . . . .	236
138	Tensile Strength versus Percent Closed Porosity for ATJ-S Billet L-6-3 Across Grain at 70°F, 3000°F, and 4500°F . . . . .	237
139	Tensile Strength versus Section Ultrasonic Velocity for ATJ-S Billet L-6-3 Across Grain at 70°F, 3000°F, and 4500°F . . . . .	238
140	Slab Cutting Plan for ATJ-S Billets L-9-10, L-10-6, and L-11-4 . . . . .	239
141	Cutting Plan for Slab 1 of ATJ-S Billets L-9-10, L-10-6, and L-11-4 . . . . .	240
142	Tensile Test Specimen Configuration Used for ATJ-S Billets L-9-10, L-10-6, and L-11-4 . . . . .	241
143	Tensile Stress-Strain Curves for ATJ-S Billet L-9-10 With Grain at 70°F . . . . .	242
144	Tensile Stress-Strain Curves for ATJ-S Billet L-9-10 With Grain at 4500°F . . . . .	243

# LIST OF ILLUSTRATIONS - Continued

Figure		Page
145	Tensile Stress-Strain Curves for ATJ-S Billet L-9-10 Across Grain at 70°F . . . . .	244
146	Tensile Stress-Strain Curves for ATJ-S Billet L-9-10 Across Grain at 4500°F . . . . .	245
147	Tensile Strength versus Section Bulk Density for ATJ-S Billet L-9-10 With Grain at 70°F and 4500°F	246
148	Tensile Strength versus Percent Absorption for ATJ-S Billet L-9-10 With Grain at 70°F and 4500°F	247
149	Tensile Strength versus Percent Total Porosity for ATJ-S Billet L-9-10 With Grain at 70°F and 4500°F	248
150	Tensile Strength versus Percent Open Porosity for ATJ-S Billet L-9-10 With Grain at 70°F and 4500°F	249
151	Tensile Strength versus Percent Closed Porosity for ATJ-S Billet L-9-10 With Grain at 70°F and 4500°F	250
152	Tensile Strength versus Ultrasonic Velocity for ATJ-S Billet L-9-10 With Grain at 70°F and 4500°F	251
153	Tensile Strength versus Section Bulk Density for ATJ-S Billet L-9-10 Across Grain at 70°F and 4500°F . . . . .	252
154	Tensile Strength versus Percent Absorption for ATJ-S Billet L-9-10 Across Grain at 70°F and 4500°F . . . . .	253
155	Tensile Strength versus Percent Total Porosity for ATJ-S Billet L-9-10 Across Grain at 70°F and 4500°F . . . . .	254

# LIST OF ILLUSTRATIONS - Continued

Figure		Page
156	Tensile Strength versus Percent Open Porosity for ATJ-S Billet L-9-10 Across Grain at 70°F and 4500°F . . . . .	255
157	Tensile Strength versus Percent Closed Porosity for ATJ-S Billet L-9-10 Across Grain at 70°F and 4500°F . . . . .	256
158	Tensile Strength versus Section Ultrasonic Velocity for ATJ-S Billet L-9-10 Across Grain at 70°F and 4500°F . . . . .	257
159	Tensile Stress-Strain Curves for ATJ-S Billet L-10-6 With Grain at 70°F . . . . .	258
160	Tensile Stress-Strain Curves for ATJ-S Billet L-10-6 With Grain at 4500°F . . . . .	259
161	Tensile Stress-Strain Curves for ATJ-S Billet L-10-6 Across Grain at 4500°F . . . . .	260
162	Tensile Stress-Strain Curves for ATJ-S Billet L-10-6 Across Grain at 4500°F . . . . .	261
163	Tensile Strength versus Section Bulk Density for ATJ-S Billet L-10-6 With Grain at 70°F and 4500°F	262
164	Tensile Strength versus Percent Absorption for ATJ-S Billet L-10-6 With Grain at 70°F and 4500°F	263
165	Tensile Strength versus Percent Total Porosity for ATJ-S Billet L-10-6 With Grain at 70°F and 4500°F	264
166	Tensile Strength versus Percent Open Porosity for ATJ-S Billet L-10-6 With Grain at 70°F and 4500°F	265

# LIST OF ILLUSTRATIONS - Continued

Figure		Page
167	Tensile Strength versus Percent Closed Porosity for ATJ-S Billet L-10-6 With Grain at 70°F and 4500°F . . . . .	266
168	Tensile Strength versus Section Ultrasonic Velocity for ATJ-S Billet L-10-6 With Grain at 70°F and 4500°F . . . . .	267
169	Tensile Strength versus Section Bulk Density for ATJ-S Billet L-10-6 Across Grain at 70°F and 4500°F . . . . .	268
170	Tensile Strength versus Percent Absorption for ATJ-S Billet L-10-6 Across Grain at 70°F and 4500°F . . . . .	269
171	Tensile Strength versus Percent Total Porosity for ATJ-S Billet L-10-6 Across Grain at 70°F and 4500°F . . . . .	270
172	Tensile Strength versus Percent Open Porosity for ATJ-S Billet L-10-6 Across Grain at 70°F and 4500°F . . . . .	271
173	Tensile Strength versus Percent Closed Porosity for ATJ-S Billet L-10-6 Across Grain at 70°F and 4500°F . . . . .	272
174	Tensile Strength versus Section Ultrasonic Velocity for ATJ-S Billet L-10-6 Across Grain at 70°F and 4500°F . . . . .	273
175	Tensile Stress-Strain Curves for ATJ-S Billet L-11-4 With Grain at 70°F . . . . .	274
176	Tensile Stress-Strain Curves for ATJ-S Billet L-11-4 With Grain at 4500°F . . . . .	275



# LIST OF ILLUSTRATIONS - Continued

Figure		Page
177	Tensile Stress-Strain Curves for ATJ-S Billet L-11-4 Across Grain at 70°F . . . . .	276
178	Tensile Stress-Strain Curves for ATJ-S Billet L-11-4 Across Grain at 4500°F . . . . .	277
179	Tensile Strength versus Section Bulk Density for ATJ-S Billet L-11-4 With Grain at 70°F and 4500°F	278
180	Tensile Strength versus Percent Absorption for ATJ-S Billet L-11-4 With Grain at 70°F and 4500°F	279
181	Tensile Strength versus Percent Total Porosity for ATJ-S Billet L-11-4 With Grain at 70°F and 4500°F . . . . .	280
182	Tensile Strength versus Percent Open Porosity for ATJ-S Billet L-11-4 With Grain at 70°F and 4500°F	281
183	Tensile Strength versus Percent Closed Porosity for ATJ-S Billet L-11-4 With Grain at 70°F and 4500°F	282
184	Tensile Strength versus Section Ultrasonic Velocity for ATJ-S Billet L-11-4 With Grain at 70°F and 4500°F	283
185	Tensile Strength versus Section Bulk Density for ATJ-S Billet L-11-4 Across Grain at 70°F and 4500°F	284
186	Tensile Strength versus Percent Absorption for ATJ-S Billet L-11-4 Across Grain at 70°F and 4500°F . .	285
187	Tensile Strength versus Percent Total Porosity for ATJ-S Billet L-11-4 Across Grain at 70°F and 4500°F	286
188	Tensile Strength versus Percent Open Porosity for ATJ-S Billet L-11-4 Across Grain at 70°F and 4500°F	287

# LIST OF ILLUSTRATIONS - Continued

Figure		Page
189	Tensile Strength versus Percent Closed Porosity for ATJ-S Billet L-11-4 Across Grain at 70°F and 4500°F . . . . .	288
190	Tensile Strength versus Section Ultrasonic Velocity for ATJ-S Billet L-11-4 Across Grain at 70°F and 4500°F . . . . .	289
191	Tensile Strength versus Total Strain to Fracture for ATJ-S Billet L-16-7 and NS-4 Data With Grain at 70°F . . .	290
192	Tensile Stress-Strain Curve for Strain Disparate S10-4 from ATJ-S Billet L-16-7 Evaluated in the With Grain Direction at 70°F . . . . .	291
193	Tensile Stress-Strain Curve for Strain Disparate S6-3 from ATJ-S Billet L-16-7 Evaluated in the With Grain Direction at 70°F . . . . .	292
194	Tensile Strength versus Initial Elastic Modulus for ATJ-S Billet L-16-7 and NS-4 Data With Grain at 70°F . . .	293
195	Tensile Strength versus Density (Blank and Section) for ATJ-S Billet L-16-7 With Grain at 70°F . . . . .	294
196	Developed Relations for Tensile Strength versus Percent Open Porosity for ATJ-S Billet L-16-7 With Grain at 70°F . . . . .	295
197	Total Axial Strain to Fracture versus Percent Open Porosity for ATJ-S Billet L-16-7 With Grain at 70°F . . .	296
198	Initial Elastic Modulus in Tension versus Percent Open Porosity for ATJ-S Billet L-16-7 Including NS-4 Data With Grain at 70°F . . . . .	297

# LIST OF ILLUSTRATIONS - Continued

Figure		Page
199	Typical Photograph of Pulse-Echo Display from Opposing Ends of Tensile Blank Specimen for ATJ-S Billet L-16-7 --Alcohol Coupler . . . . .	298
200	Pulse-Echo Signal Enhancement Technique Using Aligned End Signals from Opposing Ends of Tensile Blank -- Alcohol Coupler . . . . .	299
201	Pulse-Echo Signal Enhancement Technique Using Shift in Time Base to Improve Signal-to-Noise Ratio from Opposing Ends of Tensile Blank--Alcohol Coupler . . . . .	300
202	Flick Inspection Results and 10X Black and White Photographs of Fracture Faces of Disparate S8-6, ATJ-S Billet L-16-7 . . . . .	301
203	Flick Inspection Results and 10X Black and White Photographs of Fracture Faces of Disparate S6-5, ATJ-S Billet L-16-7 . . . . .	302
204	Flick Inspection Results and 10X Black and White Photographs of Fracture Faces of Disparate S2-3, ATJ-S Billet L-16-7 . . . . .	303
205	28X Photograph of Cavity Observed after Initial Filing of Fracture Face of Disparate S6-5, ATJ-S Billet L-16-7 . . . . .	304
206	100X Photomicrograph of Cross Section of Disparate S6-5, 21 mils below Fracture Face, No Impregnation, ATJ-S Billet L-16-7 . . . . .	305
207	100X Photomicrograph of Cross Section of Disparate S6-5, 36 mils below Fracture Face, Epoxy Impregnated, ATJ-S Billet L-16-7 . . . . .	306

# LIST OF ILLUSTRATIONS - Continued

Figure		Page
208	100X Photomicrograph of Cross Section of Average ATJ-S (Specimen S8-4), No Impregnation, ATJ-S Billet L-16-7 . . . . .	307
209	100X Photomicrograph from Strong ATJ-S Billet Evaluated at Southern, No Impregnation . . . . .	308
210	Flick Inspection Results and 10X Black and White Photographs of Fracture Faces of Highest Open Porosity Specimen S2-2, ATJ-S Billet L-16-7 . . . . .	309
211	100X Photomicrograph of Cross Section from Highest Open Porosity Specimen S2-2, 15 mils below Fracture Face, No Impregnation, ATJ-S Billet L-16-7 . . . . .	310
212	100X Photomicrograph of Cross Section from Highest Open Porosity Specimen S2-2, 30 mils below Fracture Face, Epoxy Impregnated, ATJ-S Billet L-16-7 . . . . .	311
213	Strength versus Percent Open Porosity Showing Mean and 1 and 2 Standard Deviations of Strength for Multiple Lumped L-16-7 Data . . . . .	312
214	Design Allowable Strength versus Truncating Density for ATJ-S Billet L-16-7 . . . . .	313
215	Section Ultrasonic Velocity versus Percent Open Porosity for ATJ-S Billet L-16-7 . . . . .	314
216	Tensile Strength versus Avco $K\rho V^2$ and Southern $k\rho V^2$ for ATJ-S Billet L-16-7 . . . . .	315
217	Specimens 7-1-1 and 7-1-2 Correlation with Tensile Strength-Open Porosity Relation Developed for ATJ-S Billet L-16-7 With Grain at 70°F . . . . .	316

# LIST OF ILLUSTRATIONS - Continued

Figure		Page
218	Correlation of Specimen 7-1-1 and 7-1-2 with Ultrasonic Velocity-Open Porosity Relation of ATJ-S Billet L-16-7 . . . . .	317
219	Tensile Strength versus Total Strain to Fracture for ATJ-S Billet L-1-4 and NS-4 Data With Grain at 70°F . . . . .	318
220	Tensile Strength versus Density (Blank and Section) for ATJ-S Billet L-1-4 With Grain at 70°F . . . . .	319
221	Tensile Strain to Fracture versus Percent Open Porosity for ATJ-S Billet L-1-4 With Grain at 70°F . . . . .	320
222	Tensile Stress-Strain Curve for Specimen A10W from ATJ-S Billet L-1-4 With Grain at 70°F . . . . .	321
223	Tensile Stress-Strain Curve for Disparate Specimen A12W from ATJ-S Billet L-1-4 With Grain at 70°F . . . . .	322
224	Regression Analysis Results for Tensile Strength versus Percent Open Porosity for ATJ-S Billet L-1-4 With Grain at 70°F . . . . .	323
225	Flick Inspection Results and 10X Black and White Photographs of Fracture Faces of Disparate Specimen A12W from ATJ-S Billet L-1-4 . . . . .	324
226	Flick Inspection Results and 10X Black and White Photographs of Fracture Faces of Specimen A10W from ATJ-S Billet L-1-4 . . . . .	325
227	Section Ultrasonic Velocity versus Percent Open Porosity for ATJ-S Billet L-1-4 With Grain at 70°F . . . . .	326
228	Tensile Strength versus Total Strain to Fracture for ATJ-S Billet L-1-4 and NS-4 Data Across Grain at 70°F . . . . .	327

# LIST OF ILLUSTRATIONS - Continued

Figure		Page
229	Relation between Tensile Strength and Section Bulk Density for ATJ-S Billet L-1-4 Across Grain at 70°F . . . . .	328
230	Relation between Tensile Strength and Percent Open Porosity for ATJ-S Billet L-1-4 Across Grain at 70°F . . . . .	329
231	Flick Inspection Results and 10X Black and White Photographs of Fracture Faces of Specimen B14A from ATJ-S Billet L-1-4 . . . . .	330
232	Section Ultrasonic Velocity versus Percent Open Porosity for ATJ-S Billet L-1-4 Across Grain . . .	331
233	Tensile Strength versus Total Strain to Fracture for ATJ-S Billet L-1-8 With Grain at 70°F . . . . .	332
234	Relation between Tensile Strength and Blank Bulk Density for ATJ-S Billet L-1-8 With Grain at 70°F. .	333
235	Relation between Tensile Strength and Section Bulk Density for ATJ-S Billet L-1-8 With Grain at 70°F	334
236	Relation between Tensile Strength and Section Ultrasonic Velocity for A Specimens from ATJ-S Billet L-1-8 With Grain at 70°F . . . . .	335
237	Relation between Tensile Strength and Section Ultrasonic Velocity for B Specimens from ATJ-S Billet L-1-8 With Grain at 70°F . . . . .	336
238	Relation between Tensile Strength and Gage Electrical Resistivity for A Specimens from ATJ-S Billet L-1-8 With Grain at 70°F . . . . .	337
239	Relation between Tensile Strength and Gage Electrical Resistivity for B Specimens from ATJ-S Billet L-1-8 With Grain at 70°F . . . . .	338

# LIST OF ILLUSTRATIONS - Continued

Figure		Page
240	Relation between Tensile Strength and Percent Closed Porosity for ATJ-S Billet L-1-8 With Grain at 70°F . .	339
241	Regression Analysis Results for Tensile Strength versus Percent Open Porosity for ATJ-S Billet L-1-8 With Grain at 70°F . . . . .	340
242	Total Tensile Strain to Fracture versus Percent Open Porosity for ATJ-S Billet L-1-8 With Grain at 70°F . . . . .	341
243	Tensile Stress-Strain Curve for Specimen A20W from ATJ-S Billet L-1-8 With Grain at 70°F . . . . .	342
244	Flick Inspection Results and 10X Black and White Photographs of Fracture Faces of Disparate Specimen A30W from ATJ-S Billet L-1-8 . . . . .	343
245	Flick Inspection Results and 10X Black and White Photographs of Fracture Faces of Weak Specimen A18W from ATJ-S Billet L-1-8 . . . . .	344
246	Flick Inspection Results and 10X Black and White Photographs of Fracture Faces of Specimen A32W from ATJ-S Billet L-1-8 . . . . .	345
247	100X Photomicrograph of Cross Section from Weak Specimen A18W about 10 mils below Fracture Face, No Impregnation, ATJ-S Billet L-1-8 . . . . .	346
248	Comparison of Open Porosity by Absorption to Porosity by Other Methods . . . . .	347
249	Relation between Section Ultrasonic Velocity and Percent Open Porosity for ATJ-S Billet L-1-8 With Grain at 70°F . . . . .	348

# LIST OF ILLUSTRATIONS --Continued

Figure		Page
250	Tensile Strength versus Total Strain to Fracture for ATJ-S Billet L-1-8 Across Grain at 70°F . . . . .	349
251	Tensile Strength versus Blank Bulk Density for A and B Specimens from ATJ-S Billet L-1-8 Across Grain at 70°F . . . . .	350
252	Relation between Tensile Strength and Section Bulk Density for ATJ-S Billet L-1-8 Across Grain at 70°F . . . . .	351
253	Relation between Tensile Strength and Percent Total Porosity for ATJ-S Billet L-1-8 Across Grain at 70°F . . . . .	352
254	Relation between Tensile Strength and Percent Closed Porosity for ATJ-S Billet L-1-8 Across Grain at 70°F . . . . .	353
255	Relation between Tensile Strength and Percent Open Porosity for ATJ-S Billet L-1-8 Across Grain at 70°F . . . . .	354
256	Relation between Section Ultrasonic Velocity and Percent Open Porosity for ATJ-S Billet L-1-8 Across Grain at 70°F . . . . .	355
257	Tensile Strength versus Total Strain to Fracture for ATJ-S Billet L-4-6 With Grain at 70°F . . . . .	356
258	Tensile Strength versus Total Strain to Fracture for ATJ-S Billet L-4-6 With Grain at 3000°F . . . . .	357
259	Properties versus Specimen Location in Billet, Slab 2 of ATJ-S Billet L-4-6 With Grain at 3000°F . . . . .	358
260	Properties versus Specimen Location in Billet, Slab 4 of ATJ-S Billet L-4-6 With Grain at 70°F . . . . .	359
261	Properties versus Specimen Location in Billet, Slab 6 of ATJ-S Billet L-4-6 With Grain at 3000°F . . . . .	360



# LIST OF ILLUSTRATIONS - Continued

Figure		Page
262	Properties versus Specimen Location in Billet, Slab 8 of ATJ-S Billet L-4-6 With Grain at 70°F . . .	361
263	Properties versus Axial Position for Specimens in Billet, ATJ-S Billet L-4-6 With Grain . . . . .	362
264	Profiles of Internal Pressure while Pressing a Uniform Powder . . . . .	363
265	Relation between Blank Ultrasonic Velocity and Blank Bulk Density for ATJ-S Billet L-4-6 With Grain	364
266	Regression Analysis Results for Tensile Strength versus Percent Open Porosity for ATJ-S Billet L-4-6 With Grain at 70°F . . . . .	365
267	10X Photographs of Fracture Faces for Weak/Strong Specimens 44 and 42 from Slab 4 of ATJ-S Billet L-4-6 With Grain at 70°F . . . . .	366
268	10X Photographs of Fracture Faces for Weak/Strong Specimens 91 and 93 from Slab 8 of ATJ-S Billet L-4-6 With Grain at 70°F . . . . .	367
269	Flick Inspection Results of Fracture Faces of Weak Specimen 44 from Slab 4 of ATJ-S Billet L-4-6 . . .	368
270	Flick Inspection Results of Fracture Faces of Weak Specimen 91 from Slab 8 of ATJ-S Billet L-4-6 . . .	369
271	100X Photomicrograph of Center of Cross Section from Weak Specimen 44, No Impregnation, ATJ-S Billet L-4-6 . . . . .	370
272	100X Photomicrograph of Center of Cross Section from Weak Specimen 91 about 10 mils below Fracture Face, No Impregnation, ATJ-S Billet L-4-6 . . . . .	371

# LIST OF ILLUSTRATIONS - Continued

Figure		Page
273	Relation between Tensile Strength and Section Bulk Density for ATJ-S Billet L-9-10 With Grain at 70°F and 4500°F . . . . .	372
274	Relation between Tensile Strength and Section Ultrasonic Velocity for ATJ-S Billet L-9-10 With Grain at 70°F and 4500°F . . . . .	373
275	Regression Analysis Results for Tensile Strength versus Percent Open Porosity for ATJ-S Billet L-9-10 With Grain at 70°F and 4500°F . . . . .	374
276	10X Photographs of Fracture Faces for Disparate Specimen T5W and Weak Specimen T7W from ATJ-S Billet L-9-10 . . . . .	375
277	100X Photomicrograph of Strip Section across Diameter 10 mils below Fracture Face of Weak Specimen T7W from ATJ-S Billet L-9-10 . . . . .	376
278	Progressive Plot of Point Count on T7W from ATJ-S Billet L-9-10 . . . . .	377
279	Flick Inspection Results and 10X Black and White Photographs of Fracture Faces of Weak Specimen T1W from ATJ-S Billet L-9-10 . . . . .	378
280	Correlation between Tensile Strength and Open Porosity for Average Values of Billets and Weak Specimens Compared to Regression of ATJ-S Billet L-16-7 . . . . .	379
281	Correlation of Average Values of Section Ultrasonic Velocity and Percent Open Porosity for Various ATJ-S Billets with Data Fit for ATJ-S Billet L-16-7 . . . . .	380
282	Comparison of Average Tensile Strength and Density for Various ATJ-S Billets with L-16-7 Regression . . . . .	381

## LIST OF ILLUSTRATIONS - Continued

Figure		Page
283	Comparison of Average Tensile Strength and Velocity of Various ATJ-S Billets with Predicted L-16-7 Relation . . .	382
284	Composite Comparison of Open Porosity by Absorption to Porosity by Other Methods . . . . .	383
285	Relation between Ultrasonic Velocity and Open Porosity for Various ATJ-S Billets with Respect to the Regression of ATJ-S Billet L-16-7 . . . . .	384



## LIST OF TABLES

Table		Page
1	Tensile Properties at 70°F of Even Slabs From ATJ-S Billets L-16-7 and L-7-1 . . . . .	385
2	Tensile Properties at 70°F of ATJ-S Billet L-1-4 . .	386
3	Tensile Properties at 70°F of ATJ-S Billet L-1-8 . .	387
4	Tensile Properties at 70°F and 3000°F of Slabs 2, 4, 6, and 8 From ATJ-S Billet L-4-6 . . . . .	388
5	Tensile Properties at 70°F, 3000°F, 4500°F and 5500°F of ATJ-S Billet L-6-3 . . . . .	389
6	Tensile Properties at 70°F and 4500°F of ATJ-S Billet L-9-10 . . . . .	390
7	Tensile Properties at 70°F and 4500°F of ATJ-S Billet L-10-6 . . . . .	391
8	Tensile Properties at 70°F and 4500°F of ATJ-S Billet L-11-4 . . . . .	392
9	Results of Density, Absorption, Porosity, and Section Ultrasonic Velocity Measurements for Specimens from Even Slabs of ATJ-S Billet L-16-7 and Specimens From ATJ-S Billet L-7-1 . .	393
10	Results of Density, Absorption, Porosity, and Section Ultrasonic Velocity Measurements for Specimens From ATJ-S Billet L-1-4 . . . . .	394
11	Results of Density, Absorption, Porosity, and Section Ultrasonic Velocity Measurements for Specimens From ATJ-S Billet L-1-8 . . . . .	396

# LIST OF TABLES - Continued

Table		Page
12	Results of Density, Absorption, Porosity, and Section Ultrasonic Velocity Measurements for Slabs 2, 4, 6, and 8 of ATJ-S Billet L-4-6 . . . . .	398
13	Results of Density, Absorption, Porosity, and Section Ultrasonic Velocity Measurements for ATJ-S Billet L-6-3 . . . . .	401
14	Results of Density, Absorption, Porosity, and Section Ultrasonic Velocity Measurements for ATJ-S Billet L-9-10 . . . . .	402
15	Results of Density, Absorption, Porosity, and Section Ultrasonic Velocity Measurements for ATJ-S Billet L-10-6 . . . . .	403
16	Results of Density, Absorption, Porosity, and Section Ultrasonic Velocity Measurements for ATJ-S Billet L-11-4 . . . . .	404
17	Average Values for Tensile Properties and Section Monitors for Material From Various ATJ-S Billets . . . . .	405
18	UM721 Reflectoscope Settings Used on ATJ-S Billet L-16-7 . . . . .	407
19	Property-Monitor-NDT Fact Sheet for ATJ-S Billet L-16-7 . . . . .	408
20	Results of Property-Monitor-NDT Correlations for ATJ-S Billet L-16-7 . . . . .	409
21	Design Impact From Results of Evaluations on ATJ-S Billet L-16-7 . . . . .	410

# LIST OF TABLES - Continued

Table		Page
22	Weak/Strong Summary of Multiple Specimens From Same Test Conditions for Various Monitoring Properties Material L-4-6, ATJ-S, Slabs 4 and 8 . . . . .	411
23	Properties and Monitors of Primary Interest for Tensile Specimens From ATJ-S Billet L-9-10 . . . . .	412
24	Summary of Disparate With Grain Specimens Selected From Open Porosity Relation at 95% Probability . . . . .	413
25	Summary of Weak Specimens Selected From Composite Regressions of Tensile Strength Versus Open Porosity at 95% Probability . . . .	414
26	Inspection by Point-Count Porosity . . . . .	415





# A STRENGTH ANALYSIS OF POLYGRAPHITE

## INTRODUCTION

The major thrust of this program was to enhance the understanding of polygraphites as used on Air Force hardware by combining input from Lockheed concerning design and systems, input from Avco concerning NDT, input from Southern Research Institute concerning the flaw versus strength (property) relation, input from Union Carbide concerning materials technology, and input from the Air Force concerning requirements. As a matter of fact, many of the inputs were overlapping in an attempt to better define the interfaces. For example, in our case it became necessary to develop capabilities in the nondestructive testing and evaluation of specimen blanks, specimens, and even fractured specimens. It became clear quite early that the proper definition of a flaw required the proper definition of the material at the fracture face. This led to the concept of monitors or profilers such as density, porosity, electrical resistivity, velocity, and others so that one could describe the material at the fracture zone in the specimen. Then one could relate these signals to the comparable energies used in NDT techniques. This meant that we had to apply our own NDT methods such as pulse-echo and radiography in order to relate monitors and flaws to displays generated by others.

We hope that it is clear throughout the report where Avco conducted the NDT work and where we did. In general, all data on billets are by Avco, data on blanks are by Avco and Southern, and data on specimens or fractured pieces are by Southern. Where there is conflict in NDT techniques, we consider the Avco results as predominant. We bear the responsibility for analysis and conclusions in this report.

Many of the specimens were tested for Lockheed by Southern under a different program. Through agreement with Lockheed, these specimens were NDT'd by Avco prior to testing at Southern. The program as originally planned was modified considerably. Specimens from only seven of the originally intended 23 billets were examined due to slips in schedules and other reasons. Two additional billets of ATJ-S were substituted into the program for evaluation.

In relating flaws to strength reduction, Southern established an inspection procedure for the purpose of searching for causes of weakness or strength in the tensile specimens. Although a number of techniques were used, all of the techniques were not used on all of the materials,

since it was not known at the beginning of the program which inspection techniques would be most effective. Generally, the policy was to be as thorough as time and techniques permitted. This procedure involved inspection before and after mechanical property testing.

Upon receiving NDT'd blanks from Avco, Southern began its inspection procedure. The normal steps of the inspection procedure were:

1. Visual inspection of blanks
2. Measurements of bulk density, ultrasonic velocity, and electrical resistivity on blanks
3. Pulse-echo inspection of blanks
4. Specimen blanks ground to final test configuration -- during this phase, machinists were instructed to inspect for and call attention to any flaws or anomalies encountered
5. Specimen inspected visually
6. Measurements of electrical resistivity on gage section of specimen
7. Destructive test conducted and peculiarities of test and fracture were noted

At this stage of evaluation, post-fracture inspection was started:

8. Visual inspection of fracture faces for flaws
9. Photomicrographs (10X) and flicks (10X) were taken of fracture faces of flawed and of weak/strong specimens.

At this stage, the normal procedure called for returning the fracture specimens to Avco for their post inspection. The specimens were then returned to Southern for completion of its post-fracture inspection procedure:

10. On " $\frac{1}{4}$ -inch fracture section" (fracture plus  $\frac{1}{4}$  inch axially) from long end obtain dry weight, saturated weight, and suspended weight using mineral spirits -- calculated bulk density, apparent density, percent absorption, percent total porosity (using  $2.22 \text{ gm/cm}^3$  as the true density of polygraphite), and percent open porosity.

11. Repeated on next  $\frac{1}{4}$  inch of the long end ( $\frac{1}{4}$  inch-removed section).

12. Obtained ultrasonic velocity on  $\frac{1}{4}$ -inch fracture section of short end. Note: in order to expedite inspections, frequently the fracture face (long end) plus  $\frac{1}{8}$  inch was removed, the section  $\frac{1}{8}$  to  $\frac{3}{8}$  inch behind the fracture face was removed and machined for velocity measurements. Absorption was then performed using both the fracture face plus  $\frac{1}{8}$  inch and the  $\frac{1}{4}$  inch velocity specimen. The procedure preserved the short end of the specimen for any future evaluations desired. Other inspection techniques included alcohol penetrant tests, visual inspection under ultra-violet light, attempts to record ultrasonic emission during loading, and photomicrographs (100X) with and without prior vacuum impregnation.

Then, in order to determine and characterize major strength reducers, Southern compared the results provided by Avco NDT and Southern's results from its weak/strong inspection procedure to its mechanical property tests. In the cases where the entire procedure was performed, a rather vast collection of information resulted. It was learned that different monitors were required to define the disparate variability of a material. For example, bulk density may be a good monitor of porosity and, hence, of strength reduction due to high porosity; however, a specimen may have nominal porosity but fail at a low strength value due to a disparate inclusion. The inclusion being local would not be detected from density measurements but hopefully could be found with ultrasonic pulse-echo or radiography. As a result, Southern plotted tensile strength versus the various monitors of velocity, electrical resistivity, absorption, density, open porosity, closed porosity, and inspected both for disparate behavior to profilers, as well as for behaviors that followed analytical predictions. From these inspections, weak and disparate specimens were determined and defined. Further investigations were performed on these specimens to determine the cause of their disparate behavior and for their NDT signatures.

## MATERIALS

Materials used or referenced in this program included 9 billets of ATJ-S, one billet of NS-4<sup>1</sup>, several billets of ATJ, and one of HLM. This report includes all of the data on the ATJ-S, only reference information on NS-4 since the detailed data were termed proprietary, reference information on ATJ to provide insight into the effects of material densification on strength-monitor relations, and reference information on HLM to provide comparison to another precursor.

<sup>1</sup>Not commercially available.

All of the ATJ-S billets were uncored and nominally 8-inch diameter by 14 inches long. More detailed information on these billets is available from Avco, Lockheed, and Union Carbide, in addition to the Air Force. Southern's characterization of the billets is included in the results for each billet as that was the essence of the program.

## THE DESIGN PROCESS AND MATERIAL VARIABILITY

The ultimate objective of a program of this type is to improve hardware. In order to better understand how this work fits into the design process, consider the steps required in this process.

Fundamentally the design process involves (1) a preliminary selection of shape based on aerodynamic and/or loading consideration, (2) selection of candidate materials based on size, loads, temperatures, etc., (3) a stress analysis, (4) a properties analysis of the candidate materials, (5) selection of performance criteria, (6) the design decision, and finally (7) the production, testing, and service. The solution to the design problem is often formulated in terms of the relation of physical properties to the stress analysis; usually a strength to maximum stress ratio (i. e., safety factor).

The properties analysis is concerned with thermal and mechanical properties such as thermal expansion and conductivity, and fracture strengths and strains, failure modes, volume effects, sensitivity to stress concentration, and the total variability of the material since it establishes working strength for a specified reliability.

Polygraphites have a total variability made up of several factors which can contribute to strength reduction. Total variability in graphite includes background and disparate variabilities both of which result primarily from voids, inclusions, macrocracks, or structure-nuances, either individually or aligned in lines, planes, or volumes. The premise here is that one can detect and characterize these major strength reducers and be sure that they do not exist in the hardware any more severely than in test specimens from the same billet, and if one can be sure that their effect will be similar in both cases, then one can statistically predict the hardware performance. That is to say, if one can assure that there are no serious or other unique flaws in the hardware, then the remaining variability will be the inherent variability of the material which is established by background flaws. This leads to the problem of characterizing the different types of flaws and variations, and selecting methods to detect and characterize them.

Before proceeding further, the terms mentioned above should be defined and discussed from the standpoint of description, probable sources, types of nondestructive tests that might monitor, and their influence on strength and the type of fracture obtained in specimens. Observe that they influence both reproducibility (between pieces) and uniformity (within a piece).

### Background Flaws

Background flaws establish the inherent variability and determine the base line properties for a given graphite. This inherent variability is established by voids, inclusions, and macrocracks acting in the material. Consider first the void. In most granular materials there is a rather uniform distribution of voids by virtue of the fact that melting did not occur during the process. For example, for a typical aerospace graphite such as ATJ, these typical voids are 5 to 10 mils in major axis and are rather uniformly spaced in the solid material. These voids are the void or pore background that is typical of the material and contribute to establish a background flaw system that results in an inherent variability. This means that voids that might be introduced by other than normal means of the process of making the material would not be strength reducers unless they were larger than the voids that exist in the void or pore background. Much physical insight concerning the background voids can be gained from photomicrographs.

By a similar line of reasoning, one can conclude that there is an inclusion background and a macrocrack background that are intrinsic or inherent to a given graphite made by a given process, and that these two combine with the void background to act upon the material and provide resultant properties with an inherent variability. Another way to say this is that the inherent variability in a property of a given material cannot be altered beyond some value without making changes in the process that result in a different material. That is, if one altered the inherent variability significantly by process changes, then one probably would change the base properties at the same time and should change the name of the material.

### Disparate Voids

Disparate voids are voids that are larger than those that make up the void or pore background of the particular graphite and contribute to strength reduction by virtue of stress intensification rather than area reduction. A disparate void big enough to cause area reduction is a hole

and would indicate immediate rejection of the piece rather than an effort at characterization. These disparate voids are caused by gas pockets, burn out, pitch excess, and other sources. They are detectable by pulse-echo, radiography for thin sections, surface inspection, and other methods. Remember, however, that the same void does not behave the same in all graphites. For example, a 20-mil void in a typical POCO graphite with quite small background pores of about 1 mil reduces specimen strength perhaps 25 percent below the average at about any temperature up to the initiation of plasticity at 4000°F to 4500°F. This same void size may have little influence on the strength of a more porous graphite, such as ATJ, which has a void or pore background (inherent voids in the structure) made up of voids about 5 to 10 mils in major diameter. Thus, in POCO, one would want nondestructive methods to detect voids down to perhaps 5 to 10 mils, but in ATJ, the nondestructive method would need to detect no smaller than 20 to 30 mil voids. (Noise level is different also because of different background void sizes.) In a fractured specimen, these voids may cause an irregular fracture plane; as often as not, the void will appear as a cavity and will be surrounded by a smooth surface that proceeds to the more jagged or irregular area.

#### Disparate Inclusion

The disparate inclusion is a small zone where either the chemistry or structure is different and acts as a local hard or soft spot from the mechanics point of view. As an impurity, the degree of hardness may not be the most important criteria. Sources of inclusions include incidental ones such as when an impurity is dropped in the raw powder, general impurities in the starting raw materials that persist to the end product, poor size range in the starting material, binders that persist to the end product, particles or grains of the flour that do not choose to behave as the others (dead or inactive grains) during the process, poor impregnation, and many others. A few of these are strength reducers, and a few are not. For example, calcium compounds can persist from the raw materials to the end product, but may end up occupying the inherent voids of the material in such a way that there is no deleterious effect. That is, calcium present in this fashion may be objectionable for other reasons, but not as a strength reducer. The presence of poorly bonded grains acts as a strength reducer in specimens and probably in hardware. These types of flaws are extremely difficult to categorize; and the detection is equally difficult. Radiographs catch many of these flaws, particularly in thin sections (but perhaps not for billets). Pulse-echo may catch a few. Perhaps the best way to handle this type of flaw is by careful examination of sections of the different billets by photomicrographs, visual examination

of the fracture faces on all specimens, radiographs on thin sections, and then the use of this information as a guide to the specific inspection necessary for the hardware. Radiographs of the hardware probably remain as the best detector where the hardware has a thin section and geometry permits. In a fractured specimen, the appearance of the fractured surface often depends quite strongly on the type of disparate inclusion. Hard spots, such as grains that seemed not to bind, will usually reduce strength and look like pull outs and may give a fracture pattern much like voids.

### Disparate Macrocracks

Disparate macrocracks are seen in photomicrographs to extend across one or a few adjacent grains and appear essentially as a small crack. Undoubtedly they result from grain anisotropy, extrusion actions, pressing actions, plus point and bulk residual stresses. Disparate macrocracks may be detectable by pulse-echo, radiography for thin sections, plus surface inspection. They usually result in a reduced strength and an angled fracture, assuming, of course, that the original orientation was angled. Perhaps these zones appear smooth in the fracture and can be separated from high velocity flat zones from the point of view that they are shinier, particularly when they were originally aligned in the grain, as in the "c" direction.

### Striations

Striations result from planar alignment of voids, inclusions, and/or macrocracks. The specific type of aligned flaw results from many things, such as flow lines or slippage lines that occur during extrusion, parting planes that occur when a mold is partially filled, then pressed, then partially filled and pressed again, pitch segregation, and many others. Obviously, these striations can be either high or low density areas and may or may not be strength reducers, particularly in a specimen. There is a reasonable argument that the striations would introduce very steep gradients in some properties and that in an application such as a leading edge, these property gradients could introduce stress (not necessarily strength) gradients. Thus, even though there was not strength reduction, the stress increase could be disastrous. Local plasticity and load redistribution would be the only guard against failure. This type flaw may be detected by dye penetrant at the outcrop in some cases, perhaps by pulse-echo in some cases, and in some cases by radiography. In thin-walled hardware, dye penetrant techniques and radiography seem adequate at this state until we know more about the real effect upon strength. In a fractured specimen, the striation may not be seen directly but results in a fractured plane that is often angled, and often stepped.

### Void Cluster

The void cluster is a zone where the void sizes are larger or the frequency greater. A cluster may be large, such as a dry core where impregnation did not reach the axis, or it may be small where the impregnant bypassed a zone. Void clusters do result in strength reduction in specimens and undoubtedly in hardware. In addition to strength reduction, the permeability may be high and thermal conductivity low, thus introducing problems to the design process other than those related to strength. This general type of flaw often can be detected by dye penetrants where it outcrops, pulse-echo in some cases, velocity measurements, radiography, radiometry, and perhaps others; the sensitivities of these methods depend on the size of the zone affected and the total distance or thickness through which one had to inspect. In hardware with wall thickness of  $\frac{1}{2}$  inch or so, dye penetrants and radiography should be quite sufficient. In a fractured specimen, the void cluster usually results in strength reduction and an irregular and angled fracture plane.

### Structure Nuances

This type of flaw is described as differences in properties that result from microdifferences in the material. These property differences usually are the gradual ones that are well recognized and often are plotted, for example, as density versus length of the billet, or density versus radial or circumferential position, or as a biased difference in property levels between two billets. This variability undoubtedly results from many things, including powder segregation, pressing differences, and firing differences, within a given billet or from billet to billet. Nondestructively, these differences sometimes can be detected by velocity measurements through the billet, radiometric measurements, and radiographs, among others. Since these differences are usually gradual, the fractures in specimens are usually normal, and the presence of this variability cannot be suspected from fractology. The destructive strength values usually do correlate with such things as the density profile, but the correlation can be quite weak.

### Nonuniformity

Nonuniformity is the differences in a property within a given billet or shape resulting from the different flaws in their different geometric assemblies and their frequency of occurrence.



## Nonreproducibility

Nonreproducibility is the billet-to-billet variation in properties that may result from any of the flaws plus unknown and subtle differences in the process while making different billets. These process differences can result in different nuances, different background flaws, and different disparate flaws such as voids, inclusions, and macrocracks. Thus we see that even the background flaw system can vary from billet to billet for a given type graphite. Since this variability in reproducibility results from all of the basic causes of different types of variabilities and flaws, it is obvious that all of the causes of these other variabilities are active; that is, poor reproducibilities result from subtle process differences, careless process differences, and all of the impurities and other things that cause the separate disparate flaws. It also is obvious that all of the nondestructive test methods are applicable and that the specimen fracture pattern and destructive strength will depend on the particular cause. Remember that this is a billet-to-billet variability. This makes the design problem clear and thus leads to a solution. The solution involves two general approaches. One is to maintain a leverage on the producer to exercise extreme care during manufacture and thus probably eliminate this type of variability. The second solution is to always pull a few samples from each billet and test them both destructively and nondestructively to establish that they are typical. Finally, compare carefully the values of the data from the "use billet" with those of the "data billet" and those minimal values obtained for "other billets" which may be spares or else ones used specifically to check reproducibility.

## SUMMARY ON DESIGN AND VARIABILITY

In treating the total variability of polygraphites in order that they may be used successfully as critical hardware, it becomes obvious that the total variability must be related quantitatively by destructive data on specimens to nondestructive signals, then to properties, and finally to performance of hardware. Specifically, studies are necessary in (1) relating nondestructive signals to types of flaws, and (2) relating the types of flaws to their actions as strength reducers by specimen testing. Then a relation between nondestructive testing displays and strength reduction for a given graphite would be available. After this initial relationship is established, the loop could be completed by testing flight hardware with different types of flaws in critical areas to relate both the specimen-testing and nondestructive signatures with hardware. Then a realistic factor of safety could be developed to handle the uncertainty resulting from the total variability of the material.

Note that flaw types were related to strength reduction rather than to stress intensification or to a highly theoretical type of Griffith crack. There is a specific inference in this approach. The information needed now is of the engineering type that will assist in developing a design process for graphite. This approach of relating nondestructive displays to strength reduction should provide a pragmatic solution to the problems of the design process within the reasonably near future. It is doubtful that studies of stress intensification of flaws and studies of the nature of Griffith cracks in a material like graphite can provide useful engineering information now. By the time that such studies could be helpful, it is quite probable that the nature of the graphite itself would be different. First order estimates of stress intensification of notches (such as holes or fillets) in graphites can be presently made. This solution requires the concurrent treatment of the effect of volume on strength, and the effect of nonlinearity of the stress-strain curve on the stress fields, since both of these parameters are involved in the events that occur around a small void as it acts as a stress intensifier. Insight into these latter two problems is being gained. Certainly, current work on crack blunting will lend to the total analysis at some future time. However, even a casual thought of these problems of stress intensification, volume, and crack blunting should make it obvious that the more pragmatic treatment of strength reduction is more likely to bring a reasonable success within the near future in terms of treating total variability and thus gaining one leg on selecting a factor of safety.

## TEST METHODS

The primary test methods used at Southern are described in the following part of the text. Descriptions of Avco's NDT methods can be found in their report.

### Tensile Apparatus

The tensile evaluations were performed in a gas-bearing tensile facility. A typical tensile facility is shown in the photograph in Figure 1 and in the schematic in Figure 2. The primary components are the gas bearings, the load frame, the mechanical drive system, the 5500°F furnace, the optical strain analyzers, and associated instrumentation for measurement of load and strain. The load capacity is 15,000 pounds.

The load frame and mechanical drive system are similar to those of many good facilities. The upper crosshead is positioned by a small electric motor connected to a precision screw jack. This crosshead is stationary during loading and is moved only when assembling the load train. The lower crosshead is used to apply the load to the specimen through a precision screw jack chain driven by a variable speed motor and gear reducer.

Nonuniaxial loading, and therefore bending stresses, may be introduced in tensile specimens not only from (1) misalignment of the load train at the attachment to the crossheads either initially or during loading, but also from (2) eccentricity-kinks within the load train, (3) unbalance of the load train, and (4) external forces applied to the load train by such items as electrical leads and clip-on extensometers. Although the bending moments from some of these sources may seem relatively slight, the resulting stress distortions are quite significant in the evaluation of the extremely sensitive brittle materials. Now consider each individually.

To confirm that the gas bearings had eliminated nonuniaxial loading resulting from the point of attachment of the load train to the crossheads, the frictional moment was determined at a load of 5000 pounds by measuring the torque required to produce initial motion within the system with the bearings in operation. This torque was found to be a maximum of  $6.6 \times 10^{-3}$  inch-pounds. The equation

$$M_o = \frac{2 \mu P}{3} R_2 \left[ \frac{R_2^3 - R_1^3}{R_2^2 - R_1^2} \right] \quad (1)$$

was then applied to the system to calculate the kinetic friction where  $M_o$  was the resisting moment due to kinetic friction and  $\mu$  represented the coefficient of kinetic friction. The calculated value of  $\mu$  was then equal to a maximum of only  $4.5 \times 10^{-7}$ .

The bending stress equation

$$S = \frac{Mc}{I} \quad (2)$$

was then employed to obtain the stress that could be induced in the specimen due to this bending moment. This value was 0.16 psi, or less than 0.002 percent of the tensile stress produced within a typical graphite specimen. These low values clearly indicate the elimination of problems of bending stress in the specimen imposed by misalignment at the crosshead attachments, either initially or during loading.

Emphases in the design of the load train were placed on (1) large length-to-diameter ratios at each connection, (2) close sliding fits (less than 0.005 inch) of all mating connections, (3) the elimination of threaded connections (4) the use of pin connections wherever possible, and (5) increasing the size of components to permit precise machining of all mating surfaces. All members were machined true and concentric to within 0.0005 inch, and the entire load train was checked regularly to ensure overall alignment following assembly of the individual members. This process ensures concentricity and no kinks in the system.

The problems of unbalance within the load train and of external forces applied to the load train have been explored and corrected. The entire load train is statistically balanced to less than 0.01 inch-pound for normal operation.

The standard configuration of the tensile specimen provides a relatively large L/D ratio in the gripping area to ensure good alignment. All surfaces in the gripping area are cylindrical in order to make precision machining easier and repeatable from specimen to specimen. This specimen also has double breakdown radii from the gripping area to the gage section. This double breakdown allows a uniform transition of the stress pattern and reduces the frequency of radius (out of gage) fractures. This specimen provides a uniform gage section which gives a definable volume of material under stress and permits accurate measurements of strain. The flags for the measurement of axial strain are positioned 1 inch apart so that unit strain is recorded directly. The flag attachment for measurement of lateral strain is positioned between the flags for axial strain; see Figure 3. Some specimens used in this program actually were not standard and are discussed later.

A schematic of the precision tensile grip is shown in Figure 4. The design is much like the jaws of the lathe head or the chuck of a drill motor made with precision. Observe from the figure the long surface contact of the mating parts and the close fits to establish precise alignment with the specimen. As the load is applied, the wedges maintain alignment to fracture.

Figure 5 is a sketch of the 5500°F furnace used for tension showing the basic components. The furnace consists of a resistively heated graphite element insulated from a water-cooled shell by thermatomic carbon. The furnace and specimen are purged with helium to provide an inert atmosphere. Ports with visual openings are provided on opposite sides of the furnace as a means of allowing the strain analyzers to view the gage flags of the specimen. Specimen temperatures are determined by optical pyrometer readings taken

through another small sight port containing a sapphire window. A calibration curve was established for the loss through the sapphire window, and since the furnace cavity acts essentially as a blackbody, true temperature readings are obtained. Power is supplied to the heating element by means of a 25 KVA variable transformer.

Strain measurement consists of measuring optically the elongation between two flags, or targets, which are mounted on the specimen and separated initially by a predetermined gage length. The travel of the targets is measured by sensing the displacement of the image of the edge of the targets and then electromechanically following the image displacement. The relative travel of the two targets provides the strain measurement. Readout is continuous and automatic on a millivolt recorder. A schematic of the analyzer is shown in Figure 6.

A brief summary of the mechanical motions of the components involved in monitoring the strain is helpful in understanding the detailed performance. A tracking telescope follows the upper target and carries a second telescope mounted on its carriage. The second telescope is capable of independent motion to follow the lower target. The relative displacement between the upper and lower telescopes, as strain occurs, defines the strain. The system usually is operated so that the tracking telescope follows the upper target and the strain is monitored by the relative displacement of the aperture rather than the telescope following the lower target. With this procedure the maximum range is the maximum displacement available for the lower aperture, or about  $\frac{1}{8}$  inch, and the sensitivity is limited by the optics and the noise level of the detector. Using both telescopes, the range is about  $\frac{3}{4}$  inch.

To provide optical references on the specimens, targets are affixed to the test specimen as mentioned. When the specimen is heated to temperature, the targets are self-luminous and are observed optically. The optics view past the luminous targets into a cooled cavity in the opposite furnace wall. The self-luminous targets are then visible against a dark background. To obtain data below 2000°F, a light beam is directed from behind the flags providing a shadow image for the detection system.

The image of the glowing target is focused through a rotating shutter (chopper) and onto a rectangular aperture. Small slits in the aperture pass a portion of the upper and lower edges of the light beam. A photocell receives the light thus transmitted, and an electronic circuit detects whether the energy passed by the two slits is equal. A servo drives the apertures to let a balanced quantity of light pass through the two slits and thus maintains an optical null.

Calibrations of the analyzers are performed in various ways including absolute correlations to precision micrometers, strain gage extensometers, and direct plots of stress-strain for reference materials such as steel, plexiglas, magnesium, and aluminum. Precision is within  $\pm 0.000020$  inch.

Instrumentation includes primarily a stress-strain measurement system composed of a 1000-pound SR-4 Baldwin load cell, a constant d. c. voltage power supply, an optical strain analyzer, and an X-Y recorder. Specimen temperature is monitored with an optical pyrometer. Stress (load) is measured by a commercial load cell. The cell receives a constant d. c. voltage input from the power supply and transmits a millivolt signal (directly proportional to load) to the X-Y recorder. Simultaneously, the optical strain analyzer measures the axial strain and transmits a millivolt signal (proportional to strain) to the X-Y recorder. Thus, continuous plots of stress-axial strain are recorded.

### Ultrasonics

Ultrasonic measurements for velocity and flaw detection are made using a Sperry UM721 reflectoscope. Acoustic velocity is determined by the through-transmission, elapsed-time method. The Sperry UM721 is used as the pulser, and a Tektronix 564 oscilloscope complete with a 3B3 time base (precision of 1 percent) and a 3A3 vertical amplifier are used as signal measuring devices. The detection of macro flaws is accomplished using the pulse-echo, reflection technique. Frequently used test specimens are the tensile blank specimen having dimensions of  $\frac{1}{2}$  inch diameter by 4 to 6 inches long and the  $\frac{1}{4}$  inch long segment from gage section of a fractured tensile specimen which is removed and machined after the tensile test has been performed. Ultrasonic inspection is performed on specimens having machined, flat surfaces normal to the longitudinal axis of the specimen.

In using the through-transmission, elapsed-time technique for measuring acoustic velocity, a short pulse of longitudinal-mode sound is transmitted through the specimen. An electrical pulse originates in a pulse generator and is applied to a ceramic piezoelectric crystal (SFZ). The pulse generated by this crystal is transmitted through a short delay line and inserted into the specimen. The time of insertion of the leading edge of this sound beam is the reference point on the time base of the oscilloscope which is used as a high-speed stop watch. When the leading edge of this pulse of energy reaches the other end of the specimen, it is displayed on the oscilloscope. The difference between the entrance and

exit times is used with the specimen length in calculating ultrasonic velocity. A short lucite delay line is used to allow time isolation of the sound wave from electrostatic coupling and to facilitate clear presentation of the leading edge of the entrant wave resulting in a more accurate "zero" for time. Transducers having resonance frequencies of 1mHz and a  $\frac{1}{2}$  - inch diameter cross section are used. Alcohol is used as the couplant to reduce errors incurred by solid couplants. The precision of measurement for tensile test blanks is  $\pm 0.002$  inch per microsecond; for the  $\frac{1}{4}$  - inch removed section,  $\pm 0.010$  inch per microsecond.

In using the pulse-echo, reflection technique of ultrasonics to detect macro flaws, test blocks from a similar material are used as calibration references for estimating the location, depth, and size of any discontinuities. These blocks are normally about  $\frac{5}{8}$  inch square by 2, 3, and 4 inches long. At one end, a single hole is drilled along the longitudinal axis to a depth of 1 inch. The hole sizes range from  $\frac{1}{32}$  to  $\frac{1}{4}$  inch in  $\frac{1}{32}$  inch increments. Thus, several test blocks having bottom reference holes of various sizes at the varying depths of 1, 2, and 3 inches from the incident surface are available for reference. Instrument settings are duplicated as much as practical for specimens of similar material. For evaluations of graphite, an ultrasonic frequency of 1mHz is used. At 1mHz, propagation of acoustical energy is limited by attenuation to distances of the order of 12 inches. When using pulse-echo, this means a specimen 6 inches long is within test range, Alcohol is used as the couplant for this evaluation also.

Using a Tektronix Oscilloscope C-12 camera, two techniques are used in recording pulse-echo signals from specimen blanks. The first technique involves signal addition by taking photographs of the signal as transmitted from both ends of the specimen to determine "standing signals" and the position which maximizes these signals by reverse overlay of the displays. The second technique involves recording a multiple trace (smear) of the signal. This is done by revolving the specimen on the face of the transducer on about a  $\frac{1}{8}$  inch radius with the camera shutter open. This technique tends to define the "standing signals" because they are more repetitive, thus resulting in greater exposure to the film.

### Radiography

Radiography of graphite materials is performed using state-of-the-art X-ray techniques for low-absorptive materials. The radiographic unit is a Radifluor 360 manufactured by Torr X-ray Corporation, a division of Phillips Electronics. This unit is rated for operation from 0 to 120 kv at either 3 or 5 ma, making it ideal for graphite thicknesses up to about 2 inches. It

incorporates basic characteristics which are required for examination of low-absorptive materials. For example, the X-ray tube is equipped with a 0.015 inch thick beryllium window and has a focal spot size of 0.35 mm. The beryllium window provides low inherent filtration for the low energy rays, thus allowing them to pass from the tube for utilization. The small focal spot lends to providing distortion-free imaging of small discontinuities. The sensitivity of this unit using extra-fine grain film is better than 2 percent.

Operational and film development procedures used are consistent with conventional radiographic practices for obtaining good radiographs. For example, lower power settings are used and development time is extended in order to produce images having good contrast. Extra-fine grain film (Eastman Type M) is used so that image unsharpness is not enhanced by the grain size of the film emulsion. Further, image unsharpness is further reduced by placing the specimen as far as practical from the source of radiation (usually about 42 inches). Image quality is checked by a penetrameter made from a similar material. Drilled holes indicate 2 and 4 percent sensitivities. No intensifying screens, filters, or masks are used to affect imaging for graphite thicknesses up to 2 inches. Film processing is consistent with good standard practices. Examination of radiographs is made using a variable, high intensity spot illuminator.

#### Electrical Resistivity

Electrical resistivity is measured by the potentiometer method shown in Figure 7. The test specimen may be either a specimen blank or a finished specimen configuration having a uniform gage length of 1 inch or more. The attachment taps to the specimen are spring-loaded graphite discs. Potential taps are normally clipped to the specimen and have a gage length of 1 inch.

The procedure used in the potentiometer method involves comparing the voltages for a standard resistor with a specimen of unknown resistance when a common, known current flows through both. As shown in Figure 7, with 1 amp flowing through the specimen and standard 5000  $\mu$  ohm resistor, the potentiometer leads are connected across the standard 5000  $\mu$  ohm resistor, the potentiometer set on 5000  $\mu$ V, and the rheostat adjusted until there is no current flow through the galvanometer. Then, the potentiometer leads are switched to the specimen. The potentiometer is adjusted for zero current flow through the galvanometer, and the voltage across the specimen is read.



From the relation

$$R = \frac{E}{I} \quad (3)$$

the relationship between the standard resistance, the unknown resistance, and the associated voltages can be expressed as

$$\frac{R_x}{R_s} = \frac{E_x}{E_s} \quad \text{or} \quad R_x = R_s \frac{E_x}{E_s} \quad (4)$$

where

- $R_x$  = Resistance of specimen
- $R_s$  = Resistance of standard resistor (5000  $\mu$  ohm in this case)
- $E_x$  = Voltage drop across specimen
- $E_s$  = Voltage drop across standard resistor.

A full-wave rectified dc power supply operated by an ac regulated power source is used to induce current flow through the specimen. A galvanometer having a sensitivity of 0.8  $\mu$ V per millimeter with a 1000 ohm series resistor is used with a potentiometer having a dial graduation of 0.0005  $\mu$ V to measure voltage.

Using the measured voltage drop across the specimen, the known current flow, and the dimension measurements from the specimen, the volume electrical resistivity is calculated using the equation

$$\rho = \frac{A}{L} \frac{V_x}{I} \quad (5)$$

where

- $\rho$  = Volume electrical resistivity
- $A$  = Cross-sectional area of specimen
- $V_x$  = Voltage drop across gage length of specimen (corrected for open-circuit voltage)
- $I$  = Current flow through specimen, and
- $L$  = Gage length of specimen

The normal uncertainty for the value of electrical resistivity determined from this apparatus is  $\pm 2$  percent.

#### Open and Closed Porosity by Liquid Absorption

At Southern, liquid absorption measurements are made to further characterize the nature of a material. A vacuum-impregnation technique using mineral spirits (s. g. of 0.774) as the impregnant is used. Using this technique, the three weights—dry weight, suspended weight, and saturated weight—are determined for evaluating the absorption, density, and porosity of a material. This technique is used frequently to characterize material near the fracture zone of tensile specimens. For such evaluations,  $\frac{1}{4}$ -inch segment or segments from the long and/or short halves of the tensile specimens are used. A  $\frac{1}{4}$ -inch "fracture" section is a  $\frac{1}{4}$ -inch long section including the fracture face. A  $\frac{1}{4}$ -inch "removed" section is a section behind the  $\frac{1}{4}$ -inch "fracture" section; that is, a section from  $\frac{1}{4}$  to  $\frac{1}{2}$  inch behind the fracture face.

The normal procedure used in making liquid absorption measurements involves first of all thorough drying and then precise weighing of specimens to determine dry, suspended, and saturated weights (recorded to nearest 0.0001 gram). First, the specimens are oven dried at 300°F for two hours to drive out absorbed moisture and then weighed to determine dry weight. Individual specimens are then placed in small beakers which are placed on their sides in a desiccator. After the desiccator is sealed off, a vacuum of 50 microns of Hg is pulled and held for two hours to remove entrapped air from the specimens. The desiccator is then purged with mineral spirits until the beakers containing the specimens are submerged. The desiccator is then vented, and the specimens are left in the desiccator for 20 minutes to allow vapor inside the specimens to condense.

The suspended weight is obtained by weighing the saturated specimen while suspended in the mineral spirits. The specimens are kept submerged by righting the beakers in the desiccator to maintain the mineral spirits level above the specimen. Figure 8 illustrates the procedure used for suspending the specimen in mineral spirits from a balanced beam. The tare weight of the basket, which is subtracted from the total suspended weight to determine the suspended weight of the specimen, is determined by weighing

the suspended basket submerged in mineral spirits to the same depth that the specimen is weighed. Care is exercised to ensure that no air bubbles cling to the basket and that a clearance between the basket and sides of the beaker is maintained.

For determining saturated weight, the specimens are removed from the mineral spirits and wiped carefully to remove excessive surface mineral spirits. The specimens are then weighed immediately to determine the saturated weight.

From the three weights taken for each specimen (dry weight, suspended weight, and saturated weight) percent water absorption, open porosity, bulk density, and apparent density are determined. The total porosity is also derived when the true density of the material is known. The equations used for these calculations are:

$$W_a = \left( \frac{W_{sa} - W_d}{W_d} \right) \left( \frac{\rho_w}{\rho_m} \right) \times 100 \text{ percent} \quad (6)$$

$$P_o = \left( \frac{W_{sa} - W_d}{W_{sa} - W_{su}} \right) \times 100 \text{ percent} \quad (7)$$

$$\rho_b = \left( \frac{W_d}{W_{sa} - W_{su}} \right) \times \rho_m \quad (8)$$

$$\rho_a = \left( \frac{W_d}{W_d - W_{su}} \right) \times \rho_m \quad (9)$$

$$P_t = \left( \frac{\frac{W_{sa} - W_{su}}{\rho_m} - \frac{W_d}{\rho_t}}{\left( \frac{W_{sa} - W_{su}}{\rho_m} \right)} \right) \times 100 \text{ percent} \quad (10)$$

where

- $W_a$  = water absorption
- $W_{sa}$  = weight of sample when saturated with liquid m
- $W_d$  = dry weight of sample
- $W_{su}$  = weight of sample when suspended in liquid m
- $\rho_m$  = density of liquid m (0.744 gm/cm<sup>3</sup> for mineral spirits)
- $\rho_w$  = density of liquid water

$\rho_t$  = true density of sample  
 $\rho_b$  = bulk density of sample  
 $\rho_a$  = apparent density of sample  
 $P_o$  = open porosity  
 $P_t$  = total porosity

Weights for this evaluation are determined using an analytical balance sensitive to 0.0001 gram. Instrument precision for measuring absorption is  $\pm 0.10$ , bulk density is  $\pm 0.002$  gm/cm<sup>3</sup>, open porosity is  $\pm 0.15$ , and total porosity is  $\pm 0.05$ .

### Porosity by Point Count

Volume fraction analysis<sup>1</sup>, a frequently used tool in metallography, is used for estimating the volume fraction of a constituent within a given volume. Three techniques are commonly in use: areal, lineal, and point fractions. These techniques involve the sampling of measurements from a two-dimensional plane (usually a polished surface) for estimating the volume fraction of a constituent. The fundamental relation for, say, the point-count technique is that a point placed at random within a given volume has a probability of that point falling within a given constituent equivalent to the volume fraction of that constituent. The accuracy of the analysis is determined primarily by the number of observations and is not dependent on whether the observation is in measurements of intercepted area, length, or the identification of the constituent occupied by a point. Further, the basis for selecting a method of analysis is not one of accuracy, but the one which is most efficient requiring the least amount of effort on the part of the investigator.

The point-count method used by Southern in evaluating the porosity volume fraction within a given graphite is a random, one-dimensional array technique. Using this technique, a one-dimensional array of points is distributed in a regular fashion along a line. The line (scale) is then applied randomly to a photomicrograph of a polished section of material, and the number of occupied points versus the number of points applied is recorded. A point is considered occupied when the constituent whose fractional volume is being evaluated falls under one

---

<sup>1</sup>Information regarding technique and equations extracted from Delhoff, R. T. and Rhines, F. N. : "Quantitative Microscopy," McGraw Hill, New York, 1968.

of the regular spaced points along the line of the array. In the case where some points fall close to a boundary and it is not possible to decide which constituent should be applied, such points are counted as one-half. When the total number of points have been applied, the porosity of the area is determined from the relation

$$P_p = \frac{P_\alpha}{P} = V_v \quad (11)$$

where

$P_p$  = Point fraction  
 $V_v$  = Volume fraction  
 $P_\alpha$  = Total number of points falling in voids  
 $P$  = Total points applied

The number of points to be applied by an investigator is determined by the maximum error that can be tolerated. The number of points needed to achieve a desired accuracy can be calculated from the expression

$$P = \frac{1}{\sigma^2_{(V_v)}} [V_v (1 - V_v)] \quad (12)$$

where

$P$  = Total number of points applied  
 $\sigma$  = Standard deviation  
 $V_v$  = Volume fraction

An estimate of the volume fraction ( $V_v$ ) can be obtained for determining the total number of points  $P$  by applying a few points to the specimen.

In using this point-count technique, two basic assumptions are made:

1. Areas of porosity occur as discrete areas randomly distributed throughout the material.
2. The spacing between points is large enough to prevent two or more points from falling within the same area of porosity.

In evaluating porosity of ATJ-S by the point-count technique, a 100X photomicrograph of either impregnated or unimpregnated material is used. Because the background void size of ATJ-S is on the order of 0.006 inch, the point-counting increments are equally spaced at 1 inch. This spacing provides sufficient distance between points to prevent two or more points from falling within the same area of a void. In making the point count, all voids greater than 0.001 inch are considered. In evaluating the porosity of impregnated versus unimpregnated ATJ-S, the voids for an impregnated material appear smaller and gray instead of black. The minor axis of the voids in the impregnated material is smaller because the epoxy prevents the edges from breaking off in this dimension during polishing. The major dimension, perhaps a little smaller, remains about the same size as for the unimpregnated material. Therefore, porosity measurements for unimpregnated material result in somewhat higher values than those for impregnated material (usually about 14 percent for unimpregnated and 9 percent for impregnated). In both cases, porosity by point count is relatable to open porosity by absorption. In the case of the impregnated material, the porosity by point count is about equal to open porosity as measured by absorption.

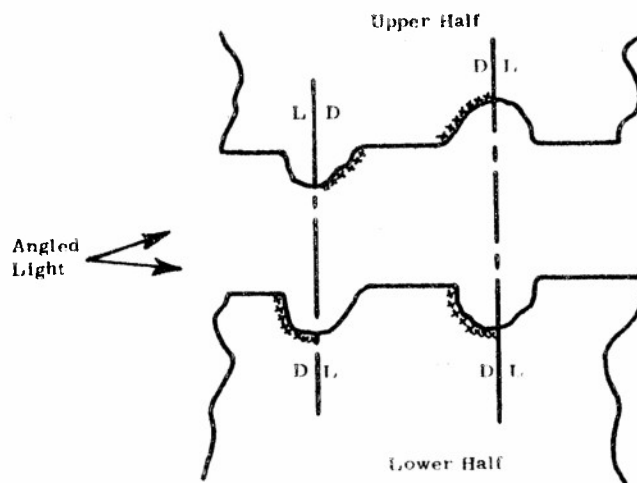
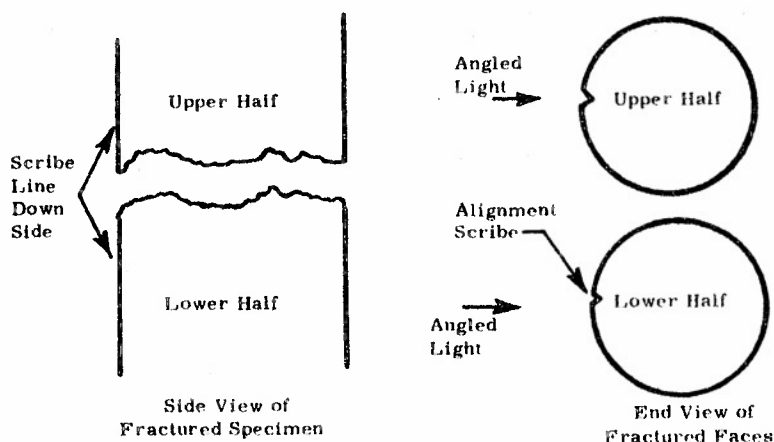
As mentioned earlier, the degree of accuracy depends on the number of points applied. In measuring open porosity of ATJ-S by absorption, the value of one standard deviation normally varies from below one percent to as high as two percent. Therefore, considering the variability of the material, point counts providing accuracies better than one — two percent (0.01 - 0.02) are considered unnecessary. Referring to equations (11) and (12), for accuracies providing a standard deviation of 0.01 a total of 1200 points would be applied. For an accuracy of 0.02, a total of only 300 points would need to be applied. Of these, one would expect to have about 170 of the 1200 and 40 of the 300 points to be occupied by voids. Normally, for ATJ-S, the inspection of a specimen is continued until 50 occupied points have been obtained. Such inspection provides an accuracy within 0.02.

#### Inspection of Fracture Faces by Flicks

Inspection of fracture faces by flicks is a visual evaluation made on overlays of transparent photographs (one reversed) taken on both fracture faces of a specimen. The term "flicks" is used because the transparent overlays are placed on a light box and inspected by flicking the upper transparency with respect to the lower one. The transparencies are viewed at a slight angle so that the images of the upper and lower transparencies can be superimposed during the flicking action. The flicks

technique provides a useful tool for inspecting fracture faces for voids common to both faces.

The fracture face is positioned normal to the view direction of the camera, and light is directed from an angle toward the fracture face (about  $60^\circ$  to the normal to the fracture face). The fracture faces are oriented so that the light hits the specimen from the same side. The effect here is that when the transparencies are properly aligned with one another and overlaid, voids common to both halves of the fracture face incur shadow reinforcement, whereas, hills and valleys do not reinforce. This effect is depicted by the sketch shown below.



Positive transparencies used in the flick technique are made with a Polaroid MP-3 camera using Type 146L film (or equivalent). The transparencies are photographed at 10X magnification.

#### Weight/Volume Bulk Density

Each specimen is initially machined to a predetermined blank size, and the bulk density of each blank is determined from direct measurements of weight and dimensions. Weight measurements are made on an analytical balance having a sensitivity of 0.0001 gm. Dimensional measurements are made to the nearest 0.0005 inch using micrometers.

#### Application of Alcohol Penetrant for Evaluation of Surface Porosity

Alcohol (either methyl or isopropyl) is used on graphite as a nondestructive penetrant test for surface discontinuities, gross porosity, wide density variations, large inclusions, and cracks. When a piece of graphite is wetted with alcohol, porous areas and cracks remain wet for a longer period of time than the surrounding material. This effect is discernable by visual observation. Although this technique is not quantitized (it probably could be), it is effective in revealing surface discontinuities.

The alcohol inspection procedure involves the following:

1. Application of alcohol to surface of specimen usually for 5 to 10 seconds. This can be done by flooding, brushing, or immersing.
2. Inspection of specimen surface as alcohol evaporates. Porous areas will remain wetted while the surrounding smooth areas will dry. Cracks also will remain wetted depending primarily upon the depth and width of the crack.
3. Record is made of visual observations.

This technique is useful for revealing the need of other NDT methods of inspection such as ultrasonics and X-ray for determining the extent of the surface discontinuity internally.

#### Other Methods of Inspection

Other techniques used to a lesser extent for particular inspections included normal usage of electron microscopy, electron microprobe, porisimetry, pycometry, and light microscopy.



## EXPERIMENTAL RESULTS

The testing results are tabulated in Tables 1 through 17. Tables 1 through 8 provide the results from the tensile evaluations for the various ATJ-S billets, and Tables 9 through 16 provide the results from the section monitor evaluations. Table 17 gives a summary of the average values and the standard deviations for tensile properties and section monitors for the various billets. The results are plotted in composite plots of specimens from the various ATJ-S billets in Figures 9 through 14. Figures 9 through 13 are plots of tensile strength versus the section monitors bulk density, open porosity, closed porosity, velocity, and electrical resistivity. Figure 14 is a composite plot of the section monitors-gage electrical resistivity versus open porosity. The significance of these composite plots will become more apparent as the data are presented and discussed.

The data for this report will be grouped and presented according to billet. This seems appropriate since each billet was evaluated separately and since the reader should find the data less confusing when so organized.

### ATJ-S Billet L-16-7

The scrap from the even numbered slabs from Billet L-16-7 was released by Lockheed for the purpose of the flaw significance studies. The original cutting plans for the billet and even numbered slabs are shown in Figures 15 and 16. Figures 17 through 21 are sketches made from Avco photographs of the five slabs which described the locations of the porous regions. Figures 22 through 26 are Avco drawings of the original cutting plans for the even numbered slabs and show radiometric densities in the slabs as measured by Avco. Figures 27 through 31 are schematics of the slabs which present the positions and relative size of ultrasonic flaw indications as found by Avco. In addition to these data, Avco radiographs were available for study. The porous regions located as shown in Figures 17 through 21 were clearly visible and well defined in the radiographs. Using the radiographs and ultrasonic indications from Figures 27 through 31, cutting plans were made for positioning as many flaw indications as possible in the gage sections of 4-inch long tensile specimens. The cutting plans for the five slabs are shown in Figures 32 through 36. Avco removed specimen blanks according to the plans, performed additional nondestructive examination, and sent the tensile blanks shown in Figure 37 to Southern for further inspection to determine the causes for weak-strong specimens, for machining to test configuration, and destructive testing.

The inspection procedure to determine causes for weak/strong specimens described earlier was performed by Southern and included measurements for ultrasonic velocity and pulse-echo, for electrical resistivity, and for section density, absorption, and porosity by liquid absorption measurements.

The blanks were machined into the 4-inch long tensile specimen configuration shown in Figure 38 and then loaded to fracture in the gas-bearing tensile testing apparatus. All evaluations were with grain at 70°F. An attempt was made to record acoustic emission from the specimens during loading; however, extraneous electrical noise and other problems precluded reliable results within the scope of this program. Our acoustic emission recording capability for graphite is still in the developmental stages.

Subsequent to post testing inspection, the fracture locations were recorded, the fracture faces were photographed at 10X magnification, and the specimens were shipped to Avco for inspection. Upon return to Southern, a  $\frac{1}{4}$ -inch long section was removed from adjacent to the fracture face of the long end of each specimen. Ultrasonic velocity, density, absorption and porosity measurements were made on these  $\frac{1}{4}$ -inch sections.

The results of testing on L-16-7 (including L-7-1 scrap) are tabulated in Tables 1 and 9. Photographs showing multiple traces of pulse-echo signals (smears) along with fracture locations for all specimen blanks are presented in Appendix A. Original stress-strain curves are provided in Appendix B. A composite of all the stress-strain curves is given in Figure 39. The mechanical properties of the L-16-7 specimens are presented in Table 1, and the section bulk density, percent absorption, apparent density, porosity and ultrasonic velocity of the  $\frac{1}{4}$ -inch sections adjacent to the fracture faces are tabulated in Table 9. The fracture locations are shown on the cutting plans in Figures 32 through 36. The only fracture located over an Avco ultrasonic flaw indication is that for Specimen S2-6. A study of the 10X fracture face photograph did not reveal any identifiable flaw. Further, the specimen exhibited a strength which was higher than the average for Slab 2. As expected, in every case where a portion of the specimen gage sections fell in the porous or dry core region, the specimens fractured in that portion, and several cases of these were the weakest specimens from their respective slabs.

The average with grain tensile strength for L-16-7 was 4763 psi with a standard deviation of 499 psi. The strength of this billet is low compared to the average value of strength obtained for all ATJ-S tested at Southern prior to March 10, 1969 (4960 psi with a standard deviation of 610 psi). In view of this lumped test data, several specimens from L-16-7 were

weak by one standard deviation or more (4350 psi or less). The weak specimens were S2-2 at 3680 psi, S2-3 at 4320 psi, S4-2 at 3910 psi, S6-1 at 3990 psi, S6-4 at 4240 psi, S6-5 at 4020 psi, and S8-6 at 4260 psi.

Upon inspecting the test data from L-16-7 for correlations between tensile strength and the various monitors, the curves shown in Figures 40 through 47 were plotted. Figure 40 is a plot of average blank density, average blank ultrasonic velocity, and average tensile strength versus the various slab positions. The average blank ultrasonic velocity is seen to be a rather good monitor of the average slab strength, whereas average blank density is not so good as a monitor for this group of data.

Figures 41 through 45 are plots of tensile strength versus the section monitors density, absorption, and porosity. All these monitors correlate strength with the exception of closed porosity. Figure 41 shows a direct relation between tensile strength and bulk density; whereas, Figures 42, 43, and 44 show inverse relations between tensile strength and absorption, total porosity, and open porosity. Little or no relation between tensile strength and closed porosity is shown in Figure 45. For these data, the closed porosity values are tight, thus rendering any relation to strength unapparent. The results of the other monitors, section ultrasonic velocity and electrical resistivity, used to correlate strength are given in Figures 46 and 47. Figure 46 shows a direct relation between tensile strength and section ultrasonic velocity, and Figure 47 shows an inverse relation between tensile strength and gage electrical resistivity.

Visual inspection of the fracture faces revealed that S6-5 and S8-6 contained visible flaws of 0.030 inch and 0.075 inch major dimensions, respectively. Further discussion including 10X photographs of these fracture faces will be presented in the next section on the discussion of experimental results. Photographs showing the multiple traces from the pulse-echo signals from Specimens S6-5 and S8-6 are provided in Figure 48. The fracture locations are indicated. Strong signals are revealed in the vicinities of the failures; however, these signals were of no particular significance when compared with signals from other specimens for locations where specimens did not fail. In order to further characterize disparate S6-5, a more detailed inspection using a microprobe and electron microscopy was made. The results of this inspection are presented in Appendix C.

During the post testing inspection at Southern, pulse-echo smears on all specimens and radiographs of weak specimens were included. As shown

in Appendix A, the fracture location for each specimen was recorded. Although the fracture frequently occurred in the vicinity of strong signals, no strong relation is apparent. However, a relation of low-hash for dry-core specimens was observed. Radiographs on weak specimens were inspected for macro-sized voids, cracks, striations, and inclusions. No particular significance could be attached to the fracture location, Southern pulse-echo signals, or Avco pulse-echo flaw indications shown in Figures 32 through 36. Of seven specimens which had strong Avco pulse-echo indications in the gage, only one, S2-6, failed at the indication. It was noted from radiographs that L-16-7 had high absorptive spots throughout which are larger than usual for ATJ-S. Frequently, these spots appeared to be collected into clusters. However, since none of these clusters were observed in the fracture zone, they are not considered to be strength reducers. Figure 49 is a photograph of the radiograph of Specimen S2-2. It is typical for L-16-7 and also depicts a dense cluster.

#### ATJ-S Billet L-7-1

The original specimens from ATJ-S graphite Billet L-7-1 were not NDT'd by Avco since the work was started prior to the initiation of this program. It was intended that several specimens be removed from L-7-1 scrap for use in this program; however, due to the size of the scrap pieces only two specimens could be removed. These were NDT'd by Avco and sent to Southern for destructive testing. The two specimens from L-7-1 were NDT'd and destructively tested concurrently with those from the even slabs of L-16-7. The data are presented along with that from L-16-7 in Tables 1 and 9 for purposes of comparison. Generally, the behavior of the two specimens was similar to L-16-7 except that L-7-1-2 had a lower value of ultrasonic velocity than was expected. Strengthwise, the specimens seem to fit the L-16-7 strength-open porosity relation shown in Figure 44.

#### ATJ-S Billet L-1-4

Billet L-1-4 was substituted into the program to replace material which was not received due to changes by Lockheed. L-1-4 was thoroughly NDT'd by Avco and was found to exhibit many flaw indications. Avco made cutting plans for 6-inch tensile blanks locating as many flaw indications as possible in the gage section of the blanks. Avco machined the blanks to the dimensions of  $\frac{5}{8}$  inch x  $\frac{5}{8}$  inch x 6 inches, nondestructively reexamined the blanks to assure that flaws were in the desired location, and then shipped the blanks to Southern. Avco's cutting plan for L-1-4 was not available for inclusion in this report. However, the billet was sectioned in half, as shown in Figure 50, and specimens from the top and bottom

halves were designated as A and B specimens, respectively. The results of Avco's ultrasonic inspection on the specimen blanks are presented in Appendix D. The fracture location for each specimen is indicated by the solid line.

Upon receipt of specimen blanks from Avco, Southern again conducted its inspection procedure for weak-strong specimens, machined specimen blanks to the specimen test configuration shown in Figure 51, and then loaded the test specimens to fracture in the gas-bearing tensile testing apparatus.

During machining to test configuration, a large void was found in Specimen A12W. This void is shown in Figures 52a, b, and c. Figure 52a shows the specimen before the final gage section was ground. Figure 52b is a 9.2X photograph of the void indicated by the arrow in Figure 52a. Figure 52c shows the void after final grinding and polishing. The flaw happens to fall in the first breakdown radius, and the specimen failed at this point. Avco's ultrasonic flaw detection described this void as a large to very large indication. As shown in Figure 52b, the void had a major dimension of at least 0.027 inch.

The results of testing on L-1-4 are tabulated in Tables 2 and 10. The mechanical properties are presented in Table 2 and section bulk density, percent absorption, apparent density, porosity, and section ultrasonic velocity are tabulated in Table 10. Photographs showing multiple traces of pulse-echo signals along with fracture locations for the with grain specimen blanks are presented in Appendix E. Original stress-strain curves are presented in Appendix F. A composite of all the with grain stress-strain curves is presented in Figure 53, and all of the across grain stress-strain curves in Figure 54.

The average with grain and across grain tensile strengths for L-1-4 were 4909 psi with a standard deviation of 338 psi and 4026 psi with a standard deviation of 397 psi. These values are comparable to the lumped data obtained for ATJ-S at Southern prior to March 10, 1969 (4960 psi with a standard deviation of 610 psi with grain, and 4060 psi with a standard deviation of 380 psi). In view of these lumped data, only Specimens A12W at 3890 psi and B14A at 1850 psi were weak by one standard deviation or more (4350 psi or less with grain and 3680 psi or less across grain). As mentioned earlier, A12W had a large void. Specimen B14A had a large dark spot in both fracture faces. A more complete discussion on these two specimens will be presented in the next section on the discussion of the experimental results.

Subsequent to post testing inspection, the fracture locations were recorded, and 10X black and white photographs and 10X flicks were made of fracture faces on Specimens A10W, A12W, A22W, A24W, and B14A. The 10X black and white photographs of the fracture faces of A10W, A12W, and B14A will be presented in a later discussion on the flick evaluations for these specimens. In order to expedite the program, these fractured specimens were not shipped to Avco for inspection. Southern resumed its post testing inspection by removing a  $\frac{1}{4}$ -inch section from adjacent to the fracture face of the long end of each specimen and making measurements of ultrasonic velocity and of section density, absorption, and porosity by the liquid absorption technique.

Test results for the with grain evaluations are plotted in Figures 55 through 61. Figures 55 through 59 are plots of tensile strength versus section monitors density, absorption, and porosity. Similar relations between strength and section monitors are seen for L-1-4 with grain as were observed for L-16-7. Figure 55 shows a direct relation between tensile strength and bulk density; whereas, Figures 56, 57, and 58 show inverse relations between strength and absorption, total porosity, and open porosity. It is of interest to note that the section bulk density of L-1-4 is tight (COV = 0.4 percent) compared to L-16-7 (COV = 1.0 percent). Figure 59 shows no relation between strength and closed porosity. Again, the data for closed porosity were tight and in the 8 to 10 percent range. Figures 60 and 61 are plots of tensile strength versus the section monitors ultrasonic velocity and gage electrical resistivity, respectively. The relation between strength and velocity are weakened here because of the tightness of the velocity data. However, a strong inverse relation is again shown for strength and electrical resistivity. For the relations between strength and the monitors of section density, absorption, and porosity, weak Specimen A12W is not so obvious because it seemingly profiles. However, in the relations of strength and section velocity and gage resistivity, weak Specimen A12W does appear more obvious. A more detailed discussion on this will be presented in the next section on the discussion of the results.

Test results for the across grain evaluations are plotted in Figures 62 through 68. Figures 62 through 66 are plots of tensile strength versus section monitors density, absorption, and total porosity, and open porosity. Similar relations between strength and section monitors are seen for across grain as were seen for with grain. Figure 62 shows a direct relation between tensile strength and bulk density; whereas, Figures 63, 64, and 65 show inverse relations between strength and absorption, total porosity, and open porosity. Note that the section bulk density data in the across grain direction were not quite as tight as the with grain data (COV of 0.6

percent compared to 0.4 percent). Figure 66 shows a direct relation between strength and closed porosity when the end points B25A and B34A are considered. Without these, however, the relation is weakened significantly. Figures 67 and 68 are plots of tensile strength versus section ultrasonic velocity and gage electrical resistivity. The velocity data are tight; however, an indirect relation between strength and velocity seems apparent, especially when the few scattered data points are disregarded. No relation between strength and electrical resistivity is apparent. Note here that weak Specimen B14A obviously misses the strength-monitor profiles.

During the post testing inspections at Southern on L-1-4, pulse-echo smears on all specimens and radiographs of weak specimens were again included. Smears on the with grain specimens showing the fracture locations for each specimen are presented in Appendix E. Similar to L-16-7, relating the fracture to pulse-echo signals was somewhat a hit-and-miss proposition. Pulse-echo smears on two weak Specimens A12W and B14A are presented in Figure 69. Strong signals are revealed in the vicinity of both fractures. Inspection of radiographs on weak specimens revealed no significant relationship between fracture location and high and low absorptive spots. However, as shown by Figure 70, the size of the high absorptive spots for L-1-4 was somewhat smaller than for L-16-7.

#### ATJ-S Billet L-1-8

Billet L-1-8 was also substituted into the program to replace other material. L-1-8 was treated similarly to L-1-4. Avco made a thorough NDT inspection of the billet, made cutting plans for 6-inch tensile blanks and machined  $\frac{5}{8}$  inch x  $\frac{5}{8}$  inch x 6-inch tensile blanks. Avco's cutting plan for L-1-8 was not available for inclusion in this report. However, similar to L-1-4, the billet was sectioned in half, as shown in Figure 50, and specimens from the top and bottom halves of the billet were designated A and B respectively. Many flaw indications were found. Avco NDT'd slabs before making cutting plans to locate flaw indications over specimens and then NDT'd the tensile blanks after machining to ensure that the flaw indications were within the gage section of the blanks. The results of Avco's ultrasonic inspection on the specimen blanks are presented in Appendix G. Fracture locations are indicated by solid lines. After completing their inspections, Avco shipped the blanks to Southern.

Upon receipt of specimen blanks, Southern again conducted its inspection procedure for weak-strong specimens, machined specimen blanks to the specimen test configuration shown in Figure 71 (the same configuration used for L-1-4), and then loaded the test specimens to fracture in the gas-bearing tensile testing apparatus.

The results of testing on L-1-8 are tabulated in Tables 3 and 11. The mechanical properties are presented in Table 3, and the liquid absorption results along with section ultrasonic velocity are tabulated in Table 11. Pulse-echo smears from L-1-8 with grain specimens are presented in Appendix H. Original stress-strain curves are presented in Appendix I. Composites of the with grain and across grain stress-strain curves are presented in Figures 72 and 73, respectively.

The average tensile strength for L-1-8 in the with grain direction was 5007 psi with a standard deviation of 283 psi. In the across grain direction, the average strength was 4087 psi with a standard deviation of 114 psi. This compares with the average with grain and across grain strengths of all ATJ-S tested at Southern prior to March 10, 1969 (4960 psi with a standard deviation of 610 psi and 4060 psi with a standard deviation of 380 psi, respectively). In comparison, the strength of L-1-8 was slightly higher with tighter data scatter than for the average ATJ-S tested at Southern. The weakest specimens from L-1-8 were A18W at 4450 psi, A30W at 4170 psi, A32W at 4350 psi, B11A at 3800 psi, and B22A at 3810 psi. However, in view of all data evaluated at Southern prior to March 10, 1969, only specimens A30W and A32W can be viewed as weak by one standard deviation (4350 psi for with grain, 3680 psi for across grain). No macro-size flaws were observed for any of the specimens during any of Southern's inspections and machining operations.

Subsequent to post testing inspections, the fracture locations were recorded and 10X black and white and 10X flicks were made of the fracture faces on weak Specimens A18W, A30W, and A32W. These 10X black and white photographs will be presented with the flick inspection of these fracture faces in the next section on the discussion of the data. Similar to L-1-4, fractured specimens from L-1-8 were not returned to Avco for inspection in order to expedite the program. Southern resumed its post testing inspection by removing a  $\frac{1}{4}$ -inch long section from adjacent to the fracture faces on the long end of each specimen and making measurements of ultrasonic velocity and of section density, absorption, and porosity using the liquid absorption technique.

Test results from the with grain evaluations are plotted in Figures 74 through 80. Figures 74 through 78 are plots of tensile strength versus section monitors density, absorption, and porosity. The relations seen earlier for L-16-7 and L-1-4 between strength and these section monitors were consistent; that is, a direct relation between strength and bulk density (Figure 74), inverse relation between strength and absorption (Figure 75), total porosity (Figure 76), and open porosity (Figure 77).



It should be noted, however, that this trend holds for A and B specimens lumped, is strongest for A specimens alone, but is considerably weaker for B specimens alone. Again, as shown in Figure 78, little, if any, relation is shown between strength and closed porosity. However, note that the values of closed porosity are tight in the 9 percent range. Figures 79 and 80 are plots of tensile strength versus the monitors section ultrasonic velocity and gage electrical resistivity, respectively. Again, the trends seen earlier for L-16-7 and L-1-4 were consistent. Figure 79 shows a strong direct relation between strength and velocity for the A specimens alone; however, the trend weakens somewhat when lumped with the results from the B specimens. Figure 80 shows a strong inverse relation between strength and electrical resistivity. The A specimens again show the stronger relation, but the relation is perhaps only shifted slightly upward when lumped with the B specimens. The weak Specimens A18W, A30W, and A32W appear to fit the strength-monitor profiles in all of the plots and appear obvious on each plot.

Test results for the across grain evaluations are plotted in Figures 81 through 87. Tensile strength versus absorption monitors bulk density, absorption, total porosity, open porosity, and closed porosity are plotted in Figures 81 through 85, respectively. Tensile strength versus section velocity and blank electrical resistivity are plotted in Figures 86 and 87. The L-1-4 across grain strength-monitor relation was similar to the relation noted for the with grain direction. However, for L-1-8 across grain, the strength-monitor relations as shown by the figures seem insignificant. However, it should be noted that most of the with grain specimens from L-1-8 were from the A segment (top) of the billet and that the with grain A specimens showed a somewhat stronger strength-monitor correlation than did the B specimens (bottom segment of the billet); whereas, all but four of the across grain specimens were from the B segment of the billet. Although there appears to be a significant difference in the profilability for the A and B segments of L-1-8, no noticeable strength variation exists between the two segments, as shown in Table 3.

Pulse-echo smears on all specimens and radiographs on weak Specimens A18W, A30W, and A32W were included in Southern's post testing inspection. Smears on the with grain specimens showing the fracture location for each specimen are presented in Appendix H. Smears on weak Specimens A18W, A30W, and A32W are presented in Figure 88. A photograph of the radiograph made of weak Specimens A18W, A30W, and A32W is shown in Figure 89. The radiograph gave no insight into why these three specimens were weaker. The size of the high absorption spots (about the same as that observed for L-1-4 but much smaller than those observed for L-16-7) was considered about normal for ATJ-S.

While inspecting the pulse-echo smears for L-1-8, it was noted that most specimens failed at or near large signal/noise indications. A simple test was conducted to examine for a relation between these large signals, the fracture location, and strength. This test consisted of selecting those smears from the L-1-8 with grain group where fracture occurred at or near quite large signal/noise indication within the gage section on the basis that they should be weak. From the 46 specimens, 11 were selected to be weak on this basis. The results of this inspection are given in the following table.

<u>Specimen</u>	<u>Tensile Strength psi</u>	Relation to L-1-8
		<u>Strength, With Grain</u> Mean = 5007 psi Standard Deviation = 283 psi
A5W	5180	Above average
A10W	5300	1 Standard deviation strong
A11W	5000	Average
A14W	5090	Average
A21W	5030	Average
A28W	5160	Above average
A29W	4780	Almost 1 standard deviation weak
B27W	5020	Average
B36W	5290	1 Standard deviation strong
B38W	5000	Average
B43W	4950	Below average

Photographs of the smears complete with fracture location indications for 11 specimens are shown in Figures 90 through 95. Of the 11 selected to be weak, 2 were one standard deviation above the mean strength, 2 were classed as above average strength, 5 were average strength, 1 was below average strength, and 1 was almost one standard deviation below the mean strength. Thus, for this group of specimens only 1 out of the 11 selected as being weak could be classed as weak, while the other 10 would be classed in the average/strong category. In summary, fracture occurs near large signals, but large signals do not necessarily indicate weakness.

#### ATJ-S Billet L-4-6

Lockheed had previously used L-4-6 in a round robin evaluation conducted at four locations. L-4-6 became part of this program by Lockheed releasing Southern's destructive data on 28 tensile bars to Avco. Avco had previously performed NDT tests on these 28 bars; however, the results of

these NDT tests were not available for inclusion in this report. The complete results of Southern's destructive tests on L-4-6 were reported to Lockheed.

The cutting plan for L-4-6 and machining of specimen blanks were done by Lockheed. The cutting plan is shown in Figures 96 through 105. The 28 tensile bars tested by Southern were from Slabs 2, 4, 6, and 8 and were oriented in the with grain direction. Upon receipt of the tensile blanks from Lockheed, Southern made density measurements and machined the blanks to the tensile test configuration shown in Figure 106. The specimens were loaded to failure at 70°F and 3000°F using the gas-bearing tensile testing apparatus. This testing was done during the early stages of development of Southern's weak/strong inspection procedure; therefore, some of the inspections used for the other billets such as pulse-echo and electrical resistivity were not performed.

The results of testing on L-4-6 are tabulated in Tables 4 and 12. The mechanical properties are presented in Table 4, and the liquid absorption results along with the ultrasonic velocity measurements for the  $\frac{1}{4}$ -inch sections are tabulated in Table 12. Stress-strain curves were presented in the work previously referenced, and thus will not be included in this report. The envelope for the stress-strain curves complete with points of fracture for the 70°F evaluations (Slabs 4 and 8) is presented in Figure 107.

The average with grain tensile strength for the L-4-6 specimens tested at Southern at 70°F was 4910 psi with a standard deviation of 380 psi. At 3000°F, the average with grain tensile strength was 6065 psi with a standard deviation of 345 psi. The 70°F evaluation of L-4-6 is comparable to the average with grain strength of 4960 psi with a standard deviation of 610 psi for all ATJ-S tested at Southern prior to March 10, 1969. Overall, the with grain strength at 3000°F for L-4-6 was below 6300 psi, which is about average for the ATJ-S tested at Southern. However, of the two slabs from L-4-6 that were evaluated at 3000°F, Slab 2 had an average strength of 5930 psi while Slab 6 had an average strength of 6200 psi, which is comparable to other ATJ-S tested at Southern. From the 70°F evaluation, the two weak specimens were T44W at 4200 psi and T91W at 4300 psi. In view of the ATJ-S data evaluated at Southern prior to March 10, 1969, both specimens were weak by at least one standard deviation in strength (4350 psi).

Specimens from L-4-6 were perhaps the first to undergo a formal post testing inspection procedure at Southern. Black and white photographs at 10X were made of the fracture faces for the weak/strong Specimens.

mens T44W and T91W/T42W and T93W. Also, 10X flicks were made on weak Specimens T44W and T91W. These will be included in the discussion on the flick inspection for these specimens to be presented in the next section on the discussion of experimental results. The post testing inspection for L-4-6 consisted primarily of liquid absorption measurements on the  $\frac{1}{4}$ -inch fracture and  $\frac{1}{4}$ -inch removed sections from the long end of the fractured specimen and velocity measurements on a  $\frac{1}{4}$ -inch section taken from about  $\frac{1}{8}$  to  $\frac{3}{8}$ -inch behind the fracture face of the short end of the specimen. The liquid absorption and ultrasonic velocity measurements were among the first made at Southern on graphite. In fact, the velocity measurements were made on hand-cut sections. Therefore, these measurements were unrefined and somewhat inaccurate when compared with the later measurements.

Test results from L-4-6 are plotted in Figures 108 through 114. Figures 108 and 109 are plots of tensile strength versus section bulk density and absorption, respectively. The relations observed earlier between strength, density, and absorption were again confirmed; that is, direct relation between strength and density, and indirect relation between strength and absorption. Note that this same relation held for the 3000°F evaluations also. The relation at 70°F appears much stronger when weak Specimens T44W and T91W are omitted.

As mentioned previously, these absorption measurements represent our earlier efforts and thus are somewhat inaccurate. The following table compares various absorption values measured for L-4-6 to those measured later for L-1-4 and L-1-8:

Billet	Sec Density (gm/cm <sup>3</sup> )		% Absorption		% Total Porosity		% Open Porosity		UTS (psi)	
	Avg	s.d.	Avg	s.d.	Avg	s.d.	Avg	s.d.	Avg	s.d.
L-1-4	1.818	0.008	4.7	0.4	18.1	0.4	8.6	0.6	4909	338
L-1-8	1.812	0.009	5.2	0.3	18.4	0.4	9.5	0.4	5007	283
L-4-6 Slab 4	1.79	0.01	5.8	0.3	19.5	0.3	10.3	0.4	4710	282
Slab 8 (Initial Evaluation)	1.80	0.04	5.6	1.4	19.0	2.0	9.9	2.2	5110	375
Slab 8 (Current Evaluation)	1.826	0.004	4.7	0.2	17.7	0.2	8.6	0.2	5110	375

Inspection of this table reveals a systematic shift in the absorption results. For example, the strengths of the billets are fairly comparable, although it is apparent that Slab 4 of L-4-6 was clearly the weakest sample. Note that although Slab 8 was the strongest material, it had low density, high absorption, and high porosity when compared with L-1-4 and L-1-8. If true, this would negate the relations reported thus far between strength and the monitors density, absorption, and porosity. Some of the specimens from Slab 8 were later vacuum dried and rerun--these data are also shown in the table above. Note that the corrected density is the highest value and the values of absorption and porosity are the lowest of those shown in the table. Thus, the previous relations of strength and porosity remain intact.

Continuing, Figures 110 through 113 are plots of section bulk density, porosity, 0.02 percent offset tensile strength, blank ultrasonic velocity, blank bulk density, and ultimate tensile strength versus specimen position for Slabs 4 and 8 (70°F evaluations). The absorption data plotted here were from the early evaluations and were on the  $\frac{1}{4}$ -inch fracture section of the long end of the specimen. Although these data include inaccuracies primarily resulting in a systematic shift, many of the trends observed earlier still are reflected. For example, in Figures 110 and 112 for Slabs 4 and 8, a 0.02 percent offset strength-section bulk density correlation is in evidence, although the values for density seem to be oversensitive at a few points. Perhaps the best correlation is depicted in Figure 112 for Slab 8 between 0.02 percent offset strength and the monitors open and total porosity. A relation here is fairly consistent for all specimen positions. Figures 111 and 113 show fairly consistent correlations between tensile strength and the blank monitors and density for both Slabs 4 and 8. Here it is perhaps significant that Figure 111 depicts three curves for blank velocity, density, and tensile strength which are, in effect, concave upward; whereas, Figure 113 depicts these same three curves concave downward. This may relate to pressing conditions.

Figure 114 is a plot of tensile strength versus blank ultrasonic velocity for L-4-6 at 70°F and 3000°F. Here it is significant that similar relations of increasing strength with increasing velocity still hold at both temperatures. The relation at 70°F appears much stronger when weak Specimens T44W and T91W are omitted.

Figure 115 is a photograph of the radiograph of weak Specimen T91W. Inspection of the radiograph revealed no significant relationship between the fracture location and high and low absorption spots. It is of interest to note that the low-absorptive appearing line, parallel with the longitudinal

axis, appearing on the small fracture segment of the short end of the tensile specimen was a scribed line on the surface of the specimen and not a flaw in the material.

### ATJ-S Billet L-6-3

Billet L-6-3 was part of the overall program conducted for Lockheed to characterize graphite for design data. The destructive data were later released to Avco by Lockheed for use in this program. Lockheed made the cutting plan given in Figures 116 through 118. Avco executed the cutting plan by removing specimen blanks from the billet and nondestructively testing each of them. The results of Avco's ultrasonic and alcohol penetrant inspections complete with fracture locations are given in Appendix J. After completion of the NDT evaluations, the blanks were forwarded to Southern where density measurements were made on the blanks, the blanks were machined to the test configuration shown in Figure 119, and the specimens were loaded to failure in the gas-bearing tensile testing apparatus. Evaluations were made in the with and across grain directions at 70°F, 3000°F, 4500°F, and 5500°F. The complete results of Southern's destructive tests on L-6-3 were reported to Lockheed. Upon completion of destructive tests, the fractured specimens were sent to Avco for further inspection before being subjected to Southern's post testing inspection.

Similar to L-4-6, L-6-3 was evaluated when Southern's weak/strong inspection procedure was in its early stages of development. As result, the pretest inspections of electrical resistivity and ultrasonic velocity measurements and pulse-echo smears were not made on blank specimens. However, the liquid absorption measurements were made later in the program and, unlike L-4-6, contain the high degree of precision that was developed during the course of the program.

The results of testing on L-6-3 are tabulated in Tables 5 and 13. The mechanical properties are presented in Table 5, and the liquid absorption results along with the section ultrasonic velocity measurements are presented in Table 13. Stress-strain curves for the with grain evaluations at 70°F, 3000°F, 4500°F, and 5500°F are given in Figures 120 through 123, respectively; for the across grain evaluations, at 70°F, 3000°F, 4500°F, and 5500°F in Figures 124 through 127, respectively.

For L-6-3 in the with grain direction, only 4 specimens were tested at 70°F and 3 each at 3000°F, 4500°F, and 5500°F. In making the cutting plan, no intent was made to position specimens over NDT flaw indications. At 70°F, tensile strength ranged from 4520 to 5500 psi with an average strength of 5010 psi. At 3000°F, tensile strength ranged from 6080 to

7140 psi with an average of 6770 psi; at 4500°F, from 7240 to 8160 psi with an average of 7550 psi; at 5500°F, two values of 4450 and 3320 psi with an average of 3880 psi. It should be noted that the tensile strengths reported for 5500°F were not true ultimate values because there was no peaking and fractures were not obtained at this temperature. For these runs, total length of the specimen increased from 6.000 to 6.375 inches. The strength values reported are those for a total axial strain level of 0.025 in./in. in the specimen. Specimen T2W at 4700 psi and T3W at 4520 psi were regarded as being weak. However, in view of all ATJ-S tested at Southern prior to March 10, 1969, these were not weak by one standard deviation of the mean (4350 psi or less).

In the across grain direction, three specimens were tested at 70°F, three at 3000°F, four at 4500°F, and three at 5500°F. At 70°F, tensile strength ranged from 4040 to 4350 psi with an average of 4200 psi; at 3000°F, from 5040 to 5520 psi with an average of 5320 psi; at 4500°F, from 6300 to 7000 psi with an average of 6820 psi; at 5500°F, from 3150 to 4180 psi with an average of 3600 psi. None of these high temperature specimens were considered weak.

Test results from L-6-3 are plotted in Figures 128 through 139. Strength versus the with grain monitors section bulk density, absorption, total porosity, open porosity, closed porosity, and section ultrasonic velocity are given in Figures 128 through 133, respectively. Strength versus these same across grain monitors are given in Figures 134 through 139, respectively. Because of so few data points for each evaluation, and because the monitor data were tight, no trends in the data are apparent.

#### ATJ-S Billet L-9-10

Scrap from Billet L-9-10 and the next two billets to be presented (L-10-6 and L-11-4) consisted of a total of 60 bars which were tested together. All three billets were part of the overall program conducted for Lockheed to characterize graphite for design data. The cutting plan shown in Figures 140 and 141 was drawn by Lockheed and was used for all three billets. No intent was made to position specimens over NDT flaw indications. Scrap from these three billets was shipped to Avco by Lockheed for machining tensile blank specimens and for performing NDT evaluations on same. After the NDT evaluations were completed, Avco shipped the blanks to Southern for destructive testing. After completion of destructive testing, Lockheed released these data to Avco for use in this program. The complete results of Southern's destructive tests on these three billets (L-9-10, L-10-6, and L-11-4) were reported to Lockheed. The fractured specimens from all

three billets were returned to Avco for post testing inspection before being subjected to Southern's post testing inspection procedure. Some of the results from NDT performed by Avco on bars from L-9-10, L-10-6, and L-11-4 were made available to Southern, but these were not particularly revealing under the circumstances.

Upon receipt of test blanks from the three billets from Avco, Southern made bulk density measurements, machined the blanks to the tensile test configuration shown in Figure 142, and loaded the specimens to failure in the gas-bearing tensile testing apparatus. Unfortunately, all the tensile specimens were machined to a final configuration shown in Figure 142 which had too much diameter reduction in the first step-down radii. This undoubtedly influenced strengths and failure locations -- too many specimens failed at or near the flags. In most instances, this precludes the possibility of one finding a disparate strength reducer in the specimen fracture face, such as an obvious inclusion, void, or pre-existing crack. Although these specimens are not ideal for disparate flaw studies, they are useful in obtaining some information on background variability. Similar to L-4-6 and L-6-3, these specimens were tested when Southern's weak/strong inspection procedure was in its early stages of development. As result, the pretest inspections of electrical resistivity, ultrasonic velocity measurements, and pulse-echo smears were not made on the blank specimens. However, the liquid absorption measurements made on sections from the fractured specimen were of more recent date and thus reflect data results with a higher degree of precision than was obtainable at first with this procedure.

For L-9-10, tensile evaluations were made in the with grain and across grain directions at 70°F and 4500°F. Five specimens were tested for each condition. The results of testing on L-9-10 are tabulated in Tables 6 and 14, with the mechanical property results being presented in the former and the absorption results along with section ultrasonic velocity in the latter. Stress-strain curves for the with and across grain evaluations at 70°F and 4500°F are presented in Figures 143 through 146.

Billet L-9-10 was weak. In the with grain direction at 70°F, tensile strength ranged from 3290 to 4000 psi with an average value of 3730 psi; at 4500°F, from 5880 to 7340 psi with an average of 6500 psi. In the across grain direction at 70°F, tensile strength ranged from 3540 to 3820 psi with an average of 3670 psi; at 4500°F, from 5080 to 5680 psi with an average of 5540 psi. At 70°F, the strengths for L-9-10 were about 1200 psi (with grain) and 400 psi (across grain) below the average for ATJ-S tested at Southern prior to March 10, 1969. Thus, at 70°F, all five of the with



grain evaluations and three of the five across grain evaluations were weak by at least one standard deviation based on average ATJ-S tested at Southern. As mentioned earlier, the specimen configuration used resulted in an excessive number of fractures in the area of the flags and the tangent to the gage diameter, refer to Table 6. At 4500°F, the with grain strength showed a 74 percent increase over the value at 70°F (from 3750 to 6500 psi). Perhaps the elevated temperature helped to solve some of the L-9-10 problems evidenced by the low strengths at 70°F.

Specimen T7W, weakest at 70°F in the with grain direction, fractured outside of the gage section in the radius. Our pulse-echo inspection indicated a large number of  $\frac{1}{16}$ -inch flaw indications in this specimen. This was the only specimen to provide such indications and was the only with grain specimen to fracture in the radius. As photographs of pulse-echo signals were not being made at the time of this inspection, the signals observed for this specimen cannot be illustrated.

Before subjecting the failed specimens to liquid absorption measurements, the fracture faces for specimens from L-9-10 were examined visually for flaws, and the location of the fracture with respect to the center of the gage section for each specimen was recorded. Also, the fracture faces of the weak-strong specimens were photographed at a magnification of 10X for further study. From these, photographs of the fracture faces of Specimens T5W and T7W will be presented in the later discussion of the results.

Test results for L-9-10 are plotted in Figures 147 through 158. With grain strength at 70°F and 4500°F versus the density, absorption, total porosity, open porosity, closed porosity, and section ultrasonic velocity are plotted in Figures 147 through 152, respectively. Across grain strength at 70°F and 4500°F versus these same section monitors are plotted in Figures 153 through 158. Although a limited number of data points were available for each test condition, good strength-monitor correlations are shown for the with grain direction. As observed earlier, tensile strength had a direct relation with the section monitors bulk density and velocity but had an indirect relation with the section monitors, absorption, total porosity, and open porosity. The same relations hold for the 4500°F evaluations as for the 70°F evaluations. A surprisingly strong direct relation is shown in Figure 151 between with grain tensile strength at 70°F and closed porosity. Previously, the relation here has been weak primarily because of the narrow range in the values measured for closed porosity. At 4500°F, this relation though weaker is still apparent. The across grain tensile strength-section monitor relations were not so well defined. This resulted primarily because the range of the monitor data in

the across grain direction was small. However, at 70°F the across grain strength-section monitor relations observed earlier for the with grain evaluations were confirmed in general; that is, direct relation between tensile strength and bulk density and velocity; indirect relation between tensile strength and absorption, total porosity, and open porosity. At 70°F, the relation between across grain tensile strength and closed porosity is somewhat obscure. At 4500°F, the relations between across grain tensile strength and the section monitors appear to have the opposite relations that have been observed thus far. However, the relations appearing here for this evaluation stem primarily in each case from Specimen T4A which had low strength.

#### ATJ-S Billet L-10-6

Recall that scrap from billets L-9-10, L-10-6, and L-11-4 consisted of 60 bars which were tested together to obtain design data for Lockheed. Avco machined blank specimens and performed NDT on the bars. No intent was made to position specimens over NDT flaw indications. Southern machined the bars to tensile test configuration, conducted tensile tests, and performed its weak/strong inspection procedure. The tensile data were released to Avco by Lockheed for use in this program. The complete discussion on the handling and processing of L-9-10, L-10-6, and L-11-4 specimens was given in the previous section on L-9-10.

For L-10-6 (as for L-9-10 and L-11-4), tensile evaluations were made in the with and across grain directions at 70°F and 4500°F. Five specimens were tested for each condition. The results of testing for L-10-6 are tabulated in Tables 7 and 15 with the mechanical property results being presented in the former and the absorption results along with section ultrasonic velocity in the latter. Stress-strain curves for the with and across grain evaluations at 70°F and 4500°F are presented in Figures 159 through 162. Individual stress-strain curves for each evaluation are presented in the referenced report.

Of the three billets (L-9-10, L-10-6, and L-11-4), Billet L-10-6 had intermediate values of strength. In the with grain direction at 70°F, tensile strength ranged from 4150 to 5510 psi with an average of 4690 psi; at 4500°F, from 6500 to 8040 psi with an average of 7150 psi. In the across grain direction at 70°F, tensile strength ranged from 3240 to 4070 psi with an average of 3570 psi; at 4500°F, from 5560 to 5960 psi with an average of 5720 psi. Thus, the 70°F strengths for L-10-6 are only about 300 psi (with grain) and 500 psi (across grain) below the average ATJ-S tested at Southern prior to March 10, 1969. At 70°F, two with grain specimens, T3W at 4350 psi and T9W at 4150 psi, and two across grain specimens,

T5A at 3240 psi and T9A at 3480 psi, were weak by at least one standard deviation based on average ATJ-S evaluated at Southern. Again, the specimen configuration used resulted in an excessive number of fractures in the area of the flags and the tangent to the gage diameter, refer to Table 7. At 4500°F, the with grain strength showed a more normal 52 percent increase (from 4690 to 7150 psi).

Before subjecting the failed specimens to liquid absorption measurements, the fracture faces for specimens from L-10-6 were examined visually for flaws, and the location of the fracture with respect to the center of the gage section for each specimen was recorded. The fracture faces of the weak/strong specimens were photographed at 10X magnification for further study -- no significant flaws were observed in the fracture faces.

Test results for L-10-6 are plotted in Figures 163 through 174. With grain strength at 70°F and 4500°F versus the section monitors bulk density, absorption, total porosity, open porosity, closed porosity, and section ultrasonic velocity are plotted in Figures 163 through 168, respectively. Across grain strength at 70°F and 4500°F versus these same monitors are plotted in Figures 169 through 174. It is apparent in inspecting these figures that the section monitors offer poor correlations for tensile strength for this billet. It is probable that the specimen configuration was the overriding factor affecting this result. Therefore, these data are presented primarily for the purpose of comparing the average properties of L-10-6 with those of L-9-10 and L-11-6 (the next billet to be presented) from the standpoint of demonstrating the effects of bad specimen configuration upon results. Since all the specimens are of the same configuration, the average strengths may be some measure of relative background strengths of the three billets.

#### ATJ-S Billet L-11-4

Again recall that scrap from Billets L-9-10, L-10-6, and L-11-4 consisted of 60 bars which were tested together to obtain design data for Lockheed. Avco machined blank specimens and performed NDT on the bars. No intent was made to position specimens over NDT flaw indications. Southern machined the bars to tensile test configuration, conducted tensile tests, and performed its weak/strong inspection procedure. The tensile data were released to Avco by Lockheed for use in this program. The complete results of Southern's tensile evaluations were reported to Lockheed. The complete discussion on the handling and processing of L-9-10, L-10-6 and L-11-4 specimens was given in the prior section on L-9-10.

For L-11-4 (as for L-9-10 and L-10-6), tensile evaluations were made in the with grain and across grain directions at 70°F and 4500°F. Five specimens were to be tested at each condition. However, for L-11-4, Specimens T8W and T2A were broken in process before test. The results for testing for L-11-4 are tabulated in Tables 8 and 16 with mechanical property results being presented in Table 8 and the absorption results along with section ultrasonic velocity in Table 16. Stress-strain curves for the with and across grain evaluations at 70°F and 4500°F are presented in Figures 175 through 178.

Of the three billets (L-9-10, L-10-6, and L-11-4), Billet L-11-4 provided the highest values for strength. In the with grain direction at 70°F, tensile strength ranged from 4450 to 5170 psi with an average value of 4830 psi; at 4500°F, from 7140 to 8380 psi with an average value of 7760 psi. In the across grain direction at 70°F, tensile strength ranged from 3770 to 4240 psi with an average value of 3950 psi; at 4500°F, from 6020 to 6500 psi with an average value of 6300 psi. Thus, the 70°F strength for L-11-4 is only about 100 psi below the average ATJ-S tested at Southern prior to March 10, 1969, in both the with and across grain directions. At 70°F, no specimens, with or across grain, were weak by one standard deviation based on the referenced average. Also, at 70°F the specimen configuration used resulted in an excessive number of fractures in the area of the flags and the tangent to the gage diameter, refer to Table 8. However, at 4500°F, the location of the fractures had a more normal distribution. Also, at 4500°F, the with grain tensile strength showed a 61 percent increase (from 4830 psi to 7760 psi).

Before subjecting the failed specimens to liquid absorption measurements, the fracture faces for specimens from L-11-4 were examined visually for flaws, and the location of the fracture with respect to the center of the gage section for each specimen was recorded. The fracture faces of the weak/strong specimens were photographed at 10X magnification for further study -- no significant flaws were observed in the fracture faces.

Test results for L-11-4 are plotted in Figures 179 through 190. With grain strength versus the section monitors bulk density, absorption, total porosity, open porosity, closed porosity, and section ultrasonic velocity, respectively, are plotted in Figures 179 through 184. Across grain strength at 70°F and 4500°F versus these same monitors are plotted in Figures 185 through 190. Although the specimen configuration was a factor (especially for L-10-6) and only a limited number of data points were available for each test condition, the strength-monitor relations observed up to this point were confirmed, especially in the with

grain direction at 70°F. As shown in Figures 179 and 184, tensile strength had a direct relation with the section monitors bulk density and velocity. The relation at 4500°F was less apparent. As shown in Figures 180 through 182, tensile strength had an indirect relation with the section monitors absorption, total porosity, and open porosity. The same relations seem to hold for the 4500°F evaluations. As shown in Figure 183, the relation between tensile strength and closed porosity is remote at both temperatures -- the closed porosity data were tight within the 9 to 10 percent range. In the across grain direction, although perhaps less apparent, these same relations seem to hold. As shown in Figures 185 and 190 at 70°F, tensile strength showed a direct relation to the section monitors bulk density and velocity. The relation at 4500°F again is remote. As shown in Figures 186 through 188 at 70°F, tensile strength showed an indirect relation with the section monitors absorption, total porosity, and open porosity. At 4500°F the relation is remote. As shown in Figure 189, the tensile strength relation to closed porosity is again remote.

## ANALYSIS AND DISCUSSION OF RESULTS

Recall that the prime objective of this program is to determine the major flaws of ATJ-S graphite. Of course, there was hope that we could converge upon a failure mode and failure criteria and relate the behavior to theoretical and empirical arguments. Also recognize that when we speak of flaws, we are speaking of departures from the normal heterogeneity of this kind of material to the extent that a property is altered significantly.

There is general information available in the literature and developed here that seems to describe differences in different types of graphite with some fair degree of anticipation. For example, we presented information to the Air Force in a private symposium on April 19, 1968 supporting the argument that the strengths of different types of graphite are inversely proportional to some relation of the porosity when one considers only graphites of the same general maximum sieve size. This is to say that graphites with maximum sieve sizes of about 1 to 4 mils seem to follow the same porosity rule, those with maximum sieve sizes of 4 to 10 mils seem to follow the same rule with values shifted, and those with larger maximum sieve sizes seem to follow the same rule only shifted again. Still speaking of graphites in general, the same argument seems to hold for the relation of modulus to porosity. The authors also presented evidence at the same meeting that the strengths of different graphites (covering different sieve sizes) were inversely proportional to some relation of the background void size which is defined presently as the larger voids that occur repetitively.

Other authors have presented evidence that the strength is inversely proportional to some relation of the grain size.

Earlier in this report, we presented composite plots of strength versus density, open porosity, closed porosity, electrical resistivity, sonic velocity, and other monitors for the ATJ-S involved in this program. These composite plots indicated that there were some correlations between this property and some of these monitors.

Now we propose to inspect in more detail from single billets to see if the same relations still exist, if the relationships can be tightened by a more articulate inspection, and if the correlations can be described by relationships meaningful to the mechanic.

#### ATJ-S Billet L-16-7

The first billet to be inspected is L-16-7. This billet was a bad one in that it had a dry core (detected by both dye penetrant and radiography) resulting from the impregnant not reaching the center 2 or 3 inches of the cylinder. Even though this may have represented poor impregnation, it did provide a gradient in the material that permitted an inspection of its effect even back to the state of the precursor. As a matter of record, the average strength of all specimens from this billet was 4763 psi with a coefficient of variance of 10.5 percent.

Recall that the general data for this billet have been presented earlier under the section of "Experimental Results." Also recall that different types of inspections were made including those on the billet, the slabs, the blanks which are oversized specimens, on the fracture section which includes the fracture face plus up to one-fourth inch, and on the quarter-inch removed section which is a quarter-inch removed from a location extending from one-fourth to one-half inch back from the fracture face. Also, we will be speaking of the short end and the long end where the short end is simply the short half of the broken specimen and the long end is the long half of the broken specimen.

First, let us inspect L-16-7 in terms of the relation between the variables such as strength at fracture versus strain at fracture, as shown in Figure 191. The first observation is that as one of these variables increases, so does the other, essentially in a linear fashion. This is consistent with our prior observations for this graphite and many others. All stress-strain curves fall within a typical envelope, and any given specimen proceeds in the envelope in some random position and fails at

some random point. This is to say that the weak ones are not on the bottom of the envelope nor the strong ones on the top. It is also to say that one cannot assume a single value for strain at failure and calculate strength for a given specimen. It also suggests that there is no detectable relation between ultrasonic or initial modulus and strength or strain at failure in terms of the mechanics of the material.

Values for plus and minus one standard deviation for strength are plotted on the curve. These values were obtained from about 200 different points for several ATJ-S billets and not restricted solely to the data points for L-16-7. We will call them "multiple lumped values." This provides a large sample size from an apparently similar population. These values will be used on other figures to provide a good yardstick for making judgments of disparate behavior of different billets as well as of single specimens -- that is, whether a particular billet or specimen is stronger or weaker than most. Limits are also shown on the curve for strain. These limits were obtained by plotting the standard deviations for strength on the stress-strain envelope and picking off the strains at the maximum and minimum intersects with the envelopes. Thus, the strain limits represent the strain range that one should expect if there were only one standard deviation in strength. This is to say that the range of scatter in strain must be outside of these limits if the arguments concerning the envelope are valid and particularly if this variable has its own inherent scatter. A line has been plotted on the curve for a secant modulus of  $1 \times 10^6$  psi at fracture, and another line has been plotted to fit the data. As you can see, a given range in strength does result in a larger range in strain, resulting from the slope of the line through the experimental data.

A plot of this type can be used in another way that will become quite useful as we proceed to the remaining analyses. One can consider that those specimens with a value below one standard deviation on the negative side are disparate in strength, and those to the left of the minimum strain limit are disparate in strain. Thus, those specimens which are disparate in strength would include 4-2, 6-4, 6-5, 8-6, 6-1, 2-2, and 2-3. Of these, four were from the core, and two had visual flaws in the fracture face. One had high open porosity. The data points to the left of the strain limit include 10-4, 6-3, 2-3, 6-4, 4-2, and 6-5. Of these, two were from the core, one had a visual flaw in the fracture face, one had high open porosity, and one (10-4) had a bad stress-strain curve which makes it suspicious that indeed its strain probably was higher and it was not strain-disparate. This stress-strain curve is shown in Figure 192. The remaining specimen that was disparate in strain was 6-3. We have found nothing wrong with this specimen, even though it was marginal on strength. The stress-strain curve for this specimen is shown in Figure 193 -- it looks all right.

The real disparates may be those that show in the lower lefthand corner of Figure 191 which are in the zone of being disparate both from the standpoints of stress and strain. These specimens include 2-3, 6-4, 4-2, and 6-5. Of these, two were from the core, one had a visual disparate in the fracture face, and one had a high open porosity. Thus, all are accountable. Later we will give more detail for each of these disparates. The envelope within the strength and strain limits may represent the inherent behavior of the material that can be improved only by production methods and truncating profiles. As a matter of interest, the strength and strain at fracture for NS-4 are also plotted on Figure 191. Recall that NS-4 is a precursor for ATJ-S. It is interesting and probably more than fortuitous that the values for NS-4 fall rather closely on a straight line extrapolation of the data for the ATJ-S. This infers that the enhancement resulting from impregnation is an orderly thing related to some changing parameter and does not involve a shift to an entirely new mechanism of failure for this graphite after impregnation.

Now let us inspect another plot of variables as shown in Figure 194, where we have strength versus initial elastic modulus. Our observation here would be that there is no relationship that one could relate to mechanics or could relate by correlation, not merely because all the data for the ATJ-S fall within an extremely tight range of values for modulus compared to scatter, but also because by no law of mechanics known by us could this small change in modulus induce an increase in strength that could account for the range shown. When one inspects the curves we mentioned earlier for graphites in general, one does not find this strong a relationship. Certainly for the ATJ-S data alone the variance is such that no relation could be extracted. It seems that covariant influences must be operating such as test scatter in modulus, reading the stress-strain curve, lattice variability in the material, or other material phenomena.

Figure 195 is a plot of strength versus density where density was measured first from the blanks and then later from the fracture section. First, one notes that there does seem to be a trend of increased strength with increased density, although the relation is not tight. Secondly, one notices that contrary to expectations, the use of section densities did not tighten the data compared to using the blank densities. Further, one would expect the section densities statistically to fall to the left of the blank densities, but this did not happen. There is a question of the precision of measurement of density, particularly for the thermogravimetric technique on the smaller sections. We have not resolved this entirely in terms of the observation that we are making at this point, but the precisions seem to be within 2 to 3 percent.



Recall from the composite plots that closed porosity was not a monitor of strength in that all specimens, weak or strong, had about the same closed porosity at about 9 percent. Surprisingly, even NS-4 had about the same closed porosity as ATJ-S. Thus we pass this monitor.

As seen in Figure 196, the relation between strength and open porosity was rather tight; whereas the coefficient of variance for the lumped data was about 11.0 percent, the coefficient of variance about the curve as obtained in a regression analysis even without truncating the disparates was only about 7.6 percent. Thus, each specimen that had a different open porosity was, in effect, a different material. The disparate specimens, as obtained from this plot of strength versus open porosity, would fall outside of the limits of two standard deviations (95 percent) from the curve and would include 6-5, 8-6, and perhaps 2-3. Note that this list does not include 4-2, 6-4, and 2-2 (which had been selected as disparate from the plot of strength versus strain at fracture) because they had high open porosity or were from the core; when inspected in relation to the open porosity curve, they are not disparates but are a different material. This is profiling of gradients rather than truncation of disparates in this case.

Other information is shown on Figure 196. The solid curve designated as Curve ① is a least squares fit of Knudsen's porosity relationship which was used for the regression analysis. It fits the data rather well and gives a coefficient of variance of about 7.6 percent before truncating disparates and 6.3 percent after such truncation. Curve ② is a plot of a relationship developed by the author using the original Griffith relation, correcting the nominal strength by total porosity to obtain a net strength, and assuming that half-crack length is proportional to open porosity. There is a physical reason for this assumption that half-crack length is proportional to open porosity in that inspection of the photomicrographs suggests that impregnation fills the larger background voids first and progressively reduces their size. If the general relation to strength for background voids mentioned earlier is valid and can be applied to different background void sizes in a given graphite, then it follows that the same relation could be used with open porosity in a given graphite. This does not infer that open porosity could be used for comparing different graphites because the impregnation might not reduce the background void size and porosity in the same manner in all cases.

The scatter in values at any given open porosity requires analysis but seems elusive now. After truncating the disparates, the coefficient of variance about the curve is 6.3 percent. This represents the total scatter for testing, material variability, covariant effects, and other

unknowns except for open porosity and disparates. If one were to assume that the parasitic stresses from testing techniques were as high as 2 percent (and they are closer to 0.5 percent), the scatter in the material itself (by difference in variance) would be described by a coefficient of variance of about  $5\frac{1}{2}$  percent. This scatter probably can be attributed to real events such as crack shape, residual stresses, point source variation in graphitization, and other phenomena characteristic of the material. Actually, this is a tolerable range for designers and about the same as reported in the literature for some cast irons.

Figure 197 is a plot of total axial strain versus open porosity. From this view, one can see the same relationship of strain at fracture decreasing with increasing open porosity. However, the range is worse for reasons as described earlier, and the standard deviation is more ill defined. A detailed analysis of the strain behavior is necessary and should be made. Perhaps these data can be so treated at a later date in a fashion similar to that used for strength.

Initial elastic modulus versus open porosity is plotted in Figure 198. There seems to be a general decrease in modulus with increasing open porosity when we include the values for NS-4, but the relationship is not a very strong one. For ATJ-S, no correlation exists. This is to say that the scatter is large compared to the change in property. When lumping the data, the average modulus is about  $1.45 \times 10^6$  psi, and the coefficient of variance is about  $8\frac{1}{2}$  percent.

In all of the open porosity studies, it seems apparent in hindsight that we should have obtained open porosity on both fracture sections from a given specimen and used the highest value. This should tighten the relationships. Much time would have been lost by this procedure, so a trade-off was made.

Thus, the strongest relationship from data inspection seems to be between strength and open porosity, and the problem remains to explain the departure of the disparates from this relationship. First consider radiography on the disparates. Recall that the disparates are Specimens 8-6, 6-5, and 2-3. These specimens were inspected by radiography, and no reproducible high density or low density zones were found. High absorbing specks were seen in about all. However, this was common to both weak and strong specimens. Specimen 2-2 (not disparate to the regression) which had the highest open porosity also had extremely large high absorbing spots. On one specimen, 6-5, the microprobe was used on a polished section in an attempt to describe the specks (results of this inspection are given in Appendix C). No calcium or other foreign element could be

detected. We would conclude at this point that a disparate void would have to be worse than a threshold strength reducer in order to be detectable by our radiography for ATJ-S graphite. Conversely, discontinuities can be seen that are not strength reducers. Really extreme disparates could be truncated in all probability.

Next, the pulse-echo signals that had been obtained on the blanks were inspected to see if that information could be used to describe uniquely the disparates. Several different techniques were used in evaluating the pulse-echo capability. The general approach for handling the logistics of information was to take pictures of the pulse-echo displays on the blanks as obtained for the different modes of operation and then later compare the fracture position with the display. First, the artful technique was used by adjusting the pulse-echo unit to try to maximize the spike during the original pulse-echo work; this proved unsuccessful. Second, the smears were developed. Smears are displays made by photographing the signal on the display tube of the pulse-echo while translating the transducer in a rotary fashion on a one-eighth inch diameter at one end of the specimen. By this technique, the noise being random with position becomes a smear, and a signal stands out as a rather clean spike. This technique seems to hold promise in that about all fractures on good and bad specimens occurred near a rather significant, clean spike on the display for the original blank. However, one could not have picked out the disparate specimens before the fact with sufficient confidence with a signal-to-noise ratio of two to one, or less. This simply means that a flaw in the material became a strength reducer before it provided a large enough signal on the smears to be detected uniquely. However, the fact that most of the fractures in all specimens occurred near a clean spike on the smears of the original blanks makes us suspicious that we may be able to enhance this technique to provide useful information before the fact. The third technique used was to take pictures of pulse-echo signals from both ends of the specimen blanks and then add the signal so that the noise would tend to randomize and the signal would add. Typical pictures of the pulse-echo displays from opposing ends of the blanks are shown in Figure 199; instrument settings are shown in Table 18; the added signal is shown in Figure 200, where the time bases were aligned by the back face signal; added signals are shown in Figure 201, where the time bases were shifted by visual choice. There seems to be an improvement in signal-to-noise ratio when one arbitrarily selects the alignment position. Certainly this method can be justified since the base is really time and not distance. However, much more work on this technique will be necessary before one can say it would do the job before the fact. All of this work is similar to auto-correlation and requires a technique for putting it on the computer so that one can obtain necessary information to judge its value. The time required to construct plots manually is extensive.

The pulse-echo signals were inspected from other points of view and some consistencies were observed. For example, all of the specimens removed from the core had low noise for a given signal input. Thus, one might truncate a flawed area of the nature of a dry core in a given billet. Also, plots of back-face signal strength versus position may provide useful information and a method that would be amenable to thin shapes. Specific experiments on blanks have confirmed some promise in this technique. A table will be presented later wherein we discuss other aspects of pulse-echo. However, the general conclusion at this time is that our pulse-echo techniques can detect large flaws but cannot detect those disparities at the threshold of becoming strength reducers.

Thus, to this point we have not discussed a method to tag those specimens that behaved in a disparate fashion in relation to the curve for strength versus open porosity. The next procedure was to inspect the fracture faces to see if there was evidence of flaws in the fracture plane that might not have extended down into the volume of material and been detectable as a volume effect. Such flaws would have been hard to detect by any of the techniques discussed to this point. Both regular and transparency pictures were made of the fracture faces from both the short and long ends of the specimen. These pictures for the disparities are shown in Figures 202, 203, and 204 for 8-6, 6-5, and 2-3. As you can see, this effort was fruitful. For example, an aligned discontinuity or striation is immediately obvious on the fracture face of the short end of 8-6 as seen in the upper lefthand side of Figure 202. This discontinuity appears to be carbon in nature, plus an alignment of large voids. No foreign element could be found by the microprobe on the rough fracture face; but it is not really intended for use on this rough surface. To enhance visual inspection, the transparencies were overlaid to obtain reinforcement of the fracture pattern. This technique is called the "flicks" because the transparency overlays are placed on a light box, and the upper one is flicked slightly while viewing at a slight angle to normal to see the lower one. Since angled light oriented from the same side on both ends of the specimen has been used in making the pictures, one obtains shadow reinforcement where the voids exist in both fracture faces and lack of reinforcement on the bottom and sides of valleys and ridges. The point is that the void shadow must appear aligned on both views. A pencil sketch of part of what was seen on Specimen 8-6 is included on Figure 202, and one can note the pattern similarity for the aligned discontinuity to that of the regular photograph in the upper lefthand corner. It is quite surprising the number of voids that exist in both fracture faces that do match and enhance each other. During the flicking action one sees hundreds of such voids (connected by curved lines) that seem to be of normal background void size of 6 mils for this material, and then occasionally one sees the larger voids as noted for 8-6. The normal voids are

shown as black dots, and the oversized ones by open symbols. It is difficult to assign dimensions to the voids and the flaw (void cluster, for example) they create. However, the author has chosen to describe the dimension of the cluster in terms of its maximum penetration in toward the center of the specimen and its chordal width. This means that it is not a flaw unless it returns to the circumference or else is extremely severe. Such a conclusion is made primarily because aligned voids on a radius, for example, are found in the strongest specimens and do not seem to be strength reducers.

Now that we have taken care of disparate 8-6, let us consider disparate 6-5. As seen in Figure 203, a collection of large voids that returned to the circumference was found on the flicks for this specimen, also. This specimen was subjected to considerable further treatment in that (1) a replica was made, (2) it was scanned by a microprobe, (3) it was filed down to a plane below the maximum cavity that could be measured before filing, (4) it was polished 6 mils further and a photomicrograph was obtained, and (5) it was vacuum impregnated with epoxy, polished an additional 15 mils, and an additional photomicrograph was obtained. The cavity observed after initial filing is shown in Figure 205. It was larger than 70 mils and may have been the source of fracture. It is difficult to be definite here because one cannot be absolutely sure that this was not simply a depression or cavity at the bottom of a valley undetected by previous measurements on the fracture face.

The 100X photomicrograph of the entire cross section of 6-5 is shown in Figure 206. It was the one obtained after the 6 mils further polish below the cavity (no impregnation), or about 21 mils from the fracture face. Some areas of rather high void count are apparent, but this is of no real disparate nature. At first we thought that the porosity looked much greater. Indeed, the background void size is about  $7\frac{1}{2}$  mils rather than 6 mils normally ascribed to ATJ-S. However, point counts were made of the porosity, and the value was about 14.6 percent. This point count was made including all voids larger than 1 mil. A point count on an average ATJ-S (8-4, not epoxy impregnated) that indeed looked like it had much less severe porosity provided a similar value for porosity of about 13.1 percent. It appeared that Specimen 6-5 looked worse because the solid portion of the structure polished differently, but that the larger voids were indeed quite typical of "good" ATJ-S. It turns out that this agreement in point-count porosity between 8-4 and 6-5 is a fortunate thing in that it lends support to the argument that Specimen 6-5 broke because there was a flaw in a plane and not because it had a higher volume porosity. Also, this corroborates the evidence obtained where porosity was measured by the absorption technique. The open porosity of 8-4 was more typical than

low. The photomicrograph obtained after 6-5 had been impregnated with epoxy and polished an additional 15 mils is shown in Figure 207. Note that the voids no longer appear as black spots, but rather as gray ones because that is the nature of the epoxy. The first observation is that indeed most of the larger voids are a part of open porosity and could be filled. The second qualitative observation is that the so-called minor axis of the voids is smaller than for prior Figure 206 where the specimen had not been epoxy-impregnated. Undoubtedly this is because the epoxy in the voids preserved their edges in this dimension during polishing. Across the major axis, the dimension for the background voids remains about the same or perhaps a little smaller than when not epoxy-impregnated. Porosity measure by point count provided a value of about 8.2 percent or considerably less than the value of 14.6 percent found just 15 mils away but where there had not been epoxy-impregnation. The value of 8.2 percent is quite close to the average value of open porosity from absorption of 9 percent and probably is the better measure of real porosity in that polishing without impregnant would break off the edges of the voids.

Figure 208 shows a photomicrograph of Specimen 8-4 with no impregnation, just mentioned. This specimen had average values of strength and porosity by absorption and is included for comparison later.

As a matter of side interest, a typical photomicrograph from one of the stronger ATJ-S billets that we have inspected in all our work is shown in Figure 209. The smaller background void sizes and lower frequency seem apparent. The view was not large enough to justify a point count.

Thus, we see that disparate 8-6 had average values of open porosity near the fracture as measured by point counts. More data on the point-count method will be presented later. Let us return to the final disparate.

Photographs and flicks of Specimen 2-3 are shown in Figure 204. Note in Figures 191 and 196 that it was borderline in terms of one standard deviation for the lumped values of strength and fell about on the 95 percent probability limit for the regression to open porosity. Unfortunately, there was material loss from one large zone. Hence, the 75 x 150 mil zone of aligned voids would represent a minimum flaw size in plane. This flaw is clear in the regular photograph of the short end. The flicks must be viewed to confirm that the aligned larger voids occur in both halves of the fracture face.

Now we have accounted for those specimens that are disparate by one standard deviation to the lumped values or by 95 percent probability

to the curve of strength versus open porosity. All three had flaws in the fracture face that would not have influenced a volume sufficient to influence open porosity on a fracture section.

As a matter of interest in the sensitivity of the point-count method, photographs and flicks of Specimen 2-2 are shown in Figure 210. This specimen had the highest open porosity by absorption and the lowest strength. Since it fell on the curve of strength versus open porosity, it was not disparate to this curve. Note that there were large background voids (open circles on the flick sketch) over the entire surface inevitably returning to the circumference. This specimen was polished to 15 mils below the fracture surface without impregnation (see Figure 211), where a point count provided a porosity of 29 percent. This is about twice the value of 13.1 percent obtained by point count on 8-4, which was an average specimen. The specimen was then epoxy-impregnated, polished 15 mils, and a point count of 16.5 percent obtained, Figure 212. The comparison of values of porosity by absorption and point count ( $> 1$  mil) can be seen in the following table for all data discussed to this point:

<u>Specimen</u>	<u>Open Porosity by Absorption</u>	<u>Closed Porosity by Absorption</u>	<u>Porosity by Point Count on Nonimpregnated Specimen</u>	<u>Porosity by Point Count on Epoxy Impregnated Specimen</u>
8-4 (average)	8.3	8.6	13.1	-
2-2 (highest open porosity)	14.7	8.5	29.0	16.5
6-5 (disparate)	8.2	8.9	14.6	8.2

Thus, the point-count method is qualitatively related to open porosity by absorption. Also, the higher open porosity of Specimen 2-2 is confirmed since it has been shown that most of the porosity above 1 mil is open.

Background void sizes also were obtained on Specimen 2-2 from Figure 211. They were larger than is typical for ATJ-S (6 mils) and in the range of 8 to 11 mils. More inspection would be necessary to converge more tightly on the value.

Now let us see if other monitors exist by inspecting Tables 19 and 20 wherein we have arbitrarily chosen a "selector" and determined whether or not that selector correlated with strength, a monitor, with NDT, or with some other selector. A correlation was assumed to exist when a selector was capable of picking out a particular performance over half of the time. Actually, in making up Table 19, the facts from the various data were assembled and analyzed from the standpoint of the chosen selector. Table 20 was then prepared as a summary of Table 19. Note that the mean and standard deviation values for strength are based on the multiple billets as used for the comparison in the discussion on open porosity and not on L-16-7 data alone. The mean and standard deviation for the other various selectors are based only on L-16-7 data.

In inspecting Table 20, remember that we are searching for selectors that offer promise for correlating behavior. Thus, the ability of a selector to profile is not evaluated here -- only the limits of correlations are inspected. The real question of Table 20 lies in those selectors which do or do not correlate with dry core, weak-strong-average, disparate flaws, and density.

The dry core in L-16-7 was detected successfully. Avco was successful in its efforts using such selectors as pulse-echo, radiometric measurements, and dye penetrant. Southern, too, was successful in detecting the dry core in its tensile specimens using strength, monitors, and NDT as selectors. The successful monitors were high open porosity, high electrical resistivity, and low section density. Successful NDT was pulse-echo of blank specimens in which a low-hash signal was observed for the dry core specimens. Surprisingly, the section velocity did not show correlation to dry core material -- but then NS-4 has about the same velocity as ATJ-S. Further, when using specimen blanks, both density and velocity revealed no correlation.

Correlating weak-strong-average strength met with some success. Here the successful selectors were Southern pulse-echo, the test specimen, and various blank and section monitors. Since low-hash signals on Southern pulse-echo were used as a selector for dry core material earlier, high-hash was then used as a selector for average and high strength (only two specimens, 8-1 and 8-2, being in the high strength category). A good correlation was found here. Further, since high-hash correlated with average and strong specimens and low-hash indicated dry core material, dry core was then used as a selector for low strength. Here, four out of six dry core specimens were weak. Then, to go further, the test specimen itself was used as a selector for weak strength. The criterion here was failure outside the gage section of the tensile specimen. A good correlation was



found for dry core material but not so for material outside the dry core. All six of the dry core specimens failed within a zone defined as the tangent of the gage diameter to the end shanks. This zone included material up to  $\frac{1}{16}$  inch outside the point of tangency. Of these six, four were weak and two were average strength. Thus, we are saying here that the specimen configuration was disparate for the dry core material but was not for regular material. The next selector used was electrical resistivity of the gage section. Good correlation was found in correlating average and strong. High resistivity also was used as a selector to correlate low strength, and low resistivity was used to correlate high strength. However, no correlation was indicated.

Continuing, the section monitors of density, open porosity, and velocity were used as selectors for correlating strength. In correlating low strength, the three selectors used were low density, high open porosity, and low velocity. Low density was the only monitor to indicate a correlation here. Similarly, in correlating high strength, high density, low open porosity, and high velocity were used as selectors. No correlation was indicated here. Then, primarily because there were only two high strength specimens (8-1 and 8-2), average and high strength were lumped together for correlation. The section monitors used for selectors were average and high density, average and low open porosity, and average and high velocity. Good correlations were indicated in each case.

Briefly, the final item to be considered is flaws by pulse-echo. This item is of particular interest because pulse-echo is considered to hold promise for hardware truncation. Avco reported several flaws that were determined by pulse-echo in the slabs of L-16-7 used in this program. Of these, Southern was able to locate specimen gage sections over seven of the indications in the various slabs. Only one specimen of the seven failed at one of these pulse-echo flaws. Further, the two strong specimens, 8-1 and 8-2, were reported as having a cluster and a 40 to 70 percent full CRT scale flaw, respectively. Neither failed at these flaw indications. Efforts by Southern to relate strong signal-to-noise indications to flaws in the fracture face or fracture location were also fruitless.

In conclusion of Tables 19 and 20, L-16-7 contained a dry core which was detectible by various monitors and NDT. Further, dry core material had low strength, high open porosity, and should be regarded as different material from the regular ATJ-S. Being porous in nature, the dry core material was somewhat correlatable using low-hash pulse-echo and the section monitors of low density and high open porosity. Similarly, high resistivity in the gage section correlated. Section velocity did not correlate.

Further, it should be mentioned that the validity and strength of correlations for both dry core and regular material were weakened somewhat due to the limited amount of data available to the various categories and perhaps by the bounds of the categories. For example, there were only six confirmed dry core specimens, only seven low strength specimens of which at least two contained visual flaws, and only two high strength specimens. The bounds were diminishing in that plus or minus one standard deviation was used for all the various selectors and items being correlated; when perhaps correlations could have been tightened by more careful consideration of the bounds for each individual selector.

Now let us consider the effect on design of being able to profile and truncate specimens (and eventually hardware). There are several ways to inspect this question in terms of this billet. Table 21 contains average strengths, variances, standard deviations, and coefficients of variance calculated by different methods. In one case, all values are lumped together, an average is obtained, and variance calculated. This means that there is no consideration of the effect of open porosity or the fact that each specimen is indeed a different material, nor of disparates such as flaws in the fracture faces. In another case the means and variances are calculated by a regression analysis wherein the coefficient of variance represents the departure from the curve of strength versus porosity. In both cases for lumped and regression treatments, values for means and variances have been calculated with and without disparates. To establish typical ranges, some data on Billets L-1-4 and L-1-8 are included for comparison, although these billets will be discussed later. It is apparent that the average strengths of all billets are reasonably close when one learns how to profile and truncate properly. For L-16-7 it is interesting to note that the coefficient of variance for all data lumped together was a high 11.0 percent, reduced to only 10.5 percent by truncating disparates, reduced to 7.6 percent by the proper consideration of the effect of open porosity, and further reduced to 6.3 percent after profiling and truncation of the disparates. Obviously, most of the effect was attributable to open porosity. If one were designing to a 99 percent confidence interval, the design allowable would be about 3400 psi for the lumped data and 4015 psi when one knows how to profile open porosity and truncate disparates. This is a 17.7 percent increase or a significant difference when one is using a factor of safety of 1.2, and justifies efforts to learn to profile and truncate. If design were based on minimum values, the gain would be about 10 percent. The major gain, however, is in confidence of performance that a designer must have in his material and in relaxing from the 99 percent confidence level, as we will justify later.

Another way of inspecting the data is to over plot curves for 1, 2, and 3 standard deviations on the open porosity curve for that case where these values have been obtained from the regression analyses and compare them with the statistics of the lumped values. This has been done in Figure 213 with data points removed for clarity. Refer back to Figure 196 to inspect the positions of data points.

As a compromise between a goal of one standard deviation for profiling and a field practice of 99 percent probability (about the same as minimum values) used in same design, let us compare results at 95 percent probability. Observe in Figure 213 that using 95 percent confidence on lumped values is the equivalent of assuming no open porosity over 11 percent. This would be a total porosity of about 20 percent, or a minimum density of  $1.77 \text{ gm/cm}^3$ . In order to raise the design allowable to 4400 psi at the same confidence, the open porosity would have to be less than about 8.5 percent, or the density at  $1.828 \text{ gm/cm}^3$  or better. Thus, the density limit as determined by this analysis is quite consistent with the experience generated in the field. Obviously different billets could have systematically different means and variances resulting from covariant effects, but a given graphite or billet might be well defined this way. We will inspect this question later.

It also is obvious from the probability limits that considerable increase in design allowable could be obtained if the relation for open porosity does tighten to one standard deviation and if one could truncate to this level either by production techniques or inspection. For example, at  $8\frac{1}{2}$  percent open porosity, the design level could be raised from about 4350 psi to about 4700 psi.

Figure 214 shows a plot of design allowable versus truncation density for different confidence levels on the lumped values and different probabilities for the regression. These are crossplotted from Figure 213. The payoffs are obvious, particularly for moving from two standard deviations to one by profiling and truncation. Again, it is obvious that the assumptions usually made by hardware people based on experience have had a valid analytical basis.

From an inspection of all data to this point, the argument has evolved that strength is a function of open porosity and that open porosity has meaning to the mechanic. Since it may be difficult to inspect small volumes of a billet for open porosity, it would be fortuitous for inspection purposes if there were a relation between open porosity and some other monitor. Fortunately there is, since both ultrasonic velocity and

electrical resistivity correlate with open porosity. This is not a one-to-one correlation for individual specimens and would not work for disparates. But it does exist as an overall trend and is tight with a scatter of only about  $\pm 2$  percent over the base value. See Figure 215 for the plot.

Figure 216 shows a plot of strength versus the Avco  $K\rho v^2$  obtained from Figure E3 of their part of this report and a plot of our value of  $k\rho v^2$ , where the analytical relation of strength versus open porosity and the correlation of velocity versus open porosity shown in Figure 215 have been used. Small  $k$  normalizes to  $1.24 \times 10^6$  psi.

Note that the Southern  $k\rho v^2$  is an analytical prediction based on the basic relation between strength and open porosity plus the correlation between velocity and open porosity, while Avco  $K\rho v^2$  is, by claim, simply a correlation to a line between with grain and across grain strengths. Figure 216 shows a separation of the two curves by about 16 percent while going from  $1.2 \times 10^6$  to  $1.7 \times 10^6$  psi, suggesting that a systematic error of 16 percent would be generated by assuming that the with and across grain relation is valid. However, velocity is a good measure of open porosity for this graphite and hence  $k\rho v^2$  could correlate rather well with strength if the correlation were made directly through open porosity. Unfortunately, velocity does not truncate the disparates and would add the additional 16 percent systematic error in trying to predict absolute values unless the correlation accommodated the open porosity interrelation. Perhaps the correlation between open porosity and velocity can be tightened now that it has been uncovered as such an apt descriptor for this material.

A similar conclusion can be reached for electrical resistivity; however, the correlation is not so tight and again disparates cannot be truncated so well.

This is the story that has evolved from Billet L-16-7. Specifically, failure mode seems to be from void to void, failure criteria may be by equivalent tensile strain, open porosity includes most voids larger than 1 mil, open porosity is a good monitor of strength, and open porosity is relatable to strength by mechanics. Some monitors exist for open porosity such as velocity and electrical resistivity. Disparates such as 70 mil voids (cavities) and gathered large voids (clusters, perhaps) that return to the circumference on 125 mil chords are strength reducers. We must learn to profile and truncate to these limits so design allowables can be increased up to 30 percent. The inherent material variability (with grain) is described by a coefficient of variance of about 6.3 percent. For this

graphite and our current ability to inspect blanks and specimens, 95 percent probability on the regression of strength to open porosity encompasses all data points suggesting that the strength clusters around the mean and may not have the extreme values of a normal distribution curve. Thus, 99 percent confidence may not be necessary.

It is necessary to inspect these arguments in terms of the information obtained from the remainder of the billets. Unfortunately, on most of the other billets the ranges of the properties and monitors were not so broad so that one does not have the opportunity to make such a broad inspection, as you will see. However, they do provide data that permits inspection of limited ranges of the variables, and they provide single specimens having high porosity and disparate natures.

#### ATJ-S Billet L-7-1, With Grain

Billet L-7-1 was used to generate design data for Lockheed, and most of the data went for that purpose. Avco inspected the scrap in a search for disparities and positioned new Specimens 7-1-1 and 7-1-2 over apparent flaws. The important results for the overall data generated for Lockheed and these two special specimens are shown in the following table:

	<u>Specimen</u>	<u>Blank Density gm/cm<sup>3</sup></u>	<u>UTS psi</u>	<u>Section Density gm/cm<sup>3</sup></u>	<u>Ultrasonic Velocity in./μ sec</u>	<u>% Open Porosity by Absorption</u>
Regular Data Specimens	T1W	1.815	5120	1.812	-	
	T2W	1.802	4600	1.799	-	
	T3W	1.793	4000	1.799	-	
	T16W	1.825	4200	1.800		
		1.803	4480	1.802		
Selected Weak Ones	7-1-1	1.778	4420	1.809	0.1032	10.0
	7-1-2	1.771	4220	1.797	0.1010	11.2

Indeed, 7-1-1 and 7-1-2 were weak specimens having strengths of 4200 and 4400 psi. The reason for their low strength was that they had high open porosity, as shown in Figure 217. The data points for these two specimens fall quite close to the relationship of strength versus open porosity that was established for L-16-7 and well within 95 percent confidence.

Velocity did serve as a monitor in this case, as shown in Figure 218, where the values for the data points fell quite close to the curve developed for L-16-7 for velocity versus open porosity. Thus, again, we see that velocity is a good correlator for strength when the cause of strength reduction is high open porosity.

#### ATJ-S Billet L-1-4, With Grain

L-1-4 was another ATJ-S billet where Avco obtained pulse-echo information on slabs and then removed the blanks so that a flaw would be in the gage section of subsequent specimens. After receiving the blanks, we exposed them to our NDT and monitor inspections, machined them to specimens, obtained stress-strain to fracture, and then submitted the sections to the inspection by monitors.

Generally these blanks seemed to have a quite narrow range of density, as though they had been truncated by virtue of their selection from the billet or that indeed this billet was extremely uniform. The average mean with grain strength for lumped values with the disparates was 4909 psi. The coefficient of variance was 6.8 percent. With truncation of two disparates, the mean strength was 4962 psi, and the coefficient of variance 5.5 percent. The mean density of the blanks was 1.824 gm/cm<sup>3</sup> with one standard deviation of 0.004 gm/cm<sup>3</sup>. These numbers demonstrate the uniformity of the blanks.

This billet did provide us with one new disparate and a further opportunity to check the confidence that one can have in a 95 percent probability about a regression relation to open porosity.

The stress-strain envelope for all specimens is shown in Figure 53. Note again that the point of fracture seems to be random in the envelope. However, it does appear that two of the weaker ones, A10W and A12W, fractured on the upper end of the envelope in this case.

Values for strength were plotted against strain at failure as shown in Figure 219. NS-4 data are included for comparison. Also, the values for one standard deviation for the lumped data on multiple billets and for the data on L-1-4 are included. Strain limits are shown as determined for prior Billet L-16-7. The first observation is that A12W was disparate in strength, and A12W plus A10W were disparate in strain. All other specimens fell above the strength and strain limits established for one standard deviation for the lumped data of multiple billets. Again there appears to be a linear relation between strength and strain at failure having a slope of less than unity when one ignores the NS-4 data.

The next plot of properties is shown on Figure 220, where we have strength versus blank and section densities. The strength versus density for L-16-7 is plotted on the curve and passes quite near the mean value for L-1-4. Contrary to the behavior observed for L-16-7, the density of the sections was less than the density of the respective blank in every case but four. This infers that fracture does seek out a low density zone, since we are quite sure that the precision of our section density measurements was adequate in this case.

Additional plots of one property versus another are not presented here for this billet because they revealed nothing significant and can be found in earlier sections of the report.

Now let us discuss the regular NDT inspections that were conducted on these blank specimens. First consider pulse-echo. Avco did find a "large" signal for A12W but not for A10W. For our smears, there were large spikes at the fracture face for both specimens, but these were not much different from spikes seen on average specimens so that, before the fact, we did not predict that these were weak specimens. Further, even with hindsight and with further review of the smears, we could not separate the signals seen for these two from the signals seen for the others. The signals are there, but one does not seem to be able to make a judgment. Pictures of all smears and the fracture location were presented earlier.

Our radiography uncovered nothing unique about any of these specimens. Only a few specimens were inspected for this billet.

The plot of tensile strength versus the section velocity is shown in Figure 60. There appears to be no correlation from visual inspection; an inspection by rank correlation reveals that one cannot reject the hypothesis of no relation with 95 percent probability. It is also rather obvious that one could not have picked out the disparates with a velocity relationship in a unique fashion. The velocity for A12W was lower than the average but above that of several; the velocity for A10W was near average.

The plot of strain at failure versus open porosity is shown in Figure 221 and does show a positive correlation of decreasing strain with increasing open porosity. The extent that A10W and A12W were strain disparates is quite obvious on this particular plot. The strain values for all other specimens fell within the one standard deviation for the multiple lumped values. The stress-strain curves for A10W and A12W are shown in Figures 222 and 223 and were both normal.

Strength versus open porosity is plotted in Figure 224 with curves shown for the mean and the 68, 95, and 99 percent probability as obtained from the regression analysis for this billet. The same curve form developed for L-16-7 was used in this analysis, and the mean strength versus open porosity curve for that billet is shown for comparison. Notice that all of the data are rather tight within one standard deviation based on lumped values of 95 percent probability based on the regression analysis, except for the disparate A12W. Thus, we see that A10W was not disparate when considered in light of its open porosity. Also, the mean strength curve is in close agreement with the one obtained for L-16-7. Although they are not plotted, the 95 percent probability values are in good agreement for the two billets. A rank correlation test on the relation between strength and open porosity provided a 99 percent confidence that one could reject the hypothesis of no correlation between the two whether one did or did not include the disparates.

The coefficient of variance about the regression was 5.2 percent with the disparates included and 4.5 percent without them. This is a small coefficient which is in good agreement with the value obtained for L-16-7 about its regression.

Now let us review the search that was made for an explanation of the behavior of the disparate. For Specimen A12W, the search was not difficult. Note in Figure 52 that this specimen had an obvious void at its surface (uncovered during the machining operation) that was about 27 mils across the major axis. The pictures of fracture faces are shown in Figure 225 along with a sketch made from the flicks. From the pictures the hole appears to have a depth of about 35 mils and a width around the circumference of perhaps 35 mils. From the flicks, the dimensions of the hole are quite close to those of the pictures. Also, from the flicks there appears to be a general area of voids larger than the background void sizes across the lower third of the specimen. These must have been essentially in a plane since the open porosity of this specimen was not particularly high.

Specimen A10W was inspected in a similar manner to A12W since it was disparate when considered in all ways except by open porosity. The search was not so fruitful, as can be seen in Figure 226. Judging from the defocus obtained on the long end and the focus that was possible on the short end, there was material loss. An alignment of large voids was found, as shown for one of the views obtained from the flicks, but this cluster did not seem particularly severe. As a matter of side interest, additional information has been shown on the views obtained from the flicks for this



specimen showing the many background voids that are obvious and the scalloped nature of the line that seems to connect them. These are not flaws but a typical view of the fracture face as seen in the flicks. Perhaps one should not expect to find an obvious flaw in A10W since it was disparate in strain but not much in strength and not at all in terms of its open porosity.

There were some interesting side observations made while developing Figure 224 and making the search for the disparates. At first, we had listed A10W, A12W, and A28W as disparates. Of course, A12W was immediately tracked down by the large void observed after machining the specimen. But a review of the open porosity relation and the flicks could not find an explanation for A10W and A28W. When open porosity was obtained on the short ends of the specimens, the value for A28W was increased from 6.8 percent to 8.6 percent and the value for A10W increased from 8.7 percent to 10.4 percent. In both cases, these new values of open porosity caused the data points to fall almost on the curve for strength versus open porosity that had been developed for L-16-7 and L-1-4. This provided much confidence in open porosity as a major factor in strength. It also reconfirms our prior remarks that one should obtain open porosity from both ends of the specimen and use the larger value in developing the relationship since the fracture could occur at either end of a large cluster.

When we review the data for L-1-4, we find that for the lumped values the mean was 4909 psi, and the coefficient of variance 6.8 percent when A12W and A10W are included; the mean increased to 4962 psi at a reduced coefficient of variance of 5.5 percent when the two specimens are excluded. From the regression analysis, the coefficient of variance is reduced to 5.2 percent with A12W and A10W and reduced further to 4.5 percent without A12W and A10W. The general observations made earlier for L-16-7 concerning 95 percent probability as a reasonable goal when profiling and truncating remains essentially valid.

Again we ask the question as to whether or not open porosity can be correlated to an inspection technique that can be employed on specimens, billets, and shapes. Figure 227 is a plot of open porosity versus velocity and includes a curve for the relation found for L-16-7. Note that the data points for L-1-4 are systematically below the curve for L-16-7. Another way of saying this is that the open porosity values are systematically about 1 percent lower for a given velocity than would be predicted from L-16-7. Thus one would miss a strength prediction by 250 psi if one used the same velocity to open porosity correlation for these two different billets. When

the L-1-4 relationship of velocity versus open porosity is inspected by rank correlation, one cannot reject the proposition of no relation within a probability of 95 percent.

In summary, L-1-4 did not contain the dry core of L-16-7, and the density of the blanks as received seemed quite tight. Design allowables were quite close to those obtained for L-16-7 after truncating open porosities at about 11 percent. Also, specimens from L-1-4 with high open porosity resulting from "islands" behaved similarly to those from L-16-7 from the dry core. Further, the L-1-4 specimens having average porosity behaved about the same as those from L-16-7 that were not in the dry core or had large open porosities. Truncated means and variances were about the same. The rank correlations obtained for the different relationships were revealing. At 95 percent confidence one could not reject the hypothesis that there was no relation between strength and velocity or between velocity and open porosity. But one could reject the null hypothesis for strength versus open porosity with a 99 percent confidence. Thus, open porosity for this billet was the only monitor of strength but seemed to defy being monitored by some other available monitor. This is not alarming since the scatter was small anyhow after truncating two disparates.

#### ATJ-S Billet L-1-4, Across Grain

Several across grain specimens were prepared from Billet L-1-4 to permit at least a preliminary look at the behavior in the material in this orientation. Avco removed blanks from the billet, conducted NDT, and sent them to us for our work. As a matter of reference, the across grain strength for this billet (without disparate B14A) was 4090 psi with a coefficient of variance of 2.9 percent. This value of mean strength for L-1-4 compares with a value of 4060 psi for the lumped multiple billets that have been used as reference for the with grain direction. Thus, the across grain strength for L-1-4 is fairly typical. The coefficient of variance is lower than usual since the value for multiple billets was about 9.5 percent. It is typical that the scatter in with grain data is higher than the scatter for across grain. Since the values from most of the properties monitored were so tight, very little information was gained for relationships and correlations, but one important disparate was uncovered.

The plot of strength versus strain at fracture is shown in Figure 228 with mean and one standard deviation values for the multiple billets and the mean value for the lumped data for this billet. Values for NS-4 in the across grain direction are included. The same observation holds for this type of plot as for the with grain direction in that strength

increases linearly with strain at fracture. A single straight line fits rather tightly on the data ranging from the disparate B14A with a strain at fracture of only 2.4 mils to the precursor NS-4 with a strain at fracture of 3.7 mils to the average value for the across grain direction of about 6 to 6.5 mils. It is immediately obvious from this figure that the only disparate is B14A in that all other values fall well within one standard deviation for strength.

Strength versus section bulk density is shown in Figure 229. Curves are included relating these two variables for the with grain direction and for the across grain direction as predicted analytically from the open porosity relationship discussed earlier. There is a correlation between strength and density in this case. Again, B14A shows us an obvious disparate.

Other plots of variables revealed no strong relationships and are not included.

The NDT records were inspected to see if one could have predicted the disparate B14A by either pulse-echo or radiography. In the case of pulse-echo, Avco indicated "small" and "medium" signals at the position of fracture. We found a good signal in our smears near the location of the fracture. However, it is our judgment that this specimen could not have been singled out as a disparate before the fact. As before, the signal seems to be there, but so are others equally strong so that the low signal-to-noise ratio destroys one's confidence in using it or in assigning it a value.

The X-rays of B14A revealed the high absorbing specks common to all specimens. These were considerably smaller than seen in L-16-7, but quite sharp. No other abnormalities were obvious.

Most of the monitors were quite unrevealing. A plot of strength versus section velocity was shown in Figure 67. Obviously the range of velocity is too tight compared to the variances in strength obtained to permit much confidence in a correlation by visual inspection. B14A does stand out as a disparate but could not have been detected by velocity.

Electrical resistivity was inspected as a monitor of strength. As was shown in Figure 68, there was no visual correlation. Rank correlation indicated that one could reject no correlation at only 50 percent probability. Thus, resistivity could not be used as an effective monitor in this case. Also, observe that B14A could not have been detected as a disparate by electrical resistivity.

Strength versus closed porosity is shown in Figure 66. As for the with grain orientation, the closed porosity was quite tight. However, a rank correlation does exist even though visual inspection leaves doubt to significance.

Strength versus open porosity is shown in Figure 230 with multiple lumped values for the mean and one standard deviation and with an analytical curve developed from open porosity in the same fashion as was done for the with grain orientation. In this case the measured mean density was used to calculate an equivalent open porosity, and the curve was positioned by that calculated value and the mean measured strength. Since true density is a somewhat arbitrary value of  $2.22 \text{ gm/cm}^3$ , the curve does not fall through the mean of the data points on Figure 230. It does show the relationship that one should expect. It is visually obvious in Figure 230 that a relationship does exist between strength and open porosity and that only 2 points depart significantly. One is the B14A and the other is B20A. Detailed inspection of B20A revealed nothing. Really, this is not surprising since its strength was within 160 psi of the mean. However, the strength was appreciably less than it would have been predicted from a strength open-porosity curve.

It was not difficult to find the disparate in the fracture face of B14A. As seen in Figure 231, there was a large black spot on the fracture faces about 85 mils on the chord and 90 mils radially into the specimen. The pictures of this spot and the outline obtained on the flicks are shown in Figure 231. The spot was actually an inclined plane with a black, low reflectance appearance, containing small pores, with no pullouts, and surrounded by ridges and valleys of a structure like that found in normal faces. The specimen was polished in a plane normal to the fracture face so that one could observe the nature of the structure of the material below this spot. There was no large inclusion nor body of material that had a different nature of porosity. Also, there was no common particle in both fracture faces that might have cleaved on a common plane. The solid matrix below the spot also seemed typical. The only odd feature was a layer of dust about 0.2 mil thick that seemed to be at the fracture face. This was seen at 400X. Perhaps this evidence alone supports a suspicion that a small tab of paper or some such material was in the flour mix and separated the particles at that stage. Another suspicion was that there was a high or low density compaction plane in this billet and/or specimen. Verbal communication with Arnold Schultz of Avco revealed that a high density "ribbon" 1 inch wide did extend through this billet (from radiography) and intersected Specimens B13A through B25A with the exception of B20A and this one. He also confirmed the small and medium pulse-echo signals obtained on the blank.

The fracture surface for B14A outside of the zone occupied by the spot was fairly typical being flat and rough. However, normal background voids that show as reinforced shadows in both views of the flicks were not so obvious and indeed were difficult to find. Either failure in this direction is not so clearly from void to void, or else the voids were shaped so that they were more difficult to define by the eye. The author suspects the latter.

The results presented here are too meager to make many comments concerning their impact on design. Perhaps the important remarks would be the scatter was typically less than with grain and that dispartes are as active as they are in the with grain direction. Perhaps the designer can gain confidence from the fact that the coefficient of variance of only 2.9 percent would include scatter of both the material and of testing. Certainly it is obvious that most of the scatter in the with grain direction is from the material by this evidence alone.

The data were inspected to see if monitors existed for strength and/or open porosity, and particularly to see if there was a correlation between velocity and open porosity. As shown in Figure 232, visual inspection of the relationship reveals no correlation. Rank correlation indicated that one could reject no correlation at only 80 percent probability, thus confirming the visual observation. (In rank correlations on these types of data, at least 90 percent probability must be obtained before results seem to agree with visual inspection on the scales used. Scales are selected to relate to mechanics.) Good precision was not obtained on velocity for these specimens in that reruns showed scattered results. Perhaps the passages were contaminated in a way not known by us.

In summary, the mean across grain strength was 4090 psi with a coefficient of variance of 2.9 percent indicating typically small scatter for this orientation. The relationship between strength and strain at fracture persists as a linear one as it is for the with grain direction. The range in densities of these specimens was too narrow to obtain meaningful relations or correlations between most properties or between properties and most monitors. Correlations did exist between strength and both density and open porosity. Velocity did not monitor strength or open porosity. The only new observation is that strength may indeed increase with increased closed porosity. An 85 to 90 mil dispartes was a significant strength reducer; unfortunately, none of the inspection techniques found this dispartes before the fact, even though a signal does seem to exist within the noise when one reviews the fracture location in relation to these signals for the blanks. A high density compaction line cut through several specimens but did not appear to be a strength reducer. Ironically

perhaps, this ribbon missed B14A and B20A which were the disparates off of the strength versus open porosity plot.

#### ATJ-S Billet L-1-8, With Grain

Avco subjected Billet L-1-8 to nondestructive testing, cut it on the diameter in two halves called A and B, performed more nondestructive testing on the sections, selected the sites of apparent flaws, removed blanks from over the flaws, and inspected the blanks. These blanks were shipped to Southern where we conducted our nondestructive test, obtained the monitors, machined them into specimens, tested them, and inspected the remnants. The specimens were divided into the two groups from the sections designated A and B. There was some systematic difference in results obtained on these groups, as will be noted. All with grain specimens were from the A section except B26 through B43. A6, A10, A13, A14, A18, A19, A20, A24, A25, A29, and A30 were within  $1\frac{1}{2}$  inches of the center. B28, B31, B35, B38, B41, and B43 were within  $1\frac{1}{2}$  inches of the center.

The average strength on all specimens obtained from this billet was 5007 psi with a coefficient of variance of 5.6 percent. The average density was 1.815 gm/cm<sup>3</sup> with a standard deviation of 0.008. Thus, we see that the density of this billet was a bit low, but that its strength was comparable or slightly higher than the others. Also, we see that there was very little scatter in the strength, even though the specimens had been positioned over flaws. The envelope of stress-strain curves for both A and B specimens is shown in Figure 72. The envelope is fairly typical in that the scatter in extracted properties is fairly tight.

This billet also was quite uniform. Axially, the average strength was 4899 psi for the specimens taken from the top-center and 4935 psi for those taken from the bottom center. The average strength for all top specimens was 4999 psi and for all bottom specimens was 5020 psi. Thus, the radial gradient was equally small for both the top and bottom with the edges having a somewhat higher strength in both cases. The maximum difference in strengths for different zones was  $2\frac{1}{2}$  percent.

Figure 233 is the plot of strength versus strain at fracture, including (1) NS-4 data, (2) the mean and one standard deviation for the multiple lumped billets, and (3) the mean and one standard deviation for this billet. It is immediately obvious that only one specimen, A30W, was a disparate in strength or in strain when compared to the envelope developed for the multiple lumped billets. If one considers only the

data for L-1-8, then the disparates became A18W, A30W, and A32W. For the remainder of the discussion on this billet, we will consider A30W as a disparate, and A18W and A32W were specimens having low values of strength.

The plot of strength versus blank bulk density shown in Figure 234 indicates a systematic shift of the data points to a higher strength than was developed from this relationship for L-16-7. The fact that A18W, A30W, and A32W are different from the other specimens is rather obvious, although density did not seem to explain this difference. By rank correlation one could reject the null hypothesis at a 99.2 percent probability. Hence, again the relationship is seen between strength and density.

The plot of strength versus section bulk density shown in Figure 235 leads to about the same conclusions that were obtained from blank bulk density. The rank correlation was just about the same value at 99.8 percent for a null hypothesis. This is to say that by this analysis the section densities do correlate with strength but no better than do the blank densities.

Both Avco's and Southern's pulse-echo provided no significant guidance to the preselection of the disparate or the weaker specimens. It is true that A18W and A32W had "large" signals, and, indeed, they were two of the three weakest specimens. However, A30W did not have a large signal and, indeed, A5W, A8W, A14W, A16W, A19W, A21W, A27W, A31W, B25W, A32W, and B39W all had large signals but were not weak. From the smears, the eleven largest signal to noise ratios were selected. Eight of these were stronger than the average. Four fractured in the signal; six at the edge of the signal; one fractured away from a signal. Thus, the correlation was negative. One wonders if there were no clusters to scatter a large reflected signal.

By radiography no evidence was obtained that would permit preselection of the weak specimens.

The monitors provided some interesting information on L-1-8. Figure 236 shows a plot of strength versus section velocity and indicates a visual correlation, although a systematic change from that obtained from L-16-7 is shown by the curve on the figure. One could reject the null hypothesis at a 99.9 percent probability. In this case the three weak specimens might have been preselected by low velocity, although only A32W (highest open porosity of all) did indicate positive preselection. The

fact that there does seem to be a relation between strength and velocity for this billet is the first evidence that all of the weak ones may suffer from high open porosity since we have already seen that low velocity, high open porosity, and low strength go together.

A similar plot of strength versus velocity for the B type specimens is shown in Figure 237. Again, the data points are systematically shifted from the curve shown for L-16-7 but in this case do not seem to indicate a correlation.

Plots for strength versus electrical resistivity for the Type A and B specimens are shown in Figures 238 and 239. One could reject the null hypothesis at 99.82 percent probability and, indeed, visual inspection indicates extremely good correlation for Type A. Two of the three weak specimens had the highest electrical resistivity. The third one, A18W, would be difficult to preselect.

At first glance, it appears that strength is a function of closed porosity, as shown in Figure 240. It is interesting to note that the careless use of rank correlation can mislead one. In this case, one would reject the null hypothesis at 98.3 percent probability; it is obvious from visual inspection of the data that there would be a rank correlation. However, the inference that the strength would increase from about 4200 psi to about 5500 psi as the closed porosity increased from 8.7 to 9.2 percent seems ridiculous on the face of it. Undoubtedly the relation is covariant.

Strength versus open porosity with the 95 percent probability limits are shown in Figure 241. Also included are some notes that describe the other monitors for the three weak ones, A18W, A30W, and A32W. It is apparent in this plot that A30W is the only specimen that is appreciably disparate to the 95 percent probability line. Even it falls quite close. It is also apparent in this plot that A32W had the highest open porosity (the two ends were similar at 9.9 and 10.1 percent) of all specimens. One could reject the null hypothesis that there was no correlation between strength and open porosity with 99.96 percent probability. The curve for this relationship for L-16-7 is included on Figure 241 and is not coincidence with the curve obtained for the mean of L-1-8. Obviously there is a systematic difference. However, it falls well within the 95 percent probability limit and within the one standard deviation for the multiple lumped billets.



The relationship for strain to fracture versus open porosity is shown in Figure 242. It was noted earlier that none of the specimens were disparate when compared to the strain limits for the multiple lumped billets. However, A18W, A30W, and A32W remain as the poor specimens and are joined by A20W. Since this was the only place that A20W shows as a disparate or as a poor performer, its stress-strain curve was inspected and found reasonably normal, as shown in Figure 243.

Detailed inspections were conducted on the three weak specimens to gain more information as to why they were weak. A visual flaw was found in the fracture face of A30W, as shown in Figure 244. Note the squiggly at five o'clock on the 10X view of the long end. Inspection under flicks revealed that this area had many voids larger than the background void size. This squiggly is similar to one we found for an earlier specimen where no foreign element (other than carbon) could be found. However, an inspection was not made of this specimen because inspection for foreign elements seems difficult.

The inspections of the two weak ones, A18W and A32W, did not reveal obvious visual flaws in the fracture face. Pictures of the fractures and the flicks are shown in Figures 245 and 246. In both cases one can see the evidence that the fracture proceeded from void to void and that scalloped lines seemed to connect these lines. This is typical for average specimens. Also, one can find numerous voids larger than the background void size in both cases. Since A32W could be explained as having the highest open porosity, A18W was selected for further inspection. It was polished to 10 mils below the fracture face, and 100X pictures obtained across the diameter as shown in Figure 247. The void cluster that was seen in the flicks is immediately obvious on the left side of the picture. Point counts were made of all voids larger than 1 mil in zones on each end and in the middle, as marked in Figure 247. In the zone of the cluster, the point-count porosity was 19.5 percent. Proceeding across the specimen, the values were 13.0 and 12.7 at the right edge. These values would correspond to true open porosities of about 10.7 percent and 8 percent, as obtained by absorption measurements, if one can use the relationships shown in the table presented in the discussion on L-16-7 and plotted in Figure 248 for the numbers obtained using absorption, point count with no impregnation, and point count with impregnation. Perhaps it is only fortuitous that the open porosity of the cluster predicts a fracture strength from the analytical relation of about 4640 psi and A18W had a strength of about 4470 psi. If this evidence withstands further inspection, a void cluster of a given open porosity may be expected to be a strength reducer about to the same extent as a

larger dry core zone or zone that transgresses the entire diameter of the specimen. In the flicks, the bounds of the cluster seemed to be about 40 x 100 mils. On the photomicrograph, it seemed to be about 60 mils on the radius.

Now consider the question as to whether or not velocity could be used to monitor open porosity. As shown in Figure 249, velocity was a good correlator for open porosity with the Type A specimens, no correlator for the Type B specimens (not enough range), but a good correlator for the grouped data. The probability values for the different correlations are shown on the figure. For example, one could reject the null hypothesis at the 99.86 percent probability for the group data. It is apparent from this figure that there was a systematic shift in the data from the relationship found for L-16-7. The shift was small for Type A specimens and larger for Type B specimens. Recall that Type A specimens were from the top section and were weaker both at the center and edge of the billet. For L-1-8, one is obtaining a lower velocity for the same open porosity or the same strength. It is obvious that if one compared the two billets by velocity then one would come to a conclusion opposite to the experimental fact. That is, one would predict a lower strength for this billet than one would obtain by testing. This probably means that velocity cannot yet be used to systematically predict the difference between billets but still is useful in profiling a given billet.

In summary, L-1-8 had a slightly low density at 1.815 gm/cm<sup>3</sup>, but a slightly high strength at 5007 psi compared to Billets L-16-7 and L-1-4. The coefficient of variance was 5.6 percent, indicating little scatter even without truncating the disparates and the two weak ones.

Neither of the disparates nor the two weak specimens could have been preselected by NDT. Velocity, open porosity, and electrical resistivity all correlated the strength but were systematically shifted in comparison to the relationships for L-16-7. Thus, there must be covariant effects. Of the three weak specimens, the weakest, A30W, was easily accounted for by a visual flaw in the fracture face; A32W had the highest open porosity of all specimens and fell reasonably close to the 95 percent limit for the regression of strength to open porosity; A18W contained a void cluster about 60 mils on its bounds having an open porosity (by point-count correlation) that suggests that void clusters behave as strength reducers about to the same extent as dry cores or large zones of low porosity that transgress an entire specimen.

The rank correlations obtained for the different relationships that existed for this billet provide some insight as to their adequacy as a tool to judge data. A summary of these rank correlations is included in the following table:

Null Hypothesis: There is no Correlation

Without Specimen A30W	
<u>Rank Correlation on</u>	<u>Reject N. H. at (%)</u>
$\sigma / \rho$ Blank	99.82
$\sigma / \rho$ Sect	99.82
$\sigma$ /Velocity A Specimens	99.94
$\sigma$ /Resistivity A Specimens	99.82
$\sigma$ /Resistivity B Specimens	89.90
$\sigma$ /Closed Porosity	98.32
$\sigma$ /Open Porosity	99.96
op/Velocity A Specimens	99.98
op/Velocity B Specimens	25.1
op/Velocity A and B Specimens	99.86

The most obvious conclusions are that (1) a value of probability of over 90 percent is required for rejection, and (2) careless conclusions from rank correlations can suggest a relationship that may or may not be consistent with analysis.

#### ATJ-S Billet L-1-8, Across Grain

Recall that Billet L-1-8 had been sectioned in A and B parts for removal of with grain specimens. Across grain specimens also were removed from these same sections with most of them being from a portion near the D/4 location. B6A was from within  $1\frac{1}{2}$  inches of the center; B1A and B2A were within  $1\frac{1}{2}$  inches of the edge; A1A, A2A, A3A, and A4A were all within  $1\frac{1}{2}$  inches of the edge.

The average across grain strength was a typical 4087 psi with a low coefficient of variance of 2.8 percent (like L-1-4) and a total range of only  $\pm 5.9$  percent. This means that the variability of the test method and the across grain strength could total no more than 5.9 percent for these 29 specimens. The average density was 1.808 gm/cm<sup>3</sup> with a standard deviation of 0.011 gm/cm<sup>3</sup>. The uniformity was excellent from all indications in that the specimens removed from the center were not weaker and those removed from the edge were not stronger than the average.

The stress-strain curves are shown in Figure 73 providing further indication of the tightness of values obtained for this billet.

Figure 250 is the plot of strength versus strain at fracture, including a curve of secant modulus of fracture for  $1 \times 10^6$  psi. NS-4 data are shown for reference. Obviously there are no disparities and no specimens that are particularly weak. However, we will select B4A, B11A, and B22A as the weaker ones and observe how they behave in the remainder of the relationships.

There is not much correlation between strength and blank density as shown in Figure 251 where one would reject the null hypothesis at 91.8 percent probability. However, this correlation is tightened when one considers strength versus section density as shown in Figure 252 and the probability increases to 97.5 percent. Evidence seems to be mounting that either there is a systematic error in measuring section density or else the section density of the short end is consistently less by about 0.01 gm/cm<sup>3</sup> than the section density of the long end. Even though controlled experiments have not detected this, most checks on short ends have revealed this. If so, then there are small systematic errors in plots of some of these relationships. This systematic condition could be introduced by the geometry of the load train since any misalignments could be imagined to induce greater parasitic strains at the center than at the ends of the gage section of the specimens. However, the effect should be quite small since the total parasitic strain is less than one percent. Perhaps this is the reason that we are seeing the effect only for groups of specimens where the scatter is extremely small ( $\pm 5.9$  percent range for these specimens). As will be noted, a few more of the fractures (12 to 9) appear to occur toward the center of the gage from a smear signal than toward the end.

No significant relations were found between plots of any of the other properties.

Avco found "very large" pulse-echo signals in Specimens A1A, A2A, A3A, and a "large" one in B14A. We also found significant signals in these, as presented earlier, but no worse than in others. None of these specimens is among the 3 weakest ones. Both our smears and Avco's signals for the three weak ones would not justify preselecting them. It is interesting that we preselected the fracture location within  $\pm \frac{1}{4}$  inch for 19 of the 29 specimens. Pure chance would have given 12 for 24 specimens. For all specimens, fracture occurred in a strong signal in the smear 8 times (B1, B11, B16, B17, B18, B21, B23, and B24); to the left of a large signal and within  $\frac{1}{4}$  inch 14 times; to the right 7 times. Using another criteria, fracture occurred at the edge of a large signal toward the center of the gage 12 times and toward one end 9 times. One continues to wonder if void clusters are the primary strength reducers and minimize the strength of the signals (in terms of signal to noise ratio) from isolated flaws that happen to exist but are not in fact the operating strength reducers for ATJ-S until they become quite large. This would explain the lack of correlation between large signals and fracture location.

Radiography on these specimens indicated high absorption specks quite similar to those mentioned earlier for L-1-4 and considerably smaller for L-16-7. Since there were no particularly weak ones, one should not expect that one should uncover the weak ones by radiography for a  $\pm 6$  percent maximum variation in strength.

Since the strength range was small, one does not expect much correlation with the different monitors. As shown in Figure 86, there was no correlation between strength and velocity, nor, as shown in Figure 87, was there a correlation between strength and blank electrical resistivity. Visual inspection of strength versus total porosity shown in Figure 253 does suggest some correlation. One does not find it when one plots strength versus closed porosity, as shown in Figure 254, but it does show weakly with open porosity as shown in Figure 255. In this latter case, one can reject the null hypothesis with 93.7 percent probability when one uses the maximum open porosities for the three weaker specimens. Recall that these values are suspect of a systematic shift of perhaps 0.2 percent in open porosity. With or without this systematic shift, these three specimens all have open porosities greater than the average, and the two strongest have open porosities less than the average. We really do not intend to inspect the cause of variability for no greater range than typified by these across grain data. However, the consistency of the results makes one suspicious that such an inspection would be worthwhile if all inspection techniques were improved to, say, 1 percent reproducibility.

The relationship between velocity and open porosity is shown in Figure 256 and indicates no correlation. One could reject the null hypothesis at only 84.6 percent probability. Thus, within these narrow ranges, velocity could not be used to monitor open porosity or strength within the limits of reproducibility that we have established at this point for the two measurements. This is to say that one would have to improve the techniques for measuring both open porosity and velocity before one could inspect this material where the coefficient of variance or range was so small. Of course, one might not have to inspect it if it was always this uniform.

In summary, the across grain strength of L-1-8 was typical and averaged 4087 psi with a low coefficient of variance of 2.8 percent and a low range of only  $\pm 5.9$  percent. It is difficult to determine the incremental contribution of test methods, material variability and covariant effects that contribute to the coefficient of variance of 2.8 percent and total range of  $\pm 5.9$  percent. If one truncated open porosities at 9.25 and 9.75 percent, the range of the remaining 10 specimens would be  $\pm 2$  percent to be divided between test methods and material variability (for covariables). The uniformity of the billet axially and from center to edge was excellent. No disparities were found. There were only weak correlations between strength and density, velocity, total porosity, and open porosity. However, one would expect these correlations to be weak because the ranges were so small. There is some suspicion that a test specimen tends to fracture on the side of a low porosity zone that is toward the center of the specimen. In all probability this would be observable only in those cases where the high porosity zone was indeed not much different than its neighbor-material, and hence was not sufficiently different in structure to be much of a strength reducer. That is, we are talking of 1 percent difference in parasitics.

#### ATJ-S Billet L-4-6, With Grain

Billet L-4-6 was used by Lockheed to conduct a round robin at four locations. The original billet size was 8 inches in diameter by 14 inches long. It was cut in eight slabs or discs, numbered 1 through 8, from the top to the bottom, where the top relates to the movable ram during original pressing of the precursor. Specimens were blanked and inspected by Avco; however, at this early stage in the program, we were just developing our inspection techniques as well as our monitoring techniques and did not have the degree of precision that we developed later in the program. Slabs 4 and 8 (center and bottom) were tested at 70°F and provided strengths of 4700 and 5110 psi and average blank densities of 1.801 and 1.807, respectively. Slabs 2 and 6 (top and center) were tested at 3000°F and had strengths

of 5930 and 6200 psi and average blank densities of 1.799 and 1.816 gm/cm<sup>3</sup>, respectively. Thus, at both temperature levels, the stronger slabs were denser. Also, in both cases, the higher density was related to less open porosity, since we have seen that closed porosity was about the same regardless of density or open porosity. In general, this billet was fairly typical of ATJ-S billets, but had a density slightly lower than average; specimen location permitted the observation that the properties had very obvious profiles as a function of radial and axial positions.

The cutting plan for this billet has been presented earlier. The major points to be observed in the cutting plan include the ones just mentioned, that the billet was slabbed and that specimens were removed from different positions on the radius so that radial and axial profiles could be generated for the properties. The remainder of the discussion will concern the 70°F data unless specific reference is made to the higher temperature.

Stress/strain envelopes for specimens from Slabs 4 and 8 are shown in Figure 107. Here we have the first evidence that most of the data were tight with the exception of Specimens 44 from Slab 4 and 91 from Slab 8.

The plot of strength versus strain at fracture is shown in Figure 257 with the mean and one standard deviation for the multiply lumped values, NS-4 for reference, and two data points obtained from strain gages bonded to graphite. It is obvious that Specimens 44 and 91 are the only two that approach being disparate specimens. Indeed, they are practically on the limit for one standard deviation and will be categorized as weak rather than as disparate specimens. This will be further justified later when we see that they fall quite near the 95 percent probability limit on the regression of strength versus open porosity. The two data points shown for specimens where strain gages were used are included to the extent that they are typical of strains measured with small strain gages. This is to say that our small strain gages ( $\frac{1}{4}$  inch x  $\frac{1}{8}$  inch) systematically provide low values for strain at failure when compared with values obtained from our optical strain analyzer or with clip-on extensometers. We are conducting a detailed study of this and now believe that this is a systematic error for strain gages typical of this type of measurement related primarily to (1) poor bond between the glue and the graphite, and (2) the fact that the glue penetrates the voids of the graphite and forms a composite material several mils deep that is not in plane continuum with the remainder of the specimen. Longer strain gages are extremely difficult to install on these small specimens.

Figure 258 is a plot of strength versus strain at fracture for the data obtained at 3000°F. Since the major thrust of this report concerns room temperature data and since a relatively few number of data points were obtained at 3000°F in this program, an extensive analysis has not been made for the purpose of this report. However, it does appear that the strength increases with strain at fracture with a progressively decreasing slope as the stress/strain curves approach ultimate, just as it does at 70°F.

In order to emphasize the profiles of the properties as a function of location in the billet, the data will be presented differently than for prior billets. Figures 259 through 262 contain plots of the more important properties and monitors as a function of their radial positions in the billet. It is immediately obvious that the density and strength curves are concave upward at the top of the billet, still concave upward at the center of the billet, and concave downward at the bottom of the billet. This general observation is true considering both the 70°F and 3000°F data. A careful inspection of the scale used to plot the data suggests that a one percent profile in density is the equivalent of about 3 to 5 percent in strength. The profile for open porosity is included for Slab 8 on Figure 262 and is consistent with the density profile in the same slab. These data on open porosity provide an opportunity to inspect the precision of the measurement where sections from the short end were evaluated several months after the first inspections and found to have values of open porosity within 0.2 to 0.3 percent of the original measurements. Even the inflections on the curve agree with the prior measurements. The values obtained for sections from the short end also are plotted and confirm that there is a difference in the open porosity of sections from the short and long ends, but that this difference is more random than systematic. In three cases the long end had lower open porosity, in two cases it had the highest open porosity, and in two cases it was about the same. Thus, these specimens did not seem to leave a cluster on the short end with much statistical confidence.

Now let us return to a discussion of the profiles. The axial profiles are plotted in Figure 263 and indicate that the strength and density were both appreciably lower at the top of the billet, steadily increasing toward the bottom. At the top, the center of the billet was less dense, whereas at the bottom the center became more dense. Recall that the moving ram was at the top in the precursor. These observations were inspected in relation to the internal pressures that are generated in a powder during the pressing process, and indeed similarities are quite striking. Note from Figure 264 that the hydraulic pressures in a powder decrease proceeding from the moving ram toward the fixed ram, decrease toward the



center on the moving ram end, and increase toward the center on the fixed ram end. Thus, the radial profiles of L-4-6 were consistent with classical behavior but the axial ones were not. Since the manufacturing procedure for the precursor of ATJ-S is proprietary and not known in detail by the writer, it may be that the radial agreement just described is fortuitous. Impregnation, in fact, could be controlling.

A plot of velocity versus blank density is shown in Figure 265. There was a correlation between velocity and density at the 99.9 percent probability that one could reject the null hypothesis. Here again it is obvious that the density as well as the velocity difference was primarily a function of the location of the specimen in the billet particularly related to the slab that it came from.

The results of inspection by pulse-echo and radiography by Avco were not made available to us, so no comments are possible. We did inspect Specimen 91 (a weak one) by radiography and found the normal specks but no other significant information. This inspection was conducted after fracture.

The plot of strength versus open porosity is shown in Figure 266 using average values for Slabs 4 and 8 and specific values for Specimens 44 and 91 (weak ones). Since we suspect systematic errors and possible contamination of the open passageways in those early specimens, individual points are not plotted. It is immediately obvious that the average strengths for the two slabs are quite parallel to the regression curve for L-16-7 and that Specimens 44 and 91 are within the 95 percent probability limit.

During the initial part of the program, before the regression had been established, weak/strong and weak/average inspections were conducted in an effort to detect those properties and monitors that would best flag a weak specimen. Information such as that shown in Table 22 was prepared to permit such an inspection. Recall that these earlier data may have systematic errors; however, it is interesting to note that in this case a specific explanation as to why Specimens 44 and 91 were weak was not obvious when compared with the average values of the remainder of the specimens from the respective slabs. Inspection was a little more fruitful when the weak one was compared with the strongest one, but not consistently so. Meaningful inspection came later when the regression of strength versus open porosity was uncovered, and specimens were inspected to the 95 percent probability limits by the technique of measuring open porosity on progressively smaller portions of material until one was obtaining a point count just a few mils below the fracture face and "flick" readings at the fracture face.

Pictures of the fracture face at 10X magnification of weak/strong specimens for Slab 4 are shown in Figure 267. There was an odd appearance on the short end of Specimen 44 as can be seen at eleven o'clock where the material seemed to be chalky or loosely bonded with some discoloration. However, this appearance was not unique in that it occasionally showed on other specimens that were not weak. Similar pictures of weak/strong specimens are shown for Slab 8 in Figure 268.

Inspection of these two specimens (44 and 91) by the flicks was not particularly revealing, as shown in Figures 269 and 270, where clusters of background voids were found, as well as the ridges composed of background voids connected by scalloped lines. However, these clusters did not appear to be made up of voids larger than background voids and did not seem severe.

The odd zone mentioned earlier for Specimen 44 was inspected by the point-count method by polishing axially until that zone was exposed, as shown in Figure 271. A void cluster smaller than the diameter of the specimen is immediately obvious in the picture. As noted on Figure 271, a point count of voids larger than one mil provides a porosity of 23.2 percent for the end at the fracture face and a lower value of 17.6 percent further removed from the fracture. The average for the total view was 20.4 percent. Since it seems that the precision of this measurement is within about a percent, this may be a significant difference. It certainly appears significant visually. The average value of 20.4 percent porosity by point count would be an equivalent open porosity of about 11 percent if the relationships established for L-16-7 for the unimpregnated polishes are good for this billet. At 11 percent open porosity, this specimen would be predicted from the regression analysis for L-16-7 to have a strength of about 4300 psi, while it actually had a strength of 4200 psi. Thus, it would appear that Specimen 44 was weak because it had a void cluster or a high local porosity of a significant portion (about 60 to 70 mils) of the specimen diameter. The background void size for this area was about  $8\frac{1}{2}$  mils or somewhat larger than the value of 6 mils more typical for ATJ-S.

Similar inspection was made for Specimen 91 from Slab 8, as shown in Figure 272. In this case the specimen was polished normal to the axis to a depth of about 10 mils below the fracture face. Point count of voids larger than one mil provides a porosity of 21.4 percent on one edge of the specimen, 19.1 percent at the center, 21.8 percent on the other edge, and 20.8 percent over all. There was no apparent small cluster. It would appear that in this case there was a high porosity zone having an

equivalent open porosity of about **11** percent that transgressed the entire cross section of the specimen at the fracture but did not occupy enough of the specimen axially to have its full influence on the open porosity as measured by absorption. That is, the open porosity for Specimen **91** measured by absorption was **9.1** percent, but the equivalent open porosity from the point count was about **11.2** percent, or quite similar to that for Specimen **44**.

It is quite apparent when placing these photomicrographs next to those for typical specimens that Specimens **44** and **91** have more porosity than is typical for ATJ-S. The problem of assigning a value to this porosity, however, is quite difficult. Remember that one obtains different values for point count whether one has or has not impregnated the specimen prior to polishing. At this stage, these comparisons are more qualitative than quantitative and undoubtedly contain systematic errors, although they undoubtedly have relevant significance.

Some of this information has design impact. For example, it seems that the bottom of the billet is denser and has less severe profiles. Yet one must remember that the specimens for that area had a higher elastic modulus and no more strain at failure. Perhaps the major thought would be that one could expect to obtain specimens from key locations in a billet to establish the nature of the profile and could then expect to interpolate porosities (and strength) in the areas from which the hardware would be removed. Of course, this infers developing the ability to detect disparities and recognize small porous zones within some confidence.

In summary, Billet L-4-6 had average strengths and densities that were fairly typical for the other billets in this program but did indicate significant differences in strength and density, for example, from slab to slab. The radial strength and density profiles seem to follow some aspects of those that one would expect from the classical hydraulic pressures generated when pressing a powder, although the specific history of this precursor is not known. Both the **70°F** and **3000°F** data seem to profile. Using the Student "t" test, there was 95 percent confidence of a difference in strength between Slabs **4** and **8** (**70°F**) and between Slabs **2** and **6** (**3000°F**). Truncating Specimens **44** and **91** increased the confidence for Slabs **4** and **8** to 99.9 percent.

Two weak specimens were uncovered, **44** and **91**, and their weakness traced by a point count to high porosity at or near the fracture face. Even including the high open porosity for these two weak ones, all strength values fell within the 95 percent probability on the regression curve of strength

versus open porosity developed for L-16-7. When the porosities obtained by point count for Specimens 44 and 91 were converted to the equivalent open porosities, the values for these two specimens fell on the mean strength curve for L-16-7. This provides evidence that small clusters behave as strength reducers about the same as larger dry cores and builds some confidence in the point-count technique.

#### ATJ-S Billet L-6-3, With Grain

L-6-3 was a billet from which design data were generated for Lockheed after Avco and Southern had inspected the blanks. There was no intent to place the specimens over flaws. At 70°F, the strength of the four specimens ranged from 4500 to 5500 psi with no disparities. At 3000°F, the range in strength was 6100 psi to 7100 psi with no disparities. At 4500°F, the range was 7200 to 8200 psi with no disparities. At 5500°F, T11W had a low ultimate; however, the strains at this temperature are so large, and no fracture was obtained so that a detailed inspection of T11W was not warranted. Also, the stress-strain curve was poor.

The following table shows the significant properties and monitors for the 70°F data:

	Strength psi	Density Long End gm/cm <sup>3</sup>	Density Short End gm/cm <sup>3</sup>	Blank Velocity in./μ sec	Open Porosity Long End	Open Porosity Short End	Closed Porosity Short End
T1W	5500	1.814	1.812	0.1044	8.15	8.46	9.91
T2W	4700	1.823	-	0.1042	7.60	-	-
T3W	4520	1.828	1.829	0.1040	7.25	7.50	10.19
T16W	<u>5310</u>	<u>1.820</u>	<u>-</u>	<u>0.1048</u>	<u>7.84</u>	<u>-</u>	<u>-</u>
	5010	1.821	1.820	0.1044	7.71	7.98	10.05

There is no correlation for properties, and the monitors say little. If one applies a weak/strong comparison of T1W and T3W, the weak one was denser with a lower open porosity but did have a slightly lower velocity. All data fell within one standard deviation and the 95 percent probability of regression for strength versus open porosity. Inspection of pulse-echo data from Avco and Southern reveals little new information. Actually, no correlations or analytical relations should be expected within this small range without further inspection for clusters.

For the 3000°F experiments, T6W was the weakest but still not disparate. It had the lowest density by 0.001 gm/cm<sup>3</sup>, a slightly lower velocity, and a higher open porosity of 8.1 percent compared to 7.3 and 7.4 percent for the other two specimens at 3000°F. Closed porosity was the same for all three.

In summary, there were not enough data points at any given test condition to uncover new information from L-6-3 with grain specimens. Also, there were no new disparates that could be submitted to inspection. The only significant remark might be that the 3000°F results followed 70°F trends.

#### ATJ-S Billet L-6-3, Across Grain

The across grain results for L-6-3 were obtained as design data and were about as unrewarding in disparates as the with grain ones for this billet. Similar to the across grain specimens from other billets, the range in strengths was quite tight, being from 4000 to 4300 psi at 70°F.

Since the densities, velocities, and open porosities were also tight, and since there were no disparates, correlations and analytical relationships could not be inspected. Of course, this speaks well for the material.

#### ATJ-S Billet L-9-10, With Grain

Billet L-9-10 was a data billet from which a few specimens were tested at 70°F and 4500°F for both grain orientations. At the time the data were reported it was called simply a weak billet with low density, since at 70°F the average with grain strength was only 3730 psi and the average across grain strength 3670 psi, with average densities for the specimens of 1.813 and 1.824 gm/cm<sup>3</sup>, respectively. The low with grain strength was the result of a shifted range rather than just a few low values in that the range was 3290 to 4000 psi. The modulus was about average at 1.47 x 10<sup>6</sup> psi. At 4500°F, the strength was about 75 percent higher than the

room temperature strength compared to a typical increase of 50 percent. Thus, the billet regained some of its strength at the higher temperature.

Avco blanked the specimens, conducted NDT, and we tested them. At the time, we did not have our NDT and monitors at the precision that we developed later. Since four of the nine room temperature specimens (with grain and across grain) broke at or near the flags, we again were displeased that we had used a specimen with a diameter of 0.188 inch and a tangent radius at the gage section of only one inch. Only two or three of the specimens should have broken at or near the flags by statistical distribution. There were not enough specimens to be conclusive. The properties and some of the monitors of primary interest are shown in Table 23.

Inspection of this table confirms the fact that the average strength and density for this billet were quite low and immediately point out the two weakest specimens, T5W and T7W. Since all of the open porosities were so high, a good check of profiles was not anticipated. Strength versus density is plotted in Figure 273 for the with grain data at both 70°F and 4500°F. Correlation does seem to exist at both temperatures, even though there are insufficient data points to draw much of a conclusion or conduct a rank correlation.

The NDT inspection by Avco indicated several large signals in T7W that were outside the gage section. This specimen did have extremely high open porosity which was revealed to extend on the surface into the gage section by Avco alcohol penetrant testing. The fracture location missed both types of flaw indications. Radiography revealed little.

Now consider the monitors. Some comments can be made concerning strength versus velocity shown in Figure 274, where strength does increase at both temperatures with increasing velocity, and T7W with the lowest strength also had the lowest velocity. These specimens as a group had the lowest velocity of any billet, as was noted earlier on the composite plots. Unfortunately, data on electrical resistivity was not obtained before fracture.

A plot of strength versus open porosity is shown in Figure 275 for both 70°F and 4500°F. First, consider the 70°F data. It is immediately apparent that T7W was weak because it had a high open porosity and fell within the 95 percent probability limit for the regression of strength to open porosity. Hence, it was not a disparate in relation to this regression. T5W was disparate in that it fell well outside of the 95 percent probability

limit. It is interesting to note that the relationship seems to hold at 4500°F of decreasing strength with increasing open porosity. More data points are required.

For the 70°F with grain specimens, strength seemed to increase with increased closed porosity. This phenomenon persists.

Pictures of the fracture ends at 10X magnification are shown for T5W and T7W in Figure 276. Unfortunately, the long end of T7W was destroyed early in the program by inspection techniques used at that time. This really is not serious, because the low strength value of this specimen has been explained in terms of high open porosity measured by the more reliable technique of absorption. Do observe the chevron in the fracture face of T5W at nine o'clock on the long end. (It is also clear on the short end under stereo microscope.) Since this specimen had nominal open porosity, a flaw in the fracture face is suspect.

The usual flicks were not obtained for these specimens at the time; recall that the long end of T7W was destroyed.

The short end of T7W was polished normal to the axis to a depth of 10 mils below the fracture face, and the photomicrograph is shown in Figure 277. Point count of voids larger than one mil on an unimpregnated coupon gave a porosity of 23.15 percent and a background void size a little larger than typical of 7.5 mils. This point-count porosity provides an equivalent open porosity of 12.4 percent which is about what would be expected as compared to the open porosity of the short end of 13.79 percent as measured by absorption. Recall that the equivalent open porosity is obtained from the relationship of point count to absorption values first developed for L-16.7. Thus, open porosity remains as the explanation for the low strength of T7W.

As a point of interest in the technique of point count, Figure 278 contains a plot of points occupied over points applied versus points occupied. One can see that a reasonable precision is obtained with about 70 points occupied and perhaps with even 30 or 40 points occupied by using an internal average and truncating the one high and one low value from the first 50 points occupied. A second inspector obtained 20.6 percent porosity, and a third obtained 21.2 percent on the view shown in Figure 277. This technique needs more development as related to graphite but seems reproducible.

The following data restates the situation for Specimens T5W and T7W:

<u>Specimen</u>	<u>Tensile Strength psi</u>	<u>Open Porosity %</u>	<u>Point Count</u>	<u>Equivalent Open Porosity %</u>	<u>Remarks</u>
T5W* (Disparate)	3580	9.8	-	-	Radius break. Large Visual V-shaped discoloration
T7W (Weak)	3290	13.6	23.4	12.4	Large P-E radius break

\* Fracture location uncertain -- two breaks.

T7W provided large pulse-echo signals by Avco and Southern and was weak because of high open porosity both as measured by absorption on the fracture section and as confirmed by point count. It fell within the 95 percent probability limit for the regression of strength and open porosity. T5W probably was weak because of a disparate in the fracture face recorded visually as a large "V" but made suspect by the facts that half of the fracture face was destroyed early in the program. Also, there was a dual fracture introducing some uncertainty as to which fracture came first, and that first fracture appeared to be in a tangent radii.

Even though T1W was not disparate to this billet, it was disparate to the regression for strength versus open porosity that will be presented later for the composite data. For this reason, it was inspected under stereo microscope at 10X and by the flicks. As shown in Figure 279, a predominance of quite large voids larger than the background void size was obvious. Undoubtedly a cluster existed but did not seem worth pursuing on so "poor" a billet.

In summary, Billet L-9-10 was weak, had low density, and high open porosity. Correlations did seem to exist with density, velocity, and open porosity both at 70°F and 4500°F, although there are not enough data points to confirm this. The strength of all but one specimen was within the 95 percent probability limit developed for L-16-7. One weak specimen was well defined by open porosity and one disparate somewhat defined visually and by pulse-echo but confused by local fracture locations.



### ATJ-S Billet L-10-6, With Grain and Across Grain

Billet L-10-6 was a data billet from which only minimum information was gathered. Specimens were blanked and inspected by Avco and machined and tested at Southern prior to our full development of the monitors. The average strength was a little low, being 4690 with grain and 3570 psi across grain at 70°F. Average densities for these lots were 1.829 gm/cm<sup>3</sup> and 1.831 gm/cm<sup>3</sup>, or a little on the high side.

For these specimens a gage diameter of 0.188 inch was used rather than 0.250 inch as for most other billets excepting L-9-10, L-10-6, and L-11-4. This may have been an unfortunate decision, since nine out of ten specimens fractured at or near the flag, as reported earlier. Since we have used gage diameters as small as 0.125 inch on both ATJ and ATJ-S graphites with no apparent difficulties, and since this problem from experience seems to prevail primarily with faulty billets, we have concluded that breaks at or near the flags are aggravated by the events associated with faulty billets.

No new information was gained by us from this billet concerning NDT and the monitors. We did not receive all the NDT results from Avco, and ours were inadequate at the time. All monitors fell about where predicted from other billets but were too narrow in range to detect an effect. That is, for data at 70°F and with grain specimens, the section density range was 1.807 to 1.824 gm/cm<sup>3</sup>, the range in open porosity was 8.6 to 9.6 percent with an average of 9.2 percent, the range in closed porosity was 8.9 to 9.3 percent, and the range in velocity was 0.0996 to 0.1016 in. /μ sec with an average of 0.1007. T9W was the only specimen that might be called a disparate, but with such meager information, it was not inspected further. Actually, it fell quite near one standard deviation for this billet.

Specimen T5A (across grain) had a quite low modulus of 0.79 x 10<sup>6</sup> psi at 70°F but did not seem worth inspecting.

In summary, L-10-6 (1) was a little weaker than most billets, (2) produced questionable fracture locations, (3) had tight monitors that fell where expected, (4) had no significant disparates, and (5) provided no new input other than confirming the average values of properties and monitors within the prescribed limits.

#### ATJ-S Billet L-11-4, With Grain and Across Grain

Billet L-11-4 was another data billet for which minimum replications were obtained at 70°F and 4500°F. Specimens were blanked and inspected by NDT at Avco and then finally machined and tested at Southern during the early stages of developing our techniques for inspection and monitors. The billet was typical and had average strengths of 4830 psi with grain and 3950 psi across grain at 70°F. Average densities for these lots were 1.814 gm/cm<sup>3</sup> and 1.821 gm/cm<sup>3</sup>, respectively. This billet provides some baseline values for monitors at 4500°F.

As for L-10-6, a smaller gage diameter of 0.188 inches was used and excessive fractures at 70°F occurred near the flags and the tangent to the gage diameter. At 4500°F, fractures were distributed properly, possibly as a result of release of stress intensifications by more plasticity. Three out of eight fractured near the center of the gage.

Little NDT information was received from Avco, and it was not revealing. All monitors were tight and fell about as expected in relation to other billets. For 70°F and with grain specimens, the average open porosity was 9.6 percent, and the average velocity 0.1015 in. /μsec.

There were no disparates. If we ever pursue the questions involved on the plus side of the regression analysis, Specimen T7W will be a candidate since it had a strength of 4920 psi which is higher than the L-16-7 regression analysis predicts as 4500 psi for 10.3 percent open porosity.

In summary, this billet provided average properties and monitors with no disparates.

#### Comparison of Different Billets, With Grain

Now that we have discussed the billets individually, we will (1) compare them all to L-16-7, (2) inspect composite plots of all data for each monitor, and finally, (3) develop a table for those specimens that have been screened as disparates and those that have been screened as weak.

Table 17 provides a summary of the average strengths, densities, open porosities, and other properties and monitors for the different billets in one reference. Note that all billets had average strengths between 4909 and 5010 psi except for L-16-7, which had the dry core, and L-9-10, L-10-6, and L-11-4, which had either quite high open porosities or a suspect specimen design.

Figure 280 provides a plot of strength versus open porosity for the average values of the billets and weak specimens for the different billets compared to the regression of L-16-7. Two points are particularly apparent. One is that the average values for the different billets all fall within 95 percent probability of the regression for L-16-7, and most fall within 68 percent probability. The second observation is that the specimens which have been defined as weak ones and which have been defined as weak ones because of either high open porosity or large void clusters also fall quite close to the regression. The inference is that open porosity is a strength reducer, regardless of its particular source or nature (from a dry core or an unimpregnated island).

Figure 281 provides a plot of velocity versus open porosity obtained from a data fit for L-16-7 and the average values for the other billets. It is apparent that a rank correlation does exist between different billets, although it is certainly not as tight as previously found when one inspects the data for individual billets. This would lead one to conclude that velocity could be used to correlate with open porosity on the basis of individual billets within the precision that we are seeking for our truncations.

Figure 282 shows the plot of strength versus density, including the curve developed for L-16-7 for the regression analysis to open porosity plus averages for the different billets. With the exception of Billet L-9-10, all fall within 95 percent probability and quite close to 68 percent probability. This is inevitable, since the relation to open porosity has been developed and closed porosity remained about constant for all billets.

Figure 283 contains plots of strength versus velocity with the relationship developed for L-16-7 and includes the average for all billets. One could not use velocity to predict strengths between billets with the confidence that one could for a single billet.

The next several figures to be discussed were introduced in the earlier section of "Experimental Results" and include plots of strength versus the monitors where all data points are shown, and least squares fits with 95 percent probabilities for the composite data have been developed and are shown. Also shown is some reference information developed in the program for HLM graphite, which is another precursor for another polygraphite.

Strength versus open porosity for the composite data is plotted in Figure 9. If one truncates all specimens that have been described as disparates, then all data points except two fall within the 95 percent regression, and one of those is above the one standard deviation so it was not inspected. The second one that falls outside the limit was T1W from L-9-10, and that entire billet is considered atypical. Also, a large cluster of voids was apparent in the fracture face from inspection visually (10X) and by flicks. The disparate specimens have their data points flagged, and the number of the particular specimen is noted beside the data point. Another interesting observation can be made from this figure which is that if one then truncated all specimens with open porosity by absorption greater than 11 percent, all the data points except the one mentioned would fall within about one standard deviation from the multiple lumped mean. (This would be a tremendous advantage in establishing design allowability.) When equivalent open porosities obtained by point count are used to account for clusters, the fit becomes tighter. The fact that the dry core specimens and those with clusters as determined by point count fall rather neatly on the regression over the range of open porosity between the average for the ATJ-S and the NS-4 suggests that as one impregnates this material one is progressively filling the open porosity, and the strength increases in a uniform fashion. Perhaps even the mechanism of fractures does not change proceeding from NS-4 to ATJ-S.

Figure 10 is a composite plot of all data for strength versus the section bulk density. In this case the relationship is not so clear. Two of the weak specimens, 2-2 and 4-2, had quite low densities and were from the dry core. T7W had quite low density and low strength, but no dry core was found in that billet. The other weak specimens and the disparates are rather uniformly distributed through the density range so that we could not really expect to extract weak specimens from density alone unless they had extremely low density. This means that the fact that the closed porosity remains constant for all specimens tends to mask the more pronounced effect of open porosity, as they are both involved in the density of the material. That is, density is not as sensitive as open porosity because of the fixed closed porosity.

The plot of strength versus closed porosity is shown in Figure 11, plus a least squares fit of the ATJ-S data without including NS-4. The reason for not including NS-4 is obvious, since there is not a clear relationship between strength and closed porosity. As a matter of fact, it appears that strength increases with increasing closed porosity. This is not a new thought, but the rank correlation is quite strong. One should limit one's observations with the particular comment that about

all of the weak and disparate specimens have less than average closed porosity. Again, this is not inconsistent with prior thoughts in that more micro porosity may well tend to blunt crack extension.

The plot of strength versus ultrasonic velocity for all billets is shown in Figure 12. Again the NS-4 data were not included in the least squares fit of the Knudson regression for the obvious reason that it does not fit this relationship. As a matter of fact, the NS-4 and ATJ-S have about the same average velocity. It would appear that initial impregnation decreases the velocity, and subsequent impregnation tends to increase it until it obtains the value that might be called average for ATJ-S, which is about returning to the same value as it had initially as NS-4. This phenomenon is rather difficult to understand from the standpoint of macro mechanics and must be related to carbon-like to graphite-like transformations that take place in the period proceeding from NS-4 to the initial impregnation, to subsequent impregnations. We will return to this subject when discussing the next figure. Observe that the disparate specimens are rather equally distributed over the velocity range, which indicates that the velocity could not be used to detect disparates as they initially become large enough to be the points of discreet flaws in the material. Also observe that all but one of the weak specimens have velocities less than the average for ATJ-S. Hence, velocity does correlate with strength in this case, and the question is one of precision and degree in the case of weak specimens. Remember that weak ones had high open porosity by absorption or void clusters by the point-count method.

Figure 13 includes the plot of strength versus electrical resistivity for the different billets. The disparates are distributed over the full range of resistivity, while the weak specimens seem to distribute over the higher range of resistivity about as they intended to distribute over the lower range of velocity. The precise relationship between velocity and electrical resistivity is not understood by the author. However, one does suspect that both monitors should be quite sensitive to the micro structure and to the carbon-like versus graphite-like nature, in addition to some effects that might be related to the geometric structure. Values for NS-4 fall over an order of magnitude higher in resistivity and could not be shown on this plot and again suggest that NS-4 is more carbon-like than is ATJ-S. It would be quite difficult to explain the differences in electrical resistivity of NS-4 and ATJ-S in terms of geometric events. Lattice parameters must be involved.

Now let us summarize the arguments assembled concerning the disparate and weak specimens. Recall that disparate specimens are those in which visible discontinuities are apparent in the fracture face. We have called these discontinuities flaws to the extent that they are strength reducers. No one can say with assurance that similar discontinuities do not exist in good specimens at locations other than the fracture face. However, as we can see in Table 24, some of the evidence is quite convincing. For example, one of the flaws was a 27 mil hole that showed at the surface of the unbroken specimen before testing. Fracture occurred through this hole and revealed a major diameter of about 35 mils. That was on Specimen A12W. In Specimen T5W, there was little question that a large "grain" about 15 x 20 mils was apparent in the fracture face at one edge. Also, a large chevron type discontinuity appeared in both fracture faces. For a third specimen, A30W, the fracture faces contained a clean-cut line we have called a "squiggly" which, by experience, has been found in weak specimens of graphite of this type, which looks like a "worm" hole, which appears to have a glazed bottom, and which has never been identified beyond being carbon. For the remaining three specimens, the nature of the flaws in the fracture face is much more difficult to describe or to find. Certainly there were zones that appeared different when viewed under the stereo microscope at 10X. In some places the areas appeared as discolorations, and in others they appeared as loose granular material. In these cases the flaws could be better defined only by the technique that we have described as the "flicks" wherein a large collection of either material or voids larger than the background voids are gathered over some significant portion, but not all, of both fracture faces. In some cases we have polished down below these surfaces and found clusters, and in some cases we have not. None of the disparates could have been uniquely preselected by pulse-echo or radiography with the exception of A12W which had the large hole. It was detected by pulse-echo before the fact. Also, none of the monitors are sufficiently sensitive at this time that they could have preselected these specimens as disparate ones.

Now let us proceed to a discussion of the weak specimens which have been described as those which fall outside of the 95 percent regression and at or below one standard deviation on the lumped values, and which would not have visual flaws in the fracture face. As you can see in Table 25, three of the weak specimens were from the dry core. In these three cases, the specimens had quite high open porosity from absorption on the sections. For the remaining seven weak specimens, the section open porosities were not adequate to explain their weak value, and further inspection was necessary. The first procedure was to go to the flicks and search for void clusters, progressively polish the specimen

to an area below the fracture face, and obtain porosity measurements by the point-count method. A work table for this approach is shown in Table 26, which includes open porosity by absorption, porosity by point count measured on unimpregnated specimen and by point count measured on impregnated specimens. Figure 284 shows a plot of point-count porosities versus section open porosities by absorption so that one can obtain an equivalent open porosity of the cluster itself. Remember that this number is really more qualitative than quantitative, although the precision of the point-count technique is quite good. Now return to Table 25, and we can see that four of the remaining weak specimens can be explained in terms of void clusters, and one can go to the flicks and try to assign a physical dimension to the clusters. Usually this dimension was in the order of 60 mils. The three remaining weak specimens, 7-1-2, T9W, and T1W were not inspected by point count but by flicks. They had void clusters unconfirmed by a second technique. Thus, in summary, six of the ten weak specimens had high open porosity by absorption, and the four remaining ones had high equivalent open porosity described as void clusters by point count or flicks. Now that we have reviewed the open porosity, let us proceed to the other monitors as shown on Table 25, and consider them in terms of their ability to uniquely detect the weak ones before the fact or without concurrently preselecting too many good ones for disposal. In the case of pulse-echo, three of the ten might have been preselected by virtue of the low-hash level, two might have been selected by virtue of abnormally high signal to noise ratios, and the remaining five would have gone undetected. In the case of radiography, the three specimens from the dry core could have been detected, but the other seven would have gone undetected. In case of penetrant and radiometry, they were effective on the dry core material. Six of the ten weak ones had lower densities, four of the five upon which measurements were obtained had higher electrical resistivities, and four of the ten had lower velocities. However, two of these velocities were on the blank rather than on the section so that larger volumes were being inspected, thus confounding the conclusion.

In summary then, we had six disparates and ten weak ones. The most effective truncators were visual inspection of the fracture faces and the flicks for the disparates, and open porosity by absorption or point count for the weak ones. The major sources of strength reduction would appear to be single large voids and "grains" in the case of disparates and void clusters in the case of weak ones.

It is true that a major strength reducer for ATJ-S graphite is open porosity, then inspection techniques are necessary that will be effective not only for large dry cores in a billet, but also for small

islands of porosity that we have called void clusters. We have said that some type of auto correlation or signal extraction may be applicable in the case of pulse-echo for some void clusters; further, we have said that radiography as normally applied seems questionable. There is evidence that both electrical resistivity and velocity are monitors of open porosity and might be used in principle for inspection.

Figure 285 provides a plot of ultrasonic velocity versus open porosity for both the with grain and across grain directions for the averages of all billets. For the with grain direction, the probability that one could reject the null hypothesis is 96.5 percent, indicating a strong correlation. For the across grain direction, the probability is weak at 86.4 percent. A least squares curve fit of all the data points rather than the averages is over-plotted and shows a different slope than the one obtained for the averages. At this time, we do not know if this is the result of insufficient number of specimens in the respective populations or if these are a result of extreme values. The data fit of velocity versus open porosity for L-16-7 also is included in the plots and is quite parallel to the least squares fit for all data points. At this time, we would use the relationship for the data points rather than the one for the averages.

A plot of electrical resistivity versus percent open porosity for all data points, and the averages for a few of the billets, was shown in Figure 14. In this case the probability of a null hypothesis was 99.9 percent, indicating a quite strong correlation. The electrical resistivity of NS-4 was about 30 times that of ATJ-S and does not show on the curve. At this time we do not know if the lower electrical resistivity of ATJ-S compared to NS-4 results primarily from the heat treatments or the impregnations.

From the prior two figures it seems that the velocity and electrical resistivity are adequate monitors of open porosity and should provide a basis for inspection techniques. Since it seems that void clusters of 60 to 100 mils can be strength reducers in specimens, maybe the inspection techniques employing these two monitors would have to be sensitive to volumes of these nominal dimensions. Of course, the volume actually subjected to stress in a piece of hardware would have an influence on this observation.



## CONCLUSIONS

A major goal of this program was to establish the sources of strength reduction in ATJ-S graphite. In order to accomplish this, blank specimens from nine billets were inspected by NDT and other methods, tested in the gas-bearings under tension, and then inspected by various monitors including open porosity, ultrasonic velocity, fractology, and others. Really, a major question in this program was whether or not there was sense to the macro mechanics of the material. If so, then one should be able to determine what inspection techniques were necessary and whether or not one should proceed to micro mechanics and better inspection.

Since we are looking for strength reduction, it is obvious that we must arbitrarily select the weaker specimens from the total lot. This demands that one defines the precision of his instrument and that one establishes some reference for material variability. The precision of the gas bearings is such that the test method introduces parasitic strains no more than 1 percent and probably close to the analytical value of 0.1 percent. Also, we have seen that two criteria for setting strength limits are 68 percent or one standard deviation based on multiple lumped values and 95 percent probability or two standard deviations based on a regression of strength to open porosity. This means that indeed different materials are being inspected as open porosity varies and that more confidence is available when one accounts for this parameter.

One can think in terms of strain-at-failure as well as strength; however, this program was not directed that way because we originally did not intend to obtain strain on every specimen. If one wishes to review the data in the tables in terms of strain, the reproducibility is on the order of 50  $\mu$  inches at fracture, and the uncertainty within the same limits, except for those cases where faulty stress-strain plots have been or would be involved. Thus, the uncertainty in strain at failure due to instrumentation may be as high as 2 percent (coefficient of variance). For modulus, the uncertainty due to instrumentation would be about 5 percent (coefficient of variance). These uncertainties could be improved if the program required it.

The following are the major conclusions:

1. Disparate specimens are defined as those that had visual discontinuities in the fracture face. There were six such specimens (in the with grain direction) containing large voids, "worm" holes, large "grains," and perhaps large void clusters. Three of the six disparate flaws would be obvious even to the untrained eye, and three were found by the flicks.

In addition to the disparates, there were ten weak specimens, nine of which fell within the 95 percent regression but below one standard deviation for multiple lumped values. In every case these specimens were weak because of the high open porosity (void clusters) detected either by absorption (3 cases) on the fracture sections or by point counts (7 cases) on polishes made to below the fracture face, and by flicks (3 cases) on the fracture face. There was a total of 178 with grain specimens.

2. Our ability to preselect the disparate and weak specimens by existing NDT methods was less than satisfying. Alcohol absorption qualitatively preselected high open porosity. One disparate and five weak specimens were detected by pulse-echo. Three of the weak ones were from the dry core. Radiography was able to uniquely predetermine the three weak specimens from the dry core but no others. Thus, it appears that these techniques can detect large flaws but cannot detect with sufficient assurance flaws at the threshold where they have initially become strength reducers. Another way of saying this is that fracture occurs near large signals for pulse-echo, but large signals are not necessarily weak spots when one is searching for the flaw threshold strength. It appears that pulse-echo can be improved by techniques concerned with the principle of auto-correlation and methods involving transmission. The reader should realize that we did not know what we were looking for exactly going into the job and that the author does not profess expertise in NDT. Since the signal seems to be there, the author feels that he could do much better now, particularly with pulse-echo, for threshold flaws.

3. There were some effective monitors of the strength. Open porosity was an effective monitor of seven of the weak specimens for sure, and probably also for the remaining three where only flick data was obtained. Velocity and electrical resistivity were also effective correlators of strength.

4. Ultrasonic velocity and electrical resistivity both provided good correlation with open porosity on specimens and should provide a basis for more effective inspection on hardware when small volumes can be inspected.

5. Some information may be of assistance in improving the material. There seems no doubt that reducing the open porosity to below 10 to 11 percent, even down to small islands within a billet, would be effective (while holding closed porosity at about 9 percent). The open porosity seems to consist of void sizes greater than 1 mil and up to 6 mils, even though porosimetry data by us and others indicate that most open porosity is less than  $\frac{1}{2}$  mil. The author believes that the porosimetry data must be influenced by tortuosity or restrictions in the tunnels that form the void

system. The result of the electrical resistivity measurements indicate that NS-4 is more carbonlike than ATJ-S, and the smooth increase of strength with decreasing open porosity suggests that there are no step-wise changes in this property in the material with progressive densification by impregnation. There are profiles of open porosity, density, and velocity in the billets that cause similar profiles in strength and should be minimized. The fact that the closed porosity is about the same for NS-4 and all specimens of ATJ-S and that strength seems to increase with closed porosity suggests that these small pores are not influential as strength reducers of the material.

6. Recall that the strength increases rather uniformly progressing from NS-4 to the more dense ATJ-S. This suggests that the failure mechanism does not change with densification, accepted parameters do operate, and the event of fracture is properly described statistically by a uniform distribution. The similarity in this curve to a plot of a Griffith suggests Griffith cracks as the failure criteria in terms of propagation at least. This in turn would suggest equivalent tensile strain as a design criteria. From the progressive photomicrographs of the fractures it appears that the fracture proceeds between lamellae when they are parallel to the nominal crack path, and proceeds around the "grain" boundaries when the lamellae are normal to the nominal path. Thus, failure mode is difficult to describe. Crack initiation seems to generate around disparate, single voids of about 30 mils major diameter and from void clusters about 60 mils in major axis. Further work in fracture mechanics may define this better. The fact that increased closed porosity may increase strength suggests that work in generating fracture faces should include the blunting process.

7. Some information was obtained in the across grain direction but not sufficient for extensive conclusions; it does suggest that (1) the coefficient of variance is about  $2\frac{1}{2}$  percent in this direction, which includes both the test method and the material variability, thus providing confidence that parasitics in the test method are not more than 1 percent; (2) the presence of obvious visual disparates in the fracture face of a few specimens creates a similar situation as for the with grain direction; (3) the monitors seem to profile for the across grain orientation providing confidence that a similar inspection would be worthwhile.

8. Some data were obtained at 3000°F, 4500°F, and 5500°F. Again, the disparates seem to be active, certainly to 3000°F, and the monitors seem to profile even to 4500°F. Particularly, velocity and open porosity provided effective correlations to 4500°F in a few cases where sufficient data points were gathered.

9. Even though open porosity seems first order, there are covariant effects as demonstrated best perhaps by Billet L-9-10.



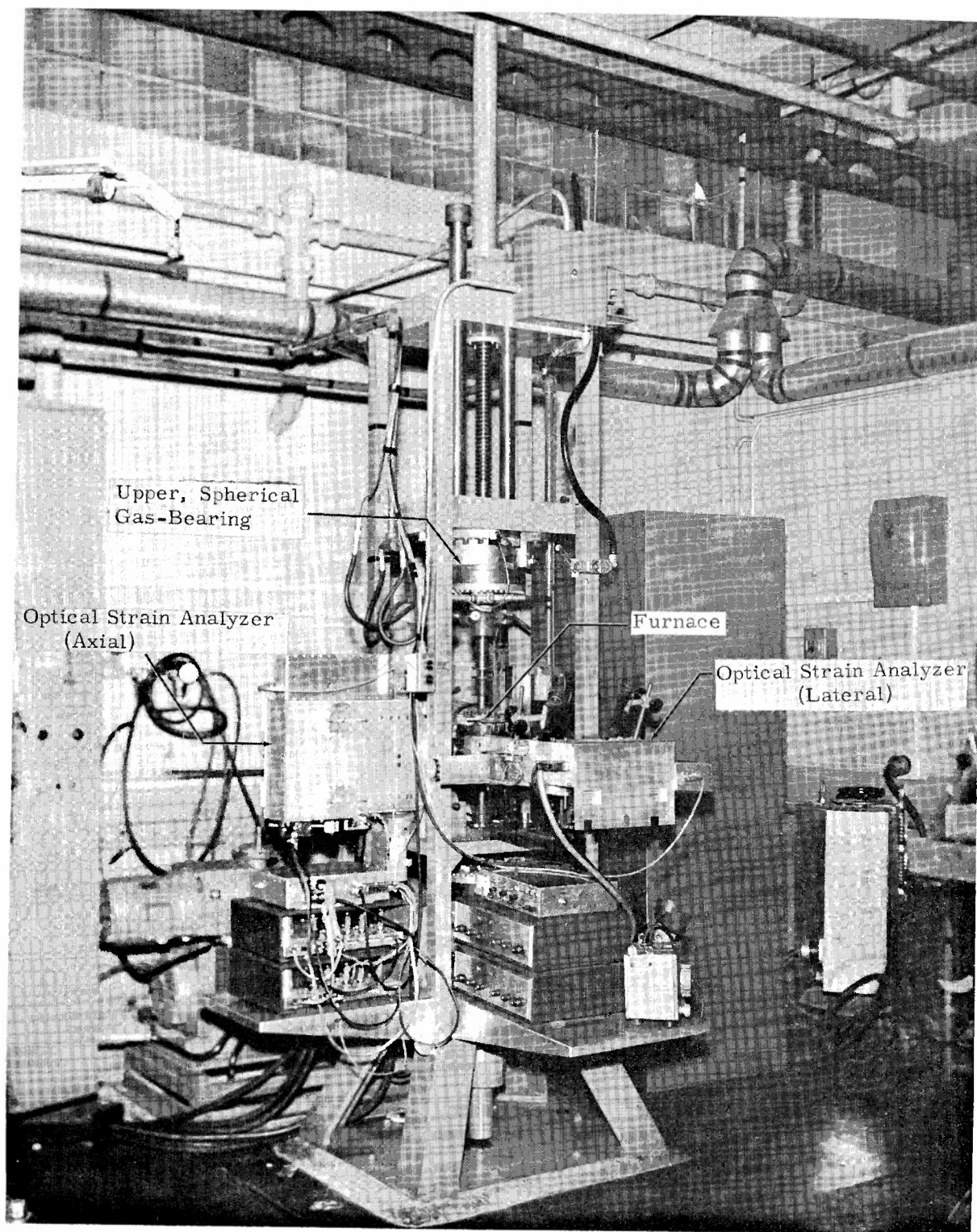


Figure 1. Picture of Tensile Stress-Strain Facility



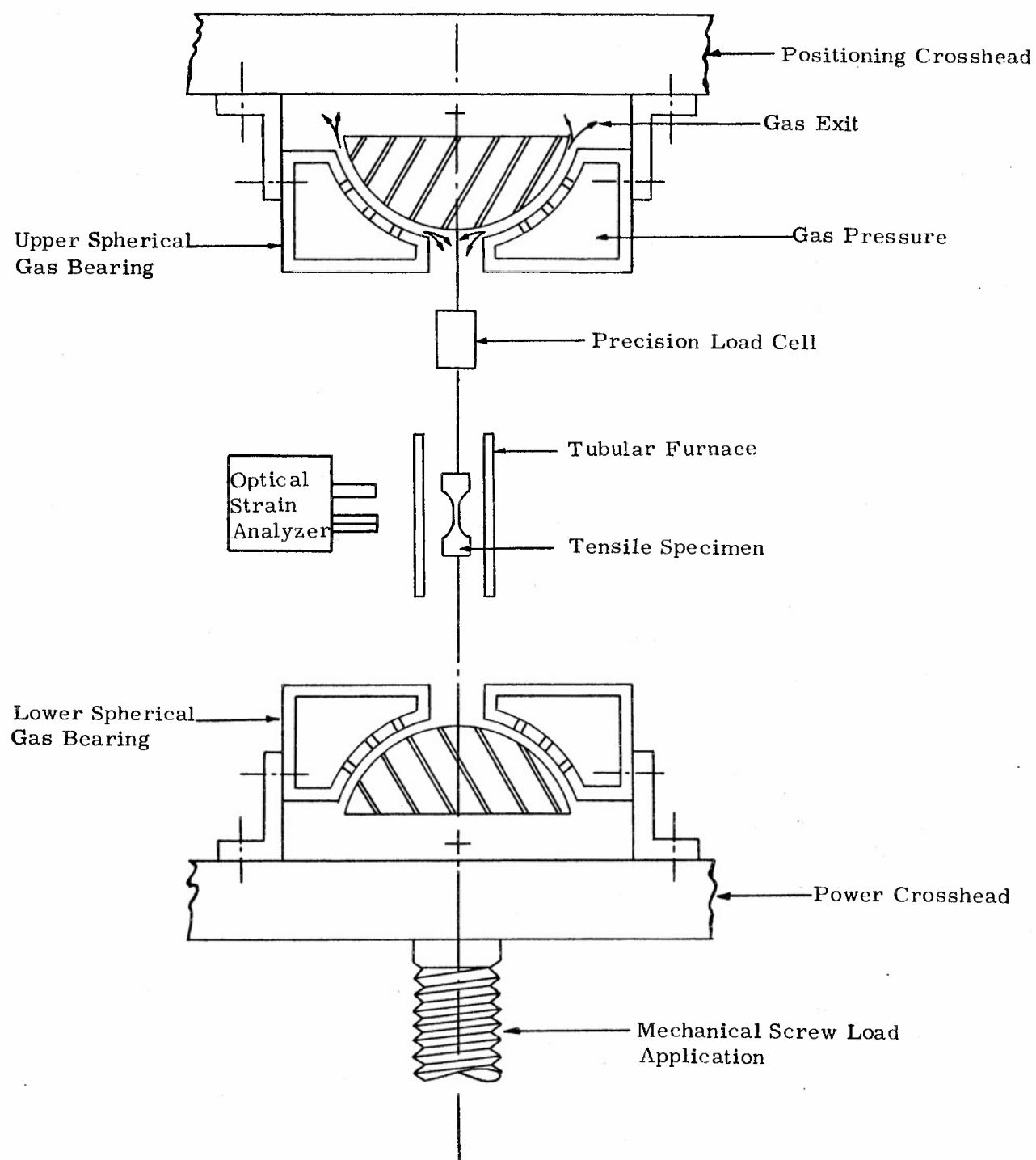


Figure 2. Schematic of the Gas Bearings and Load Train for the Tensile Apparatus

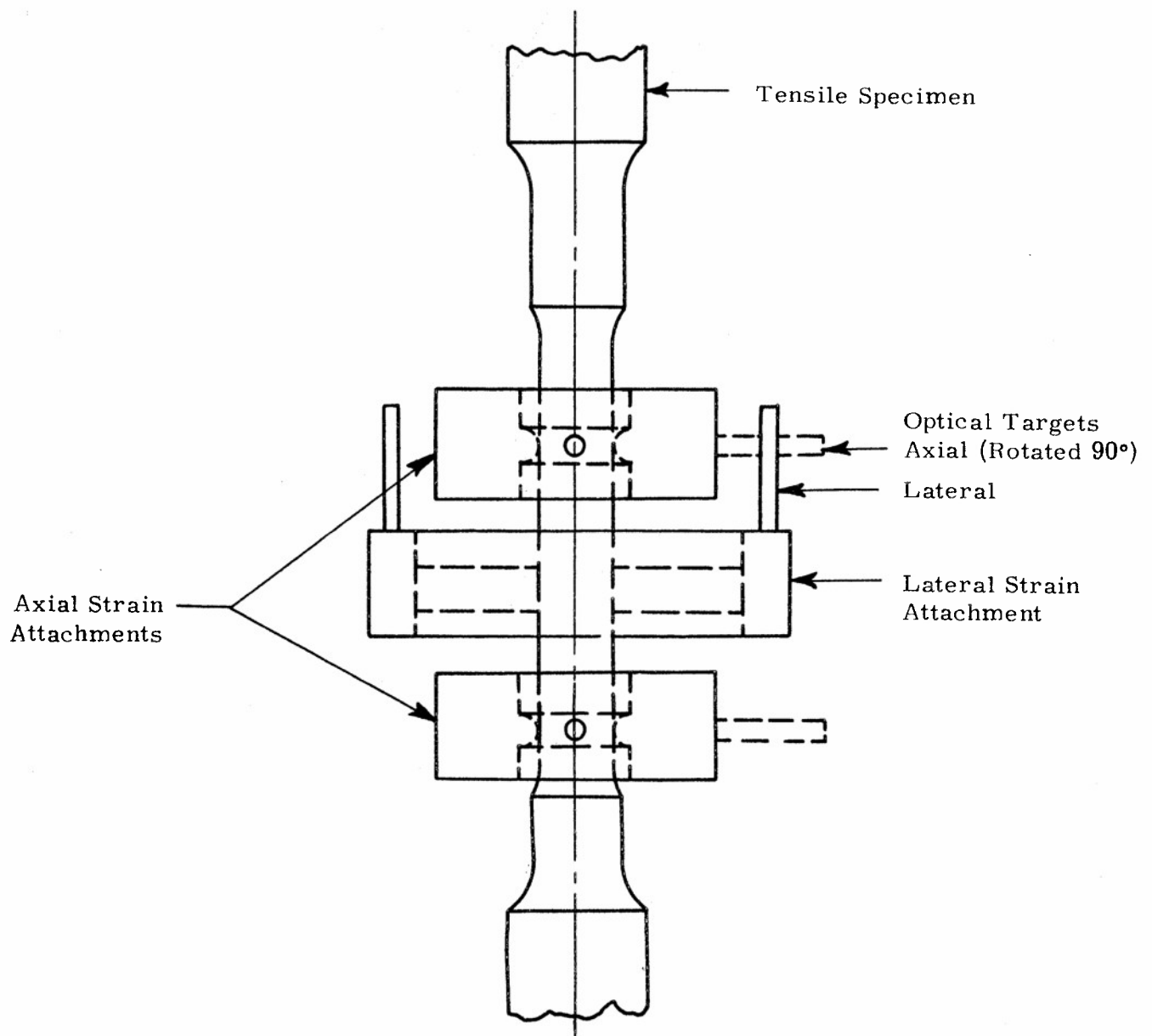


Figure 3. Location of the Flag Attachments on the Tensile Specimens



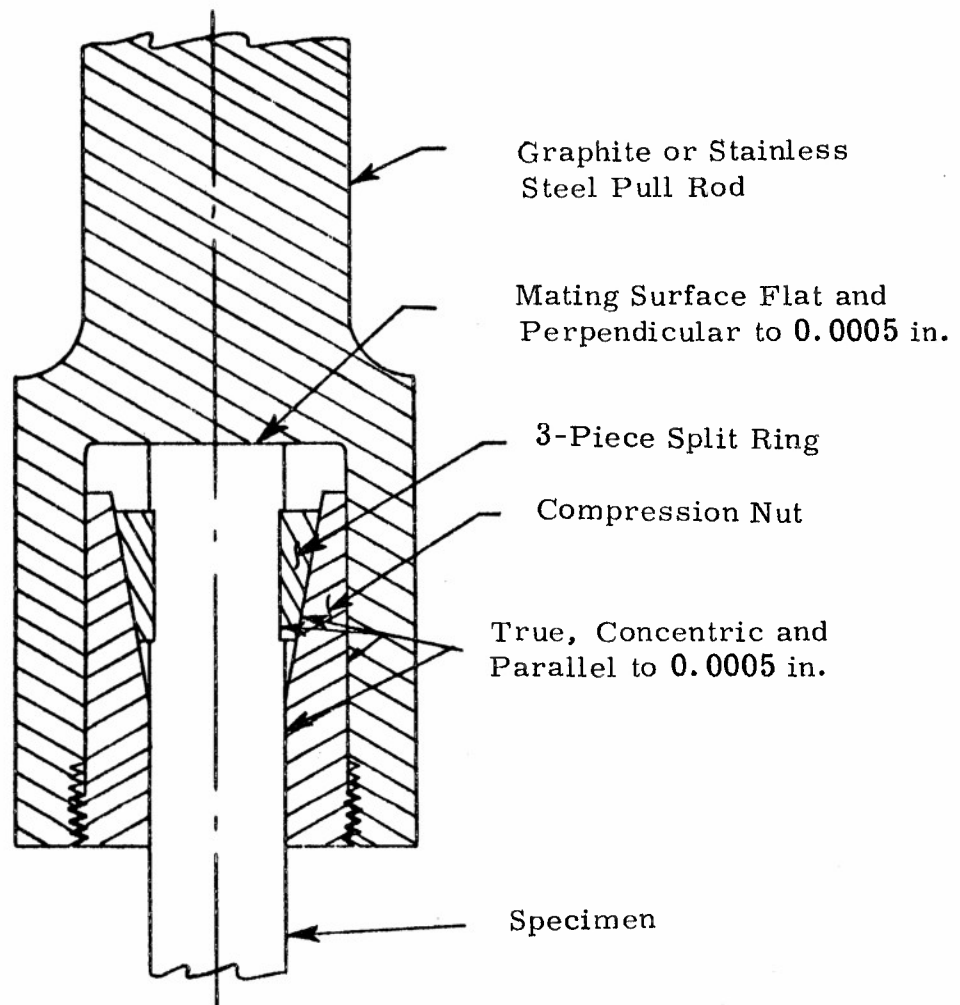
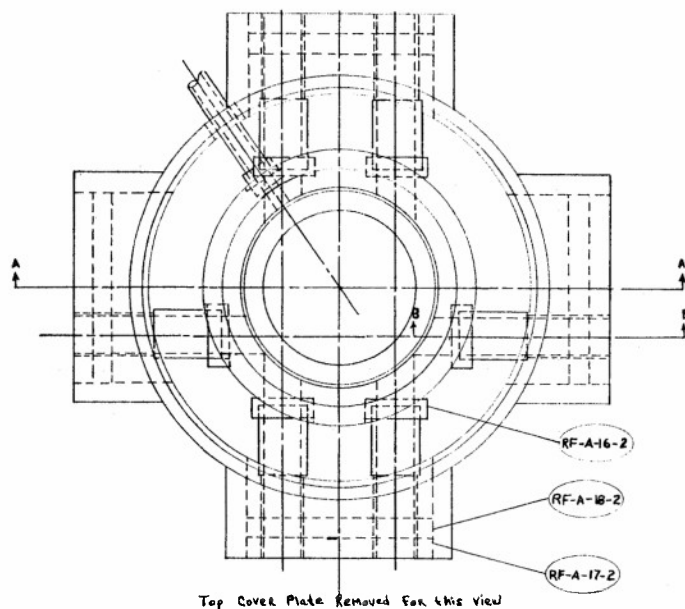
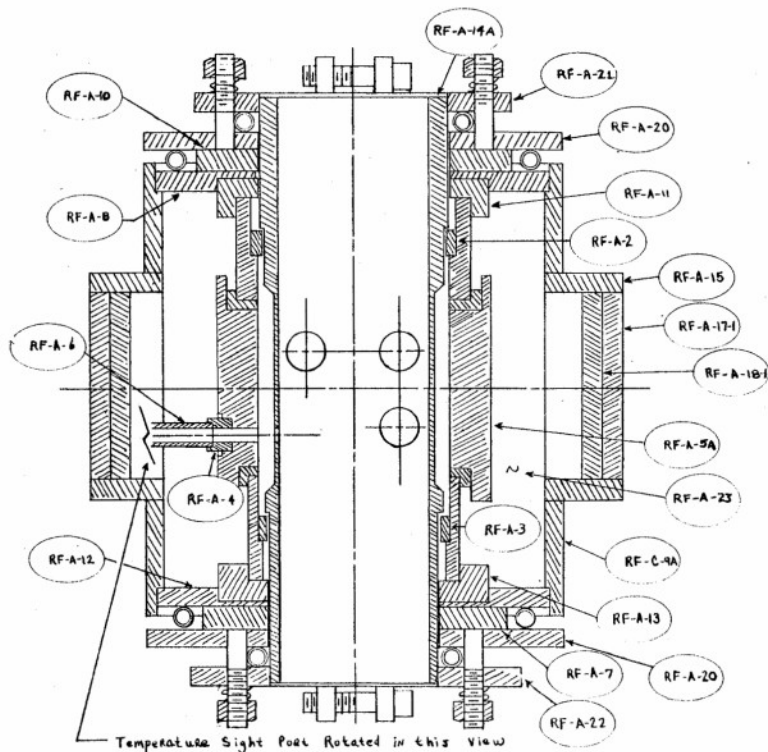


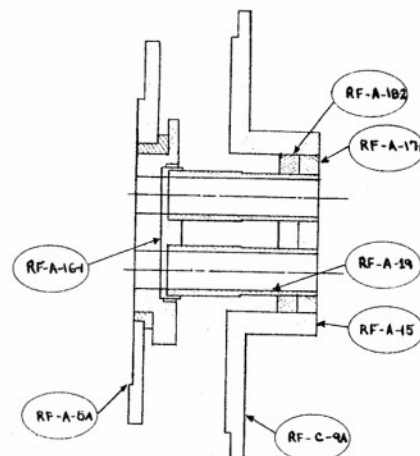
Figure 4. Precision Collet Grip for Tensile Specimens 2:1 Scale



Assy.	Item	Quan.	Description
A-2	1	Top pyrolytic graphite ring	
A-3	1	Bottom pyrolytic graphite ring	
A-4	1	Pyrolytic graphite temperature sight plate	
A-5A	1	CS graphite protector tube	
A-6	1	CS graphite temperature sight tube	
A-7	1	Bottom Micarta insulating disc	
A-8	1	Top steel base plate	
C-9A	1	Steel shell	
A-10	1	Top Micarta insulating disc	
A-11	1	Top zirconia disc	
A-12	1	Bottom steel base plate	
A-13	1	Bottom zirconia disc	
A-14A	1	CS graphite heater tube	
A-15	2	Steel sight port tube	
A-16-1	2	CS graphite sight port plate	
A-16-2	2	CS graphite sight port plate	
A-17-1	2	Firebrick sight port plate	
A-17-2	2	Firebrick sight port plate	
A-18-1	2	Zirconia sight port disc	
A-18-2	2	Zirconia sight port disc	
A-19	4	CS graphite sight tube	
A-20	2	Fiberfrax insulator	
A-21	1	Top electrode	
A-22	1	Bottom electrode	
A-23	1	Thermatomic carbon	



Section A-A



Section B-B

Figure 5. Small 5500°F Graphite Resistance Furnace

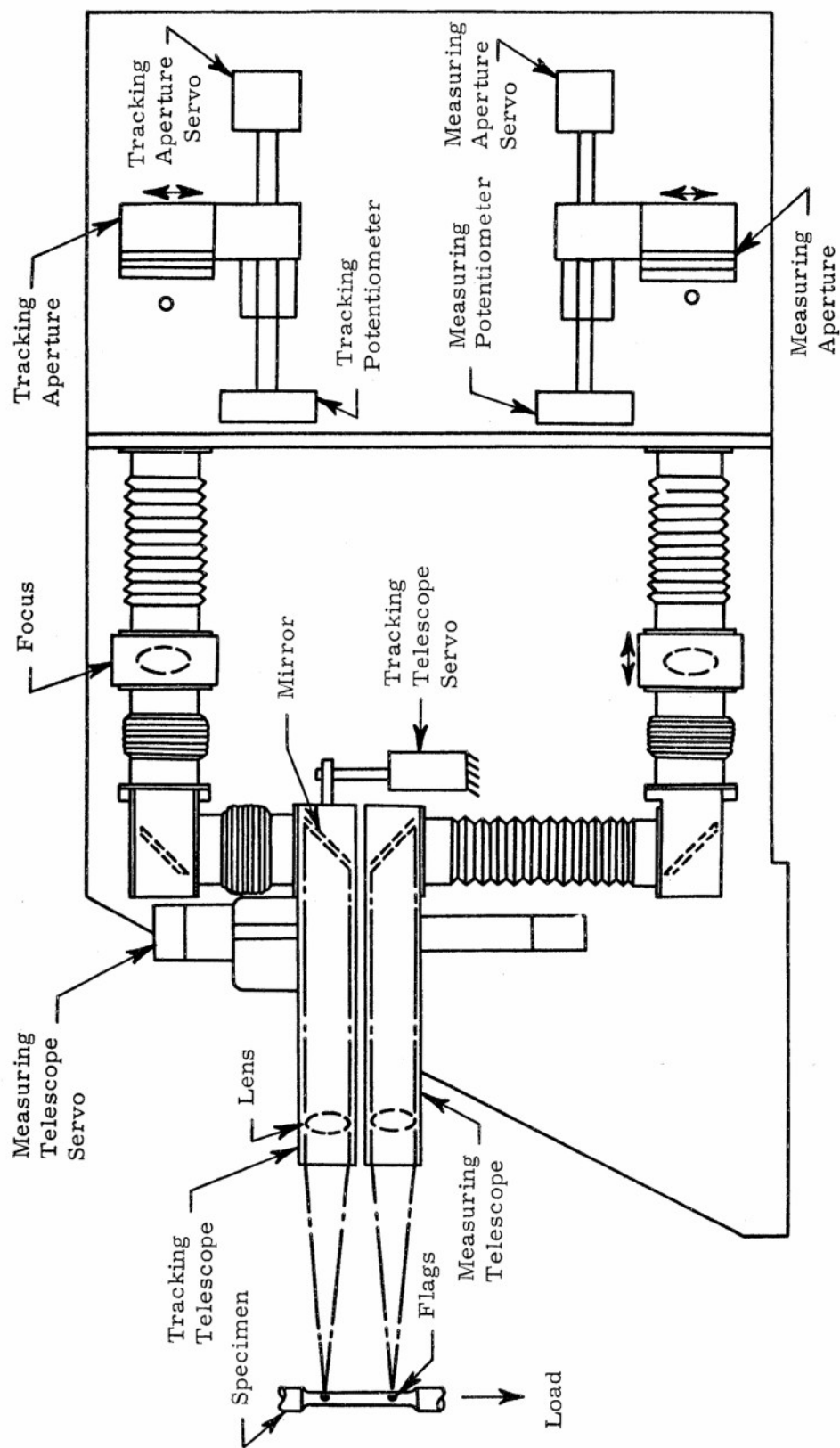


Figure 6. Arrangement of Optical Strain Analyzer

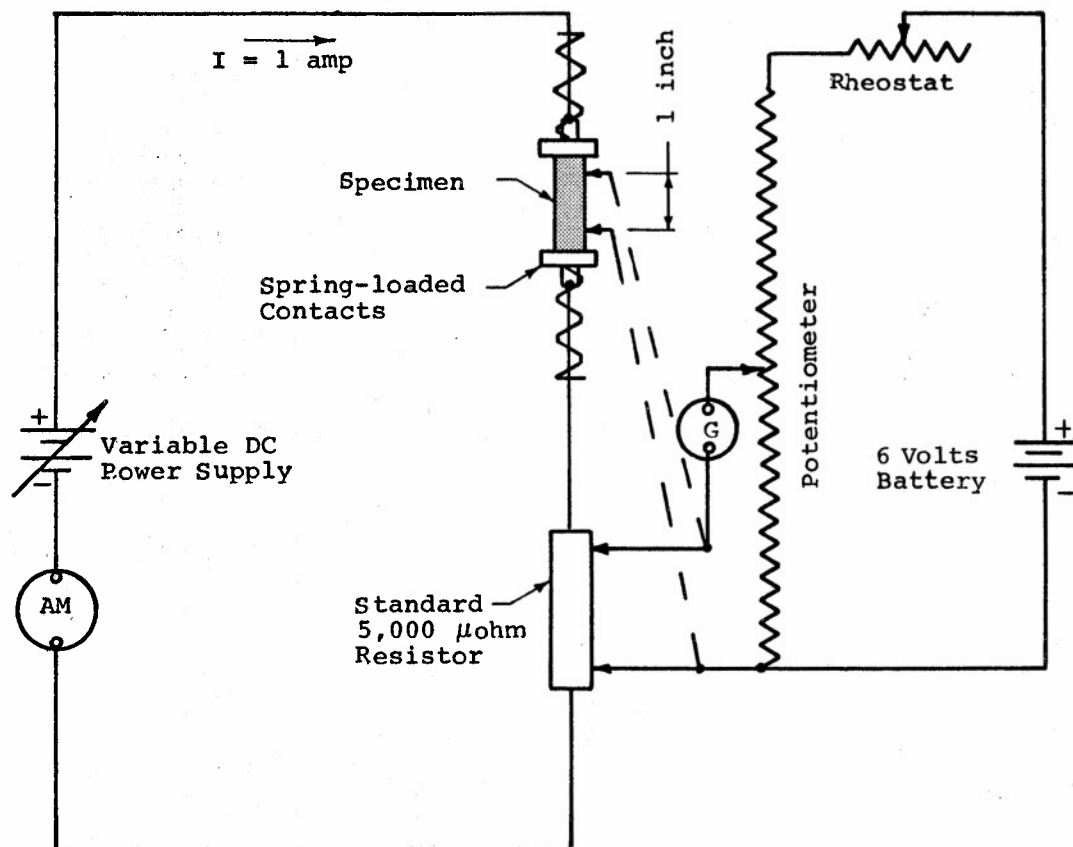


Figure 7. Potentiometer Method for Measuring Electrical Resistivity

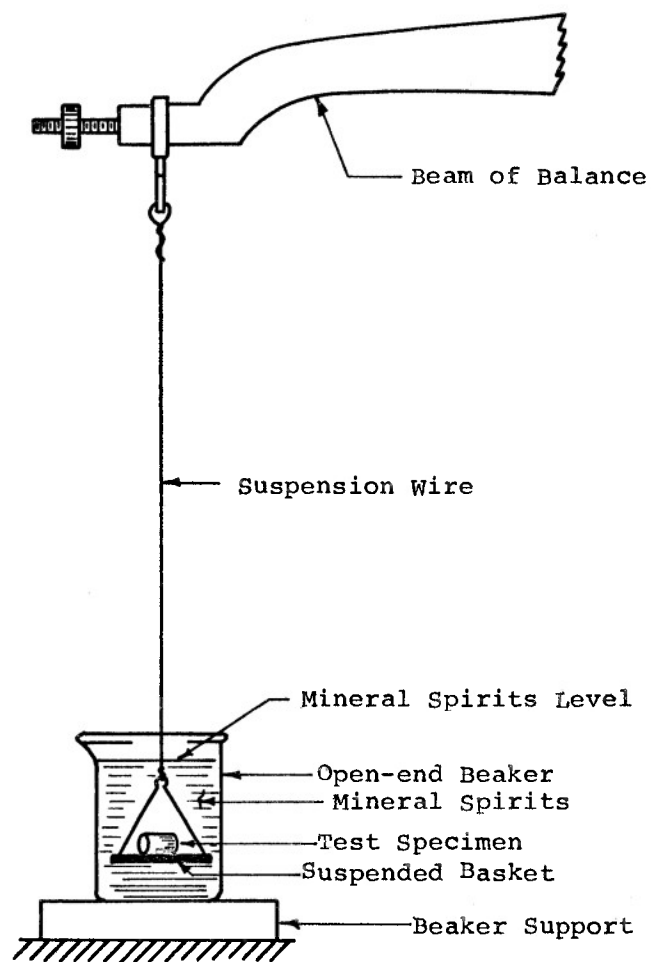
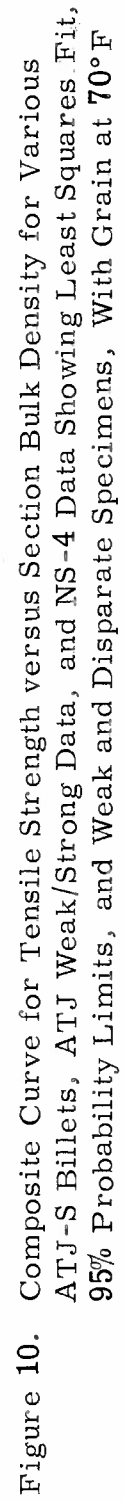


Figure 8. Setup for Determining Suspended Weight of Saturated Specimen for Liquid Absorption Evaluation







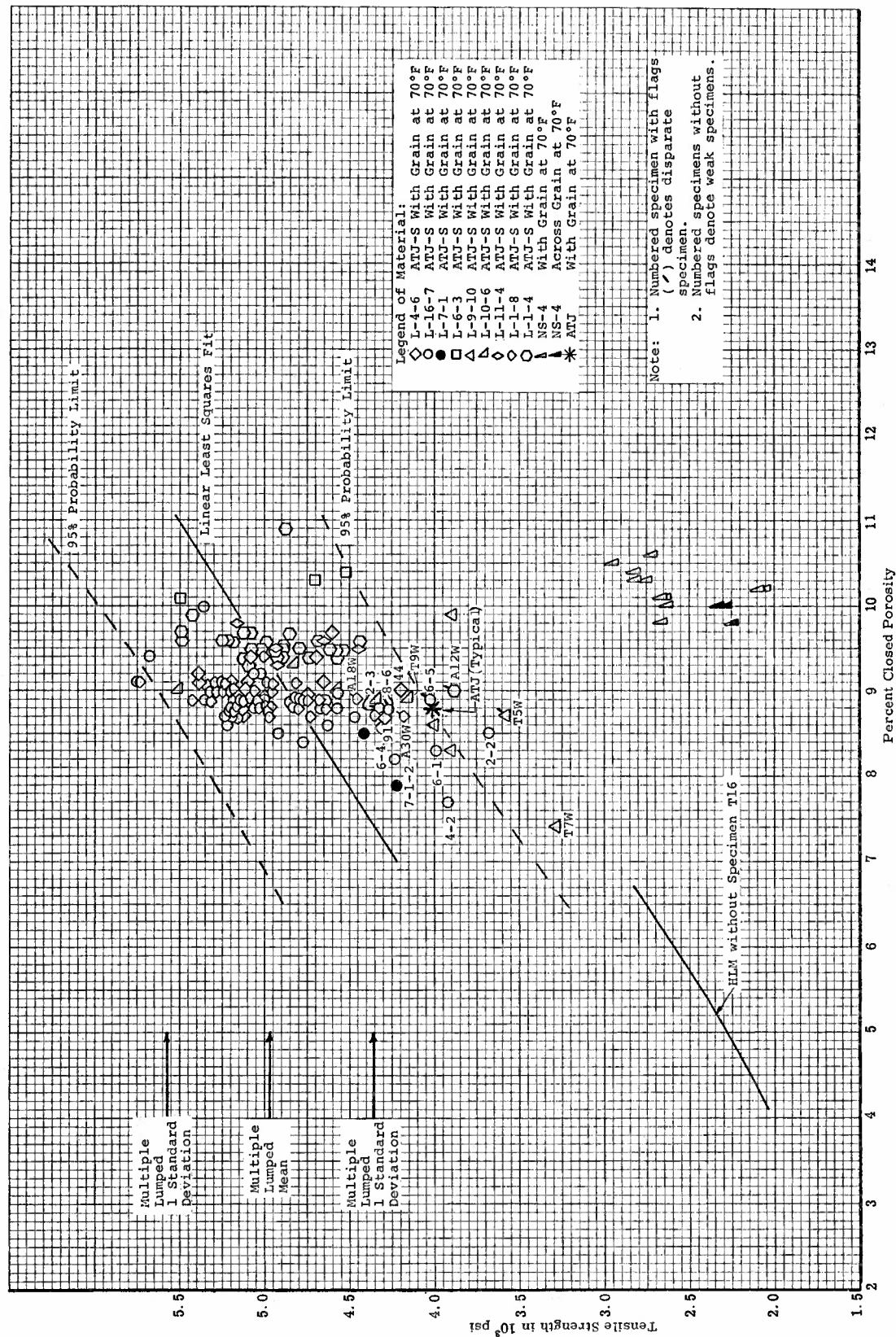


Figure 11. Composite Curve for Tensile Strength versus Closed Porosity for various ATJ-S Billets, ATJ Data, and NS-4 Data Showing Least Squares Fit, 95% Probability Limits, and Weak and Disparate Specimens With Grain at 70°F



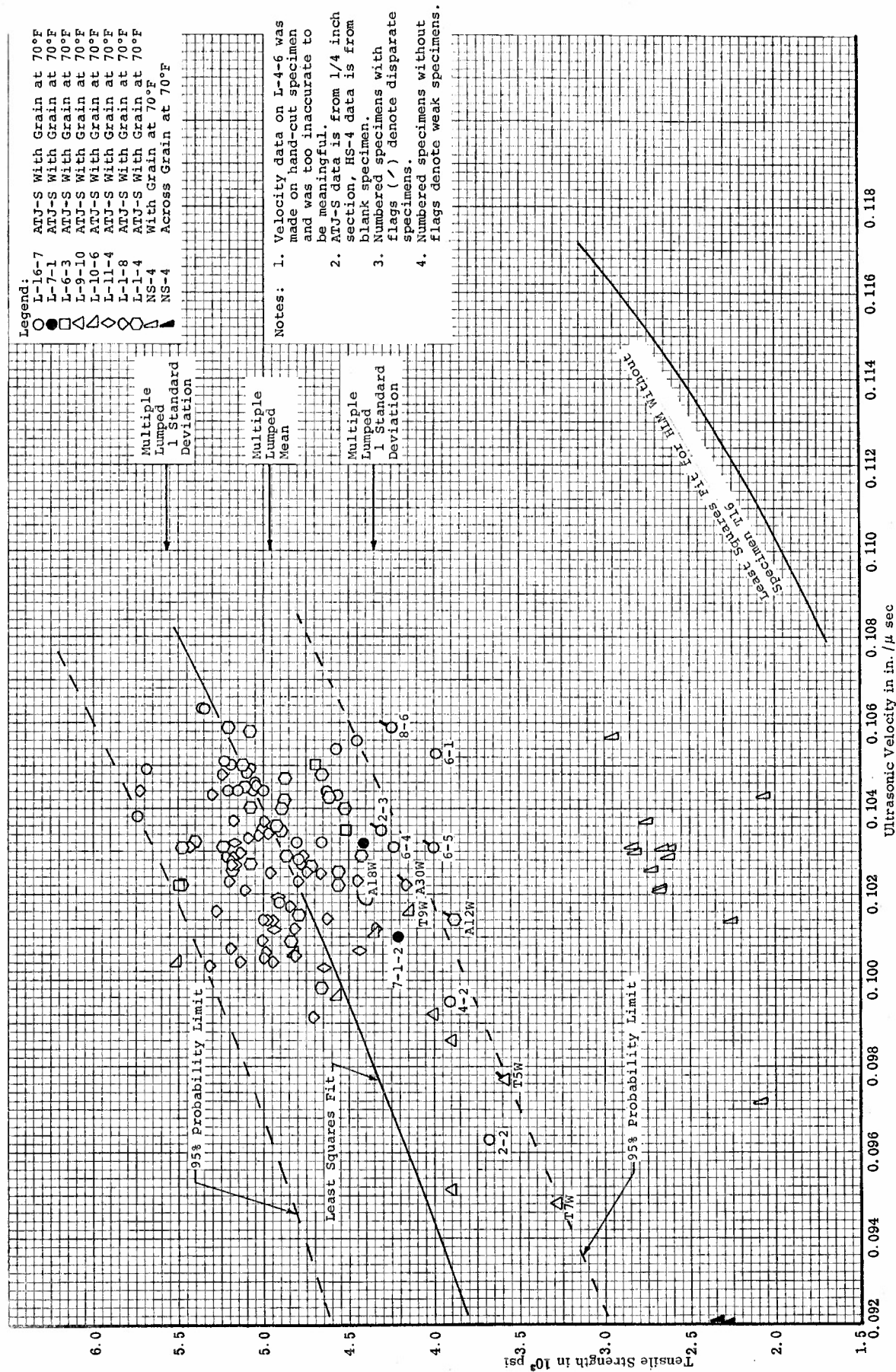


Figure 12. Composite Curve for Tensile Strength versus Velocity for Various ATJ-S Billets and NS-4 Data Showing Least Squares Fit, 95% Probability Limits, and Weak and Disparate Specimens, With Grain at 70°F

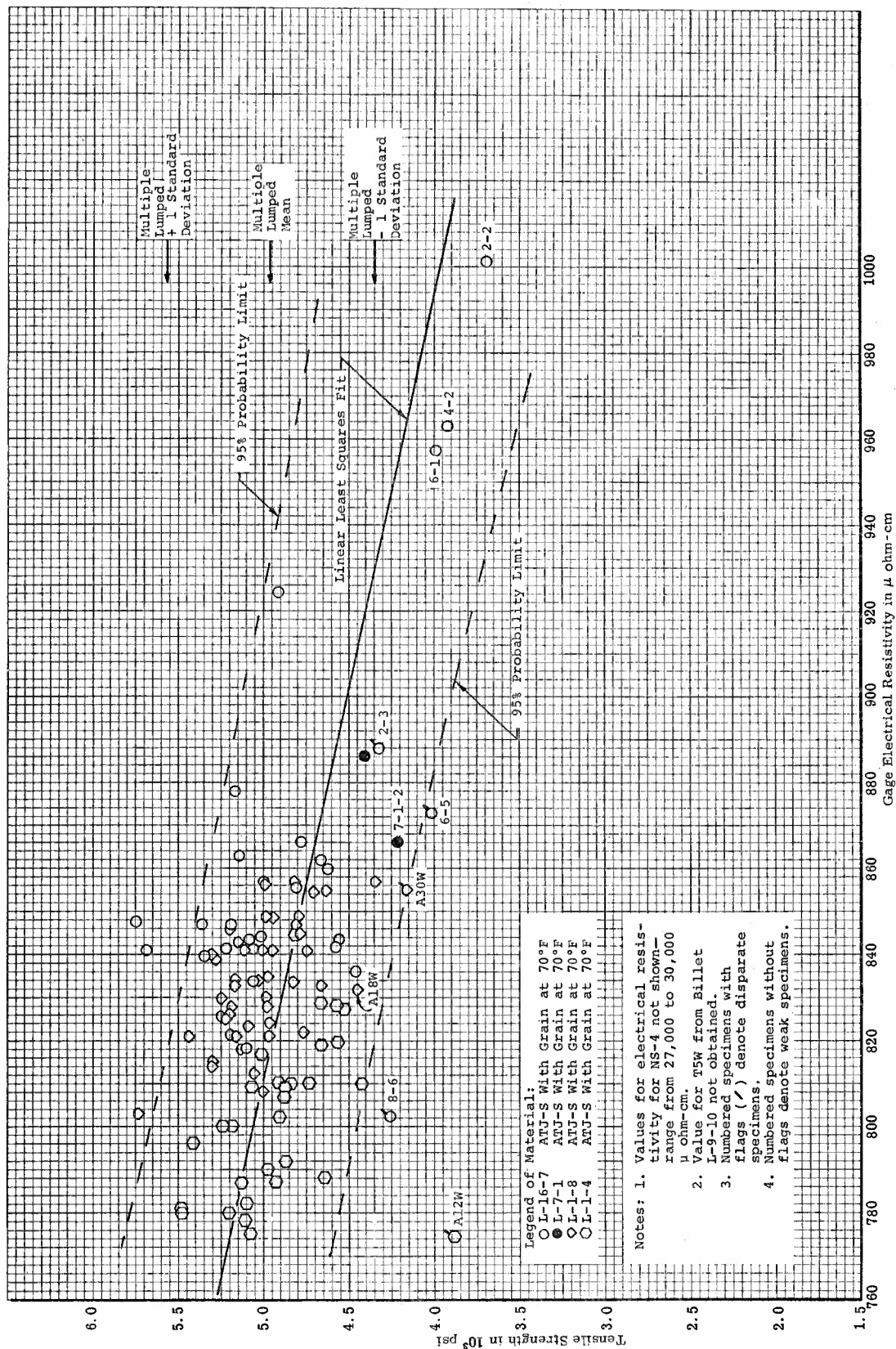


Figure 13. Composite Curve for Tensile Strength versus Gage Electrical Resistivity for the various ANJ-S Billets showing Least Squares Fit, 95% Probability Limits, and Weak and Disparate Specimens With Grain at 70°F

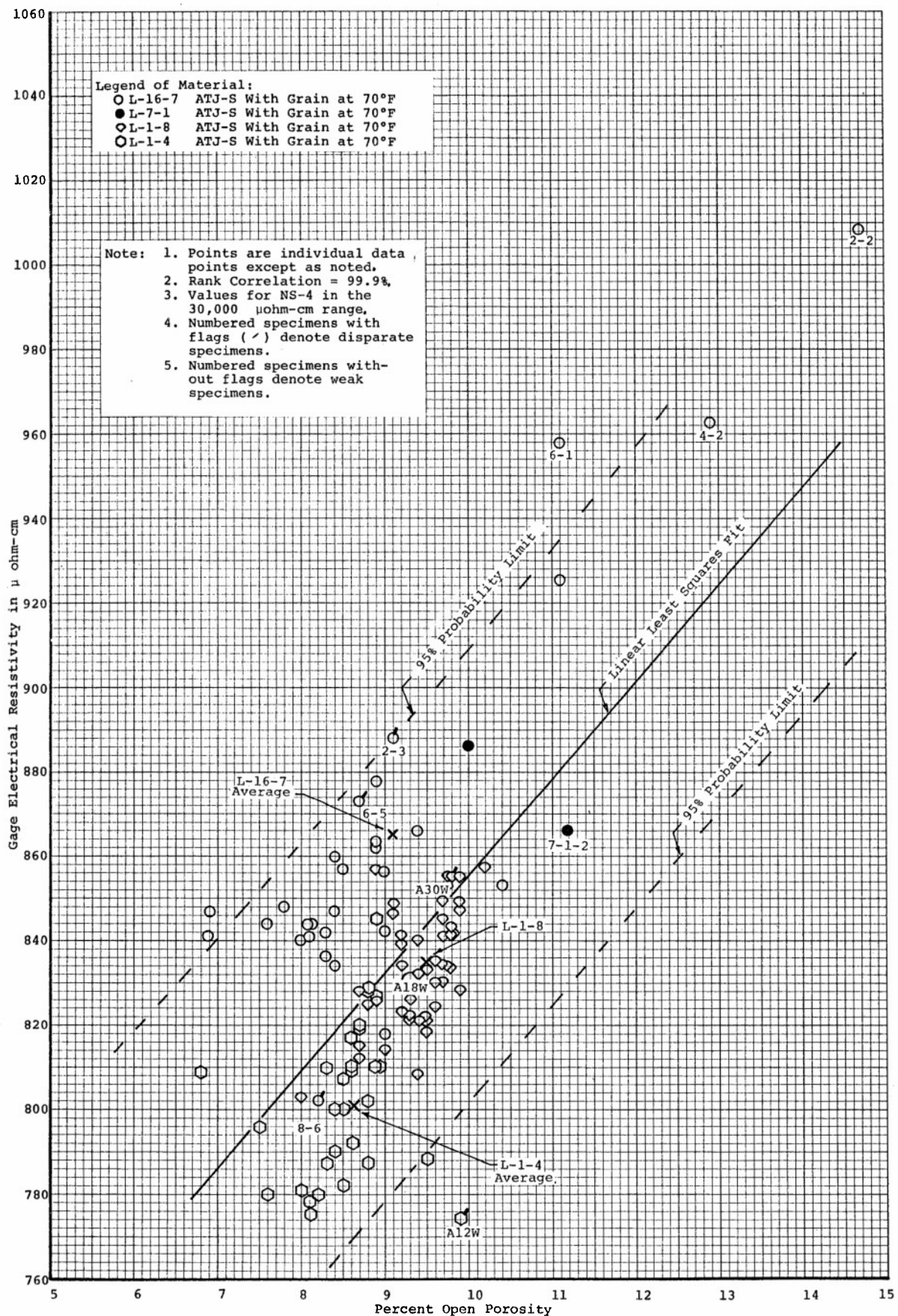
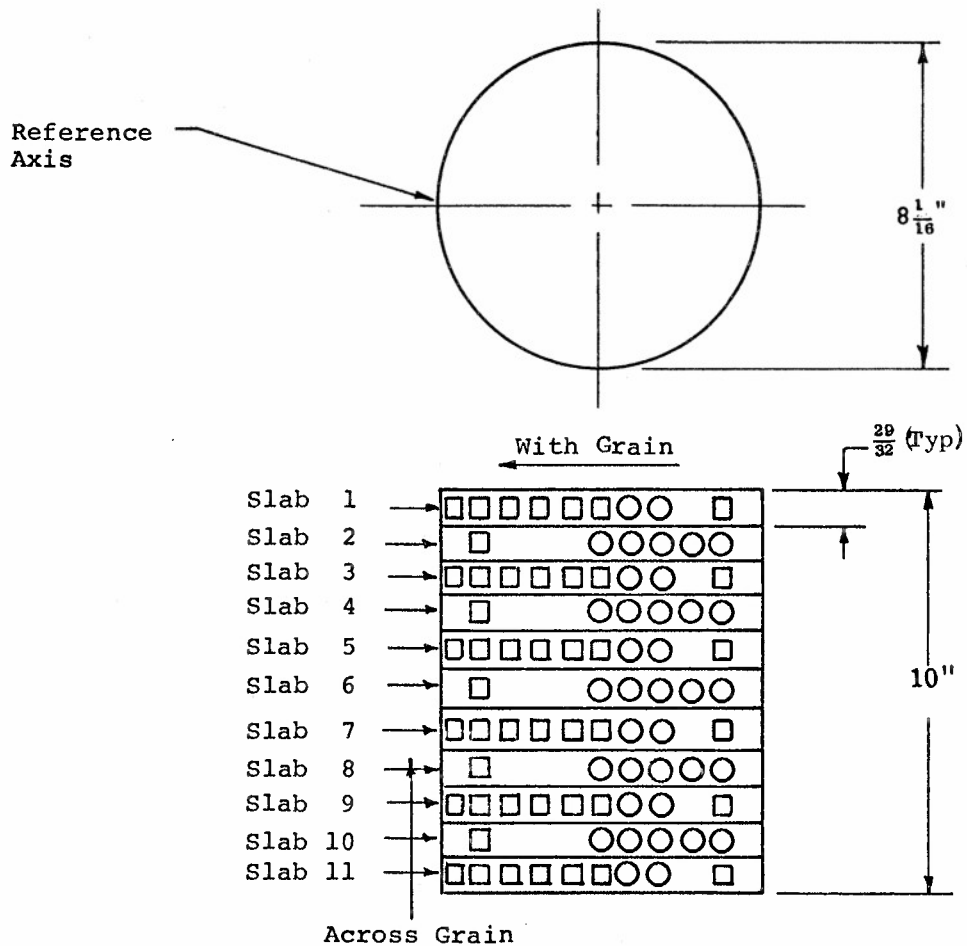


Figure 14. Composite Curve for Gage Electrical Resistivity versus Open Porosity for Various ATJ-S Billets Showing Least Squares Fit, 95% Probability Limits and Weak and Disparate Specimens, With Grain at 70°F

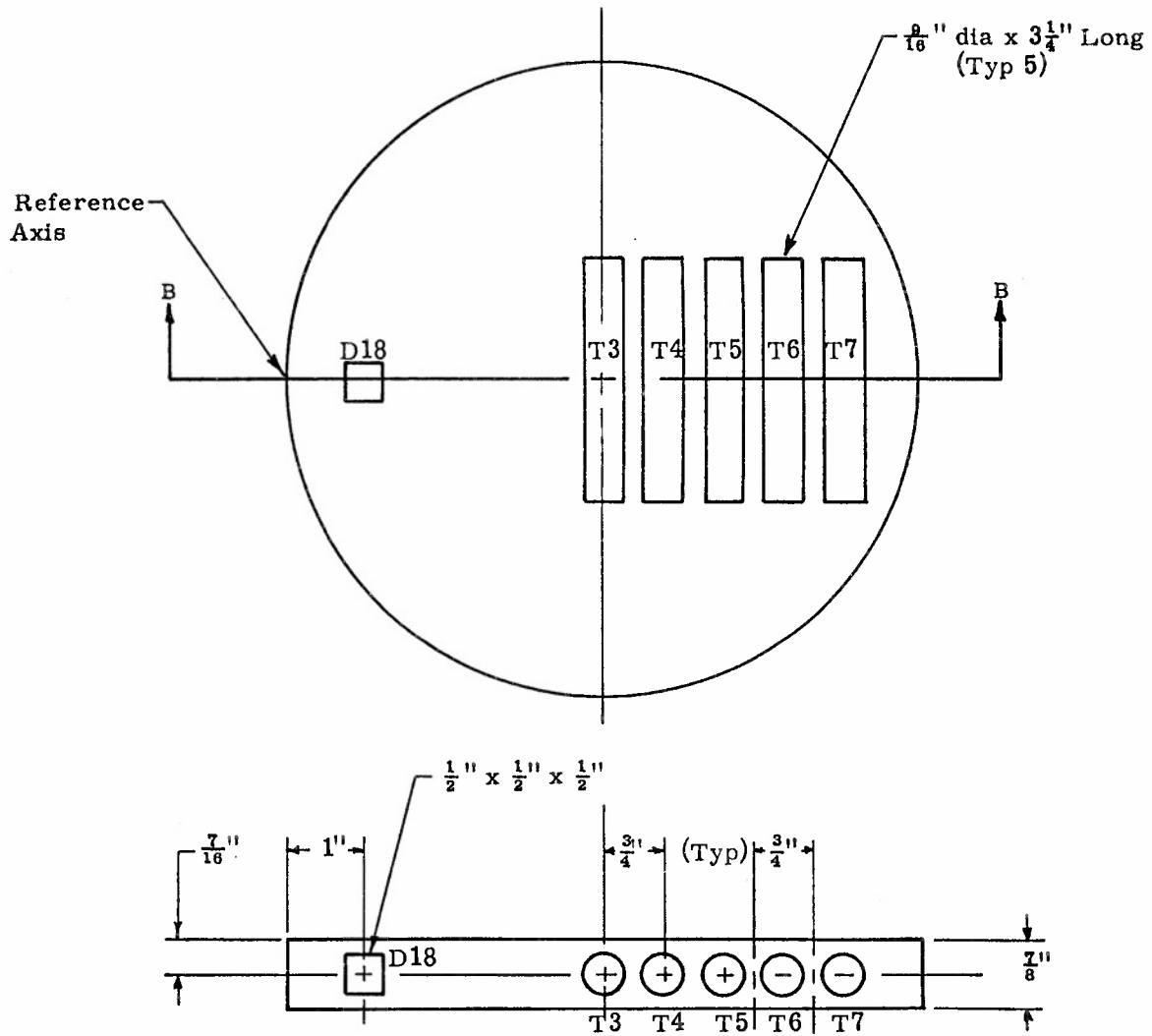


**Notes:**

1. Scribe reference line along billet length at reference axis prior to cutting.
2. Mark each specimen with number shown in the layout or place individually in marked envelope.
3. Identify and return all excess material (slab and grain).
4. Keep the material and the cut blanks in dry atmosphere at all times.
5. Visually inspect slab interfaces for cracks and flaws.

Figure 15. Cutting Plan for Billet L-16-7

Slabs: 2, 4, 6, 8 and 10



Section B - B

Figure 16. Cutting Plan for Even Numbered Slabs from Billet L-16-7

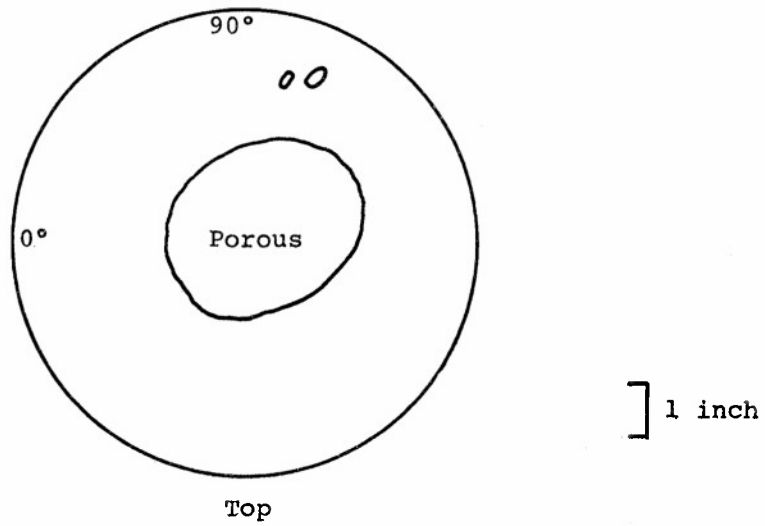
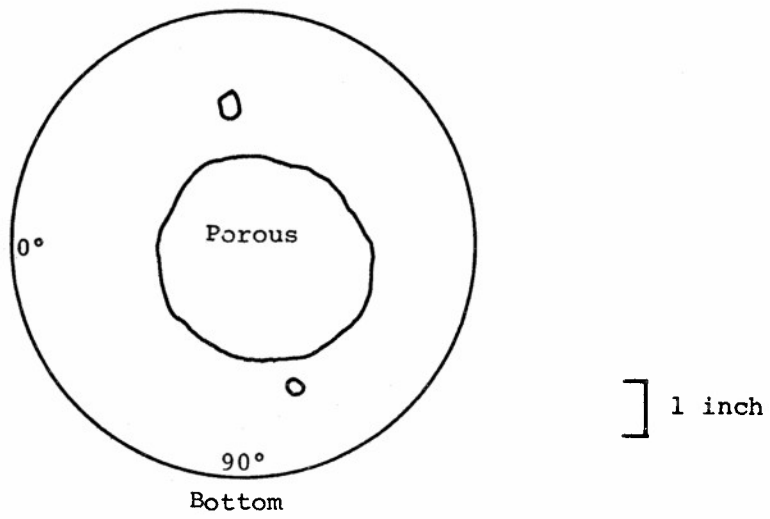
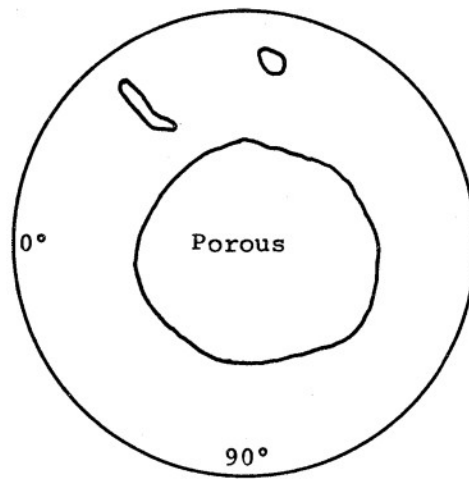
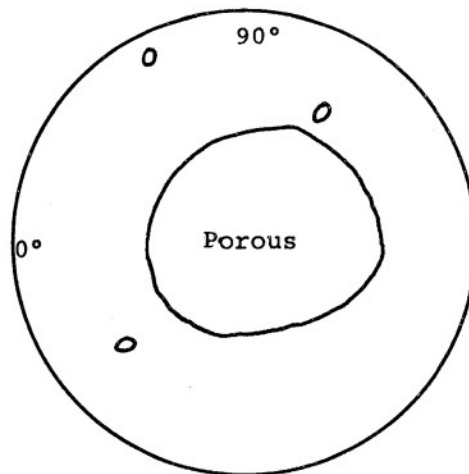


Figure 17. Sketch of Slab Number 2 Showing Porous Region as Determined by Avco, ATJ-S Billet L-16-7



Bottom

] 1 inch



Top

] 1 inch

Figure 18. Sketch of Slab Number 4 Showing Porous Region as Determined by Avco, ATJ-S Billet L-16-7

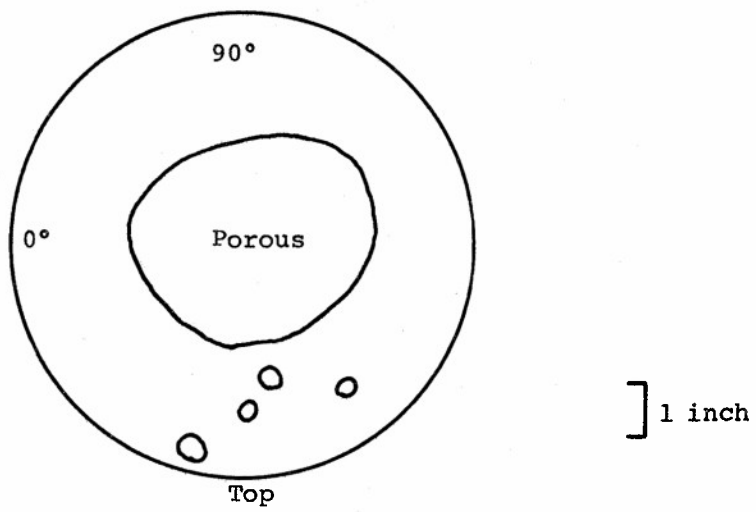
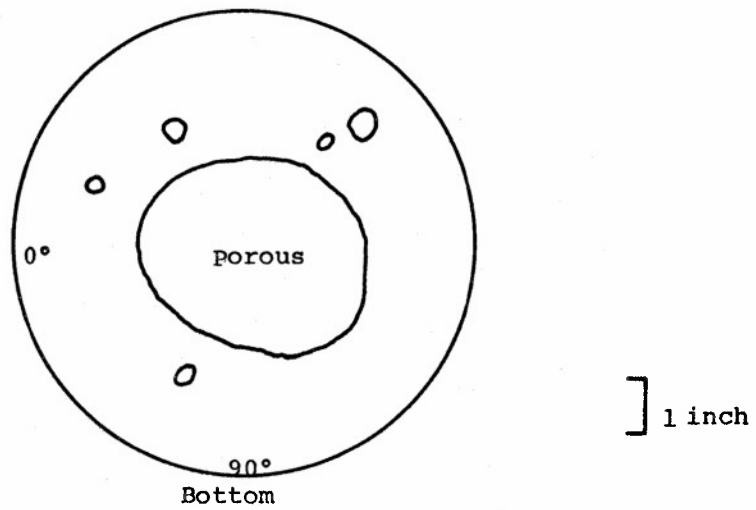


Figure 19. Sketch of Slab Number 6 Showing Porous Region as Determined by Avco, ATJ-S Billet L-16-7



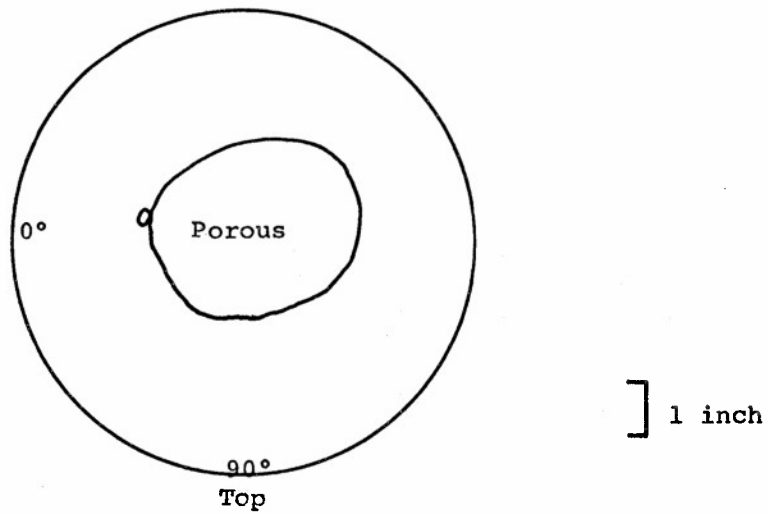
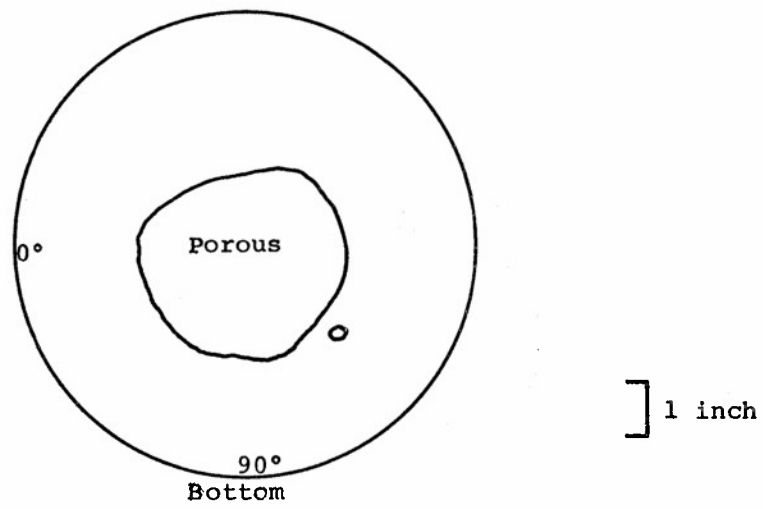
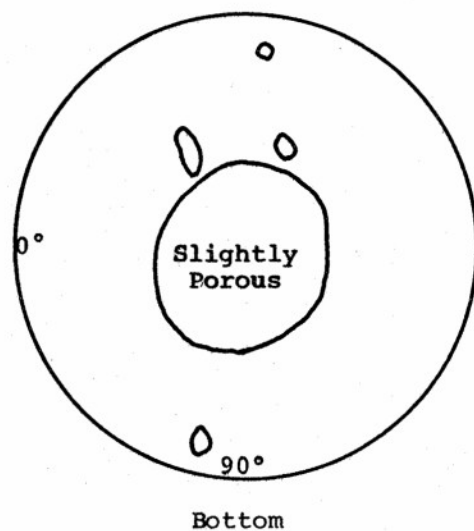
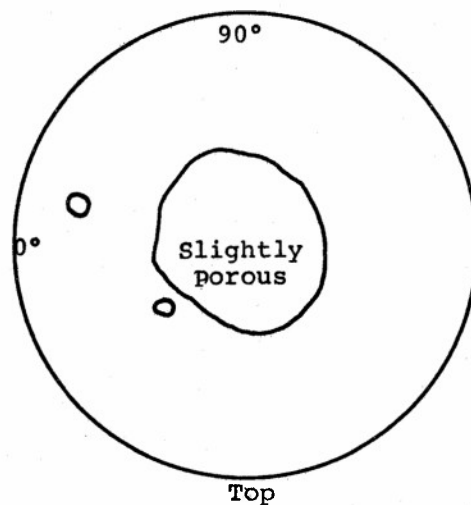


Figure 20. Sketch of Slab Number 8 Showing Porous Region as Determined by Avco, ATJ-S Billet L-16-7



] 1 inch



] 1 inch

Figure 21. Sketch of Slab Number 10 Showing Porous Region as Determined by Avco, ATJ-S Billet L-16-7

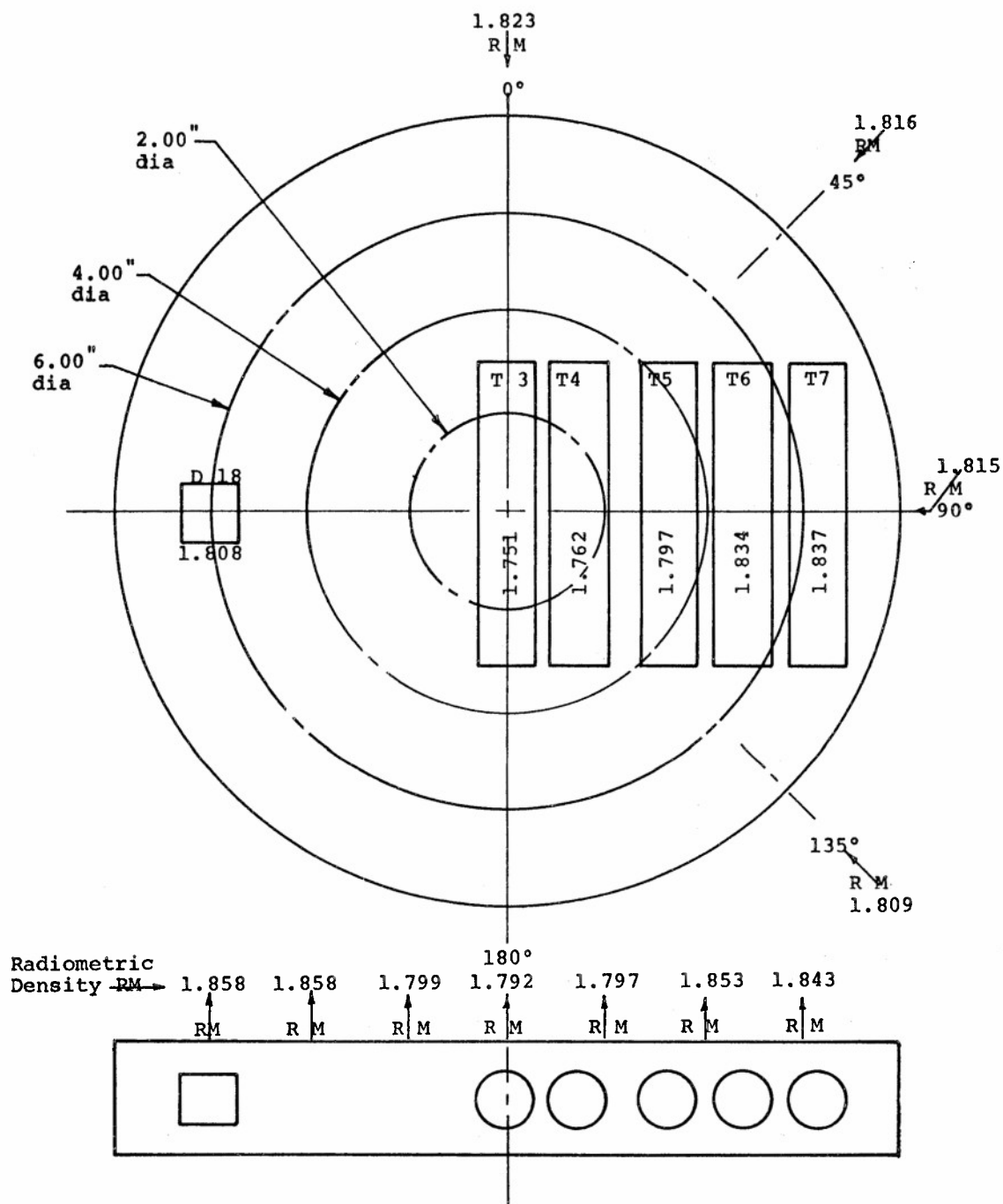


Figure 22. Original Avco Cutting Plan for Slab Number 2  
Showing Radiometric Density, ATJ-S Billet L-16-7

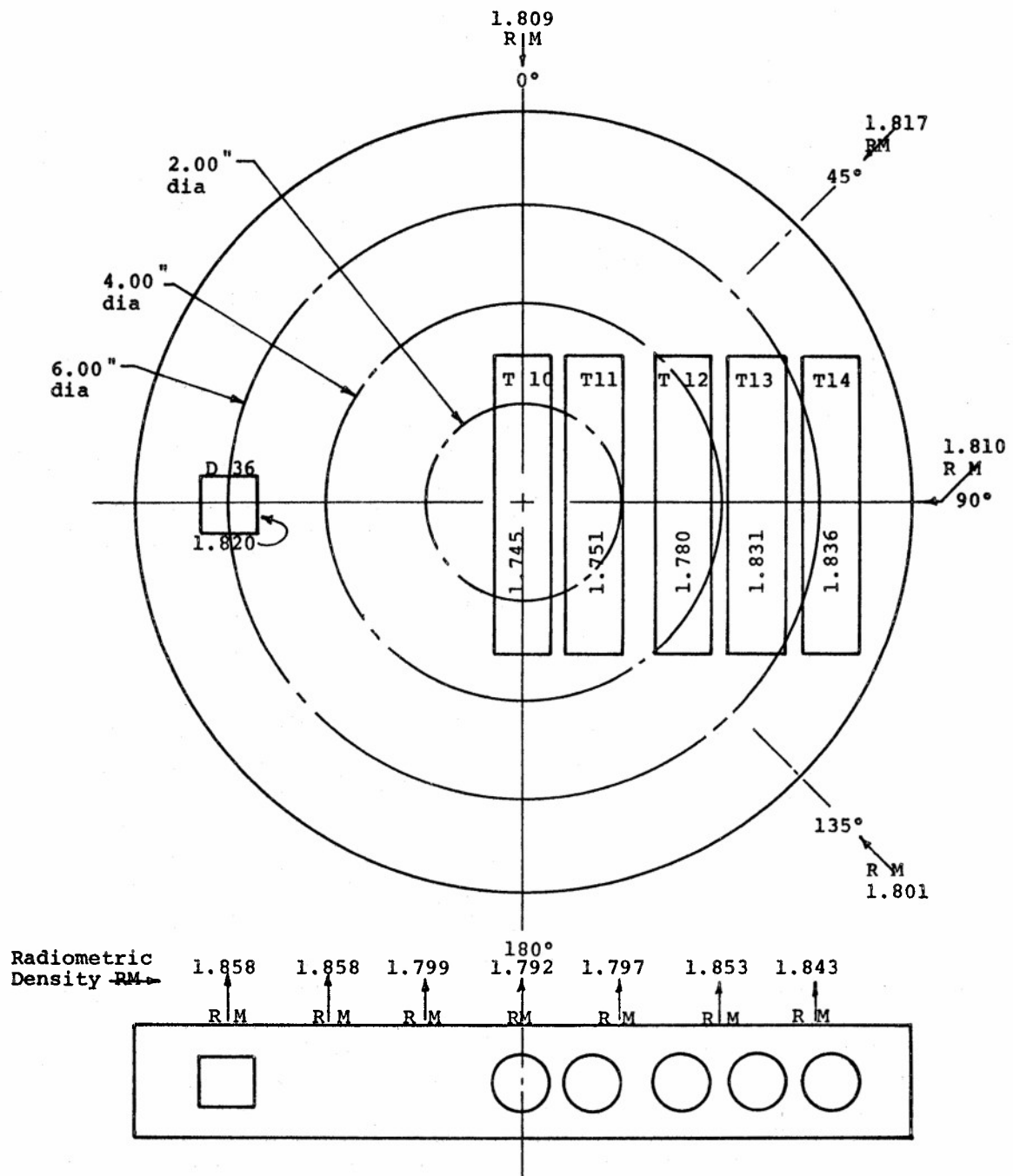


Figure 23. Original Avco Cutting Plan for Slab Number 4  
Showing Radiometric Density, ATJ-S Billet L-16-7

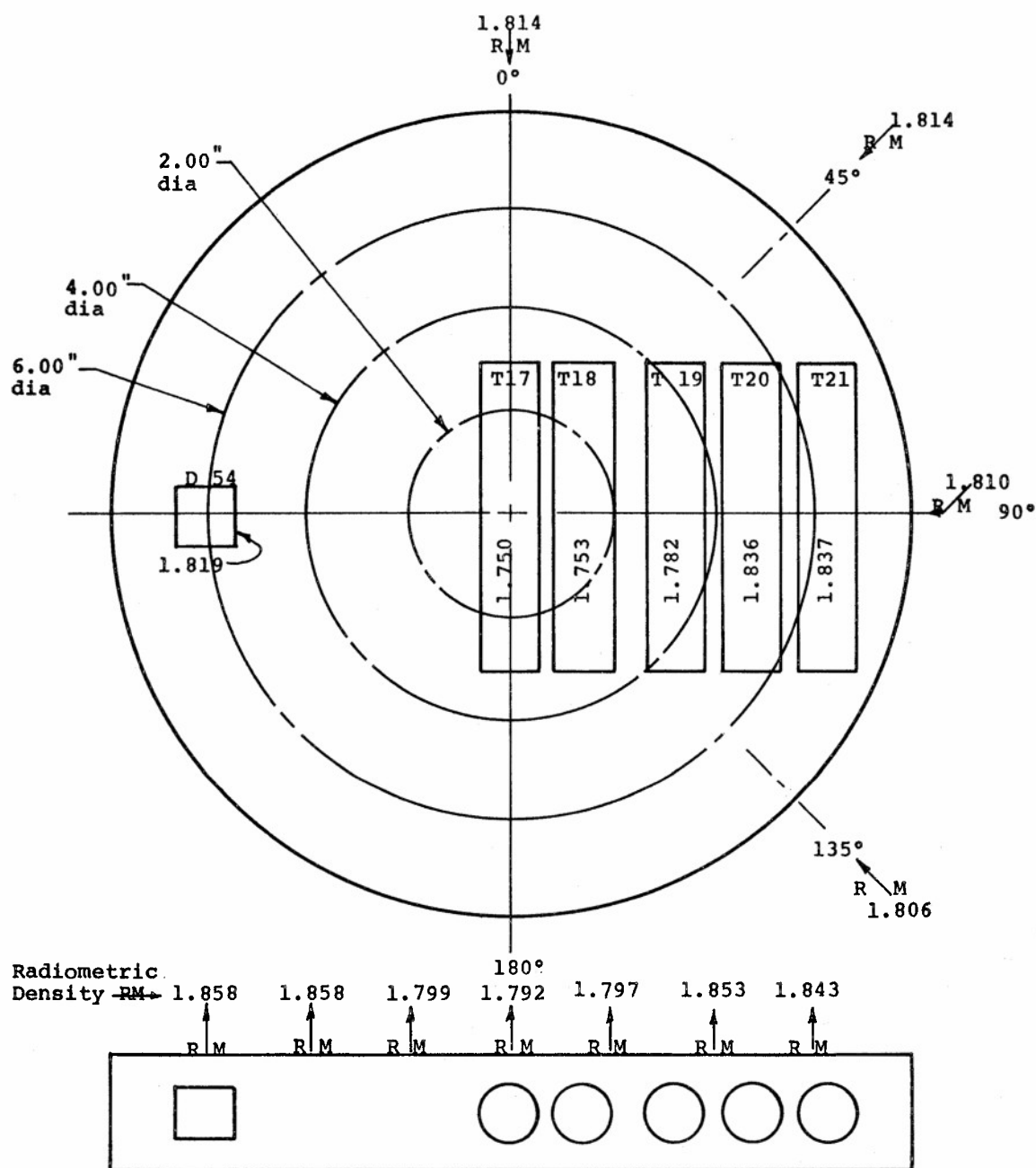


Figure 24. Original Avco Cutting Plan for Slab Number 6 Showing Radiometric Density, ATJ-S Billet L-16-7

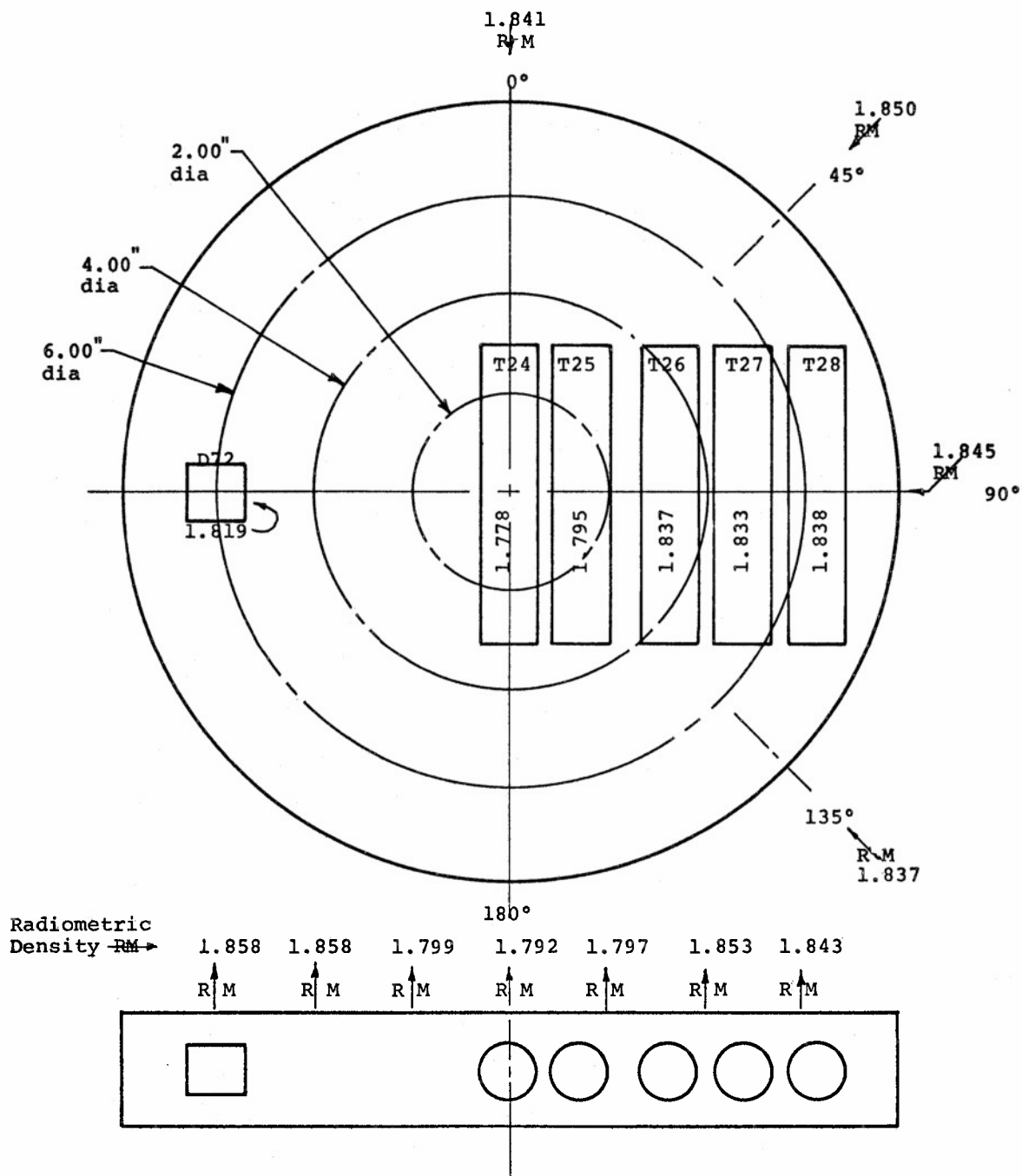


Figure 25. Original Avco Cutting Plan for Slab Number 8  
Showing Radiometric Density, ATJ-S Billet L-16-7

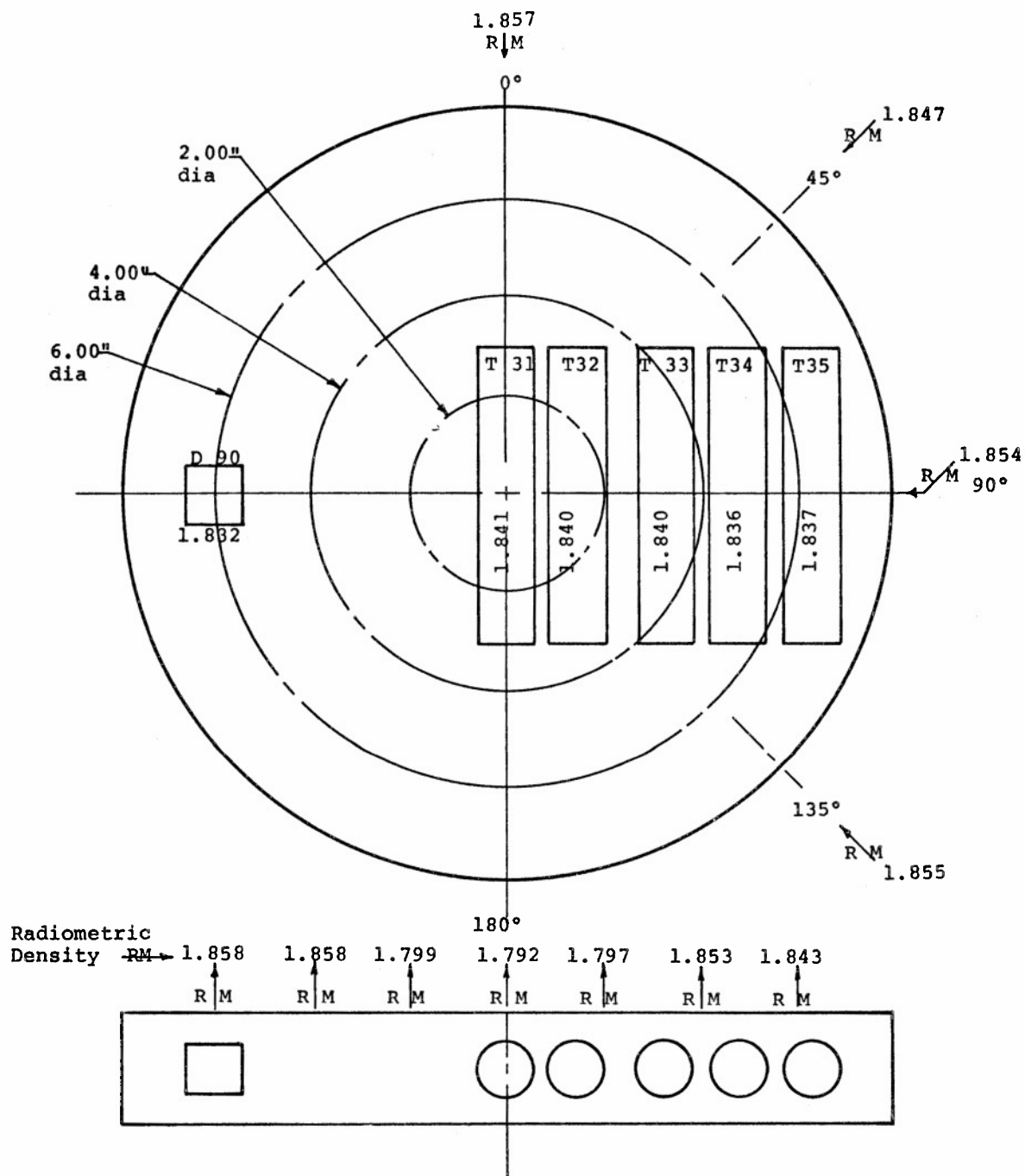
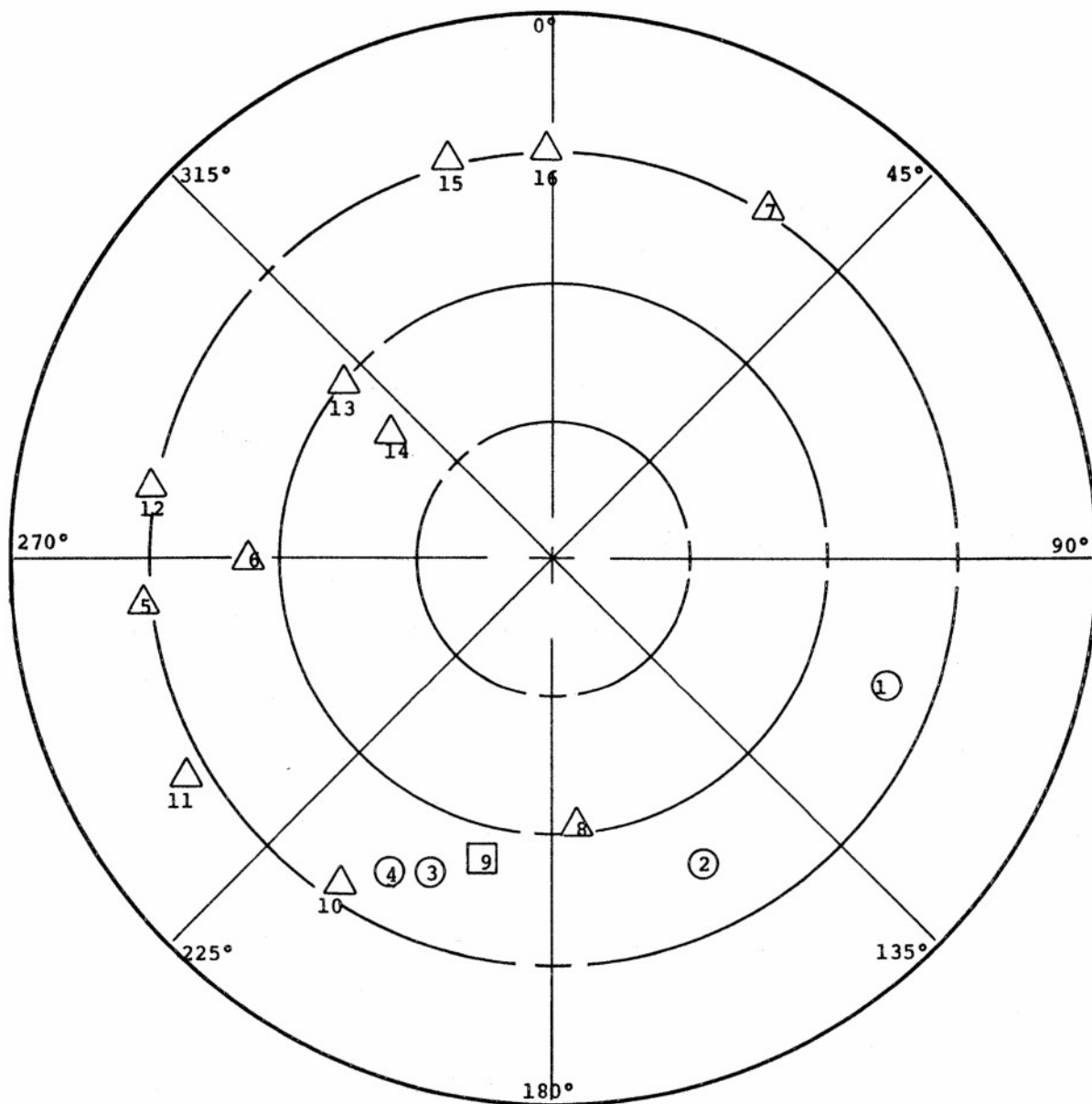


Figure 26. Original Avco Cutting Plan for Slab Number 10 Showing Radiometric Density, ATJ-S Billet L-16-7



Detected Radially: 1 - 6  
 Detected Axially: 7 - 16  
 Radial Scan: 2.25 MHZ  
 Axial Scan: 1.0 MHZ

Key

○ = 20 - 40% of Full CRT scale  
 △ = 40 - 70% of Full CRT Scale  
 □ = 70 - 100% of Full CRT Scale

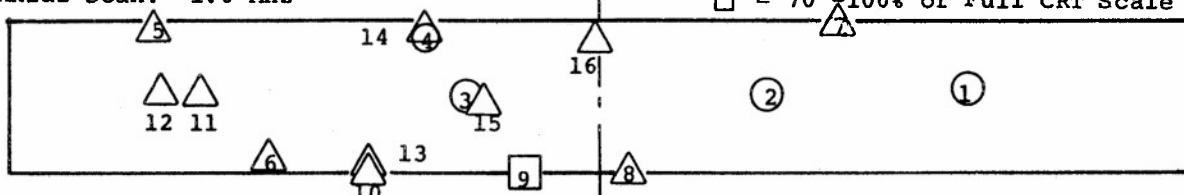
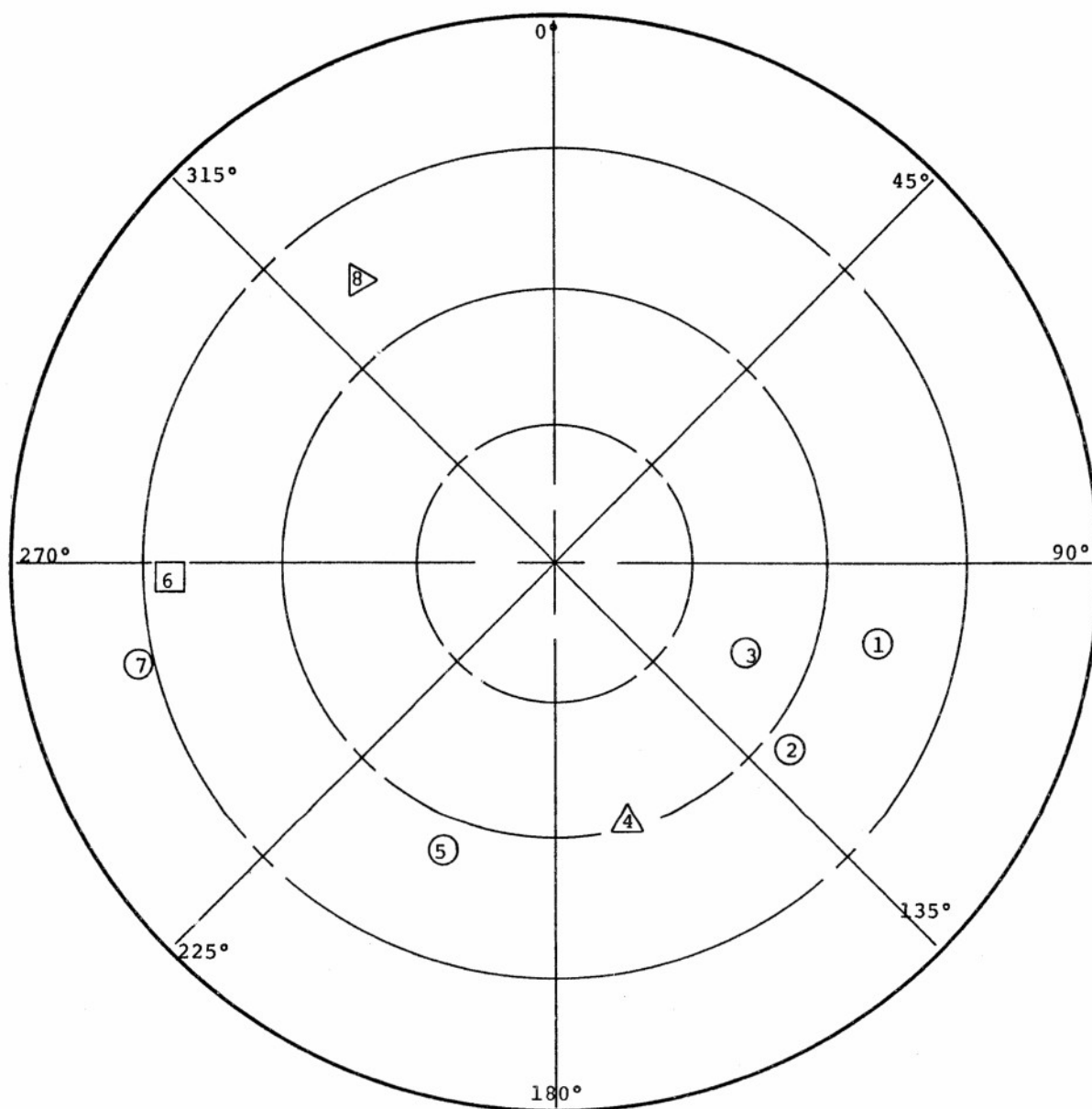


Figure 27. Avco Ultrasonic Flaw Detection, Slab Number 2, ATJ-S Billet L-16-7





Detected Radially: 1 - 7

Detected Axially: 8 only

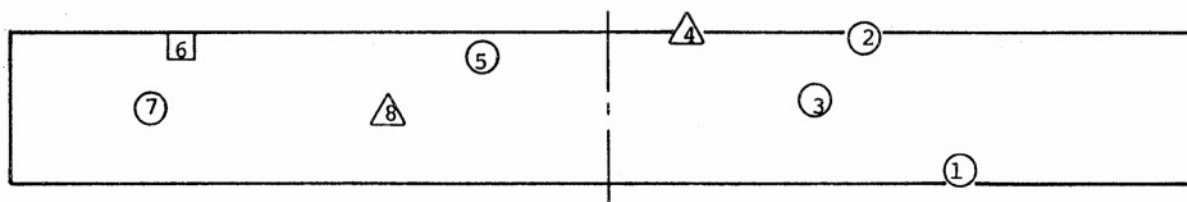
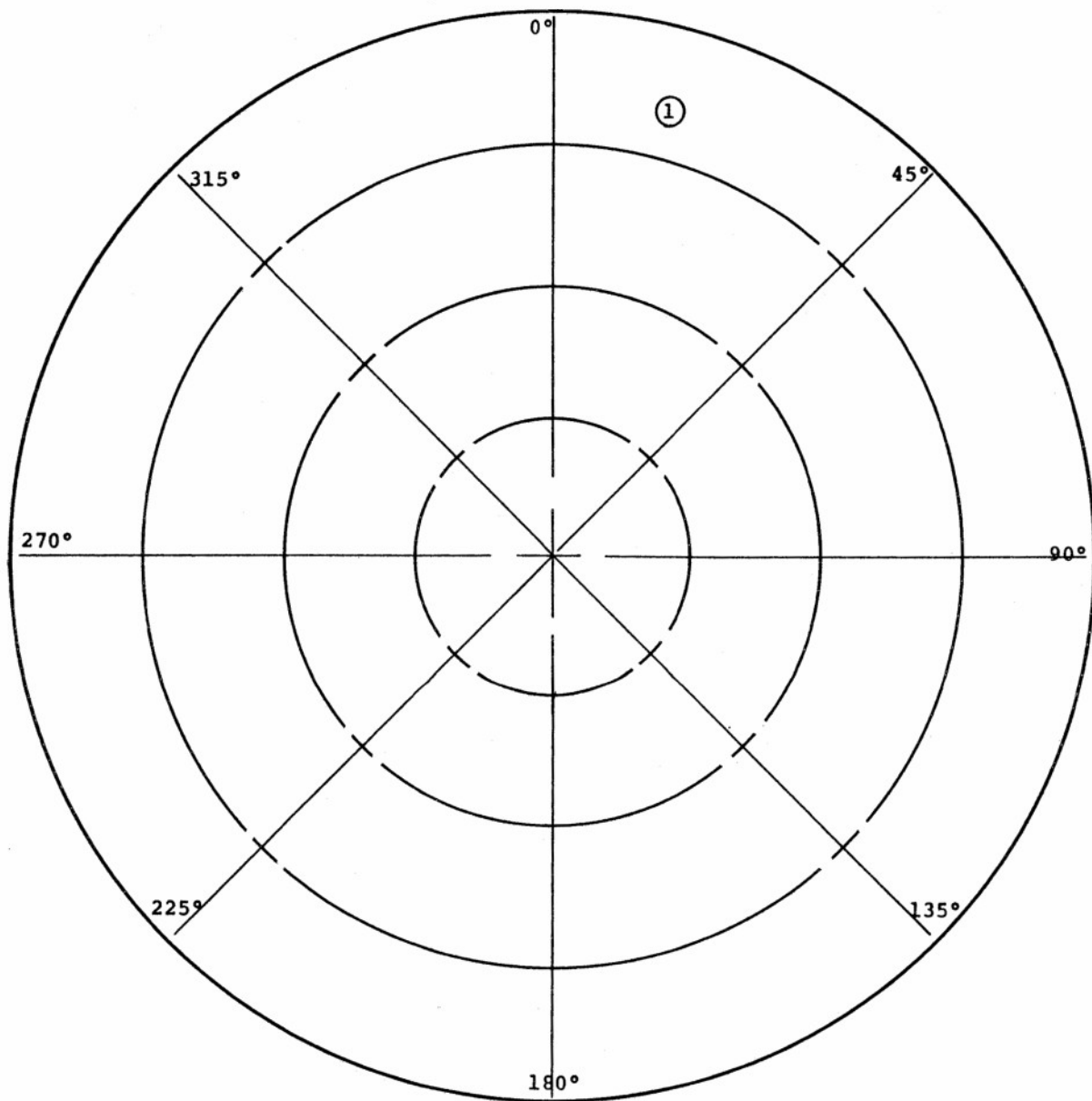


Figure 28. Avco Ultrasonic Flaw Detection, Slab Number 4, ATJ-S Billet L-16-7



Detected radially: 1  
 Detected Axially : none

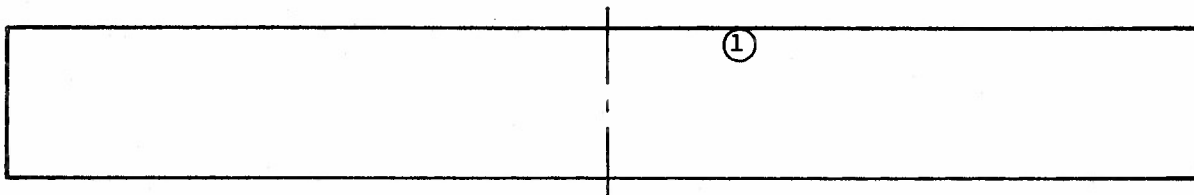
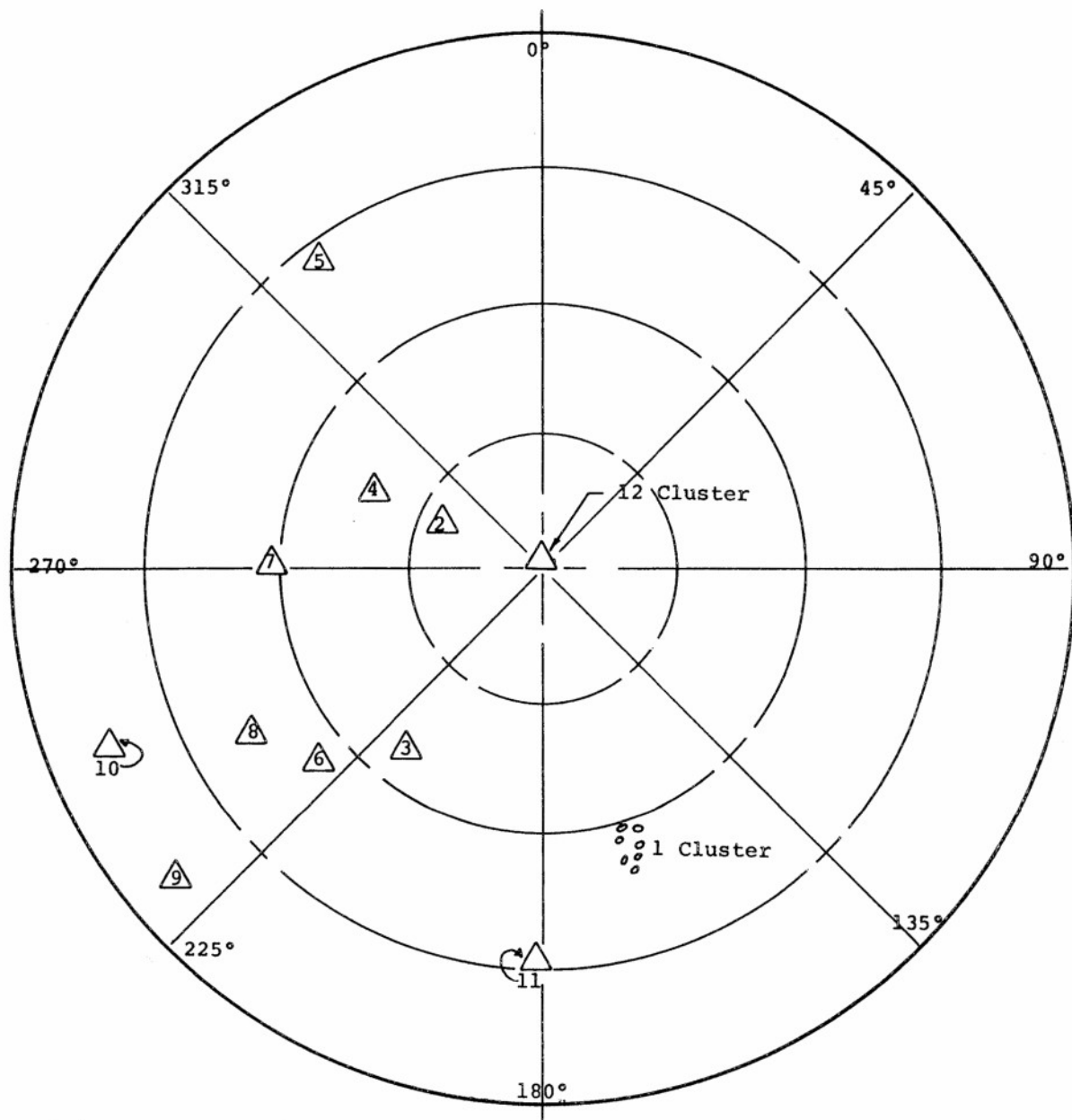


Figure 29. Avco Ultrasonic Flaw Detection, Slab Number 6, ATJ-S Billet L-16-7



Detected Radially: 1

Detected Axially: 2 - 12

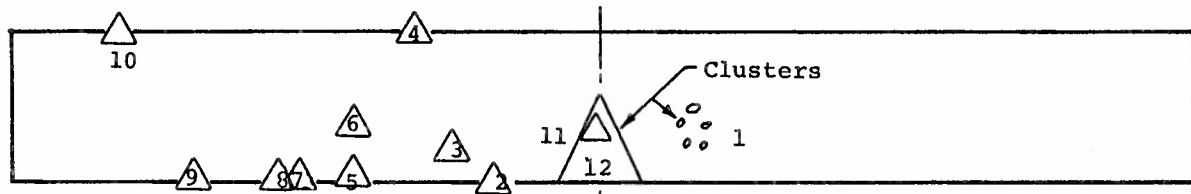
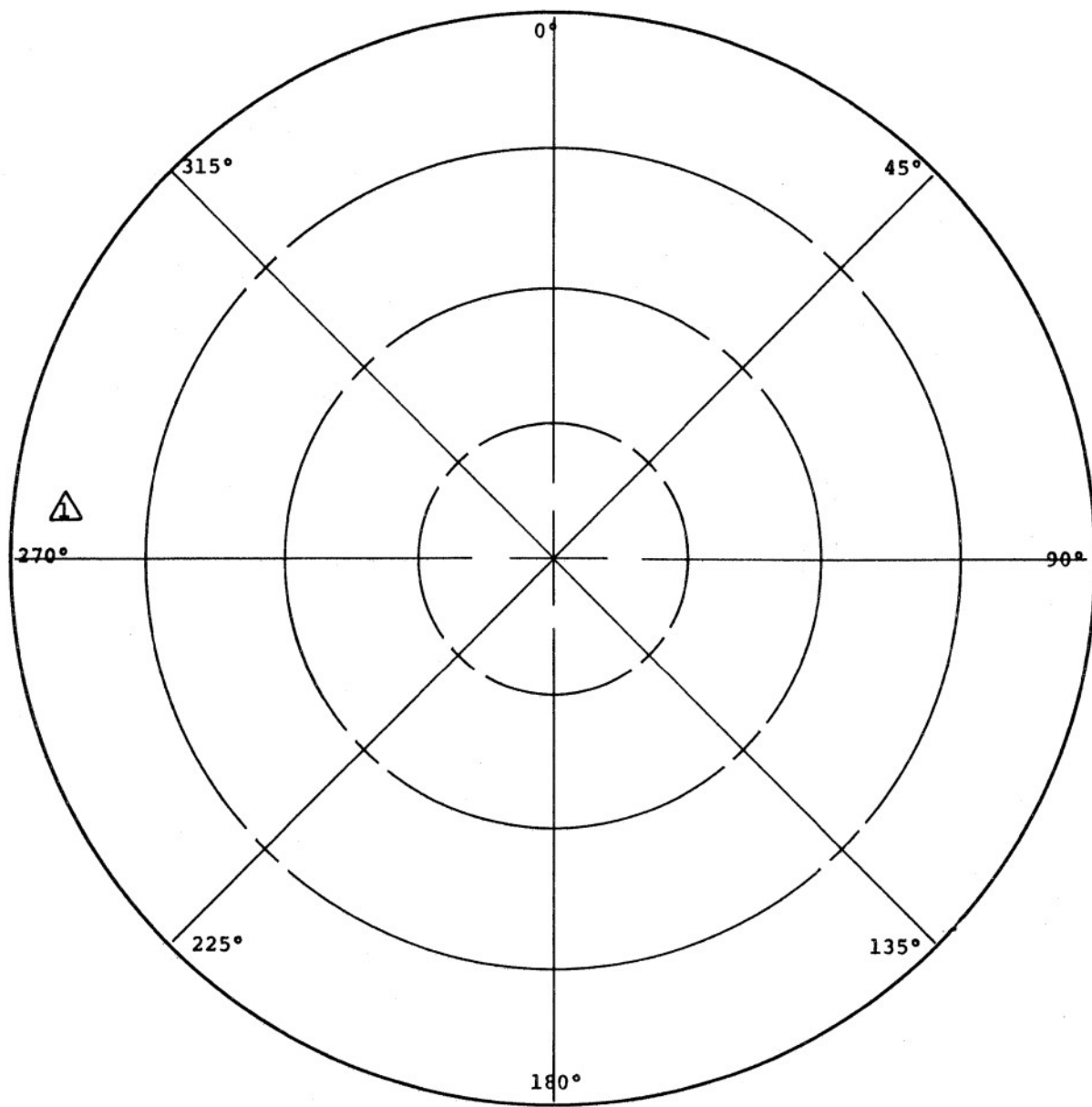


Figure 30. Avco Ultrasonic Flaw Detection, Slab Number 8, ATJ-S Billet L-16-7



Detected Radially: None  
 Detected Axially: 1 only

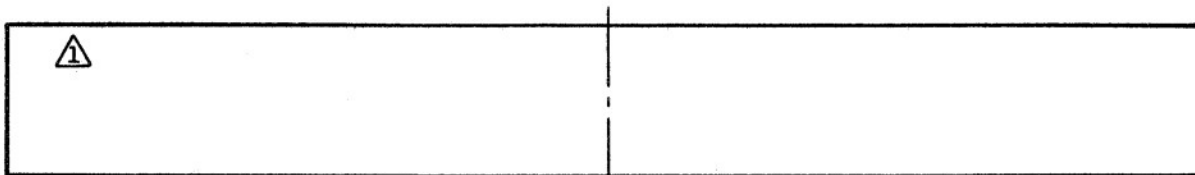


Figure 31. Avco Ultrasonic Flaw Detection, Slab Number 10, ATJ-S Billet L-16-7

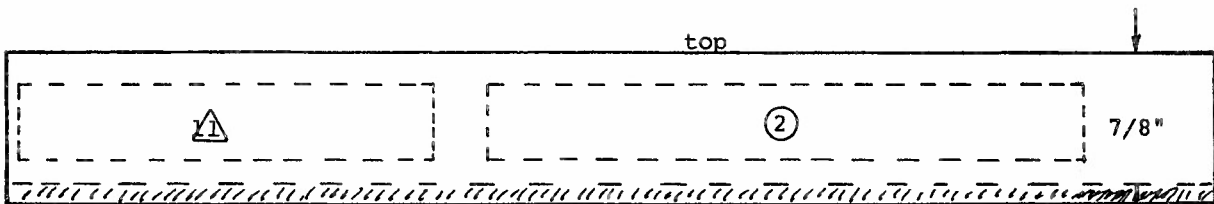
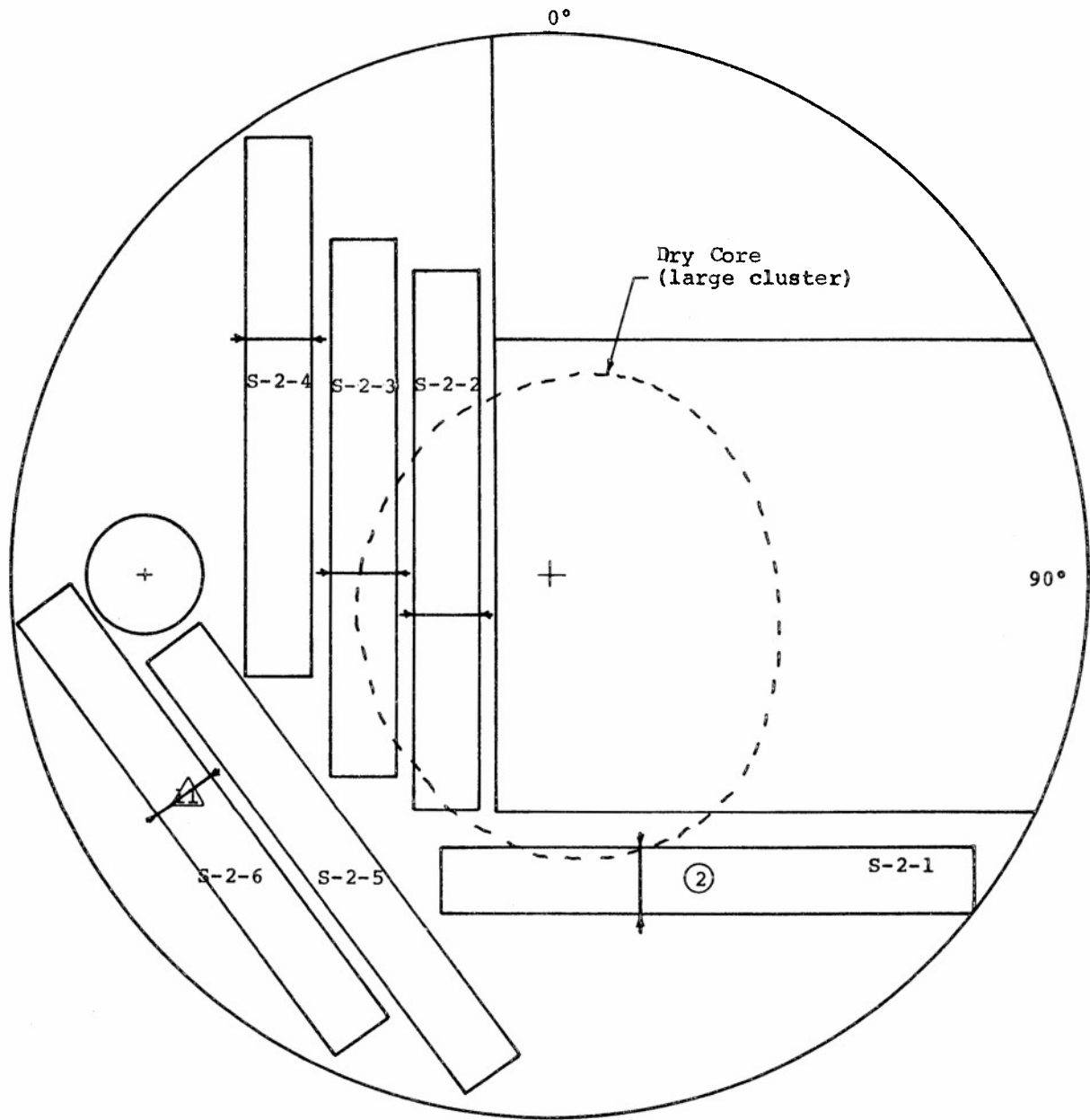


Figure 32. Cutting Plan Showing Results of Avco Ultrasonic Inspection of Specimen Blanks for Slab Number 2, ATJ-S Billet L-16-7.

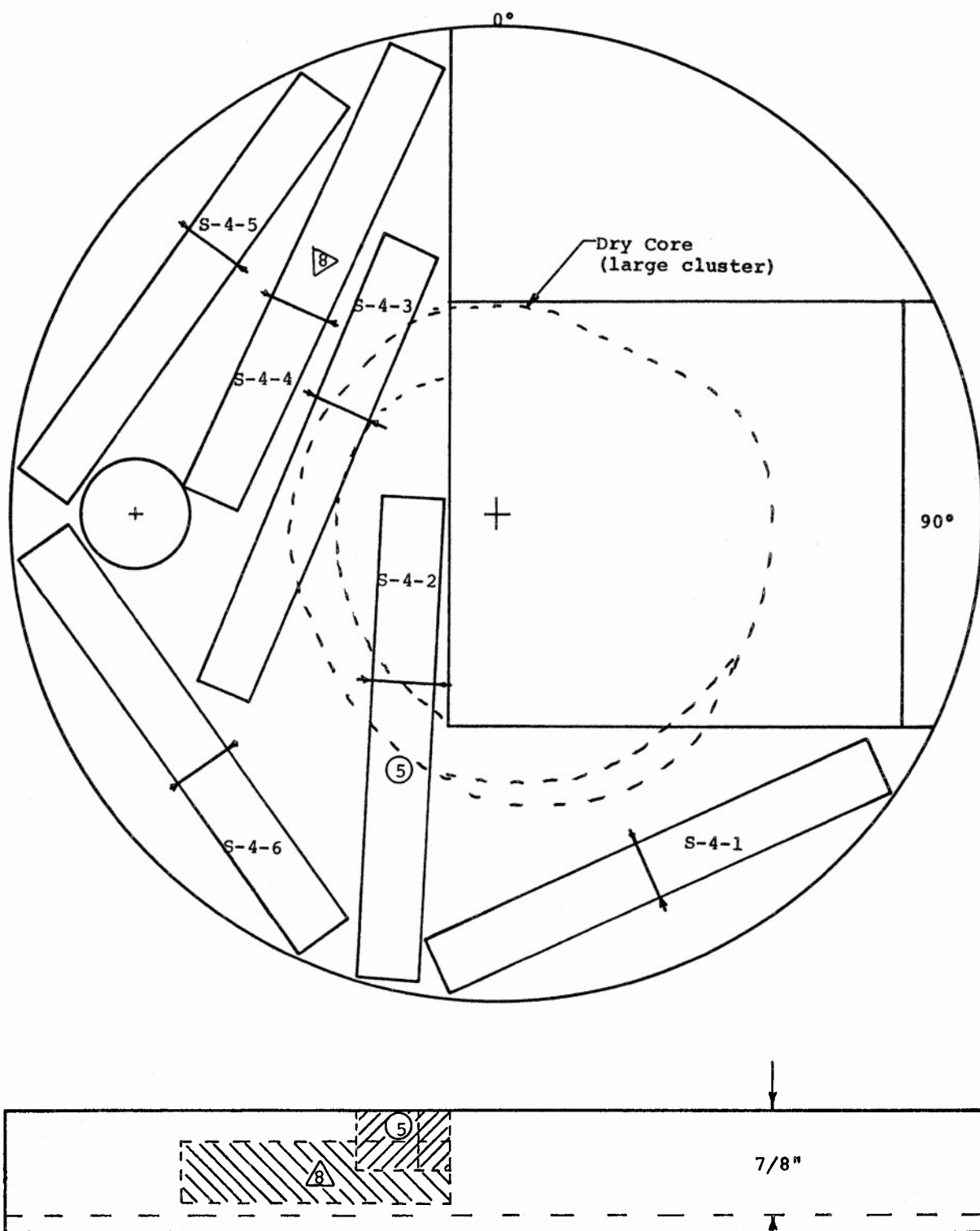


Figure 33. Cutting Plan Showing Results of Avco Ultrasonic Inspection of Specimen Blanks for Slab Number 4, ATJ-S Billet L-16-7

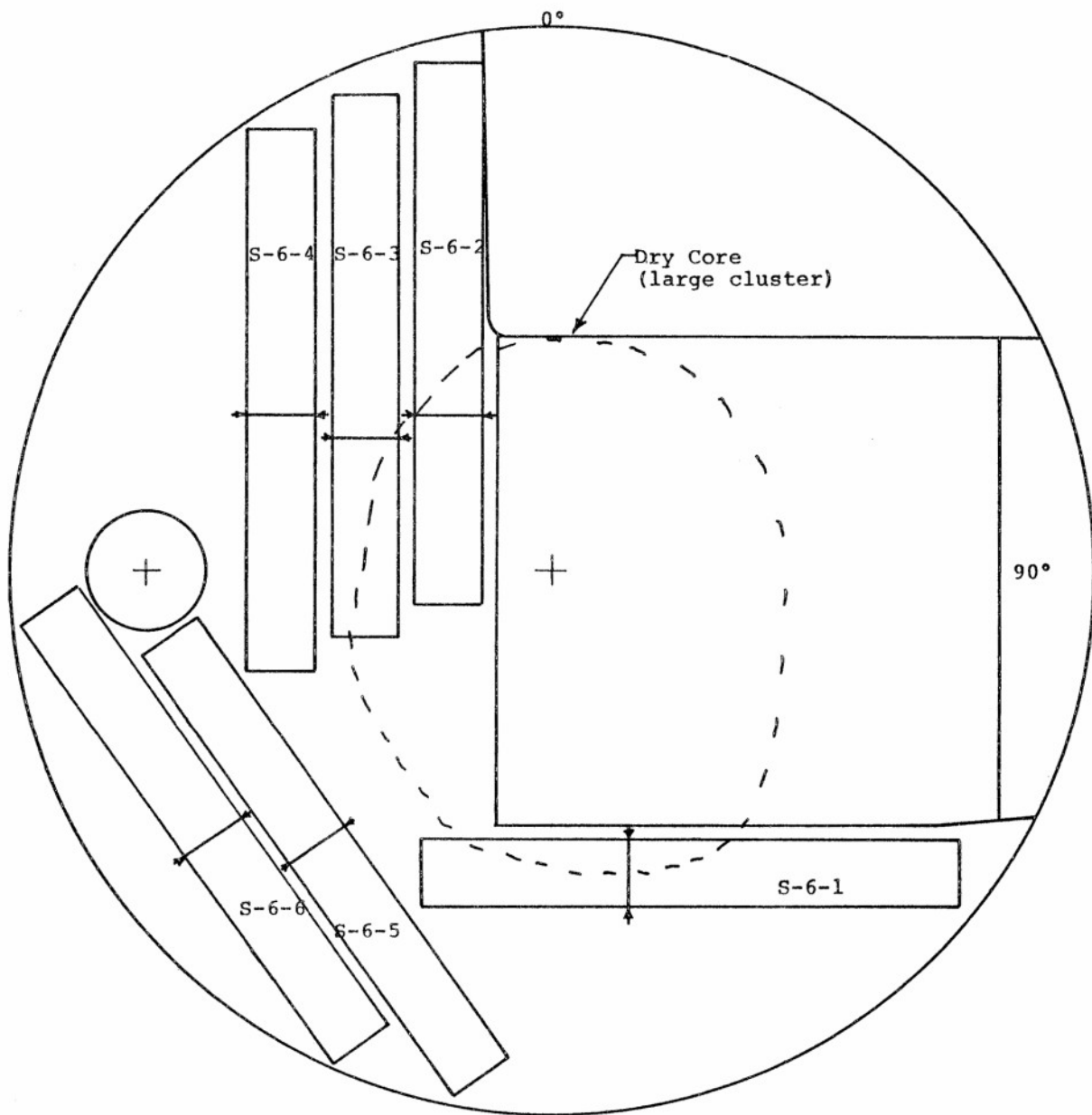


Figure 34. Cutting Plan Showing Results of Avco Ultrasonic Inspection of Specimen Blanks for Slab Number 6, ATJ-S Billet L-16-7

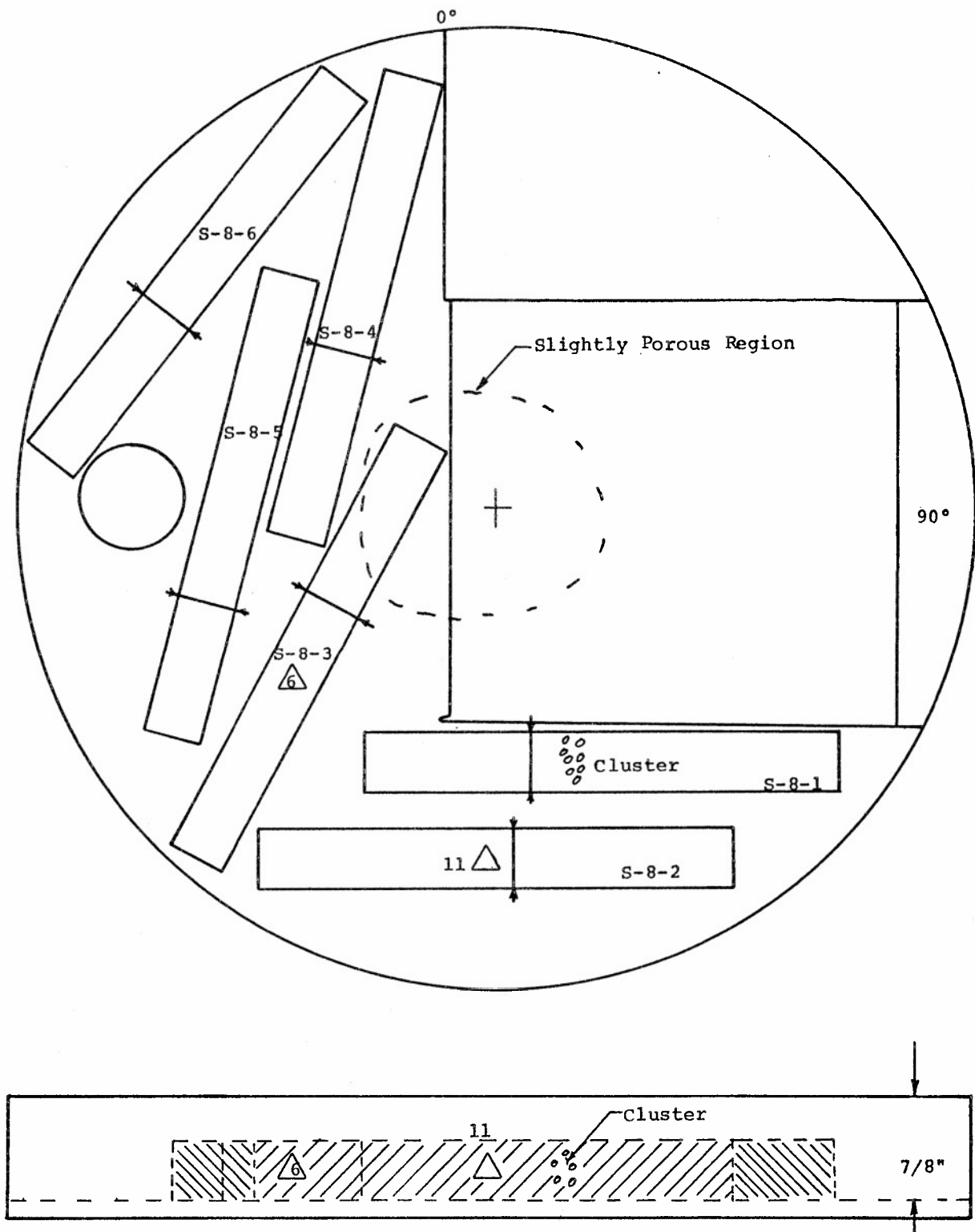


Figure 35. Cutting Plan Showing Results of Avco Ultrasonic Inspection of Specimen Blanks for Slab Number 8, ATJ-S Billet L-16-7



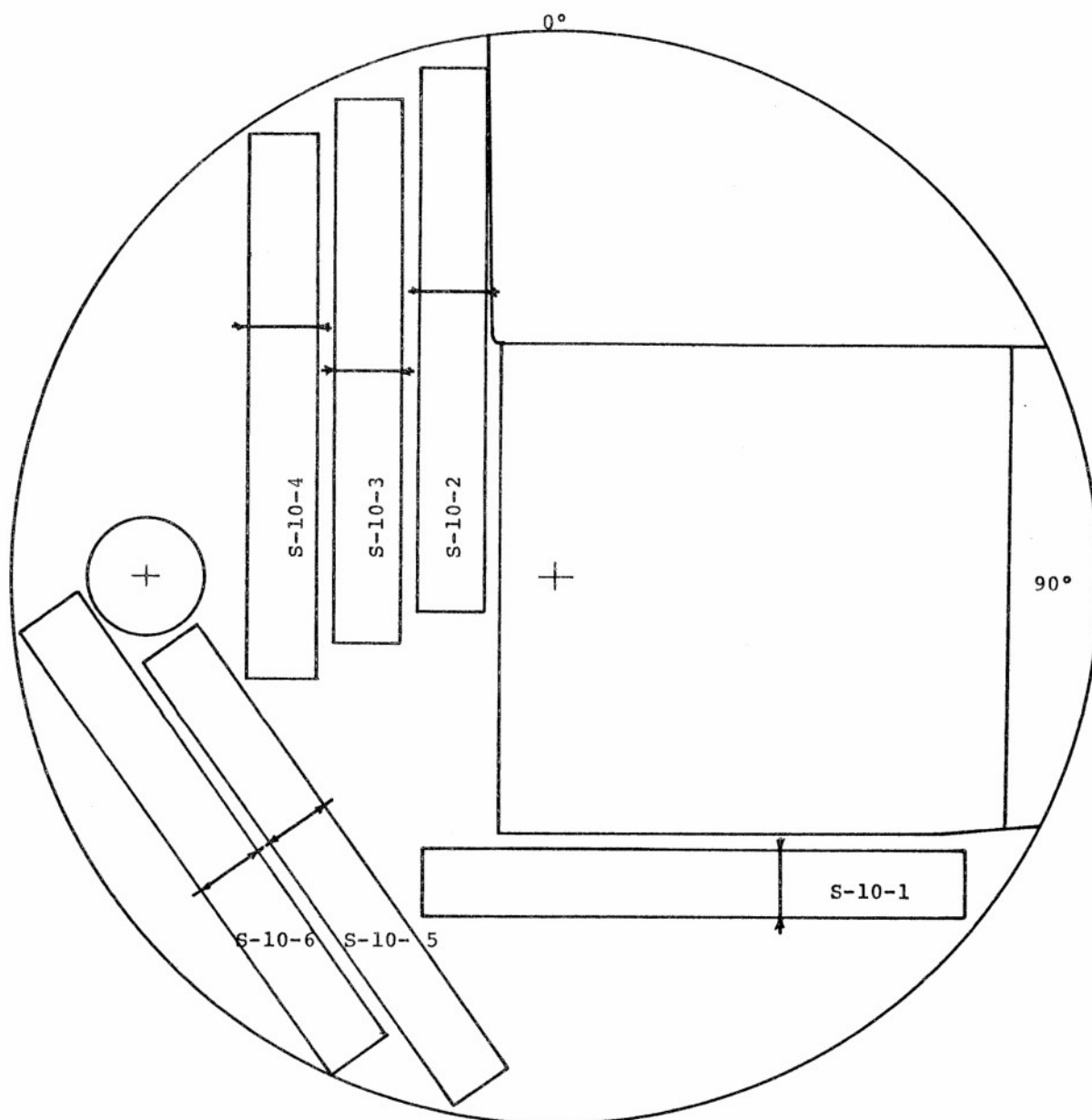
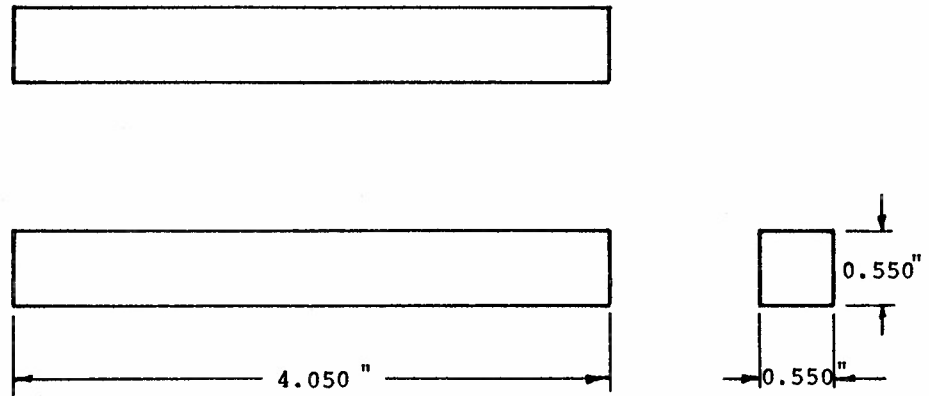
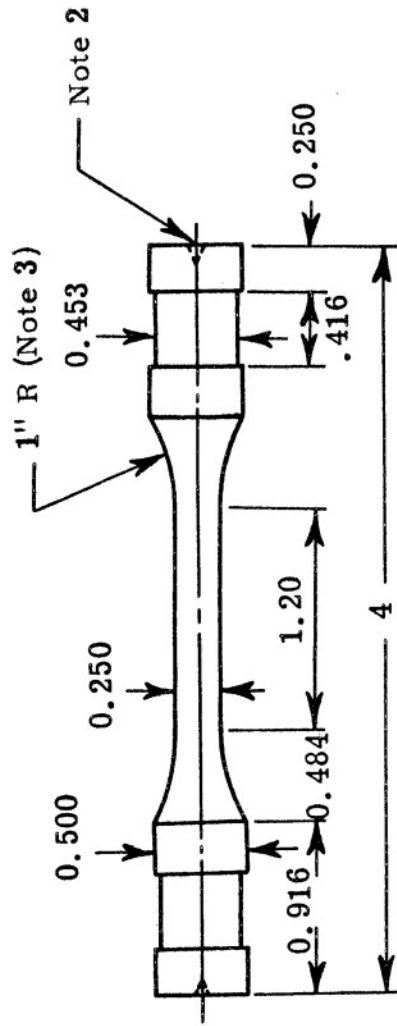


Figure 36. Cutting Plan Showing Results of Avco Ultrasonic Inspection of Specimen Blanks for Slab Number 10, ATJ-S Billet L-16-7



Note: Tolerance on all dimensions  $\pm 0.020$  "

Figure 37. Tensile Test Specimen Blank Configuration Used for ATJ-S Billet L-16-7



Notes:

1. All diameters must be true and concentric to within 0.0005 inch.
2. Both ends flat and perpendicular to  $\phi$  to within 0.0005 inch.
3. Do not under cut radii at tangent points.
4. All dimensions are in inches. Tolerances are  $\pm 0.001$  in. on diameters,  $\pm 0.005$  in. on lengths.

Figure 38. Tensile Test Specimen Configuration Used for ATJ-S  
Billet L-16-7

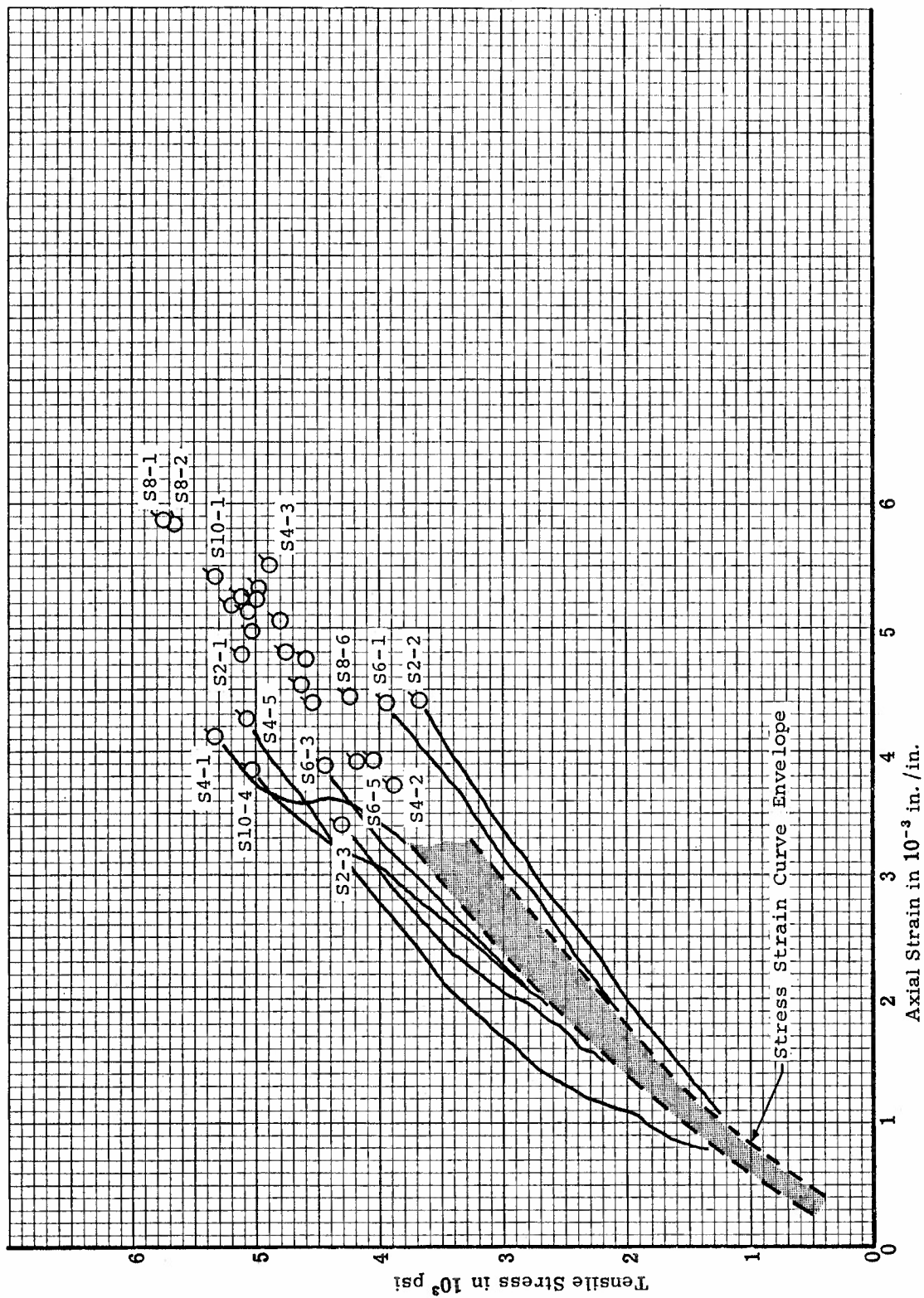


Figure 39. Tensile Stress-Strain Curve Envelope for ATJ-S Billet L-16-7 With Grain at 70°F

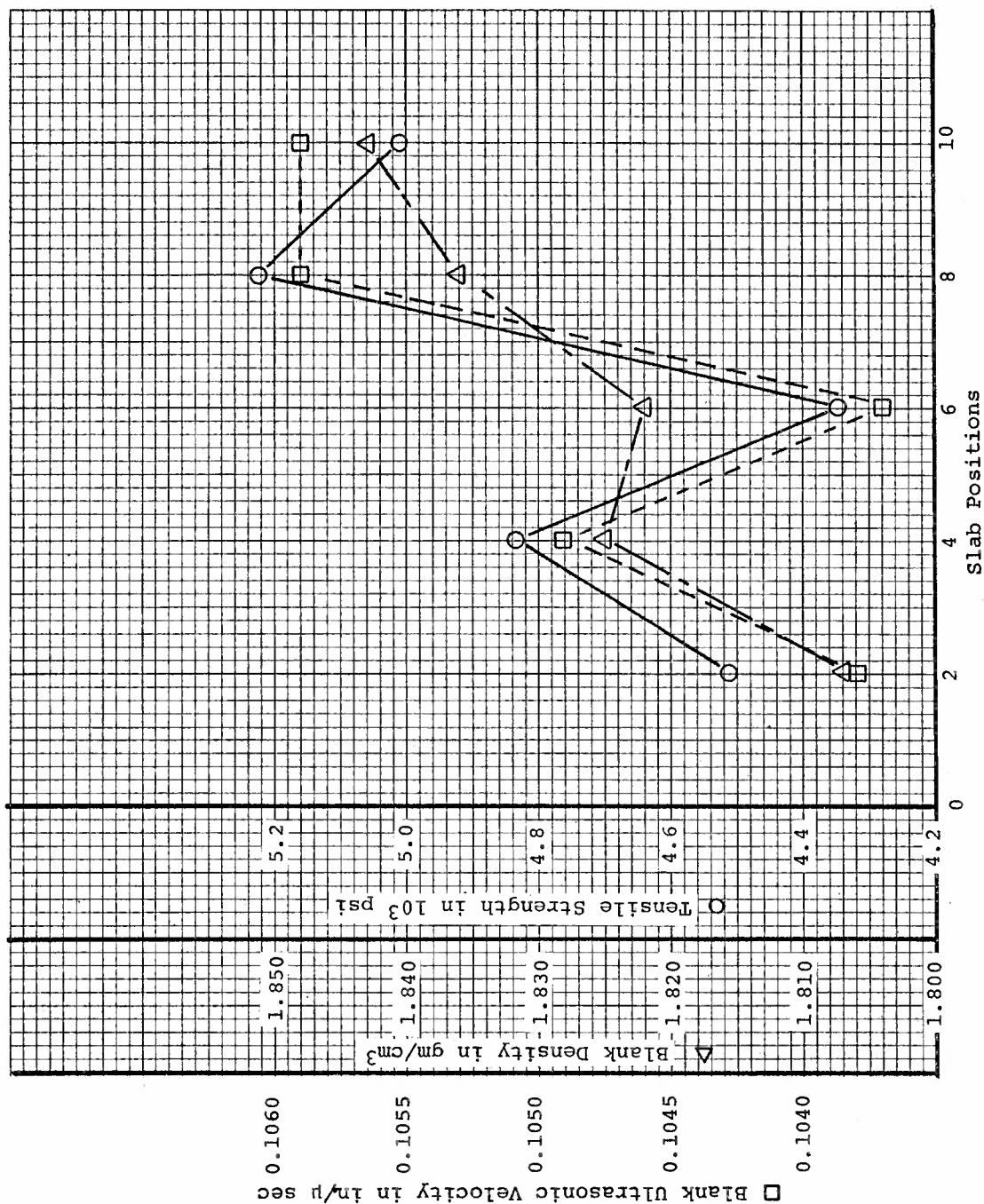


Figure 40. Average Blank Ultrasonic Velocity, Blank Density, and Tensile Strength versus Slab Position for ATJ-S Billet L-16-7

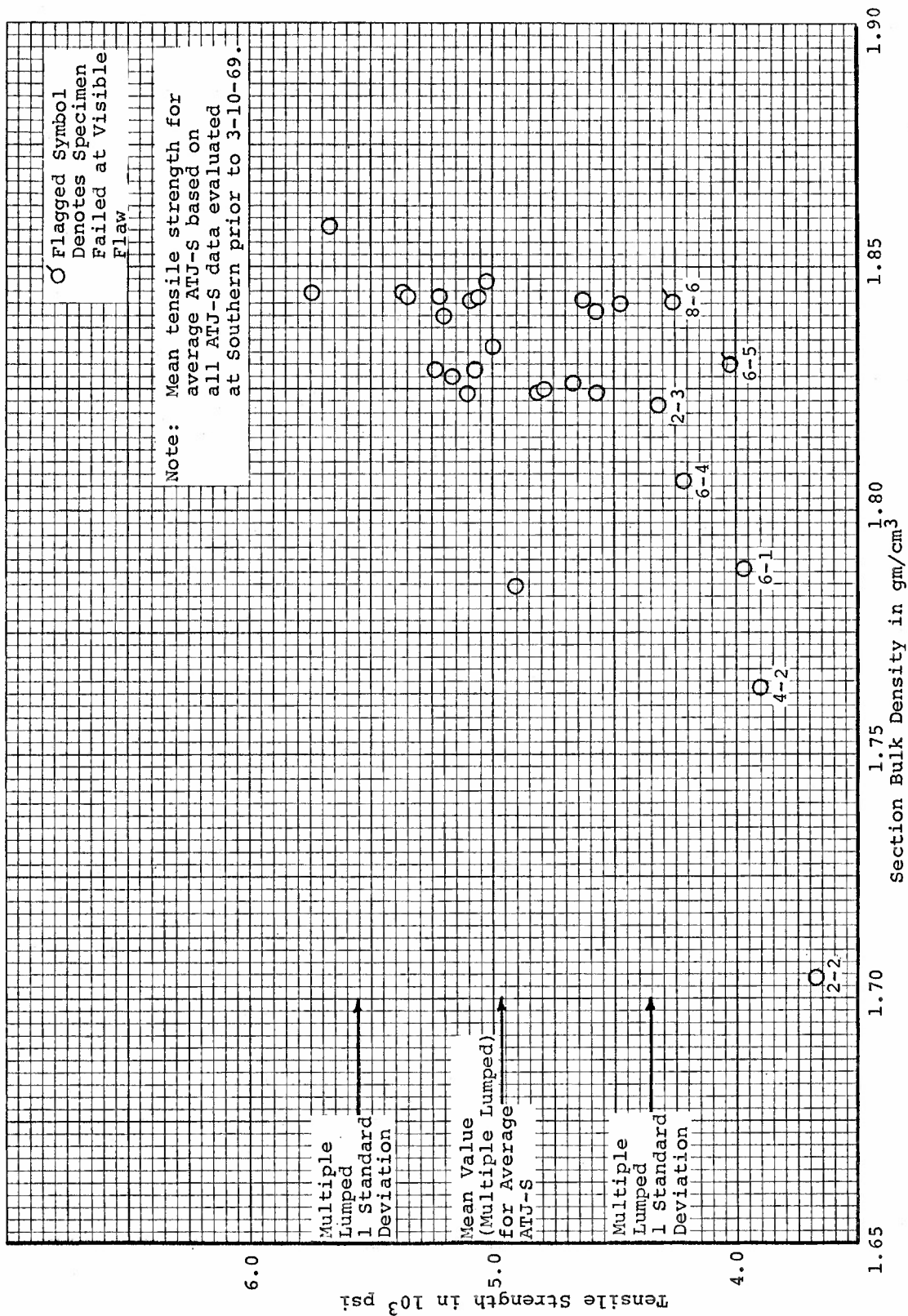


Figure 41. Tensile Strength versus Section Bulk Density for ATJ-S Billet L-16-7 With Grain at 70°F

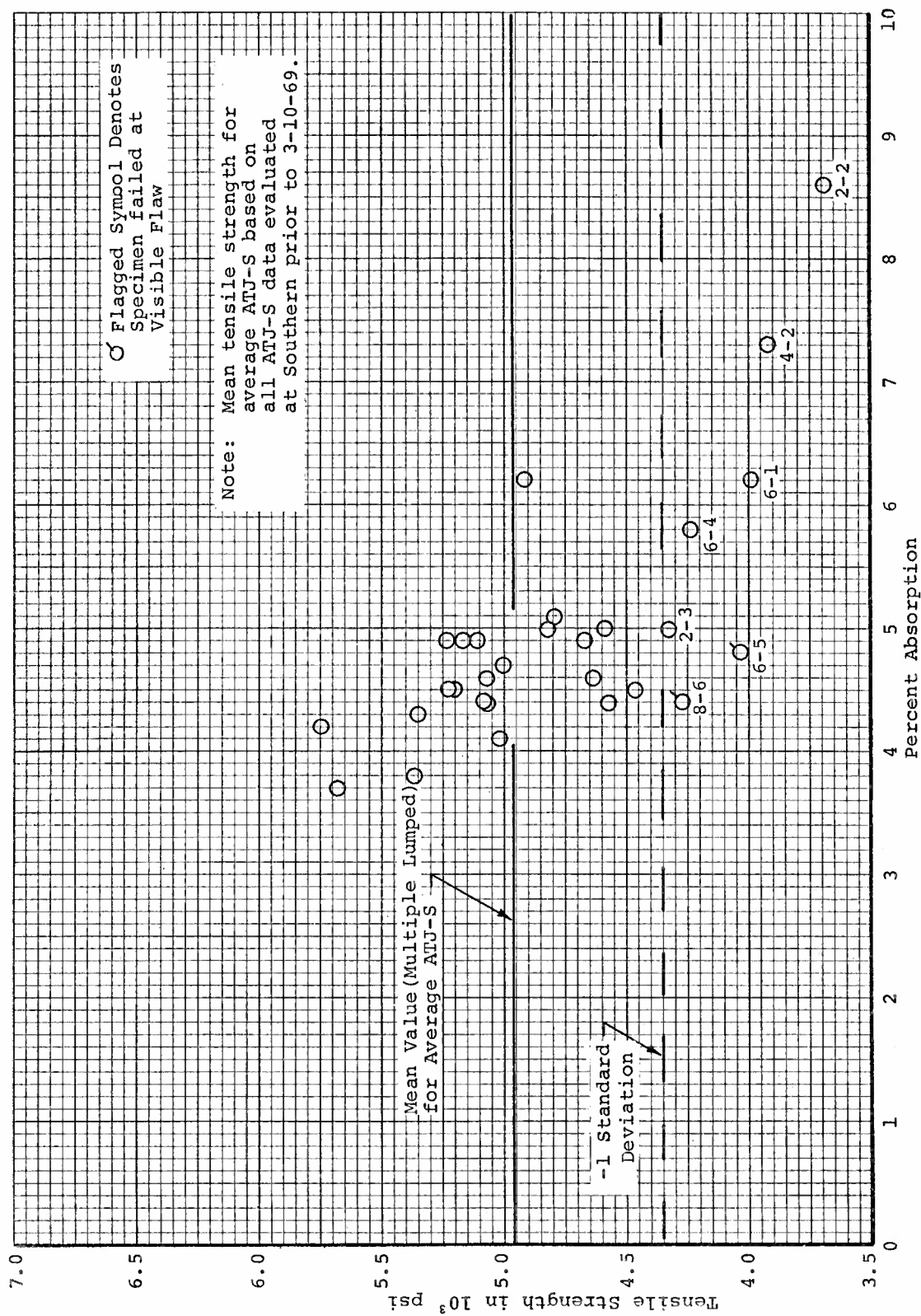


Figure 42. Tensile Strength versus Percent Absorption for ATJ-S Billet L-16-7 With Grain at 70°F

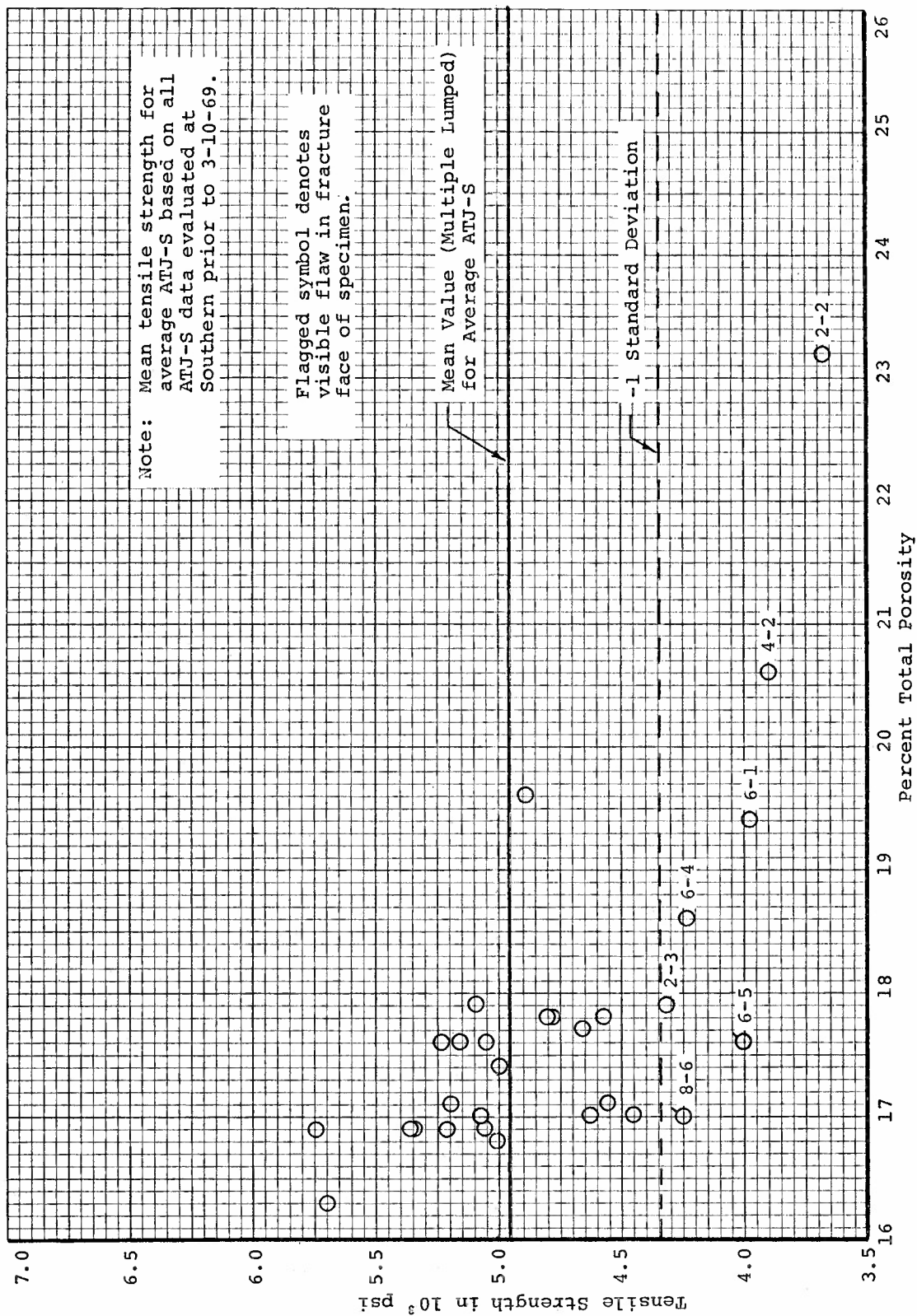


Figure 43. Tensile Strength versus Total Porosity for ATJ-S Graphite Billets L-16-7 and L-7-1 (Scrap) With Grain at 70°F



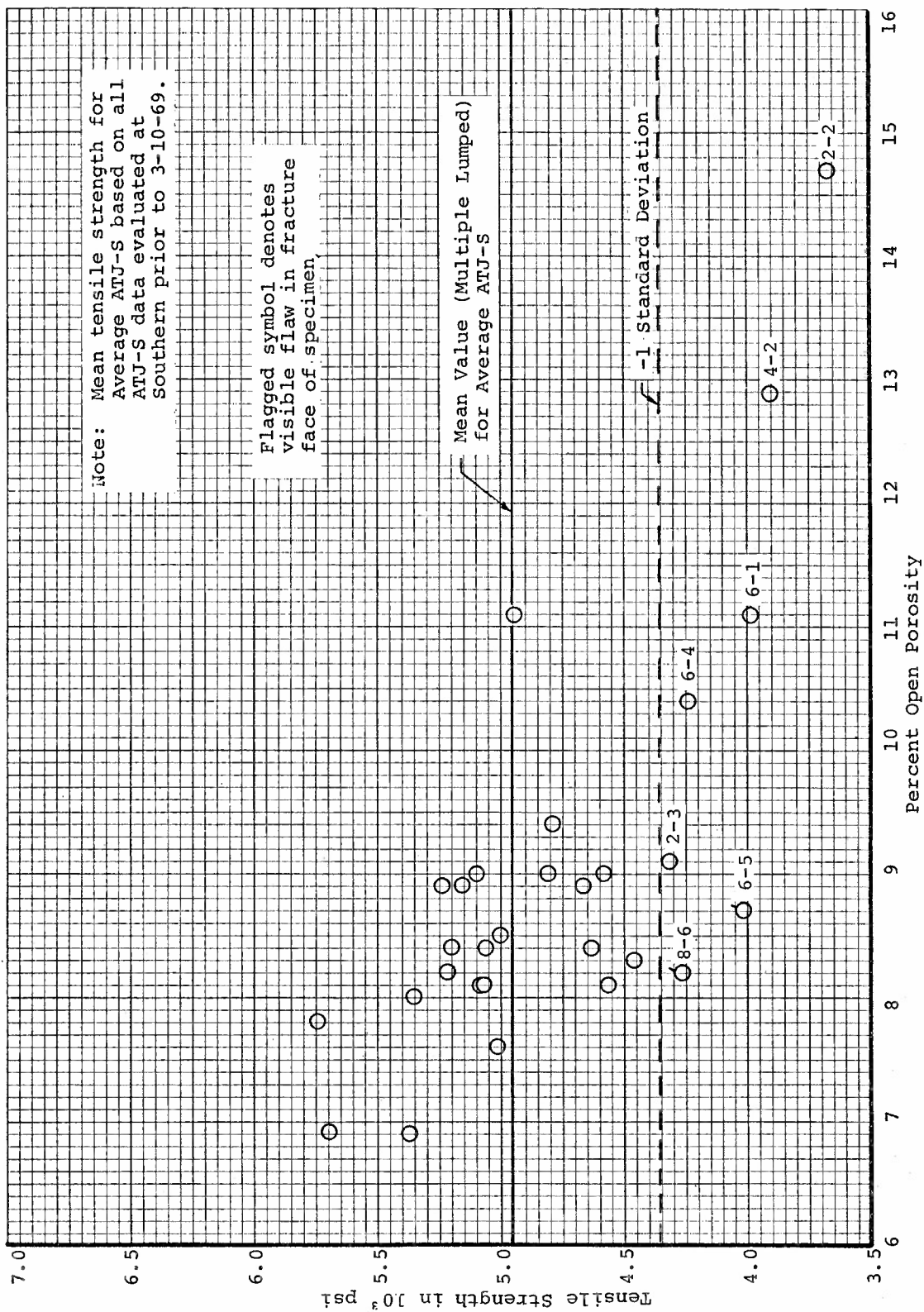


Figure 44. Tensile Strength versus Open Porosity for ATJ-S Graphite Billets L-16-7 (Including L-7-1 Scrap), With Grain at 70°F

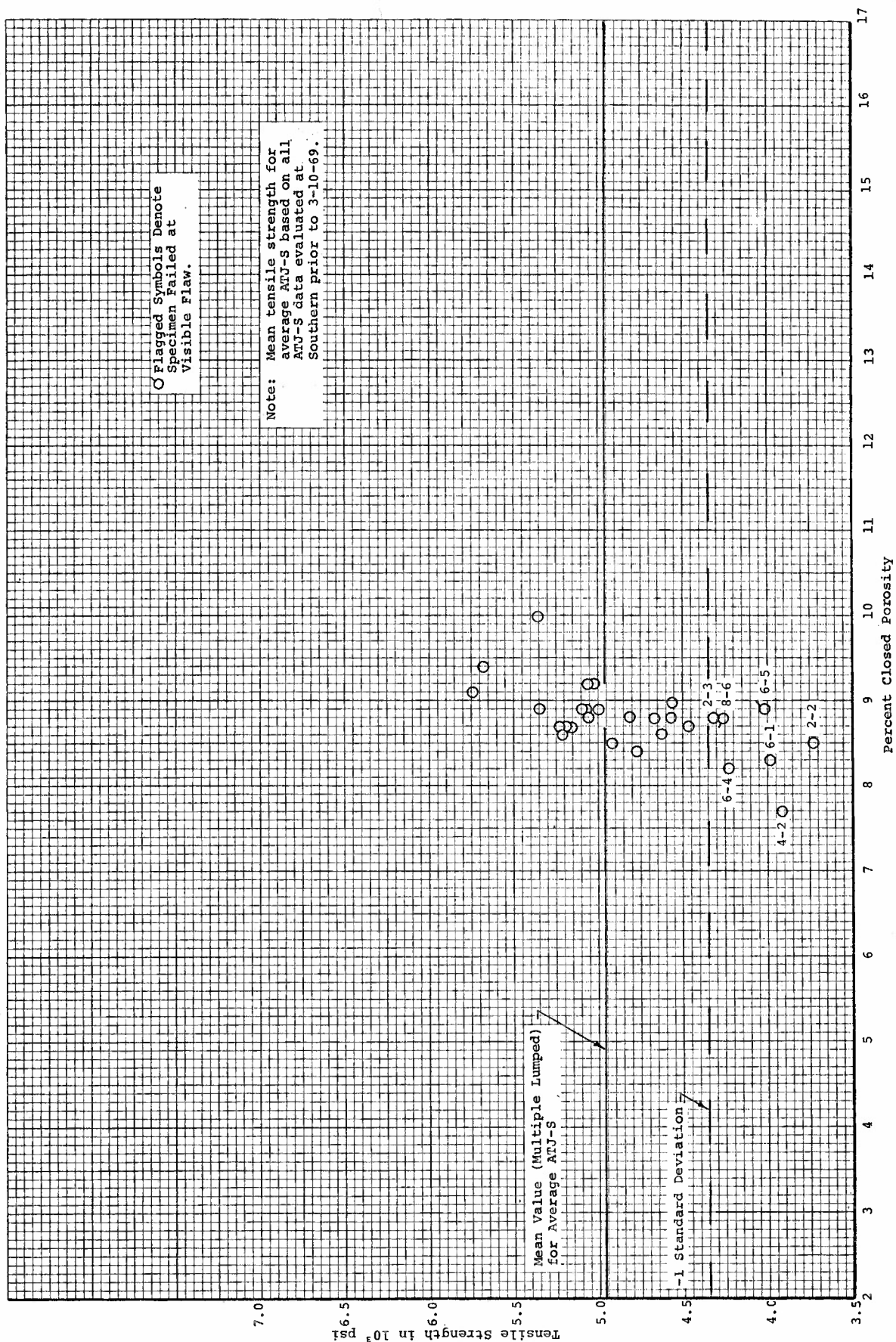


Figure 45. Tensile Strength versus Percent Closed Porosity for ATJ-S Billet L-16-7  
With Grain at 70°F

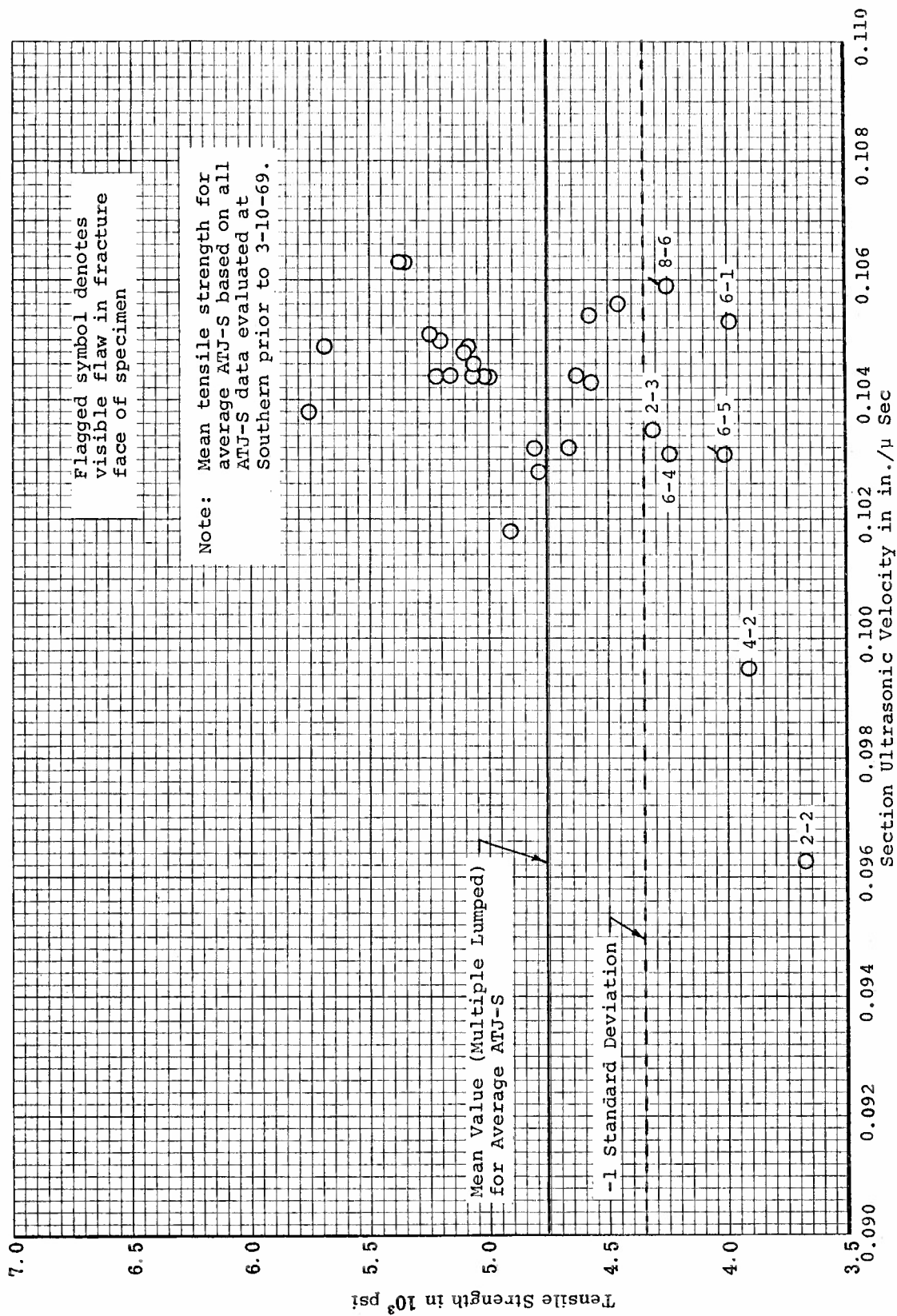


Figure 46. Tensile Strength versus Section Ultrasonic Velocity for ATJ-S Billet L-16-7 With Grain at 70°F

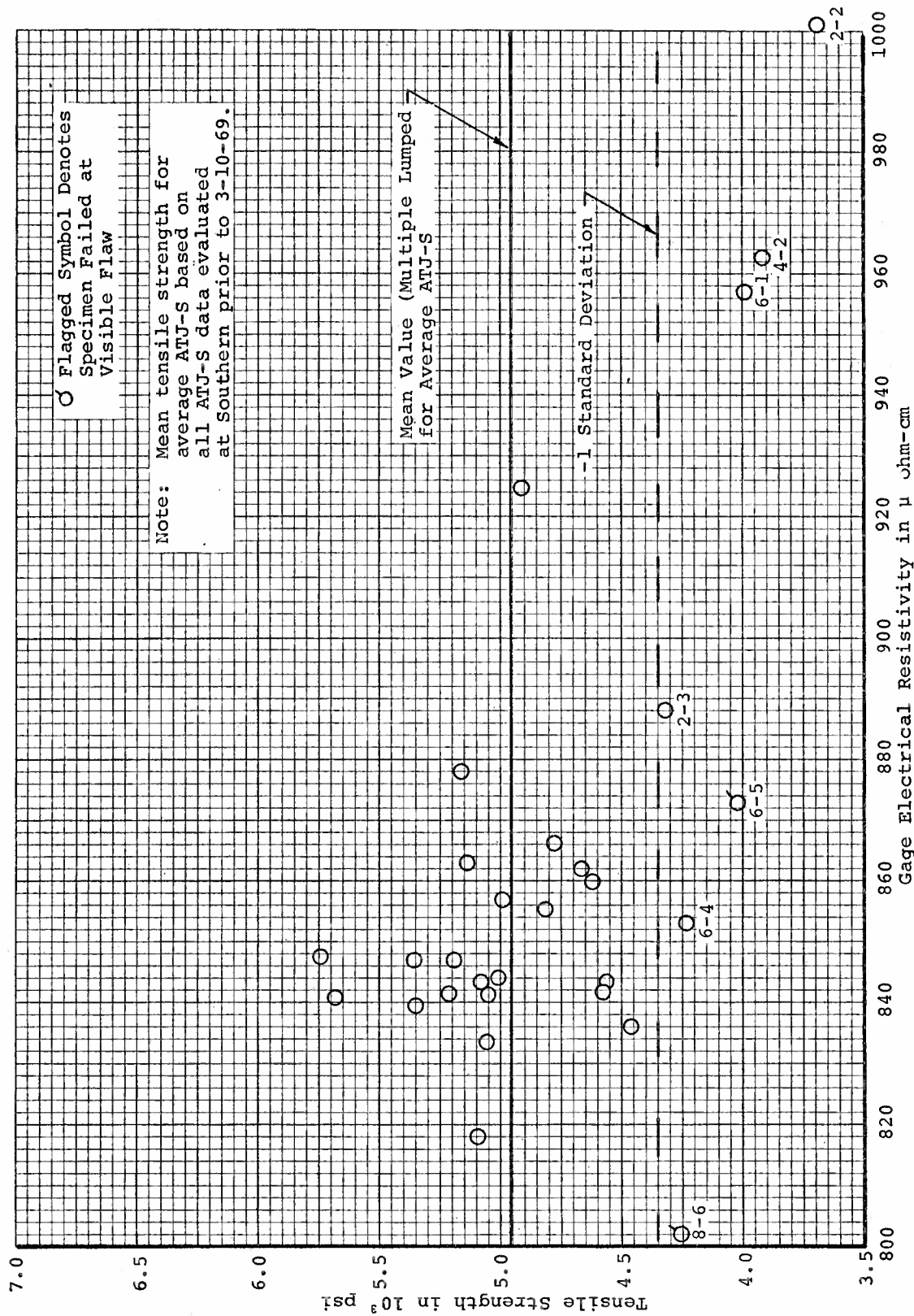


Figure 47. Tensile Strength Versus Gage Section Electrical Resistivity for ATJ-S Billet L-16-7 With Grain at 70°F

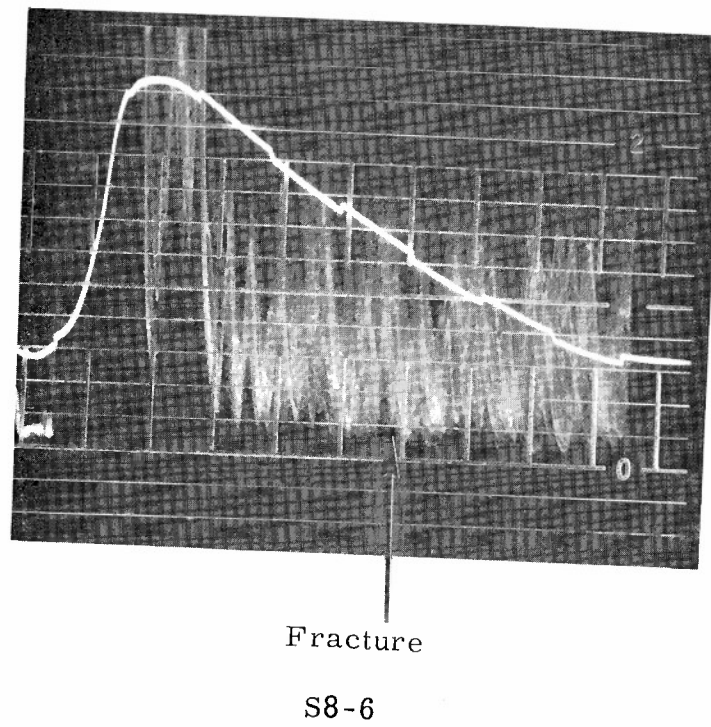
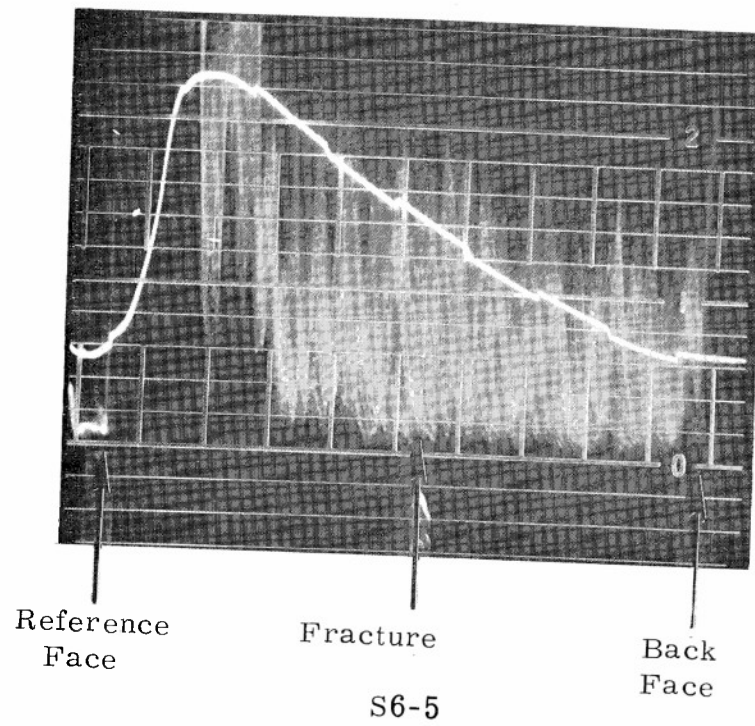


Figure 48. Pulse-Echo Smear on Disparates S6-5 and S8-6,  
ATJ-S Billet L-16-7





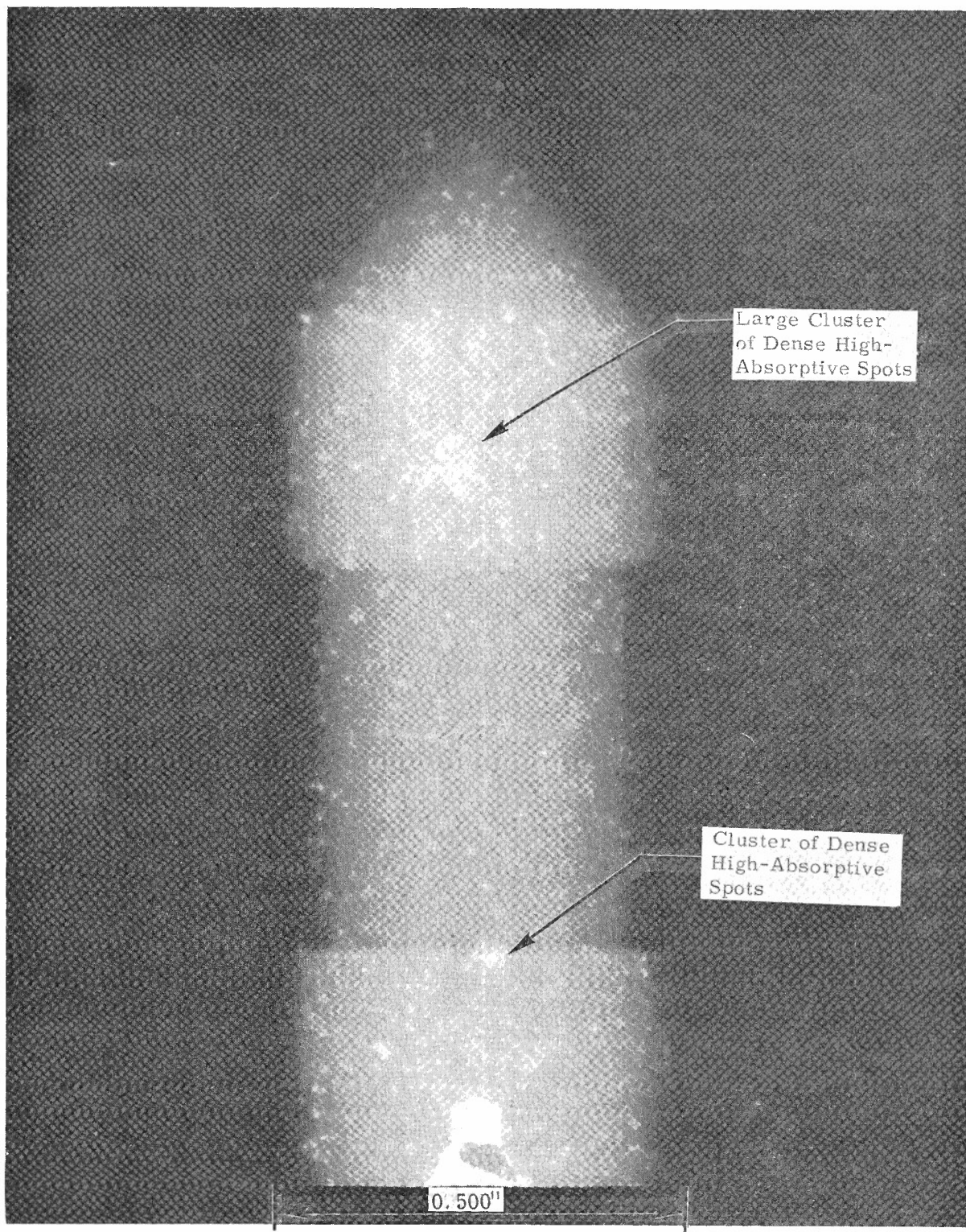


Figure 49. Radiograph of Short End of Specimen Having Highest Open Porosity (S2-2 at 14.7%) of ATJ-S Billet L-16-7





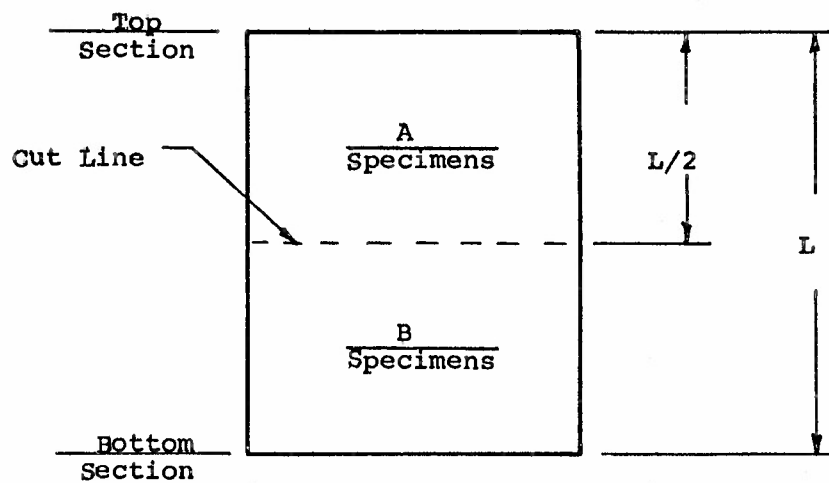
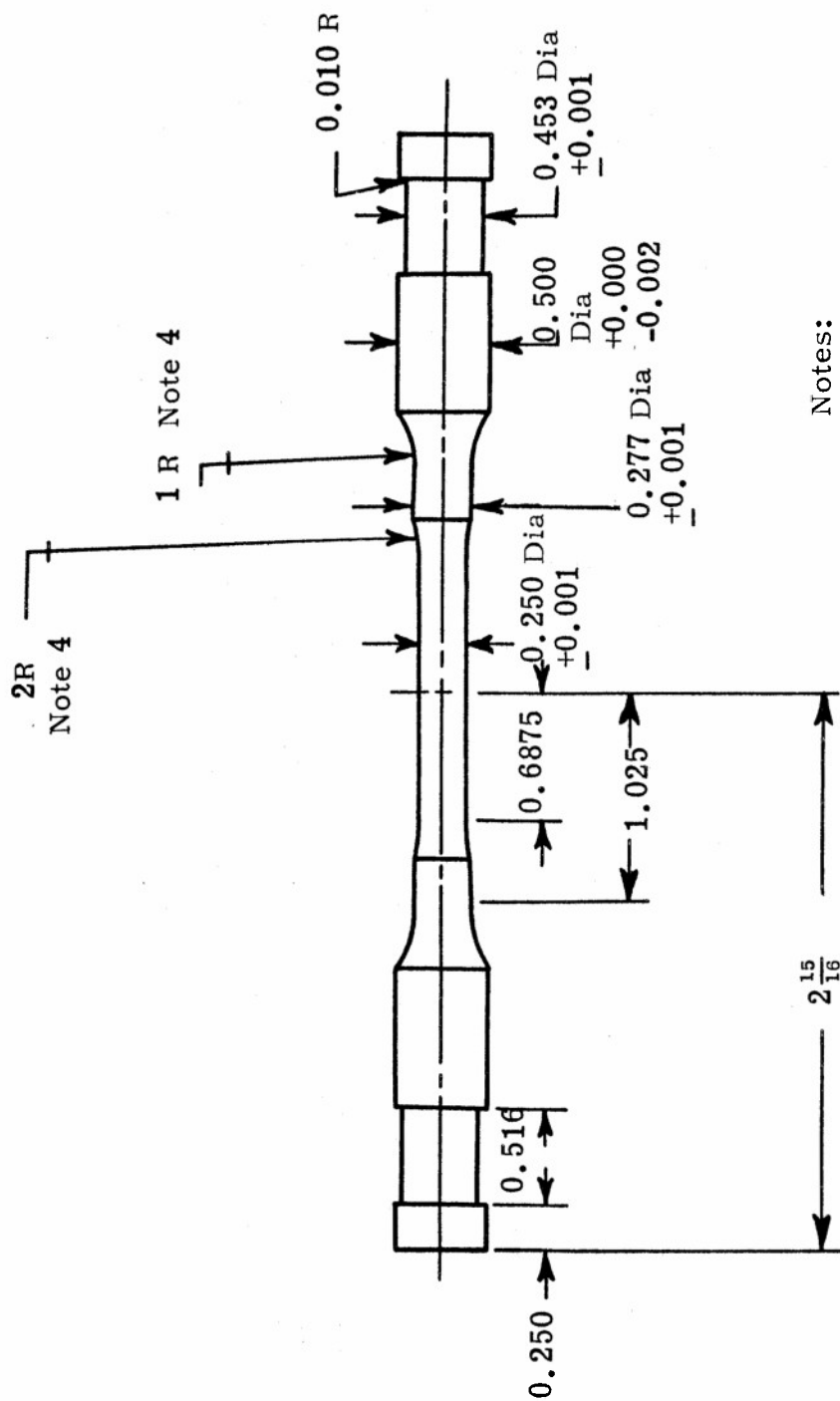


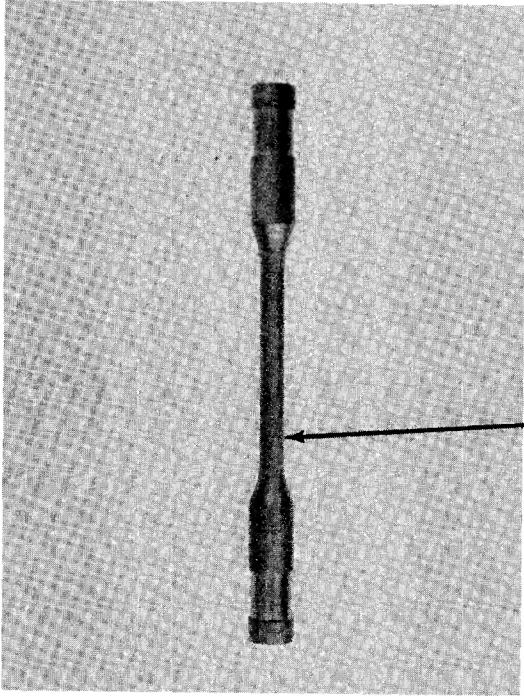
Figure 50. Avco Sectioning of Billets L-1-4 and L-1-8 and Specimen Designations



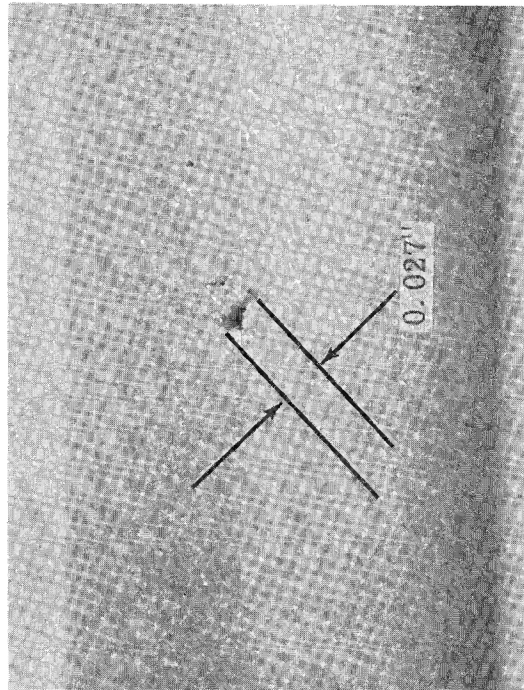
Notes:

1. All diameters true and concentric to 0.0005.
2. All lengths + 0.005.
3. Both ends flat and perpendicular to 0.0005.
4. Do not undercut at tangent point.

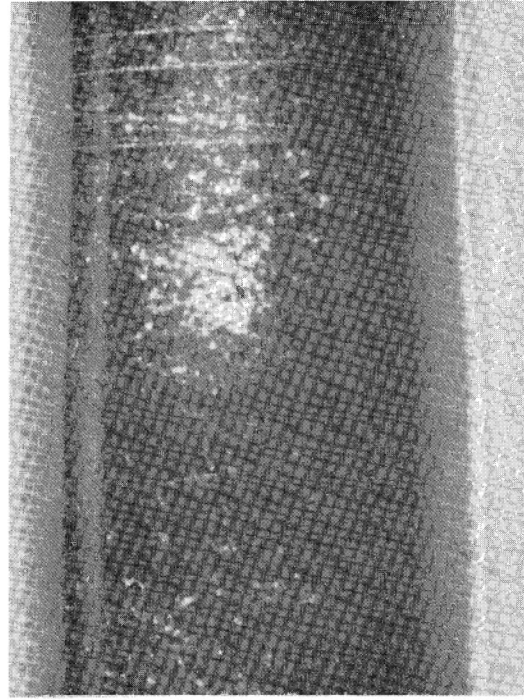
Figure 51. Tensile Test Specimen Configuration Used on ATJ-S  
Billet L-1-4



A



B



C

Figure 52. Photograph of Void Found in Disparate A12W during Machining, ATJ-S Billet L-1-4



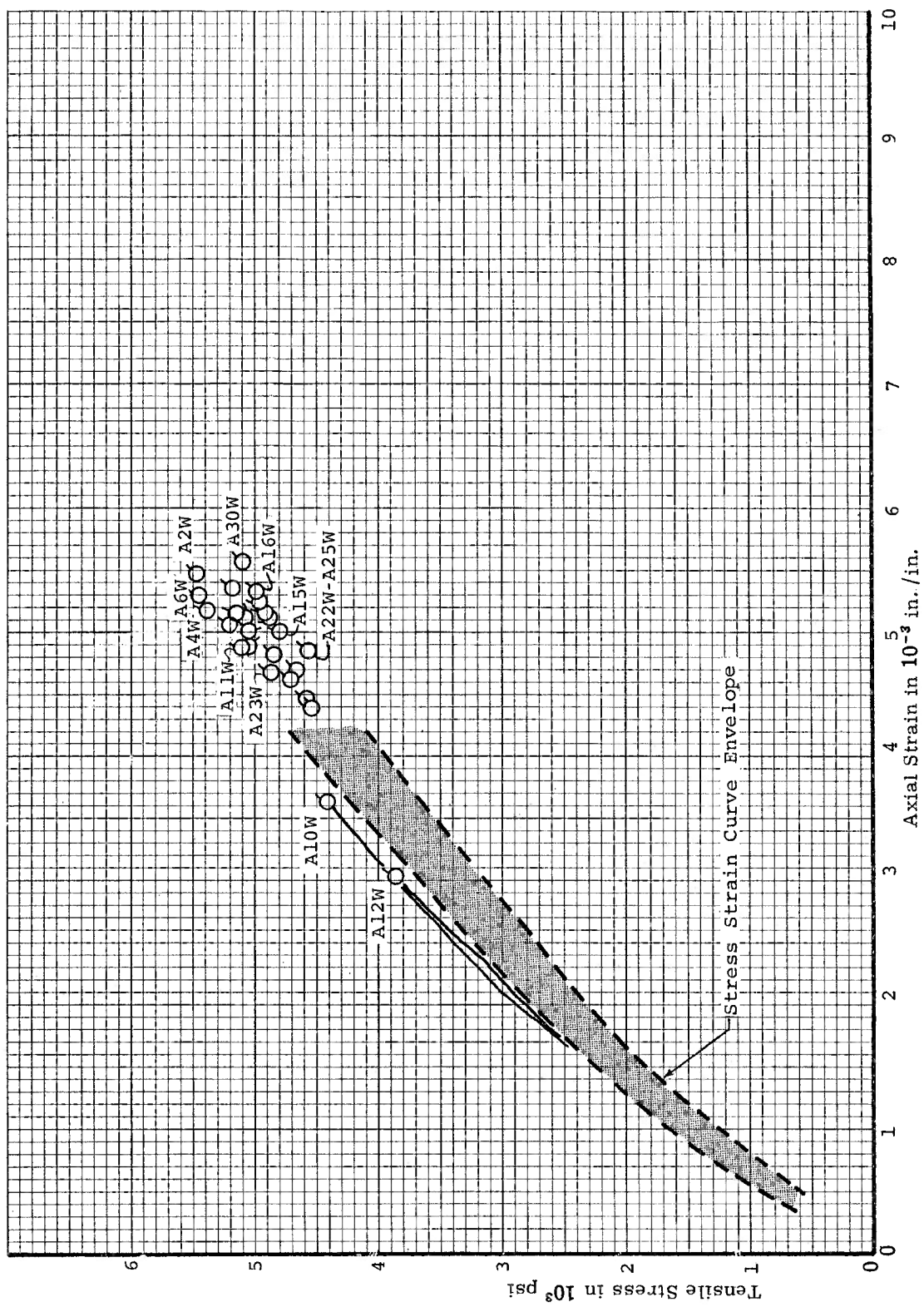


Figure 53. Tensile Stress-Strain Curve Envelope for ATJ-S Billet L-1-4 With Grain at 70°F

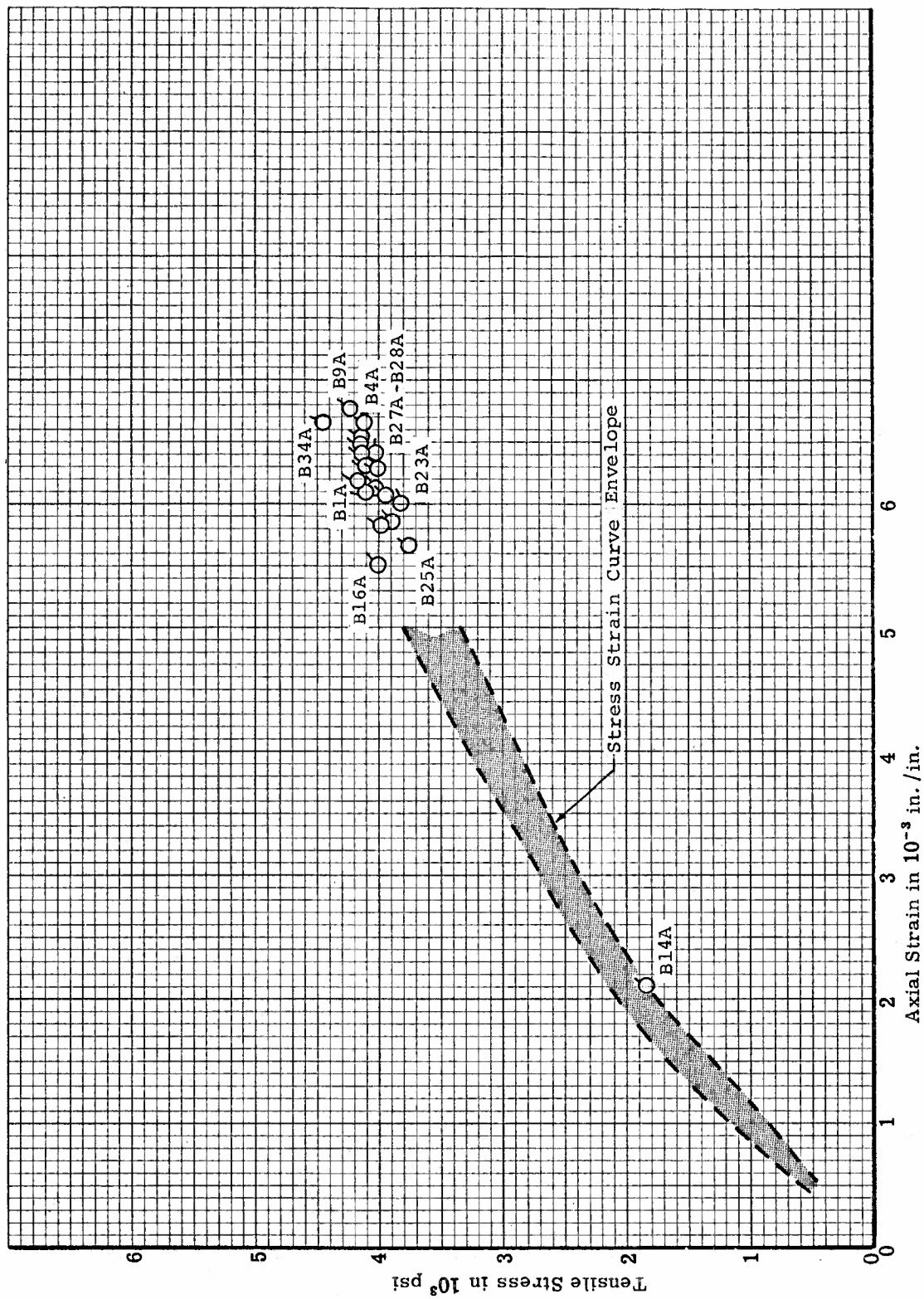


Figure 54. Tensile Stress-Strain Curve Envelope for ATJ-S Billet L-1-4 Across Grain at 70°F

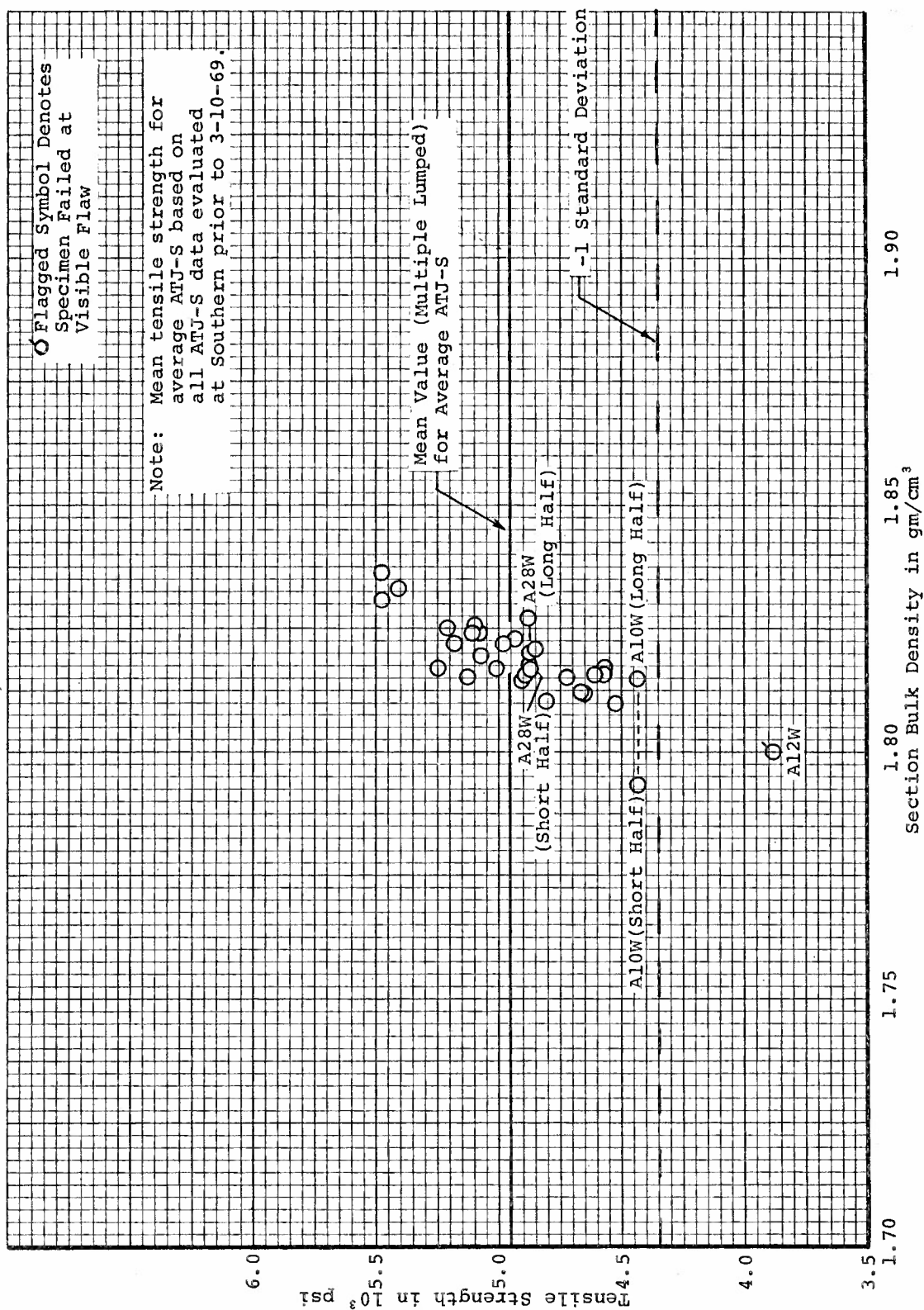


Figure 55. Tensile Strength Versus Section Bulk Density for ATJ-S Billet L-1-4 With Grain at 70°F

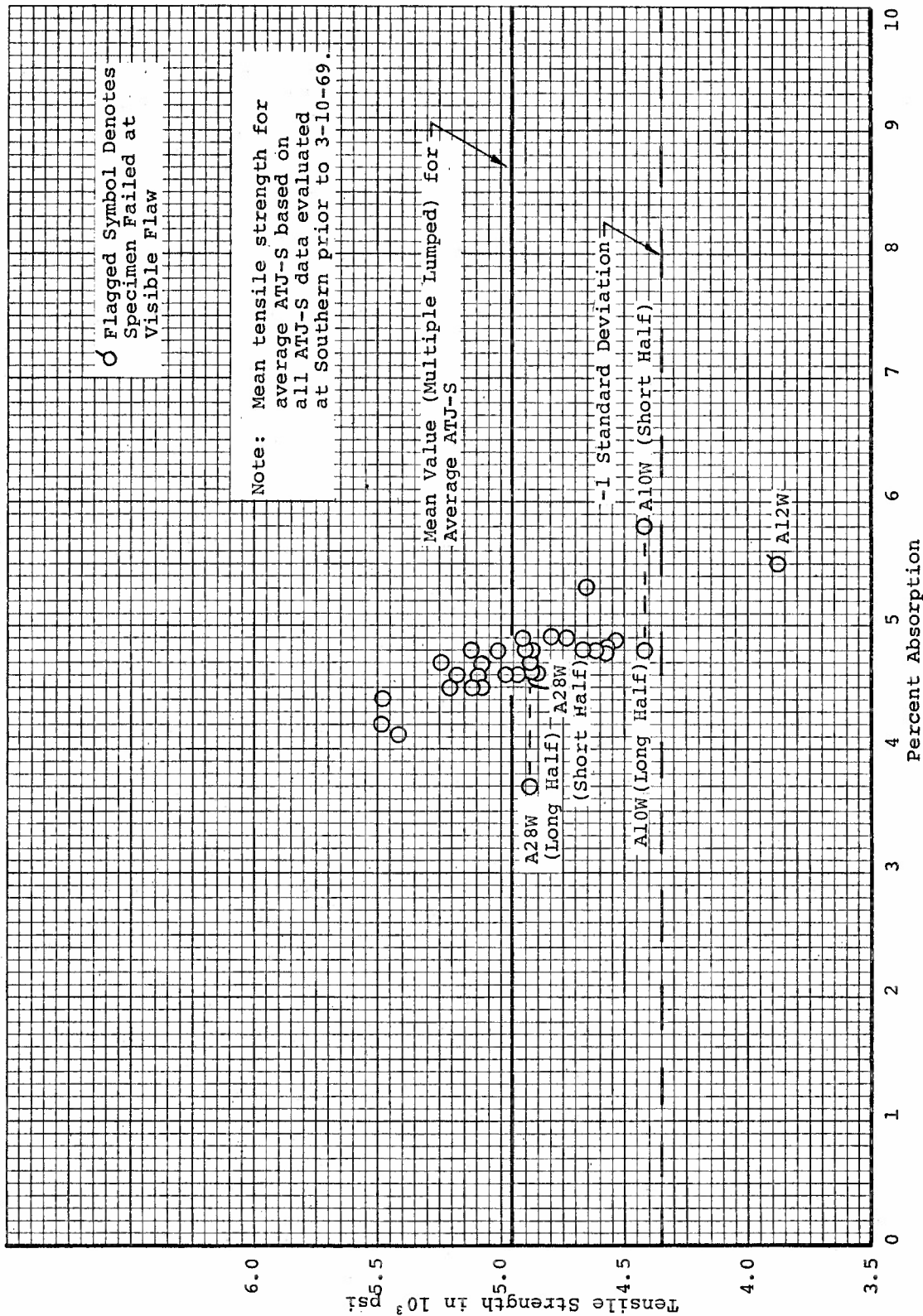


Figure 56. Tensile Strength Versus Percent Absorption for ATJ-S Billet L-1-4 With Grain at 70°F



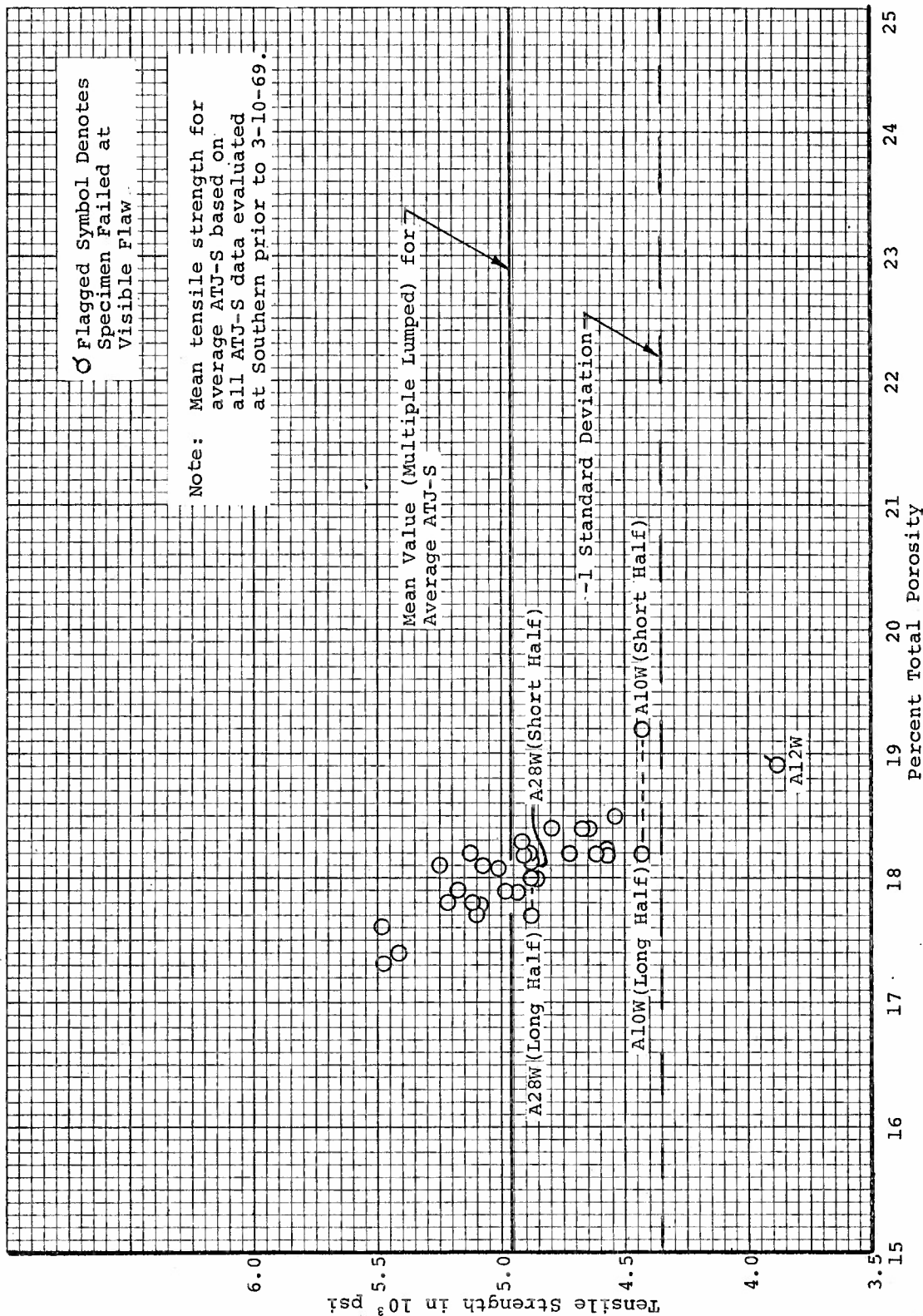


Figure 57. Tensile Strength Versus Percent Total Porosity for ATJ-S Billet L-1-4 With Grain at 70°F

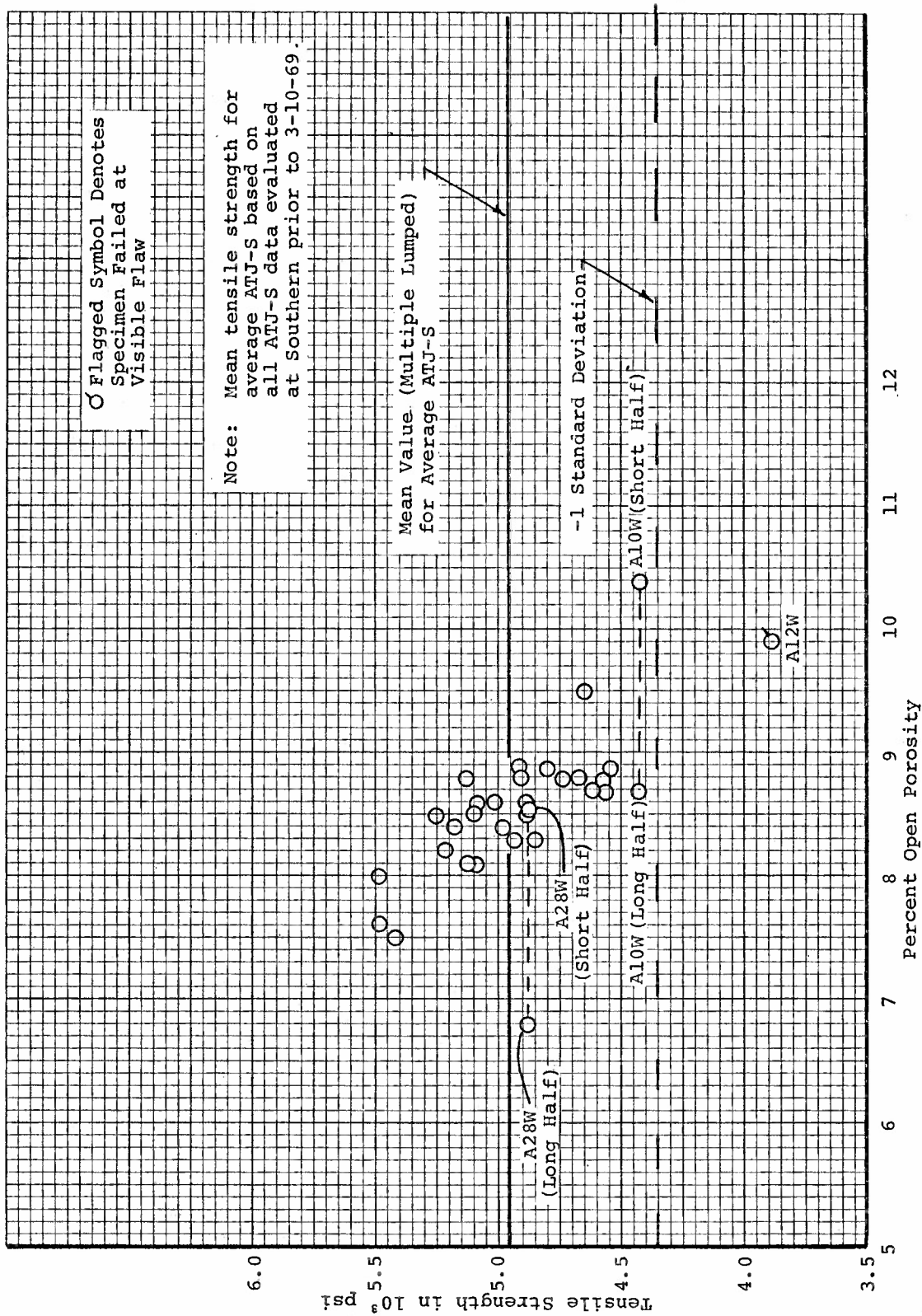


Figure 58. Tensile Strength Versus Percent Open Porosity for ATJ-S Billet L-1-4 With Grain at 70°F

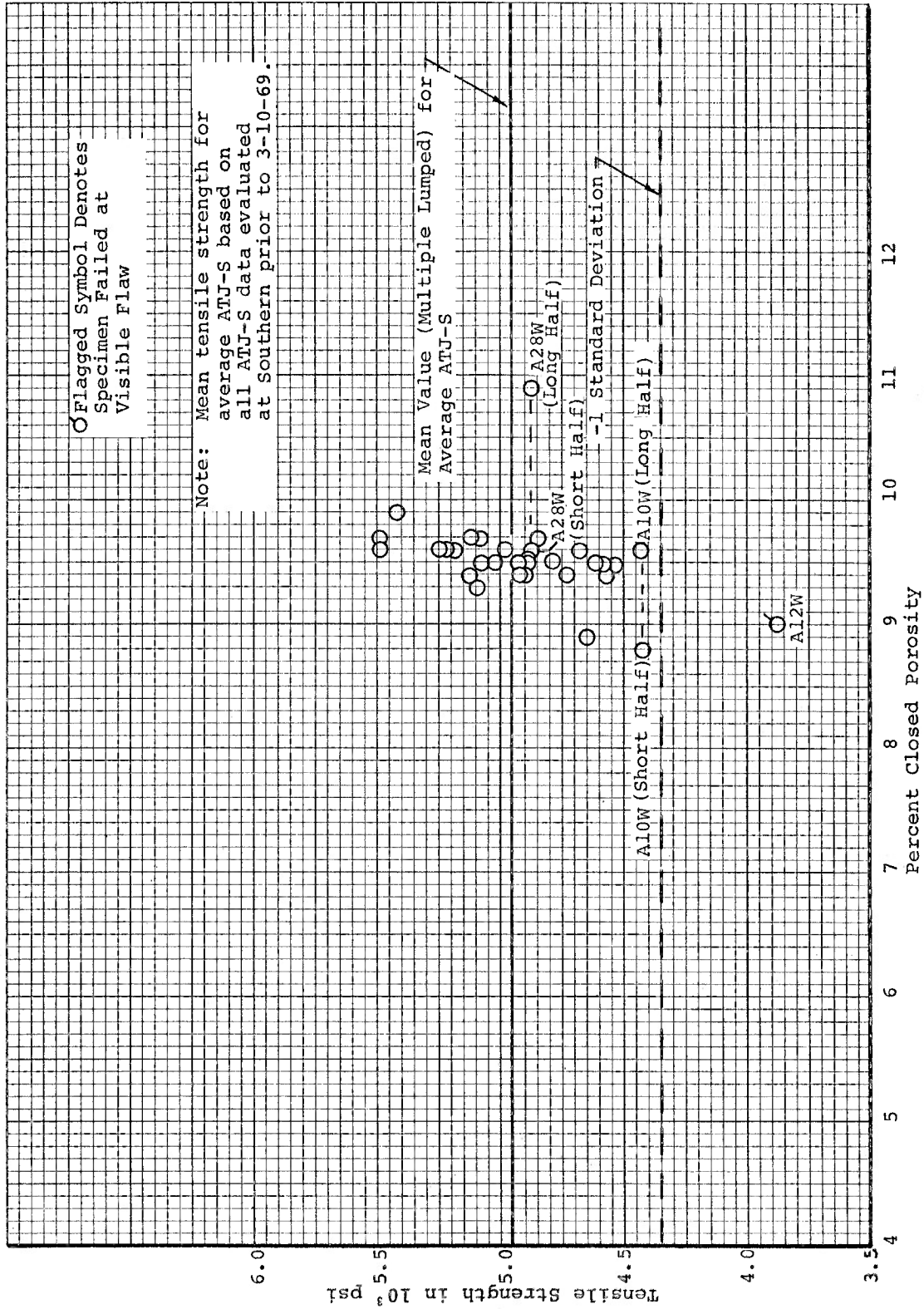
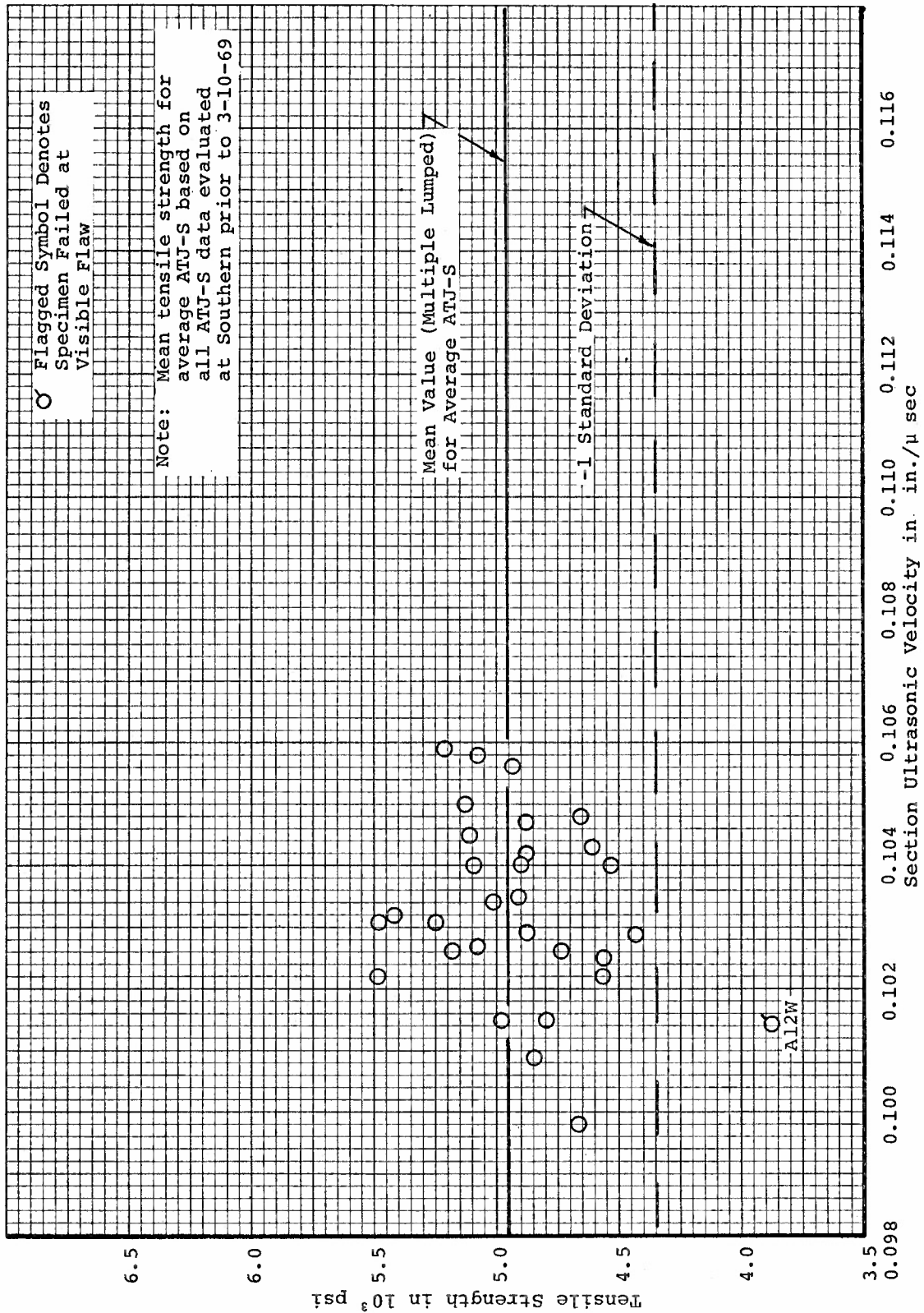


Figure 59. Tensile Strength Versus Percent Closed Porosity for ATJ-S Billet I-1-4 With Grain 70°F



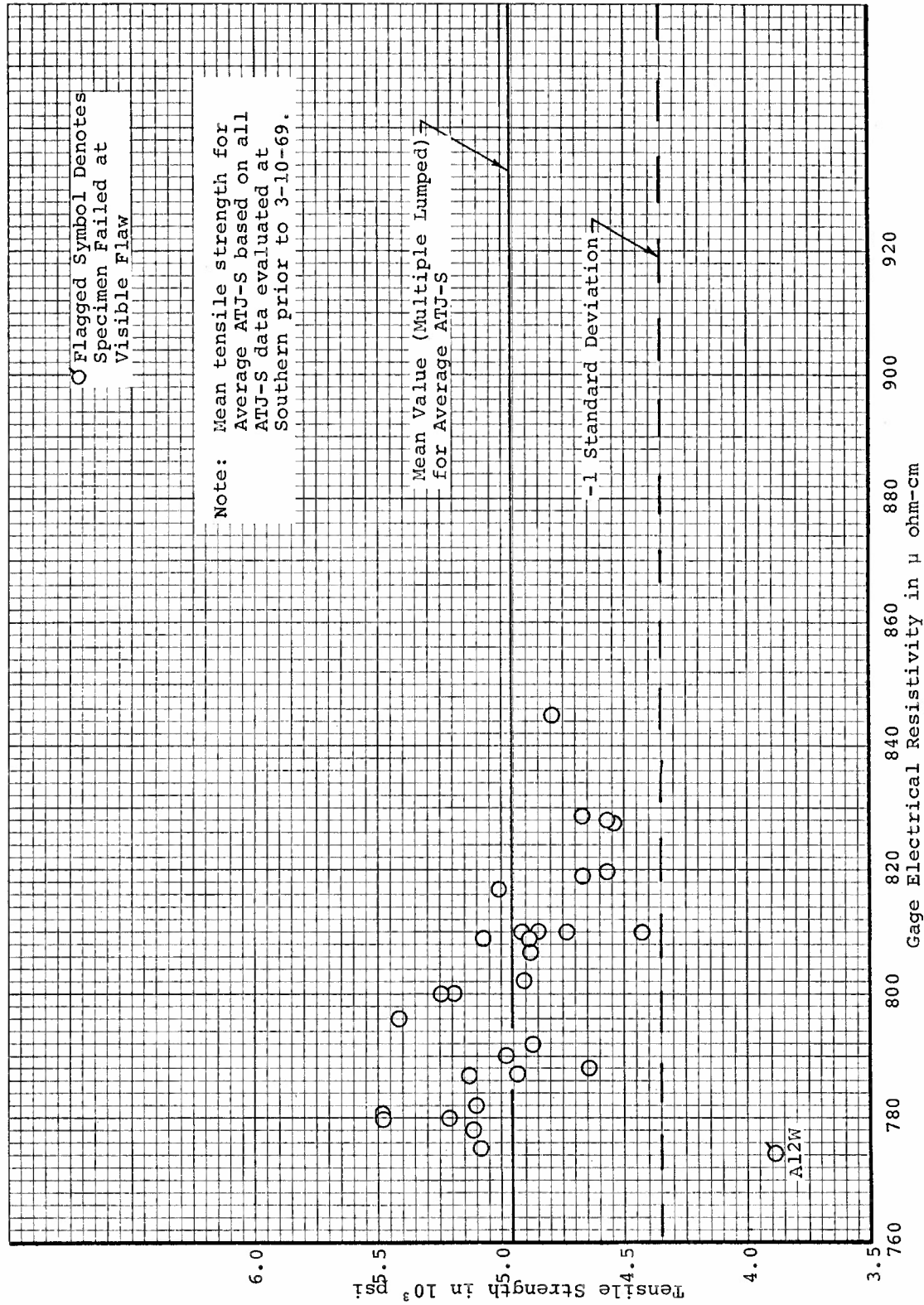
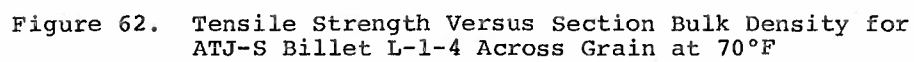


Figure 61. Tensile Strength Versus Gage Electrical Resistivity for ATJ-S Billet L-1-4 With Grain at 70°F





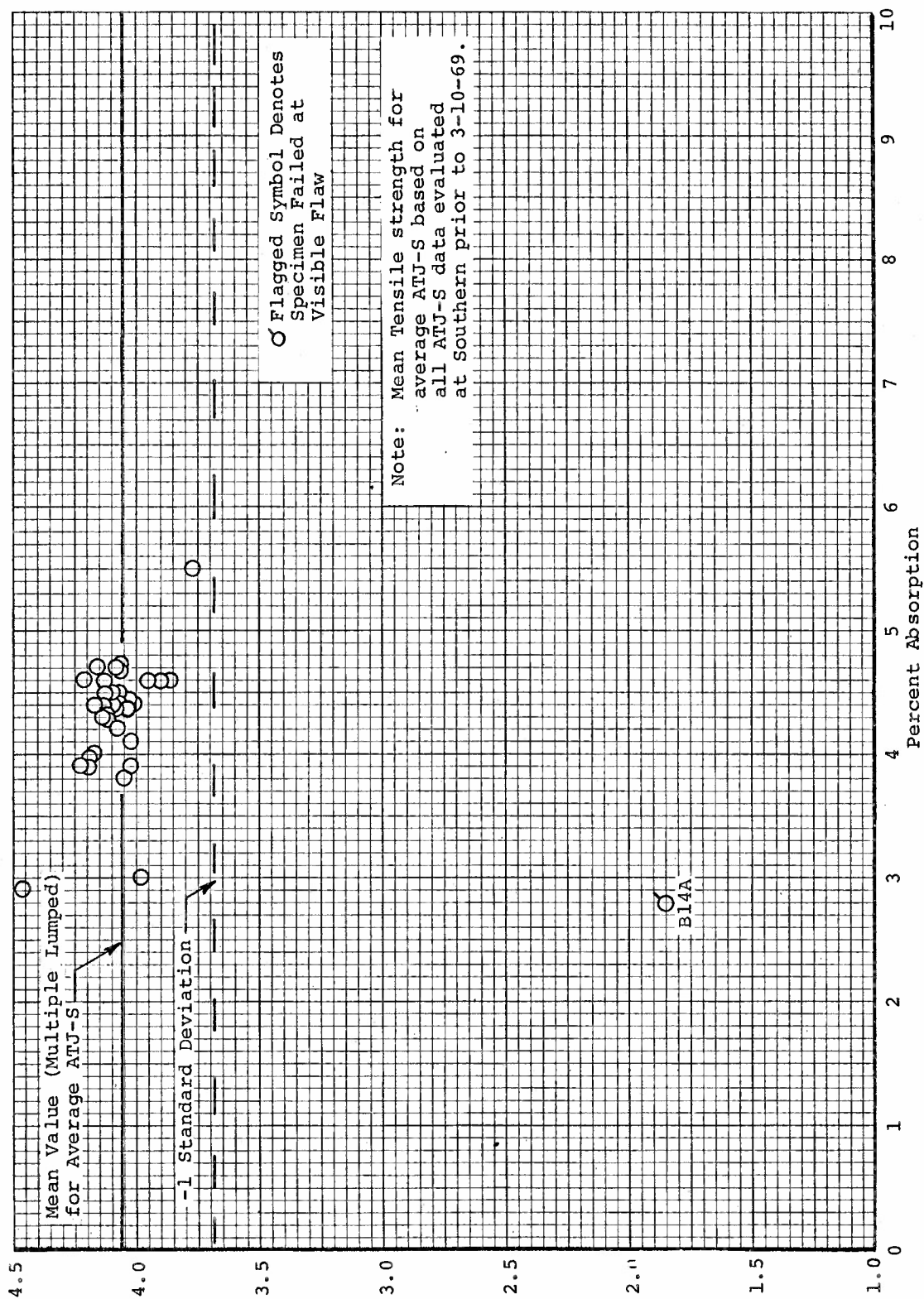


Figure 63. Tensile Strength Versus Percent Absorption for ATJ-S Billet I-1-4 Across Grain at 70°F

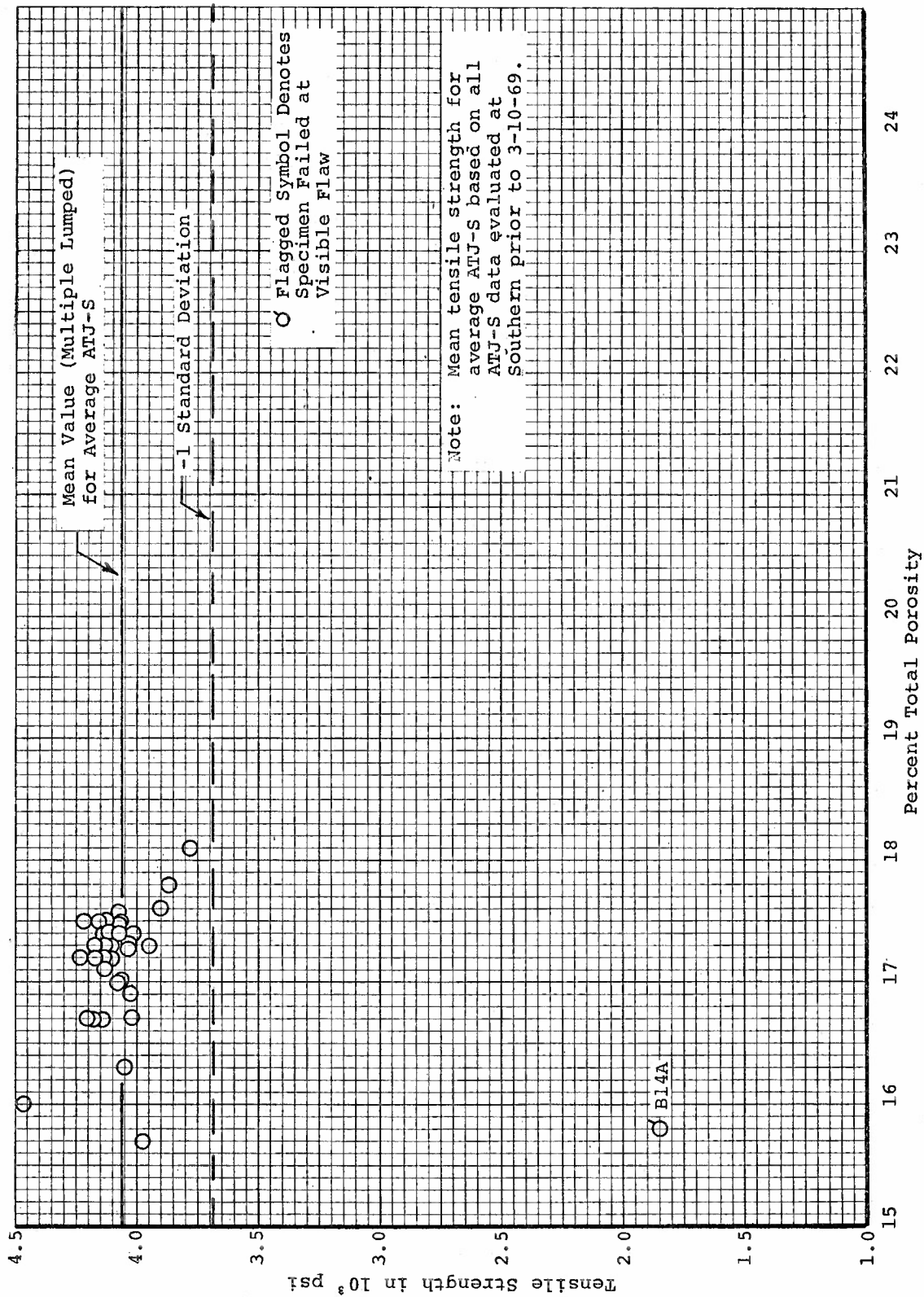


Figure 64. Tensile Strength Versus Percent Total Porosity for  
ATJ-S Billet L-1-4 Across Grain at 70°F





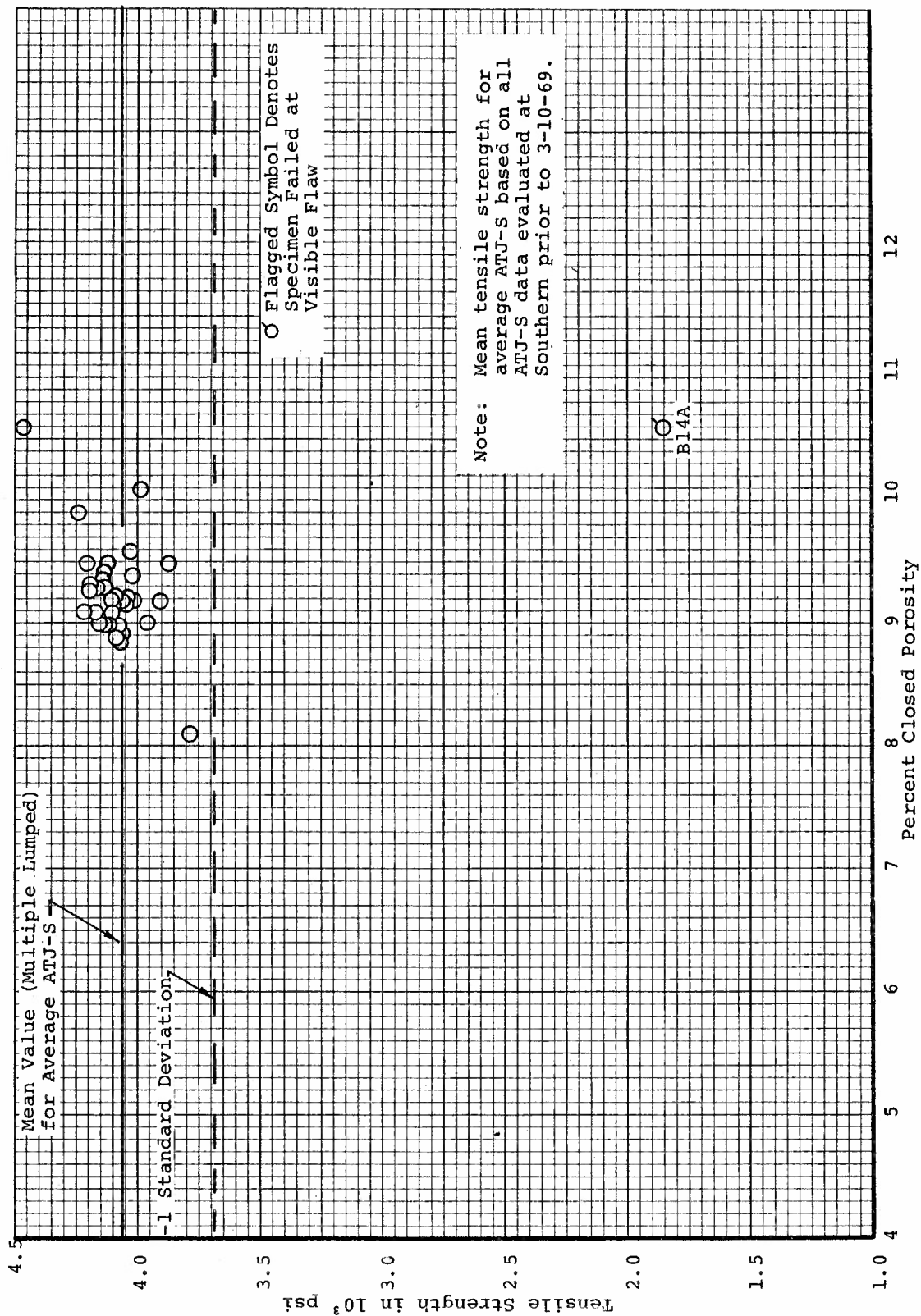


Figure 66. Tensile Strength Versus Percent Closed Porosity for ATJ-S Billet L-1-4 Across Grain at 70°F

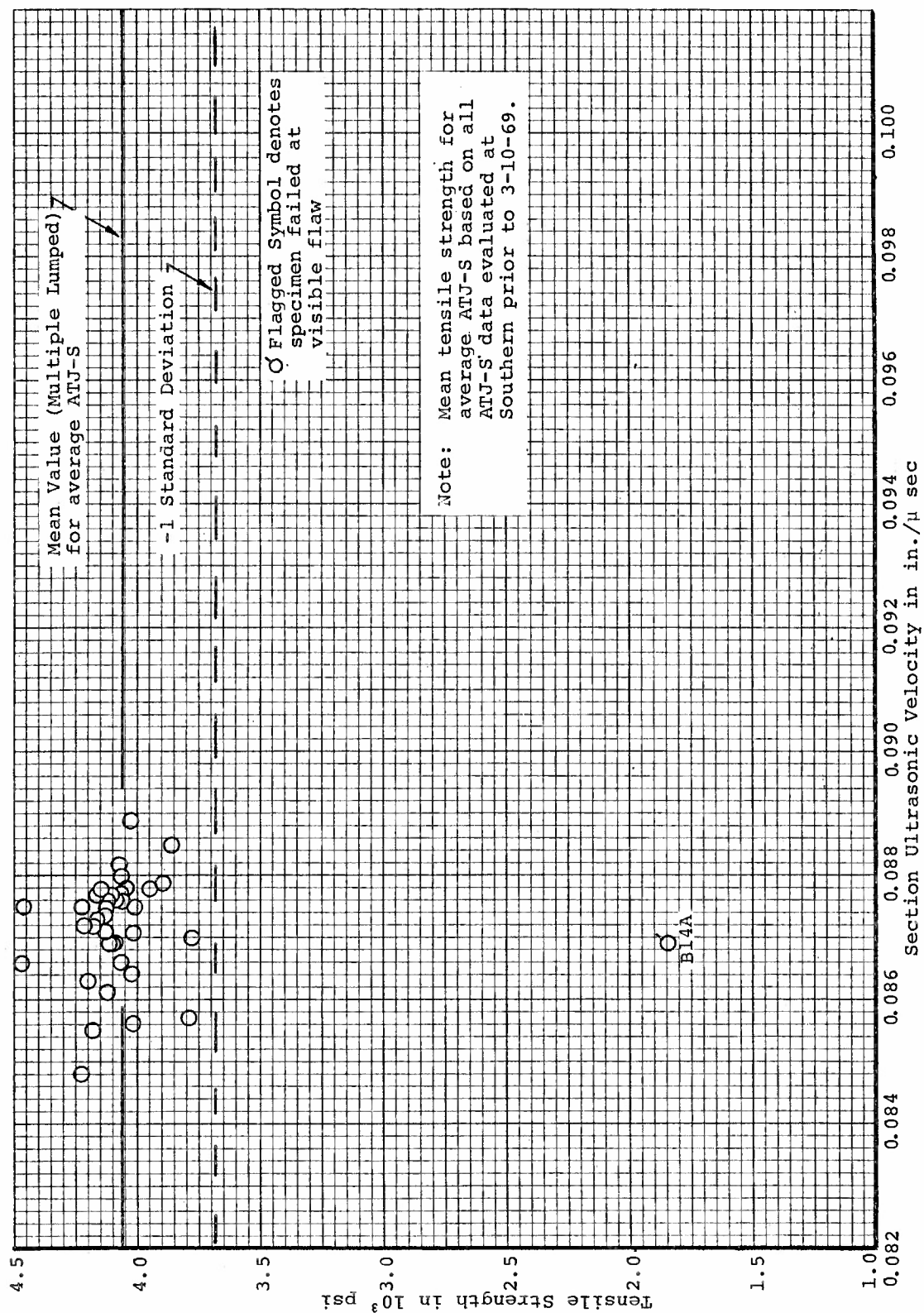


Figure 67. Tensile Strength Versus Section Ultrasonic Velocity for ATJ-S Billet L-1-4 Across Grain at 70°F

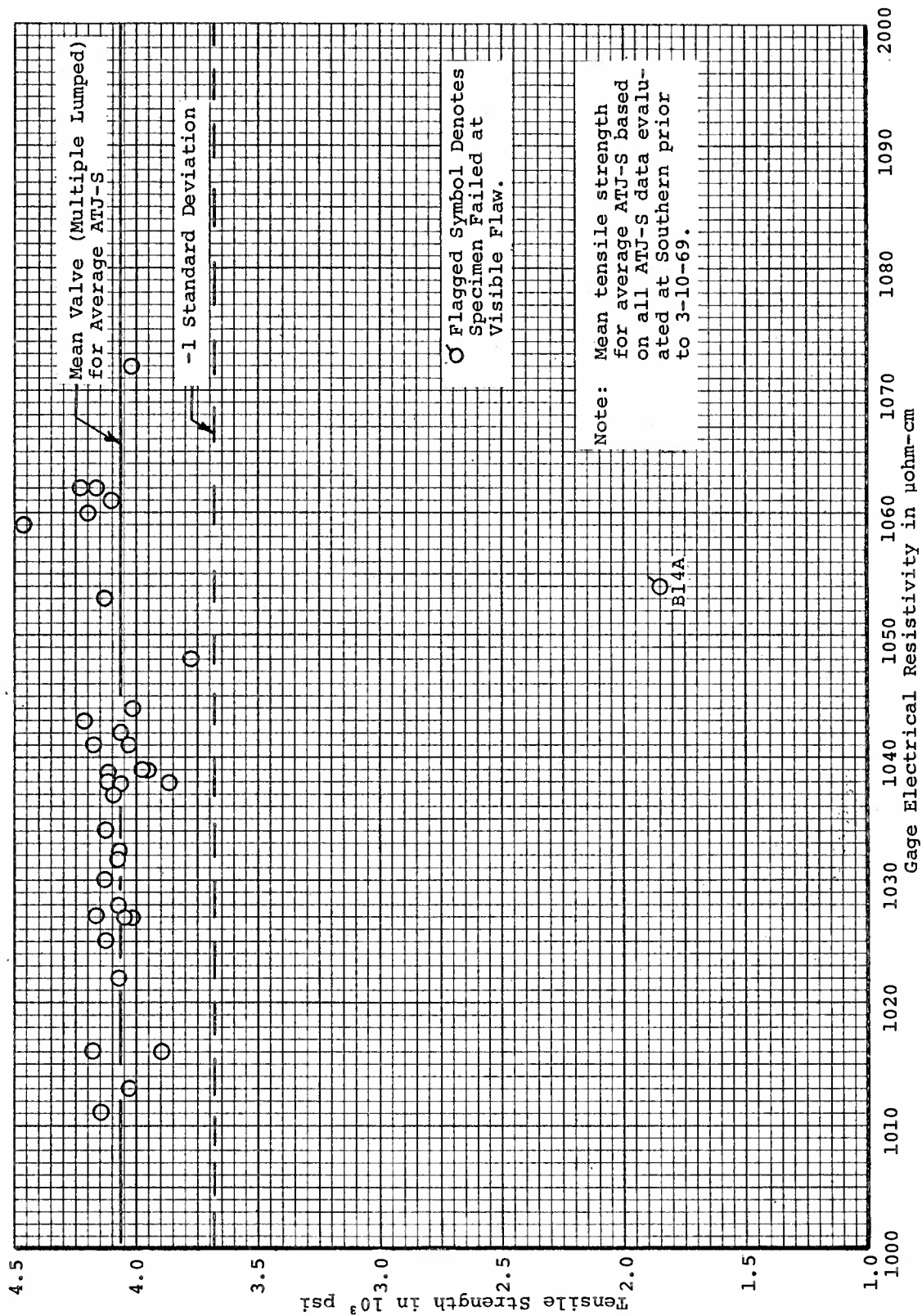
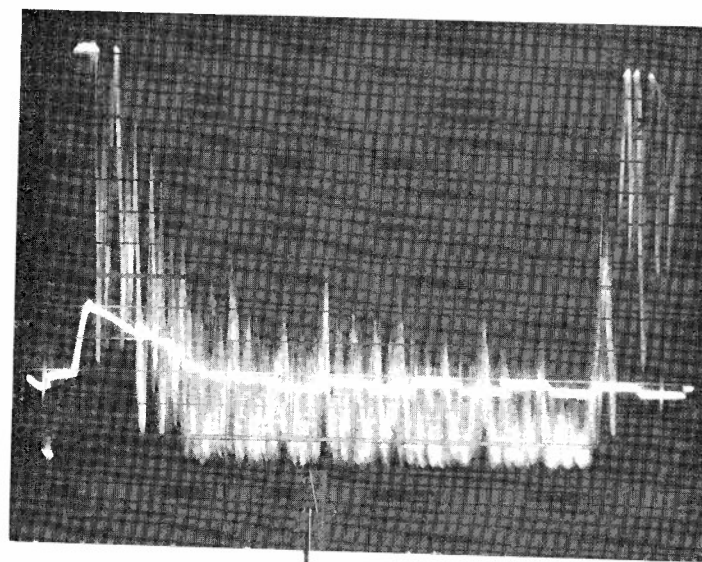
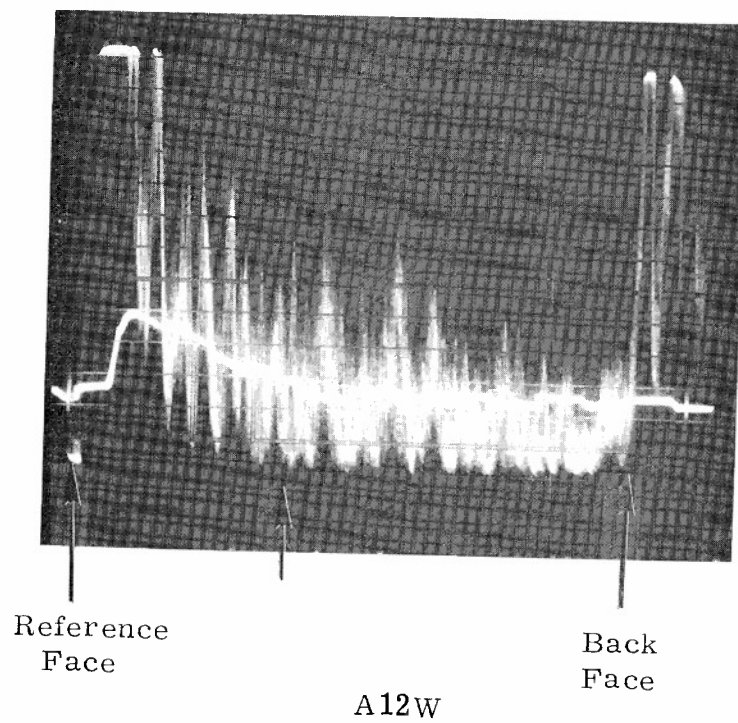


Figure 68. Tensile Strength Versus Gage Electrical Resistivity  
for ATJ-S Billet L-1-4 Across Grain at 70°F



B14A

Figure 69. Pulse-Echo Smears on Weak Specimens A12W and B14A from ATJ-S Billet L-1-4





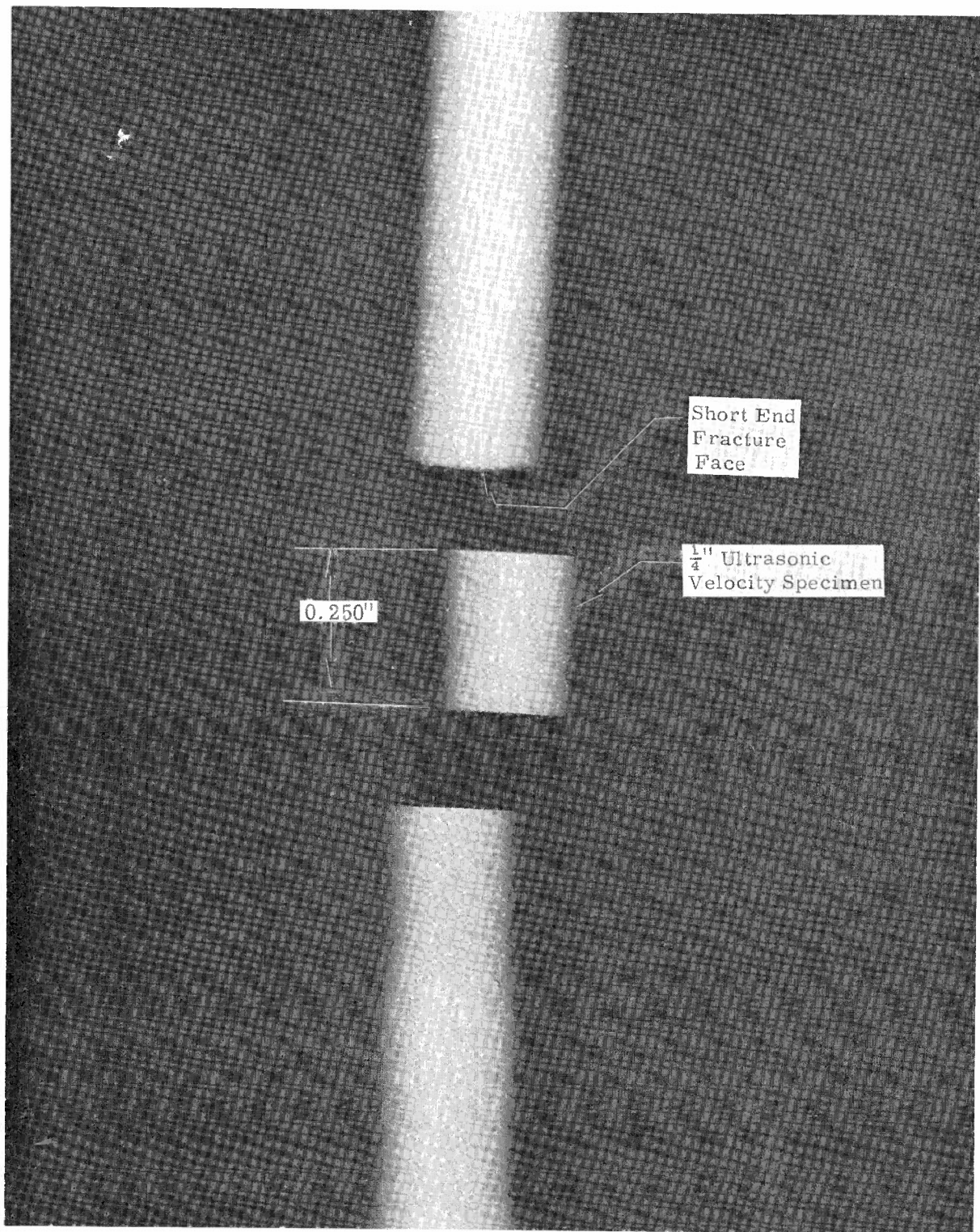
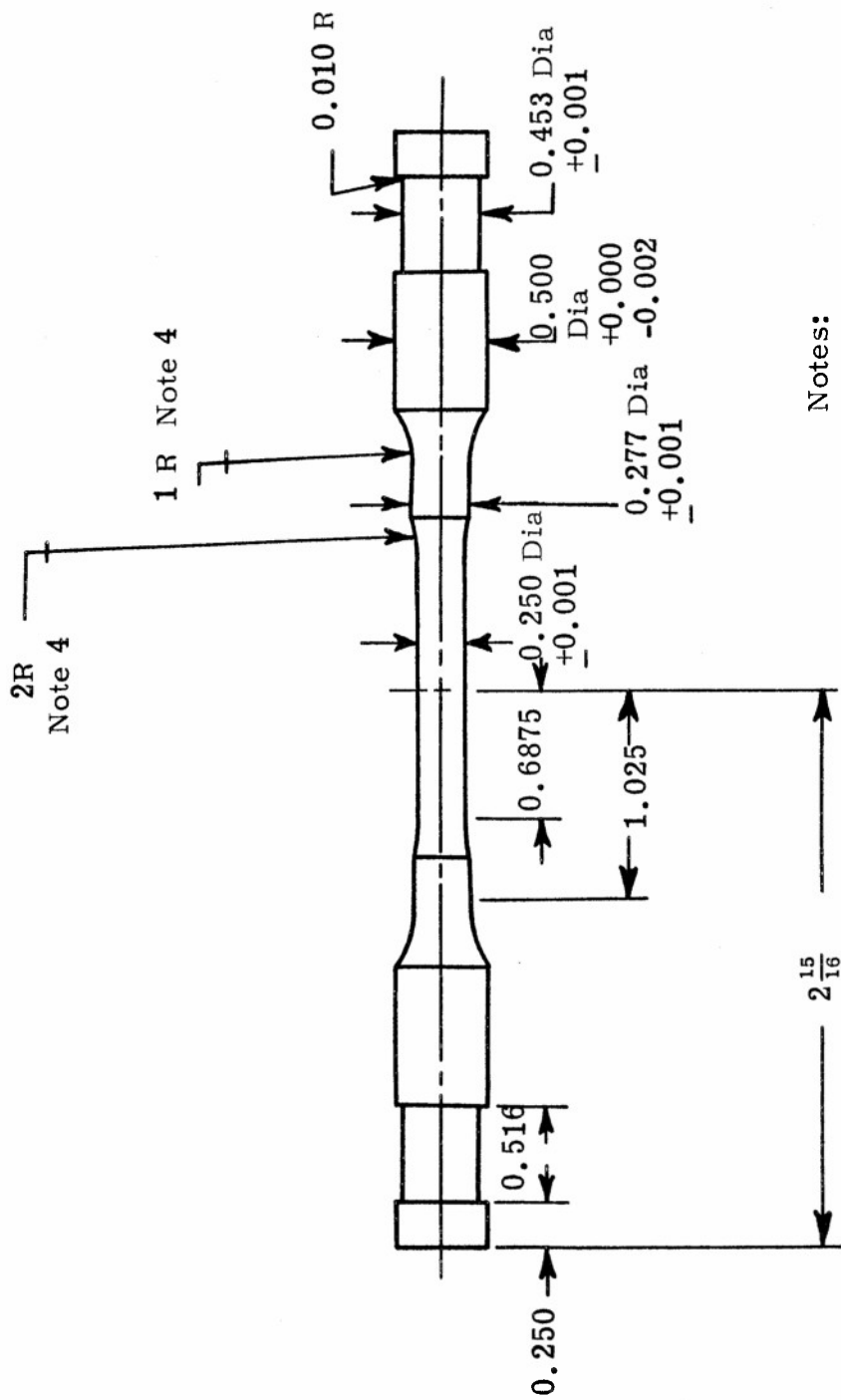


Figure 70. Radiograph of Typical Material from ATJ-S Billet L-1-4  
(Gage Section of Specimen A24W)







Notes:

1. All diameters true and concentric to 0.0005.
2. All lengths + 0.005.
3. Both ends flat and perpendicular to 0.0005.
4. Do not undercut at tangent point.

Figure 71. Tensile Test Specimen Configuration Used for ATJ-S  
Billet L-1-8

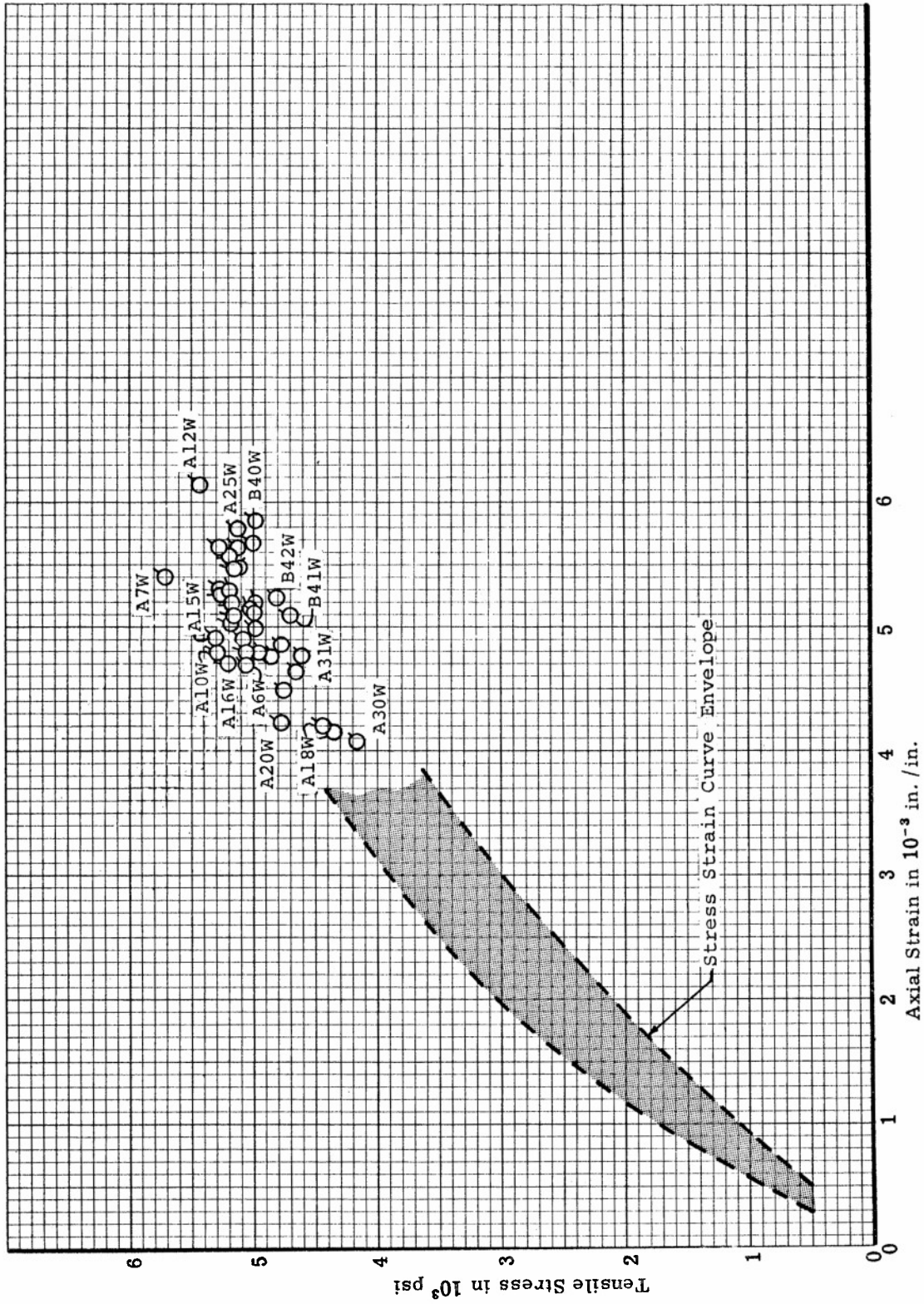


Figure 72. Tensile Stress-Strain Curve Envelope for ATJ-S Billet L-1-8 With Grain at 70°F

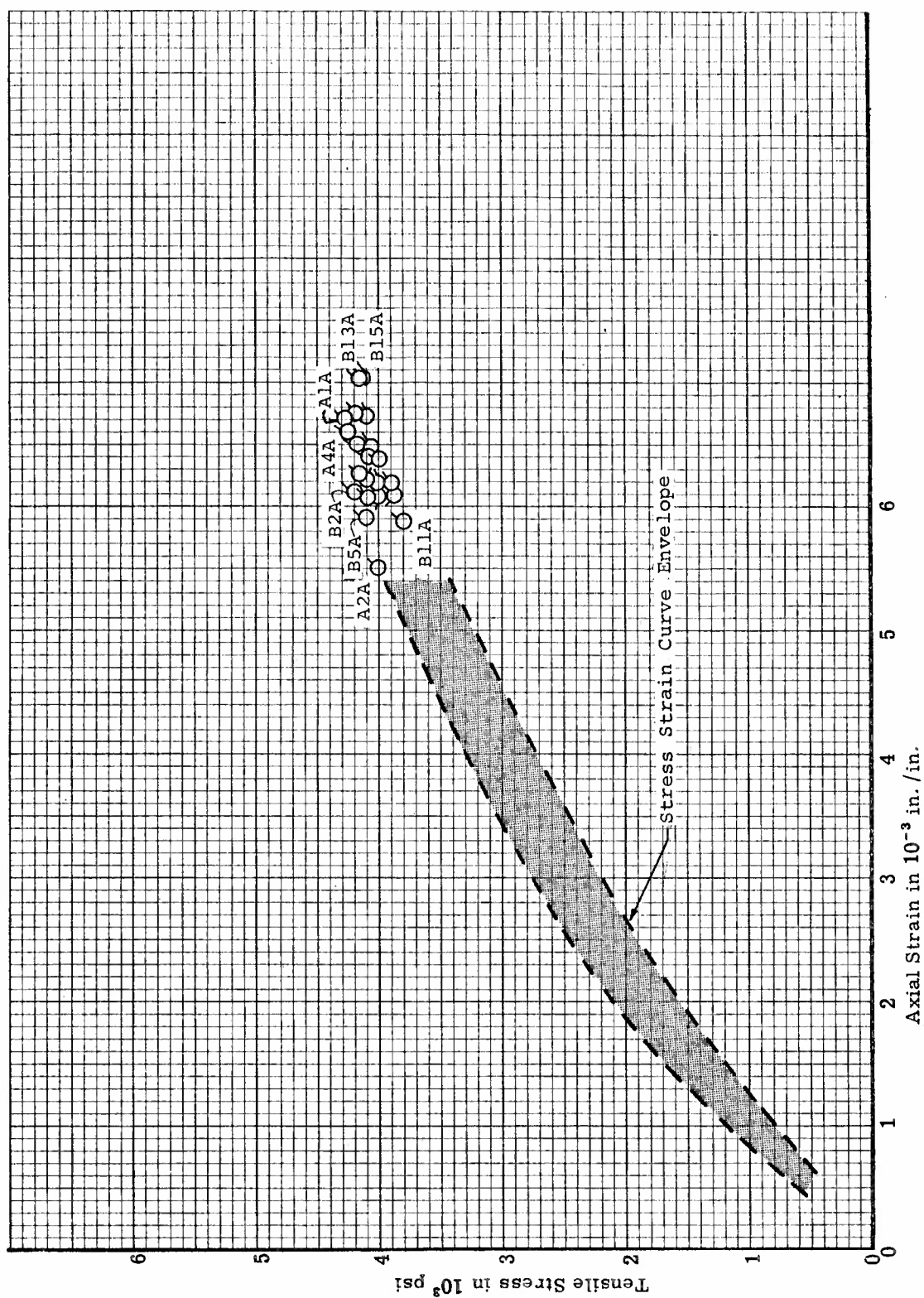


Figure 73. Tensile Stress-Strain Curve Envelope for ATJ-S Billet L-1-8 Across Grain at 70°F

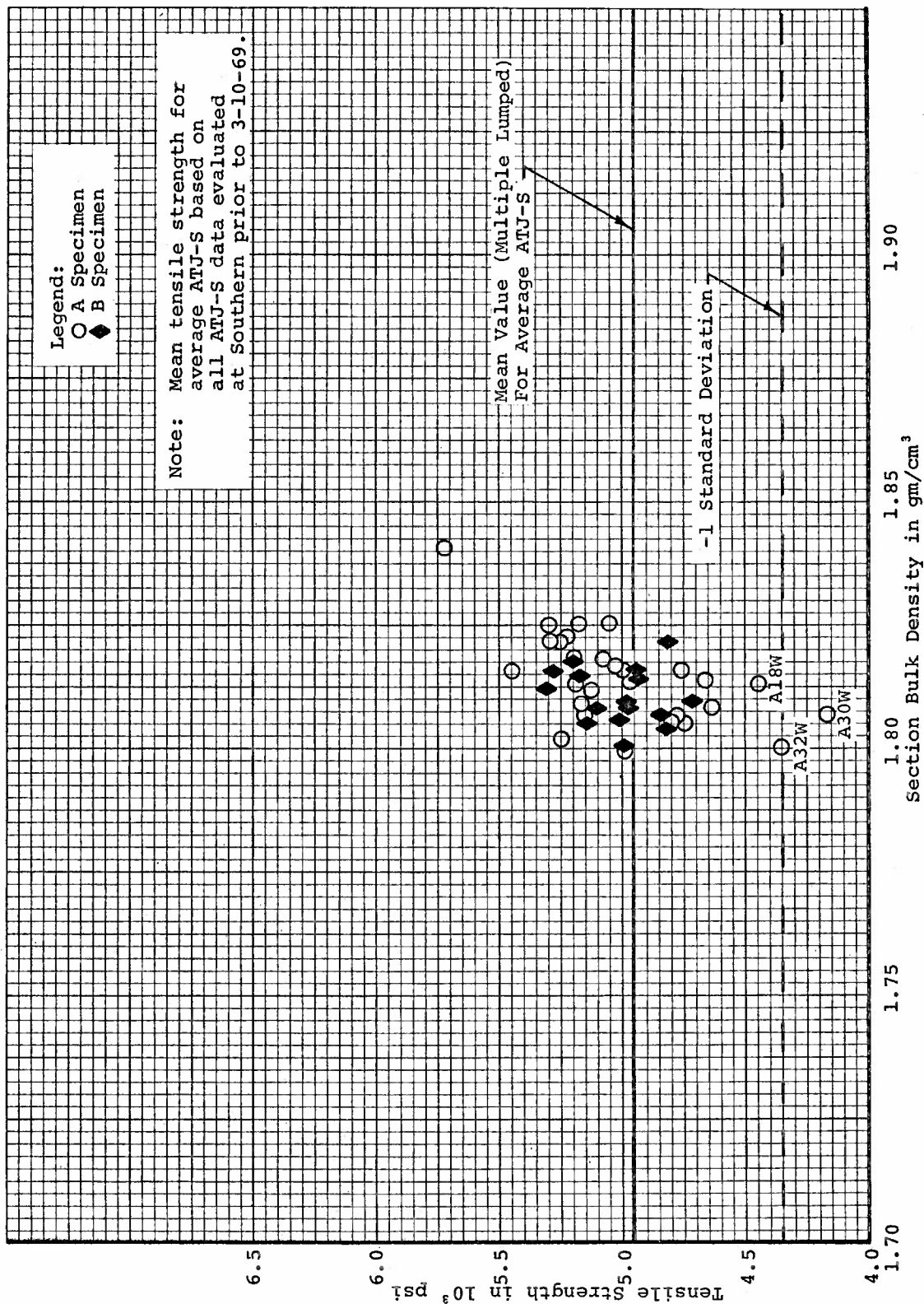


Figure 74. Tensile Strength Versus Section Bulk Density for ATJ-S Billet L-1-8 With Grain at 70°F

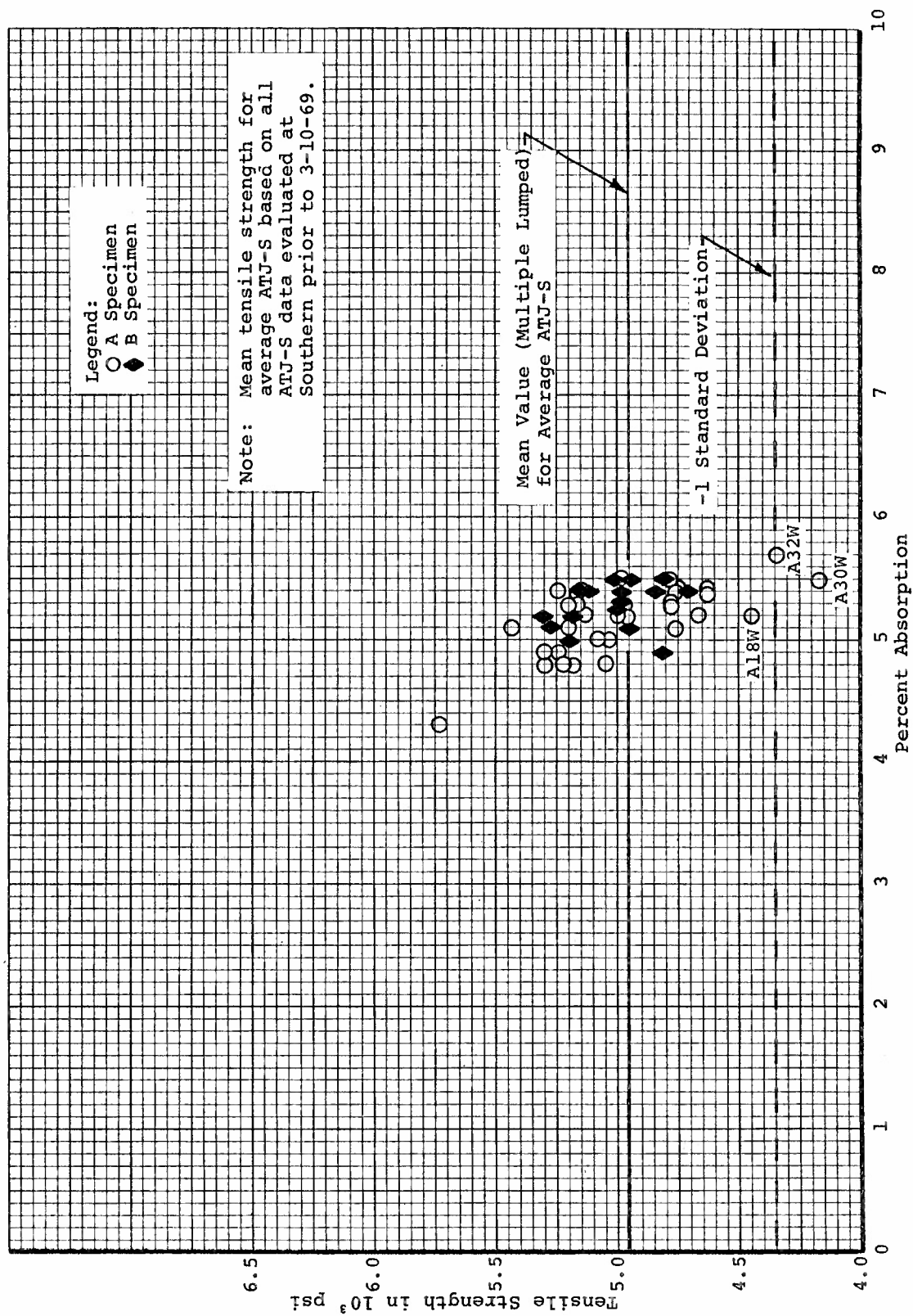


Figure 75. Tensile Strength Versus Percent Absorption for ATJ-S Billet L-1-8 With Grain at 70°F

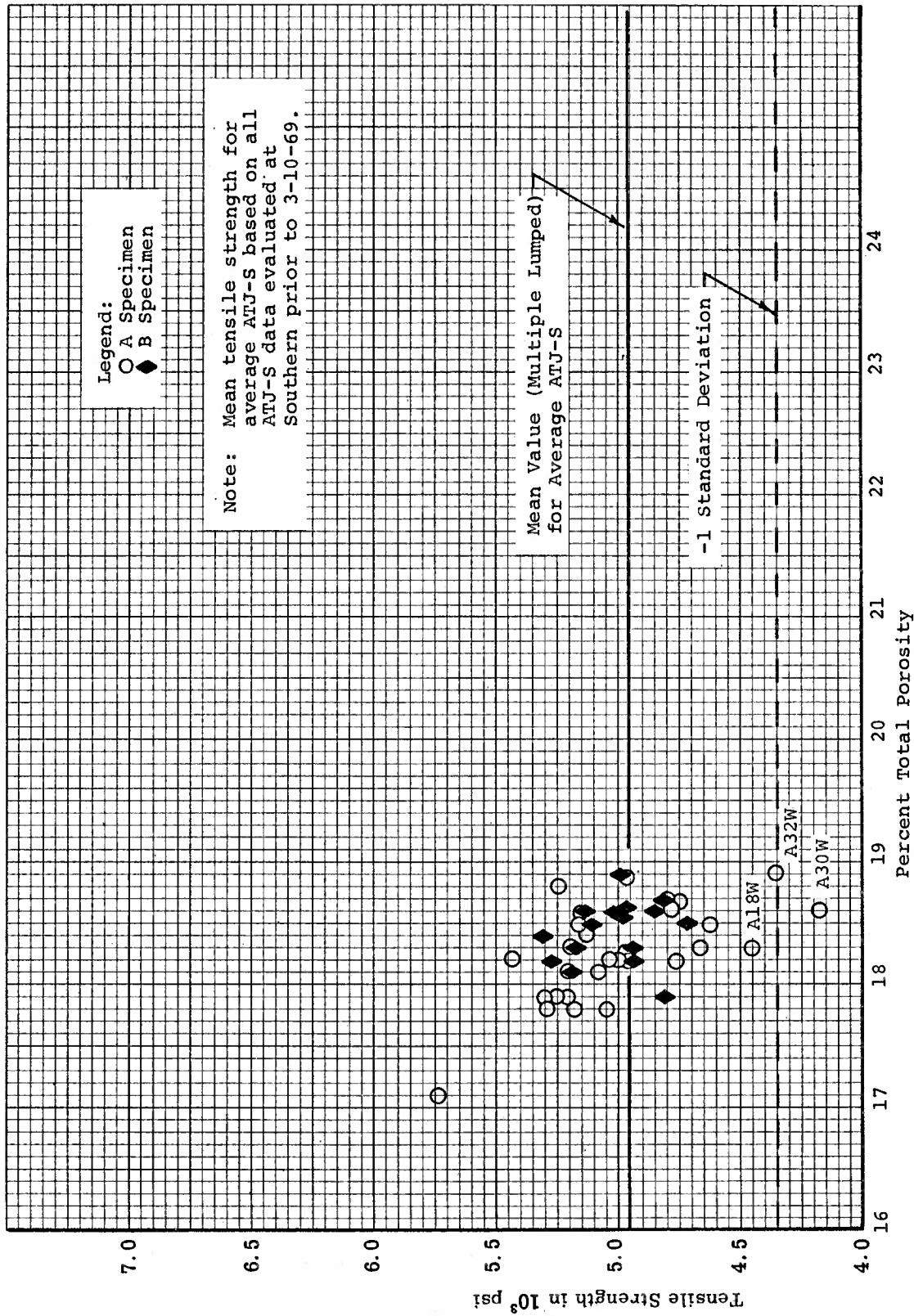


Figure 76. Tensile Strength Versus Percent Total Porosity for ATJ-S Billet L-1-8 With Grain at 70°F



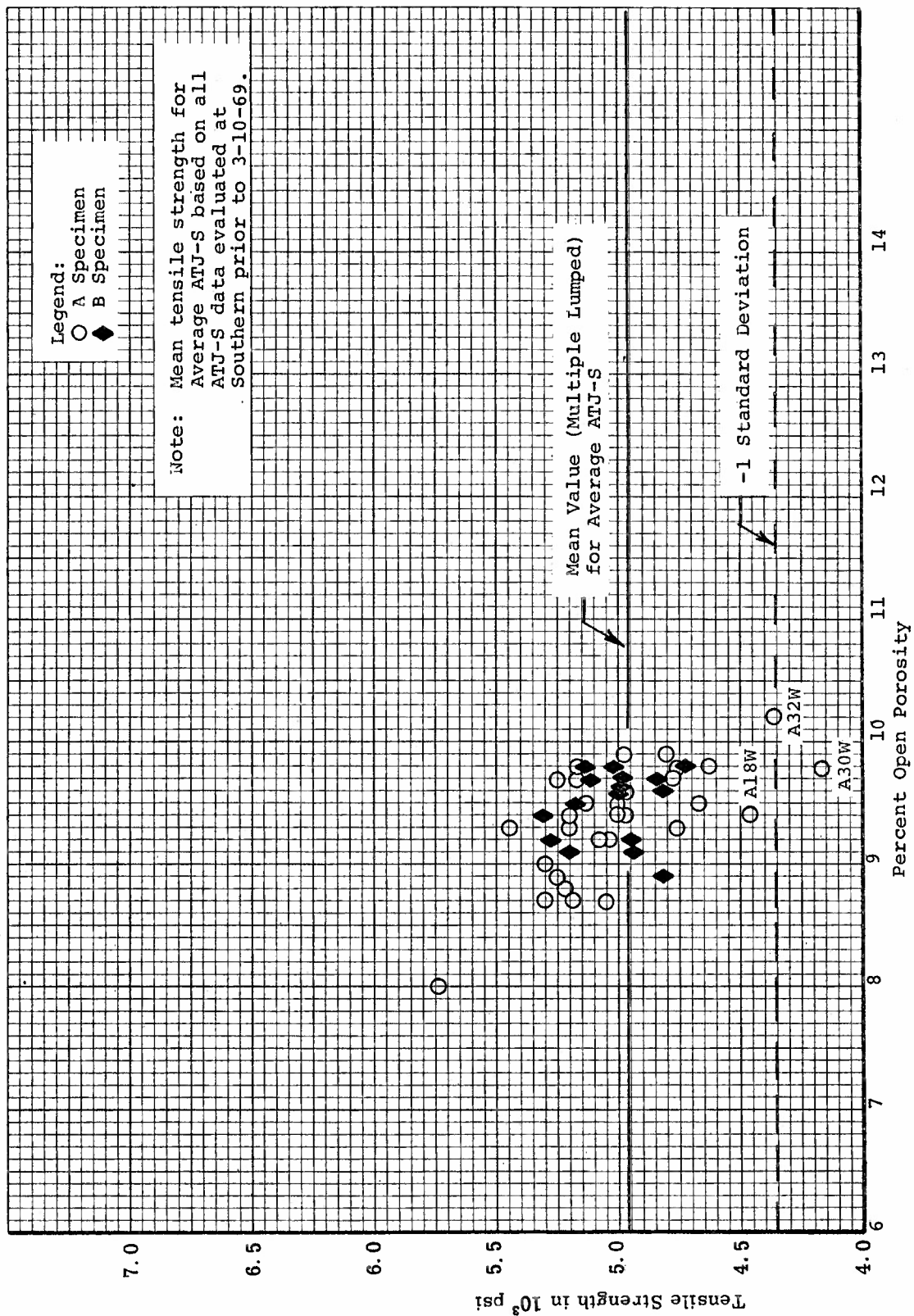


Figure 77. Tensile Strength Versus Percent Open Porosity for ATJ-S Billet L-1-8 With Grain at 70°F

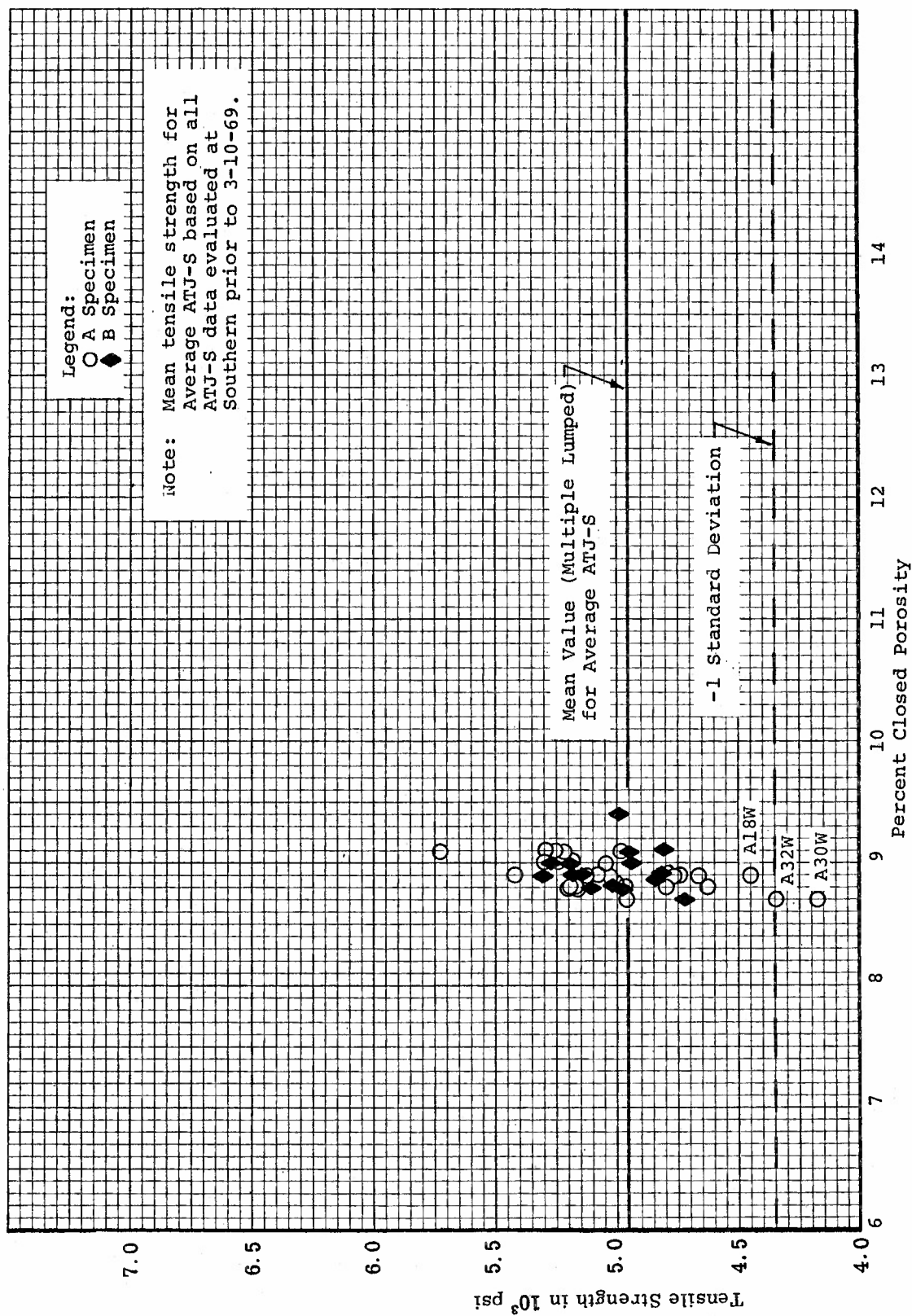


Figure 78. Tensile Strength Versus Percent Closed Porosity for ATJ-S Billet L-1-8 With Grain at 70°F



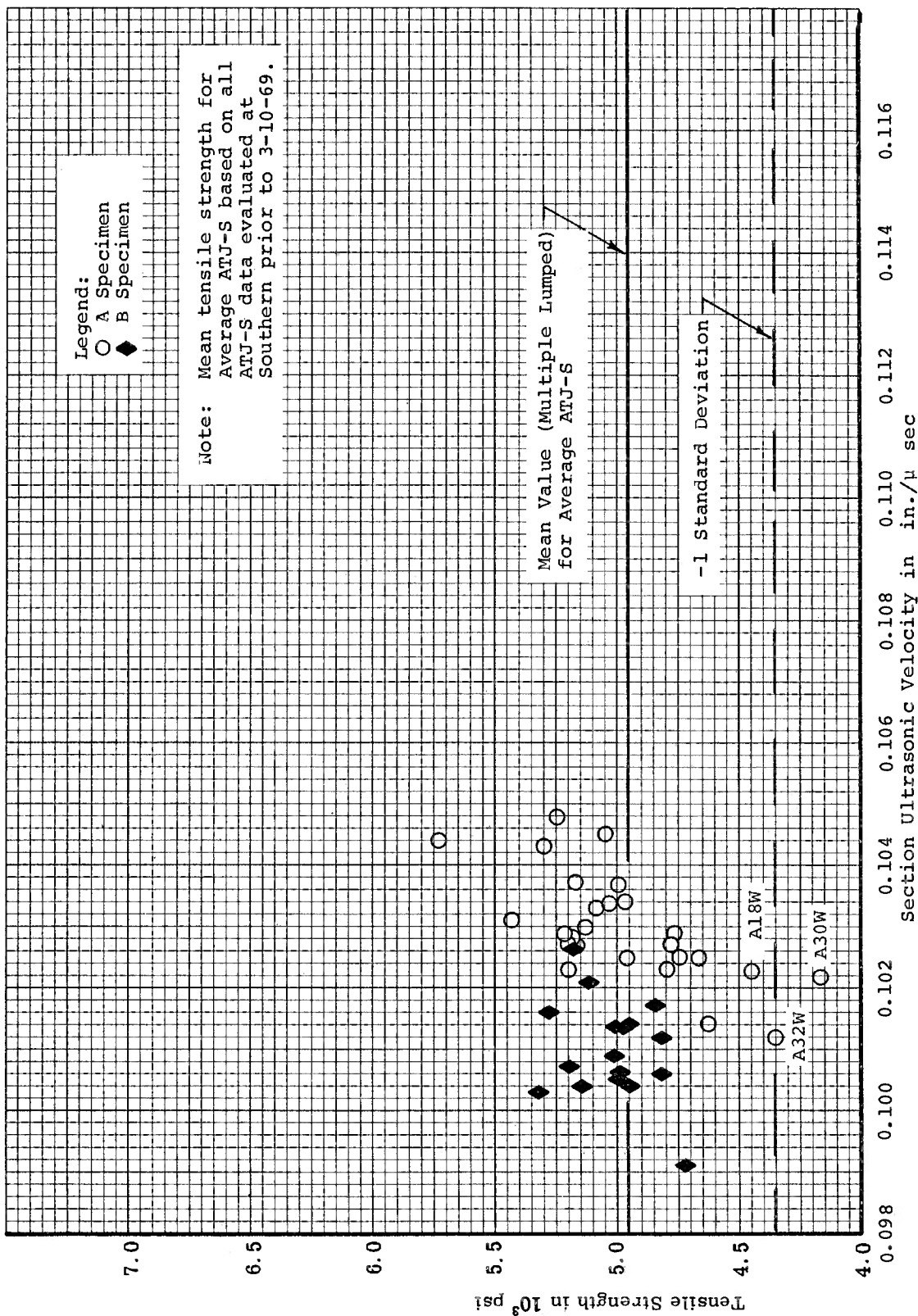


Figure 79. Tensile Strength Versus Section Ultrasonic Velocity for ATJ-S Billet L-1-8 With Grain at 70°F

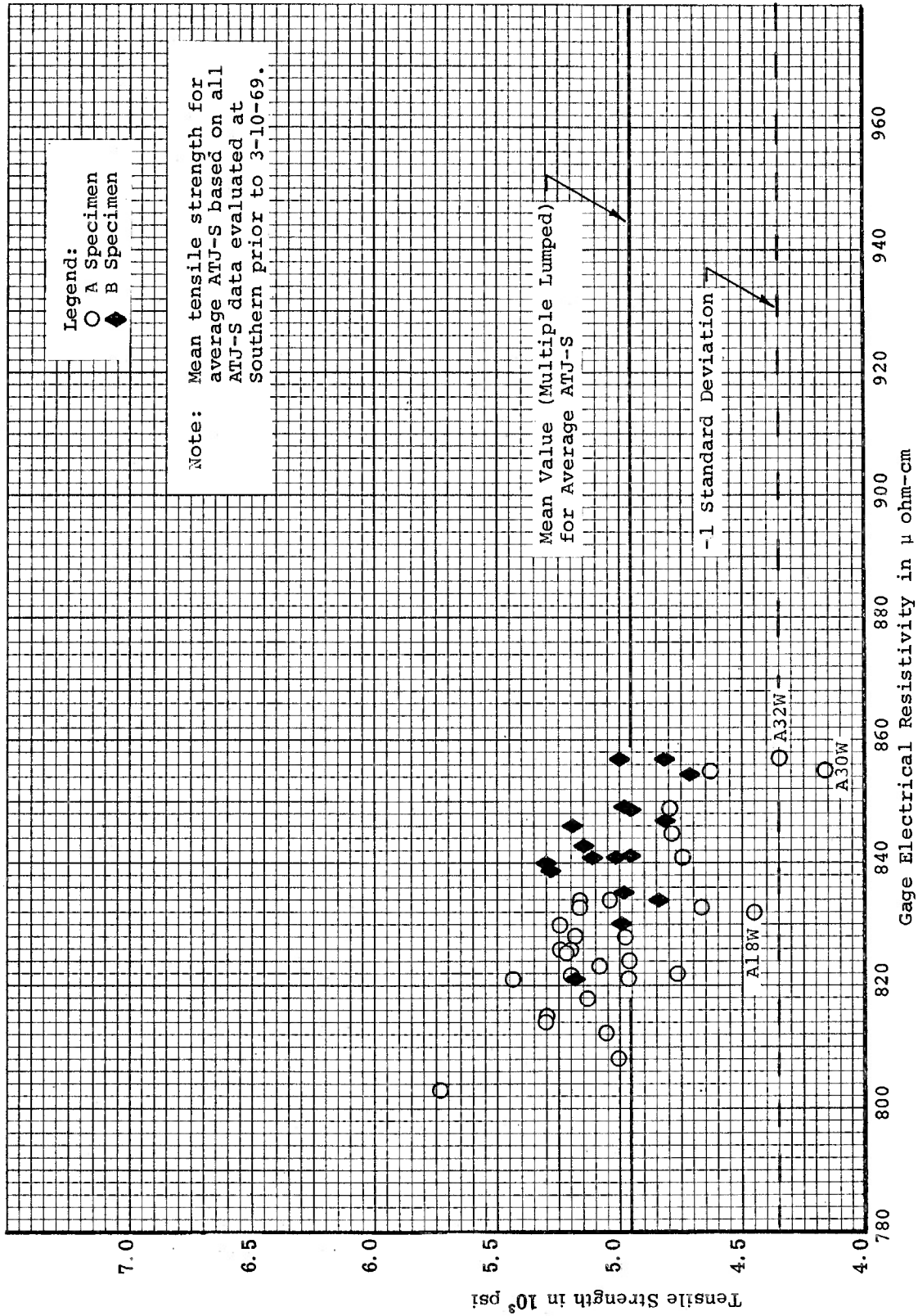


Figure 80. Tensile Strength Versus Gage Electrical Resistivity for ATJ-S Billet L-1-8 With Grain at 70°F

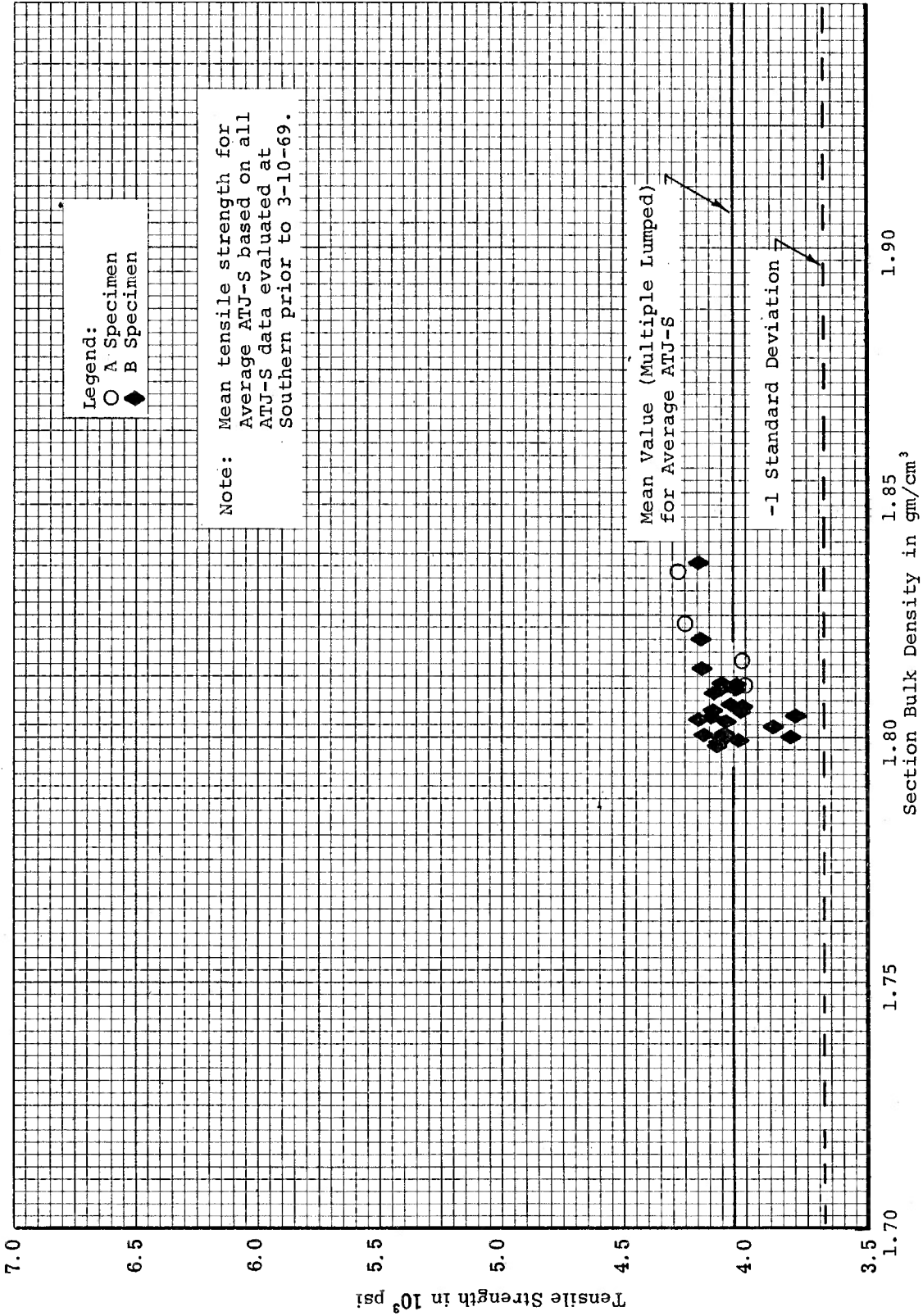


Figure 81. Tensile Strength Versus Section Bulk Density for ATJ-S Billet L-1-8 Across Grain at 70 °F

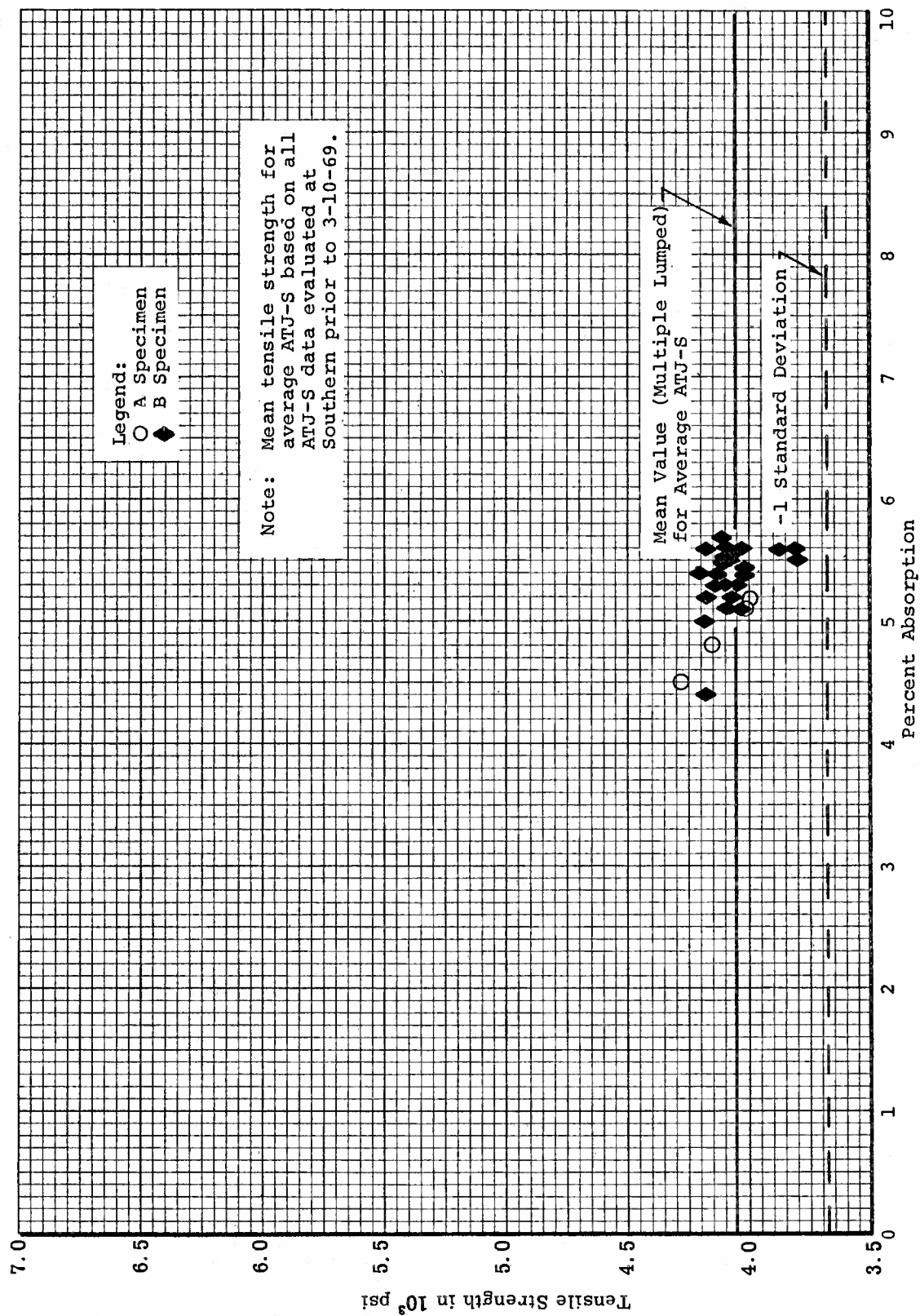


Figure 82. Tensile Strength Versus Percent Absorption for ATJ-S Billet L-1-8 Across Grain at 70°F

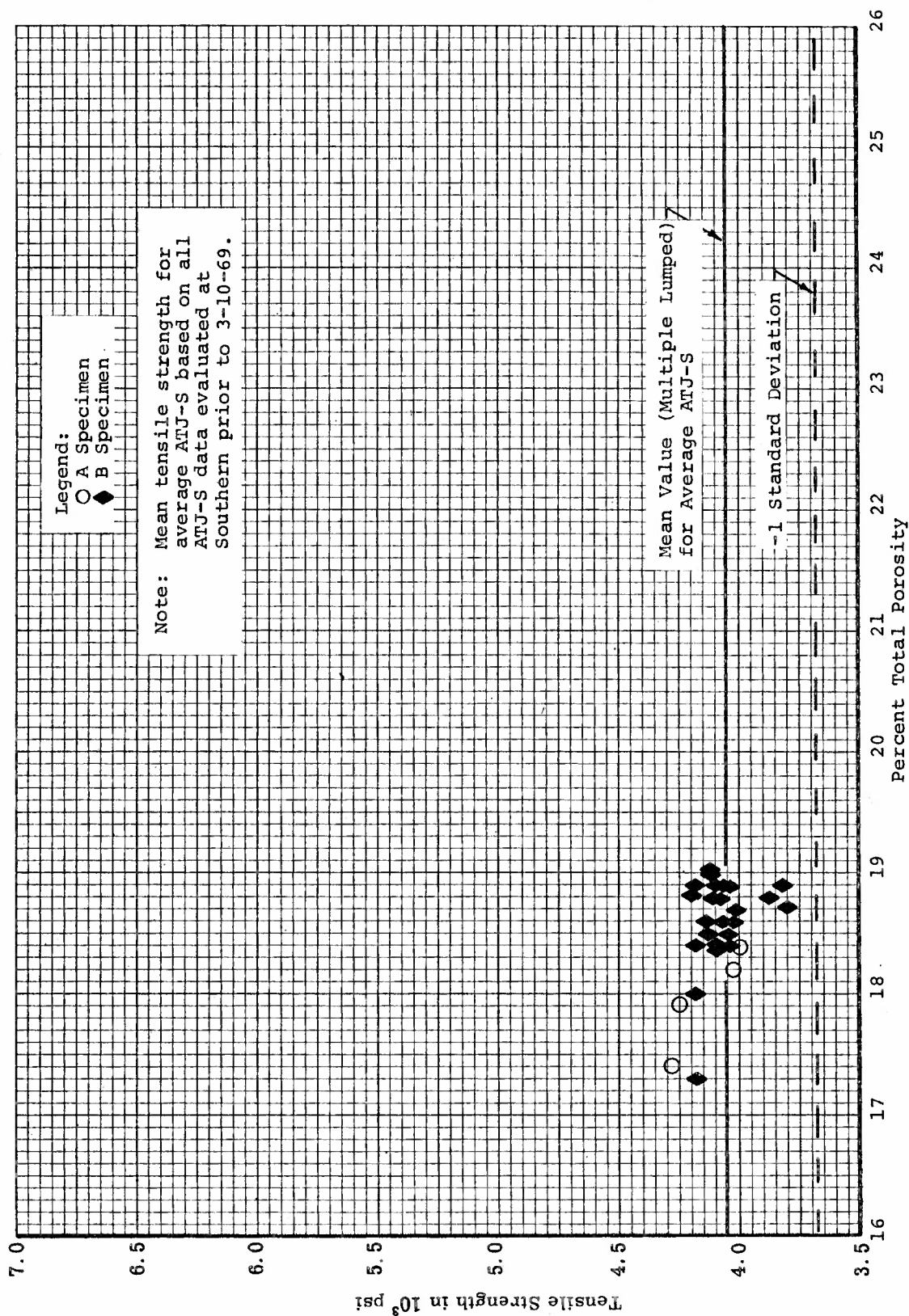


Figure 83. Tensile Strength Versus Percent Total Porosity for ATJ-S Billet L-1-8 Across Grain at 70°F

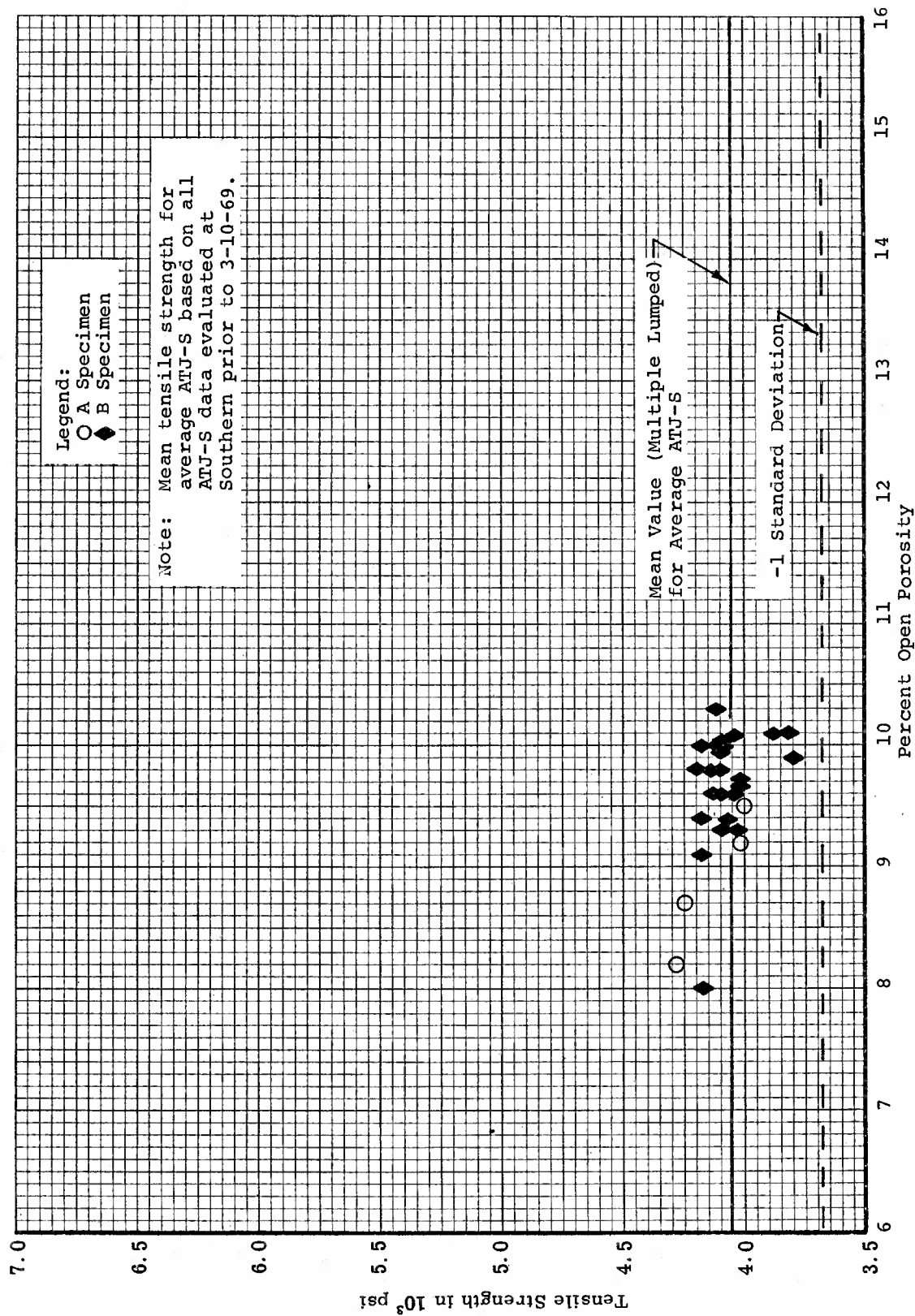
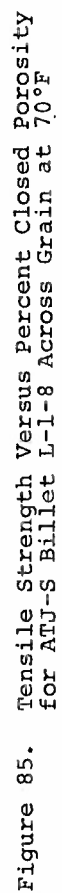


Figure 84. Tensile Strength Versus Percent Open Porosity for ATJ-S Billet L-1-8 Across Grain at 70°F





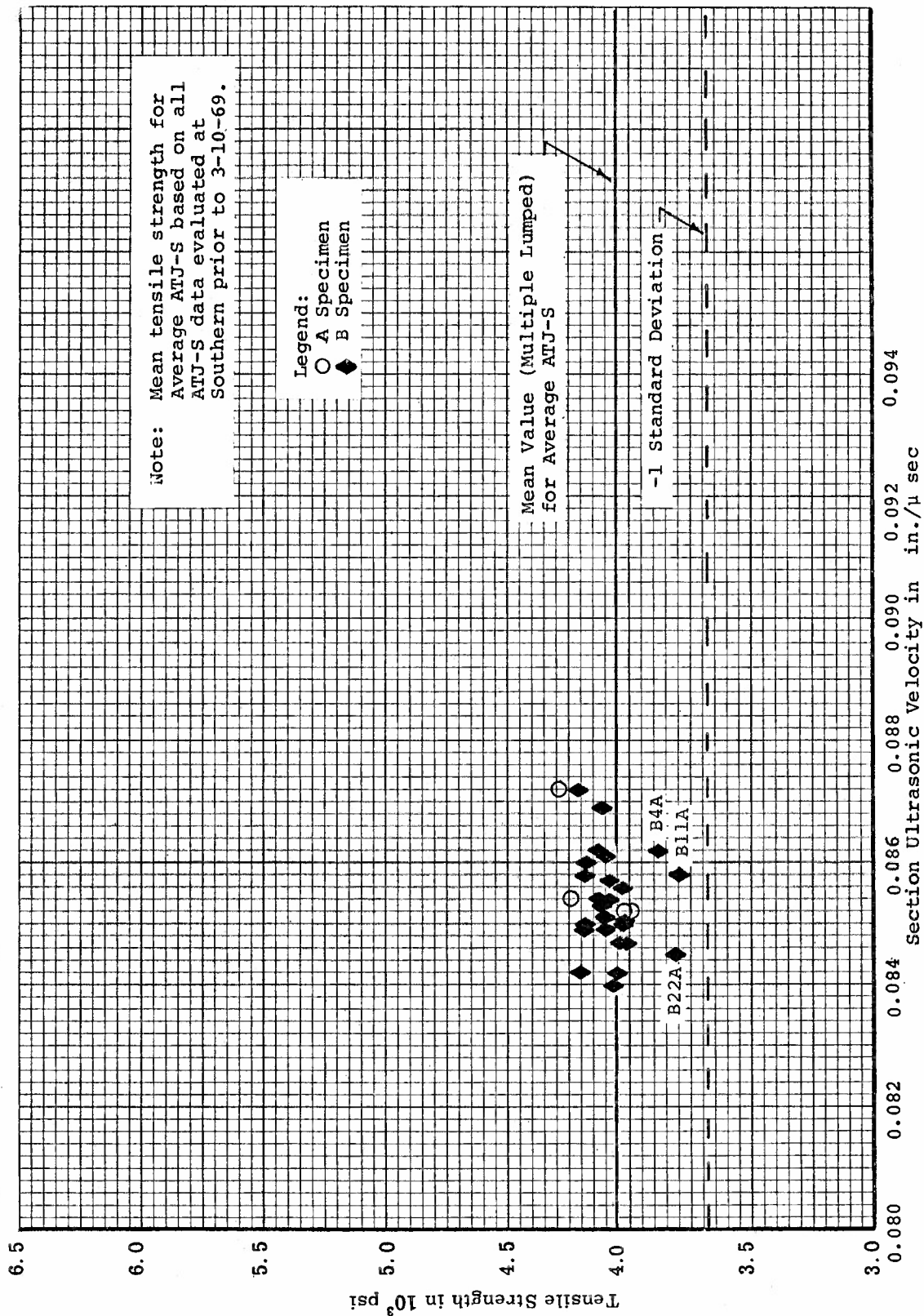


Figure 86. Tensile Strength Versus Section Ultrasonic Velocity for ATJ-S Billet L-1-8 Across Grain at 70°F



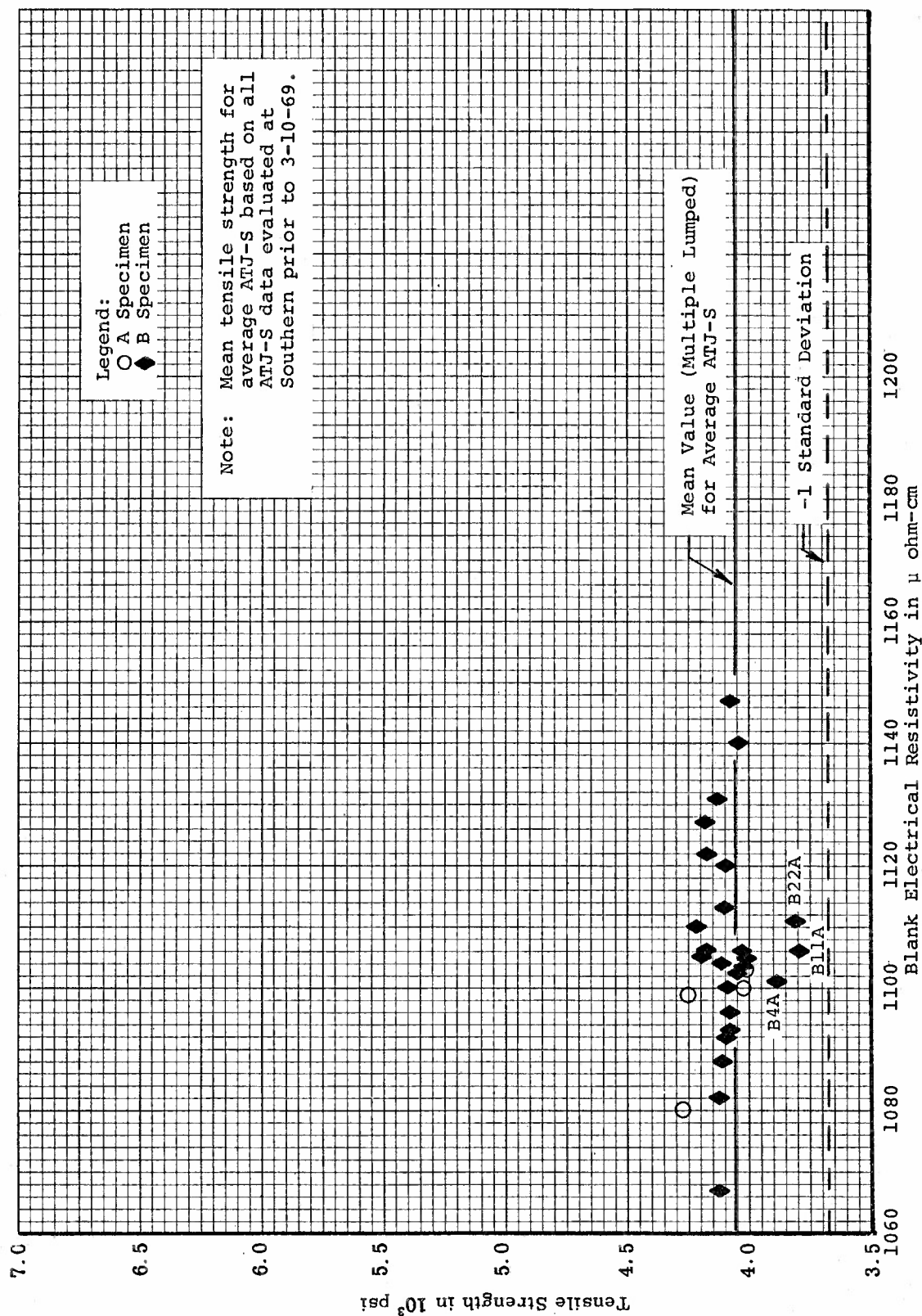
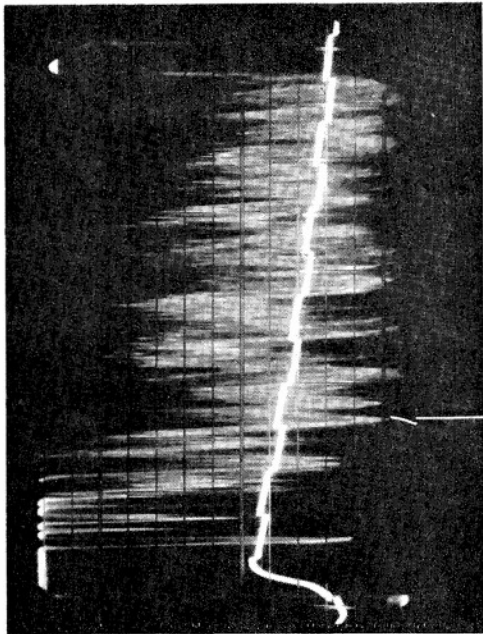
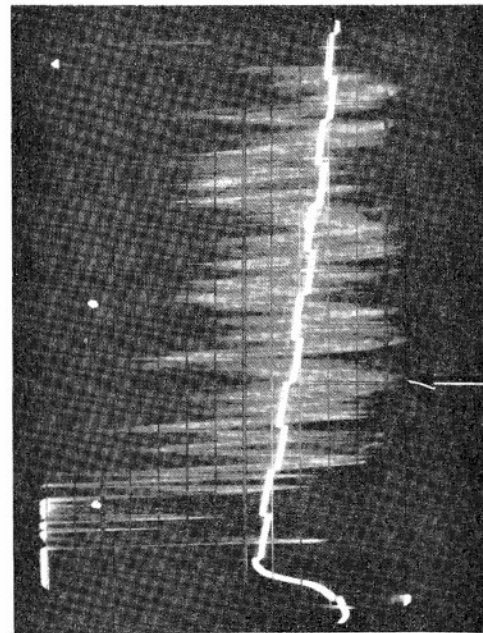


Figure 87. Tensile Strength Versus Blank Electrical Resistivity for ATJ-S Billet L-1-8 Across Grain at 70°F

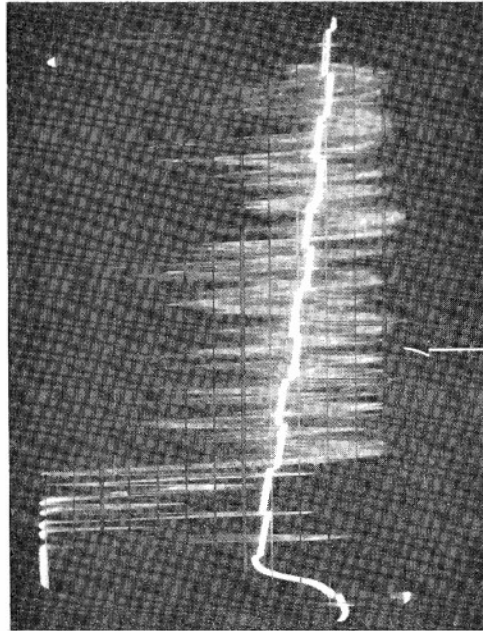




A18W



A30W



A32W

Figure 88. Pulse-Echo Smears on Weak Specimens A18W, A30W, and A32W from ATJ-S Billet L-1-8



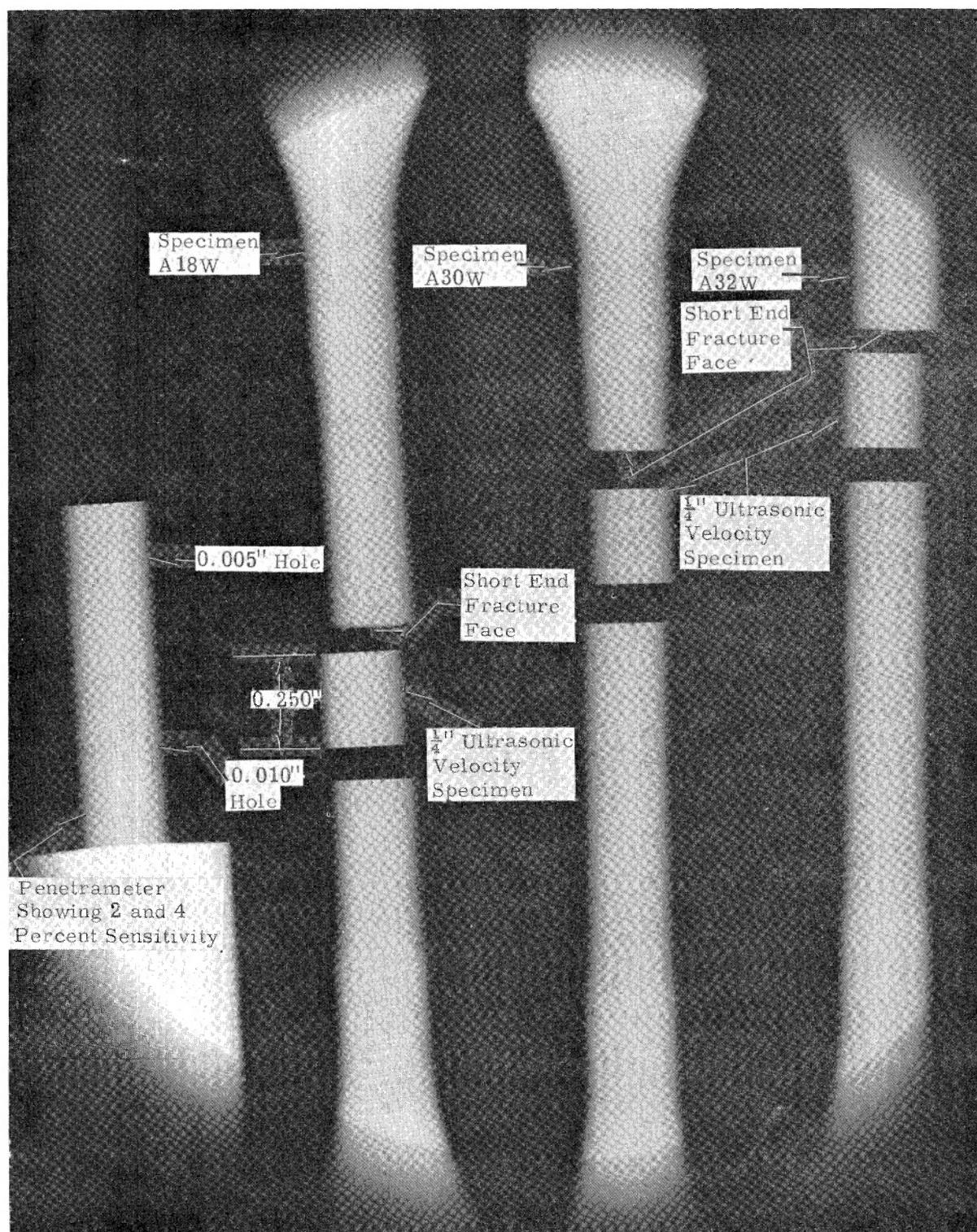
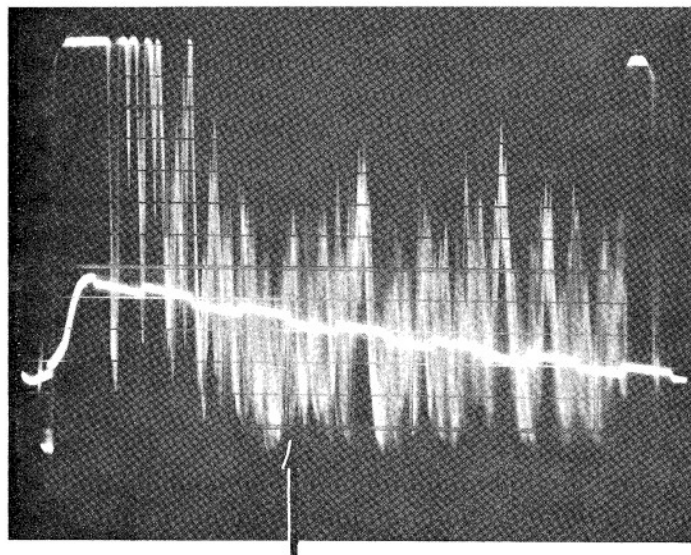
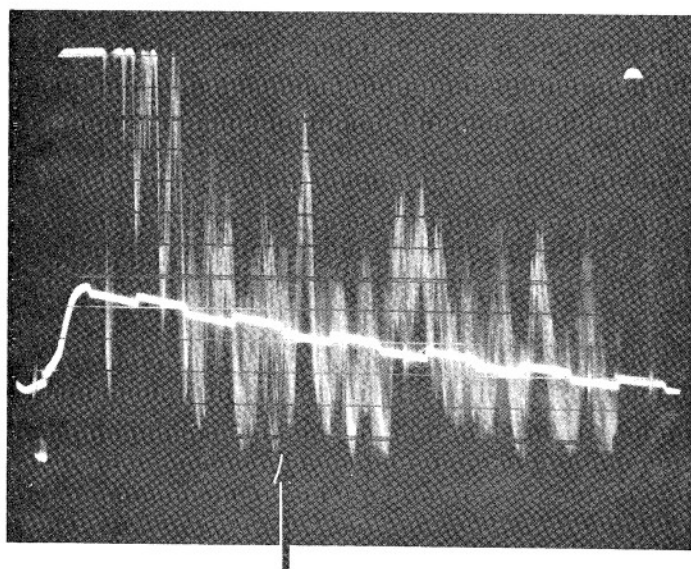


Figure 89. Radiograph of Weak Specimens A18W, A30W, and A32W of ATJ-S Billet L-1-8





A5W

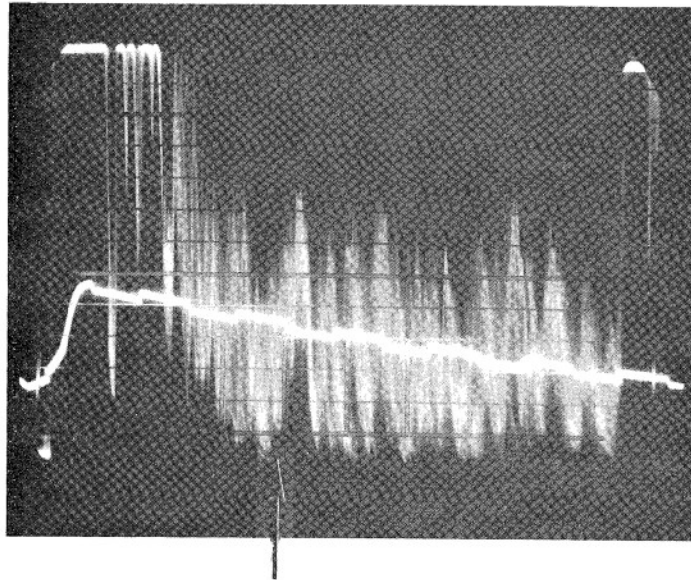


A10W

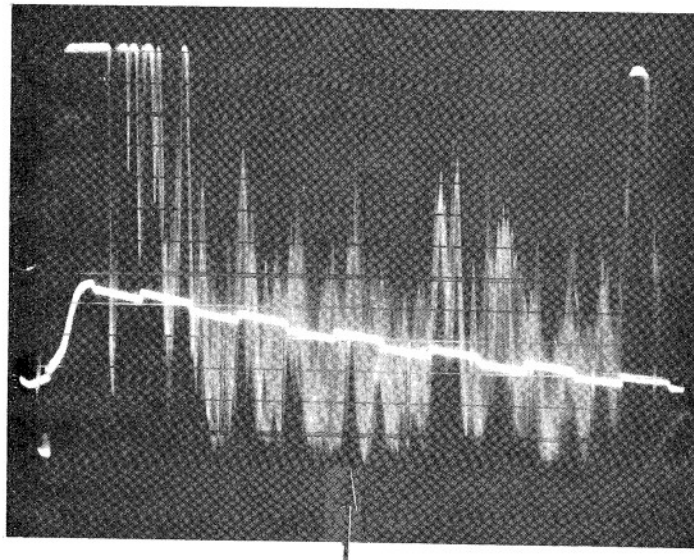
Figure 90. Pulse-Echo Smears on Selected Weak Specimens A5W and A10W from ATJ-S Billet L-1-8







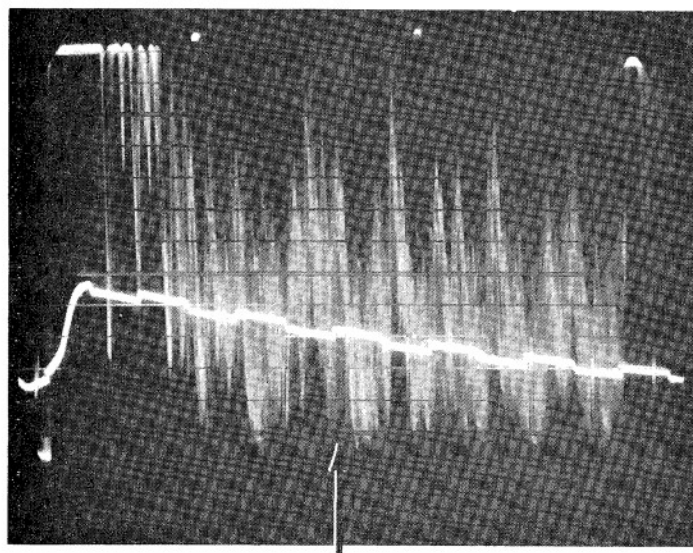
A11W



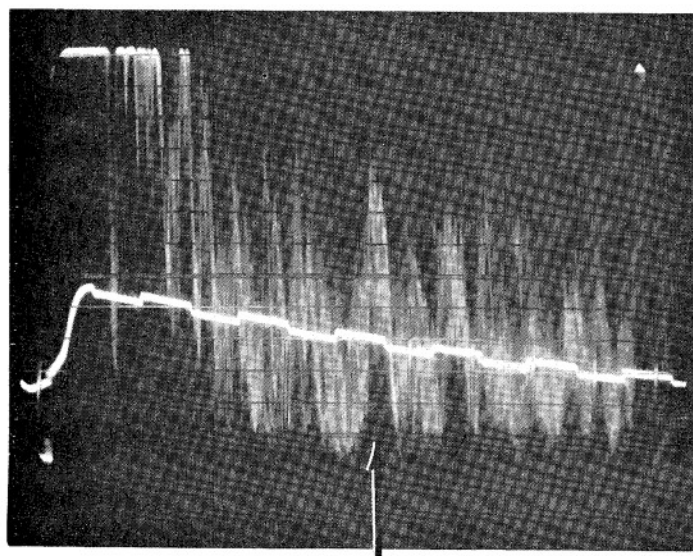
A14W

Figure 91. Pulse-Echo Smears on Selected Weak Specimens A11W and A14W from ATJ-S Billet L-1-8





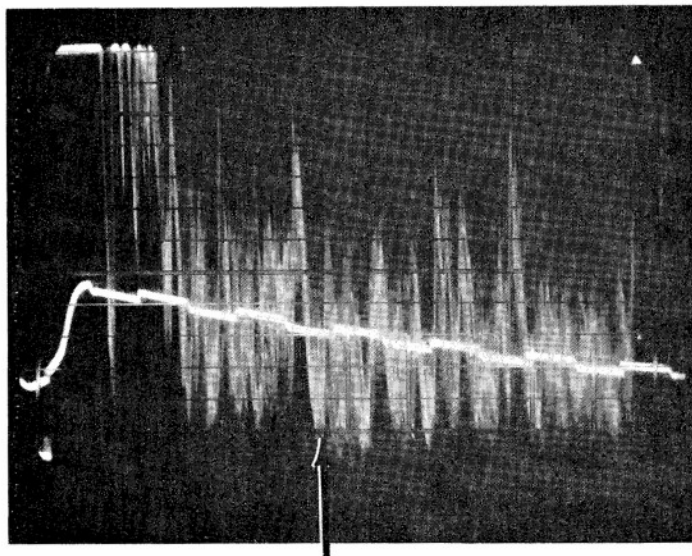
A21W



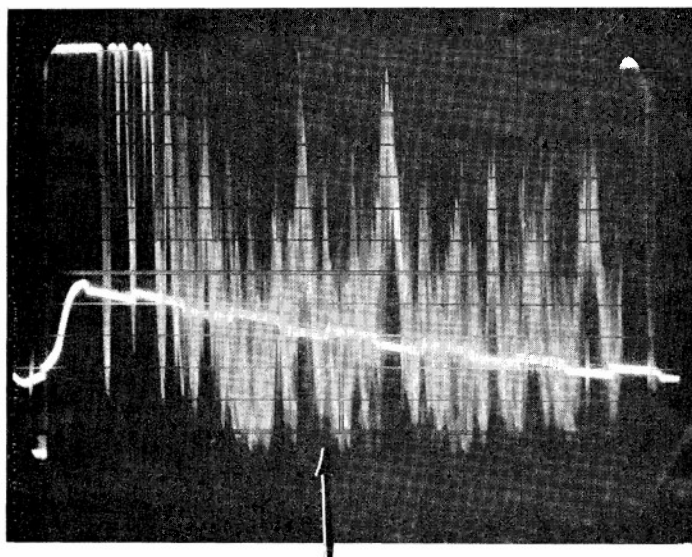
A28W

Figure 92. Pulse Echo Smears on Selected Weak Specimens A21W and A28W from ATJ-S Billet L-1-8





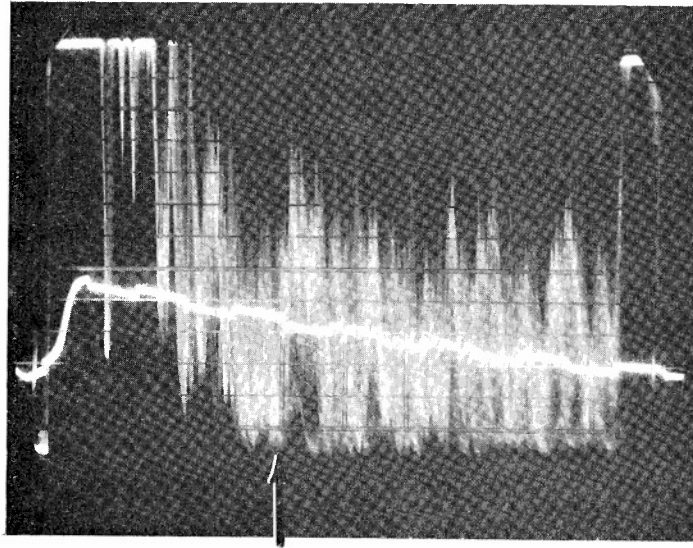
A29W



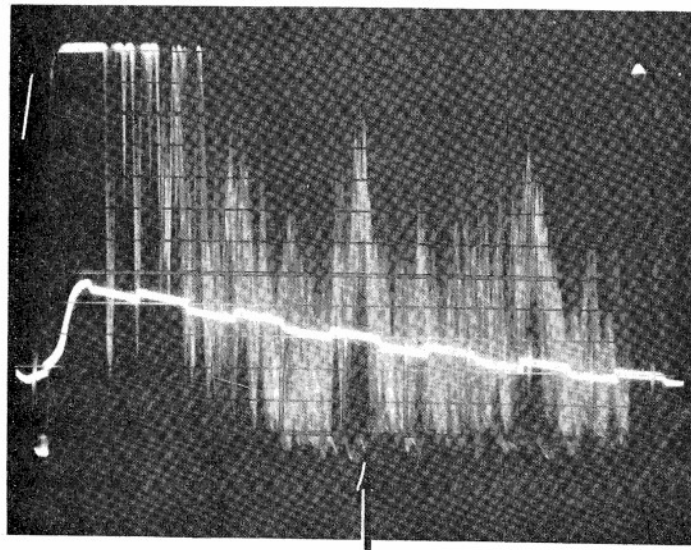
B27W

Figure 93. Pulse-Echo Smears on Selected Weak Specimens A29W and B27W from ATJ-S Billet L-1-8





B36W

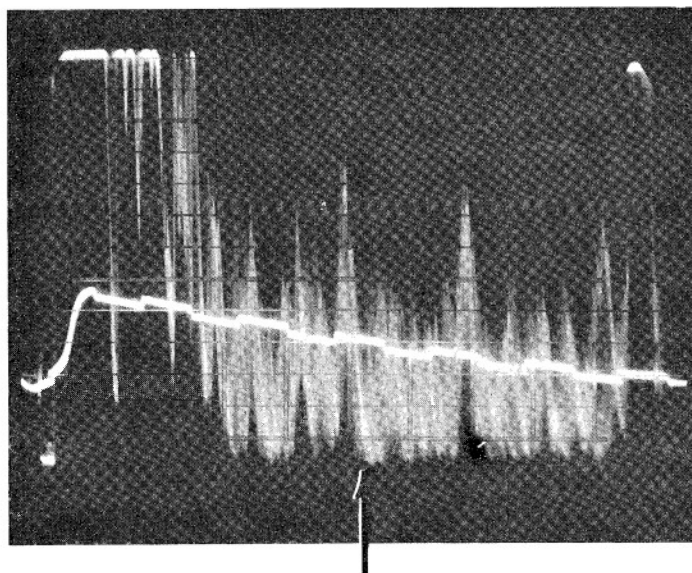


B38W

Figure 94. Pulse-Echo Smears on Selected Weak Specimens B36W and B38W from ATJ-S Billet L-1-8



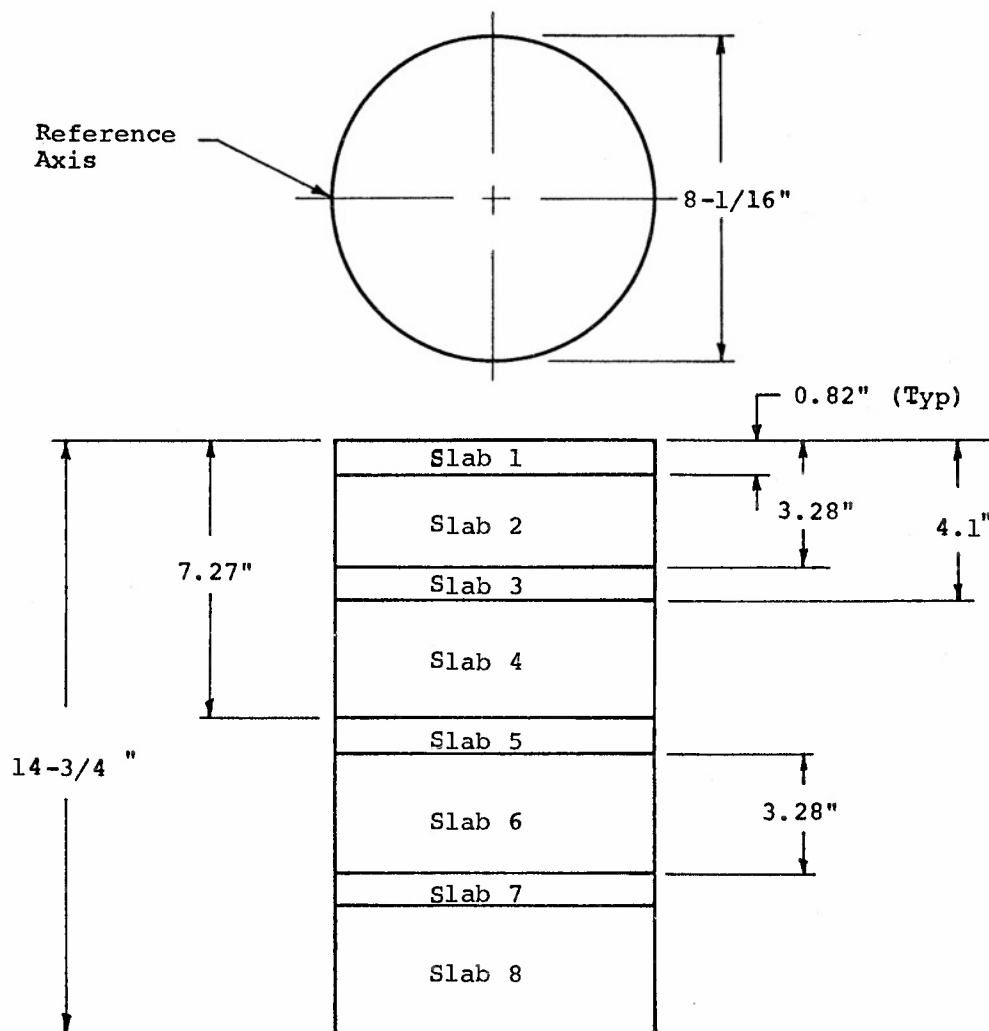




B43W

Figure 95. Pulse-Echo Smears on Selected Weak Specimen B43W  
from ATJ-S Billet L-1-8





**Note:**

1. Scribe reference line along billet length at reference axis prior to cutting.
2. Mark each specimen with number shown in the layout (use white ink, chalk, or place individually in marked envelope).
3. Identify and return all excess material.
4. Keep the graphite material in dry atmosphere at all times.
5. Visually inspect slab interfaces for cracks.

Figure 96. Slab Cutting Plan for ATJ-S Billet L-4-6

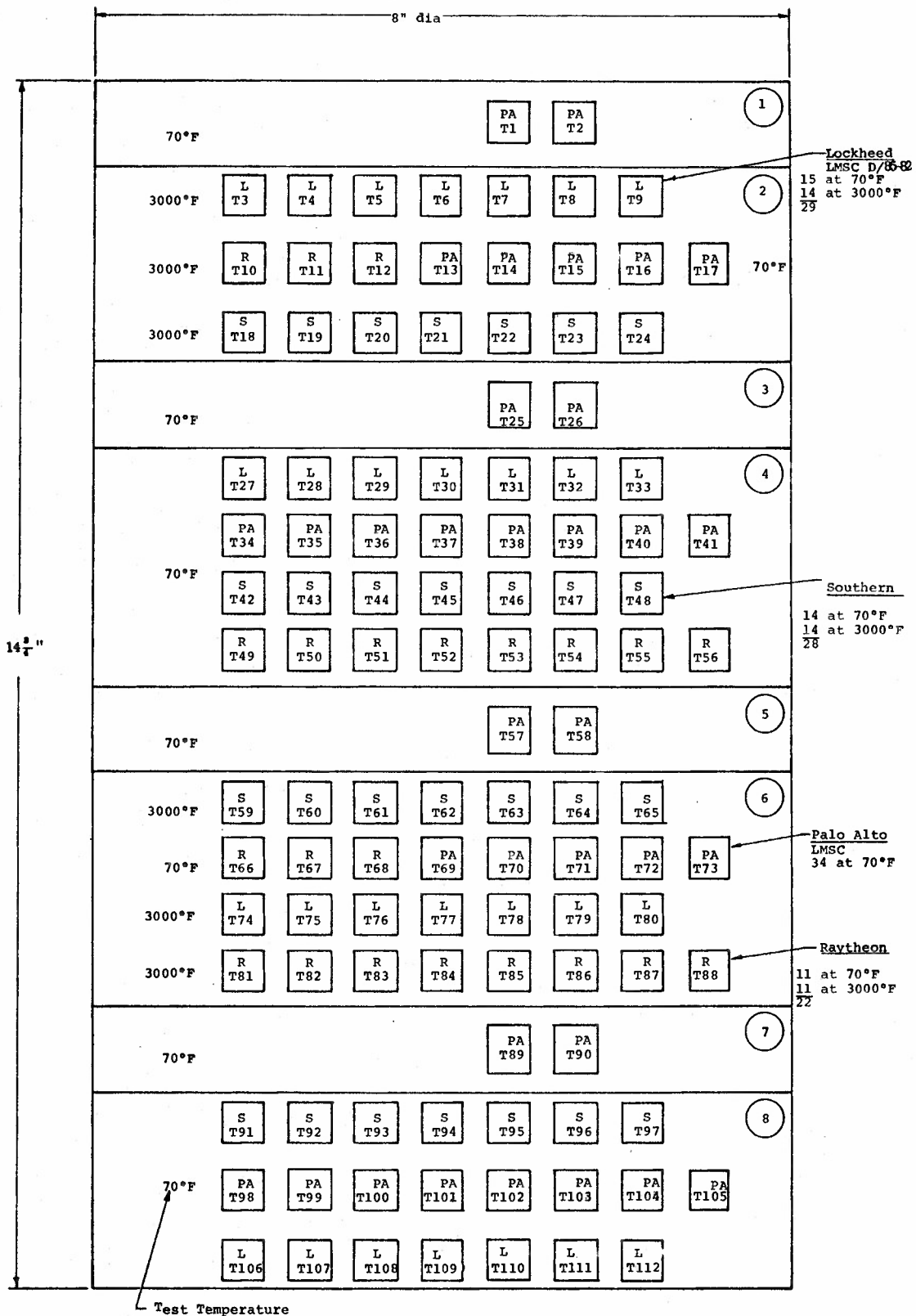
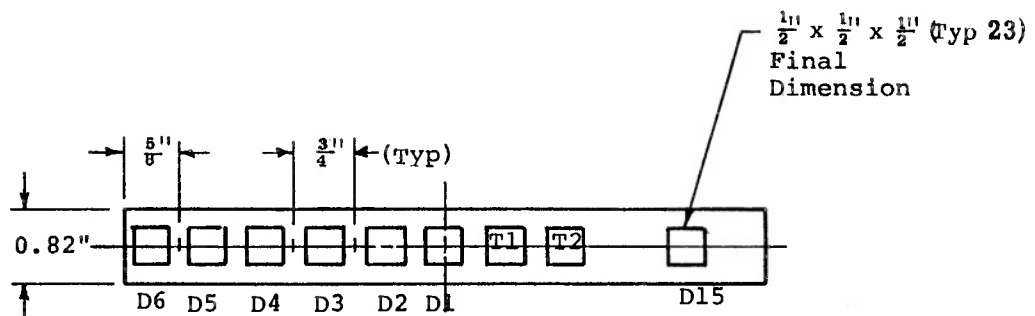
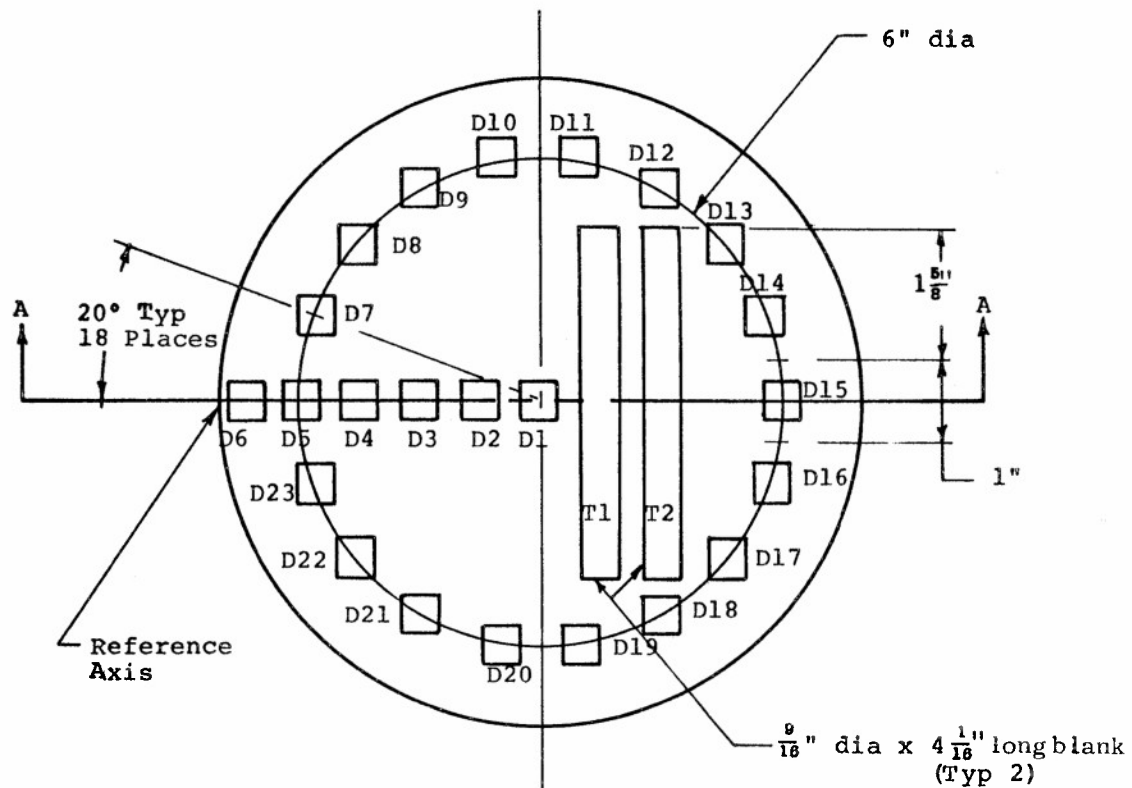


Figure 97. Tensile Specimen Cutting Plan for ATJ-S Billet L-4-6



Section A - A

Figure 98. Specimen Blank Layout for Slab 1 of ATJ-S Billet L-4-6

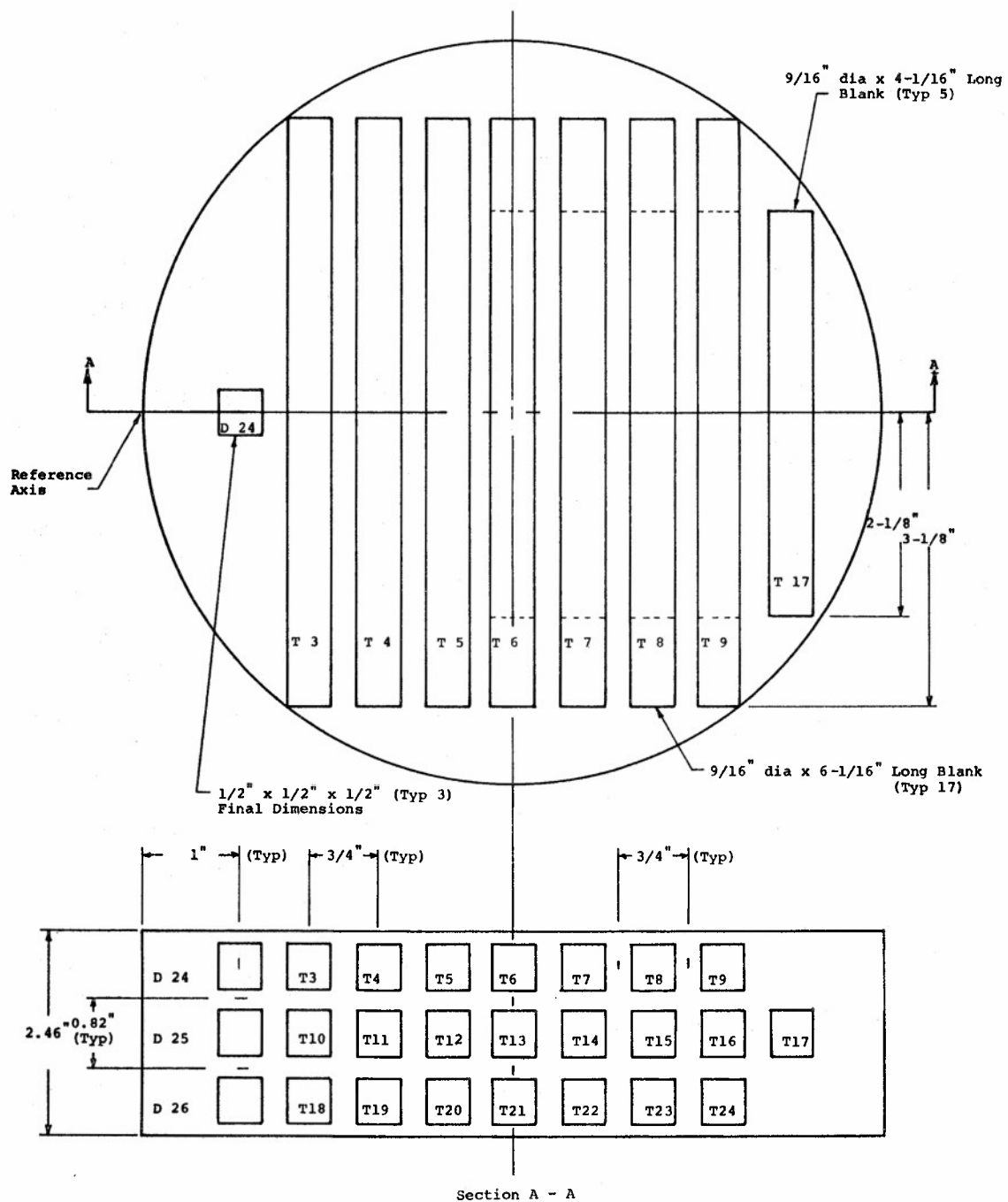
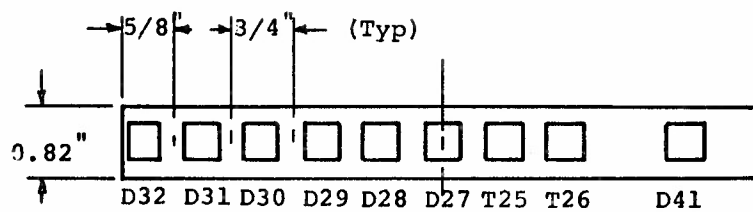
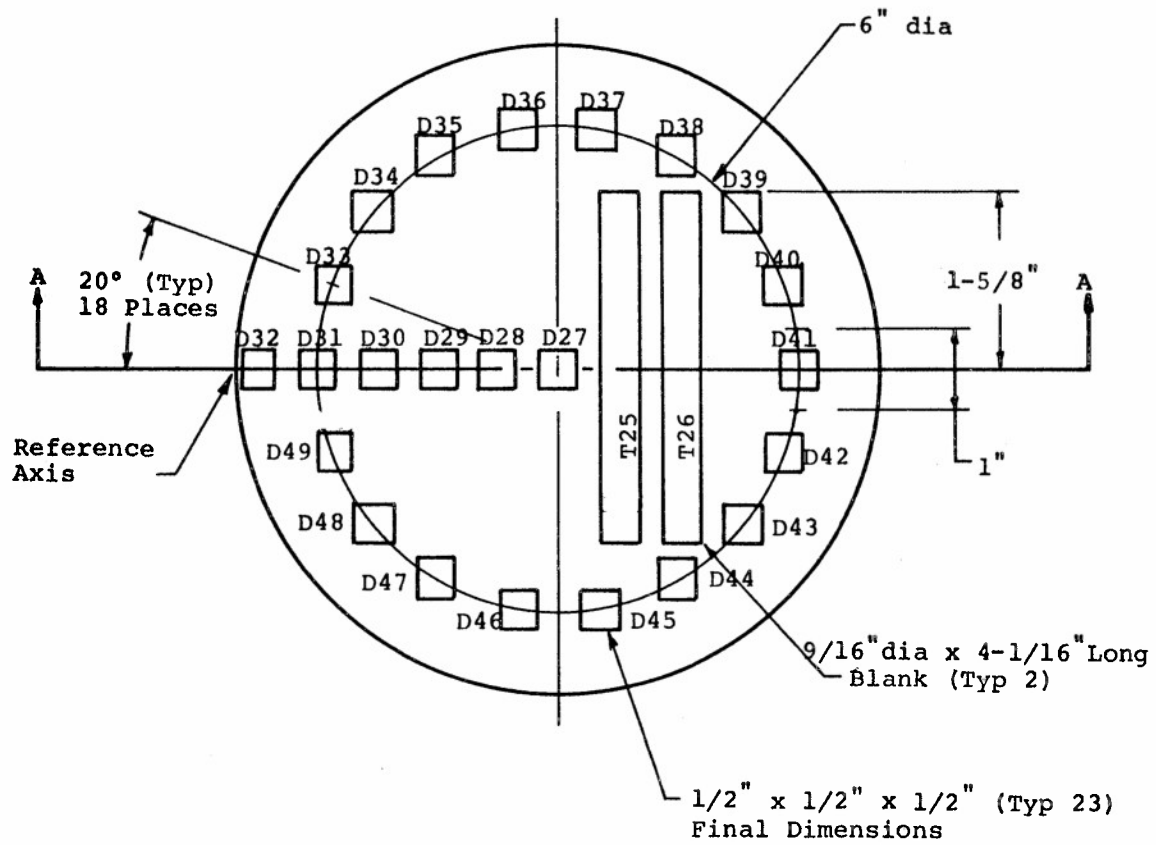
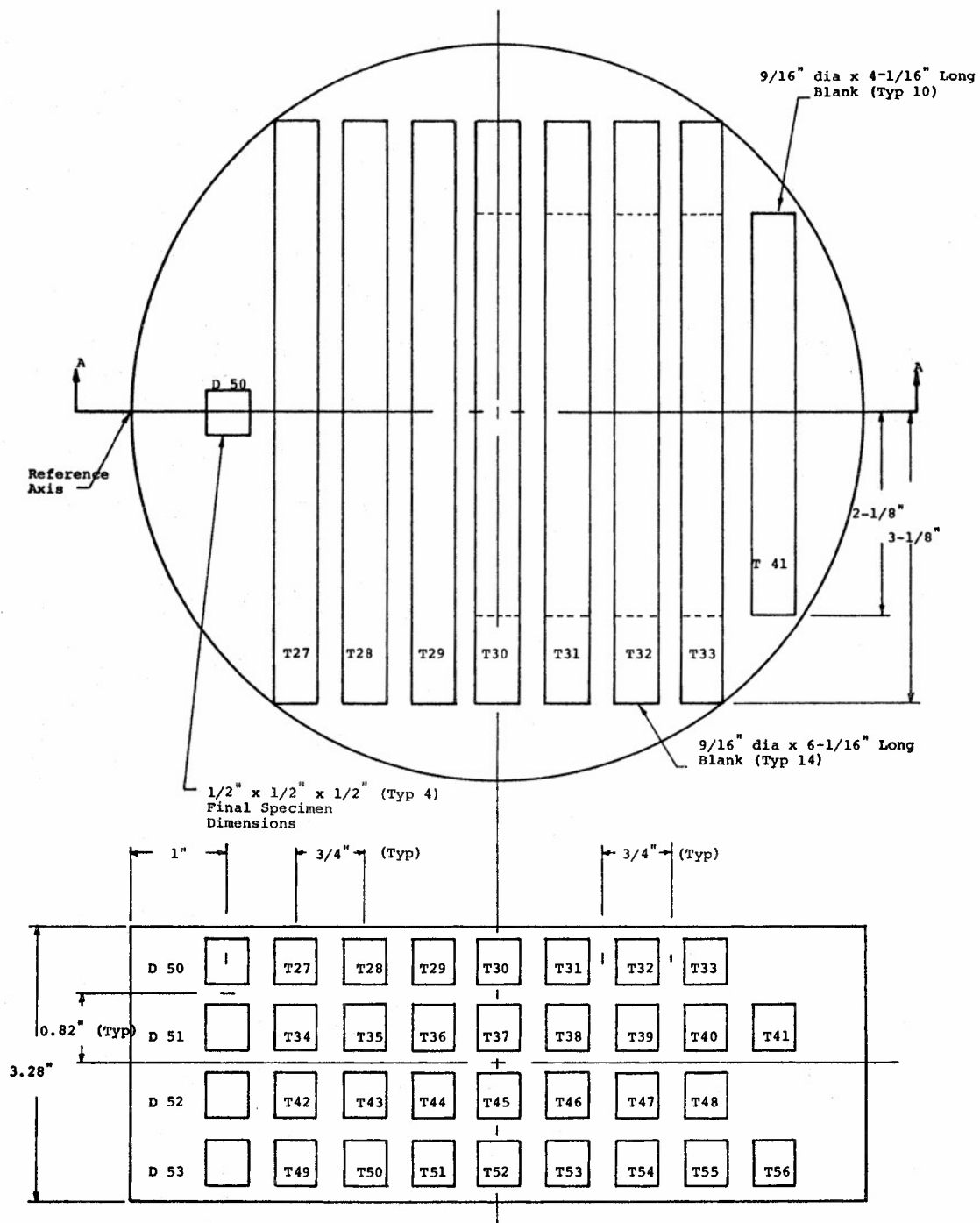


Figure 99. Specimen Blank Layout for Slab 2 of ATJ-S Billet L-4-6



Section A - A

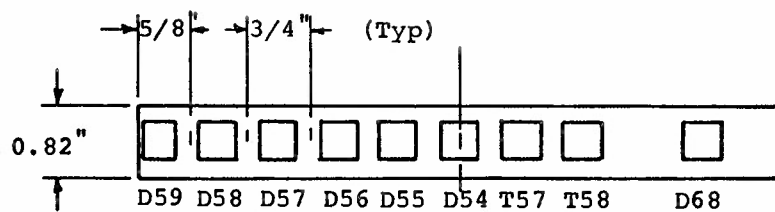
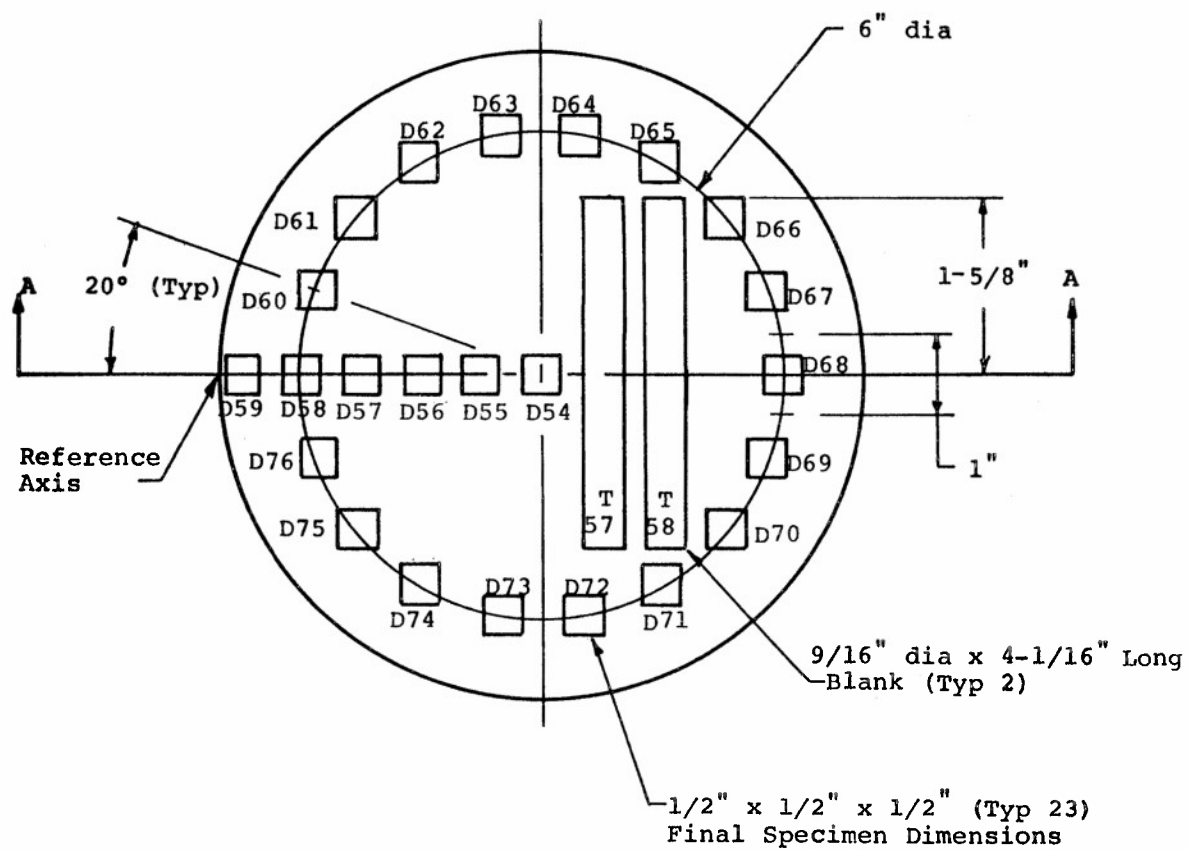
Figure 100. Specimen Blank Layout for Slab 3  
of ATJ-S Billet L-4-6



Section A - A

Figure 101. Specimen Blank Layout for Slab 4 of ATJ-S Billet L-4-6





Section A - A

Figure 102. Specimen Blank Layout for Slab 5 of ATJ-S Billet L-4-6

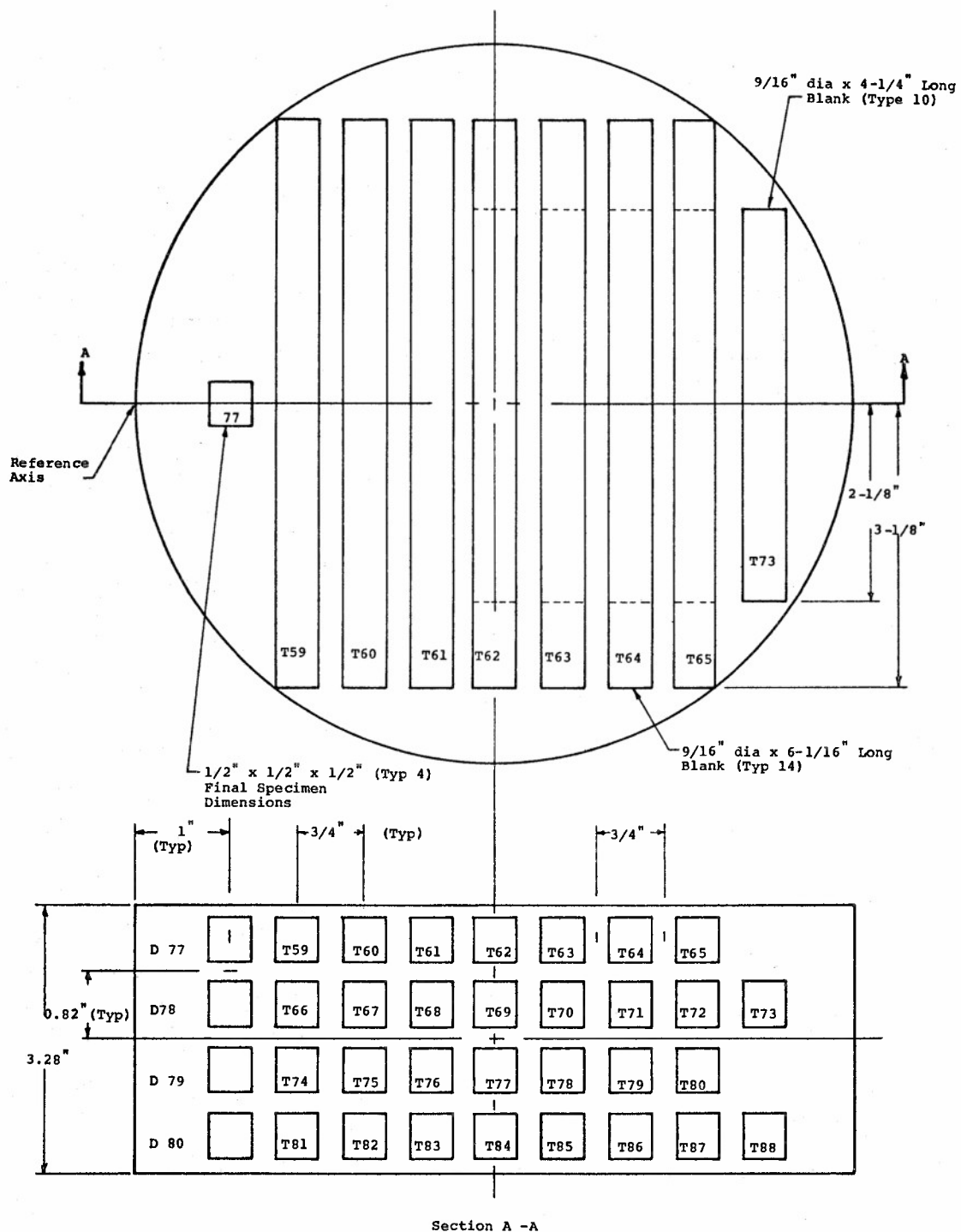
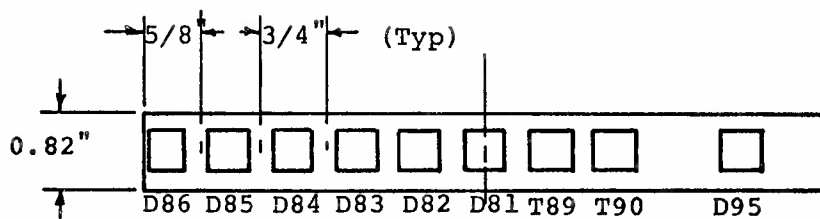
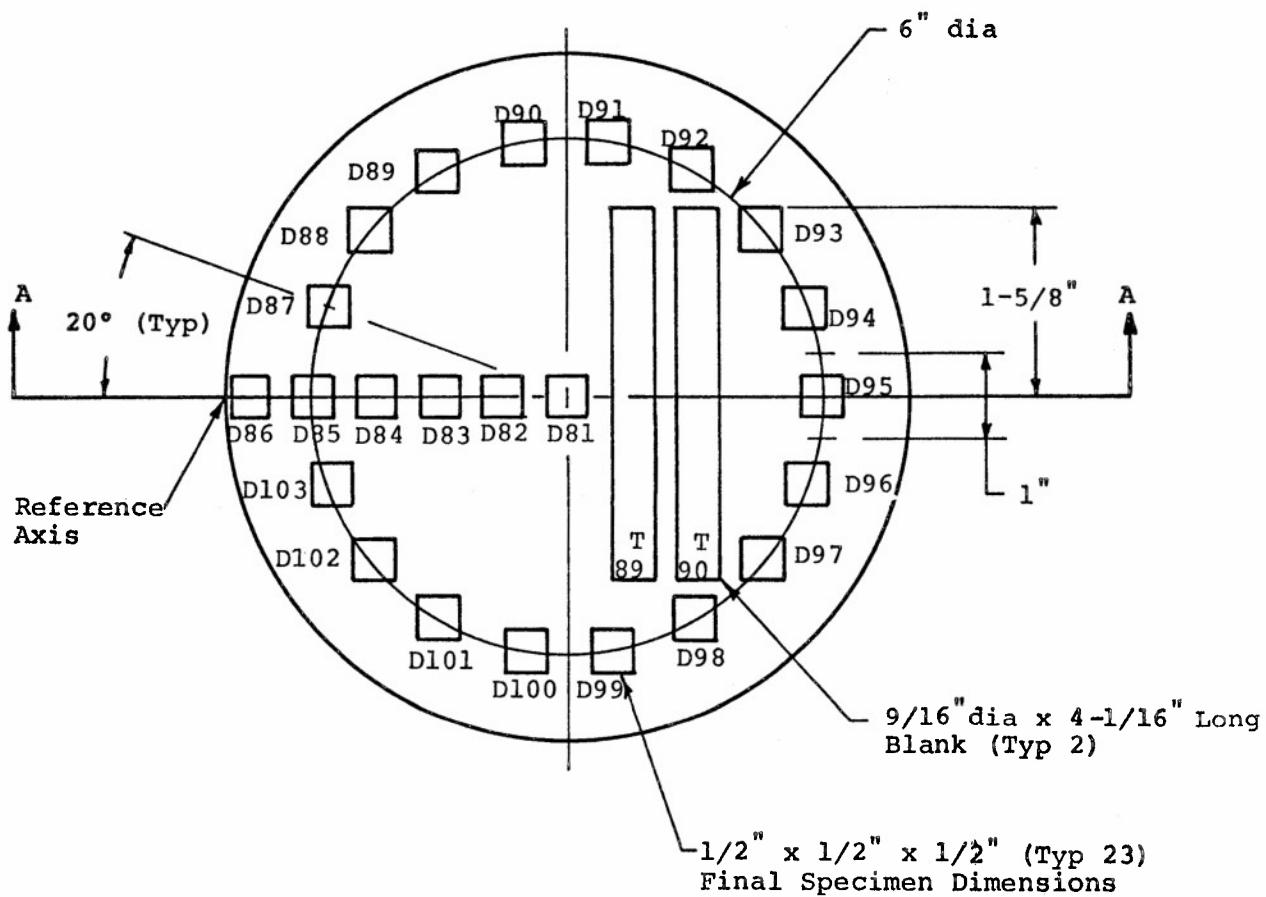


Figure 103. Specimen Blank Layout for Slab 6 of ATJ-S Billet L-4-6



Section A - A

Figure 104. Specimen Blank Layout for Slab 7 of ATJ-S Billet L-4-6

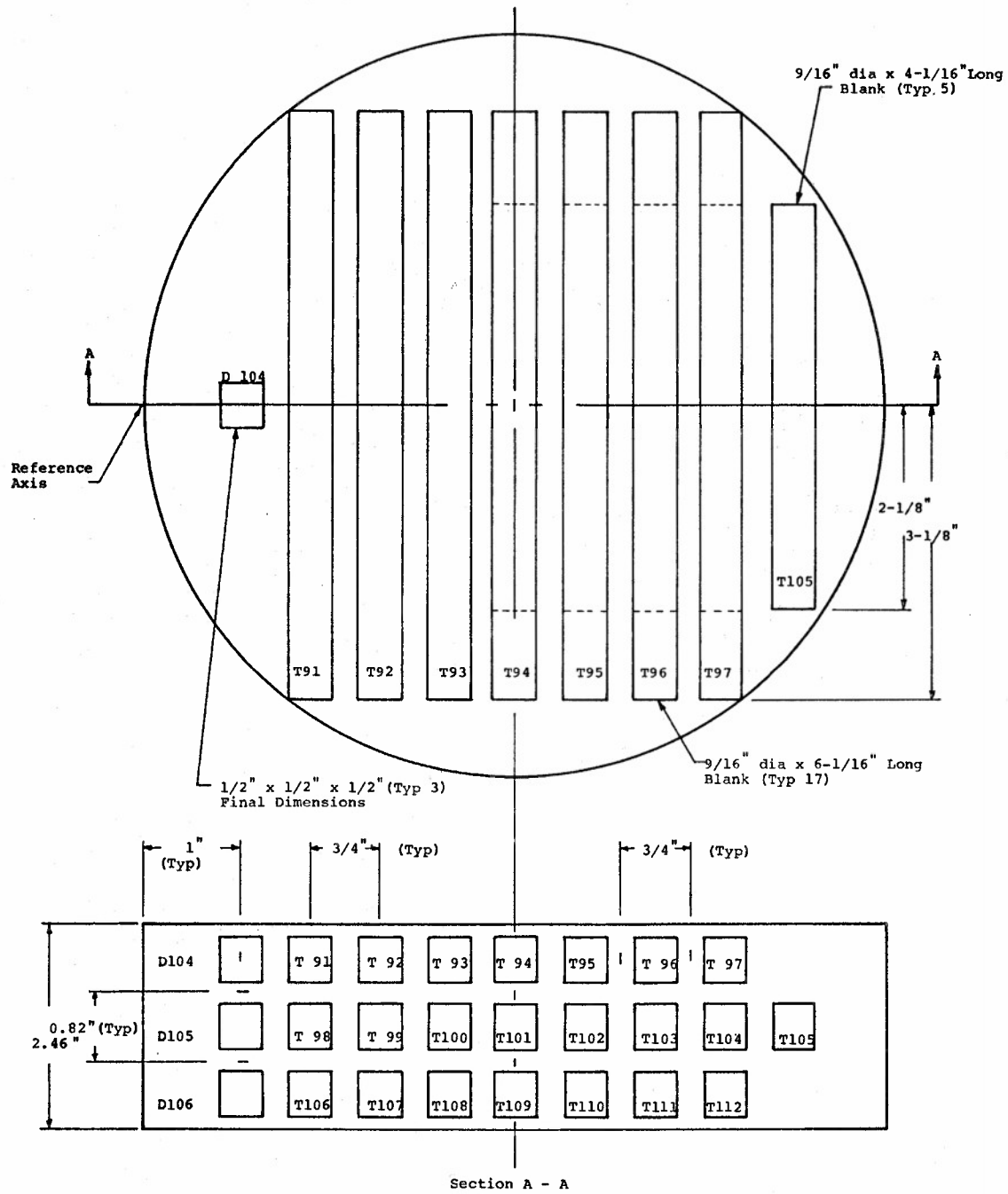
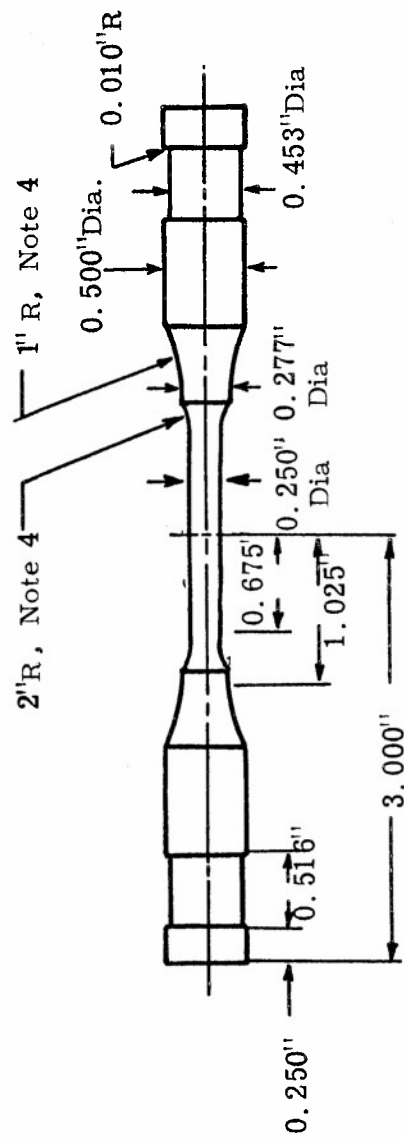


Figure 105. Specimen Blank Layout for Slab 8 of ATJ-S Billet L-4-6



Notes:

1. All diameters true and concentric to 0.0005"
2. All lengths  $\pm 0.005$ "
3. Both ends flat and perpendicular to 0.0005"
4. Do not undercut at tangent point

Figure 106. Tensile Test Specimen Configuration Used for Round Robin on ATJ-S Billet L-4-6

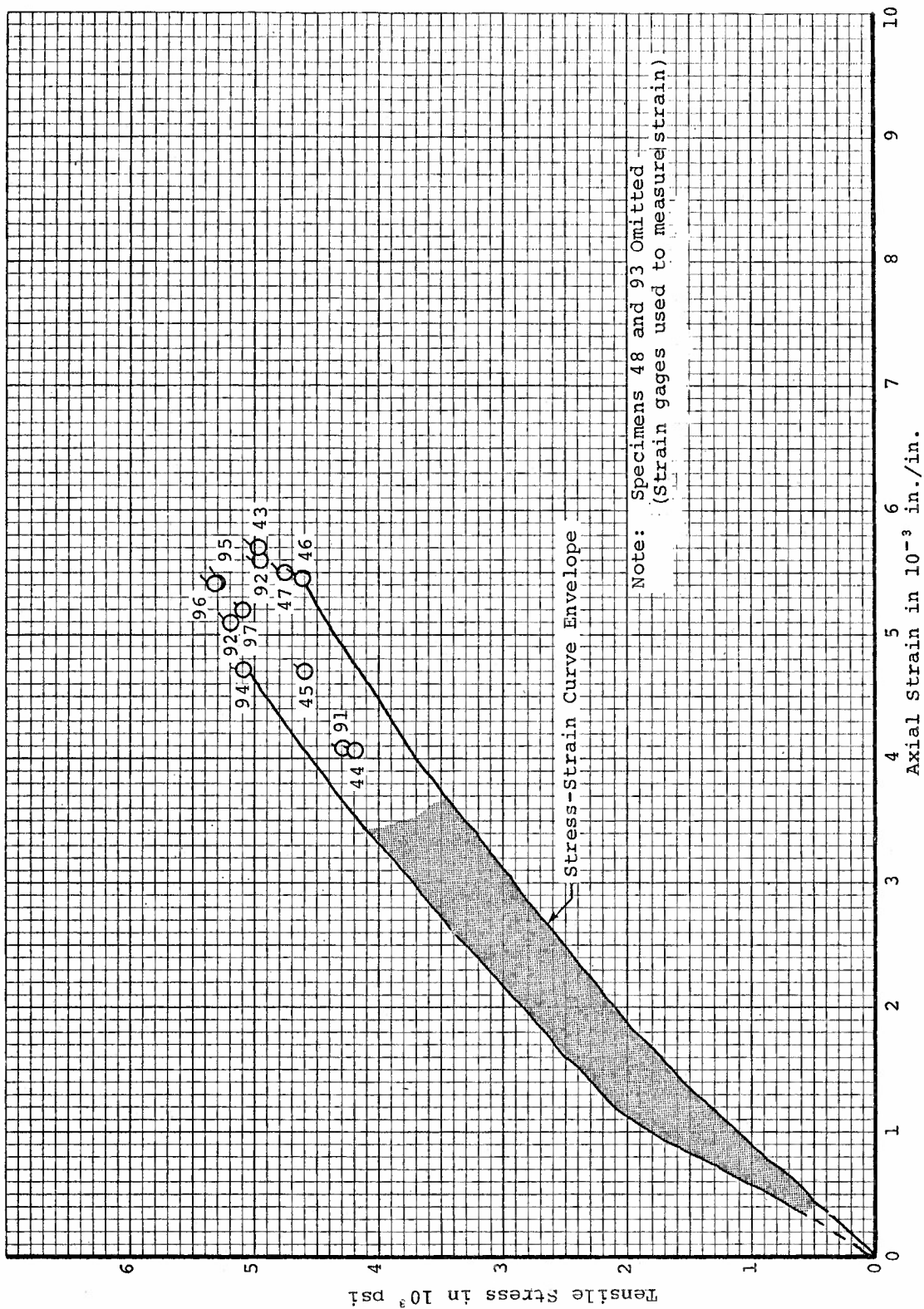


Figure 107. Tensile Stress-Strain Curve Envelope for 70°F Evaluations  
(Slabs 4 and 8) from ATJ-S Billet L-4-6

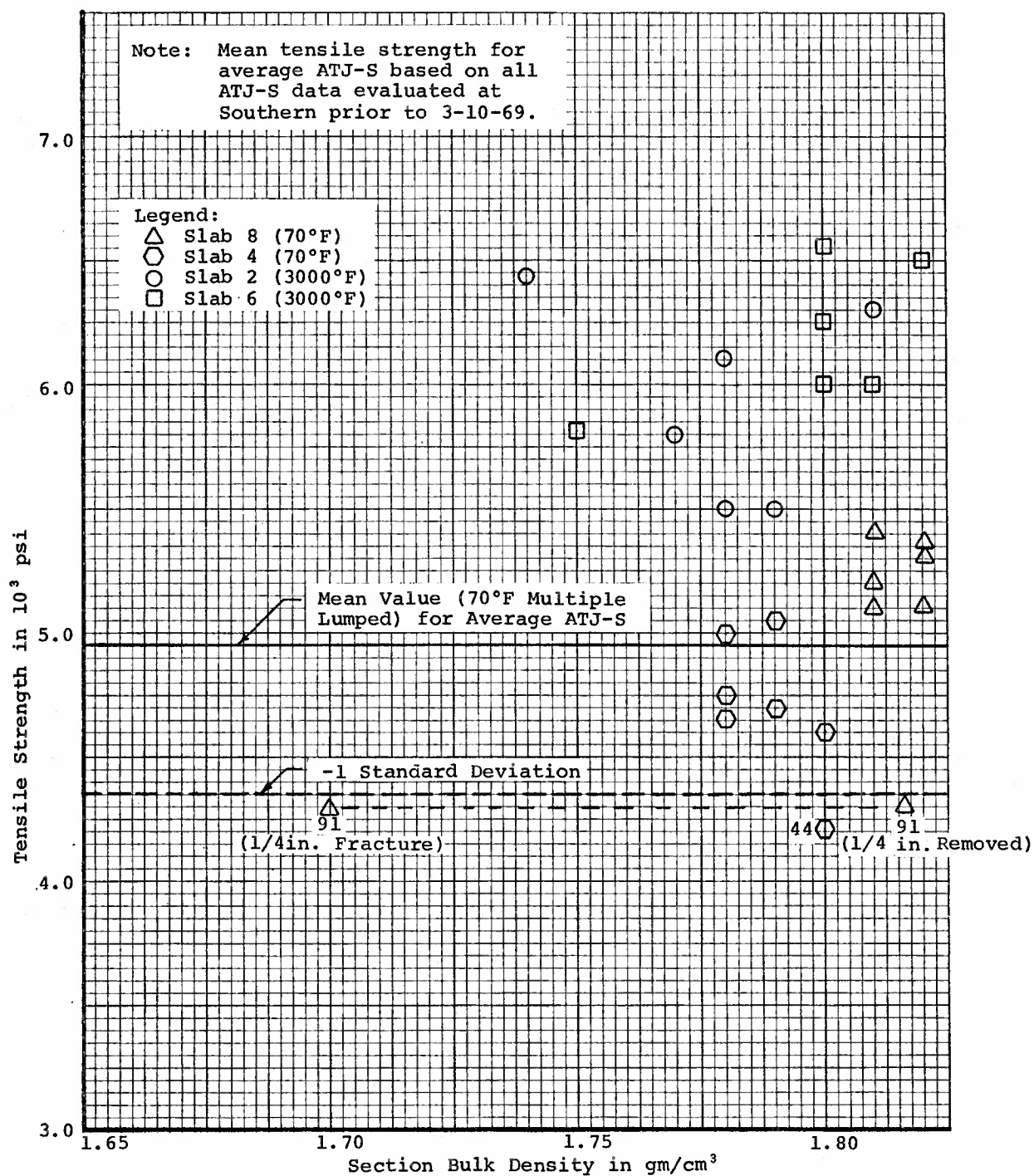


Figure 108. Tensile Strength versus Section Bulk Density (1/4 inch Fracture Section) for ATJ-S Billet L-4-6 With Grain at 70°F and 3000°F

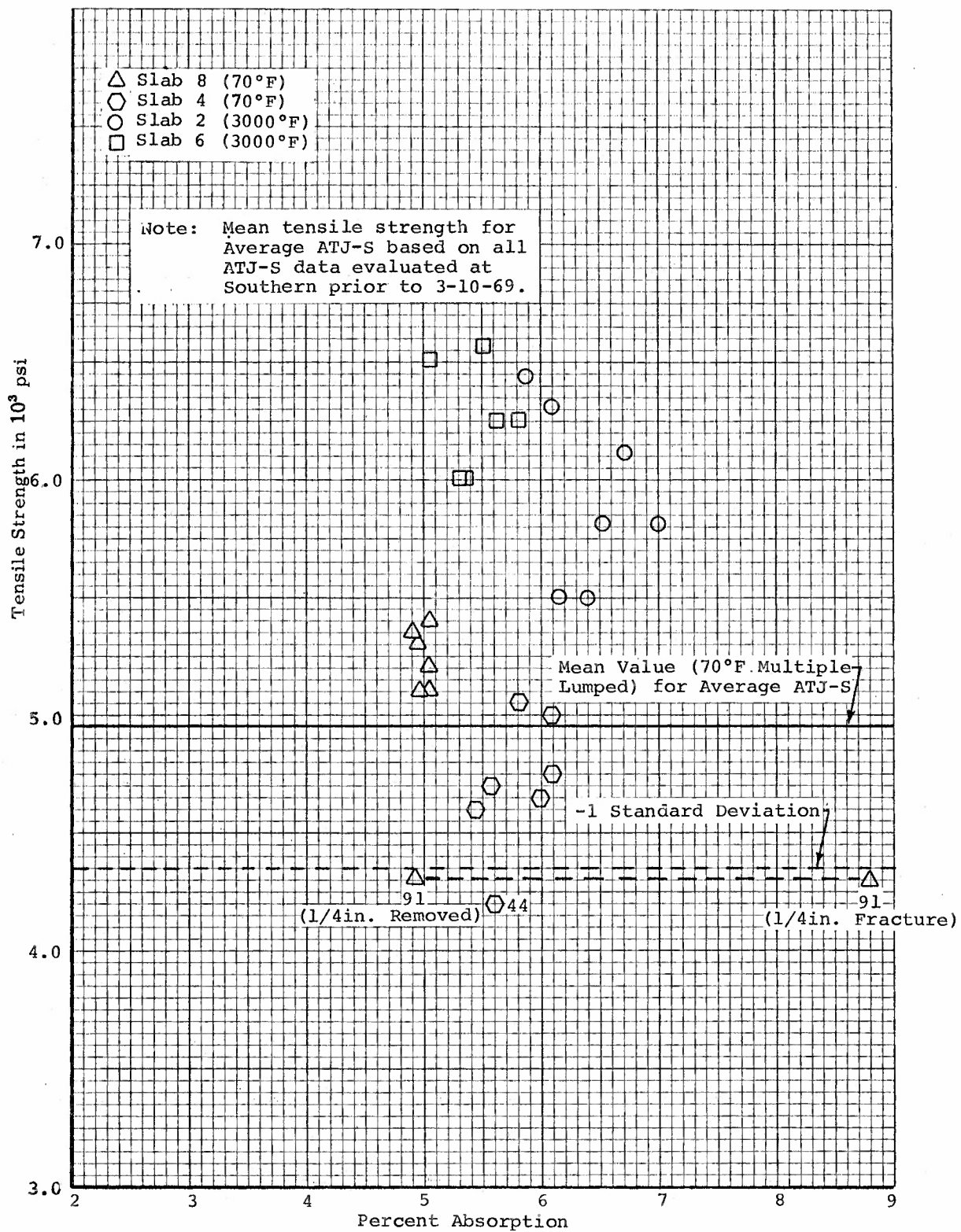


Figure 109. Tensile Strength versus Percent Absorption (1/4 inch Fracture Section) for ATJ-S Billet L-4-6 With Grain at 70°F and 3000°F



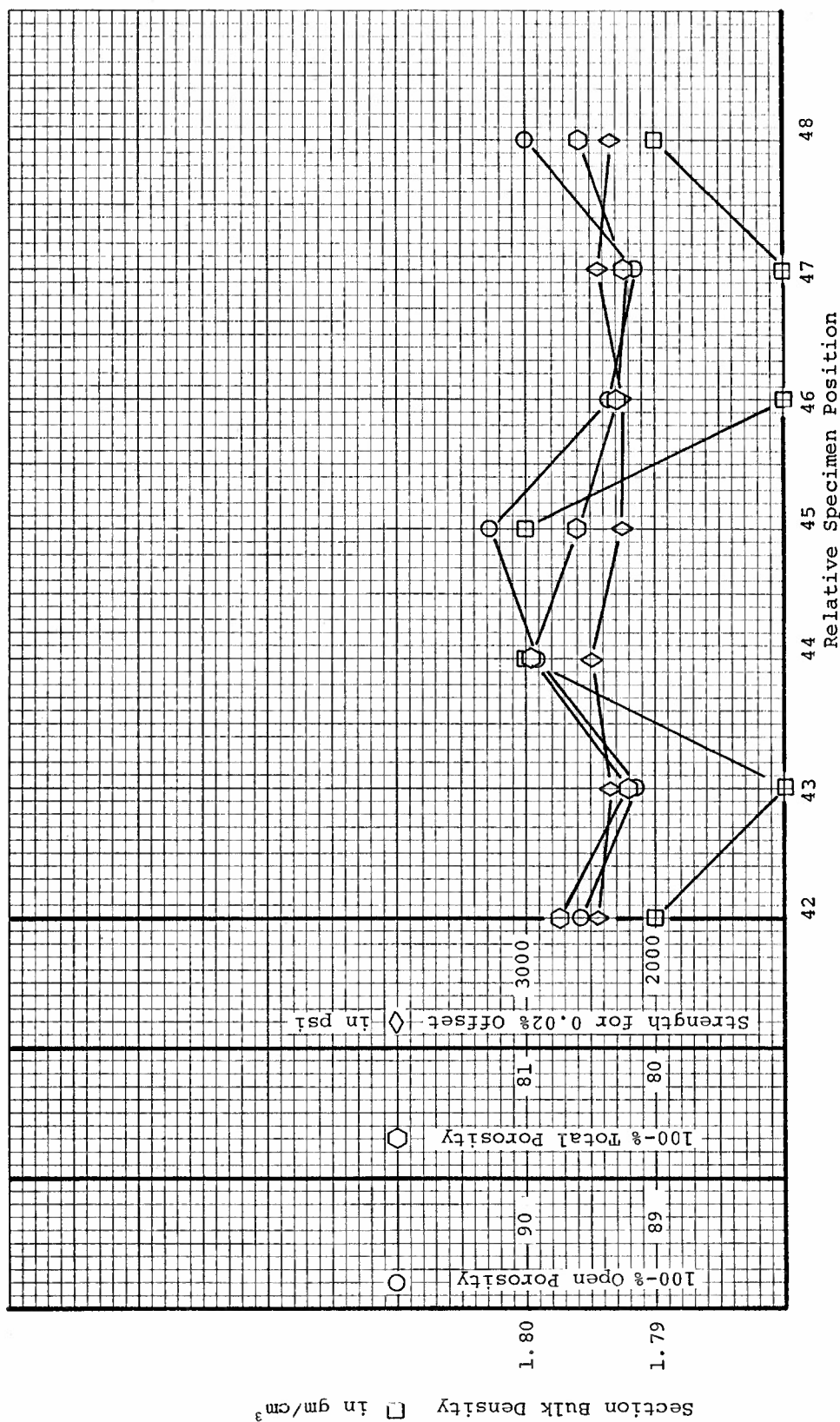


Figure 110. Specimen Position versus Section Bulk Density, Open Porosity, Total Porosity, and 0.02 Percent Offset Tensile Strength for Slab 4 of ATJ-S Billet L-4-6 With Grain at 70°F

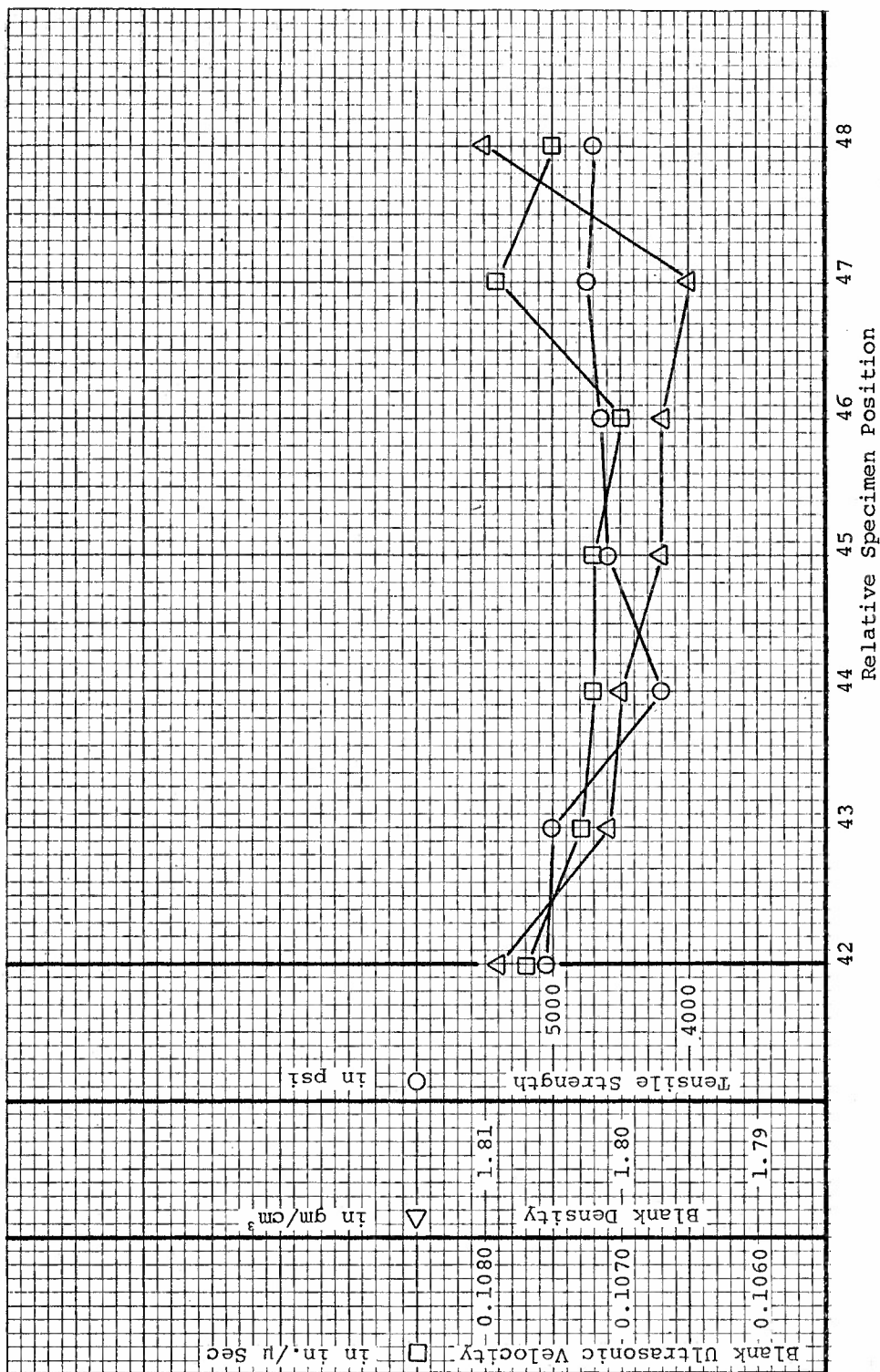


Figure 111. Specimen Position versus Blank Ultrasonic Velocity, Blank Density, and Tensile Strength for Slab 4 of ATJ-S Billet L-4-6 With Grain at 70°F



Figure 112. Specimen Position versus Section Bulk Density, Bulk Density, Open Porosity, Total Porosity, Total Porosity, and 0.02 Percent Offset Tensile Strength for Slab 8 of ATJ-S Billet L-4-6 With Grain at 70°F

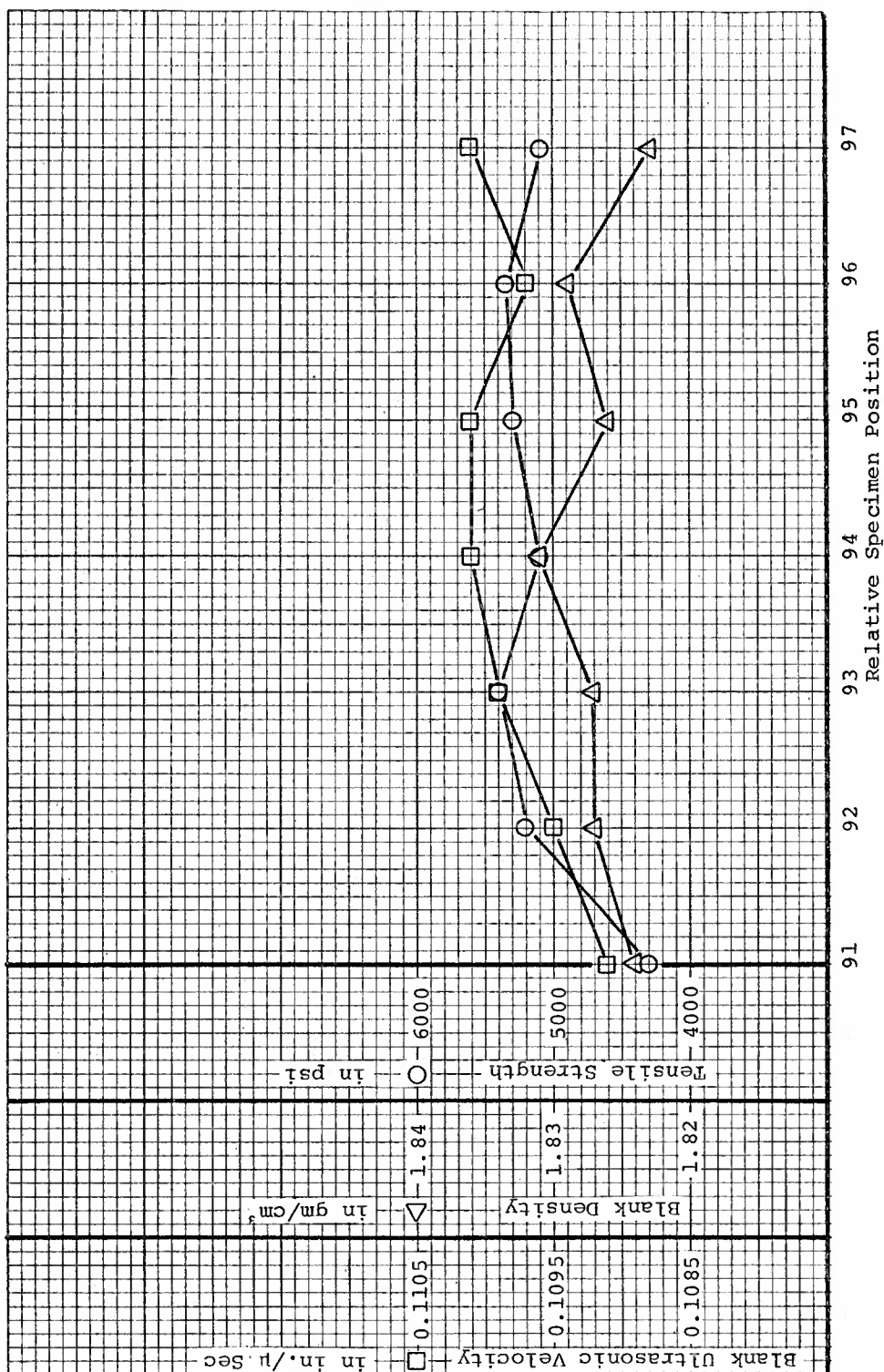


Figure 113. Specimen Position versus Blank Ultrasonic Velocity, Blank Density, and Tensile Strength of Slab 8 of ATJ-S Billet L-4-6 With Grain at 70°F

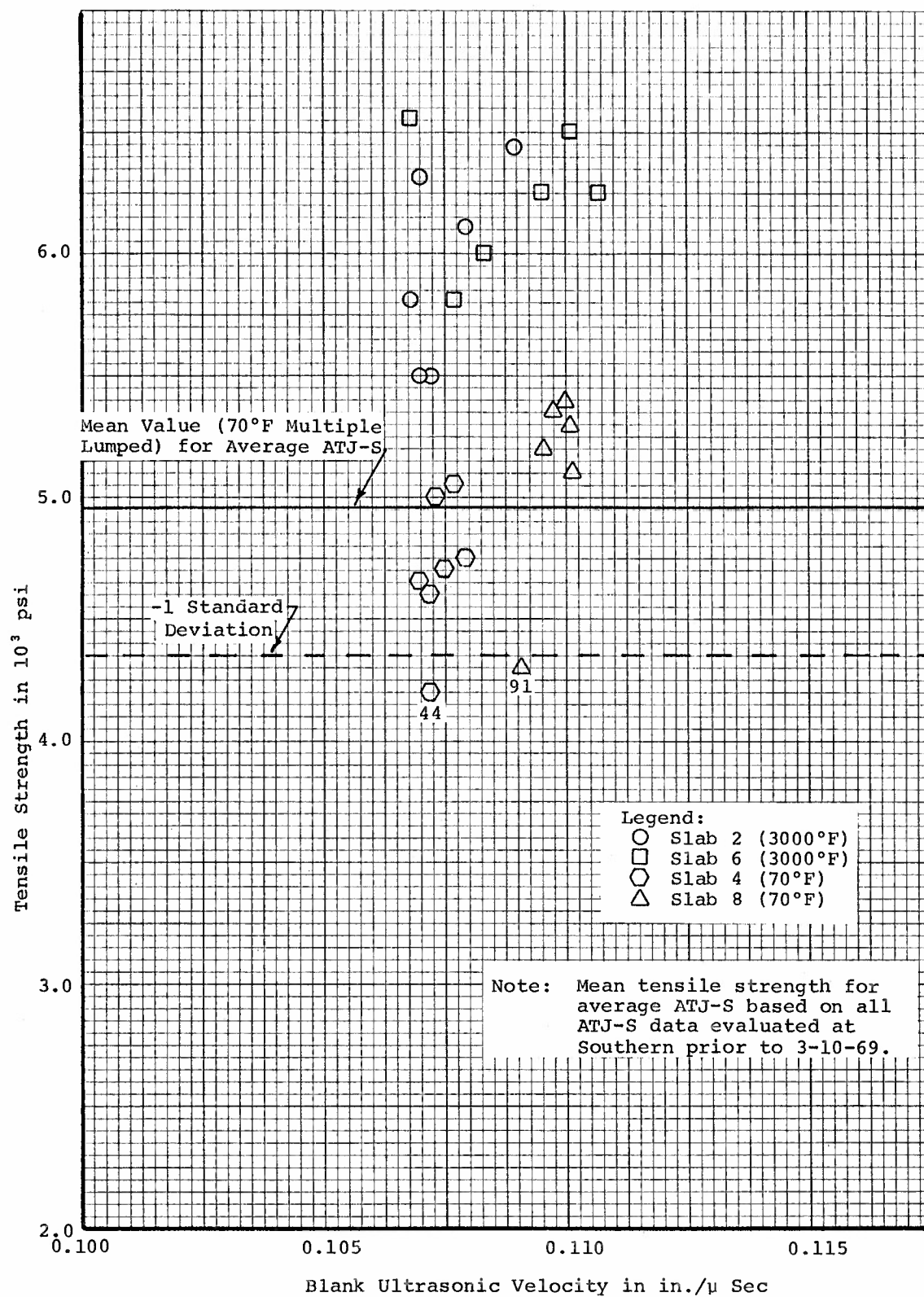


Figure 114. Tensile Strength versus Blank Ultrasonic Velocity for ATJ-S Billet L-4-6 With Grain at 70°F and 3000°F



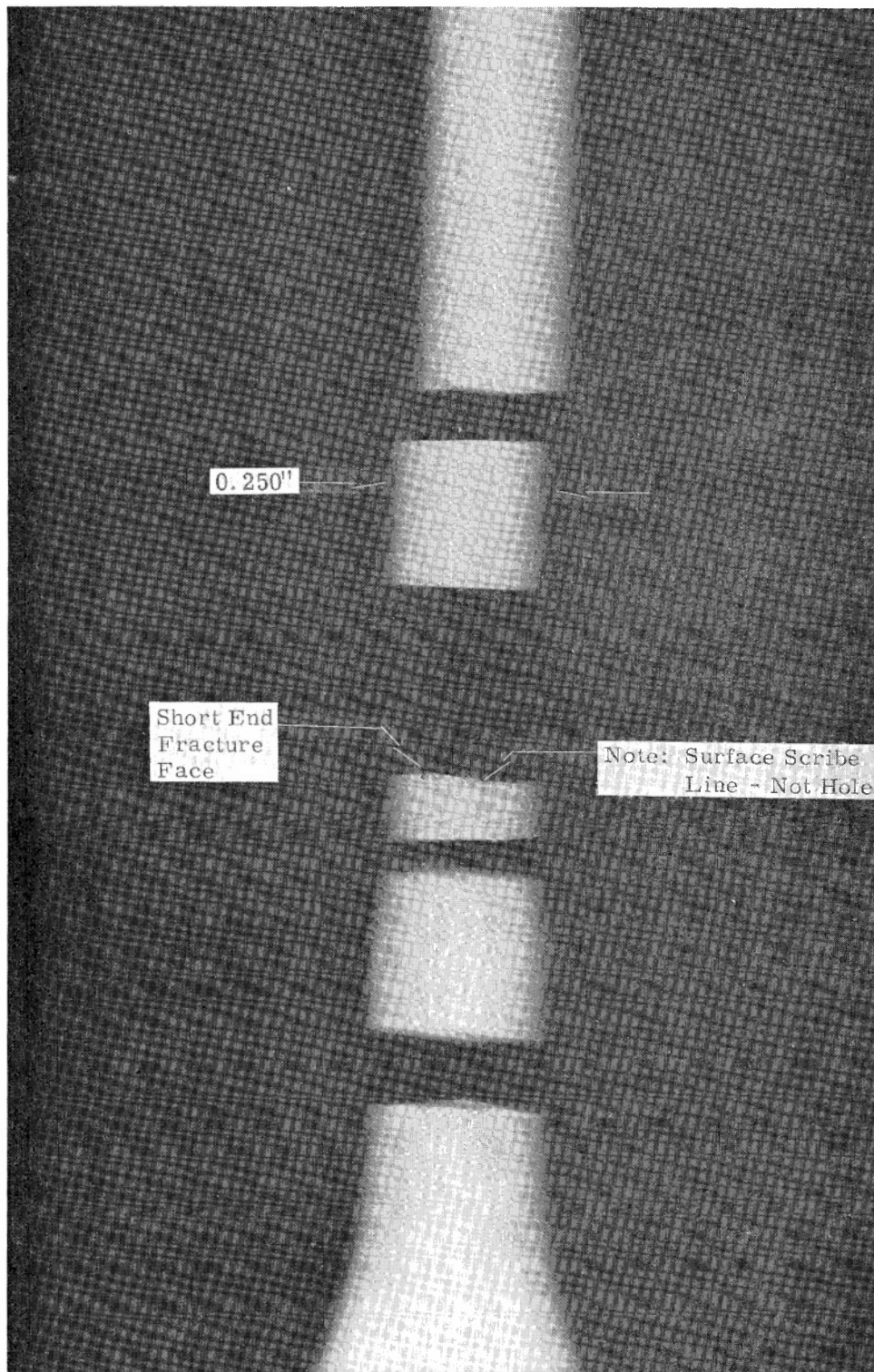
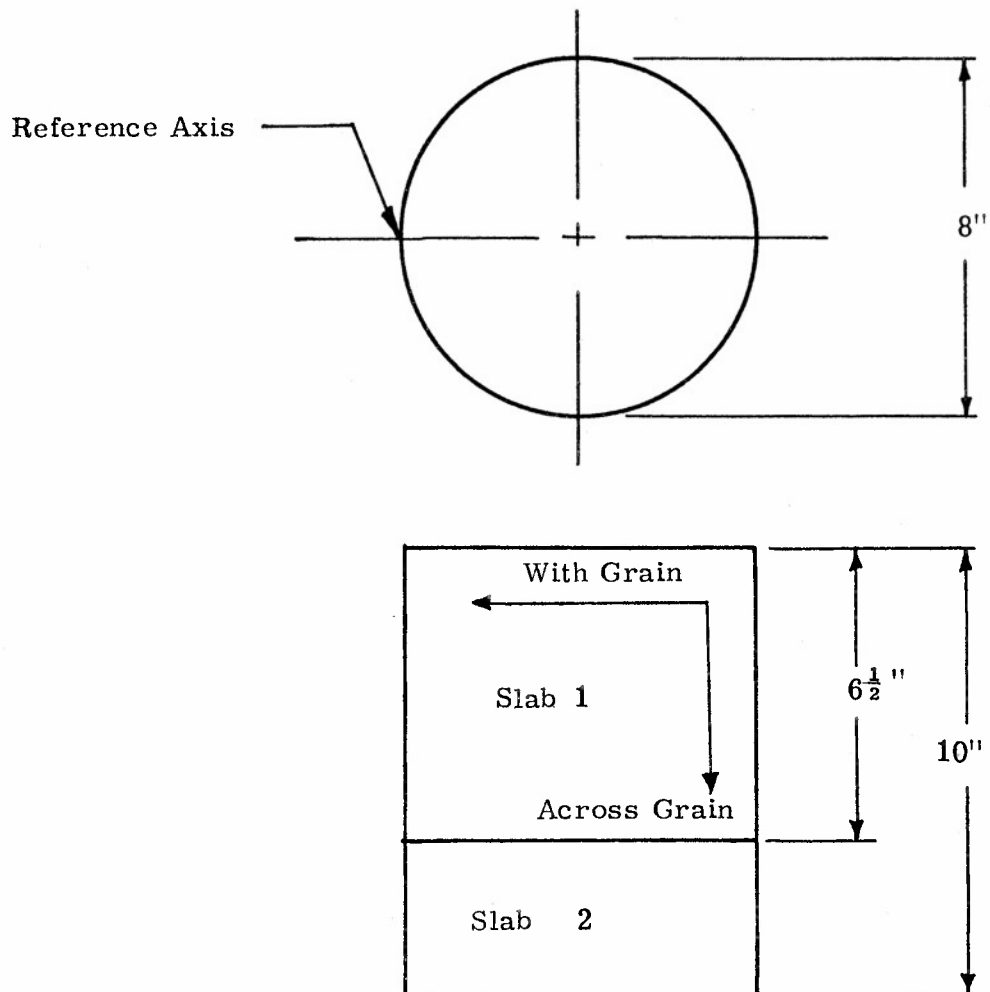


Figure 115. Radiograph of Weak Specimen T91W of ATJ-S Billet L-4-6







**Notes:**

1. Care must be exercised to maintain proper specimen identity from two billets while cutting the blanks and final machining
2. Identify all excess material and save for spare specimens which may be needed later

**Figure 116.** Slab Cutting Plan for ATJ-S Billet L-6-3

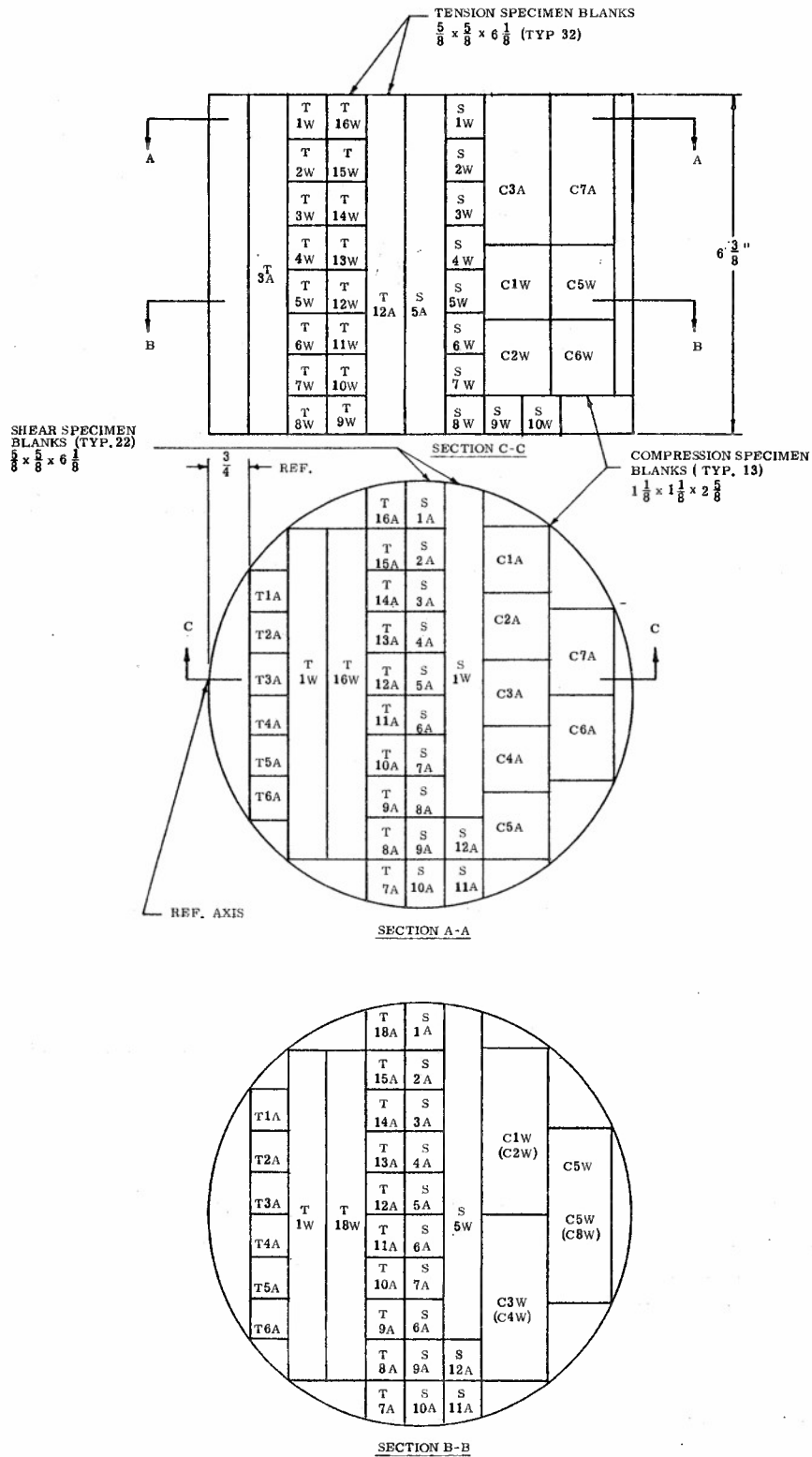
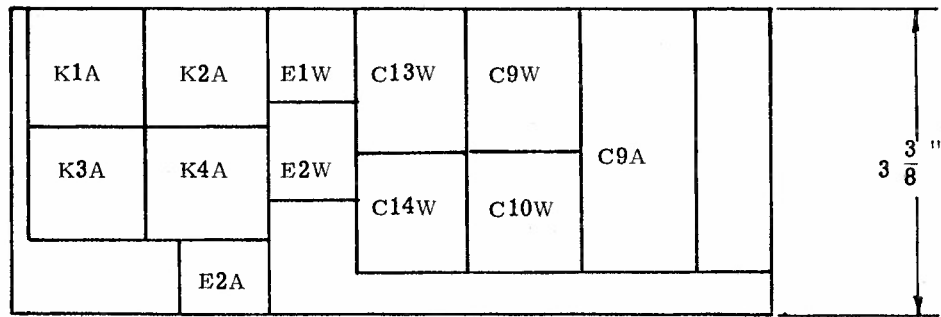
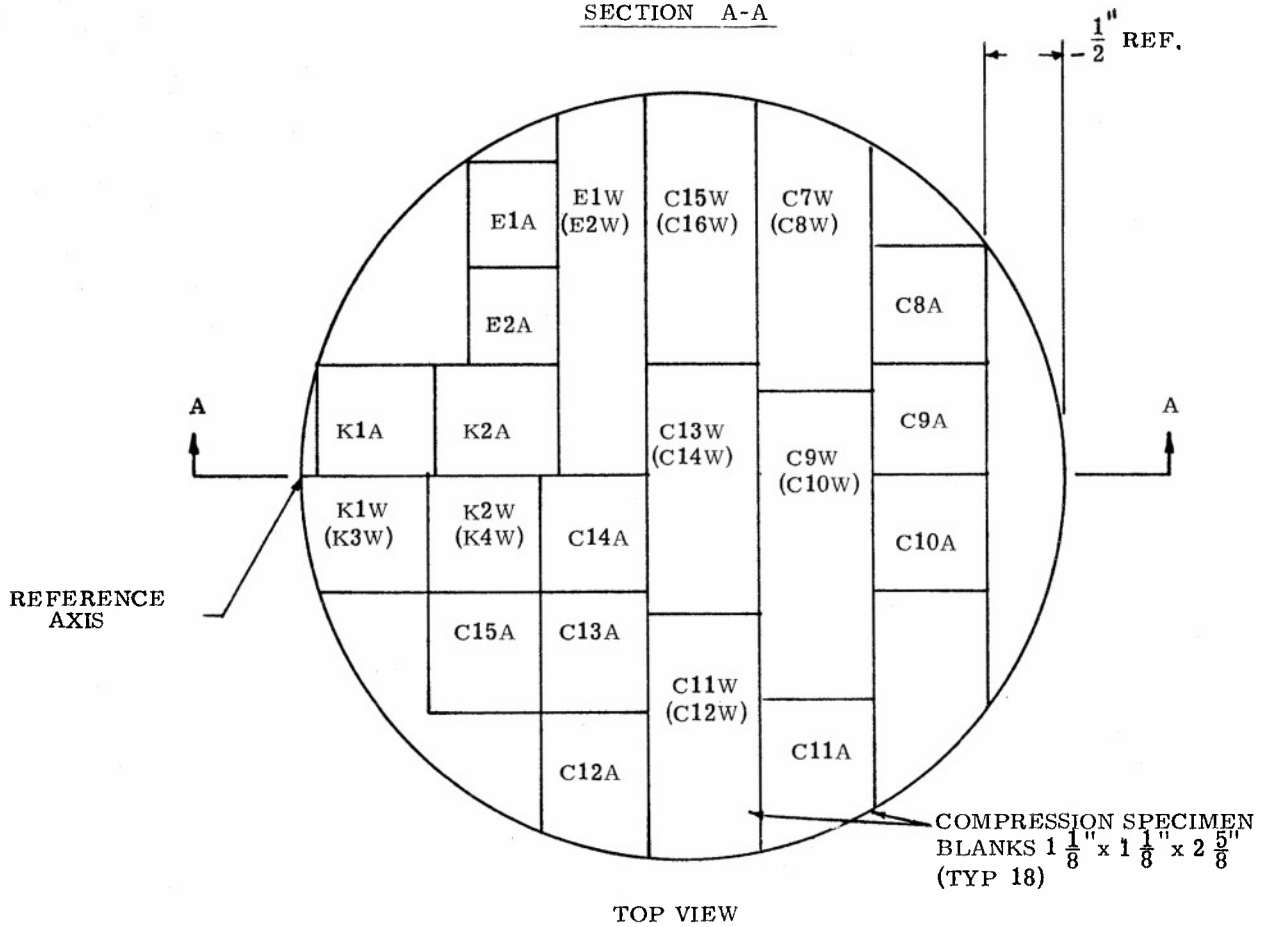


Figure 117. Cutting Plan for Slab 1 of Billet ATJ-S L-6-3

SLAB 2

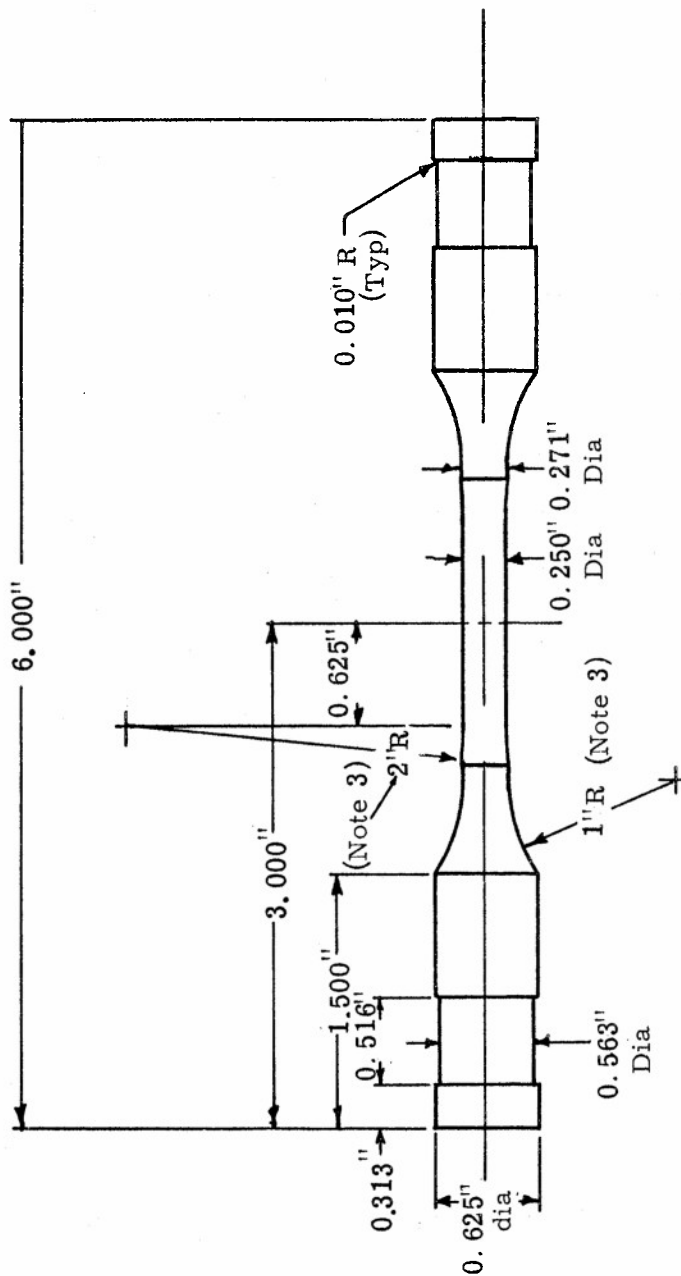


SECTION A-A



TOP VIEW

Figure 118. Cutting Plan for Slab 2 of ATJ-S Billet L-6-3



Notes:

1. All diameters true and concentric to 0.0005".
2. Both ends flat and perpendicular to 0.0005".
3. Do not undercut at tangent point.
4. Tolerances unless otherwise noted.  
 All lengths  $+0.005$   
 All diameters  $+0.001$

Figure 119. Tensile Test Specimen Configuration Used for ATJ-S  
Billet L-6-3

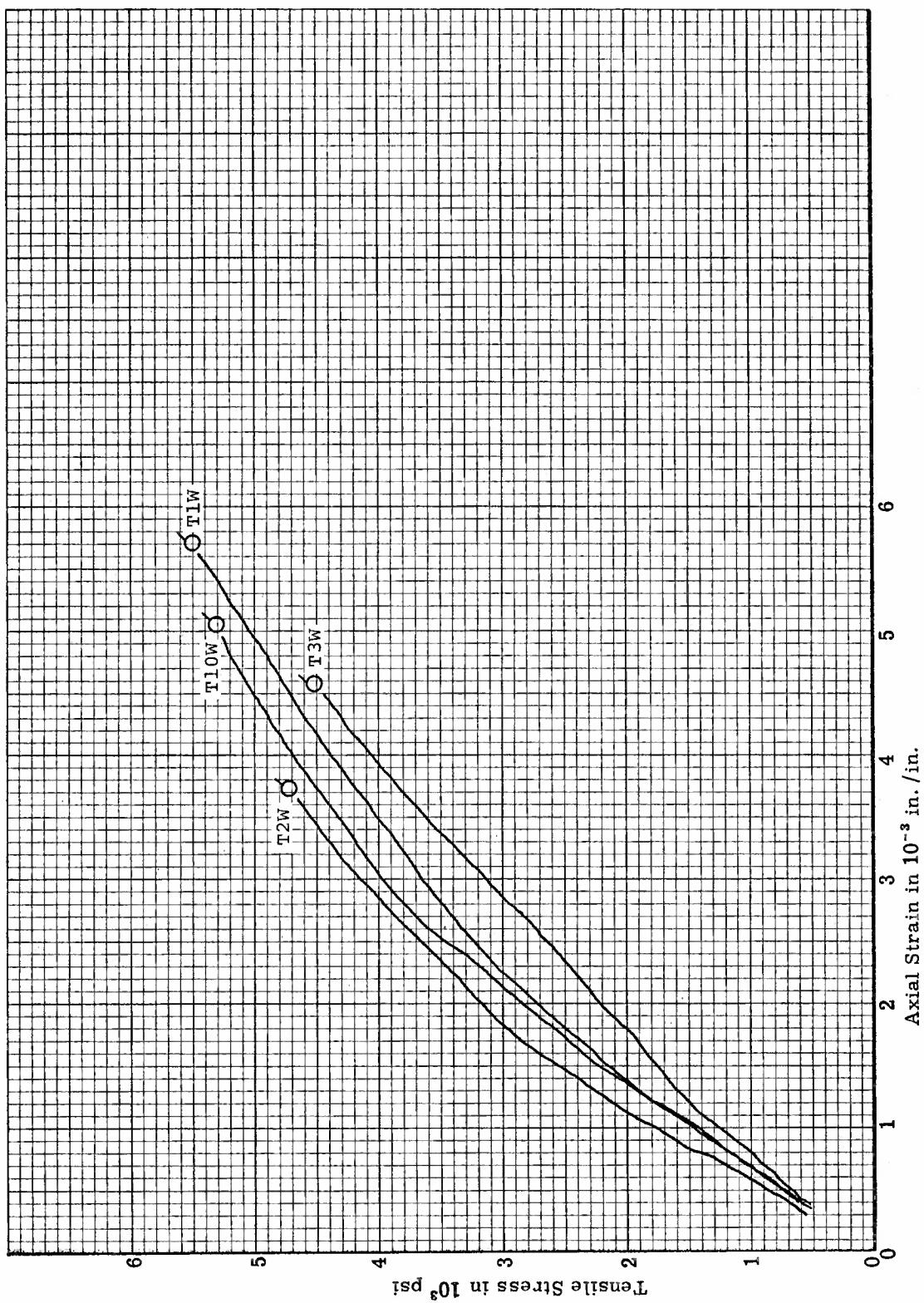


Figure 120. Tensile Stress-Strain Curves for ATJ-S Billet L-6-3 With Grain at 70°F

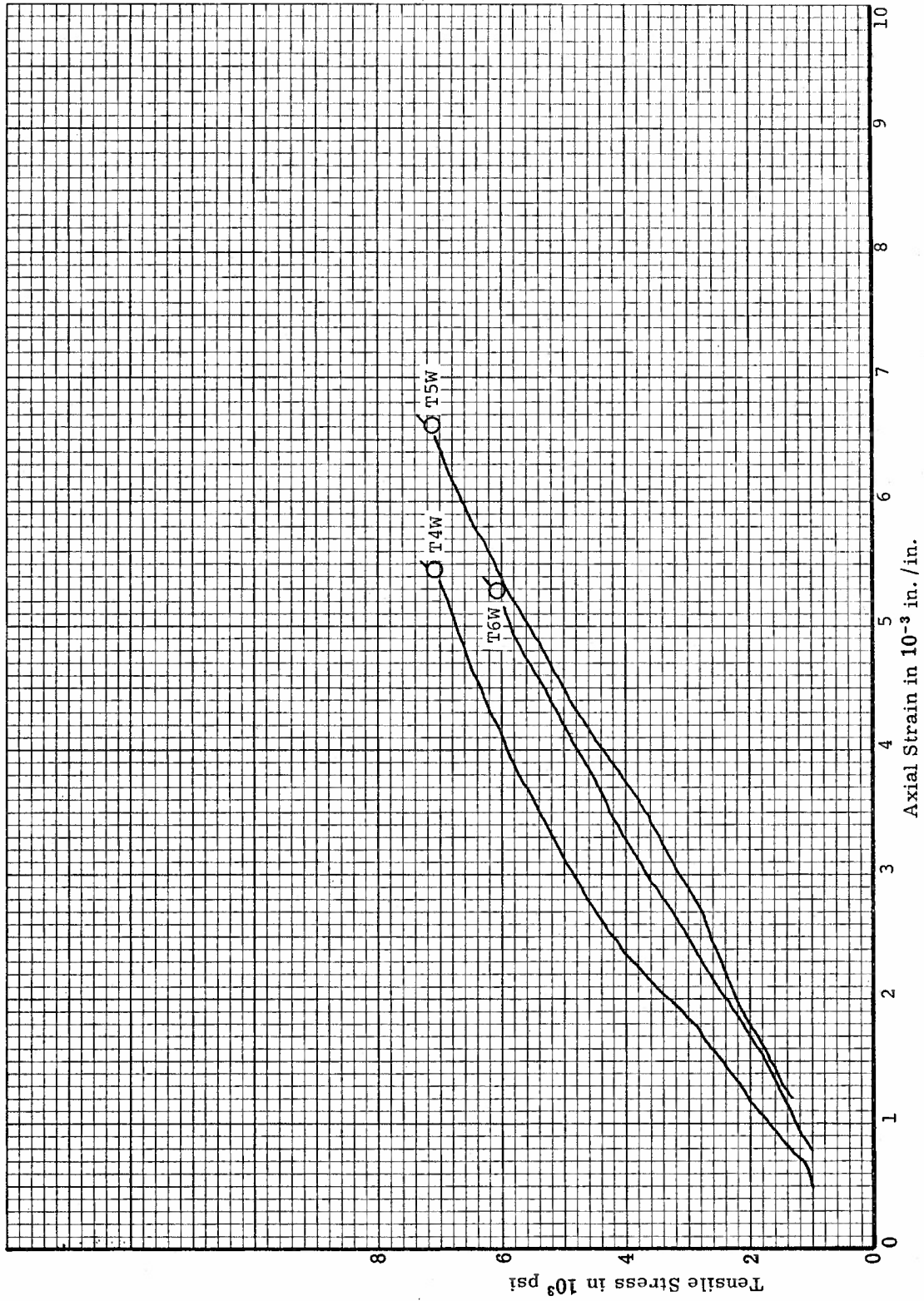


Figure 121. Tensile Stress-Strain Curves for ATJ-S Billet L-6-3 With Grain at 3000°F

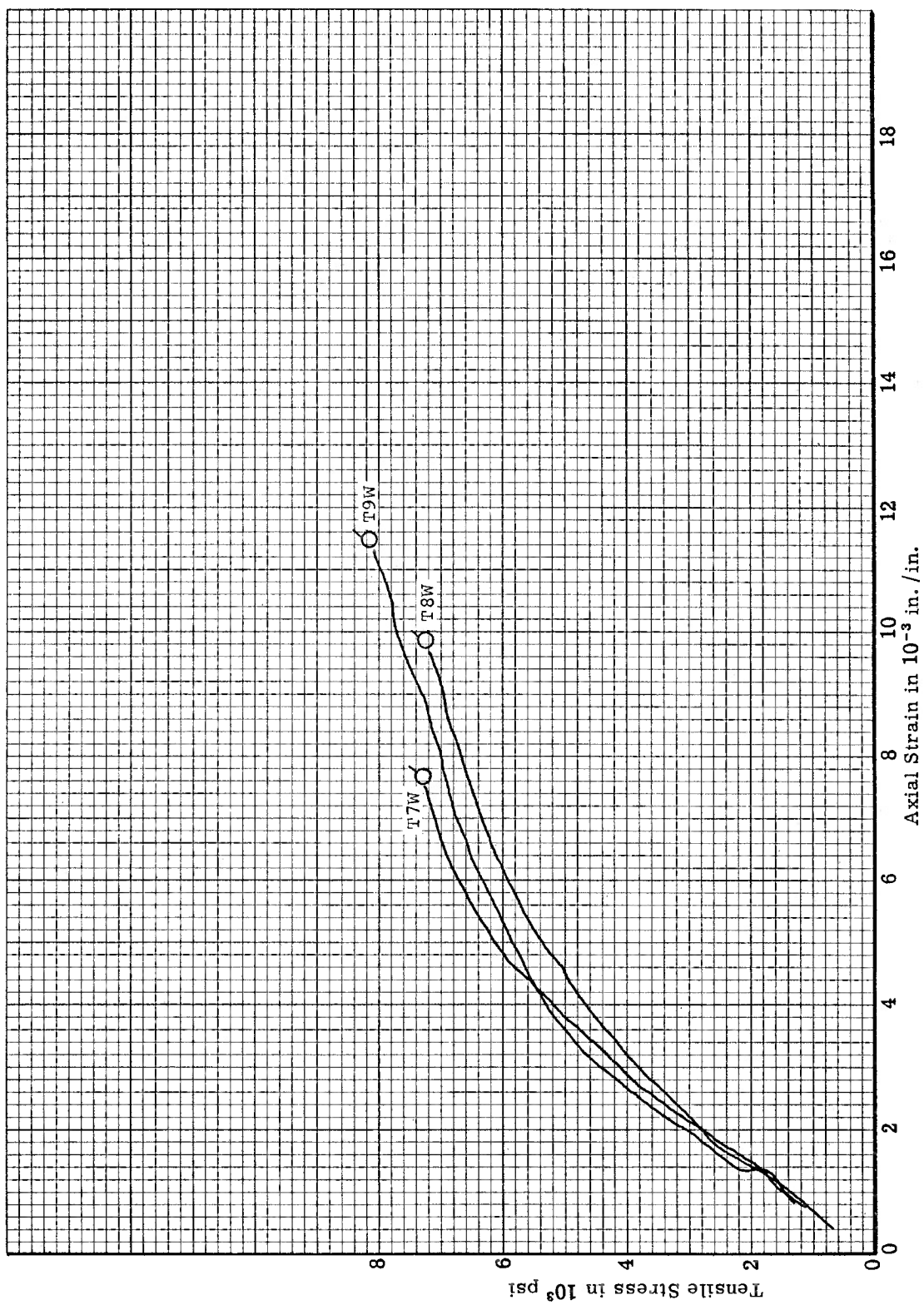


Figure 122. Tensile Stress-Strain Curves for ATJ-S Billet L-6-3 With Grain at 4500°F

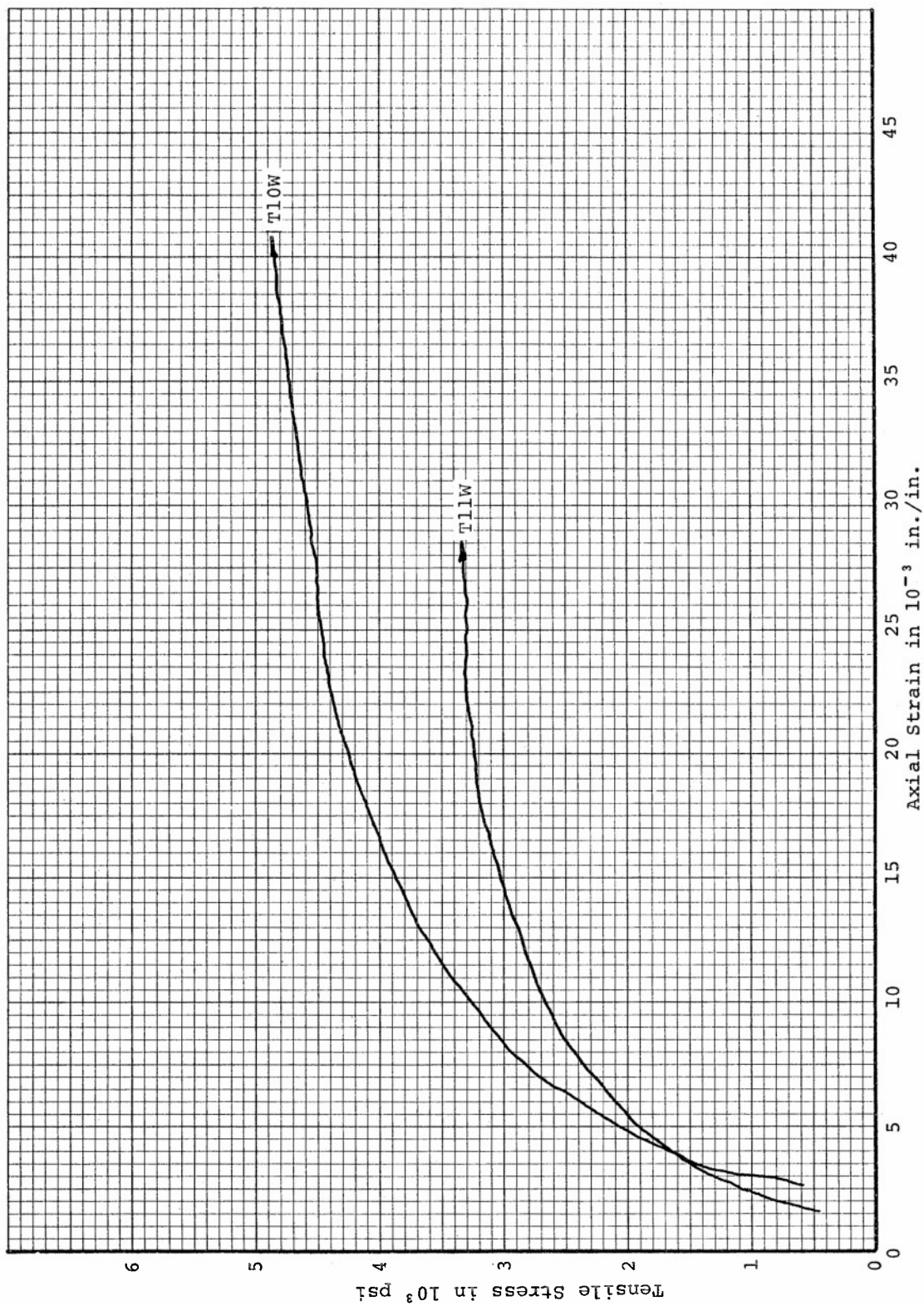


Figure 123. Tensile Stress-Strain Curves for ATJ-S Billet L-6-3 With Grain at 5500°F



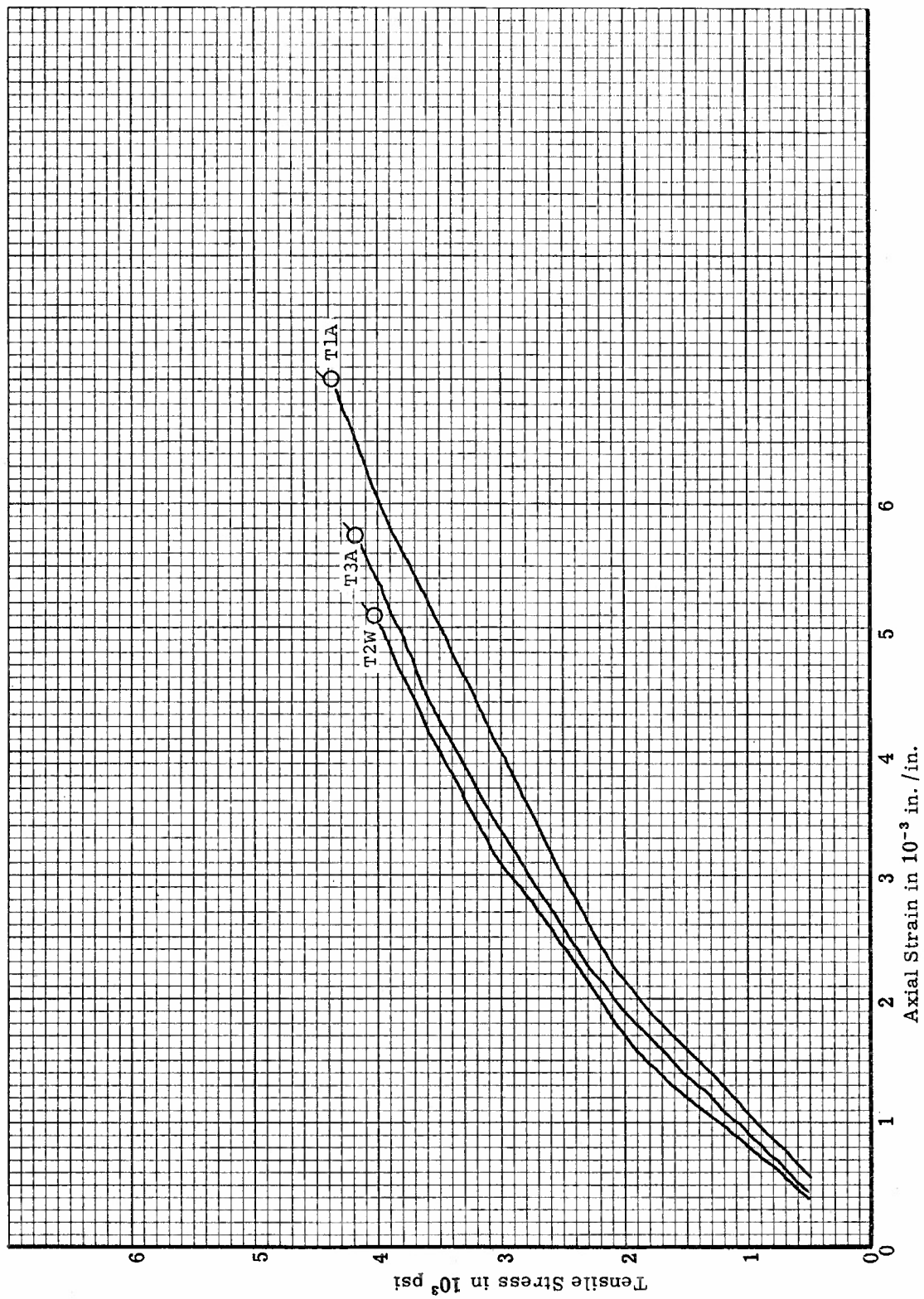


Figure 124. Tensile Stress-Strain Curves for ATJ-S Billet L-6-3 Across Grain at 70°F

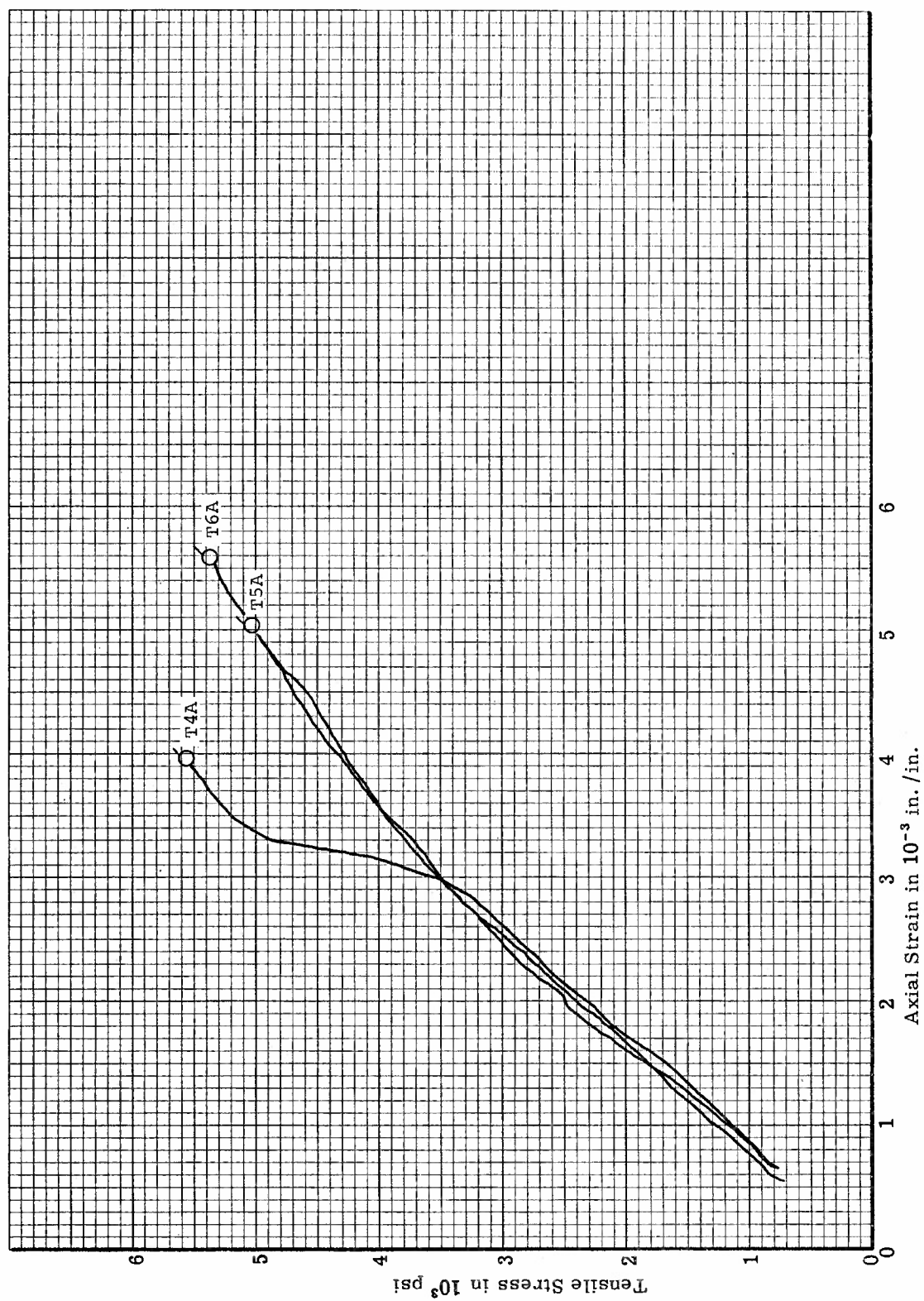


Figure 125. Tensile Stress-Strain Curves for ATJ-S Billet L-6-3 Across Grain at 3000°F

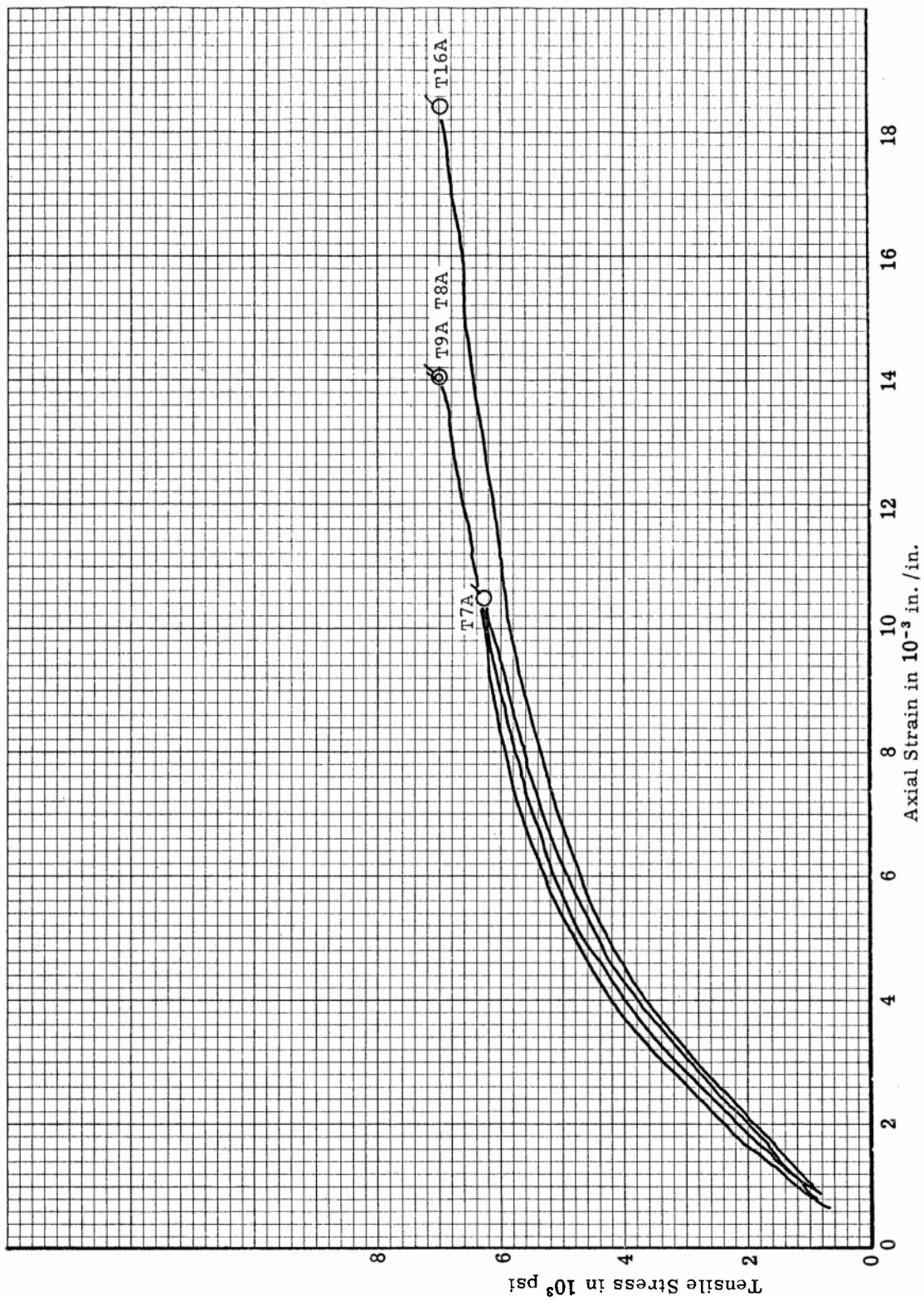


Figure 126. Tensile Stress-Strain Curves for ATJ-S Billet L-6-3 Across Grain at 4500°F

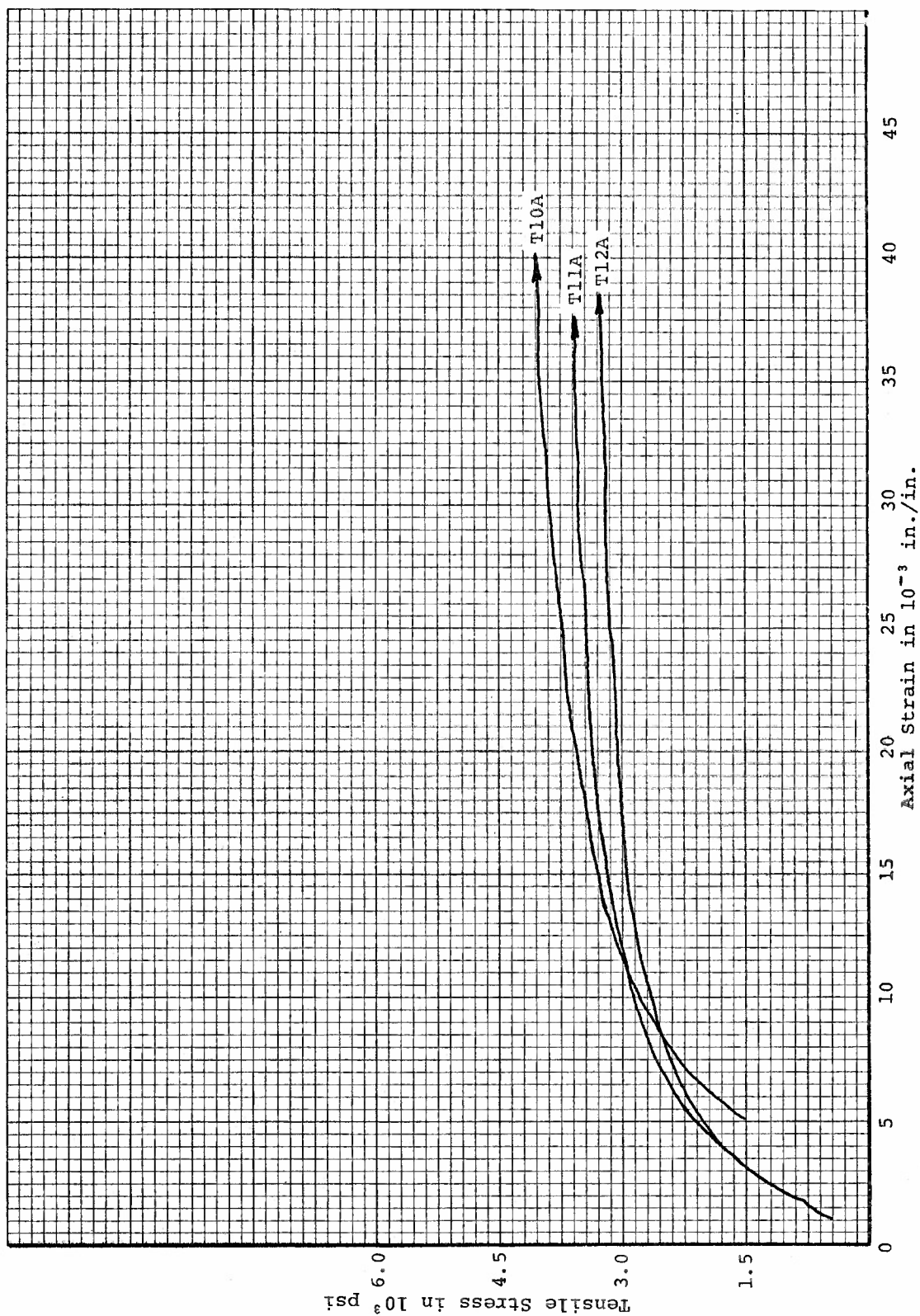


Figure 127. Tensile Stress-Strain Curves for ATJ-S Billet L-6-3 Across Grain at 5500°F

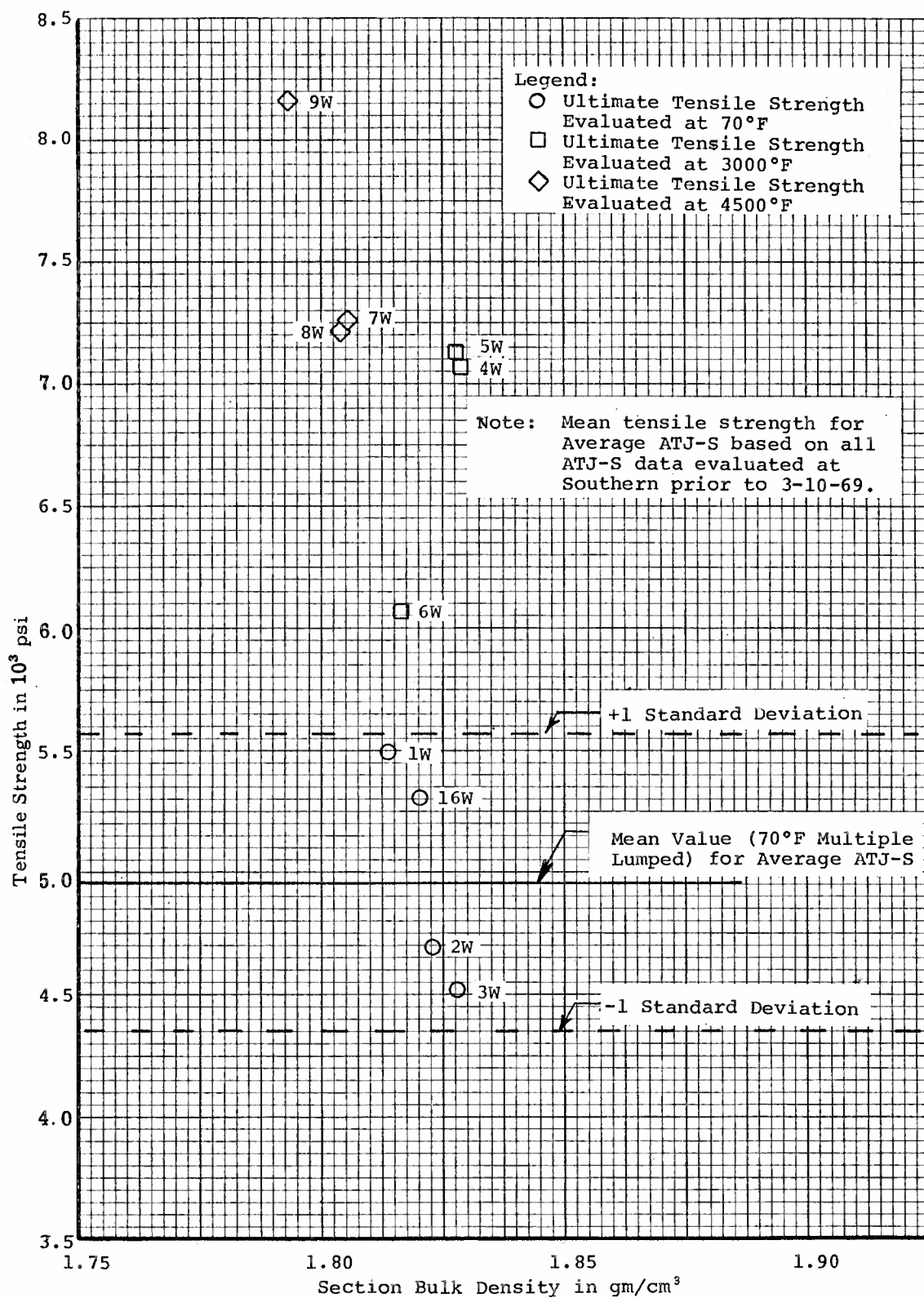


Figure 128. Tensile Strength Versus Section Bulk Density for ATJ-S Billet L-6-3 With Grain at 70°F, 3000°F, and 4500°F

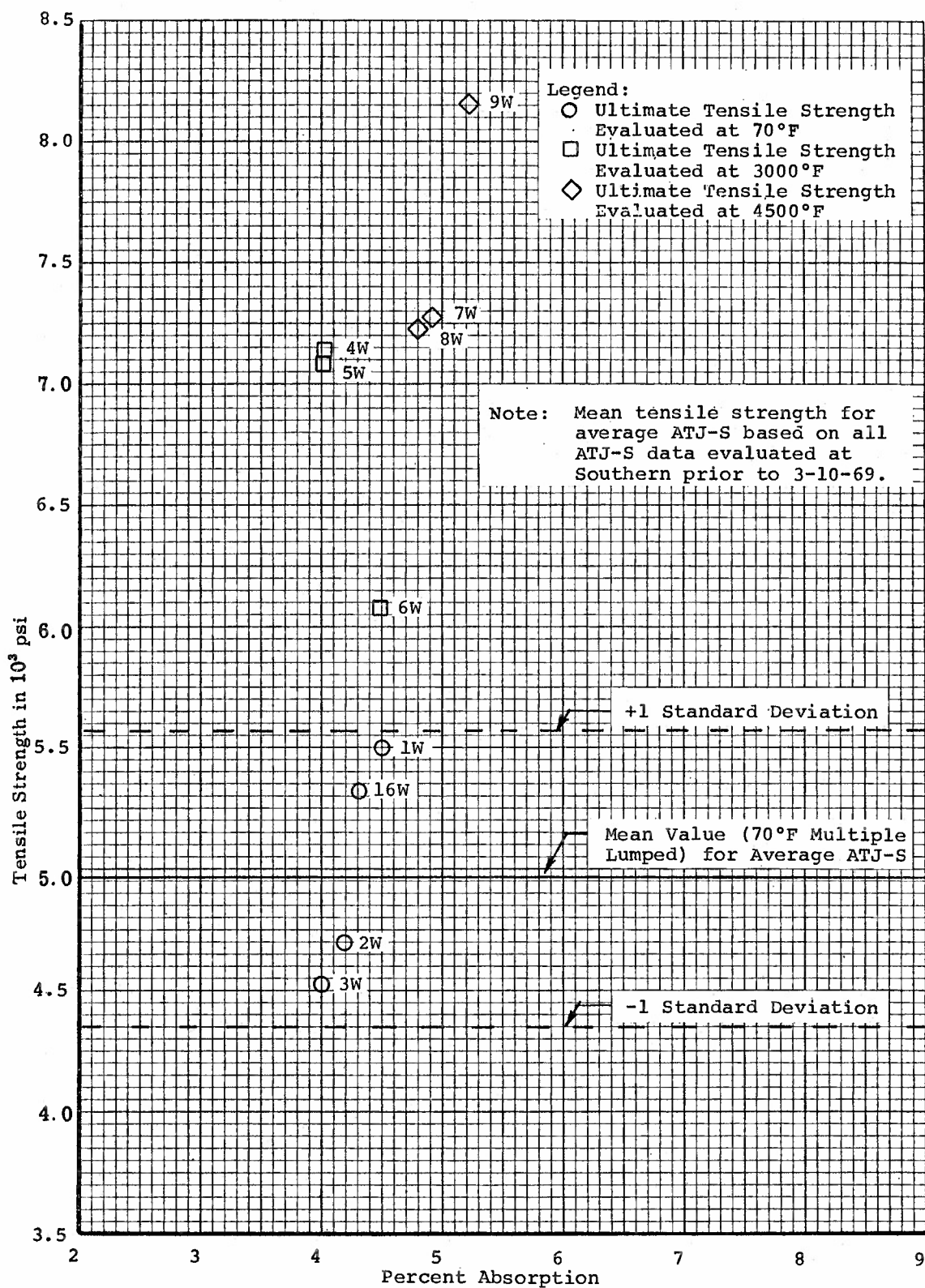


Figure 129. Tensile Strength Versus Percent Absorption for ATJ-S Billet L-6-3 With Grain at 70°F, 3000°F, and 4500°F



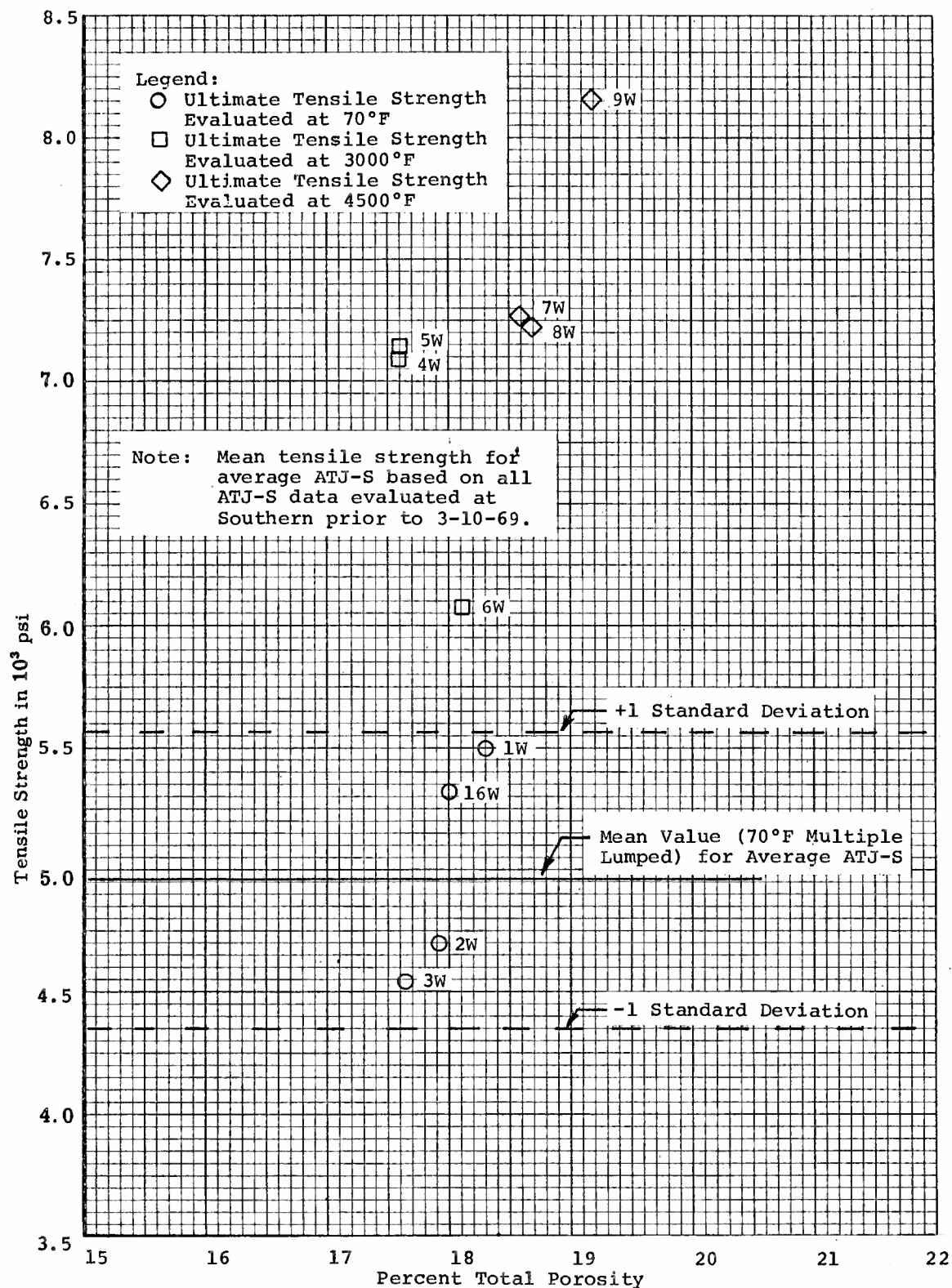


Figure 130. Tensile Strength Versus Percent Total Porosity for ATJ-S Billet L-6-3 With Grain at 70°F, 3000°F and 4500°F

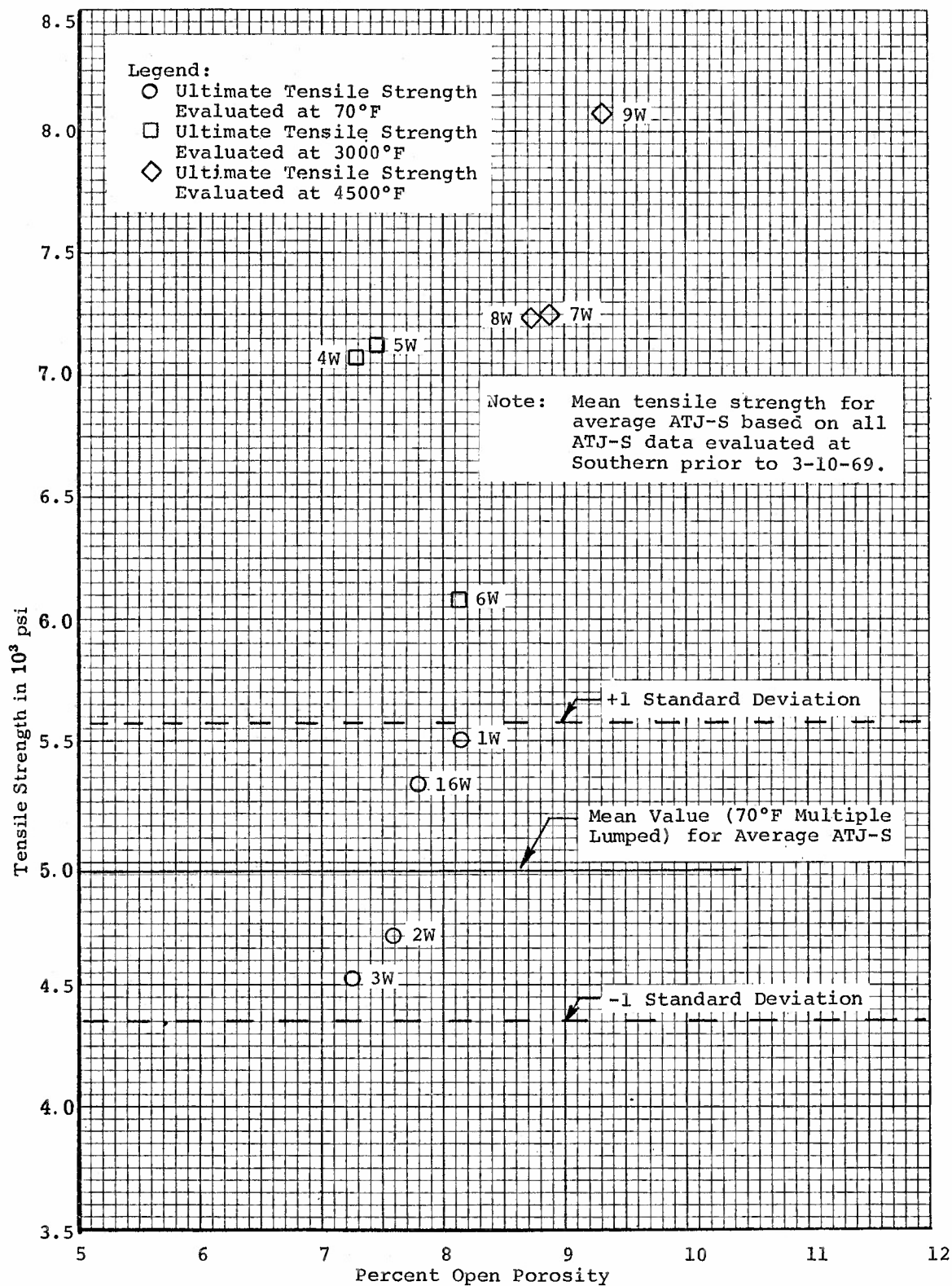


Figure 131. Tensile Strength Versus Percent Open Porosity for ATJ-S Billet L-6-3 With Grain at 70°F, 3000°F, and 4500°F



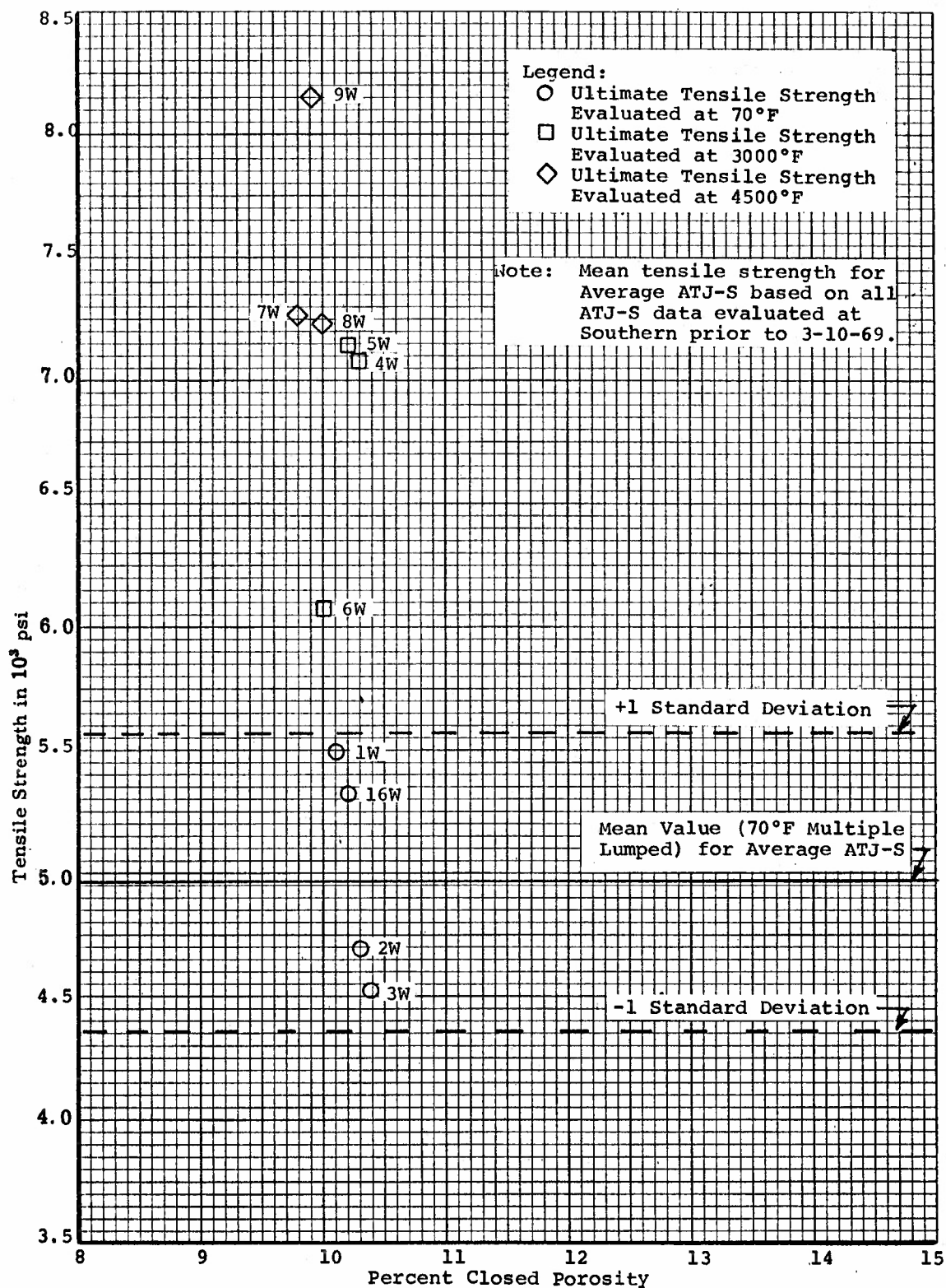


Figure 132. Tensile Strength Versus Closed Porosity for ATJ-S Billet L-6-3 With Grain at 70°F, 3000°F, and 4500°F

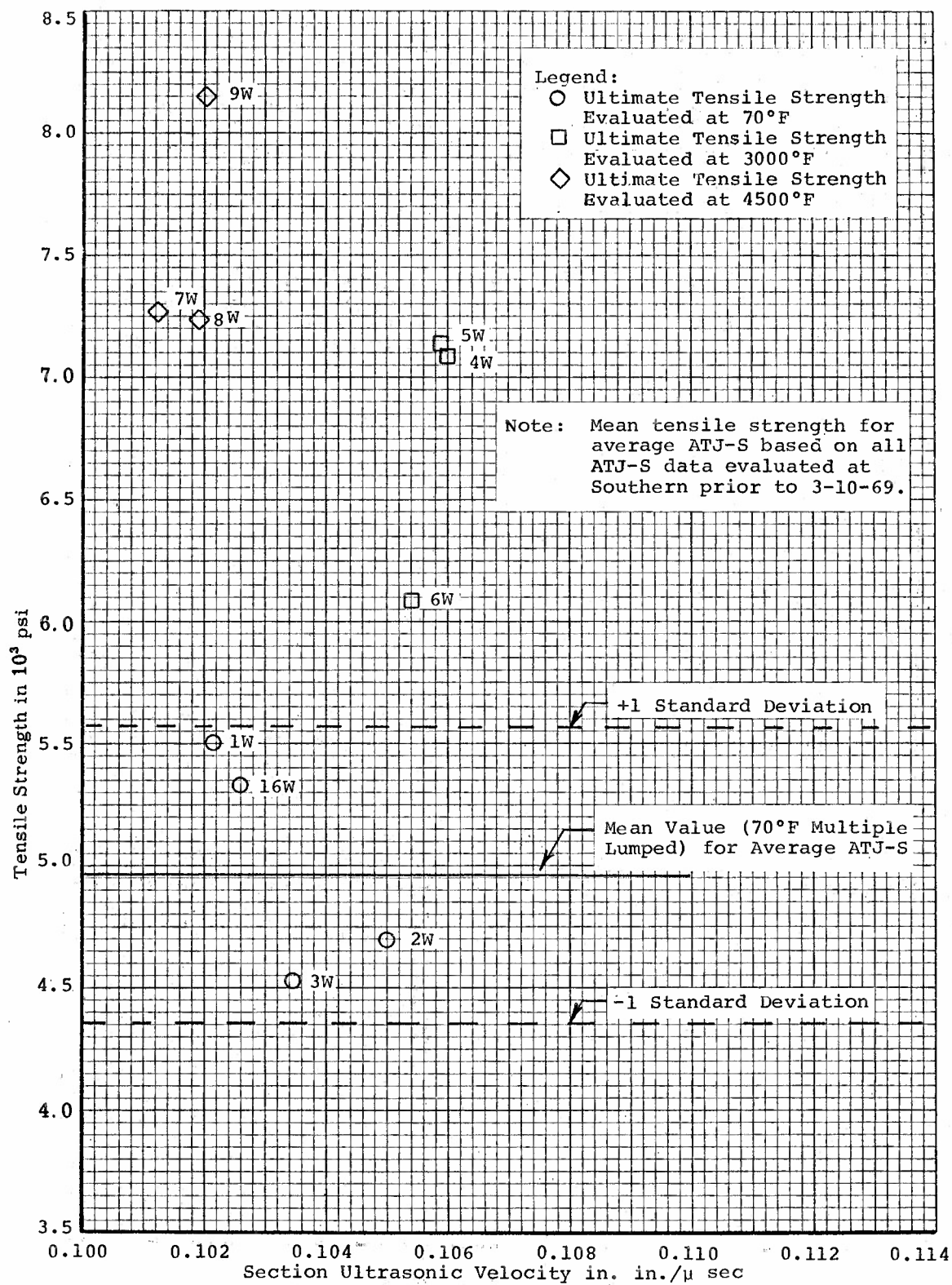


Figure 133. Tensile Strength Versus Section Ultrasonic Velocity for ATJ-S Billet L-6-3 With Grain at 70°F, 3000°F, and 4500°F

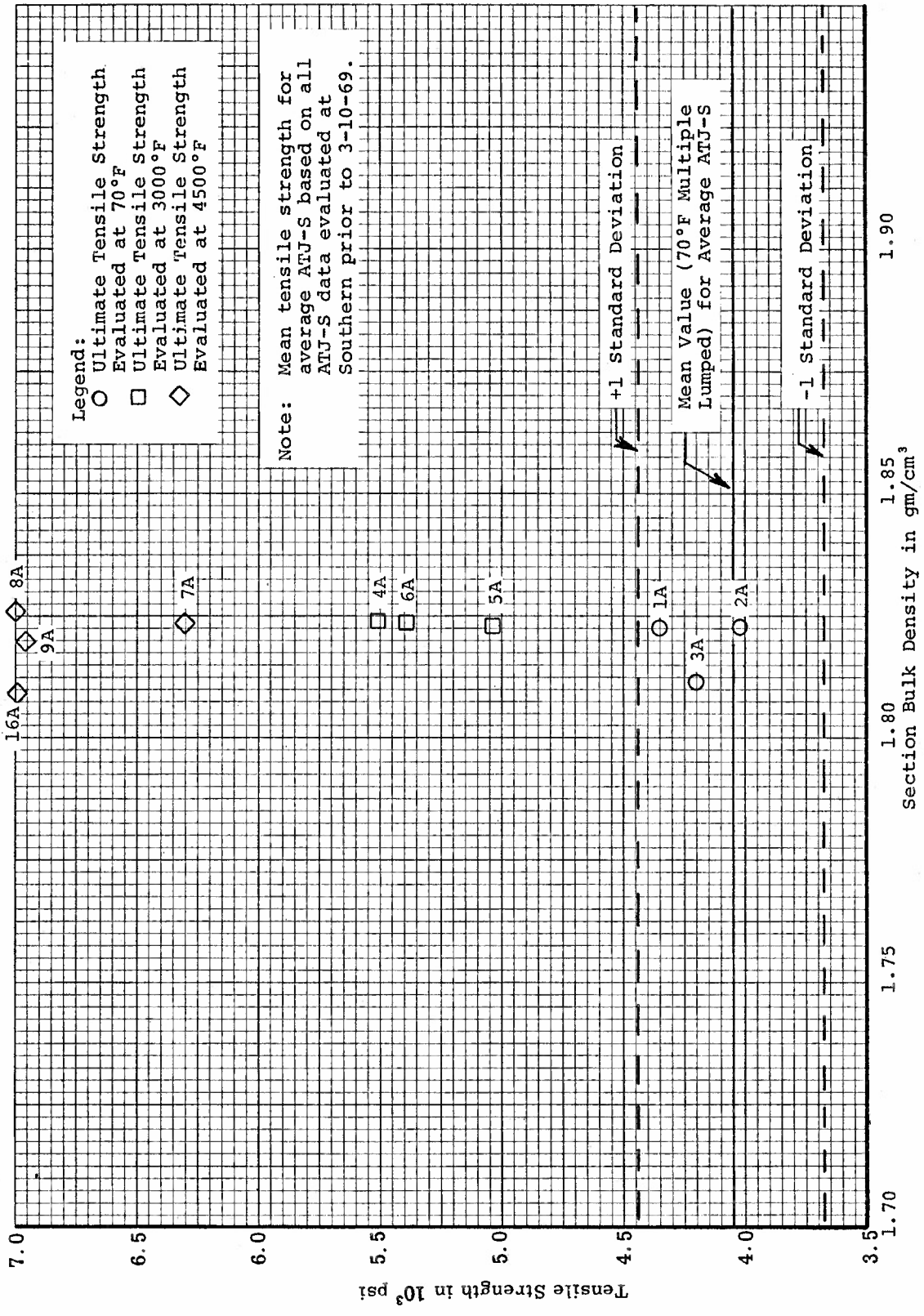


Figure 134. Tensile Strength Versus Section Bulk Density for ATJ-S Billet L-6-3 Across Grain at 70°F, 3000°F, and 4500°F

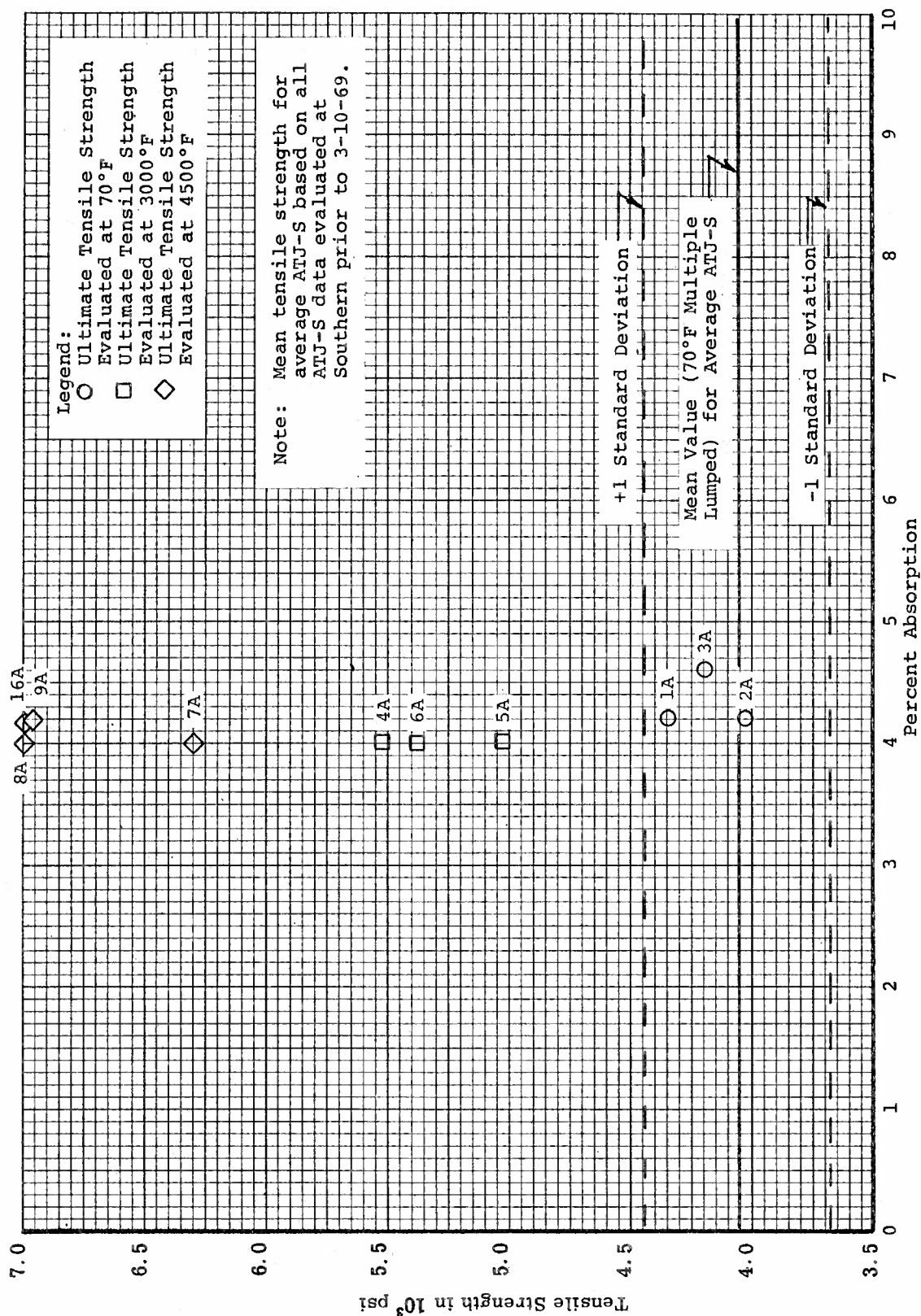


Figure 135. Tensile Strength Versus Percent Absorption for ATJ-S Billet L-6-3 Across Grain at 70°F, 3000°F, and 4500°F

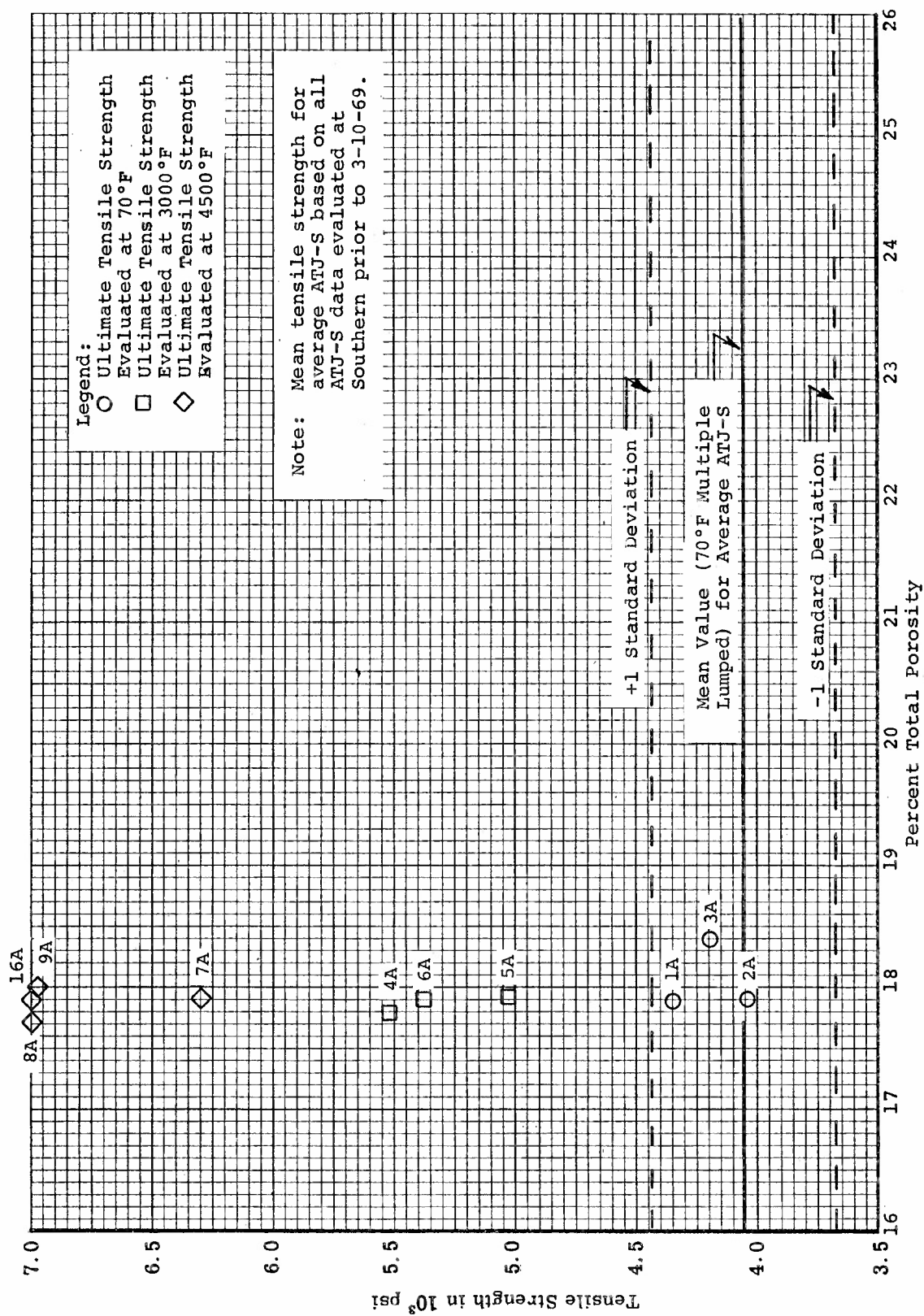


Figure 136. Tensile Strength Versus Percent Total Porosity for ATJ-S Billet L-6-3 Across Grain at 70°F, 3000°F, and 4500°F

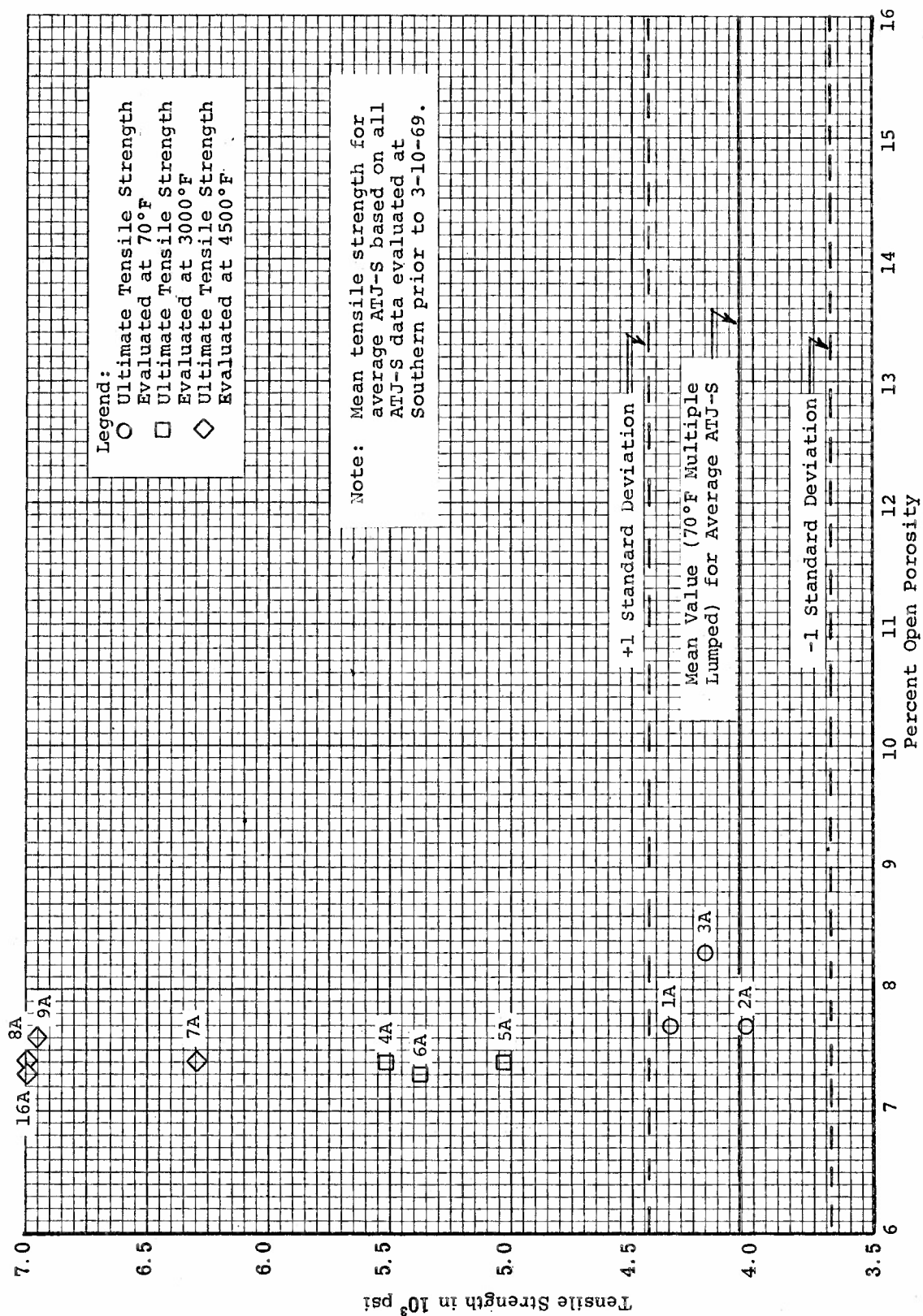


Figure 137, Tensile Strength Versus Percent Open Porosity for ATJ-S Billet L-6-3 Across Grain at 70°F, 3000°F, and 4500°F



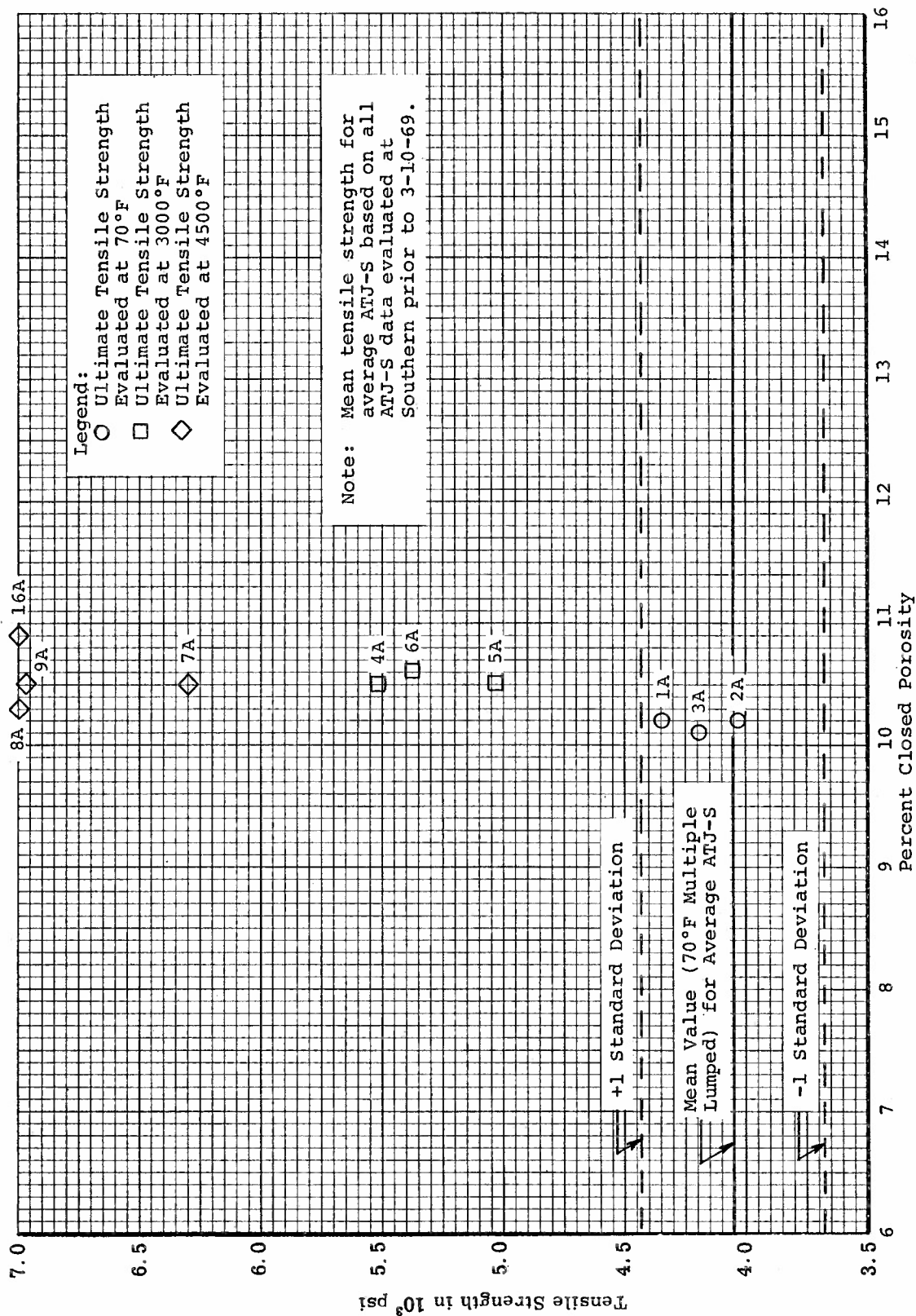


Figure 138. Tensile Strength Versus Percent Closed Porosity for ATJ-S Billet L-6-3. Across Grain at 70°F, 3000°F, and 4500°F

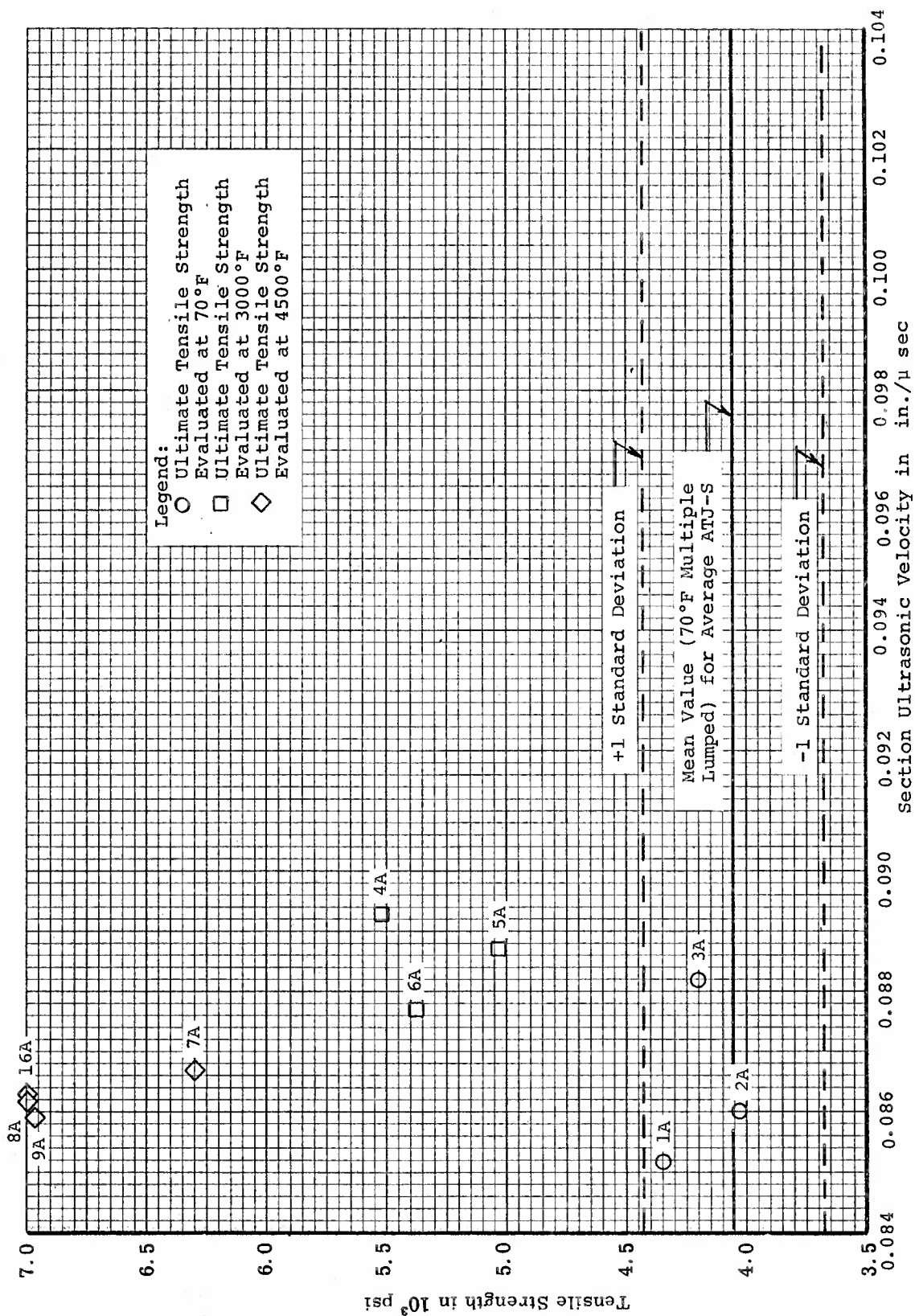


Figure 139. Tensile Strength Versus Section Ultrasonic Velocity for ATJ-S Billet L-6-3 Across Grain at 70°F, 3000°F, and 4500°F



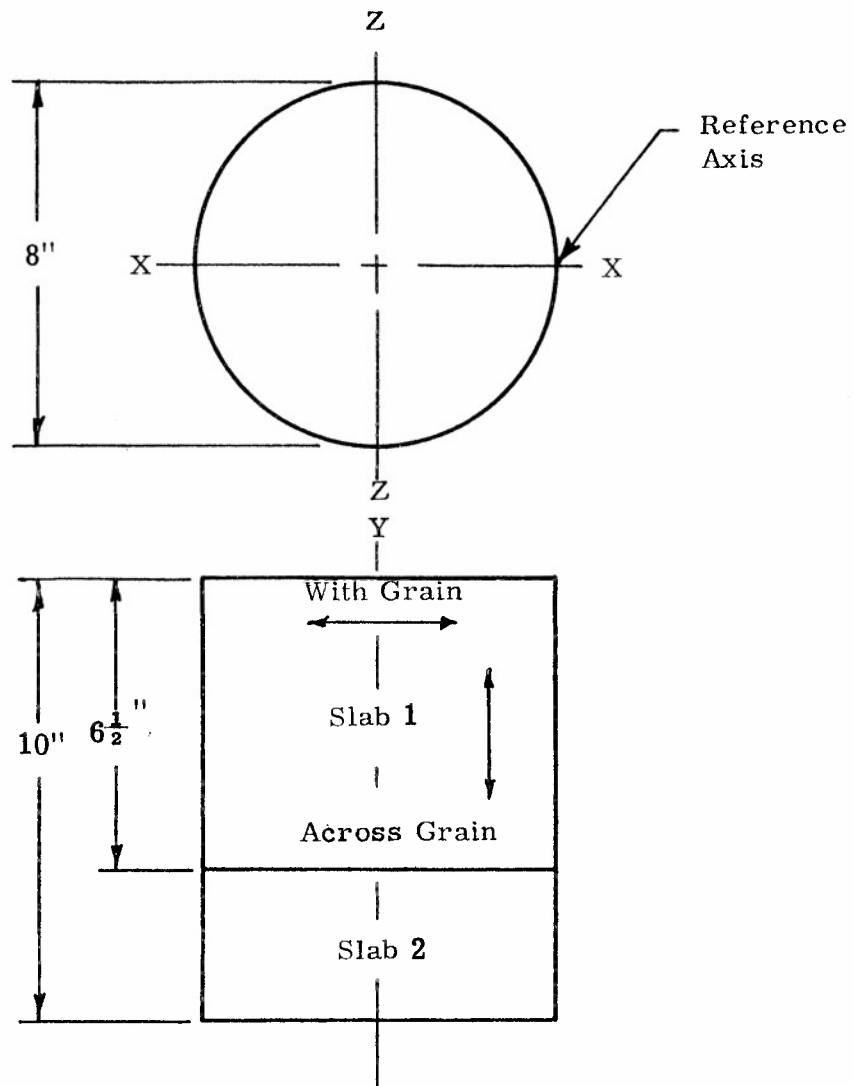


Figure 140. Slab Cutting Plan for ATJ-S Billets L-9-10, L-10-6 and L-11-4

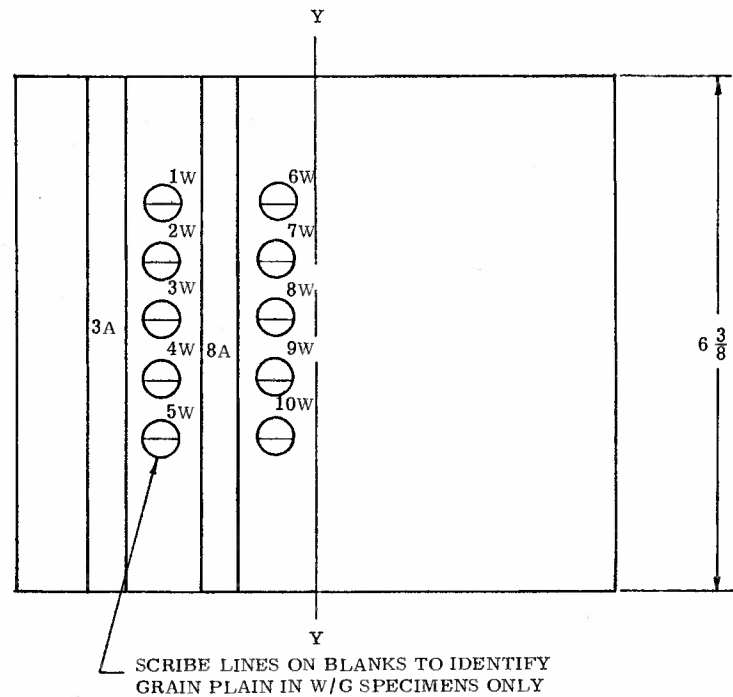
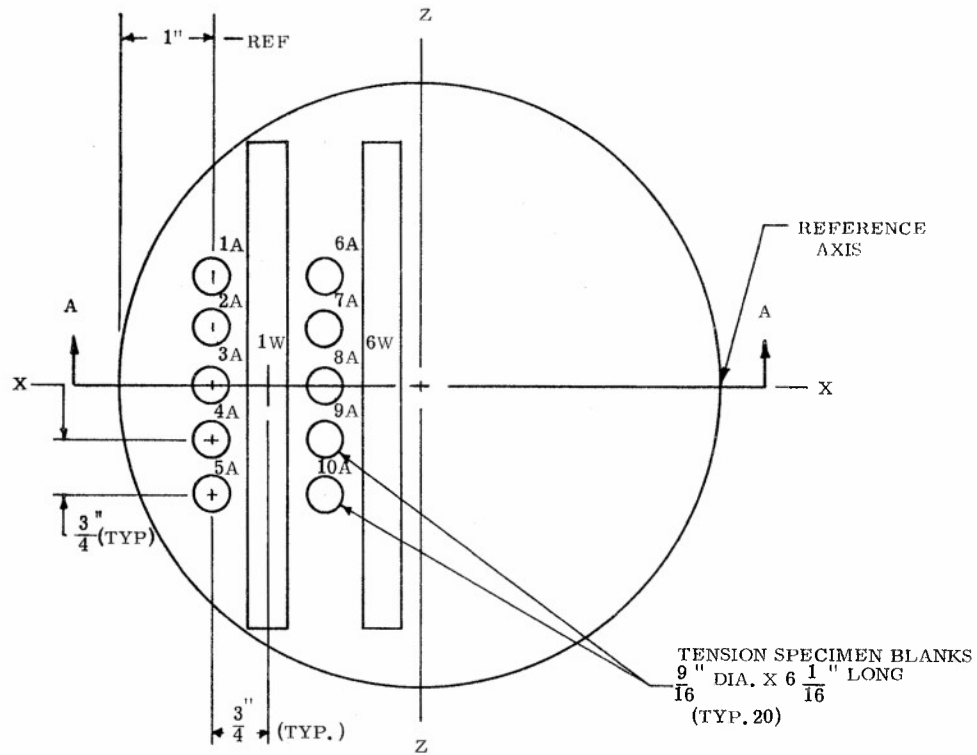
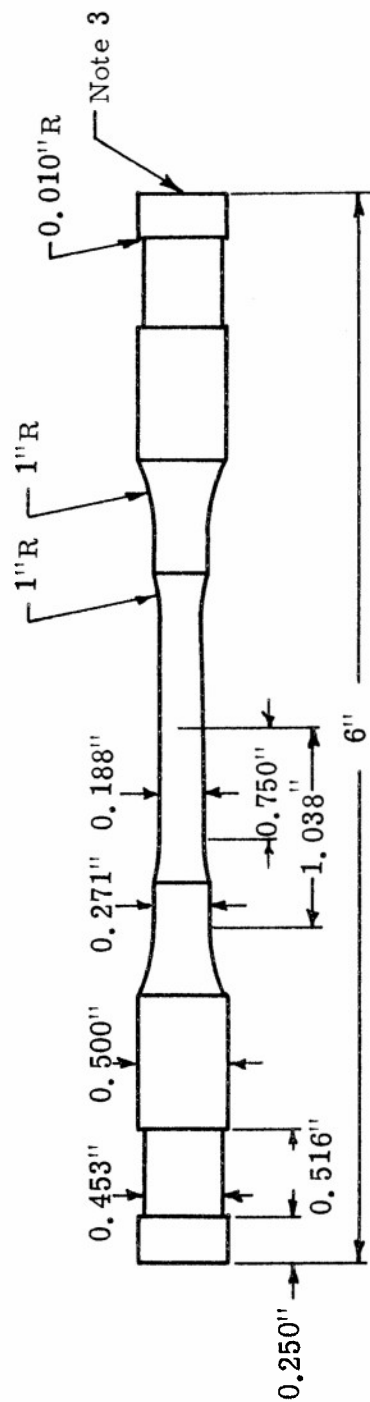


Figure 141. Cutting Plan for Slab 1 of ATJ-S Billets L-9-10, L-10-6, and L-11-4



Notes:

1. All diameters true and concentric to within 0.0005 in.
2. Do not undercut radii at tangent points
3. Both ends flat and perpendicular to  $G_L$  to within 0.0005 in.
4. All dimensions are in inches. Tolerances are:  
 $\begin{array}{l} + 0.001 \text{ on diameter} \\ \pm 0.005 \text{ on lengths} \\ - \end{array}$

Figure 142. Tensile Test Specimen Configuration Used for ATJ-S Billets L-9-10, L-10-6, and L-11-4

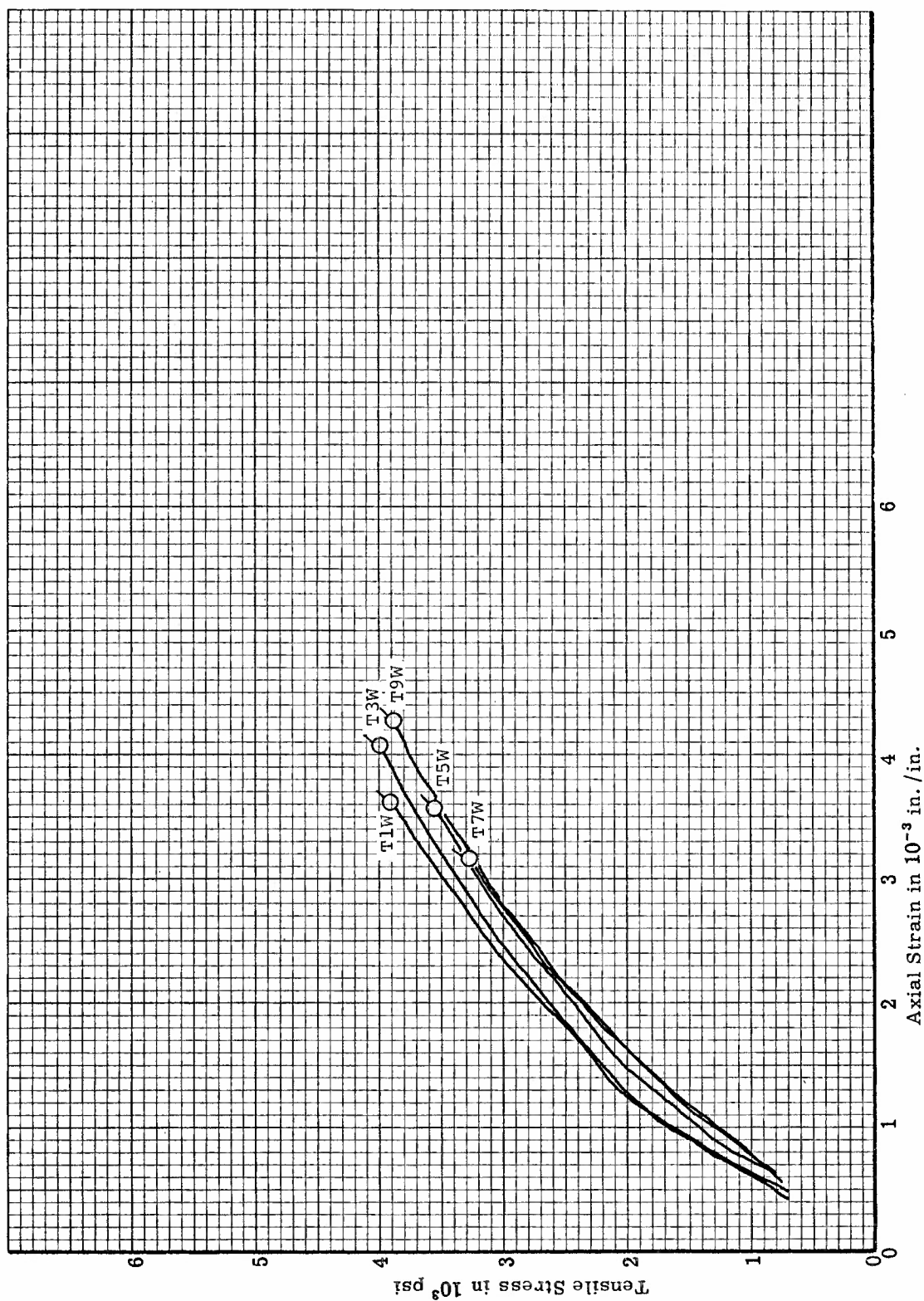


Figure 143. Tensile Stress-Strain Curves for ATJ-S Billet L-9-10 With Grain at 70°F

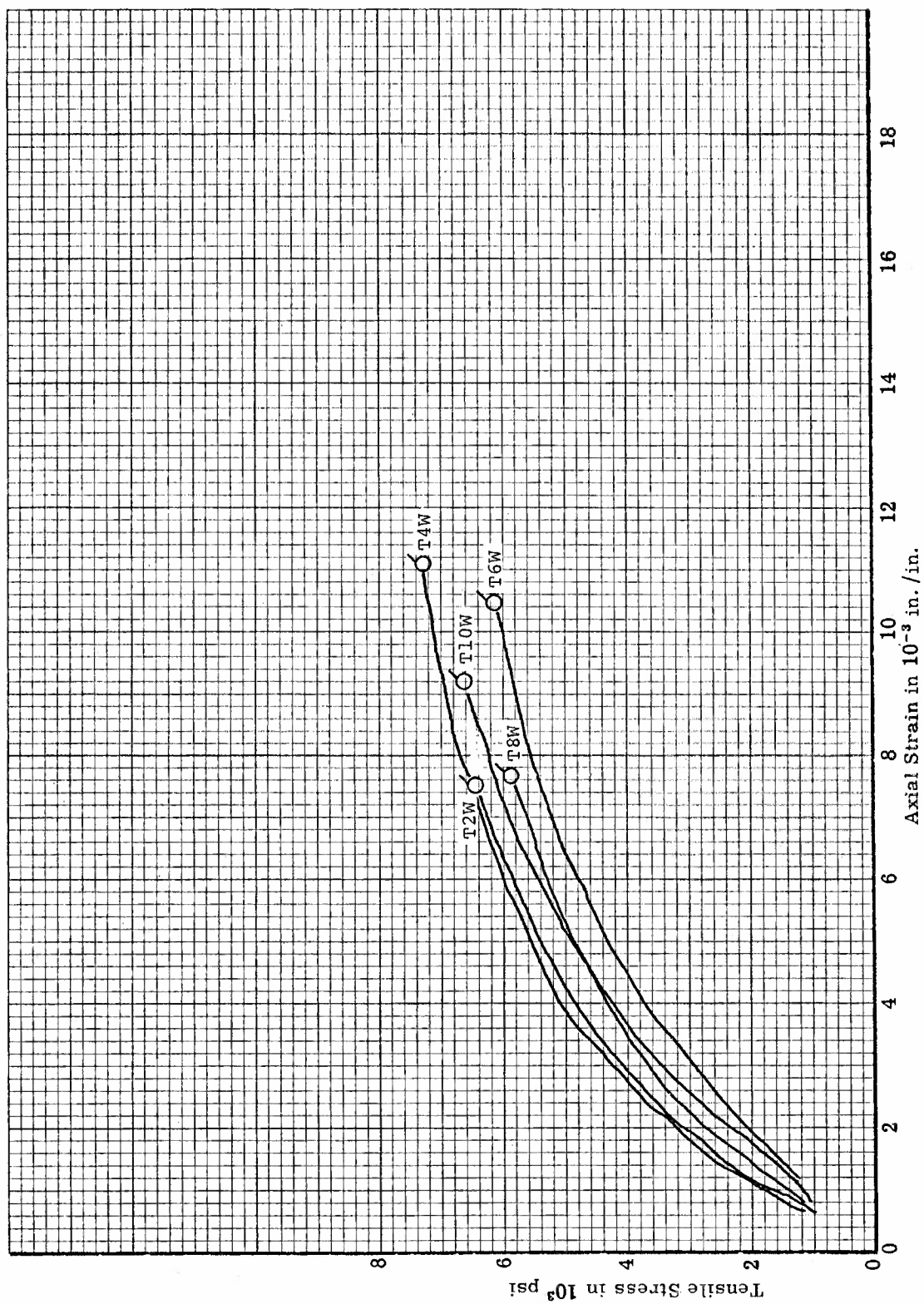


Figure 144. Tensile Stress-Strain Curves for ATJ-S Billet L-9-10 With Grain at 4500°F

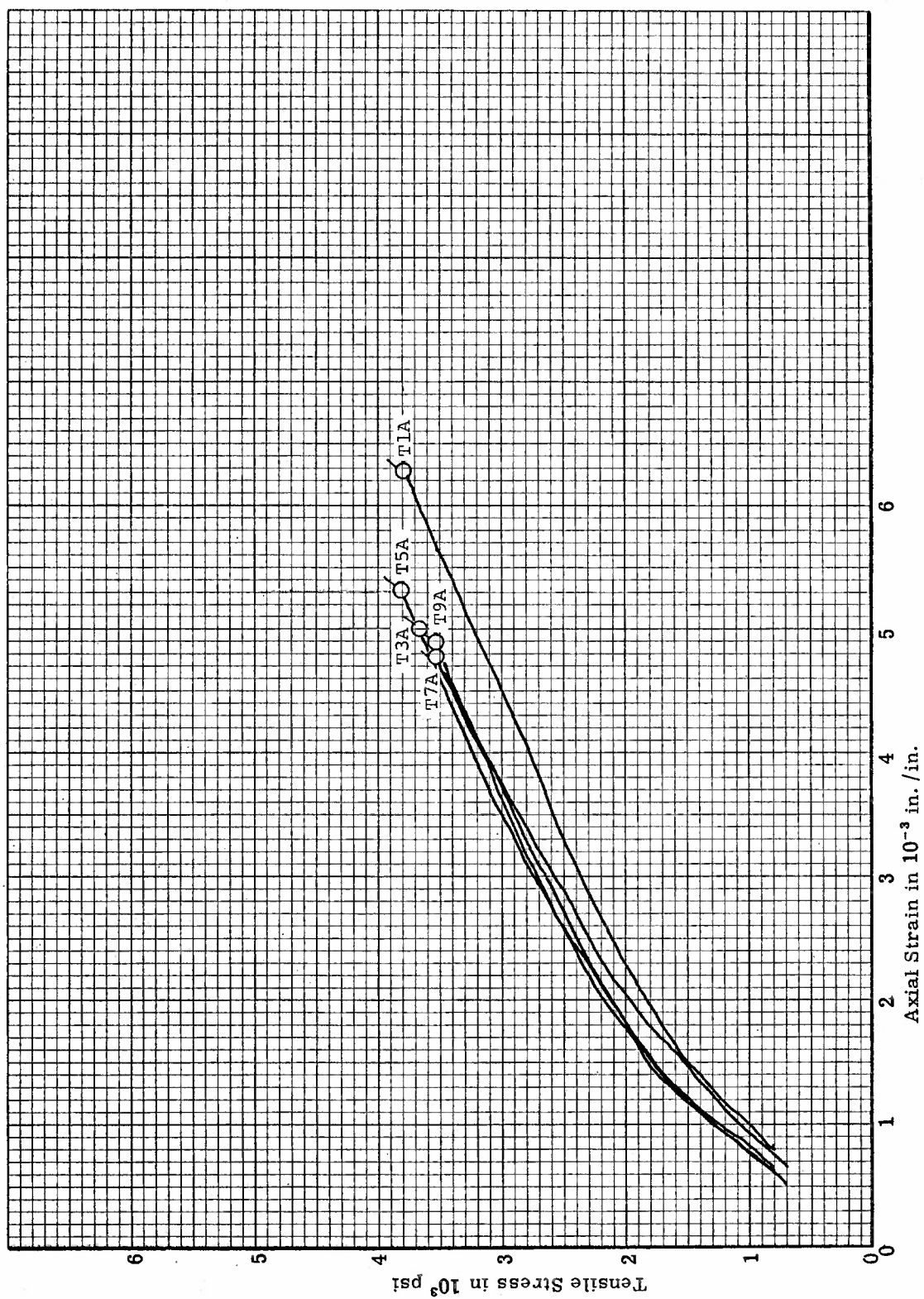


Figure 145. Tensile Stress-Strain Curves for ATJ-S Billet L-9-10 Across Grain at 70°F

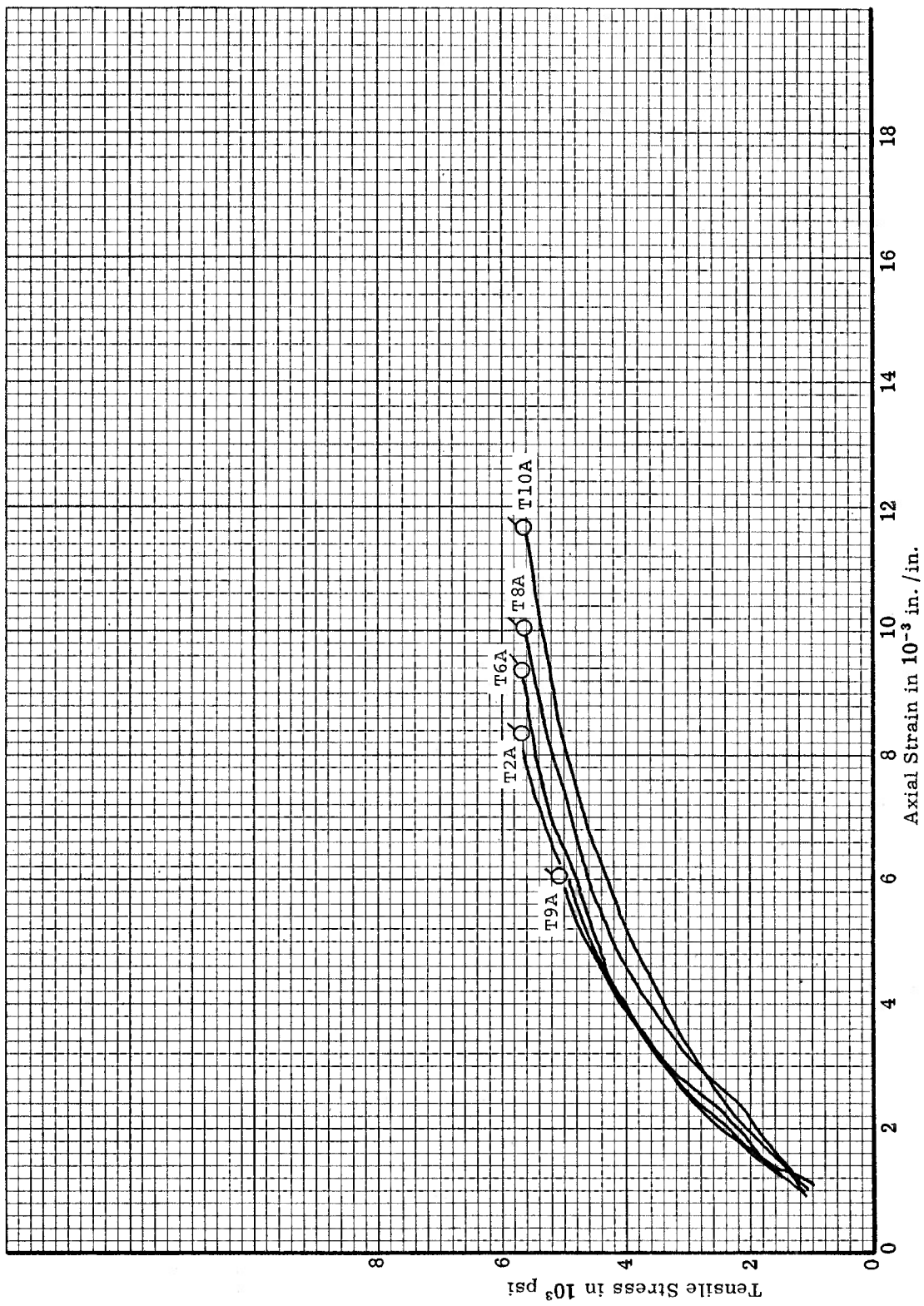


Figure 146. Tensile Stress-Strain Curves for ATJ-S Billet L-9-10 Across Grain at 4500°F

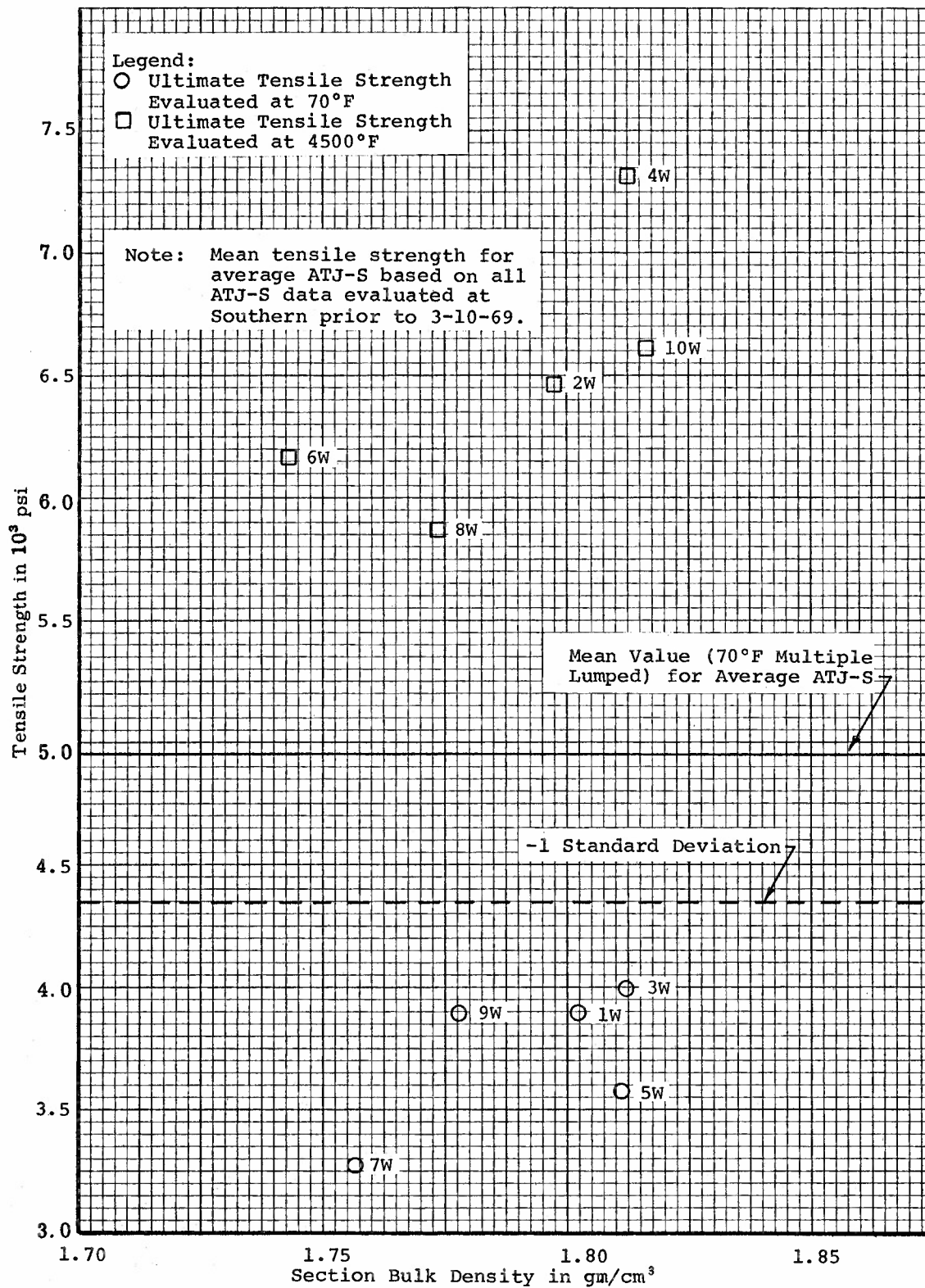


Figure 147. Tensile Strength Versus Section Bulk Density for ATJ-S Billet L-9-10 With Grain at 70°F, and 4500°F



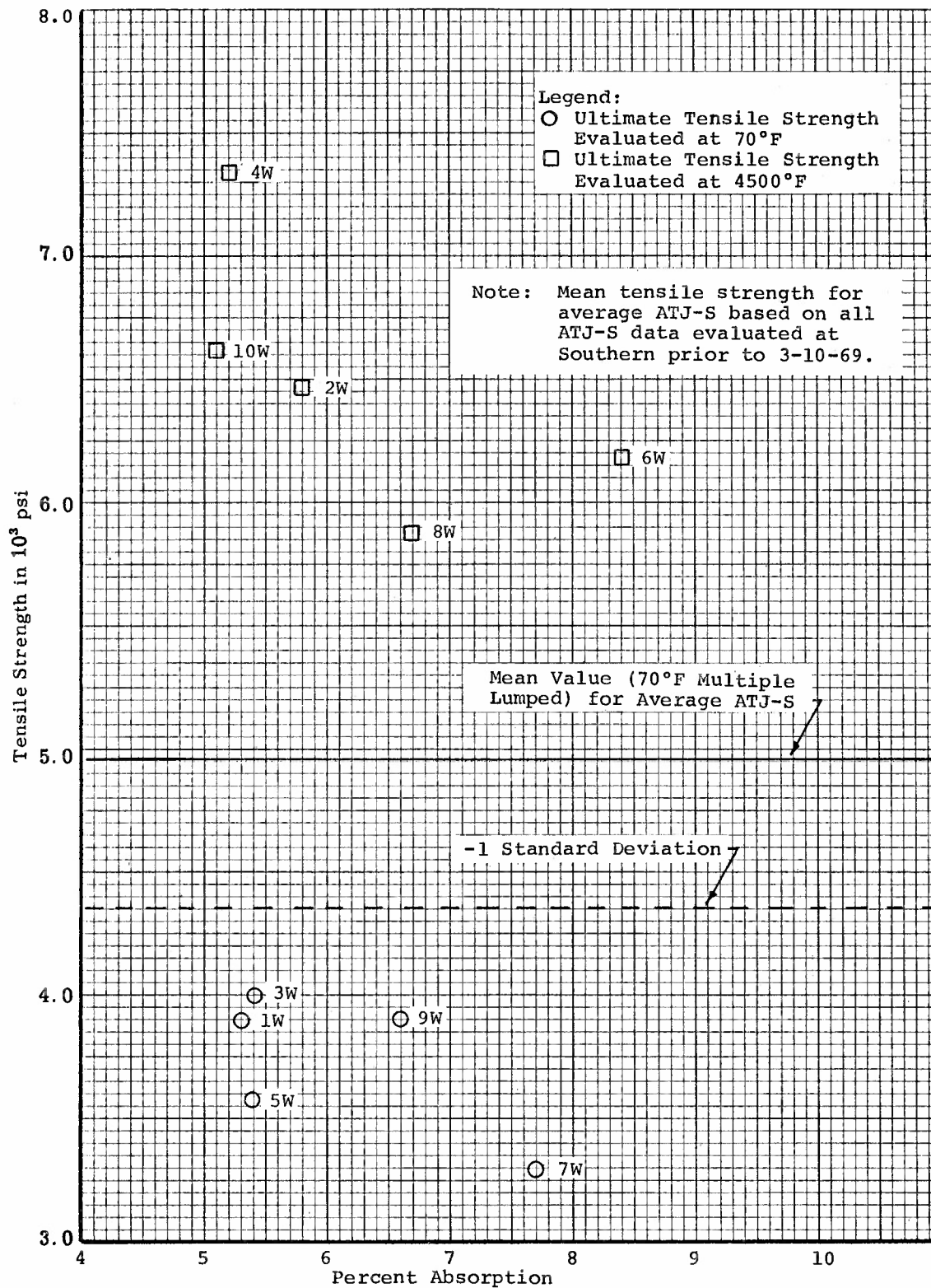


Figure 148. Tensile Strength Versus Percent Absorption for ATJ-S Billet L-9-10 With Grain at 70°F and 4500°F

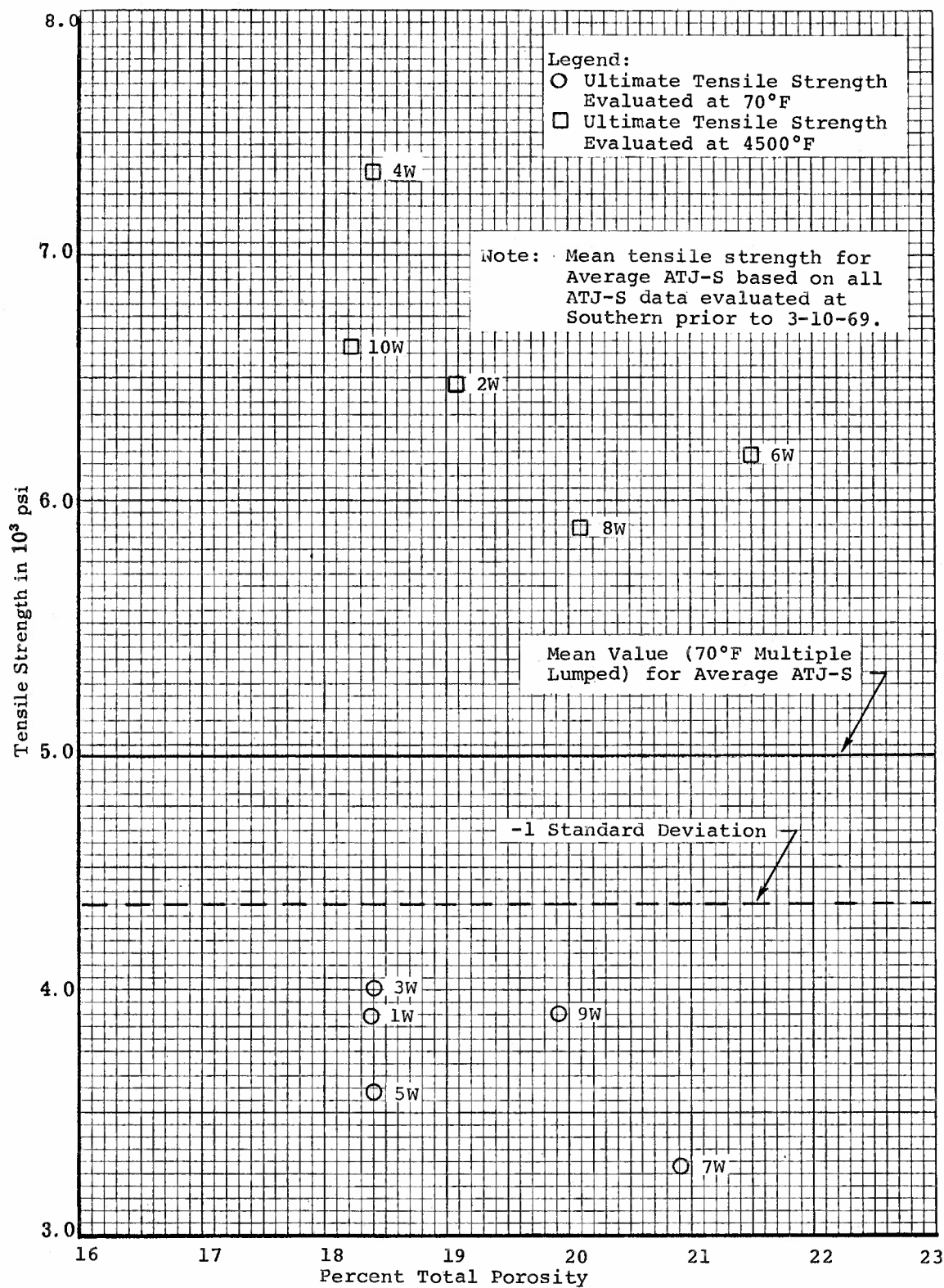


Figure 149. Tensile Strength Versus Percent Total Porosity for ATJ-S Billet L-9-10 With Grain at 70°F and 4500°F

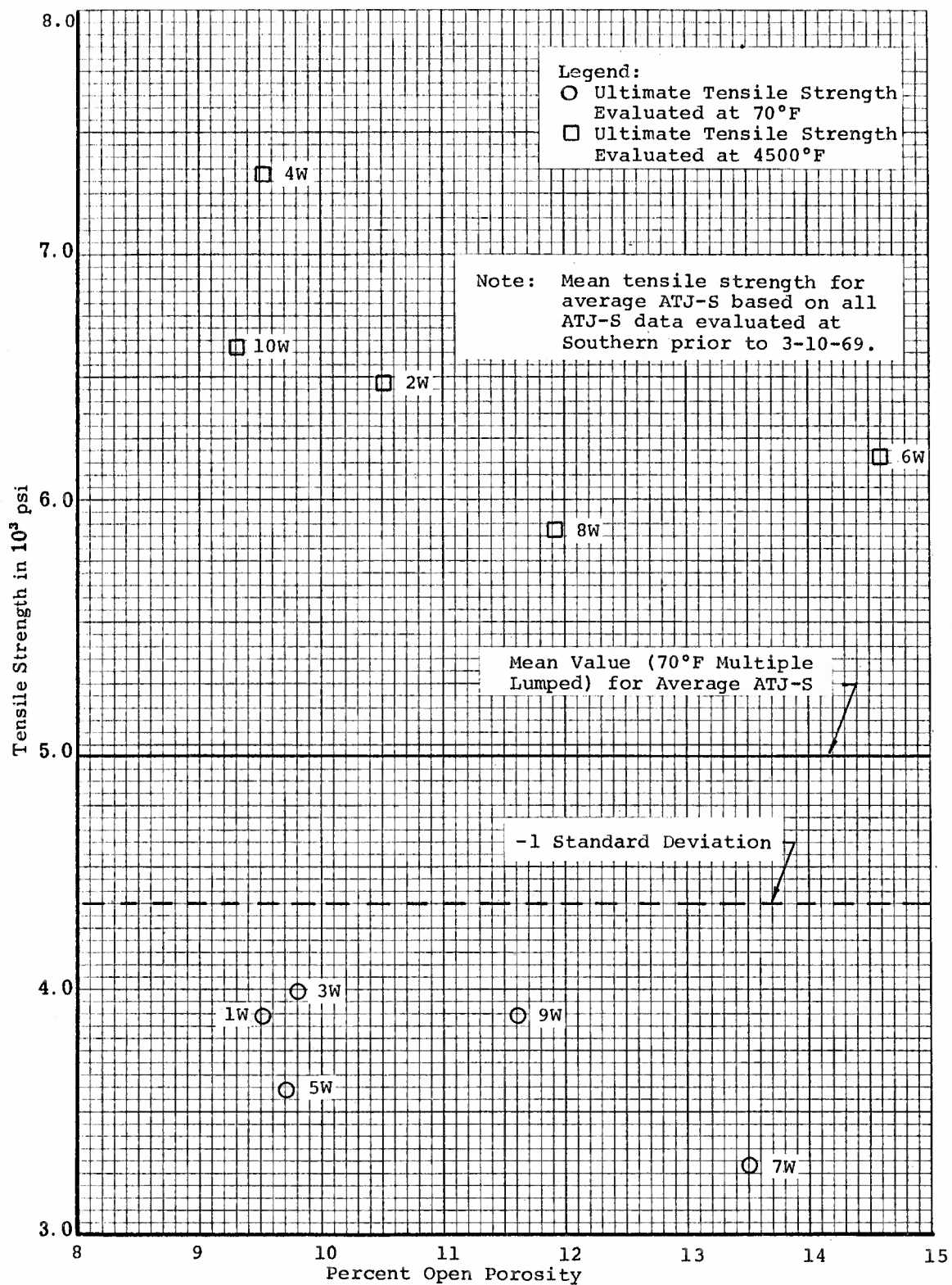


Figure 150. Tensile Strength Versus Percent Open Porosity for ATJ-S Billet L-9-10 With Grain at 70°F and 4500°F

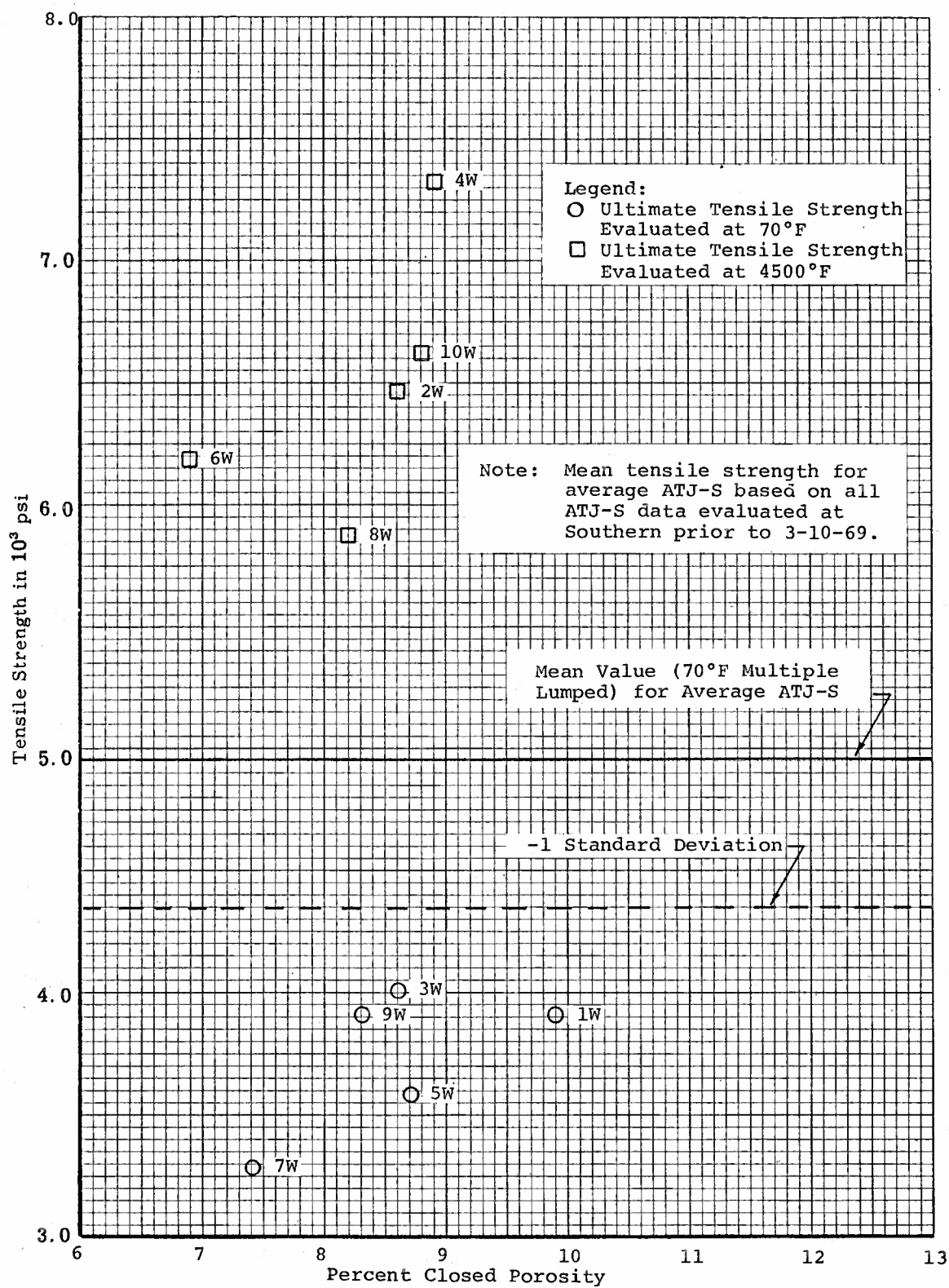


Figure 151. Tensile Strength Versus Percent Closed Porosity for ATJ-S Billet L-9-10 With Grain at 70°F and 4500°F

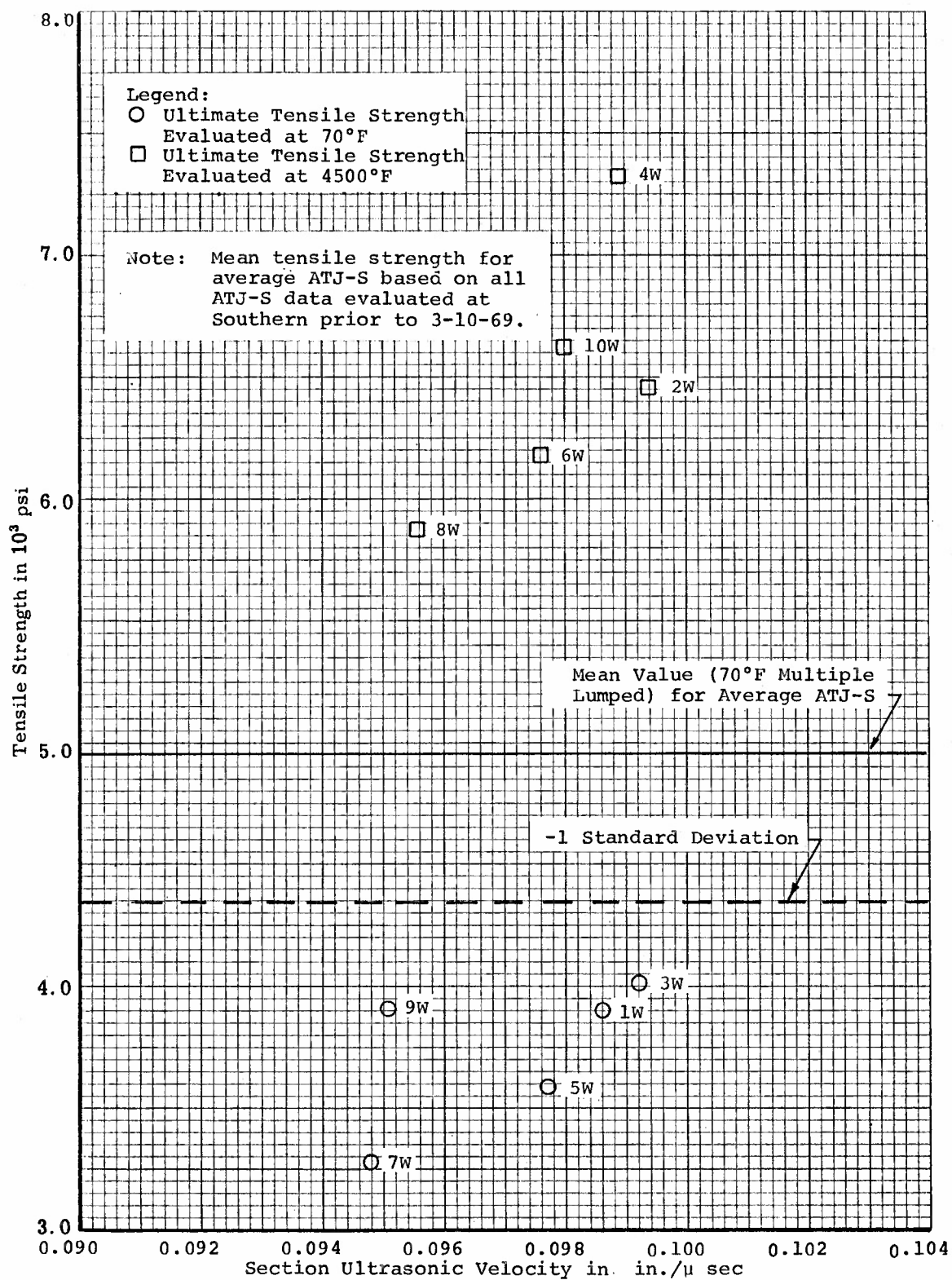


Figure 152. Tensile Strength Versus Ultrasonic Velocity for ATJ-S Billet L-9-10 With Grain at 70°F and 4500°F

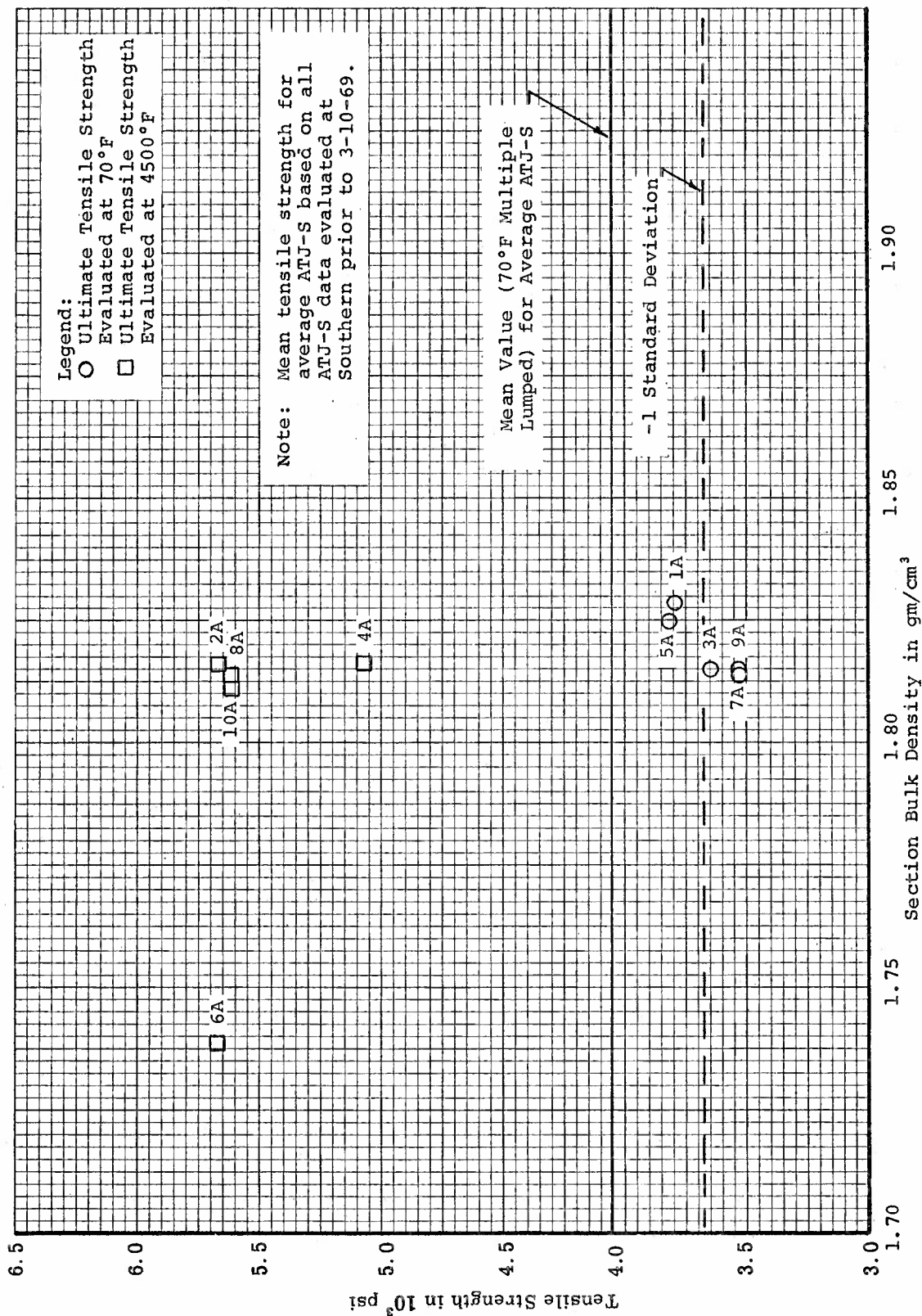


Figure 153. Tensile Strength Versus Section Bulk Density for ATJ-S Billet L-9-10 Across Grain at 70°F and 4500°F



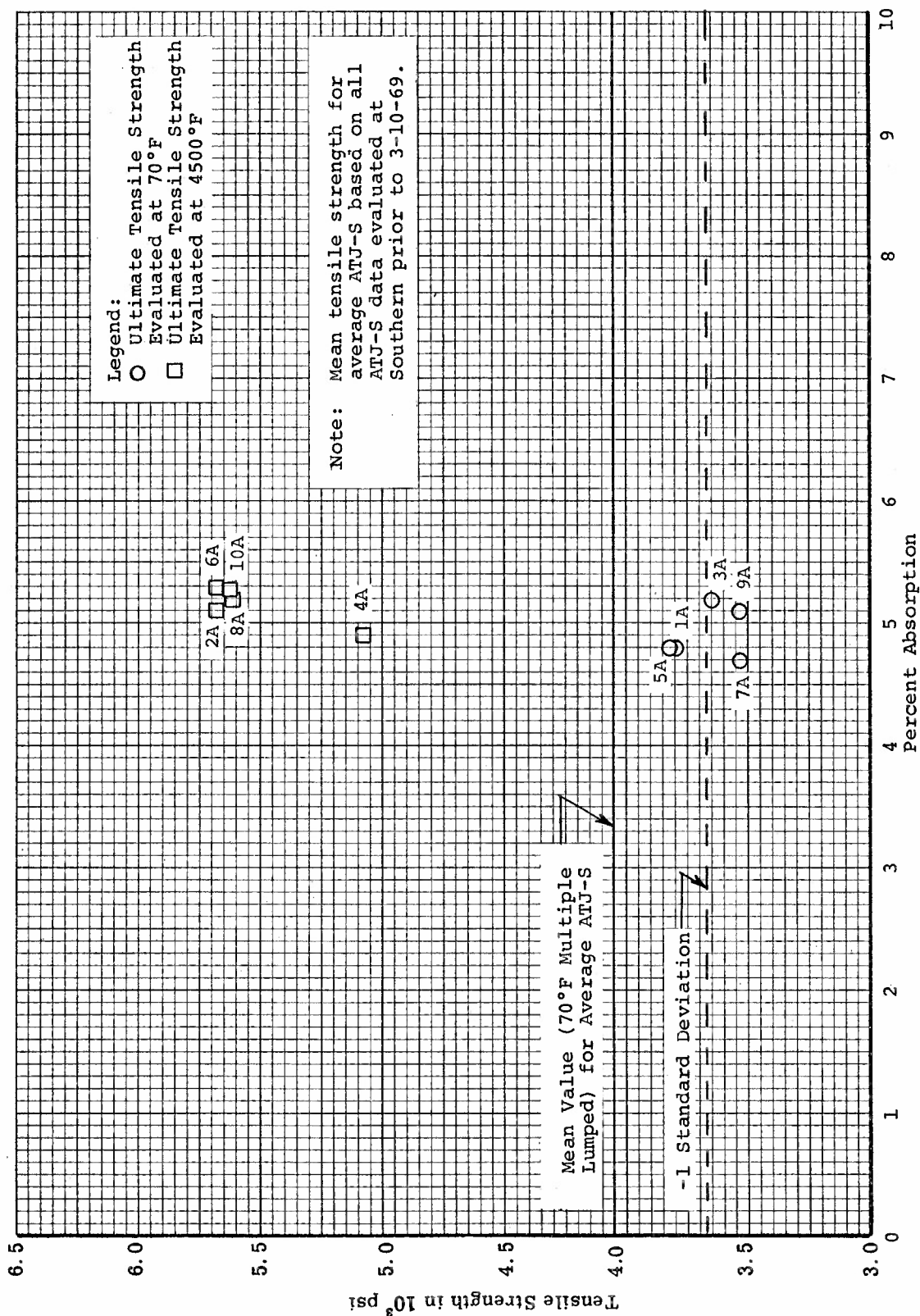


Figure 154. Tensile Strength Versus Percent Absorption for ATJ-S Billet L-9-10 Across Grain at 70°F and 4500°F

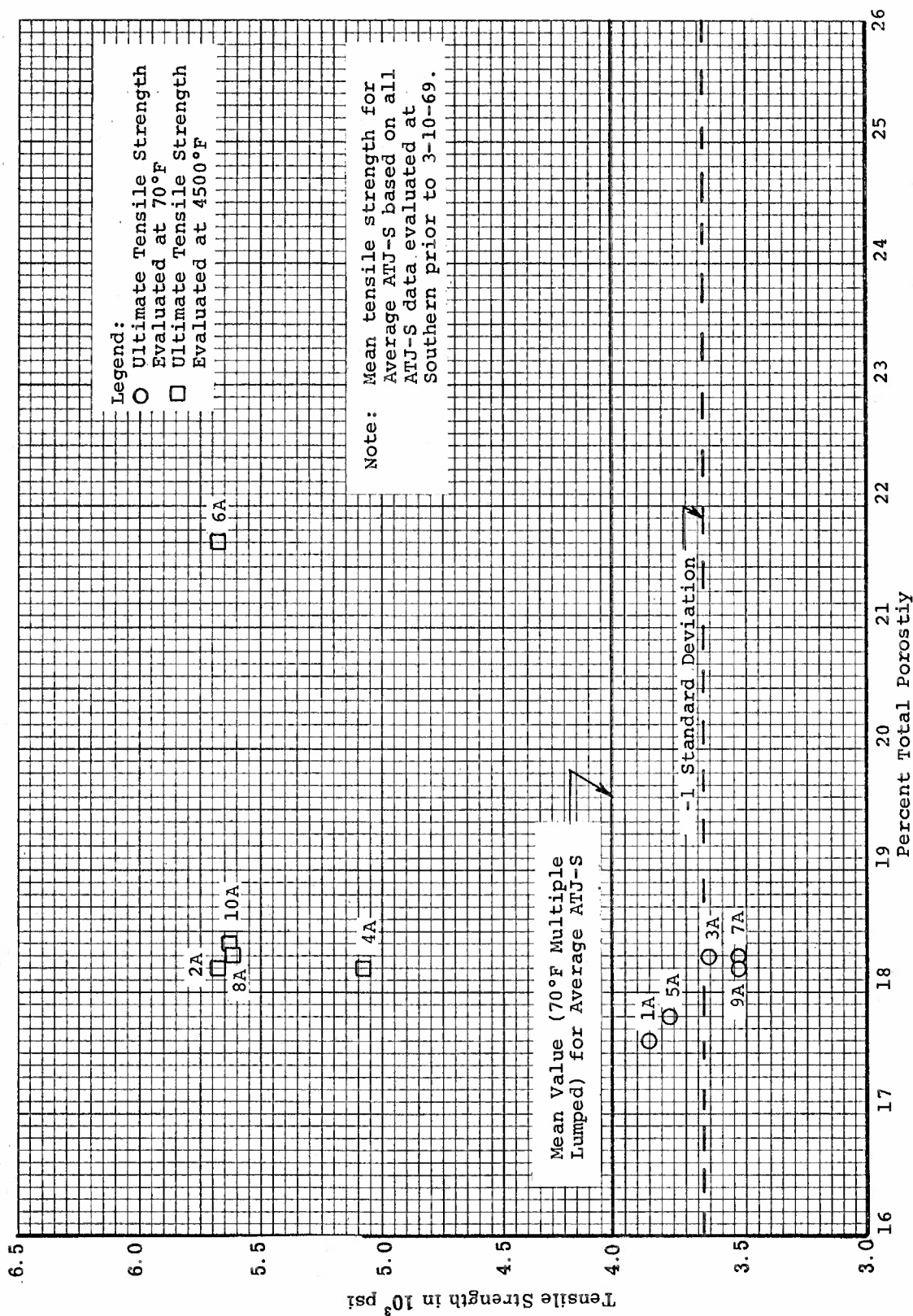


Figure 155. Tensile Strength Versus Percent Total Porosity for ATJ-S Billet L-9-10 Across Grain at 70°F and 4500°F



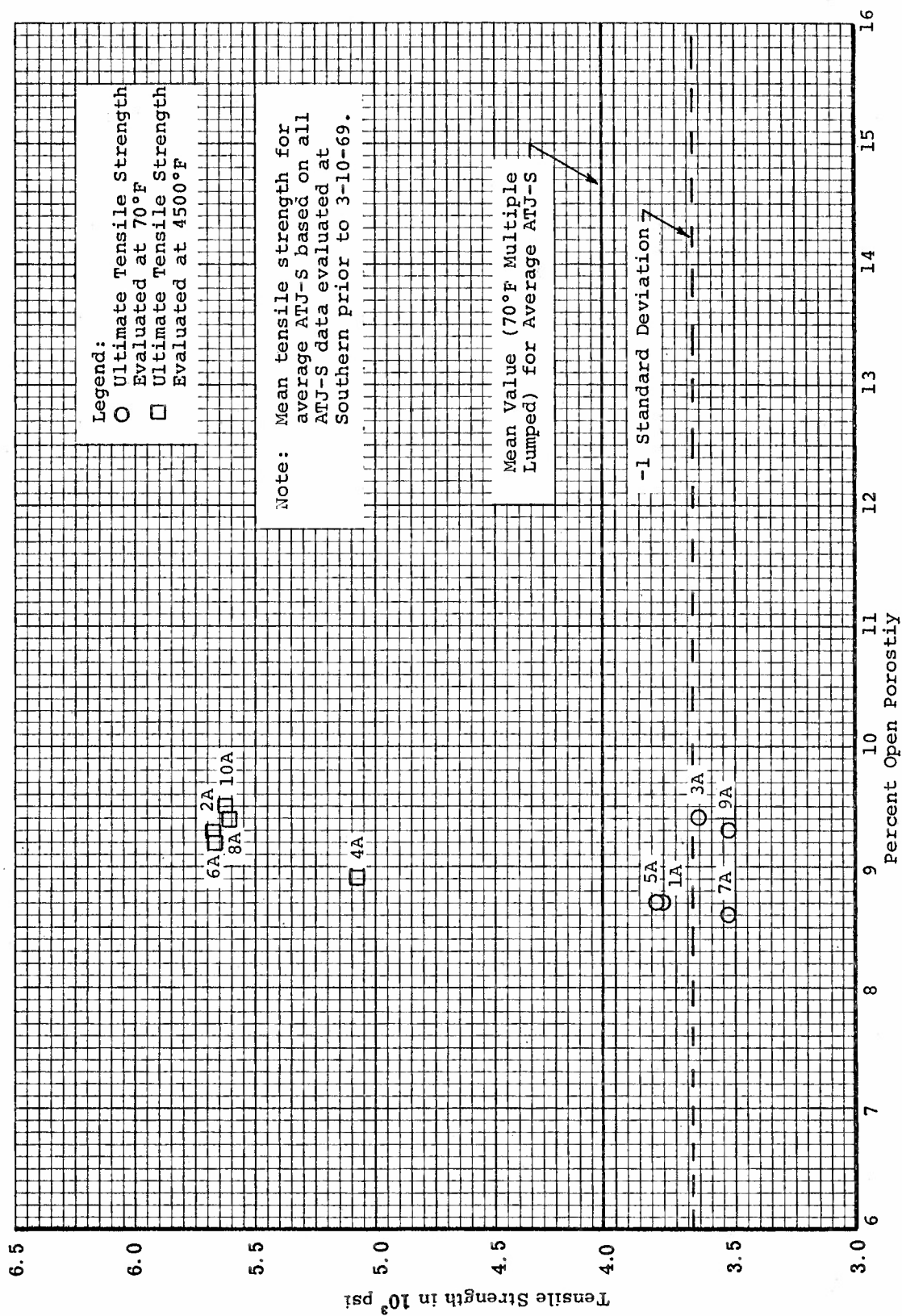


Figure 156. Tensile Strength Versus Percent Open Porosity for ATJ-S Billet L-9-10 Across Grain at 70°F and 4500°F

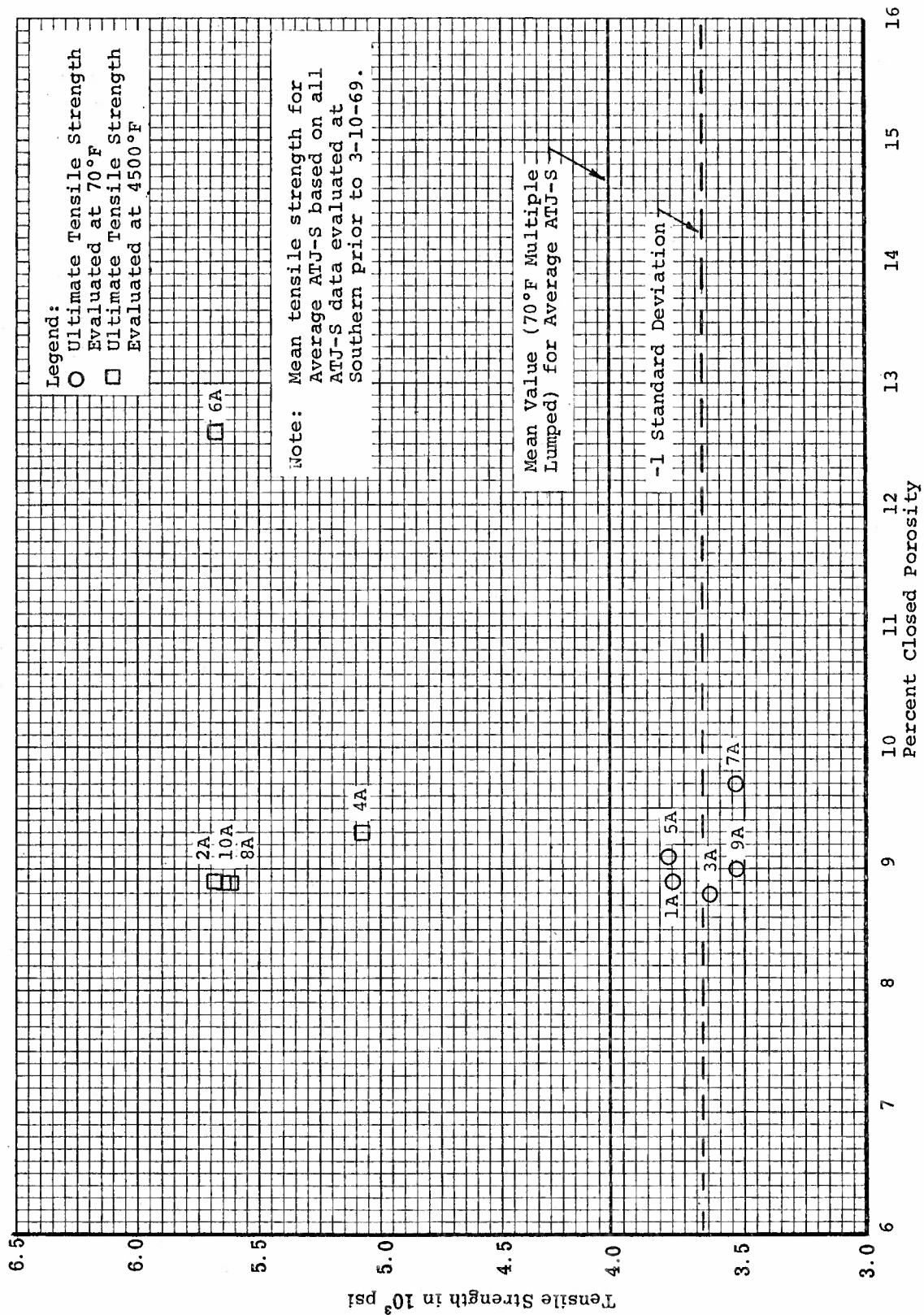


Figure 157. Tensile Strength Versus Percent Closed Porosity for ATJ-S Billet L-9-10 Across Grain at 70°F and 4500°F

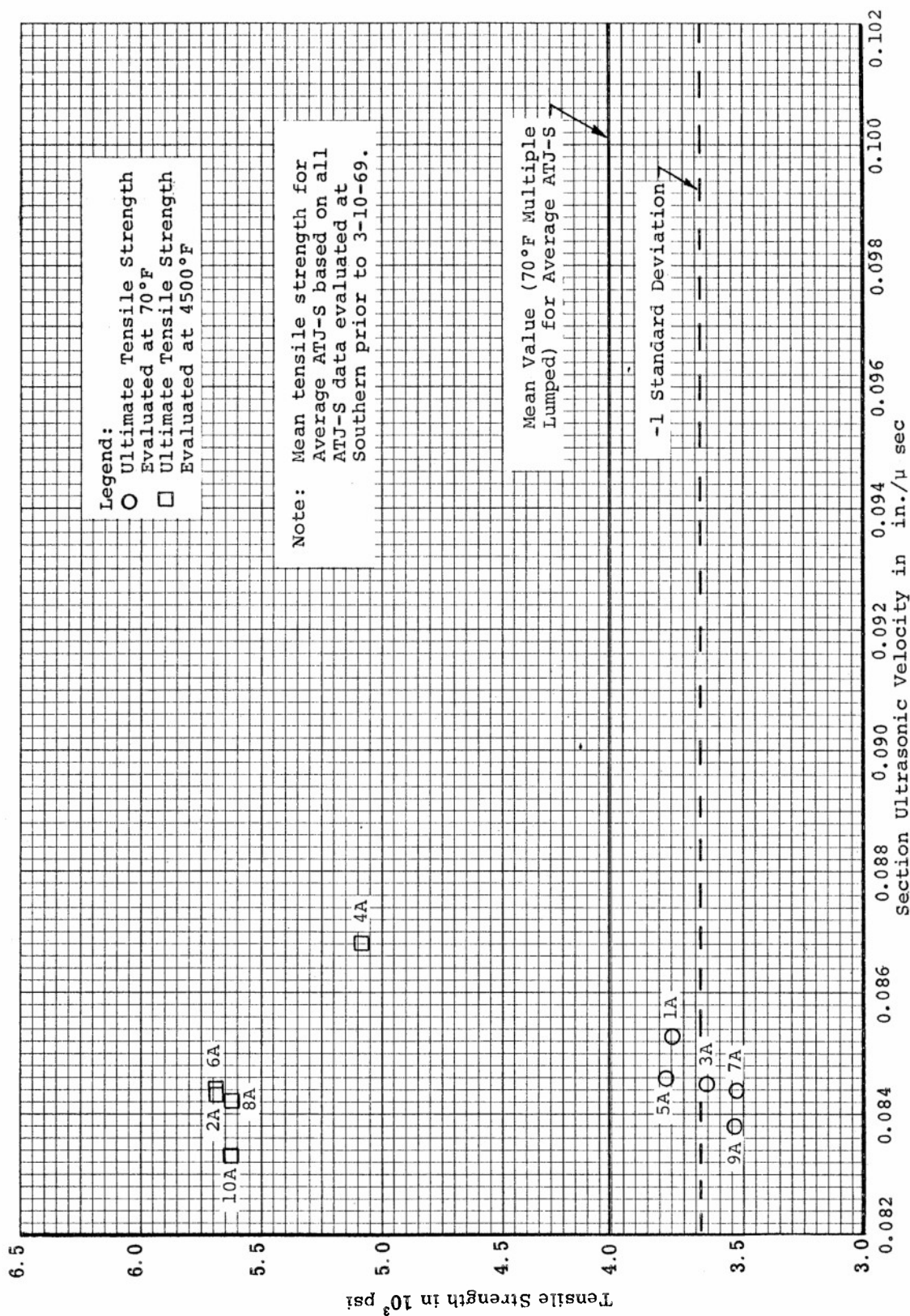


Figure 158. Tensile Strength Versus Section Ultrasonic Velocity for ATJ-S Billet L-9-10 Across Grain at 70°F and 4500°F

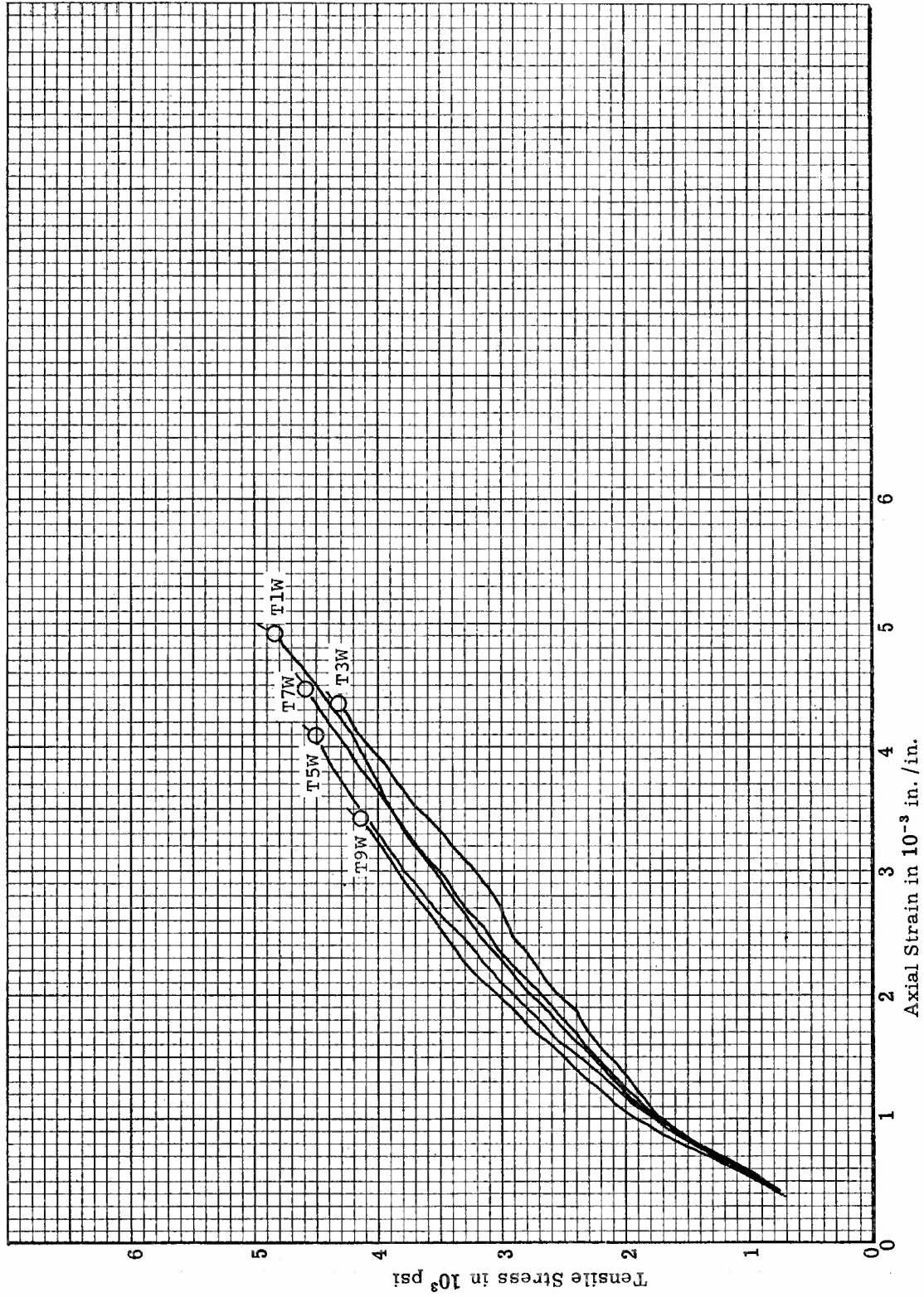


Figure 159. Tensile Stress-Strain Curves for ATJ-S Billet L-10-6 With Grain at 70°F

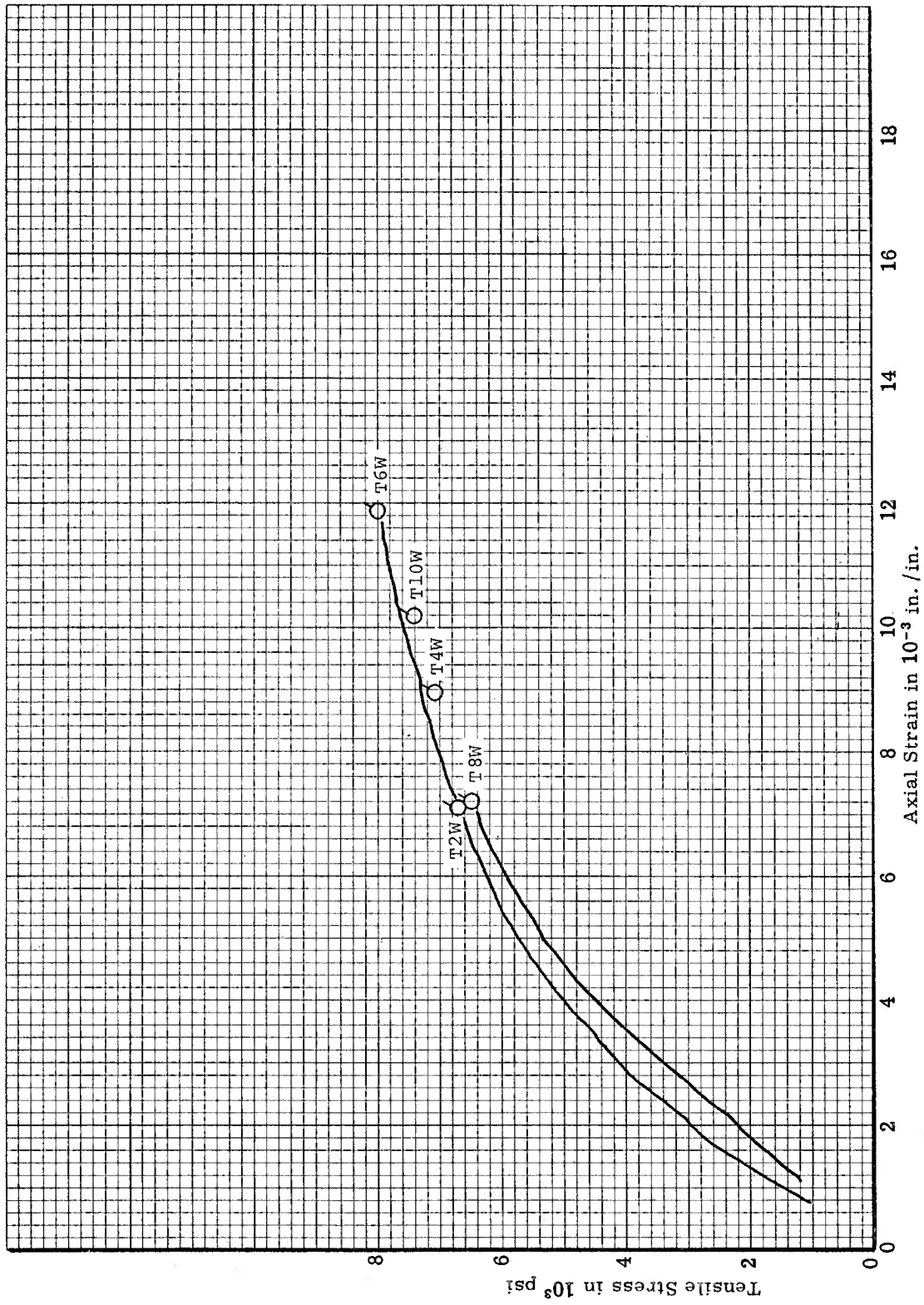


Figure 160. Tensile Stress-Strain Curves for ATJ-S Billet L-10-6 With Grain at 4500°F

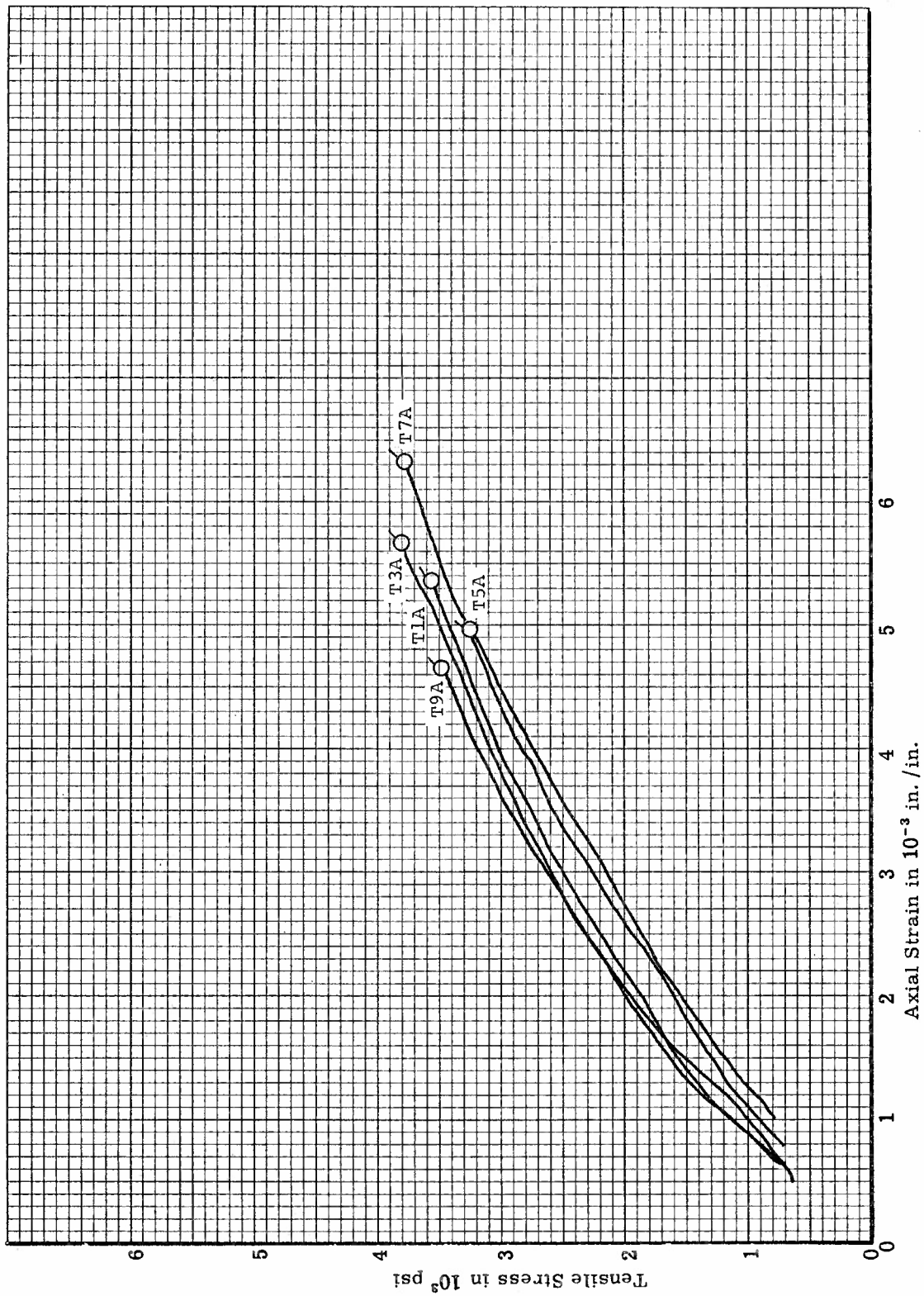


Figure 161. Tensile Stress-Strain Curves for ATJ-S Billet L-10-6 Across Grain at 70°F



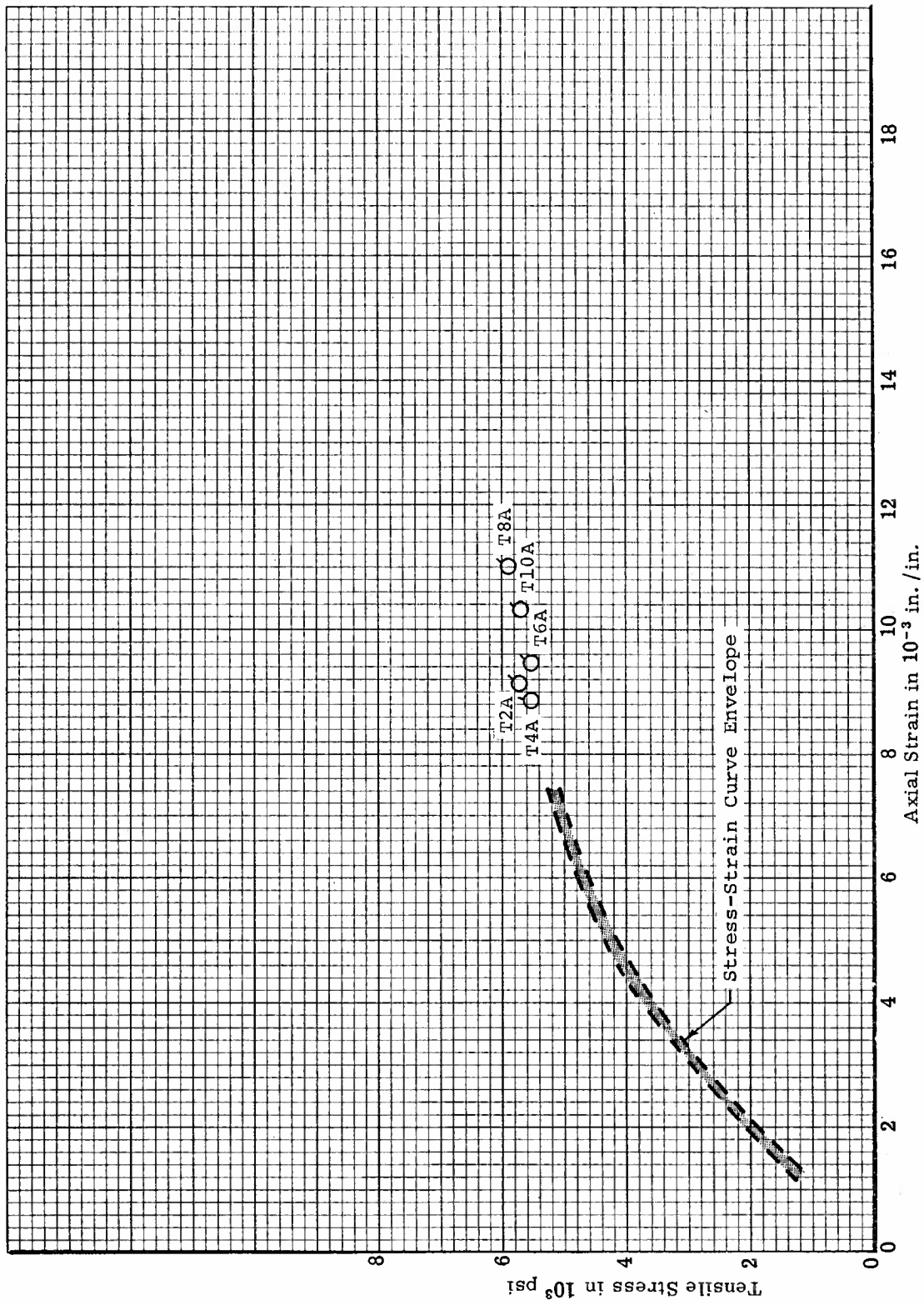


Figure 162. Tensile Stress-Strain Curves for ATJ-S Billet L-10-6 Across Grain at 4500°F

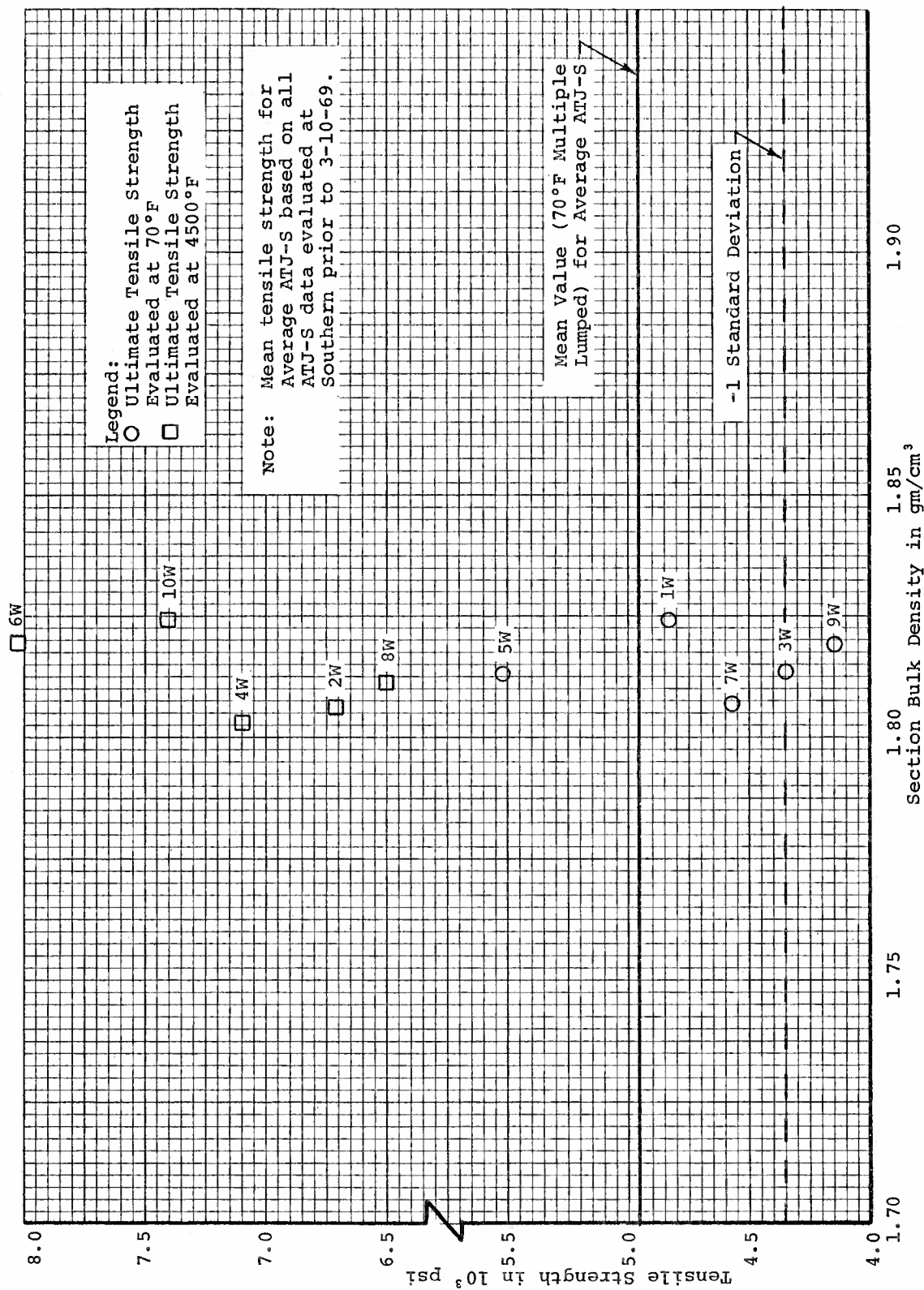


Figure 163. Tensile Strength Versus Section Bulk Density for ATJ-S Billet L-10-6 With Grain at 70°F and 4500°F



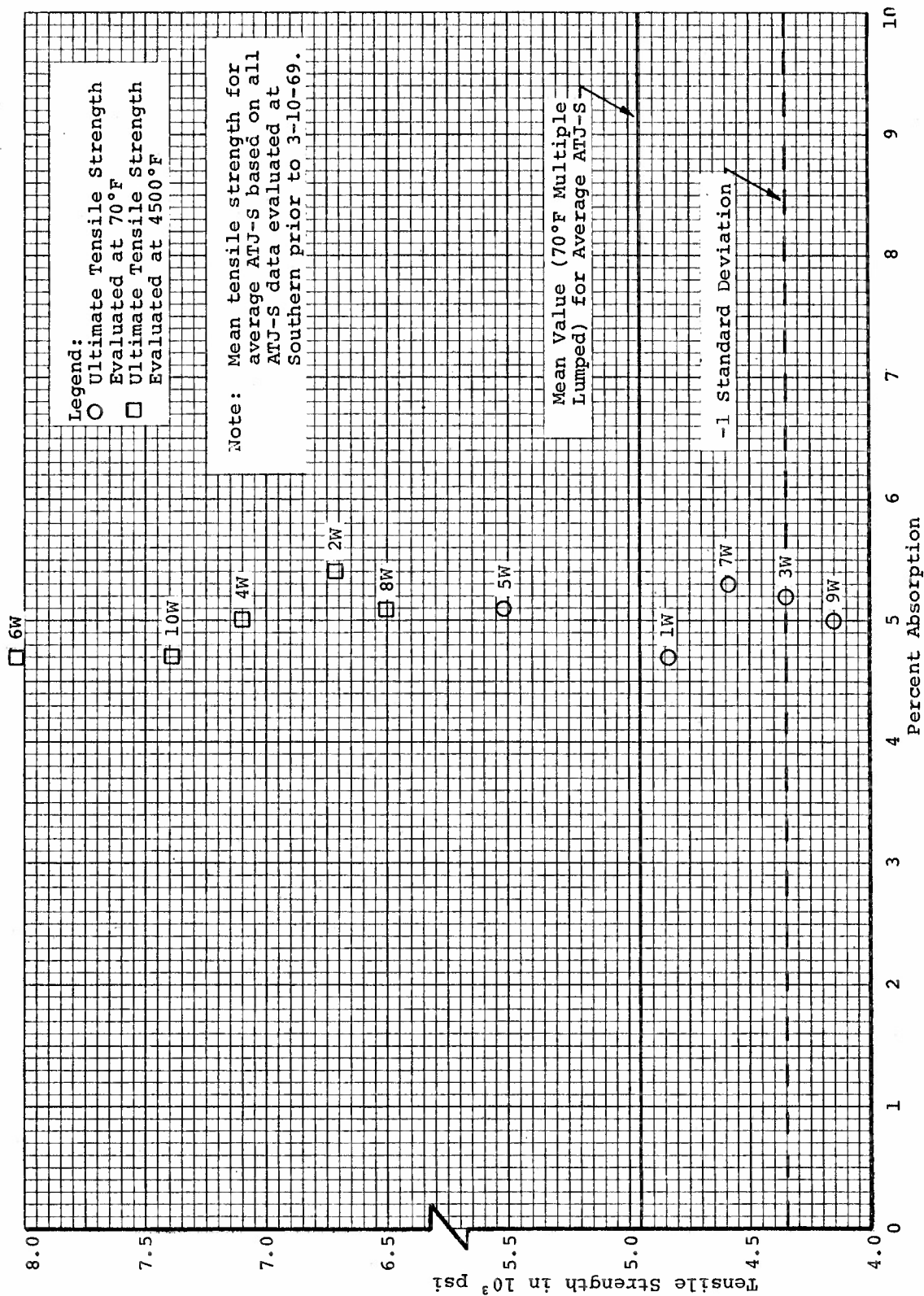


Figure 164. Tensile Strength Versus Percent Absorption for ATJ-S Billet L-10-6 With Grain at 70°F and 4500°F

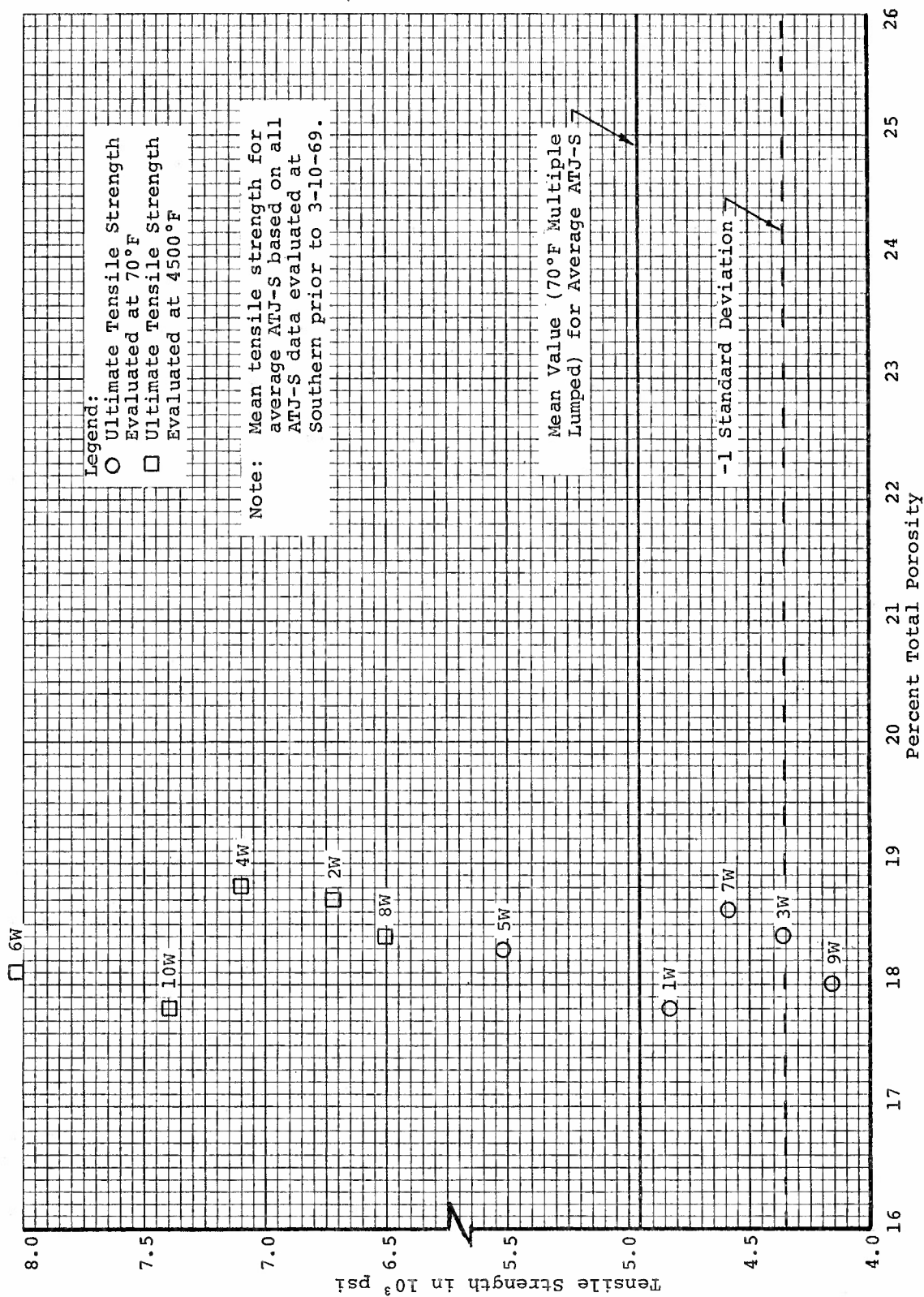


Figure 165. Tensile Strength Versus Percent Total Porosity for ATJ-S Billet L-10-6 With Grain at 70°F and 4500°F

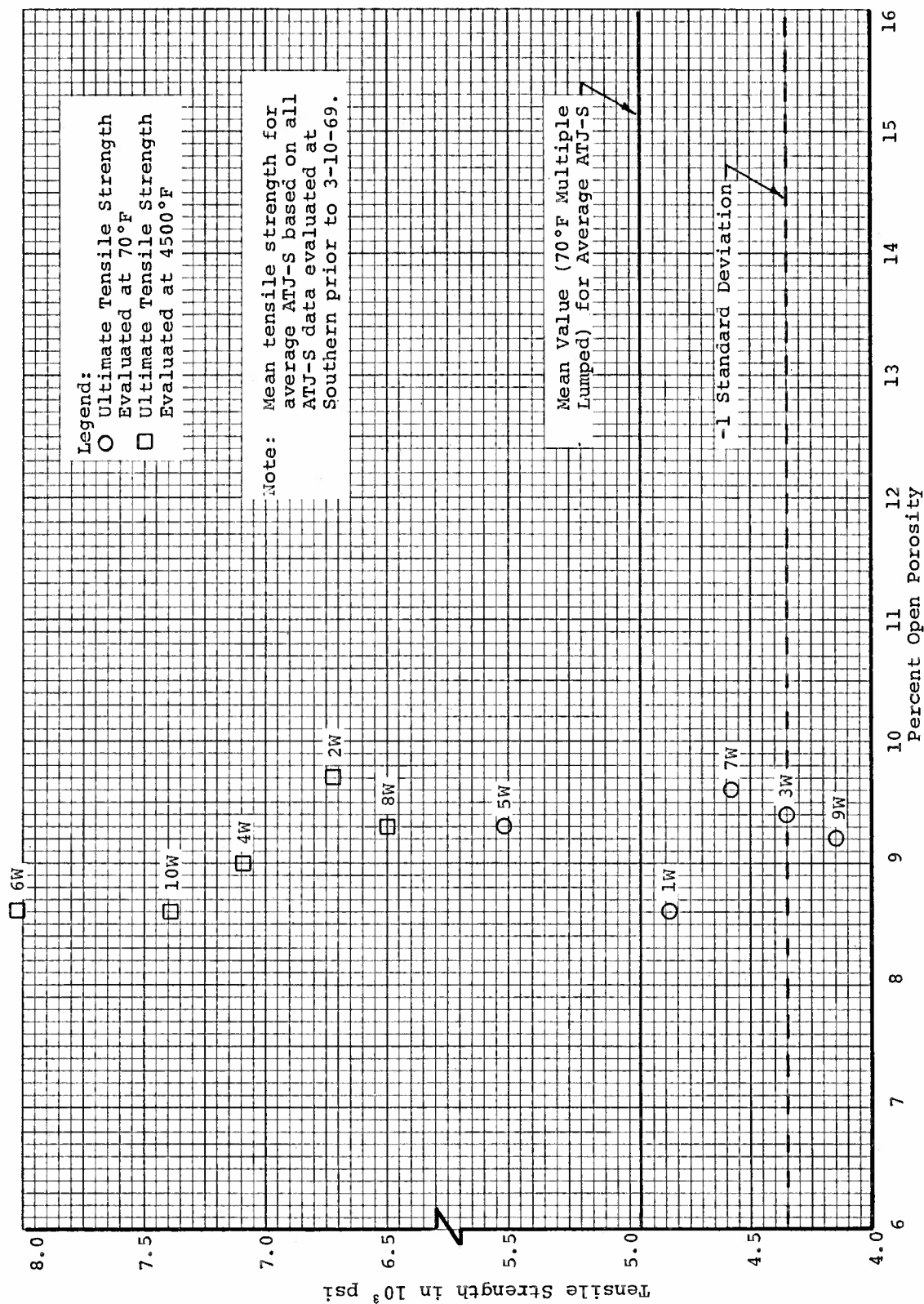


Figure 166. Tensile Strength Versus Percent Open Porosity for ATJ-S Billet L-10-6 With Grain at 70°F and 4500°F

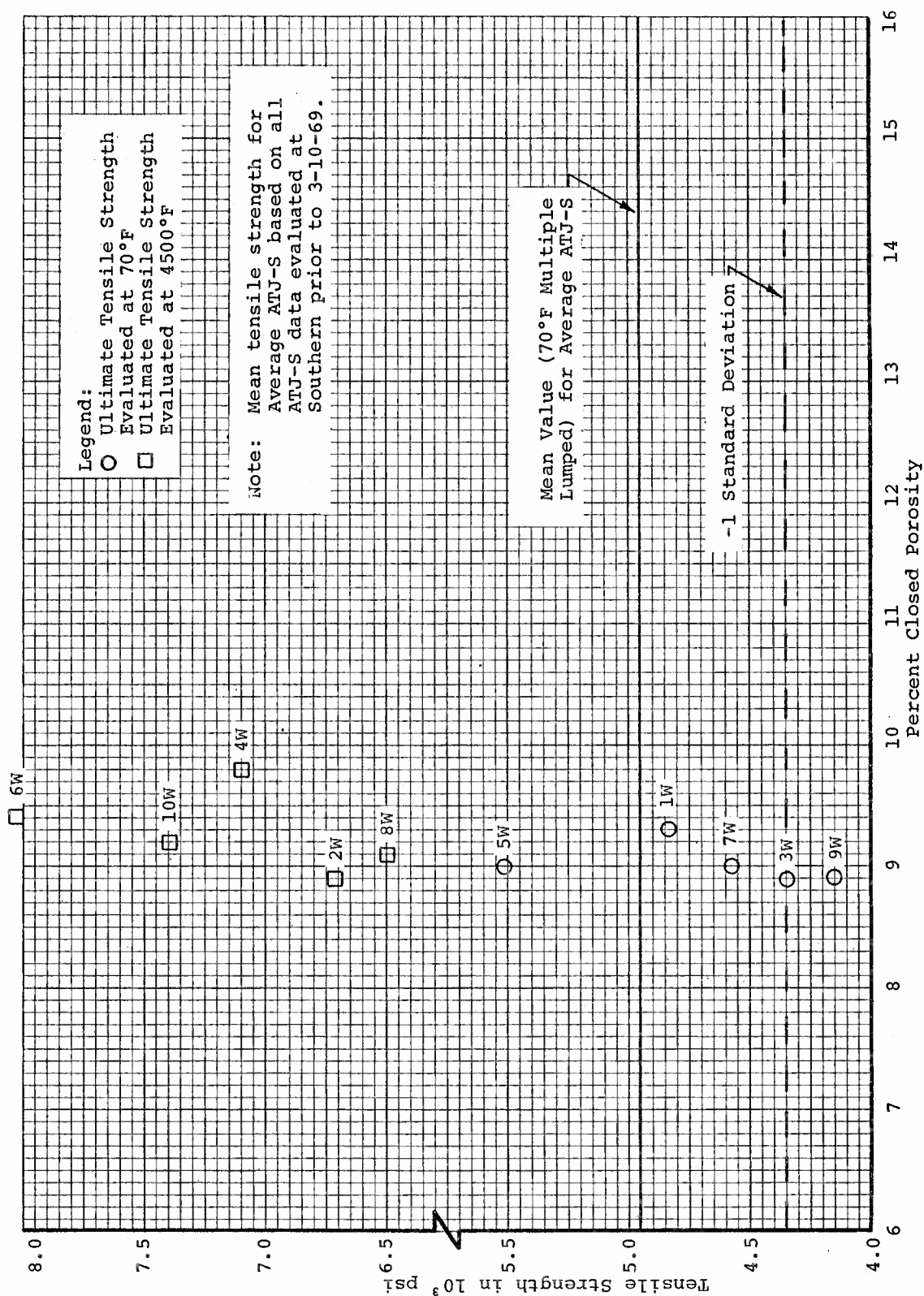


Figure 167. Tensile Strength Versus Percent Closed Porosity for ATJ-S Billet L-10-6 With Grain at 70°F and 4500°F

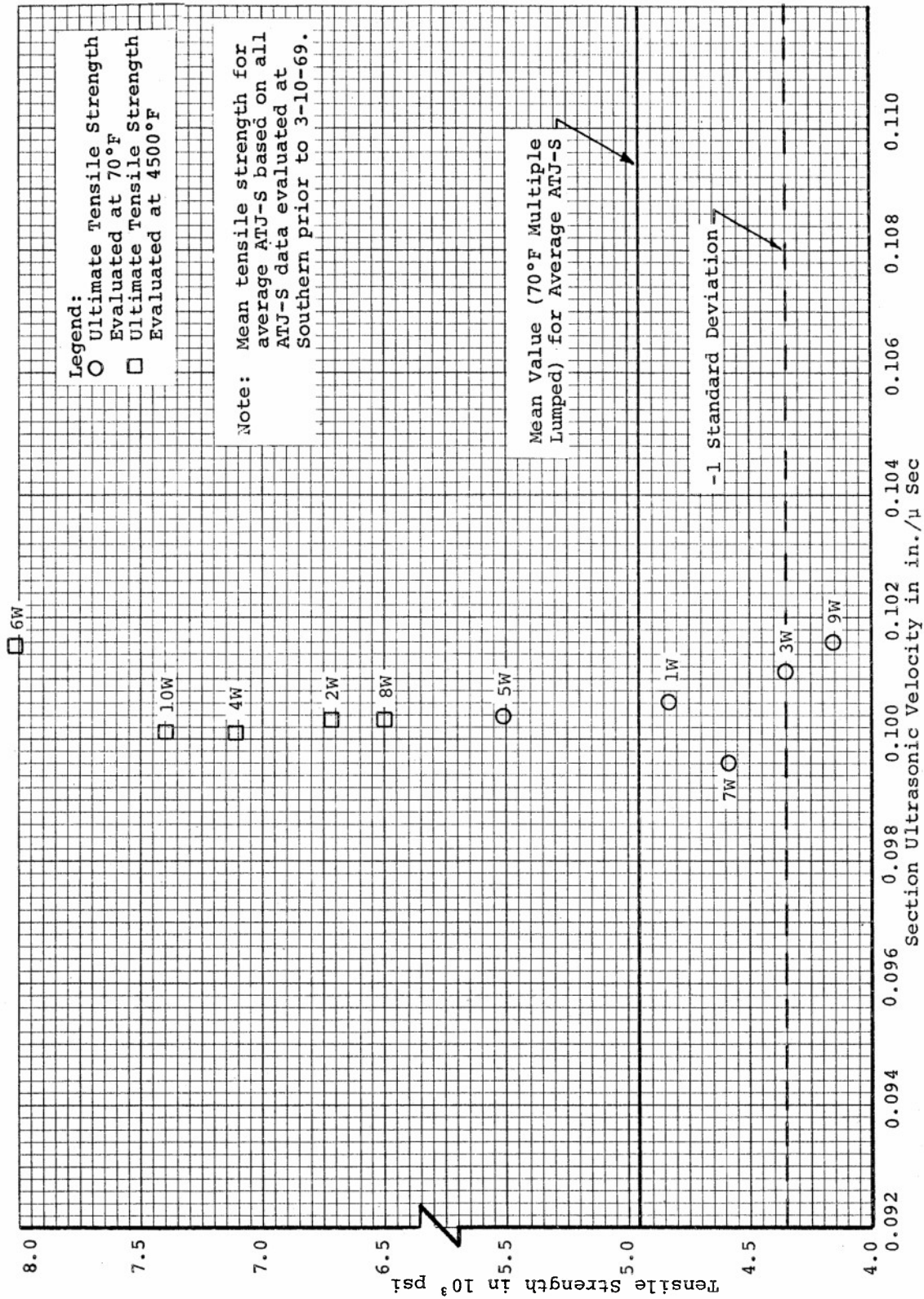


Figure 168. Tensile Strength versus Section Ultrasonic Velocity for ATJ-S Billet L-10-6 With Grain at 70°F and 4500°F

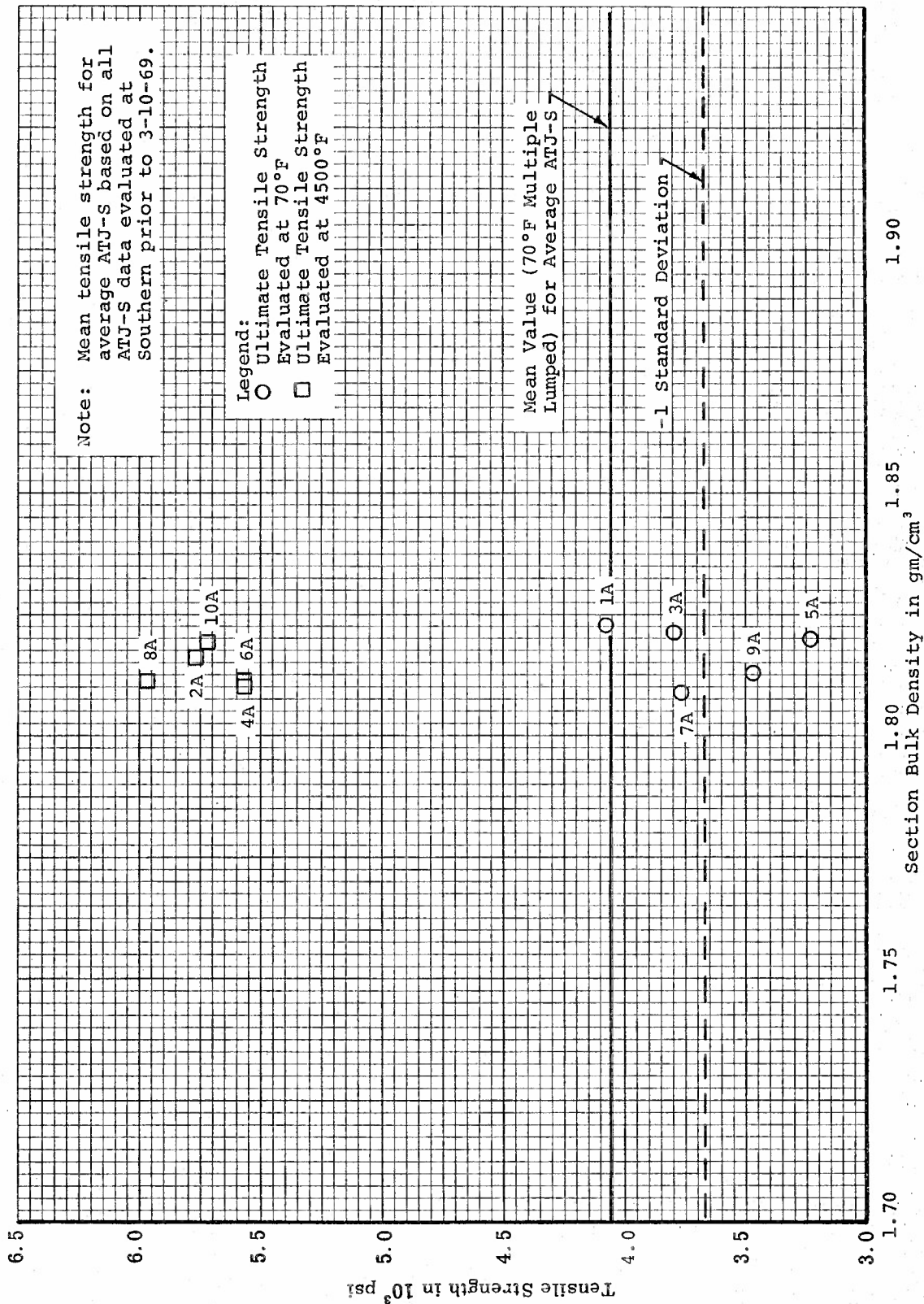


Figure 169. Tensile Strength versus Section Bulk Density for ATJ-S Billet L-10-6 Across Grain at 70°F and 4500°F



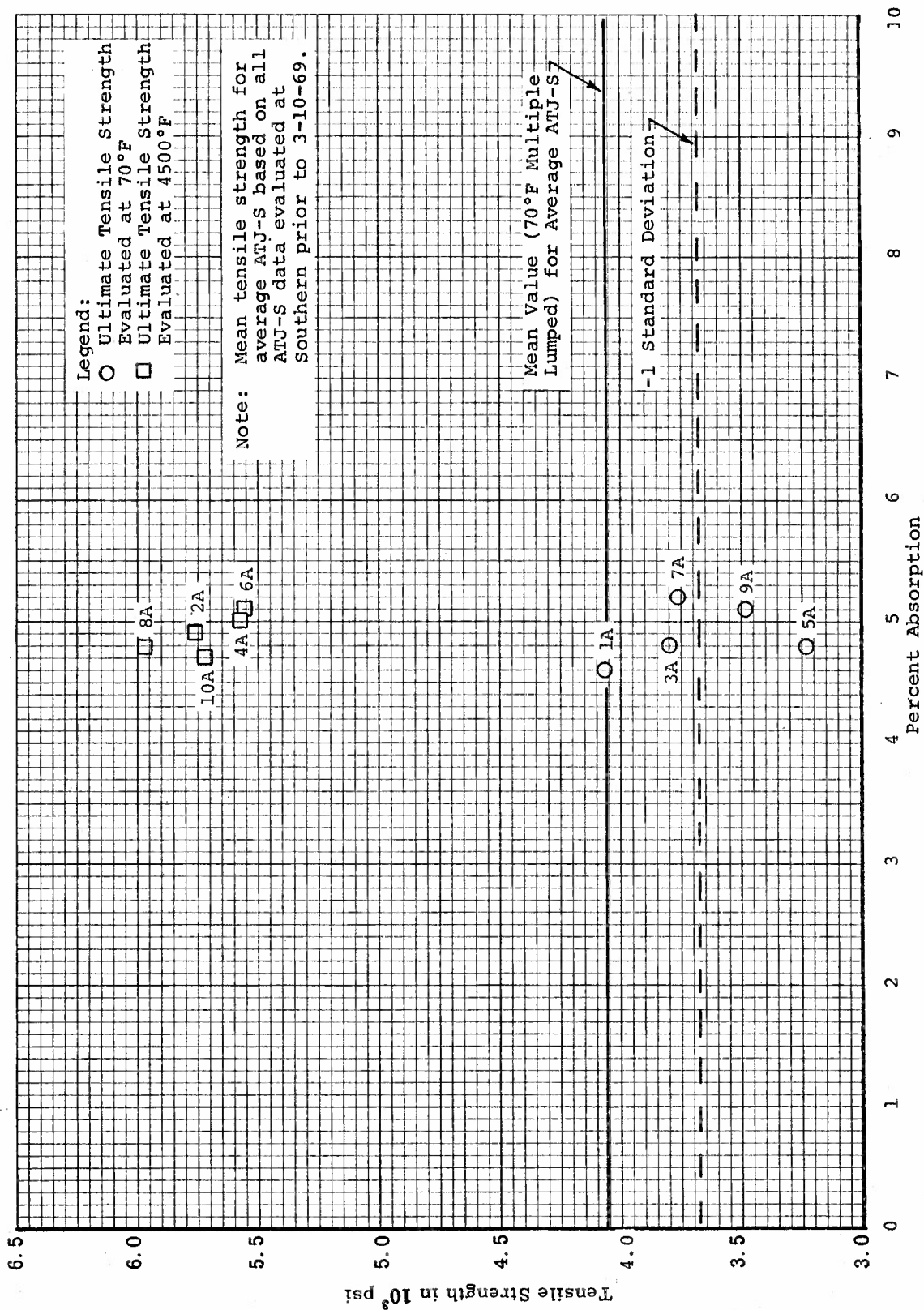


Figure 170. Tensile Strength versus Percent Absorption for ATJ-S Billet L-10-6 Across Grain at 70°F and 4500°F

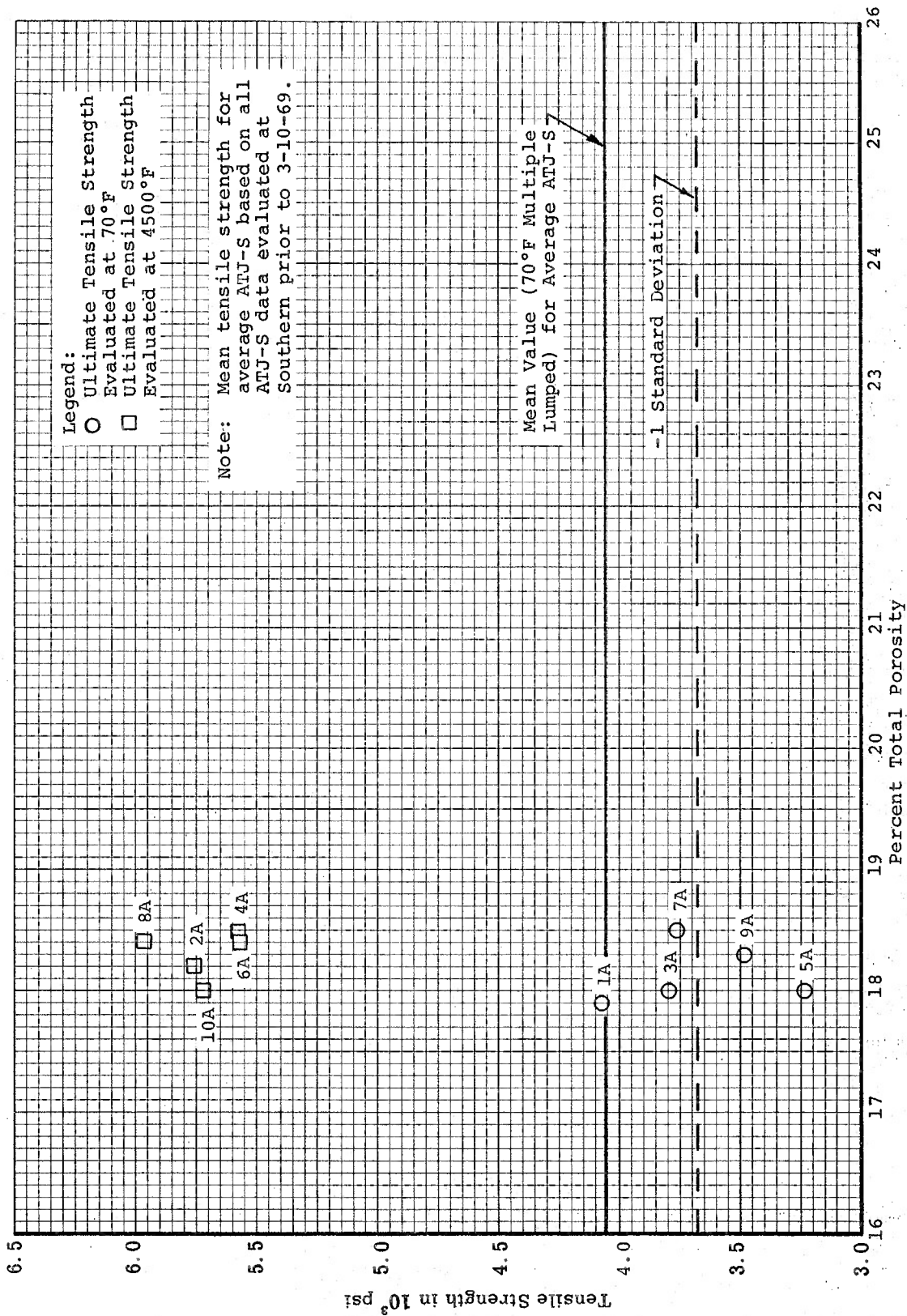


Figure 171. Tensile Strength versus Percent Total Porosity for ATJ-S Billet L-10-6 Across Grain at 70°F and 4500°F



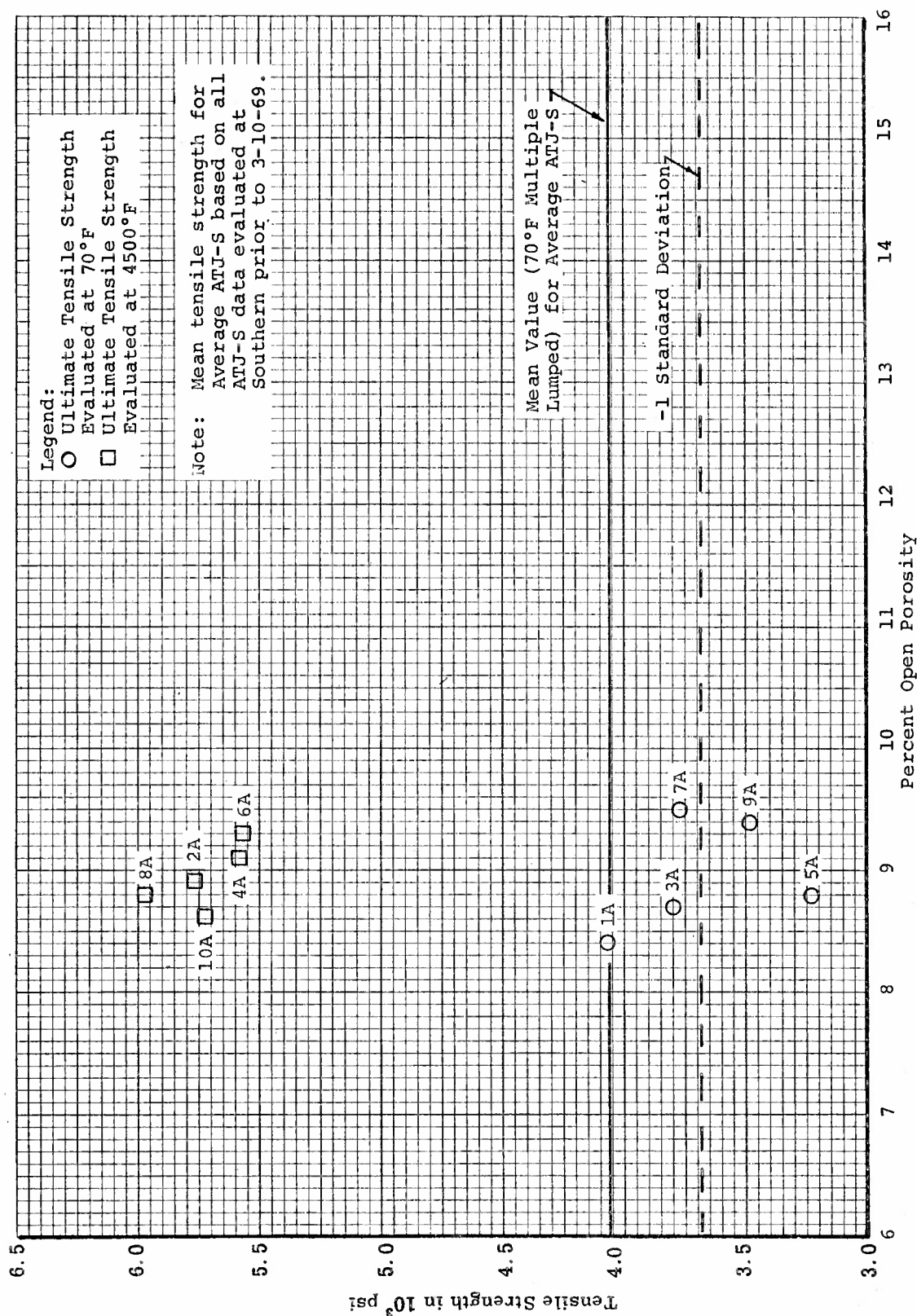


Figure 172. Tensile Strngth versus Percent Open Porosity for ATJ-S Billet L-10-6 Across Grain at 70°F and 4500°F

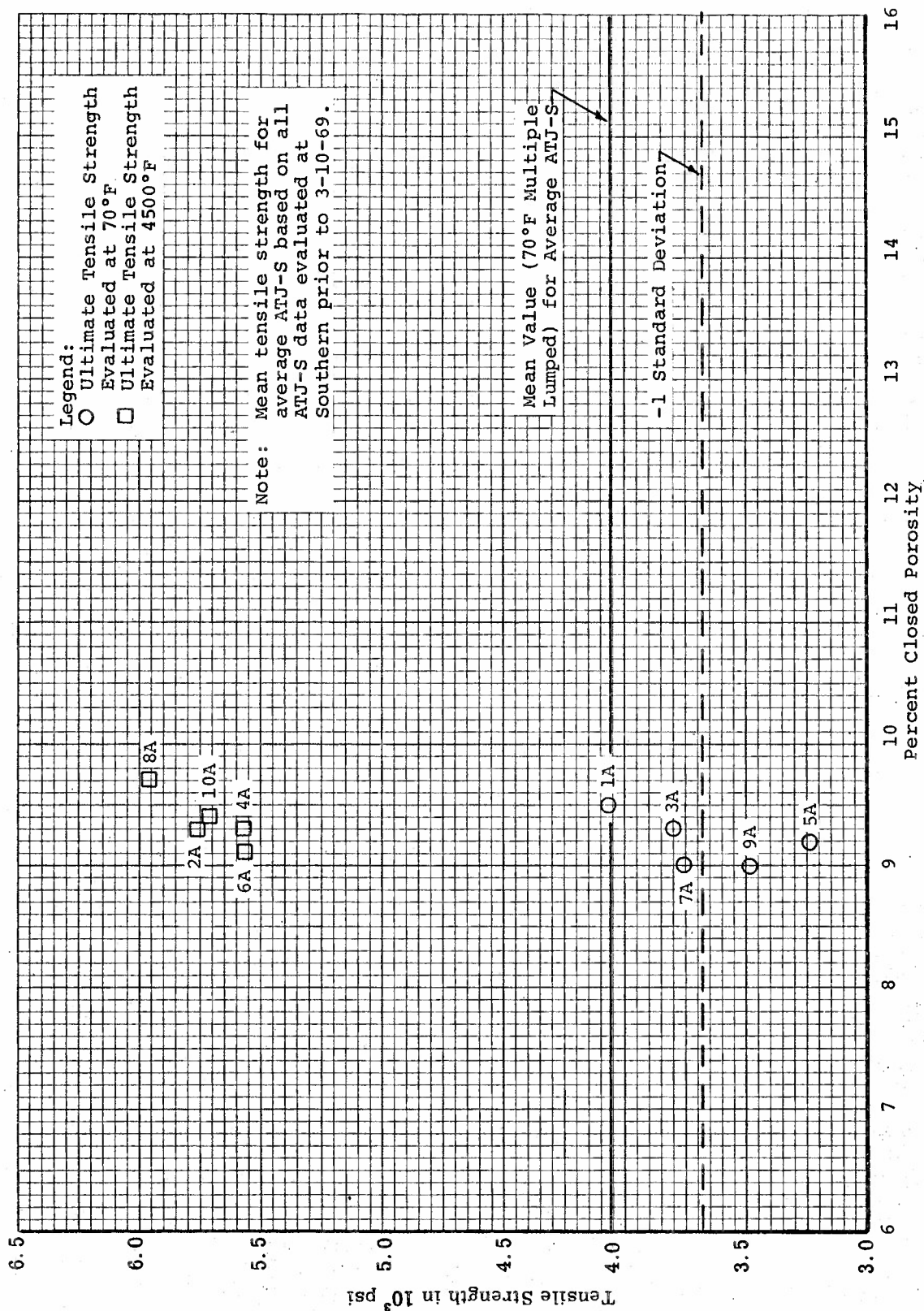


Figure 173. Tensile Strength versus Percent Closed Porosity for ATJ-S Billet L-10-6 Across Grain at 70°F and 4500°F

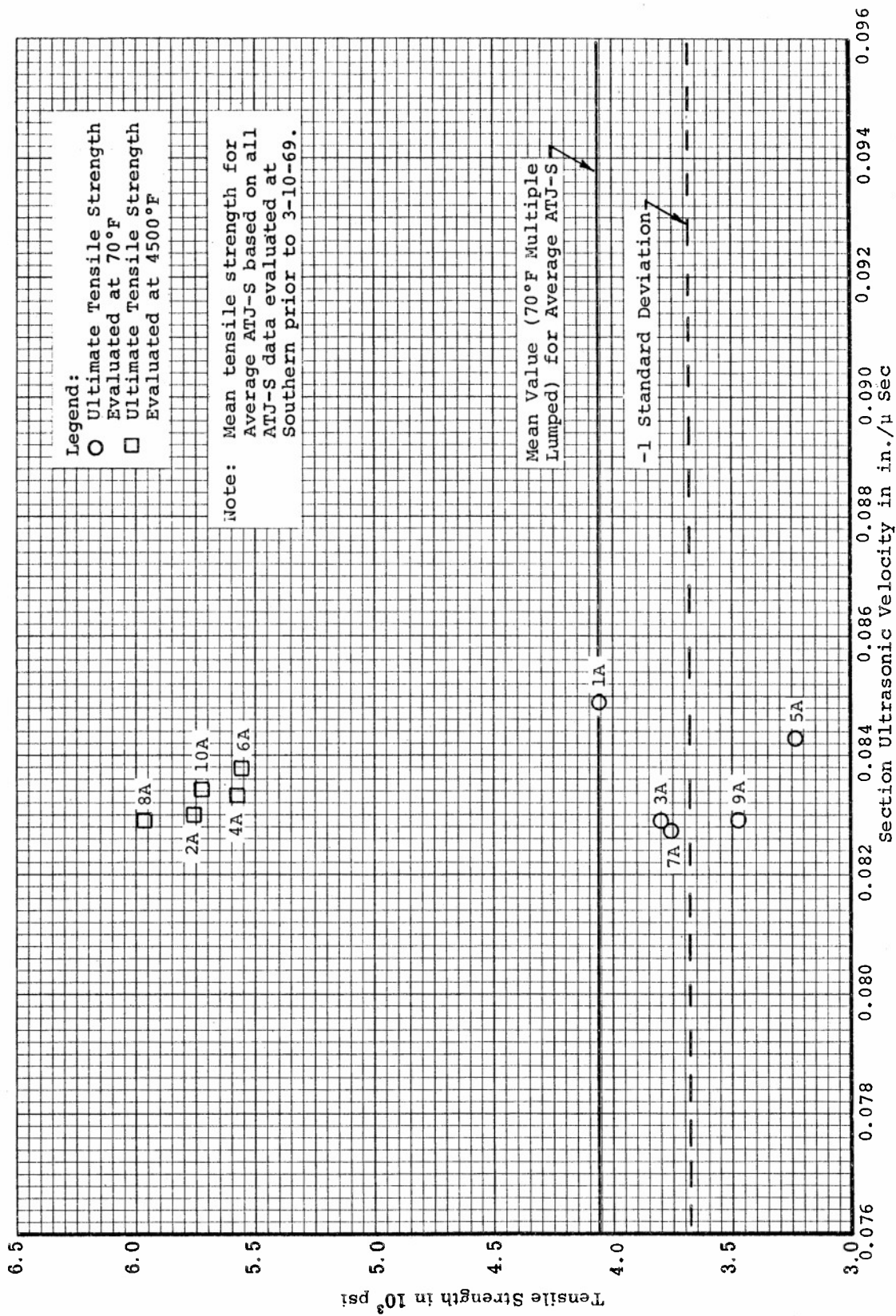


Figure 174. Tensile Strength versus Section Ultrasonic Velocity for ATJ-S Billet L-10-6 Across Grain at 70°F and 4500°F

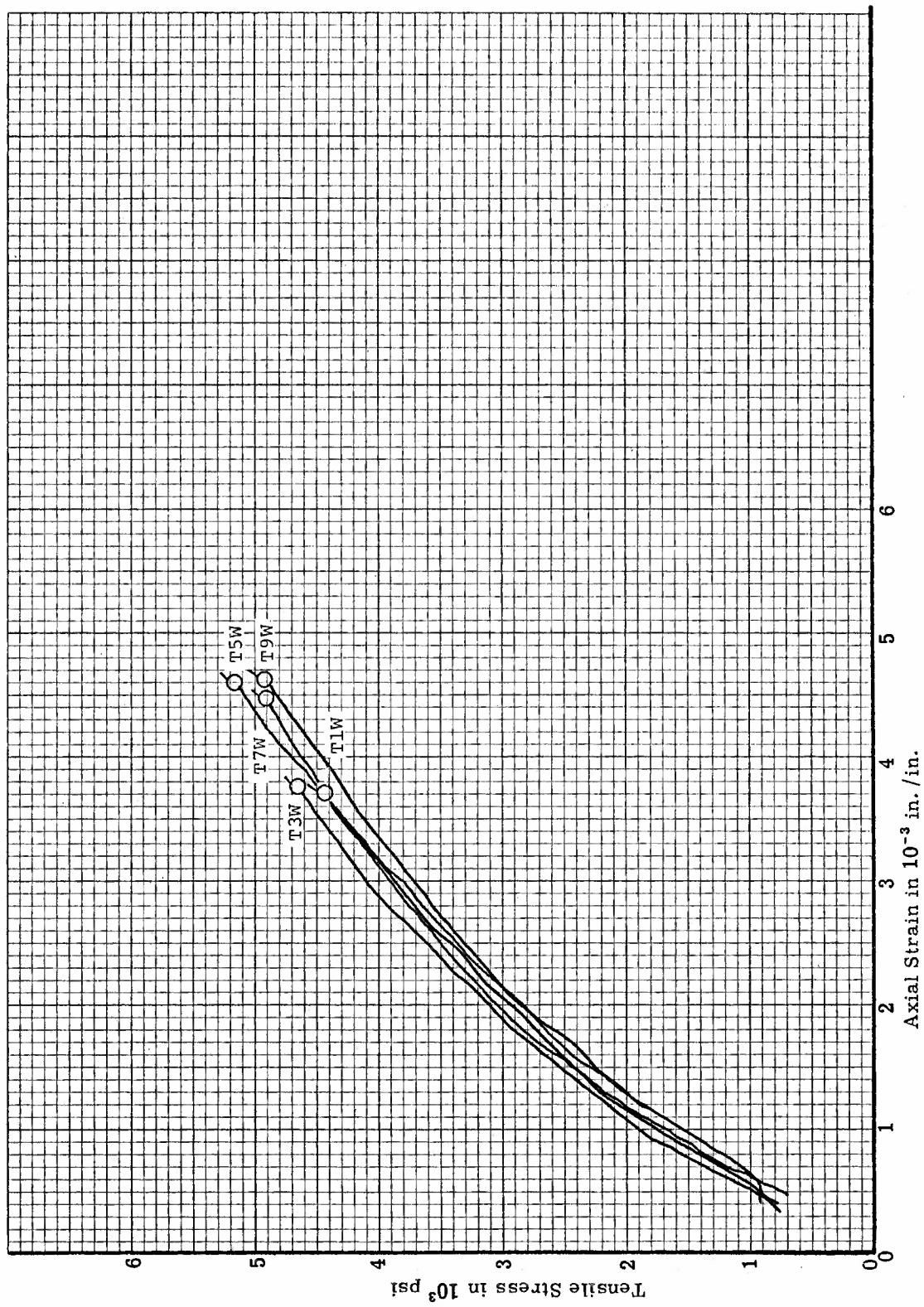


Figure 175. Tensile Stress-Strain Curves for ATJ-S Billet L-11-4 With Grain at 70°F

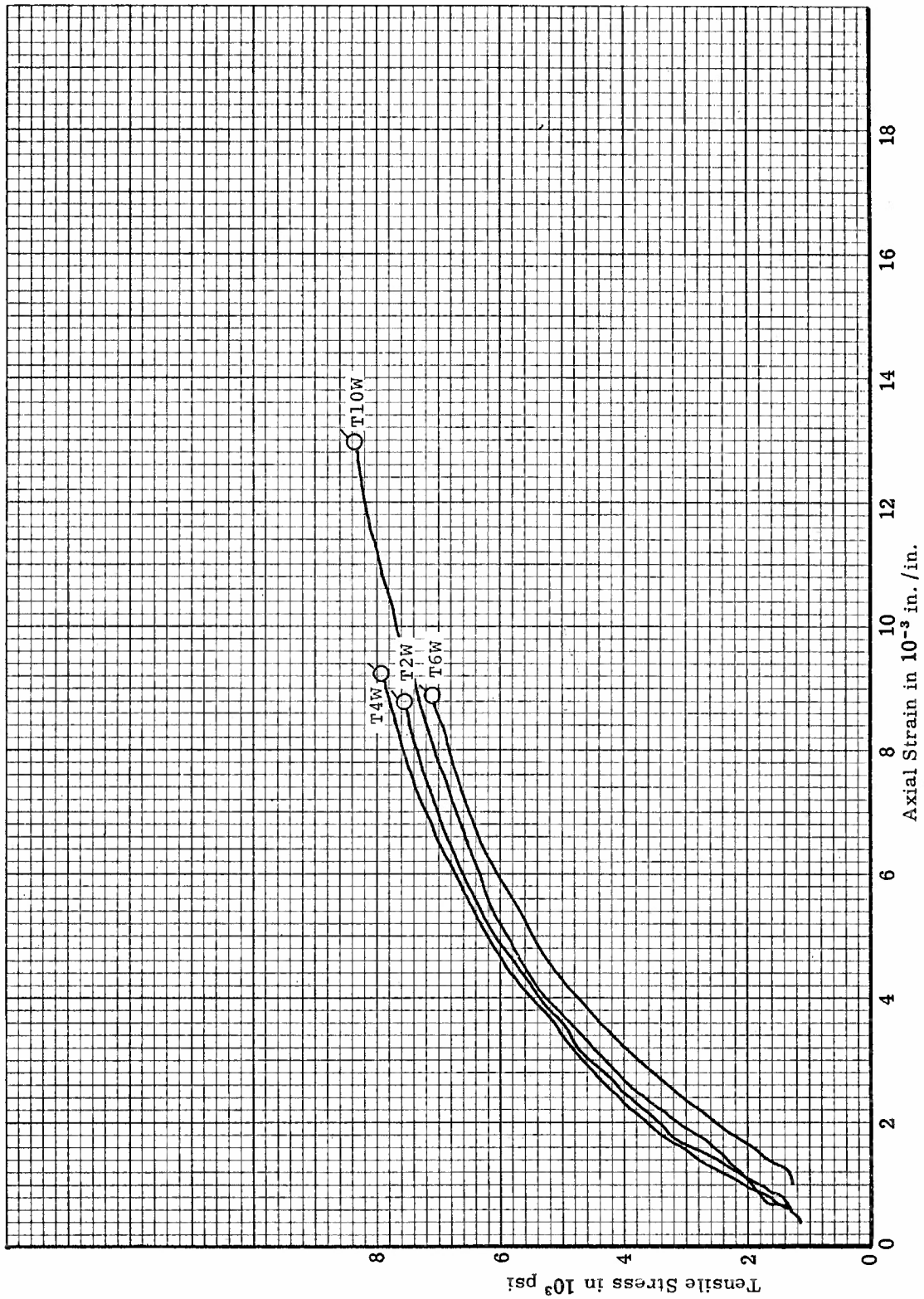


Figure 176. Tensile Stress-Strain Curves for ATJ-S Billet L-11-4 With Grain at 4500°F

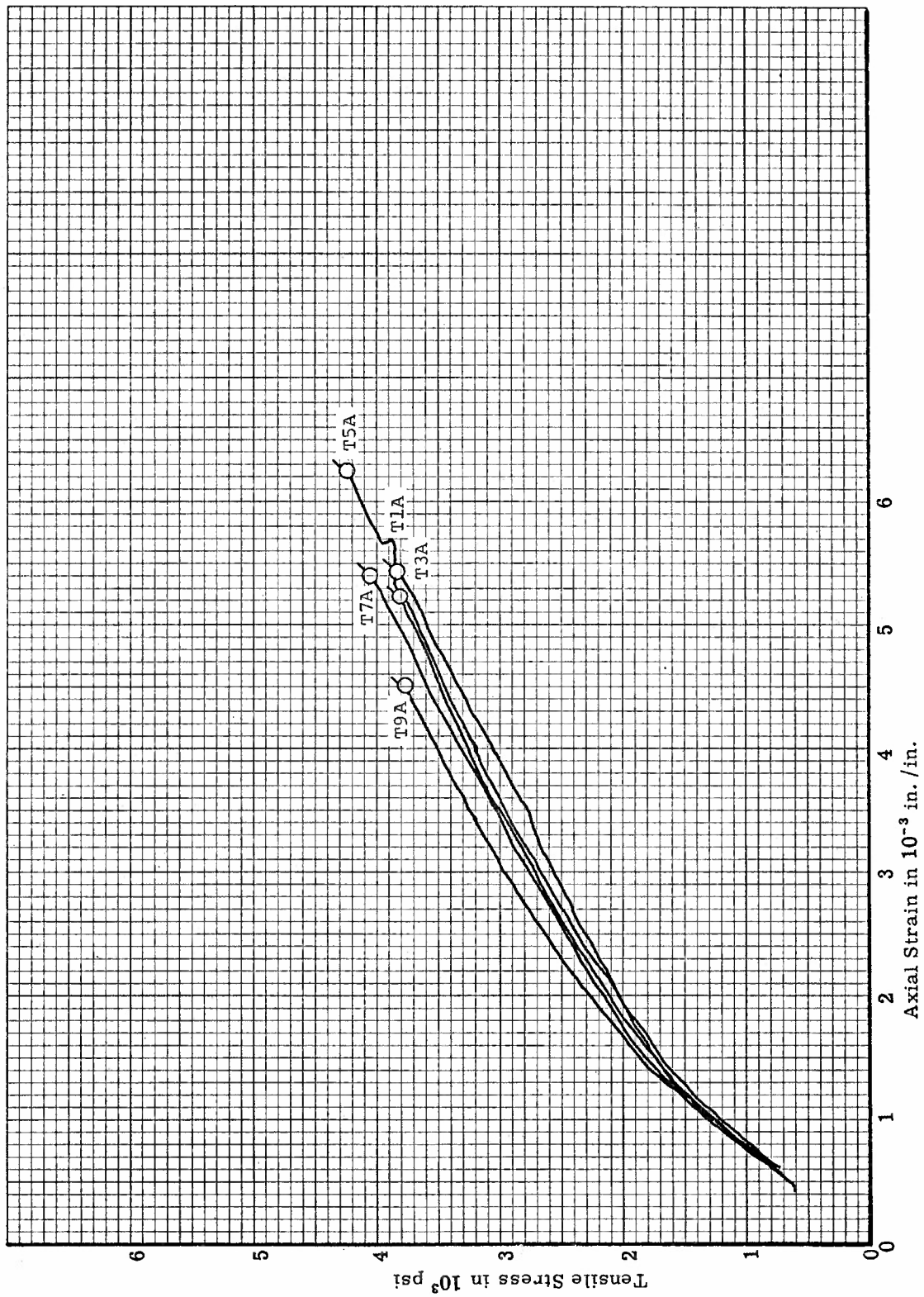


Figure 177. Tensile Stress-Strain Curves for ATJ-S Billet L-11-4 Across Grain at 70°F



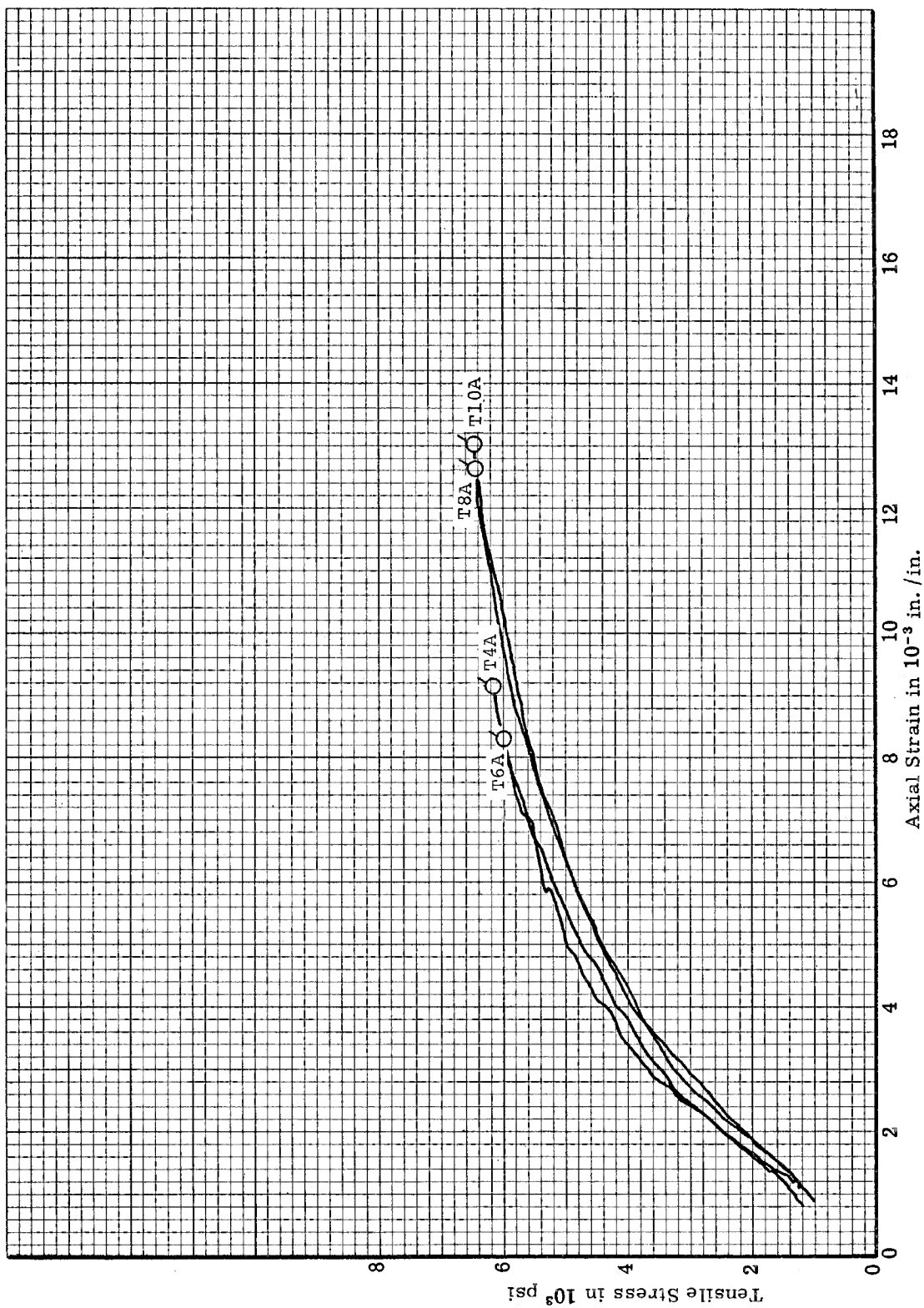


Figure 178. Tensile Stress-Strain Curves for ATJ-S Billet L-11-4 Across Grain at 4500°F

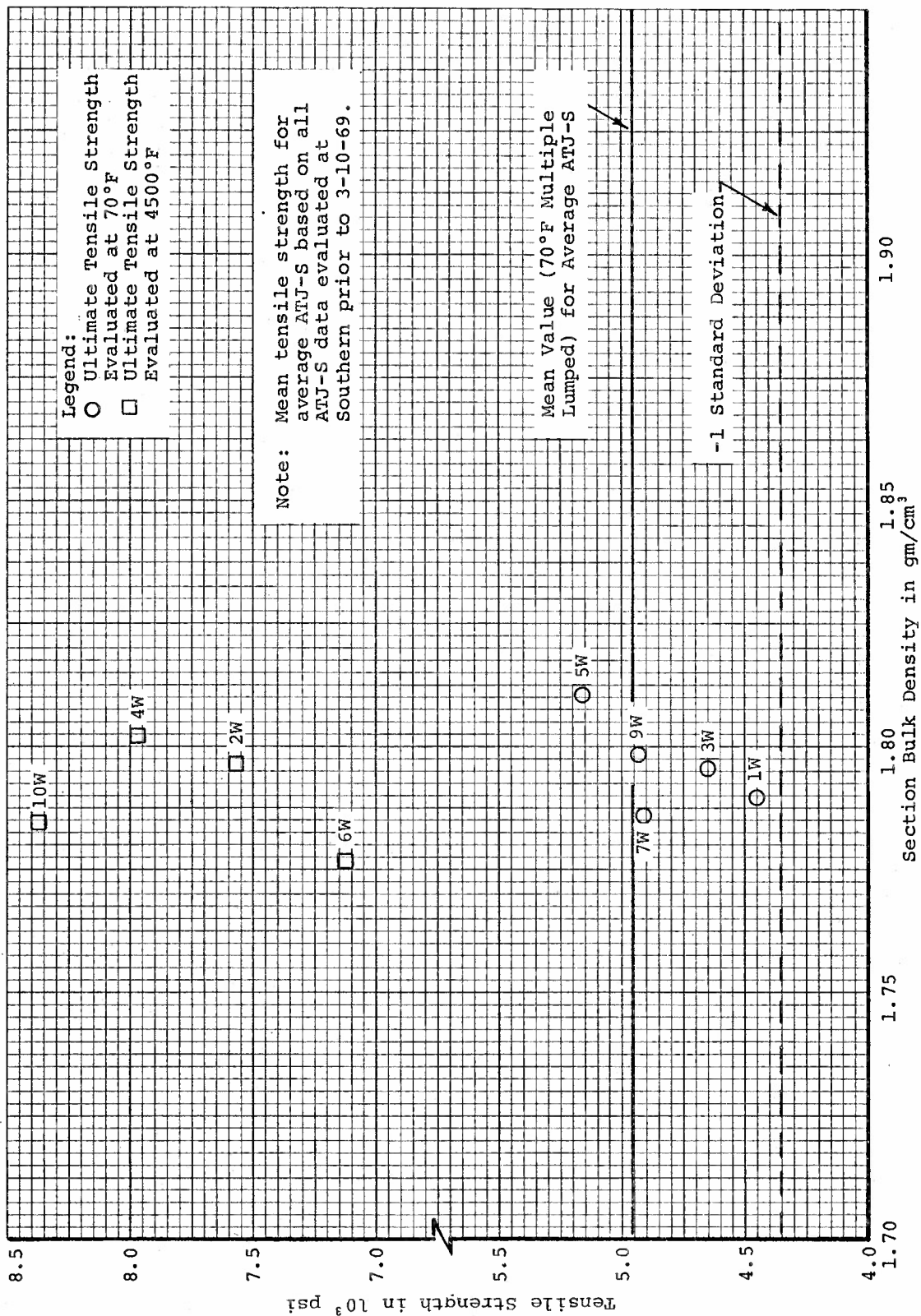


Figure 179. Tensile Strength versus Section Bulk Density for ATJ-S Billet L-11-4 With Grain at 70°F and 4500°F



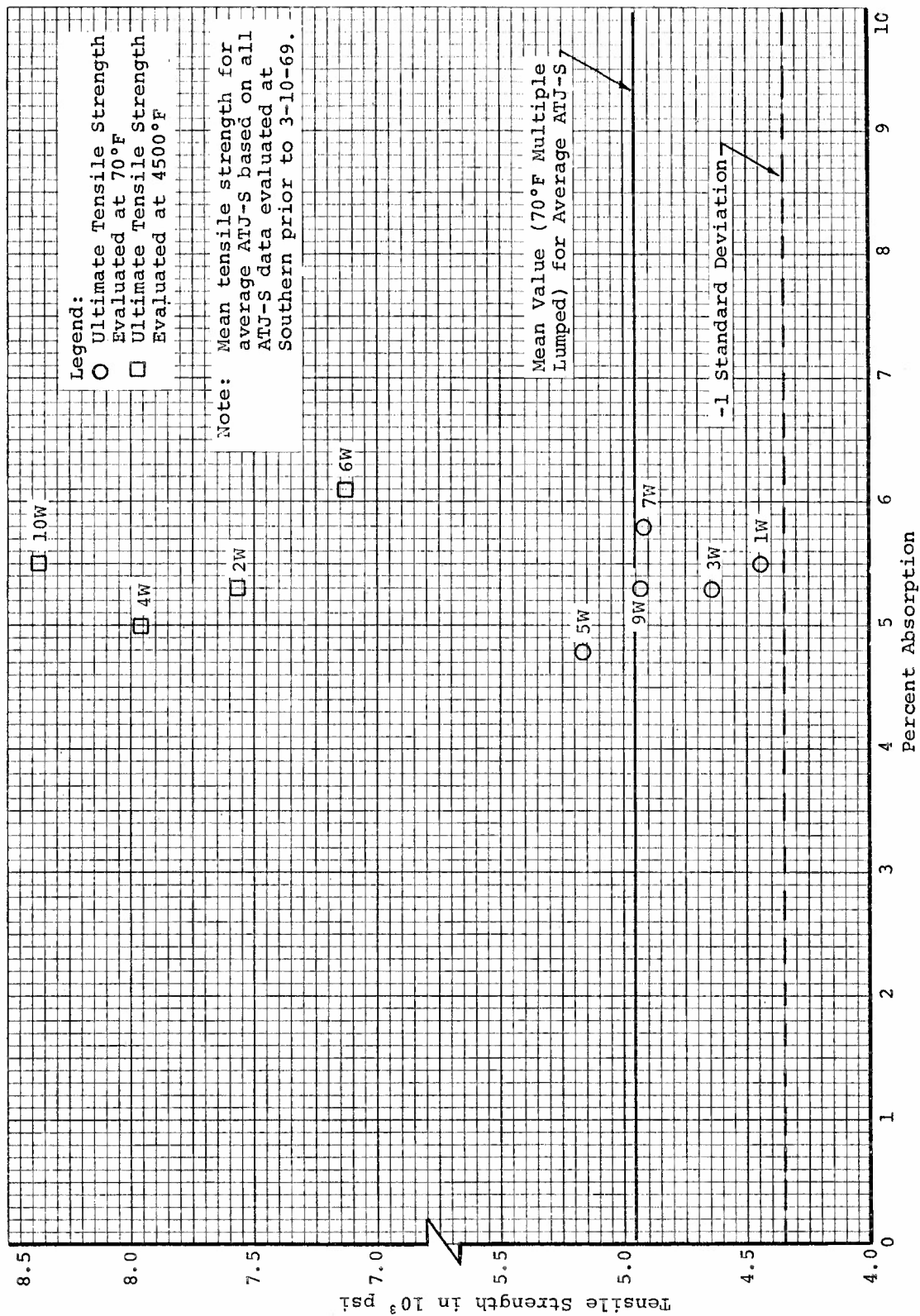


Figure 180. Tensile Strength versus Percent Absorption for ATJ-S Billet L-11-4 With Grain at 70°F and 4500°F

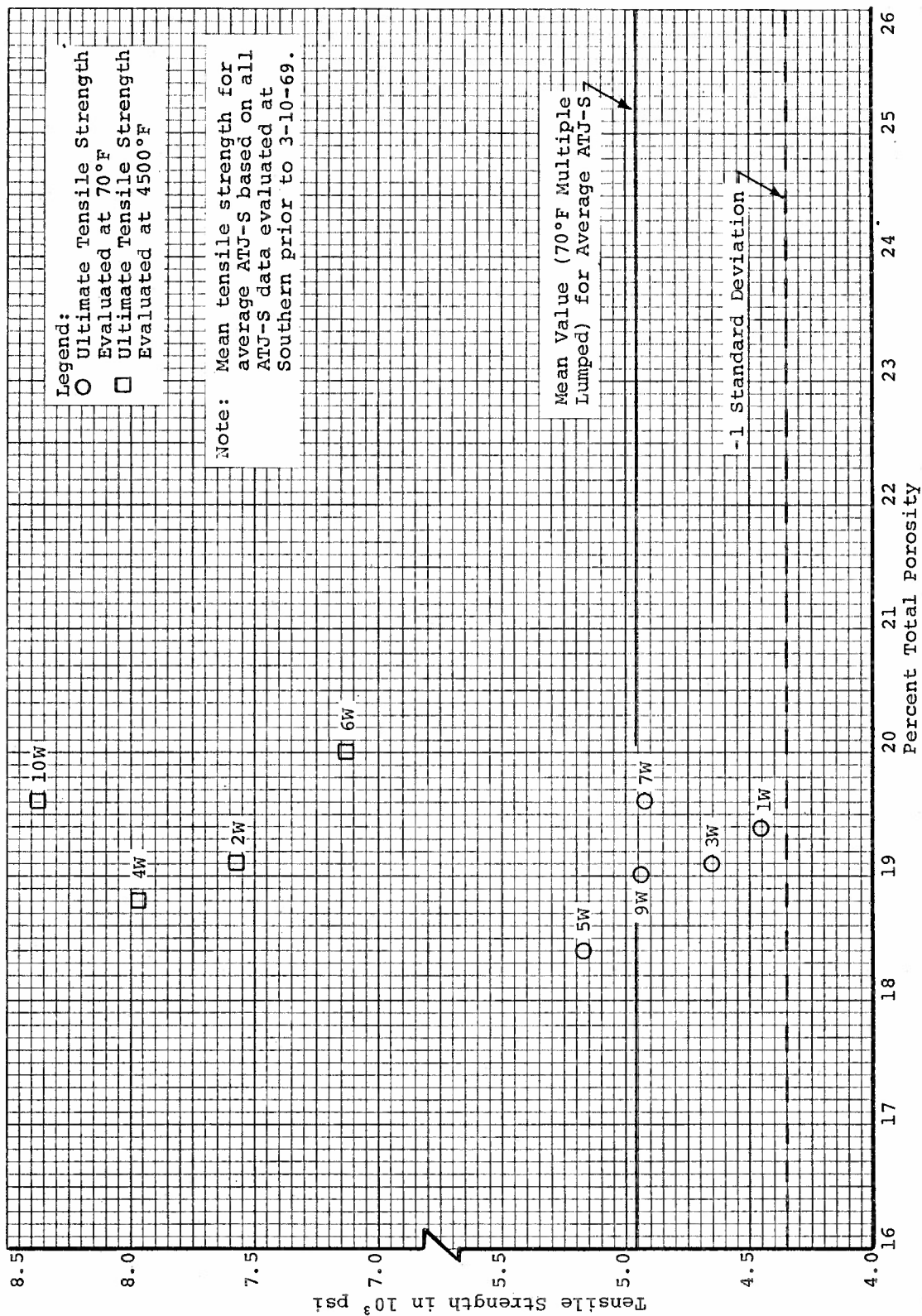


Figure 181. Tensile Strength versus Percent Total Porosity for ATJ-S Billet L-11-4 With Grain at 70°F and 4500°F

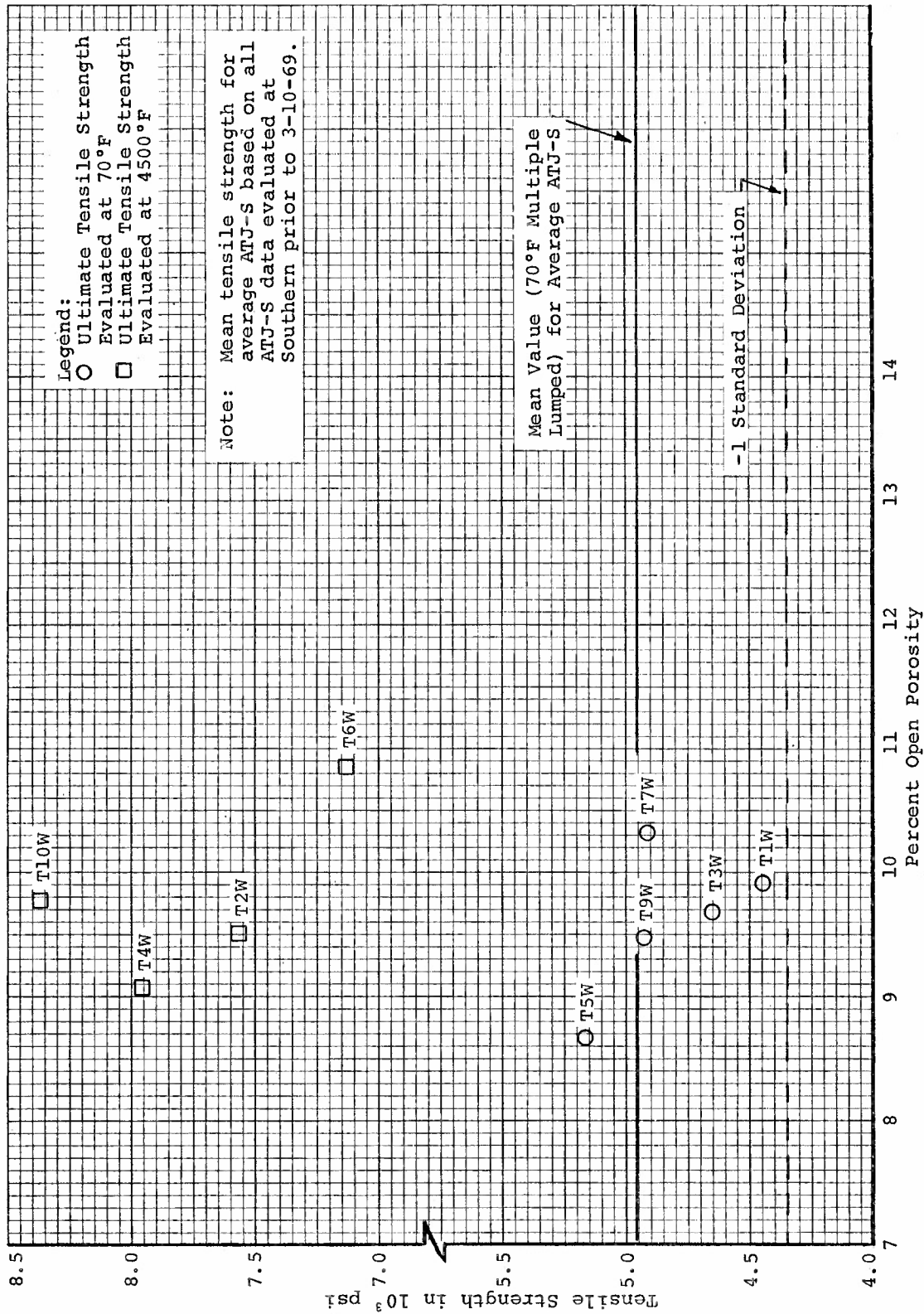


Figure 182. Tensile Strength versus Percent Open Porosity for ATJ-S Billet L-11-4 With Grain at 70°F and 4500°F

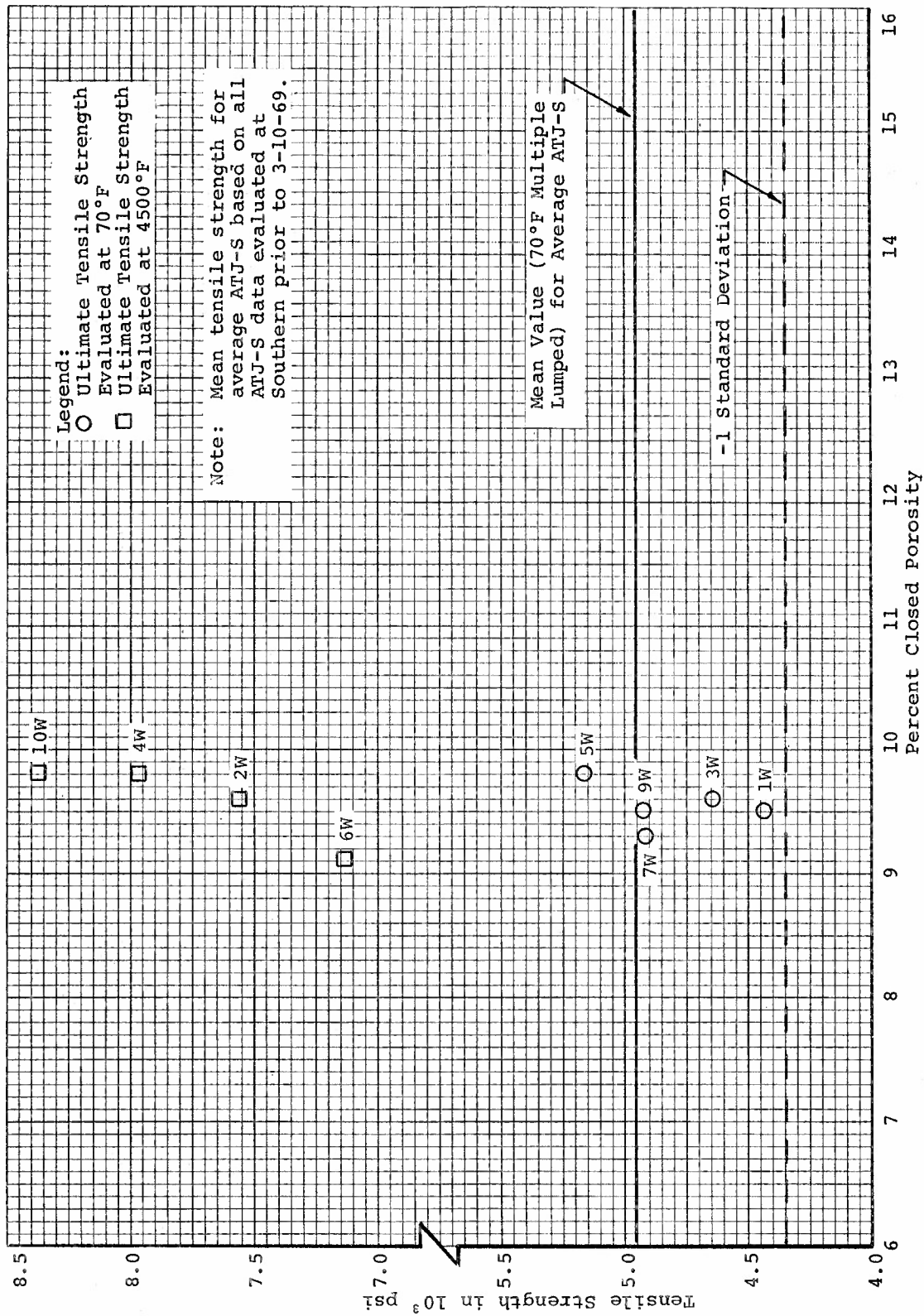


Figure 183. Tensile Strength versus Percent Closed Porosity for ATJ-S Billet I-11-4 With Grain at 70°F and 4500°F

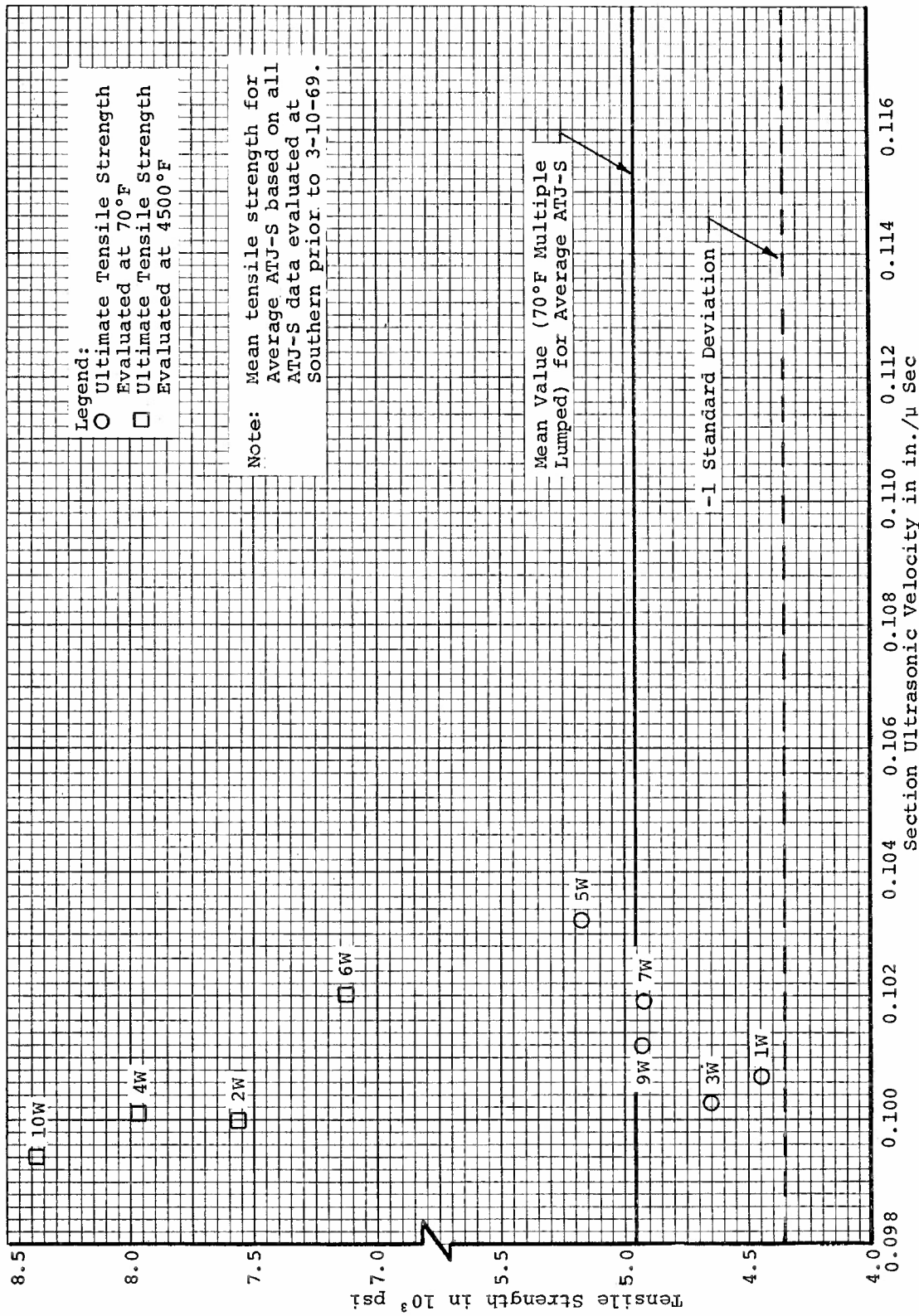


Figure 184. Tensile Strength versus Section Ultrasonic Velocity for ATJ-S Billet L-11-4 With Grain at 70°F and 4500°F

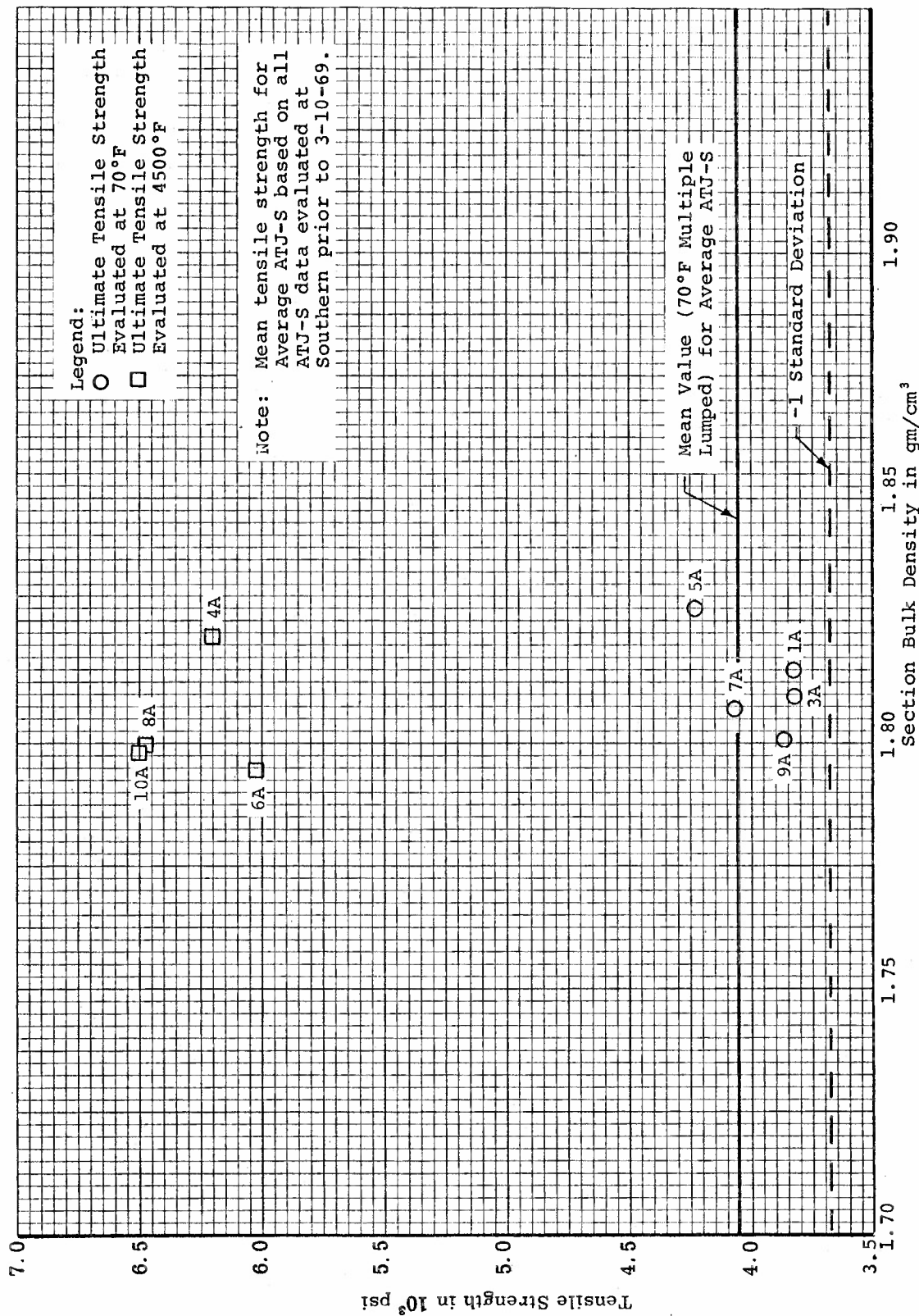


Figure 185. Tensile Strength versus Section Bulk Density for ATJ-S Billet L-11-4 Across Grain at 70°F and 4500°F



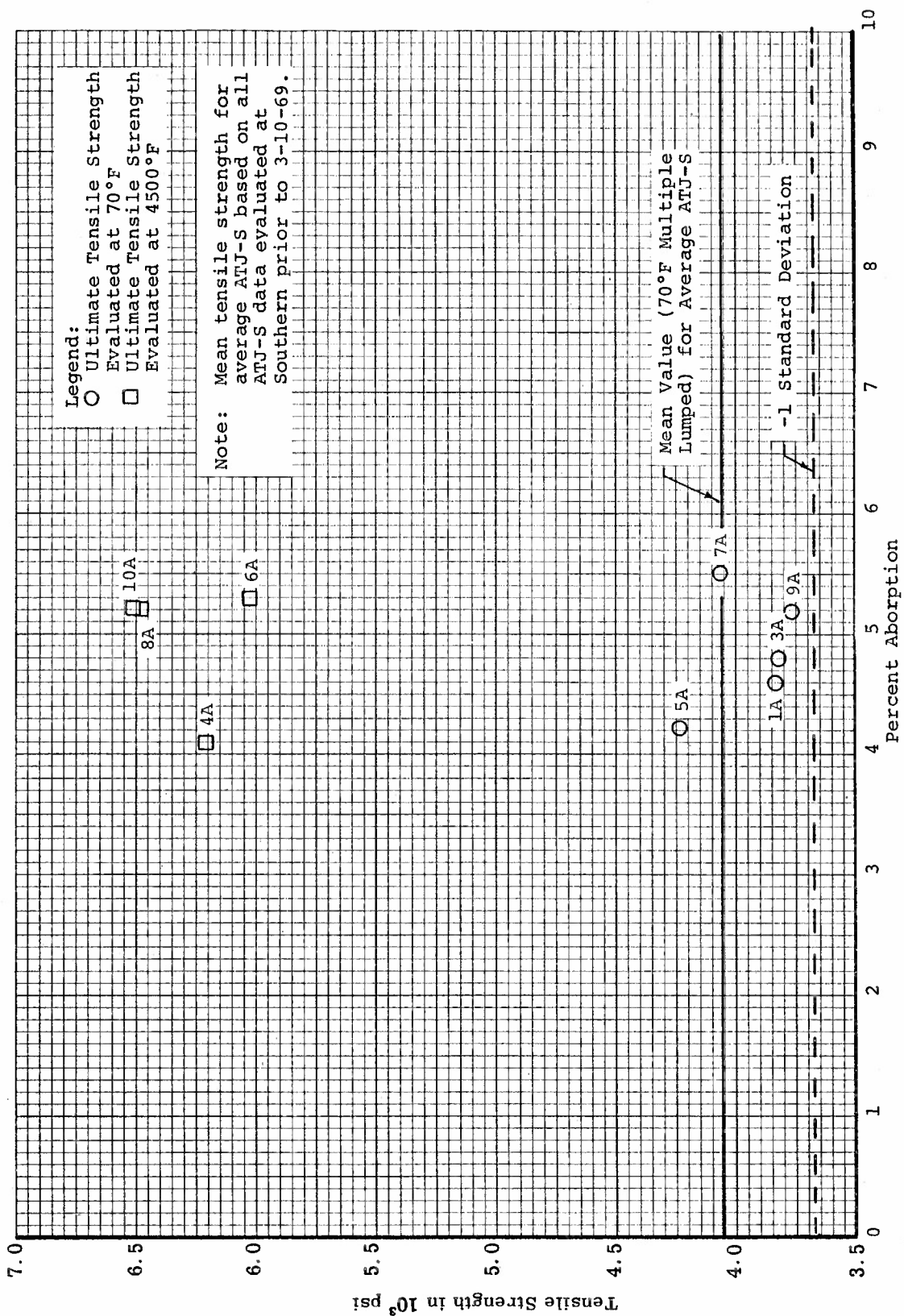


Figure 186. Tensile Strength versus Percent Absorption for ATJ-S Billet L-11-4 Across Grain at 70°F and 4500°F

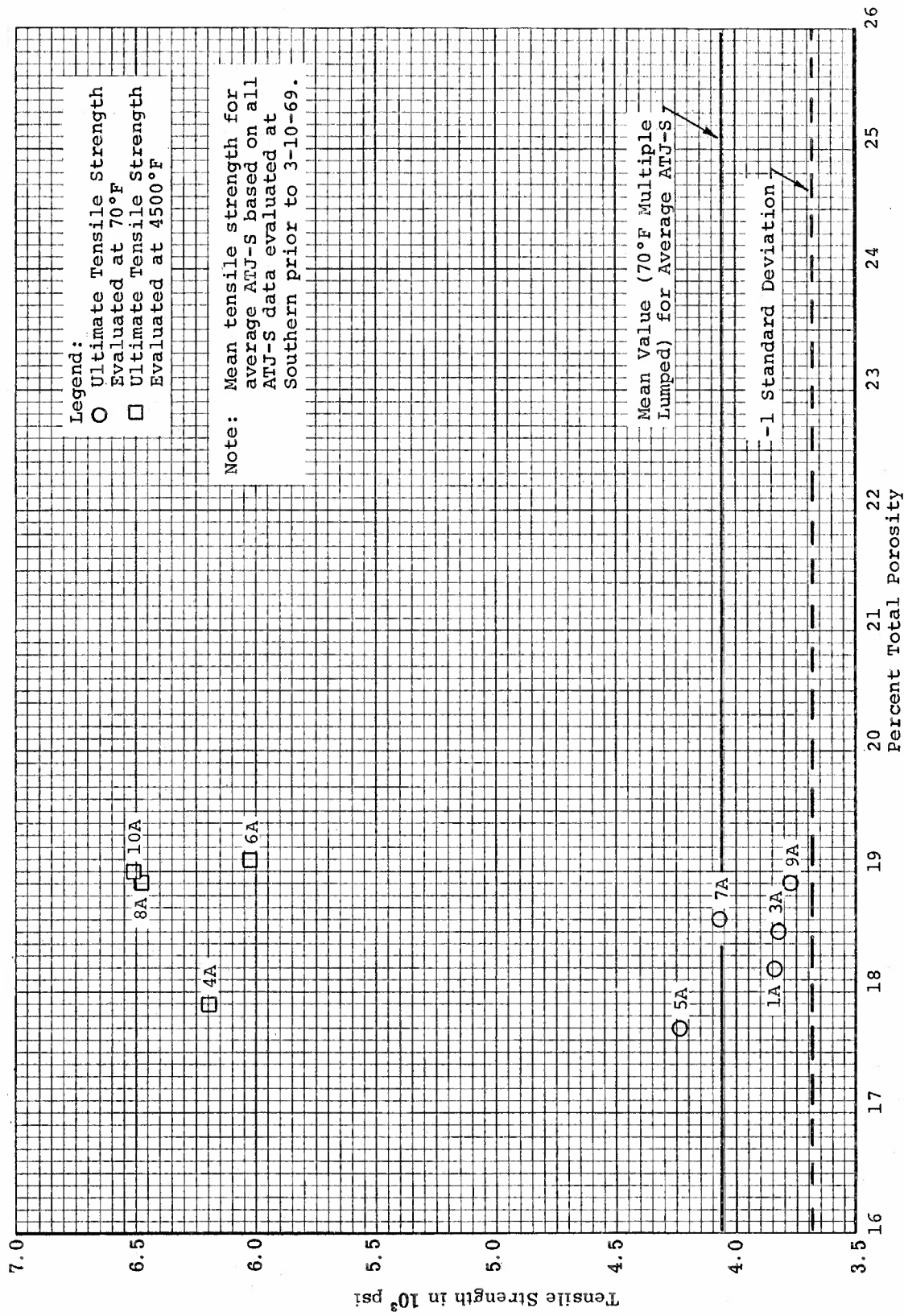


Figure 187. Tensile Strength versus Percent Total Porosity for ATJ-S Billet I-11-4 Across Grain at 70°F and 4500°F



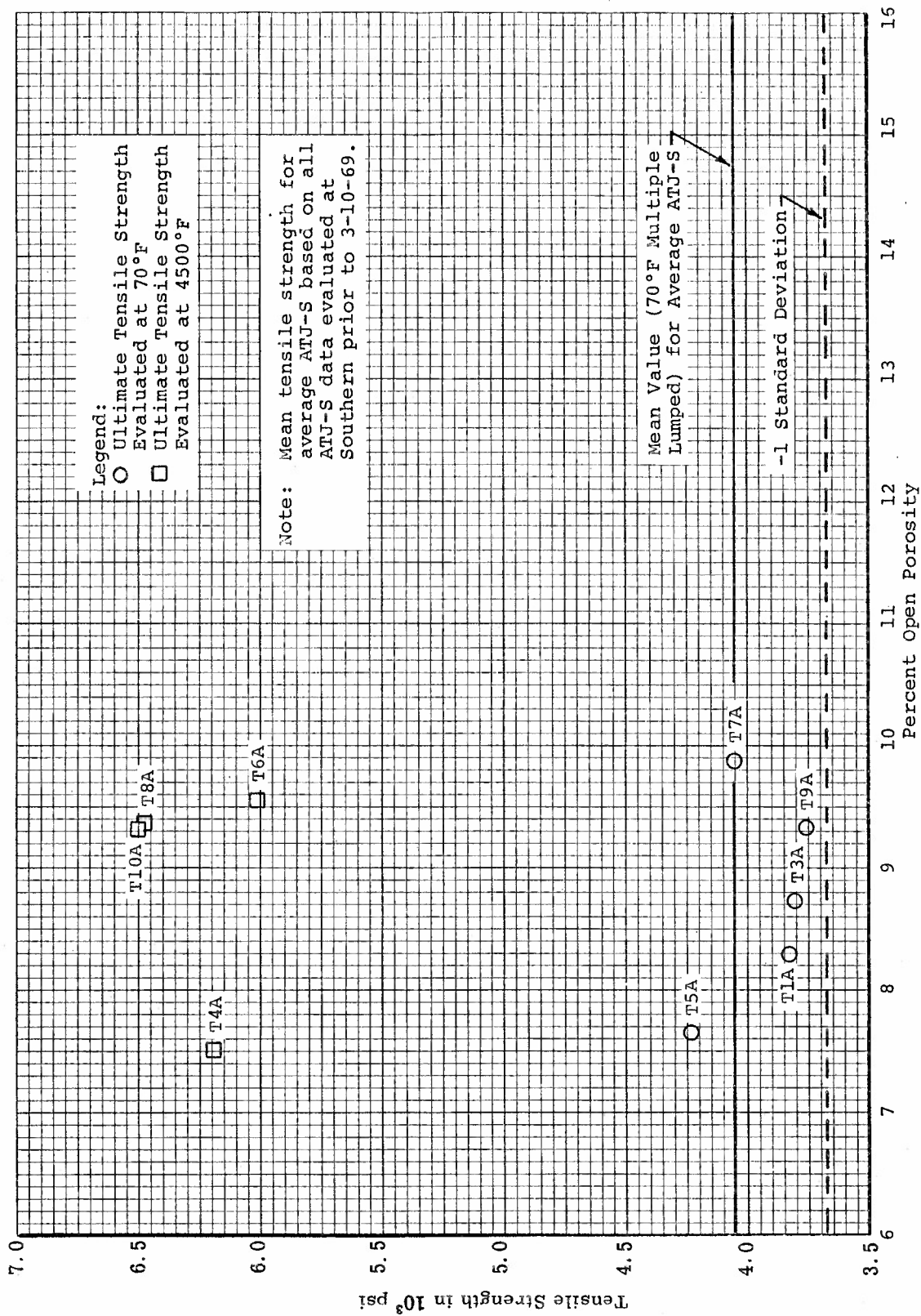


Figure 188. Tensile Strength versus Percent Open Porosity for ATJ-S Billet L-11-4 Across Grain at 70°F and 4500°F

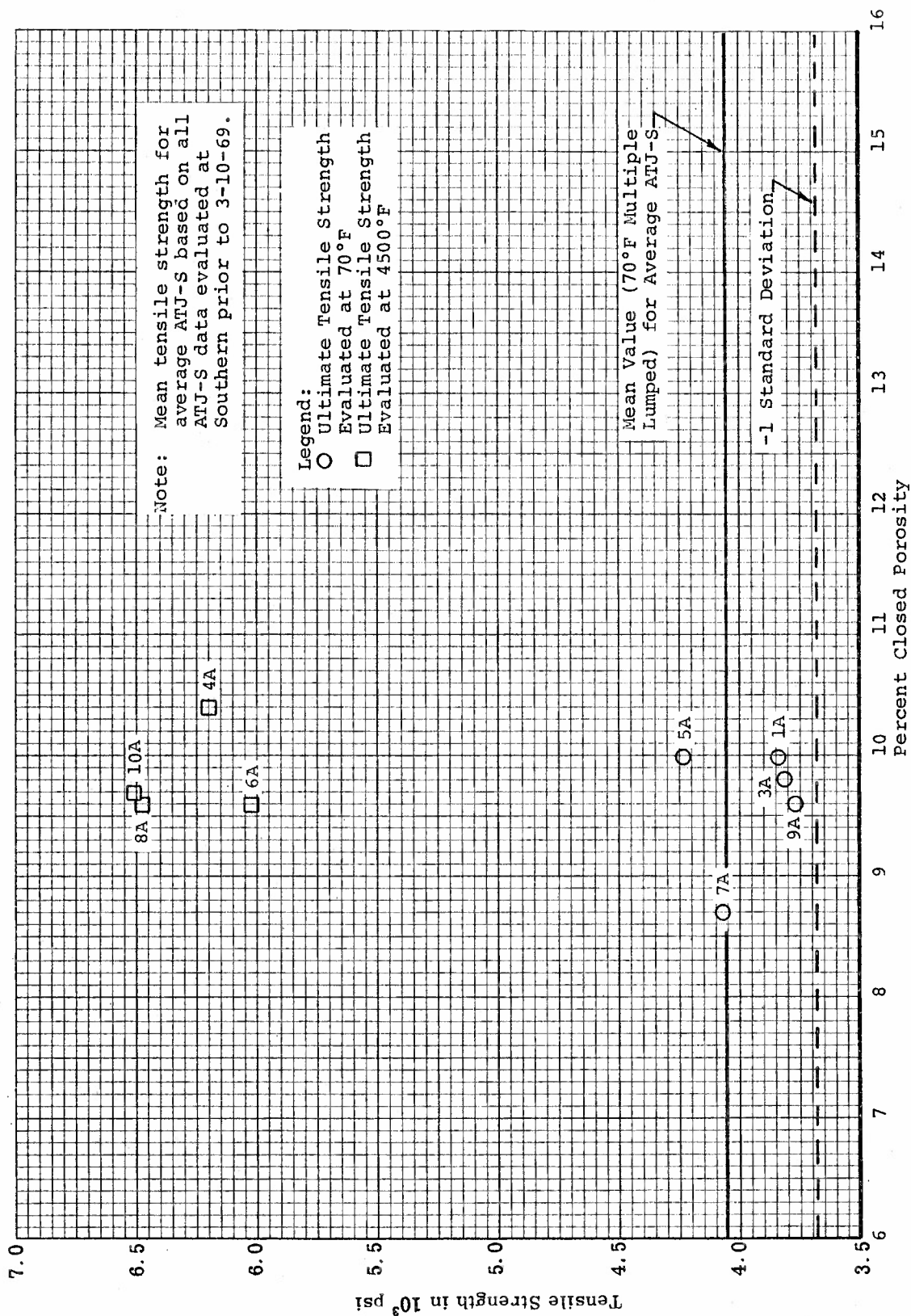


Figure 189. Tensile Strength versus Percent Closed Porosity for ATJ-S Billet L-11-4 Across Grain at 70°F and 4500°F

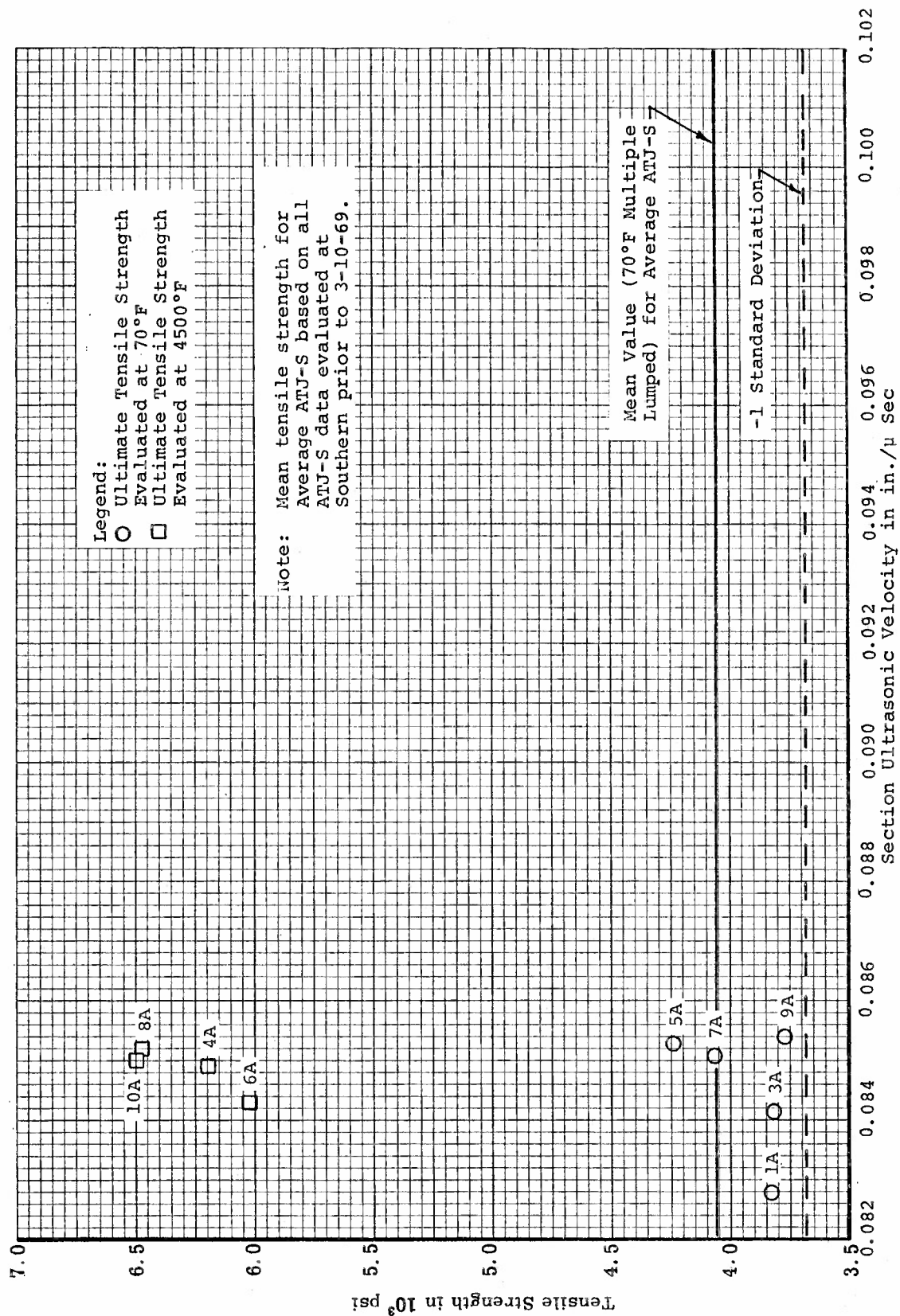


Figure 190. Tensile Strength versus Section Ultrasonic Velocity for ATJ-S Billet L-11-4 Across Grain at 70°F and 4500°F

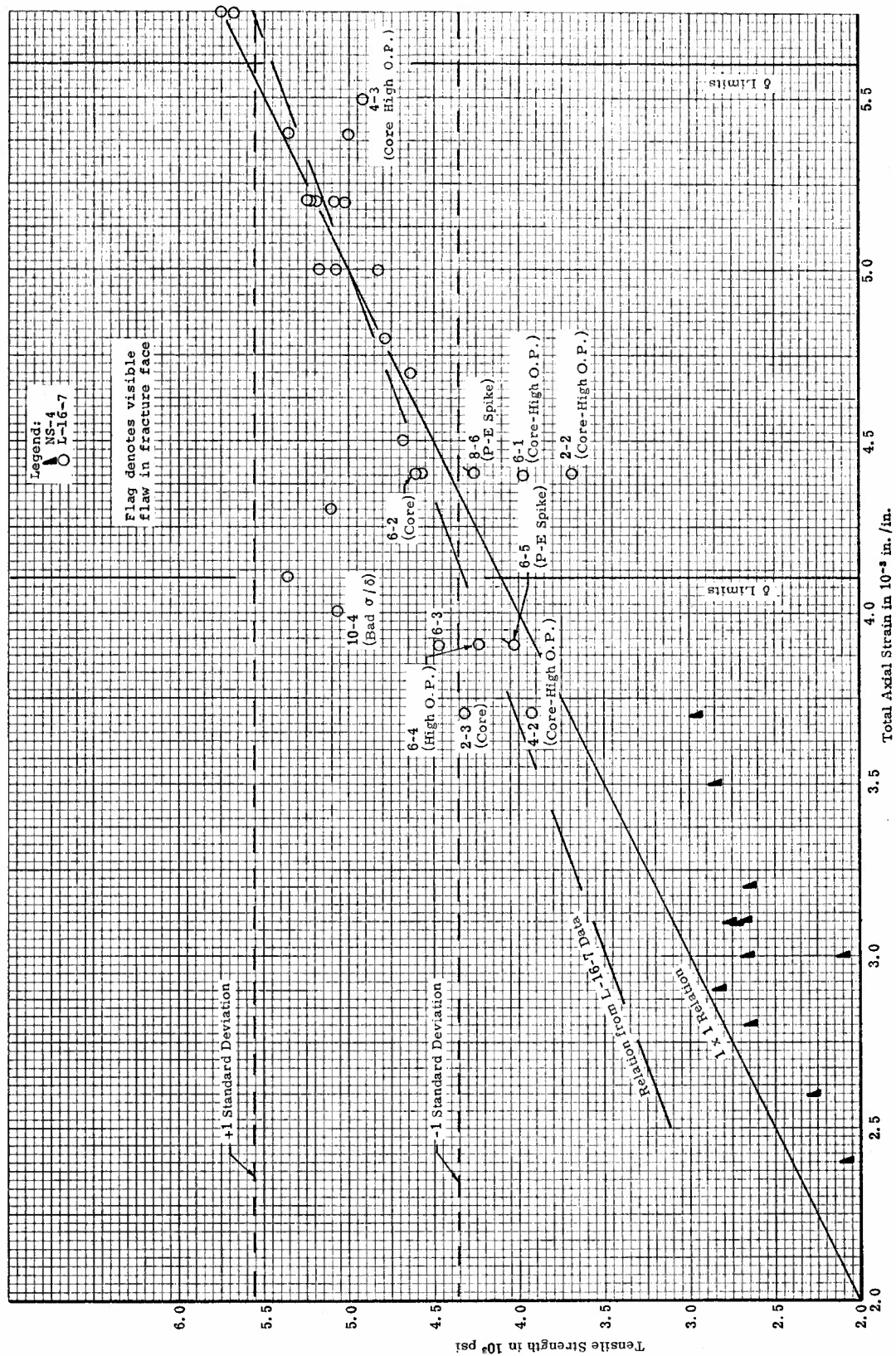


Figure 191. Tensile Strength versus Total Strain to Fracture for ATJ-S Billet L-16-7 and NS-4 Data With Grain at 70°F

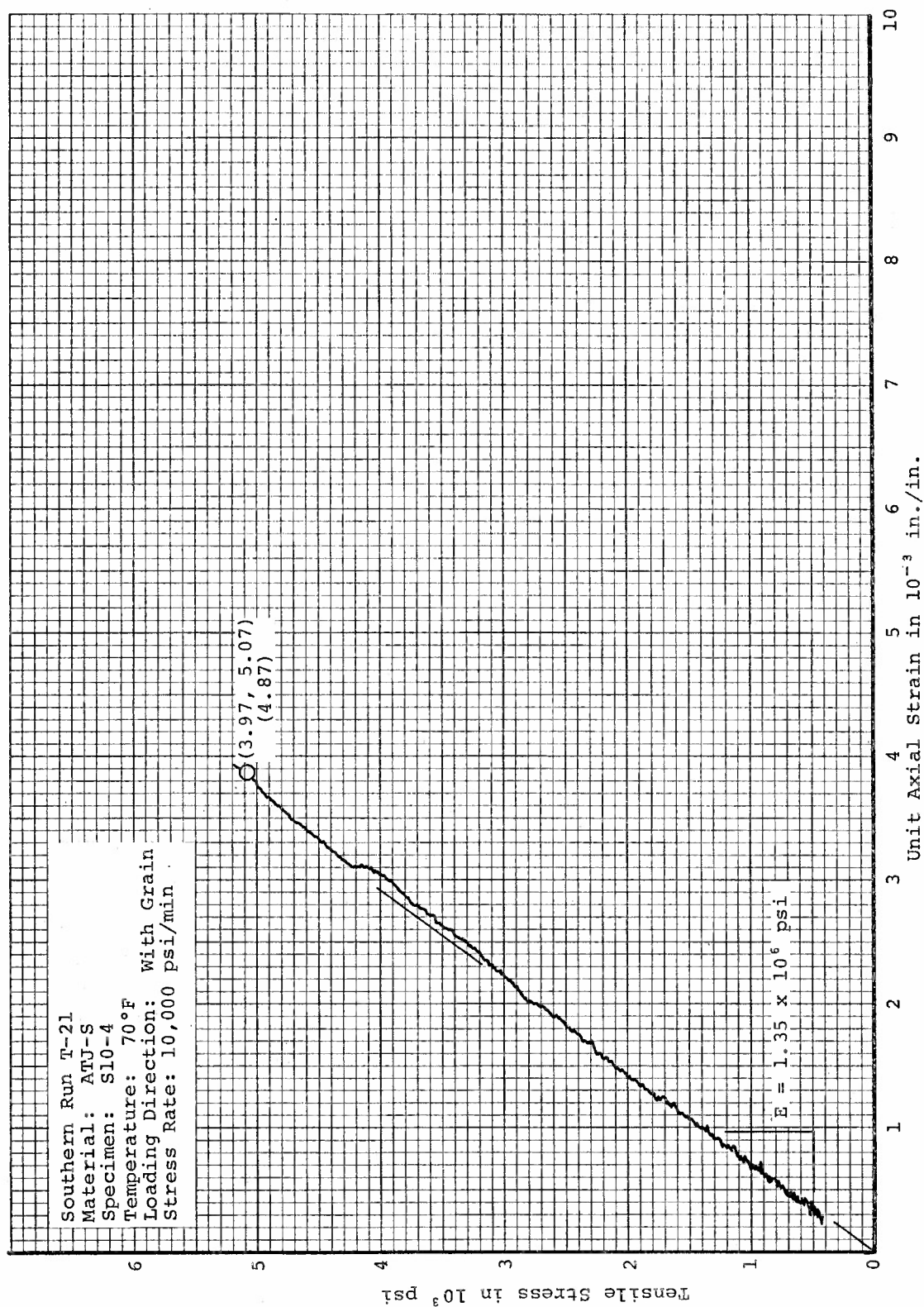


Figure 192. Tensile Stress-Strain Curve for Strain Disparate S10-4 from ATJ-S Billet L-16-7 Evaluated in the With Grain Direction at 70°F

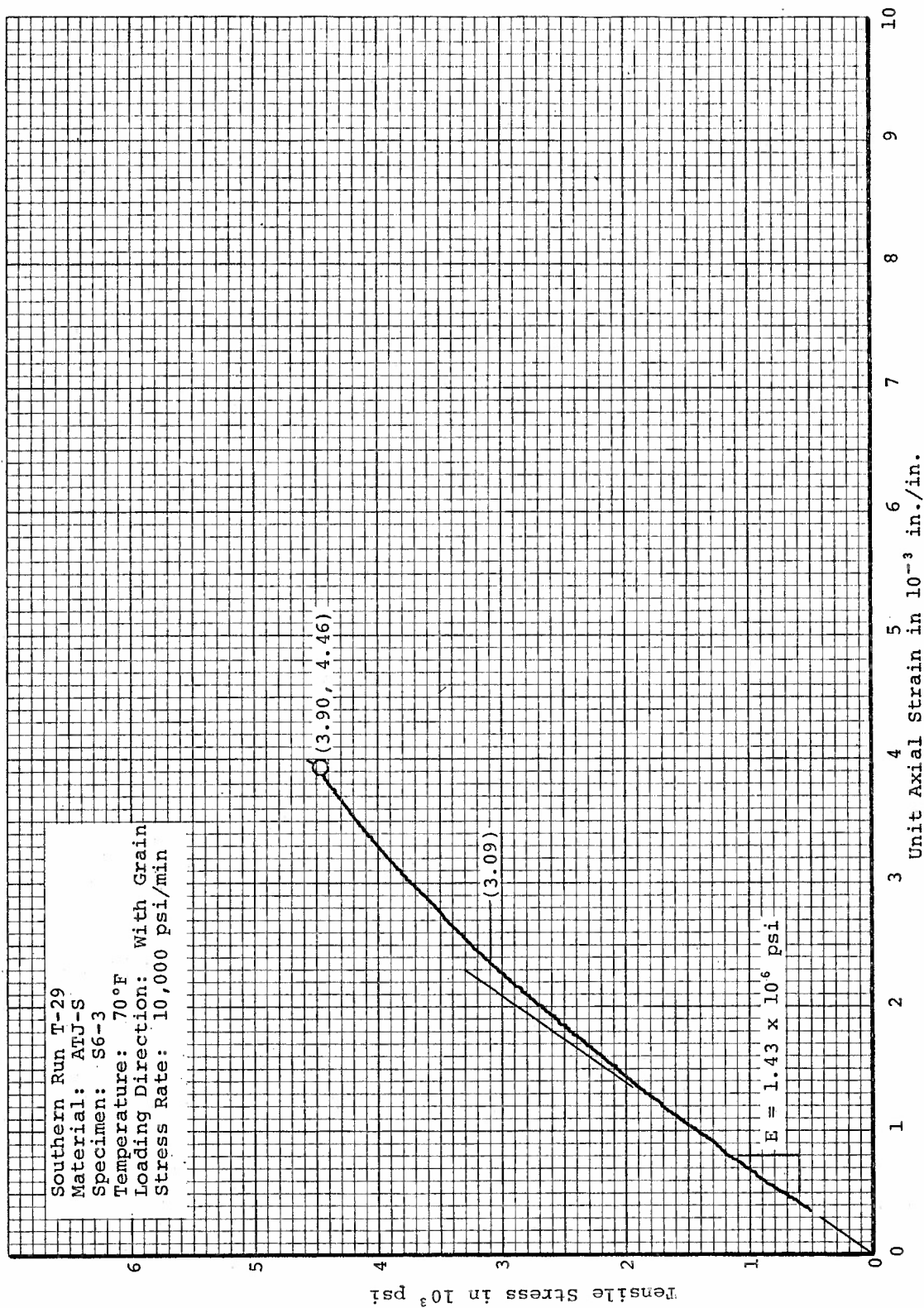


Figure 193. Tensile Stress-Strain Curve for Strain Disparate S6-3 From ATJ-S Billet L-16-7 Evaluated in the With Grain Direction at 70°F



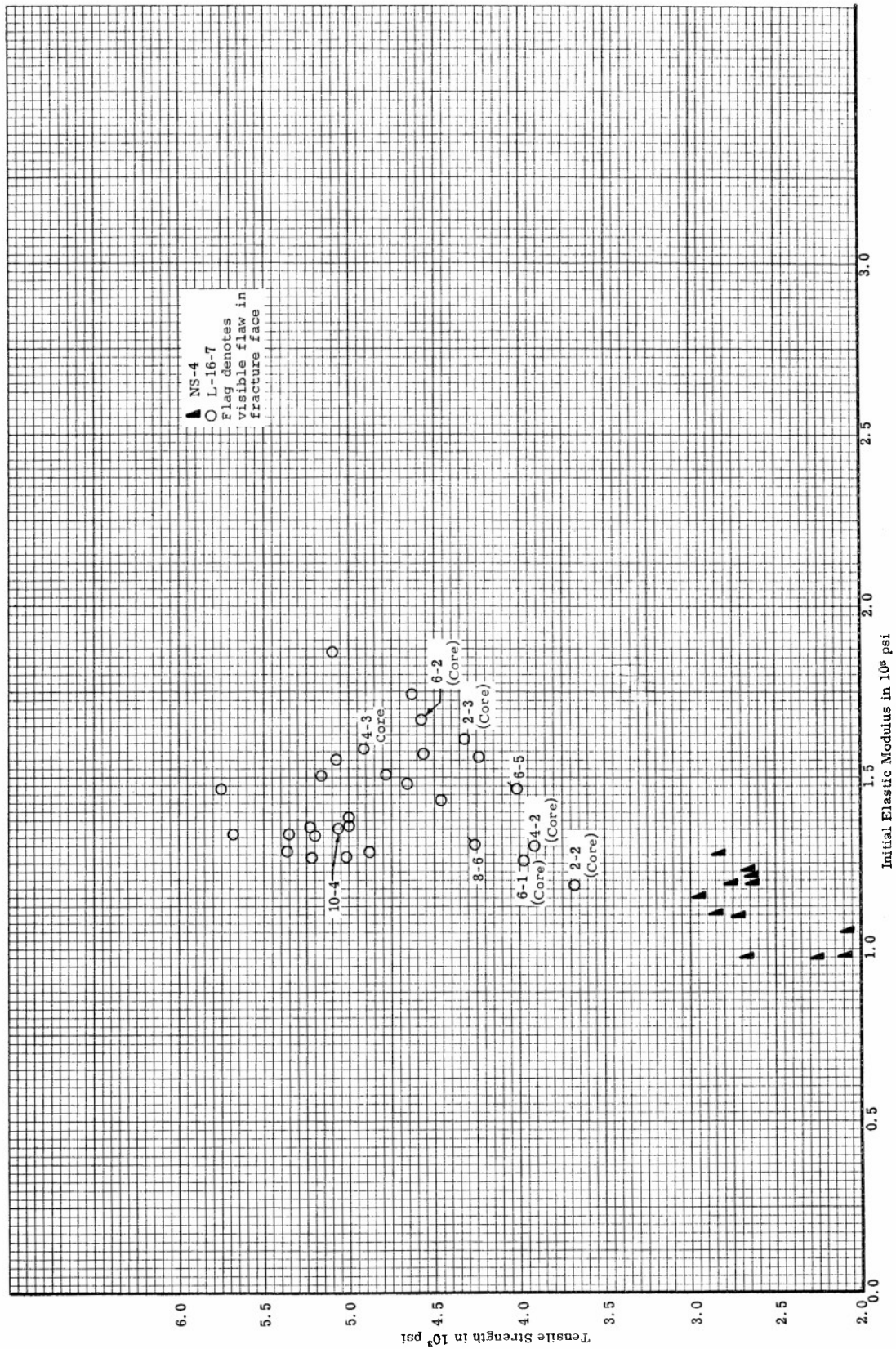


Figure 194. Tensile Strength versus Initial Elastic Modulus for ATJ-S Billet L-16-7 and NS-4 Data With Grain at 70°F

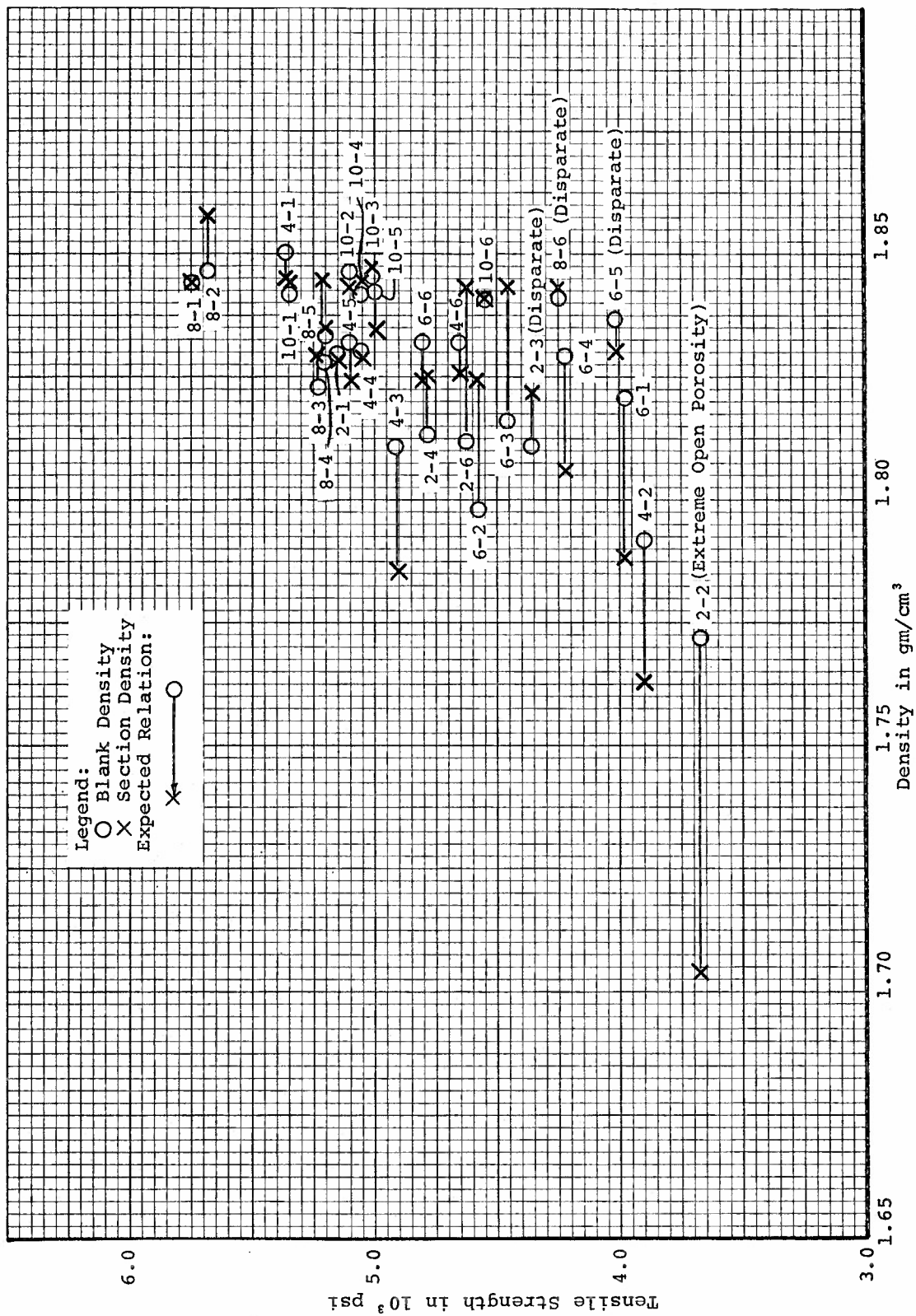


Figure 195. Tensile Strength versus Density (Blank and Section) for ATJ-S Billet L-16-7 With Grain at 70°F



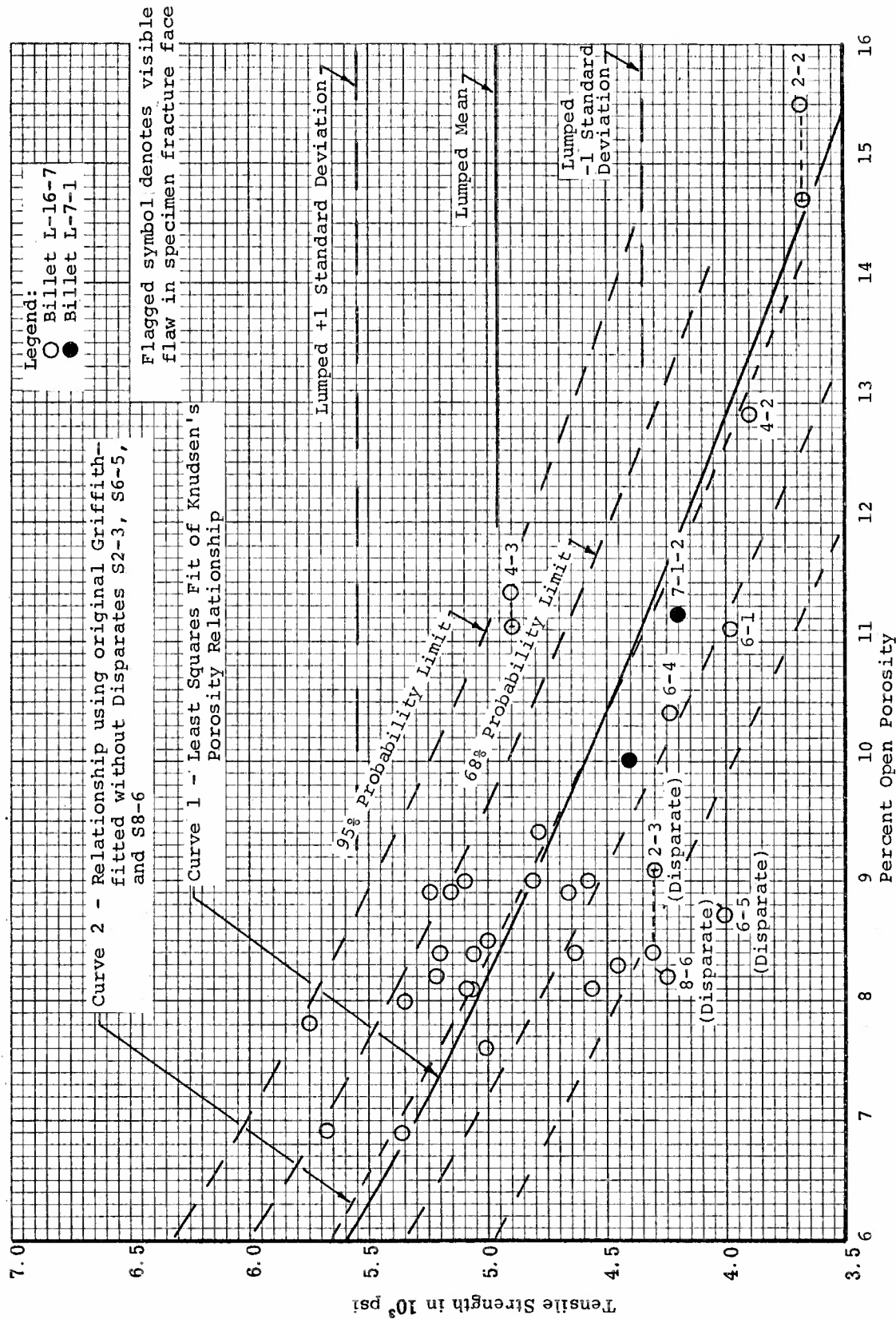


Figure 196. Developed Relations for Tensile Strength versus Percent Open Porosity for ATJ-S Billet L-16-7 With Grain at 70°F

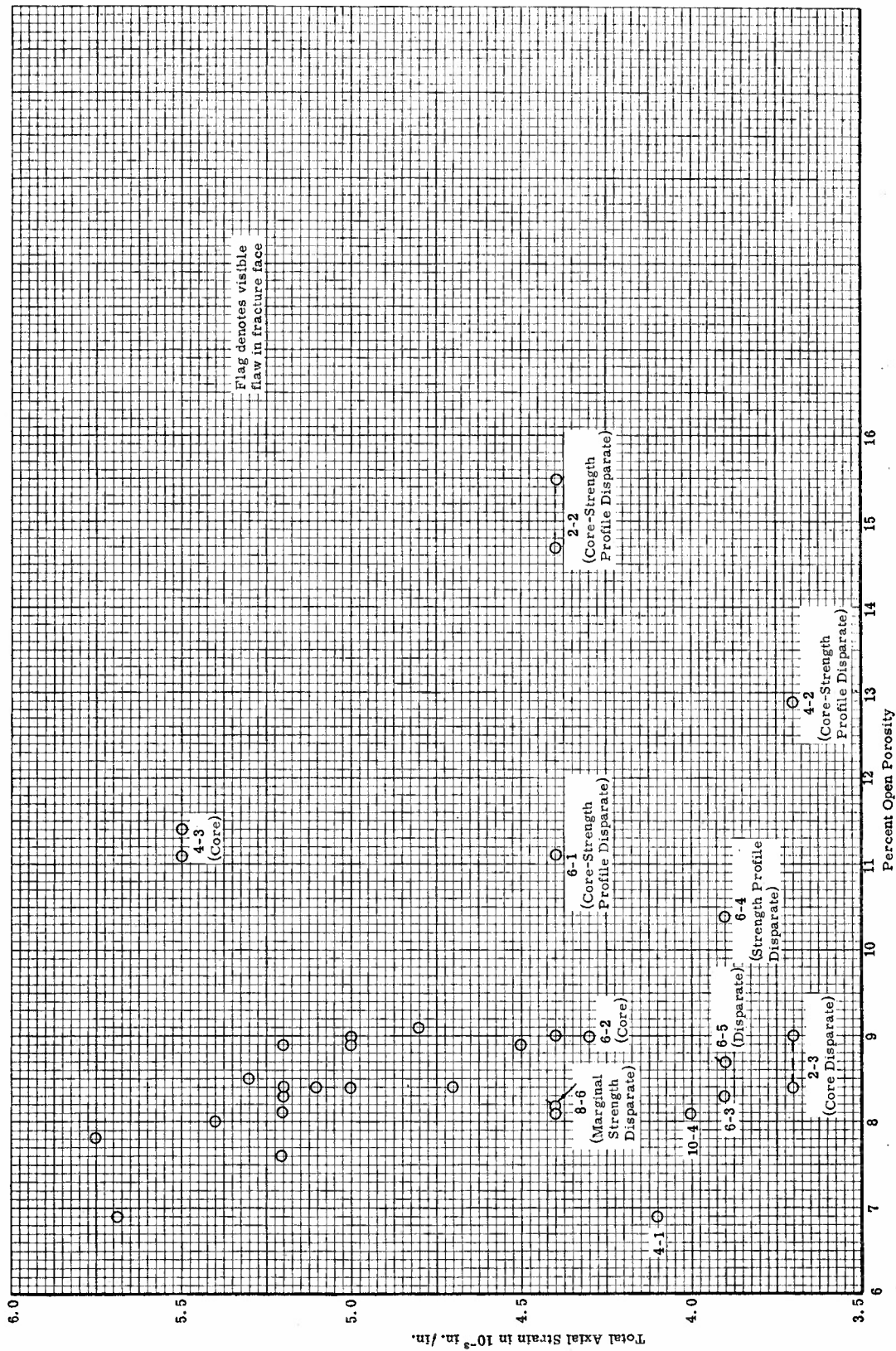


Figure 197. Total Axial Strain to Fracture versus Percent Open Porosity for ATI-S Billet L-16-7 With Grain at 70° F

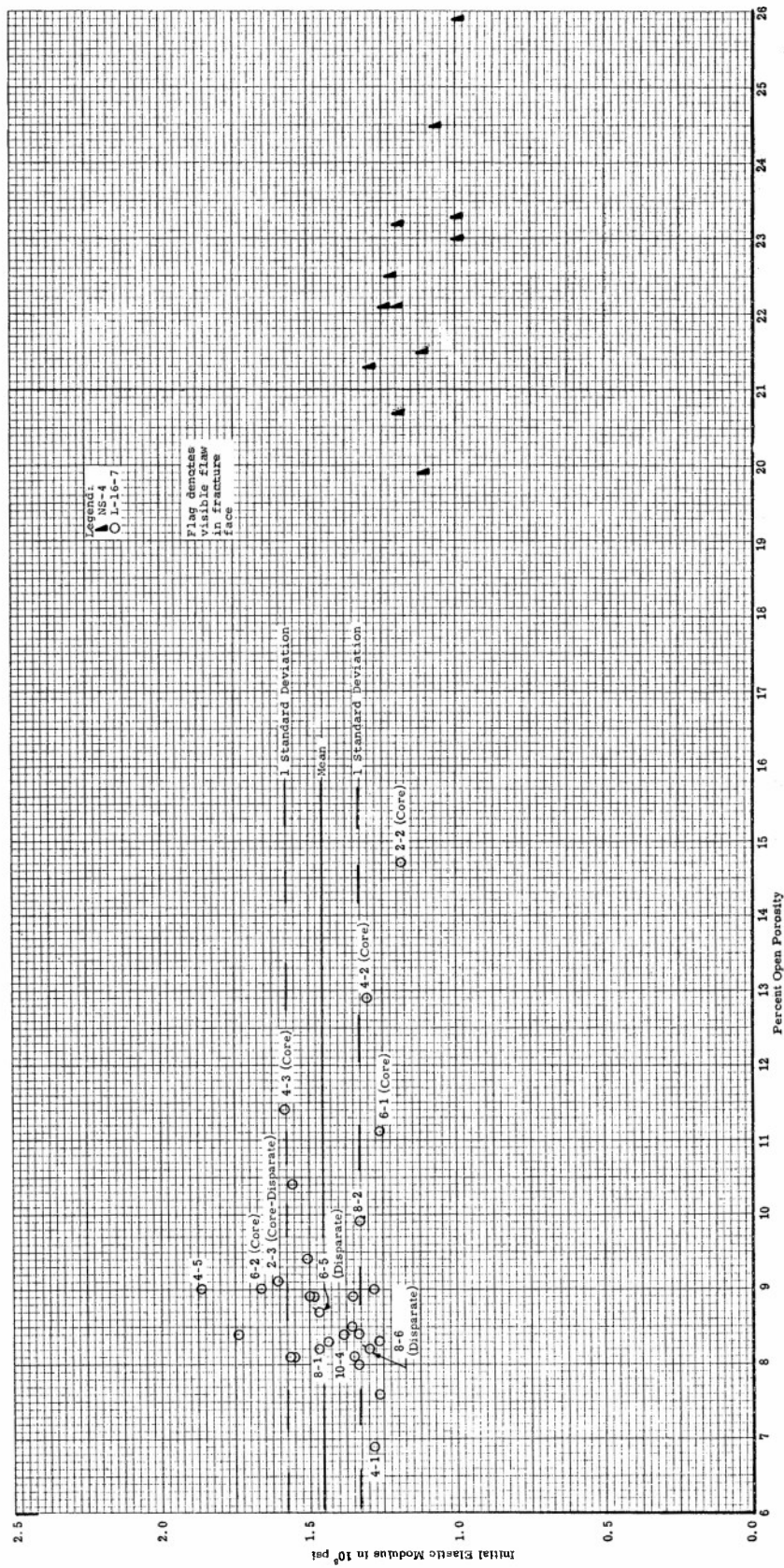


Figure 198. Initial Elastic Modulus in Tension versus Percent Open Porosity for ATJ-S Billet L-16-7 Including NS-4 Data With Grain at 70°F



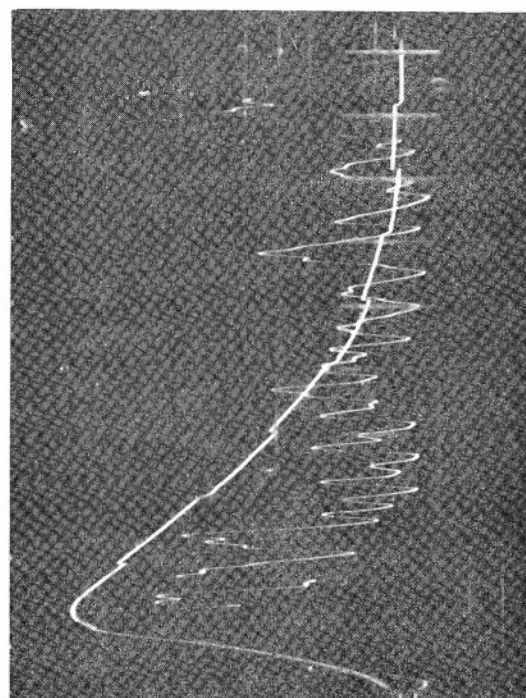
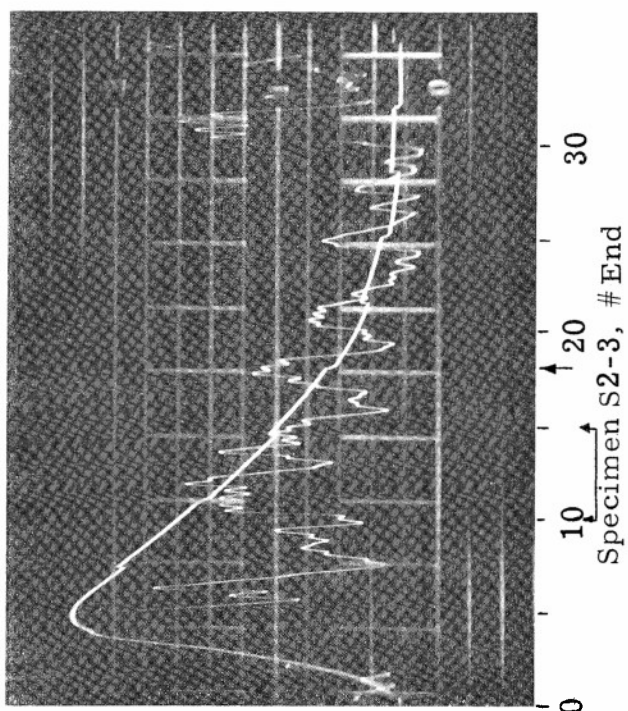
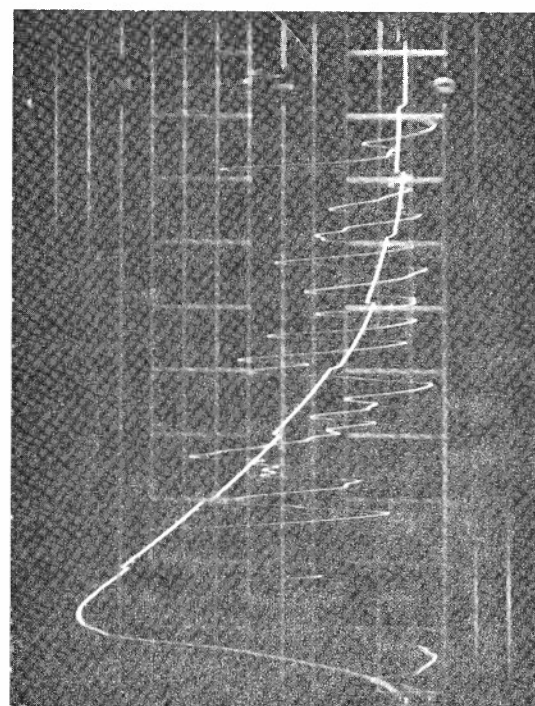
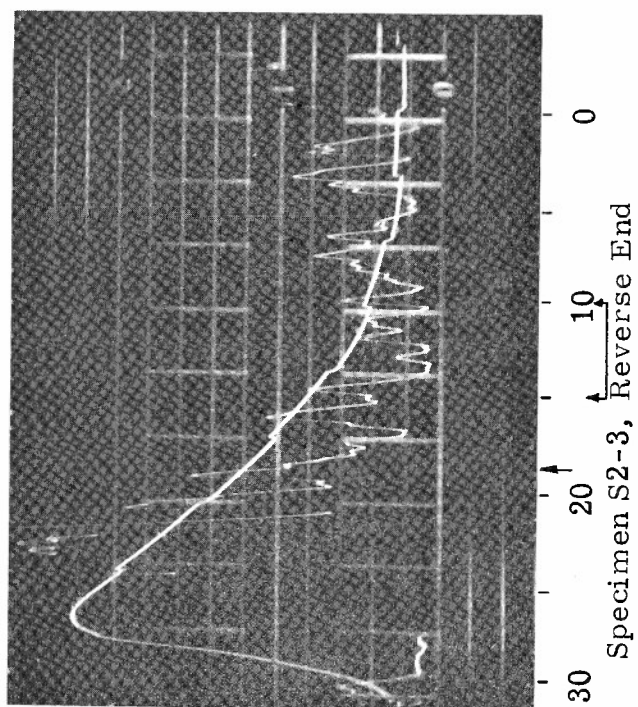


Figure 199. Typical Photograph of Pulse-Echo Display from Opposing Ends of Tensile Blank Specimen for ATJ-S Billet L-16-7--Alcohol Coupler





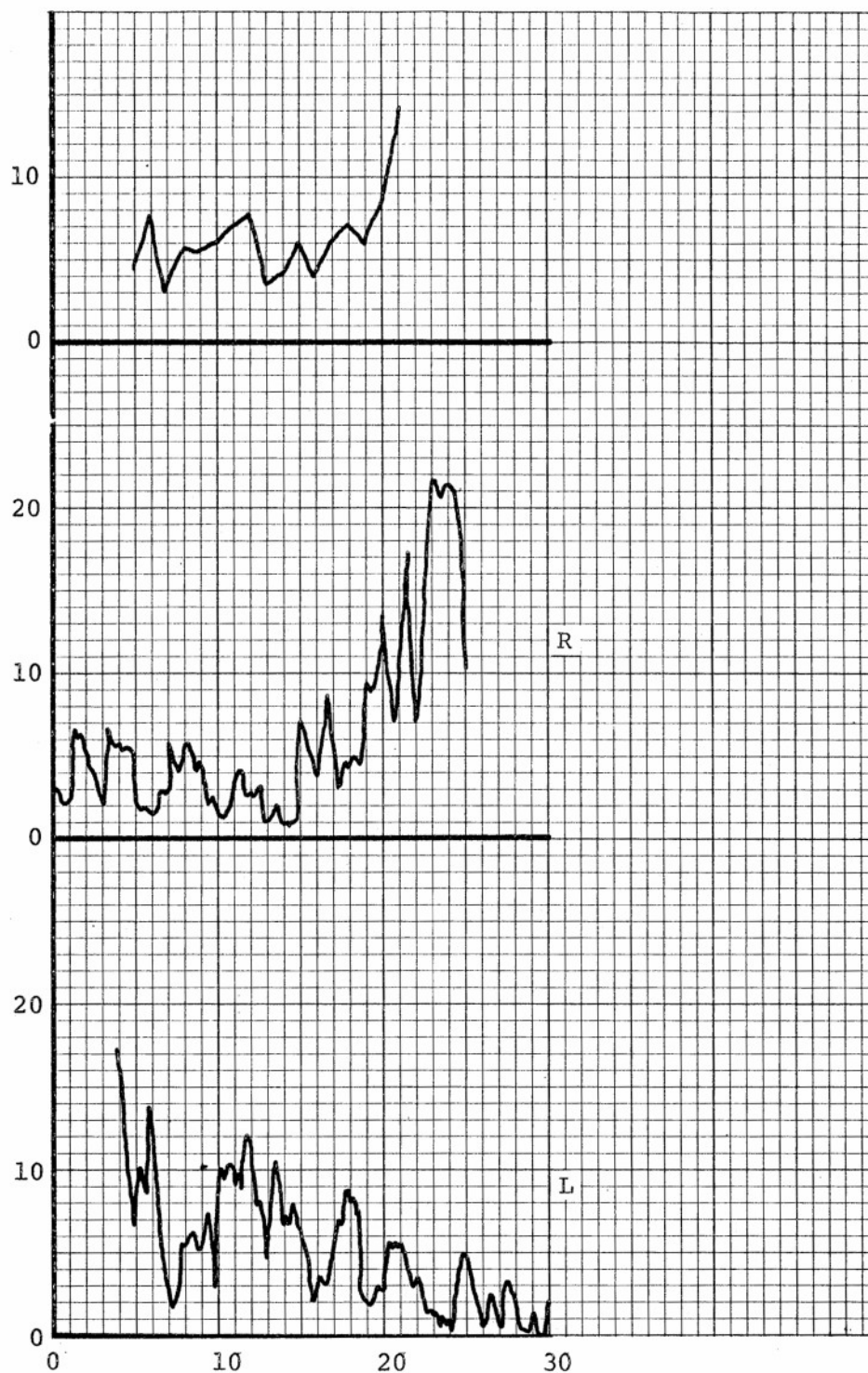


Figure 200. Pulse-Echo Signal Enhancement Technique Using Aligned End Signals from Opposing Ends of Tensile Blank-Alcohol Coupler

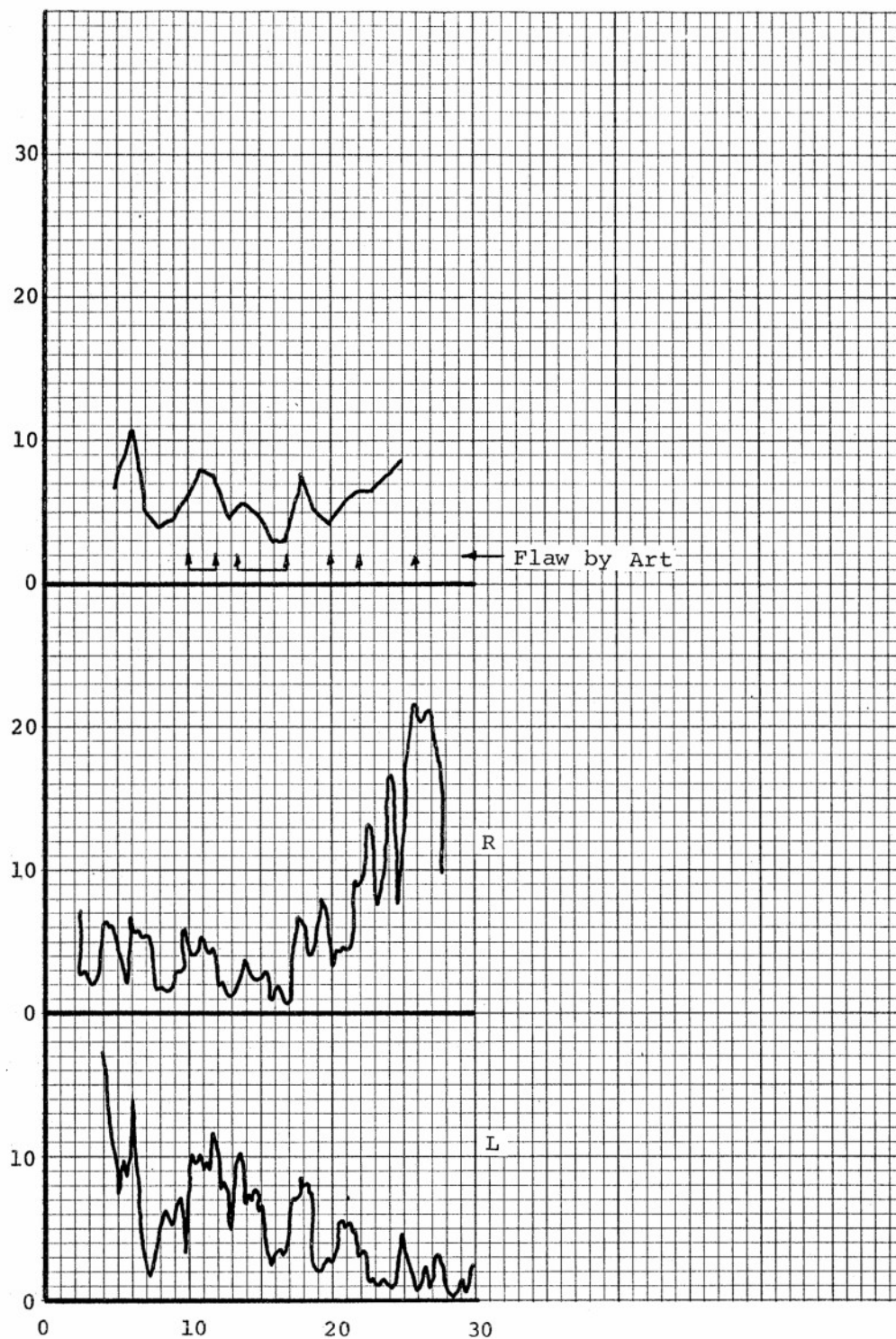
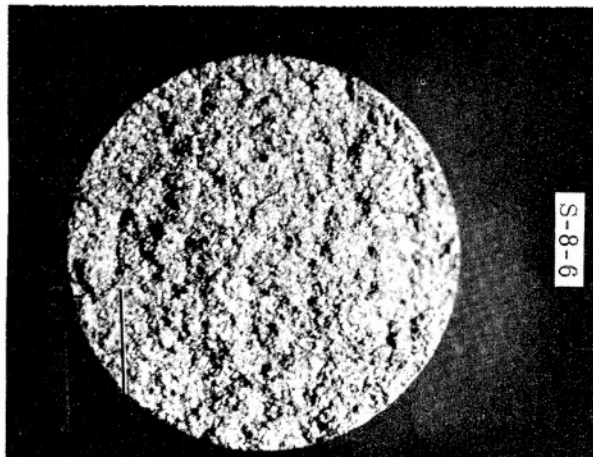


Figure 201. Pulse-Echo Signal Enhancement Technique Using Shift in Time Base to Improve Signal-to-Noise Ratio from Opposing Ends of Tensile Blank-Alcohol Coupler

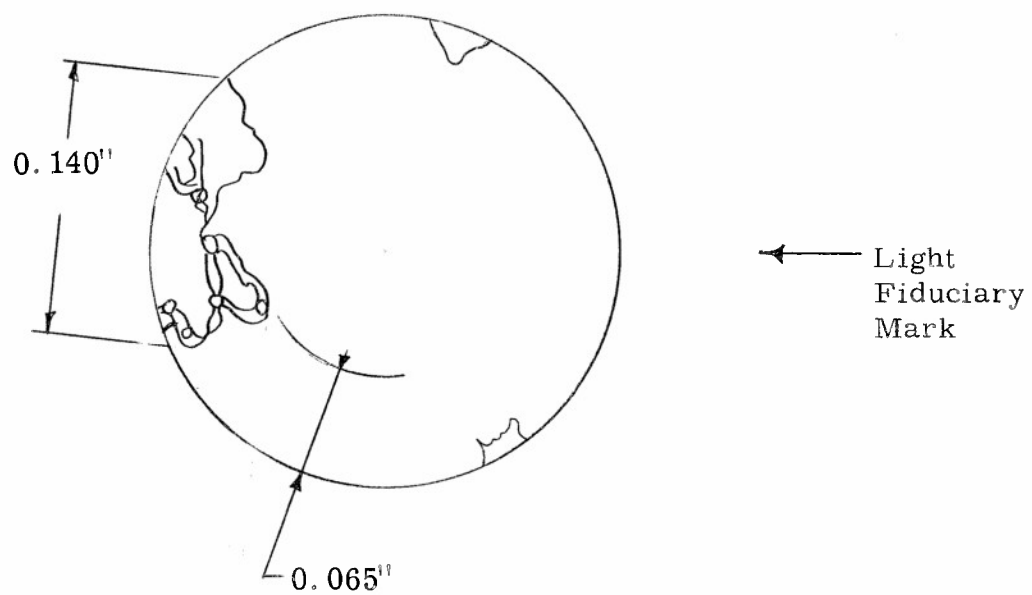




Short End



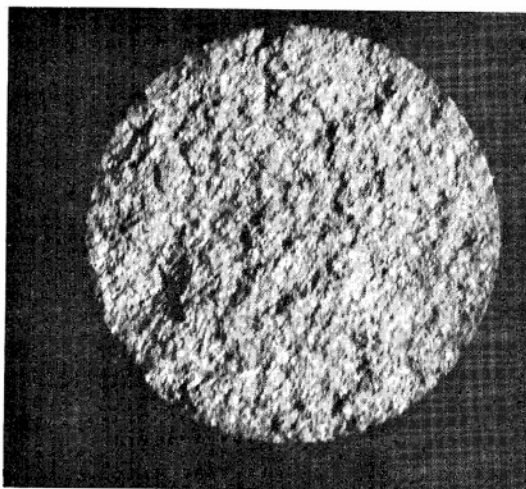
Long End



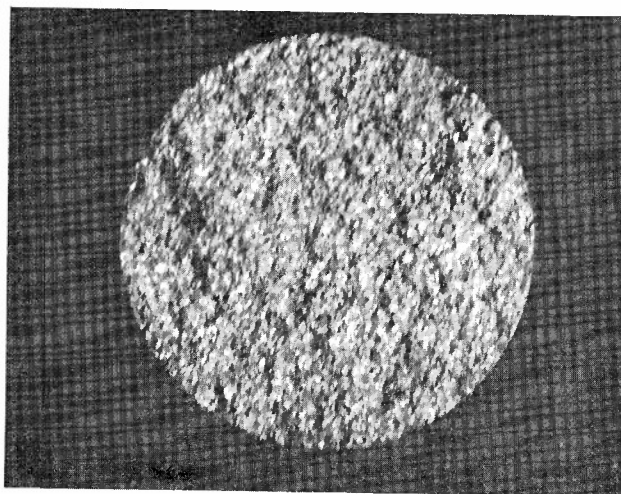
Looking toward Short End.  
Short End Predominant

Figure 202. Flick Inspection Results and 10X Black and White Photographs of Fracture Faces of Disparate S8-6, ATJ-S Billet L-16-7





Short End



Long End

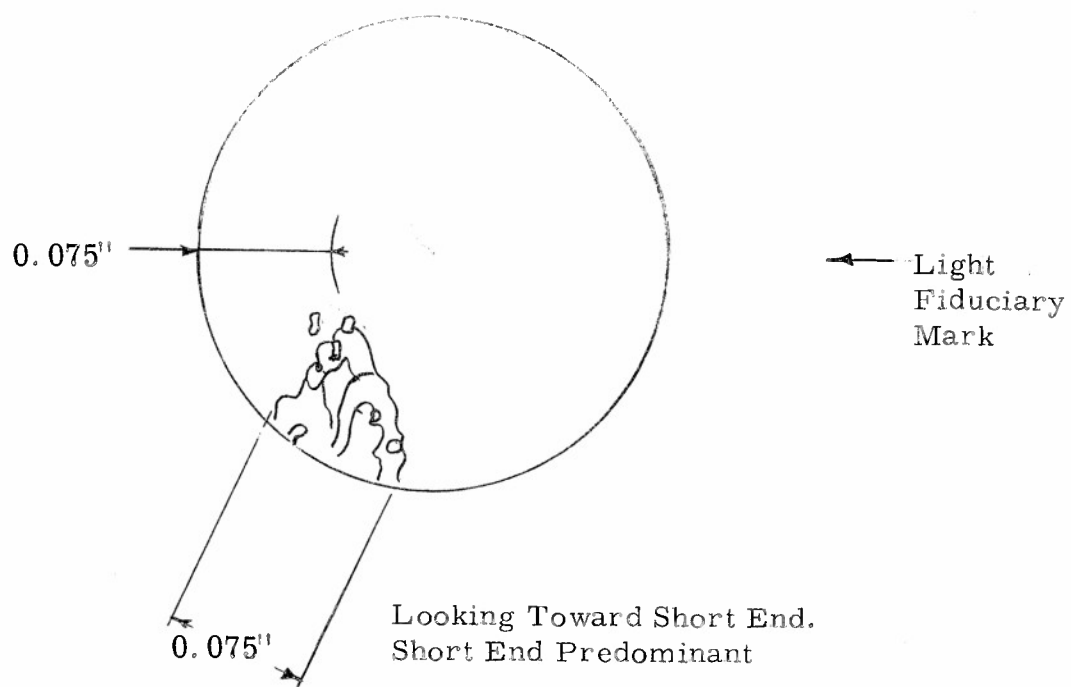
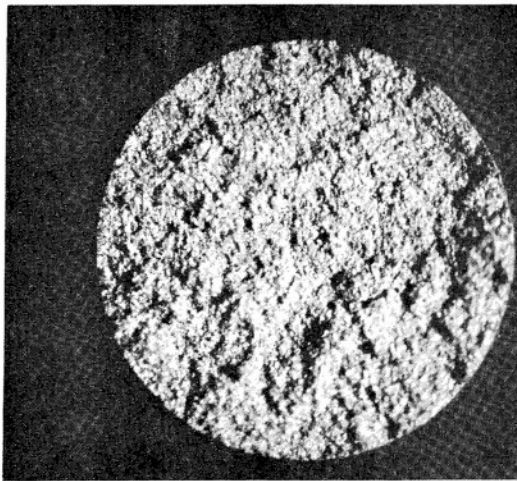
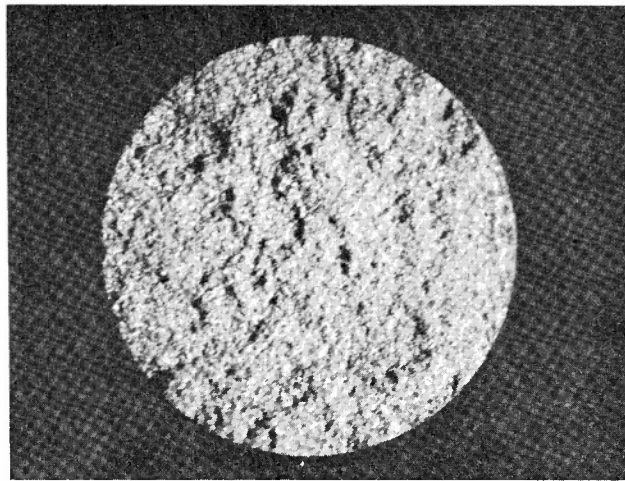


Figure 203. Flick Inspection Results and 10X Black and White Photographs of Fracture Faces of Disparate S6-5, ATJ-S Billet L-16-7





Short End



Long End

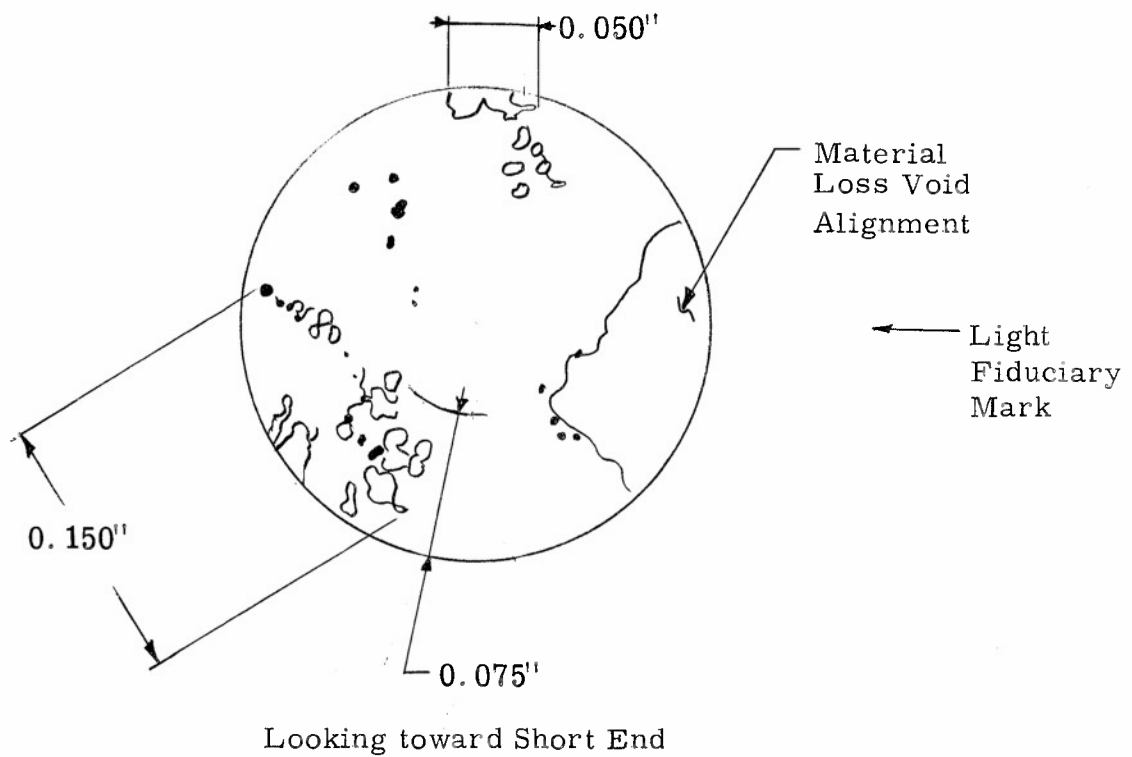


Figure 204. Flick Inspection Results and 10X Black and White Photographs of Fracture Faces of Disparate S2-3, ATJ-S Billet L-16-7



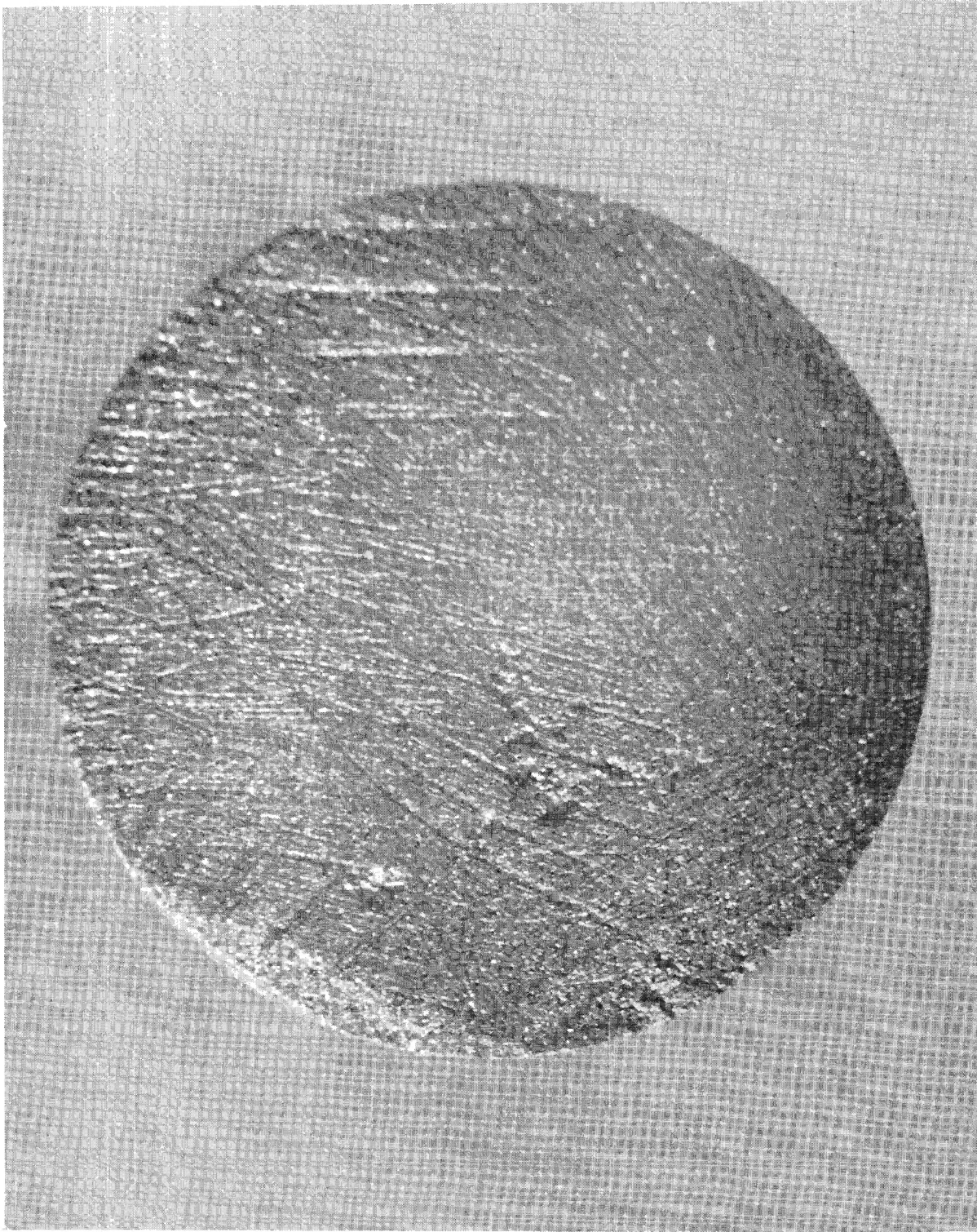


Figure 205. 28X Photobraph of Cavity Observed after Initial Filing of Fracture Face of Disparate S6-5, ATJ-S Billet L-16-7





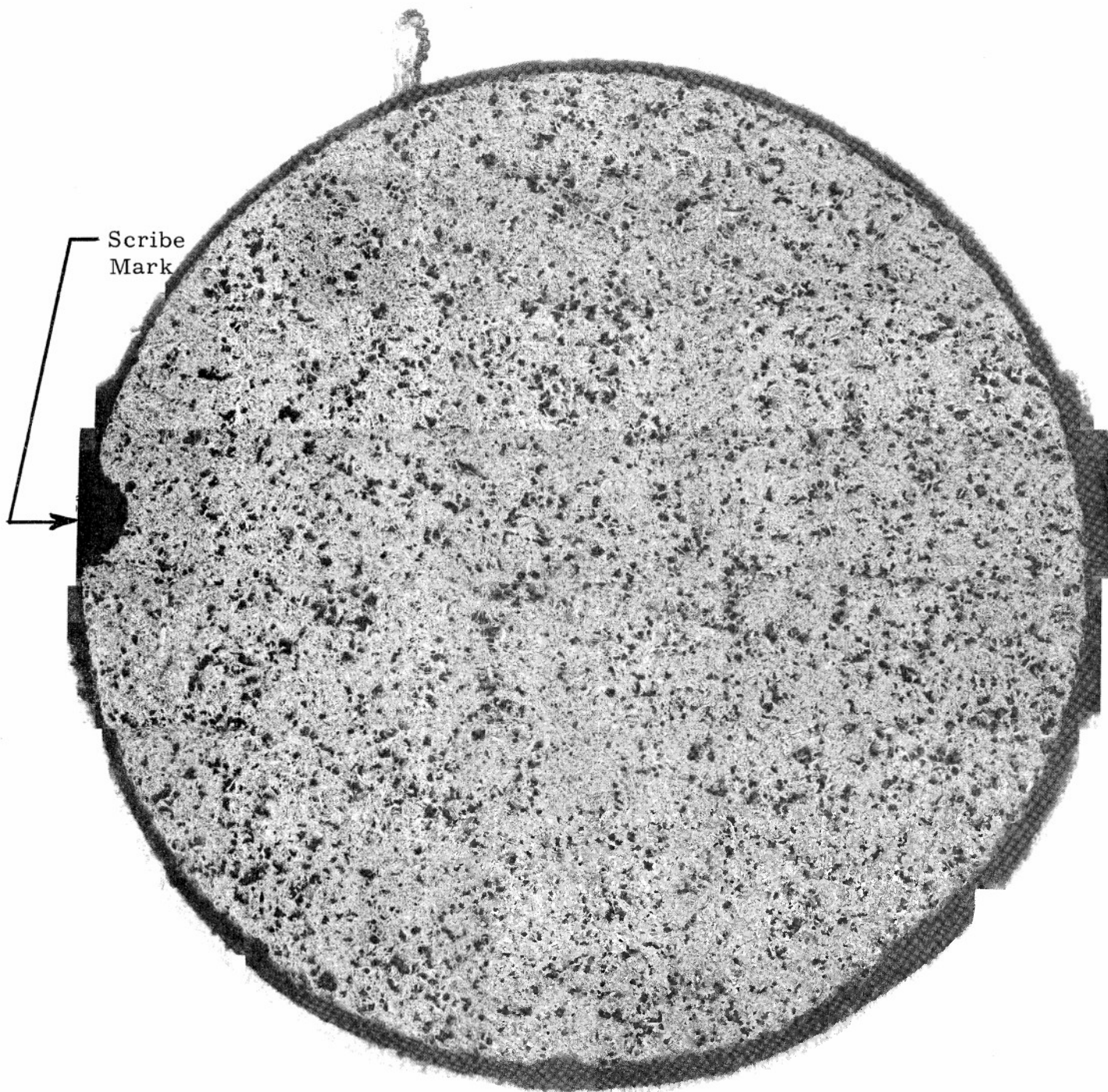
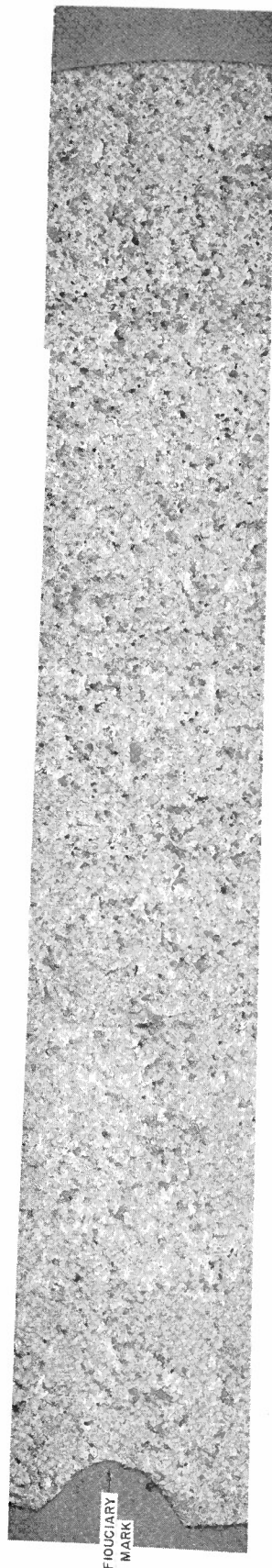


Figure 206. 100X Photomicrograph of Cross Section of Disparate S6-5, 21 mils below Fracture Face, No Impregnation, ATJ-S Billet L-16-7

2001  
M

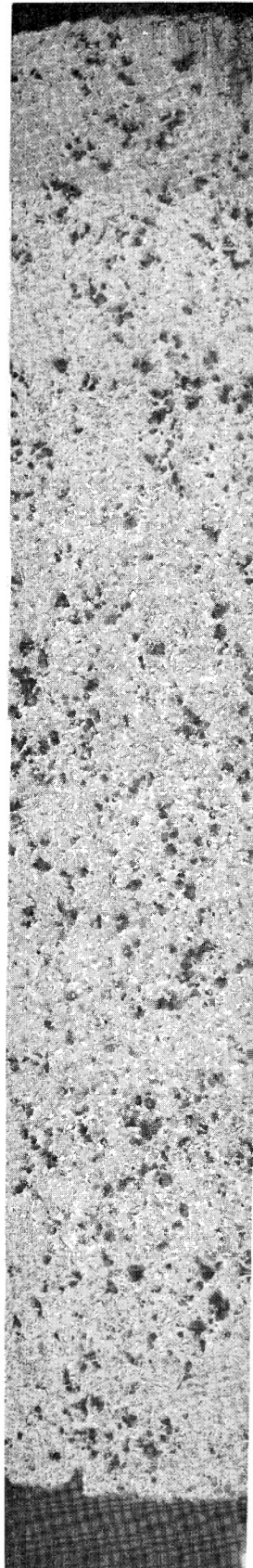
Below Pressure Recoil, 1st Impression, AT-5 Bullet L-10-V  
100% Photograph of 1st Impression of Discharge 20-6, 21 mil.



NOTE:  
POINT COUNT  $\frac{41}{504} \times 100 = 8.2\%$

Figure 207. 100X Photomicrograph of Cross Section of Disparate S6-5, 36 mils below Fracture Face, Epoxy Impregnated, ATJ-S Billet L-16-7





NOTE:  
POINT COUNT -  $\frac{52}{399} \times 100 = 13.1\%$

Figure 208. 100X Photomicrograph of Cross Section of Average ATJ-S (Specimen S8-4),  
No Impregnation, ATJ-S Billet L-16-7



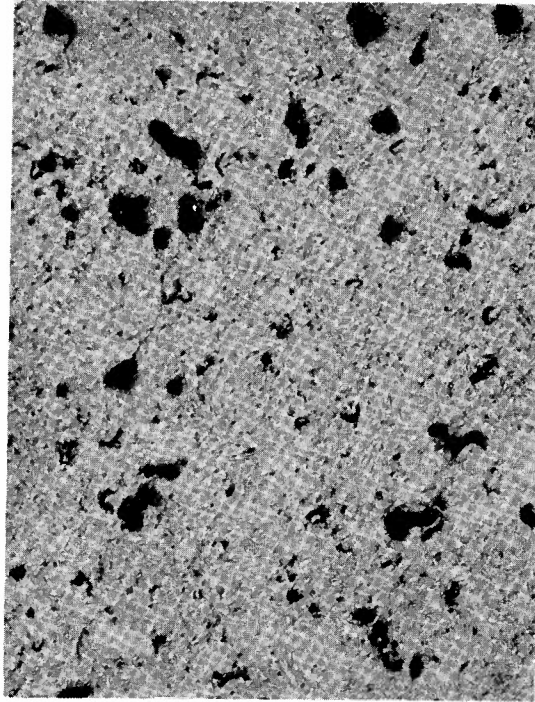


Figure 209. 100X Photomicrograph from Strong ATJ-S Billet  
Evaluated at Southern, No Impregnation



Figure 10. 10X micrograph from SEM of 10-5 filled  
Bransted at constant, No injection



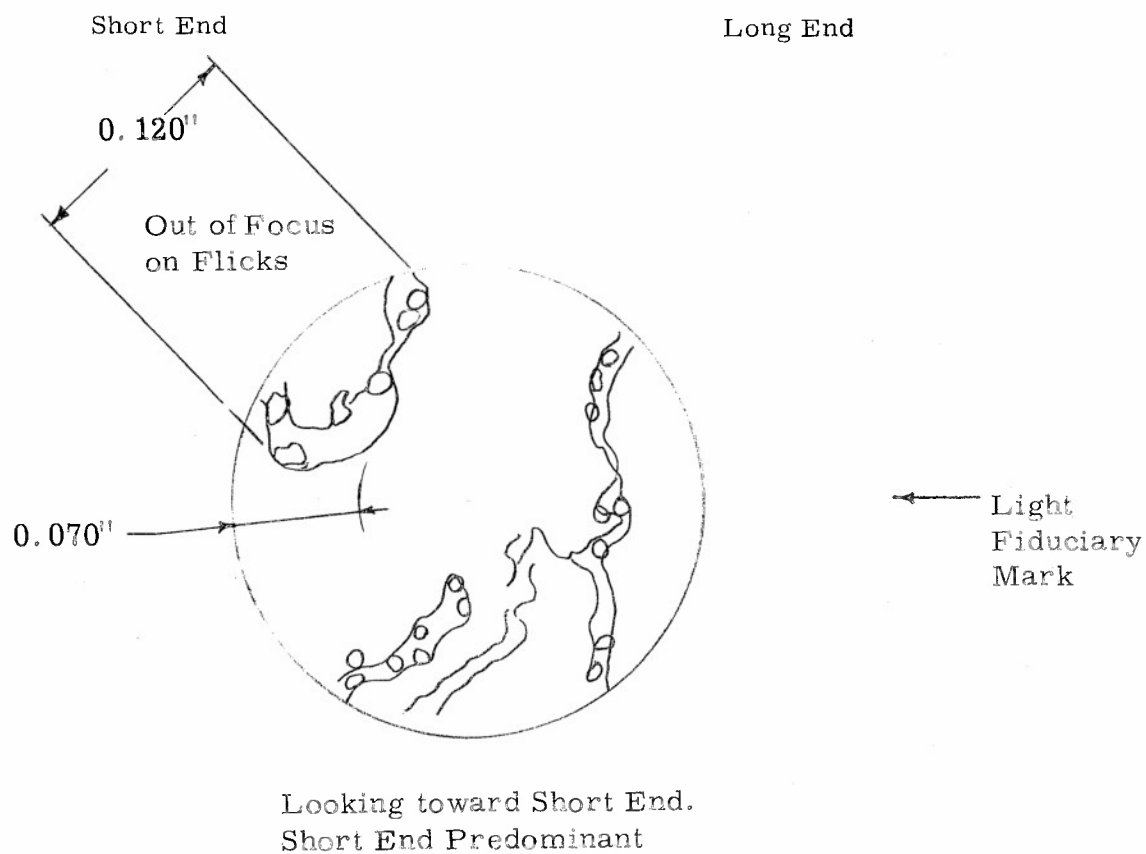
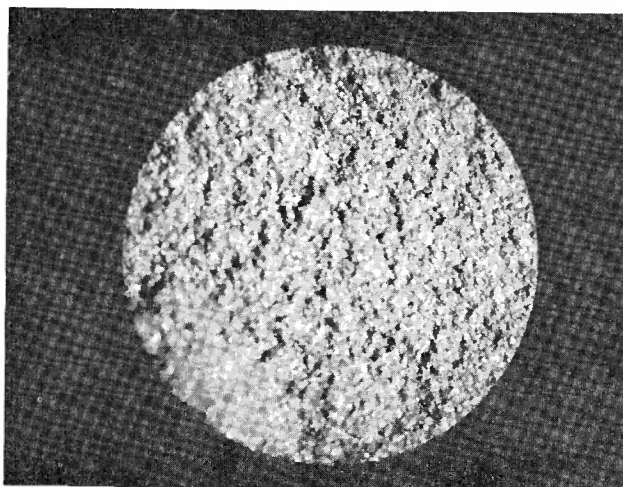
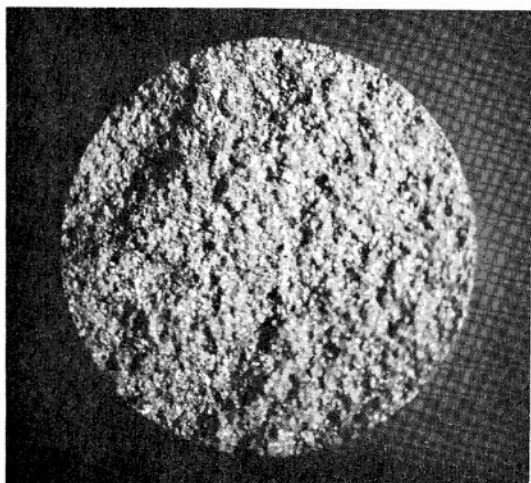
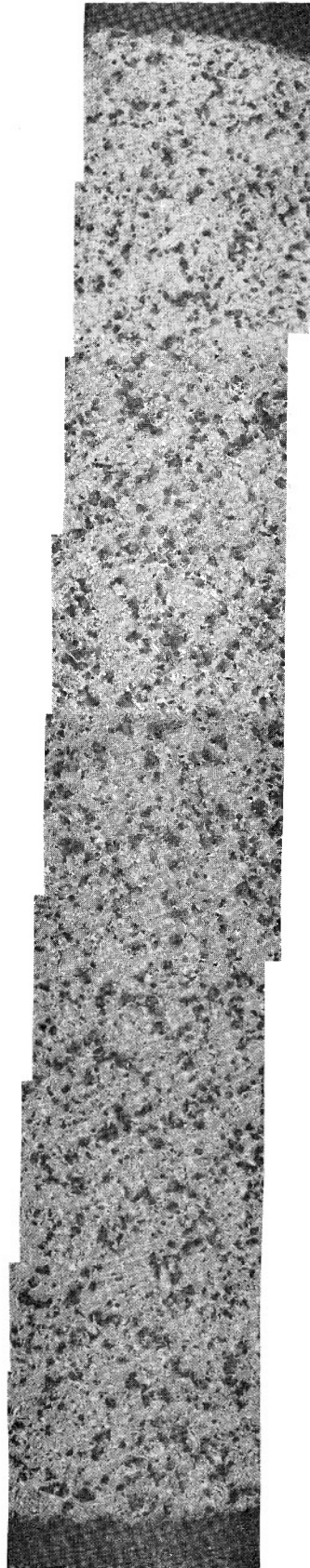


Figure 210. Flick Inspection Results and 10X Black and White Photographs of Fracture Faces of Highest Open Porosity Specimen S2-2, ATJ-S Billet L-16-7

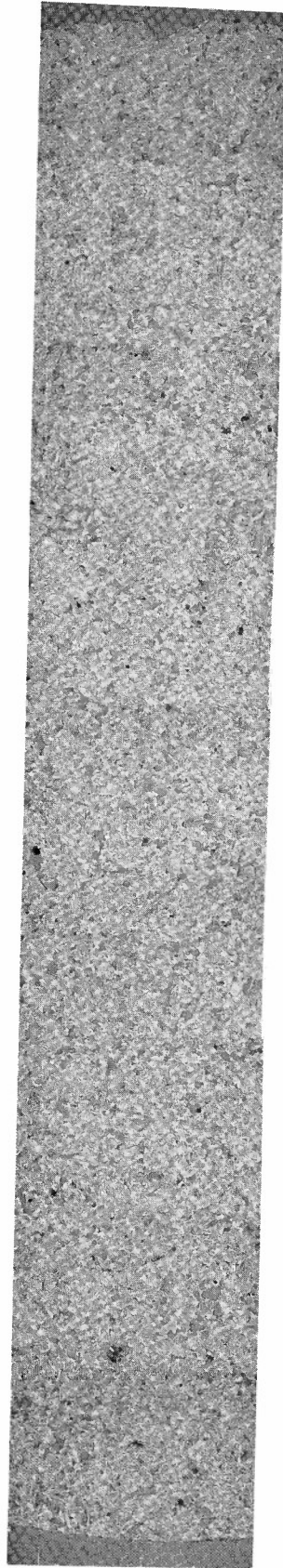




NOTE:  
POINT COUNT  $= \frac{61}{210} \times 100 = 29\%$

Figure 211. 100X Photomicrograph of Cross Section from Highest Open Porosity Specimen S2-2, 15 mils below Fracture Face, No Impregnation, ATJ-S Billet L-16-7





NOTE:  
POINT COUNT =  $\frac{52}{315} \times 100 = 16.5\%$

Figure 212. 100X Photomicrograph of Cross Section from Highest Open Porosity Specimen S2-2, 30 mils below Fracture Face, Epoxy Impregnation, ATJ-S Billet L-16-7



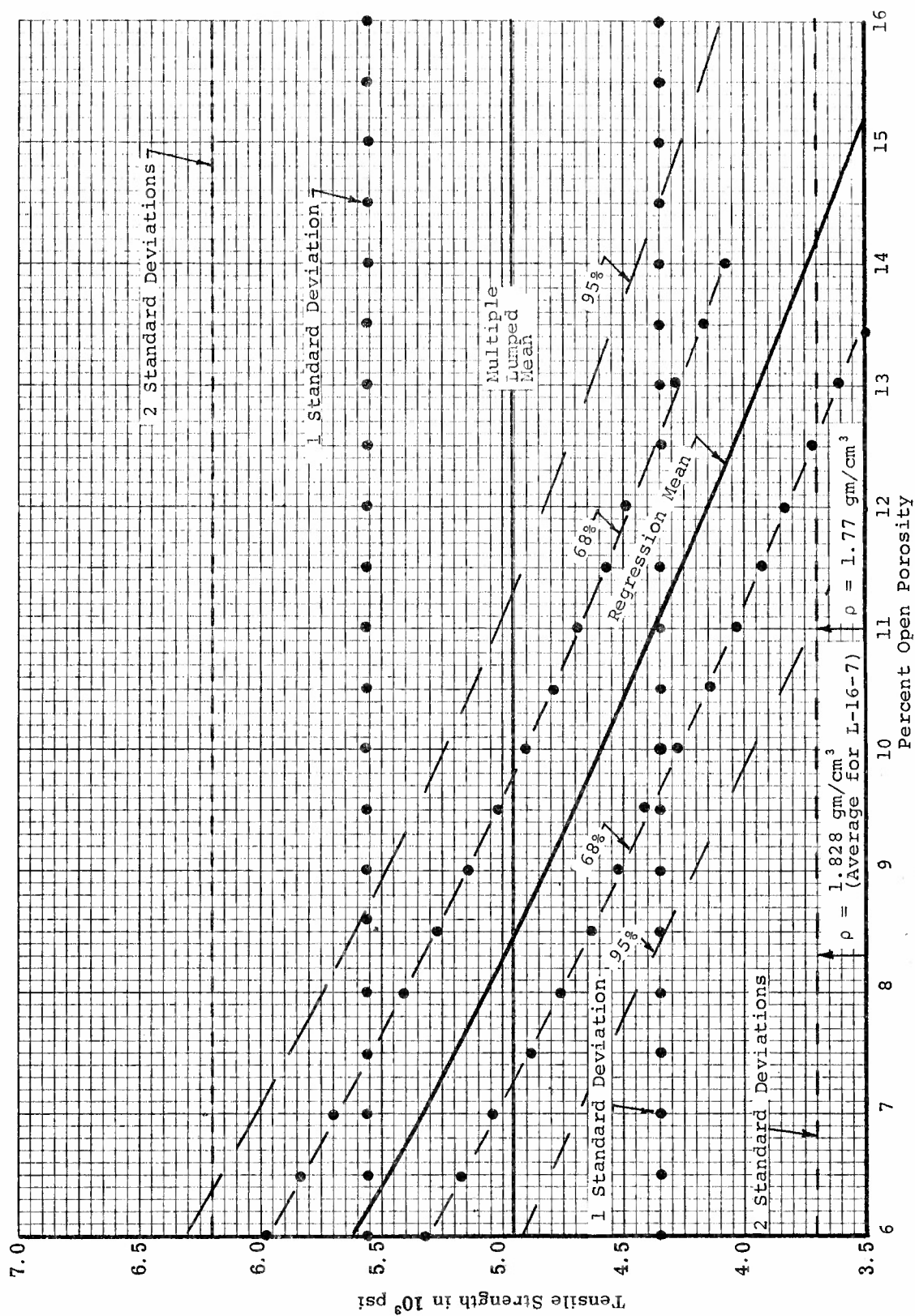


Figure 213. Tensile Strength Versus Percent Open Porosity Showing Mean and 1 and 2 Standard Deviations of Strength for Multiple Lumped L-16-7 Data

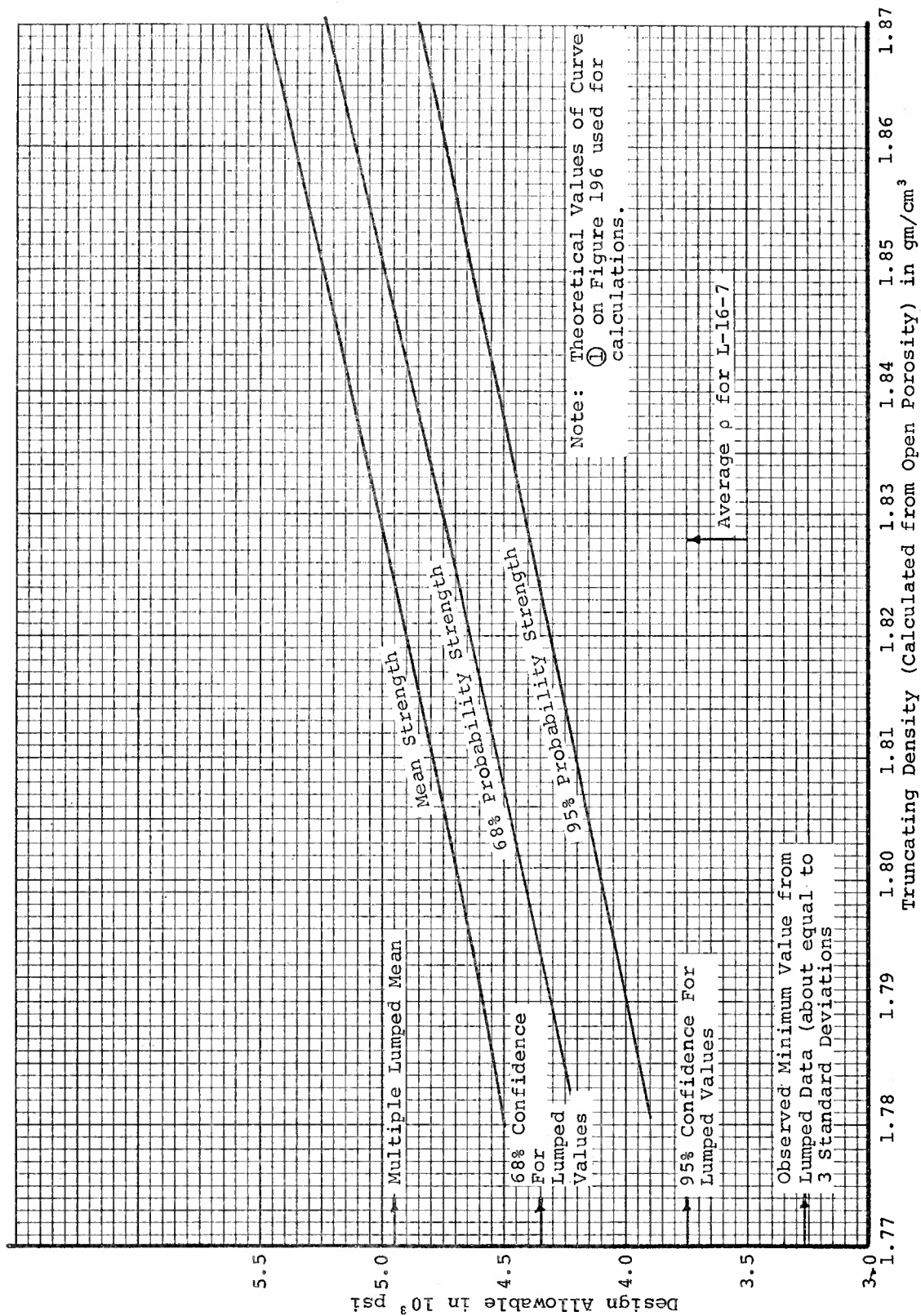


Figure 214. Design Allowable Strength versus Truncating Density for ATJ-S Billet L-16-7



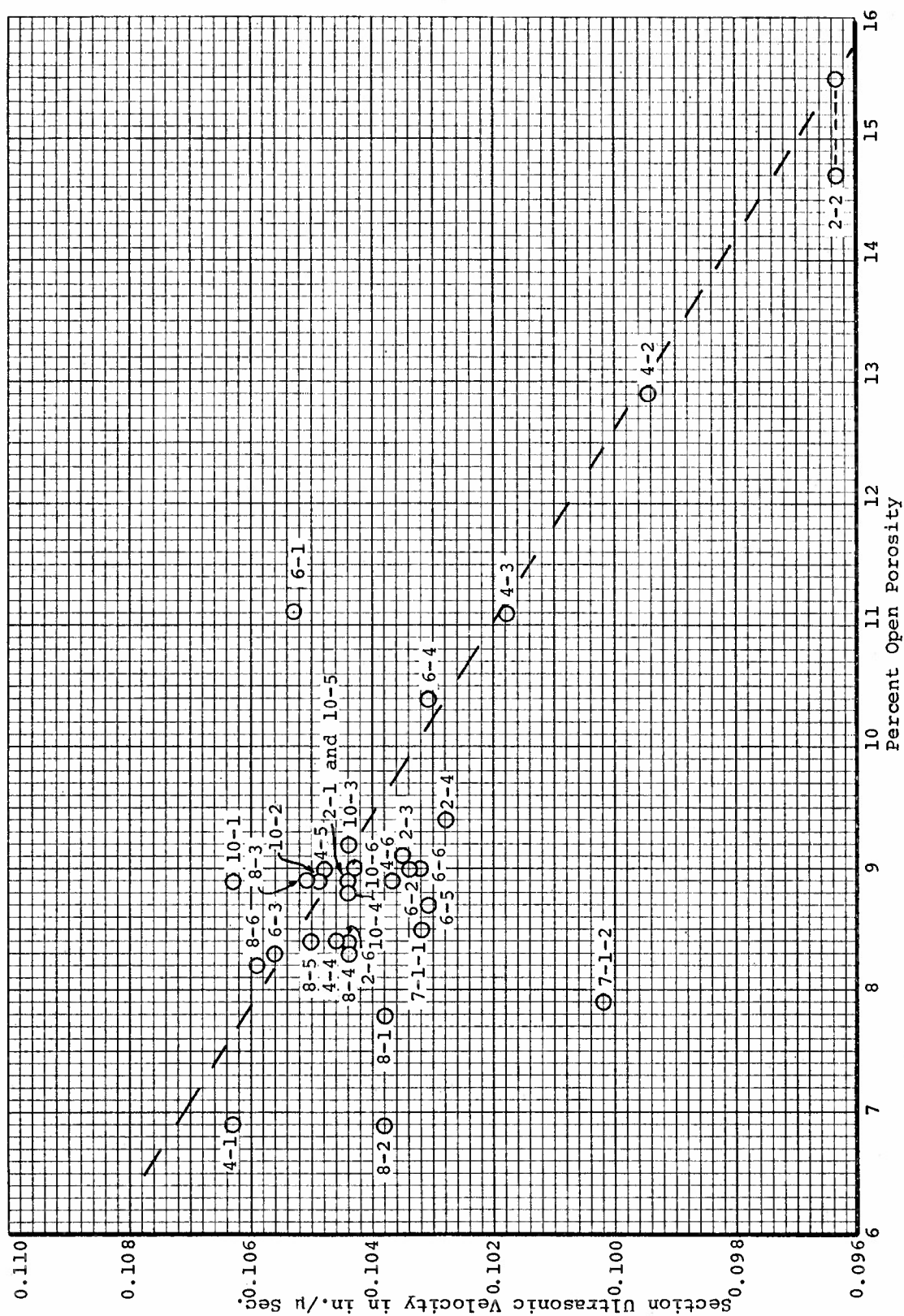


Figure 215. Section Ultrasonic Velocity versus Percent Open Porosity for ATJ-S Billet L-16-7

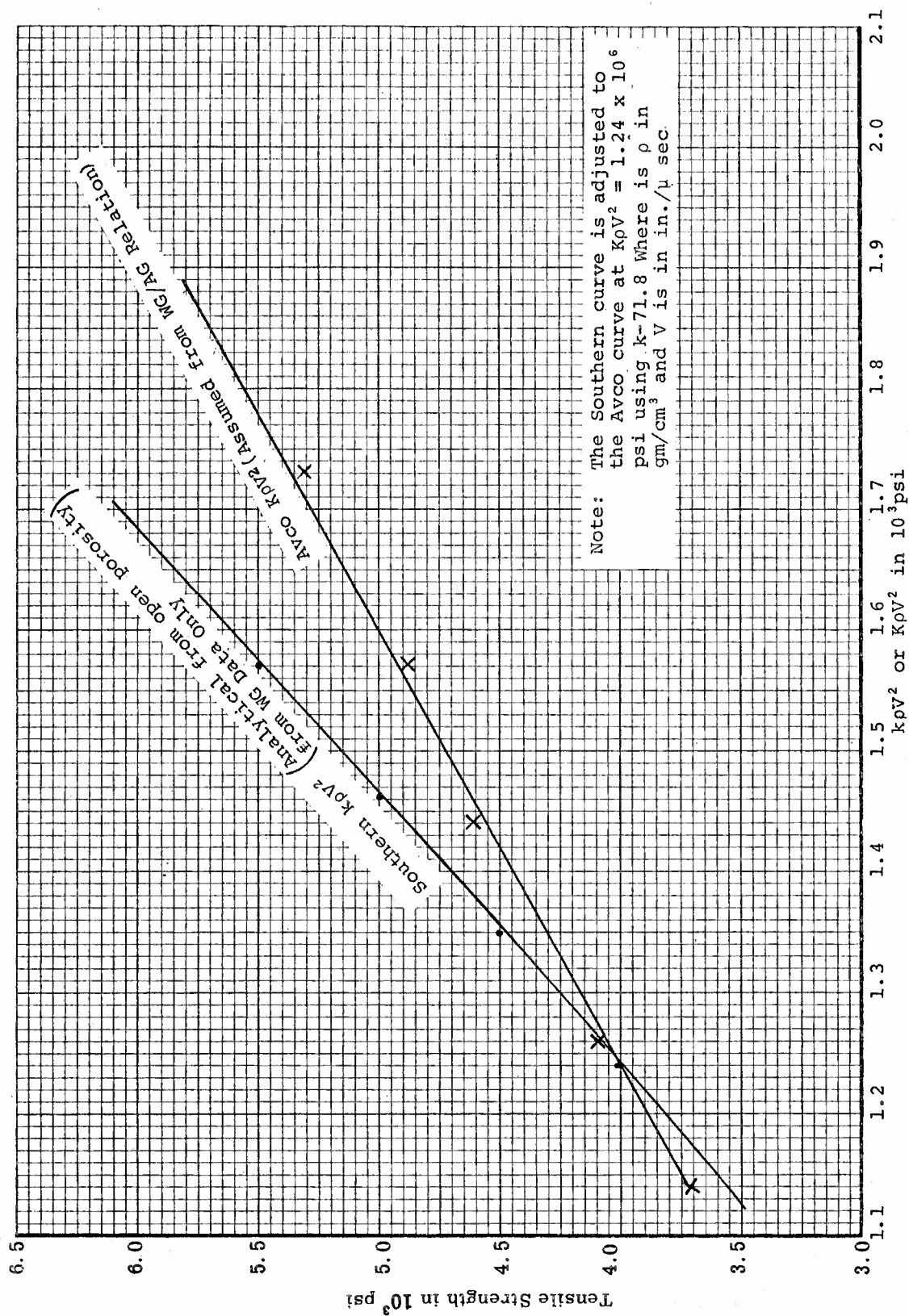


Figure 216. Tensile Strength versus Avco  $K\sigma V^2$  and Southern  $K\sigma V^2$  for ATJ-S Billet L-16-7

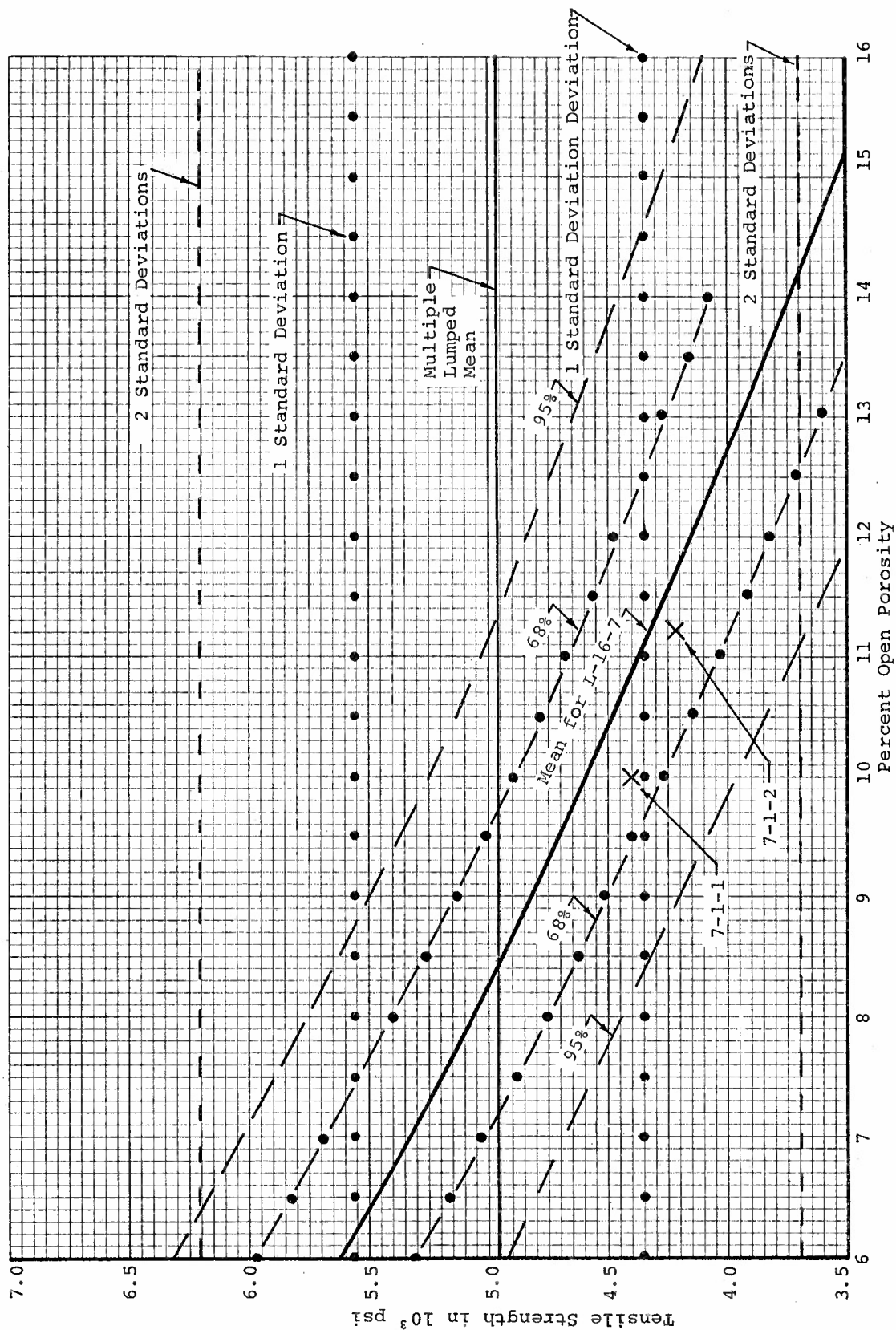


Figure 217. Specimens 7-1-1 and 7-1-2 Correlation with Tensile Strength-Open Porosity Relation Developed for ATJ-S Billet L-16-7 With Grain at 70°F

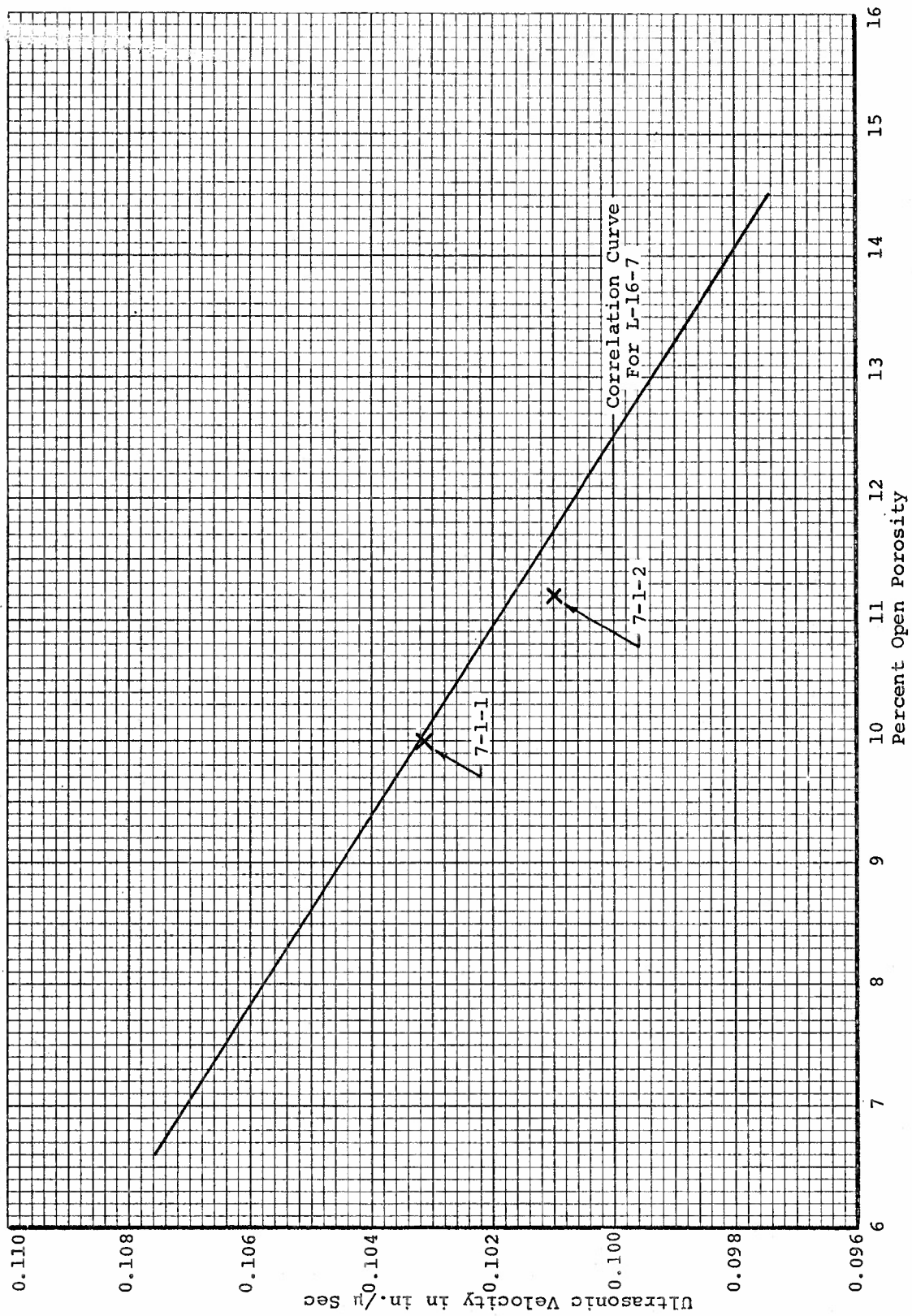


Figure 218. Correlation of Specimens 7-1-1 and 7-1-2 with Ultrasonic Velocity-Open Porosity Relation of ATJ-S Billet L-16-7



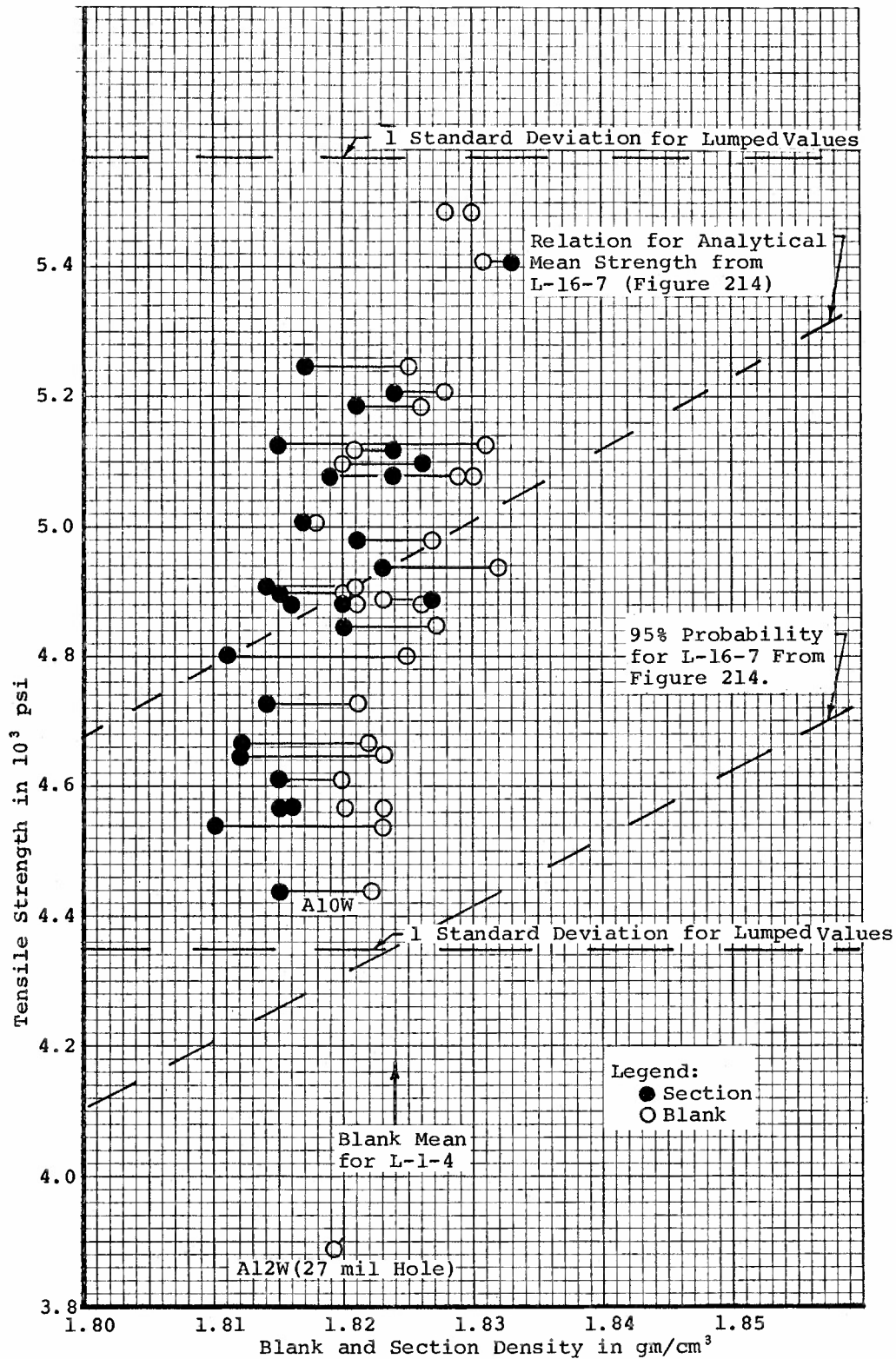


Figure 220. Tensile Strength versus Density (Blank and Section) for ATJ-S Billet L-1-4 With Grain at 70°F



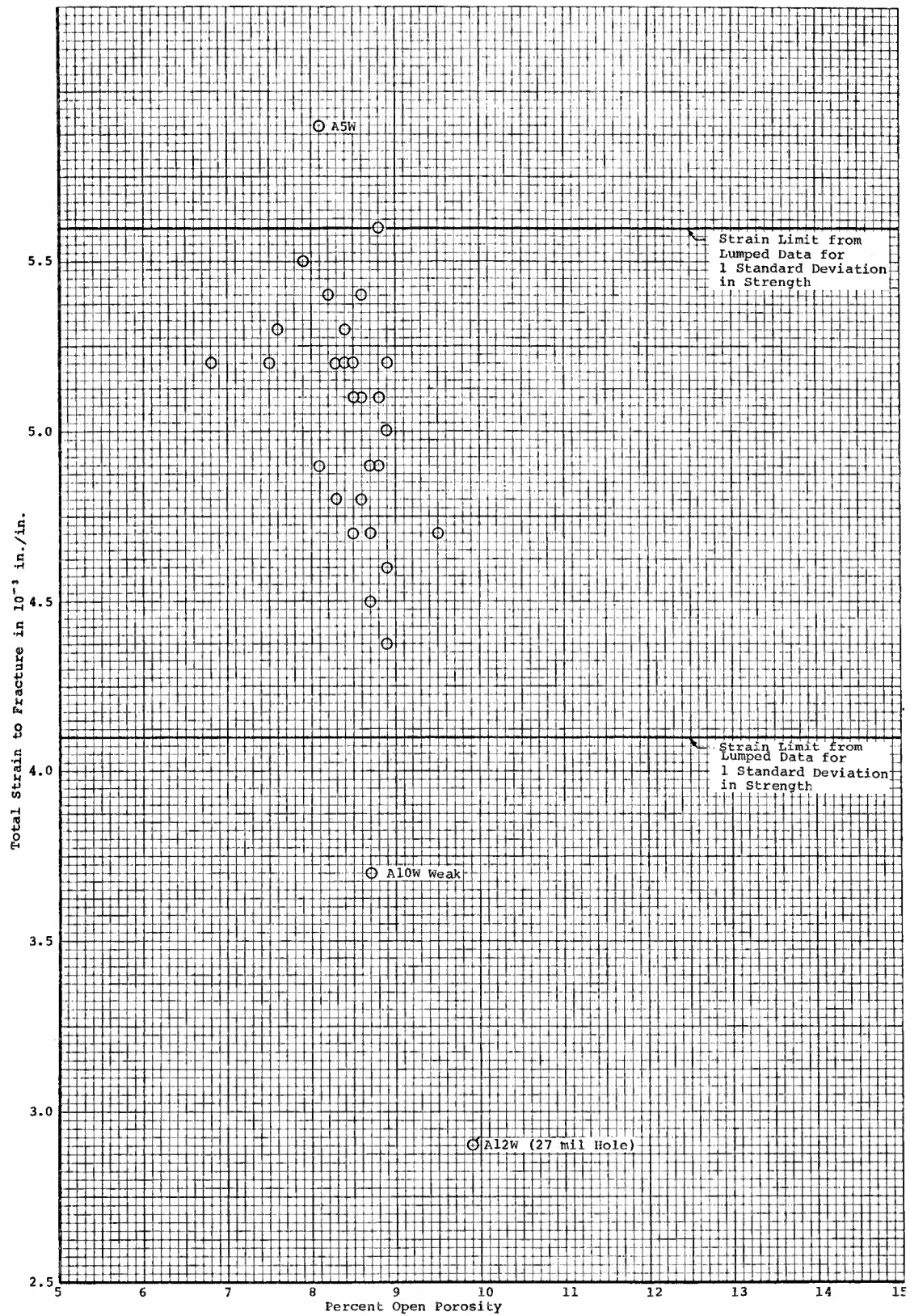


Figure 221. Total Strain to Fracture versus Percent Open Porosity for ATJ-S Billet L-1-4 With Grain at 70°F

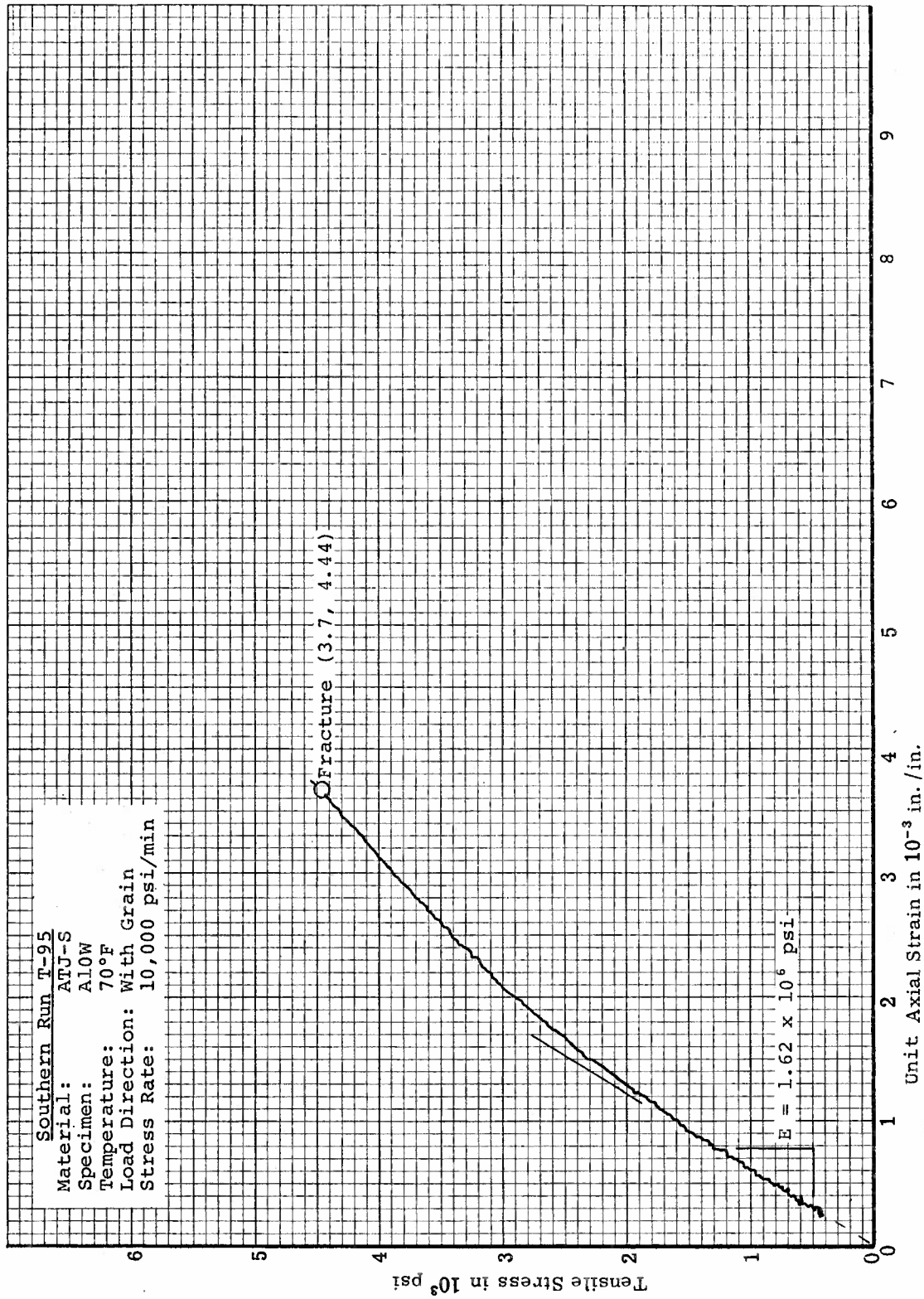


Figure 222. Tensile Stress-Strain Curve for Specimen A10W from ATJ-S Billet L-1-4 With Grain at 70°F



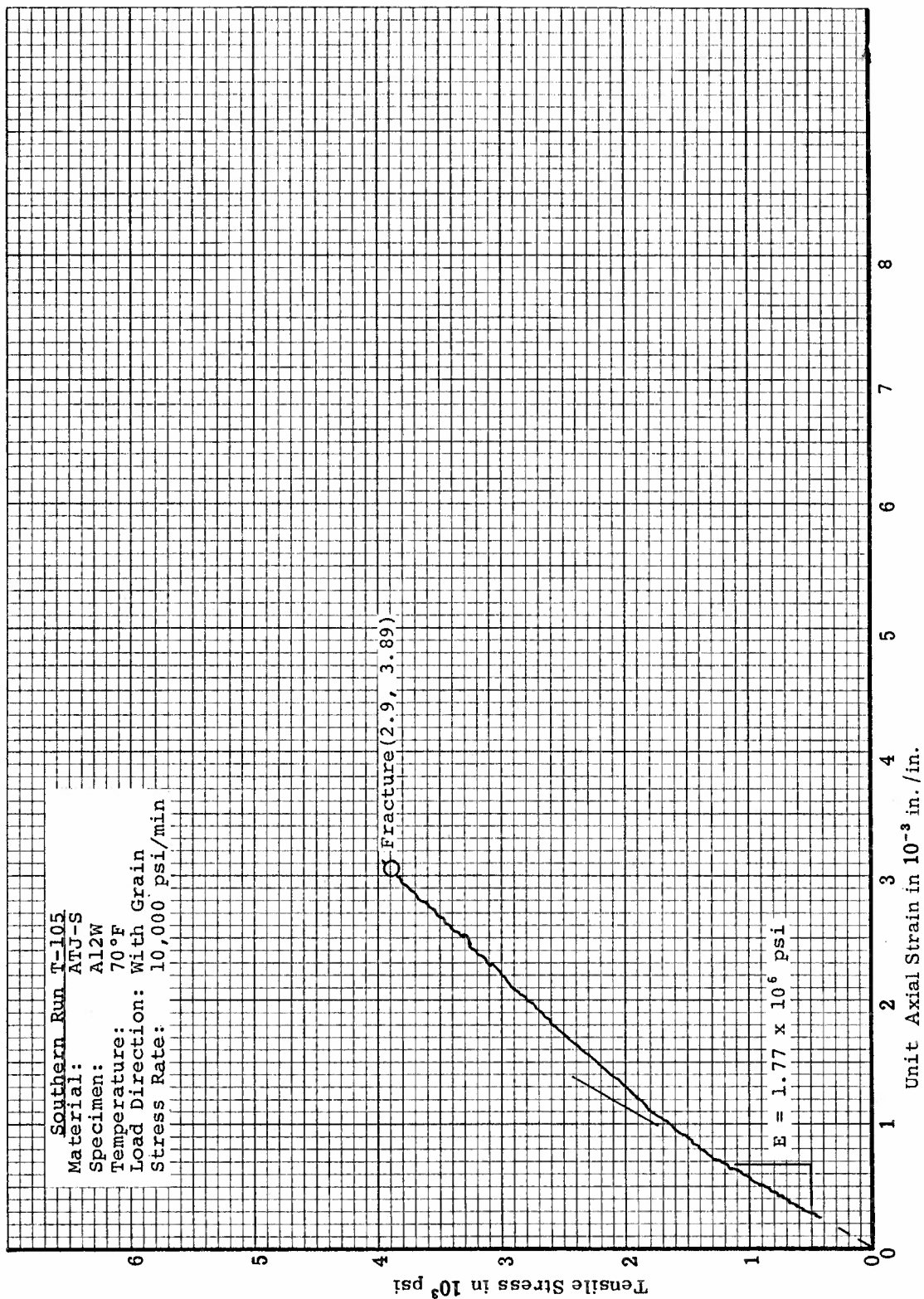


Figure 223. Tensile Stress-Strain Curve for Disparate Specimen A12W from ATJ-S Billet L-1-4 With Grain at 70°F

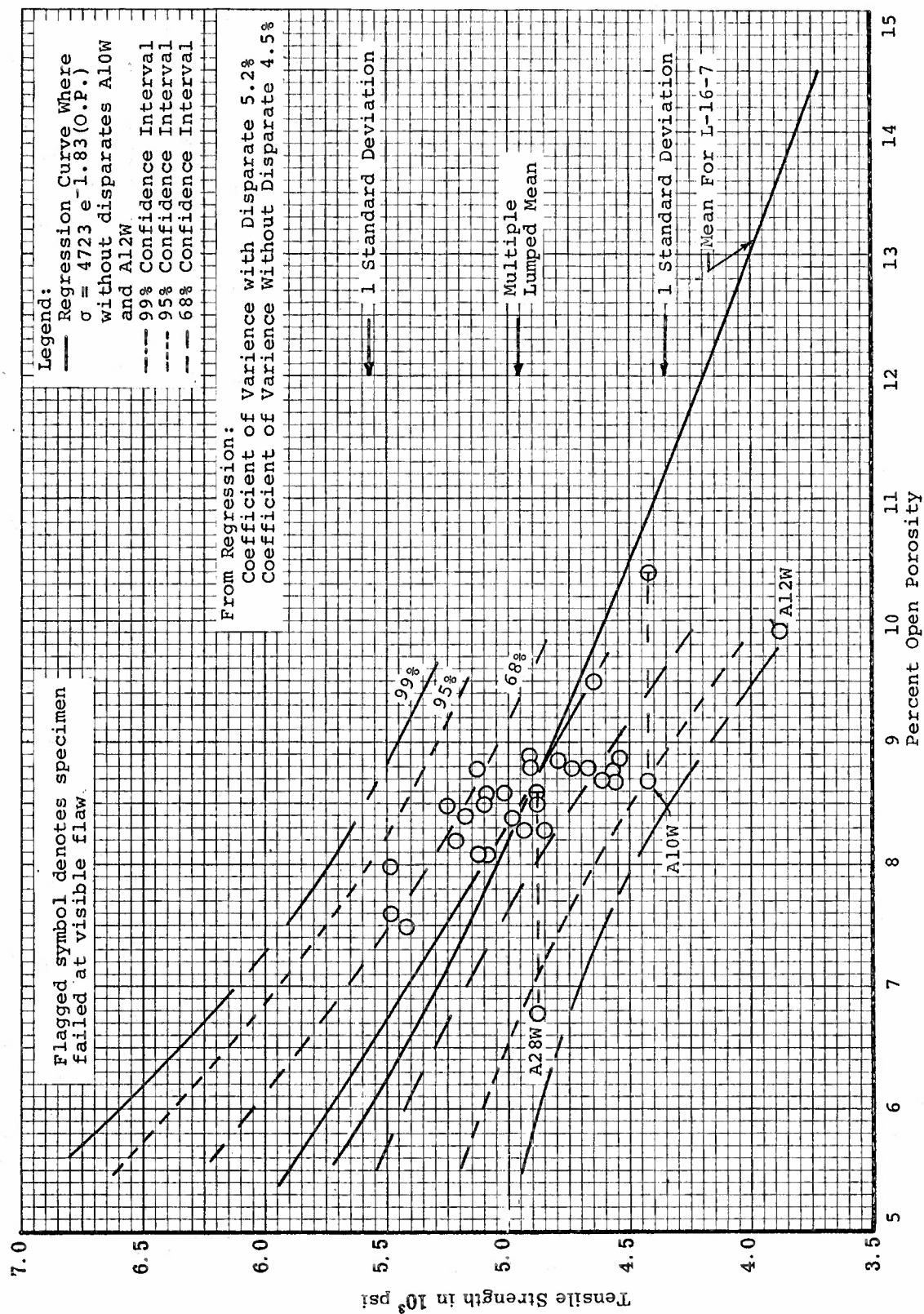
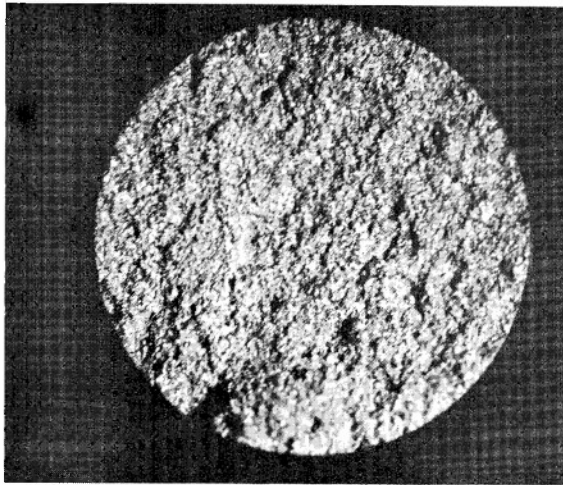
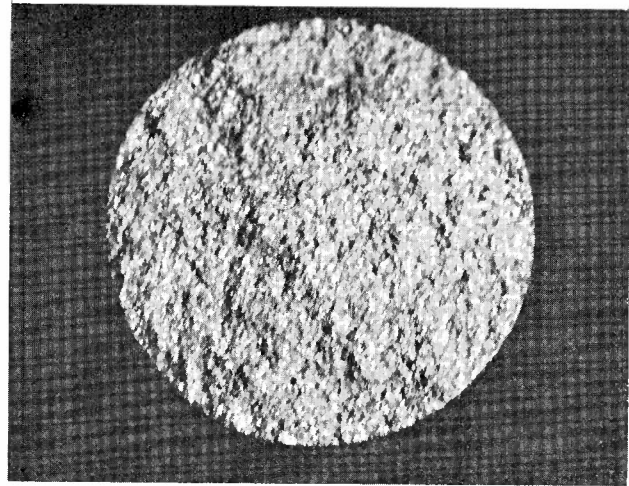


Figure 224. Regression Analysis Results for Tensile Strength versus Percent Open Porosity for ATJ-S Billet L-1-4 With Grain at 70°F



Short End



Long End

Specimen had 0.027" Hole at Surface after Machining (Fracture Occurred at Hole)

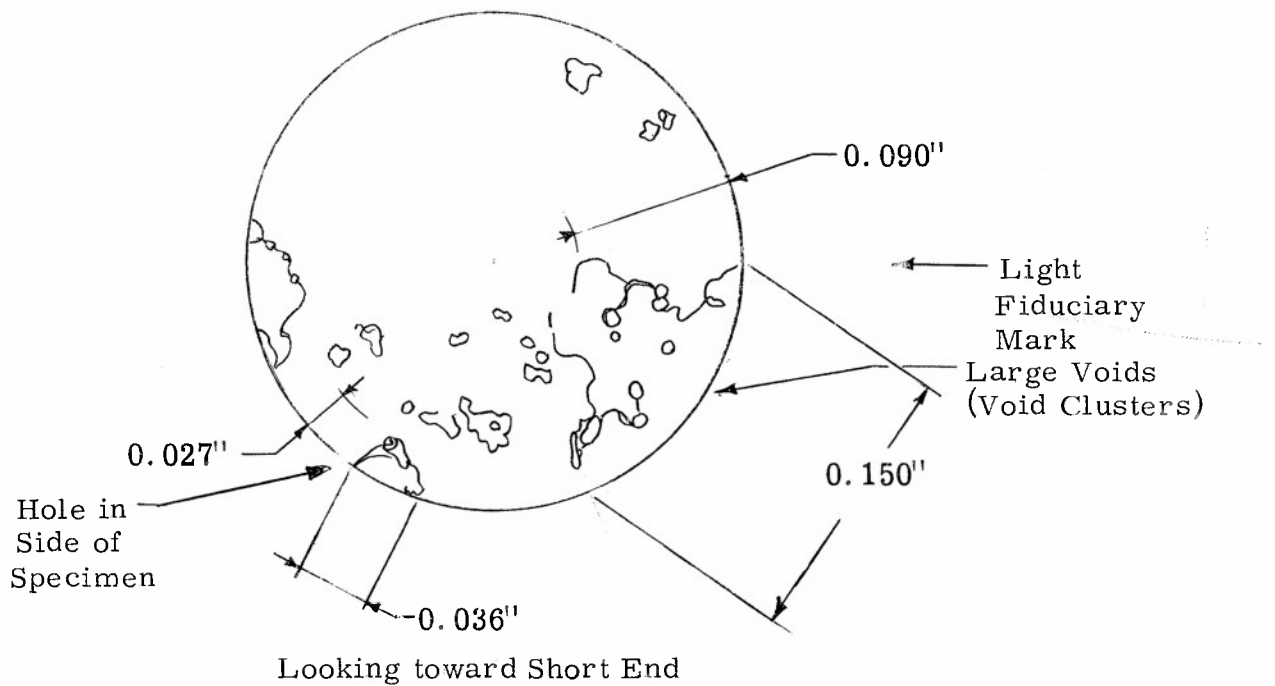
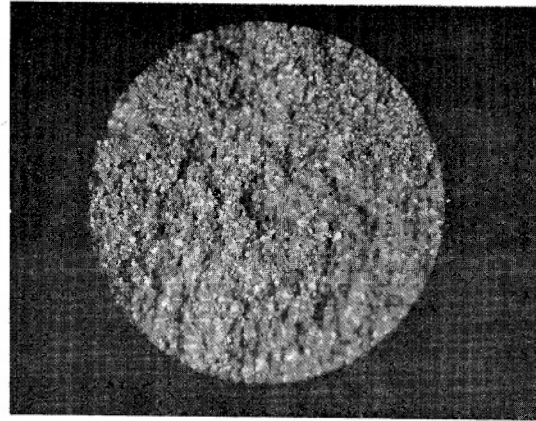
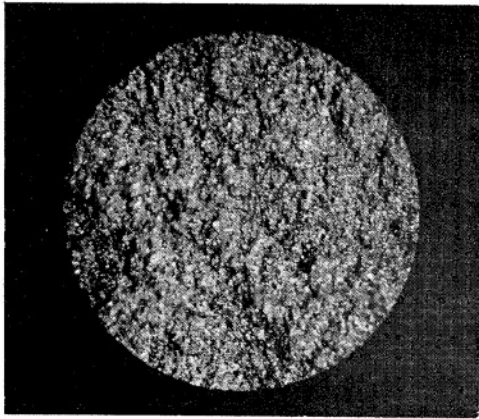


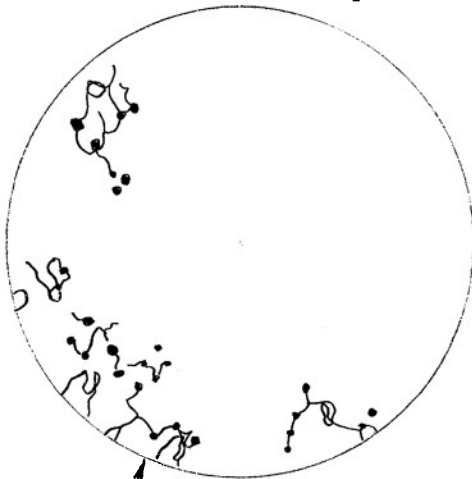
Figure 225. Flick Inspection Results and 10X Black and White Photographs of Fracture Faces of Disparate Specimen A12W from ATJ-S Billet L-1-4



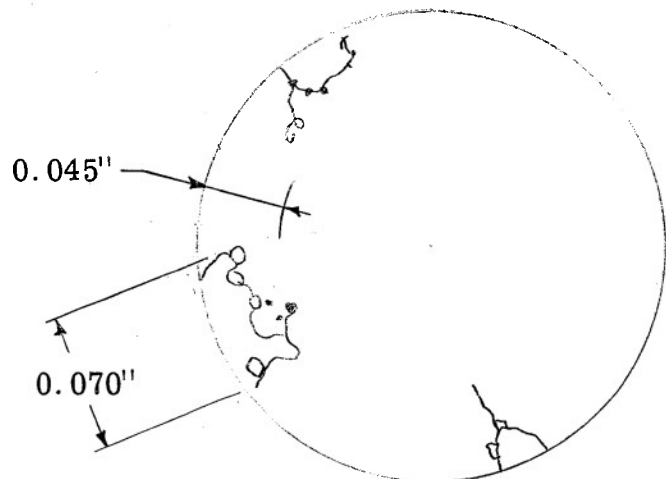


Short End  
Flicks from Transparencies

Long End  
Flicks of Regular Pictures



Typical -  
View in Flicks



Looking toward Short End. Does not Look  
too Bad. Mostly Background Void Sizes

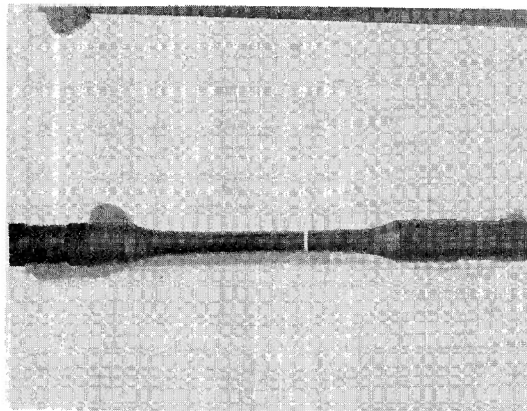


Figure 226. Flick Inspection Results and 10X Black and White  
Photographs of Fracture Faces of Specimen A10W  
from ATJ-S Billet L-1-4



Figure 100. (a) Map of the study area.

Figure 100. (b) Map of the study area.



Figure 100. (c) Map of the study area.

Figure 100. (d) Map of the study area.

Figure 100. (e) Map of the study area.

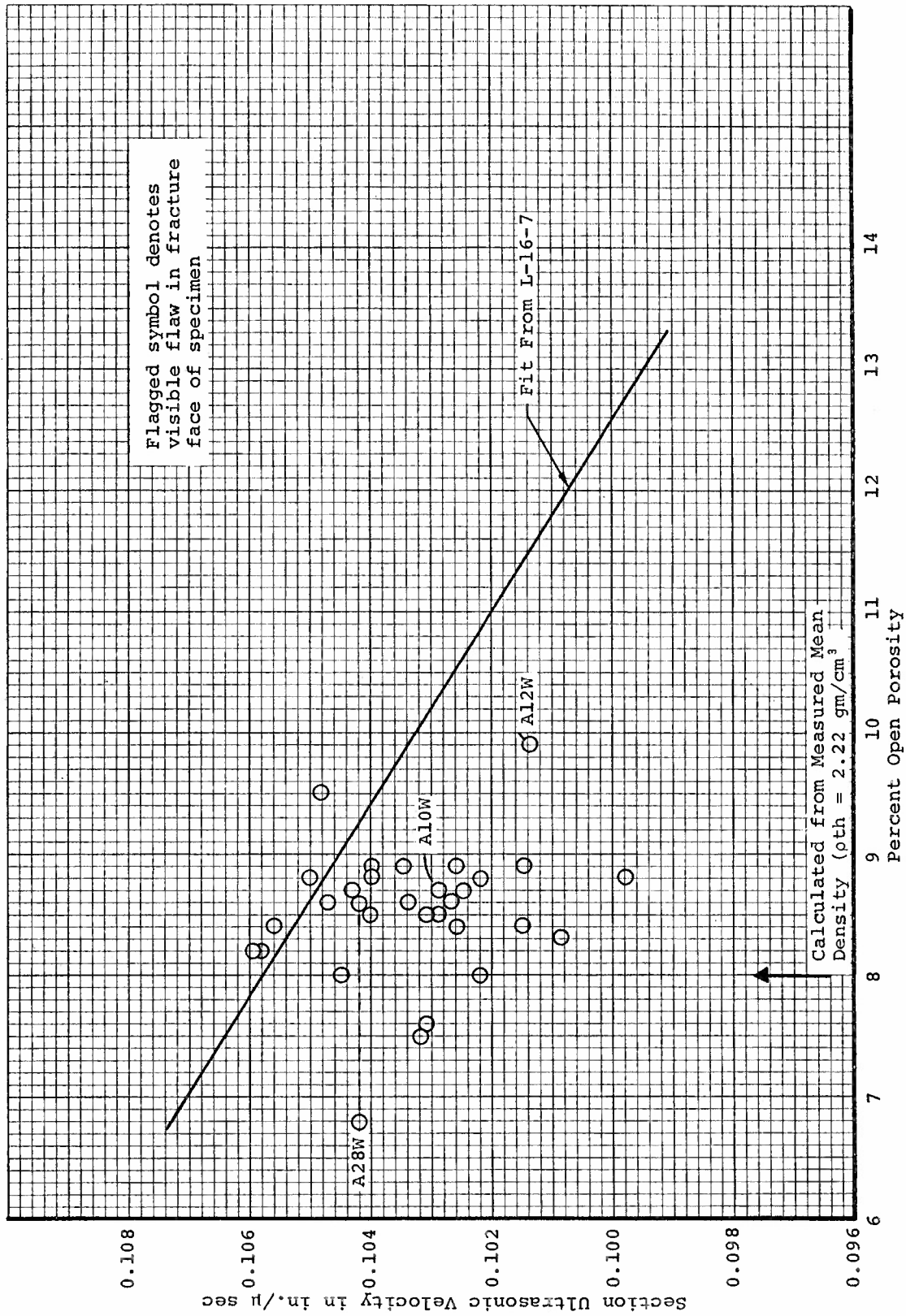


Figure 227. Section Ultrasonic Velocity versus Percent Open Porosity for ATJ-S Billet L-1-4 With Grain at 70°F



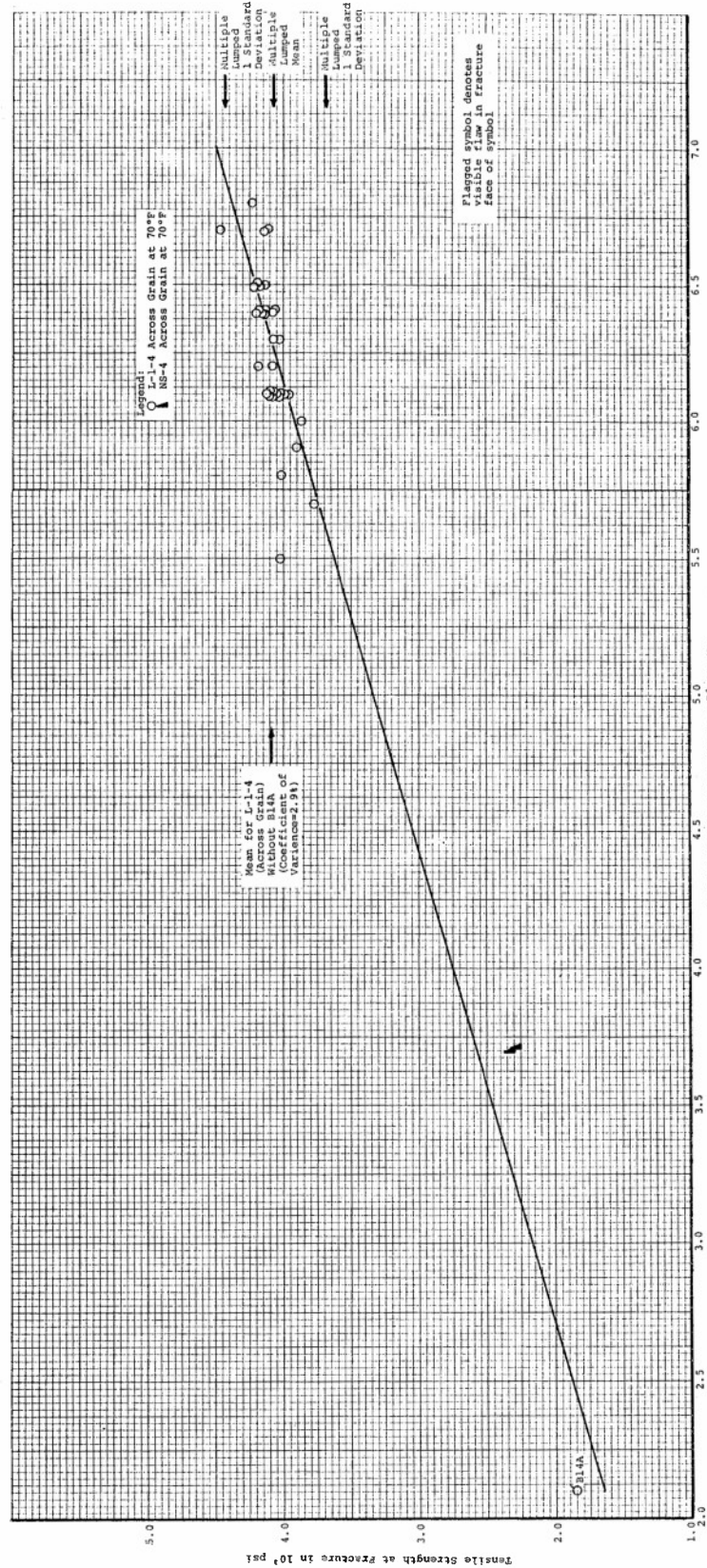
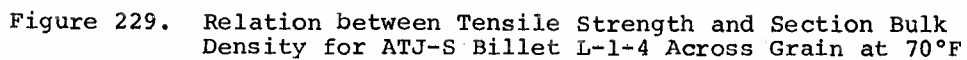


Figure 228. Tensile Strength versus Total Strain to Fracture for ATJ-S Billet L-1-4 and NS-4 Data Across Grain at 70°F





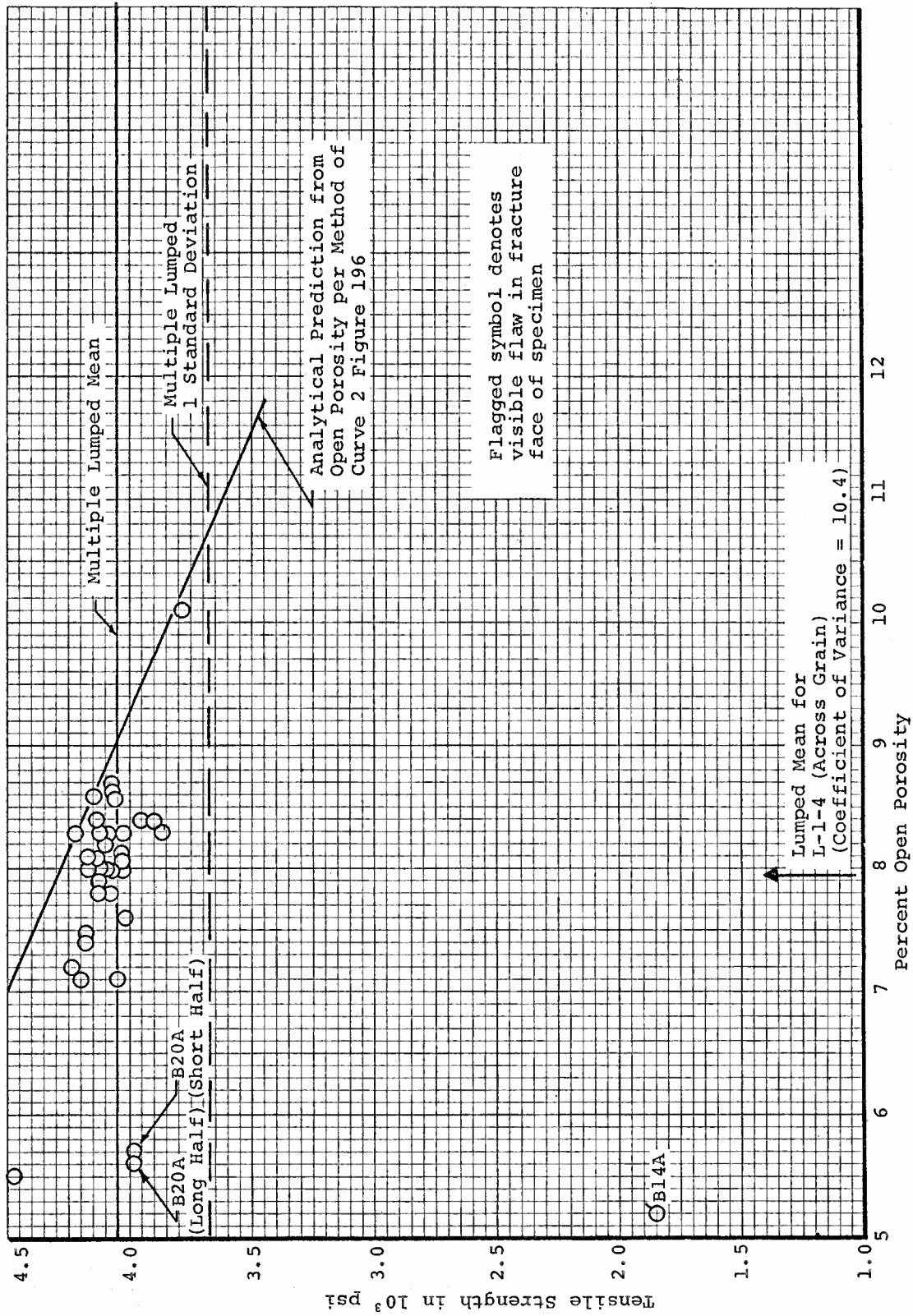
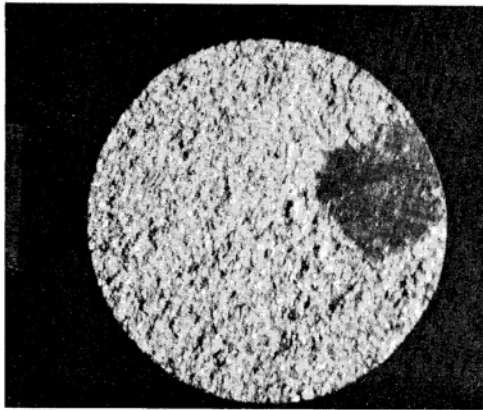
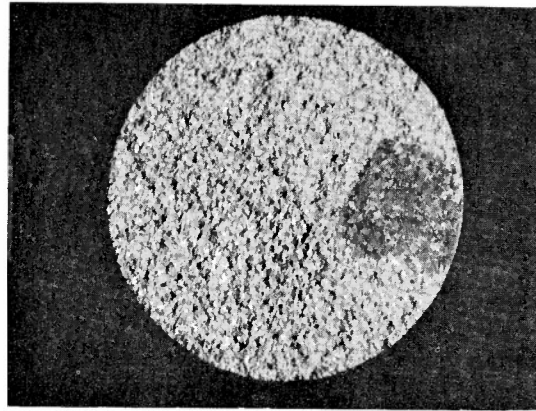


Figure 230. Relation between Tensile Strength and Percent Open Porosity for ATJ-S Billet L-1-4 Across Grain at 70°F



Short End



Long End

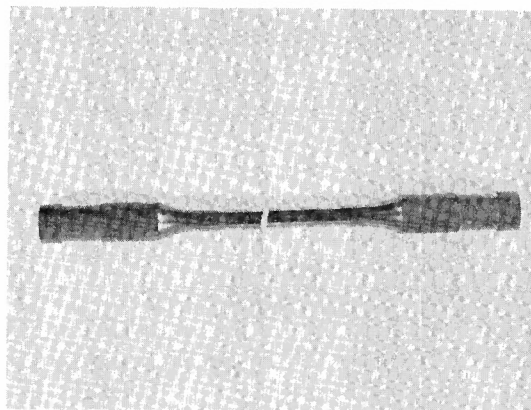
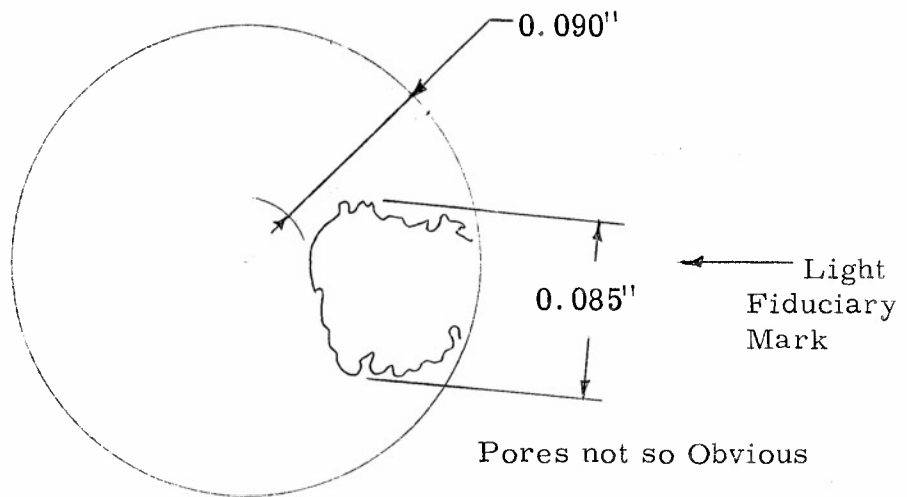


Figure 231. Flick Inspection Results and 10X Black and White Photographs of Fracture Faces of Specimen B14A from ATJ-S Billet L-1-4



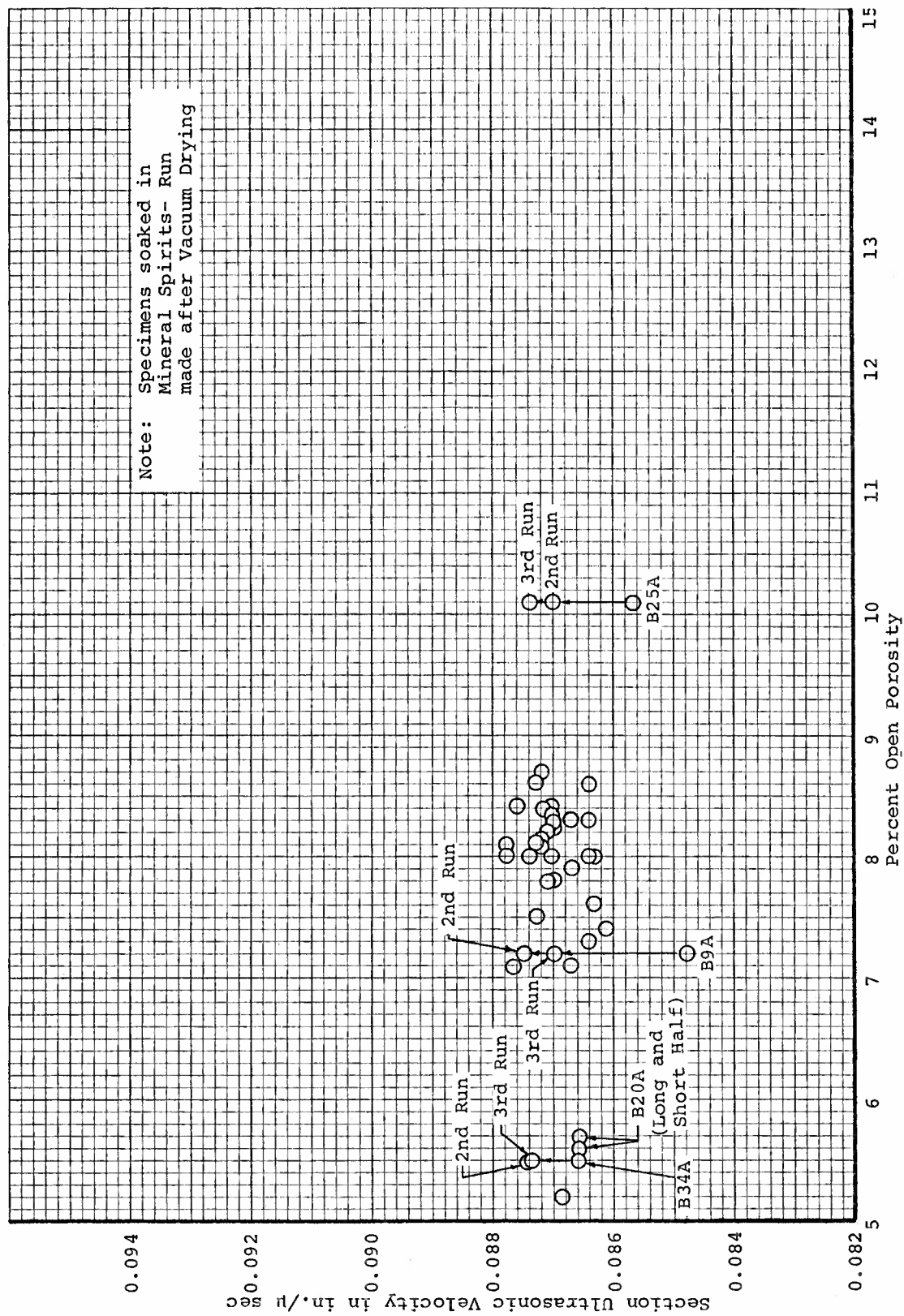
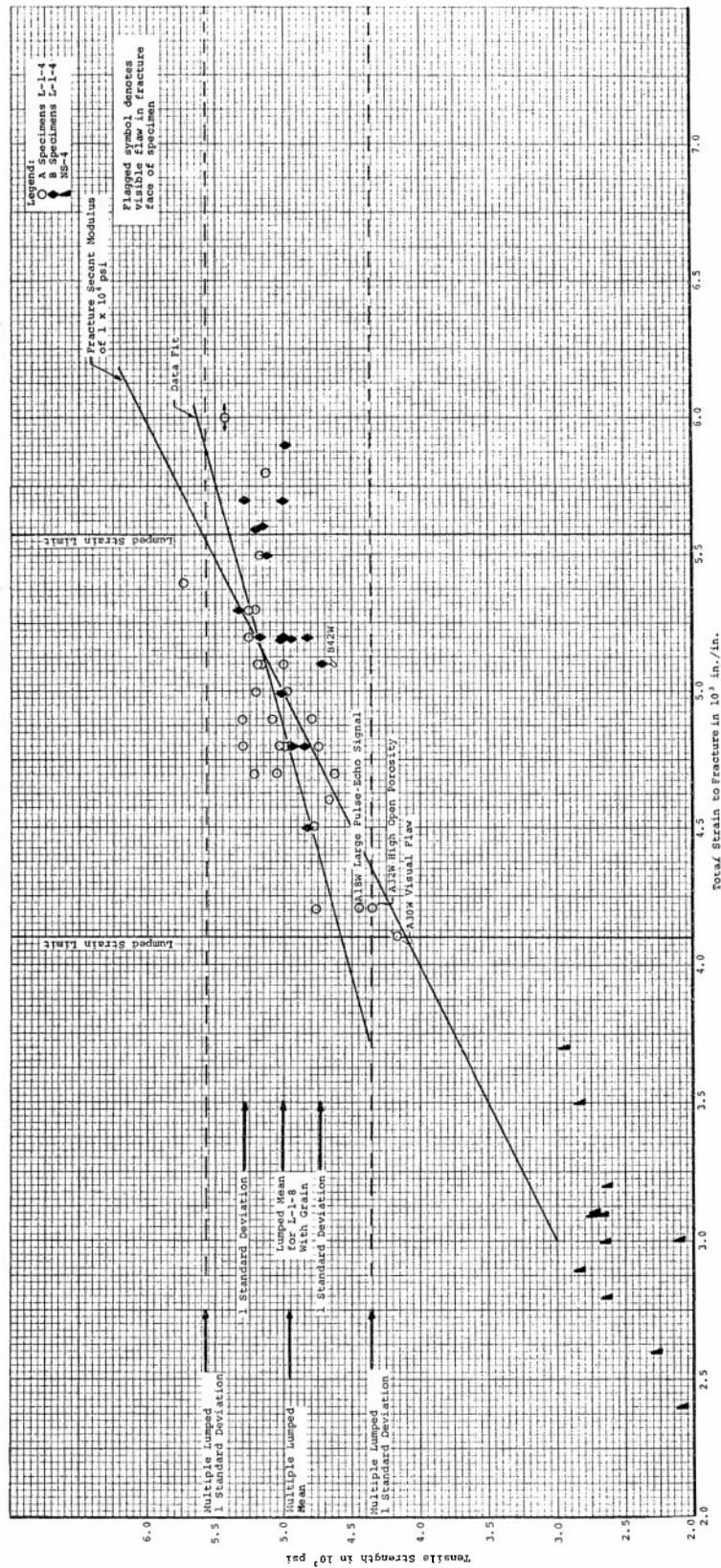


Figure 232. Section Ultrasonic Velocity versus Percent Open Porosity for ATJ-S L-1-4 Across Grain





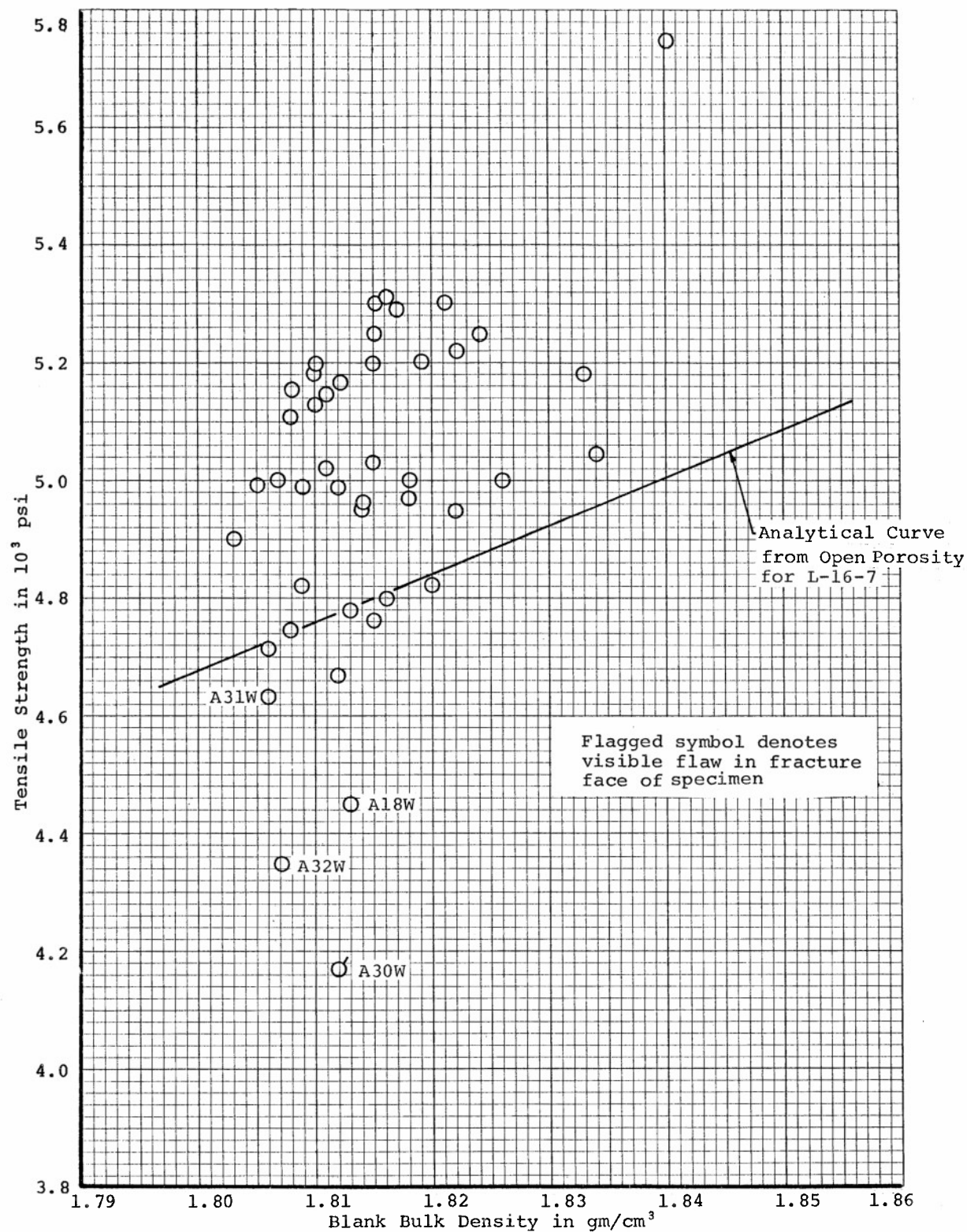


Figure 234. Relation between Tensile Strength and Blank Bulk Density for ATJ-S Billet L-1-8 With Grain at 70°F

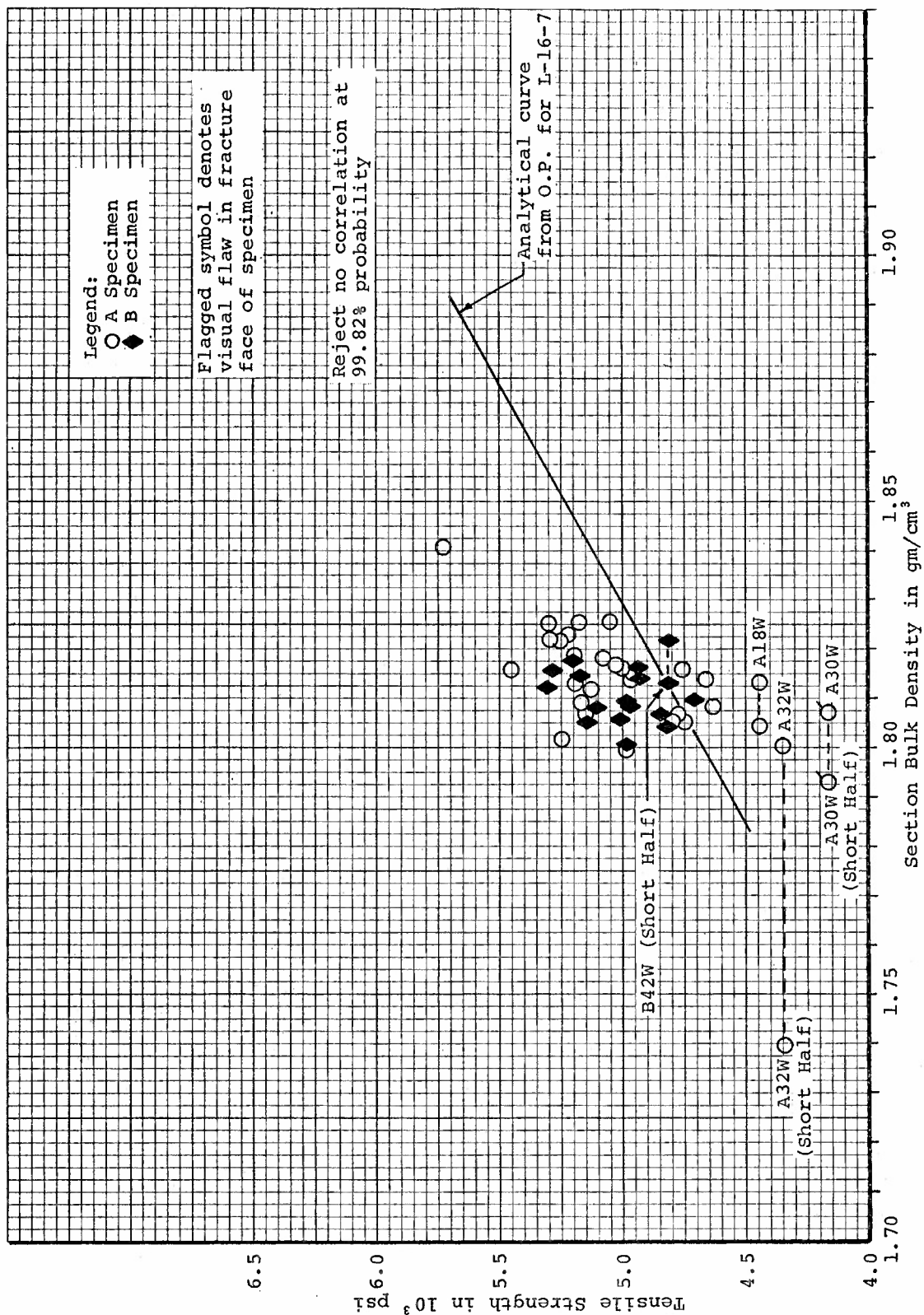


Figure 235. Relation between Tensile Strength and Section Bulk Density for ATJ-S Billet L-1-8 With Grain at 70°F



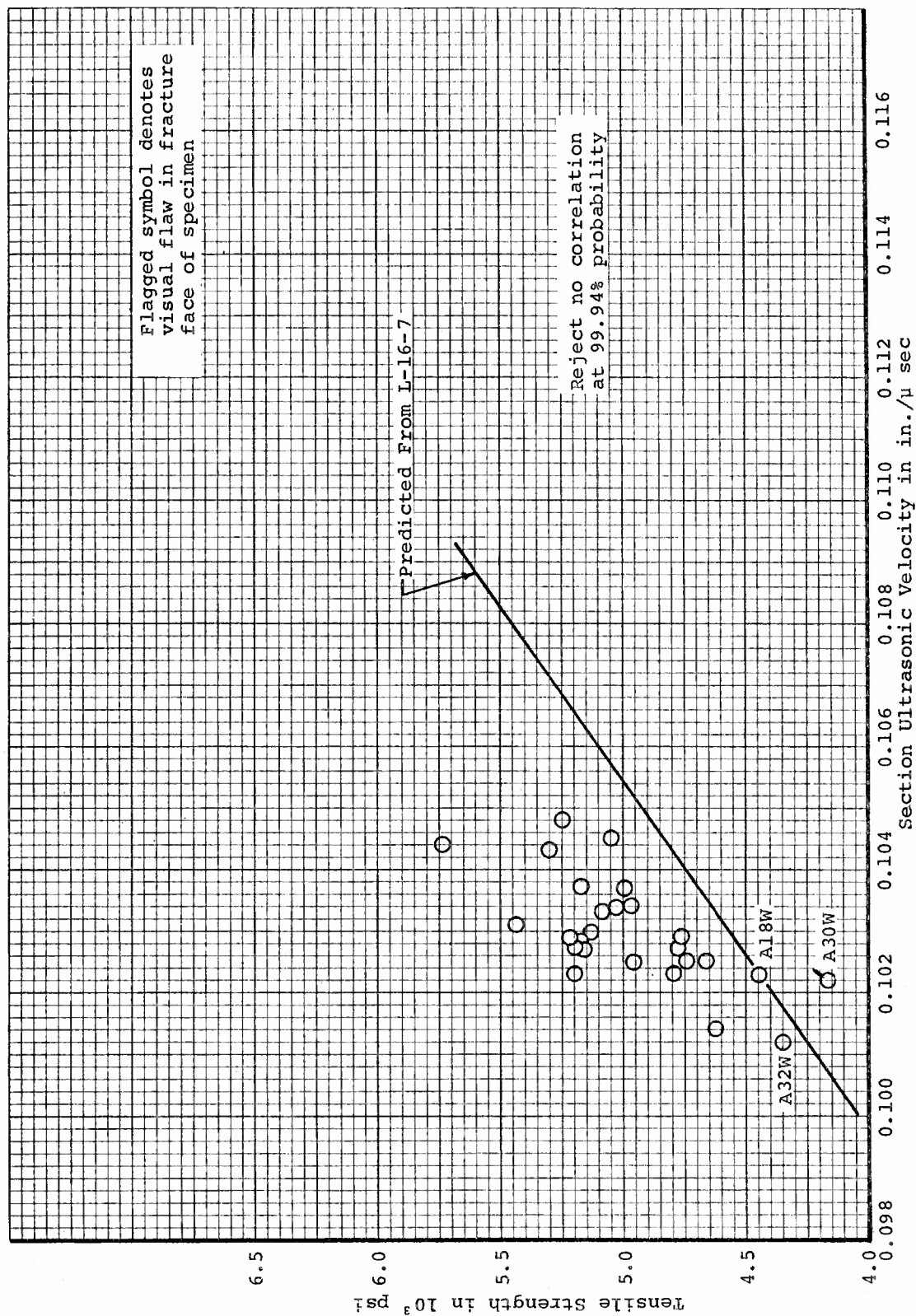


Figure 236. Relation between Tensile Strength and Section Ultrasonic Velocity for A Specimens from ATJ-S Billet L-1-8 With Grain at 70°F

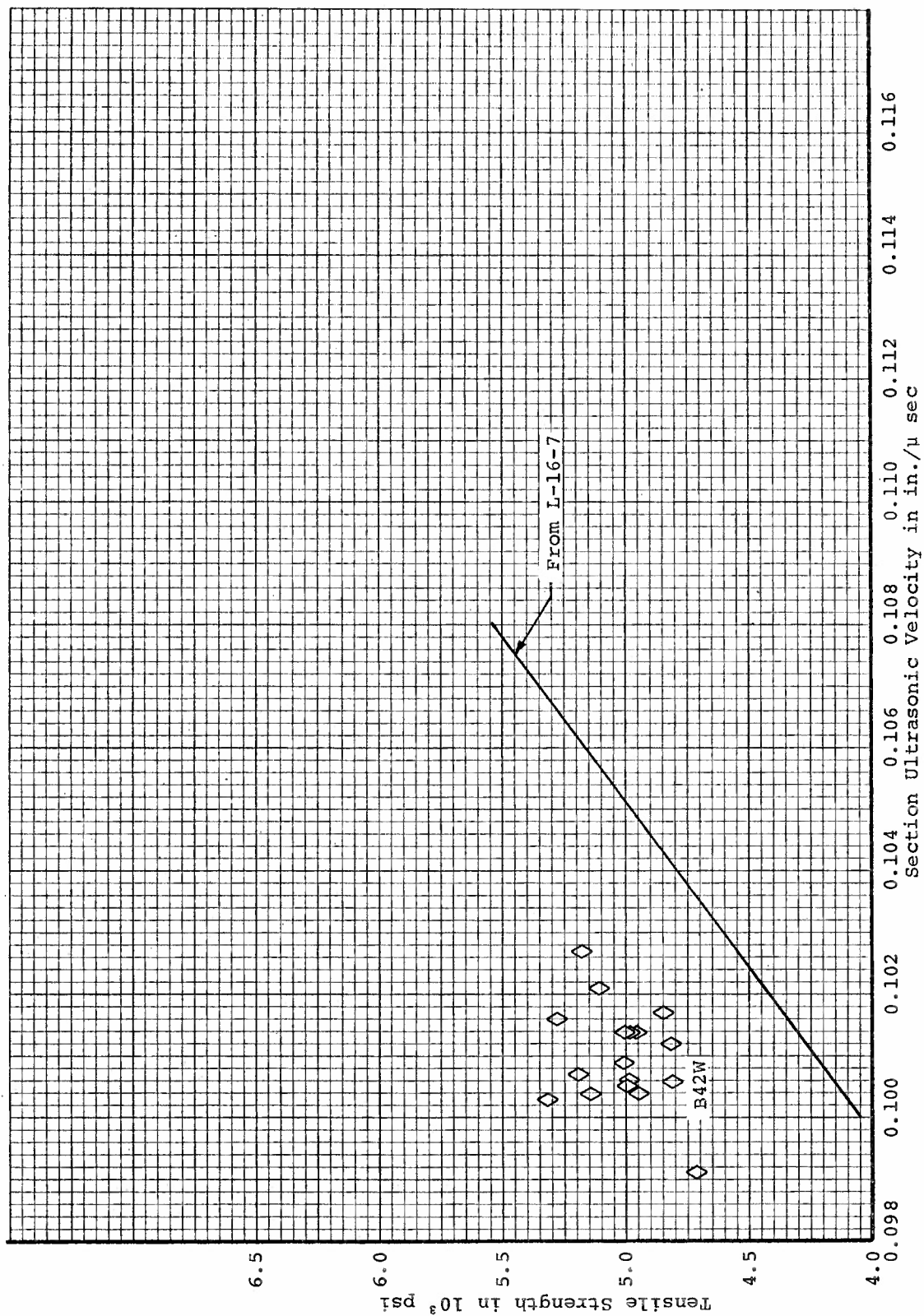


Figure 237. Relation between Tensile Strength and Section Ultrasonic Velocity for B Specimens from ATJ-S Billet L-1-8 With Grain at 70°F

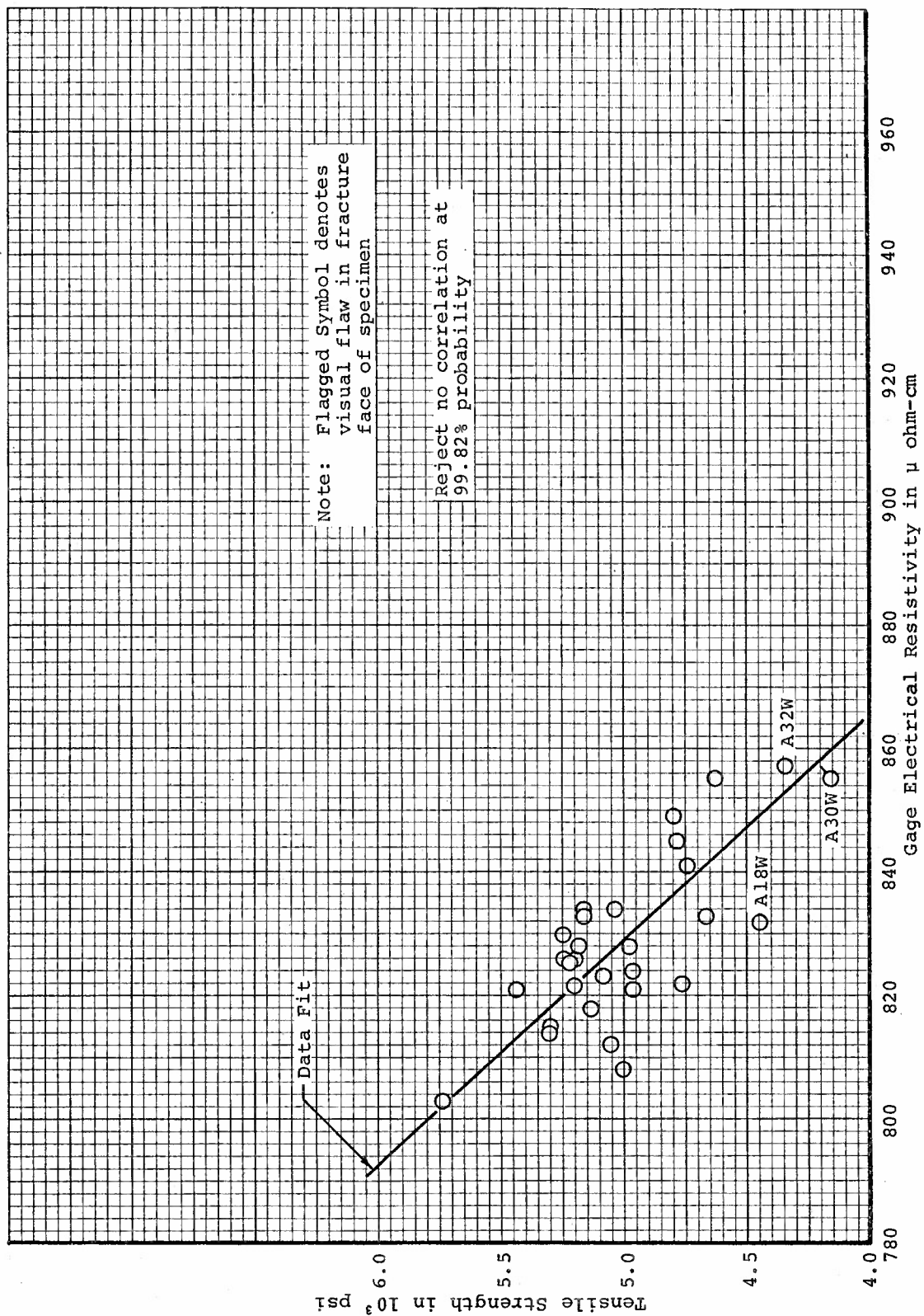


Figure 238. Relation between Tensile Strength and Gage Electrical Resistivity for A Specimens from AFJ-S Billet I-1-8 With Grain at 70°F

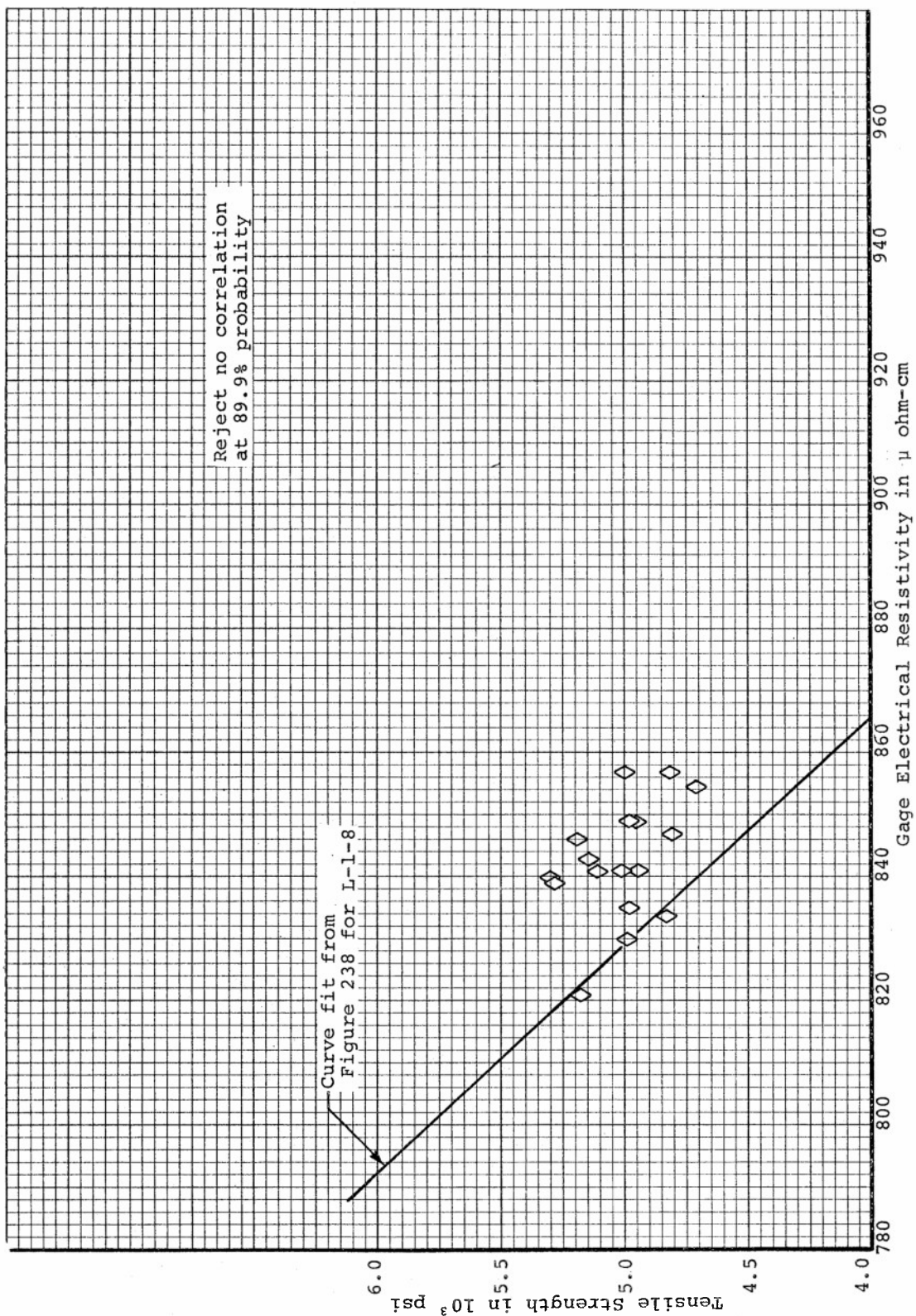


Figure 239. Relation between Tensile Strength and Gage Electrical Resistivity for B Specimens from ATJ-S Billet L-1-8 With Grain at 70°F

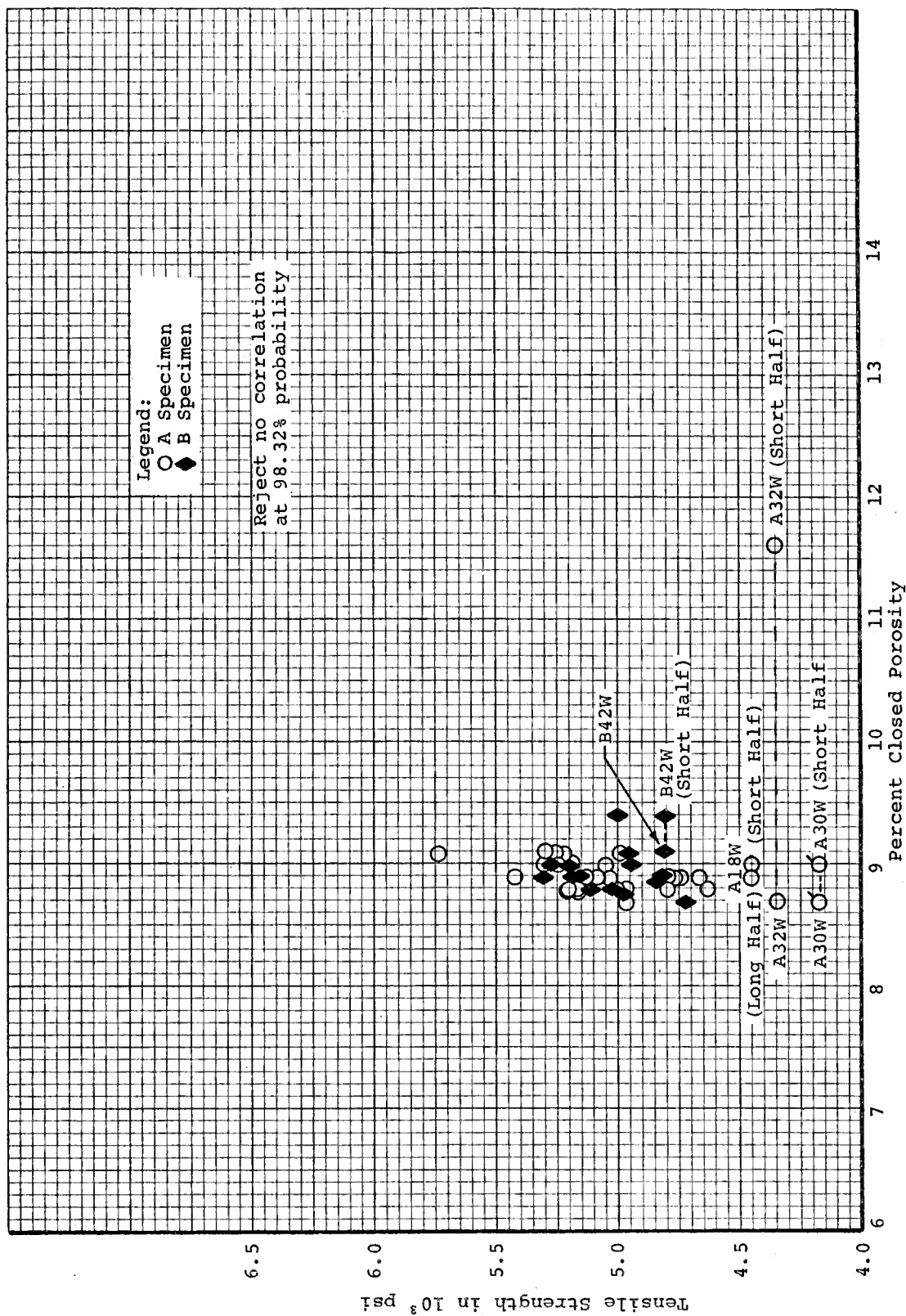


Figure 240. Relation between Tensile Strength and Percent Closed Porosity for ATJ-S Billet L-1-8 With Grain at 70°F



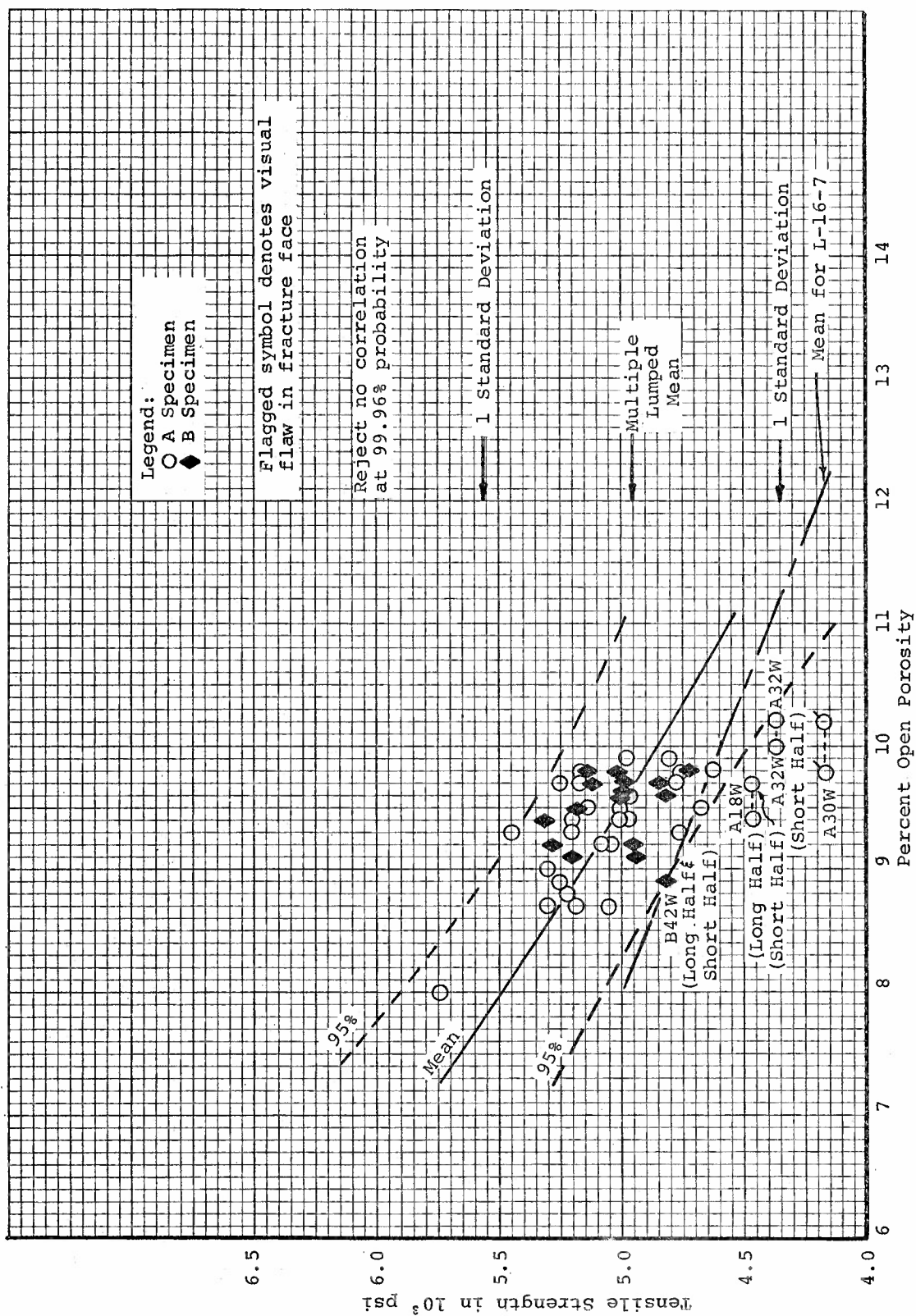


Figure 241. Regression Analysis Results for Tensile Strength versus Percent Open Porosity for ATJ-S Billet L-1-8 With Grain at 70°F

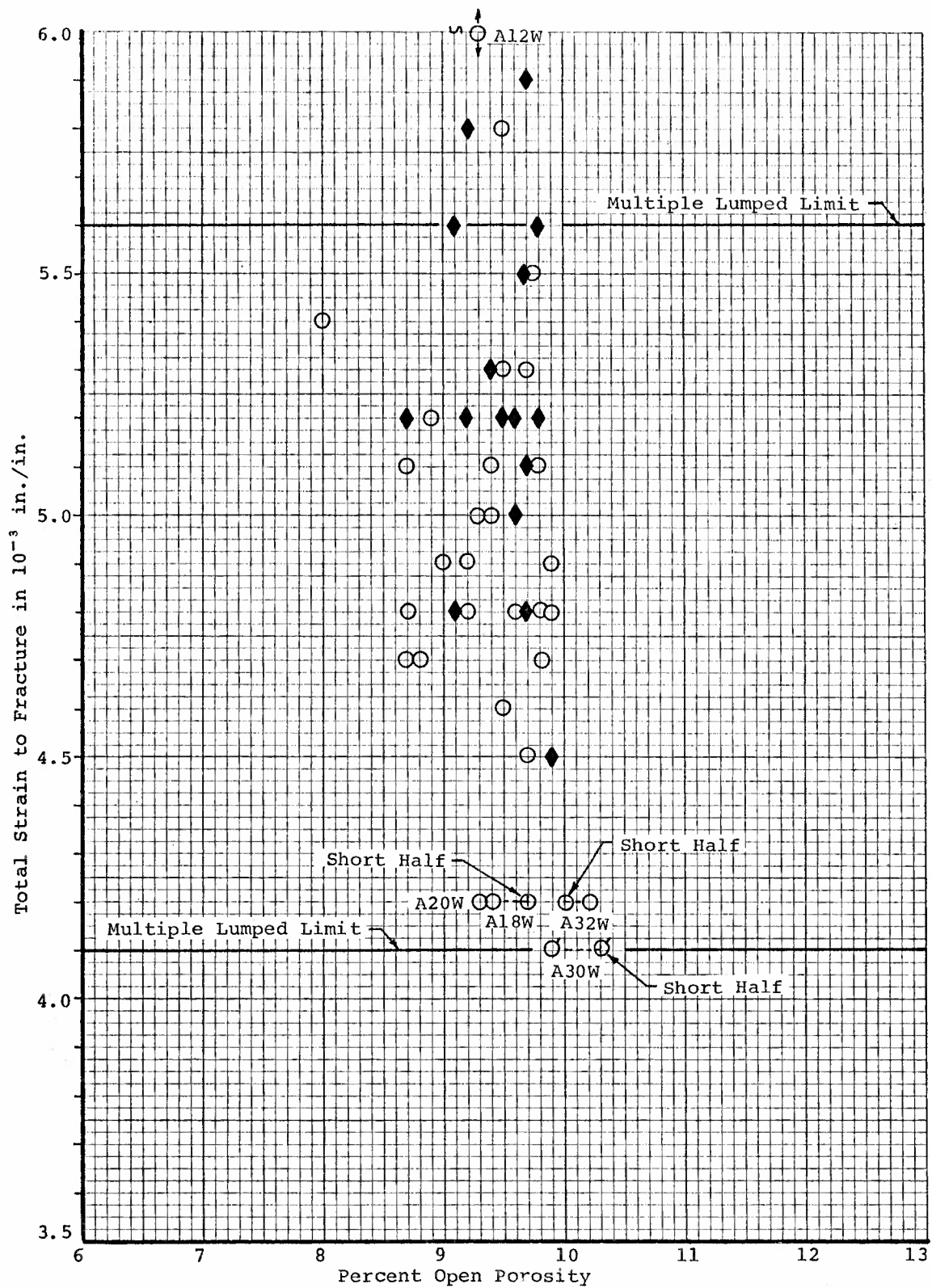


Figure 242. Total Tensile Strain to Fracture versus Percent Open Porosity for ATJ-S Billet L-1-8 With Grain at 70°F

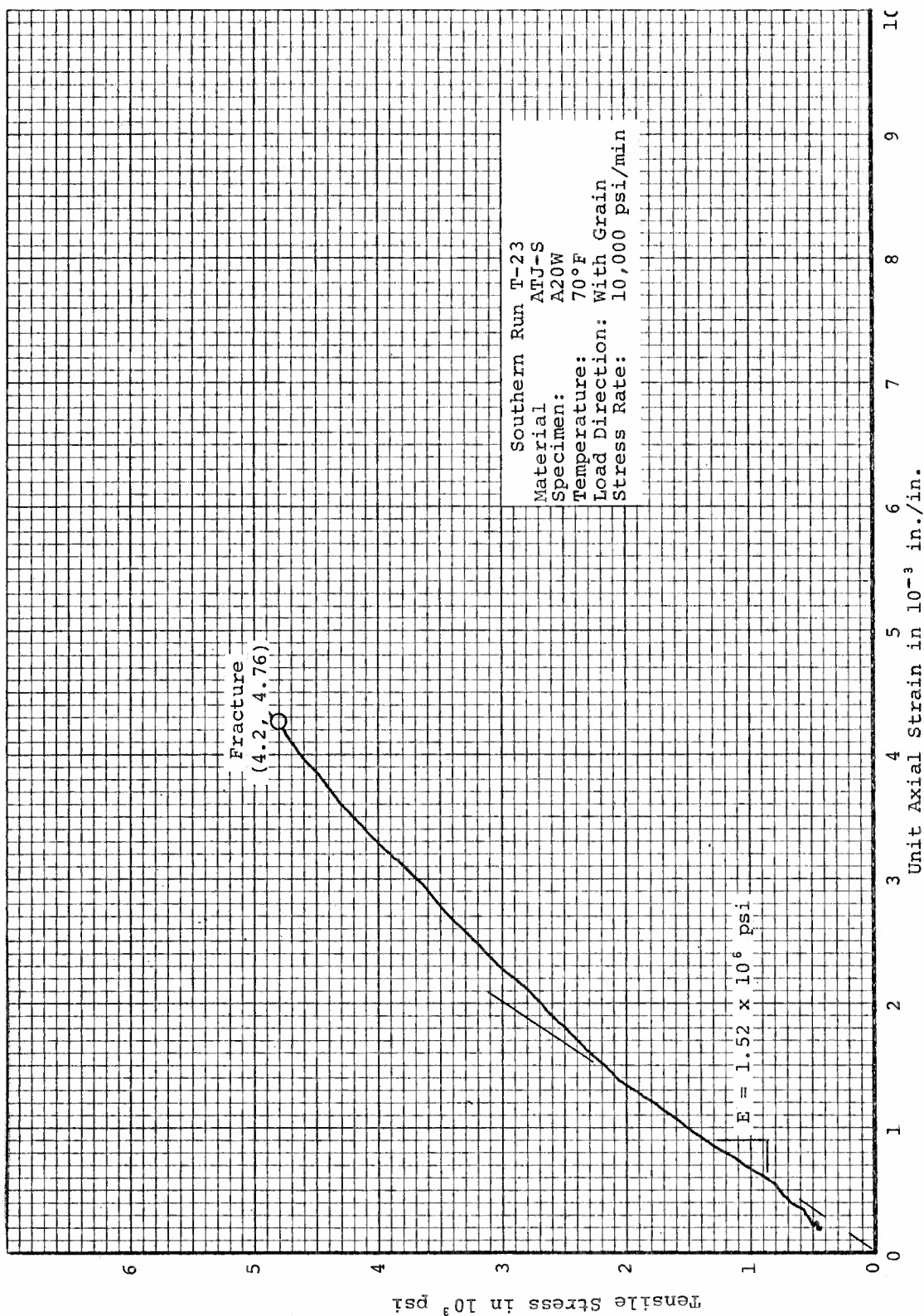
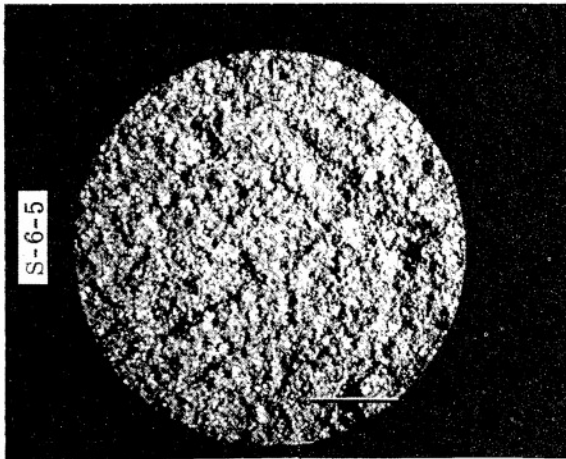
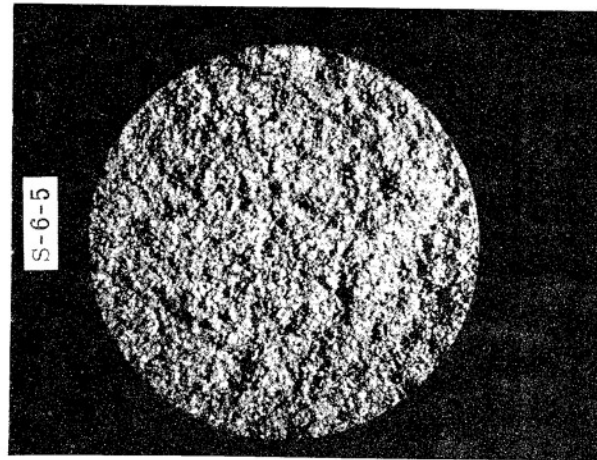


Figure 243. Tensile Stress-Strain Curve for Specimen A20W from ATJ-S Billet L-1-8 With Grain at 70°F





Short End



Long End

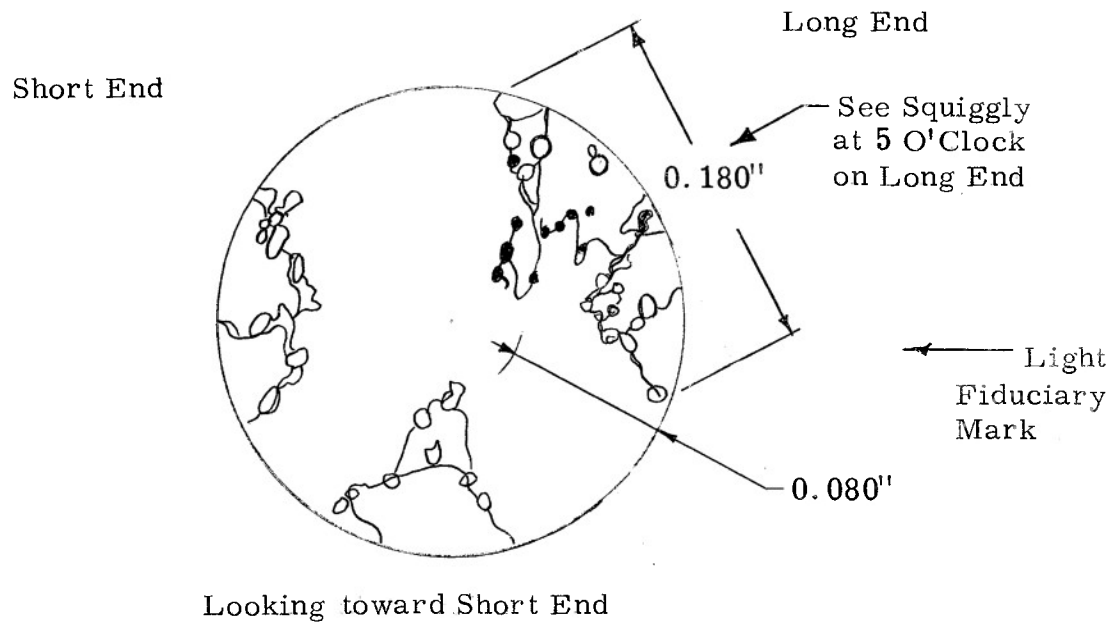
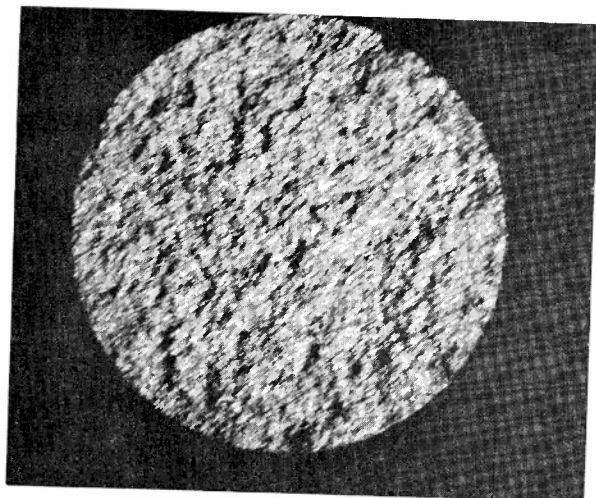
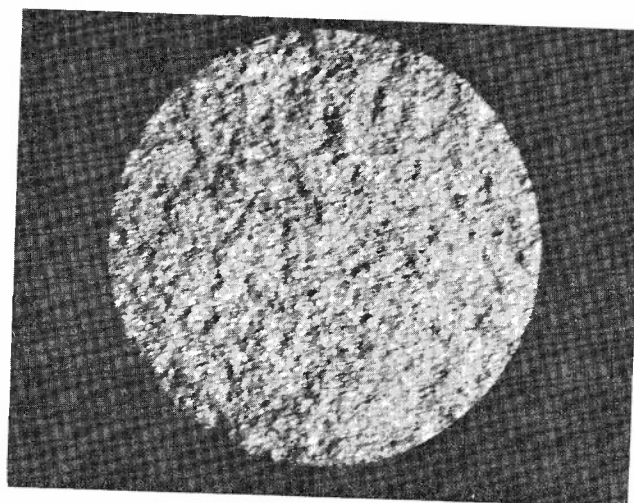


Figure 244. Flick Inspection Results and 10X Black and White Photographs of Fracture Faces of Disparate Specimen A30W from ATJ-S Billet L-1-8





Short End



Long End

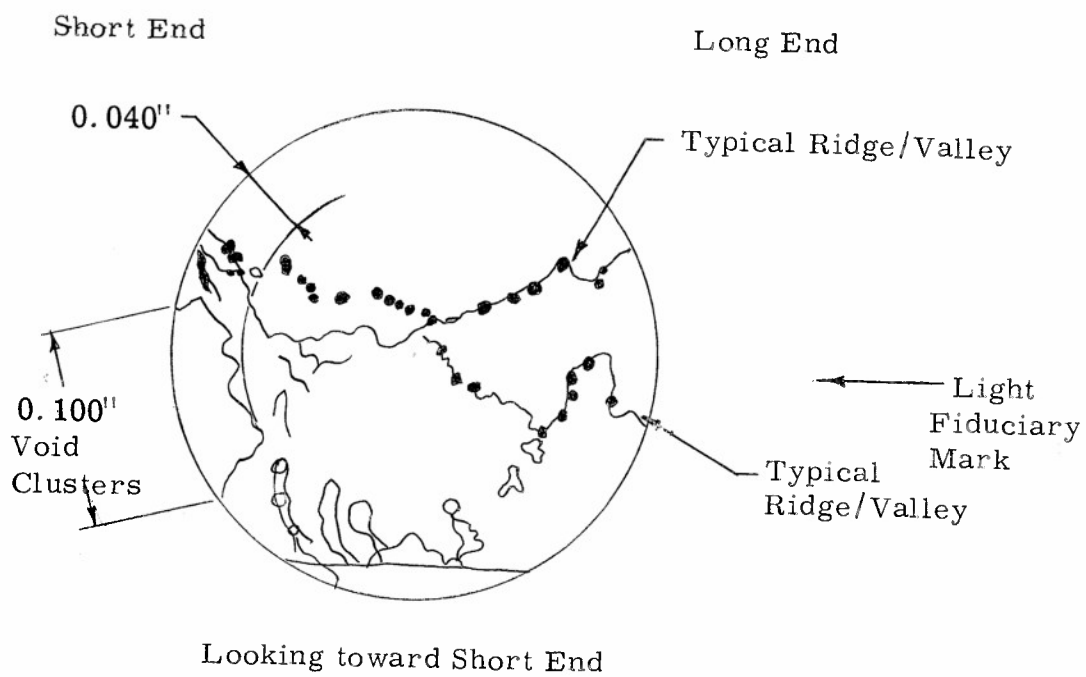
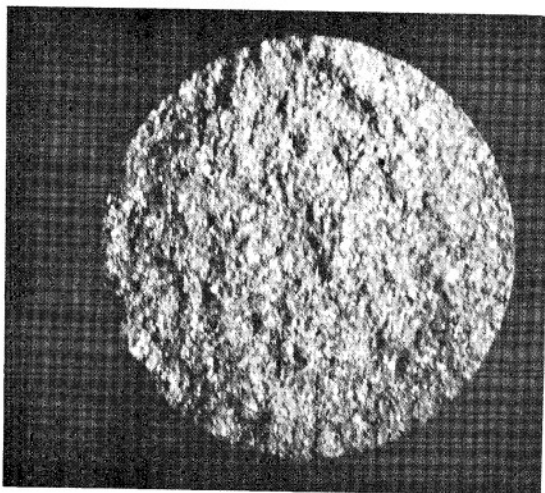
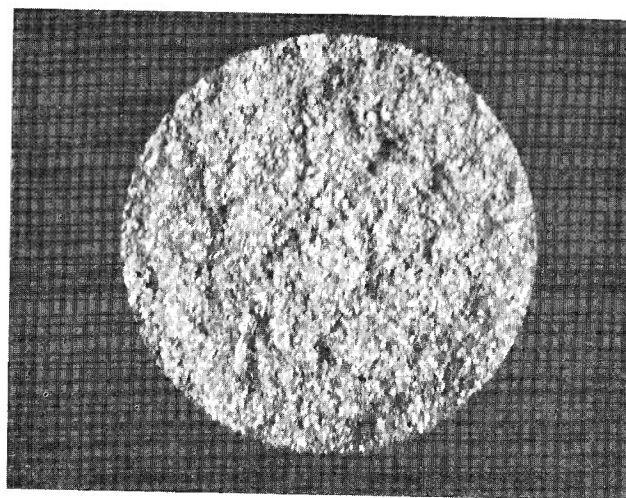


Figure 245. Flick Inspection Results and 10X Black and White Photographs of Fracture Faces of Weak Specimen A18W from ATJ-S Billet L-1-8





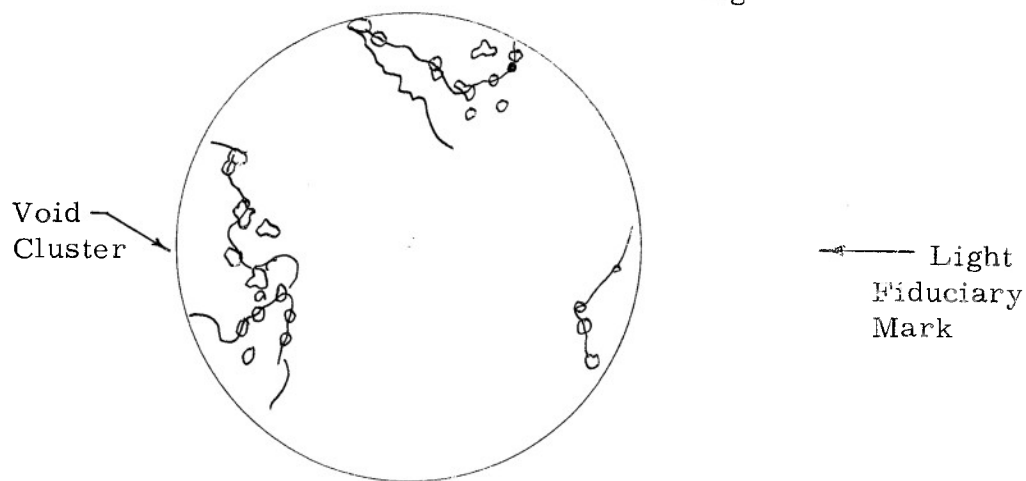
Short End



Long End

Short End

Long End



Looking toward Short End

Figure 246. Flick Inspection Results and 10X Black and White Photographs of Fracture Faces of Specimen A32W from ATJ-S Billet L-1-8



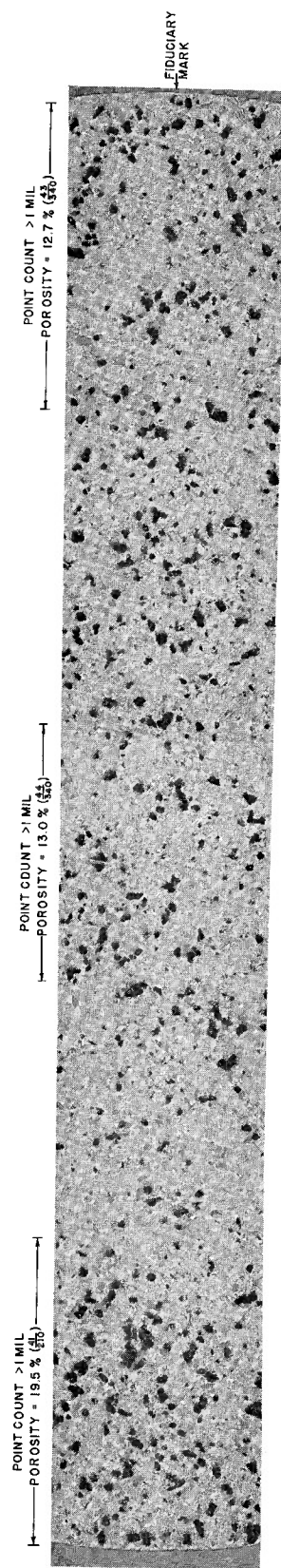


Figure 247. 100X Photomicrograph of Cross Section from Weak Specimen A18W about 10 mils below Fracture Face, No Impregnation, ATJ-S Billet L-1-8





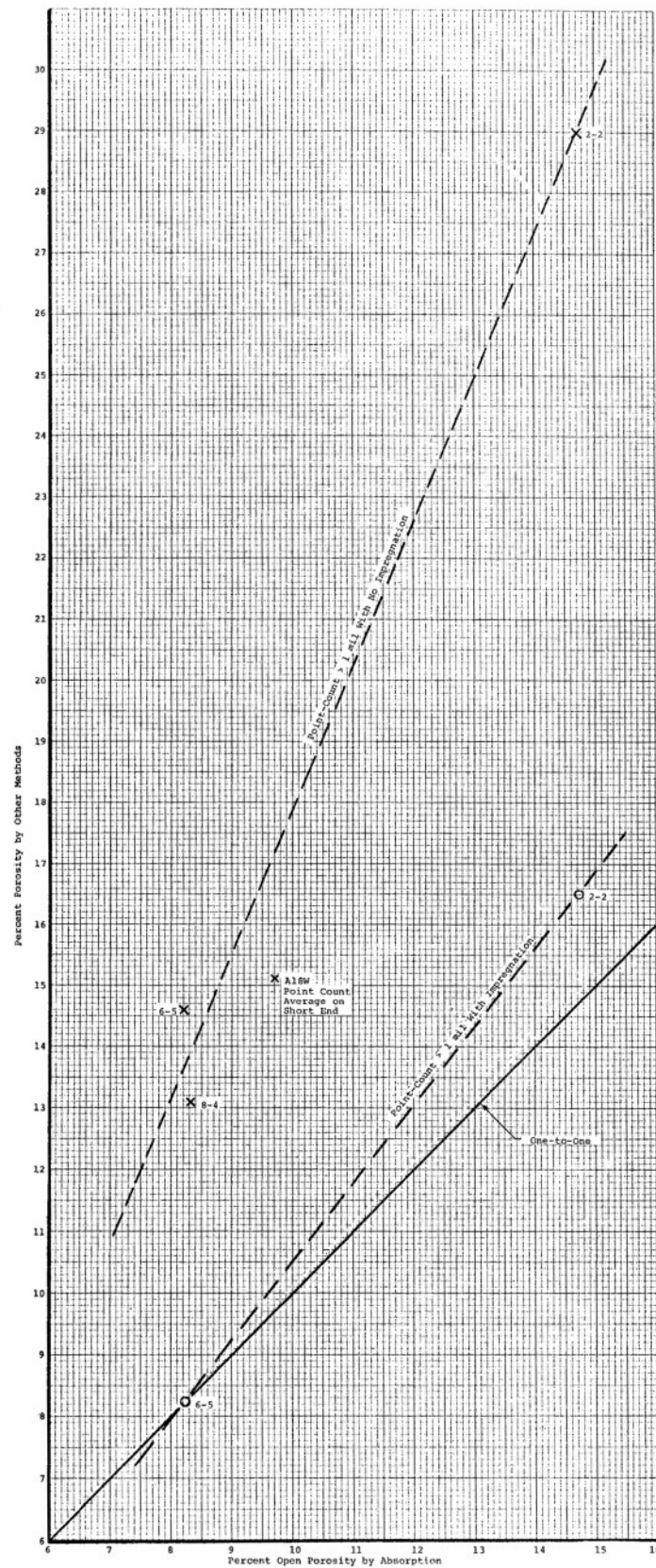


Figure 248. Comparison of Open Porosity by Absorption to Porosity by Other Methods

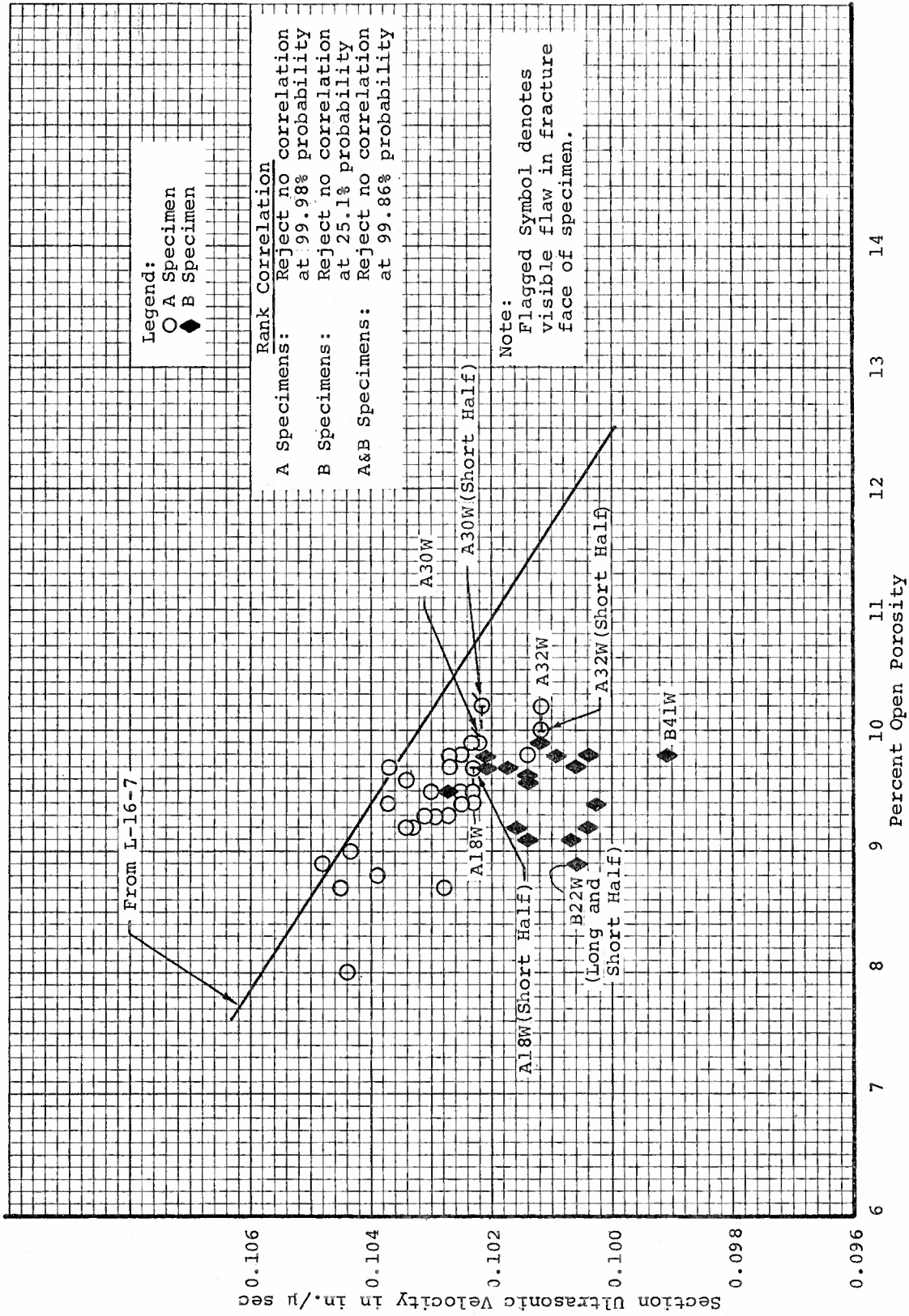


Figure 249. Relation between Section Ultrasonic Velocity and Percent Open Porosity for ATJ-S Billet L-1-8

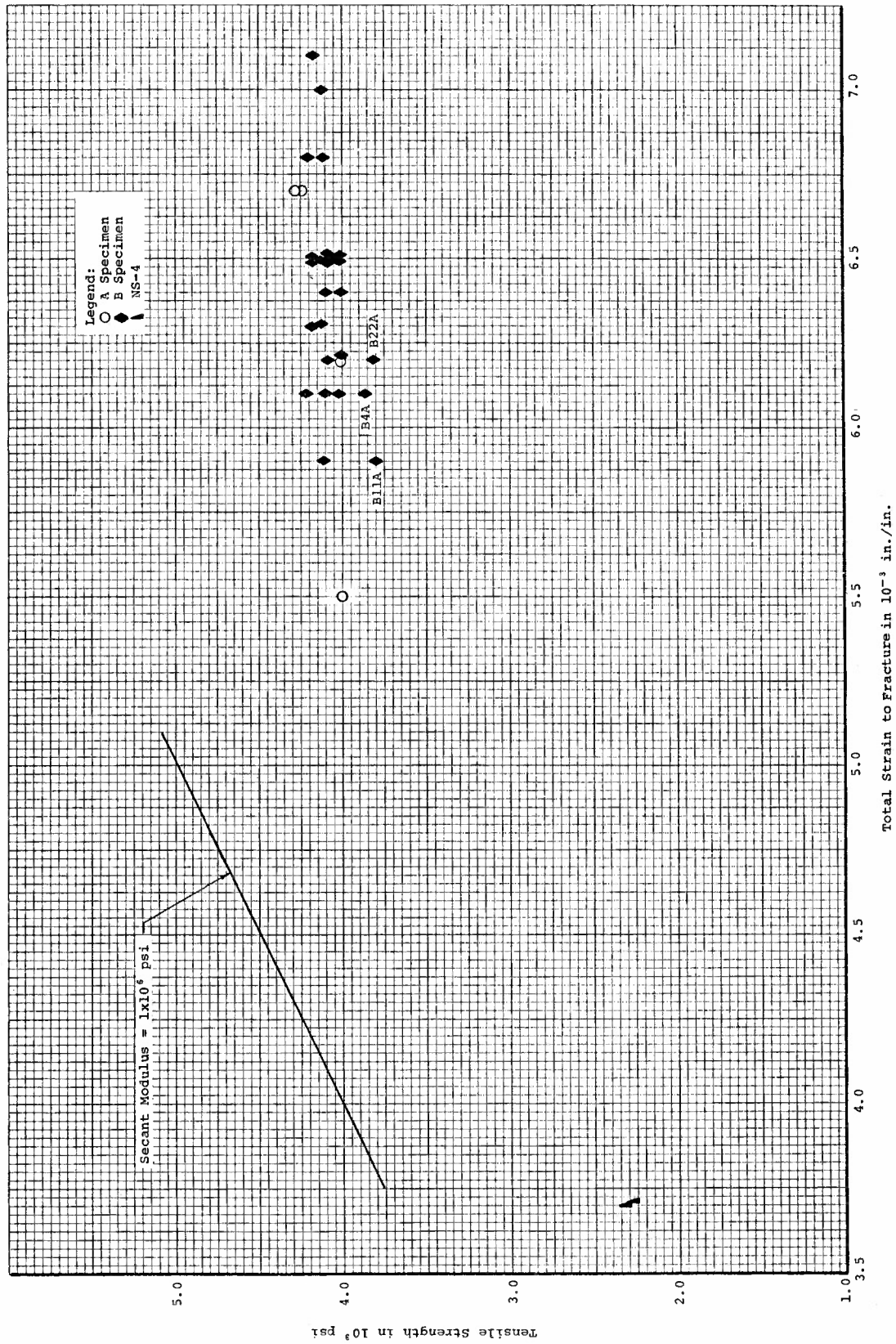
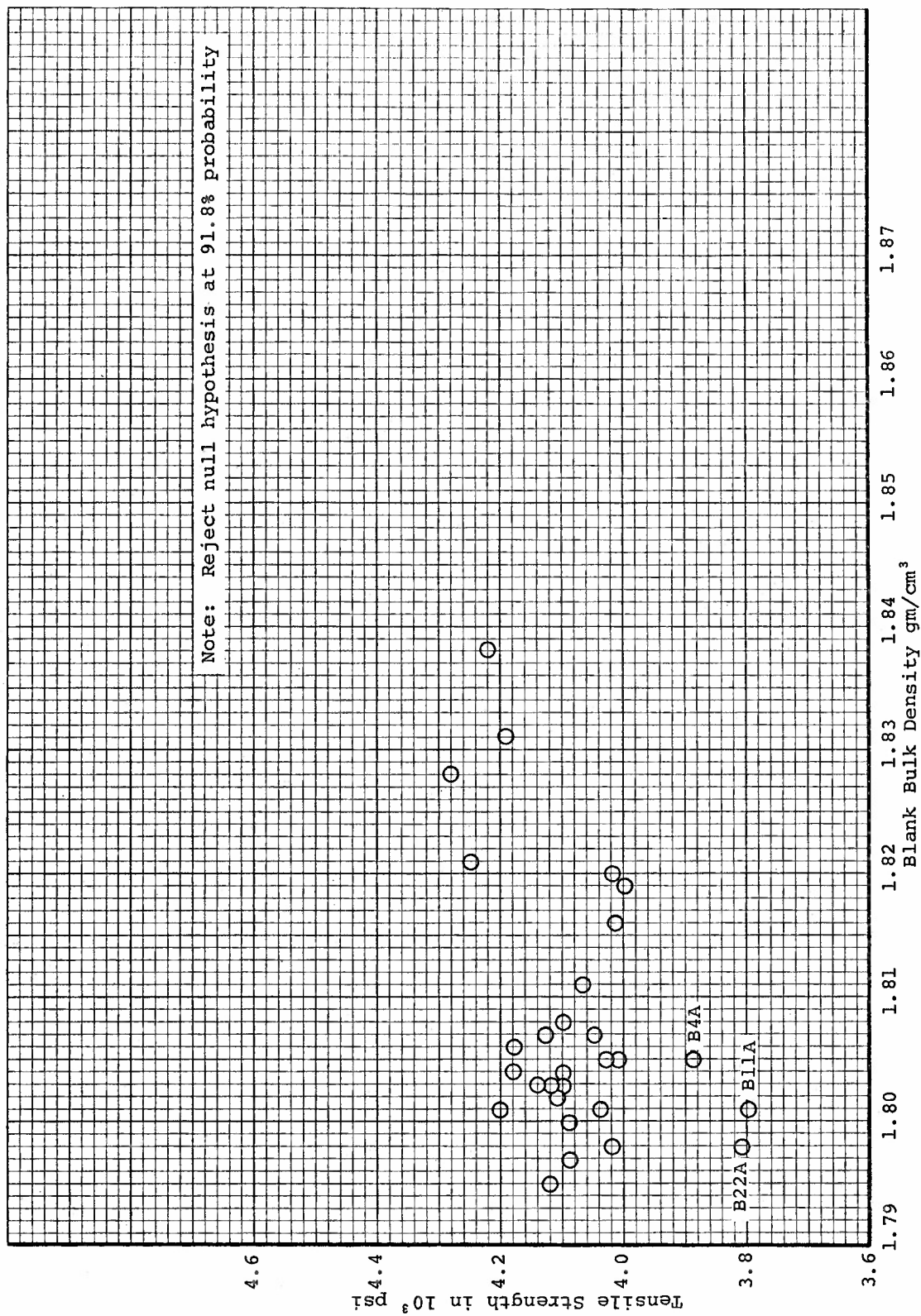


Figure 250. Tensile Strength versus Total Strain to Fracture for ATJ-S Billet L-1-8 Across Grain at 70°F



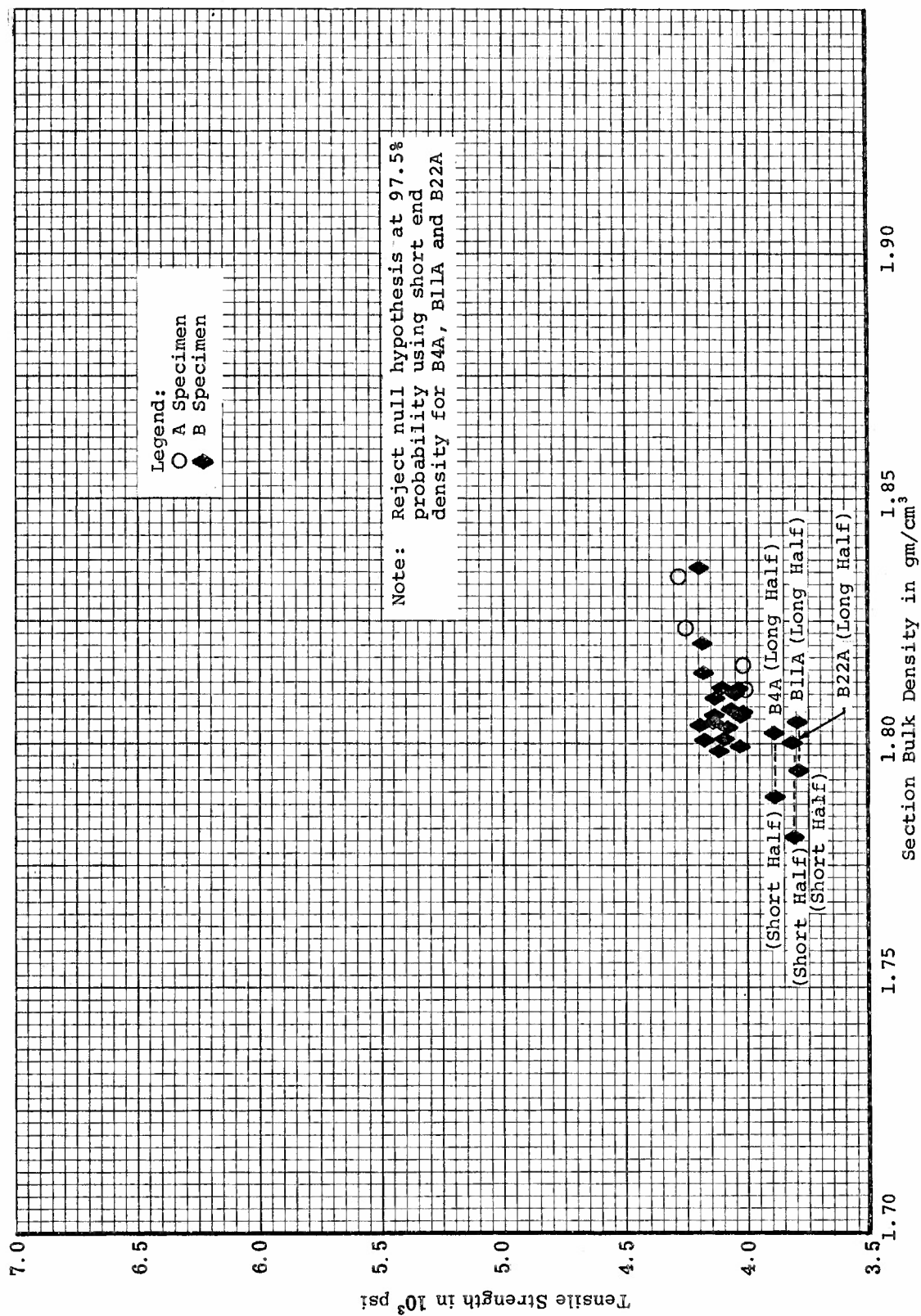
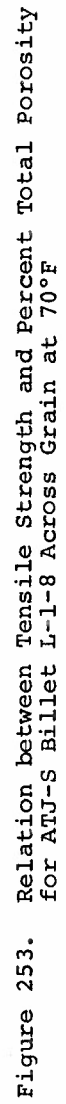


Figure 252. Relation between Tensile Strength and Section Bulk Density for ATJ-S Billet L-1-8 Across Grain at 70°F





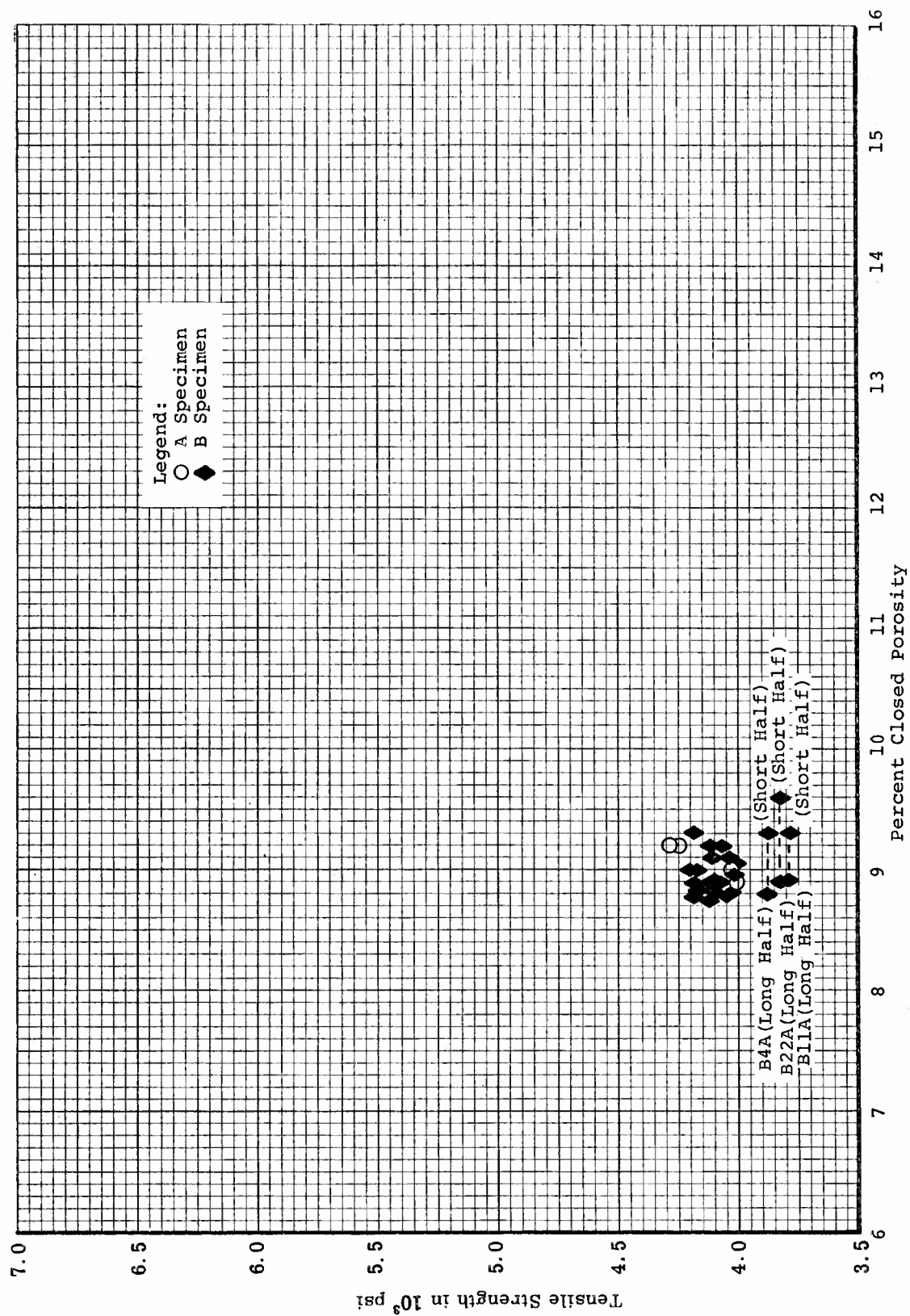


Figure 254. Relation between Tensile Strength and Percent Closed Porosity for ATJ-S Billet L-1-8 Across Grain at 70°F

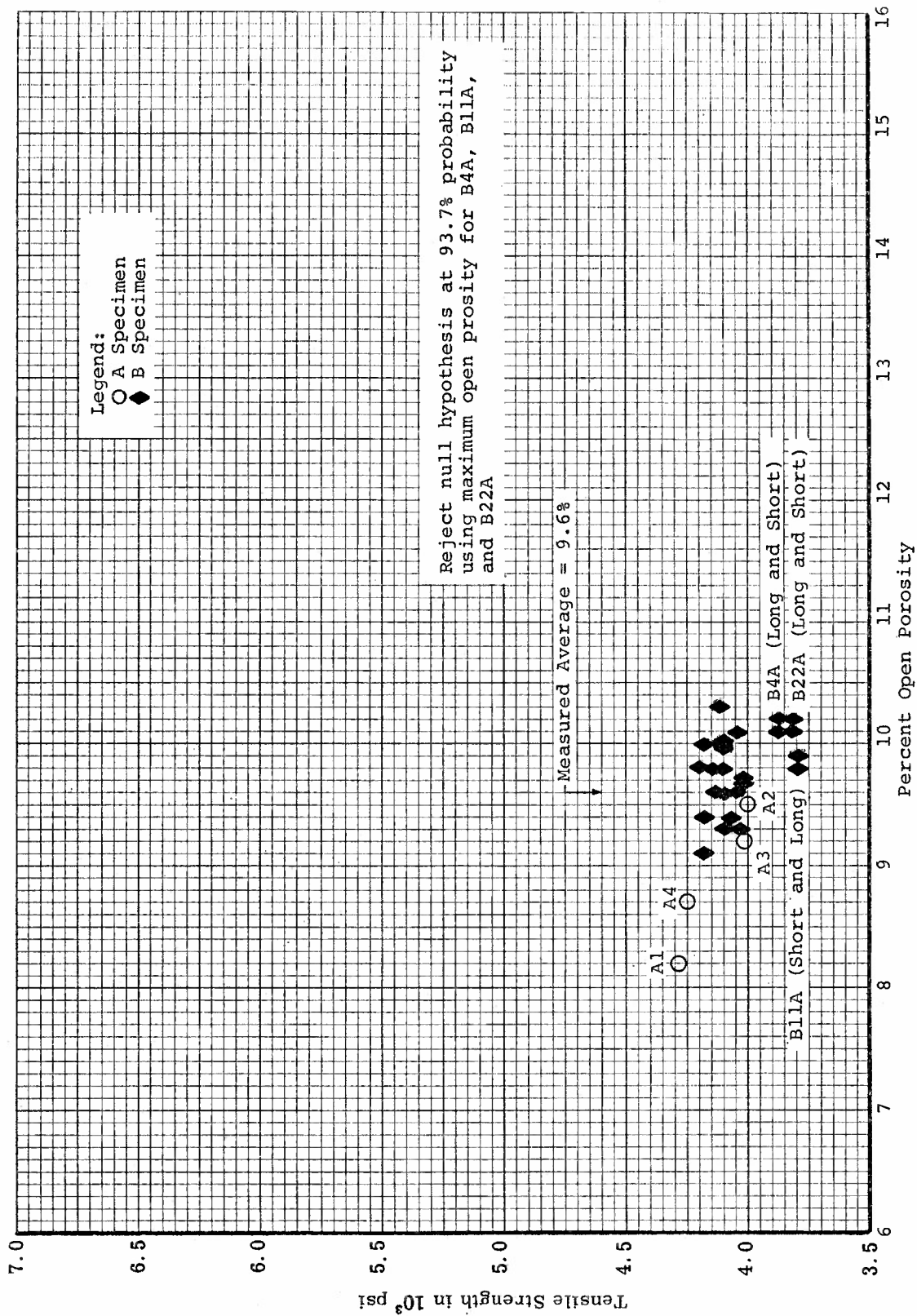


Figure 255. Relation between Tensile Strength and Percent Open Porosity for ATJ-S Billet L-1-8 Across Grain at 70°F



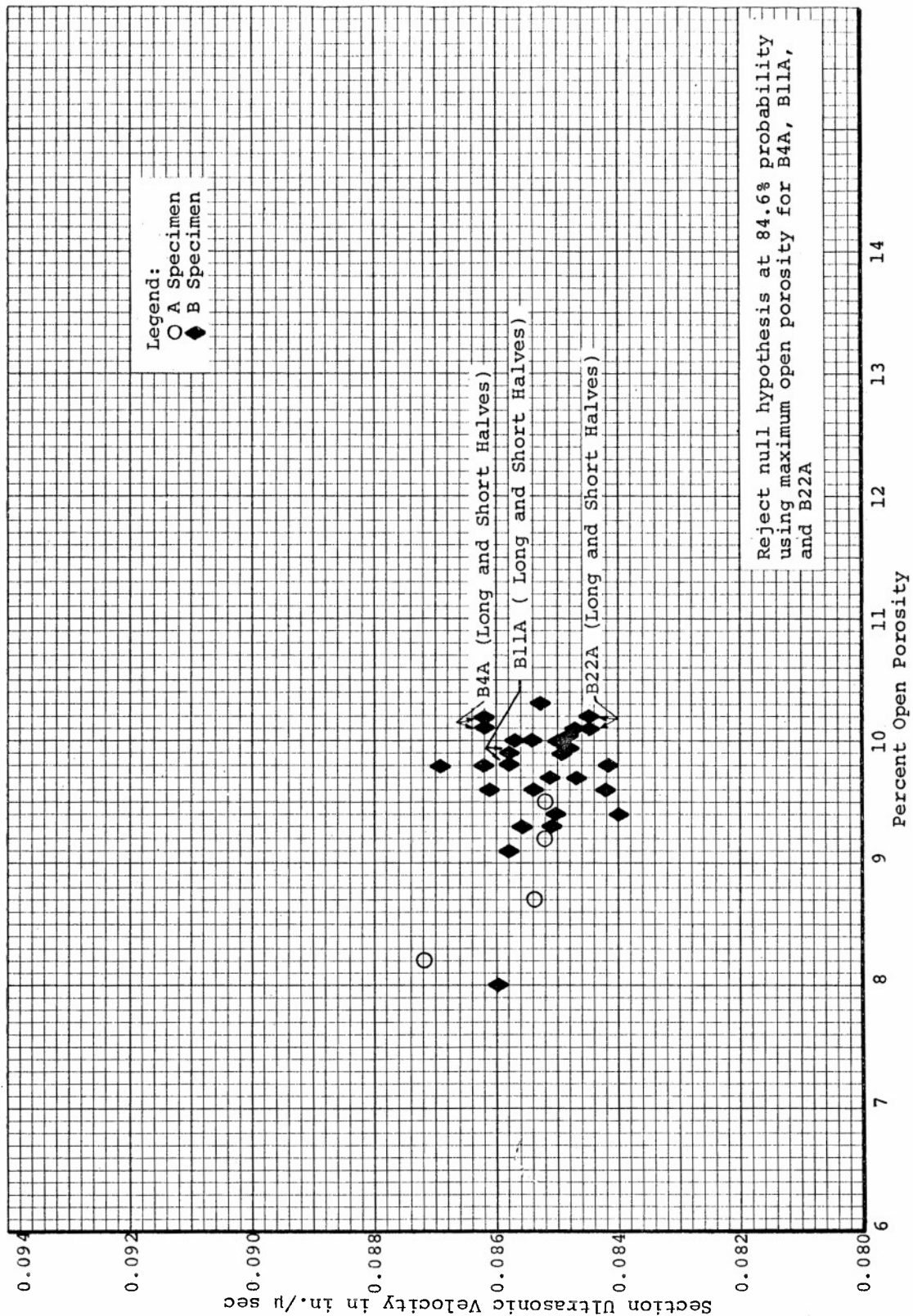


Figure 256. Relation between Section Ultrasonic Velocity and Percent Open Porosity for ATJ-S Billet L-1-8 Across Grain

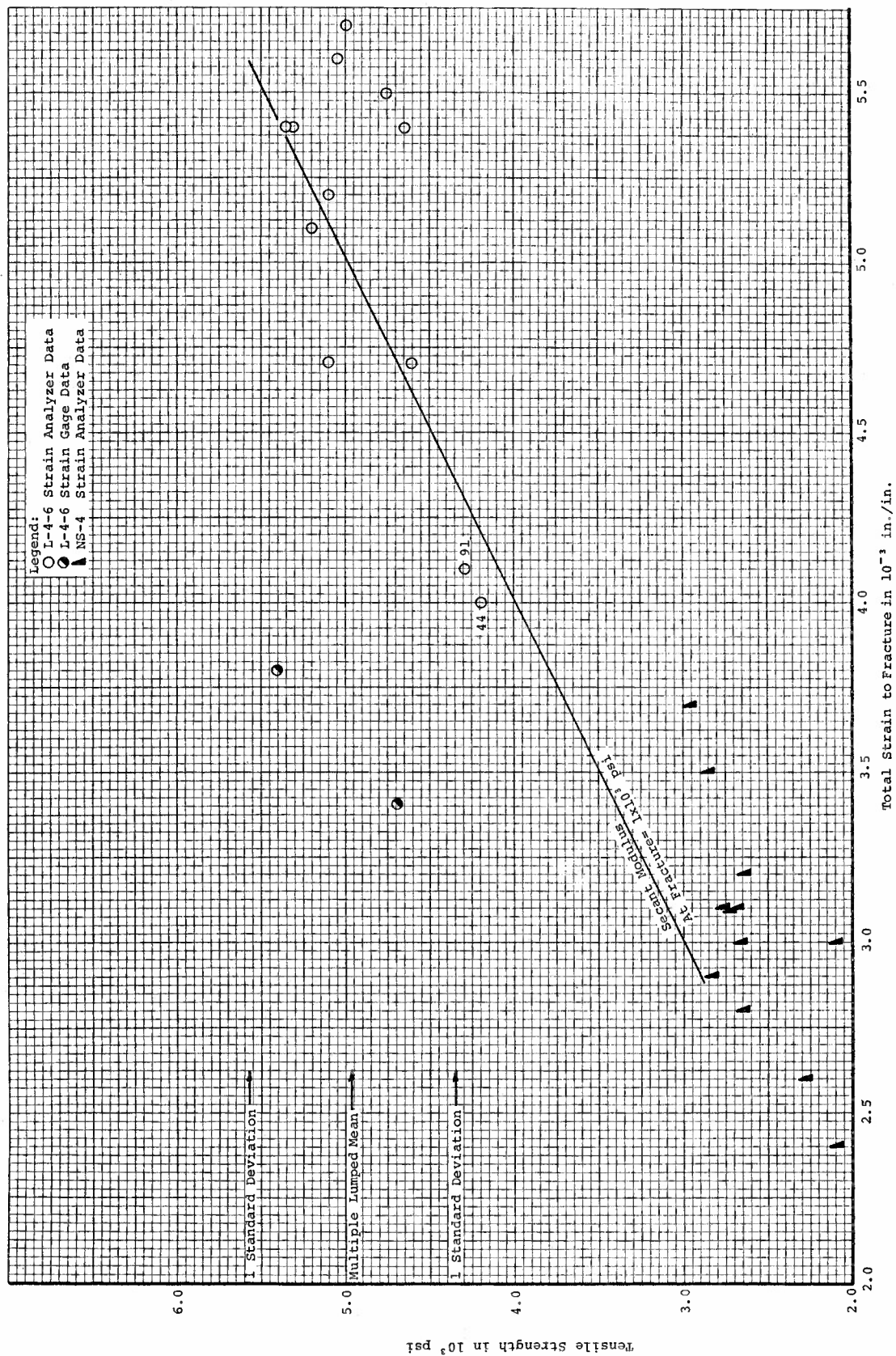


Figure 257. Tensile Strength versus Total Strain to Fracture for ANJ-S Billet L-4-6 With Grain at 70°F

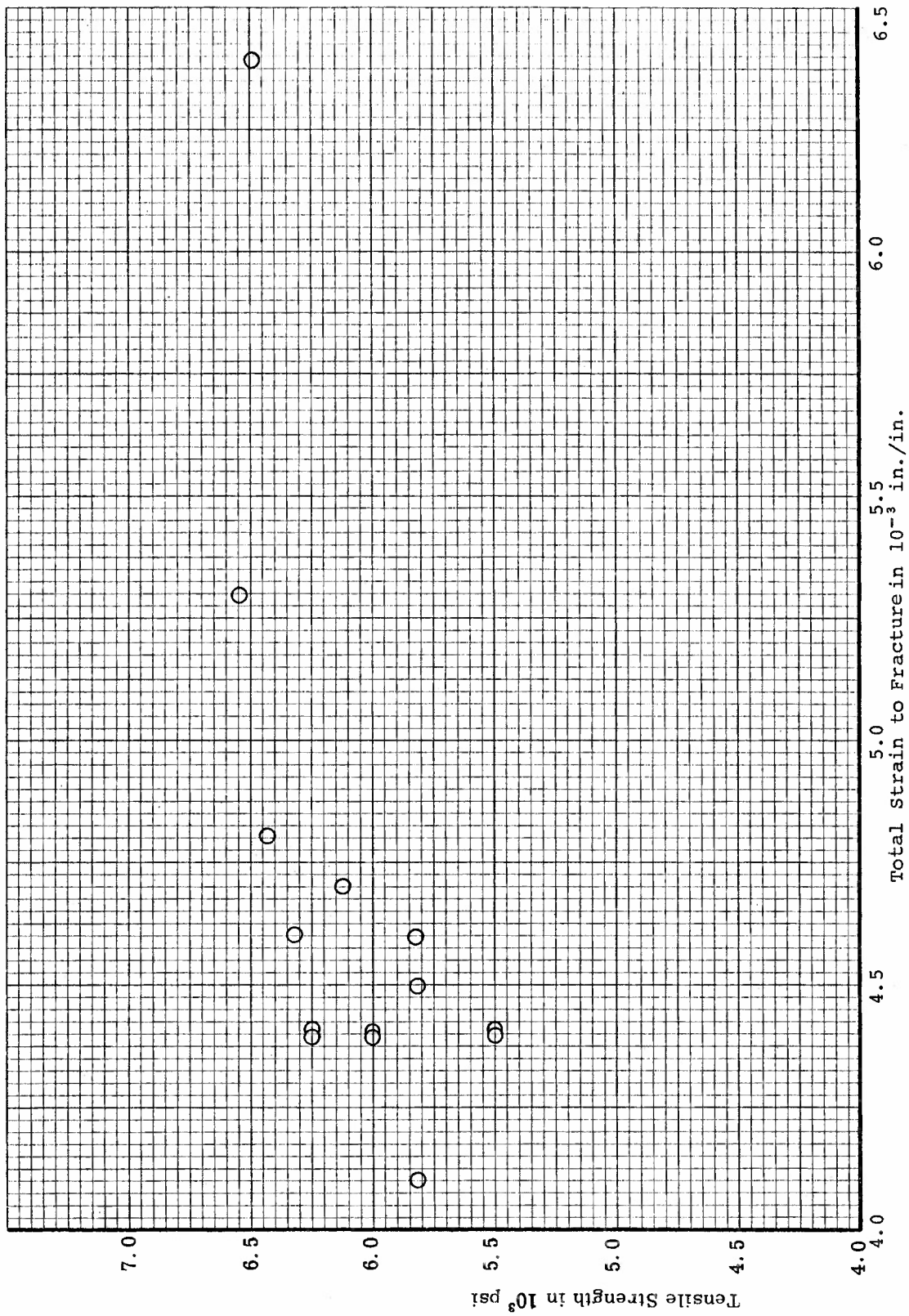


Figure 258. Tensile Strength versus Total Strain to Fracture for ATJ-S Billet L-4-6, With Grain at 3000°F

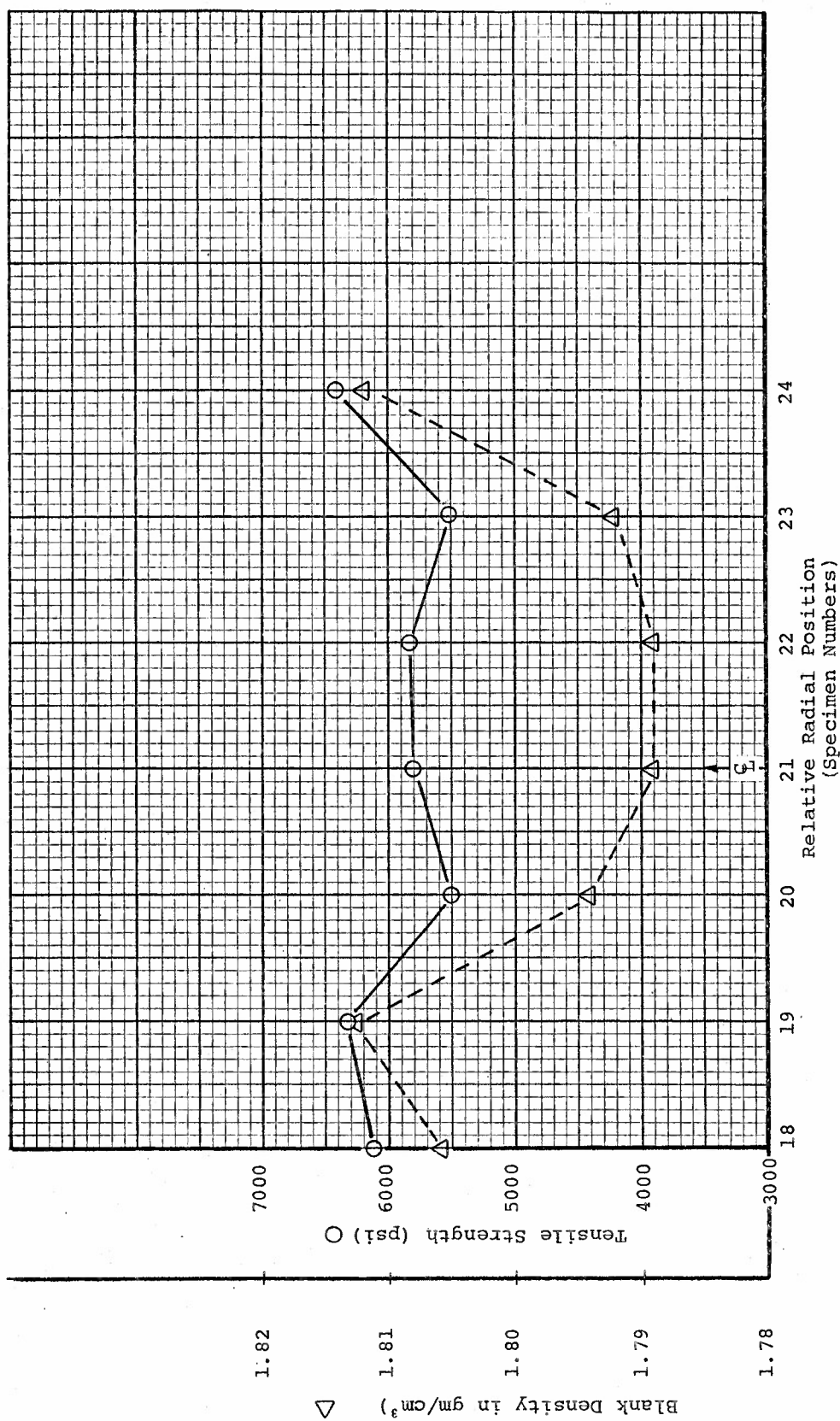


Figure 259. Properties versus Specimen Location in Billet, Slab 2 of ATJ-S Billet L-4-6 With Grain at 3000°F

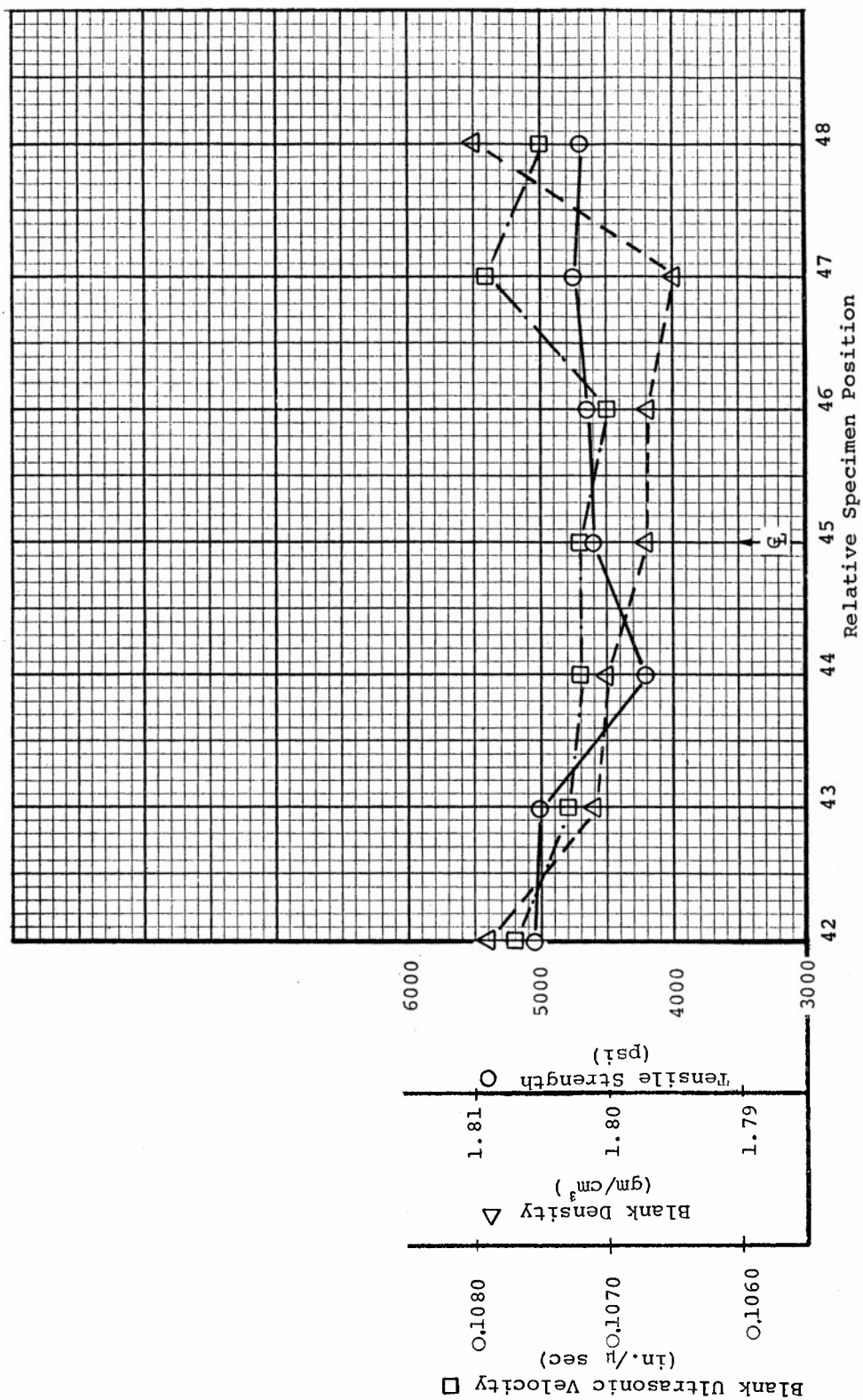


Figure 260. Properties versus Specimen Location in Billet, Slab 4 of ATJ-S Billet L-4-6 With Grain at 70°F



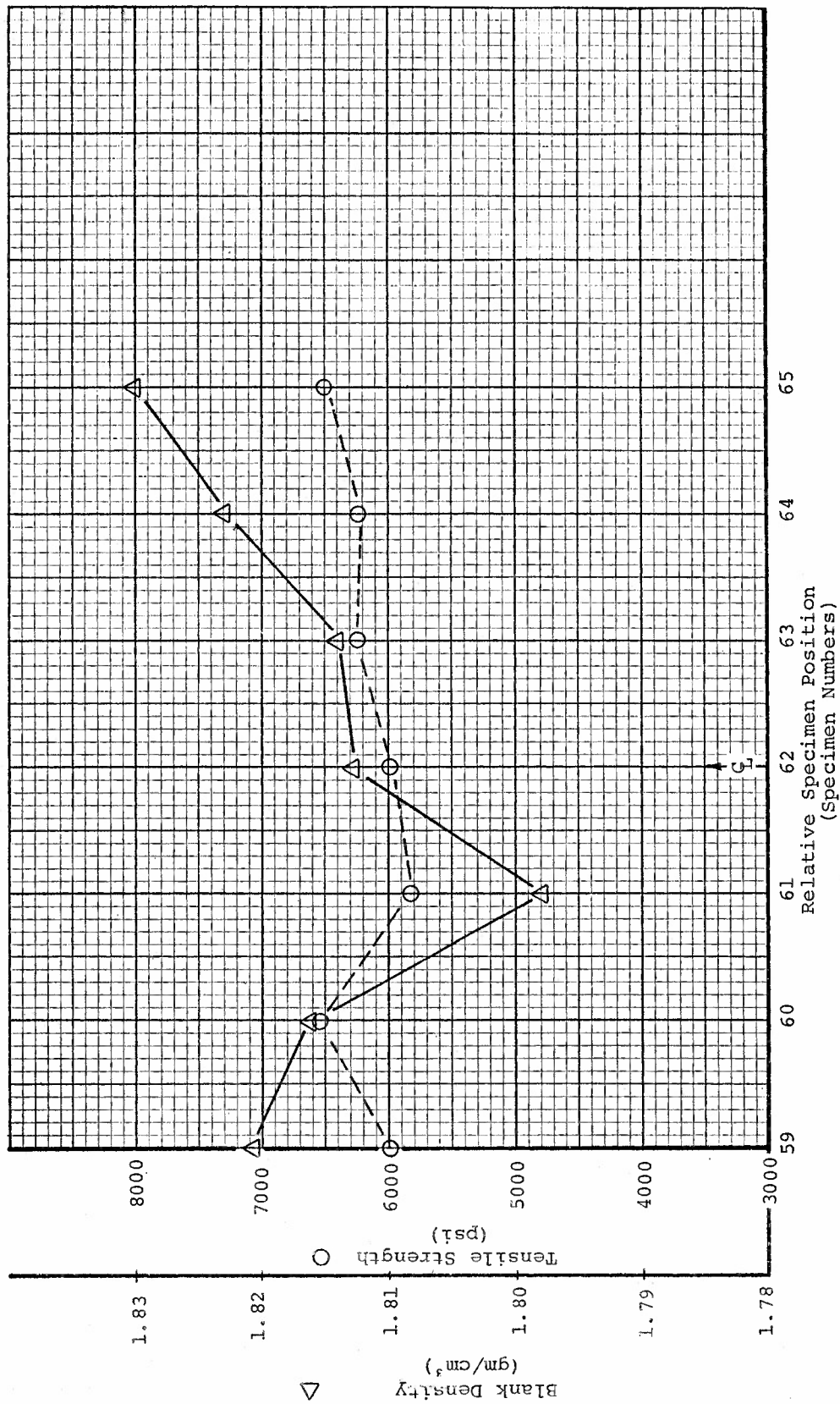


Figure 261. Properties versus Specimen Location in Billet, Slab 6 of ATJ-S Billet L-4-6 With Grain at 3000°F

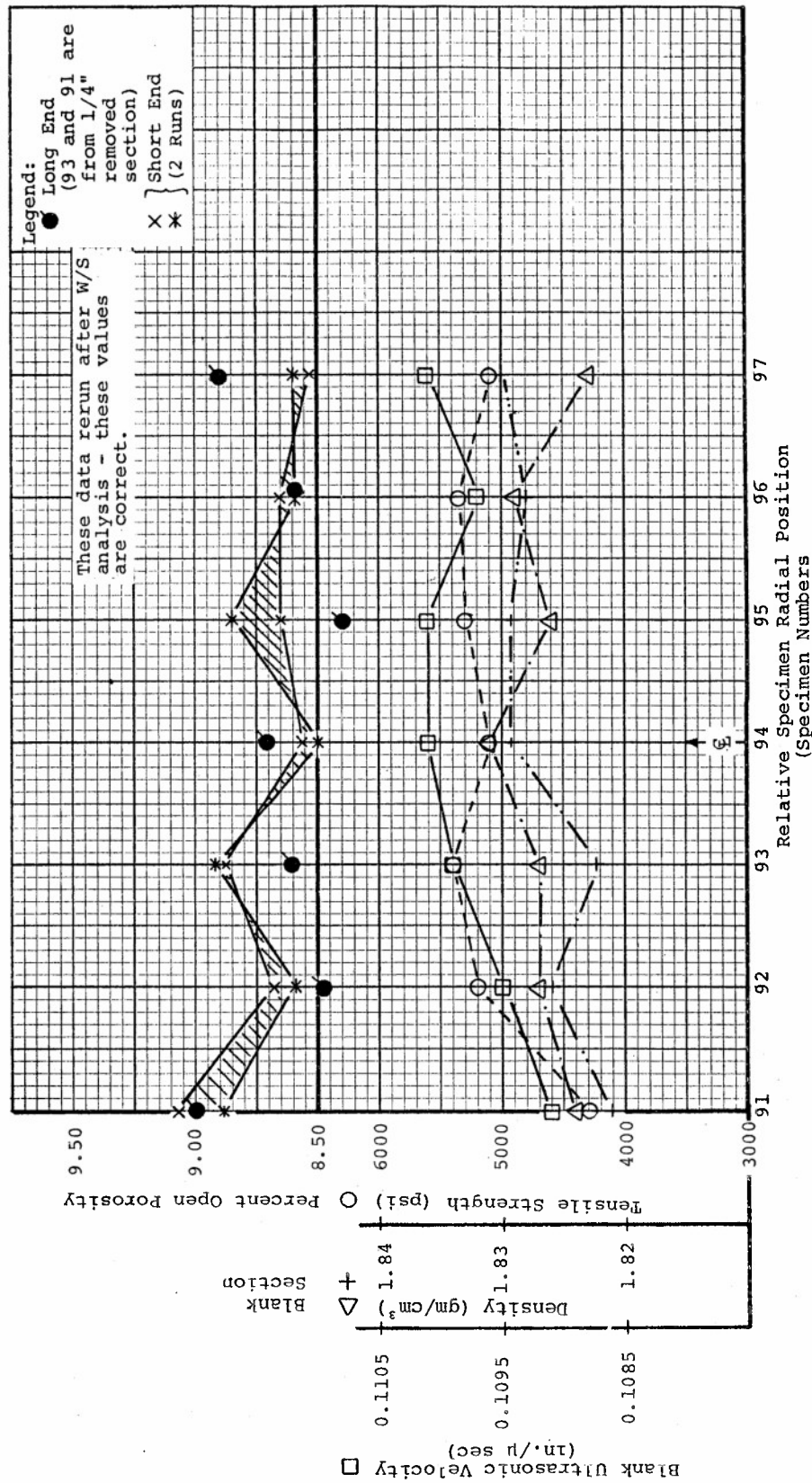


Figure 262. Properties versus Specimen Location in Billet, Slab 8 of ATJ-S Billet L-4-6 With Grain at 70°F

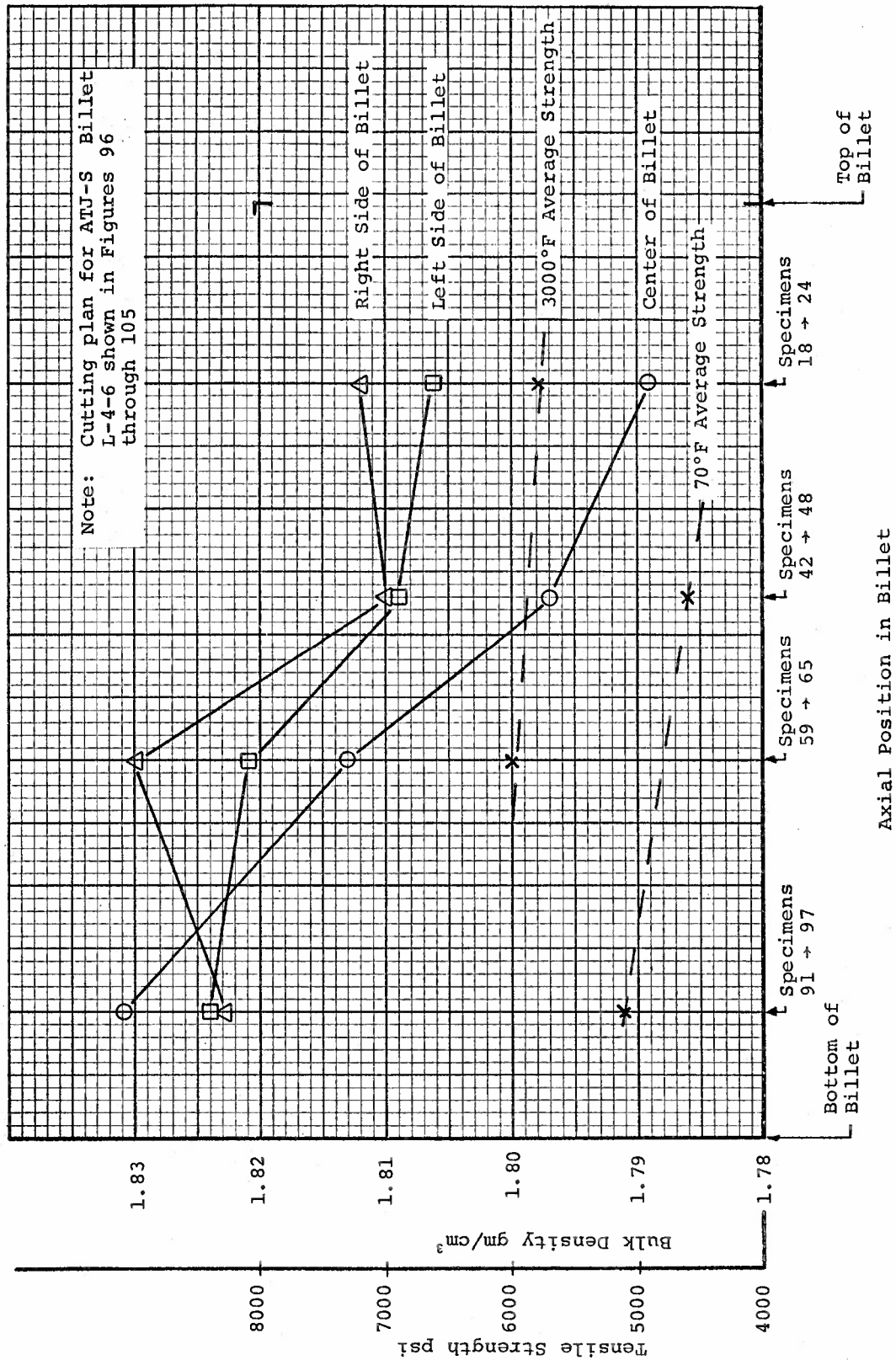
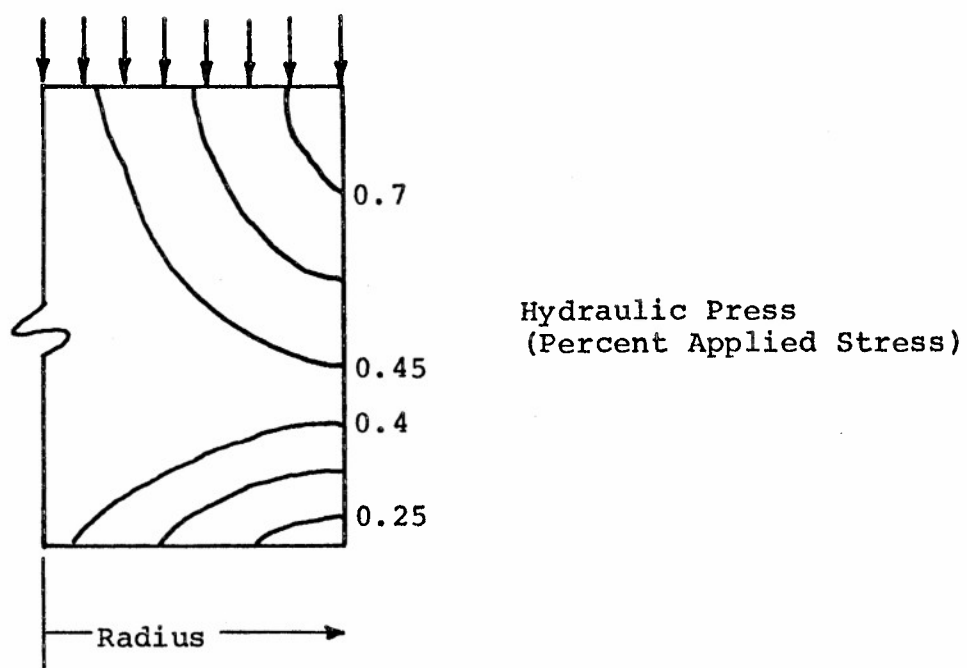


Figure 263. Properties versus Axial Position of Specimens in Billet, ATJ-S Billet L-4-6, With Grain





(See Swartz and Weinstein in Journal of ACS, July, 1965)

Figure 264. Profiles of Internal Pressure while Pressing a Uniform Powder

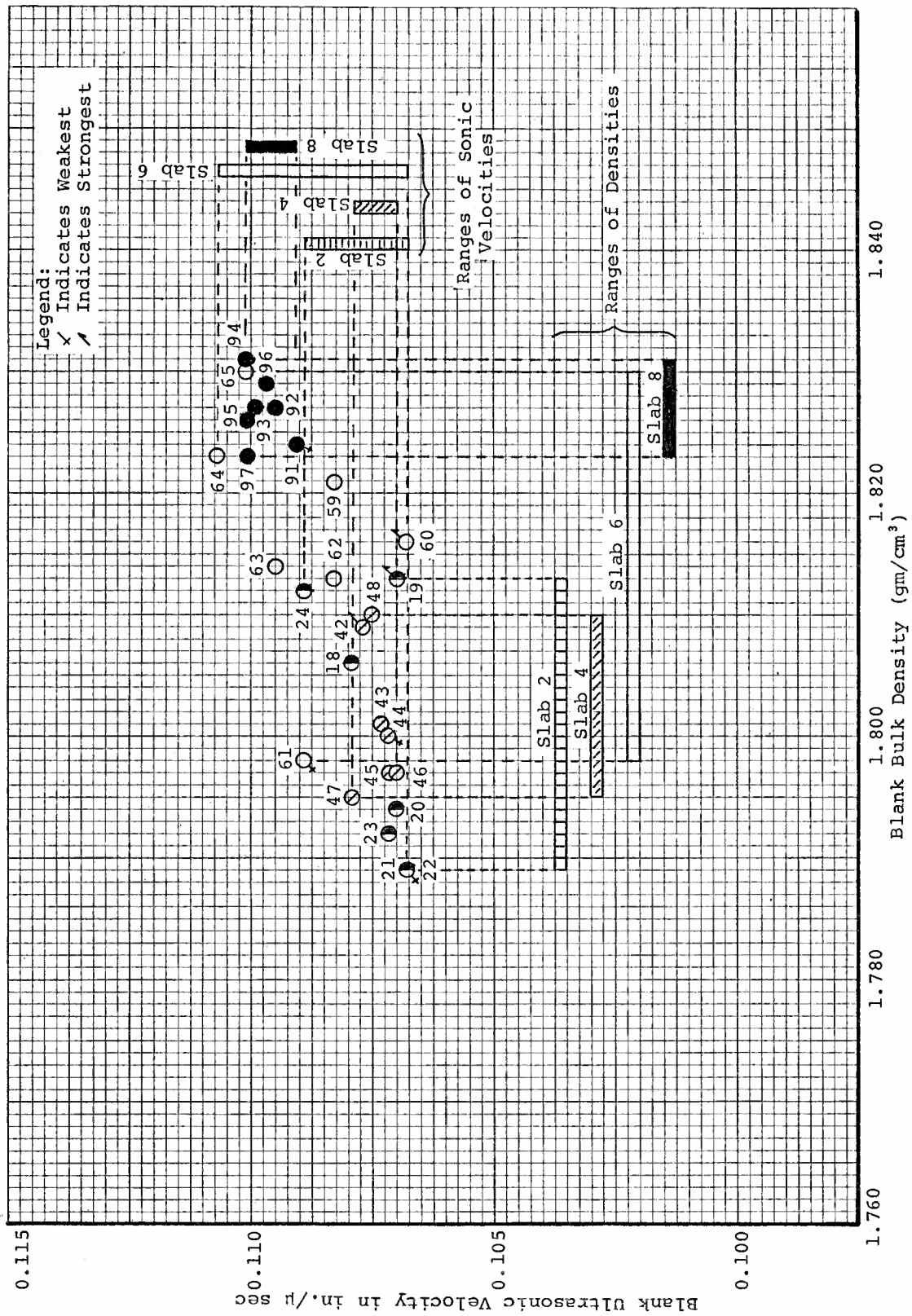


Figure 265. Relation between Blank Ultrasonic Velocity and Blank Bulk Density for ATJ-S Billet L-4-6 With Grain

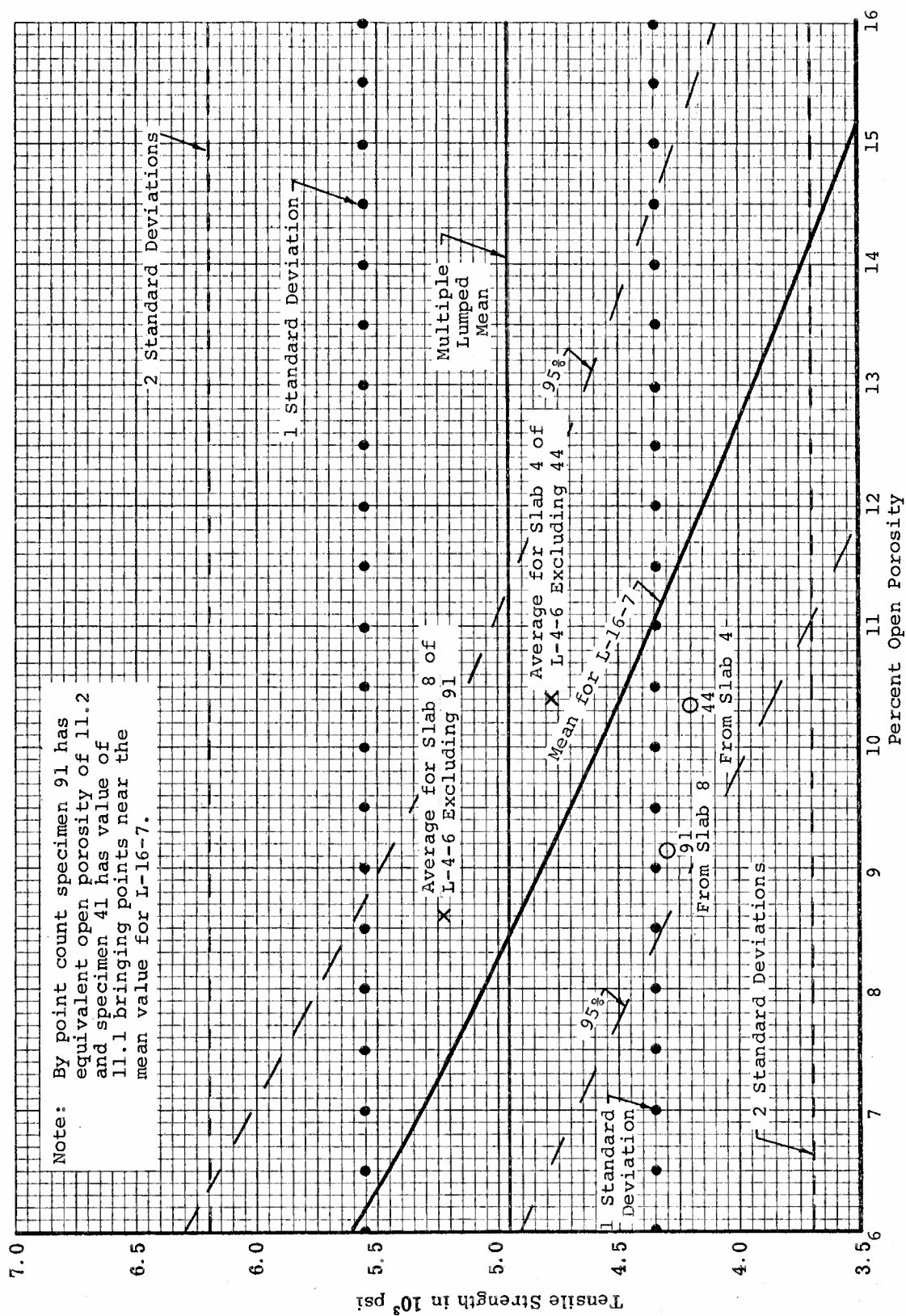
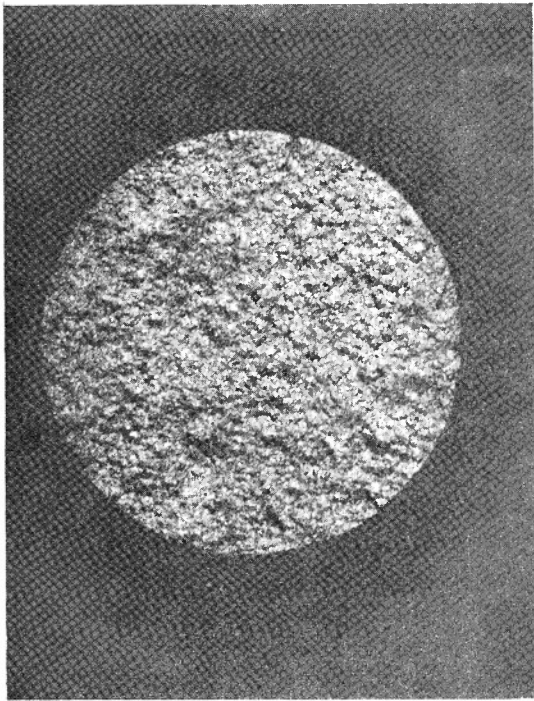
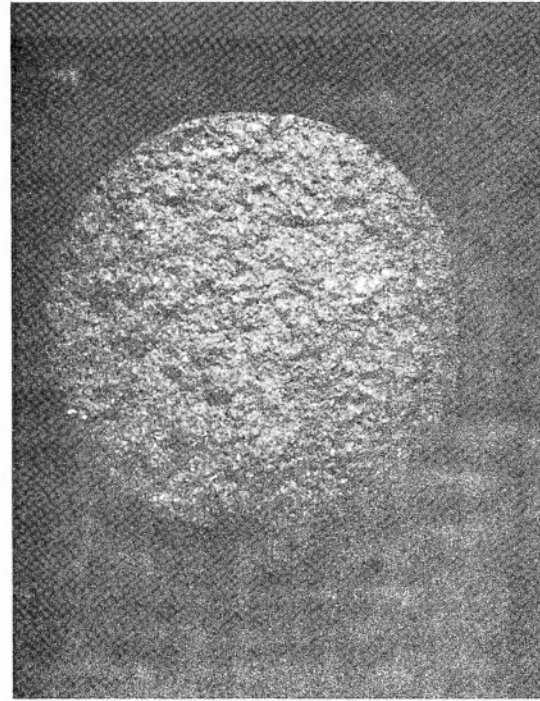


Figure 266. Regression Analysis Results for Tensile Strength versus Percent Open Porosity for ATJ-S Billet L-4-6 With Grain at 70°F

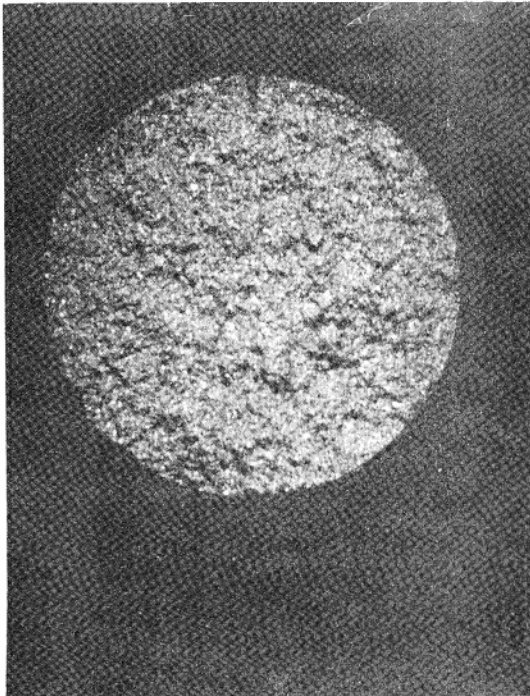




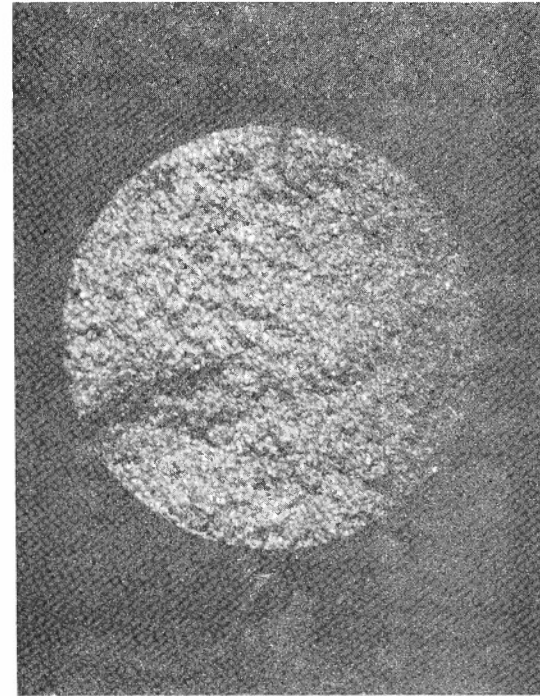
44  
Short End



44  
Long End



42  
Short End



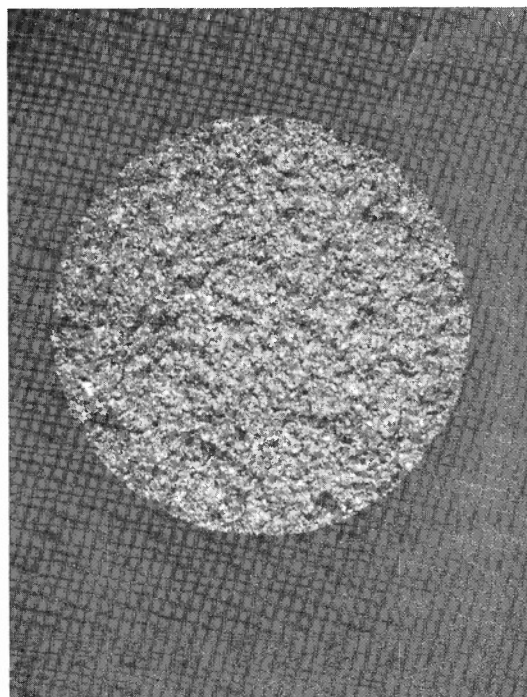
42  
Long End

Figure 267. 10X Photographs of Fracture Faces for Weak/Strong Specimens 44 and 42 from Slab 4 of ATJ-S Billet L-4-6 With Grain at 70°F

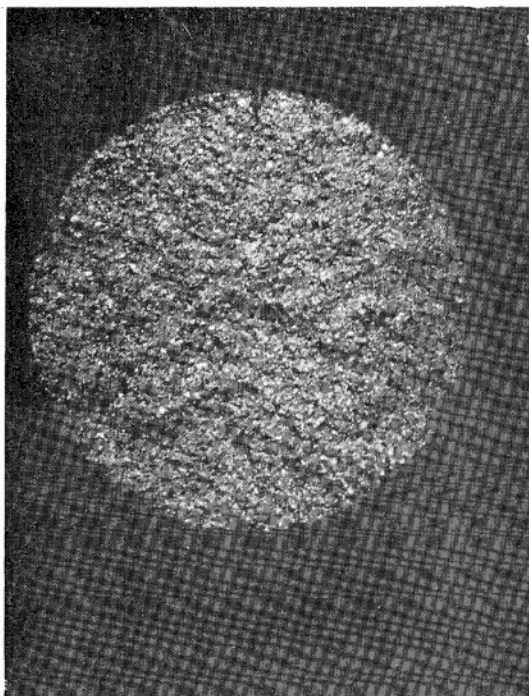




91  
Short End



91  
Long End



93  
Short End



93  
Long End

Figure 268. 10X Photographs of Fracture Faces for Weak/Strong Specimens 91 and 93 from Slab 8 of ATJ-S Billet L-4-6 With Grain at 70°F





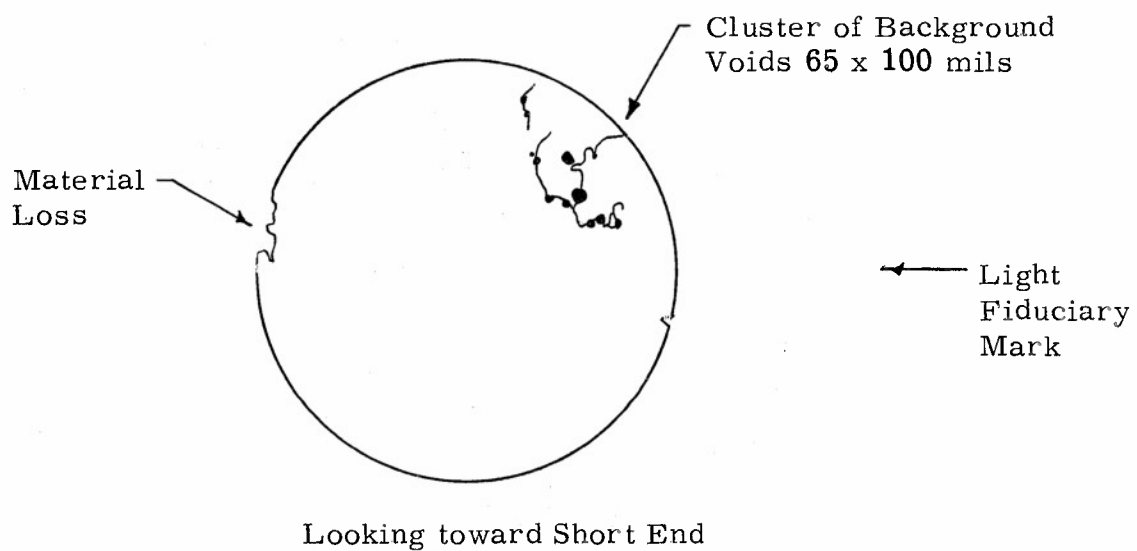
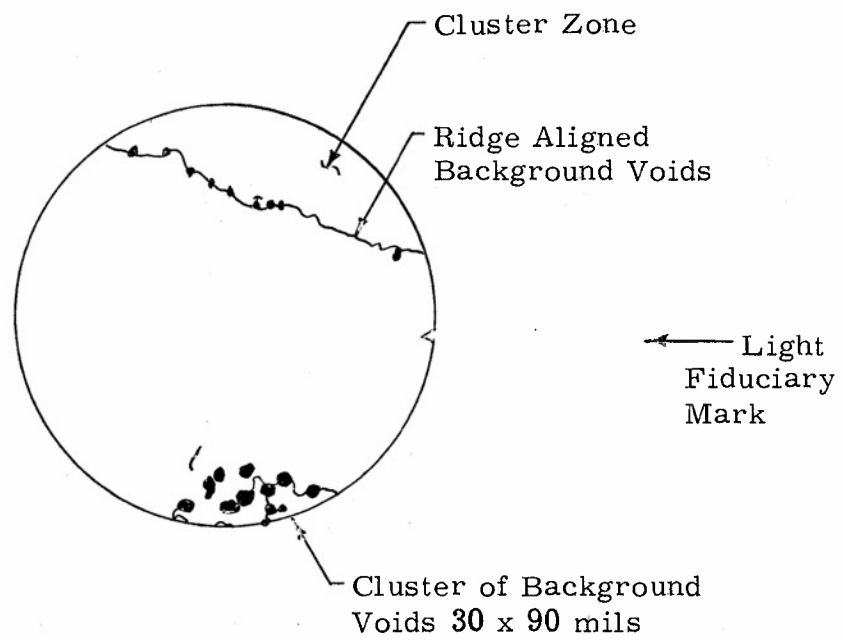
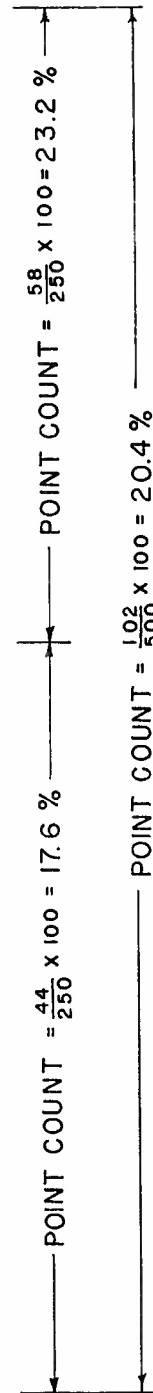
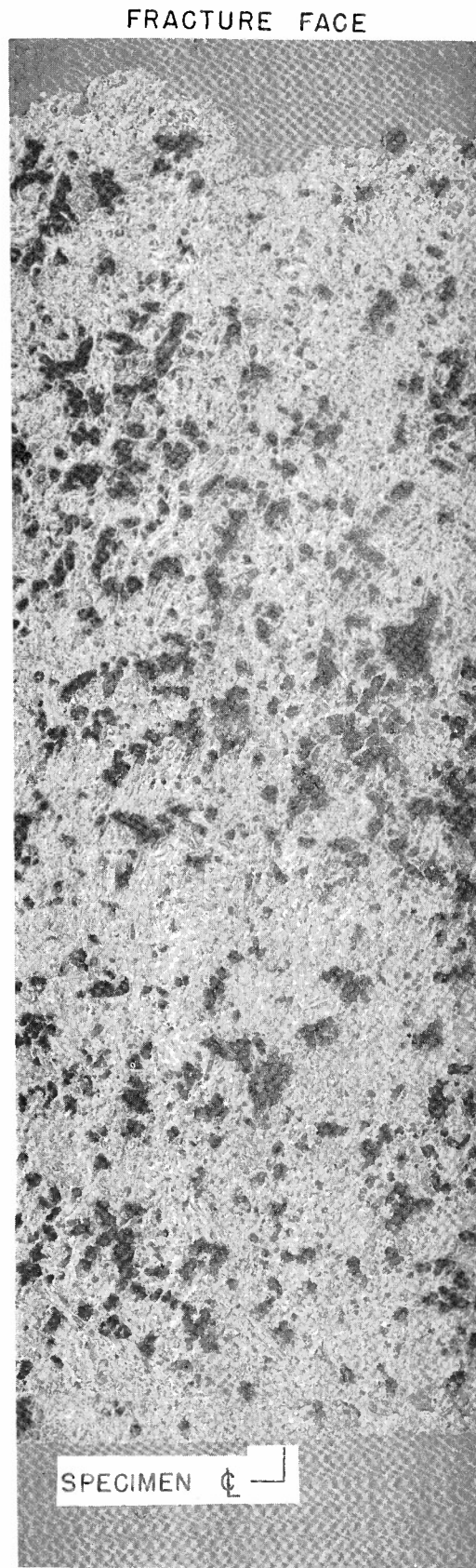


Figure 269. Flick Inspection Results of Fracture Faces of Weak Specimen 44 from Slab 4 of ATJ-S Billet L-4-6



Looking toward Short End

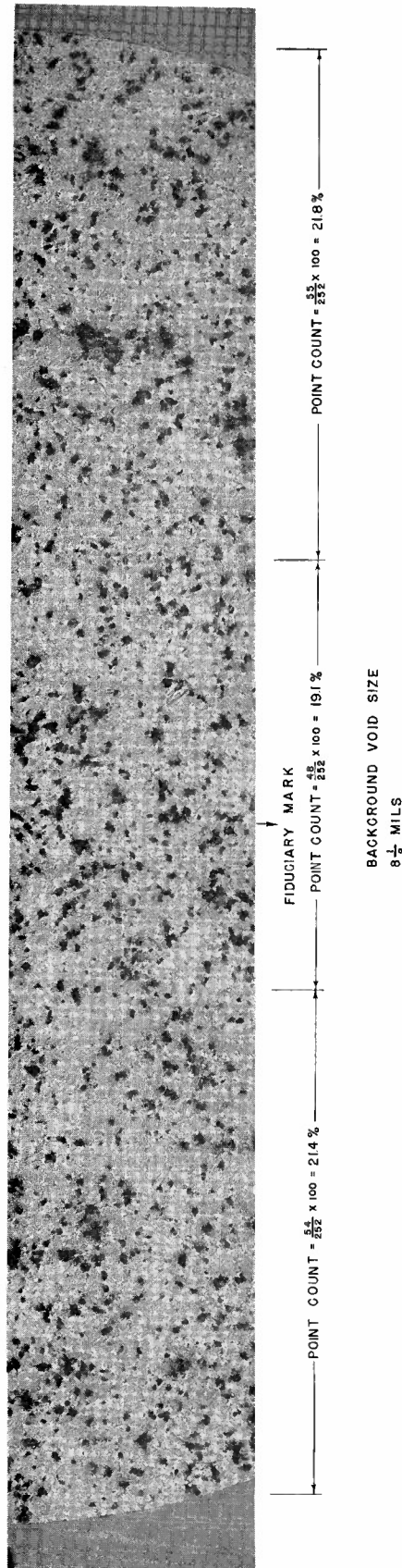
Figure 270. Flick Inspection Results of Fracture Faces of Weak Specimen 91 from Slab 8 of ATJ-S Billet L-4-6



BACKGROUND VOID SIZE  
8½ MILS

Figure 271. 100X Photomicrograph of Center of Cross Section from Weak Specimen 44,  
No Impregnation, ATJ-S Billet L-4-6





NOTE:  
 1. TENSILE STRENGTH T91W = 4300 PSI  
 2. ABSORPTION OPEN POROSITY = 91%  
 3. POINT COUNT (AVE) = 20.8% — 11.2% EQUIVALENT

Figure 272. 100X Photomicrograph of Center of Cross Section from Weak Specimen 91 about 10 mils below Fracture Face, No Impregnation, ATJ-S Billet L-4-6



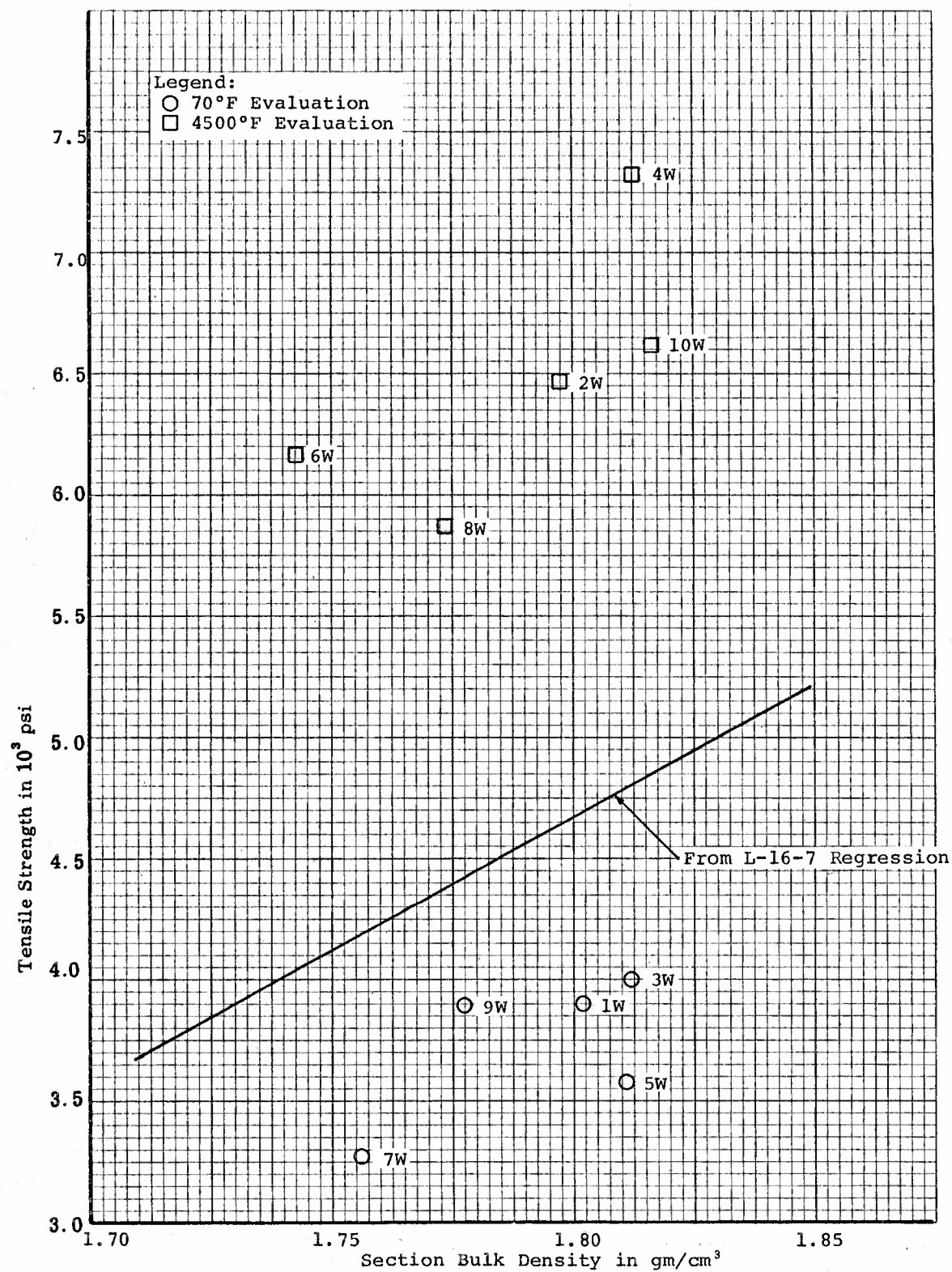
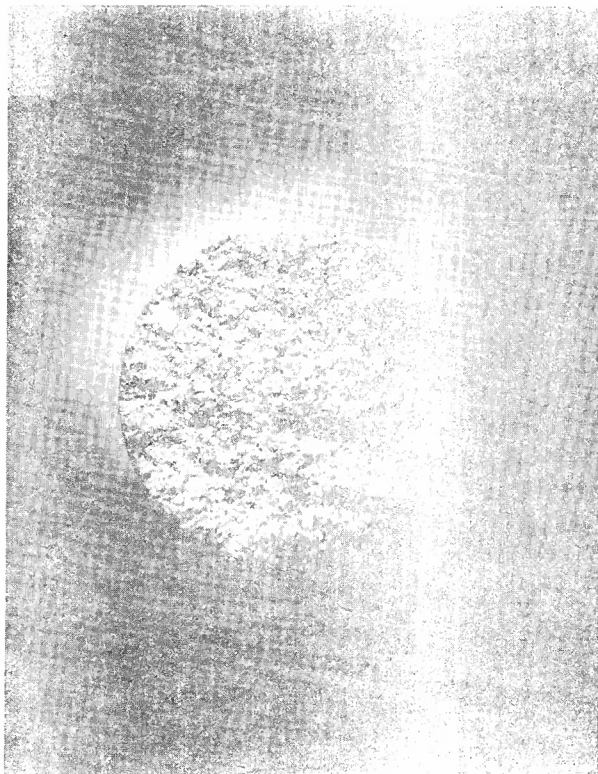


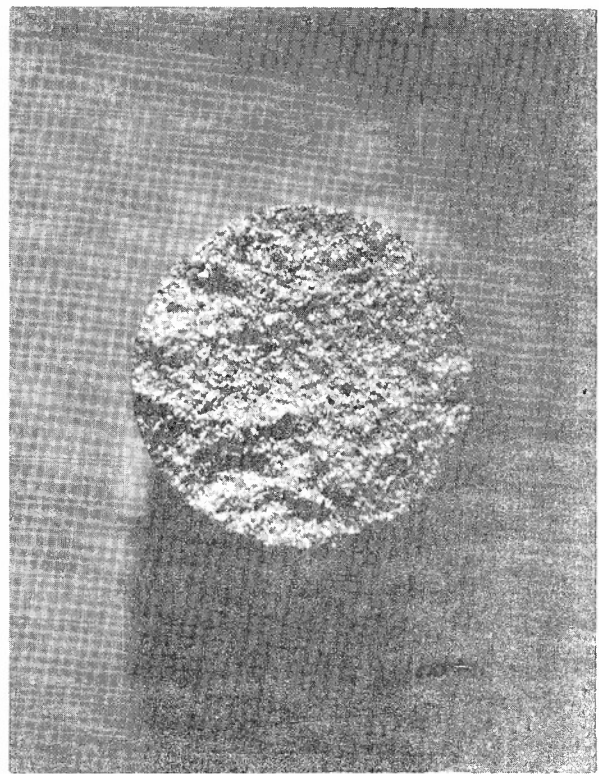
Figure 273. Relation between Tensile Strength and Section Bulk Density for ATJ-S Billet L-9-10 With Grain at 70°F and 4500°F







T5W  
Short End



T5W  
Long End



T7W  
Short End

T7W  
Long End Destroyed  
before Picture

Figure 276. 10X Photographs of Fracture Faces for Disparate Specimen T5W and Weak Specimen T7W from ATJ-S Billet L-9-10



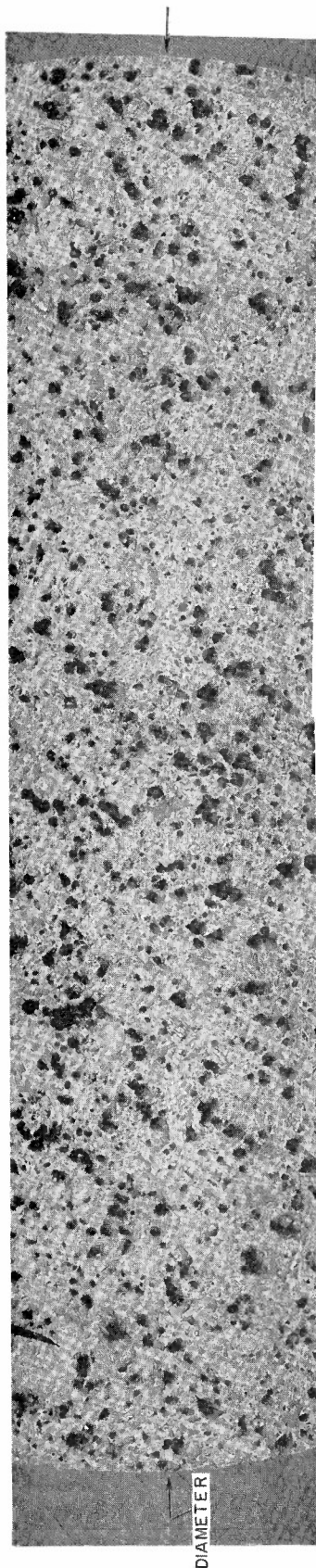


Figure 277. 100X Photomicrograph of Strip Section across Diameter 10 mils below Fracture  
Face of Weak Specimen T7W from ATJ-S Billet L-9-10



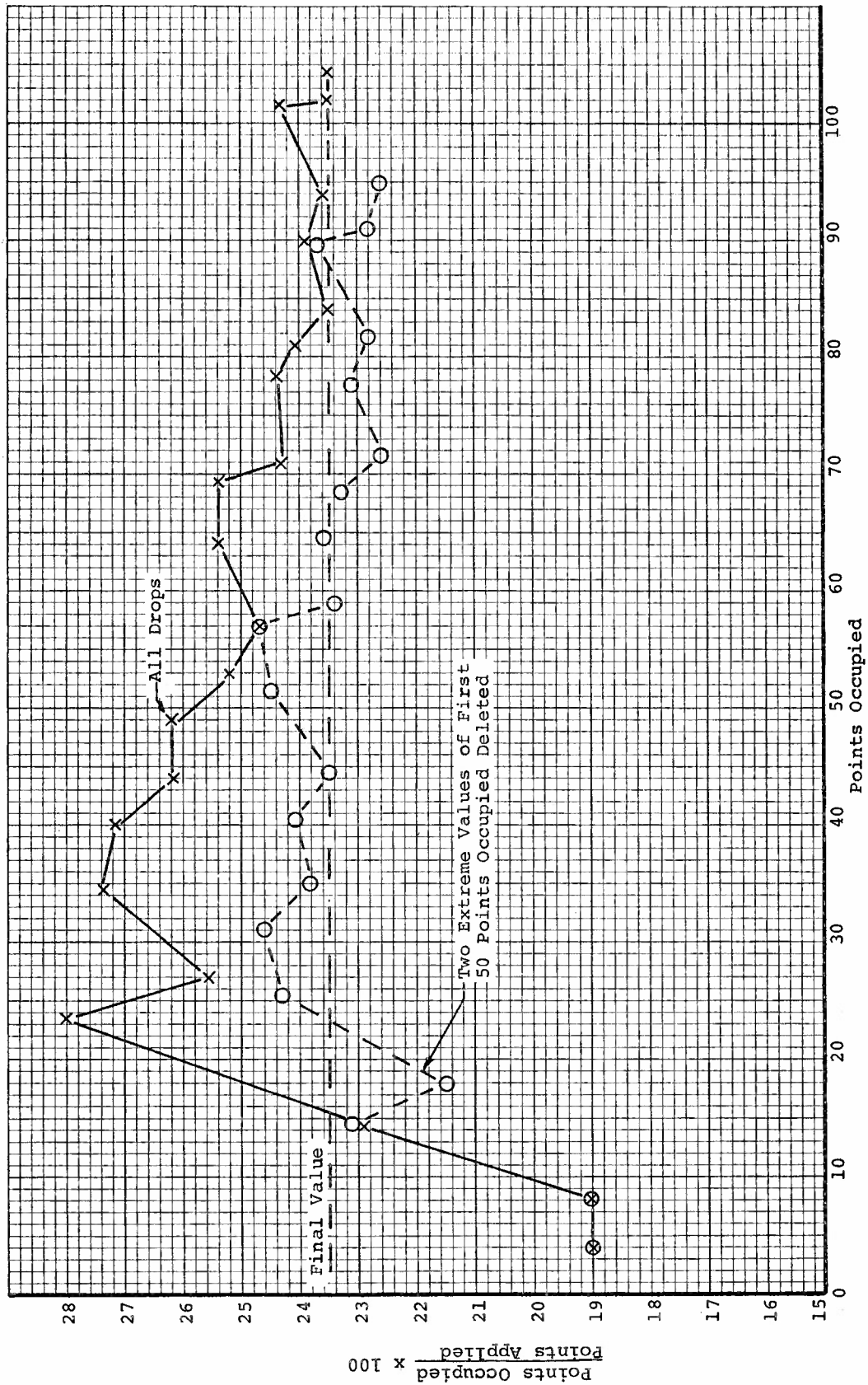
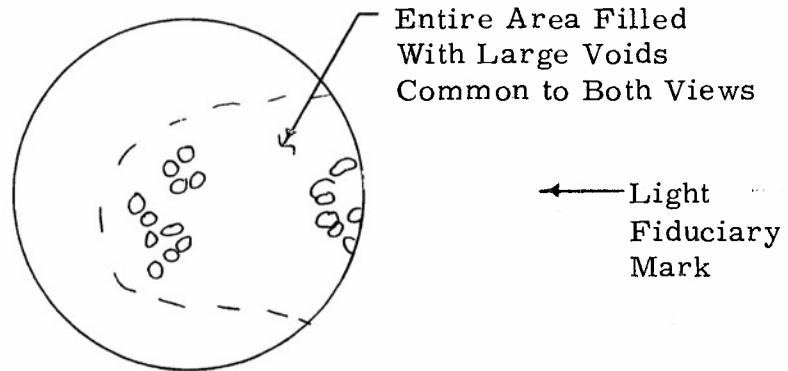
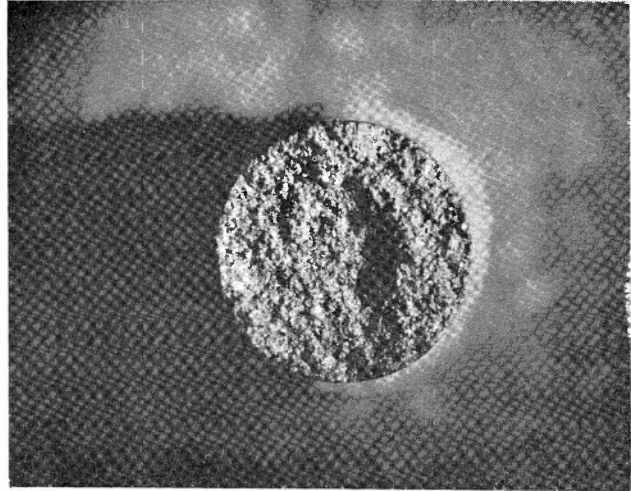
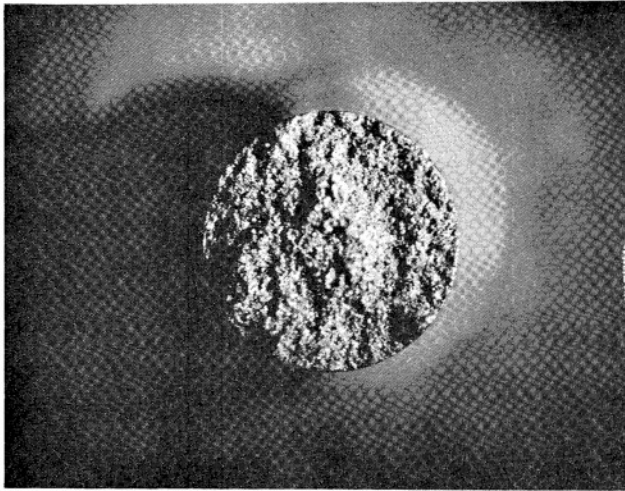


Figure 278. Progressive Plot of Point Count on T7W from ATJ-S Billet L-9-10



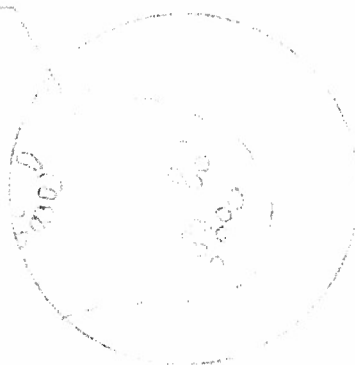


Looking toward Short End

Figure 279. Flick Inspection Results and 10X Black and White Photographs of Fracture Faces of Weak Specimen T1W from ATJ-S Billet L-9-10

Entire Area Shaded  
 With Large Voids  
 (Same as to Both Views)

Right  
 ←  
 Midway  
 Mark



Looking from Below

Figure 378. Black, brown, tan, and 10X black and white  
 photo of the same front of West Station  
 as in Fig. 377.





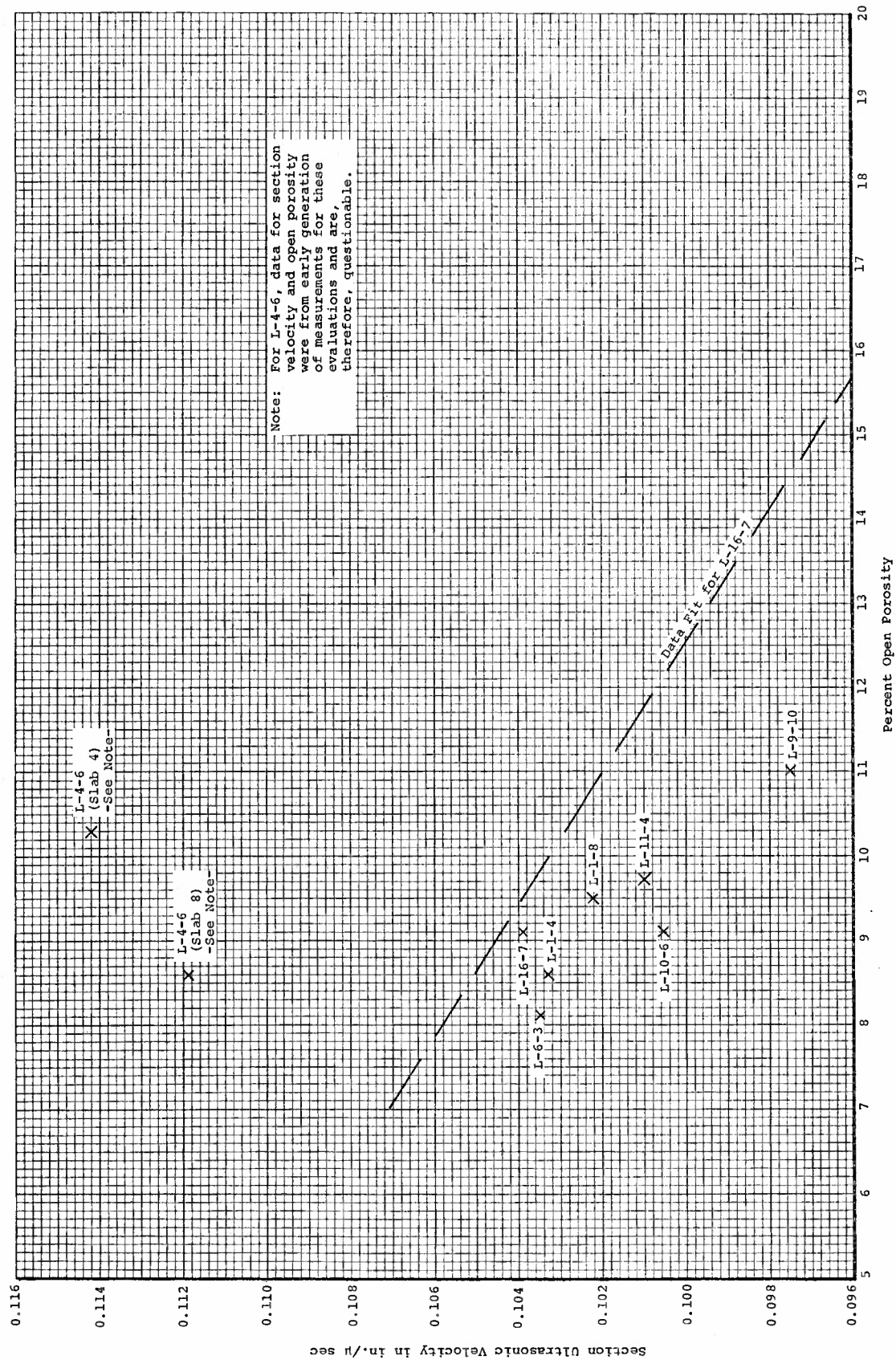


Figure 281. Correlation of Average Values of Section Ultrasonic Velocity and Percent Open Porosity for Various ATJ-S Billets with Data Fit for ATJ-S Billet L-16-7

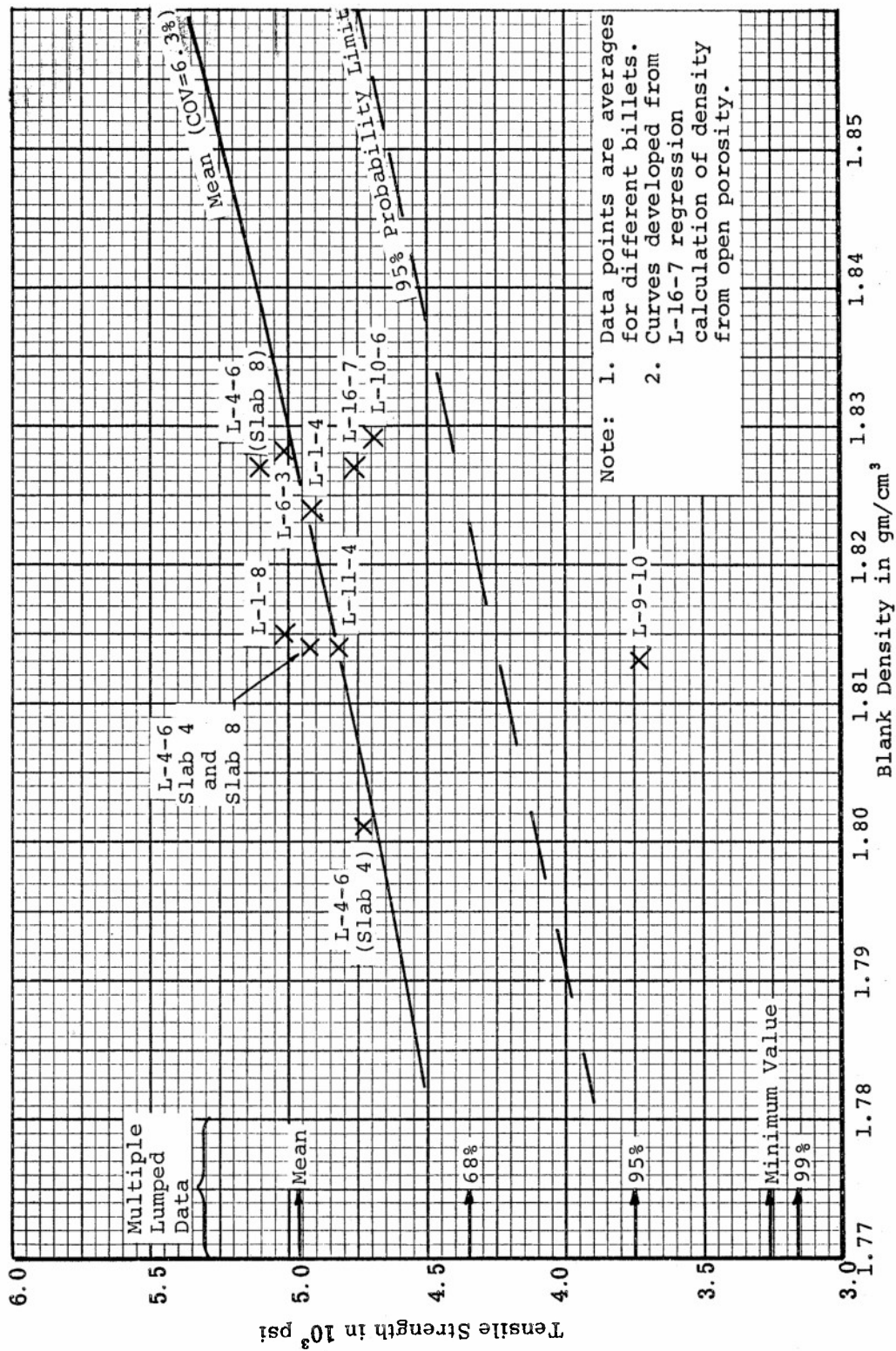


Figure 282. Comparison of Average Tensile Strength and Density for Various ATJ-S Billets with L-16-7 Regression

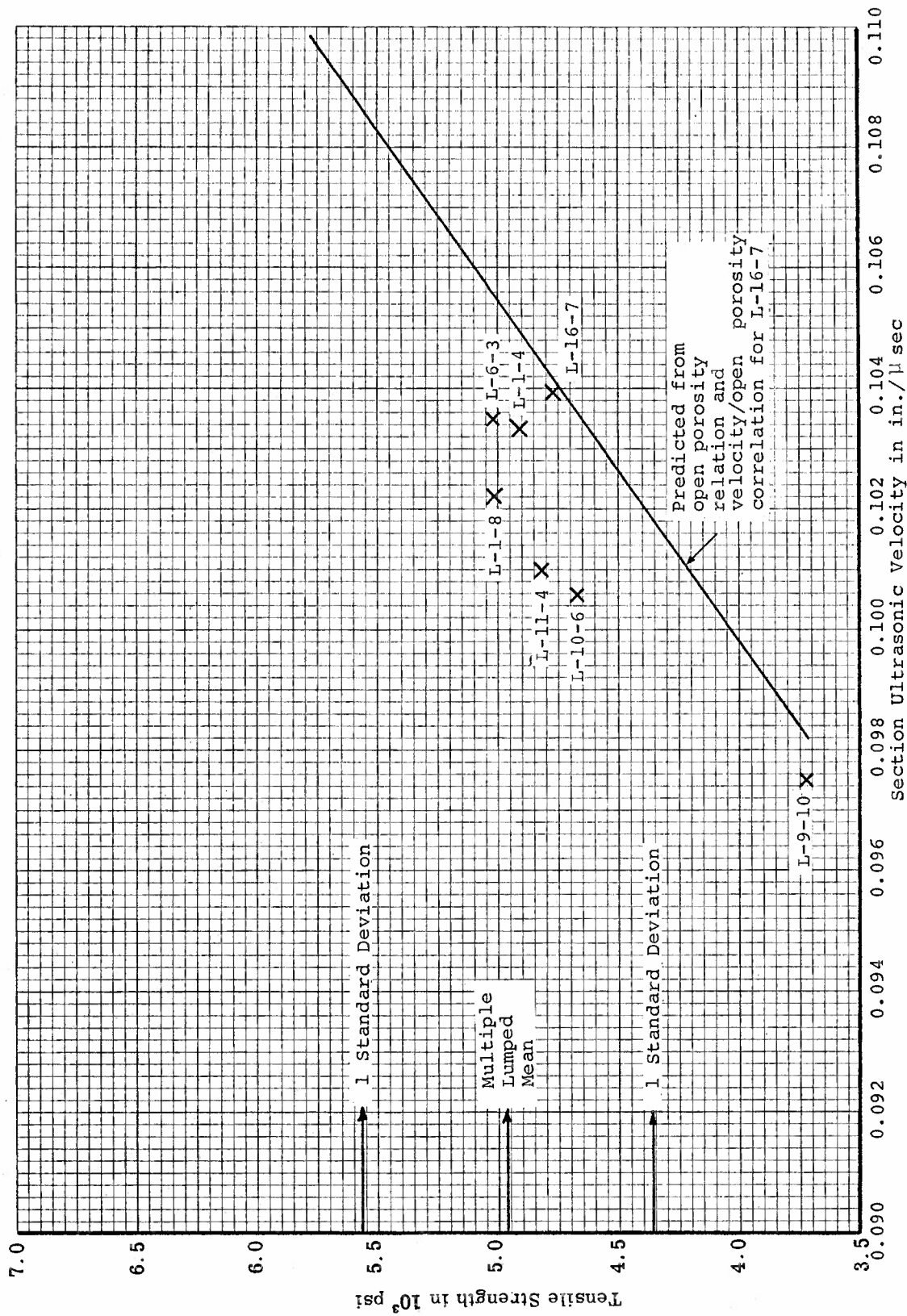


Figure 283. Comparison of Average Tensile Strength and Velocity of Various ATJ-S Billets with Predicted L-16-7 Relation

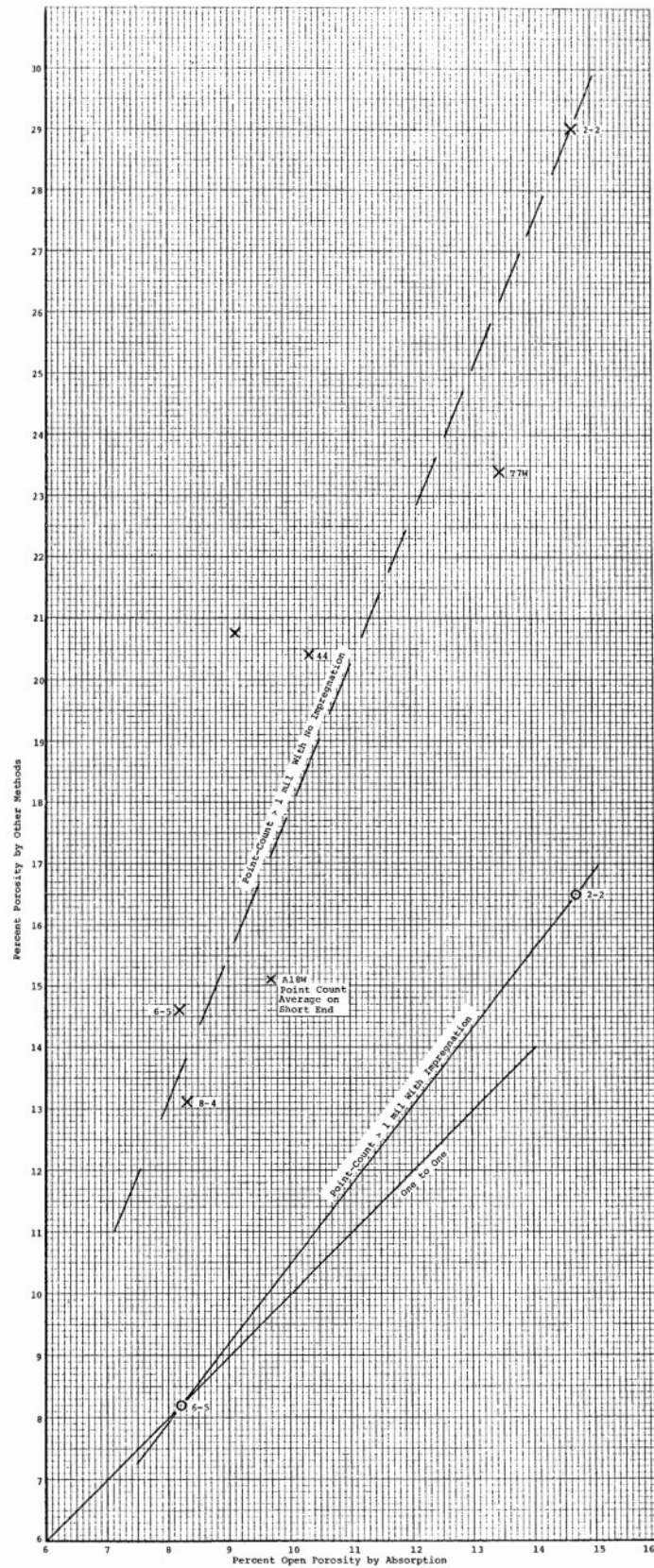


Figure 284. Composite Comparison of Open Porosity by Absorption to Porosity by Other Methods



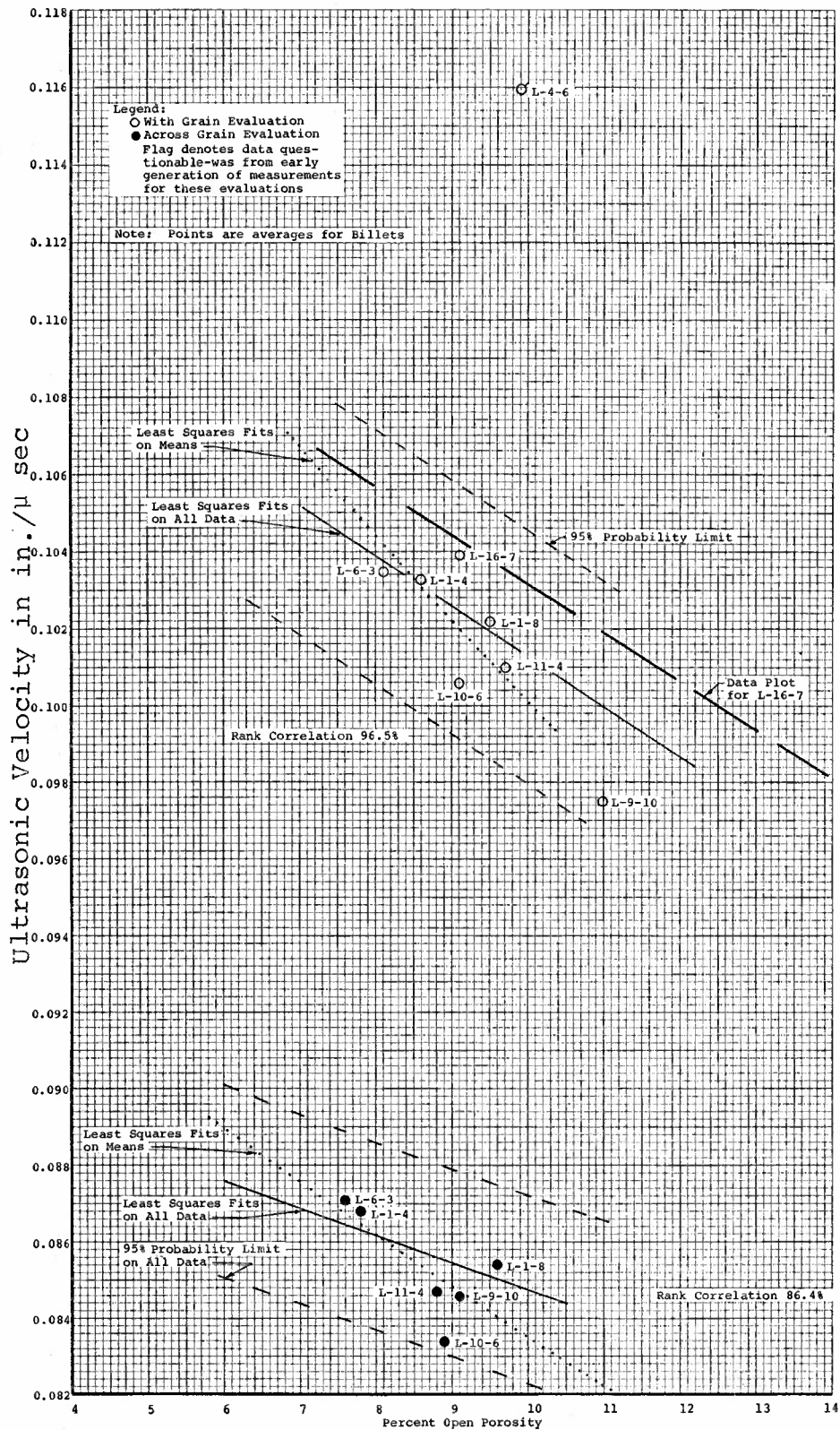


Figure 285. Relation between Ultrasonic Velocity and Open Porosity for Various ATJ-S Billets with Respect to the Regression of ATJ-S Billet L-16-7

TABLE 1

TENSILE PROPERTIES AT 70°F OF EVEN SLABS FROM ATJ-S BILLETS L-16-7 and L-7-1

Orientation	Temp °F	Stress Rate psi/min	Specimen Number	Blank Bulk Density gm/cm <sup>3</sup>	Ultimate Strength psi	Elastic Modulus 10 <sup>6</sup> psi	Total Axial Strain in. /in.	Fracture Location in. from Midspan	Blank Ultrasonic Velocity in. /μ sec	Gage Electrical Resistivity μ ohm-cm	Remarks
L-16-7 With Grain	70	10,000	S-2-1	1.829	5180	1.50 *	0.0050	0.50B	0.1056	878	
			S-2-2	1.772	3680	1.18	0.0044	0.58B	0.1002	1009	
			S-2-3	1.811	4320	1.61 *	0.0037	0.50B	0.1038	888	
			S-2-4	1.813	4790	1.51	0.0048	0.50T	0.1038	886	
			S-2-6	1.812	4630	1.74	0.0047	0.25B	0.1055	860	
			Mean	1.807	4516	1.51	0.0045		0.1038	900	
			Standard Deviation	0.021	557	0.04	0.0005		0.0022	62	
			S-4-1	1.850	5370	1.28 *	0.0041	0.10B	0.1061	847	
			S-4-2	1.792	3910	1.30	0.0037	0.50T	0.1023	963	
			S-4-3	1.811	4910	1.58	0.0055	0.53T	0.1051	926	
			S-4-4	1.830	5060	1.38 *	0.0050	0.30B	0.1060	834	
			S-4-5	1.832	5100	1.87 *	0.0043	0.42T	0.1056	818	
			S-4-6	1.832	4670	1.48 *	0.0045	0.25T	0.1045	862	
			Mean	1.825	4837	1.48	0.0045		0.1049	875	
			Standard Deviation	0.020	509	0.22	0.0006		0.0014	57	
			S-6-1	1.821	3990	1.26	0.0044	0.45B	0.0996	958	
			S-6-2	1.798	4580	1.67	0.0044	0.45T	0.1031	842	
			S-6-3	1.816	4460	1.43	0.0039	0.52B	0.1053	838	
			S-6-4	1.829	4240	1.56	0.0039	0.60B	0.1058	853	
			S-6-5	1.837	4020	1.47	0.0039	0.10B	0.1040	873	
			S-6-6	1.832	4810	1.28	0.0050	0.10T	0.1041	856	
			Mean	1.822	4350	1.45	0.0043		0.1037	870	
			Standard Deviation	0.014	325	0.18	0.0004		0.0022	45	
			S-8-1	1.844	5750	1.47	0.0058	0.62T	0.1058	848	
			S-8-2	1.847	5690	1.33	0.0058	0.15T	0.1061	841	
			S-8-3	1.823	5240	1.38	0.0052	0.42T	0.1052	863	
			S-8-4	1.828	5220	1.27	0.0052	0.40B	0.1063	842	
			S-8-5	1.833	5200	1.33	0.0052	0.35B	0.1053	847	
			S-8-6	1.841	4260	1.30	0.0044	0.45T	0.1067	802	
			Mean	1.836	5227	1.34	0.0053		0.1059	840	
			Standard Deviation	0.010	534	0.07	0.0005		0.0006	20	
			S-10-1	1.842	5350	1.33	0.0054	0.83T	0.1072	840	
			S-10-2	1.847	5080	1.55	0.0052	0.35T	0.1061	844	
			S-10-3	1.845	5010	1.27	0.0052	0.50T	0.1057	844	
			S-10-4	1.842	5070	1.35*	0.0040	0.58T	0.1055	841	
			S-10-5	1.842	5000	1.36	0.0053	0.35B	0.1055	857	
			S-10-6	1.841	4570	1.57	0.0044	0.35T	0.1054	844	
			Mean	1.843	5013	1.41	0.0049		0.1059	845	
			Standard Deviation	0.002	252	0.12	0.0006		0.0007	6	
			Mean Value	1.827	4763	1.43	0.0047		0.1049	865	
			Standard Deviation	0.018	499	0.16	0.0006		0.0017	45	
L-7-1 With Grain			L-7-1-1	1.778	4420	1.23	0.0045	0.30T	0.1043	886	
			L-7-1-2	1.771	4220	1.48*	0.0045	0.12T	0.1030	866	

\*Stress-strain curves for noted specimens were somewhat erratic due to load train motion.

TABLE 2  
TENSILE PROPERTIES AT 70°F OF ATJ-S BILLET L-1-4

Orientation	Temp °F	Stress Rate psi/min	Specimen Number	Blank Bulk Density gm/cm <sup>3</sup>	Ultimate Strength psi	Elastic Modulus 10 <sup>6</sup> psi	Total Axial Strain in./in.	Fracture Location in. from Midspan	Blank Ultrasonic Velocity in./μ sec	Gage Electrical Resistivity μ ohm-cm	Remarks
With Grain	70	10,000	A1W	1.827	4850	1.47	0.0048	0.4T	0.1033	810	0.027" Flaw in First Breakdown Radius
			A2W	1.828	5490	1.44	0.0055	0.1T	0.1041	781	
			A3W	1.832	4940	1.43	0.0052	0.6B	0.1050	787	
			A4W	1.832	5410	1.60	0.0052	0.6T	0.1044	796	
			A5W	1.829	5080	1.67	0.0059	0.6B	0.1036	775	
			A6W	1.830	5490	1.60	0.0053	0.2T	0.1034	780	
			A7W	1.828	5210	1.57	0.0054	0.6B	0.1030	780	
			A8W	1.825	5250	1.58	0.0051	0.4T	0.1027	800	
			A9W	1.822	4670	1.43	0.0047	0.1T	0.1022	829	
			A10W	1.822	4440	1.62	0.0037	0.3T	0.1030	810	
			A11W	1.821	5120	1.59	0.0049	0.2T	0.1035	778	
			A12W	1.819	3890	1.77	0.0029	0.8T	0.1030	774	
			A13W	1.826	5190	1.48	0.0052	0.0	0.1033	800	
			A14W	1.827	4980	1.52	0.0053	0.4T	0.1032	790	
			A15W	1.825	4800	1.36	0.0050	0.0	0.1023	845	
			A16W	1.818	5010	1.53	0.0054	0.5T	0.1025	817	
			A17W	1.820	4610	1.50	0.0045	0.4B	0.1027	819	
			A18W	1.820	5100	1.60	0.0052	0.8B	0.1033	782	
			A19W	1.821	4880	1.55	0.0048	0.3T	0.1037	792	
			A20W	1.823	4650	1.57	0.0047	0.0	0.1039	788	
			A21W	1.823	4540	1.41	0.0044	0.1T	0.1023	827	
			A22W	1.820	4570	1.39	0.0049	0.5B	0.1022	820	
			A23W	1.826	4880	1.29	0.0047	0.5T	0.1025	807	
			A24W	1.821	4730	1.26	0.0046	0.0	0.1020	810	
			A25W	1.823	4570	1.31	0.0049	0.5T	0.1024	828	
			A26W	1.821	4910	1.41	0.0052	0.1T	0.1028	810	
			A27W	1.820	4900	1.40	0.0051	0.7T	0.1032	802	
			A28W	1.823	4890	1.46	0.0052	0.3T	0.1033	809	
			A30W	1.831	5130	1.25	0.0056	0.6T	0.1034	787	
			A31W	1.830	5080	1.36	0.0051	0.7T	0.1032	809	
			Mean	1.824	4909	1.48	0.0049	0.7T	0.1031	801	
			Standard Deviation	0.004	338	0.13	0.0006		0.0007	18	
Across Grain	70	10,000	B1A	1.836	4190	1.04	0.0062	0.1T	0.0873	1016	Large Black Spot in Fracture
			B2A	1.830	4140	1.06	0.0064	0.5B	0.0863	1025	
			B3A	1.831	4010	1.09	0.0061	0.2T	0.0863	1027	
			B4A	1.839	4120	1.00	0.0067	0.2T	0.0865	1038	
			B5A	1.846	4020	0.87	0.0063	0.1B	0.0865	1072	
			B6A	1.835	4140	0.98	0.0067	0.1B	0.0863	1053	
			B7A	1.830	4030	0.97	0.0061	0.2T	0.0868	1041	
			B8A	1.828	3950	0.91	0.0061	0.6B	0.0866	1039	
			B9A	1.843	4240	0.90	0.0068	0.2B	0.0862	1062	
			B10A	1.828	4150	1.06	0.0064	0.6B	0.0866	1011	
			B11A	1.829	4050	0.98	0.0061	0.4B	0.0866	1027	
			B12A	1.831	4140	1.04	0.0064	0.4T	0.0863	1030	
			B13A	1.833	4100	0.95	0.0061	0.1T	0.0864	1037	
			B14A	1.864	1850	0.94	0.0021	0.2T	0.0872	1054	
			B15A	1.839	4170	1.02	0.0065	0.4T	0.0868	1062	
			B16A	1.834	4030	1.13	0.0055	0.1T	0.0872	1013	
			B17A	1.826	4080	1.04	0.0061	0.1B	0.0865	1032	
			B18A	1.832	4210	1.07	0.0065	0.4T	0.0867	1043	
			B19A	1.832	4080	1.05	0.0063	0.45T	0.0864	1032	
			B20A	1.862	3990	1.02	0.0061	0.5T	0.0872	1039	
			B22A	1.827	4130	1.00	0.0065	0.1T	0.0865	1034	
			B23A	1.830	3860	1.07	0.0060	0.5T	0.0868	1038	
			B24A	1.833	4080	1.10	0.0061	0.1B	0.0870	1028	
			B25A	1.834	3790	0.98	0.0057	0.5B	0.0870	1048	
			B26A	1.845	4200	0.95	0.0064	0.6B	0.0872	1060	
			B27A	1.832	4070	1.06	0.0064	0.5T	0.0873	1022	
			B28A	1.829	4060	0.99	0.0064	0.6B	0.0866	1038	
			B29A	1.831	4170	1.06	0.0064	0.5B	0.0867	1027	
			B30A	1.833	3900	1.02	0.0059	0.5T	0.0873	1016	
			B31A	1.831	4070	0.93	0.0061	0.5T	0.0869	1042	
			B32A	1.835	4100	1.01	0.0061	0.4T	0.0864	1061	
			B33A	1.841	4190	0.90	0.0065	0.6T	0.0860	1041	
			B34A	1.861	4470	0.94	0.0067	0.5B	0.0870	1059	
			B35A	1.835	4120	0.95	0.0061	0.5T	0.0872	1039	
			B36A	1.836	4010	1.04	0.0058	0.2T	0.0870	1044	
			B37A	1.853	----	----	-----	0.1T	0.0872	1059	
			Mean	1.837	4026	1.00	0.0061		0.0867	1039	
			Standard Deviation	0.010	397	0.06	0.0008		0.0004	17	



TABLE 3  
TENSILE PROPERTIES AT 70°F OF ATJ-S BILLET L-1-8

Orientation	Temp °F	Stress Rate psi/min	Specimen Number	Blank Bulk Density gm/cm <sup>3</sup>	Ultimate Strength psi	Elastic Modulus 10 <sup>6</sup> psi	Total Axial Strain in./in.	Fracture Location in. from Midspan	Blank Ultrasonic Velocity in./μ sec	Gage Electrical Resistivity μ ohm-cm	Remarks
With Grain	70	10,000	A5W	1.833	5180	1.46	0.0051	0.4T	0.1038	828	
			A6W	1.834	5050	1.71	0.0047	0.4B	0.1048	812	
			A7W	1.840	5730	1.69	0.0054	0.5B	0.1052	803	
			A8W	1.810	5200	1.67	0.0050	0.2B	0.1032	826	
			A9W	1.824	5250	1.54	0.0052	0.4B	0.1032	826	
			A10W	1.821	5300	1.77	0.0048	0.5T	0.1035	815	
			A11W	1.826	5000	1.43	0.0051	0.6T	0.1039	808	
			A12W	1.820	5430	1.06	0.006	0.6B	0.1030	821	
			A13W	1.818	4970	1.31	0.0050	0.6T	0.1033	821	
			A14W	1.817	5090	1.51	0.0049	0.2B	0.1033	823	
			A15W	1.815	5300	1.47	0.0049	0.6T	0.1035	814	
			A16W	1.822	5220	1.61	0.0047	0.2T	0.1038	825	
			A17W	1.814	4960	1.51	0.0048	0.5T	0.1027	824	
			A18W	1.813	4450	1.44	0.0042	0.8T	0.1029	832	
			A19W	1.815	5200	1.52	0.0053	0.3B	0.1031	822	
			A20W	1.815	4760	1.52	0.0042	0.6T	0.1028	822	
			A21W	1.815	5030	1.47	0.0048	0.0	0.1032	834	
			A22W	1.815	5250	1.26	0.0053	0.3T	0.1025	830	
			A23W	1.812	5170	1.51	0.0055	0.3T	0.1025	834	
			A24W	1.809	4990	1.46	0.0048	0.5B	0.1029	828	
			A25W	1.810	5130	1.35	0.0058	0.4T	0.1026	818	
			A26W	1.812	4670	1.51	0.0046	0.2T	0.1027	833	
			A27W	1.816	4800	1.51	0.0049	0.2T	0.1023	849	
			A28W	1.808	5160	1.49	0.0051	0.4B	0.1020	833	
			A29W	1.813	4780	1.72	0.0045	0.1T	0.1017	845	
			A30W	1.812	4170	1.48	0.0041	0.5T	0.1020	855	
			A31W	1.806	4630	1.25	0.0047	0.1B	0.1015	855	
			A32W	1.807	4350	1.41	0.0042	0.1T	0.1020	857	
			A33W	1.808	4750	1.57	0.0048	0.2T	0.1022	841	
			B26W	1.816	5310	1.45	0.0053	0.5B	0.1027	840	
			B27W	1.811	5020	1.47	0.0052	0.1T	0.1016	841	
			B28W	1.805	4990	1.41	0.0052	0.1B	0.1015	835	
			B29W	1.818	5000	1.44	0.0050	0.6T	0.1033	830	
			B30W	1.809	4820	1.61	0.0045	0.0	0.1026	847	
			B31W	1.803	4850	1.52	0.0048	0.45T	0.1018	834	
			B32W	1.822	4950	1.52	0.0048	0.4T	0.1032	849	
			B33W	1.810	5180	1.52	0.0052	0.3T	0.1032	821	
			B35W	1.808	5110	1.36	0.0055	0.0	0.1028	841	
			B36W	1.817	5290	1.45	0.0057	0.5T	0.1033	839	
			B37W	1.810	5150	1.33	0.0056	0.4T	0.1023	843	
			B38W	1.807	5000	1.29	0.0057	0.3B	0.1023	857	
			B39W	1.819	5200	1.39	0.0056	0.1B	0.1026	846	
			B40W	1.812	4990	1.12	0.0059	0.2T	0.1019	849	
			B41W	1.806	4710	1.35	0.0051	0.7B	0.1012	855	
			B42W	1.820	4820	1.29	0.0052	0.4B	0.1024	857	
			B43W	1.814	4950	1.43	0.0052	0.3B	0.1020	841	
			Mean	1.815	5007	1.47	0.0050		0.1028	834	
			Standard Deviation	0.008	283	0.13	0.0005		0.0008	14	
Across Grain	70	10,000	A1A	1.828	4280	0.88	0.0067	0.2T	0.0871	1106	
			A2A	1.819	4000	1.03	0.0055	0.4T	0.0868	1103	
			A3A	1.820	4020	0.98	0.0062	0.4T	0.0864	1110	
			A4A	1.821	4250	1.03	0.0067	0.4T	0.0863	1121	
			B1A	1.831	4190	0.99	0.0065	0.3B	0.0865	1118	
			B2A	1.838	4220	1.16	0.0061	0.4B	0.0870	1107	
			B3A	1.805	4030	0.95	0.0061	0.6B	0.0862	1096	
			B4A	1.805	3890	0.92	0.0061	0.2T	0.0859	1097	
			B5A	1.803	4120	1.07	0.0059	0.5T	0.0861	1084	
			B6A	1.803	4100	0.93	0.0065	0.3T	0.0861	1100	
			B7A	1.806	4180	1.13	0.0063	0.6T	0.0860	1111	
			B8A	1.804	4180	1.00	0.0065	0.5T	0.0859	1104	
			B9A	1.811	4070	1.00	0.0065	0.4T	0.0859	1132	
			B10A	1.795	4120	0.96	0.0065	0.5T	0.0858	1111	
			B11A	1.801	3800	1.02	0.0059	0.2T	0.0858	1087	
			B12A	1.805	4010	0.87	0.0064	0.3B	0.0861	1103	
			B13A	1.806	4180	0.82	0.0071	0.5B	0.0861	1133	
			B14A	1.807	4050	0.92	0.0065	0.4B	0.0861	1132	
			B15A	1.803	4140	0.78	0.0070	0.0	0.0862	1071	
			B16A	1.800	4090	1.05	0.0062	0.2B	0.0859	1072	
			B17A	1.802	4110	0.89	0.0068	0.3B	0.0861	1104	
			B18A	1.804	4100	1.15	0.0061	0.5B	0.0862	1111	
			B19A	1.807	4130	1.05	0.0063	0.4B	0.0864	1061	
			B20A	1.797	4090	1.00	0.0065	0.4T	0.0859	1006	
			B21A	1.798	4020	1.06	0.0062	0.55B	0.0859	1095	
			B22A	1.798	3810	0.96	0.0062	0.2T	0.0859	1100	
			B23A	1.808	4100	0.97	0.0064	0.4B	0.0864	1095	
			B24A	1.801	4200	1.09	0.0068	0.4T	0.0859	1110	
			B25A	1.801	4040	1.00	0.0065	0.4B	0.0859	1090	
			Mean	1.808	4087	0.99	0.0064		0.0862	1099	
			Standard Deviation	0.011	114	0.09	0.0003		0.0003	25	

TABLE 4

TENSILE PROPERTIES AT 70°F AND 3000°F OF SLABS 2, 4, 6, AND 8 FROM ATJ-S BILLET L-4-6

Loading Direction	Temp °F	Loading Rate psi/sec	Specimen Number	Blank Bulk Density gm/cm <sup>3</sup>	Ultimate Tensile Strength psi	Initial Elastic Modulus 10 <sup>6</sup> psi	Total Unit Axial Strain in./in.	Blank Ultrasonic Velocity in./μ sec	Remarks
With Grain	70	500	T42W	1.809	5050	1.16	0.0056	0.1077	
			T43W	1.801	5000	1.12	0.0057	0.1073	
			T44W	1.800	4200	1.47	0.0040	0.1072	
			T45W	1.797	4600	1.34	0.0047	0.1072	
			T46W	1.797	4650	1.19	0.0054	0.1070	
			T47W	1.795	4750	1.10	0.0055	0.1079	
			T48W	1.810	4700	1.59 <sup>1</sup>	0.0034 <sup>1</sup>	0.1075	
			Mean	1.801	4710	1.28	0.0049	0.1074	
			Standard Deviation	0.006	282	0.04	0.0009	0.0003	
			T91W	1.824	4300	1.33	0.0041	0.1091	
			T92W	1.827	5200	1.30	0.0051	0.1095	
			T93W	1.827	5400	1.73 <sup>1</sup>	0.0038 <sup>1</sup>	0.1099	
			T94W	1.831	5100	1.78	0.0047	0.1101	
With Grain	70	500	T95W	1.826	5300	1.39	0.0054	0.1101	
			T96W	1.829	5350	1.25	0.0054	0.1097	
			T97W	1.823	5100	1.47	0.0052	0.1101	
			Mean	1.827	5110	1.46	0.0048	0.1098	
			Standard Deviation	0.003	375	0.21	0.0006	0.0004	
			Mean	1.814	4910	1.37	0.0049	0.1086	
			Standard Deviation	0.014	380	0.21	0.0008	0.0013	
			T18W	1.806	6120	1.69	0.0047	0.1079	
			T19W	1.813	6310	1.76	0.0046	0.1070	
			T20W	1.794	5500	1.42	0.0044	0.1070	
			T21W	1.789	5810	1.87	0.0042	0.1068	
			T22W	1.789	5810	1.49	0.0045	0.1068	
			T23W	1.792	5500	1.42	0.0044	0.1072	
With Grain	3000	500	T24W	1.812	6440	1.69	0.0048	0.1089	
			Mean	1.799	5930	1.62	0.0045	0.1074	
			Standard Deviation	0.011	374	0.18	0.0002	0.0008	
			T59W	1.821	6000	1.56	0.0044	0.1083	
			T60W	1.816	6560	1.90	0.0053	0.1068	
			T61W	1.798	5820	1.49	0.0046	0.1089	
			T62W	1.813	6000	1.71	0.0044	0.1083	
			T63W	1.814	6250	1.71	0.0044	0.1095	
			T64W	1.823	6250	1.71	0.0044	0.1170	
			T65W	1.830	6500	1.28	0.0064	0.1101	
			Mean	1.816	6200	1.62	0.0048	0.1098	
			Standard Deviation	0.010	274	0.20	0.0008	0.0003	
			Mean	1.807	6065	1.62	0.0047	0.1086	
			Standard Deviation	0.013	345	0.18	0.0006	0.0026	

Note: (1) Axial Strain measured with strain gages; all other axial strain measurements were made with the strain analyzer.

TABLE 5

TENSILE PROPERTIES AT 70°F, 3000°F, 4500°F, AND 5500°F OF ATI-S BILLET L-6-3

Loading Direction	Temp °F	Loading Rate psi/sec	Specimen Number	Blank Bulk Density gm/cm <sup>3</sup>	Ultimate Tensile Strength psi	Initial Elastic Modulus 10 <sup>6</sup> psi	Total Unit Axial Strain in./in.	Measured Poisson's Ratio			Blank Ultrasonic Velocity in./μ sec	Distance of Fractured Surface from Center in.	Remarks
								$\nu_{AW}$	$\nu_{WW}$	$\nu_{WA}$			
With Grain	70	500	T1W	1.822	5500	1.46	0.0057	0.11	0.11		0.1044	0.6B	
			T2W	1.833	4700	1.71	0.0038	0.18	---		0.1042	0.6T	
			T3W	1.834	4520	1.27	0.0046		---		0.1040	0.4B	
			T16W	1.824	5310	1.45	0.0051		0.08		0.1048	0.55T	
			Average	1.828	5010	1.47	0.0048		0.12		0.1043		
	3000	500	T4W	1.836	7080	1.71	0.0056	0.11	0.09		0.1051	0.4B	
			T5W	1.834	7140	1.12	0.0066				0.1049	0.6T	
			T6W	1.833	6080	1.23	0.0053	0.08			0.1042	0.6B	
			Average	1.834	6770	1.35	0.0058	0.09			0.1047		
													Radius Break
	4500	500	T7W	1.822	7260	1.37	0.0078	---	0.17		0.1039	0.8T	
			T8W	1.818	7240	1.41	0.0099	---	---		0.1037	0.6T	
			T9W	1.812	8160	1.50	0.0115		---		0.1036	0.6T	
			Average	1.817	7550	1.43	0.0097				0.1037		
													Specimen did not fracture. Strength values are stress levels in specimen at 0.025 in. total axial strain
	5500	500	T10W	1.820	4450 <sup>1</sup>	0.41	0.025 <sup>1</sup>	0.20	---		0.1043		
			T11W	1.831	3320 <sup>2</sup>	0.43	0.025 <sup>2</sup>				0.1049		
													Specimen broke while placing in load train.
Across Grain	70	500	T12W	1.836									
			Average	1.829	3880	0.42	0.025	0.20			0.1046		
			T1A	1.827	4350	0.96	0.0071				0.0877	0.6B	
			T2A	1.826	4040	1.27	0.0051			0.07	0.0876	0.4B	
			T3A	1.829	4200	1.07	0.0057			0.06	0.0878	0.4B	
	3000	500	Average	1.827	4200	1.10	0.0060			0.09	0.0877		
			T4A	1.825	5520	1.15	---			0.10	0.0876	0.6T	
			T5A	1.827	5040	1.28	0.0050			0.07	0.0871	0.4B	
			T6A	1.826	5390	1.20	0.0056			0.14	0.0876	0.6T	
			Average	1.826	5320	1.21	0.0053			0.10	0.0874		
	4500	500	T7A	1.831	6300	0.95	0.0106			---	0.0881	0.6T	
			T8A	1.831	7000	1.12	0.0081			0.12	0.0881	0.6T	
			T9A	1.827	6960	1.06	0.0140			0.16	0.0883	0.6T	
			T16A	1.828	7000	0.94	0.0185			0.23	0.0881	0.6T	
			Average	1.829	6820	1.02	0.0143			0.17	0.0881	0.8T	
	5500	500	T10A	1.828	4180 <sup>4</sup>	0.30	0.025 <sup>4</sup>			---	0.0881		
													Specimen did not fracture. Strength values reported are stress levels in specimen at 0.025 in. total axial strain.
			T11A	1.826	3460 <sup>5</sup>	0.50	0.025 <sup>5</sup>			0.21	0.0879		
			T12A	1.830	3150 <sup>6</sup>	0.49	0.025 <sup>6</sup>			0.15	0.0880		
			Average	1.828	3600	0.43	0.025			0.18	0.0880		

1. After run total length was 6.344 in. long, and minimum gage diameter was 0.243 in.

2. After run total length was 6.438 in. long, and minimum gage diameter was 0.243 in.

3. Curve was not definitive.

4. After run specimen total length was 6.344 in. long, and minimum gage dia was 0.237 in.

5. After run specimen total length was 6.375 in. long, and minimum gage dia was 0.235 in.

6. After run specimen total length was 6.500 in. long, and minimum gage dia was 0.237 in.

TABLE 6  
TENSILE PROPERTIES AT 70°F AND 4500°F OF ATJ-S BILLET L-9-10

Loading Direction	Temp °F	Loading Rate psi/sec	Specimen Number	Blank Bulk Density gm/cm <sup>3</sup>	Ultimate Tensile Strength psi	Initial Elastic Modulus 10 <sup>5</sup> psi	Total Unit Axial Strain in./in.	Measured Poisson's Ratio			Distance of Fractured Surface from Center in.	Remarks
								$\nu_{aw}$	$\nu_{ww}$	$\nu_{wa}$		
With Grain	70	500	T1W	1.820	3900	1.66	0.0036		0.14		0.4T	
			T3W	1.817	4000	1.67	0.0041	0.09			0.6B	
			T5W	1.828	3580	1.41	0.0036		0.20		0.6B	
			T7W	1.788	3290	1.31	0.0032	---			0.6T	
			T9W	1.812	3900	1.30	0.0043		0.32		0.00	
			Mean	1.813	3730	1.47	0.0038		0.18			
			Std Deviation	0.015	294	0.18	0.0004					
	4500	500	T2W	1.802	6460	1.64	0.0075	0.16			0.6T	
			T4W	1.825	7340	1.84	0.0111		0.10		0.5T	
			T6W	1.790	6180	1.03	0.0105	0.21			0.5B	
			T8W	1.799	5880	1.43	0.0077		0.39		0.6T	
			T10W	1.820	6620	1.21	0.0092	0.11			0.6T	
			Mean	1.807	6500	1.43	0.0092		0.19			
			Std Deviation	0.015	550	0.32	0.0016					
	70	500	T1A	1.835	3800	1.08	0.0063			0.07	0.5B	
			T3A	1.827	3650	1.35	0.0050			0.12	0.5B	
			T5A	1.838	3820	1.21	0.0053			0.10	0.6B	
			T7A	1.809	3540	1.02	0.0048			0.24	0.5B	
			T9A	1.811	3540	1.30	0.0049			0.14	0.5B	
			Mean	1.824	3670	1.19	0.0053			0.13		
			Std Deviation	0.013	136	0.14	0.0006					
Across Grain	4500	500	T2A	1.828	5680	1.20	0.0084			0.13	0.5T	
			T4A	1.829	5080	1.24	0.0061			---	0.3T	
			T6A	1.812	5680	1.22	0.0094			0.16	0.6T	
			T8A	1.810	5620	0.98	0.0101			0.11	0.4T	
			T10A	1.812	5640	1.01	0.0117			0.07	0.5T	
			Mean	1.818	5540	1.13	0.0091			0.12		
			Std Deviation	0.009	258	0.12	0.0021					

TABLE 7

## TENSILE PROPERTIES AT 70°F AND 4500°F OF ATJ-S BILLET L-10-6

Loading Direction	Temp °F	Loading Rate psi/sec	Specimen Number	Blank Bulk Density gm/cm <sup>3</sup>	Ultimate Tensile Strength psi	Initial Elastic Modulus 10 <sup>6</sup> psi	Total Unit Axial Strain to Failure in./in.	Measured Poisson's Ratio			Distance of Fractured Surface from Center in.	Remarks
								$\nu_{av}$	$\nu_{wyw}$	$\nu_{wa}$		
With Grain	70	500	T1W	1.840	4840	1.85	0.0049	0.08	0.08		0.4B	Notch accidentally cut in gage section so total strain not measured
			T3W	1.828	4350	1.74	0.0044				0.6T	
			T5W	1.833	5510	1.80	0.0041				0.4B	
			T7W	1.819	4580	1.79	0.0045				0.5T	
			T9W	1.824	4150	1.89	0.0034				0.5B	
			Mean	1.829	4690	1.81	0.0043					
	4500	500	Std Deviation	0.008	527	0.06	0.0006	---	---			
			T2W	1.822	6720	1.56	0.0071				0.6T	
			T4W	1.831	7100	1.14	0.0090				0.4T	
			T6W	1.833	8040	1.38	0.0119				0.6T	
			T8W	1.826	6500	1.24	0.0072				0.6T	
			T10W	1.827	7400	1.45	0.0102				0.5T	
	70	500	Mean	1.828	7150	1.35	0.0091	0.08	0.09			
			Std Deviation	0.004	605	0.17	0.0020				0.0	
			T1A	1.839	4070	1.00	---					
			T3A	1.830	3800	1.15	0.0056				0.4B	
			T5A	1.837	3240	0.79	0.0049				0.5T	
			T7A	1.822	3760	0.90	0.0063				0.5B	
Across Grain	70	500	T9A	1.829	3480	1.15	0.0047	---	---		0.5B	
			Mean	1.831	3570	1.00	0.0054				0.5B	
			Std Deviation	0.007	262	0.16	0.0007					
	4500	500	T2A	1.833	5760	0.95	0.0091				0.7T	
			T4A	1.832	5580	1.09	0.0088				0.5T	
			T6A	1.827	5560	0.98	0.0095				0.3B	
			T8A	1.824	5960	1.01	0.0110				0.5T	
	4500	500	T10A	1.830	5720	0.95	0.0103				0.6T	
			Mean	1.829	5720	1.00	0.0097					
			Std Deviation	0.004	161	0.06	0.0009					

TABLE 8  
TENSILE PROPERTIES AT 70°F AND 4500°F OF ATJ-S BILLET L-11-4

Loading Direction	Temp °F	Loading Rate psi/sec	Specimen Number	Blank Bulk Density gr/cm <sup>3</sup>	Ultimate Tensile Strength psi	Initial Elastic Modulus 10 <sup>6</sup> psi	Total Unit Axial Strain to Failure in./in.	Measured Poisson's Ratio			Distance of Fractured Surface from Center in.	Remarks
								$\nu_{av}$	$\nu_{vw}$	$\nu_{wa}$		
With Grain	70	500	T1W	1.809	4450	1.72	0.0037	---	---	---	0.6T	Broken in handling
			T3W	1.820	4650	1.93	0.0038	0.12	---	---	0.4T	
			T5W	1.825	5170	1.53	0.0046	0.13	0.13	---	0.4B	
			T7W	1.802	4920	1.82	0.0045	0.32	---	---	0.4B	
			T9W	1.813	4940	1.55	0.0046	---	---	---	0.4T	
			Mean	1.814	4830	1.71	0.0042	0.19	---	---	---	
			Std Deviation	0.009	280	0.17	0.0005	---	---	---	---	
	4500	500	T2W	1.814	7560	1.80	0.0088	0.08	---	---	0.5T	
			T4W	1.823	7960	2.04	0.0093	0.12	---	---	0.2T	
			T6W	1.799	7140	1.28	0.0089	0.10	---	---	0.4T	
			T8W	1.810	---	---	---	---	---	---	---	
			T10W	1.818	8380	1.57	0.0130	0.10	---	---	0.1T	
			Mean	1.813	7760	1.67	0.0100	---	---	---	---	
			Std Deviation	0.009	532	0.32	0.0020	---	---	---	---	
	70	500	T1A	1.825	3840	1.29	0.0054	0.09	0.09	0.09	0.5B	Broken while machining
			T3A	1.820	3820	1.29	0.0052	0.09	0.09	0.09	0.5B	
			T5A	1.827	4240	1.21	0.0063	0.08	0.08	0.08	0.6T	
			T7A	1.816	4060	1.24	0.0055	0.18	0.18	0.18	0.7T	
			T9A	1.817	3770	1.30	0.0045	---	---	---	0.5T	
			Mean	1.821	3950	1.27	0.0054	0.11	0.11	0.11	---	
			Std Deviation	0.005	198	0.04	0.0006	---	---	---	---	
	4500	500	T2A	1.827	---	---	---	---	---	---	---	
			T4A	1.835	6200	1.25	0.0092	0.05	0.05	0.05	0.1T	
			T6A	1.821	6020	1.24	0.0083	0.22	0.22	0.22	0.6B	
			T8A	1.814	6480	1.13	0.0127	0.26	0.26	0.26	0.6B	
			T10A	1.809	6500	1.08	0.0131	0.11	0.11	0.11	0.5T	
			Mean	1.821	6300	1.18	0.0108	0.16	0.16	0.16	---	
			Std Deviation	0.010	230	0.08	0.0024	---	---	---	---	
Across Grain	70	500	T1A	1.825	3840	1.29	0.0054	0.09	0.09	0.09	0.5B	Broken while machining
			T3A	1.820	3820	1.29	0.0052	0.09	0.09	0.09	0.5B	

TABLE 9

RESULTS OF DENSITY, ABSORPTION, POROSITY, AND SECTION ULTRASONIC  
VELOCITY MEASUREMENTS FOR SPECIMENS FROM EVEN SLABS OF ATJ-S  
BILLET L-16-7 AND SPECIMENS FROM ATJ-S BILLET L-7-1

Specimen Number	Percent Absorption	Bulk Density gm/cm <sup>3</sup>	Apparent Density gm/cm <sup>3</sup>	Percent Total Porosity	Percent Open Porosity	Percent Closed Porosity	Section Ultrasonic Velocity in. / $\mu$ .sec
S-2-1	4.9	1.828	2.008	17.6	8.9	8.7	0.1044
S-2-2	8.6	1.704	1.999	23.2	14.7	8.5	0.0963
S-2-3	5.0	1.822	2.006	17.9	9.1	8.8	0.1035
S-2-4	5.1	1.825	2.014	17.8	9.4	8.4	0.1028
S-2-6	4.6	1.843	2.012	17.0	8.4	8.6	0.1044
S-4-1	3.8	1.845	1.983	16.9	6.9	10.0	0.1063
S-4-2	7.3	1.763	2.023	20.6	12.9	7.7	0.0995
S-4-3	6.2	1.785	2.009	19.6	11.1	8.5	0.1018
S-4-4	4.6	1.829	1.997	17.6	8.4	9.2	0.1046
S-4-5	4.9	1.824	2.004	17.9	9.0	8.9	0.1048
S-4-6	4.9	1.826	2.005	17.7	8.9	8.8	0.1037
S-6-1	6.2	1.788	2.013	19.4	11.1	8.3	0.1053
S-6-2	5.0	1.824	2.006	17.8	9.0	8.8	0.1054
S-6-3	4.5	1.843	2.009	17.0	8.3	8.7	0.1056
S-6-4	5.8	1.806	2.015	18.6	10.4	8.2	0.1031
S-6-5	4.8	1.830	2.005	17.6	8.7	8.9	0.1031
S-6-6	5.0	1.824	2.005	17.8	9.0	8.8	0.1032
S-8-1	4.2	1.844	2.001	16.9	7.8	9.1	0.1038
S-8-2	3.7	1.858	1.996	16.3	6.9	9.4	0.1049
S-8-3	4.9	1.829	2.008	17.6	8.9	8.7	0.1051
S-8-4	4.5	1.844	2.011	16.9	8.3	8.6	0.1044
S-8-5	4.5	1.840	2.008	17.1	8.4	8.7	0.1050
S-8-6	4.4	1.843	2.007	17.0	8.2	8.8	0.1059
S-10-1	4.3	1.844	2.005	16.9	8.0	8.9	0.1063
S-10-2	4.4	1.843	2.005	17.0	8.1	8.9	0.1049
S-10-3	4.1	1.847	1.999	16.8	7.6	9.2	0.1044
S-10-4	4.4	1.844	2.008	16.9	8.1	8.8	0.1044
S-10-5	4.7	1.834	2.005	17.4	8.5	8.9	0.1044
S-10-6	4.4	1.841	2.002	17.1	8.1	9.0	0.1043
Mean Std	5.0	1.825	2.006	17.8	9.0	8.8	0.1039
Deviation	1.0	0.031	0.007	1.4	1.7	0.4	0.0020
L-7-1-1	5.6	1.809	2.011	18.5	10.0	8.5	0.1032
L-7-1-2	6.2	1.797	2.022	19.1	11.2	7.9	0.1010

## Notes:

1. Results of second run - first run results questionable.
2. Results confirmed by second run.
3. Assumed theoretical density of 2.22 gm/cm<sup>3</sup>.

TABLE 10

RESULTS OF DENSITY, ABSORPTION, POROSITY, AND SECTION ULTRASONIC  
VELOCITY MEASUREMENTS FOR SPECIMENS FROM ATJ-S BILLET L-1-4

Specimen Number	Percent Absorption	Bulk Density gm/cm <sup>3</sup>	Apparent Density gm/cm <sup>3</sup>	Percent Total Porosity	Percent Open Porosity	Percent Closed Porosity	Section Ultrasonic Velocity in./μ sec	Remarks
A1W	4.6	1.821	1.986	18.0	8.3	9.7	0.1009	
A2W	4.4	1.830	1.989	17.6	8.0	9.6	0.1022	
A3W	4.6	1.823	1.990	17.9	8.3	9.5	0.1056	
A4W	4.1	1.833	1.982	17.4	7.5	9.9	0.1032	
A5W	4.5	1.824	1.986	17.8	8.1	9.7	0.1058	
A6W	4.2	1.836	1.988	17.3	7.6	9.7	0.1031	
A7W	4.5	1.825	1.989	17.8	8.2	9.6	0.1059	
A8W	4.7	1.817	1.987	18.1	8.5	9.6	0.1031	
A9W	4.8	1.812	1.986	18.4	8.8	9.6	0.0998	
A10W	4.8	1.815	1.988	18.2	8.7	9.6	0.1029	
A10W	4.7	1.814	1.983	18.3	8.6	9.7	----	Second Run- Vacuum Dried
A10W	5.8	1.793	2.001	19.2	10.4	8.8	----	Short Half of Fractured Spec.
A11W	4.5	1.824	1.986	17.8	8.1	9.7	0.1045	
A12W	5.5	1.800	1.998	18.9	9.9	9.0	0.1014	0.027 in. Flaw in Radius
A13W	4.6	1.822	1.988	17.9	8.4	9.6	0.1026	
A14W	4.6	1.822	1.988	17.9	8.4	9.6	0.1015	
A15W	4.9	1.811	1.989	18.4	8.9	9.5	0.1015	
A16W	4.8	1.817	1.989	18.1	8.6	9.5	0.1034	
A17W	4.8	1.816	1.989	18.2	8.7	9.5	0.1043	
A18W	4.6	1.826	1.995	17.7	8.5	9.3	0.1040	
A19W	4.8	1.817	1.989	18.2	8.6	9.5	0.1047	
A20W	5.3	1.812	2.002	18.4	9.5	8.9	0.1048	
A21W	4.9	1.810	1.988	18.5	8.9	9.5	0.1040	
A22W	4.8	1.816	1.988	18.2	8.7	9.5	0.1025	
A23W	4.7	1.820	1.989	18.0	8.5	9.5	0.1029	
A24W	4.9	1.815	1.992	18.2	8.9	9.4	0.1026	
A25W	4.8	1.817	1.992	18.2	8.8	9.4	0.1022	
A26W	4.9	1.814	1.992	18.3	8.9	9.4	0.1035	
A27W	4.8	1.816	1.990	18.2	8.8	9.4	0.1040	
A28W	3.7	1.827	1.961	17.7	6.8	10.9	0.1042	Long Half of Fractured Spec.
A28W	4.7	1.817	1.987	18.2	8.6	9.6	----	Short Half of Fractured Spec.
A30W	4.9	1.815	1.991	18.3	8.8	9.4	0.1050	
A31W	4.7	1.819	1.990	18.1	8.6	9.5	0.1027	
Mean	4.7	1.818	1.989	18.1	8.6	9.5	0.1033	
Std Deviation	0.4	0.008	0.007	0.4	0.6	0.3	0.0015	



TABLE 10 - CONTINUED

Specimen Number	Percent Absorption	Bulk Density gm/cm <sup>3</sup>	Apparent Density gm/cm <sup>3</sup>	Percent Total Porosity	Percent Open Porosity	Percent Closed Porosity	Section Ultrasonic Velocity in. / $\mu$ sec	Remarks
B1A	4.0	1.848	1.997	16.7	7.5	9.3	0.0873 <sup>1</sup>	
B2A	4.4	1.832	1.993	17.5	8.1	9.4	0.0873 <sup>1</sup>	
B3A	4.4	1.833	1.993	17.4	8.0	9.4	0.0874 <sup>1</sup>	
B4A	4.3	1.833	1.992	17.4	8.0	9.5	0.0864 <sup>1</sup>	
B5A	3.9	1.845	1.990	16.9	7.3	9.6	0.0864 <sup>1</sup>	
B6A	4.3	1.837	1.994	17.2	7.9	9.4	0.0867 <sup>1</sup>	
B7A	4.4	1.837	1.998	17.3	8.1	9.2	0.0872 <sup>1</sup>	
B8A	4.6	1.835	2.002	17.3	8.4	9.0	0.0872 <sup>1</sup>	
B9A	3.9	1.839	1.982	17.2	7.2	9.9	0.0848	
B9A	---	---	---	---	---	---	0.0870 <sup>1</sup>	
B10A	4.7	1.831	2.003	17.5	8.6	9.0	0.0873 <sup>1</sup>	
B11A	3.8	1.859	2.000	16.3	7.1	9.2	0.0877 <sup>1</sup>	
B12A	4.3	1.840	1.996	17.1	7.8	9.3	0.0871 <sup>1</sup>	
B13A	4.4	1.837	1.997	17.2	8.0	9.2	0.0870 <sup>1</sup>	
B14A	2.8	1.870	1.973	15.8	5.2	10.6	0.0869	Black Spot in Fracture Faces
B15A	4.4	1.836	1.996	17.3	8.0	9.3	0.0863 <sup>1</sup>	
B16A	4.4	1.837	1.999	17.3	8.1	9.2	0.0878 <sup>1</sup>	
B17A	4.7	1.830	2.003	17.6	8.7	8.9	0.0872 <sup>1</sup>	
B18A	4.6	1.832	1.999	17.5	8.3	9.1	0.0864 <sup>1</sup>	
B19A	4.5	1.833	1.998	17.4	8.3	9.2	0.0867 <sup>1</sup>	
B20A	3.0	1.872	1.982	15.7	5.6	10.1	0.0866 <sup>1</sup>	Long Half of Fractured Spec.
B20A	3.1	1.853	1.964	16.5	5.7	10.9	---	Short Half of Fractured Spec.
B22A	4.6	1.833	2.002	17.4	8.4	9.0	0.0871 <sup>1</sup>	
B23A	4.6	1.824	1.990	17.8	8.3	9.5	0.0870 <sup>1</sup>	
B24A	4.2	1.843	1.998	17.0	7.8	9.2	0.0870 <sup>1</sup>	
B25A	5.5	1.817	2.021	18.1	10.1	8.1	0.0857	
B25A	---	---	---	---	---	---	0.0874 <sup>1</sup>	
B26A	3.9	1.850	1.992	16.7	7.1	9.5	0.0867 <sup>1</sup>	
B27A	4.4	1.842	2.002	17.0	8.0	9.0	0.0878 <sup>1</sup>	
B28A	4.7	1.832	2.003	17.5	8.6	8.9	0.0870 <sup>1</sup>	
B29A	4.4	1.839	2.001	17.2	8.1	9.1	0.0872 <sup>1</sup>	
B30A	4.6	1.830	1.997	17.6	8.4	9.2	0.0876 <sup>1</sup>	
B31A	4.7	1.831	2.003	17.5	8.6	8.9	0.0864 <sup>1</sup>	
B32A	4.5	1.836	2.000	17.3	8.2	9.1	0.0871 <sup>1</sup>	
B33A	4.0	1.849	1.996	16.7	7.4	9.3	0.0861 <sup>1</sup>	
B34A	2.9	1.864	1.972	16.0	5.5	10.6	0.0866	
B34A	---	---	---	---	---	---	0.0874 <sup>1</sup>	
B35A	4.5	1.836	2.002	17.3	8.3	9.0	0.0870 <sup>1</sup>	
B36A	4.1	1.847	1.999	16.8	7.6	9.2	0.0863 <sup>1</sup>	
B37A <sup>3</sup>	---	---	---	---	---	---	0.0848	Flaw in Fracture Face. Premature Fracture.
Mean	4.2	1.840	1.995	17.1	7.8	9.3	0.0868	
Std Deviation	0.6	0.012	0.010	0.5	1.0	0.5	0.0007	

## Notes:

1. Noted velocity values were made on removed section after absorption measurements using mineral spirits. Specimens were vacuum dried before velocity measurements were made.
2. Assumed theoretical density of 2.22 gm/cm<sup>3</sup>.
3. Absorption data in error.

TABLE 11

RESULTS OF DENSITY, ABSORPTION, POROSITY, AND SECTION ULTRASONIC  
VELOCITY MEASUREMENTS FOR SPECIMENS FROM ATJ-S BILLET L-1-8

Specimen Number	Percent Absorption	Bulk Density gm/cm <sup>3</sup>	Apparent Density gm/cm <sup>3</sup>	Percent Total Porosity	Percent Open Porosity	Percent Closed Porosity	Section Ultrasonic Velocity in. /μ sec	Remarks
With Grain								
A5W	4.8	1.826	2.000	17.8	8.7	9.0	0.1028	No Velocity Data
A6W	4.8	1.826	2.000	17.8	8.7	9.0	0.1045	
A7W	4.3	1.840	2.000	17.1	8.0	9.1	0.1044	
A8W	5.1	1.818	2.004	18.1	9.3	8.8	0.1027	
A9W	4.9	1.822	2.001	17.9	8.9	9.0	0.1048	
A10W	4.8	1.825	1.999	17.8	8.7	9.1	-----	
A11W	5.2	1.816	2.003	18.2	9.4	8.8	0.1037	
A12W	5.1	1.816	2.002	18.2	9.3	8.9	0.1031	
A13W	5.2	1.815	2.004	18.2	9.4	8.8	0.1025	
A14W	5.0	1.818	2.002	18.1	9.2	8.9	0.1033	
A15W	4.9	1.822	2.002	17.9	9.0	9.0	0.1043	Short Half of Fractured Spec.
A16W	4.8	1.823	2.000	17.9	8.8	9.1	0.1039	
A17W	5.3	1.814	2.006	18.3	9.6	8.7	0.1034	
A18W	5.2	1.813	2.002	18.3	9.4	8.9	0.1023	
A18W	5.4	1.804	1.999	18.7	9.7	9.0	----	
A19W	5.3	1.813	2.004	18.3	9.5	8.8	0.1023	
A20W	5.1	1.816	2.003	18.2	9.3	8.9	0.1029	
A21W	5.1	1.817	2.001	18.2	9.2	8.9	0.1034	
A22W	5.4	1.802	1.996	18.8	9.7	9.1	----	
A23W	5.3	1.809	2.003	18.5	9.7	8.8	0.1037	
A24W	5.5	1.800	1.997	18.9	9.9	9.1	----	No Velocity Data
A25W	5.2	1.812	2.001	18.4	9.5	8.9	0.1030	Short End of Fractured Spec.
A26W	5.2	1.814	2.003	18.3	9.5	8.9	0.1025	
A27W	5.5	1.805	2.003	18.7	9.9	8.8	0.1023	
A28W	5.4	1.807	2.004	18.6	9.8	8.8	0.1027	
A29W	5.3	1.807	2.001	18.6	9.7	8.9	0.1027	
A30W	5.5	1.807	2.005	18.6	9.9	8.7	0.1022	
A30W	5.7	1.793	1.997	19.2	10.2	9.0	----	
A31W	5.4	1.808	2.004	18.5	9.8	8.8	0.1014	
A32W	5.7	1.800	2.004	18.9	10.2	8.7	0.1012	
A32W	5.6	1.794	1.996	19.2	10.1	9.1	----	
A32W	5.5	1.798	1.996	19.0	9.9	9.1	----	Short End of Fractured Spec.
A33W	5.4	1.805	2.001	18.7	9.8	8.9	0.1025	No Absorption Data
B26W	5.2	1.812	2.001	18.4	9.4	8.9	0.1003	
B27W	5.5	1.806	2.003	18.6	9.8	8.8	0.1009	
B28W	5.3	1.808	2.001	18.6	9.6	8.9	0.1014	
B29W	5.3	1.800	1.990	18.9	9.6	9.4	0.1014	
B30W	5.5	1.804	2.001	18.7	9.9	8.9	0.1012	
B31W	5.4	1.807	2.001	18.6	9.7	8.9	0.1017	
B32W	5.0	1.816	1.998	18.2	9.1	9.1	0.1014	
B33W	5.2	1.814	2.003	18.3	9.5	8.9	0.1027	
B34W	Specimen number skipped							
B35W	5.4	1.808	2.003	18.5	9.7	8.8	0.1021	Short Half of Fractured Spec.
B36W	5.1	1.816	2.000	18.2	9.2	9.0	0.1016	
B37W	5.4	1.806	2.002	18.6	9.8	8.9	0.1004	
B38W	---	---	---	---	---	---	0.1005	
B39W	5.0	1.818	2.000	18.1	9.1	9.0	0.1007	
B40W	5.4	1.808	2.003	18.6	9.7	8.8	0.1006	
B41W	5.4	1.810	2.006	18.5	9.8	8.7	0.0991	
B42W	4.9	1.822	1.999	17.9	8.9	9.1	0.1006	
B42W	4.9	1.813	1.991	18.3	8.9	9.4	----	
B43W	5.1	1.814	1.999	18.3	9.2	9.0	0.1004	
Mean	5.2	1.812	2.001	18.4	9.5	8.9	0.1022	
Std Deviation	0.3	0.009	0.005	0.4	0.4	0.2	0.0013	

TABLE 11 - CONTINUED

Specimen Number	Percent Absorption	Bulk Density gm/cm <sup>3</sup>	Apparent Density gm/cm <sup>3</sup>	Percent Total Porosity	Percent Open Porosity	Percent Closed Porosity	Section Ultrasonic Velocity in. / $\mu$ sec	Remarks
Across Grain								
A1A	4.5	1.834	1.998	17.4	8.2	9.2	0.0872	
A2A	5.2	1.811	2.001	18.4	9.5	8.9	0.0852	
A3A	5.1	1.816	2.001	18.2	9.2	9.0	0.0852	
A4A	4.8	1.823	1.996	17.9	8.7	9.2	0.0854	
B1A	4.4	1.837	1.996	17.3	8.0	9.3	0.0860	No Absorption Data
B2A	---	---	---	---	---	---	0.0872	
B3A	5.1	1.811	1.997	18.4	9.3	9.1	0.0856	
B4A	5.6	1.802	2.004	18.8	10.1	8.8	0.0862	
B4A	5.7	1.789	1.991	19.4	10.2	9.3	---	Short Half of Fractured Spec.
B5A	5.5	1.799	1.995	19.0	9.8	9.2	0.0869	
B6A	5.3	1.810	2.002	18.5	9.6	8.9	0.0861	
B7A	5.0	1.820	2.002	18.0	9.1	8.9	0.0858	
B8A	5.2	1.812	2.000	18.4	9.4	9.0	0.0850	
B9A	5.2	1.807	1.995	18.6	9.4	9.2	0.0840	
B10A	5.7	1.798	2.003	19.0	10.3	8.8	0.0853	
B11A	5.5	1.804	2.002	18.7	9.9	8.9	0.0858	
B11A	5.5	1.794	1.990	19.2	9.8	9.3	---	Short Half of Fractured Spec.
B12A	5.4	1.806	2.000	18.7	9.7	9.0	0.0847	
B13A	5.6	1.801	2.002	18.9	10.0	8.8	0.0849	
B14A	5.3	1.810	2.003	18.5	9.6	8.8	0.0842	
B15A	5.4	1.806	2.002	18.6	9.8	8.8	0.0862	
B16A	5.5	1.803	2.003	18.8	10.0	8.8	0.0857	
B17A	5.5	1.804	2.003	18.8	10.0	8.8	0.0850	
B18A	5.6	1.801	2.001	18.9	10.0	8.9	0.0849	
B19A	5.3	1.809	2.001	18.5	9.6	8.9	0.0854	
B20A	5.5	1.801	2.001	18.9	10.0	8.9	0.0854	
B21A	5.4	1.806	2.000	18.6	9.7	9.0	0.0851	
B22A	5.6	1.800	2.001	18.9	10.1	8.9	0.0845	
B22A	5.7	1.781	1.982	19.8	10.2	9.6	---	Short Half of Fractured Spec.
B23A	5.1	1.811	1.997	18.4	9.3	9.1	0.0851	
B24A	5.4	1.803	1.999	18.8	9.8	9.0	0.0842	
B25A	5.6	1.799	2.002	18.9	10.1	8.8	0.0847	
Mean	5.3	1.807	1.999	18.6	9.6	9.0	0.0854	
Std Deviation	0.3	0.012	0.005	0.5	0.5	0.2	0.0008	

Note:

1. Assumed theoretical density of 2.22 gm/cm<sup>3</sup>.

TABLE 12

RESULTS OF DENSITY, ABSORPTION, POROSITY, AND SECTION ULTRASONIC  
VELOCITY MEASUREMENTS FOR SLABS 2, 4, 6, AND 8 OF ATJ-S BILLET L-4-6

Specimen Number	Percent Absorption	Bulk Density gm/cm <sup>3</sup>	Apparent Density gm/cm <sup>3</sup>	Percent Total Porosity	Percent Open Porosity	Percent Closed Porosity	Section <sup>1</sup> Ultrasonic Velocity in. / $\mu$ sec	
							First Run	Second Run
Slab 2, Long End $\frac{1}{4}$ " Fracture Section - First Run								
T18W	6.7	1.78	2.02	19.9	12.0	7.9	0.1197	-
T19W	5.6	1.81	2.01	18.7	10.1	8.6	0.1229	-
T20W	6.2	1.79	2.01	19.5	11.0	8.4	0.1138	-
T21W	6.5	1.77	2.00	20.2	11.6	8.6	0.1165	-
T22W	7.0	1.77	2.03	20.1	12.4	7.7	0.1139	-
T23W	6.4	1.78	2.01	19.9	11.4	8.5	0.1111	-
T24W	5.9	1.74	1.94	21.5	10.3	11.3	0.1183	-
Mean	6.3	1.78	2.00	20.0	11.3	8.7	0.1166	
Std Deviation	0.5	0.02	0.03	0.8	0.8	1.2	0.0040	
Slab 2, Long End $\frac{1}{4}$ " Removed Section - First Run								
T18W	6.6	1.78	2.02	19.9	11.8	8.1		
T19W	5.6	1.80	2.01	18.8	10.1	8.6		
T20W	6.2	1.79	2.02	19.2	11.0	8.2		
T21W	6.5	1.77	2.01	20.1	11.6	8.6		
T22W	6.7	1.77	2.01	20.1	11.8	8.2		
T23W	6.9	1.77	2.02	20.2	12.2	8.0		
T24W	6.0	1.83	2.06	17.4	11.1	6.4		
Mean	6.4	1.79	2.02	19.4	11.4	8.0		
Std Deviation	0.5	0.02	0.02	1.0	0.7	0.7		
Slab 4, Long End $\frac{1}{4}$ " Fracture Section - First Run								
T42W	5.8	1.79	2.00	19.3	10.4	8.8	0.1060	0.1224
T43W	6.1	1.78	2.00	19.8	10.8	8.9	0.1115	0.1171
T44W	5.6	1.80	2.00	19.0	10.0	9.0	0.1154	0.1214
T45W	5.4	1.80	2.00	19.4	9.7	9.7	0.1173	0.1214
T46W	6.0	1.78	2.00	19.7	10.6	9.1	0.1190	0.1208
T47W	6.1	1.78	2.00	19.8	10.8	8.9	0.1133	0.1204
T48W	5.6	1.79	1.99	19.4	10.0	9.4	0.1167	0.1248
Mean	5.8	1.79	2.00	19.5	10.3	9.1	0.1142	0.1212
Std Deviation	0.3	0.01	0.00	0.3	0.4	0.3	0.0044	0.0023
Slab 4, Long End $\frac{1}{4}$ " Removed Section - First Run								
T42W	6.1	1.79	2.01	19.5	11.0	8.6		
T43W	5.8	1.79	2.00	19.3	10.4	9.0		
T44W	6.0	1.79	2.00	19.6	10.8	8.9		
T45W	5.7	1.79	2.00	19.4	10.2	9.2		
T46W	6.1	1.79	2.00	19.5	10.8	8.7		
T47W	5.9	1.78	2.00	20.0	10.5	9.5		
T48W	5.2	1.80	1.99	18.8	9.3	9.4		
Mean	5.8	1.79	2.00	19.4	10.4	9.0		
Std Deviation	0.3	0.01	0.01	0.4	0.6	0.3		

TABLE 12 - CONTINUED

Specimen Number	Percent Absorption	Bulk Density gm/cm <sup>3</sup>	Apparent Density gm/cm <sup>3</sup>	Percent Total Porosity	Percent Open Porosity	Percent Closed Porosity	Section <sup>1</sup> Ultrasonic Velocity in. / $\mu$ sec	
Slab 6, Long End $\frac{1}{4}$ " Fracture Section - First Run							First Run	Second Run
T59W	5.4	1.81	2.01	18.4	9.7	8.7	0.1126	-
T60W	5.5	1.80	2.00	18.8	10.0	8.8	0.1111	-
T61W	9.0	1.75	2.07	21.4	15.8	5.6	0.1065	-
T62W	5.3	1.80	2.00	18.7	9.6	9.1	0.1135	-
T63W	5.8	1.80	2.01	18.9	10.5	8.4	0.1072	-
T64W	5.6	1.80	2.01	18.8	10.1	8.6	0.1082	-
T65W	5.1	1.82	2.00	18.2	9.2	9.0	0.1130	-
Mean	6.0	1.80	2.01	19.0	10.7	8.3	0.1103	-
Std Deviation	1.4	0.02	0.03	1.1	2.3	1.2	0.0029	-
Slab 6 Long End $\frac{1}{4}$ " Removed Section - First Run								
T59W	5.4	1.81	2.01	18.4	9.7	8.7		
T60W	5.7	1.80	2.00	19.1	10.2	8.9		
T61W	6.7	1.78	2.02	19.9	11.9	8.0		
T62W	5.4	1.80	2.00	18.7	9.8	8.9		
T63W	5.8	1.80	2.00	19.1	10.3	8.7		
T64W	5.6	1.80	2.01	18.7	10.1	8.6		
T65W	5.4	1.81	2.00	18.5	9.8	8.8		
Mean	5.7	1.80	2.01	18.9	10.3	8.7		
Std Deviation	0.5	0.01	0.01	0.5	0.8	0.3		
Slab 8, Long End $\frac{1}{4}$ " Fracture Section - First Run								
T91W	8.8	1.70	1.99	23.6	15.0	8.7	0.1080	0.1238
T92W	5.1	1.81	2.00	18.3	9.2	9.1	0.1105	0.1235
T93W	5.1	1.81	2.05	18.4	9.2	9.2	0.1109	0.1193
T94W	5.1	1.82	2.00	18.2	9.2	9.0	0.1131	0.1229
T95W	5.0	1.82	2.00	18.0	9.1	9.0	0.1092	0.1224
T96W	4.9	1.82	2.00	18.1	8.9	9.1	0.1148	0.1188
T97W	5.0	1.81	1.99	18.4	9.0	9.4	0.1170	0.1214
Mean	5.6	1.80	2.00	19.0	9.9	9.1	0.1119	0.1217
Std Deviation	1.4	0.04	0.02	2.0	2.2	0.2	0.0032	0.0020
Slab 8, Long End $\frac{1}{4}$ " Removed Section - First Run								
T91W	5.1	1.81	2.00	18.4	9.3	9.0		
T92W	4.9	1.82	2.00	18.0	8.9	9.1		
T93W	5.1	1.82	2.00	18.2	9.2	9.0		
T94W	5.2	1.80	1.99	18.9	9.4	9.5		
T95W	5.1	1.82	2.00	18.0	9.4	8.6		
T96W	4.9	1.82	2.00	17.9	8.9	9.0		
T97W	4.9	1.81	2.00	18.8	9.0	9.3		
Mean	5.0	1.81	2.00	18.3	9.2	9.1		
Std Deviation	0.1	0.01	0.00	0.4	0.2	0.3		

TABLE 14

RESULTS OF DENSITY, ABSORPTION, POROSITY, AND SECTION ULTRASONIC  
VELOCITY MEASUREMENTS FOR ATJ-S BILLET L-9-10

Specimen Number	Percent Absorption	Bulk Density gm/cm <sup>3</sup>	Apparent Density gm/cm <sup>3</sup>	Percent Total Porosity	Percent Open Porosity	Percent Closed Porosity	Section Ultrasonic Velocity in./μ sec
<u>Long End</u>							
With Grain							
T1W	5.3	1.812	2.002	18.4	9.5	8.9	0.0986
T2W	5.8	1.797	2.006	19.1	10.5	8.6	0.0994
T3W	5.4	1.812	2.008	18.4	9.8	8.6	0.0992
T4W	5.2	1.812	2.002	18.4	9.5	8.9	0.0989
T5W	5.4	1.811	2.006	18.4	9.7	8.7	0.0977
T6W	8.4	1.743	2.040	21.5	14.6	6.9	0.0976
T7W	7.7	1.756	2.030	20.9	13.5	7.4	0.0948
T8W	6.7	1.774	2.013	20.1	11.9	8.2	0.0956
T9W	6.5	1.778	2.011	19.9	11.6	8.3	0.0951
T10W	5.1	1.817	2.004	18.2	9.3	8.8	0.0980
Mean	6.2	1.791	2.012	19.3	11.0	8.3	0.0975
Std Deviation	1.1	0.027	0.013	1.2	1.9	0.7	0.0017
Across Grain							
T1A	4.8	1.829	2.003	17.6	8.7	8.9	0.0853
T2A	5.1	1.816	2.001	18.2	9.3	8.9	0.0843
T3A	5.2	1.815	2.004	18.3	9.4	8.8	0.0845
T4A	4.9	1.816	1.993	18.2	8.9	9.3	0.0868
T5A	4.8	1.825	2.000	17.8	8.7	9.1	0.0846
T6A	5.3	1.738	1.913	21.7	9.2	12.6	0.0844
T7A	4.7	1.814	1.984	18.3	8.6	9.7	0.0844
T8A	5.2	1.814	2.003	18.3	9.4	8.9	0.0842
T9A	5.1	1.815	2.000	18.2	9.3	9.0	0.0838
T10W	5.3	1.811	2.003	18.4	9.5	8.9	0.0833
Mean	5.0	1.809	1.990	18.5	9.1	9.4	0.0846
Std Deviation	0.2	0.026	0.028	1.2	0.3	1.2	0.0009
<u>Short End</u>							
With Grain							
T1W	5.7	1.794	1.997	19.2	10.1	9.0	-----
T3W	5.8	1.793	2.001	19.2	10.4	8.8	-----
T7W	7.9	1.741	2.019	21.6	13.8	7.8	-----
T9W	6.0	1.786	2.000	19.5	10.7	8.9	-----

- Notes: 1. Runs on long end are data from second run after vacuum drying  
2. Assumed theoretical density of 2.22 gm/cm<sup>3</sup>

TABLE 15

RESULTS OF DENSITY, ABSORPTION, POROSITY, AND SECTION ULTRASONIC  
VELOCITY MEASUREMENTS FOR ATJ-S BILLET L-10-6

Specimen Number	Percent Absorption	Bulk Density gm/cm <sup>3</sup>	Apparent Density gm/cm <sup>3</sup>	Percent Total Porosity	Percent Open Porosity	Percent Closed Porosity	Section Ultrasonic Velocity in./μ sec
With Grain							
T1W	4.7	1.824	1.996	17.8	8.6	9.3	0.1006
T2W	5.4	1.806	2.001	18.7	9.7	8.9	0.1003
T3W	5.2	1.813	2.001	18.4	9.4	8.9	0.1011
T4W	5.0	1.803	1.980	18.8	9.0	9.8	0.1001
T5W	5.1	1.813	1.999	18.3	9.3	9.0	0.1004
T6W	4.7	1.819	1.991	18.1	8.6	9.4	0.1015
T7W	5.3	1.807	1.998	18.6	9.6	9.0	0.0996
T8W	5.1	1.811	1.997	18.4	9.3	9.1	0.1003
T9W	5.0	1.819	2.003	18.0	9.2	8.9	0.1016
T10W	4.7	1.824	1.996	17.8	8.6	9.2	0.1001
Mean	5.0	1.814	1.996	18.3	9.1	9.2	0.1006
Std Deviation	0.3	0.007	0.007	0.4	0.4	0.3	0.0006
Across Grain							
T1A	4.6	1.823	1.989	17.9	8.4	9.5	0.0849
T2A	4.9	1.816	1.993	18.2	8.9	9.3	0.0830
T3A	4.8	1.821	1.994	18.0	8.7	9.3	0.0829
T4A	5.0	1.810	1.992	18.5	9.1	9.3	0.0833
T5A	4.8	1.820	1.995	18.0	8.8	9.2	0.0843
T6A	5.1	1.811	1.996	18.4	9.3	9.1	0.0838
T7A	5.2	1.809	1.999	18.5	9.5	9.0	0.0827
T8A	4.8	1.811	1.985	18.4	8.8	9.7	0.0829
T9A	5.1	1.813	1.999	18.3	9.3	9.0	0.0829
T10A	4.7	1.819	1.991	18.0	8.6	9.4	0.0834
Mean	4.9	1.815	1.993	18.2	8.9	9.3	0.0834
Std Deviation	0.2	0.005	0.004	0.2	0.4	0.2	0.0007

Notes: 1. Assumed theoretical density of 2.22 gm/cm<sup>3</sup>

TABLE 16

RESULTS OF DENSITY, ABSORPTION, POROSITY, AND SECTION ULTRASONIC  
VELOCITY MEASUREMENTS FOR ATJ-S BILLET L-11-4

Specimen Number	Percent Absorption	Bulk Density gm/cm <sup>3</sup>	Apparent Density gm/cm <sup>3</sup>	Percent Total Porosity	Percent Open Porosity	Percent Closed Porosity	Section Ultrasonic Velocity in. / $\mu$ .sec
With Grain							
T1W	5.5	1.790	1.987	19.4	9.9	9.5	0.1007
T2W	5.3	1.797	1.984	19.1	9.5	9.6	0.1000
T3W	5.3	1.795	1.985	19.1	9.6	9.6	0.1003
T4W	5.0	1.802	1.982	18.8	9.1	9.8	0.1001
T5W	4.8	1.811	1.982	18.4	8.7	9.8	0.1032
T6W	6.1	1.777	1.993	20.0	10.9	9.1	0.1020
T7W	5.8	1.786	1.991	19.6	10.3	9.3	0.1019
T8W	5.2	1.796	1.980	19.1	9.3	9.8	0.1010
T9W	5.3	1.799	1.987	19.0	9.5	9.5	0.1012
T10W	5.5	1.785	1.978	19.6	9.8	9.8	0.0994
Mean	5.4	1.794	1.985	19.2	9.7	9.6	0.1010
Std Deviation	0.4	0.010	0.005	0.5	0.6	0.2	0.0011
Across Grain							
T1A	4.6	1.815	1.979	18.2	8.3	10.0	0.0828
T3A	4.8	1.810	1.982	18.5	8.7	9.8	0.0842
T4A	4.1	1.822	1.969	17.9	7.5	10.4	0.0849
T5A	4.2	1.828	1.979	17.7	7.7	10.0	0.0853
T6A	5.3	1.795	1.985	19.1	9.5	9.6	0.0843
T7A	5.5	1.807	2.005	18.6	9.9	8.7	0.0851
T8A	5.2	1.800	1.985	18.9	9.3	9.6	0.0852
T9A	5.2	1.800	1.986	18.9	9.3	9.6	0.0854
T10A	5.2	1.799	1.984	19.0	9.3	9.7	0.0850
Mean	4.9	1.808	1.984	18.5	8.8	9.7	0.0847
Std Deviation	0.5	0.011	0.010	0.5	0.8	0.5	0.0008

Notes: 1. Assumed theoretical density of 2.22 gm/cm<sup>3</sup>.



TABLE 17  
AVERAGE VALUES FOR TENSILE PROPERTIES AND SECTION MONITORS FOR MATERIAL FROM VARIOUS ATJ-S BILLETS

ATJ-S Billet	Grain Orientation	Number <sup>a</sup> Specimens	Blank		Tensile Properties												Total Strain to Failure in 10 <sup>-3</sup> in./in.																	
			Bulk Density g/cm <sup>3</sup>		Ultimate Strength in psi						Initial Elastic Modulus in 10 <sup>6</sup> psi						3000° F						4500° F						5500° F					
			Avg.	S.D.	70° F		3000° F		4500° F		5500° F		70° F		3000° F		4500° F		5500° F		70° F		3000° F		4500° F		5500° F							
					Avg.	S.D.	Avg.	S.D.	Avg.	S.D.	Avg.	S.D.	Avg.	S.D.	Avg.	S.D.	Avg.	S.D.	Avg.	S.D.	Avg.	S.D.	Avg.	S.D.	Avg.	S.D.	Avg.	S.D.						
L-16-7	WG	29	1.827	0.018	4763	499	-	-	-	-	1.43	0.16	-	-	-	-	-	-	4.7	0.6	-	-	-	-	-	-								
	AG	-	-	-	-	-	-	-	-	-	-	-	-	-	-	-	-	-	-	-	-	-	-	-	-									
L-1-4	WG	30	1.824	0.004	4909	338	-	-	-	-	1.48	0.13	-	-	-	-	-	-	4.9	0.6	-	-	-	-	-	-								
	AG	36	1.837	0.010	4026	397	-	-	-	-	1.00	0.06	-	-	-	-	-	-	6.1	0.8	-	-	-	-	-	-								
L-1-8	WG	48	1.815	0.008	5007	283	-	-	-	-	1.47	0.13	-	-	-	-	-	-	5.0	0.5	-	-	-	-	-	-								
	AG	29	1.808	0.011	4087	114	-	-	-	-	0.99	0.09	-	-	-	-	-	-	6.4	0.3	-	-	-	-	-	-								
L-4-6	WG	28	1.811	0.014	4910	380	8085	345	-	-	1.37	0.21	1.62	0.18	-	-	-	-	4.9	0.8	4.7	0.8	-	-	-	-								
	AG	-	-	-	-	-	-	-	-	-	-	-	-	-	-	-	-	-	-	-	-	-	-	-	-									
L-6-3	WG	13	1.827	0.008	5010	-	6770	-	7550	-	1.47	-	1.35	-	1.43	-	0.42	-	4.8	-	5.8	-	9.7	-	25 <sup>b</sup>	-								
	AG	13	1.828	0.002	4200	-	5320	-	6820	-	1.10	-	1.21	-	1.02	-	0.43	-	6.0	-	5.3	-	14.3	-	25 <sup>b</sup>	-								
L-9-10	WG	10	1.810	0.015	3730	294	-	-	6500	550	1.47	0.18	-	-	1.43	0.32	-	-	3.8	0.4	-	-	9.2	1.6	-	-								
	AG	10	1.821	0.011	3670	136	-	-	5540	258	1.13	0.14	-	-	1.13	0.12	-	-	5.3	0.8	-	-	9.1	2.1	-	-								
L-10-6	WG	10	1.828	0.008	4690	527	-	-	7150	605	1.81	0.06	-	-	1.35	0.17	-	-	4.3	0.8	-	-	9.1	2.0	-	-								
	AG	9	1.830	0.005	3570	282	-	-	5720	161	1.00	0.16	-	-	1.00	0.06	-	-	5.4	0.7	-	-	9.7	0.9	-	-								
L-11-4	WG	10	1.813	0.009	4830	260	-	-	7760	532	1.71	0.17	-	-	1.67	0.32	-	-	4.2	0.5	-	-	10.0	2.0	-	-								
	AG	10	1.821	0.008	3950	198	-	-	6300	230	1.27	0.04	-	-	1.18	0.08	-	-	5.4	0.6	-	-	10.8	2.4	-	-								

TABLE 17 - CONTINUED

	Grain Orientation	Section Monitor Evaluations														Gage	
		Percent Absorption		Section Bulk Density gm/cm <sup>3</sup>		Apparent Density gm/cm <sup>3</sup>		Percent Total Porosity		Percent Open Porosity		Percent Closed Porosity		Section Ultrasonic Velocity-in./μ sec		Electrical Resistivity μ ohm-cm	
		Avg	S.D.	Avg	S.D.	Avg	S.D.	Avg	S.D.	Avg	S.D.	Avg	S.D.	Avg	S.D.	Avg	S.D.
ATJ-S Billet																	
L-16-7	WG	5.0	1.0	1.825	0.031	2.006	0.007	17.8	1.4	9.0	1.7	8.8	0.4	0.1039	0.0020	865	45
	AG	-	-	-	-	-	-	-	-	-	-	-	-	-	-	-	-
L-1-4	WG	4.7	0.4	1.818	0.008	1.989	0.007	18.1	0.4	8.6	0.6	9.5	0.3	0.1033	0.0015	801	18
	AG	4.2	0.6	1.840	0.012	1.995	0.010	17.1	0.5	7.8	1.0	9.3	0.5	0.0868	0.0007	1039	17
L-1-8	WG	5.2	0.3	1.812	0.009	2.001	0.005	18.4	0.4	9.5	0.4	8.9	0.2	0.1022	0.0013	834	14
	AG	5.3	0.3	1.807	0.012	1.999	0.005	18.6	0.5	9.6	0.5	9.0	0.2	0.0854	0.0008	1099	25
L-4-6 <sup>3</sup>	WG	5.5	0.8	1.800	0.020	2.000	0.020	18.8	1.1	9.9	1.4	8.9	0.7	0.1160	0.0053	- <sup>4</sup>	- <sup>4</sup>
	AG	-	-	-	-	-	-	-	-	-	-	-	-	-	-	-	-
L-6-3	WG	4.5	0.4	1.817	0.012	1.975	0.003	18.2	0.5	8.1	0.7	10.1	0.2	0.1035	0.0018	- <sup>4</sup>	- <sup>4</sup>
	AG	4.2	0.2	1.821	0.006	1.970	0.005	18.0	0.3	7.6	0.3	10.4	0.2	0.0871	0.0013	- <sup>4</sup>	- <sup>4</sup>
L-9-10	WG	6.2	1.1	1.791	0.027	2.012	0.013	19.3	1.2	11.0	1.9	8.3	0.7	0.0975	0.0017	- <sup>4</sup>	- <sup>4</sup>
	AG	5.0	0.2	1.809	0.026	1.990	0.028	18.5	1.2	9.1	0.3	9.4	1.2	0.0846	0.0009	- <sup>4</sup>	- <sup>4</sup>
L-10-6	WG	5.0	0.3	1.814	0.007	1.996	0.007	18.3	0.4	9.1	0.4	9.2	0.3	0.1006	0.0006	- <sup>4</sup>	- <sup>4</sup>
	AG	4.9	0.2	1.815	0.005	1.993	0.004	18.2	0.2	8.9	0.4	9.3	0.2	0.0834	0.0007	- <sup>4</sup>	- <sup>4</sup>
L-11-4	WG	5.4	0.4	1.794	0.010	1.985	0.005	19.2	0.5	9.7	0.6	9.6	0.2	0.1010	0.0011	- <sup>4</sup>	- <sup>4</sup>
	AG	4.9	0.5	1.808	0.011	1.984	0.010	18.5	0.5	8.8	0.8	9.7	0.5	0.0847	0.0008	- <sup>4</sup>	- <sup>4</sup>

Notes: <sup>1</sup> Only 3 to 4 runs made for each evaluation.<sup>2</sup> Specimen did not fracture. Strength values are stress levels in specimen at 0.025 in. total strain.<sup>3</sup> First billet inspected at Southern by NDT and monitors—precision of measurement was lower than that later developed during course of program.<sup>4</sup> Not measured, material evaluated early in program.<sup>5</sup> ATJ-S Billet L-7-1 provided two tensile specimens not included in table.

TABLE 18

UM721 REFLECTOSCOPE SETTINGS  
USED ON ATJ-S BILLET L-16-7

Sweep Delay	- Minimum
Velocity	- 0.209 cm/ $\mu$ sec
Length	- 5 x 0.1 inches/division
Markers	- 1 cycle/inch
Pulse Length	- Minimum
Reject	- Off
Sensitivity	- 0.9 x 10
Frequency	- 1.0 Mhz
Search Unit	- 1.0/0.5 SFZ
DAC Unit	- On with curve set as shown in pictures

TABLE 19  
PROPERTY-MONITOR-NDT FACT SHEET FOR AT-5 BULLET L-16-7

Spec.	Tensile Strength -g		Core Specimen		Core Fracture		SRI PE Response				Fracture at High Tanf. $\pm \frac{1}{2}$		Core Fracture		Avco Dis- cuss Flaw by PE		Fracture Avco PE Indication		Detectable Flaw in Frac. Face		Open <sup>3</sup> Porosity		Section <sup>3</sup> Density		Section <sup>3</sup> Velocity		Case <sup>2</sup> Resistivity		Remarks			
							Fracture at High S/N Ratio		Noise Level																					Noise Level		
	Weak	Avg	Strong	Yes	No	Yes	No	Fracture in Black	Low Hash	High Hash	Yes	No	Yes	No	Yes	No	Yes	No	Yes	No	-g	Avg	-g	Avg	-g	Avg	-g	Avg		-g	Avg	-g
S2-1	X		X		X		-	X	X	-	X		X		X		X		X		X		X		X		X		X		Core in edge of blank. Avco flaw may have been machined out	
S2-2	X		X		X		-	X	X	-	X		X		X		X		X		X		X		X		X		X			
S2-3	X		X		X		-	X	X	-	X		X		X		X		X		X		X		X		X		X			
S2-4	X		X		X		-	X	X	-	X		X		X		X		X		X		X		X		X		X			
S2-5	X		X		X		-	X	X	-	X		X		X		X		X		X		X		X		X		X			
S2-6	X		This specimen not tested				-	-	-	-	-	X		X		X		X		X		X		X		X		X		X		Avco flaw may have been machined out of test block. Southern PE. Large S/N indication
S4-1	X		X		X		-	X	X	-	X		X		X		X		X		X		X		X		X		X			
S4-2	X		X		X		-	X	X	-	X		X		X		X		X		X		X		X		X		X			
S4-3	X		X		X		-	X	X	-	X		X		X		X		X		X		X		X		X		X			
S4-4	X		X		X		-	X	X	-	X		X		X		X		X		X		X		X		X		X			
S4-5	X		X		X		-	X	X	-	X		X		X		X		X		X		X		X		X		X			
S4-6	X		X		X		-	X	X	-	X		X		X		X		X		X		X		X		X		X			
S6-1	X		X		X		-	X	X	-	X		X		X		X		X		X		X		X		X		X		See S2-6 remark See S2-6 remark	
S6-2	X		X		X		-	X	X	-	X		X		X		X		X		X		X		X		X		X			
S6-3	X		X		X		-	X	X	-	X		X		X		X		X		X		X		X		X		X			
S6-4	X		X		X		-	X	X	-	X		X		X		X		X		X		X		X		X		X			
S6-5	X		X		X		-	X	X	-	X		X		X		X		X		X		X		X		X		X			
S6-6	X		X		X		-	X	X	-	X		X		X		X		X		X		X		X		X		X			
S8-1			X		X		-	-	-	-	-	X		X		X		X		X		X		X		X		X		X		Avco reported cluster (PE) Avco reported 40 - 70% CRT scale flaw (PE)
S8-2		X	X		X		-	-	-	-	-	X		X		X		X		X		X		X		X		X		X		
S8-3		X	X		X		-	-	-	-	-	X		X		X		X		X		X		X		X		X		X		
S8-4		X	X		X		-	-	-	-	-	X		X		X		X		X		X		X		X		X		X		
S8-5		X	X		X		-	-	-	-	-	X		X		X		X		X		X		X		X		X		X		
S8-6		X			X		-	-	-	-	-	X		X		X		X		X		X		X		X		X		X		
S10-1		X			X		-	-	-	-	-	X		X		X		X		X		X		X		X		X		X		Specimen had visible flaw
S10-2		X			X		-	-	-	-	-	X		X		X		X		X		X		X		X		X		X		
S10-3		X			X		-	-	-	-	-	X		X		X		X		X		X		X		X		X		X		
S10-4		X			X		-	-	-	-	-	X		X		X		X		X		X		X		X		X		X		
S10-5		X			X		-	-	-	-	-	X		X		X		X		X		X		X		X		X		X		
S10-6		X			X		-	-	-	-	-	X		X		X		X		X		X		X		X		X		X		

Legend: "o" Denotes one standard deviation  
"o" Denotes item not correlatable  
"X" Denotes correlation

Notes:  
1. Statistics based on all AT-5 tensile with grain strength data tested at Southern prior to 3/10/69.  
Mean = 4960 psi; standard deviation = 610 psi  
2. Statistics based on L-16-7 only

TABLE 20  
RESULTS OF PROPERTY-MONITOR-NDT CORRELATIONS FOR ATJ-S BILLET L-16-7

No.	Selector	Correlated											Remarks
		None	Average Strength <sup>2</sup>	High (+ S.D.) <sup>1</sup> Strength	Low (- S.D.) Strength <sup>2</sup>	Weak/Strong	Density	Core	Fracture at Flag	Fracture at Radius	Fracture at Flag-Tangent Zone ± 1/4 in.	Southern Pulse-Echo	
1	Low Hash-Southern P-E	-	-	-	4/9 No	Yes	Yes	6/10 Yes	-	-	7/16 No	-	
2	Avco Dry Core Detection	-	-	-	4/7 Yes	-	3/7 No	6/6 Yes	-	-	-	-	
3	Flag on Specimen	-	-	-	-	-	-	-	Yes for Core, No for Regular	-	-	-	
4	High Hash-Southern P-E	-	17/22 Yes	-	1/23 No	Yes	21/26 Yes for Avg and High	-	-	-	-	-	
5	Avco Discrete Flaw by P-E	None 1/7	-	-	-	-	-	-	-	-	-	4/7	Avco reported two strong ones (S6-1 and S6-2) as having cluster and 40-70% CRT scale flaw
6	Radius Break	None	-	-	-	-	-	-	-	-	-	-	
7	Fracture Insp - Visual	-	-	-	2 Yes	-	-	-	-	-	-	-	
8	Fracture Insp - Flick	-	-	-	Yes for Visual Disparates S6-5 and S6-6	-	-	-	-	-	-	-	
9	Southern PE	No on Black No on Spike	-	-	-	-	-	-	-	-	-	-	
10	Dry Core Specimen (6)	-	-	-	4/6 Yes	Yes	Blank No, Section Yes	-	3/6 Yes	-	6/6 Yes	6/6 Yes	6 Low hash indications 6 correlations
11	Weak Specimen (5)	-	-	-	-	-	-	Yes	Yes for Core, No for Regular	-	5/5 Yes	Yes for Regular	2 Weak with visual flaws (S6-5 and S6-6) dropped
12	Strong (+1 S.D.) <sup>3</sup> Specimen	-	-	-	-	-	-	-	No	-	1/2	No	
13	Velocity, Blank	-	-	No	3/6 No	-	-	3/6 No	-	-	-	-	
14	Density, Blank	-	-	No	2/7 No	-	-	3/6 No	-	-	-	-	
15	Regular Specimen	-	-	-	-	-	-	-	-	-	5/20 No	-	
16	Low (-1 S.D.) <sup>3</sup> Section Density	-	-	-	4/6 Yes	-	-	5/6 Yes	-	-	-	Low Hash 3/6 No	2 Noncorrelators with visible flaws (S6-5 and S6-6) were dropped
17	High (+1 S.D.) <sup>3</sup> and Average Section Density	-	21/23 Yes	-	-	-	-	-	-	-	-	-	2 Noncorrelators with visible flaws (S6-5 and S6-6) were dropped
18	Low (-1 S.D.) <sup>3</sup> Open Porosity	-	-	0/2 No	-	-	-	-	-	-	-	-	
19	High (+1 S.D.) <sup>3</sup> Open Porosity	-	-	-	3/6 No	-	-	4/6 Yes	-	-	-	-	2 Noncorrelators with visible flaws (S6-5 and S6-6) were dropped
20	Low (-1 S.D.) <sup>3</sup> and Average Open Porosity	-	22/25 Yes	-	-	-	-	-	-	-	-	-	2 Noncorrelators with visible flaws (S6-5 and S6-6) were dropped
21	Low (-1 S.D.) <sup>3</sup> Section Velocity	-	-	-	2/6 No	-	-	3/6 No	-	-	-	-	2 Noncorrelators with visible flaws (S6-5 and S6-6) were dropped
22	High (+1 S.D.) <sup>3</sup> Section Velocity	-	-	0/3 No	-	-	-	-	-	-	-	-	2 Noncorrelators with visible flaws (S6-5 and S6-6) were dropped
23	High (+1 S.D.) <sup>3</sup> and Average Section Velocity	-	19/26 Yes	-	-	-	-	-	-	-	-	-	2 Noncorrelators with visible flaws (S6-5 and S6-6) were dropped
24	Low (-1 S.D.) <sup>3</sup> Gage Electrical Resistivity	-	-	0/4 No	-	-	-	-	-	-	-	-	
25	High (+1 S.D.) <sup>3</sup> Gage Electrical Resistivity	-	-	-	3/6 No	-	-	4/6 Yes	-	-	-	-	2 Noncorrelators with visible flaws (S6-5 and S6-6) were dropped
26	Low (-1 S.D.) <sup>3</sup> and Average Gage Electrical Resistivity	-	20/24 Yes	-	-	-	-	-	-	-	-	-	2 Noncorrelators with visible flaws (S6-5 and S6-6) were dropped

Notes: 1. Two weak ones explained by visual disparate flaws, S6-5 and S6-6.  
2. Statistics based on all ATJ-S tensile with grain strength data measured at Southern prior 3/10/69: Mean = 4960 psi; Standard Deviation = 610 psi.  
3. Statistics based on L-16-7 only.

TABLE 21

DESIGN IMPACT FROM RESULTS OF EVALUATIONS ON ATJ-S BILLET L-16-7

	Regression Analysis						Lumped Values					
	With Disparates			Without Disparates			With Disparates			Without Disparates		
	Average $\sigma$ (psi)	Standard Deviation (psi)	COV	Average $\sigma$ (psi)	Standard Deviation (psi)	COV	Variance	Standard Deviation (psi)	COV	Variance	Standard Deviation (psi)	COV
ATJ-S Billet												
L-16-7	4766	369	7.65	4867	306	6.31	$0.275 \times 10^8$	525	11.00	$0.262 \times 10^8$	512	10.5
L-1-4	4909	260	5.20	4986	223	4.39	$0.134 \times 10^8$	338	6.88	$0.069 \times 10^8$	264	5.30
L-1-8	5007	234	4.74	5054	186	3.68	$0.080 \times 10^8$	283	5.65	$0.049 \times 10^8$	221	4.38
Compos.	4910	342	7.02	5007	251	5.02	$0.153 \times 10^8$	391	7.97	$0.068 \times 10^8$	260	5.19

TABLE 22

WEAK/STRONG SUMMARY OF MULTIPLE SPECIMENS FROM SAME TEST CONDITIONS FOR  
VARIOUS MONITORING PROPERTIES MATERIAL L-4-6, ATJ-S, SLABS 4 AND 8

	1/4" Fracture Section	Slab 4 Specimens							
		42	43	44	45	46	47	48	Average*
	Section % Absorption in Vacuum (Water); Mineral Spirits	5.81	6.08	5.60	5.45	5.97	6.08	5.58	5.83
	Section Bulk Density	1.79	1.78	1.80	1.80	1.78	1.78	1.79	1.79
	Section Velocity - in./μ Sec	0.1224 0.1060	0.1171 0.1115	0.1214 0.1154	0.1214 0.1173	0.1208 0.1190	0.1204 0.1130	0.1248 0.1167	0.1139
	Open Porosity **	10.42	10.84	10.00	9.73	10.65	10.84	10.00	10.41
Bulk and Blank Properties	Blank Bulk Density	1.809	1.801	1.800	1.797	1.797	1.795	1.810	1.802
	Blank Velocity	0.1077	0.1073	0.1072	0.1072	0.1070	0.1079	0.1075	0.1074
	Fracture Strength, (A)	5050	5000	4200	4600	4650	4750	4700	4792
	Strain and Modulus (B)	0.0056	0.0057	0.0040	0.0047	0.0054	0.0055	0.0034	0.0050
	(C)	1.16x10 <sup>6</sup>	1.12x10 <sup>6</sup>	1.47x10 <sup>6</sup>	1.34x10 <sup>6</sup>	1.19x10 <sup>6</sup>	1.10x10 <sup>6</sup>	1.59x10 <sup>6</sup>	1.25x10 <sup>6</sup>
	Blank Pulse-echo	P-E OK	P-E OK	P-E OK	P-E OK	P-E OK	P-E OK	P-E OK	
	Fracture Face Flaws	Xray Flaw		Flicks			Xray OK		
	1/4" Fracture Section	Slab 8 Specimens							
		92	93	91	94	95	96	97	
	Section % Absorption in Vacuum (Water); Mineral Spirits	5.06	5.08	8.80	5.06	4.98	4.91	4.99	5.01
	Section Bulk Density	1.81	1.81	1.70	1.82	1.82	1.82	1.81	1.82
	Section Velocity - in./μ Sec	0.1235 0.1105	0.1193 0.1109	0.1238 0.1080	0.1229 0.1131	0.1224 0.1092	0.1188 0.1148	0.1214 0.1170	0.1123
	Open Porosity **	9.18	9.21	15.00	9.21	9.07	8.93	9.03	9.10
Bulk and Blank Properties	Blank Bulk Density	1.827	1.827	1.824	1.831	1.826	1.829	1.823	1.827
	Blank Velocity	0.1095	0.1099	0.1091	0.1101	0.1101	0.1097	0.1101	0.1099
	Fracture Strength, (A)	5200	5400	4300	5100	5300	5350	5100	5242
	Strain and Modulus (B)	0.0051	0.0038	0.0041	0.0047	0.0054	0.0054	0.0052	0.0049
	(C)	1.30x10 <sup>6</sup>	1.73x10 <sup>6</sup>	1.33x10 <sup>6</sup>	1.78x10 <sup>6</sup>	1.39x10 <sup>6</sup>	1.25x10 <sup>6</sup>	1.47x10 <sup>6</sup>	1.49x10 <sup>6</sup>
	Blank Pulse-echo	P-E OK	P-E Sign	P-E OK	P-E Sign	P-E OK	P-E Sign	P-E Sign	
	Fracture Face Flaws	Xray OK	Xray OK	Flicks	Xray Sign	Xray OK	Xray OK No Flaws	Xray Sign	

Remarks: \* 44 and 91 not included in averages

\*\* Systematic error of about + 1/2% in these values developed for weak/strong analysis at time of actual testing.

- (1) Section velocities look bad - scattered.
- (2) Good comparison of slab strengths.
- (3) White specks show in fractures on 10X.

TABLE 23  
PROPERTIES AND MONITORS OF PRIMARY INTEREST FOR  
TENSILE SPECIMENS FROM ATJ-S BILLET L-9-10

Specimen	Tensile Strength <sup>3</sup> psi	Section Bulk Density <sup>1</sup> gm/cm <sup>3</sup>	Long End Open Porosity <sup>2</sup> 1st Run %	Long End Open Porosity <sup>2</sup> 2nd Run %	Short End Open Porosity <sup>2</sup> %	Closed Porosity 1st Run %	Closed Porosity 2nd Run %	Ultrasonic Velocity in./μ sec
T1W	3900	1.812	9.8	9.5	10.2	8.6	8.9	0.0986
T3W	4000	1.812	9.8	9.8	10.4	8.9	8.6	0.0992
T5W	3580	1.811	9.8	9.7	----	8.8	8.7	0.0977
T7W	3290	1.756	13.6	13.5	13.8	7.5	7.4	0.0948
T9W	<u>3900</u>	<u>1.778</u>	<u>11.7</u>	<u>11.6</u>	<u>10.7</u>	<u>8.3</u>	<u>8.3</u>	<u>0.0951</u>
Average	3730	1.794	10.9	10.8	11.3	8.4	8.4	0.0971

Notes: 1. Average blank bulk density = 1.813 gm/cm<sup>3</sup>.  
2. Other monitors shown elsewhere and obtained earlier in the program may have systematic errors.  
3. 70°F data.



TABLE 24

SUMMARY OF DISPARATE WITH GRAIN SPECIMENS SELECTED  
FROM OPEN POROSITY RELATION AT 95% PROBABILITY

ATJ-S Billet	Local Disparate	Obvious Visual Observation	Further Evidence	Comments
L-16-7	S2-3*	-	Flicks indicate 75 x 150 mil void cluster	Disparates not uniquely preselected by pulse-echo or radiography with the exception of A12W which Avco flagged as having uniquely large pulse-echo signals. Density, porosity, velocity, and electrical resistivity do not de- scribe with any statistical confidence.
	S6-5	-	1. Flicks showed 75 x 75 mil void cluster 2. Visual cavity below fracture after progressive polishing	
	S8-6	-	Flicks indicate 65 x 140 mil void cluster	
L-7-1	-	-	-	
L-1-4	A12W	27 mil hole in specimen, ob- vious before fracture	Flicks showed 35 mil hole in fracture face	
L-1-8	A30W	Squiggly in fracture visually	Flicks showed 95 x 150 mil void cluster	
L-6-3	-	-	-	
L-4-6	-	-	-	
L-9-10	T5W	Large discolored "grain" at edge of fracture visually	Flicks showed 15 x 20 mil "grain" at edge and 70 x 100 mil chevron	
L-10-6	-	-	-	
L-11-4	-	-	-	

\*Strength disparate to billet but not to the composite regression.

TABLE 25  
SUMMARY OF WEAK SPECIMENS SELECTED FROM COMPOSITE REGRESSIONS  
OF TENSILE STRENGTH VERSUS OPEN POROSITY AT 95% PROBABILITY

ATJ-S Billet	Weak Specimen	Section Open Porosity Over 11%	Specimen from Disparate Core	Evidence of Void Cluster from Flicks Plus Point Count	Evidence of Cluster from Flick Only	Other Unique Detectors					Electrical Resistivity	Section Velocity
						Pulse-Echo	Radiography	Penetrant	Radiometry	Density		
L-16-7	S2-2	Yes	Yes	-	-	(Hash Level) Yes	Yes	Yes	Yes	Yes	Yes	Yes
	S4-2	Yes	Yes	-	-	(Hash Level) Yes	Yes	Yes	Yes	Yes	Yes	Yes
	S6-1	Yes	Yes	-	-	(Hash Level) Yes	Yes	Yes	Yes	Yes	Yes	No
L-7-1	7-1-2	Yes	No	Not Inspected	Yes	-	-	-	-	Yes	Yes	Yes?
L-1-4	None	-	-	-	-	-	-	-	-	-	-	-
L-1-8	A18W	No	No	Yes - 60 mil	-	No	No	-	-	No	No	No
L-6-3	None	-	-	-	-	-	-	-	-	-	-	-
L-4-6	44	No	No	Yes - 65 x 100 mil	-	No	No	-	-	No	-	(By Blank) No
	91	No	No	Yes - 30 x 90 mil	-	No	No	-	-	Yes	-	(By Blank) No
L-9-10	T7W	Yes	No	Yes	-	Yes	-	-	-	Yes	-	Yes
	T1W	No	No	Yes	Yes	No	No	-	-	Maybe	-	Maybe
L-10-6	T9W	Yes	No	-	Yes	Yes	No	-	-	No	-	No
L-11-4	None	-	-	-	-	-	-	-	-	-	-	-

TABLE 26  
INSPECTION BY POINT-COUNT POROSITY

ATJ-S Billet	Specimen	General Strength Level of Specimen	Open Porosity by Absorption %	Closed Porosity by Absorption %	Porosity by Point Count Nonimpregnated	Porosity by Point Count Impregnated
L-16-7	S2-2	(Dry Core, High Open Porosity) Weak	14.7	~9.0	29.0	16.5
	S6-5	Disparate	8.2	~9.0	14.6	8.2
	S8-4	Average	8.3	8.6	13.1	-
	A18W	Weak	9.7	9.0	{ 19.5 at Edge 13.0 at Center 12.7 at Edge	-
L-4-6	44	Weak	10.34	8.55	20.4	-
	91	Weak	9.1	9.04	20.8	-
L-9-10	T7W	Weak	13.8	-	23.4	-



## APPENDICES

- A Southern's Multiple Traces (Smears) of Pulse-Echo Signals from Referenced End of Tensile Specimen Blanks from ATJ-S Billet L-16-7
- B Original Tensile Stress-Strain Curves for ATJ-S Billet L-16-7 and Specimens L-7-1-1 and L-7-1-2 of ATJ-S Billet L-7-1 With Grain at 70°F
- C Results of Microprobe and Electron Microscopy on Disparate S6-5 of ATJ-S Billet L-16-7
- D Results of Avco Ultrasonic Inspection of ATJ-S Billet L-1-4
- E Southern's Multiple Traces (Smears) of Pulse-Echo Signals from Referenced End of Tensile Specimen Blanks from ATJ-S Billet L-1-4 With Grain only
- F Original Stress-Strain Curves for ATJ-S Billet L-1-4 With Grain and Across Grain at 70°F
- G Results of Avco Ultrasonic Inspection of ATJ-S Billet L-1-8
- H Southern's Multiple Traces (Smears) of Pulse-Echo Signals from Referenced End of Tensile Specimen Blanks from ATJ-S Billet L-1-8 With Grain only
- I Original Stress-Strain Curves for ATJ-S Billet L-1-8 With Grain and Across Grain at 70°F
- J Results of Avco Ultrasonic Inspection and Alcohol Penetrant Test of Specimens from ATJ-S Billet L-6-3

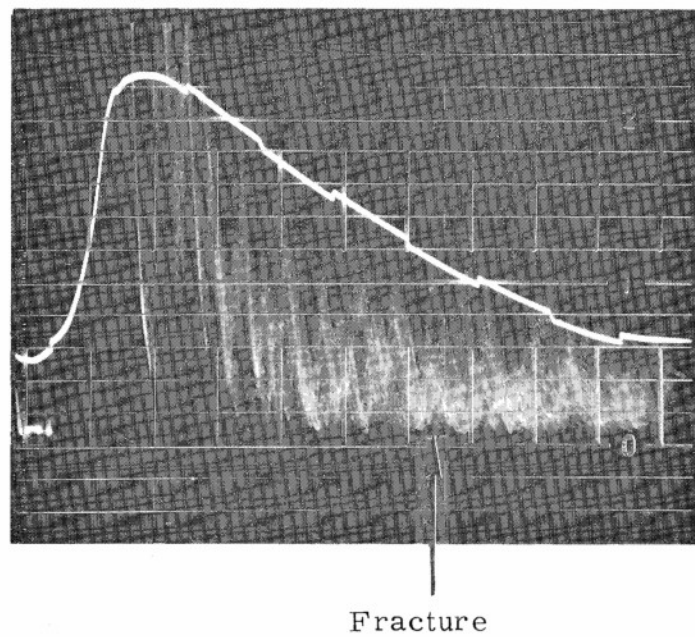
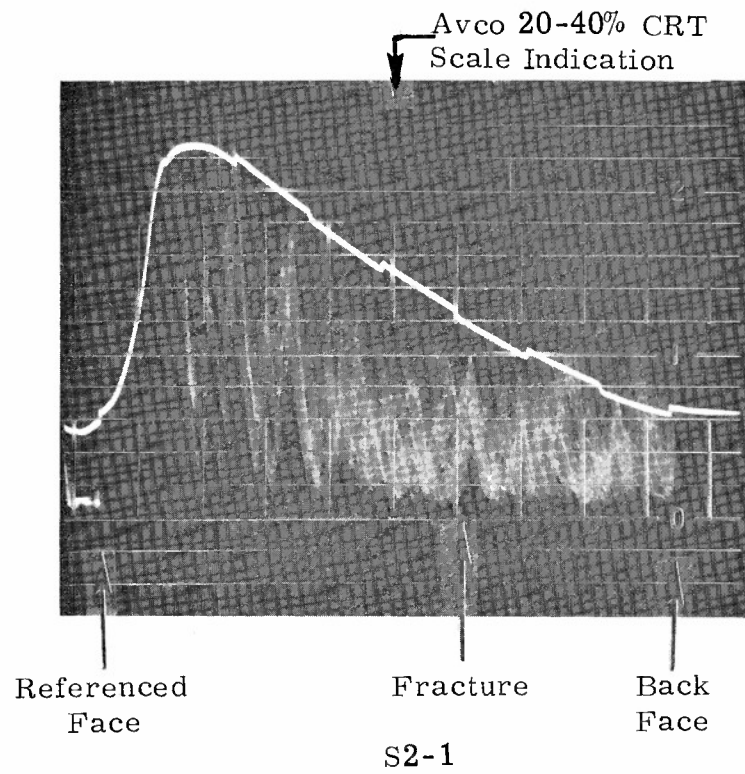


## APPENDIX A

Southern's Multiple Traces (Smears) of Pulse-Echo Signals from  
Referenced End of Tensile Specimen Blanks from ATJ-S Billet  
L-16-7



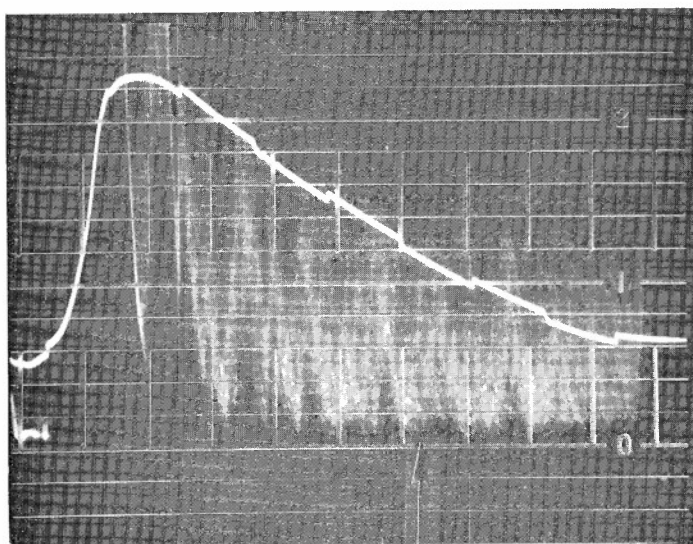




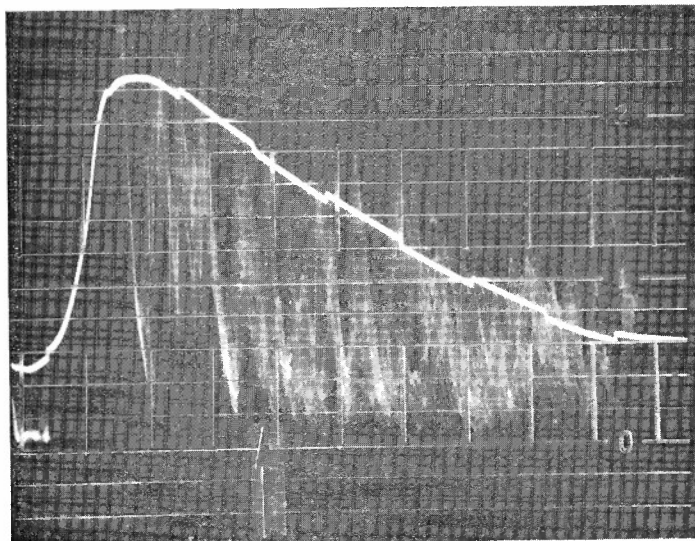
S2-2

Figure A1  
418





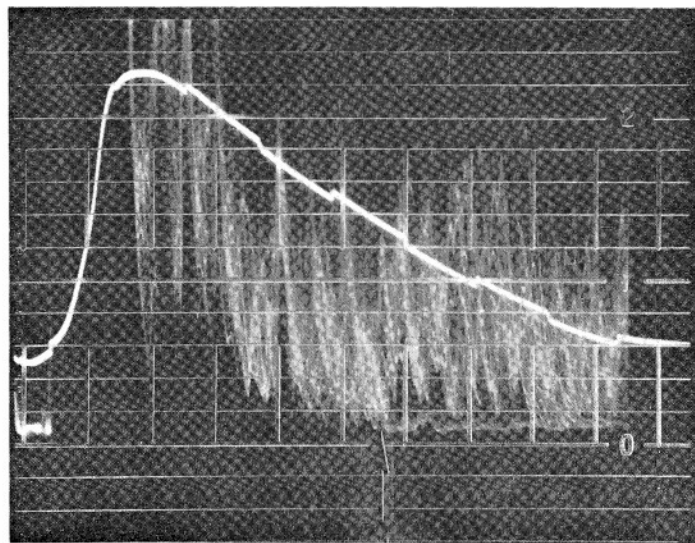
S2-3



S2-4

Figure A2



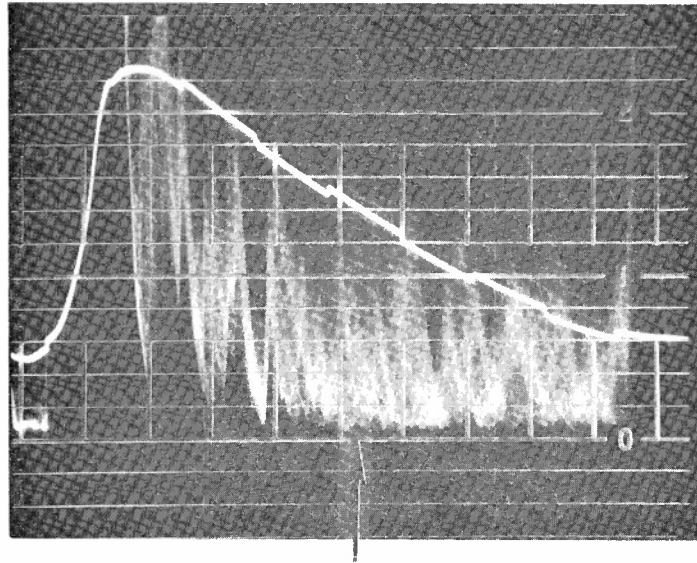


Avco 40-70% CRT  
Scale Indication

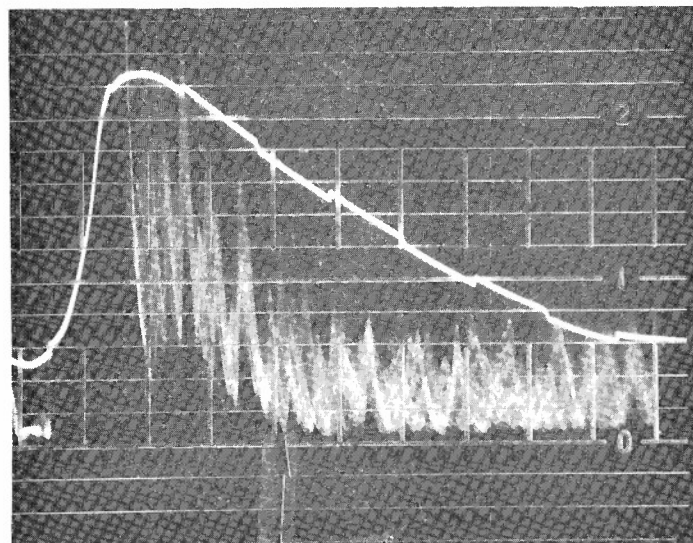
S2-6

Figure A3





S4-1



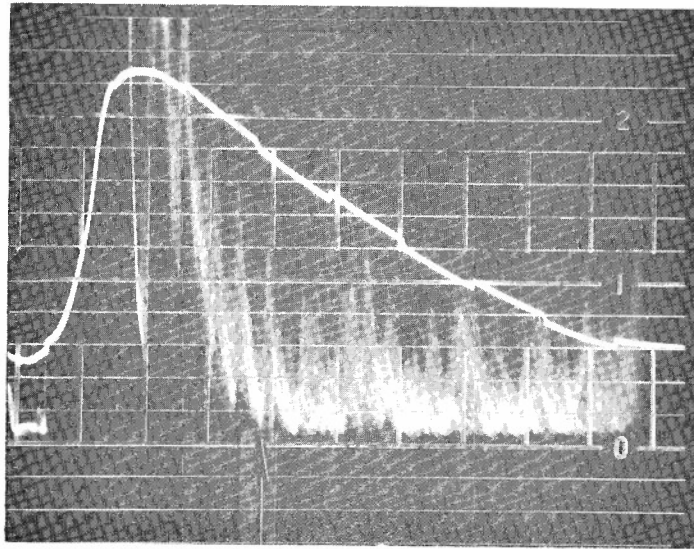
↑ Avco 20-40% CRT  
Scale Indication

S4-2

Figure A4

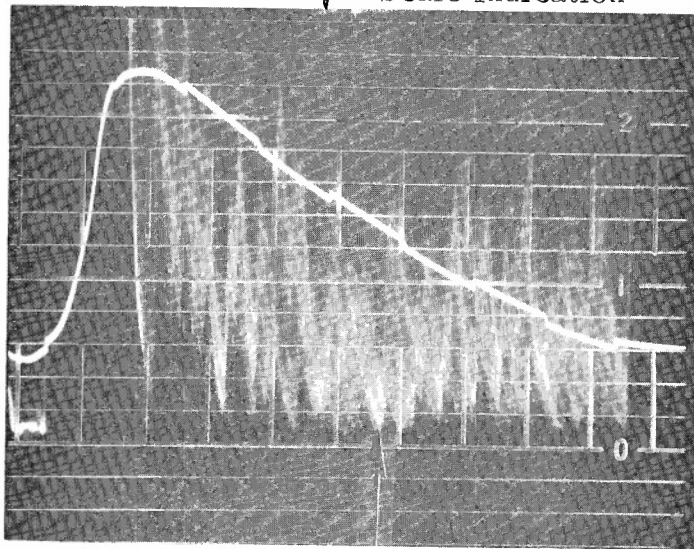






S4-3

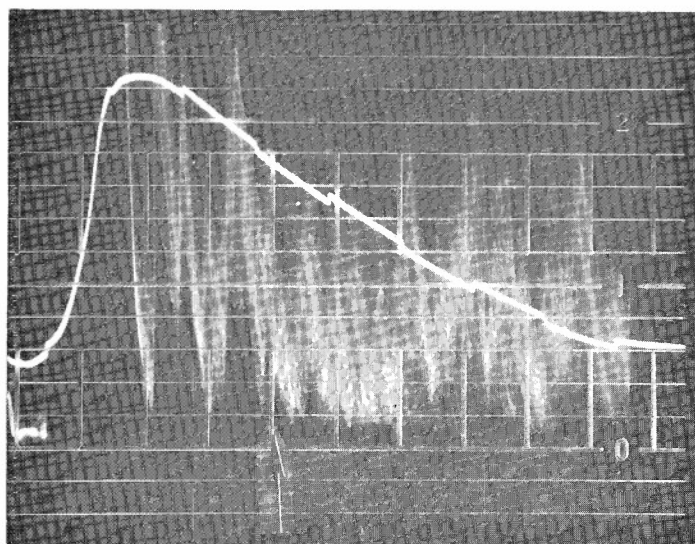
Avco 40-70% CRT  
Scale Indication



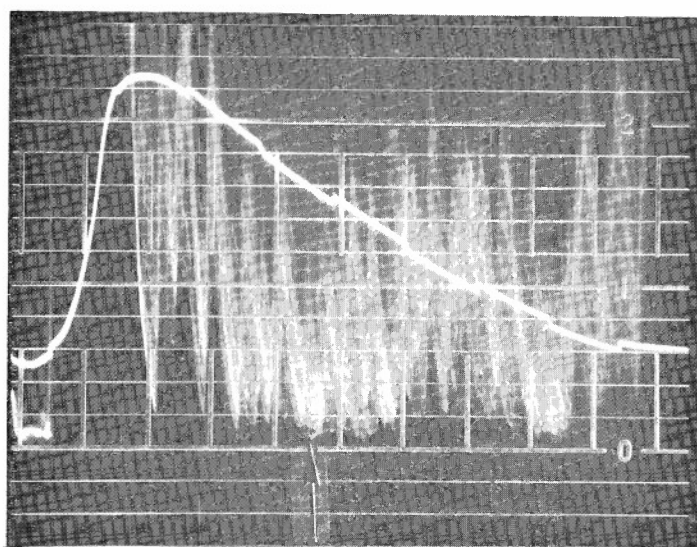
S4-4

Figure A5





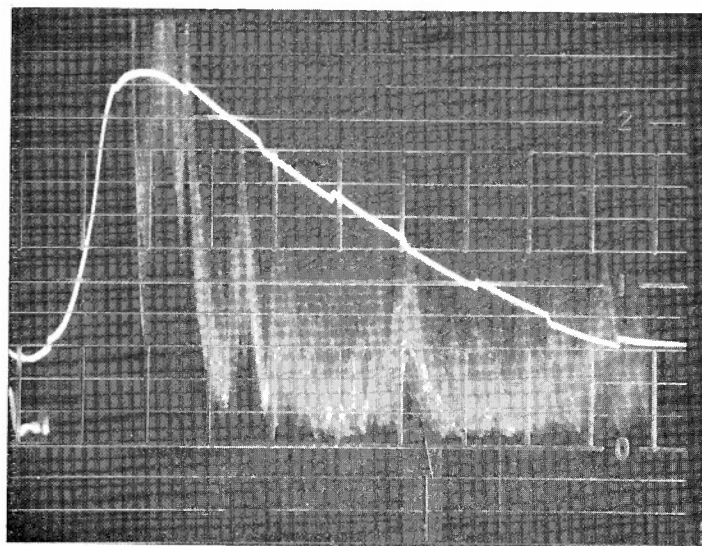
S4-5



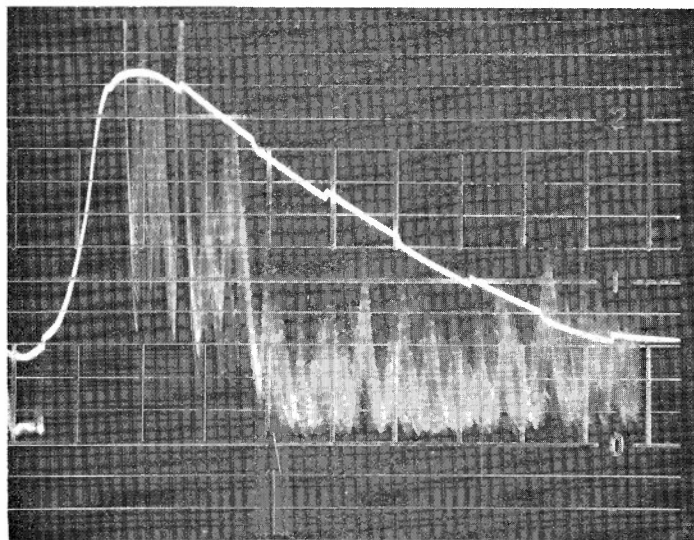
S4-6

Figure A6





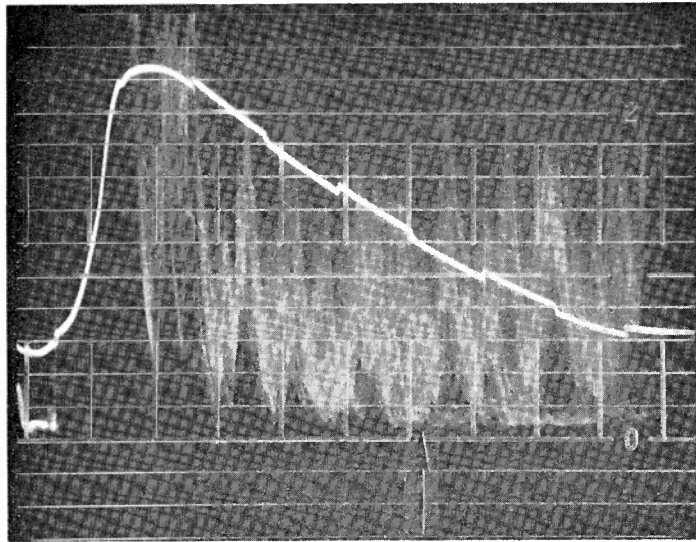
S6-1



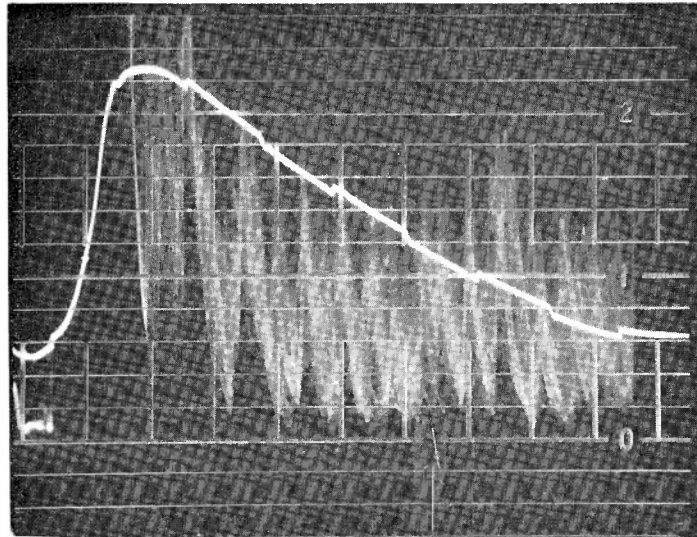
S6-2

Figure A7





S6-3

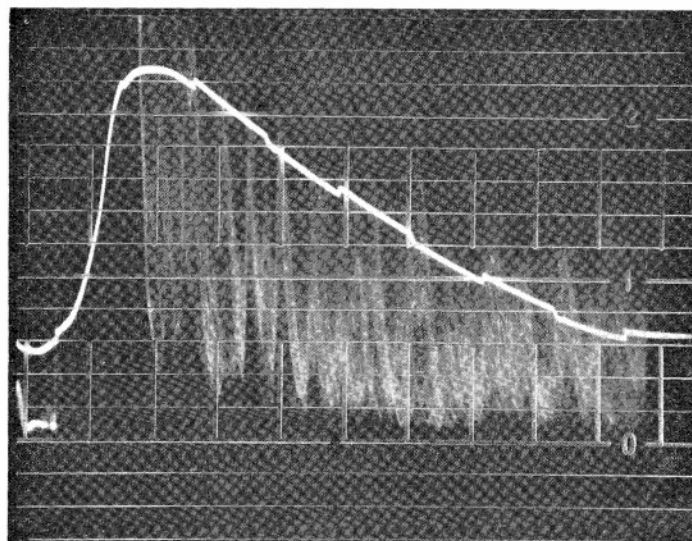
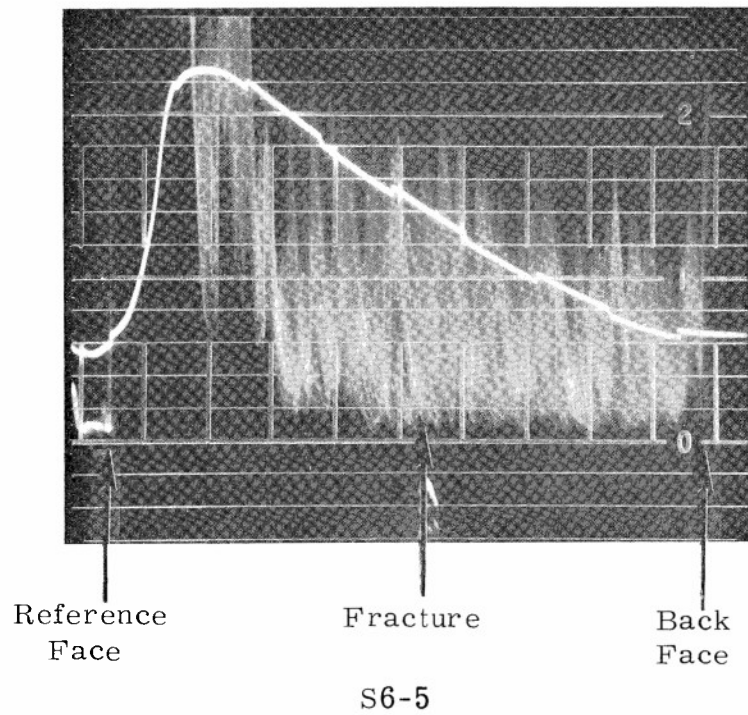


S6-4

Figure A8

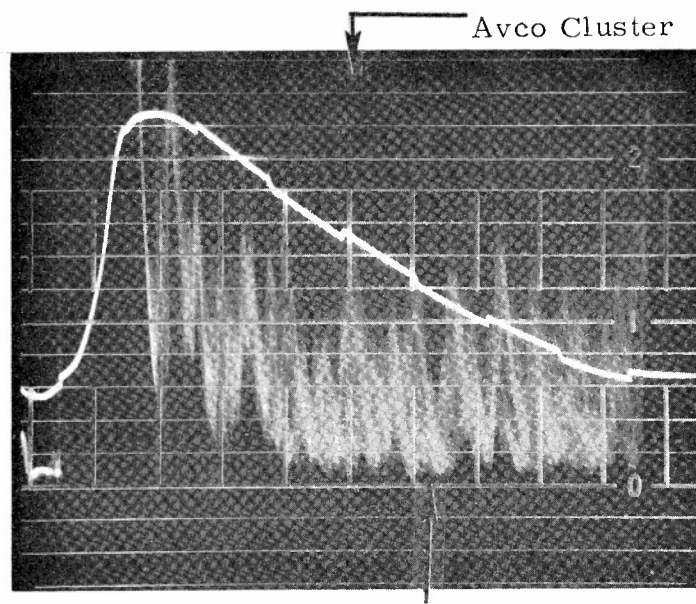




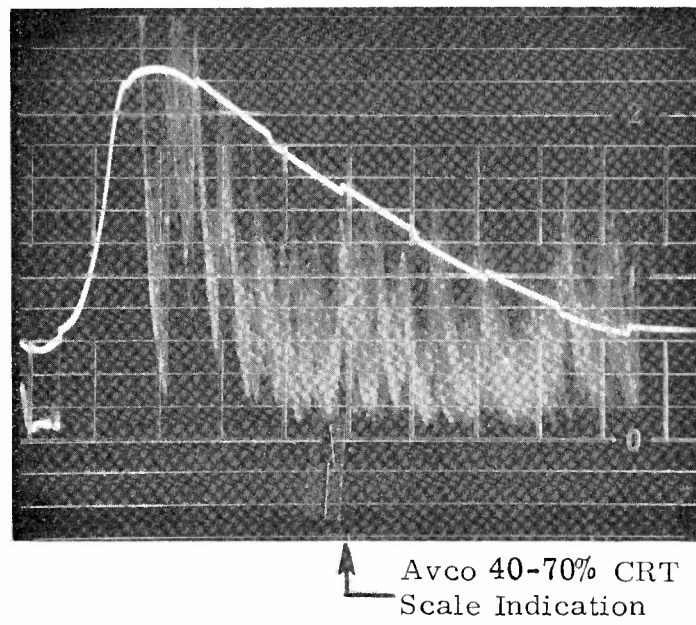


S6-6





S8-1

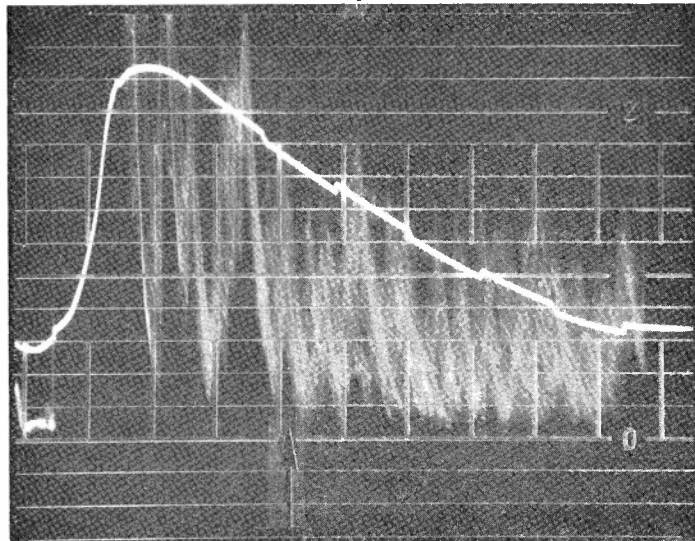


S8-2

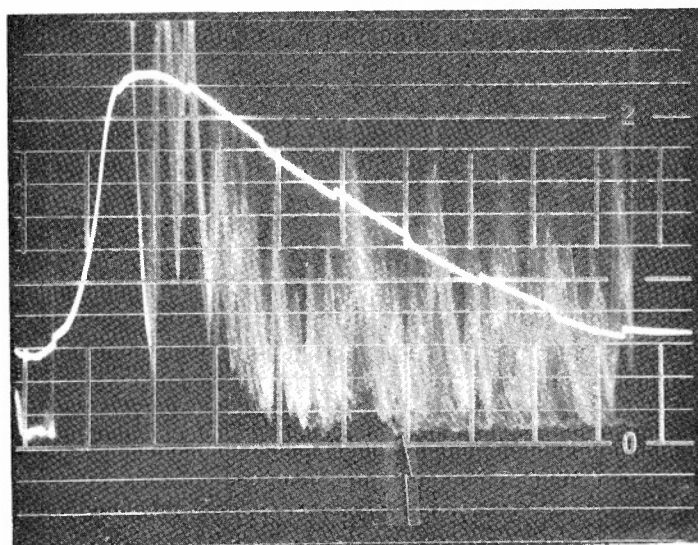
Figure A10



Avco 40-70% CRT  
Scale Indication



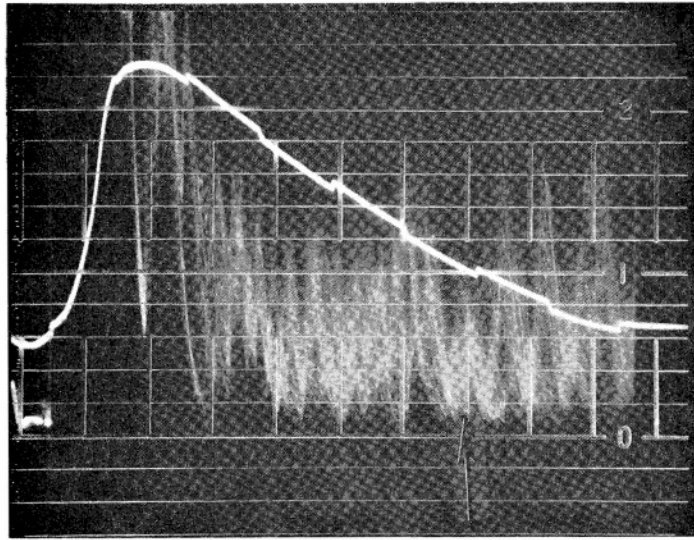
S8-3



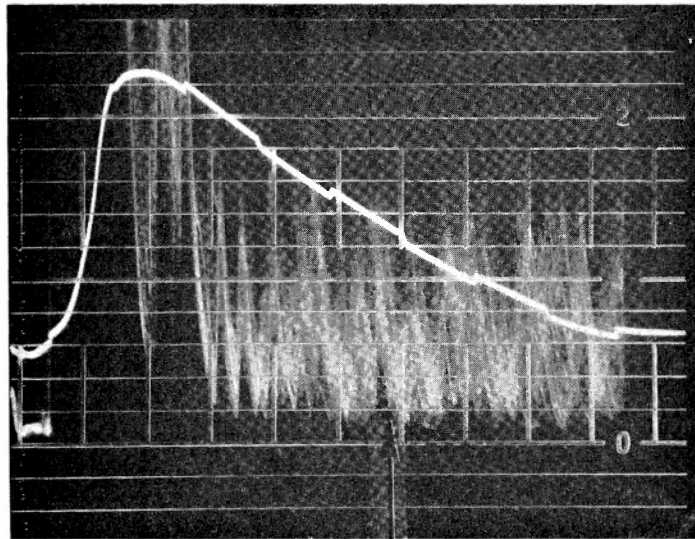
S8-4

Figure A11  
428





S8-5



Fracture

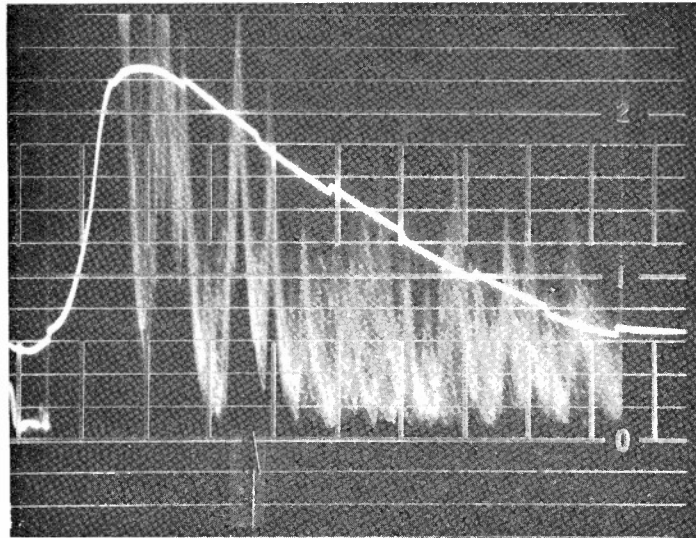
S8-6

Figure A12

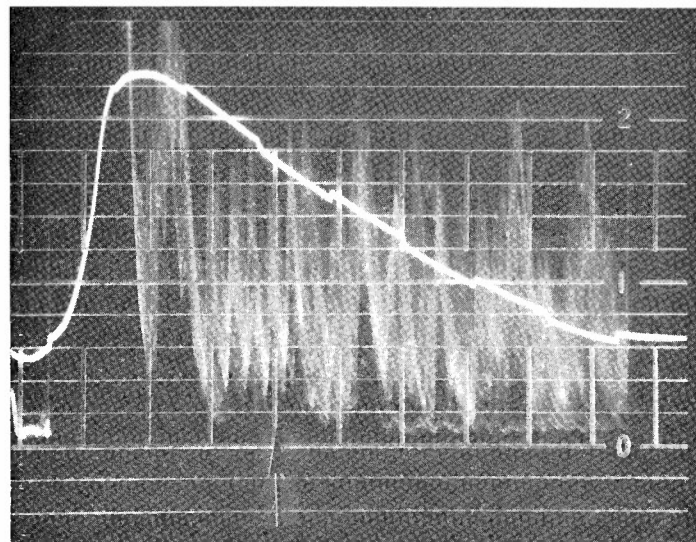
429







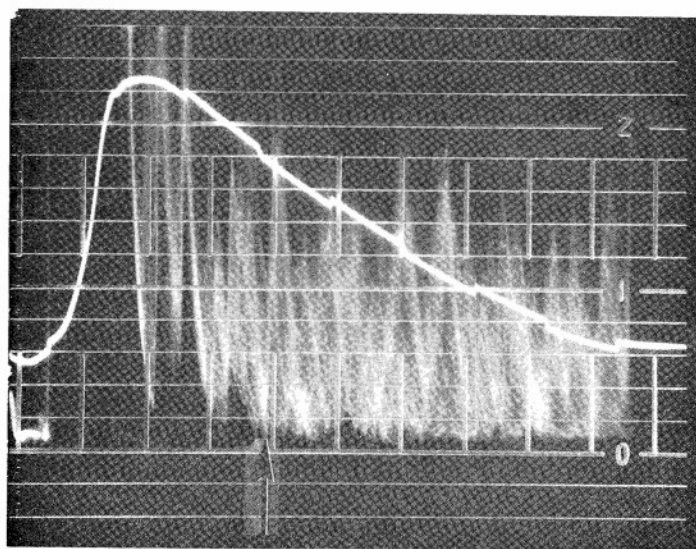
S10-1



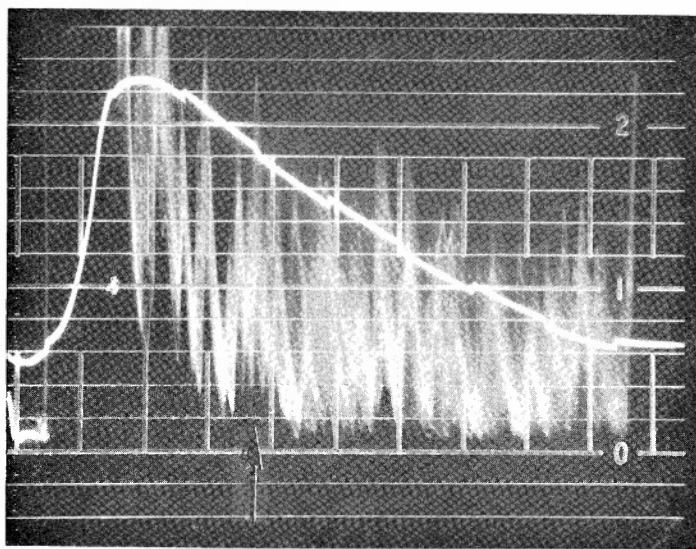
S10-2

Figure A13





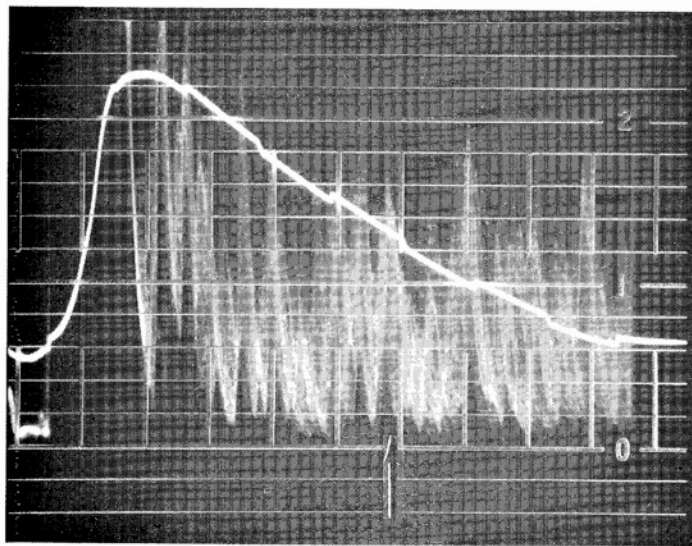
S10-3



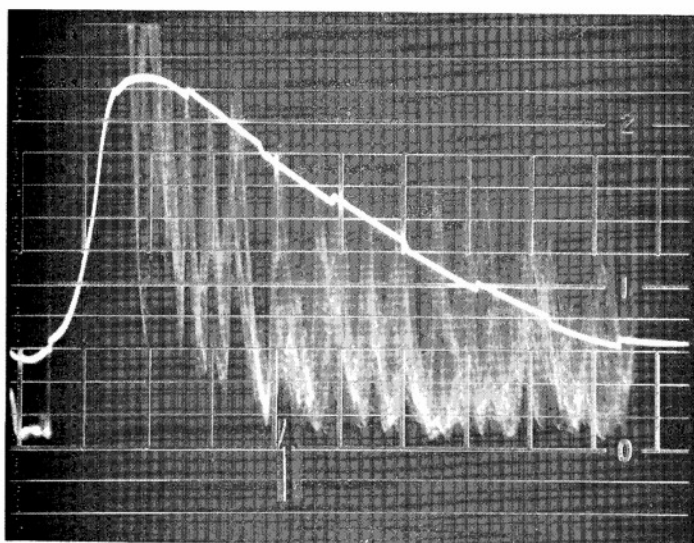
S10-4

Figure A14





S10-5



S10-6

Figure A15



## APPENDIX B

Original Tensile Stress-Strain Curves for ATJ-S Billet L-16-7  
and Specimens L-7-1-1 and L-7-1-2 of ATJ-S Billet L-7-1  
With Grain at 70°F





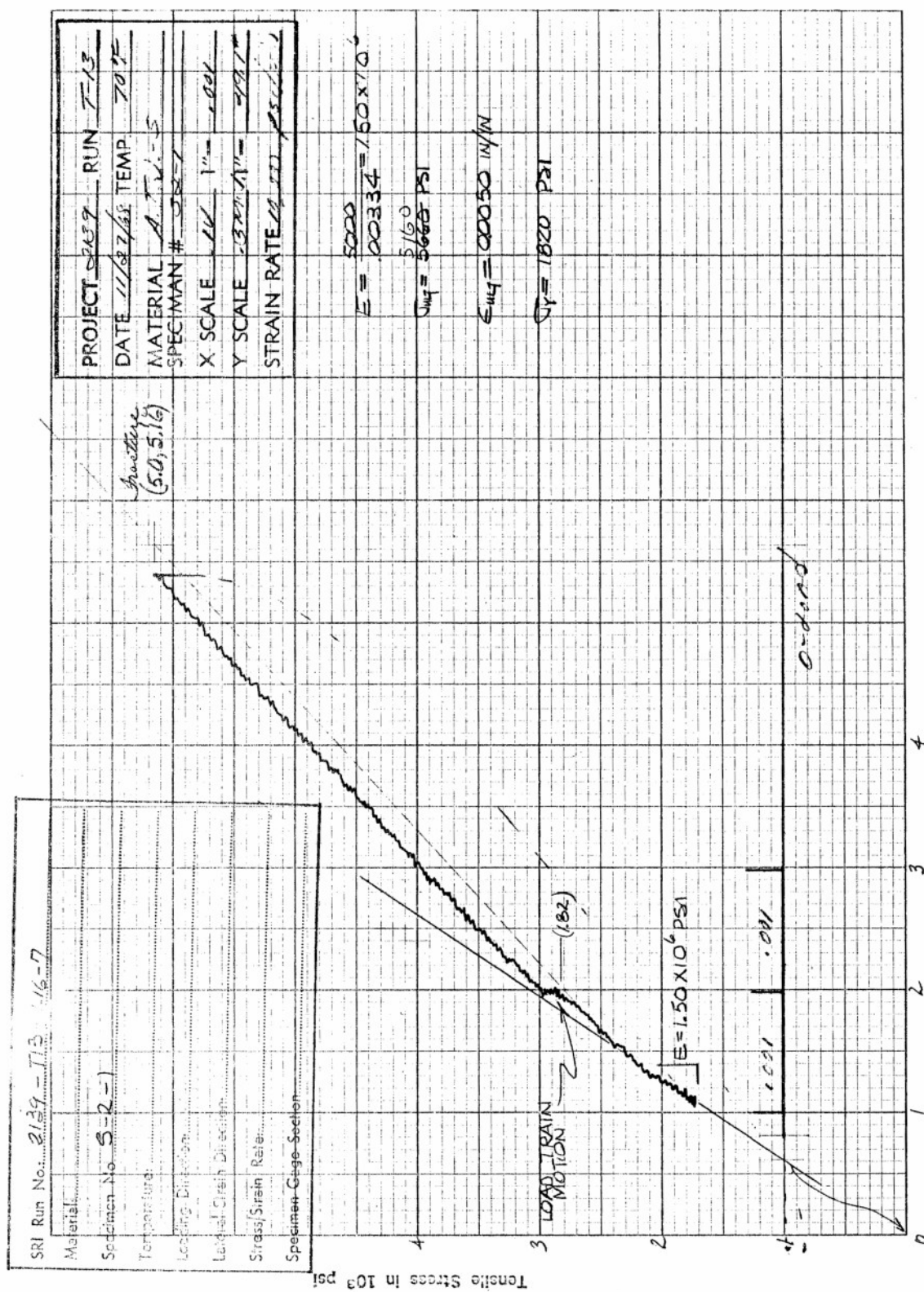


Figure B1. Tensile Stress versus Axial Strain for Specimen S-2-1 of ATJ-S Graphite at 70°F

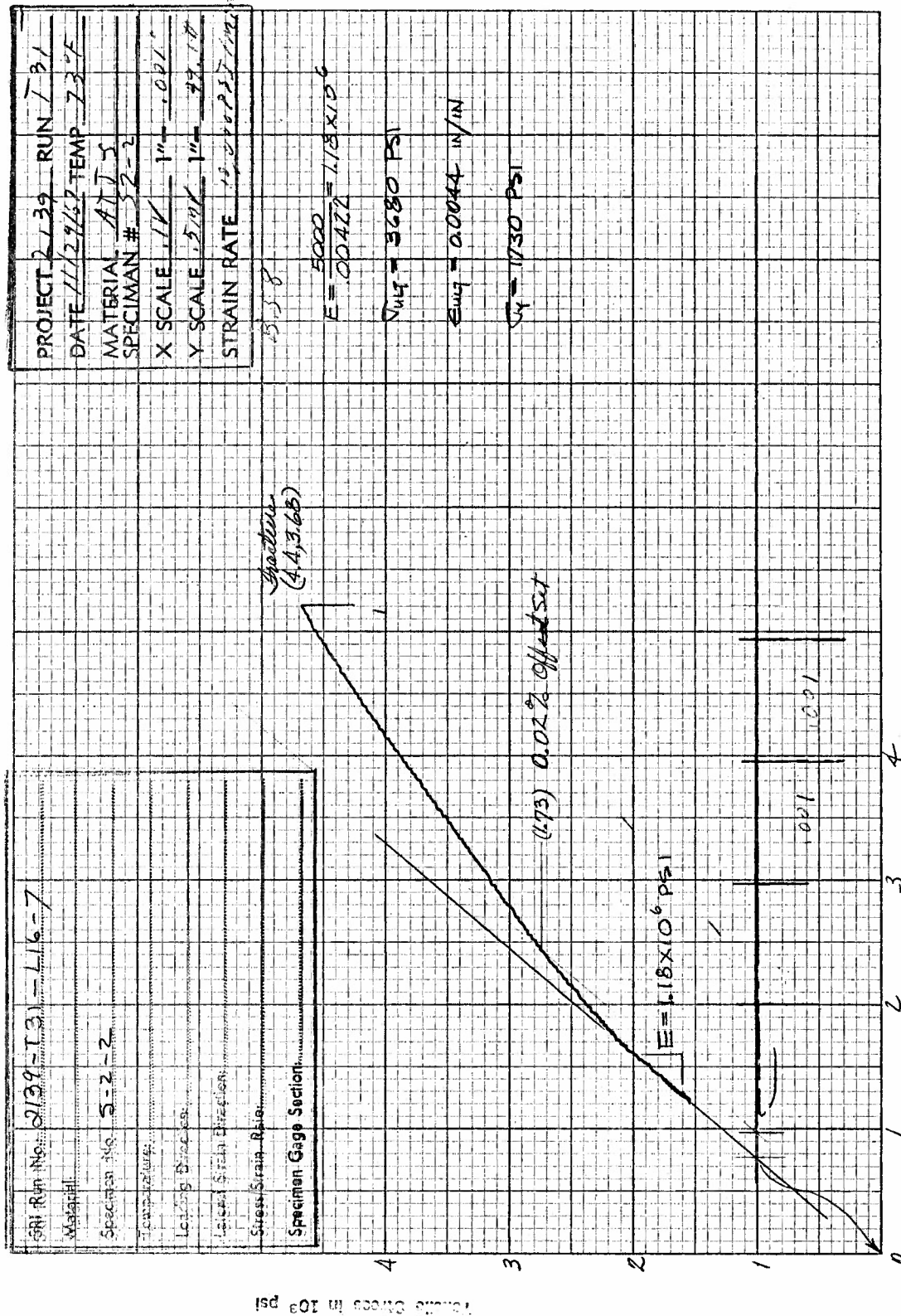


Figure B2. Tensile Stress versus Axial Strain for Specimen S-2-2 of ATJ-S Graphite at 70°F

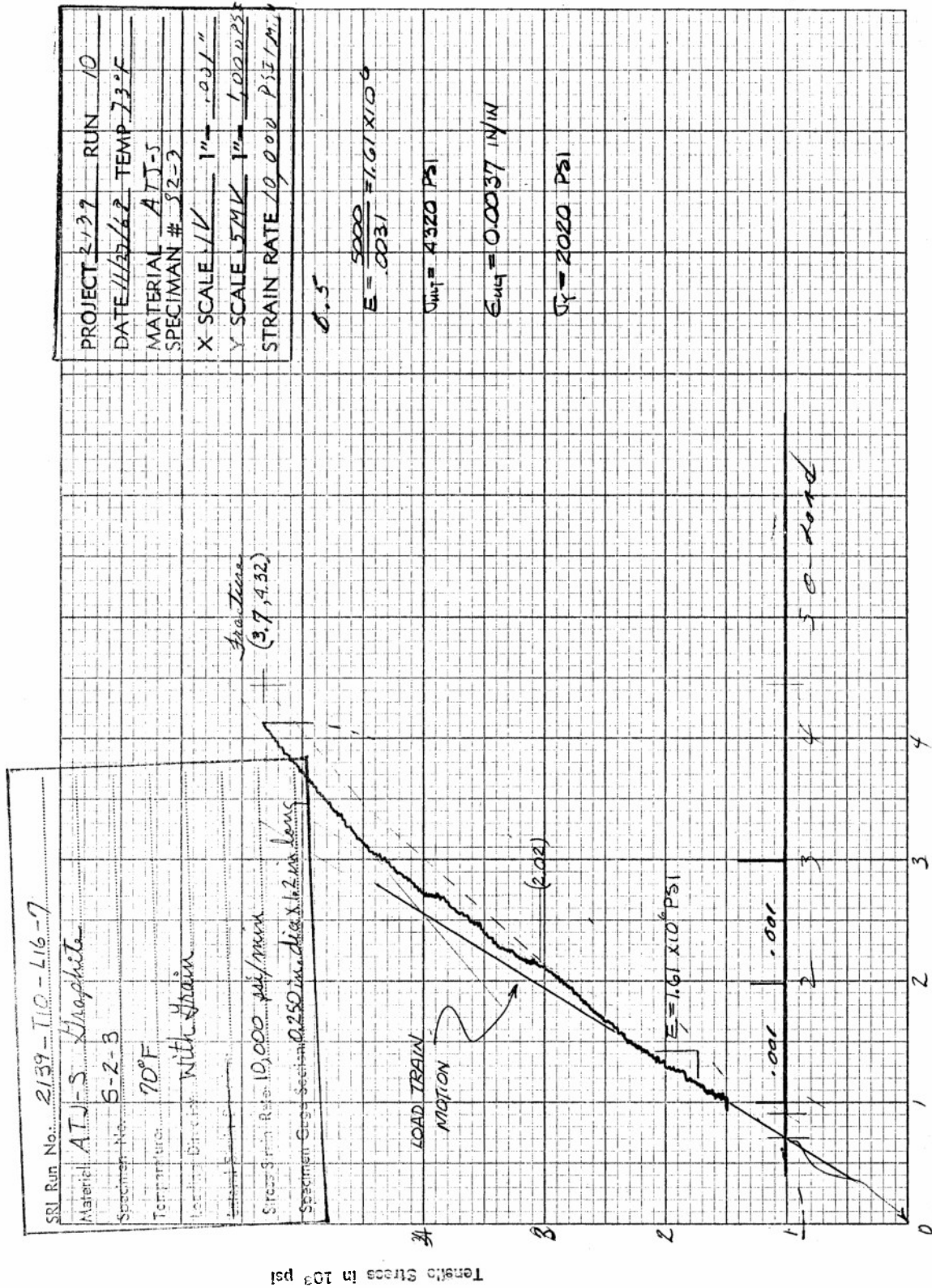


Figure B3. Tensile Stress versus Axial Strain for Specimen S-2-3 of ATJ-S Graphite at 70°F

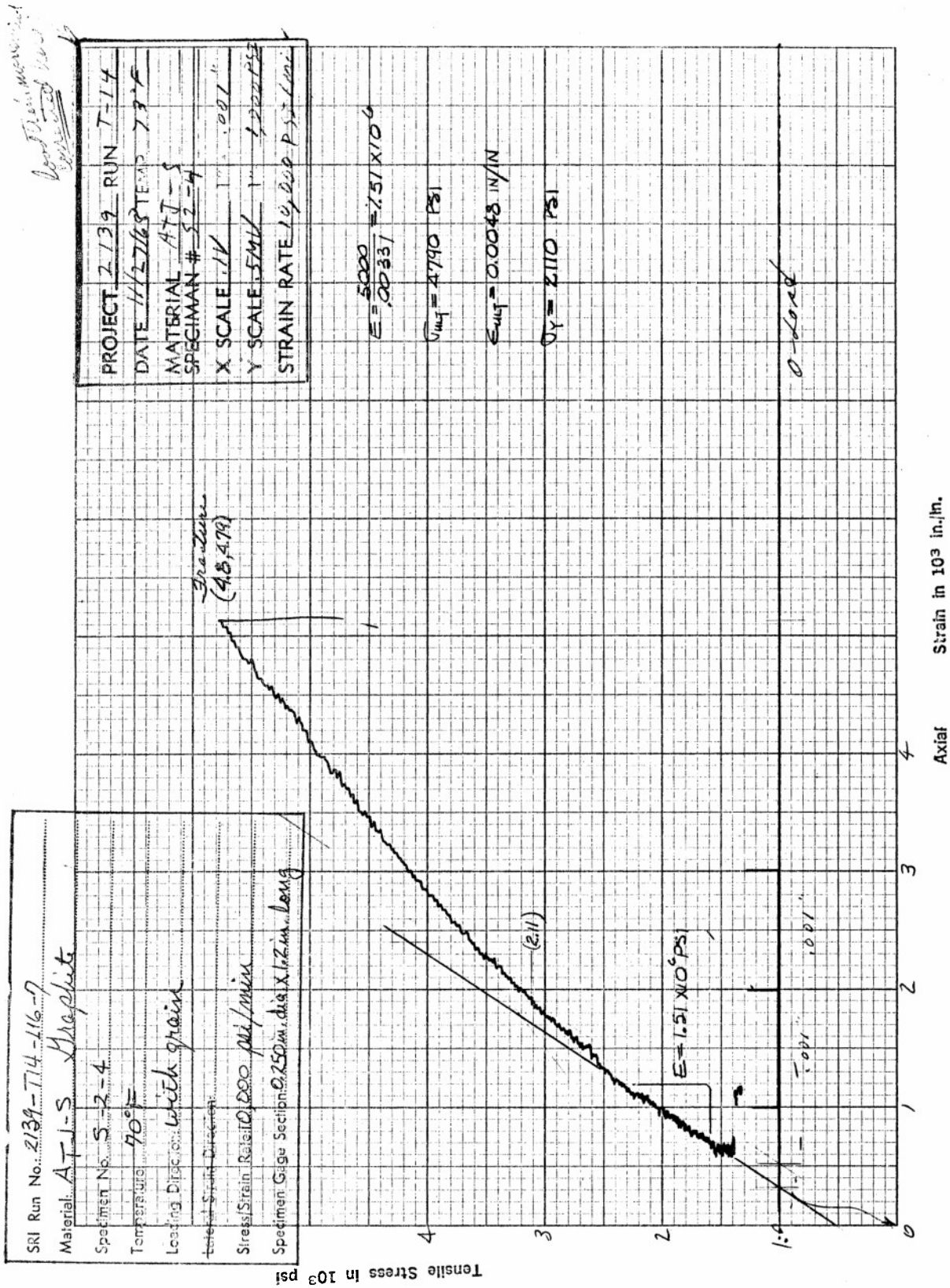


Figure B4. Tensile Stress versus Axial Strain for Specimen S-2-4 of ATJ-S Graphite at 70°F



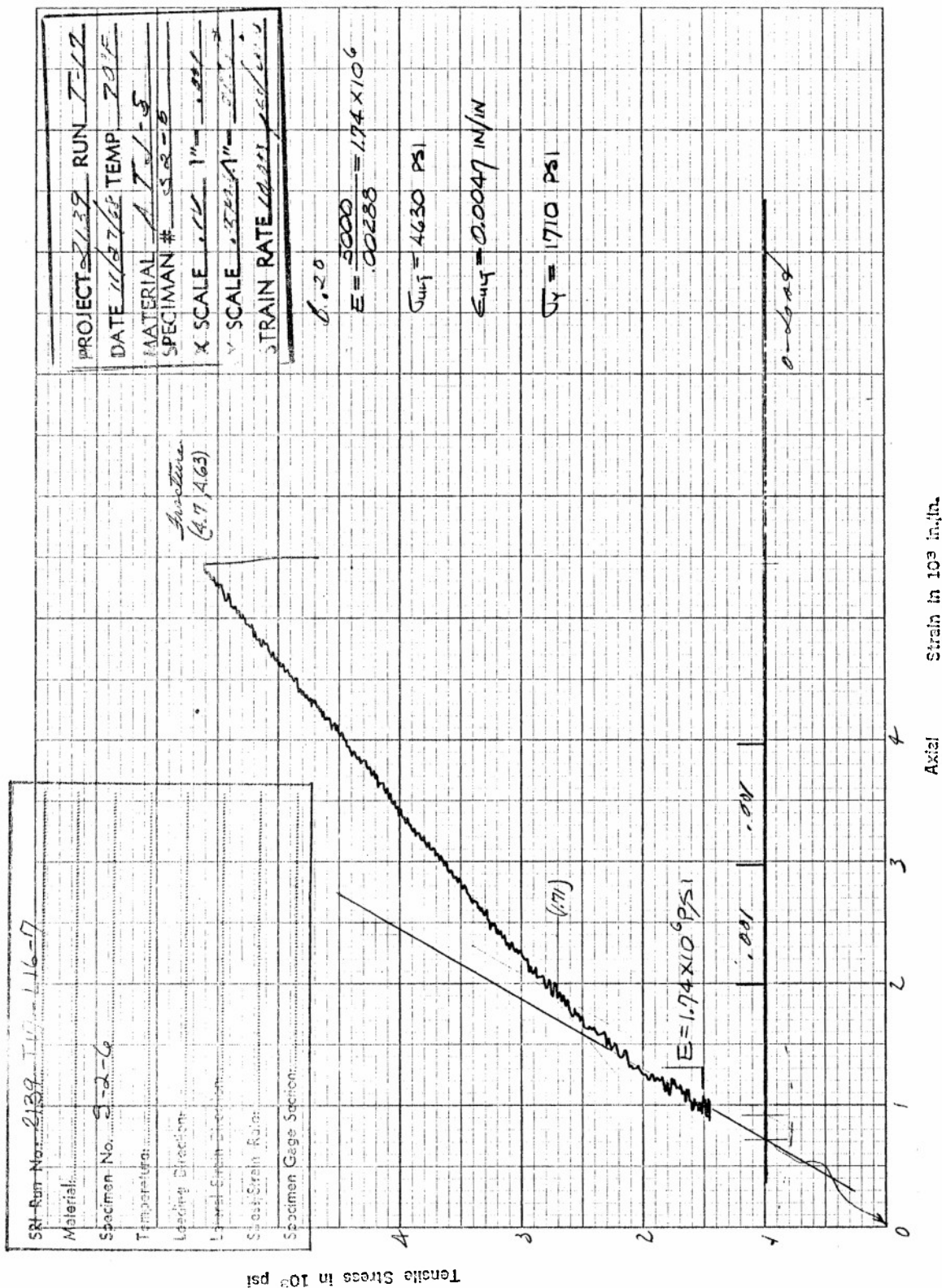


Figure B5. Tensile Stress versus Axial Strain for Specimen S-2-6 for ATJ-S Graphite at 70°F

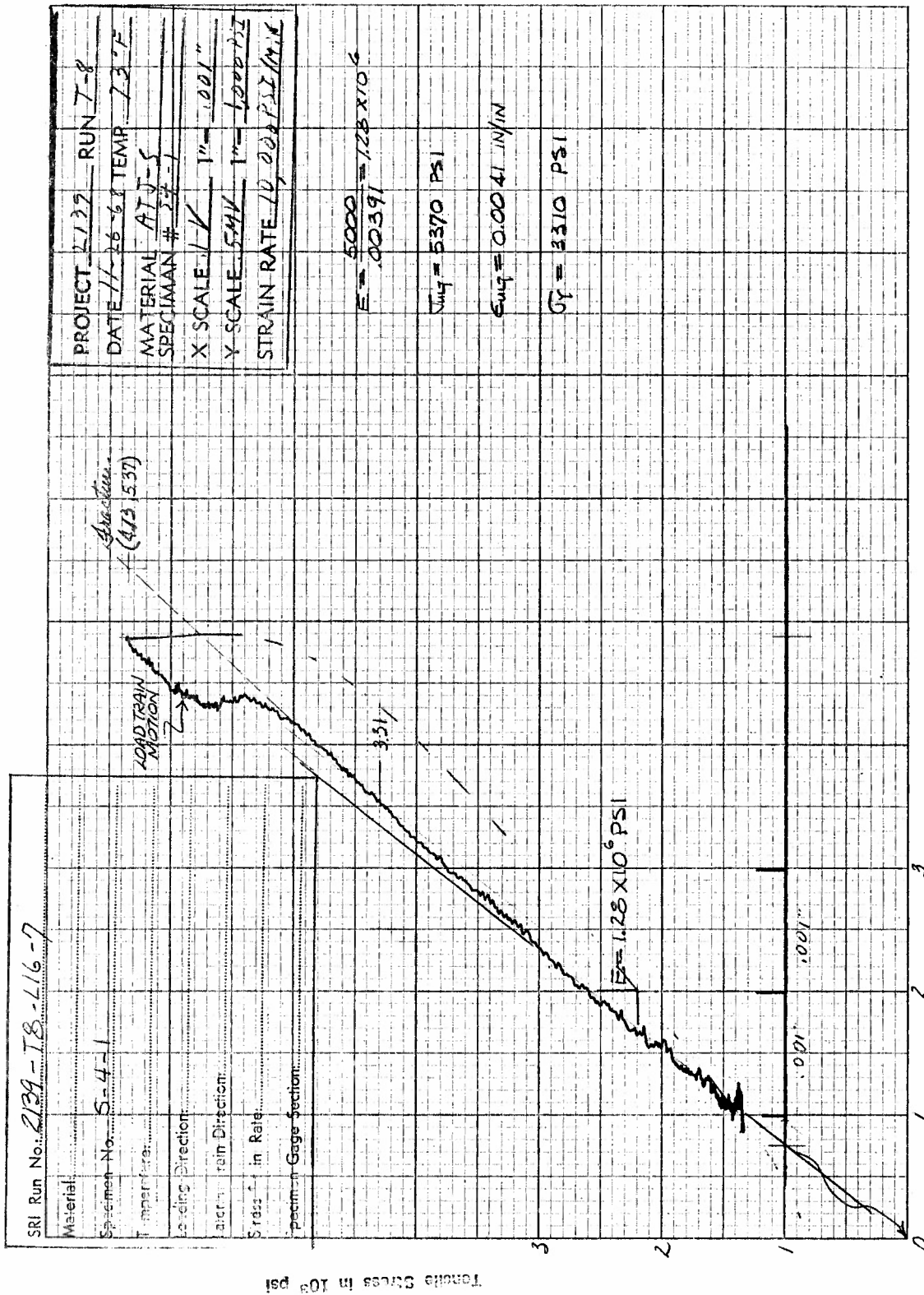


Figure B6. Tensile Stress versus Axial Strain for Specimen S-4-1 of ATJ-S Graphite at 70°F

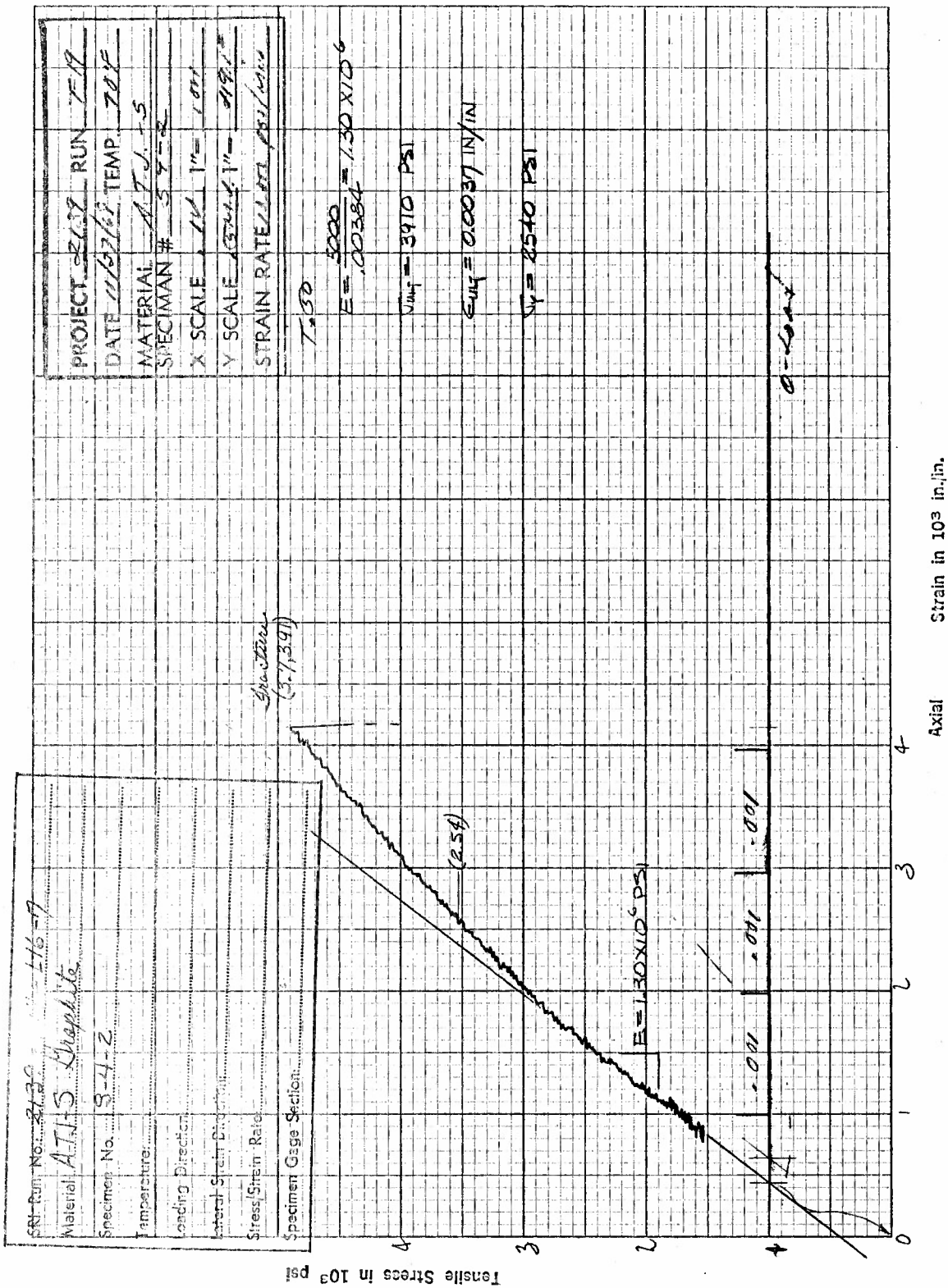


Figure B7. Tensile Stress versus Axial Strain for Specimen S-4-2 of ATJ-S Graphite at 70°F

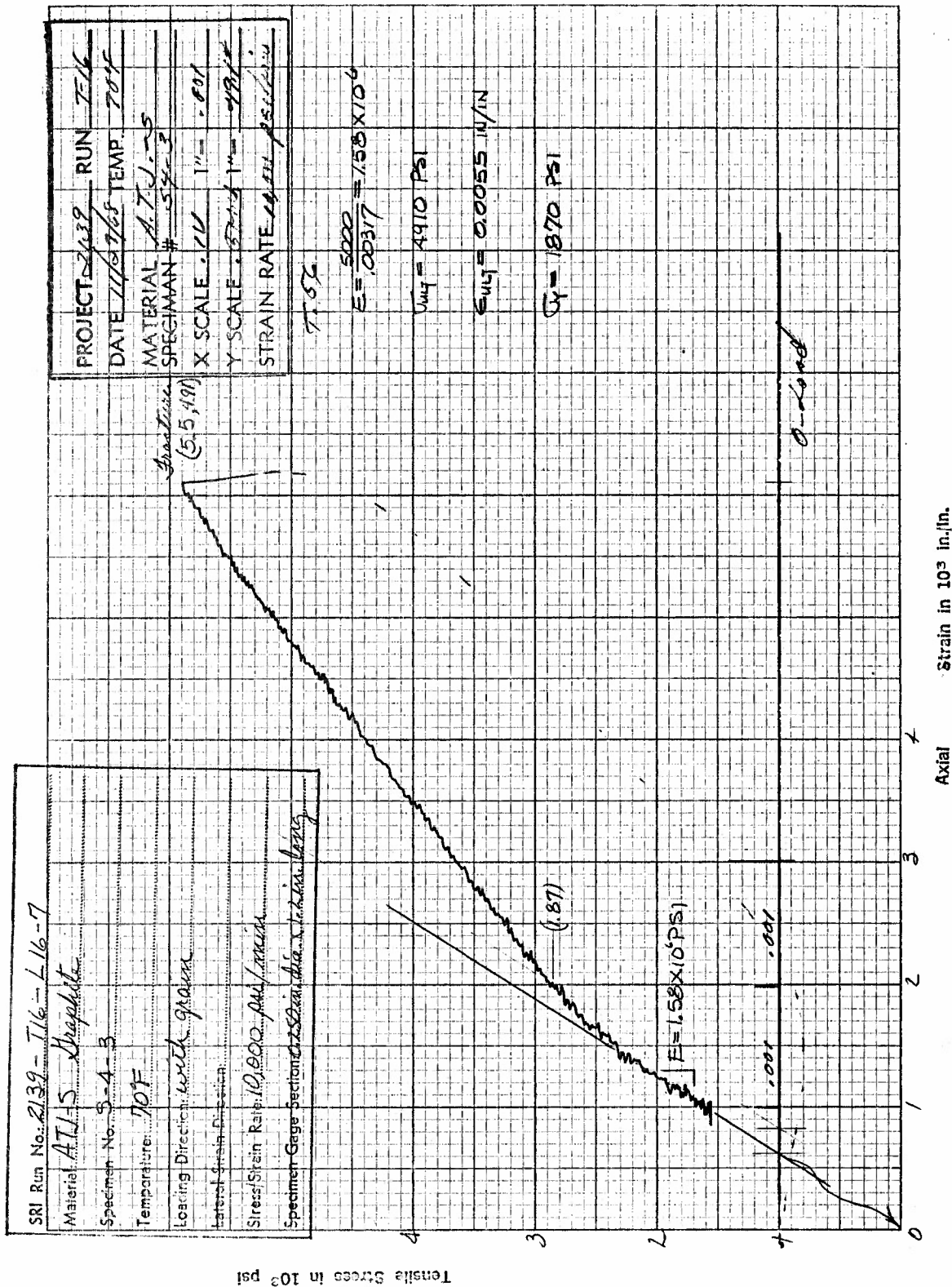


Figure B8. Tensile Stress versus Axial Strain for Specimen S-4-3 of ATJ-S Graphite at 70°F



## Material:

Material	
Specimen No.	S-4-4
Temperature	
Loading Direction	
Load/Strain Direction	
Stress/Strain Rate	
Specimen Gage Section	

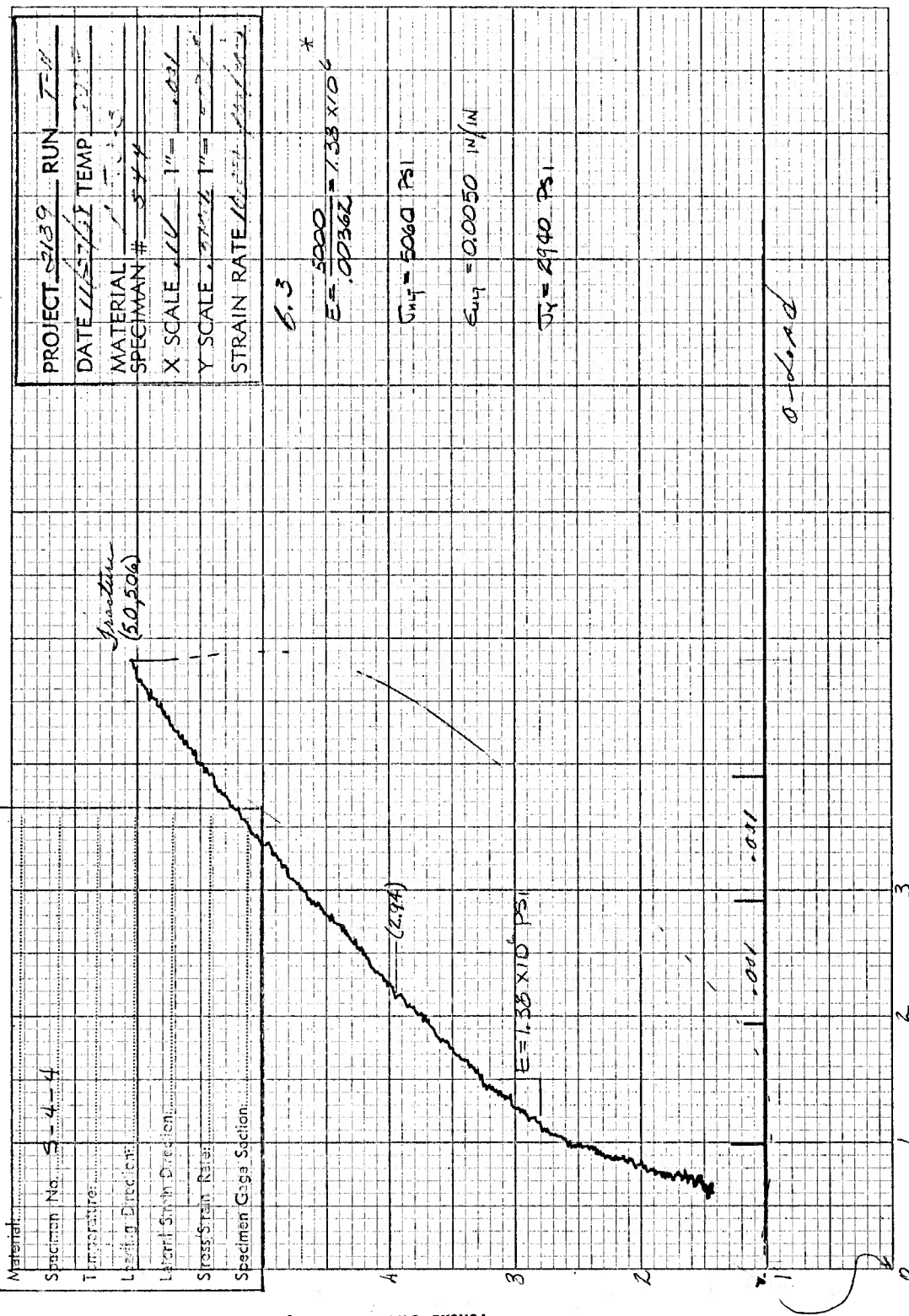


Figure B9. Tensile Stress versus Axial Strain for Specimen S-4-4 of ATJ-S Graphite at 70°F

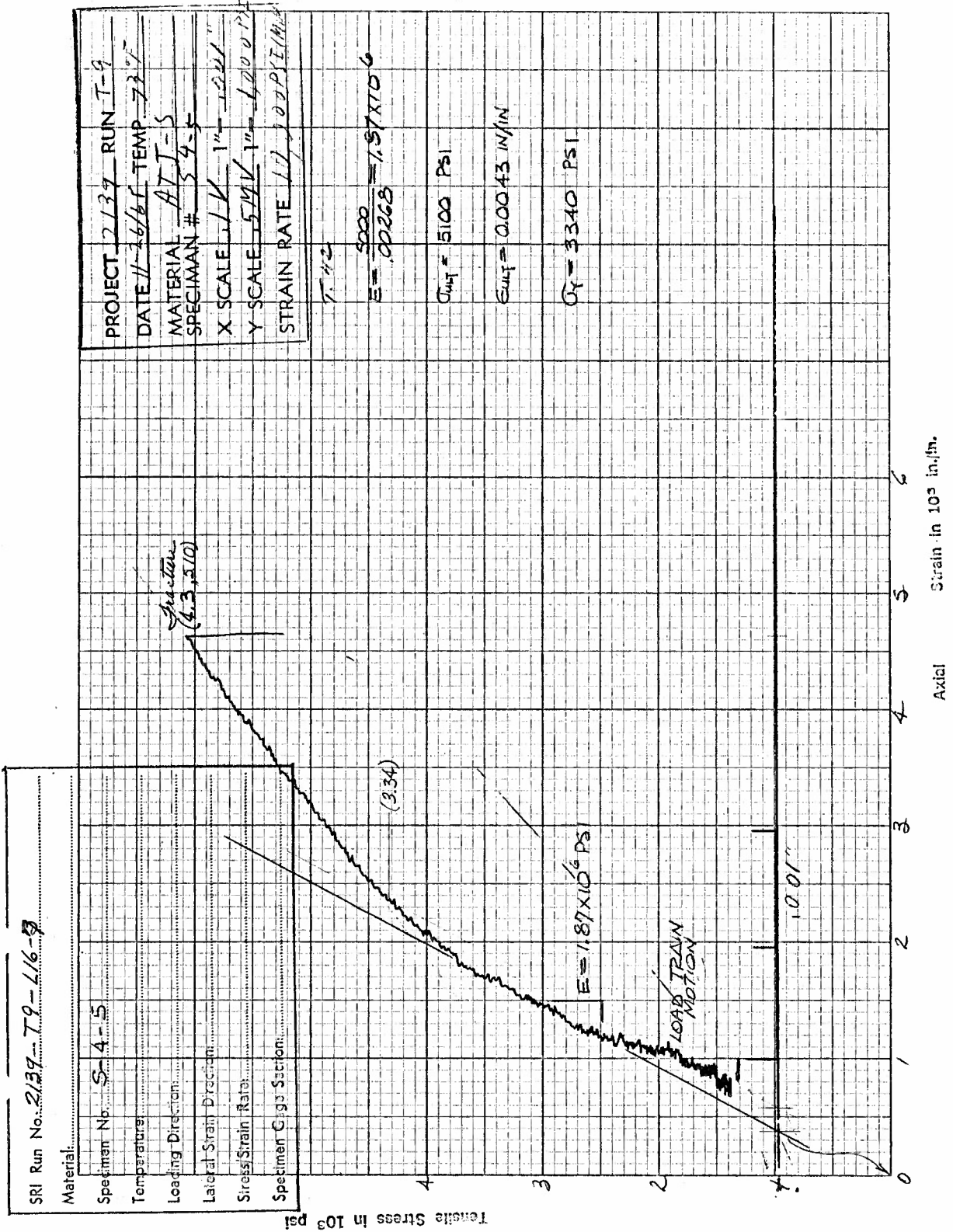


Figure B10. Tensile Stress versus Axial Strain for Specimen S-4-5 of ATJ-S Graphite at 70°F

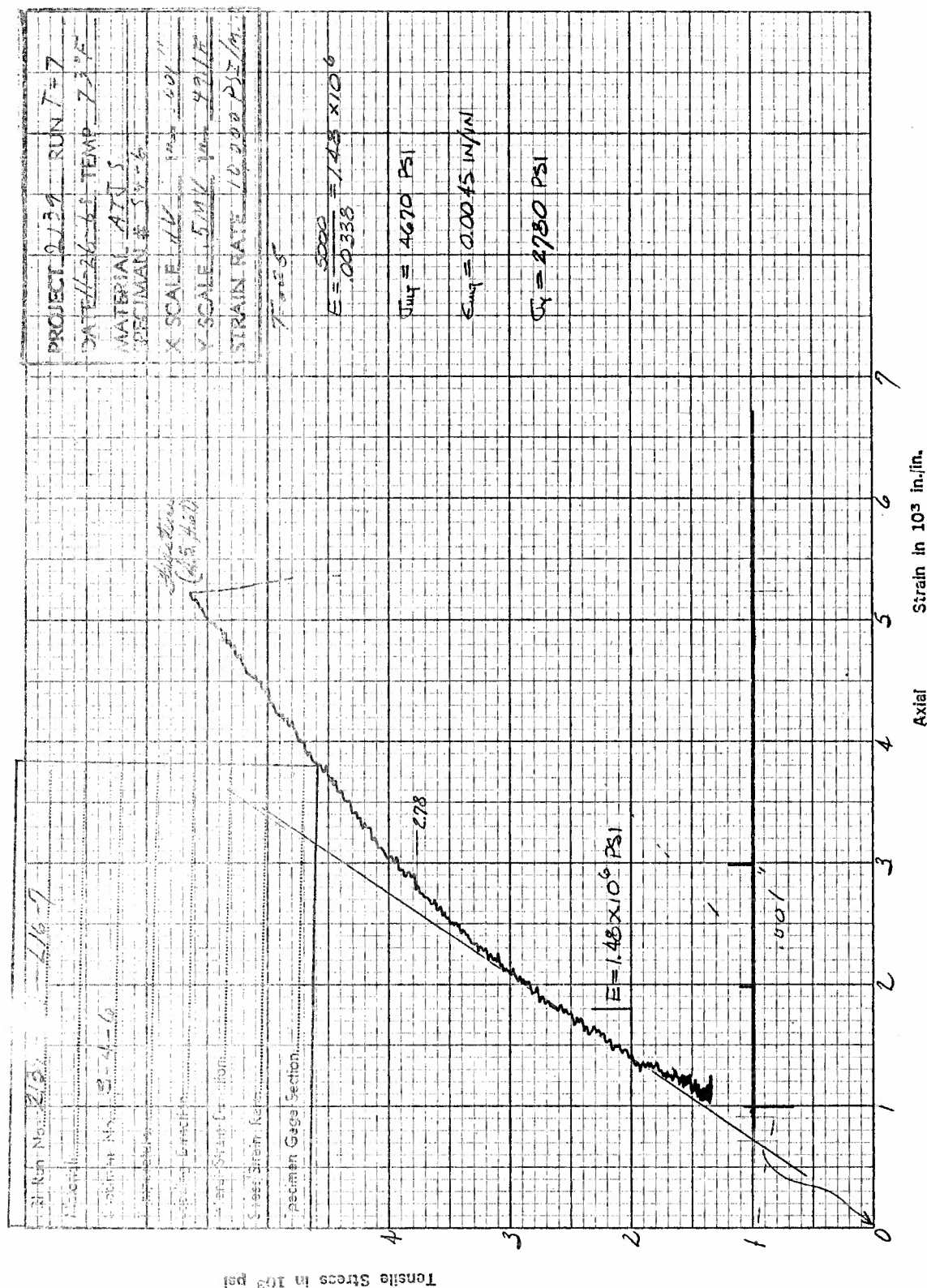


Figure B11. Tensile Stress versus Axial Strain for Specimen S-4-6 of ATJ-S Graphite at 70°F

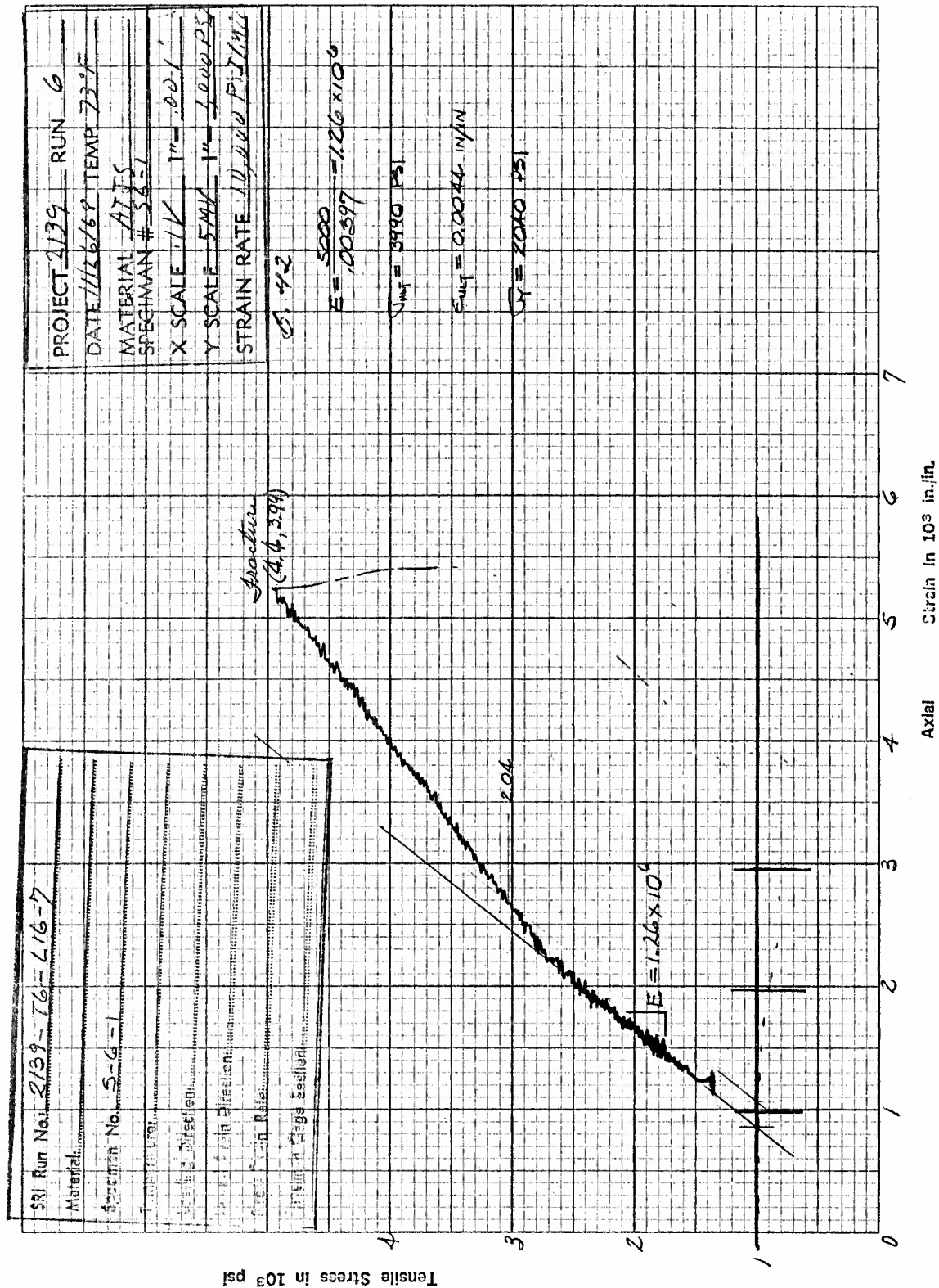


Figure B12. Tensile Stress versus Axial Strain for Specimen S-6-1 of ATJ-S Graphite at 70°F

SRI Run No. 2139 - L16-7

Material ATJ-S with green

Specimen No. S-6-2

Temperature 70°F

Loading Direction with green

Initial Strain Free

Stress/Strain Rate 10,000 psi/min

Specimen Gage Section 0.250 in. dia. Max. len.

PROJECT 2129 RUN I 2 4

DATE 11/29/68 TEMP 72°F

MATERIAL ATJ-S

SPECIMAN # S-6-2

X SCALE .1K 1" = .001"

Y SCALE 50K 1" = 49.1#

STRAIN RATE 10,000 PSI/min

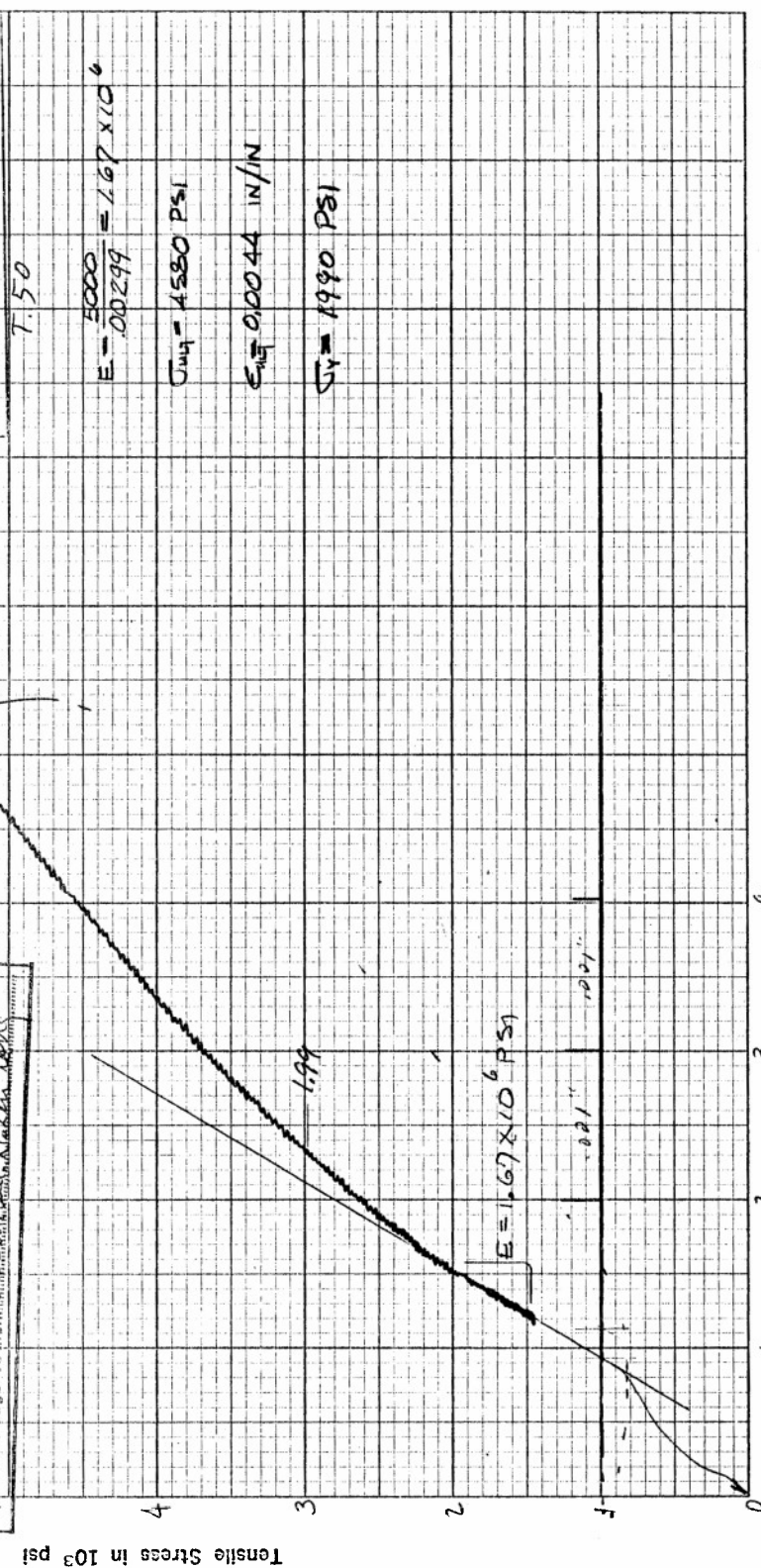


Figure B13. Tensile Stress versus Axial Strain for Specimen S-6-2 of ATJ-S Graphite at 70°F



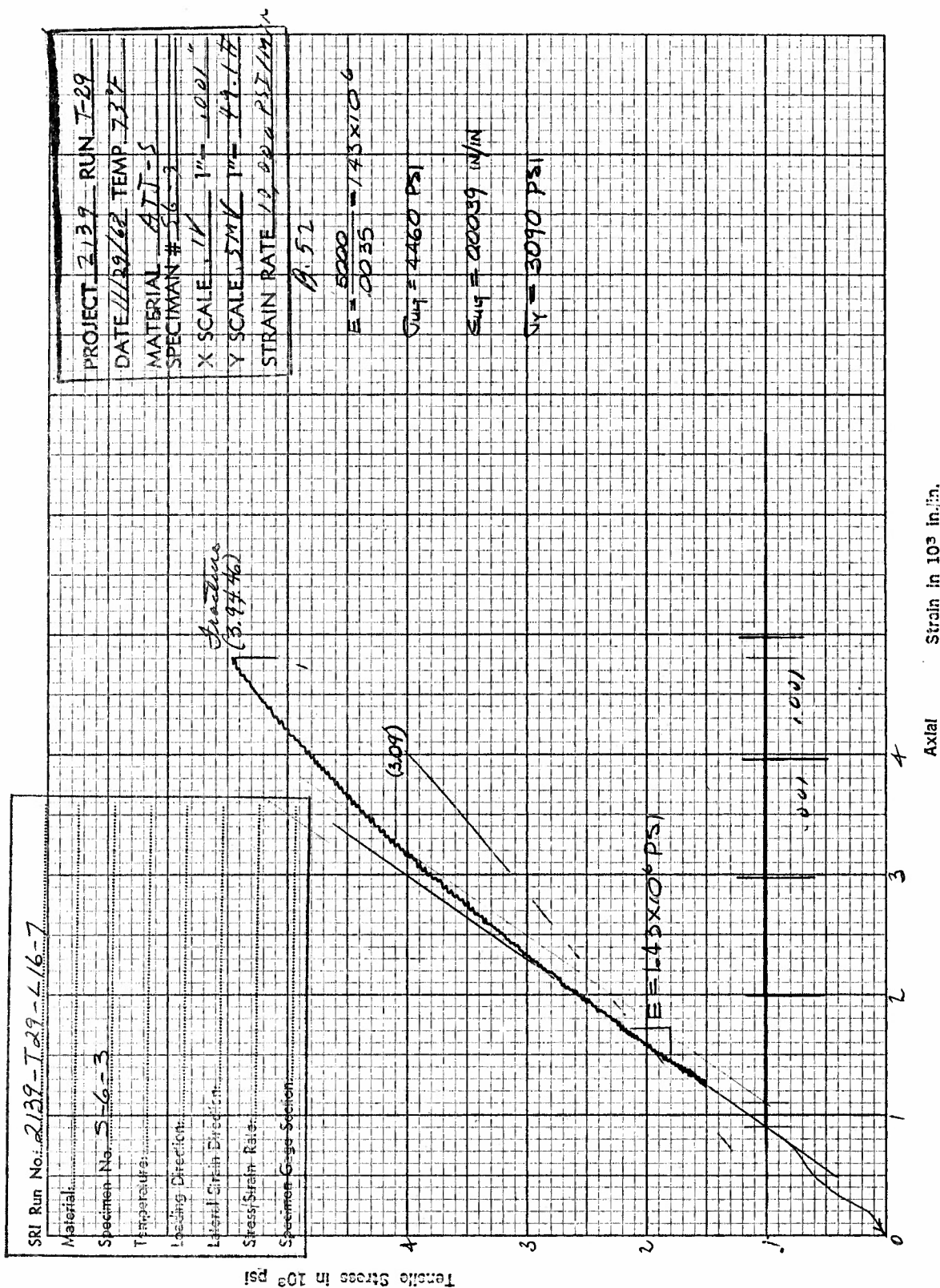


Figure B14. Tensile Stress versus Axial Strain for Specimen S-6-3 of ATT-S Graphite at 70°F

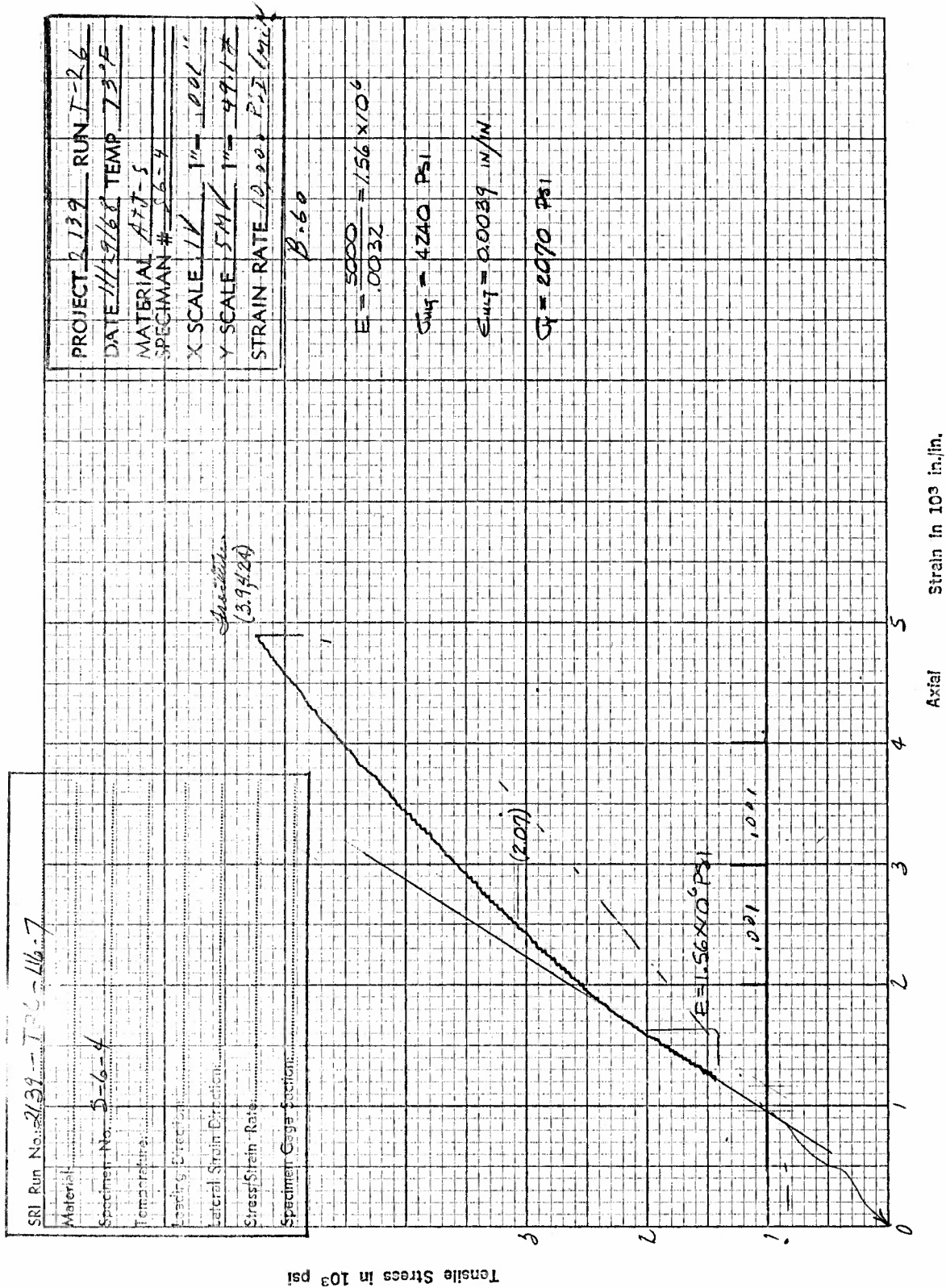


Figure B15. Tensile Stress versus Axial Strain for Specimen S-6-4 of ATJ-S Graphite at 70°F

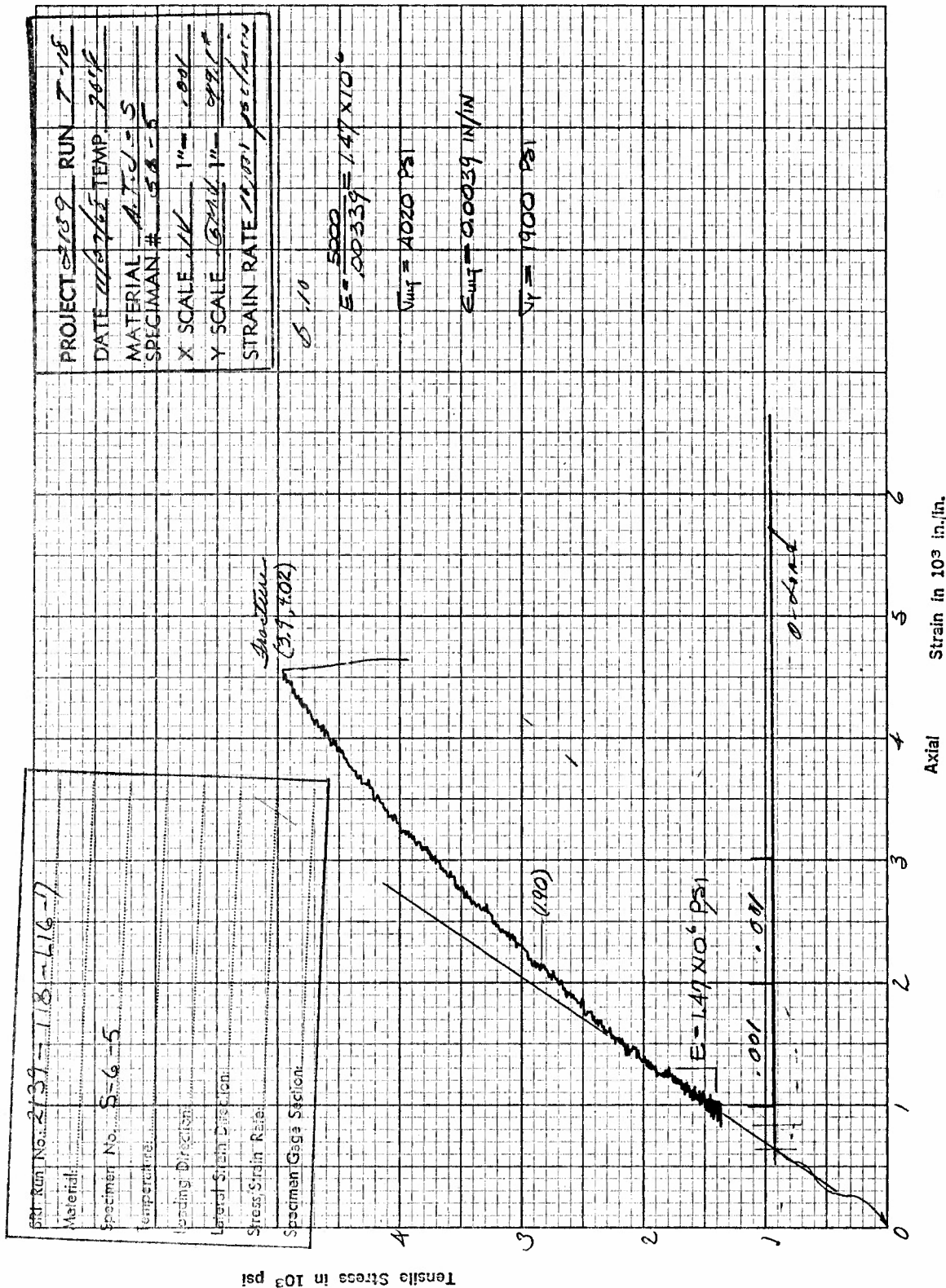


Figure B16. Tensile Stress versus Axial Strain for Specimen S-6-5 of ATJ-S Graphite at 70°F



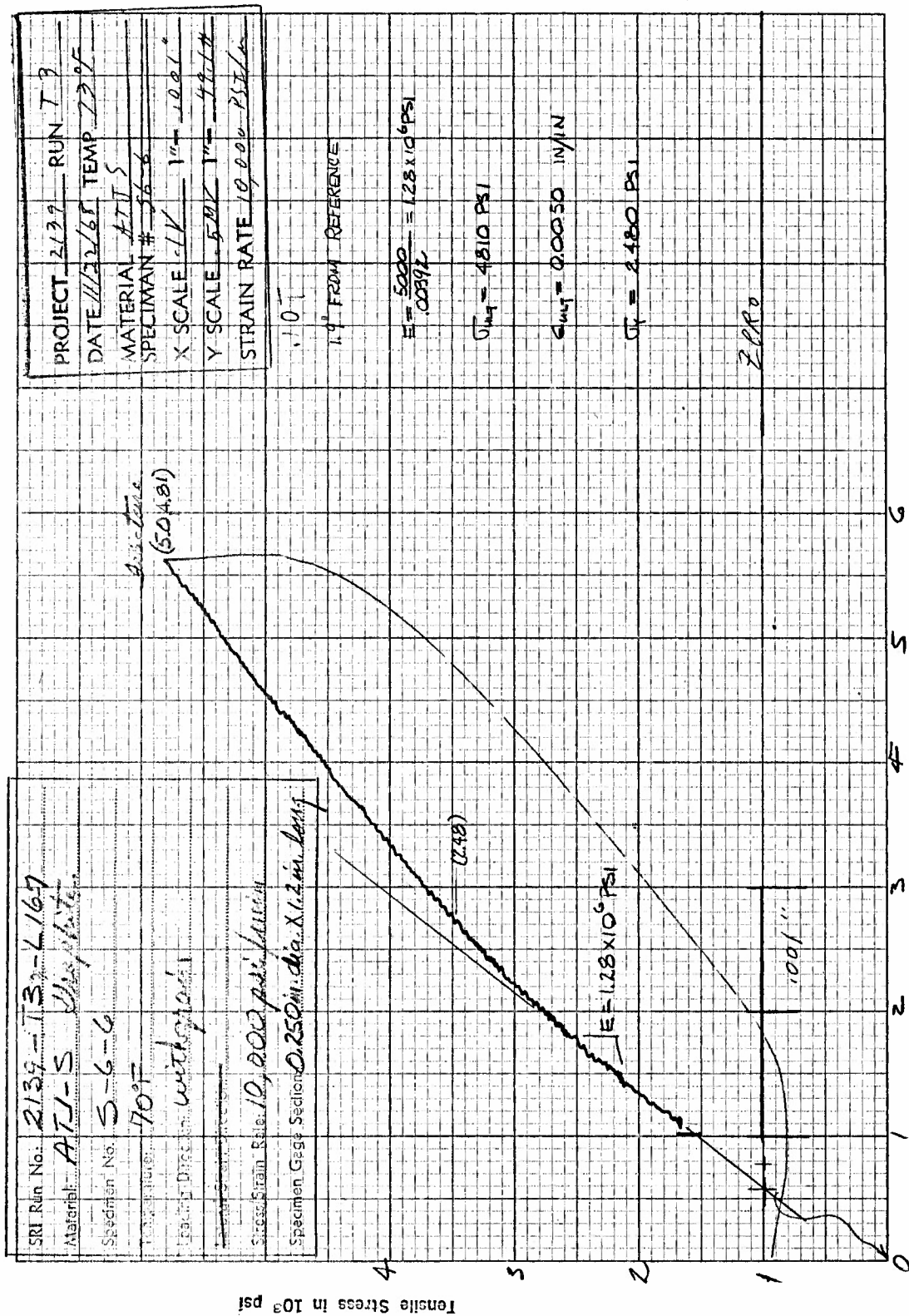


Figure B17. Tensile Stress versus Axial Strain for Specimen S-6-6 of ATL-S Graphite at 70°F

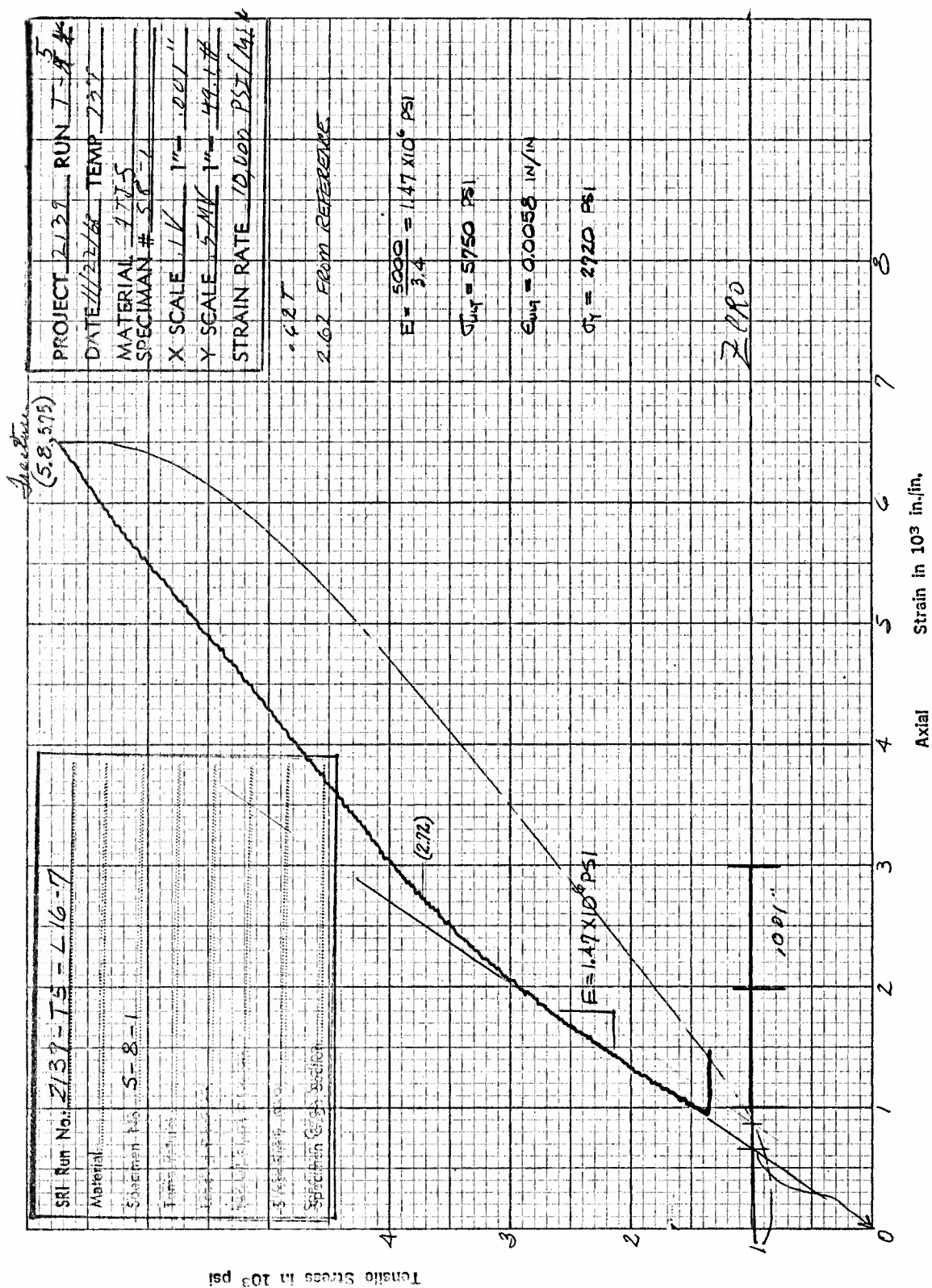


Figure B18. Tensile Stress versus Axial Strain for Specimen S-8-1 for ATJ-S Graphite at 70°F

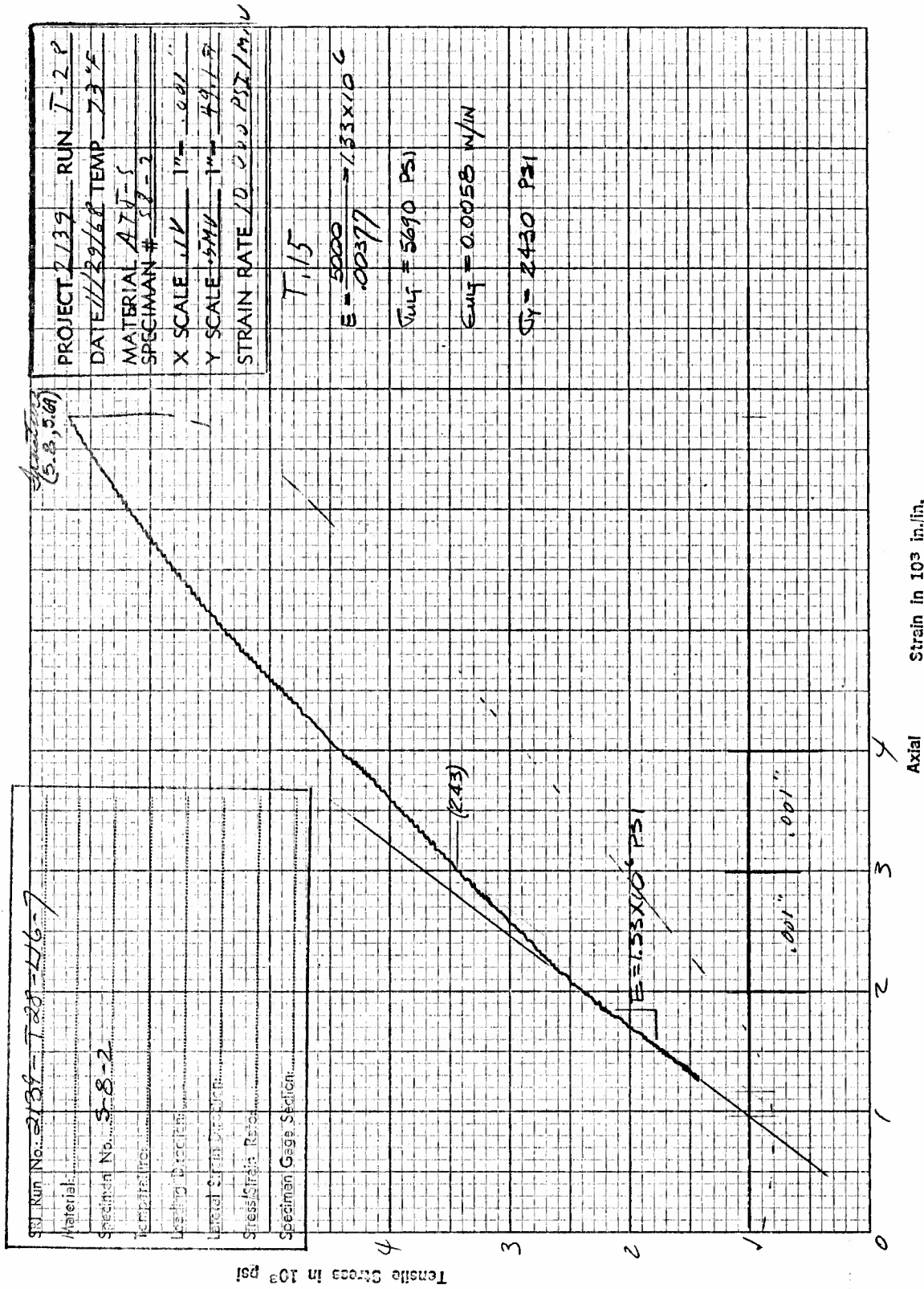


Figure B19. Tensile Stress versus Axial Strain for Specimen S-8-2 of ATJ-S Graphite at 70°F

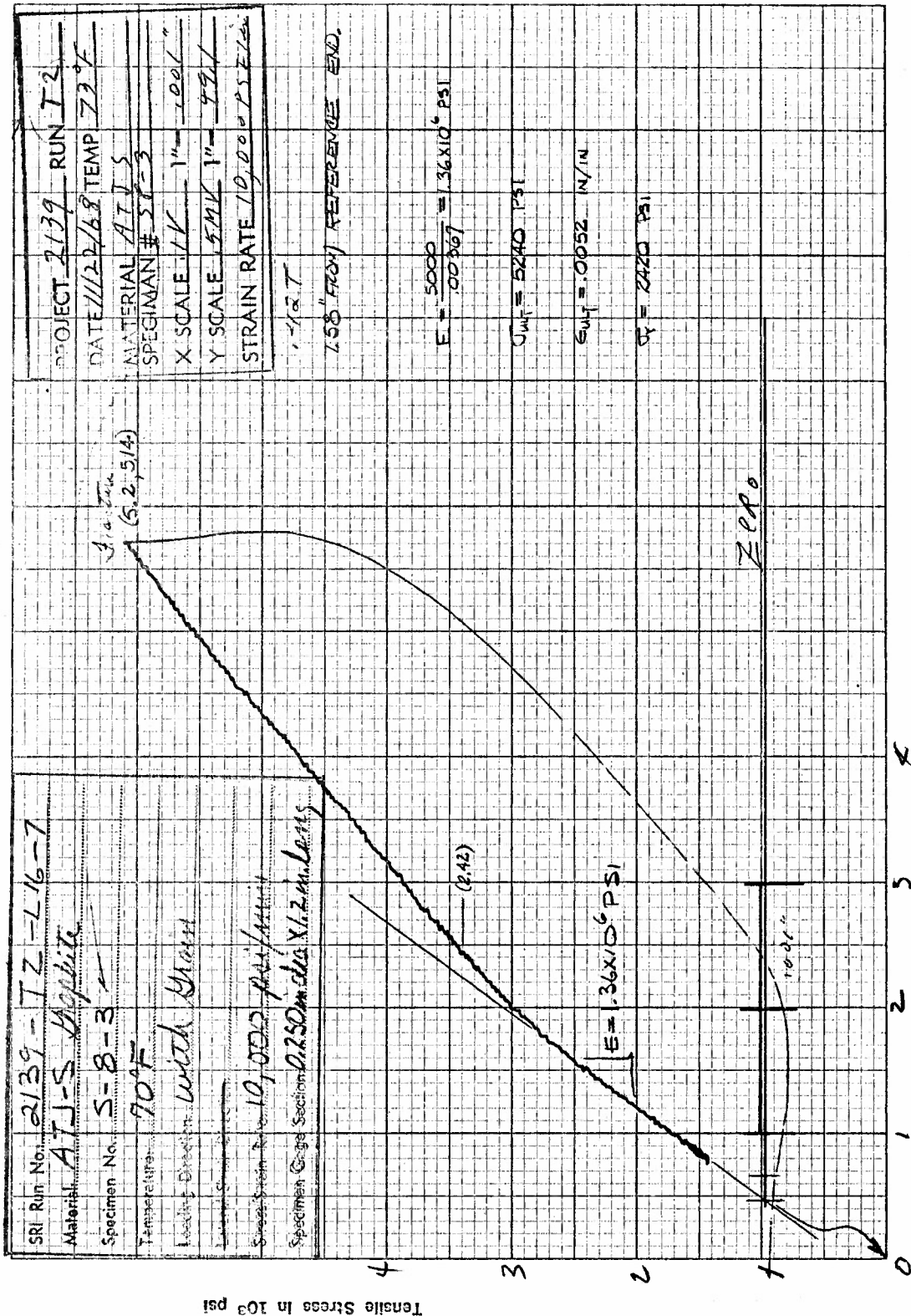


Figure B20. Tensile Stress versus Axial Strain for Specimen S-8-3 of ATJ-S Graphite at 70°F



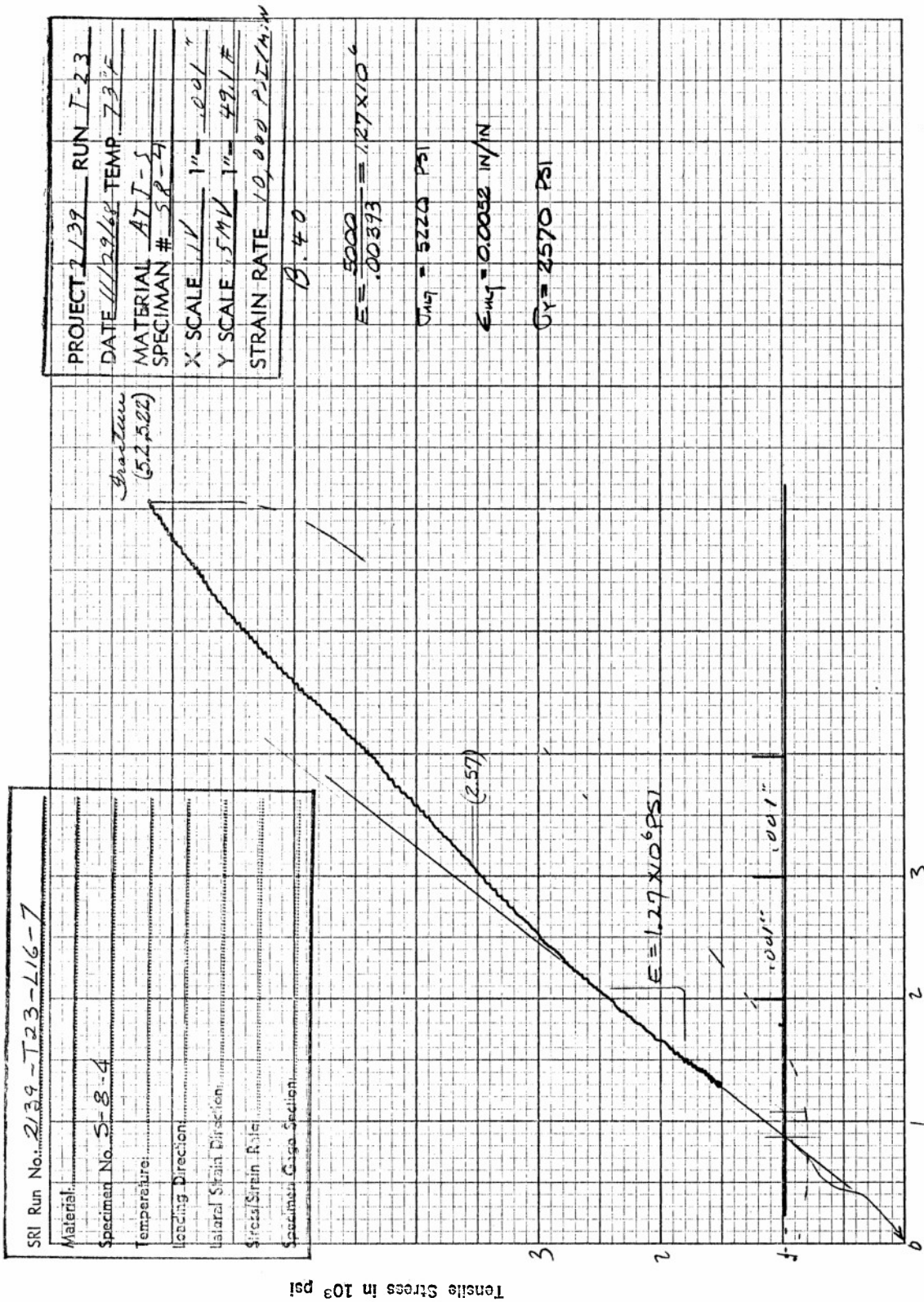


Figure B21. Tensile Stress versus Axial Strain for Specimen S-8-4 of ATJ-S Graphite at 70°F

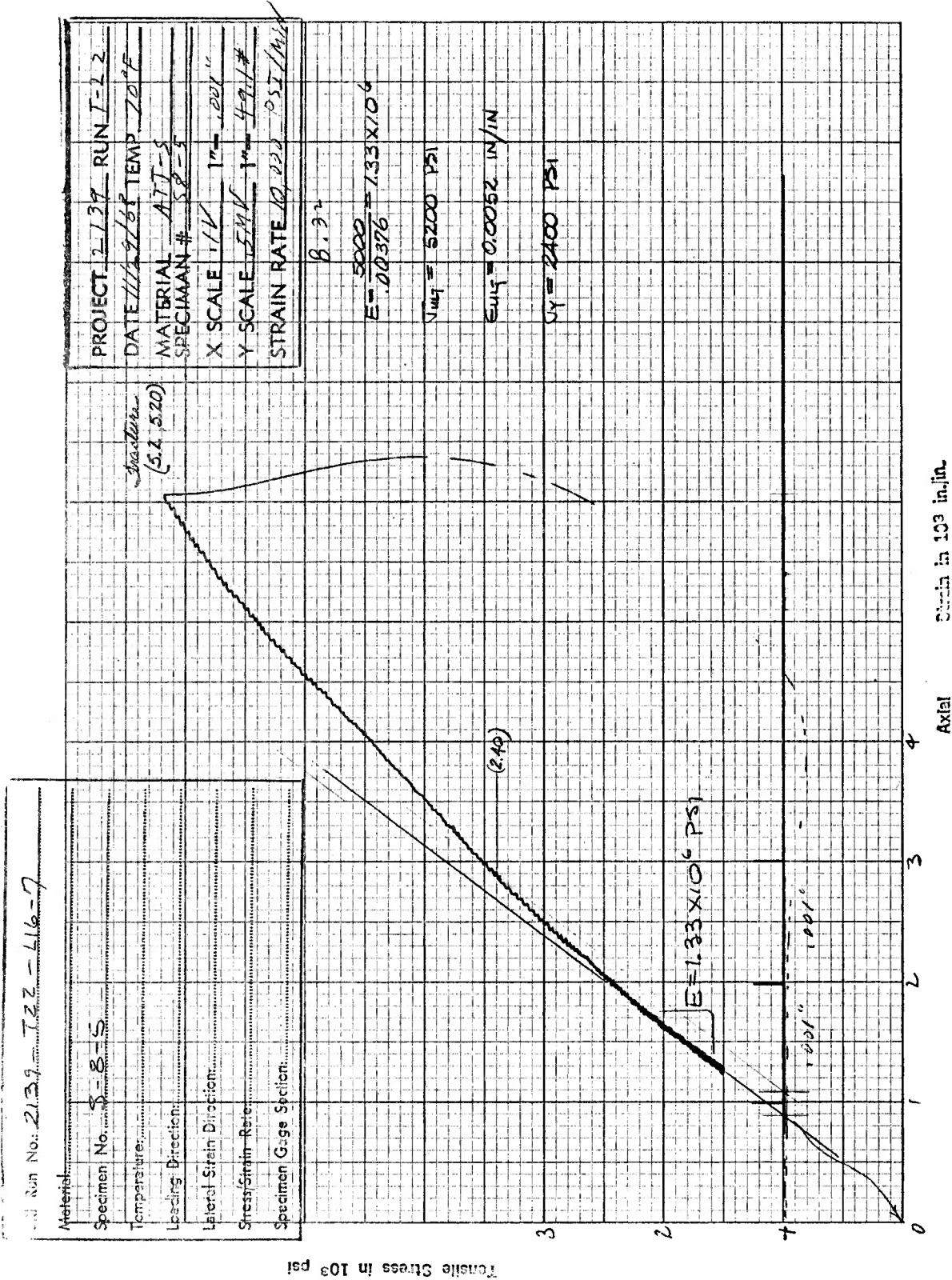


Figure B22. Tensile Stress versus Axial Strain for Specimen S-8-S of ATJ-S Graphite at 70°F

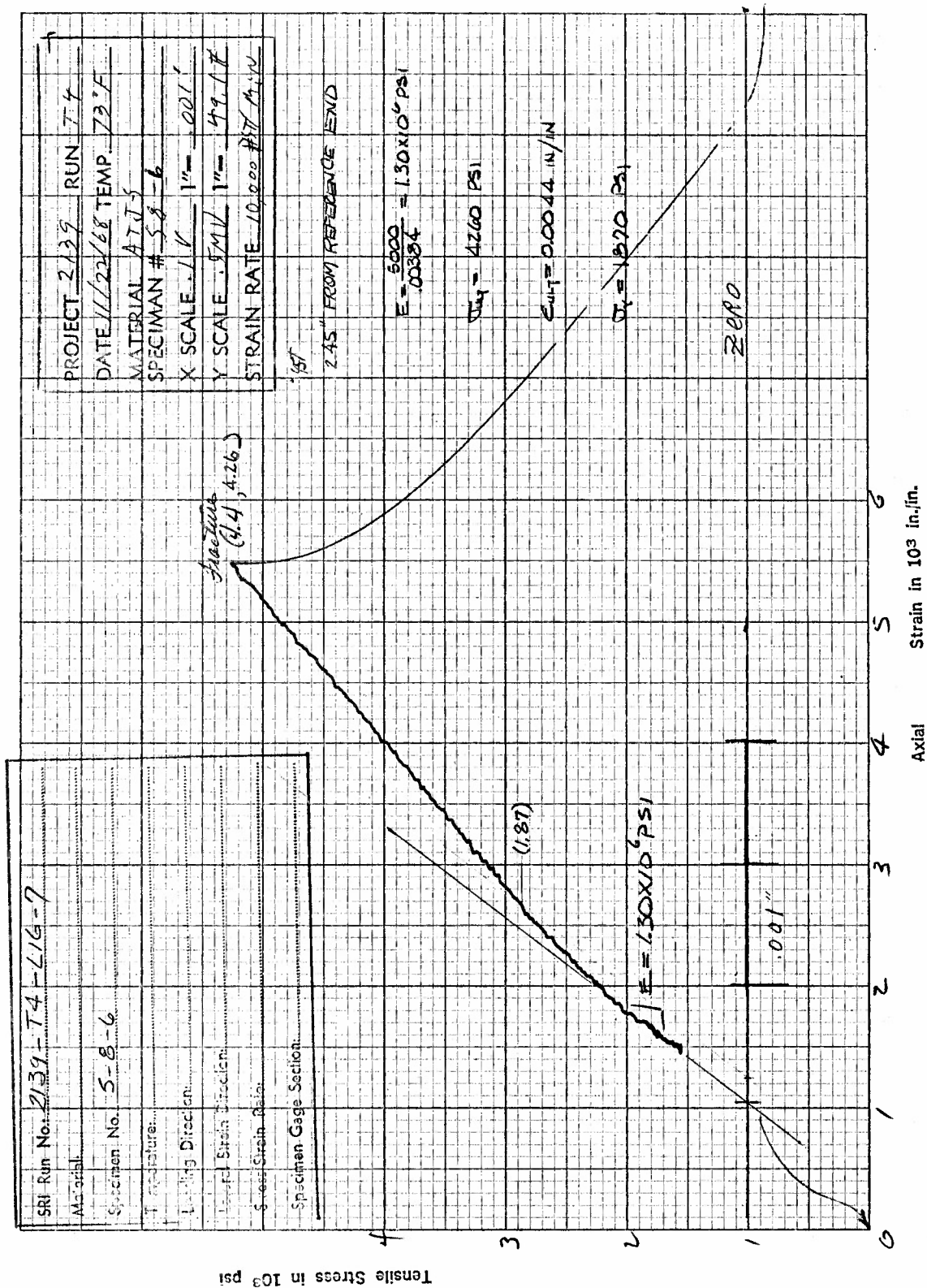


Figure B23. Tensile Stress versus Axial Strain for Specimen S-8-6 of ATJ-S Graphite at 70°F

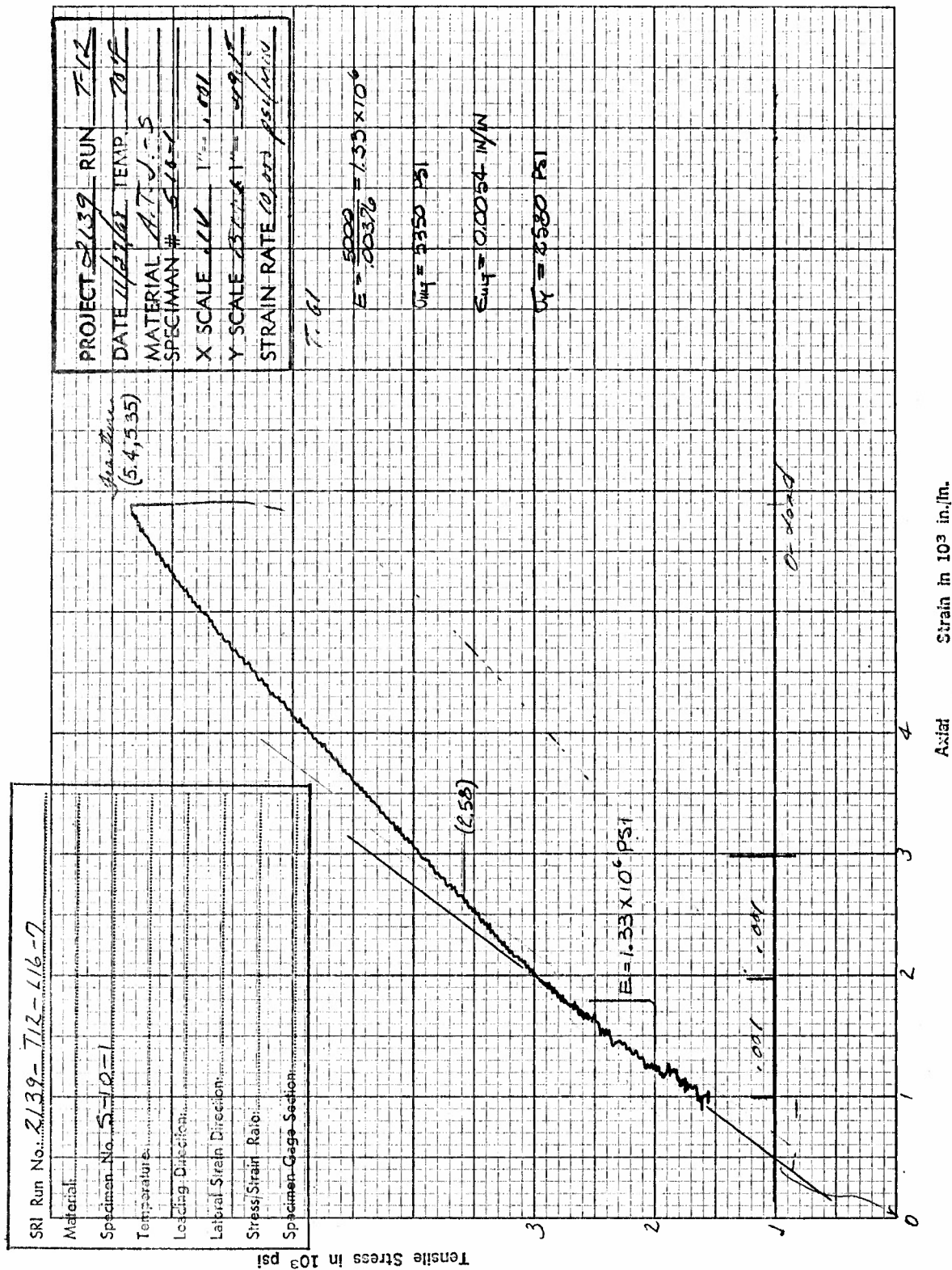


Figure B24. Tensile Stress versus Axial Strain for Specimen S-10-1 of ATJ-S Graphite at 70°F



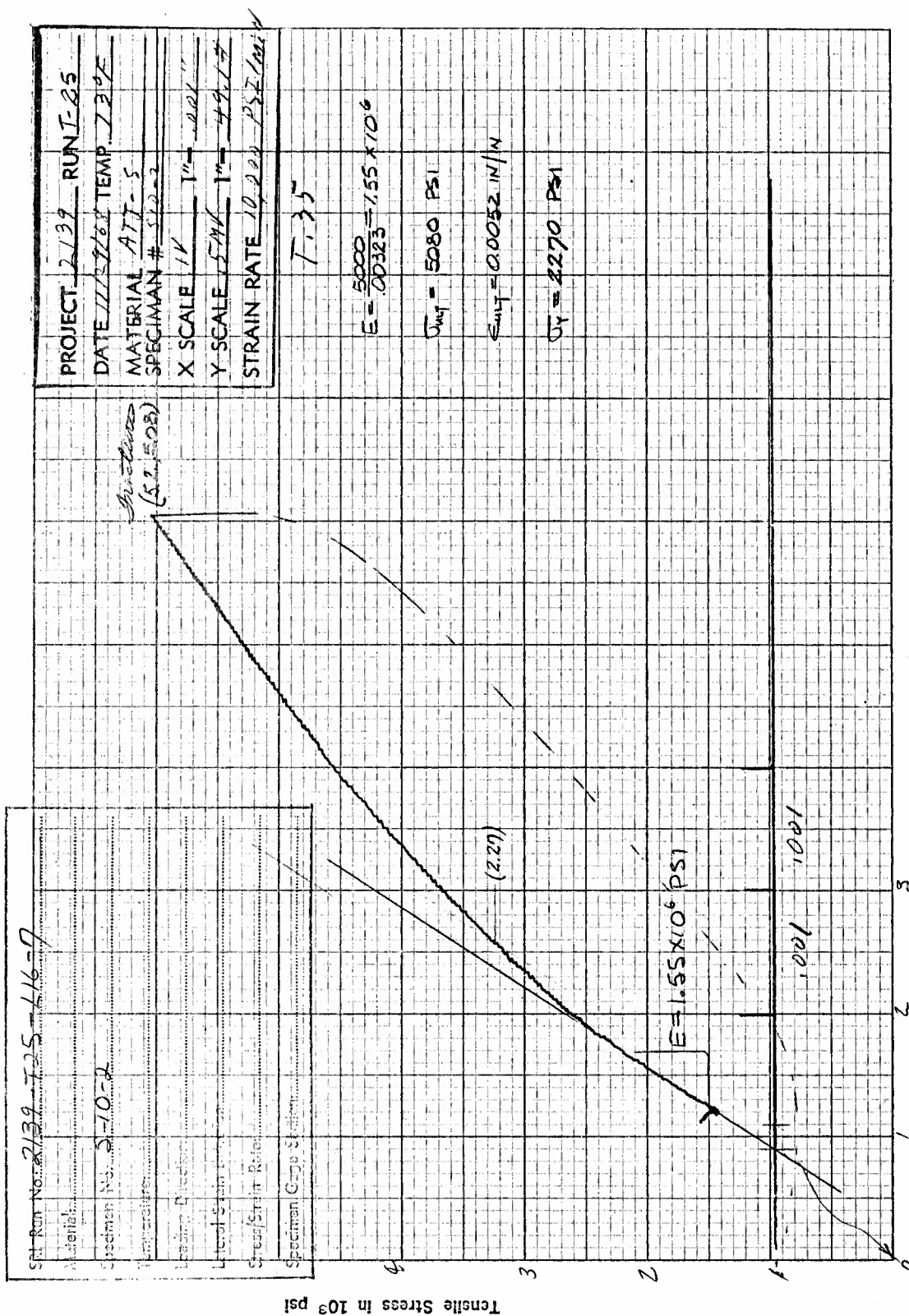


Figure B25. Tensile Stress versus Axial Strain for Specimen S-10-2 of ATT-S Graphite at 70°F

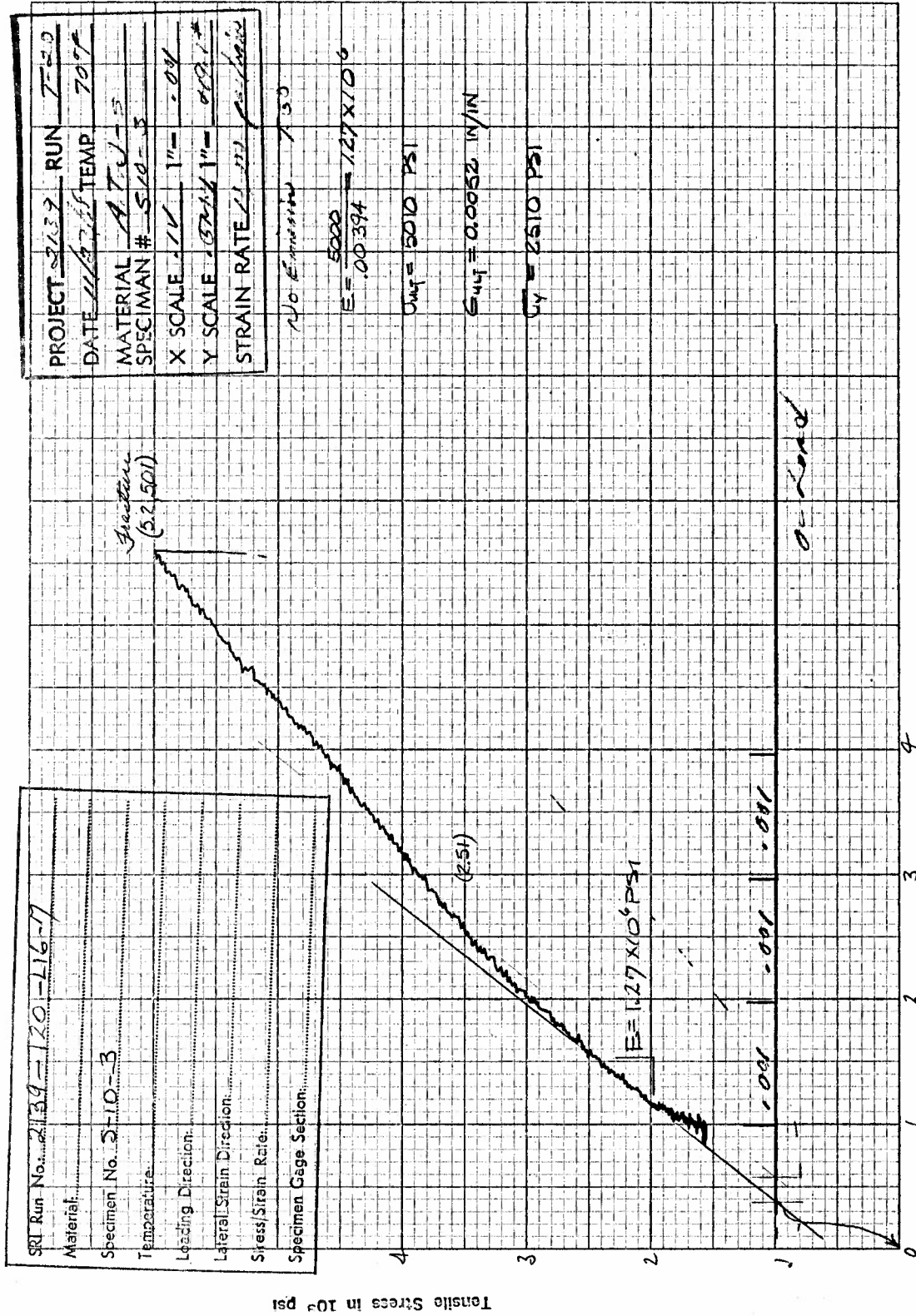


Figure B26. Tensile Stress versus Axial Strain for Specimen S-10-3 of ATJ-S Graphite at 70°F

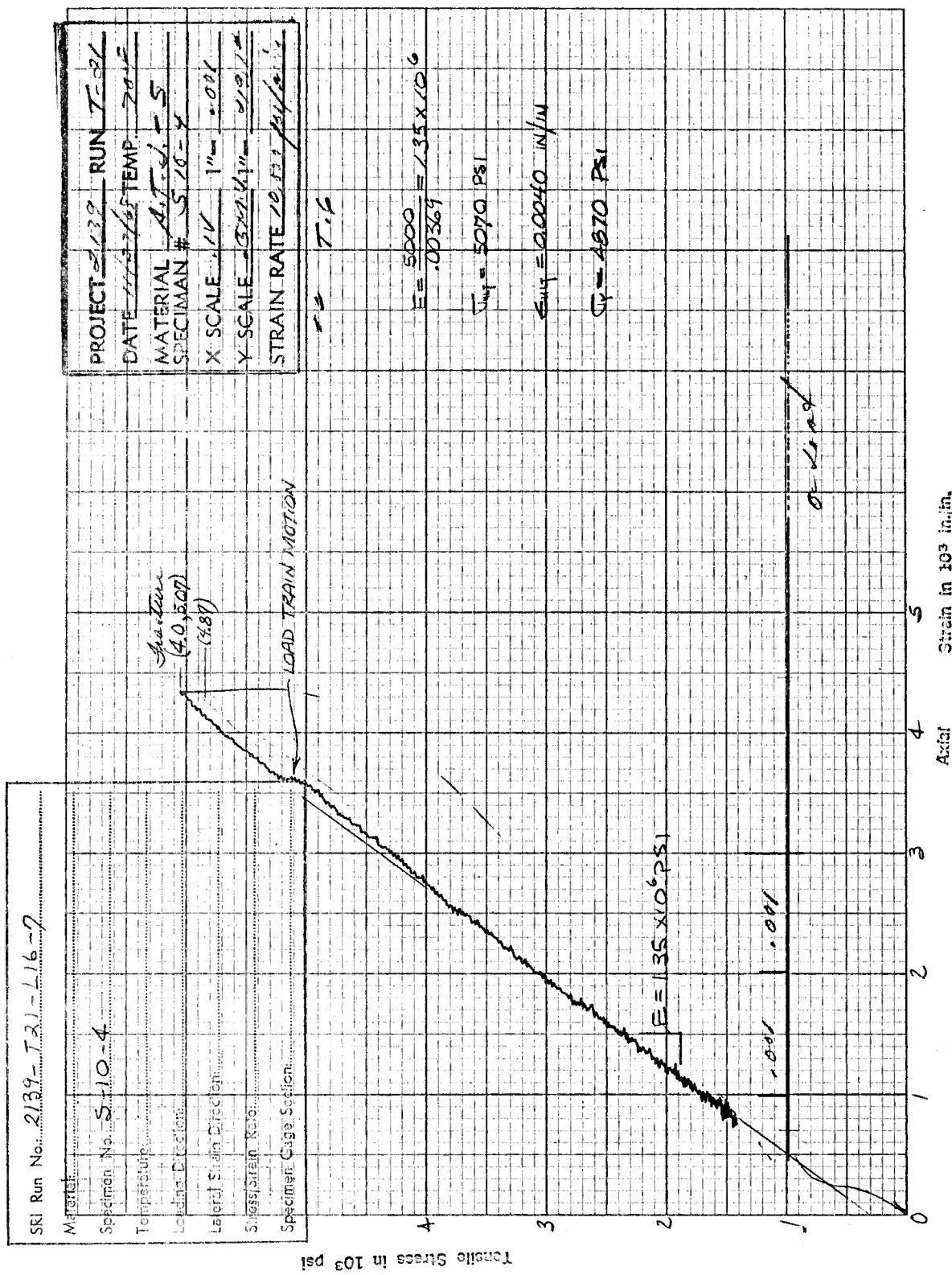


Figure B27. Tensile Stress versus Axial Strain for Specimen S-10-4 of ATJ-S Graphite at 70°F

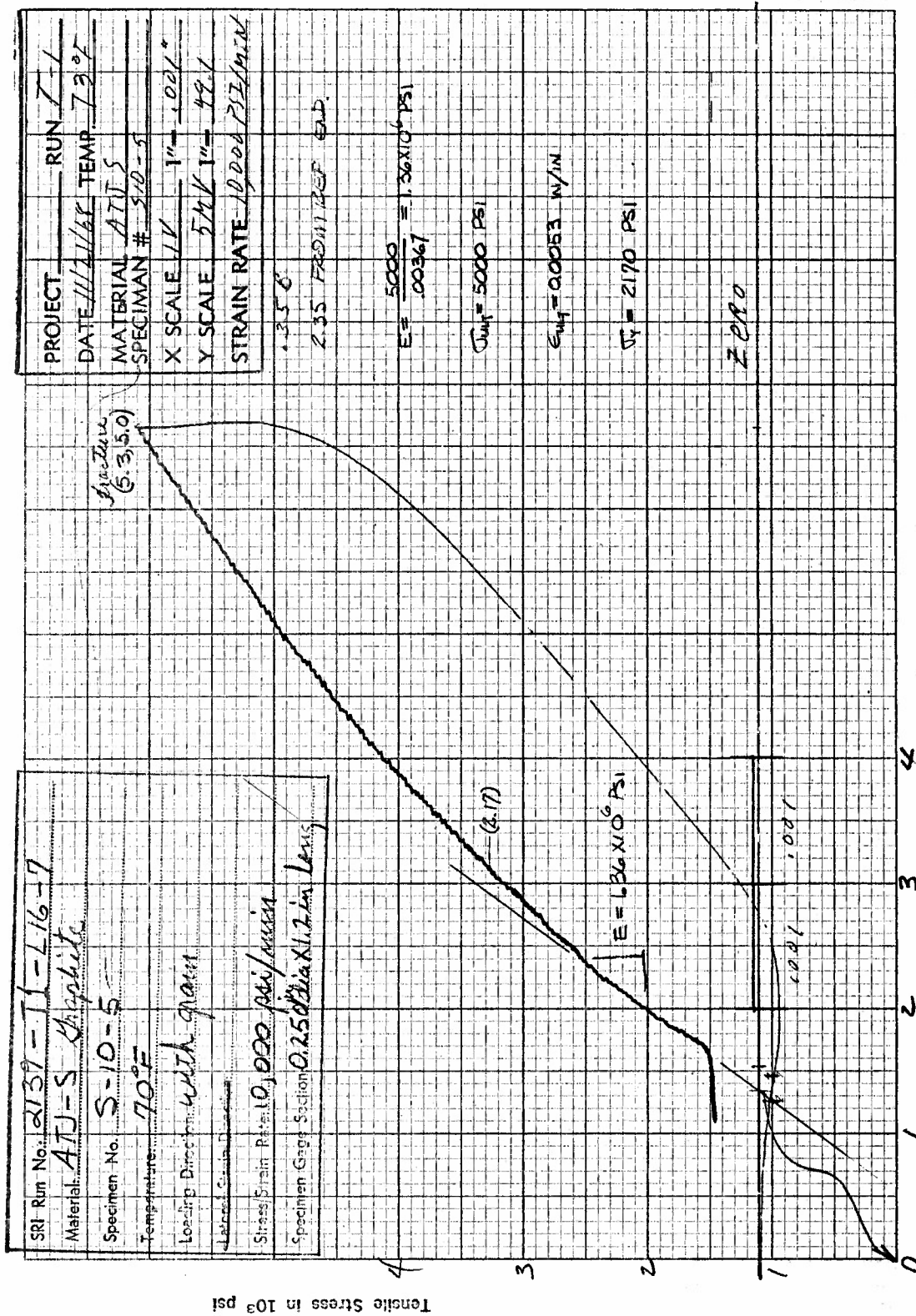


Figure B28. Tensile Stress versus Axial Strain for Specimen S-10-5 of ATJ-S Graphite at 70°F



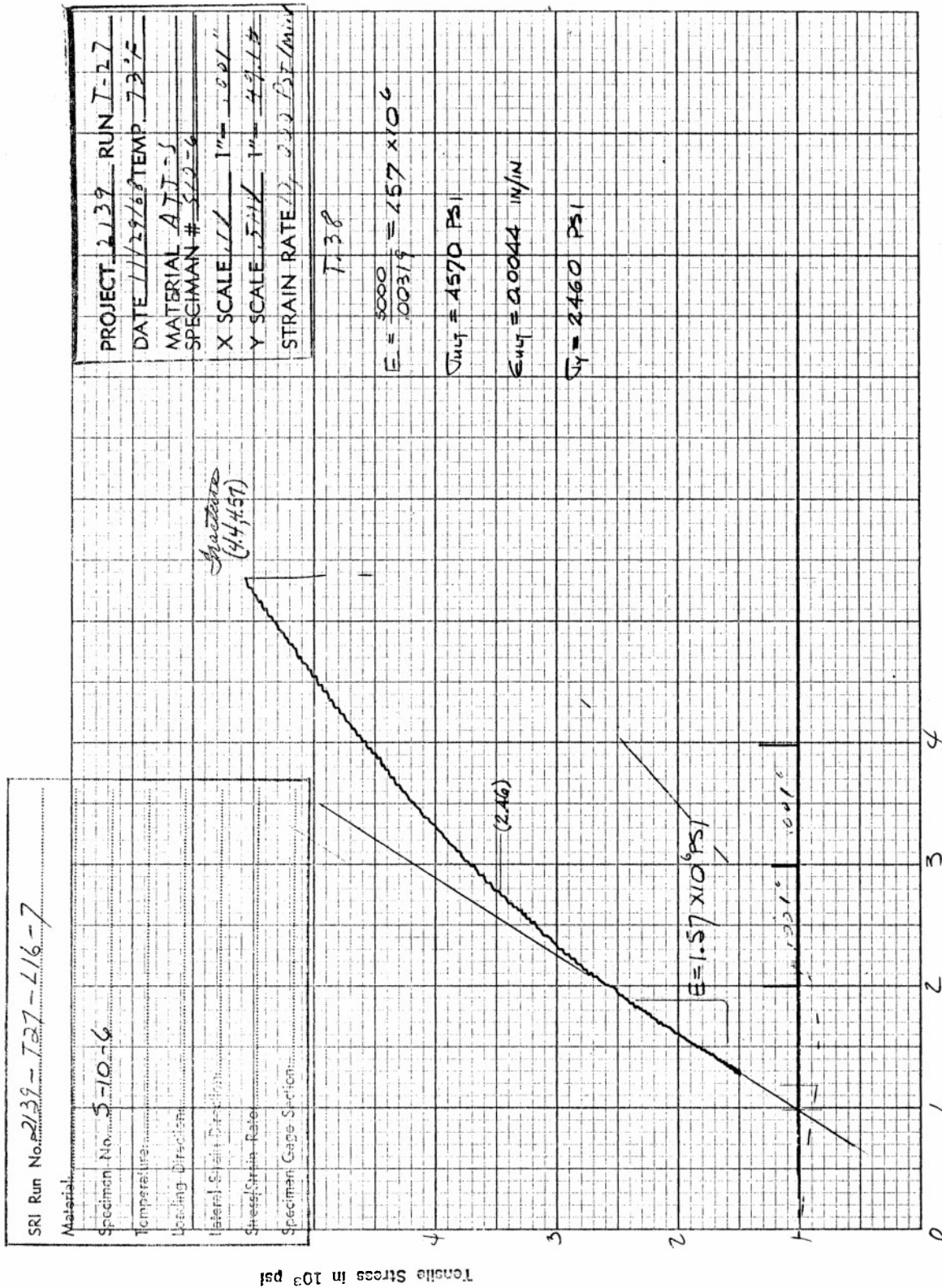


Figure B29. Tensile Stress versus Axial Strain for Specimen S-10-6 of ATJ-S Graphite at 70°F

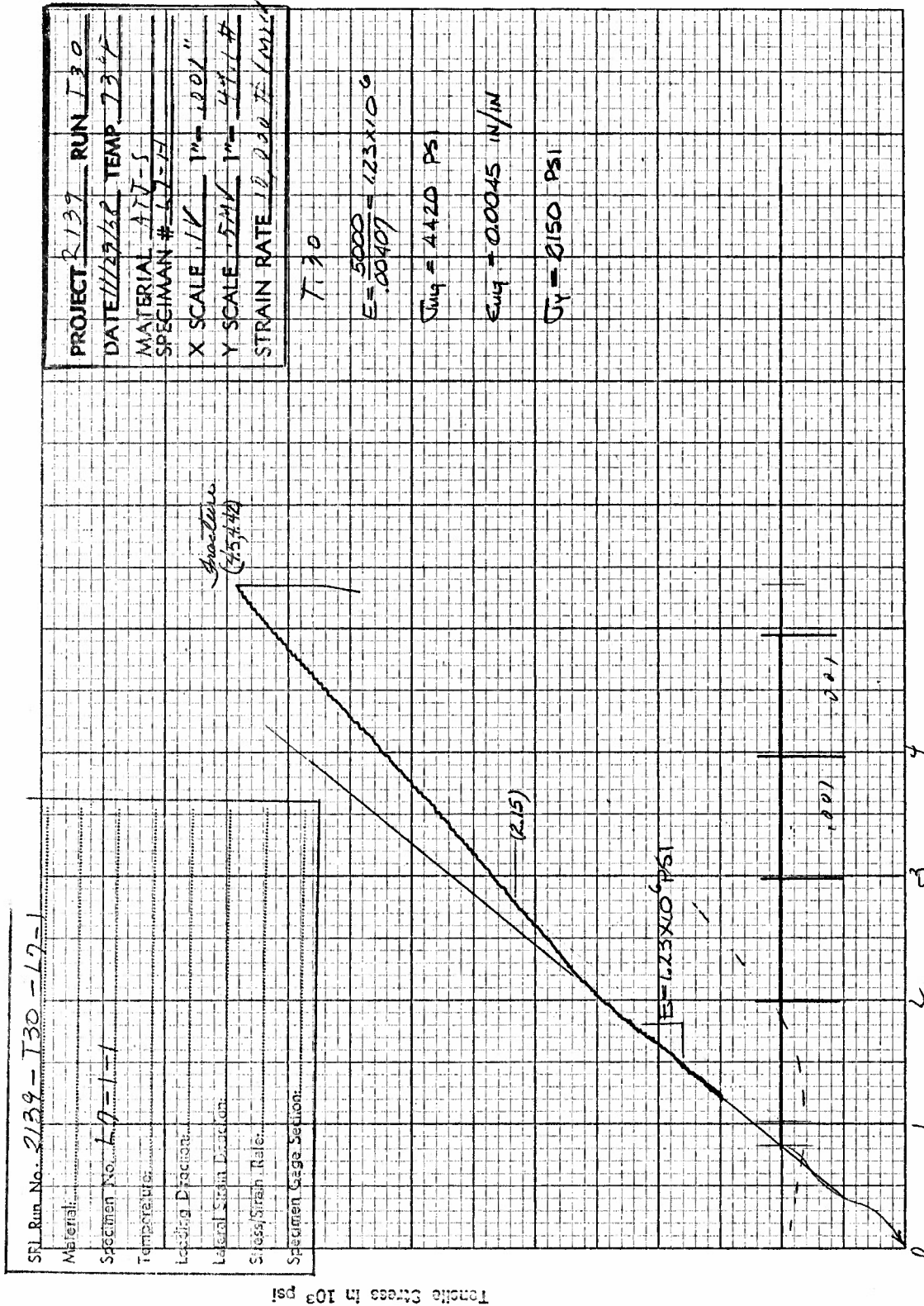


Figure B30. Tensile Stress versus Axial Strain for Specimen L7-1-1 of ATJ-S Graphite at 70°F

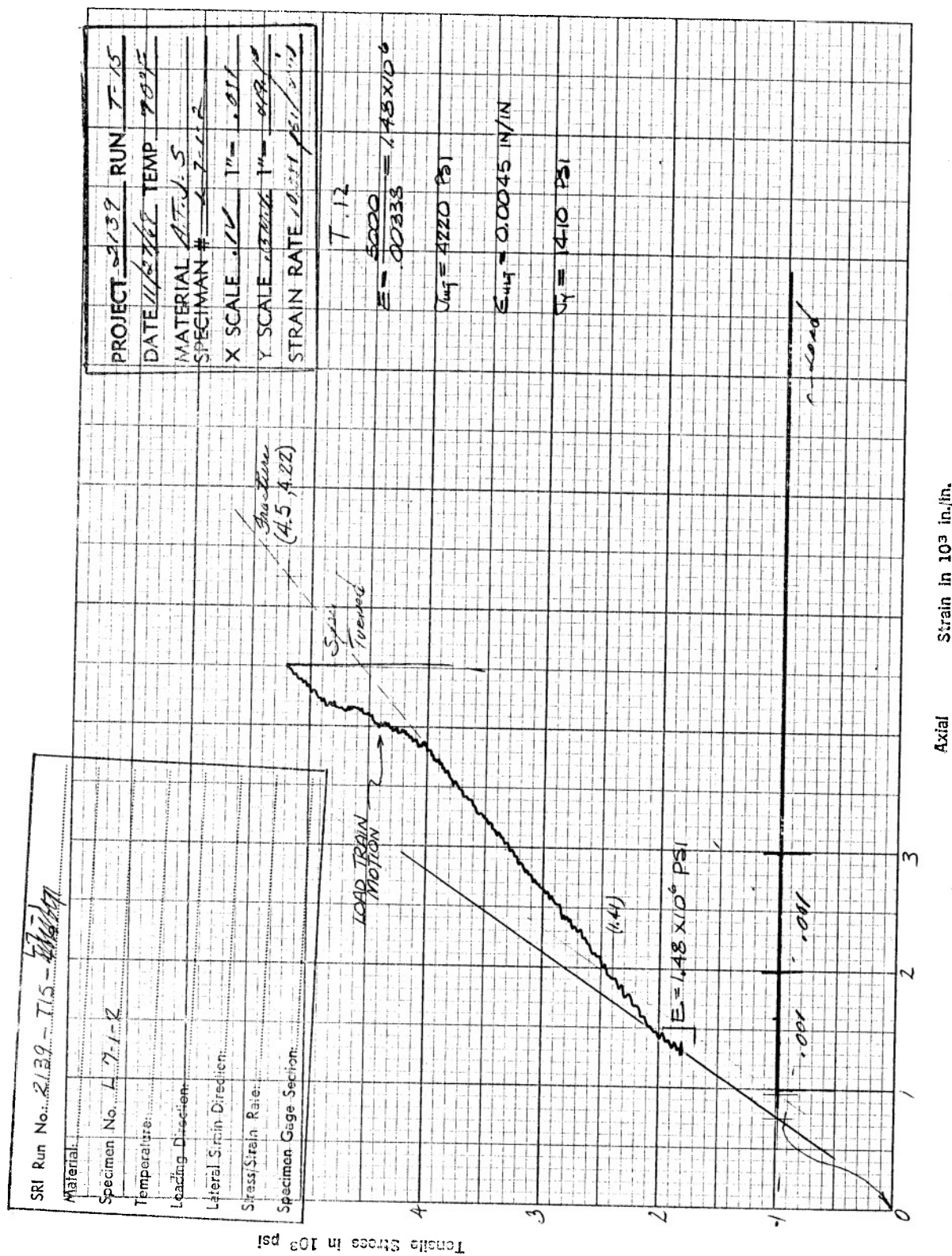


Figure B31. Tensile Stress versus Axial Strain for Specimen L7-1-2 of ATJ-S Graphite at 70°F





## APPENDIX C

Results of Microprobe and Electron Microscopy on  
Disparate S6-5 of ATJ-S Billet L-16-7



August 27, 1969

MEMO TO: C. D. Pears  
FROM: R. E. Bickelhaupt *R.E.B.*  
SUBJECT: Project 2139, Specimen S-6-5, Billet L-16-7

---

The subject specimen was one which failed at a stress lower than expected based on a plot of fracture stress versus percent open porosity. The fracture surface was examined by microprobe and electron microscopy.

The microprobe results were completely negative. No impurity was found on the fracture surface or in the sub-fracture structure as revealed by the polished section at an elevation of about 15 to 20 mils below fracture. The elements calcium and those greater in atomic number were sought.

In the process of grinding off the fracture surface, prior to making a polished section, what is thought to be a disparate void or large pore was observed. Its cross section became obvious after 5 mils of the fracture face was removed, and its presence was observed until 15 to 20 mils of material was removed. Using the replicas of the original fracture surface, an attempt was made to relate this void to the fracture surface. It was learned that the general roughness of the fracture face was about 5 mils, peaks to valleys. Therefore, the void was visible to the naked eye as soon as the general fracture roughness was eliminated. However, it was not possible to prove that the void was related to the fracture face either by the orientation or depth of the void as related to the replicated surface. As a suggestion, it might be well to impregnate and polish the remaining fracture face just on the chance that a void of similar geometry may appear in this half.

Both fracture faces were examined by electron microscopy. Photomicrographs at 7000x are available for observation. Since these are the first electron fractographs we have made of a graphitic material, interpretation is almost meaningless. Nothing relative to the critical area defined by the flicks or the large pore is apparent. Perhaps after examining many pictures of several types of graphite, both weak and strong, we may acquire a skill in this interpretation.

lg



## APPENDIX D

Results of Avco Ultrasonic Inspection of ATJ-S  
Billet L-1-4



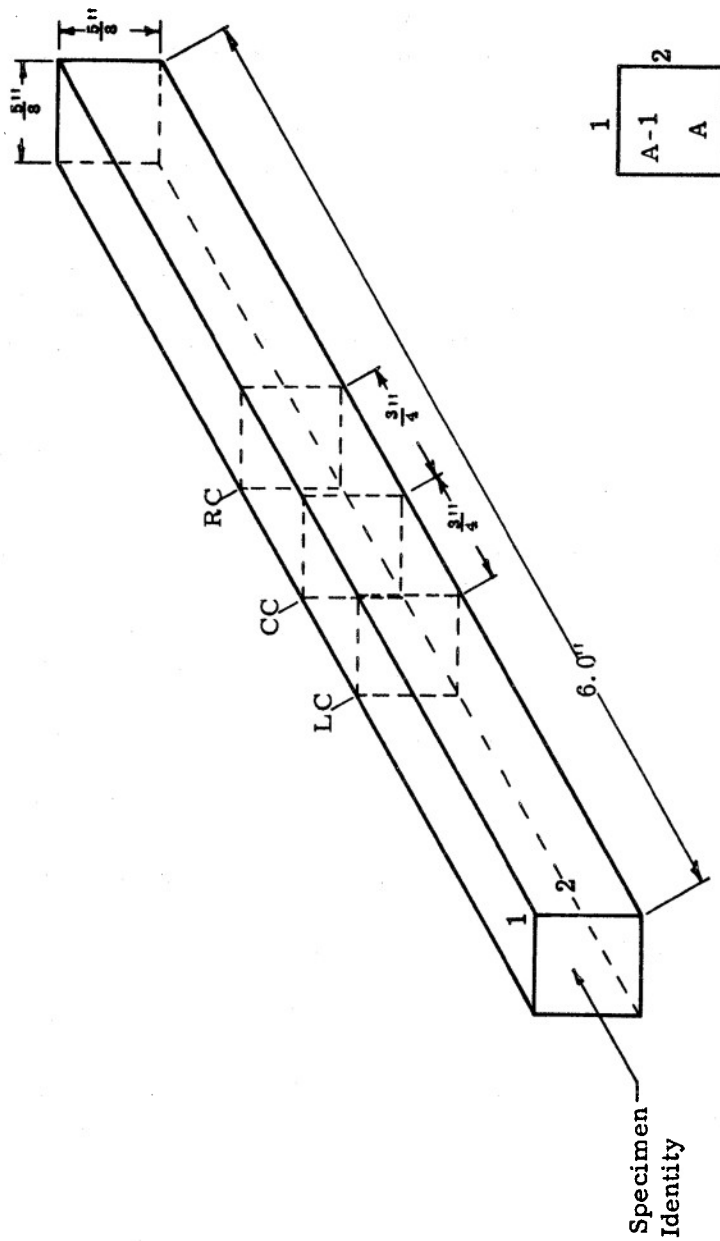
## Avco Ultrasonic Inspection Results for ATJ-S Graphite Billet L-1-4

### Explanation of Symbols:

1. Refer to Figure D1 for the significance and relationships of the numbers "1" and "2" as located on the left-hand ends of the tensile blank lay-outs.
2. The lay-outs represent two surfaces or faces of each tensile blank, even though ultrasonic testing was performed on all four faces of each specimen.
3. Circled areas designate detected discontinuities; solid circles indicating anomalies detected from sides #1 and #2, dotted circles indicating those anomalies detected from the opposite sides (i. e. those sides located 180° from sides #1 and #2).
4. The figures beside each indicated suspect area are the depths below surface at which the discontinuity may be found.
5. The letter designations refer to relative size of discontinuity thus:
  - S - Small, according to the level of test sensitivity this signal amplitude was observed just above "noise" level.
  - M - Medium, signal amplitude significantly above noise level.
  - L - Large, signal amplitude readily observed above noise level.
  - VL - Very large indication with high signal amplitude.
  - BE - Attenuation of back-echo amplitude.
  - VC - Velocity change.
6. Plotted discontinuity indications which are located outside the gauge length are included as supplementary information.
7. Solid line indicates fracture location.

Typical Identity  
of Radial Specimens

1	2
A-7	
W	



Typical Identity  
of Axial Specimens

1	2
A-1	
A	

Figure D1. Avco Sketch of Tensile Blank Specimen Describing Ultrasonic Inspection Symbols and Nomenclature



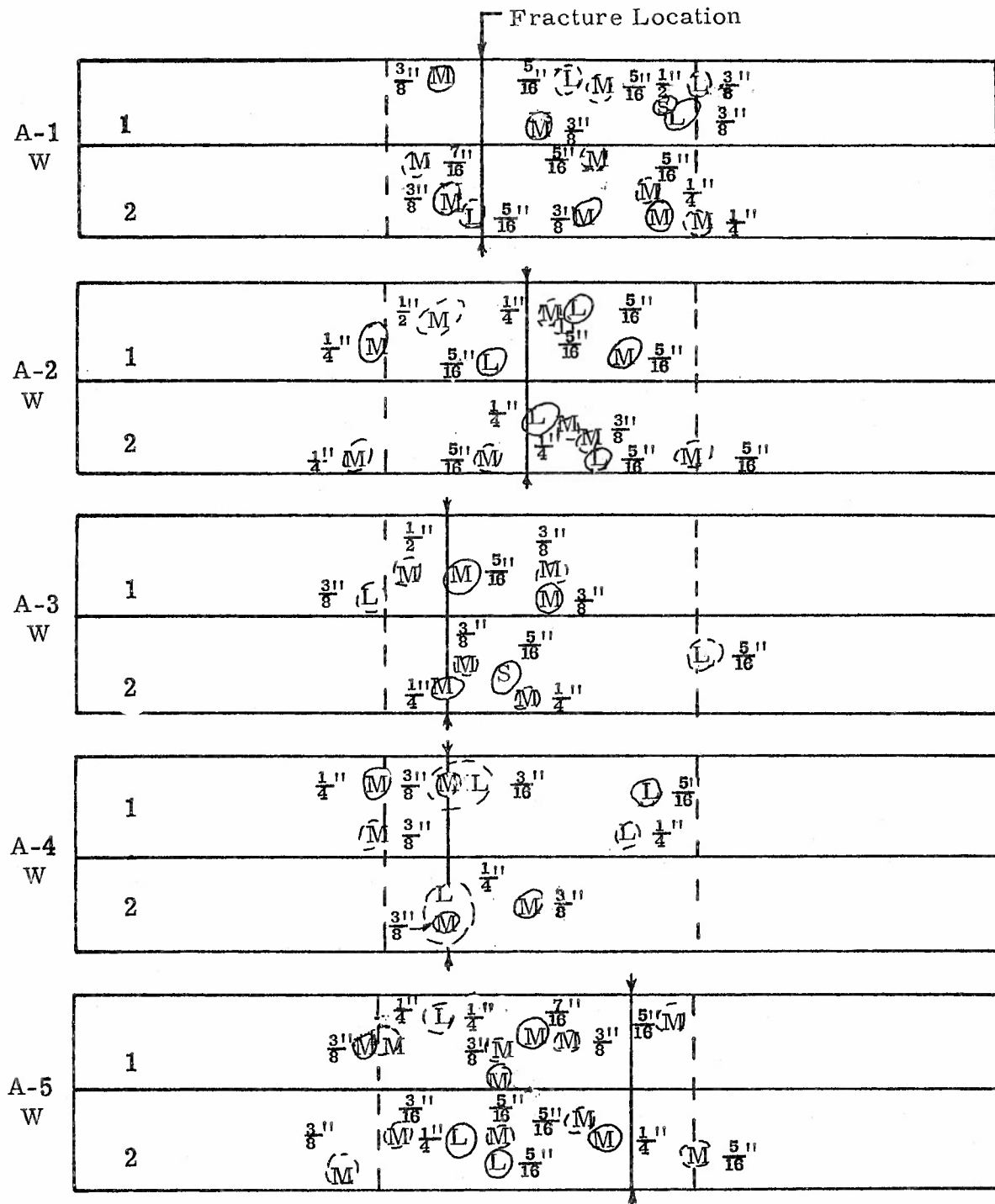


Figure D2

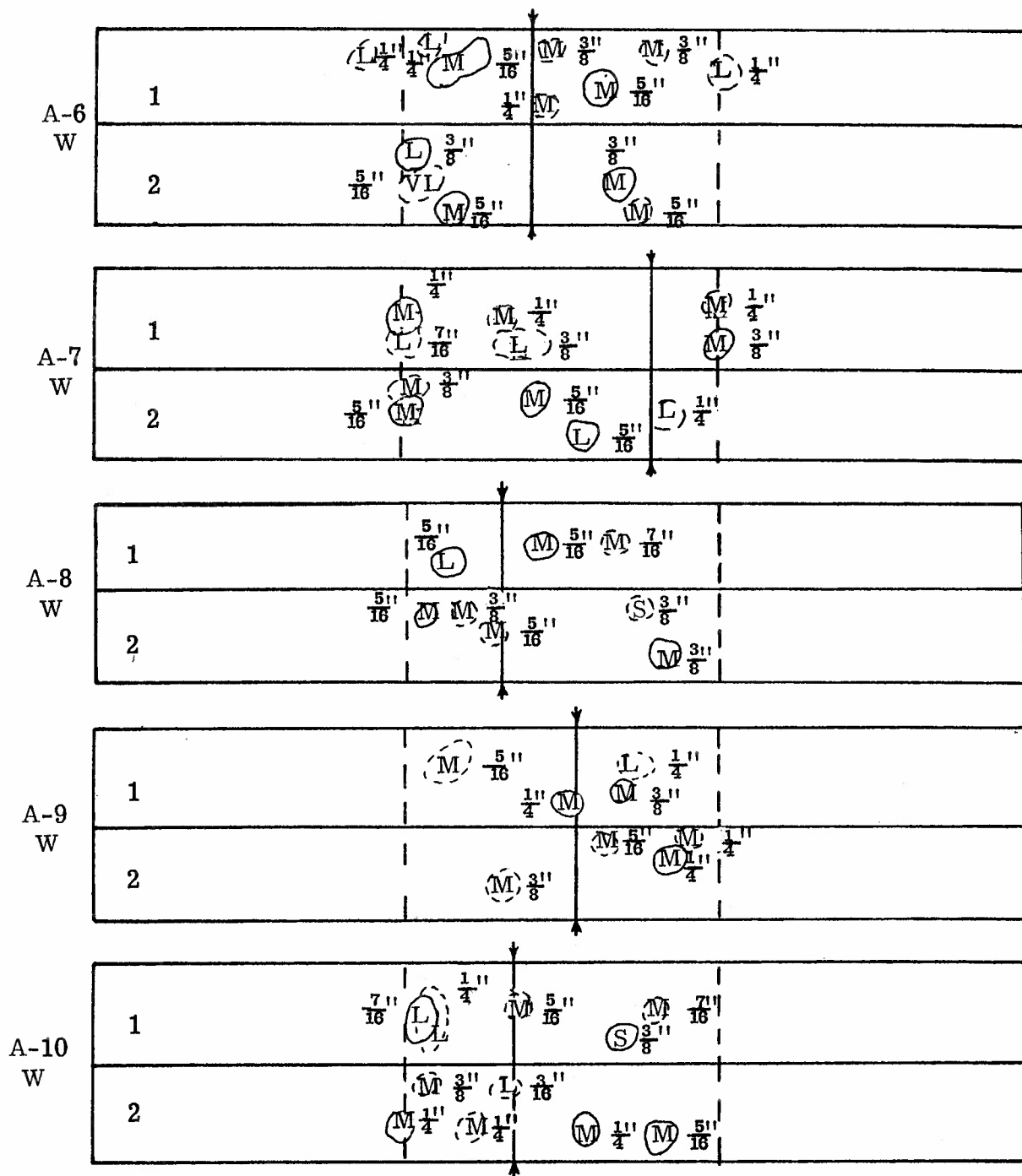


Figure D3

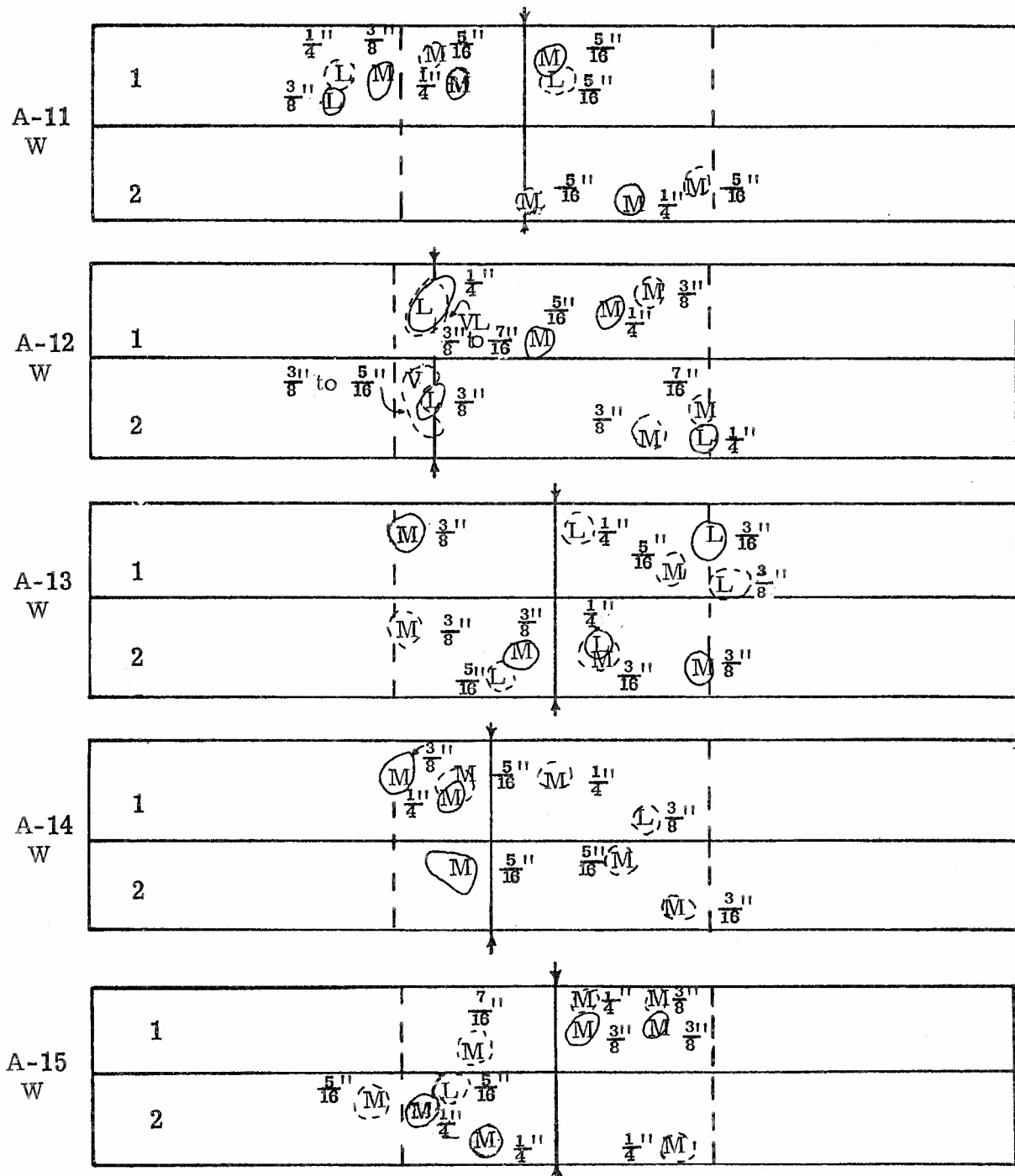


Figure D4

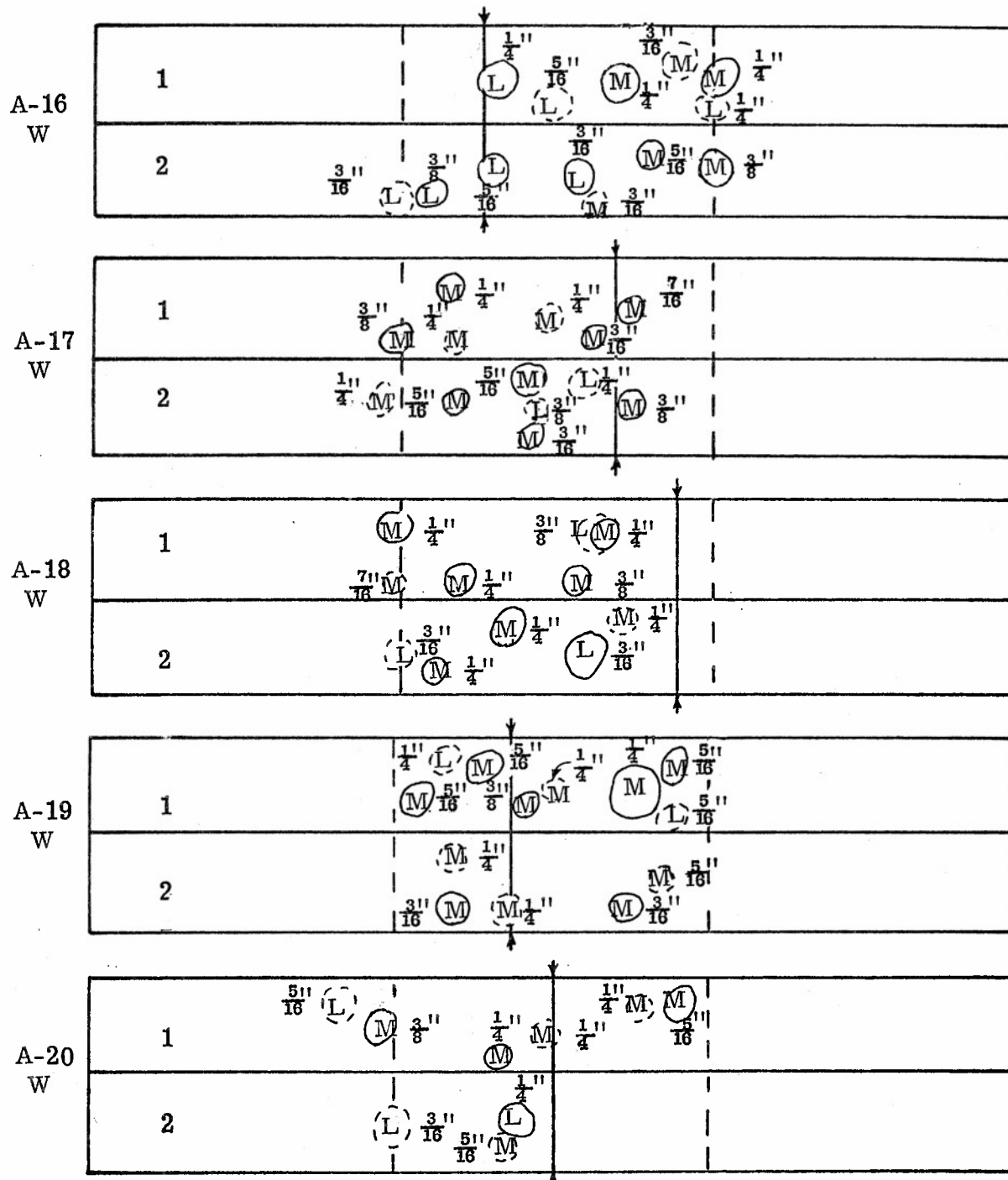


Figure D 5

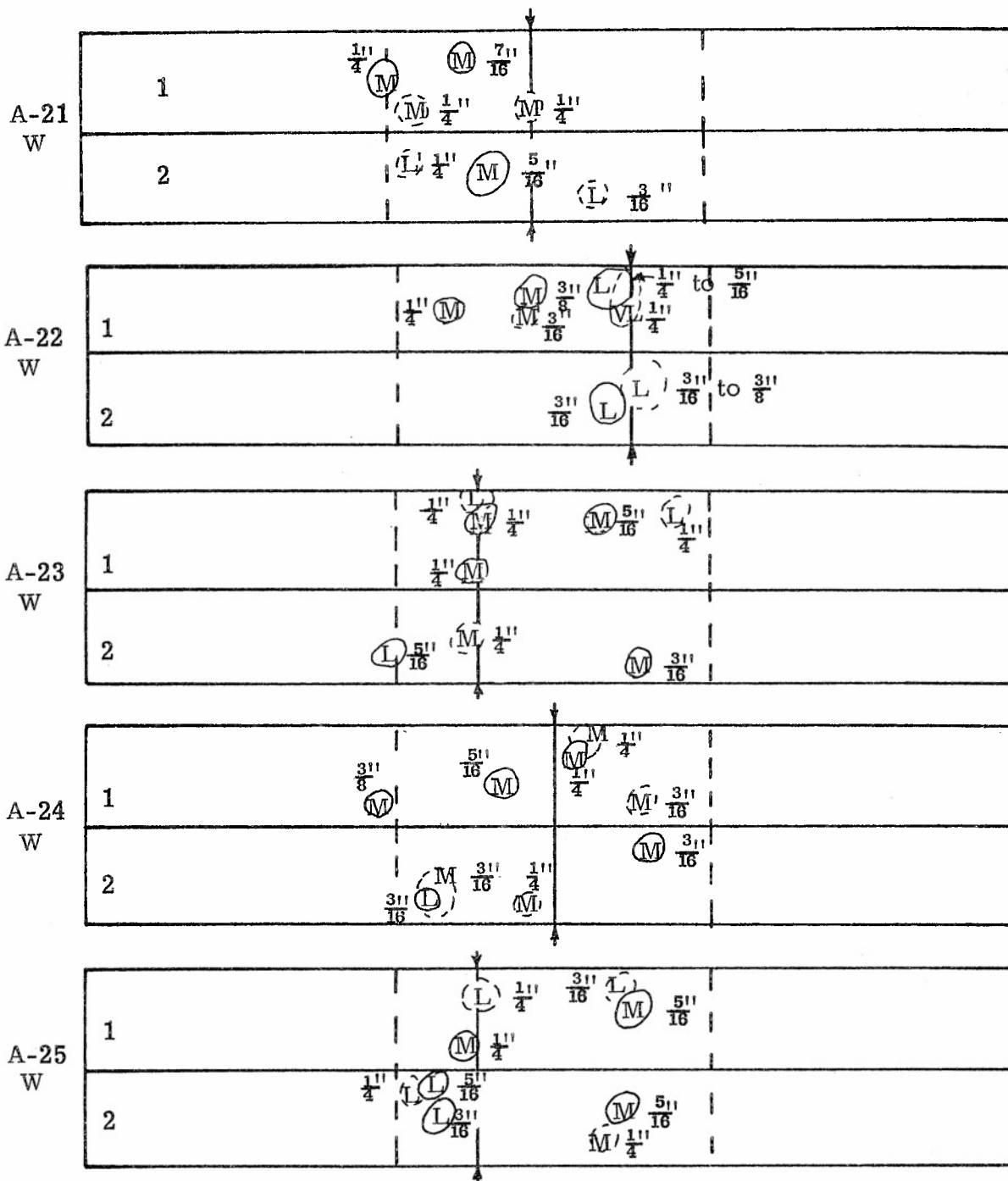


Figure D6

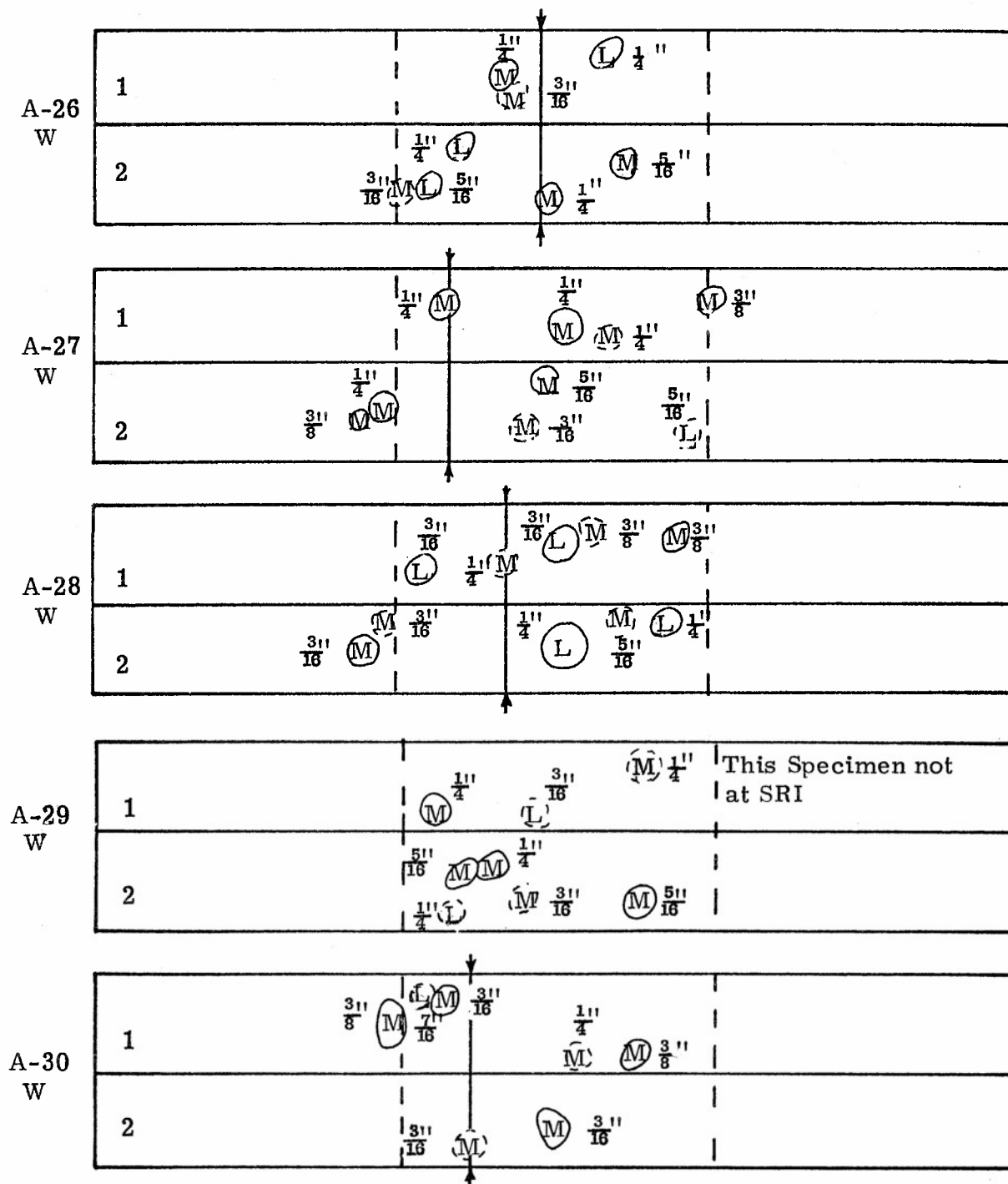


Figure D7

A-31  
W

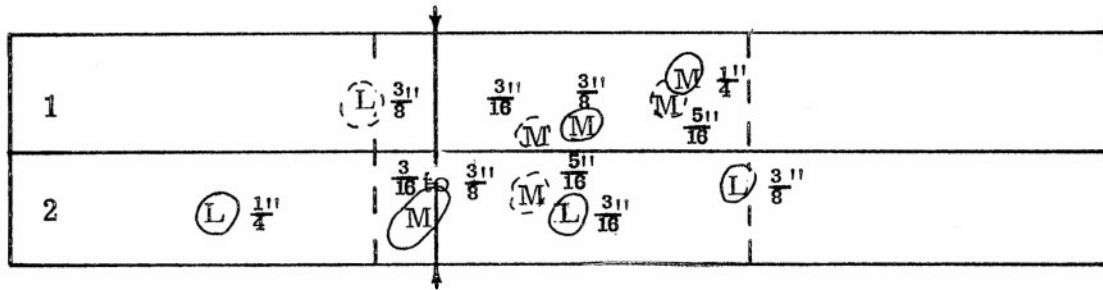


Figure D8

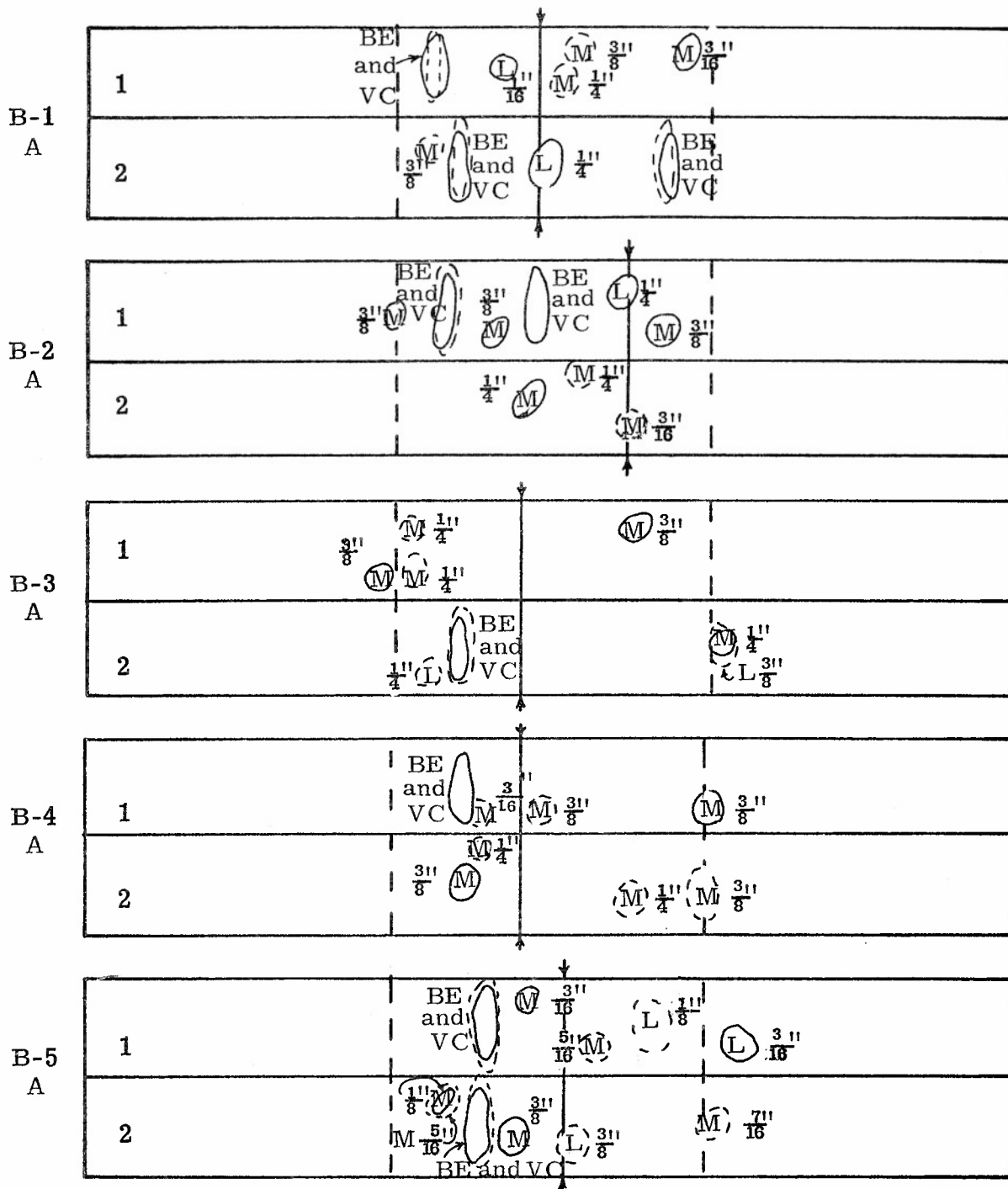


Figure D9



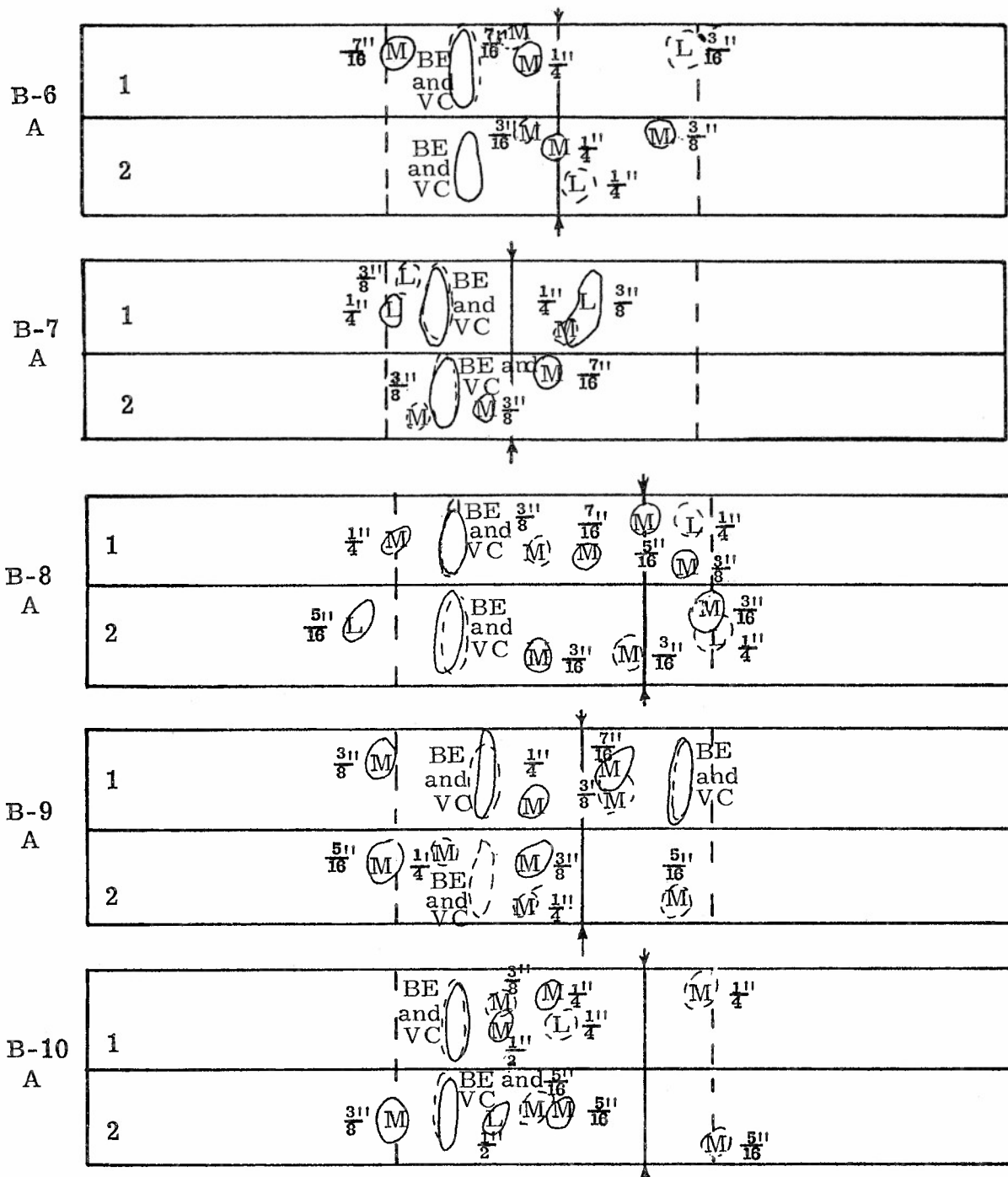


Figure D10

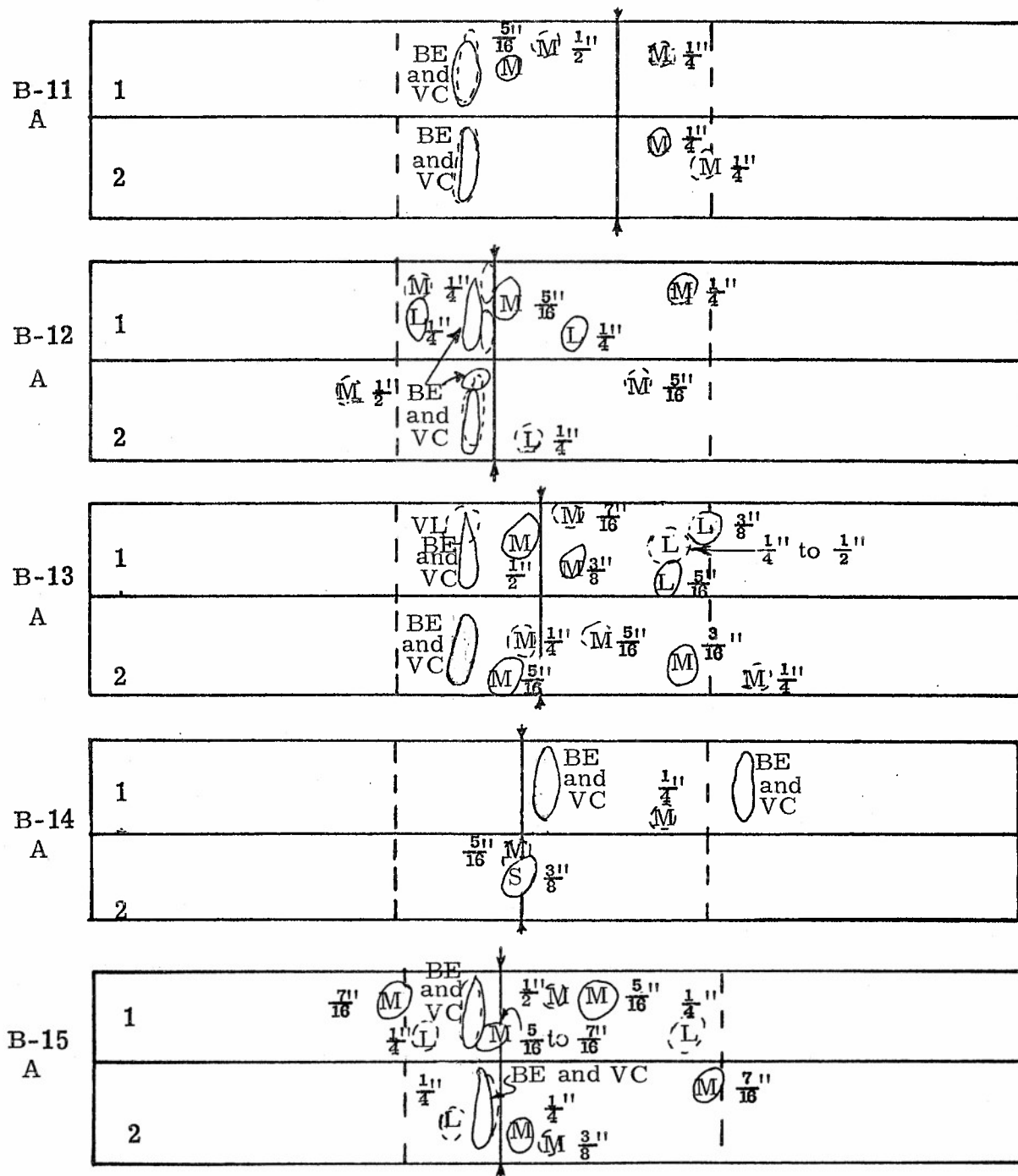


Figure D11

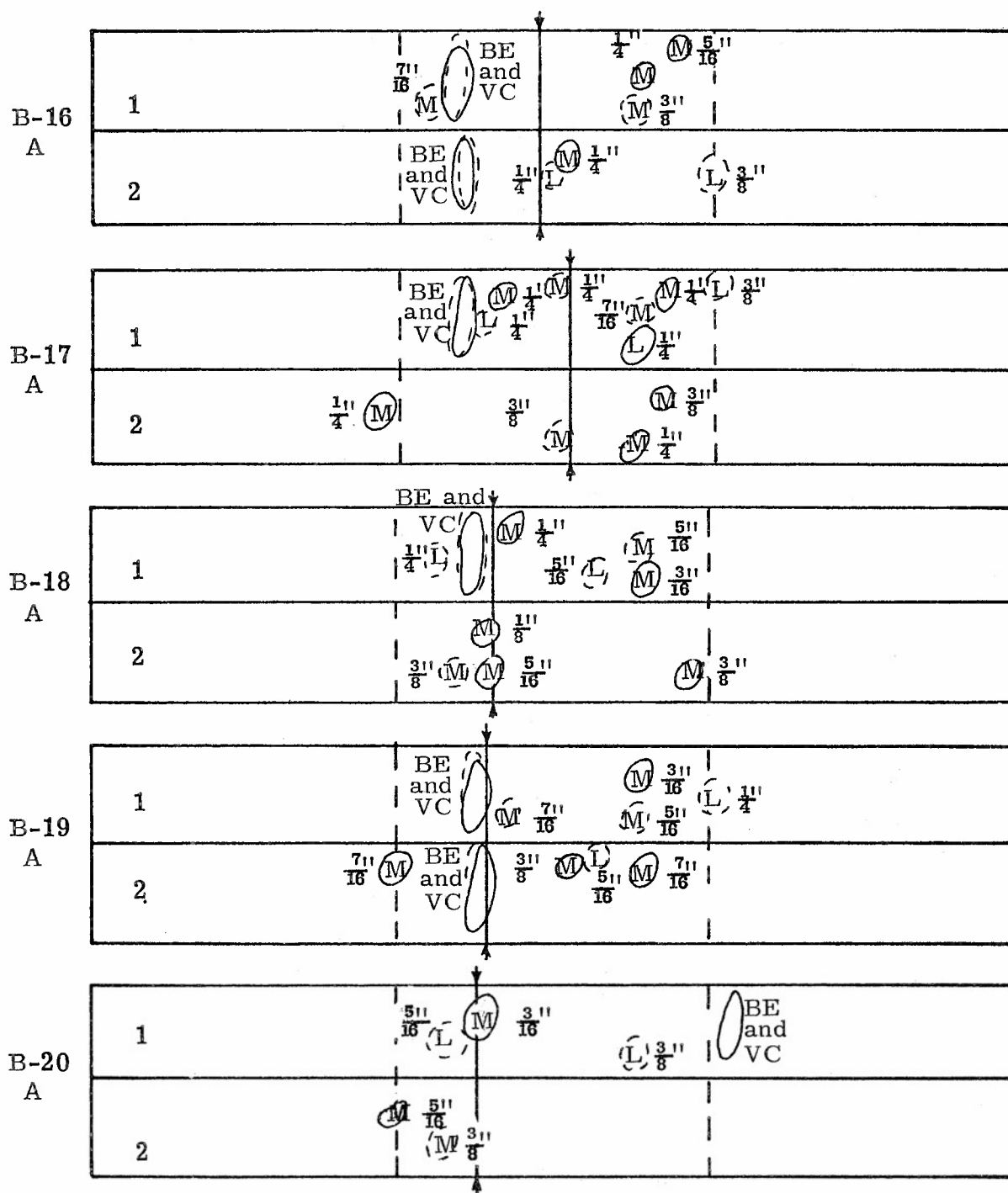


Figure D12

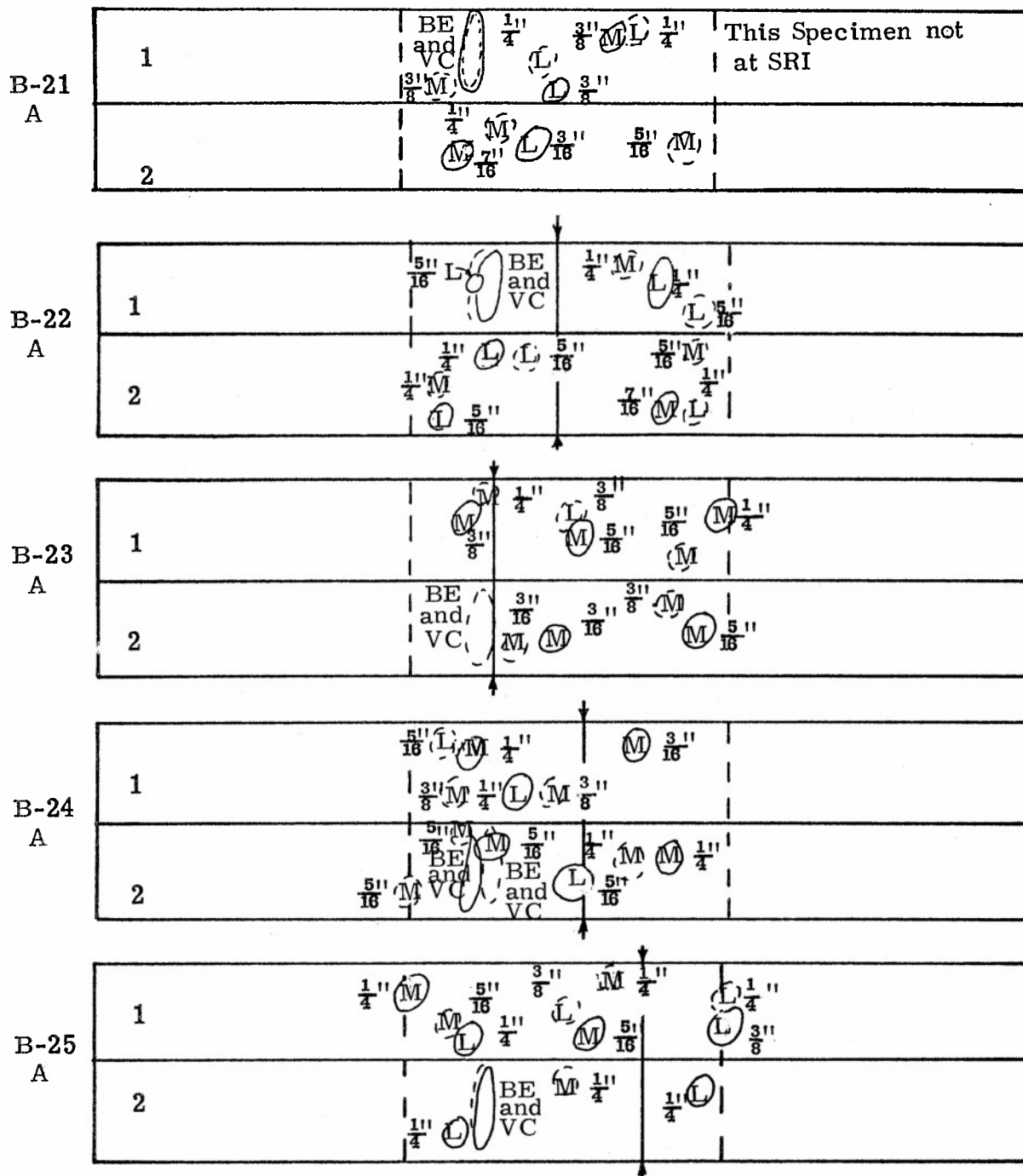


Figure D 13

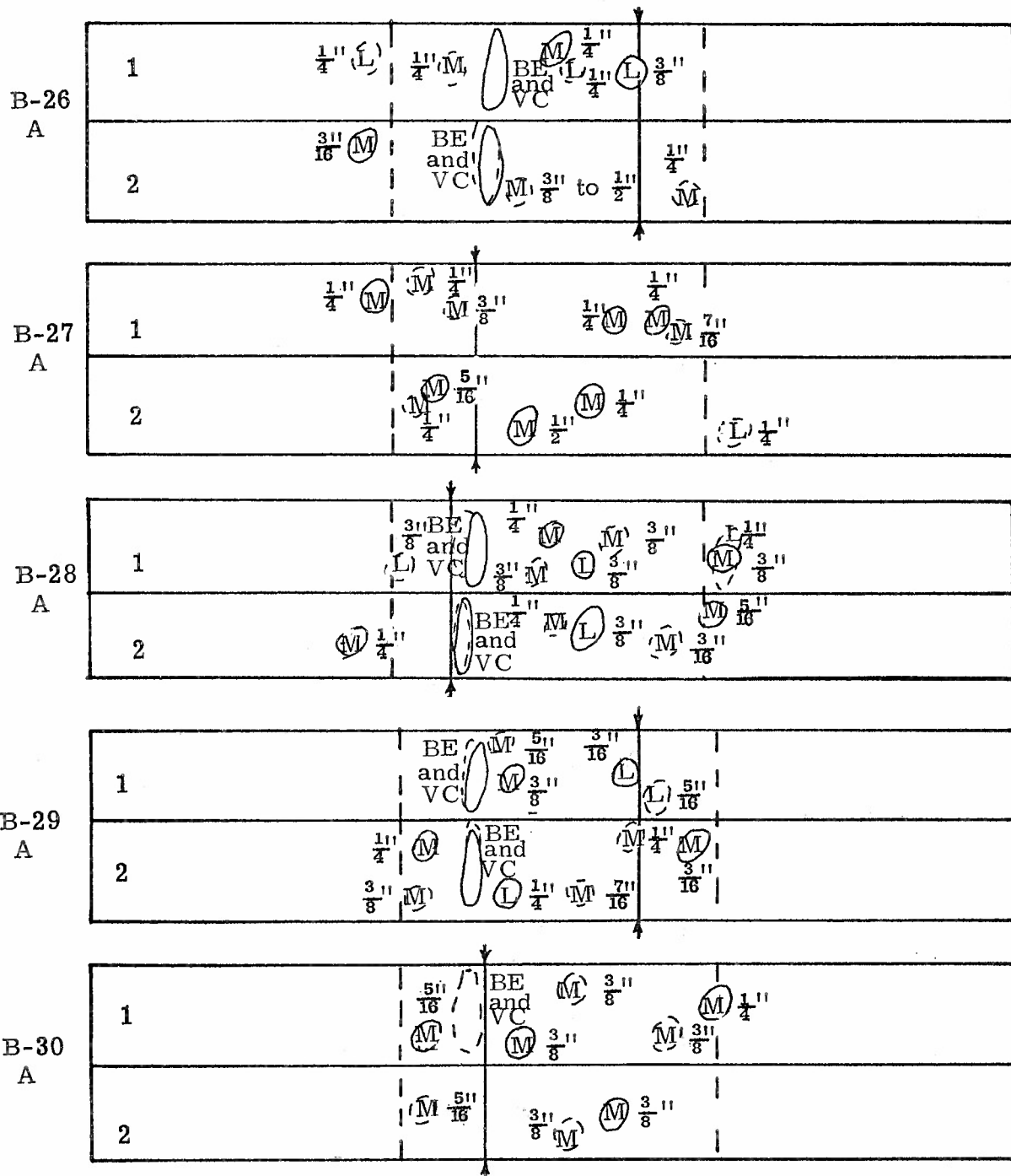


Figure D 14

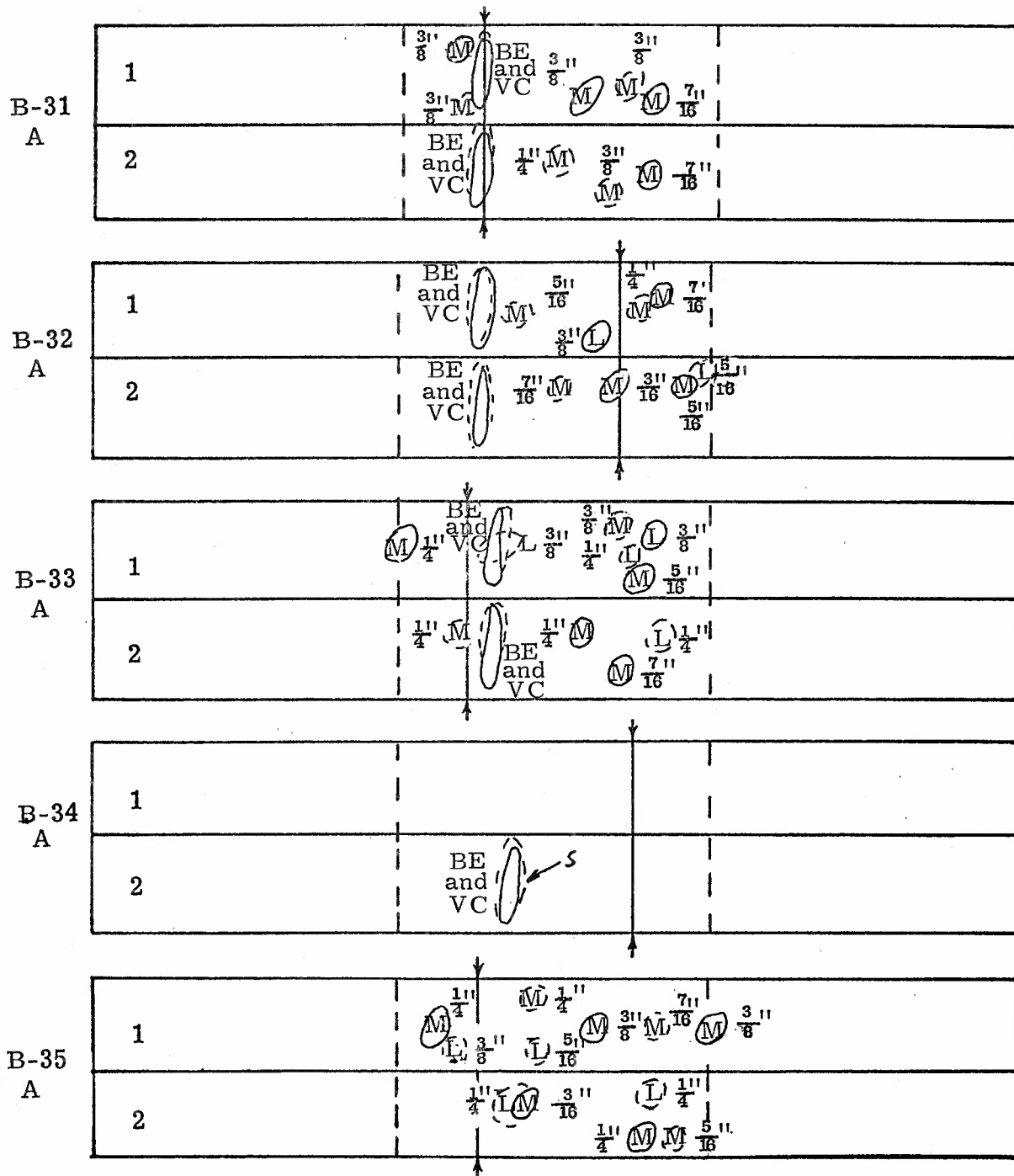


Figure D 15

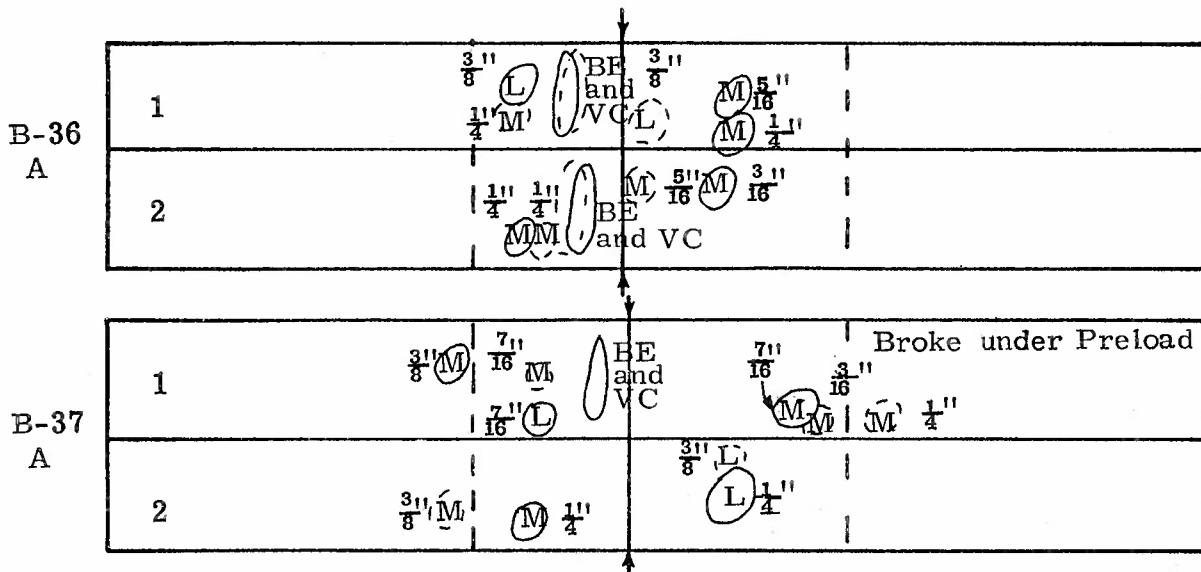


Figure D16





## APPENDIX E

Southern's Multiple Traces (Smears) of Pulse-Echo Signals from  
Referenced End of Tensile Specimen Blanks from ATJ-S Billet  
L-1-4 With Grain only



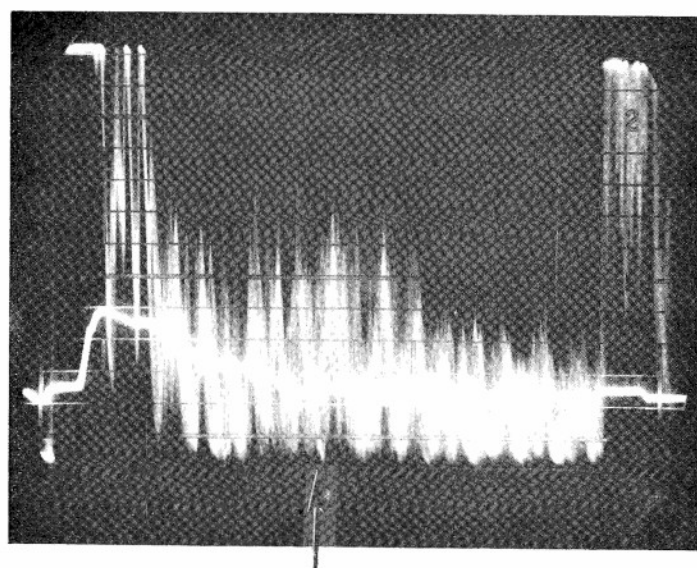
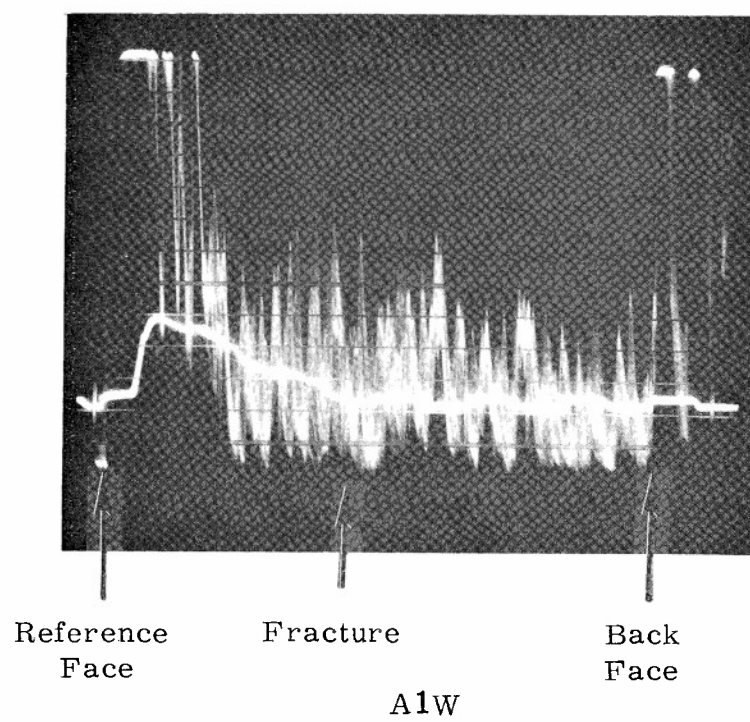
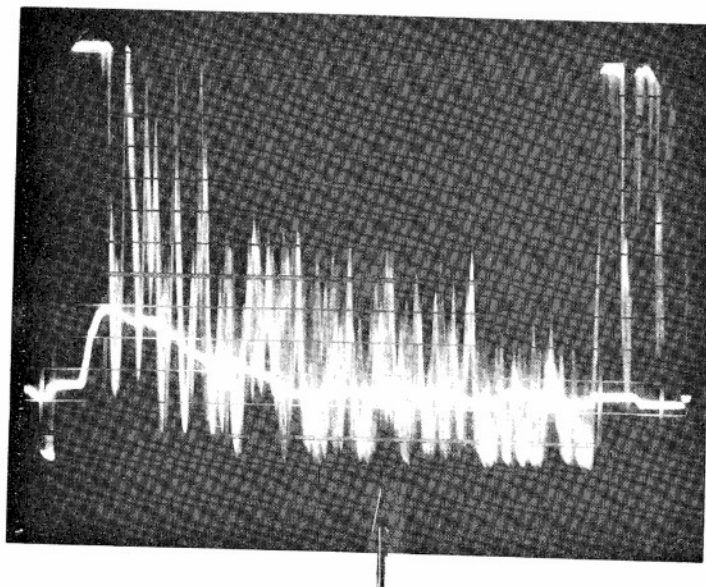
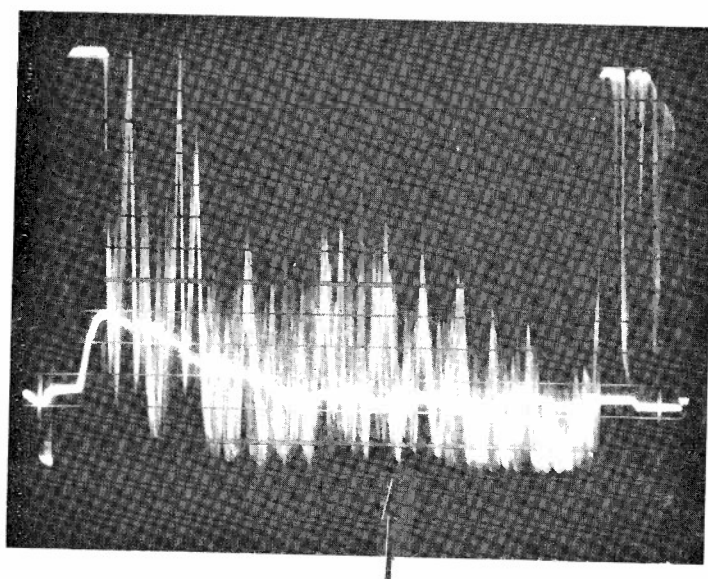


Figure E1  
486





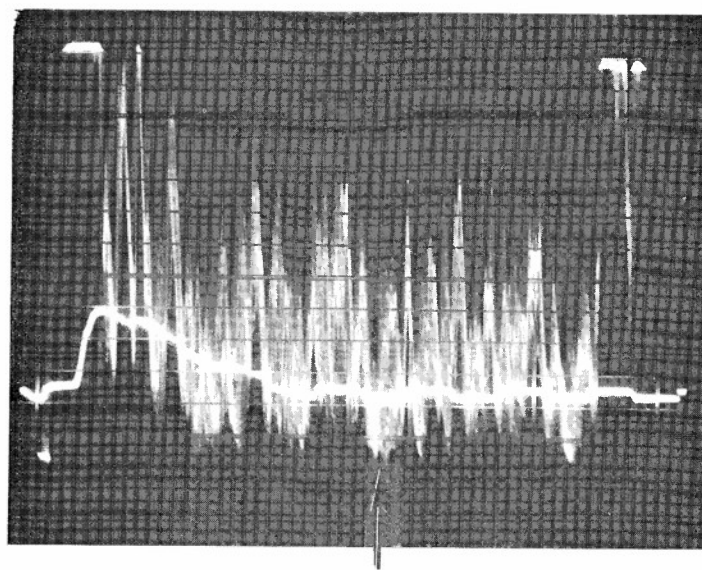
A3W



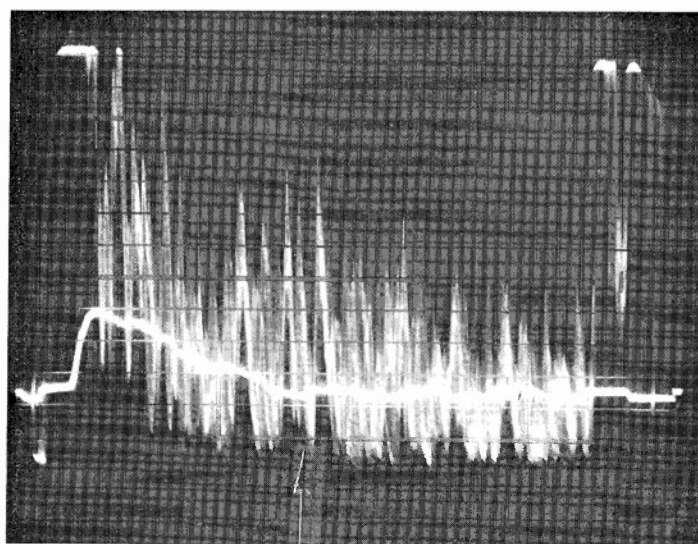
A4W

Figure E2





A5W

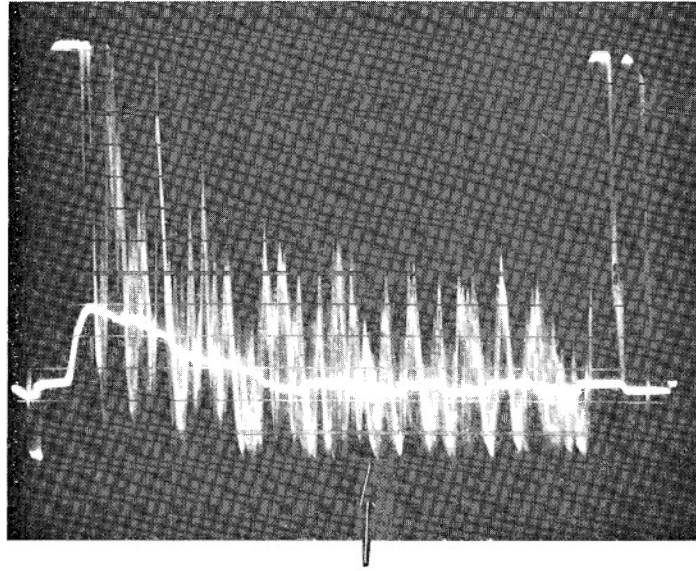


A6W

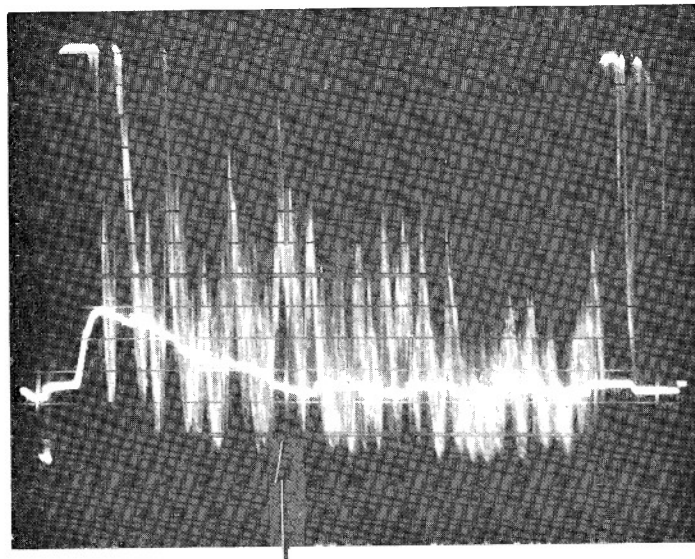
Figure E3







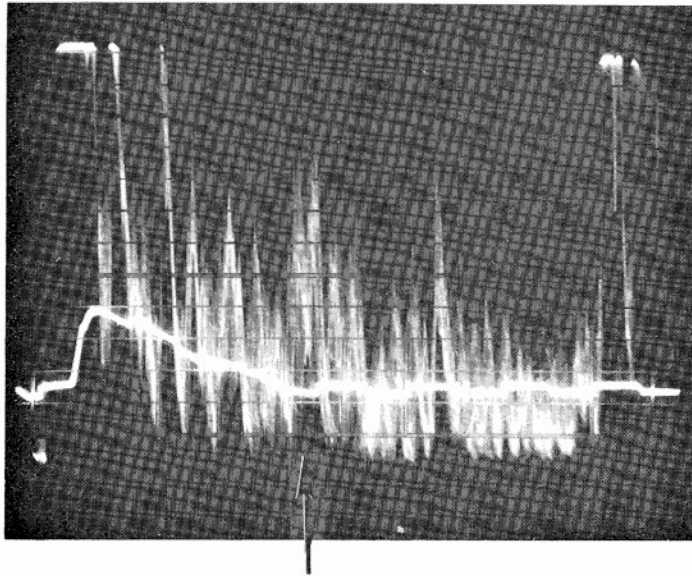
A7W



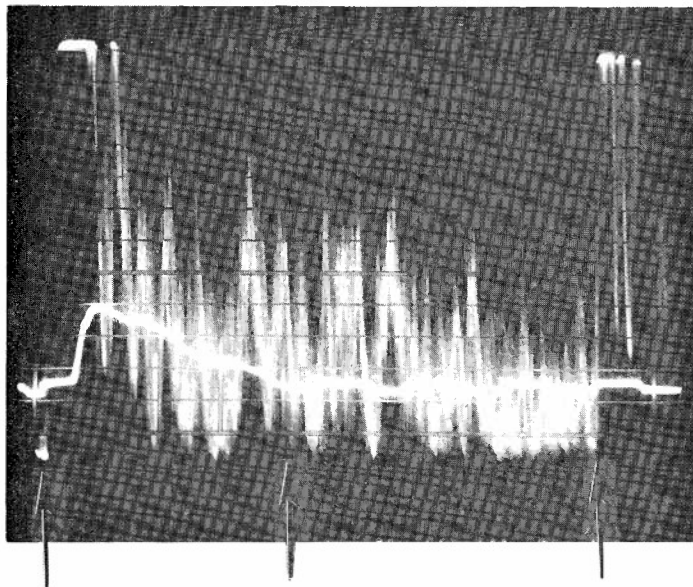
A8W

Figure E4





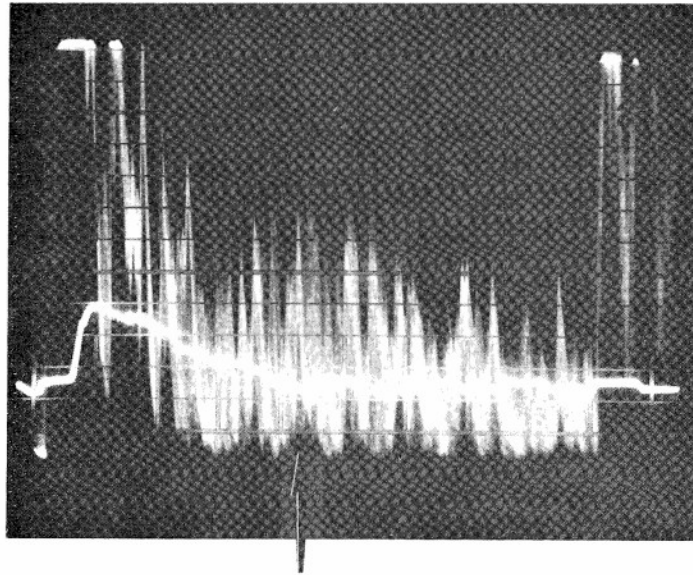
A9W



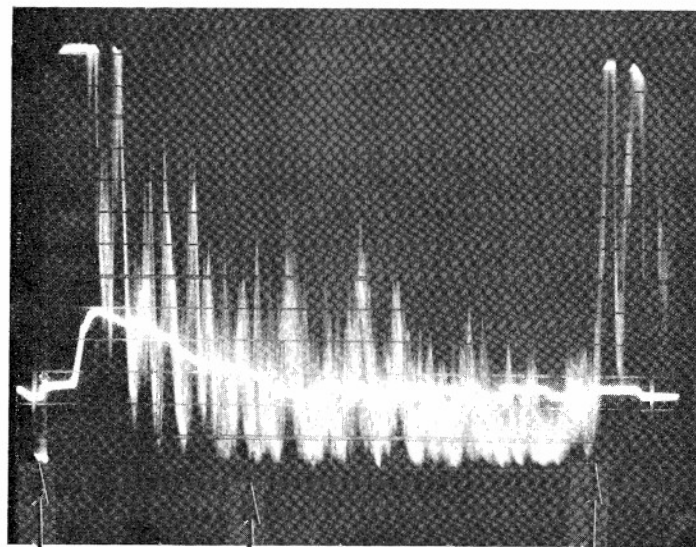
A10W

Figure E5





A11W



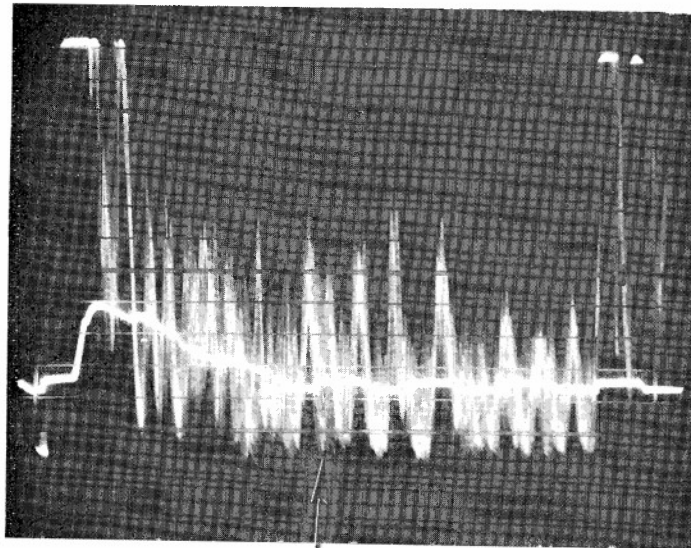
Reference  
Face

Back Face

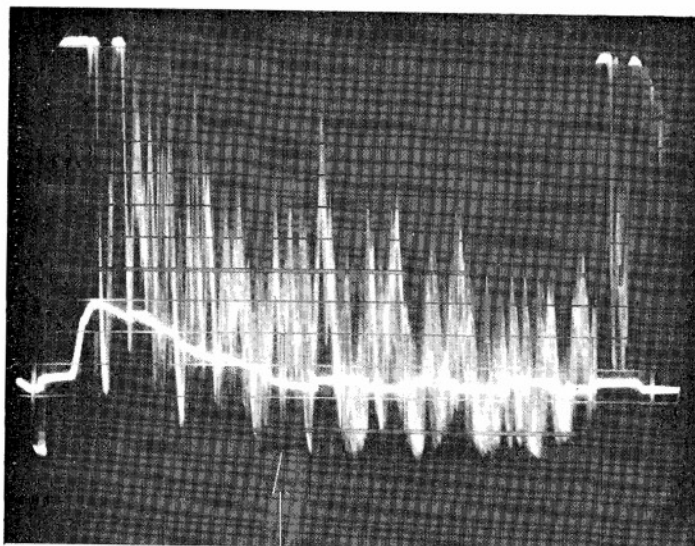
A12W

Figure E6





A13W

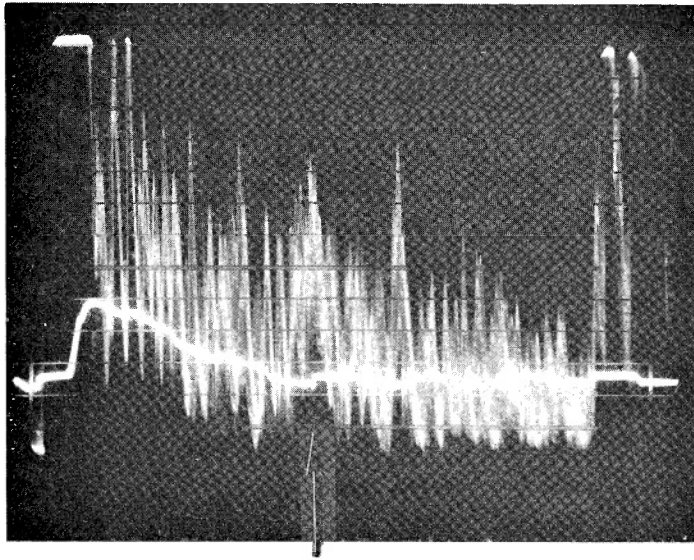


A14W

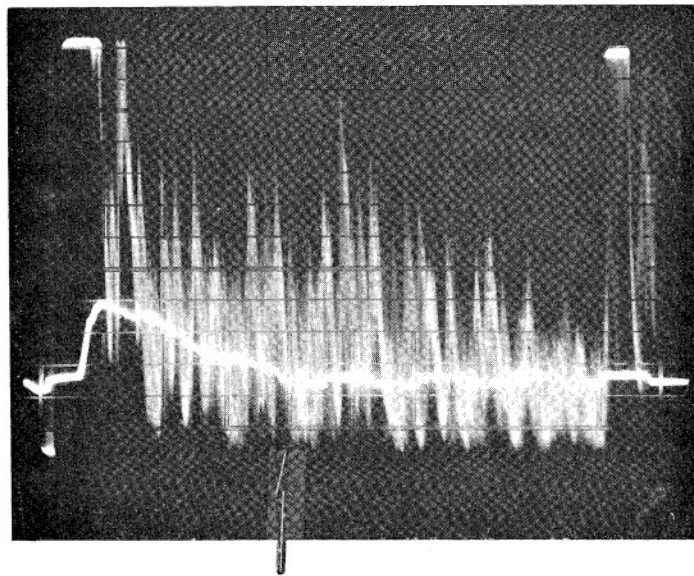
Figure E7







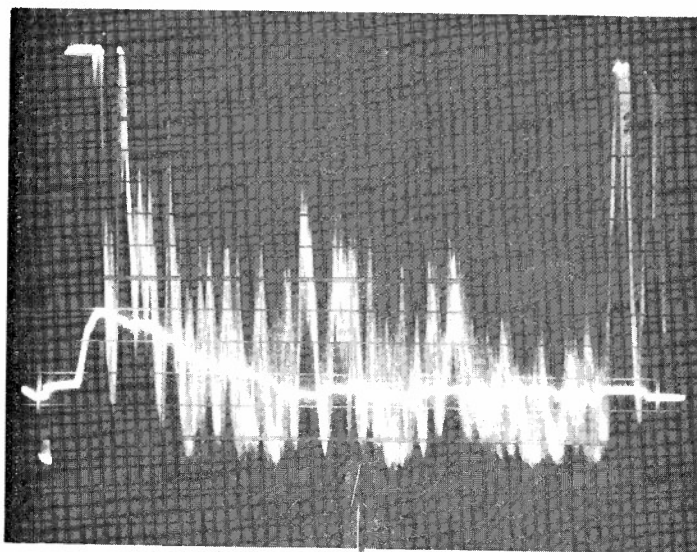
A15W



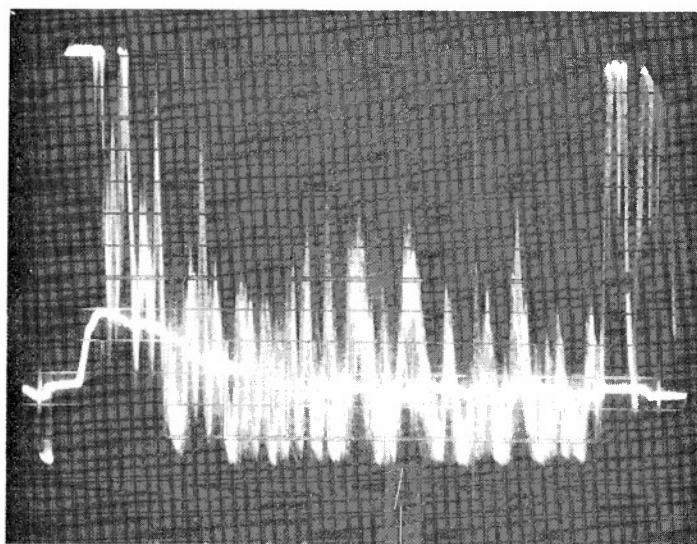
A16W

Figure E8





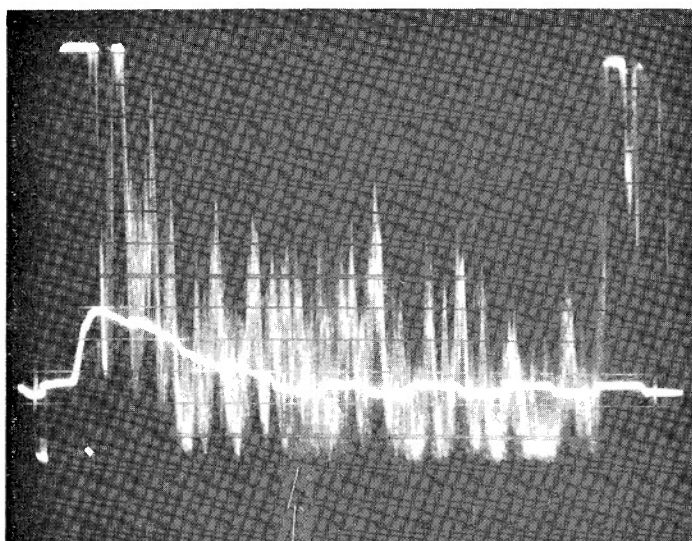
A17W



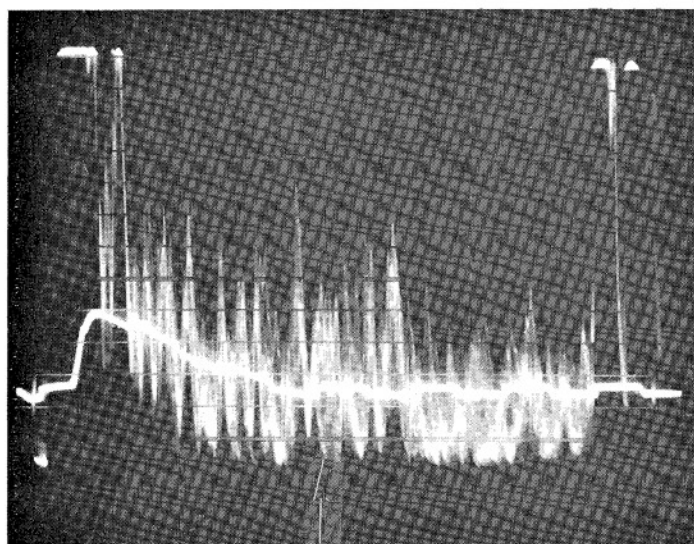
A18W

Figure E9





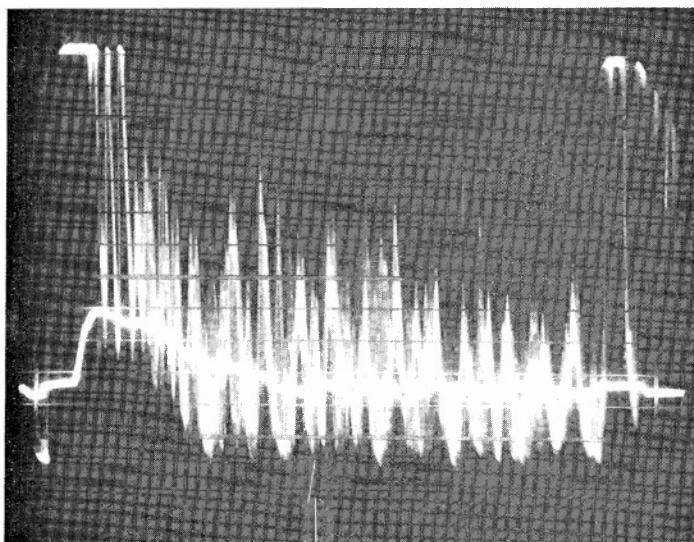
A19W



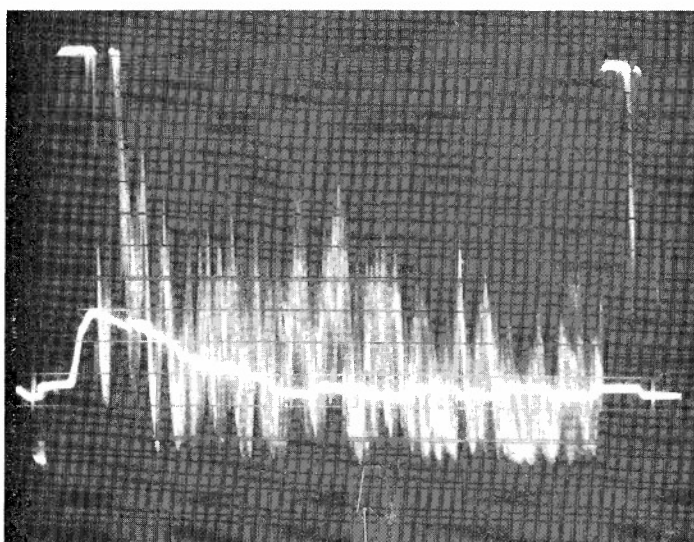
A20W

Figure E10





A21W

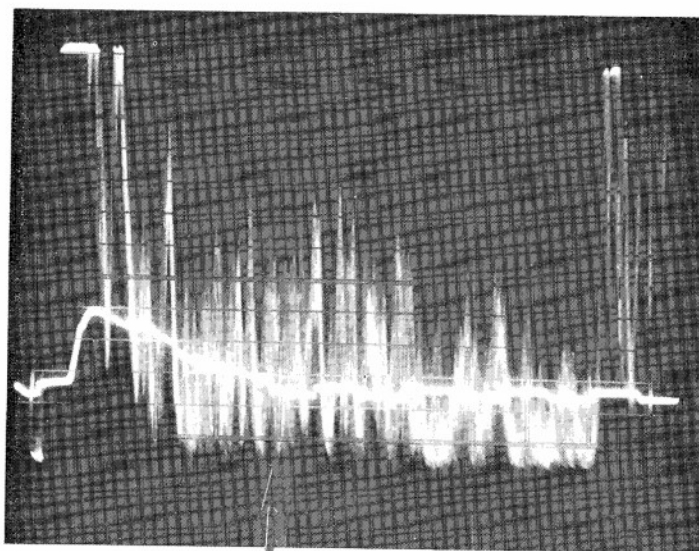


A22W

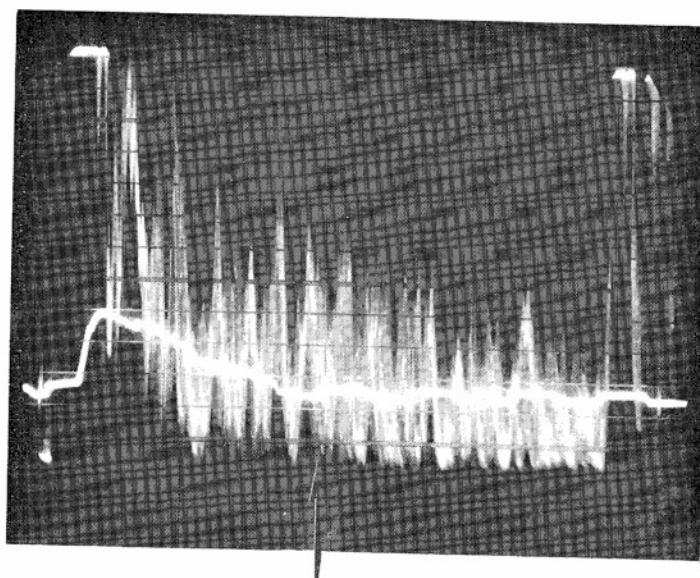
Figure E11







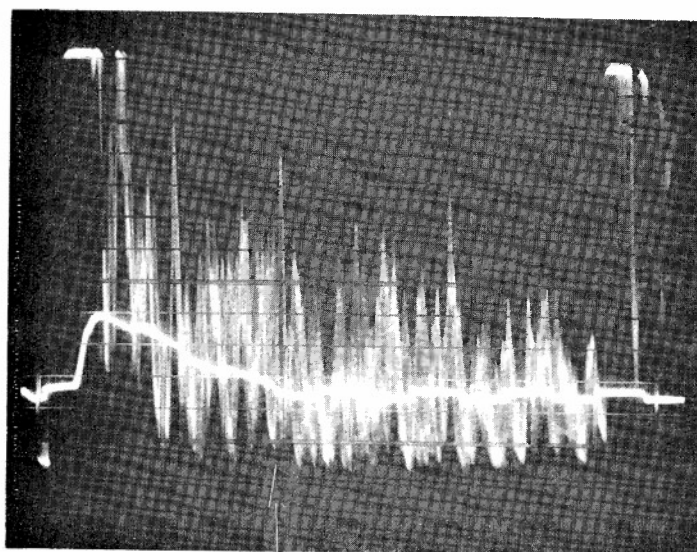
A23W



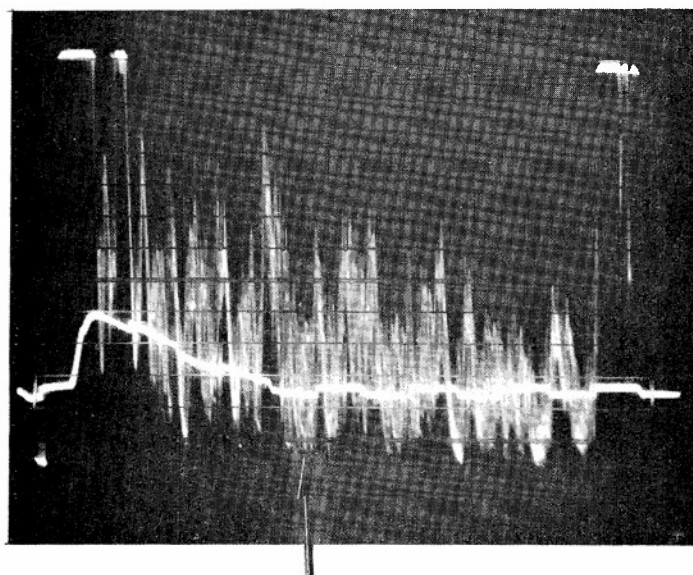
A24W

Figure E12





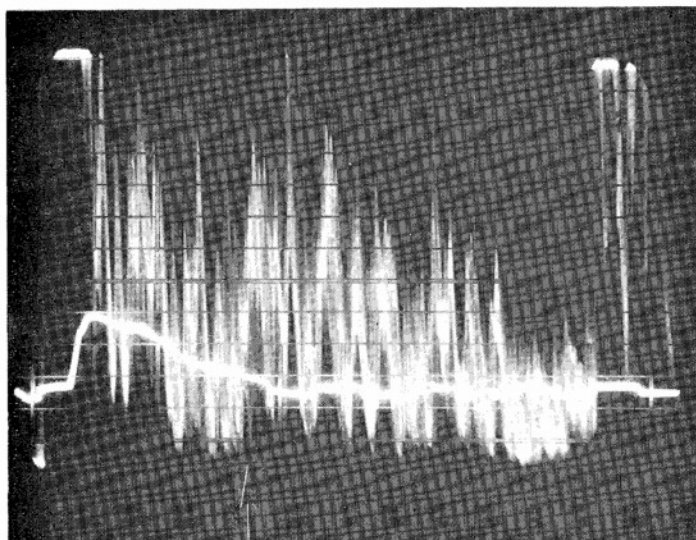
A25W



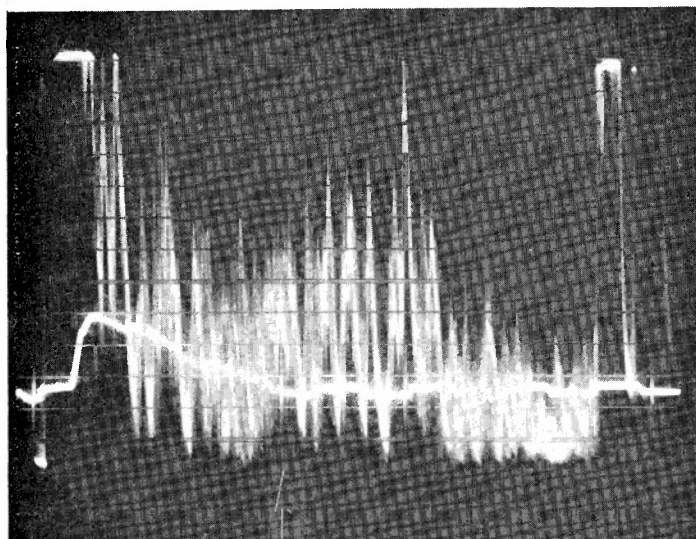
A26W

Figure E13





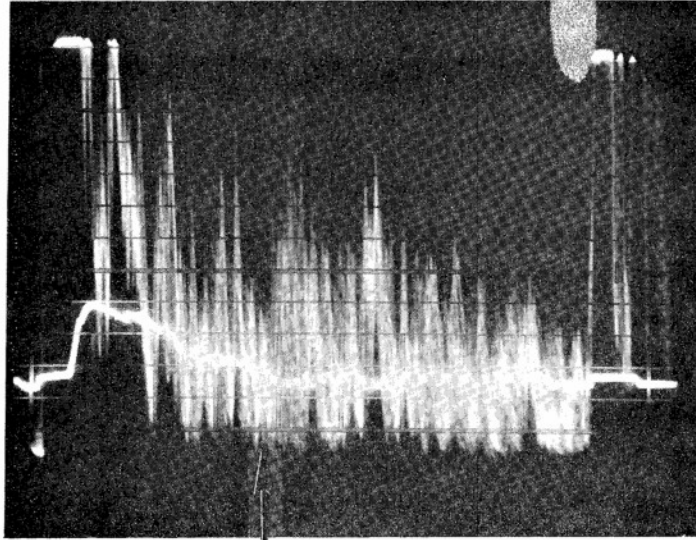
A27W



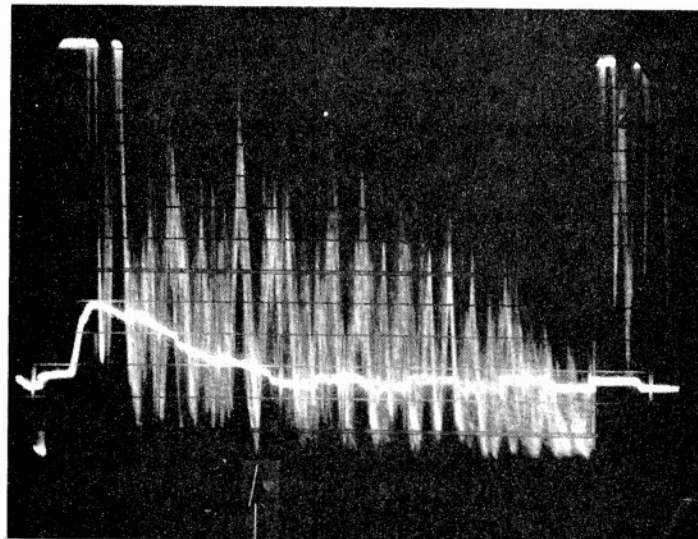
A28W

Figure E14





A30W



A31W

Figure E15





## APPENDIX F

Original Stress-Strain Curves for ATJ-S Billet L-1-4 With Grain  
and Across Grain at 70°F



SRI Run No: F118 Reel 2139

Date: 5/1/68 Temperature: 70°F

Material: ATJ-S

Specimen No.: A1W

Loading Direction: WITH GRAIN

Lateral Strain Direction: ---

Stress / Strain Rate: 10,000 psi/min

X Scale: 1" = 1001

Y Scale: 15K11 1" = 19.1K

Specimen Gage Section: 2.510 x 1.5

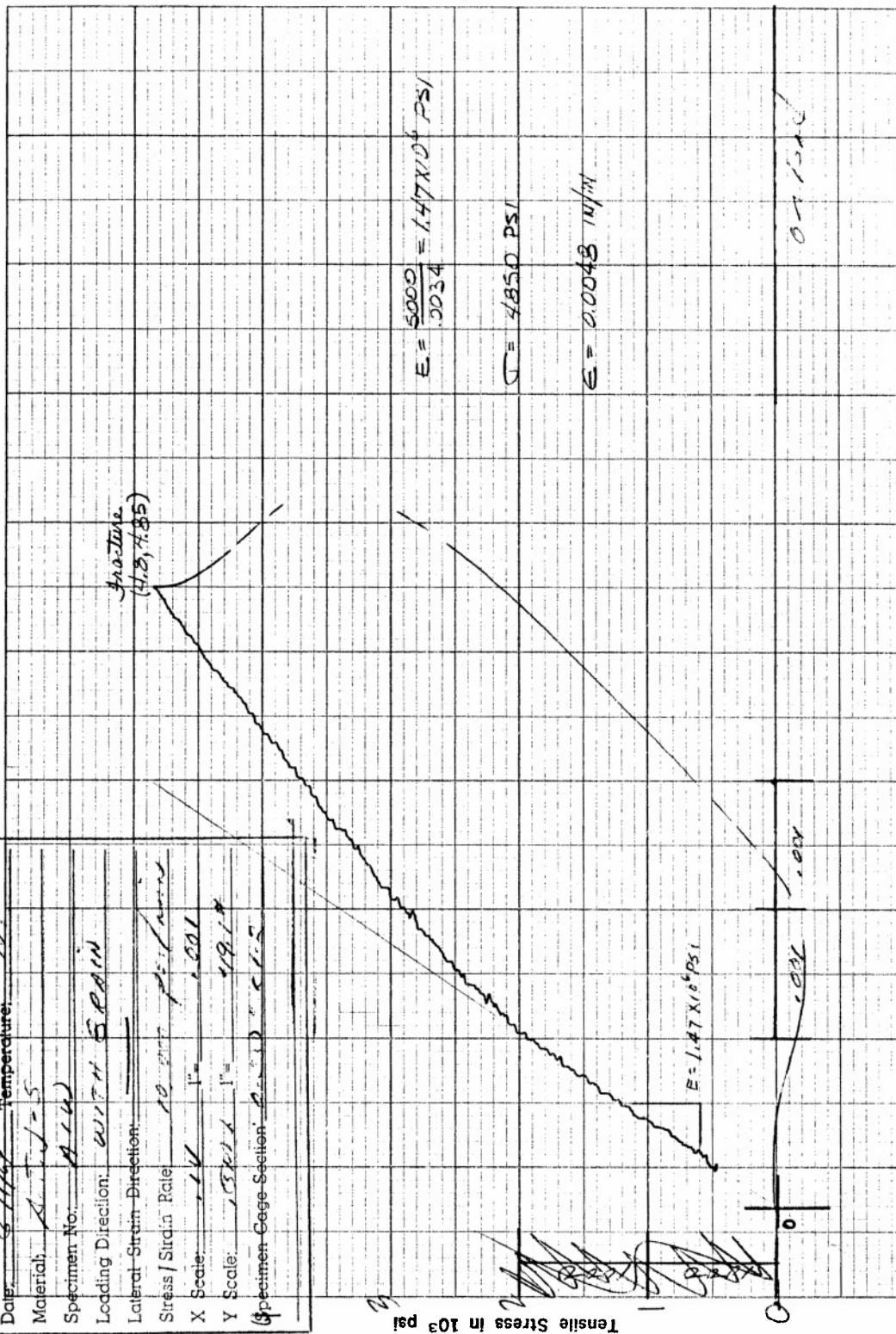


Figure F1. Tensile Stress versus Axial Strain for Specimen A1W of ATJ-S Graphite at 70°F

SRI Run No: T-144 Rev: 2/89

Date: 3/16/89 Temperature: 70°F

Material: A-2W

Specimen No.: A-2W

Loading Direction: WITH STRAIN

Lateral Strain Direction: \_\_\_\_\_

Stress / Strain Rate: 10,000 psi/min

X Scale: 1 in 1.00

Y Scale: 0.001 in 0.001

Specimen Gage Section: 0.200" x 1.2"

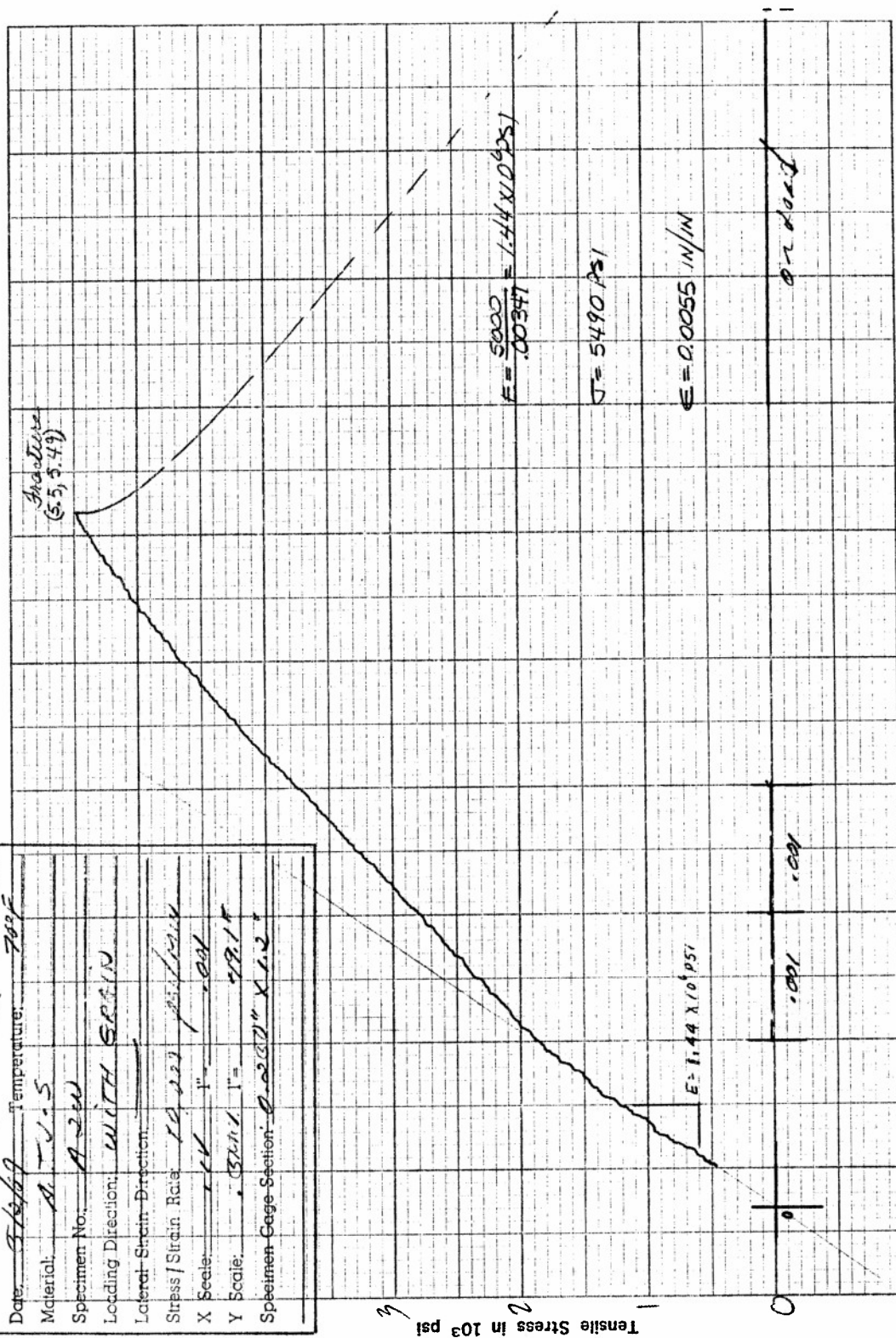


Figure F2. Tensile Stress versus Axial Strain for Specimen A2W of ATJ-S Graphite at 70°F

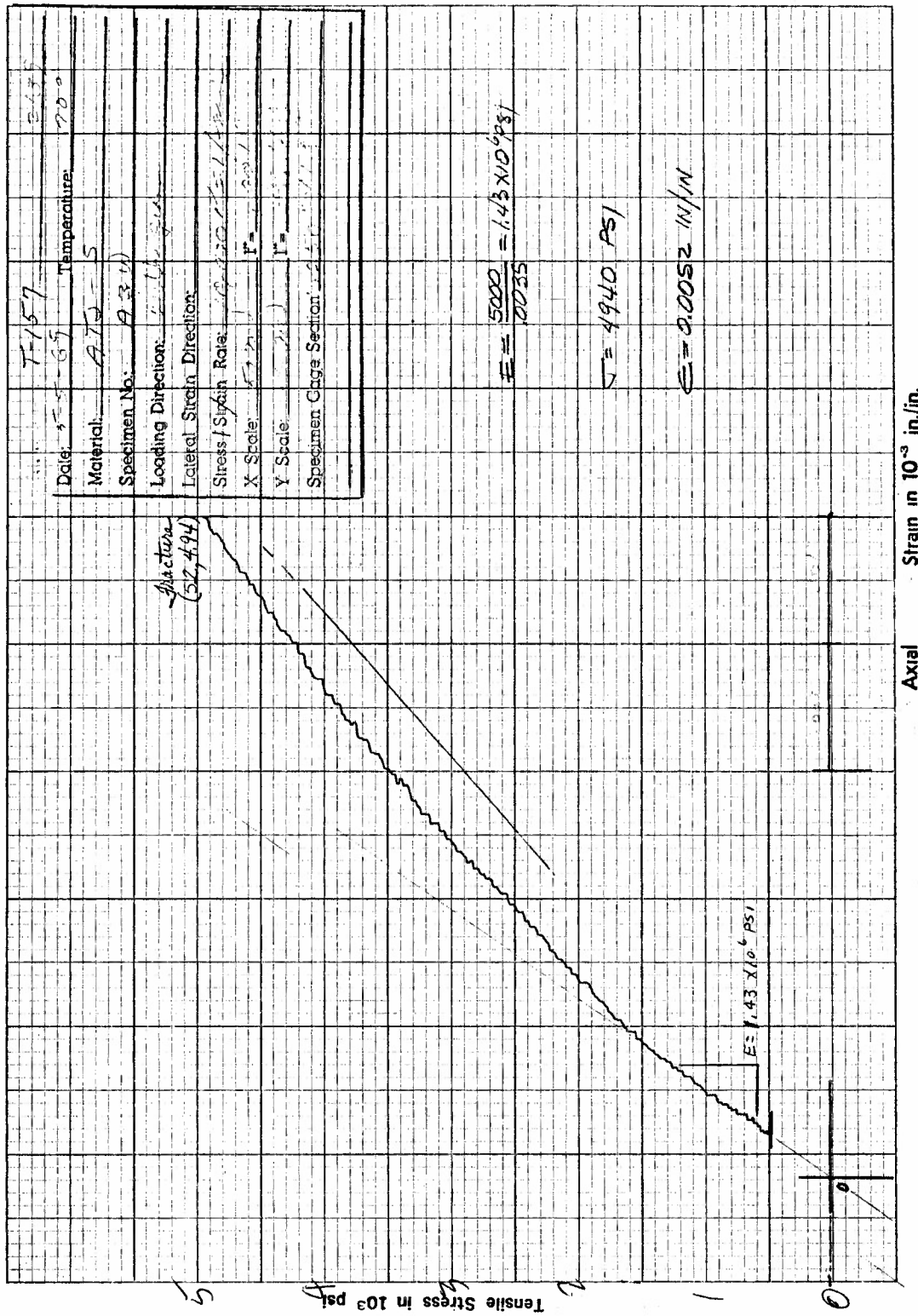


Figure F3. Tensile Stress versus Axial Strain for Specimen A3W of ATJ-S Graphite at 70°F

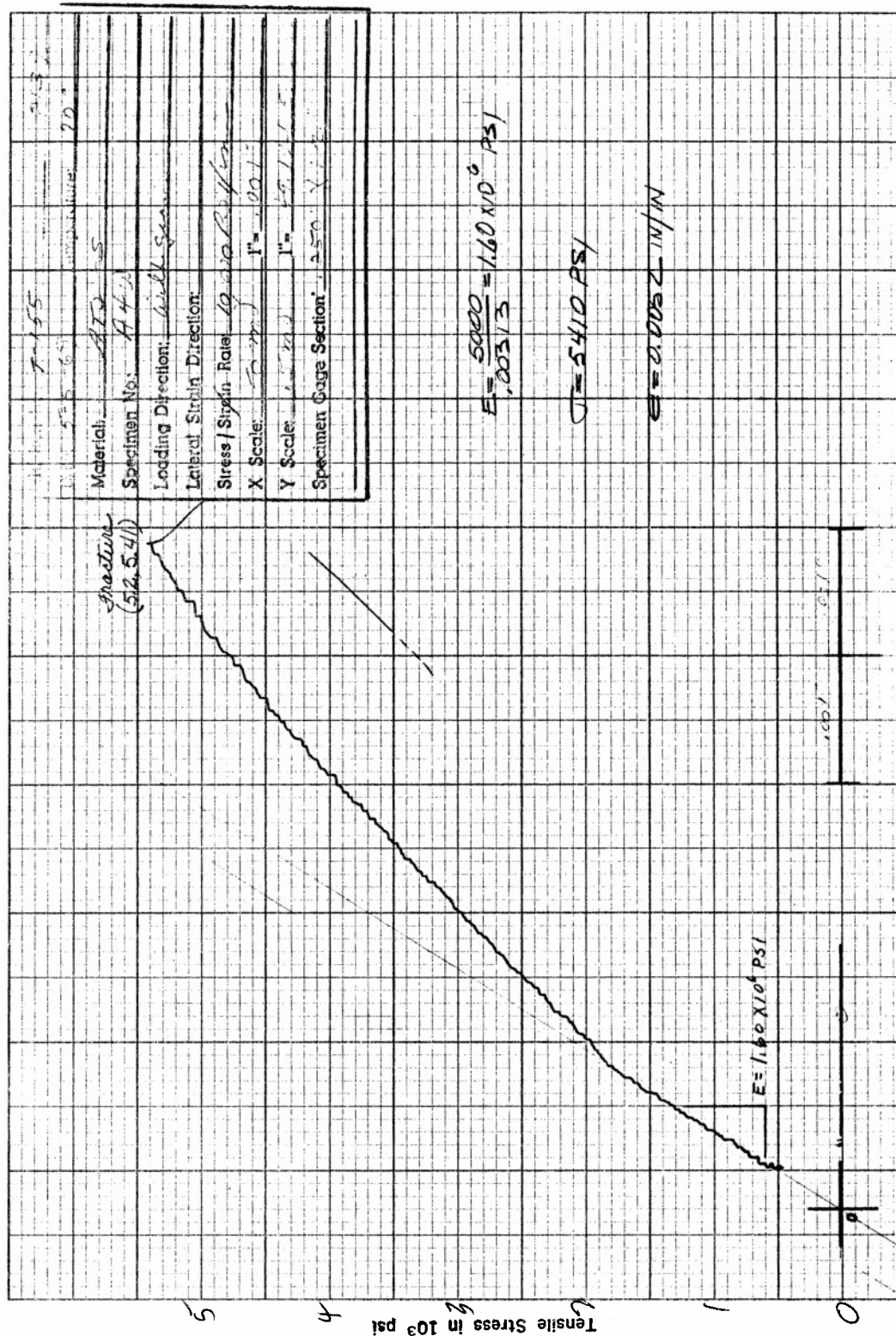


Figure F4. Tensile Stress versus Axial Strain for Specimen A4W of ATJ-S Graphite at 70°F



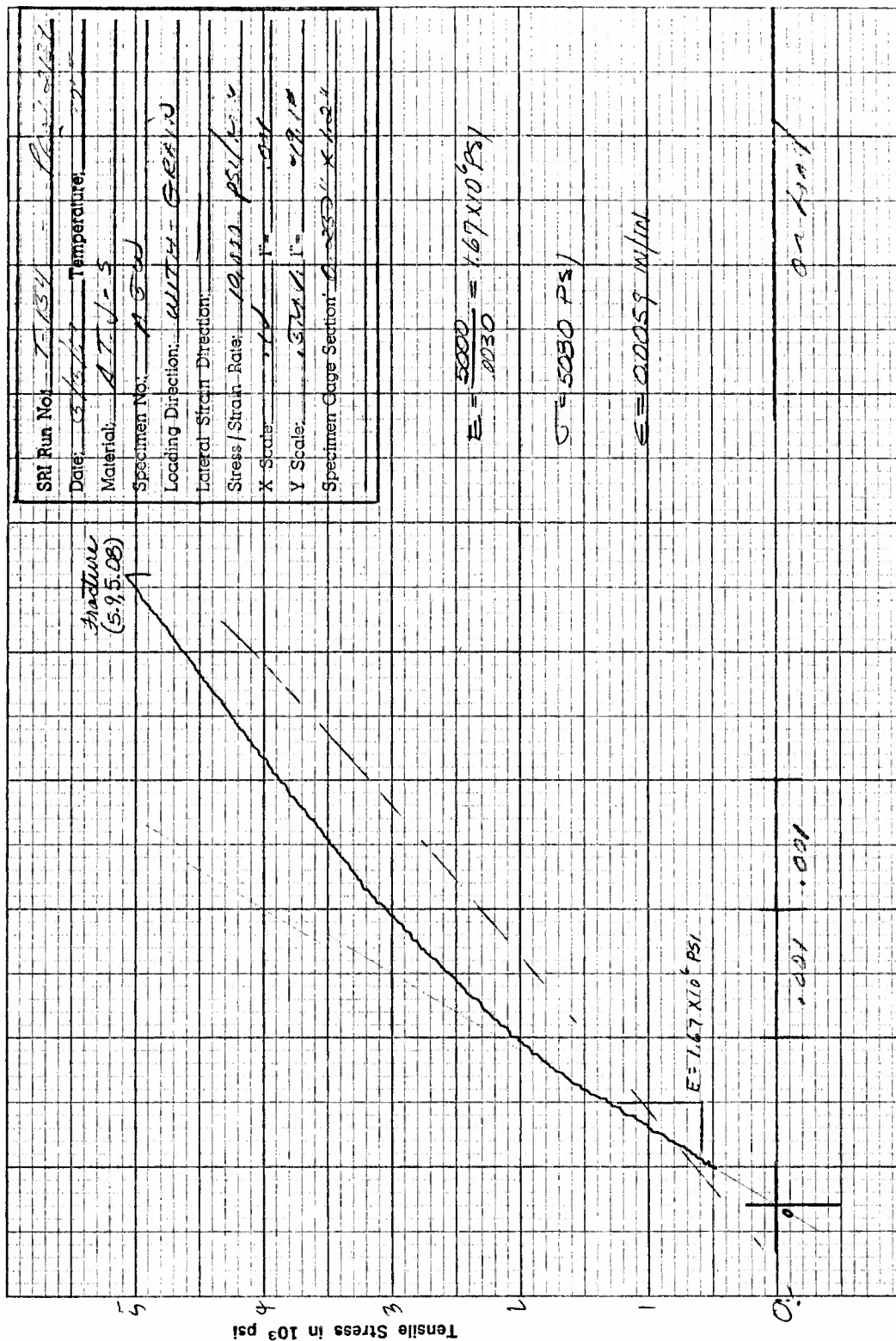


Figure F5. Tensile Stress versus Axial Strain for Specimen A5W of ATJ-S Graphite at 70°F

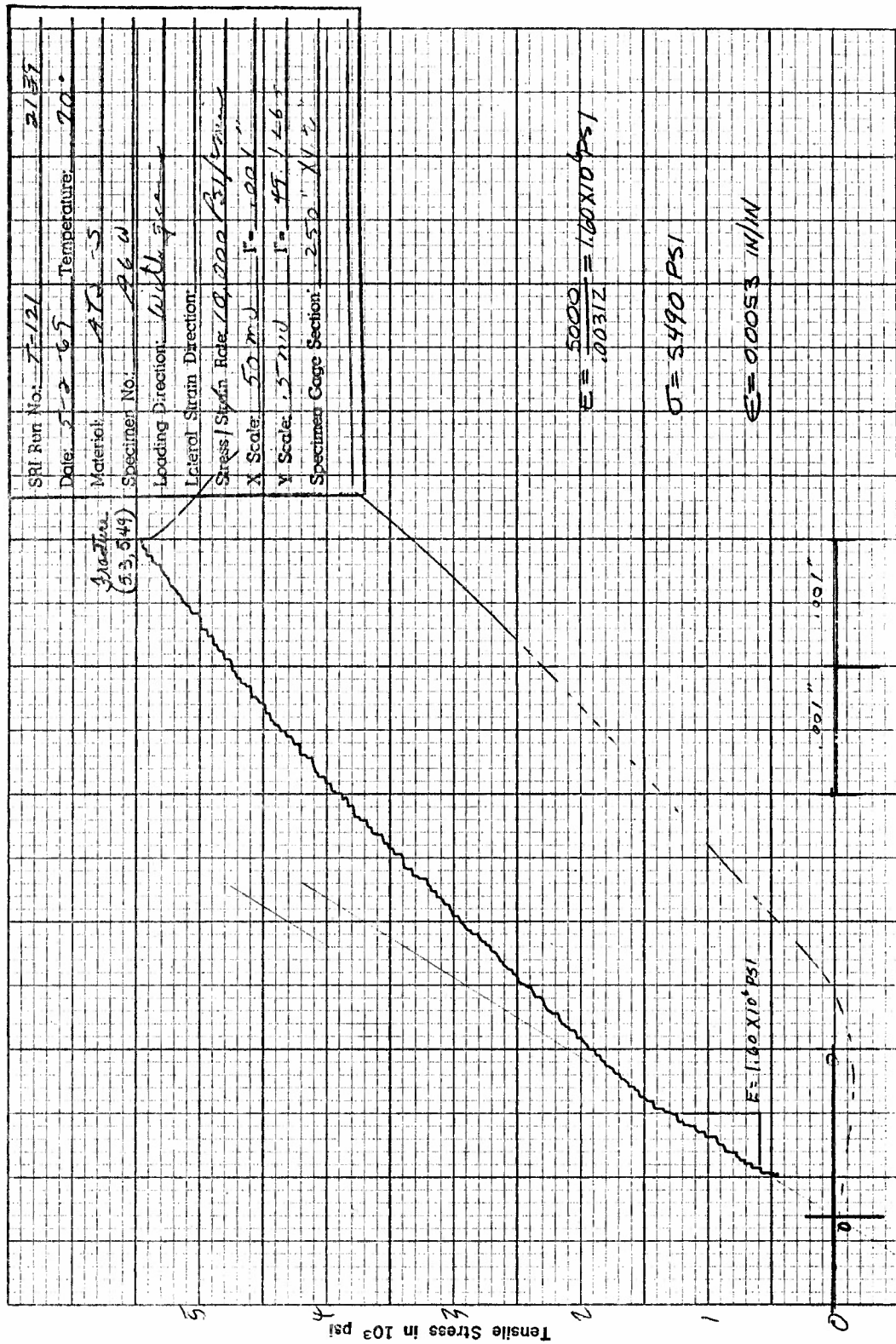


Figure F6. Tensile Stress versus Axial Strain for Specimen A6W of ATJ-S Graphite at 70°F



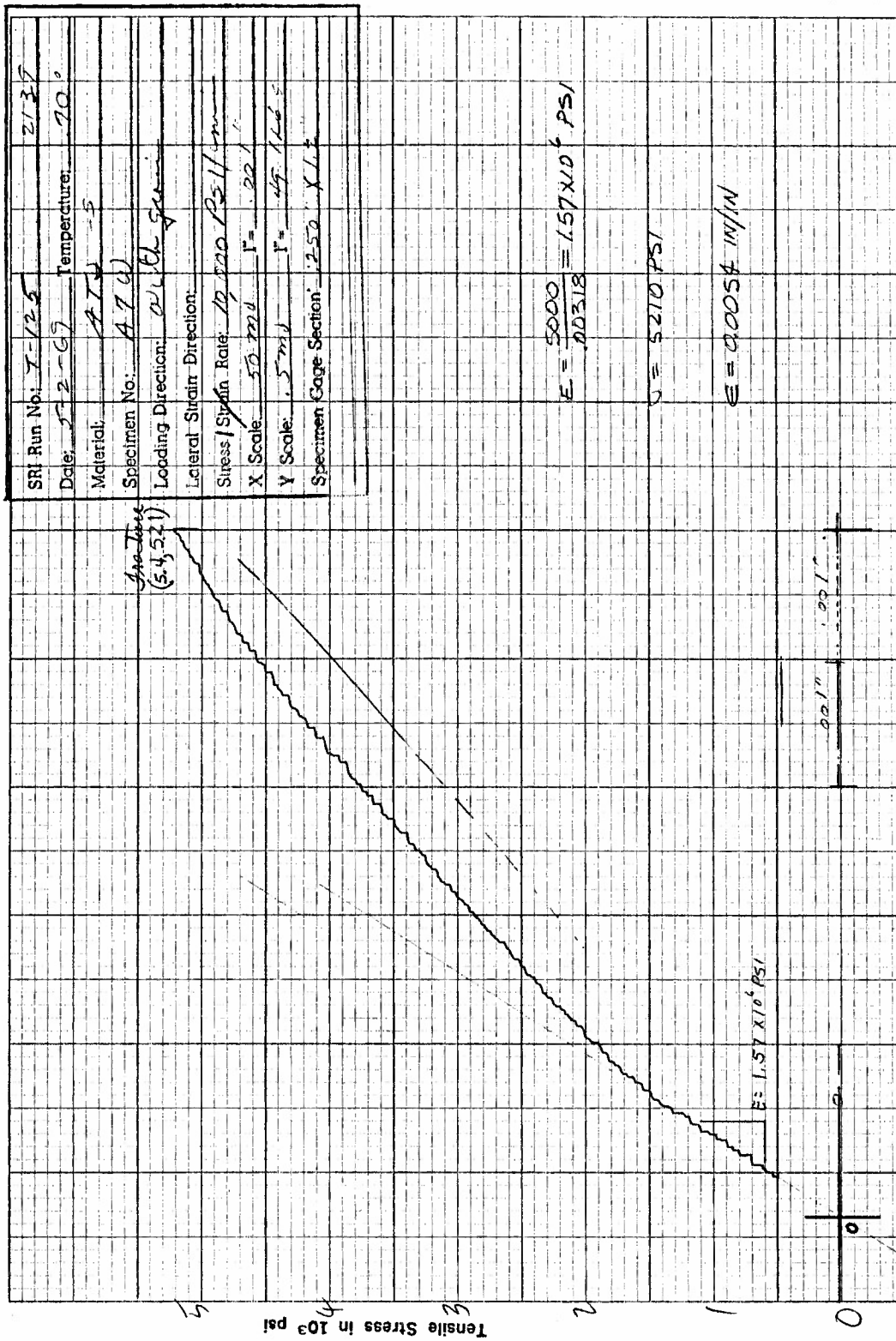


Figure F7. Tensile Stress versus Axial Strain for Specimen A7W of ATJ-S Graphite at 70°F

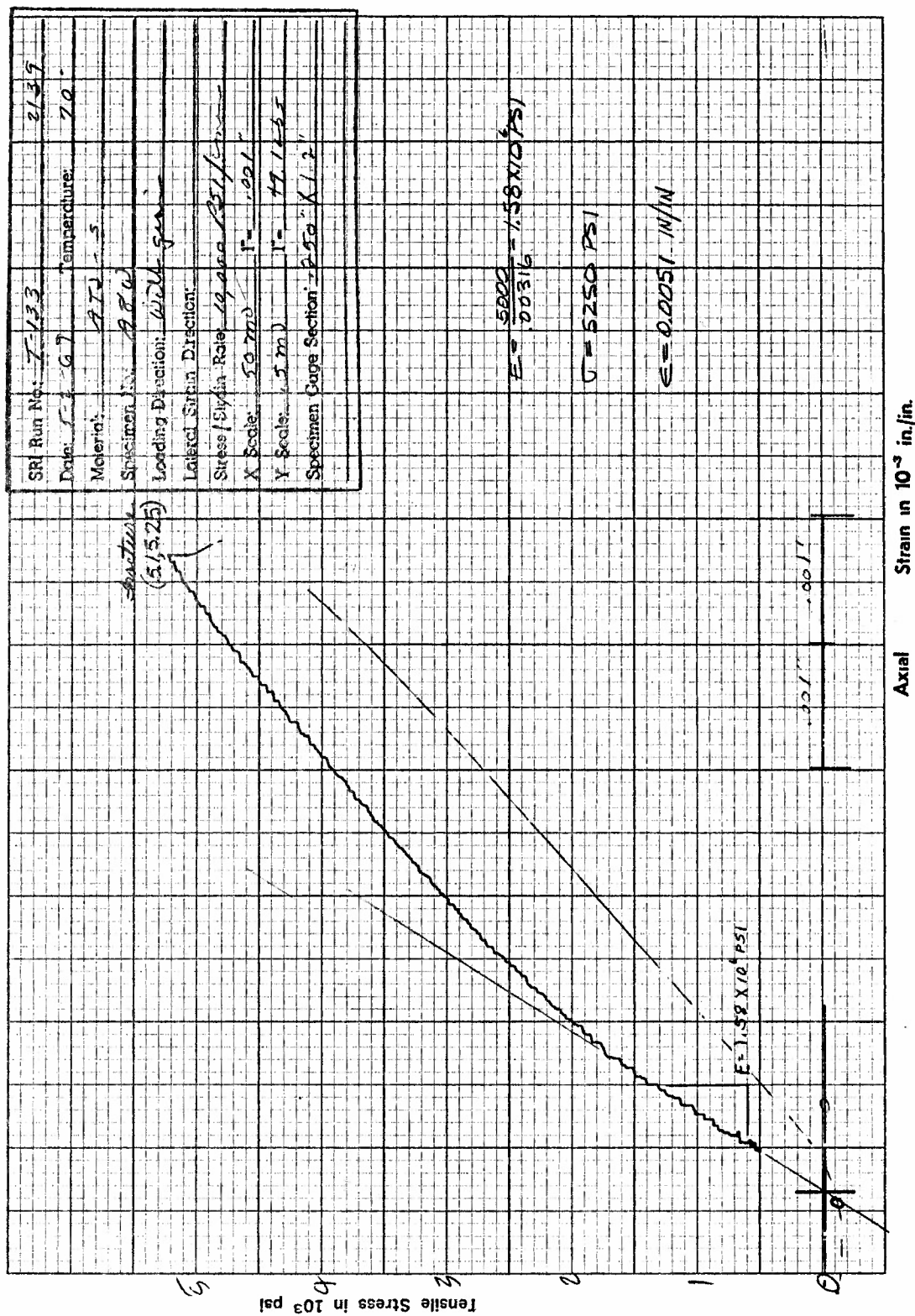


Figure F8. Tensile Stress versus Axial Strain for Specimen A8W of ATJ-S Graphite at 70°F

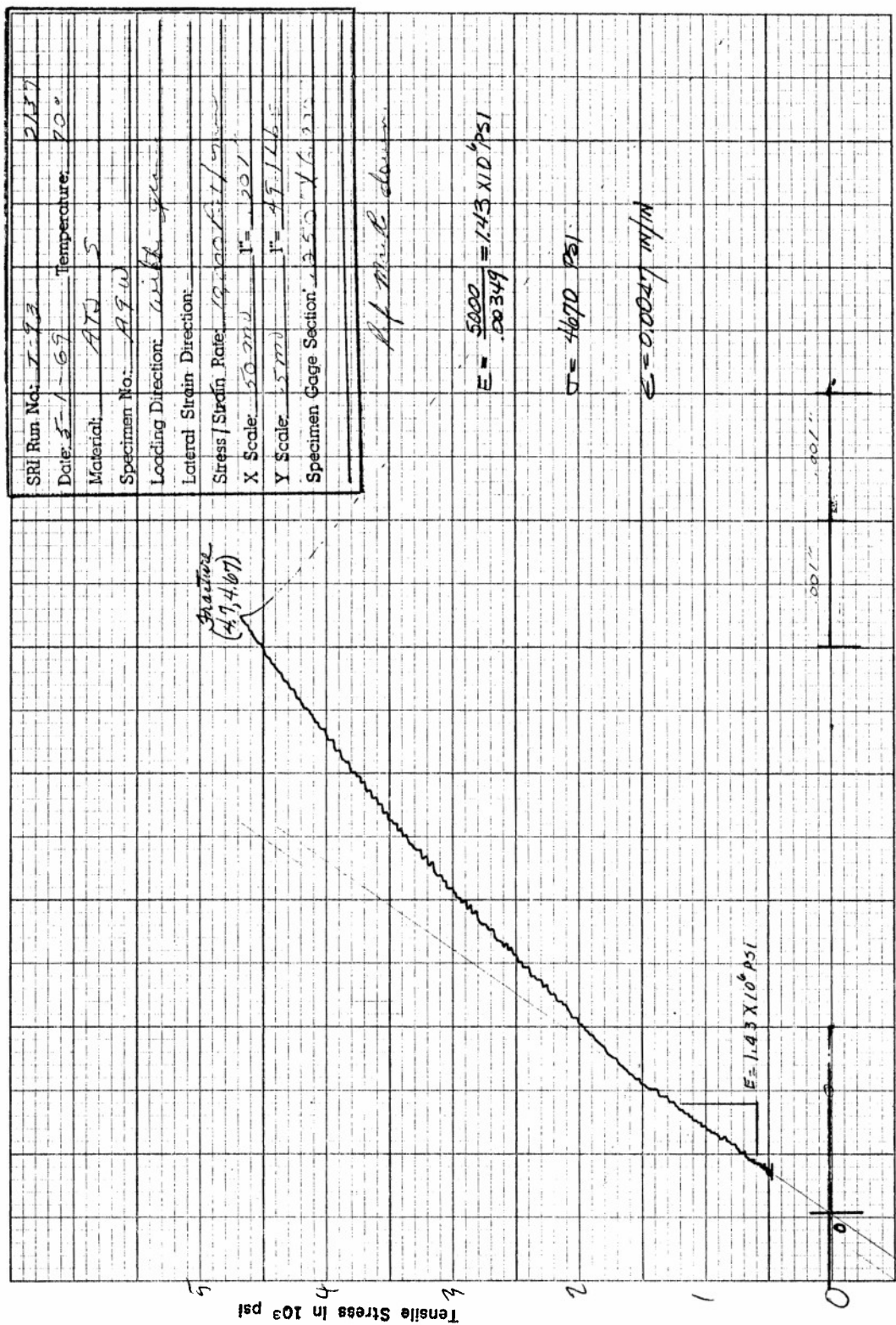


Figure F9. Tensile Stress versus Axial Strain for Specimen A9W of ATJ-S Graphite at 70°F

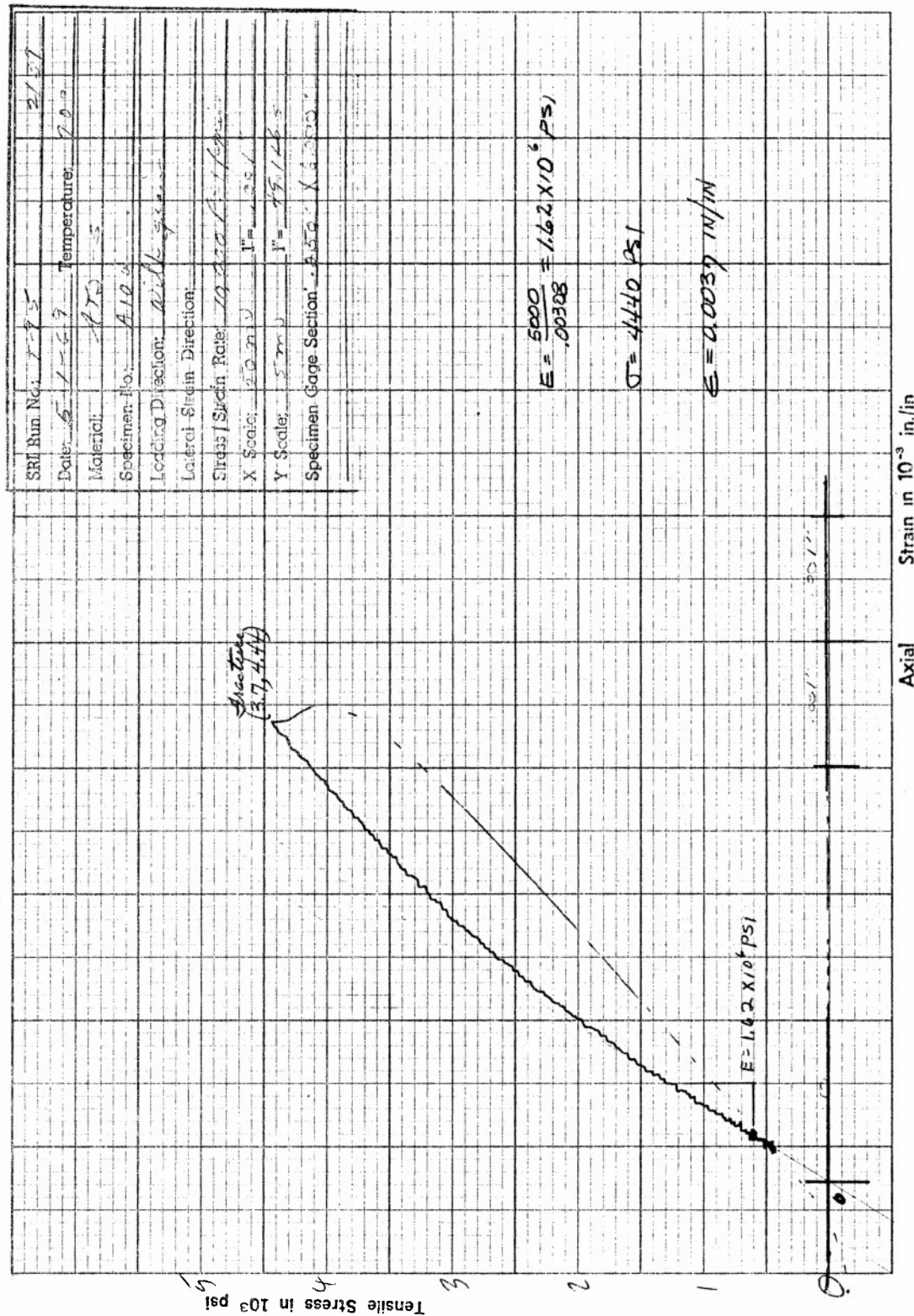


Figure F10. Tensile Stress versus Axial Strain for Specimen A10W of ATJ-S Graphite at 70°F

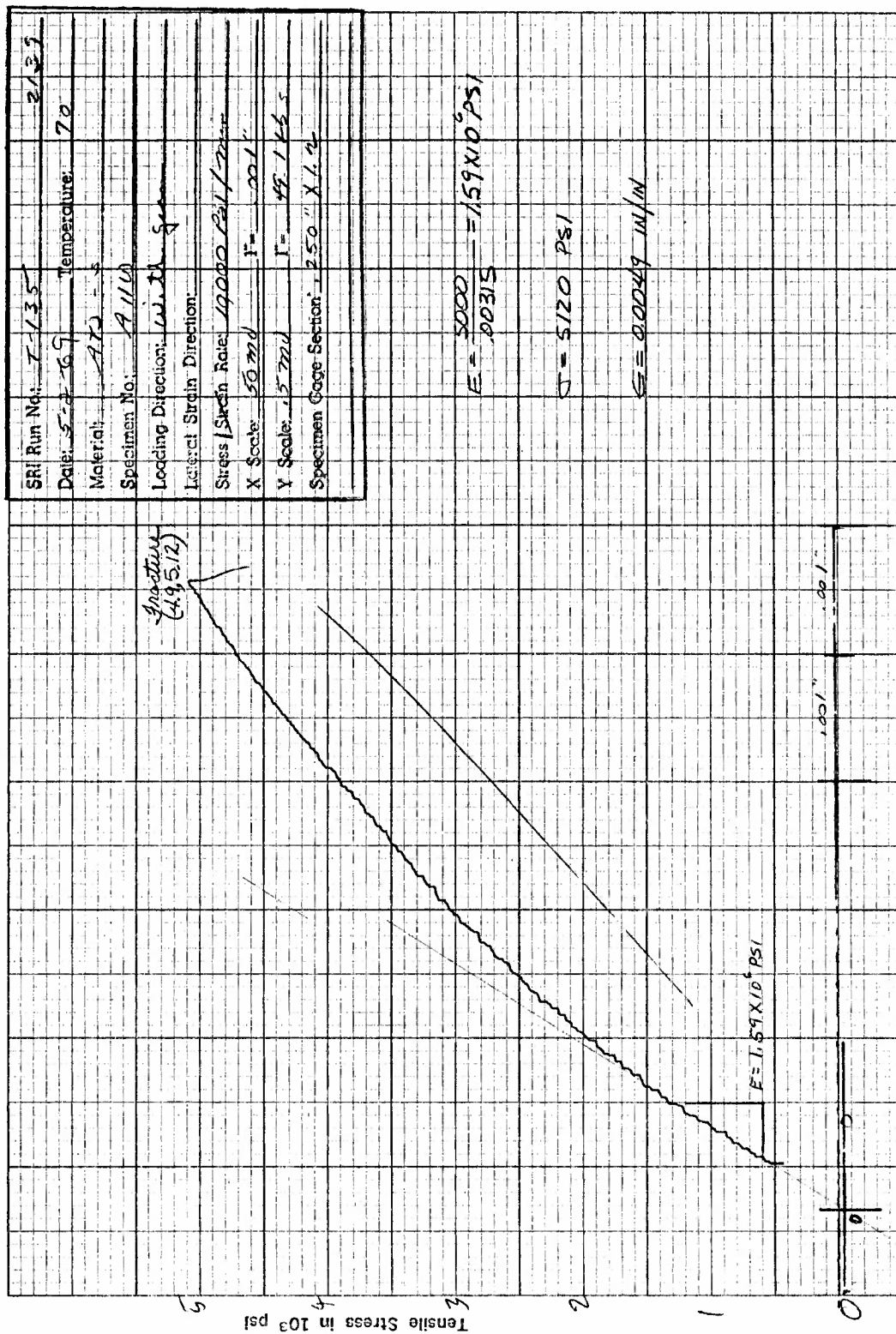


Figure F11. Tensile Stress versus Axial Strain for Specimen A11W of ATJ-S Graphite at 70°F



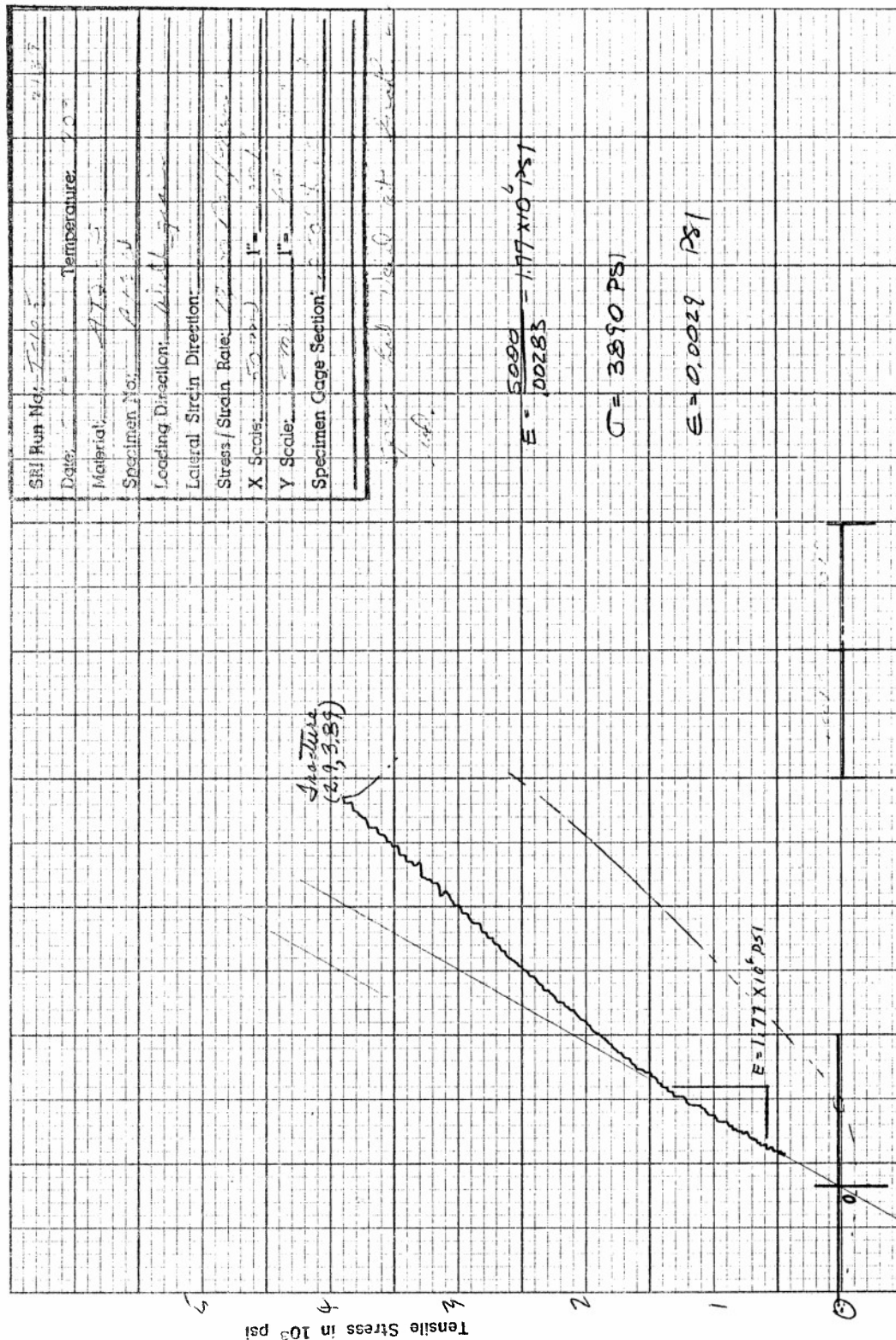


Figure F12. Tensile Stress versus Axial Strain for Specimen A12W of ATJ-S Graphite at 70°F

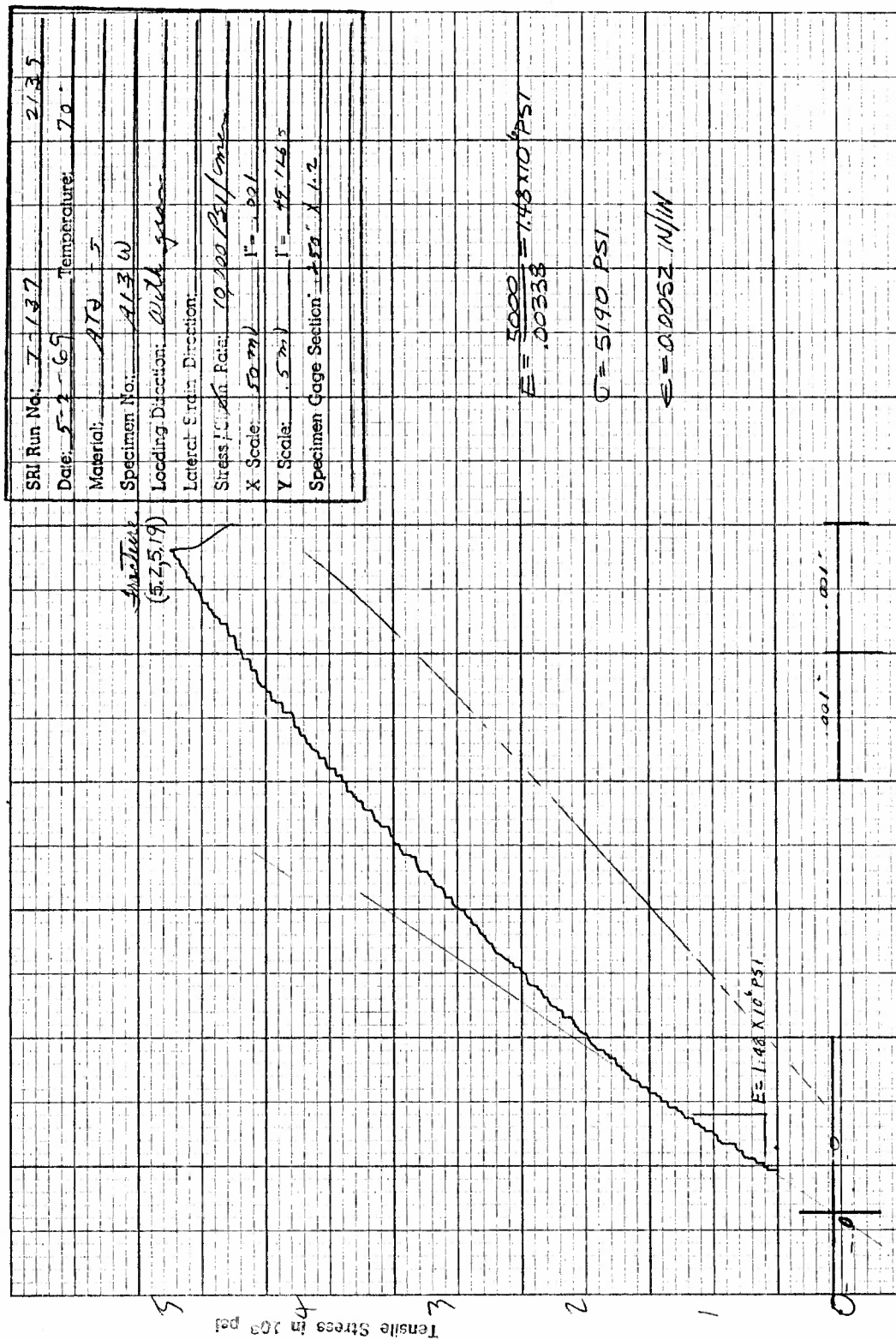


Figure F13. Tensile Stress versus Axial Strain for Specimen A13W of ATJ-S Graphite at 70°F

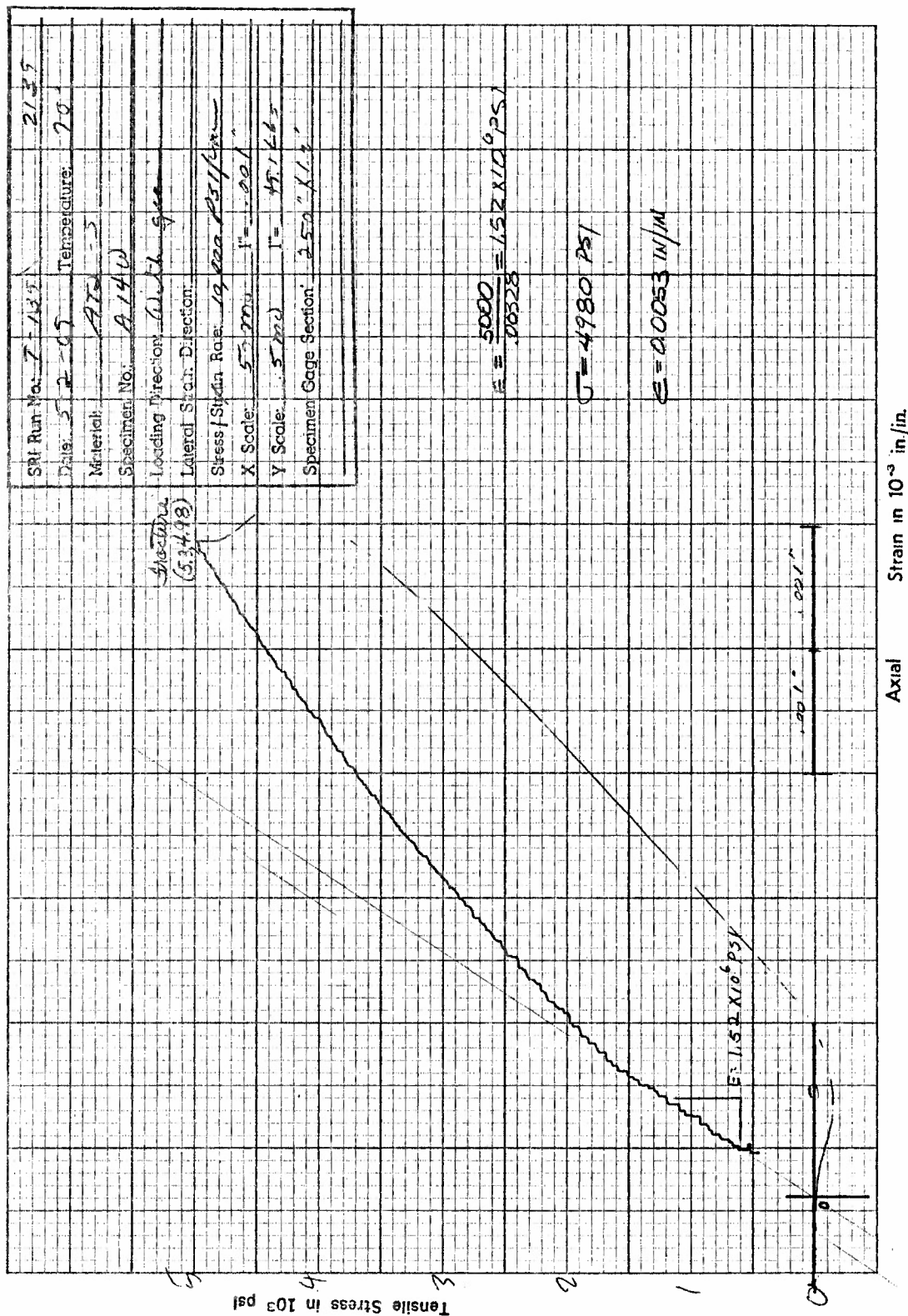


Figure F14. Tensile Stress versus Axial Strain for Specimen A14W of ATJ-S Graphite at 70°F



SRI Run No: T-122 Rev 2639  
 Date: 8/2/69 Temperature: 70°F  
 Material: A.F.J-5  
 Specimen No: A.3.11  
 Loading Direction: WITH GRAIN  
 Lateral Strain Direction: \_\_\_\_\_  
 Stress/Strain Rate: 10,000 psi/min  
 X Scale: .1V  $r = 1.021$   
 Y Scale: .020 in  $r = .0918$   
 Specimen Gage Section: 0.20 in x 1.2 in

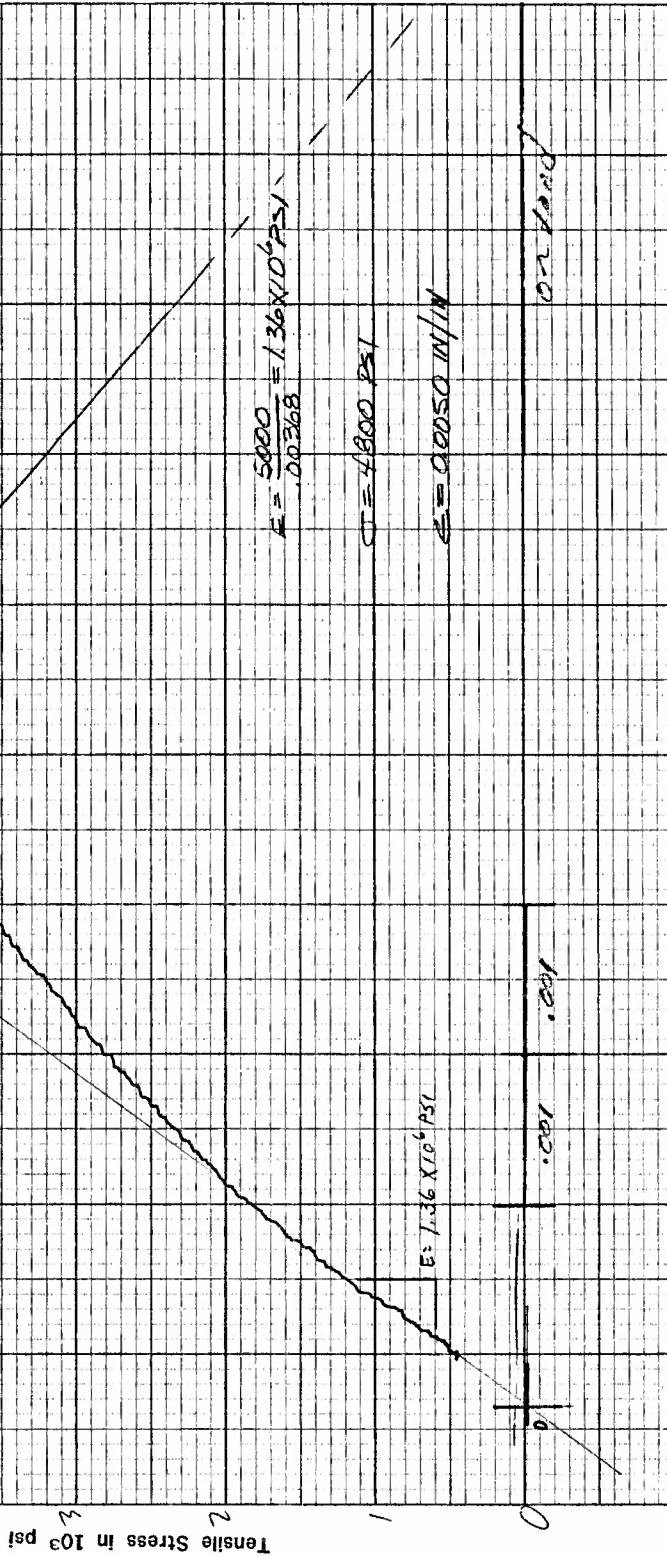


Figure F15. Tensile Stress versus Axial Strain for Specimen A15W of ATJ-S Graphite at 70°F

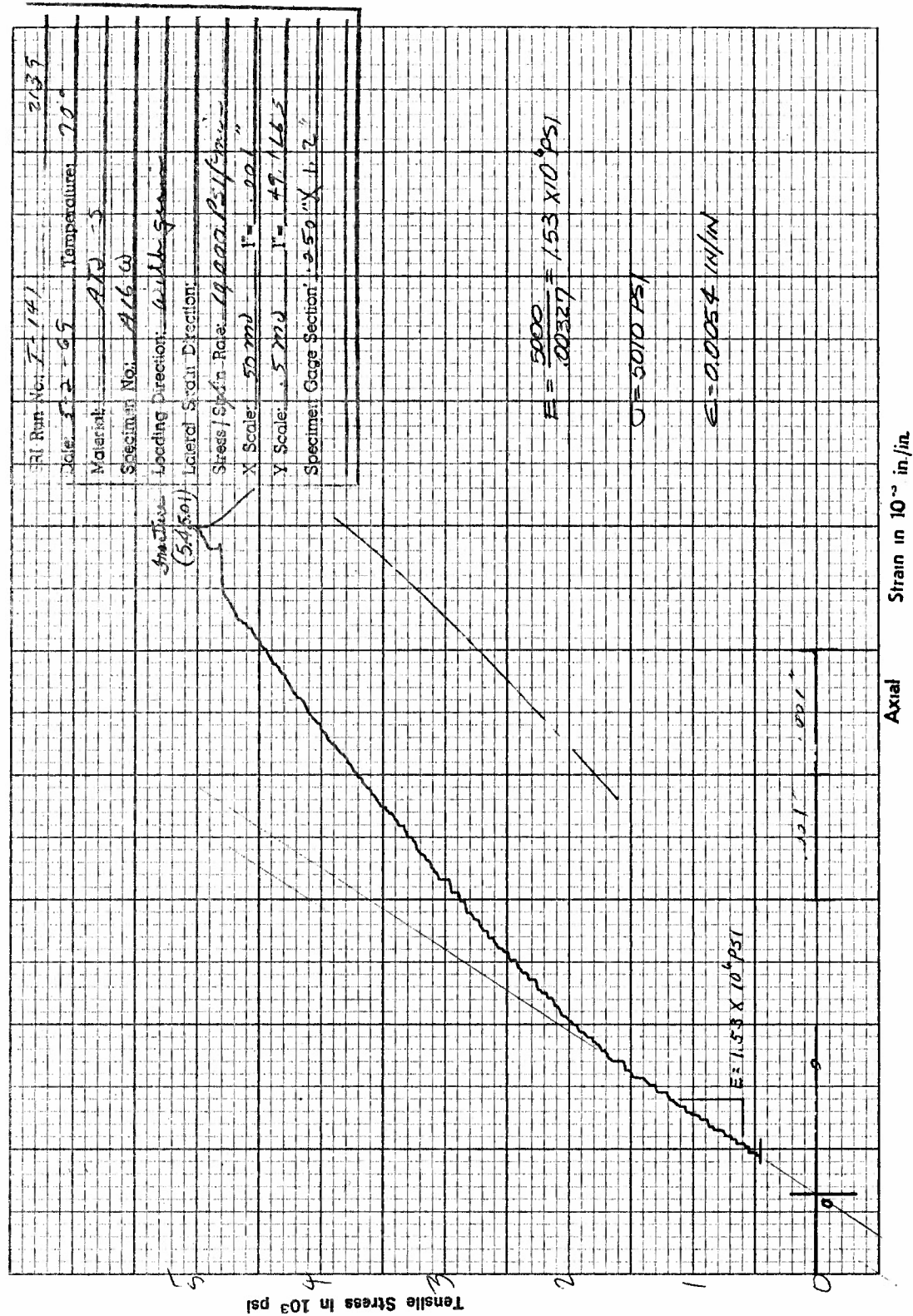
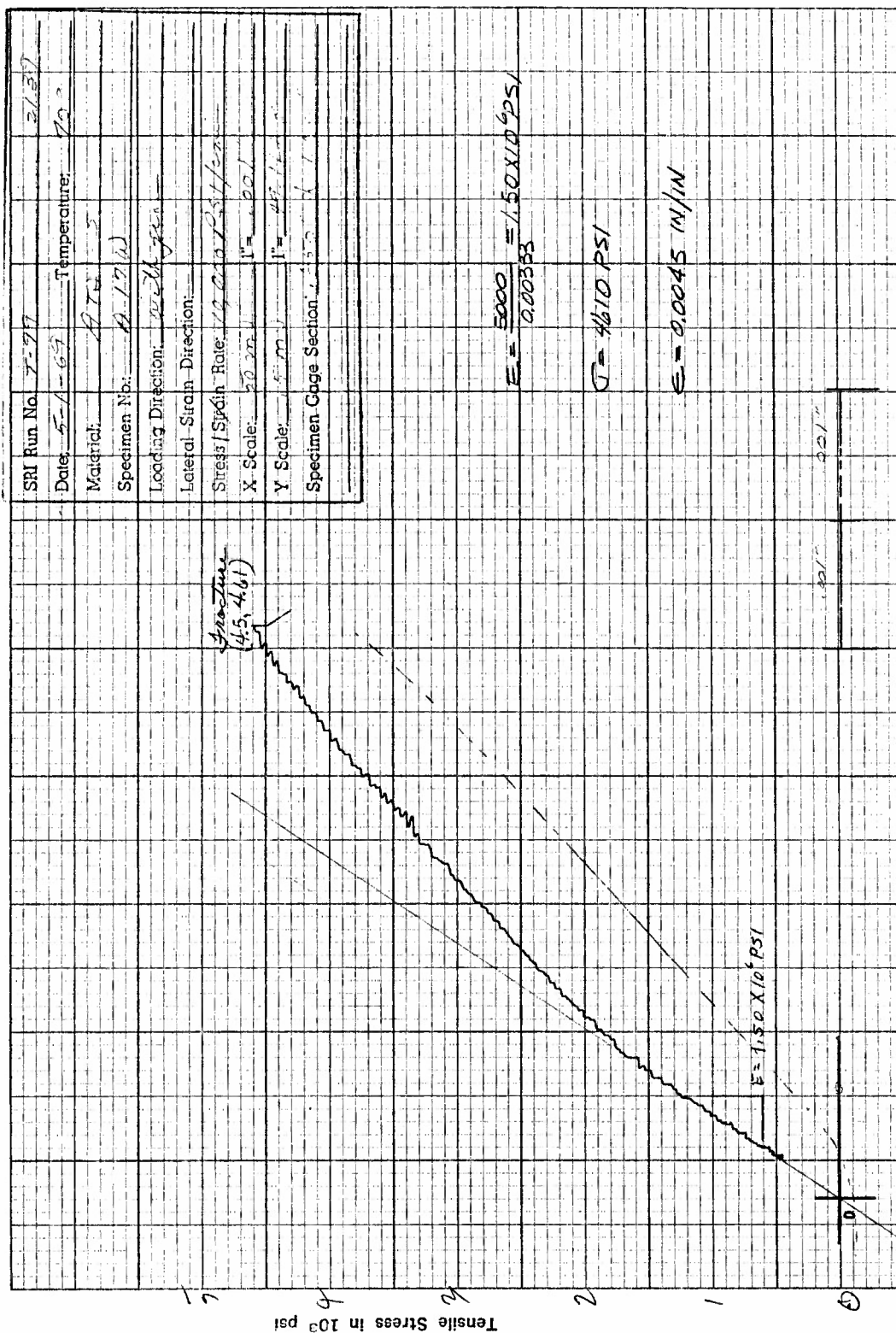


Figure F16. Tensile Stress versus Axial Strain for Specimen A16W of ATJ-S Graphite at 70°F



SRI Run No.	7-77	2137
Date	5-1-69	Temperature: 70°
Material	ATJ-S	
Specimen No.	A-17W	
Loading Direction	with grain	
Lateral Strain Direction		
Stress/Strain Rate	10,000 psi/min	
X Scale	50 mm	1" = 25.4 mm
Y Scale	5 mm	1" = 25.4 mm
Specimen Gage Section	1.50	1.1

Figure F17. Tensile Stress versus Axial Strain for Specimen A17W of ATJ-S Graphite at 70°F

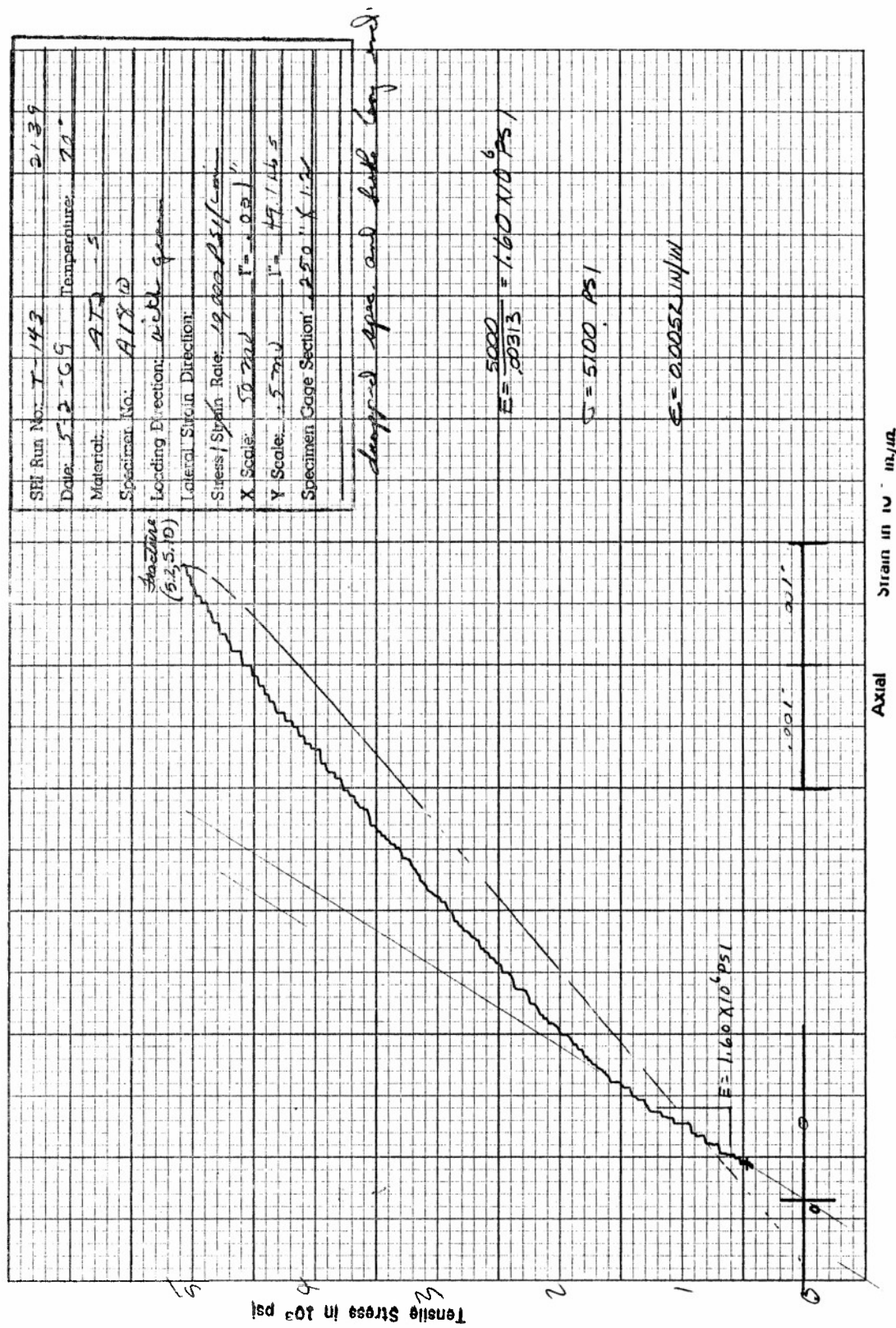


Figure F18. Tensile Stress versus Axial Strain for Specimen A18W of ATJ-S Graphite at 70°F

SRI Run No.:	T-15-2	Proj	2139
Date:	3/5/69	Temperature:	70°F
Material:	A.T.J.-5		
Specimen No.:	A-19-W		
Loading Direction:	WITH STRAIN		
Lateral Strain Direction:			
Stress / Strain Rate:	10,000	psi/min	
X Scale:	1" =	1,001	
Y Scale:	1" =	49.1	
Specimen Gage Section:	0.234" x 1.2"		

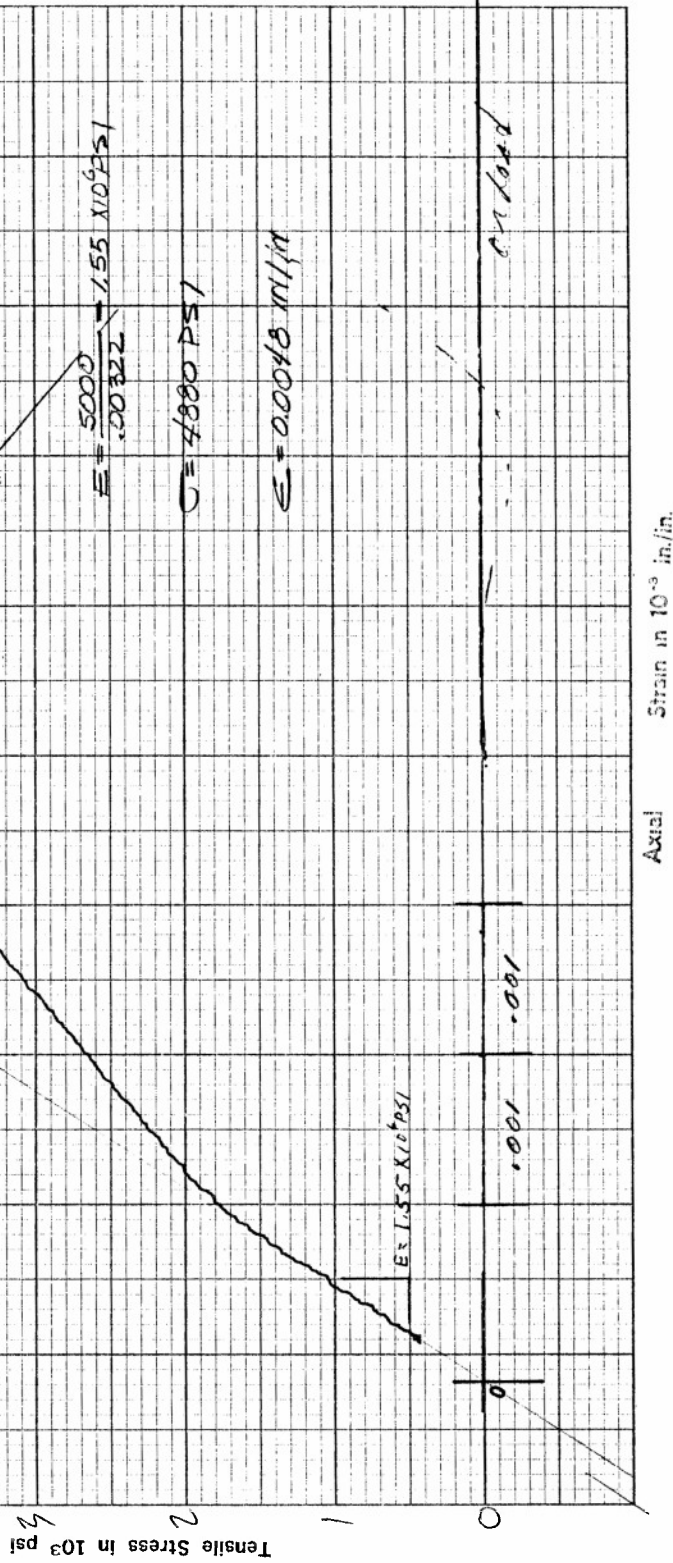


Figure F19. Tensile Stress versus Axial Strain for Specimen A19W of ATJ-S Graphite at 70°F



SRI Run No.	IF-100	Run: 5237
Date	8/12/67	Temperature: 70°F
Material	ATJ-S	
Specimen No.	A	
Loading Direction	SWITCH - LEFT	
Lateral Strain Direction		
Stress / Strain Rate	10,000 psi/min	
X Scale	1" = 1000 psi	
Y Scale	1" = 1000 psi	
Specimen Gage Section	0.25" X 1.00"	

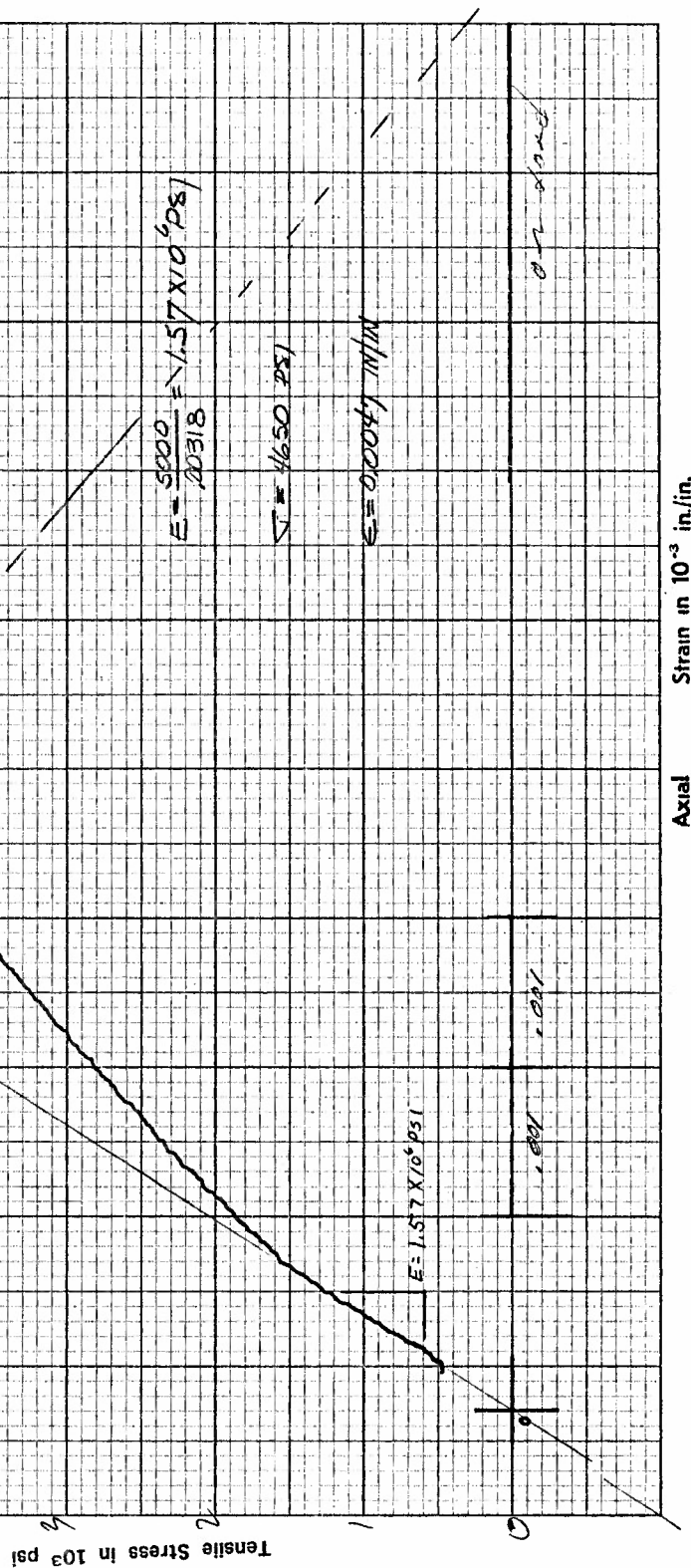


Figure F20. Tensile Stress versus Axial Strain for Specimen A20W of ATJ-S Graphite at 70°F

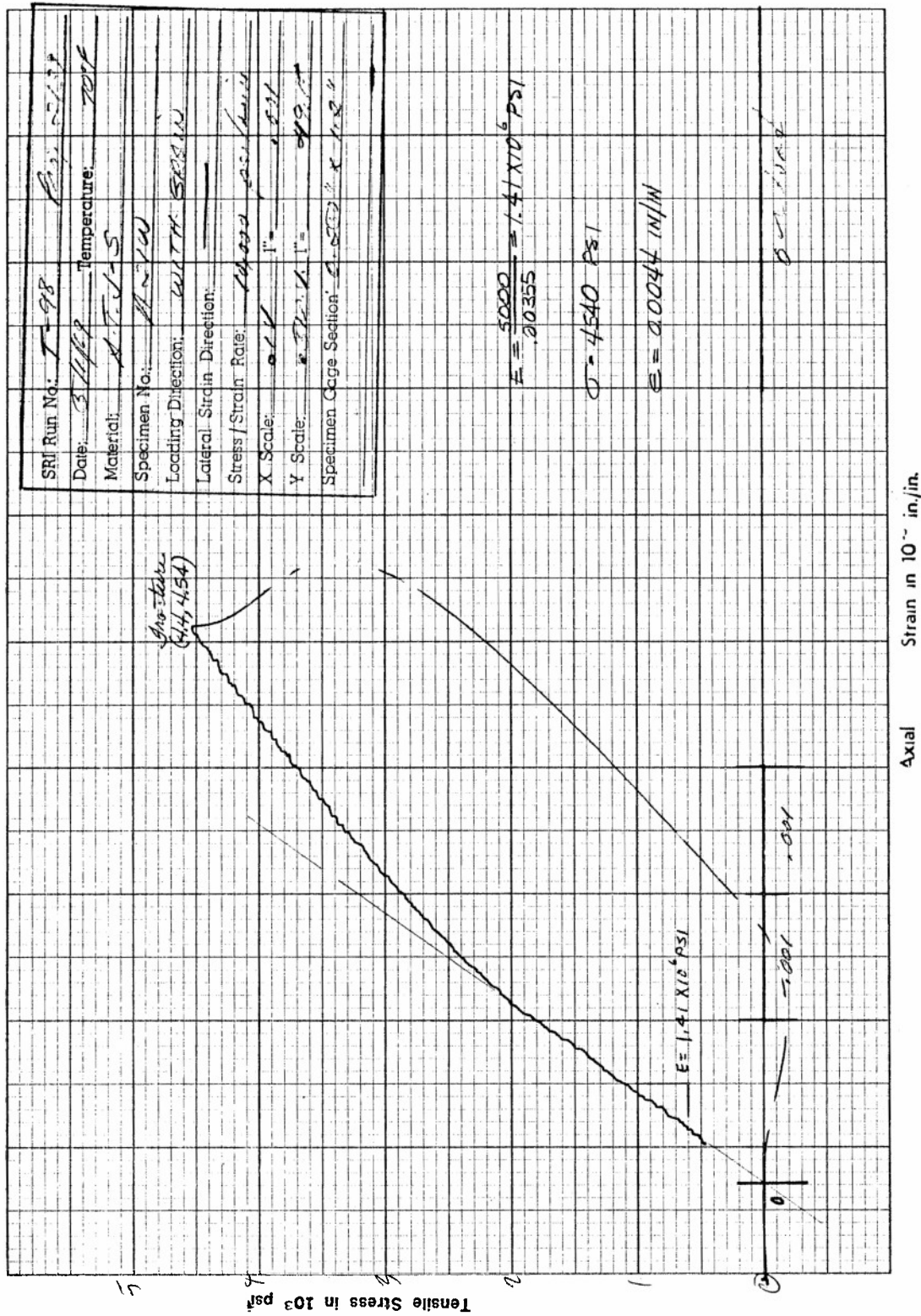


Figure F21. Tensile Stress versus Axial Strain for Specimen A21W of ATJ-S Graphite at 70°F

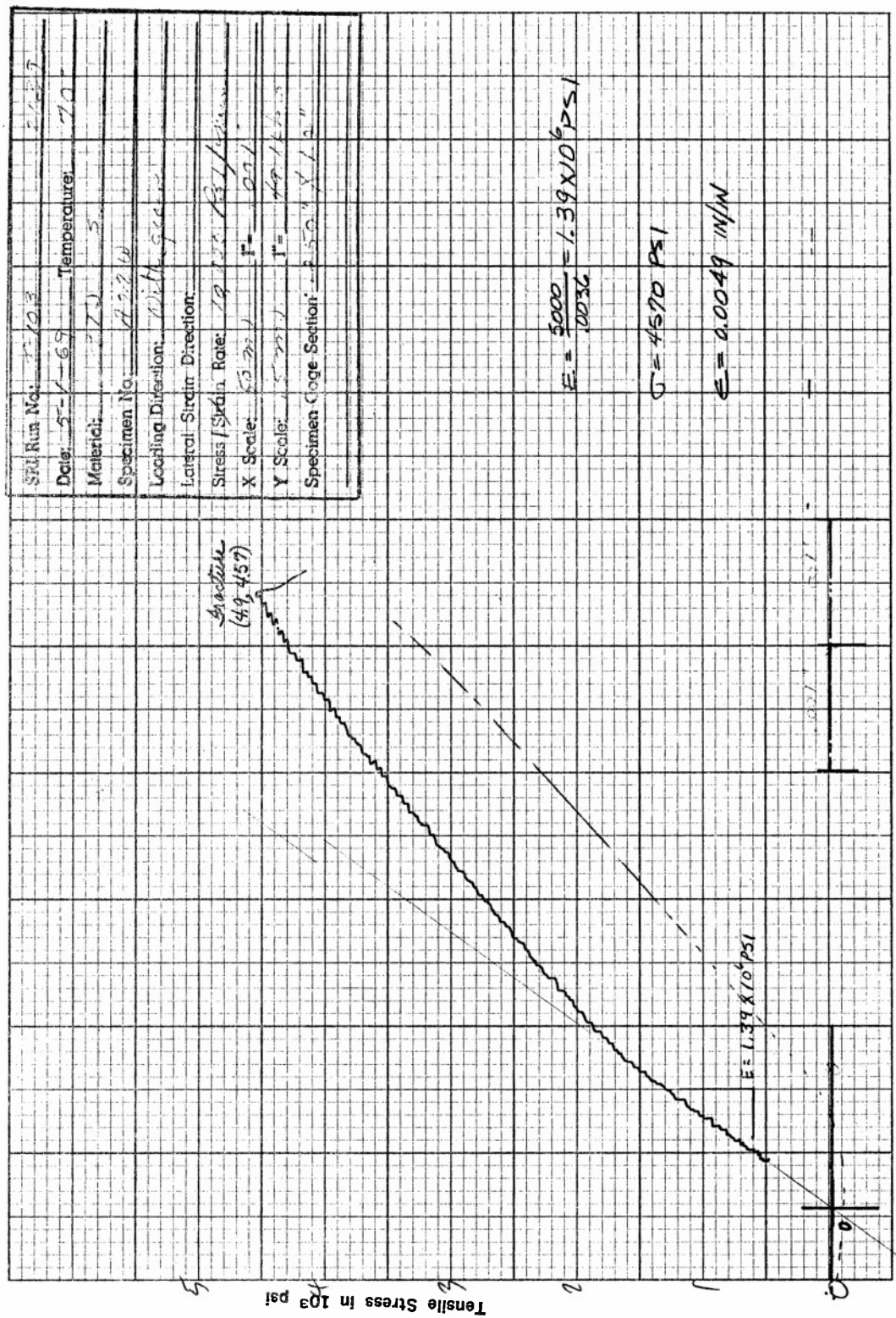


Figure F22. Tensile Stress versus Axial Strain for Specimen A22W of ATJ-S Graphite at 70°F



SRI Run No. T-148 Pci 2127

Date:	<u>3-6-69</u>	Temperature:	<u>70 F</u>
Material:	<u>ATJ-S</u>		
Specimen No.:	<u>A-23W</u>		
Loading Direction:	<u>ULTIM - GRAIN</u>		
Initial Strain Direction:	<u>—</u>		
Stress/Strain Rate:	<u>12,557 psi/min</u>		
X Scale:	<u>100</u>	1" =	<u>.001</u>
Y Scale:	<u>12,557</u>	1" =	<u>49.12</u>
Specimen Gage Section:	<u>0.230" X 1.20"</u>		

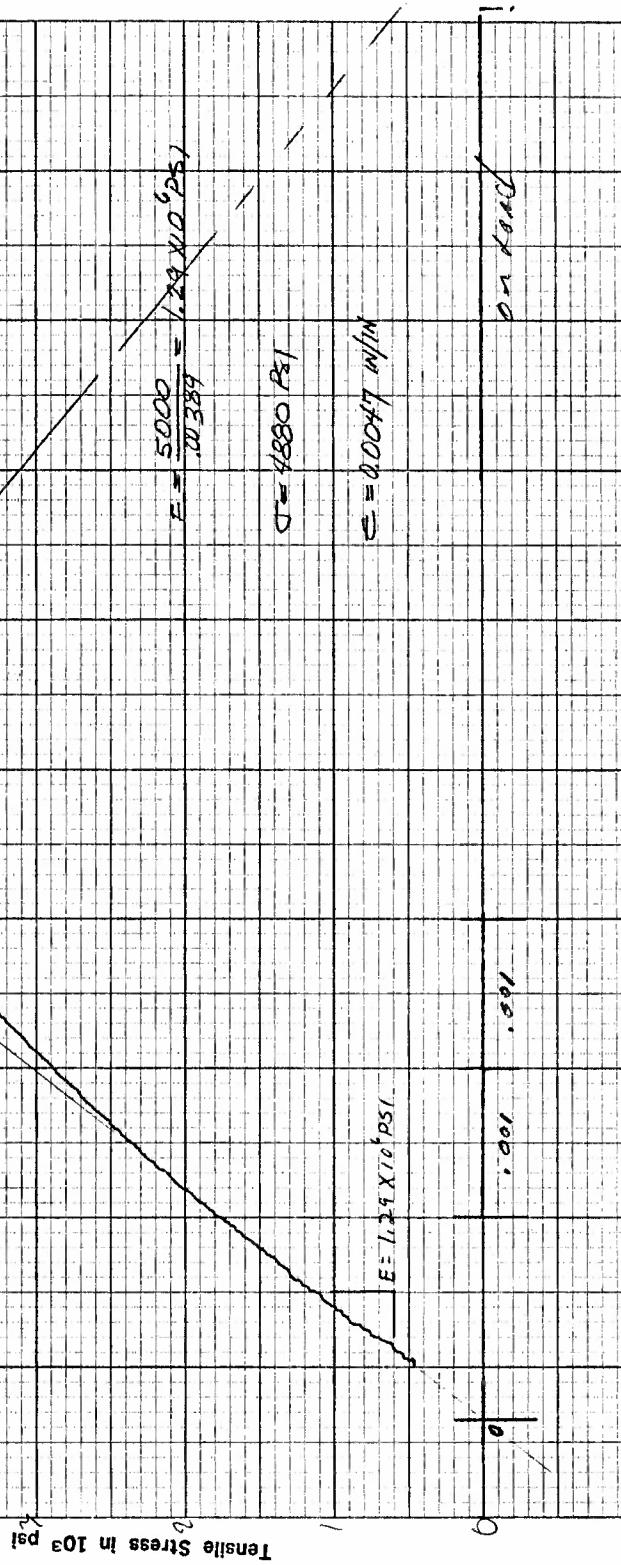


Figure F23. Tensile Stress versus Axial Strain for Specimen A23W of ATJ-S Graphite at 70°F

SRI Run No:	T-146	Per: 2139
Date:	5/24/69	Temperature: 70°F
Material:	ATJ-S	
Specimen No.:	A2446	
Loading Direction:	WITH GRAIN	
Load Strain Direction:		
Stress / Strain Rate:	10,000 psi/min	
X Scale:	10 in	
Y Scale:	13,440 in	
Specimen Gage Section:	0.250" X 1.2"	

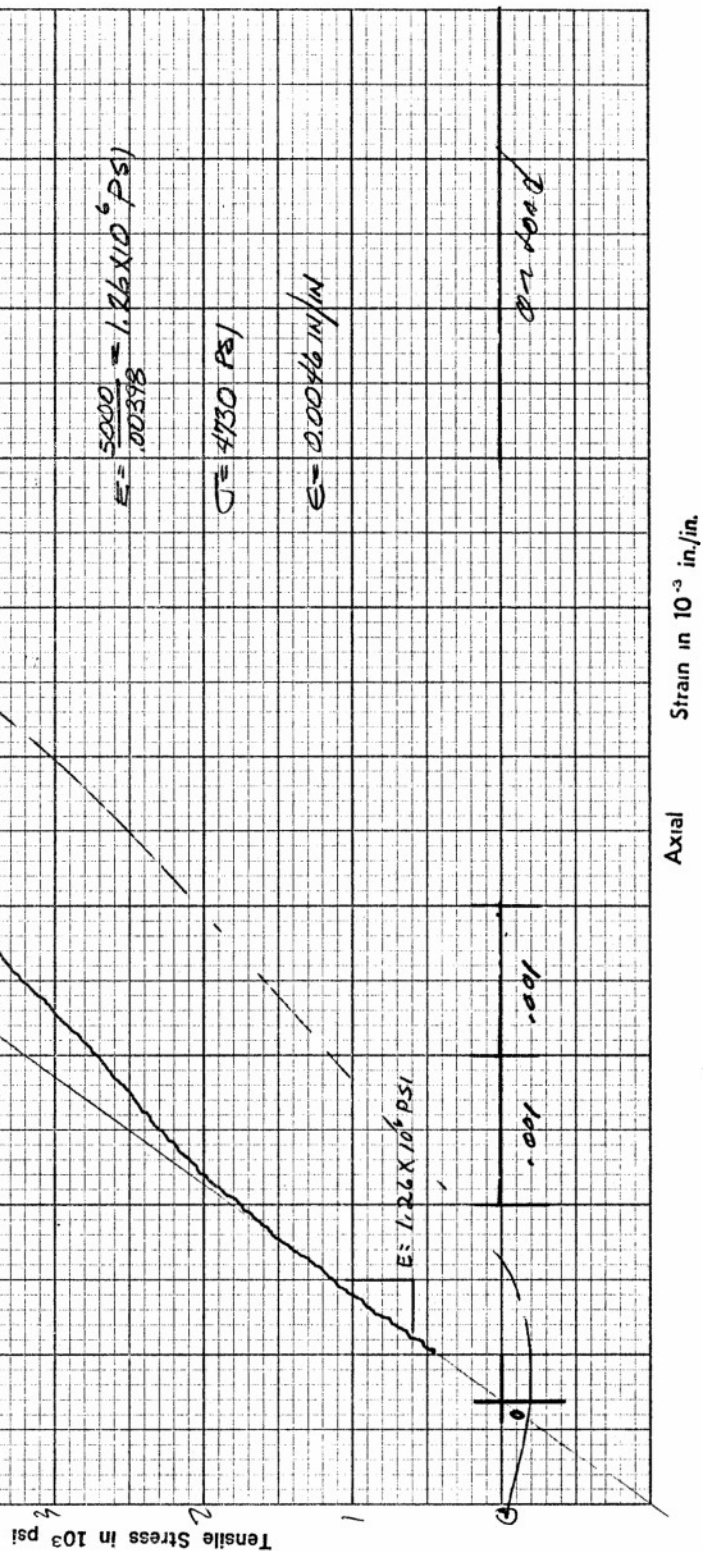


Figure F24. Tensile Stress versus Axial Strain for Specimen A24W of ATJ-S Graphite at 70°F

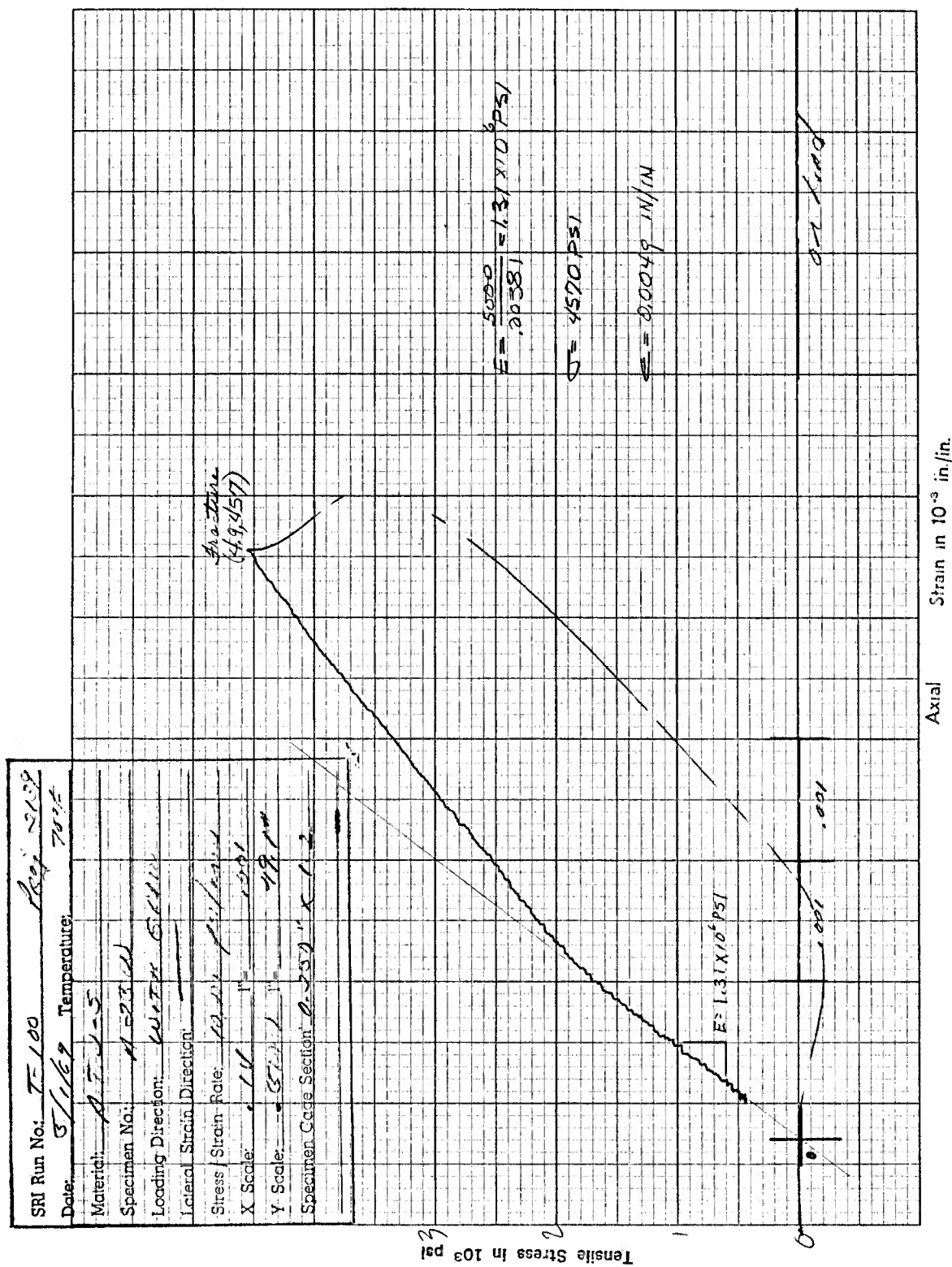


Figure F25. Tensile Stress versus Axial Strain for Specimen A25W of ATJ-S Graphite at 70°F

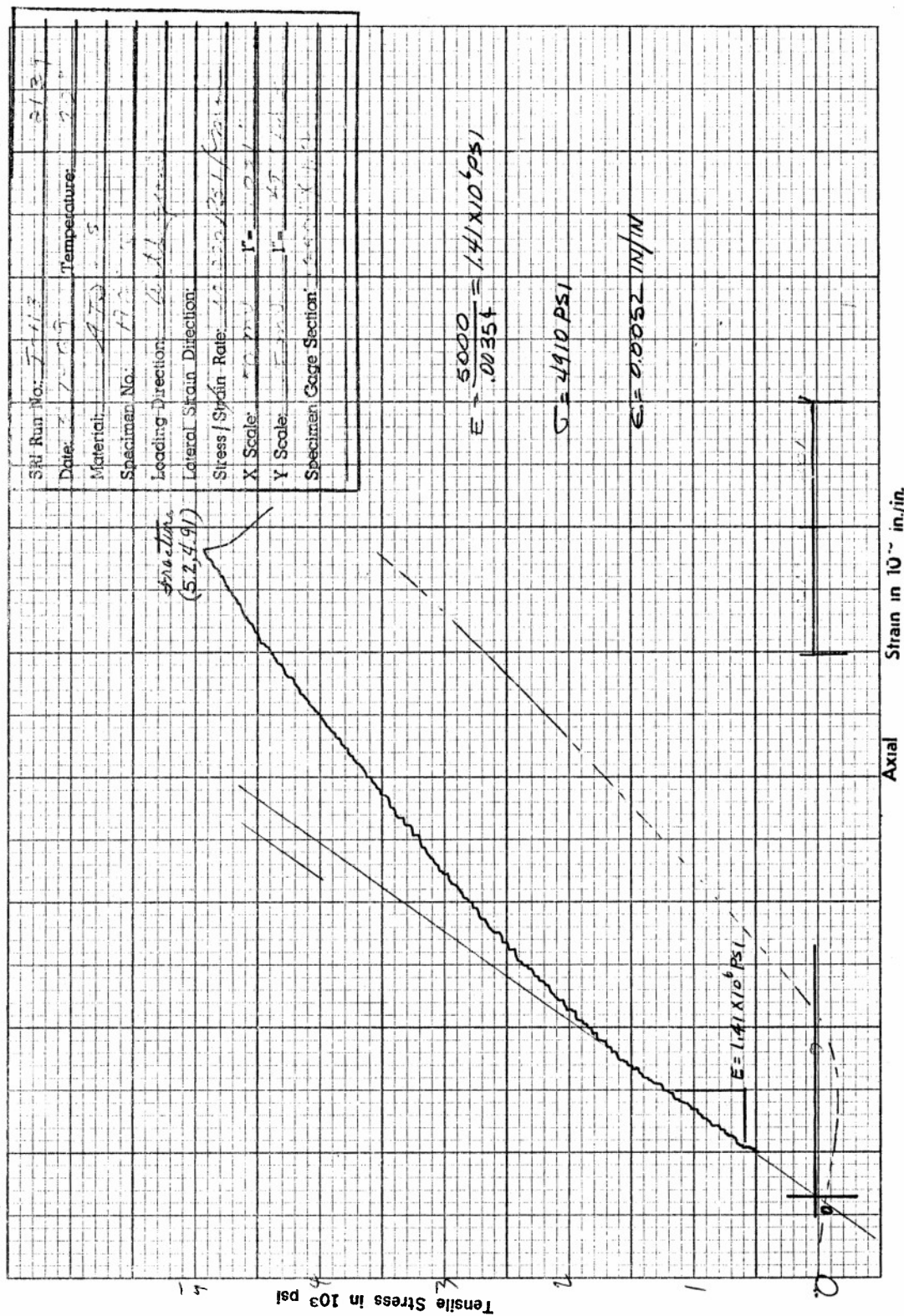


Figure F26. Tensile Stress versus Axial Strain for Specimen A26W of ATJ-S Graphite at 70°F

SRI Run No:	T-106	Proj: 22137
Date:	5/1/69	Temperature: 70°F
Material:	ATJ-S	
Specimen No:	A-27W	
Loading Direction:	WITH GRAIN	
Lateral Strain Direction:		
Stress / Strain Rate:	10,000 psi/min	
X Scale:	1" = .001	
Y Scale:	1" = 0.001	
Specimen Gage Section:	0.5" x 1.25"	

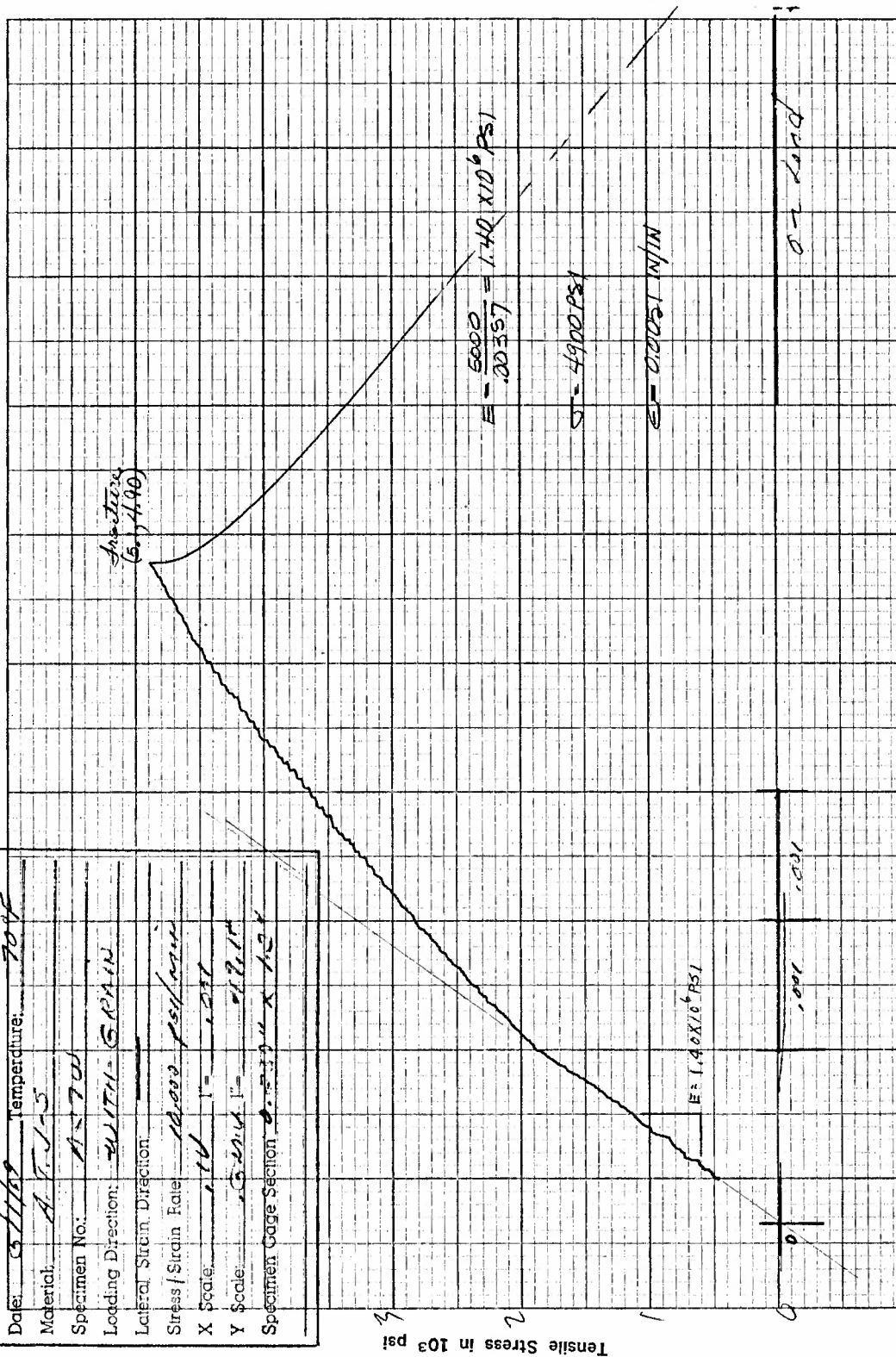


Figure F27. Tensile Stress versus Axial Strain for Specimen A27W of ATJ-S Graphite at 70°F



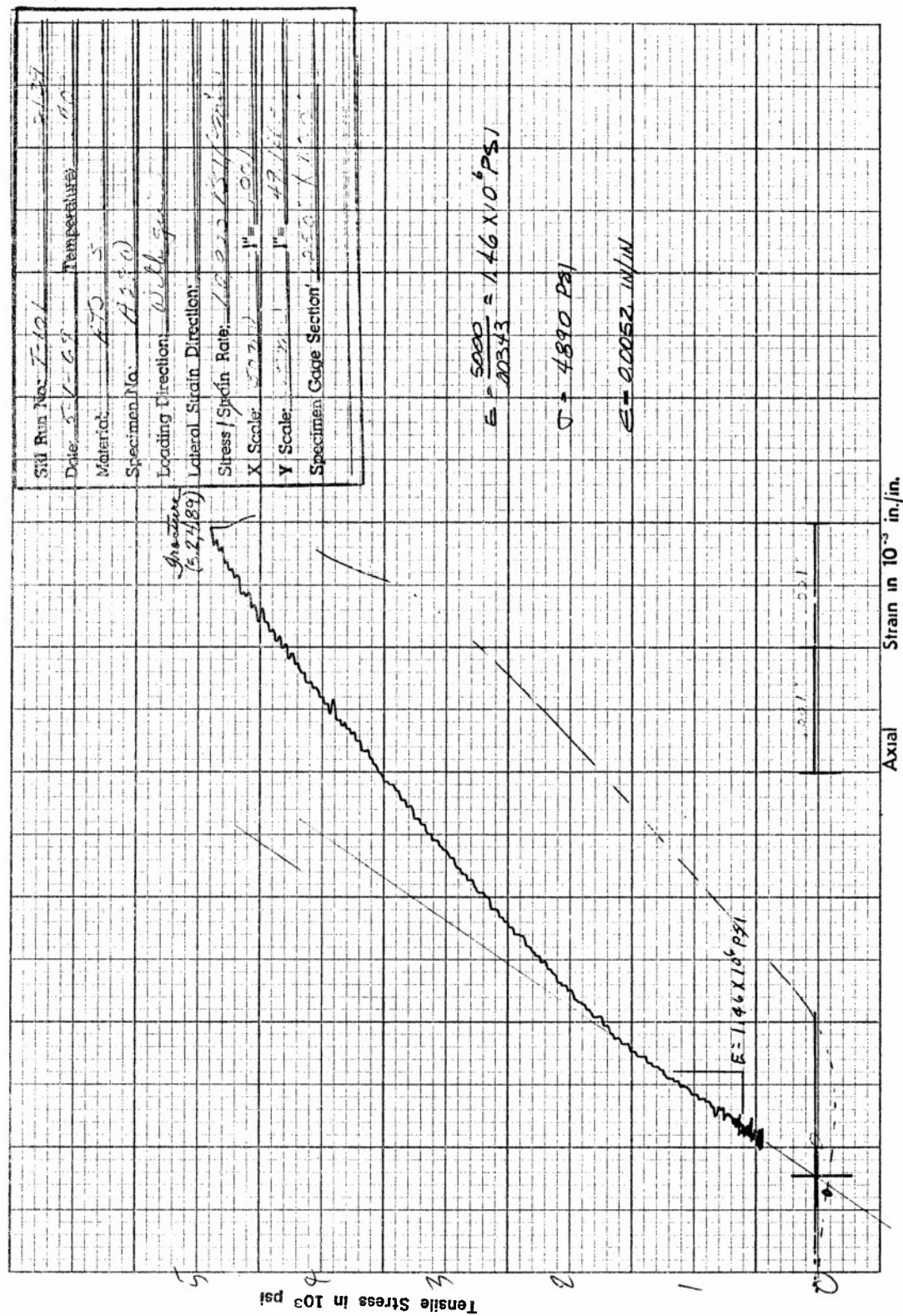


Figure F28. Tensile Stress versus Axial Strain for Specimen A28W of ATJ-S Graphite at 70°F

SRI Run No. T-108 Page 2139

Date: 8/1/68 Temperature: 70°F

Material: A.T.J-5

Specimen No.: A-32W

Loading Direction: WITON SPAIN

Lateral Strain Direction: ---

Stress/Strain Rate: 10.000 psi/min

X Scale: 1" = 1000

Y Scale: 1" = 1000

Specimen Gage Section: 0.25" x 1.0"

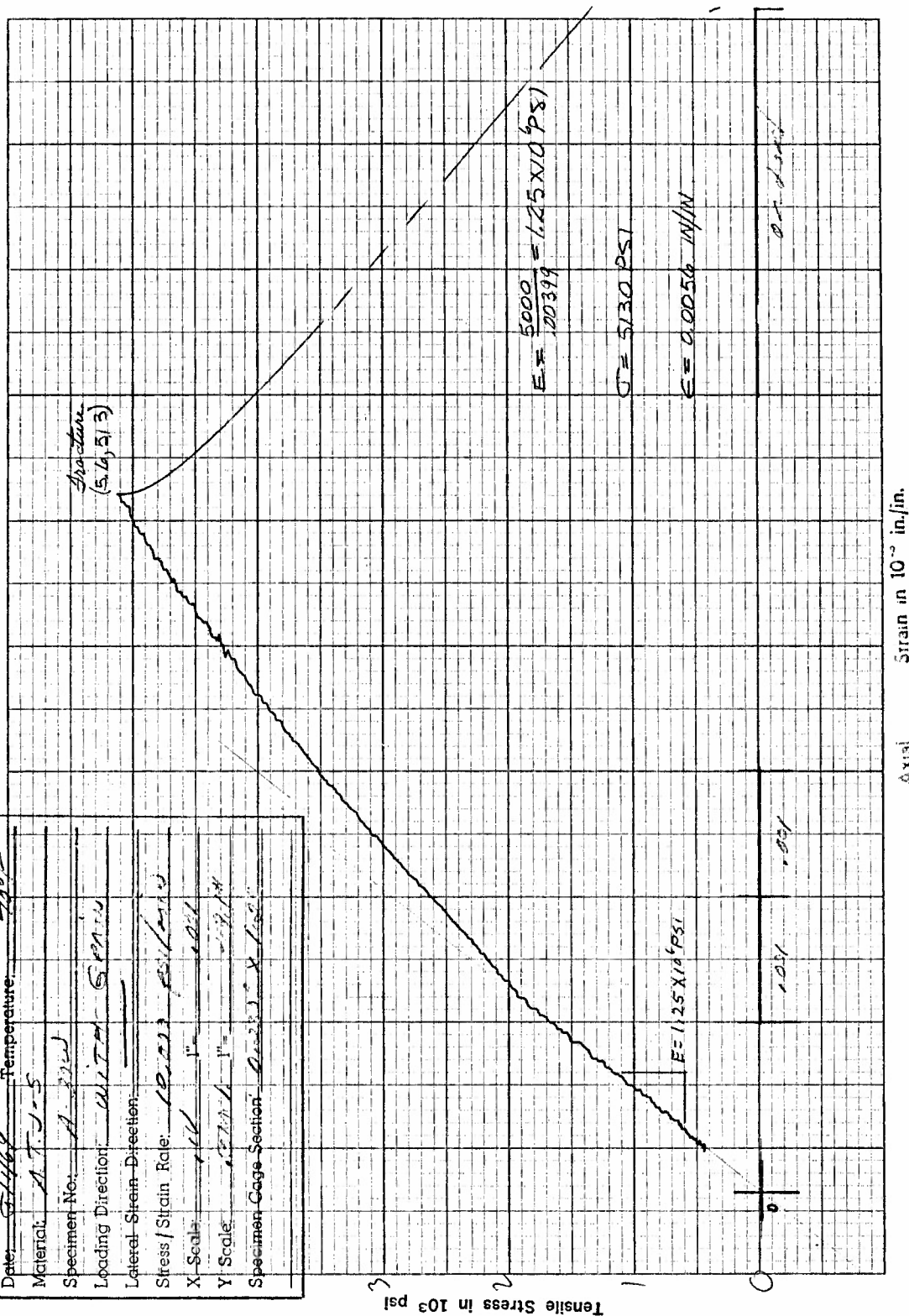


Figure F29. Tensile Stress versus Axial Strain for Specimen A30W of ATJ-S Graphite at 70°F

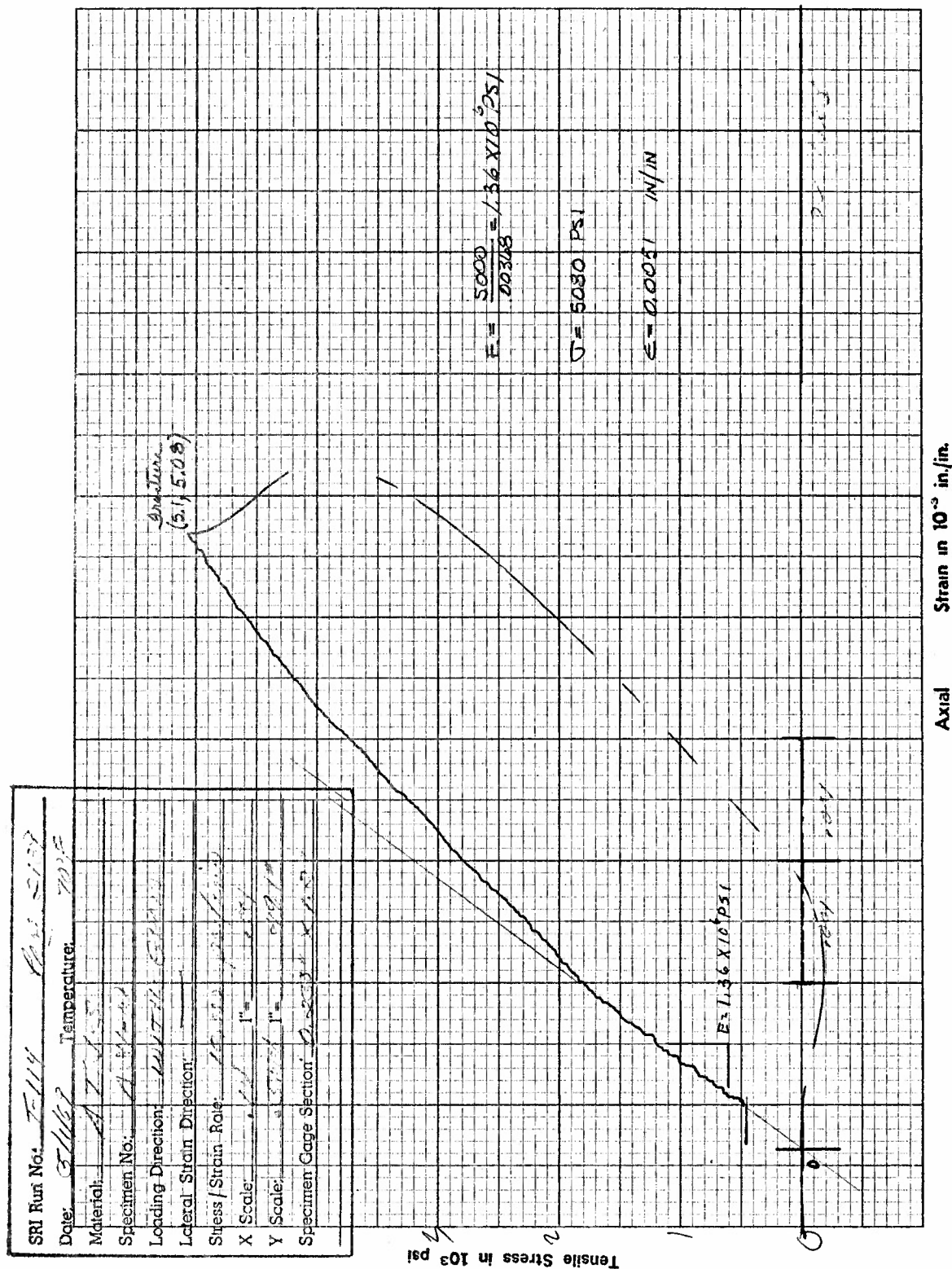


Figure F30. Tensile Stress versus Axial Strain for Specimen A31W of ATJ-S Graphite at 70°F



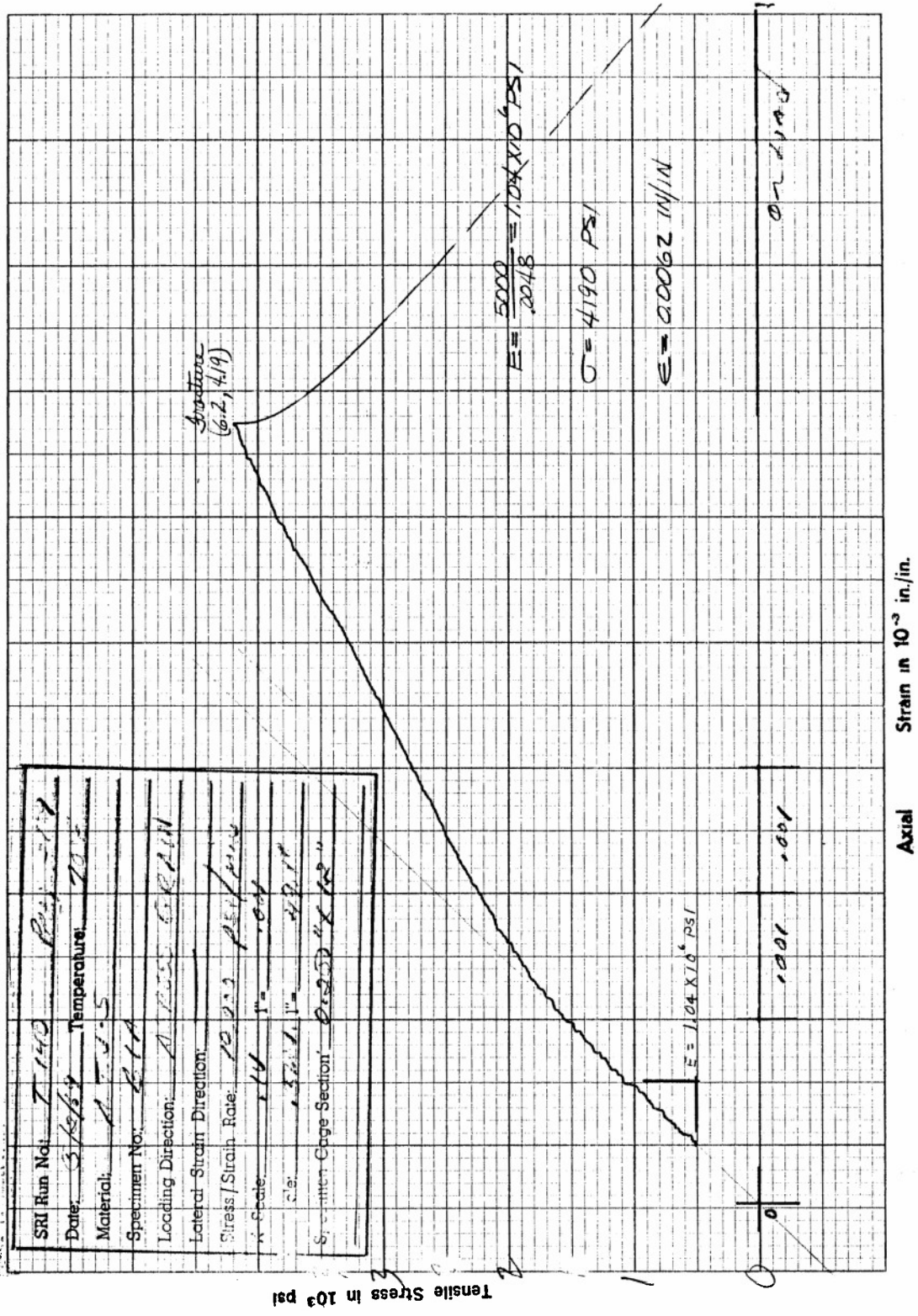


Figure F31. Tensile Stress versus Axial Strain for Specimen B1A of ATJ-S Graphite at 70°F

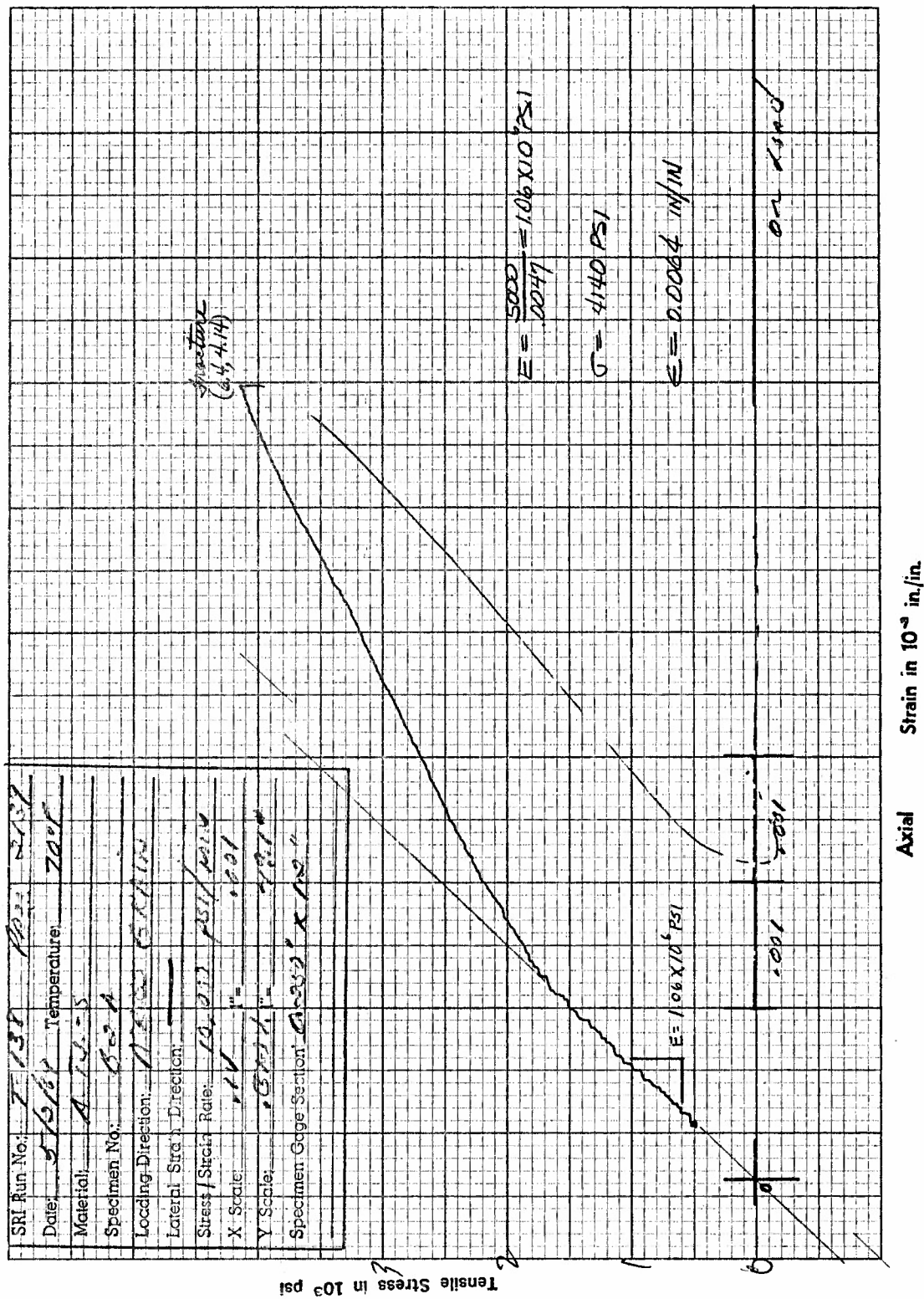


Figure F32. Tensile Stress versus Axial Strain for Specimen B2A of ATJ-S Graphite at 70°F



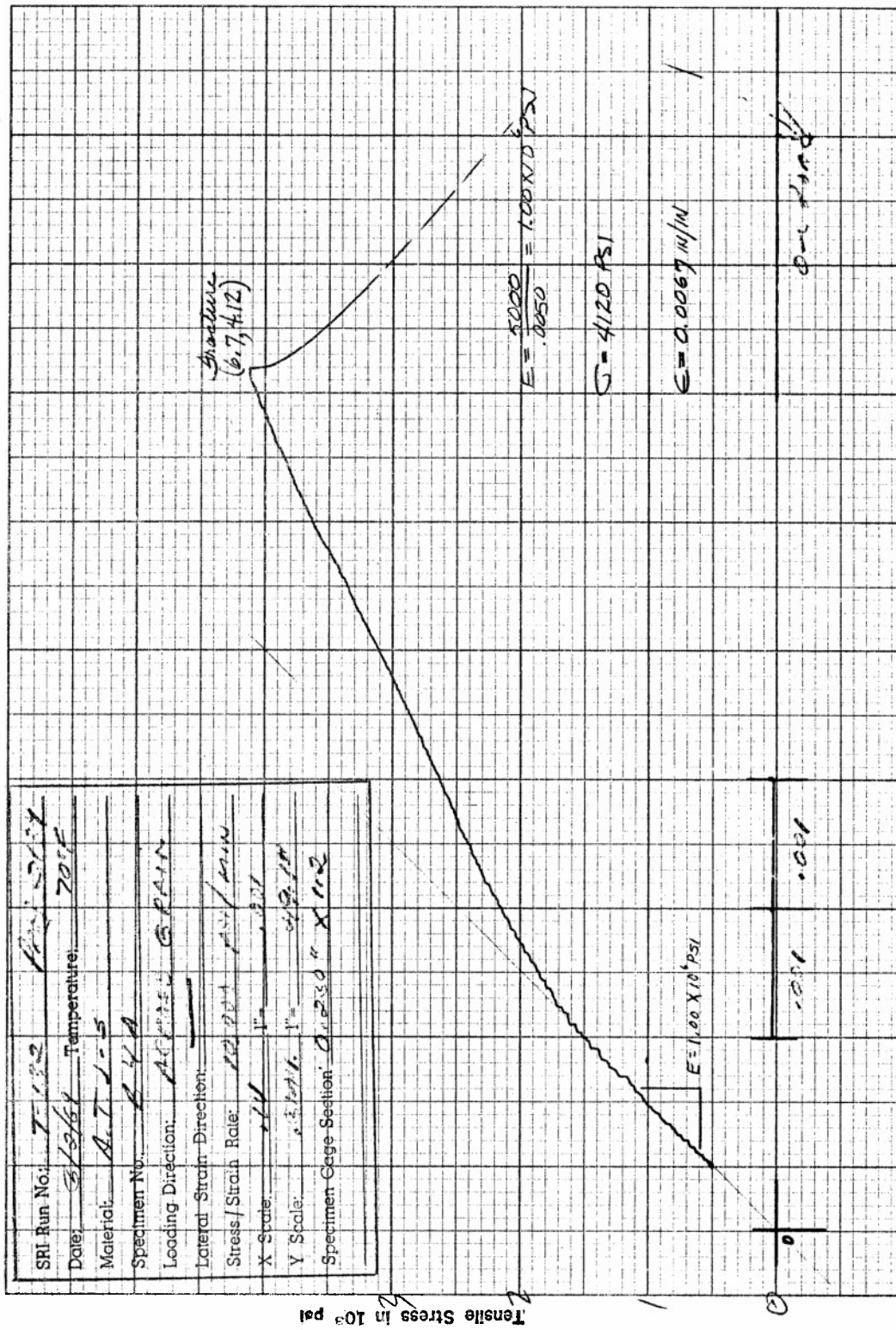


Figure F34. Tensile Stress versus Axial Strain for Specimen B4A of ATJ-S Graphite at 70°F

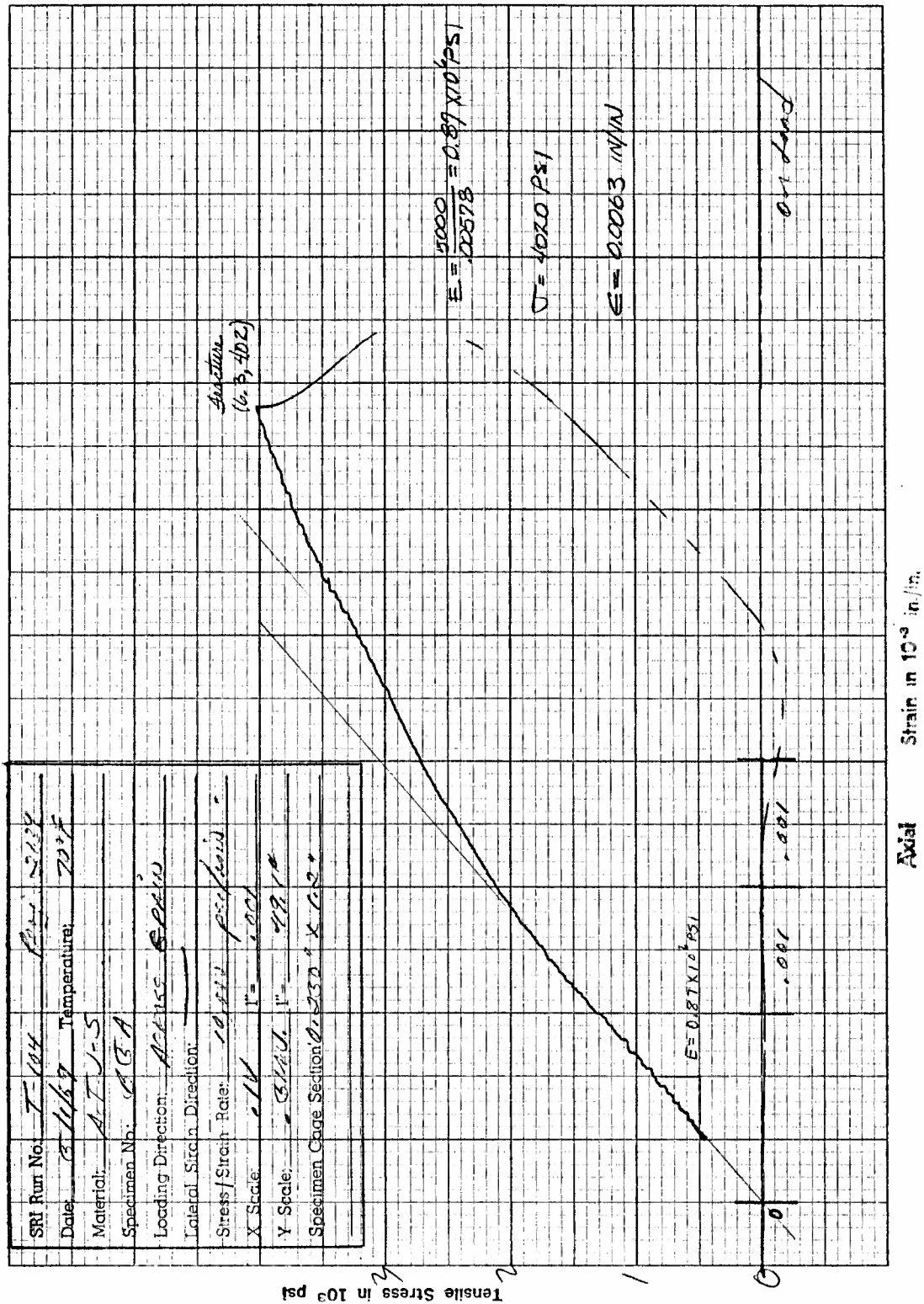


Figure F35. Tensile Stress versus Axial Strain for Specimen B5A of ATJ-S Graphite at 70°F



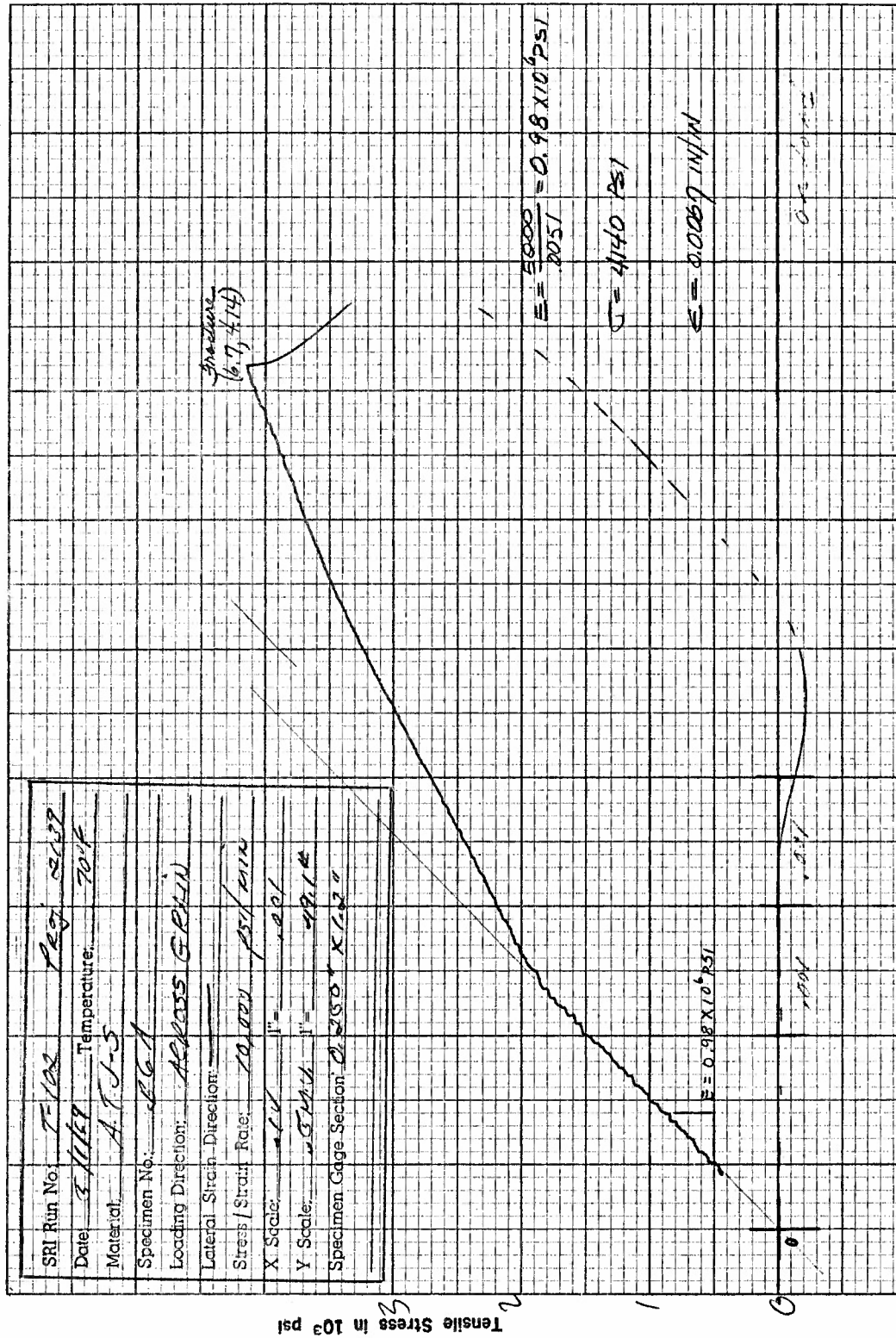


Figure F36. Tensile Stress versus Axial Strain for Specimen B6A of ATJ-S Graphite at 70°F

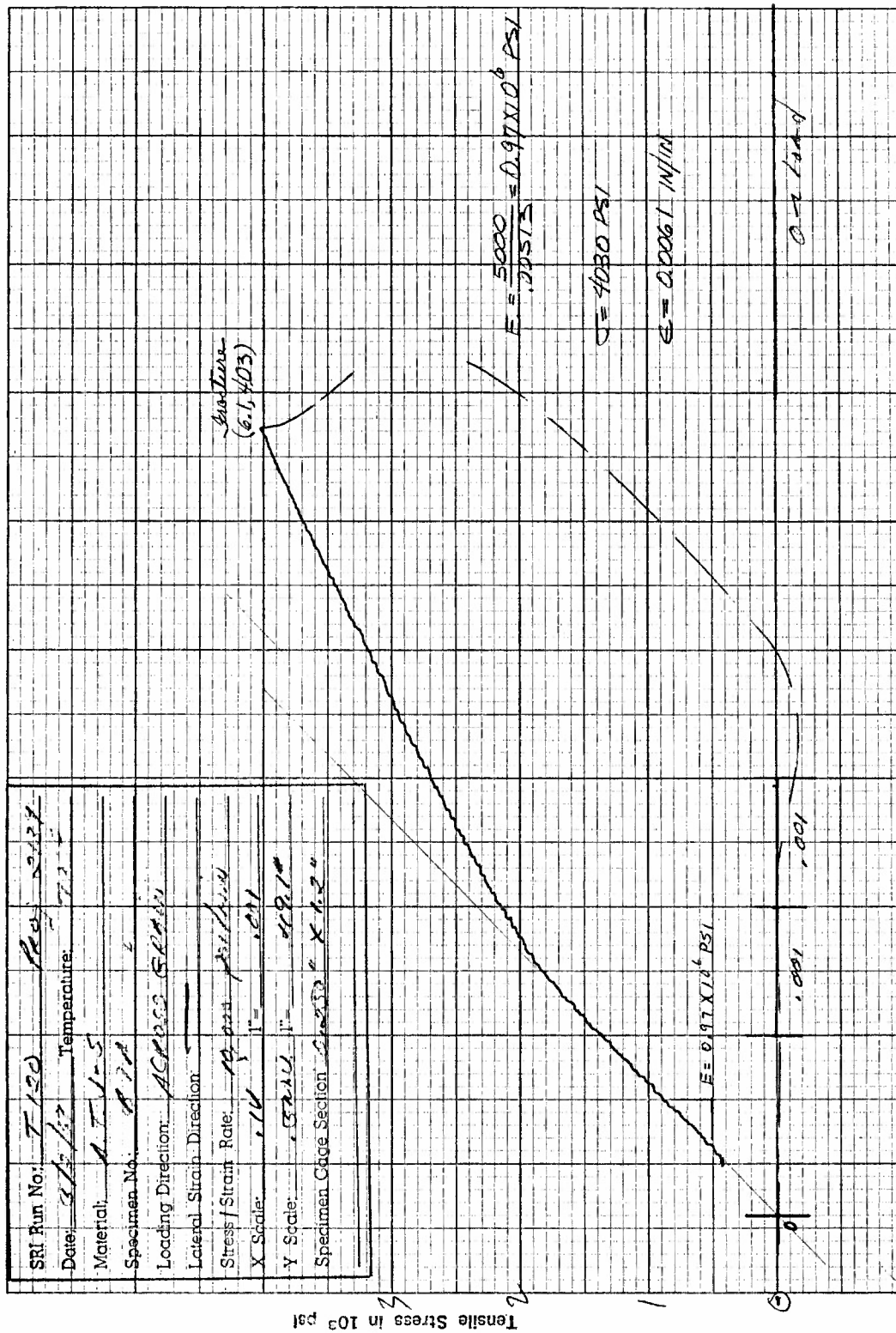


Figure F37. Tensile Stress versus Axial Strain for Specimen B7A of ATJ-S Graphite at 70°F

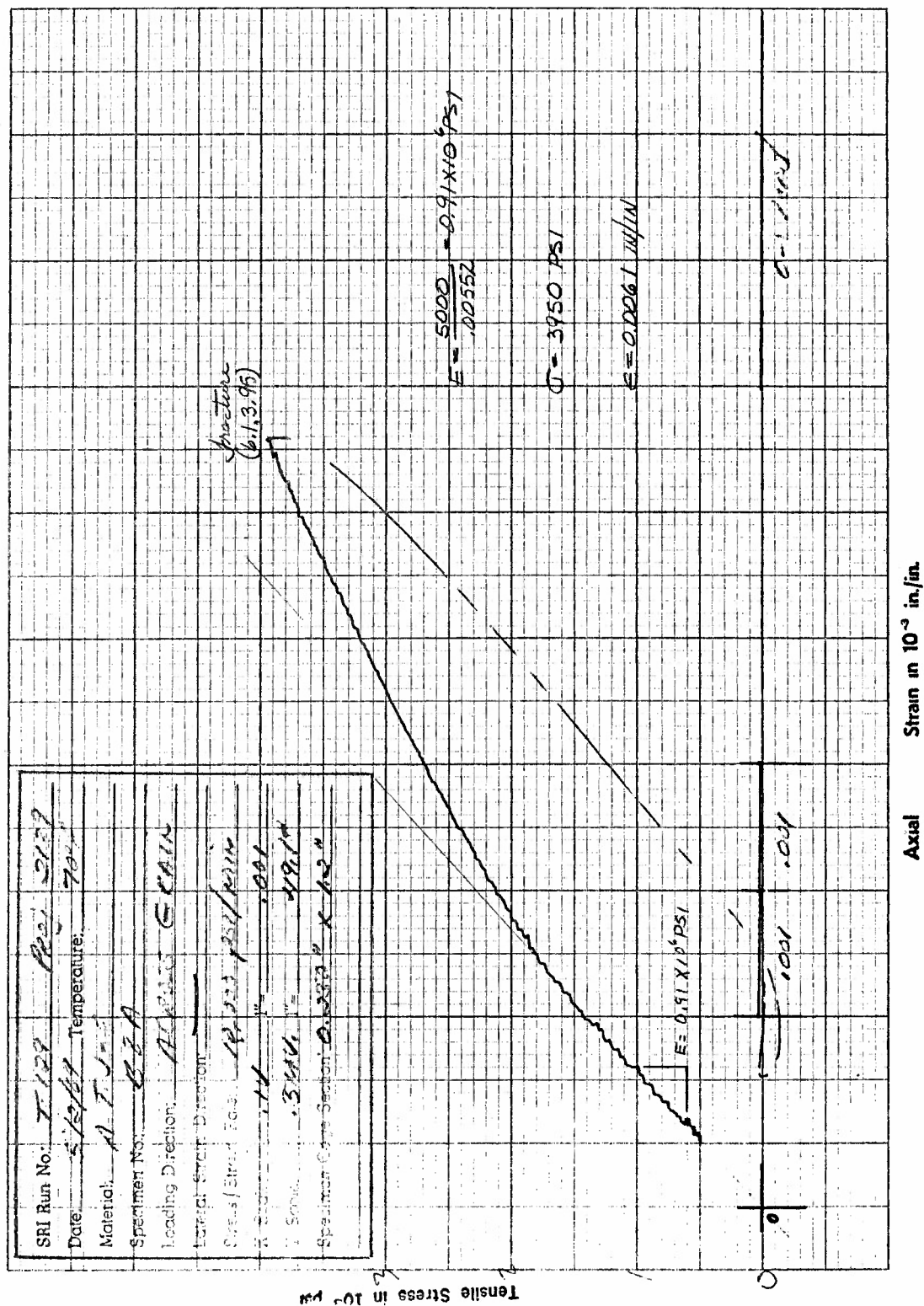


Figure F38. Tensile Stress versus Axial Strain for Specimen B8A of ATJ-S Graphite at 70°F



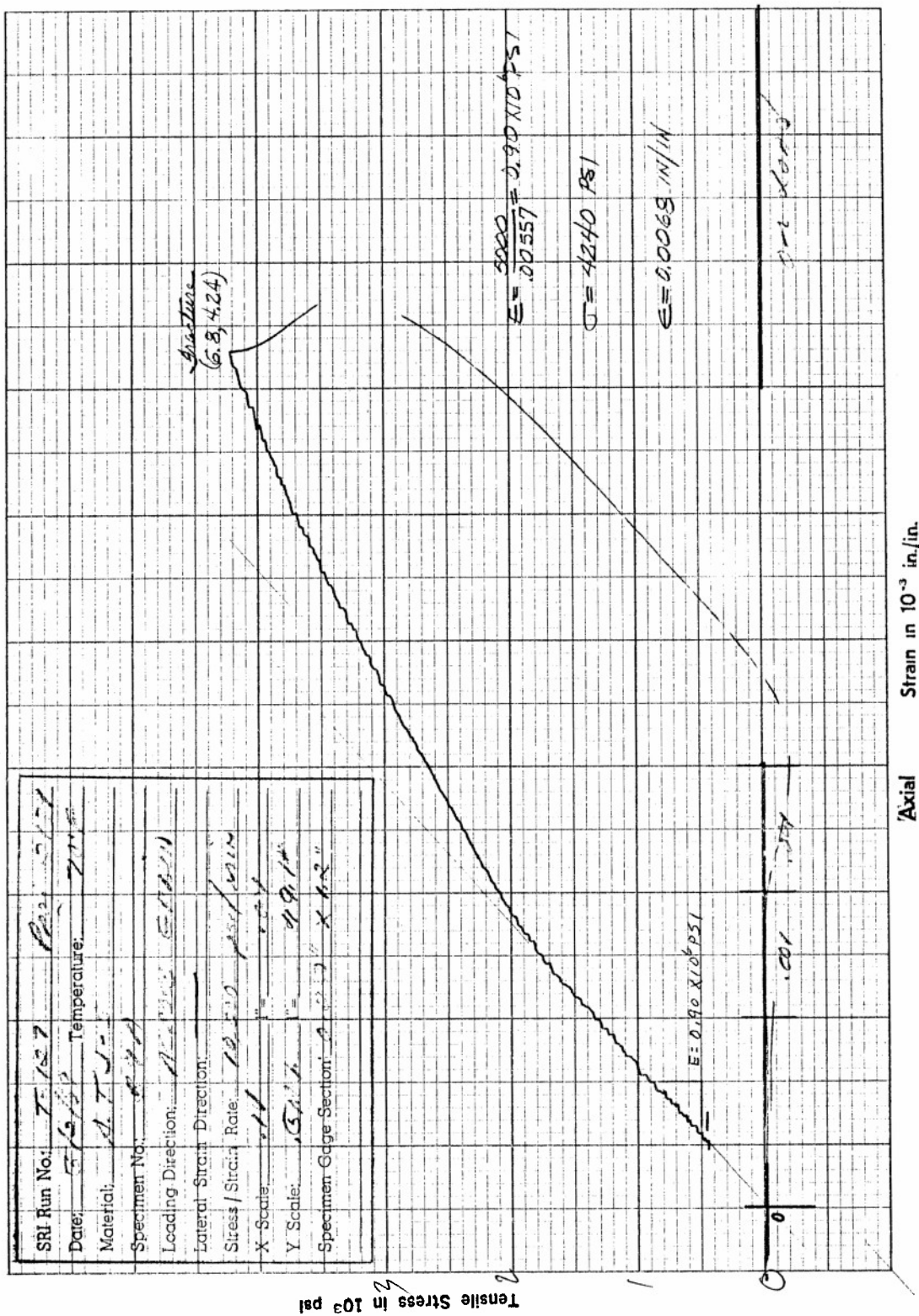


Figure F39. Tensile Stress versus Axial Strain for Specimen B9A of ATJ-S Graphite at 70°F

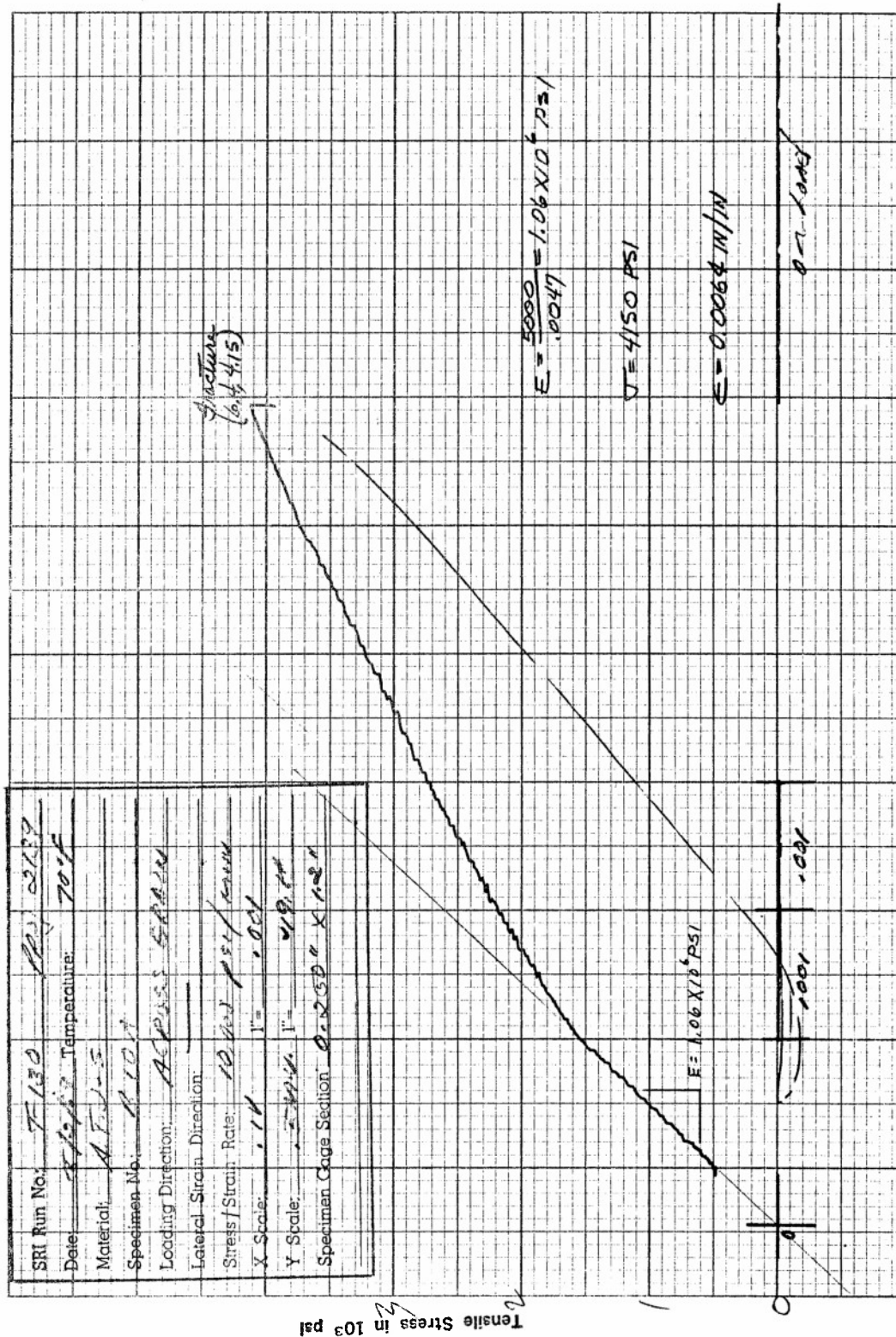


Figure F40. Tensile Stress versus Axial Strain for Specimen A10A of ATJ-S Graphite at 70°F

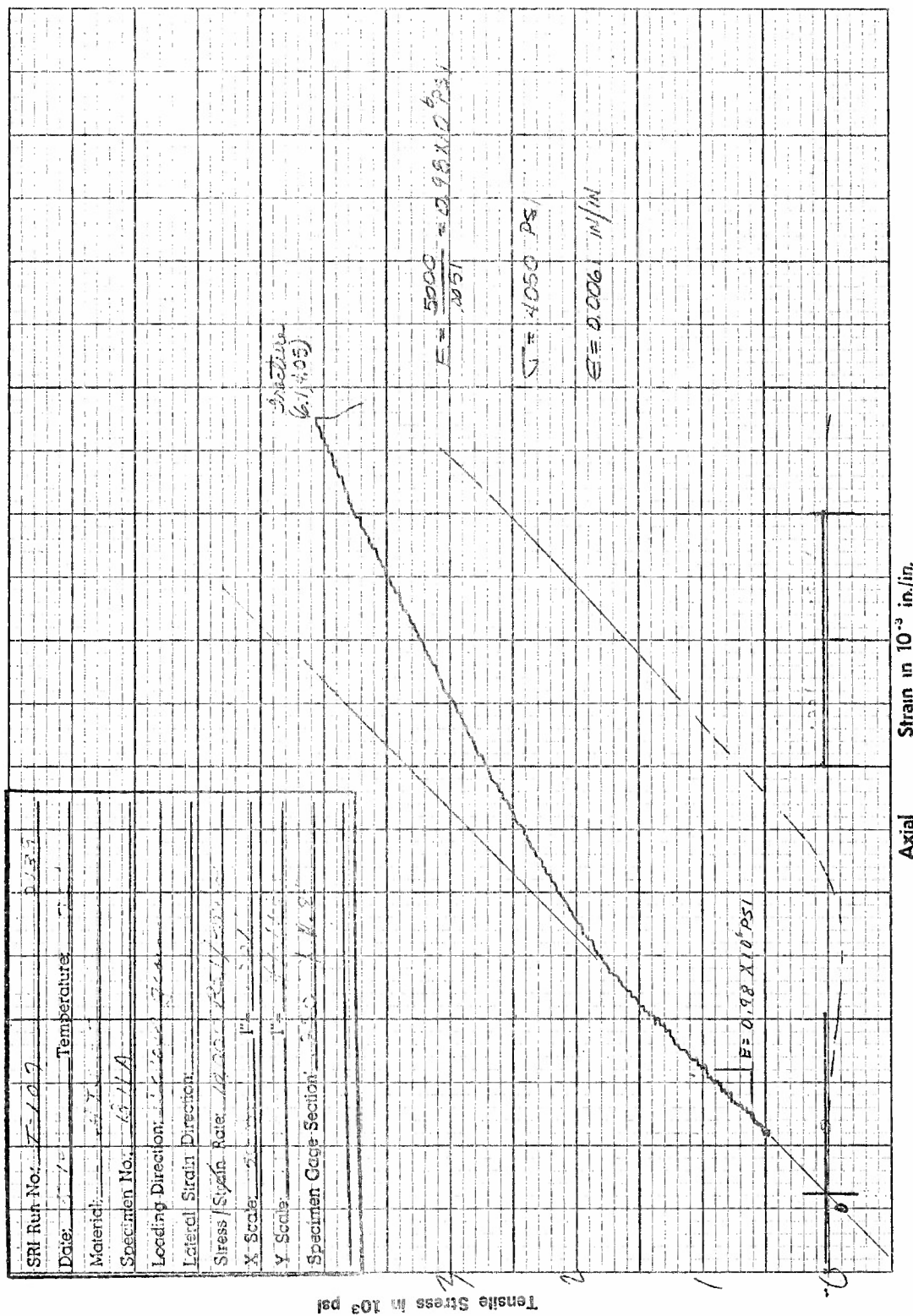


Figure F41. Tensile Stress versus Axial Strain for Specimen B11A of ATJ-S Graphite at 70°F

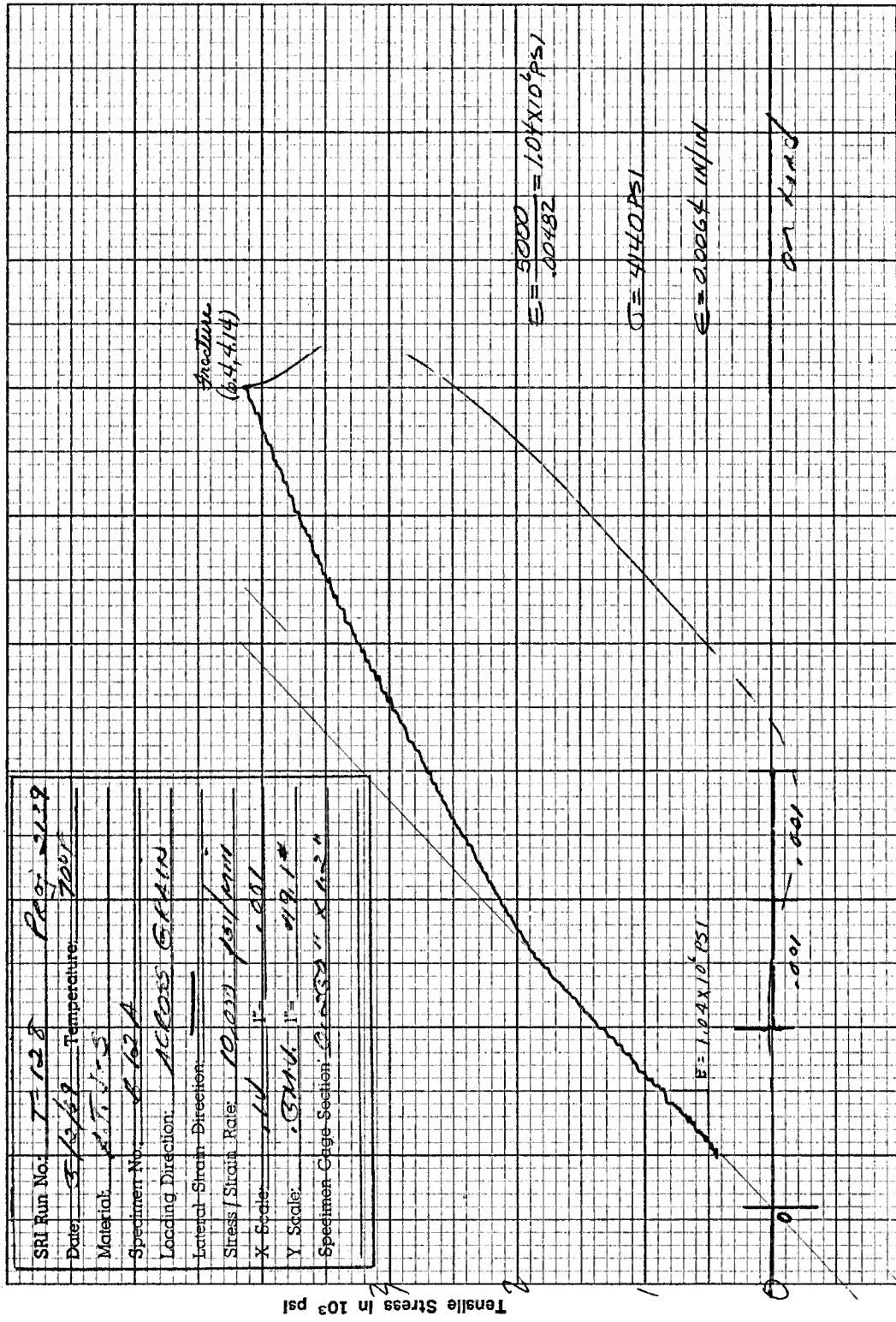


Figure F42. Tensile Stress versus Axial Strain for Specimen B12A of ATJ-S Graphite at 70°F



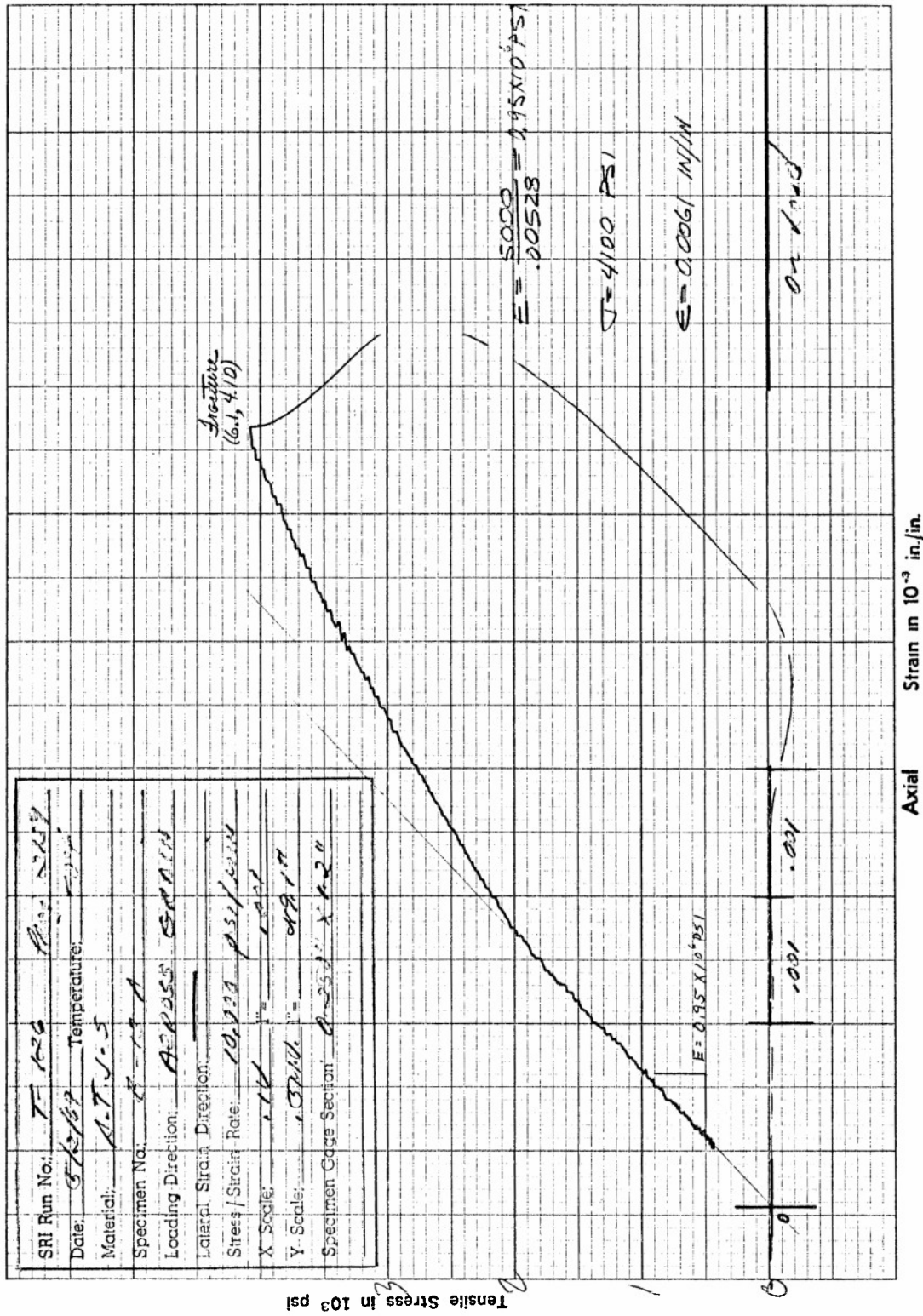


Figure F43. Tensile Stress versus Axial Strain for Specimen B13A of ATJ-S Graphite at 70°F

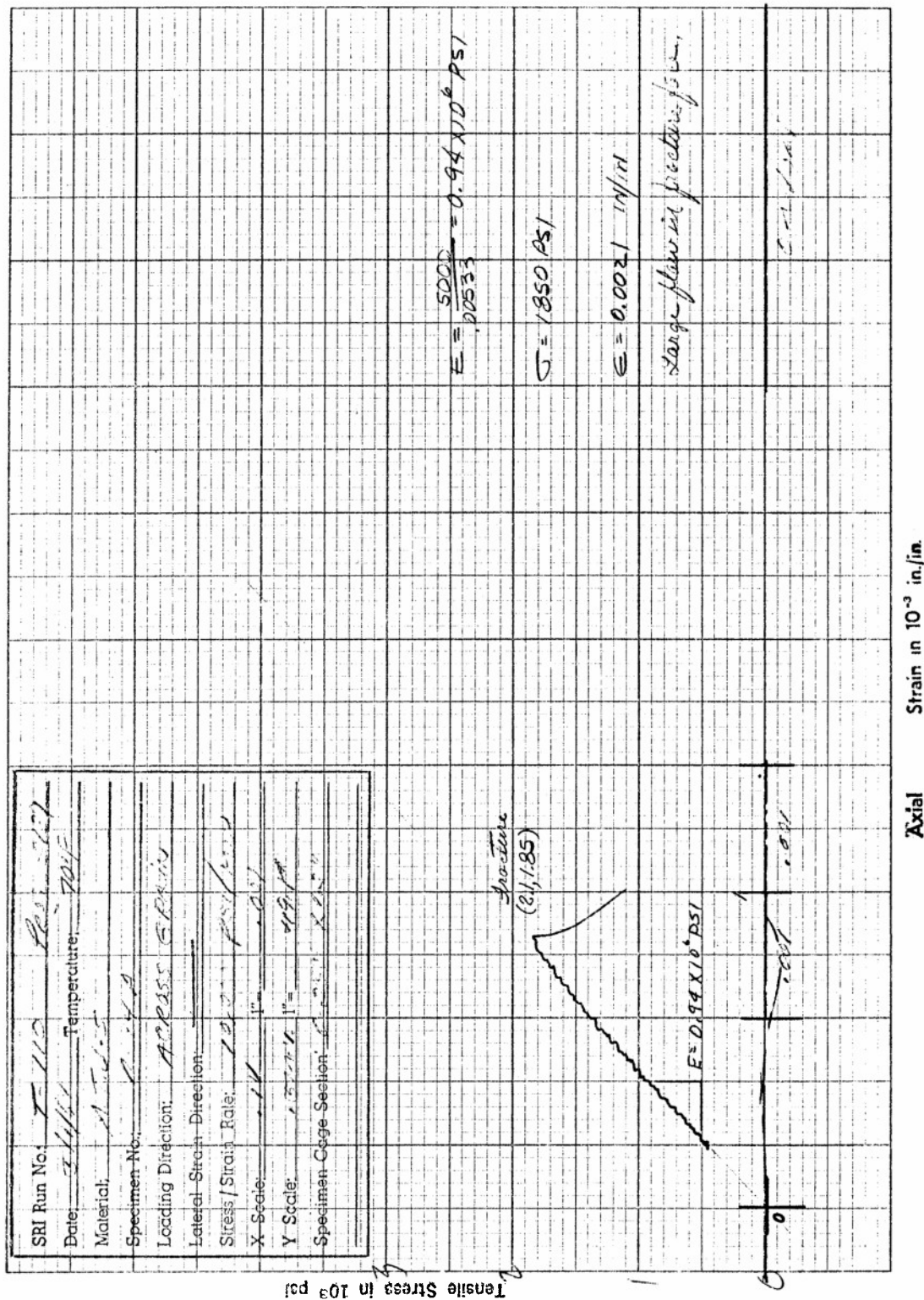


Figure F44. Tensile Stress versus Axial Strain for Specimen B14A of AGJ-S Graphite at 70°F

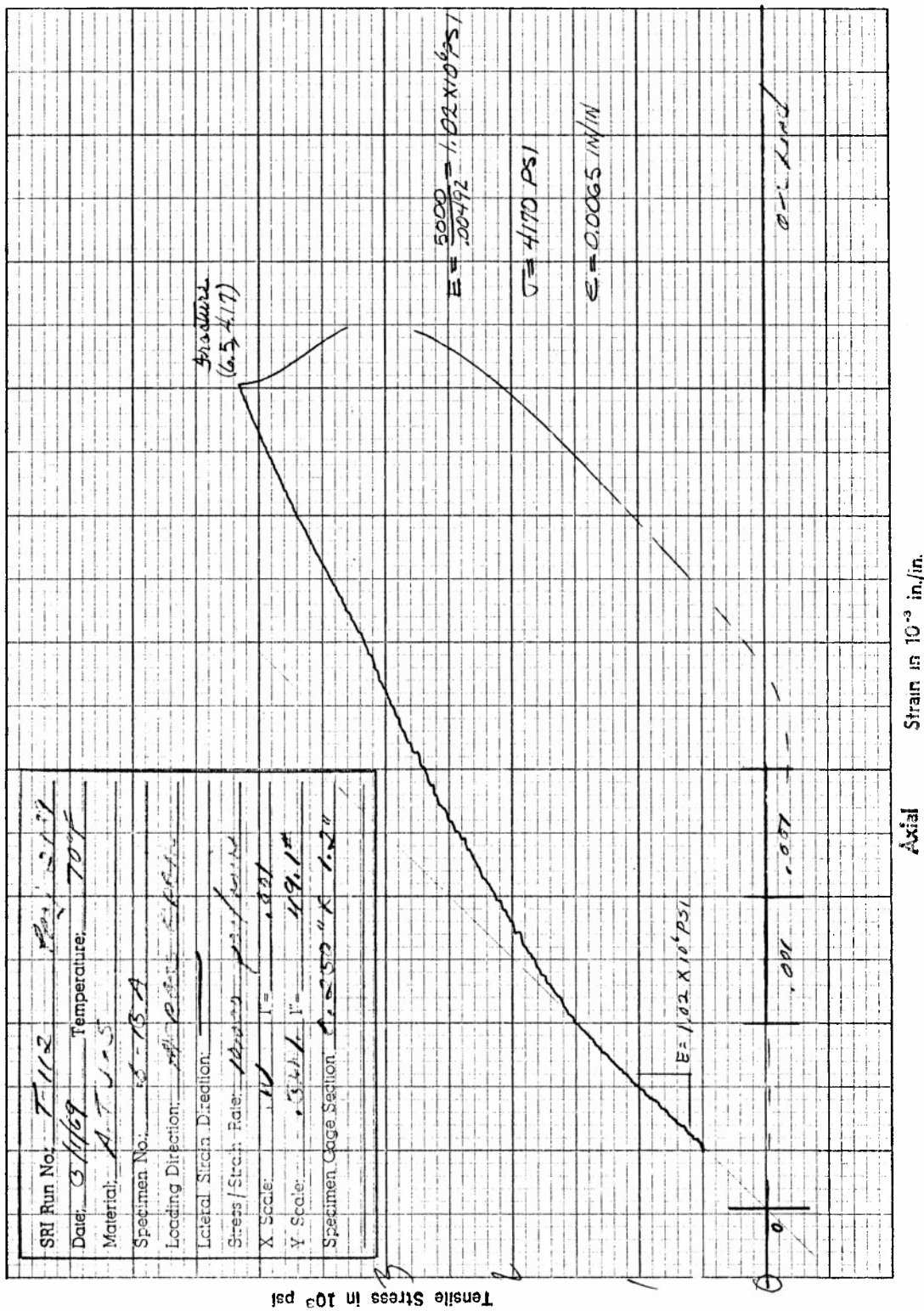


Figure F45. Tensile Stress versus Axial Strain for Specimen B15A of ATJ-S Graphite at 70°F

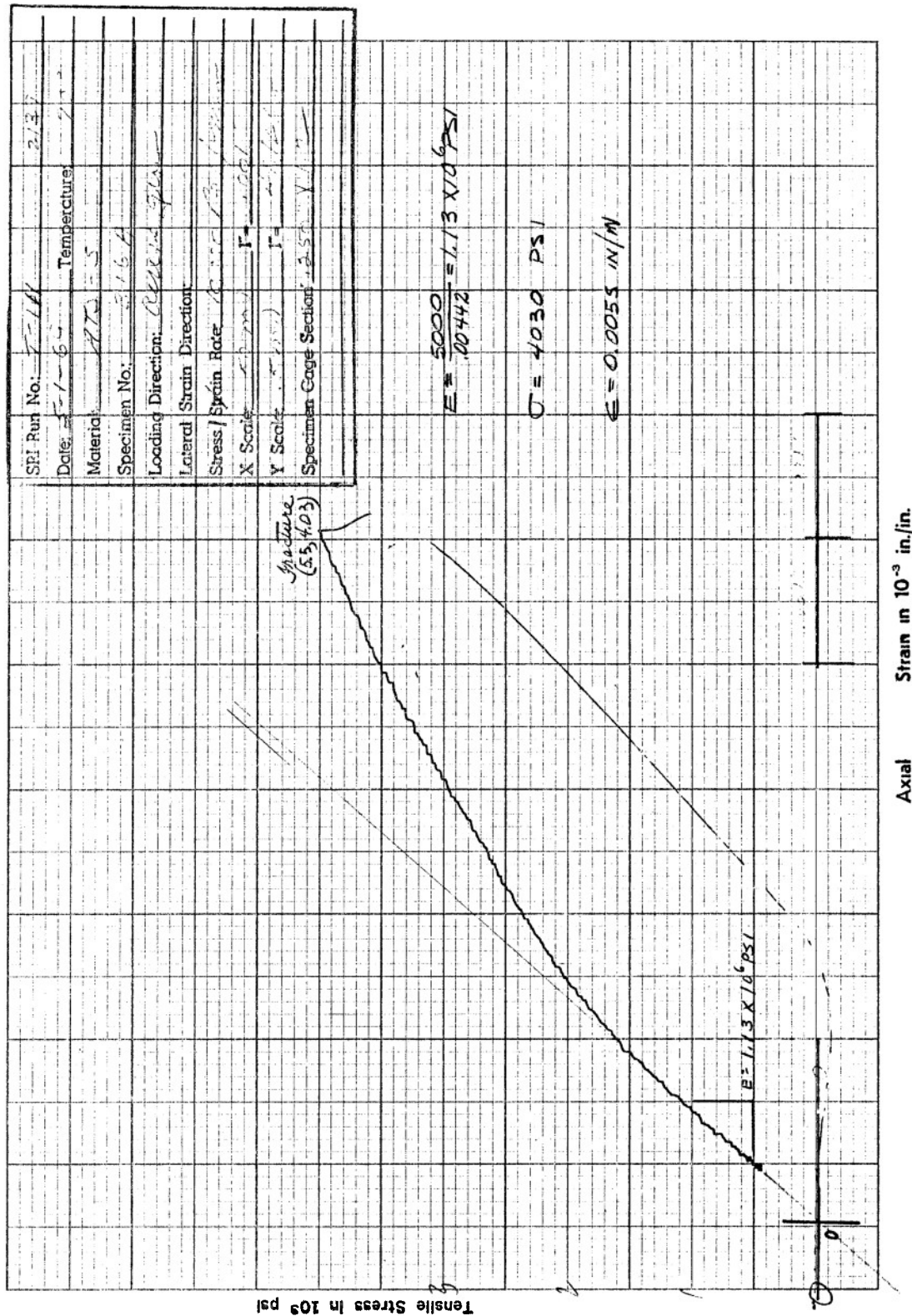


Figure F46. Tensile Stress versus Axial Strain for Specimen B16A of ATJ-S Graphite at 70°F



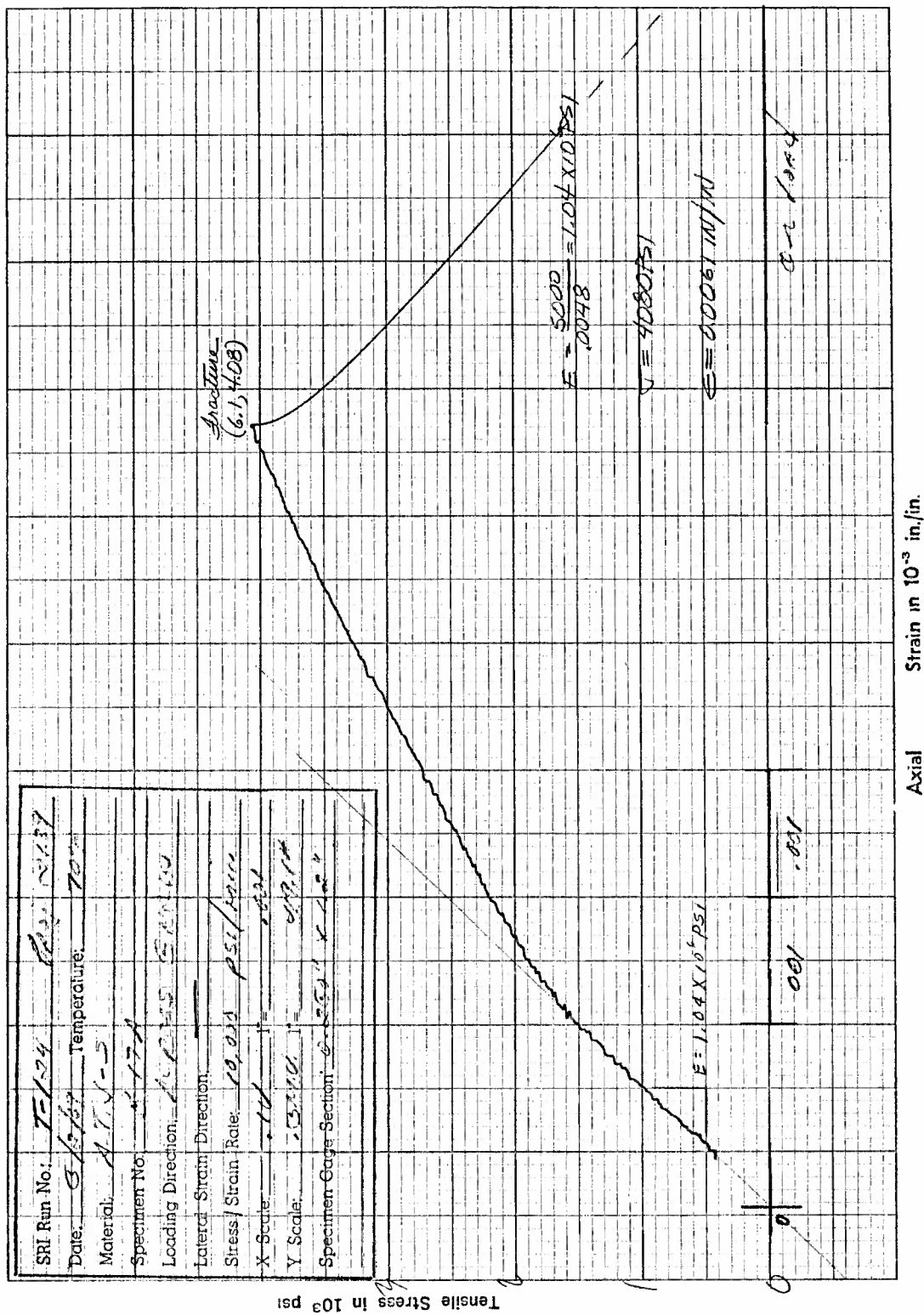


Figure F47. Tensile Stress versus Axial Strain for Specimen B17A of ATJ-S Graphite at 70°F

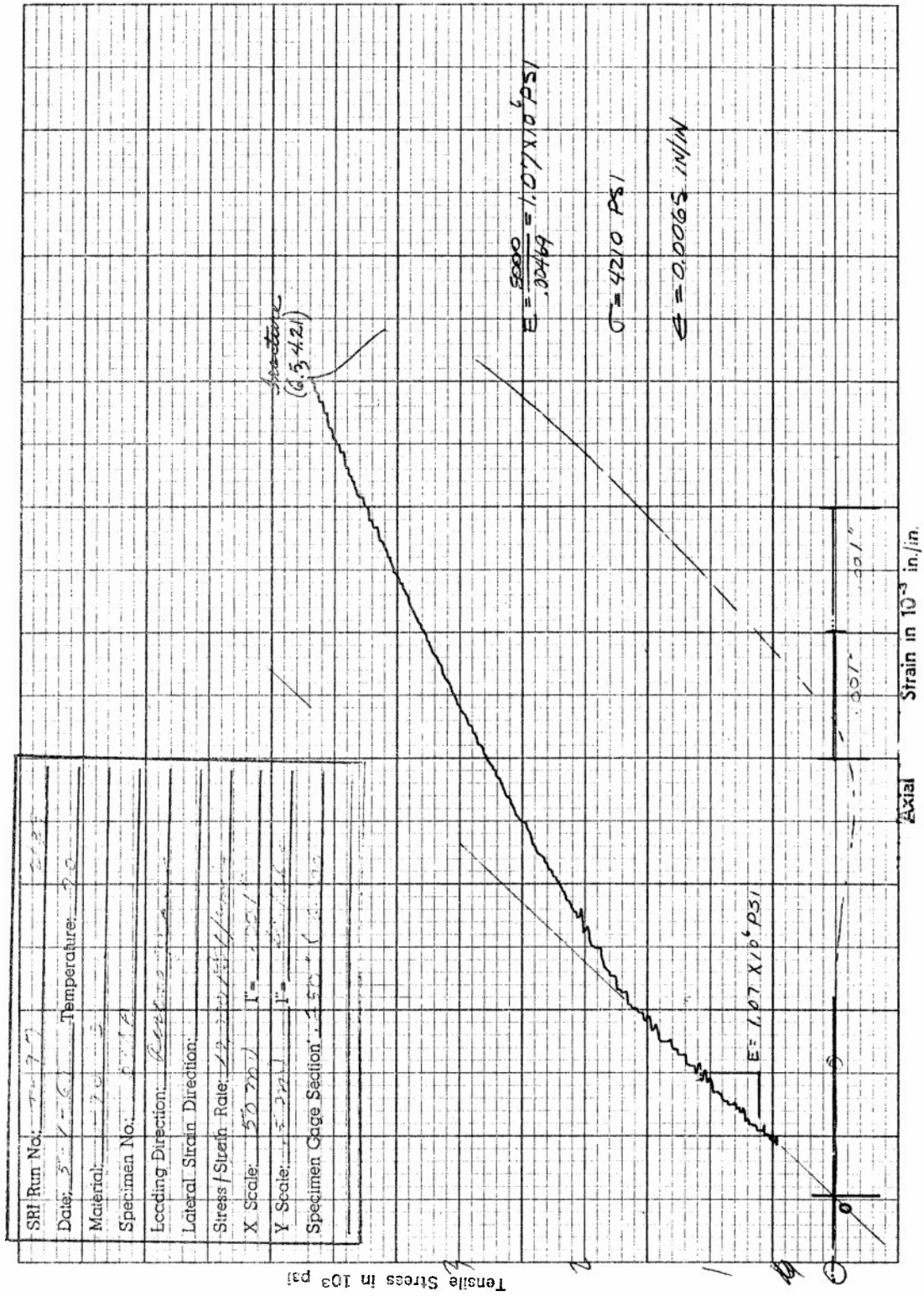


Figure F48. Tensile Stress versus Axial Strain for Specimen B18A of ATJ-S Graphite at 70°F

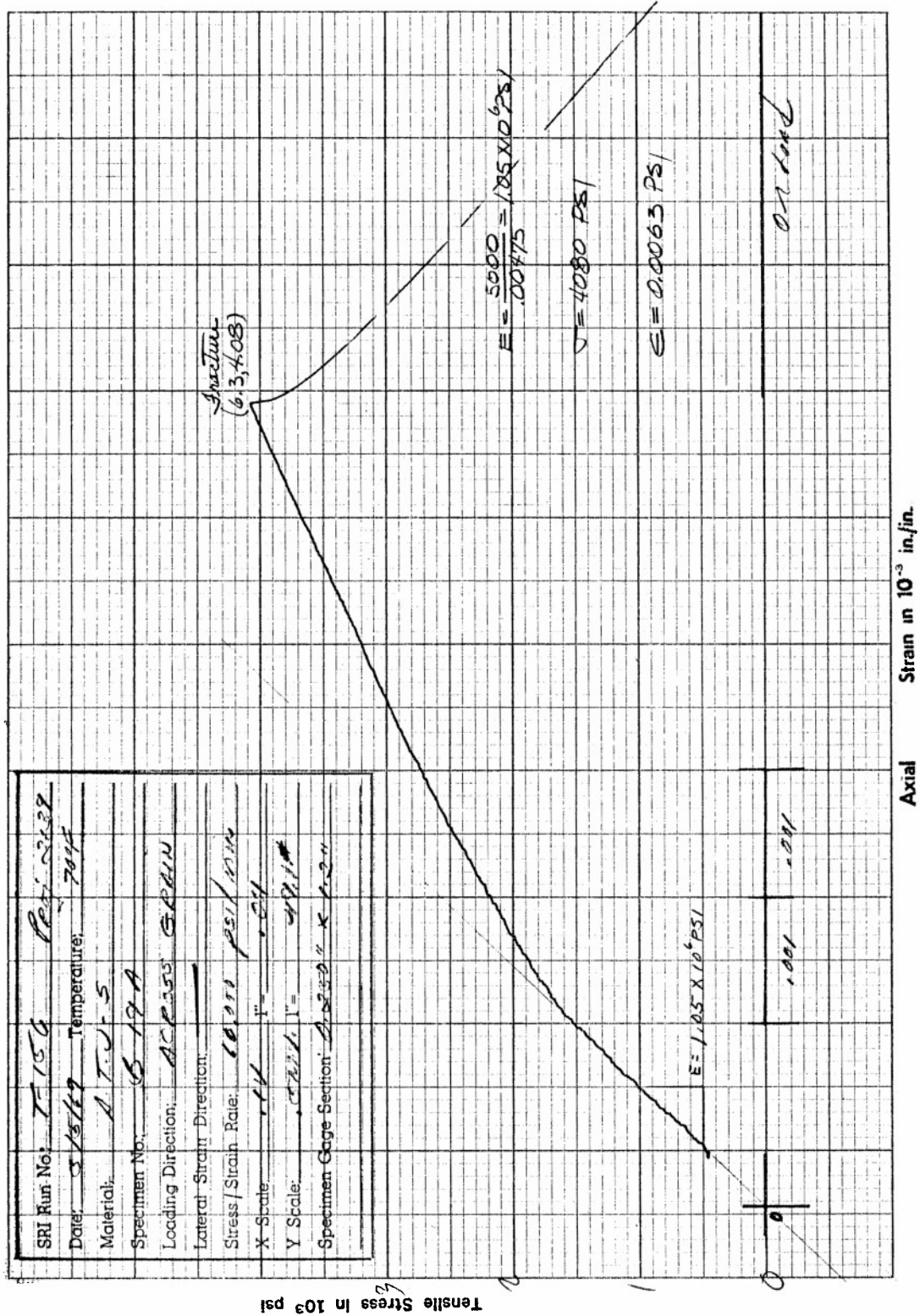


Figure F49. Tensile Stress versus Axial Strain for Specimen B19A of ATJ-S Graphite at 70°F

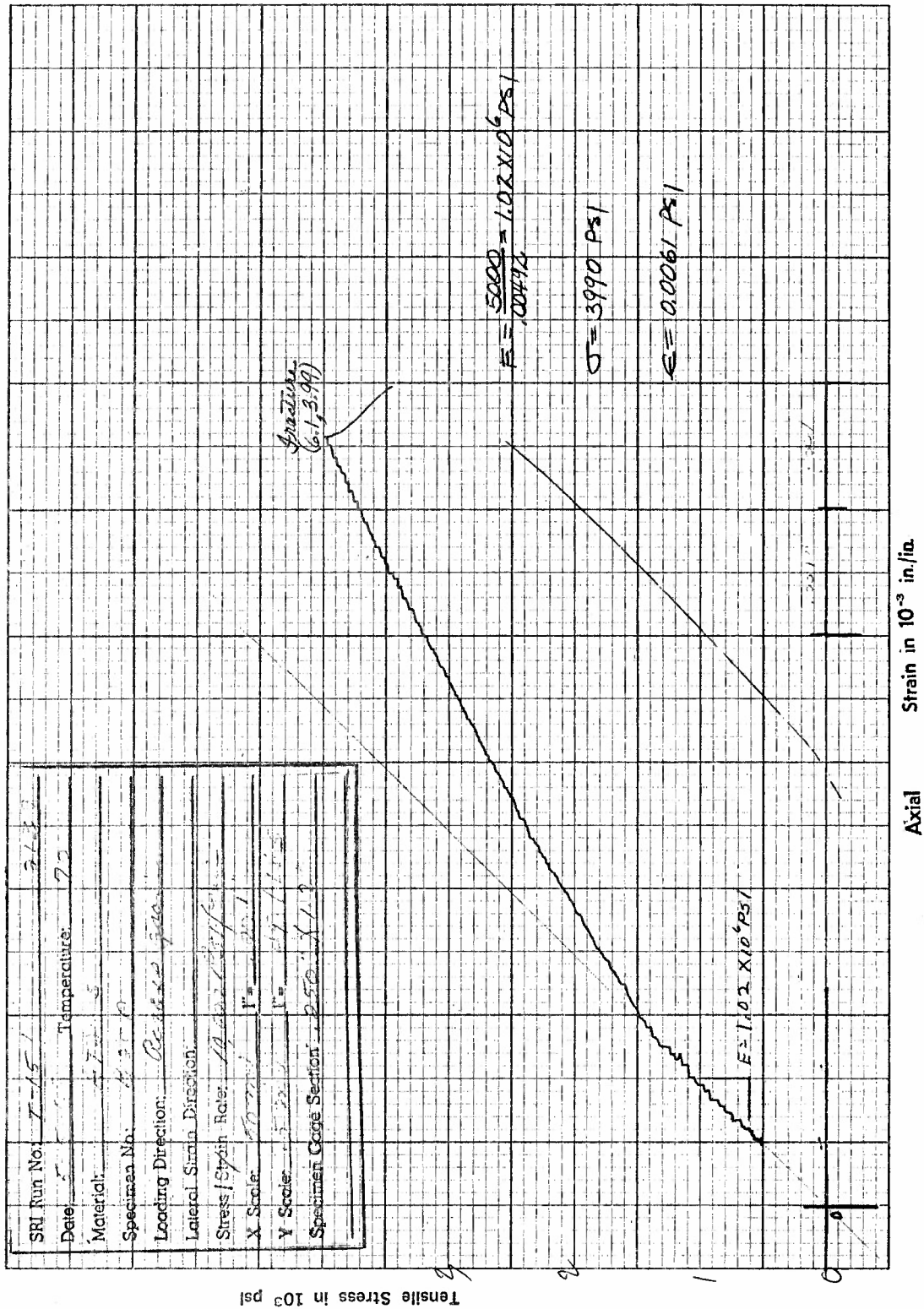


Figure F50. Tensile Stress versus Axial Strain for Specimen B20A of ATJ-S Graphite at 70°F

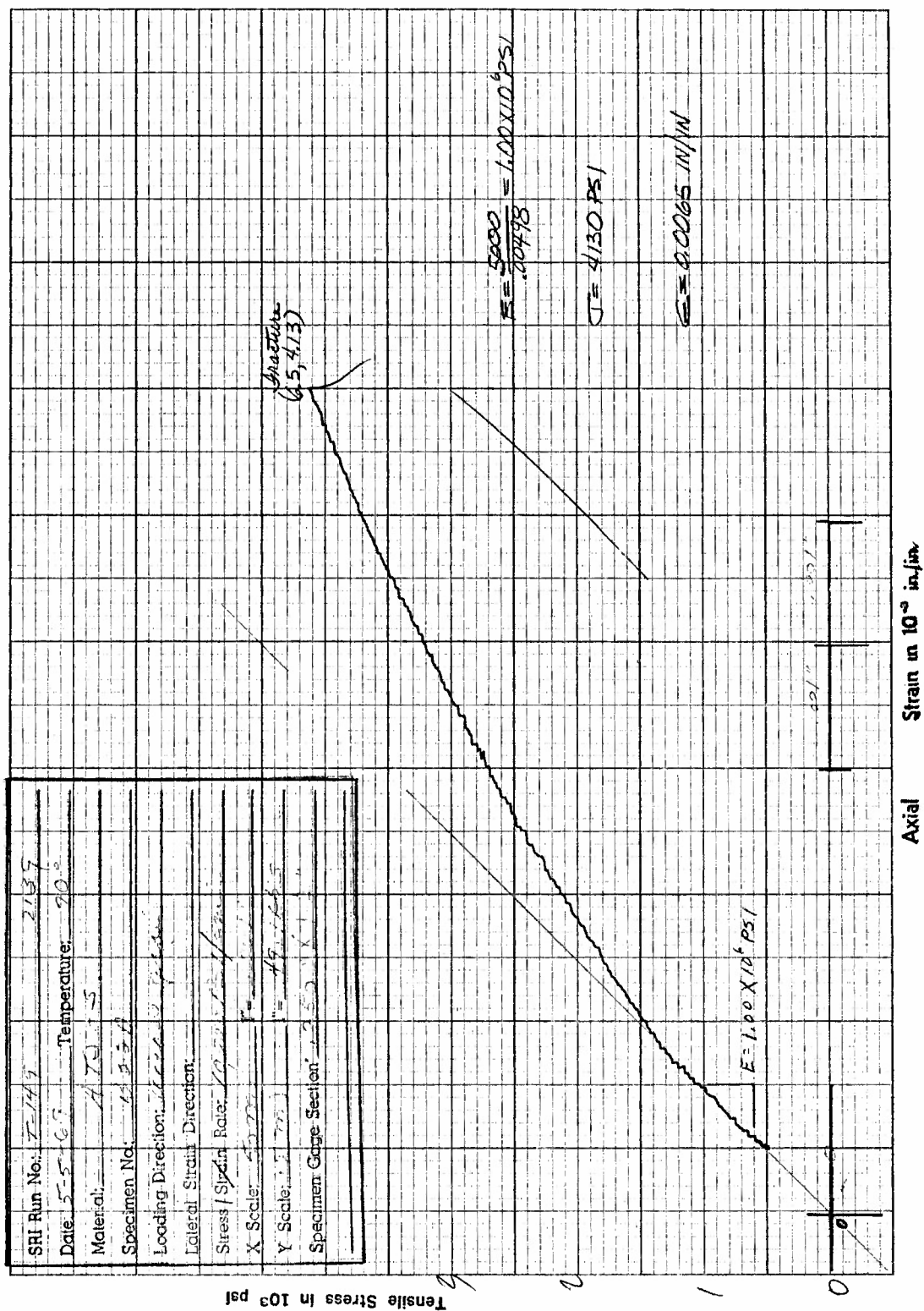


Figure F51. Tensile Stress versus Axial Strain for Specimen B22A of ATJ-S Graphite at 70°F



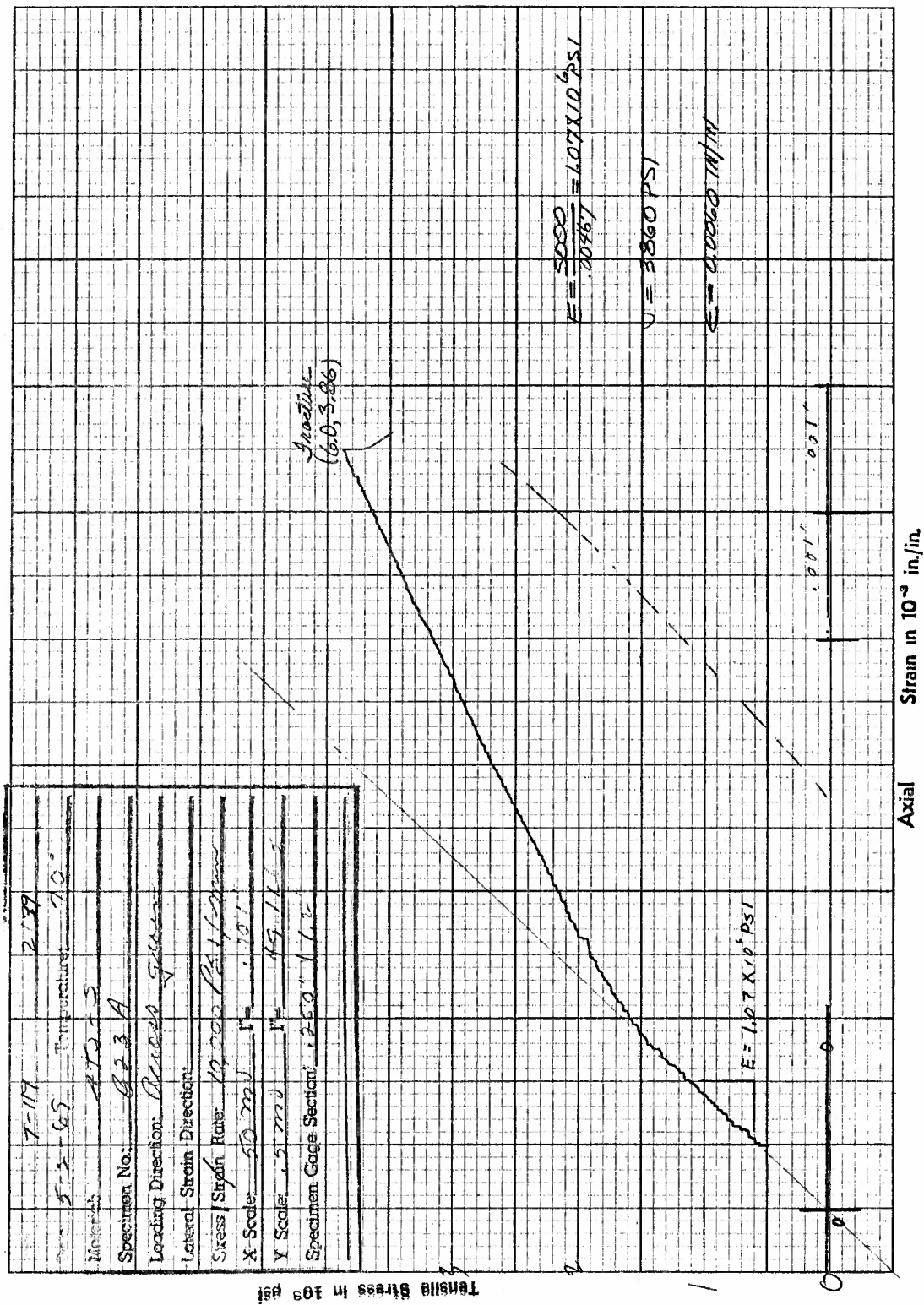


Figure F52. Tensile Stress versus Axial Strain for Specimen B23A of ATJ-S Graphite at 70°F

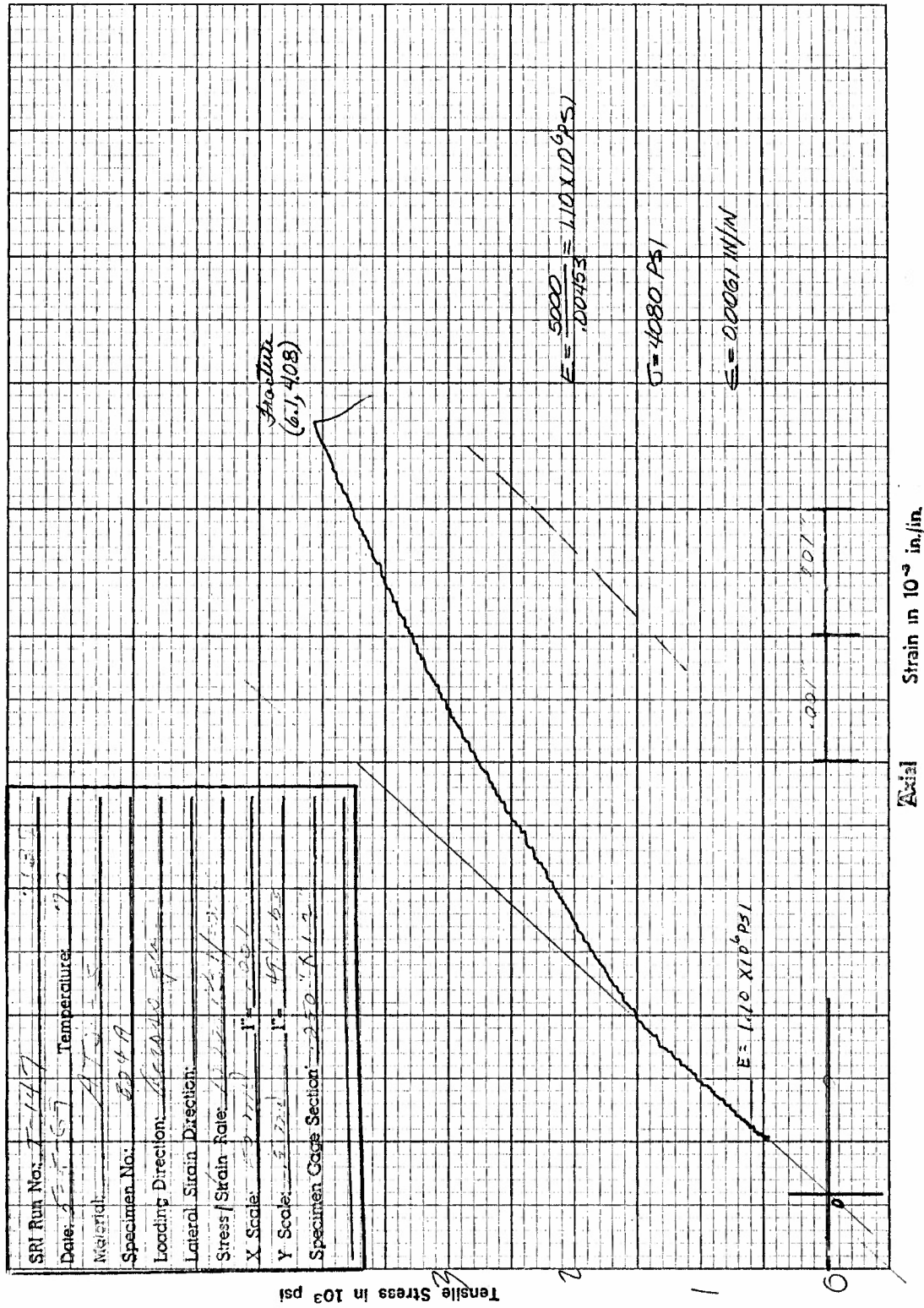


Figure F53. Tensile Stress versus Axial Strain for Specimen B24A of ATJ-S Graphite at 70°F

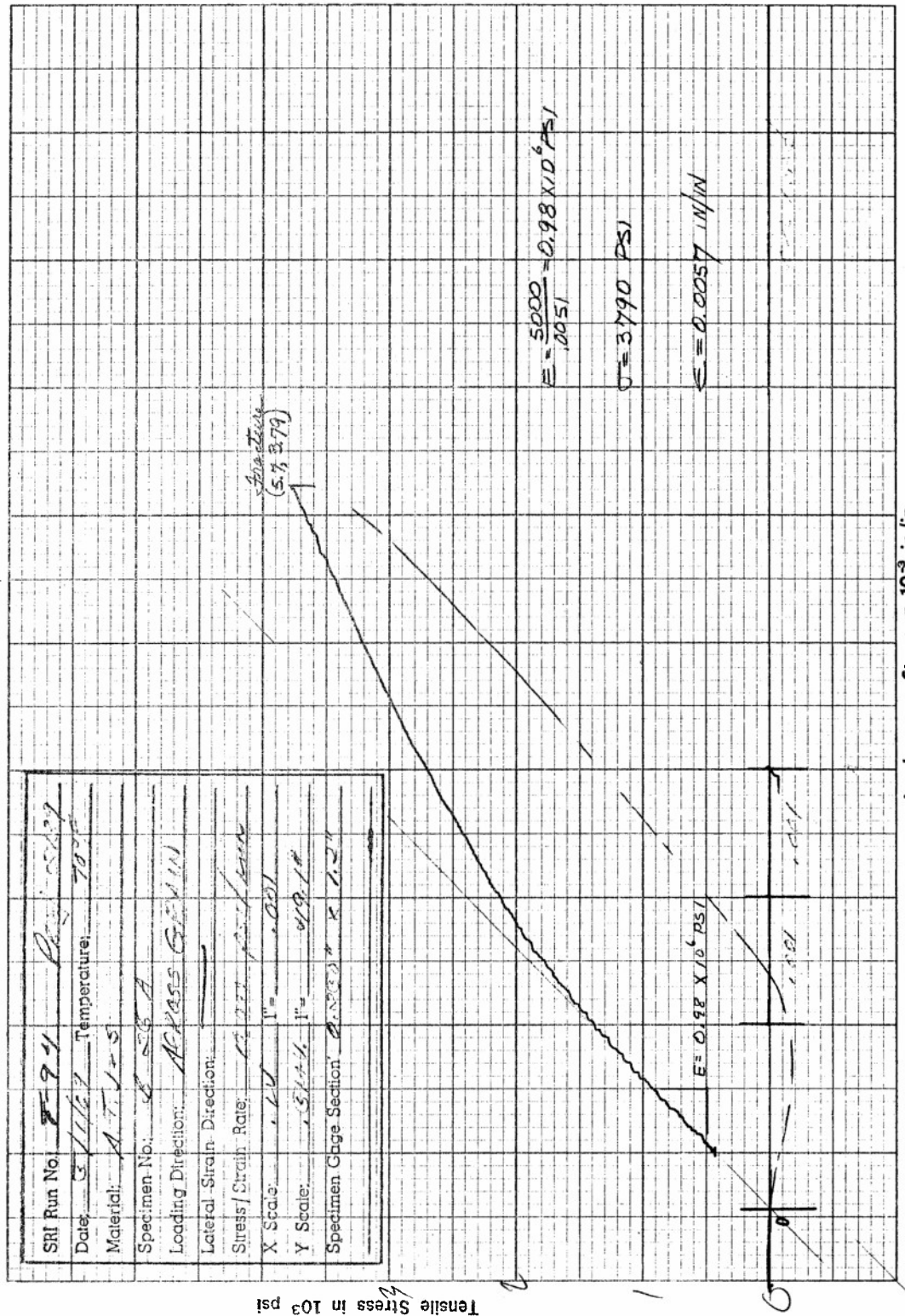


Figure F54. Tensile Stress versus Axial Strain for Specimen B25A of ATJ-S Graphite at 70°F



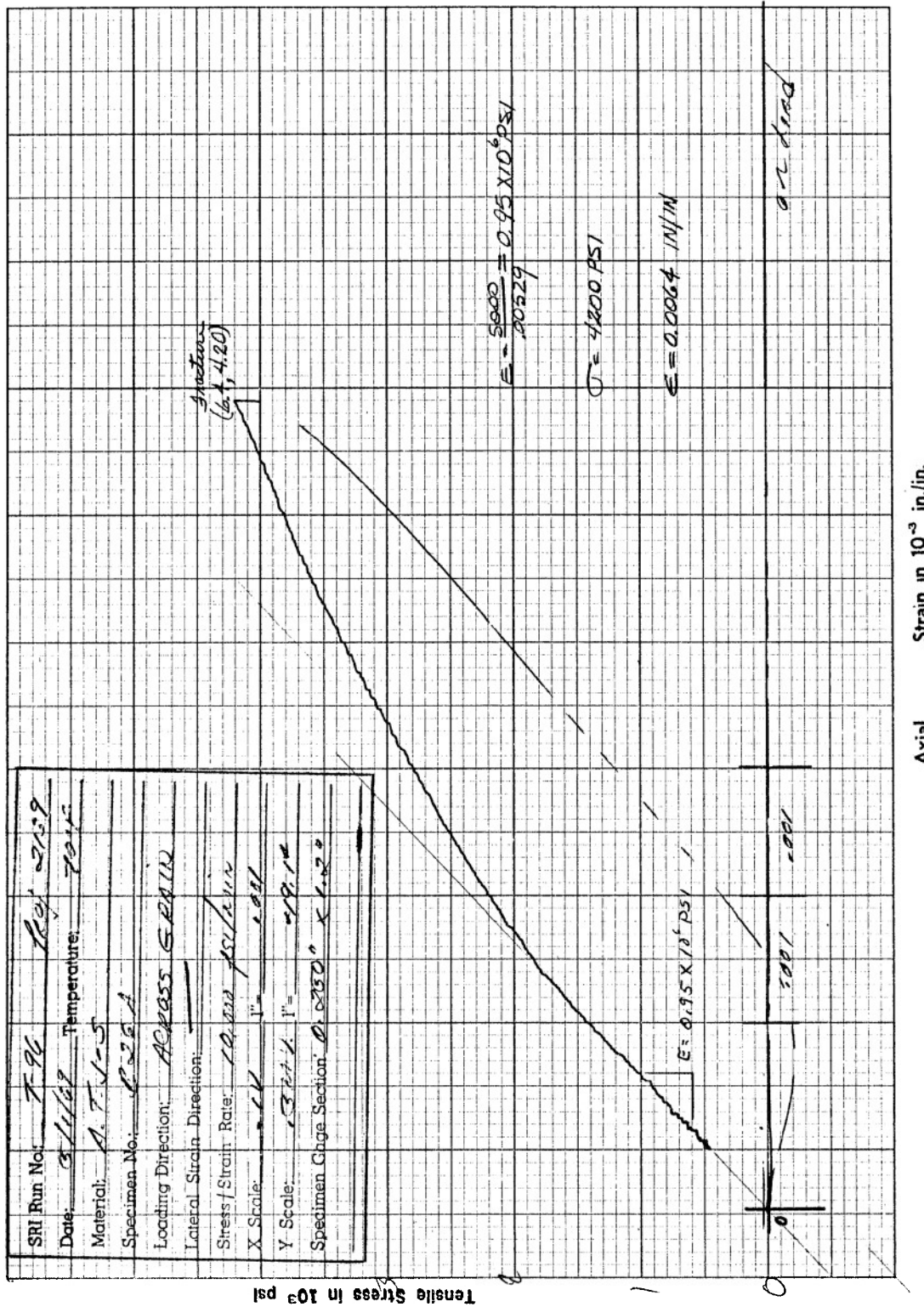


Figure F55. Tensile Stress versus Axial Strain for Specimen B26A of ATJ-S Graphite at 70°F

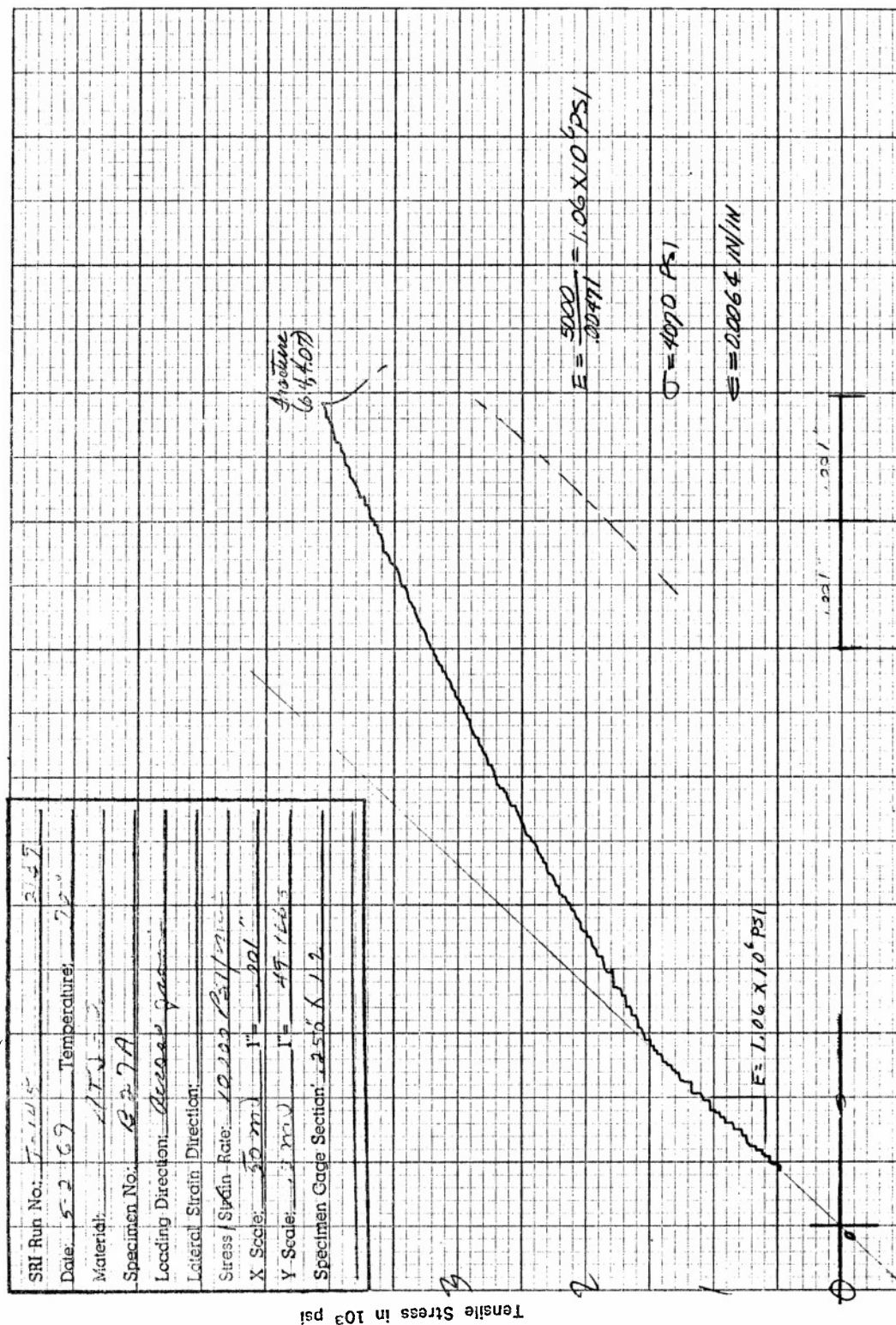


Figure F56. Tensile Stress versus Axial Strain for Specimen B27A of ATJ-S Graphite at 70°F

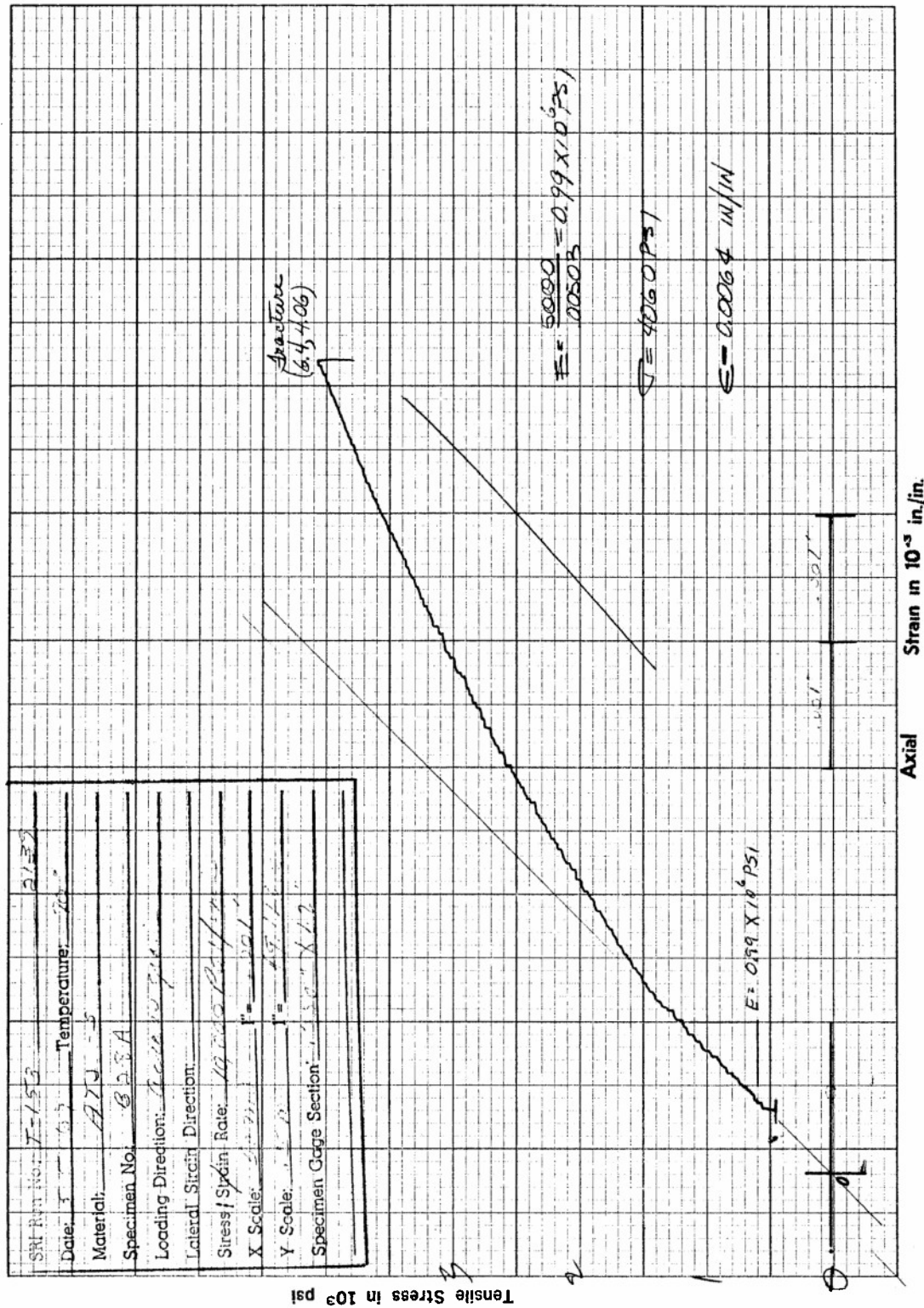


Figure F57. Tensile Stress versus Axial Strain for Specimen B28A of ATJ-S Graphite at 70°F

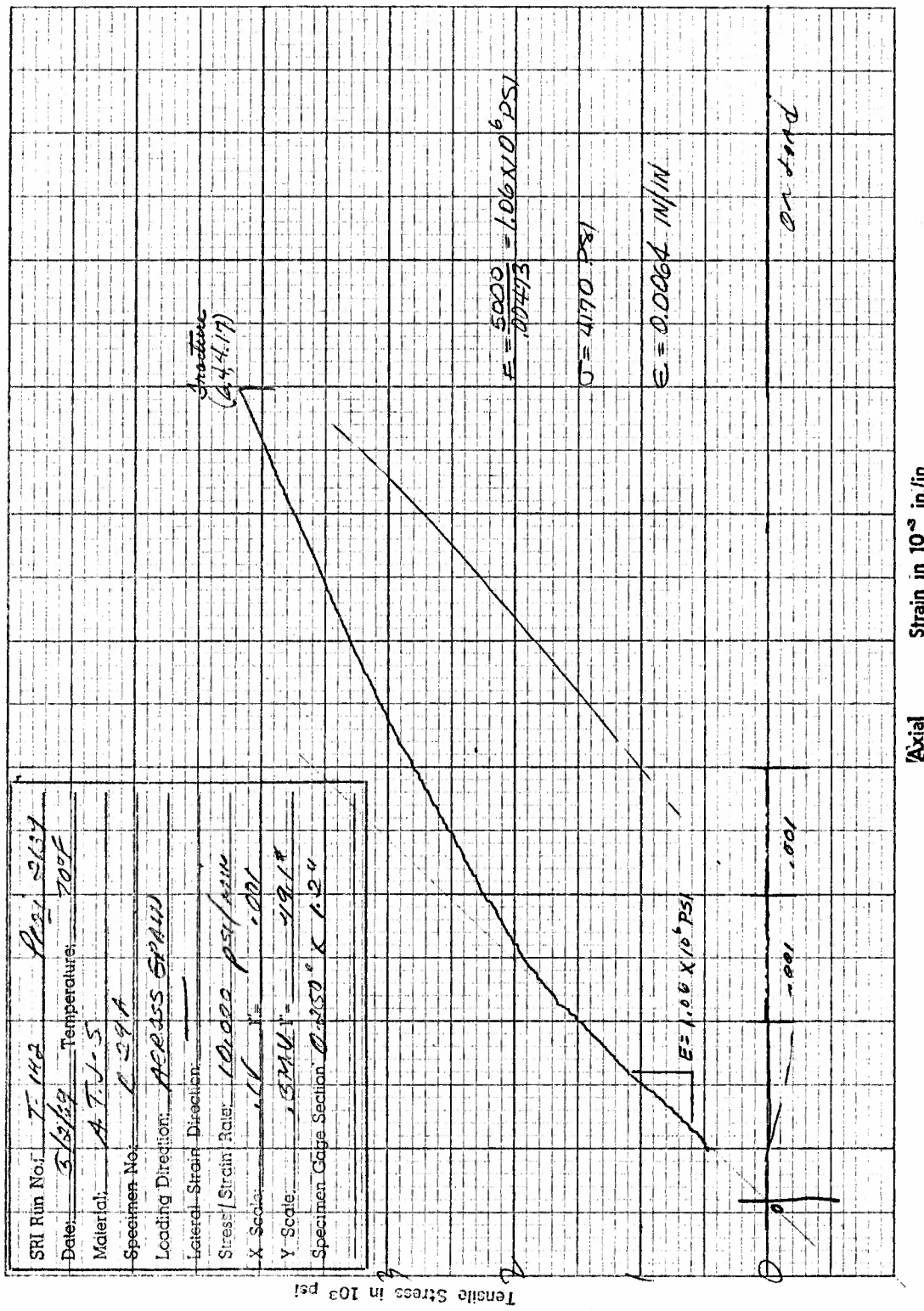


Figure F58. Tensile Stress versus Axial Strain for Specimen B29A of ATJ-S Graphite at 70°F

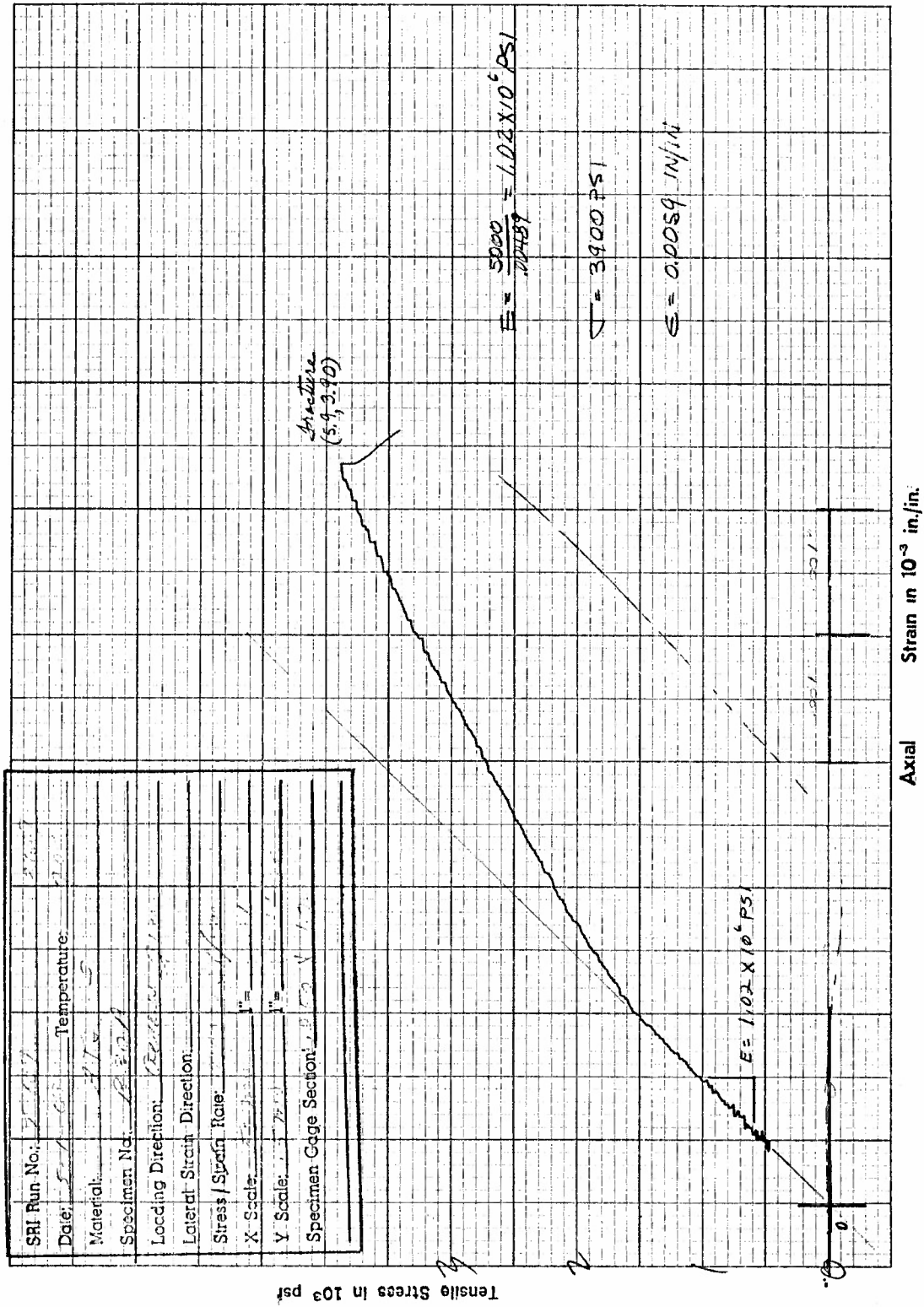


Figure F59. Tensile Stress versus Axial Strain for Specimen B30A of ATJ-S Graphite at 70°F



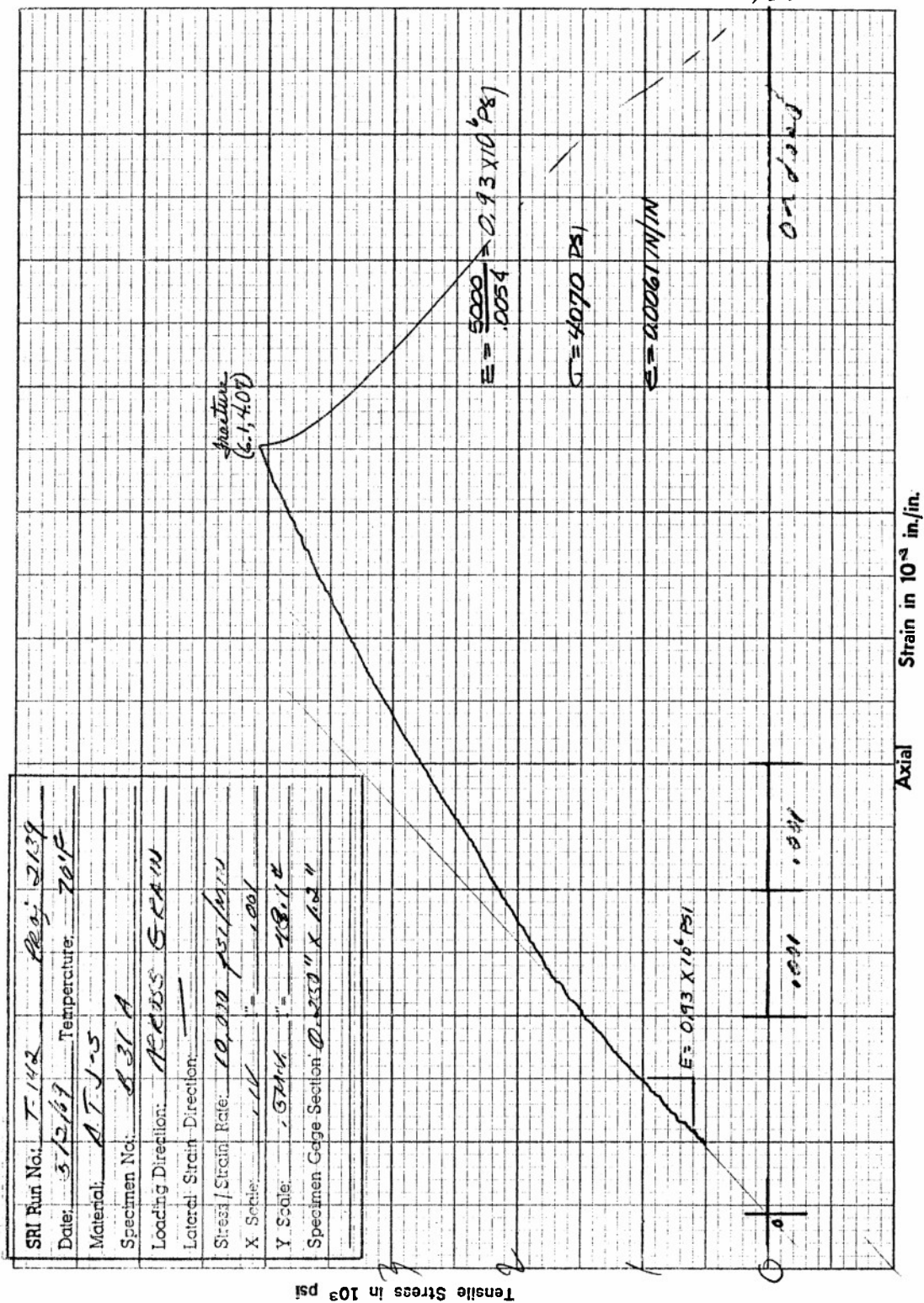


Figure F60. Tensile Stress versus Axial Strain for Specimen B31A of ATJ-S Graphite at 70°F

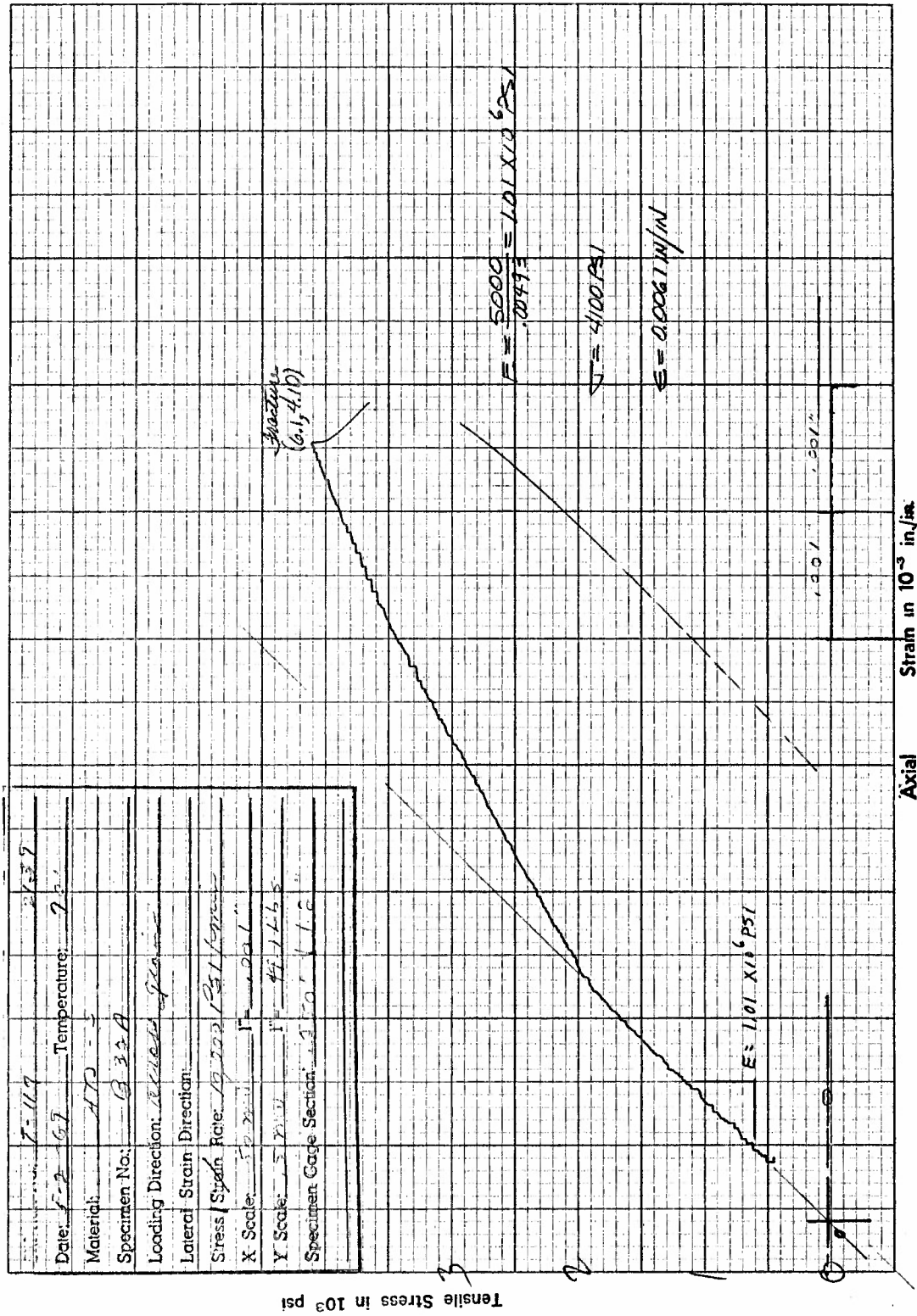


Figure F61. Tensile Stress versus Axial Strain for Specimen B32A of ATJ-S Graphite at 70°F

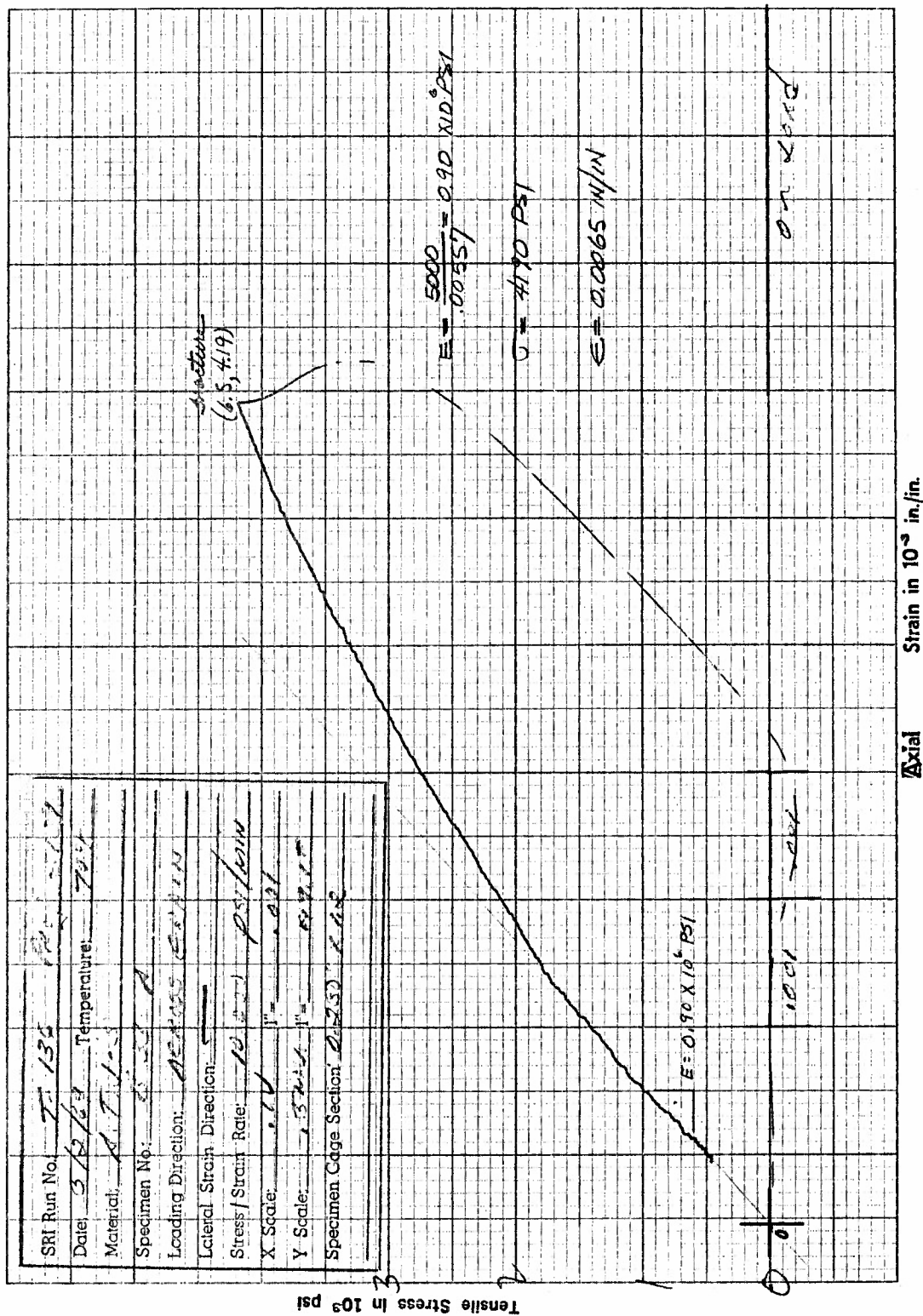


Figure F62. Tensile Stress versus Axial Strain for Specimen B33A of ATJ-S Graphite at 70°F



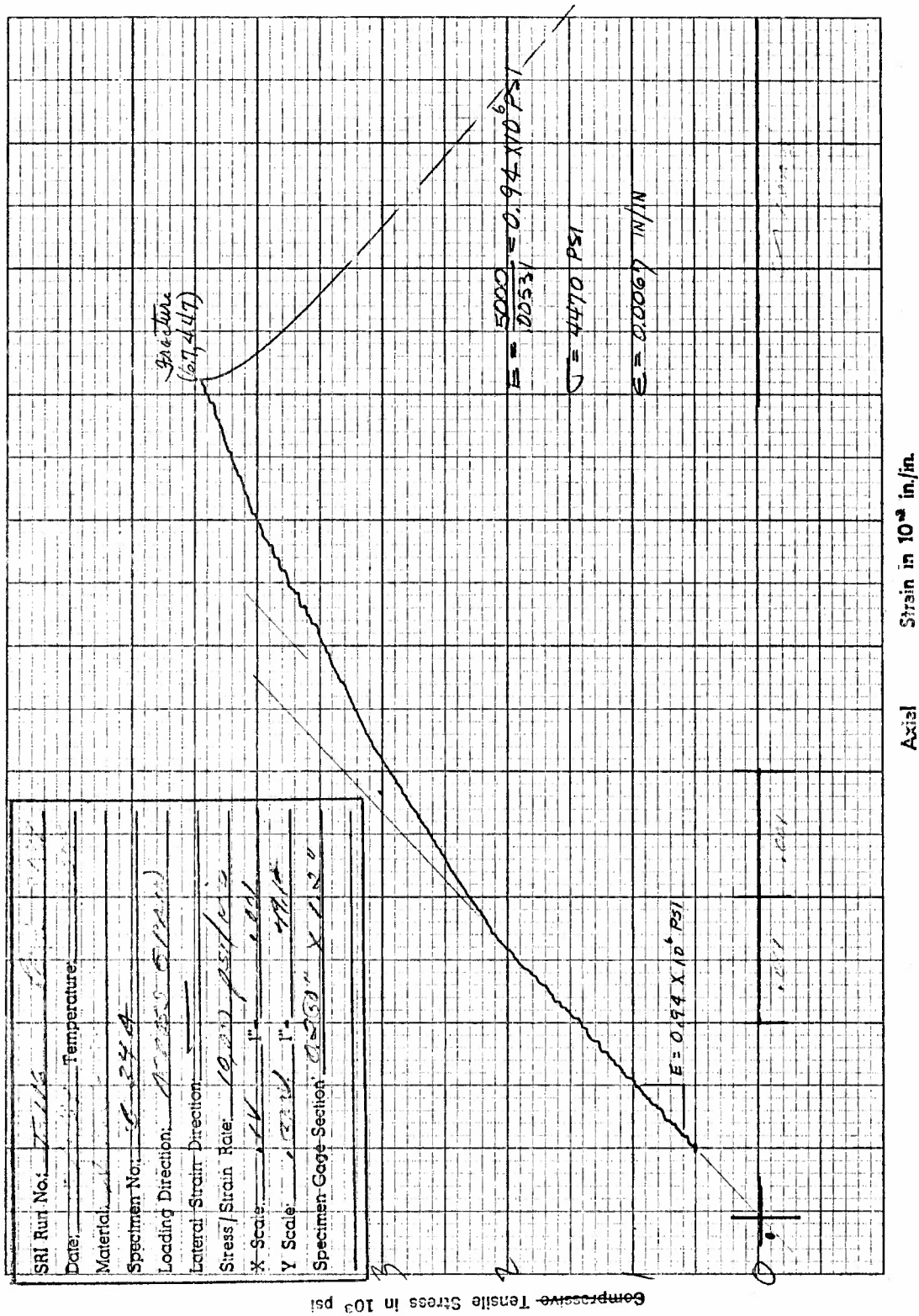
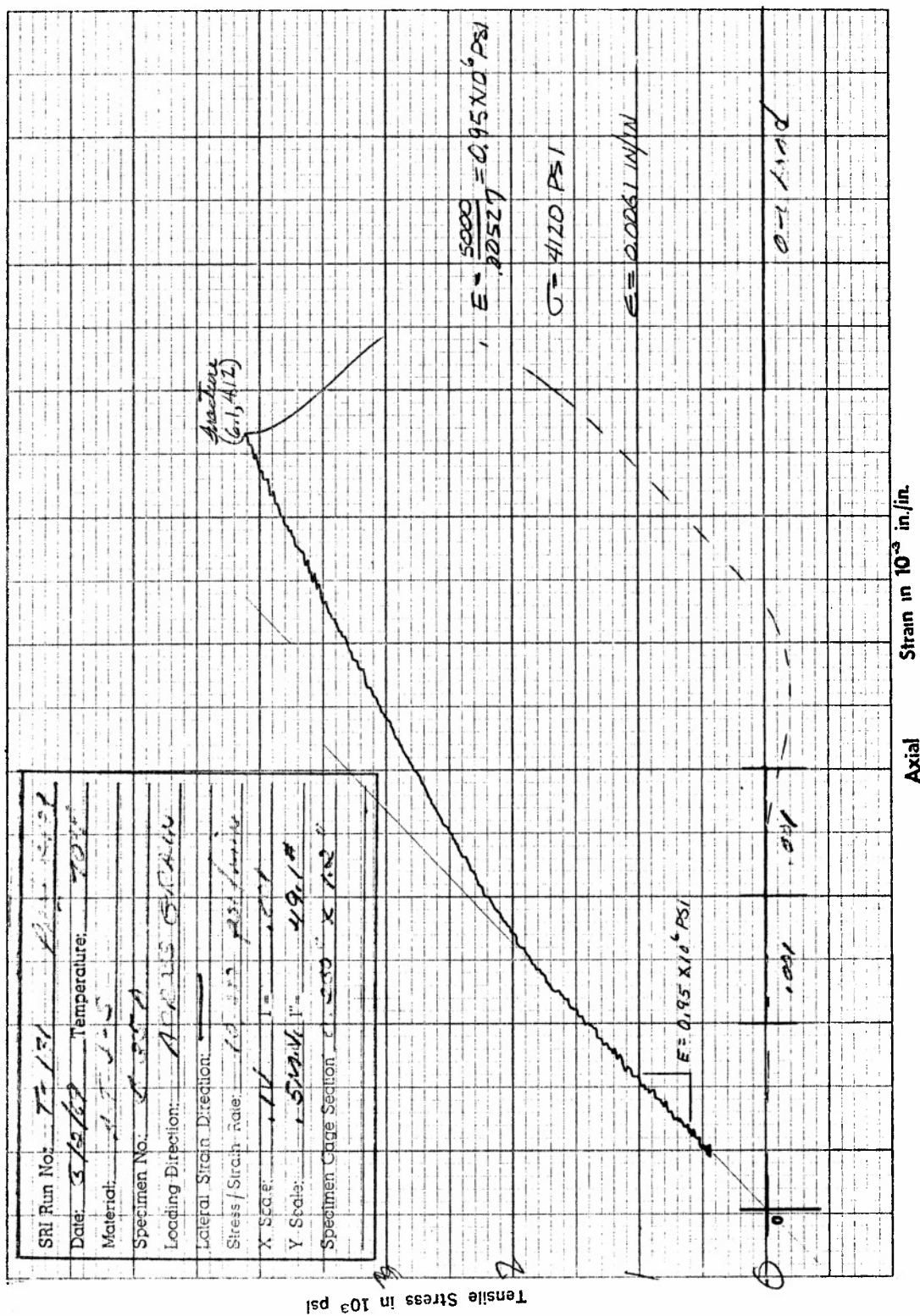


Figure F63. Tensile Stress versus Axial Strain for Specimen B34A of ATJ-S Graphite at 70°F



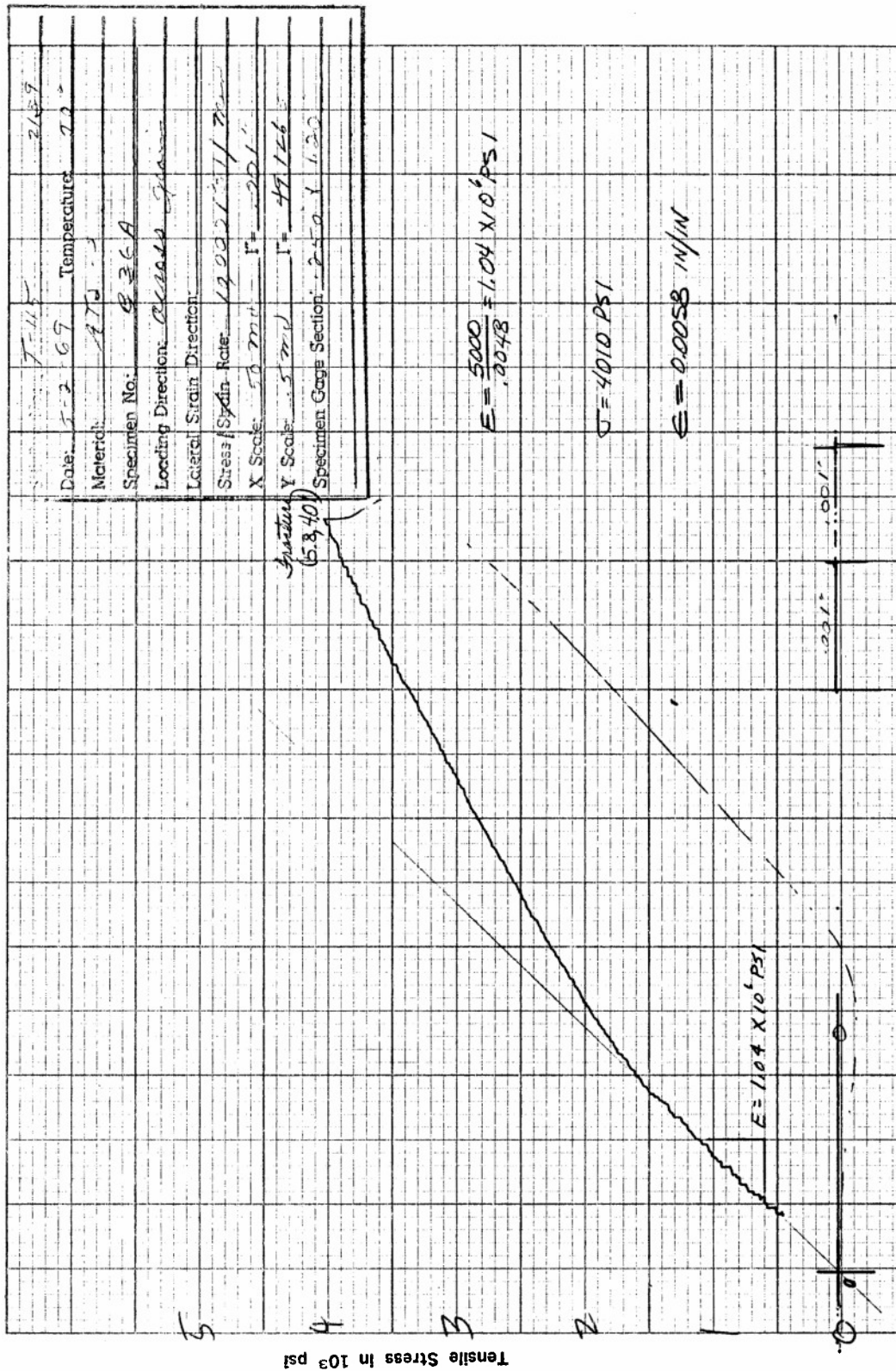


Figure F65. Tensile Stress versus Axial Strain for Specimen B36A of ATJ-S Graphite at 70°F



## APPENDIX G

Results of Avco Ultrasonic Inspection of ATJ-S Billet  
L-1-8



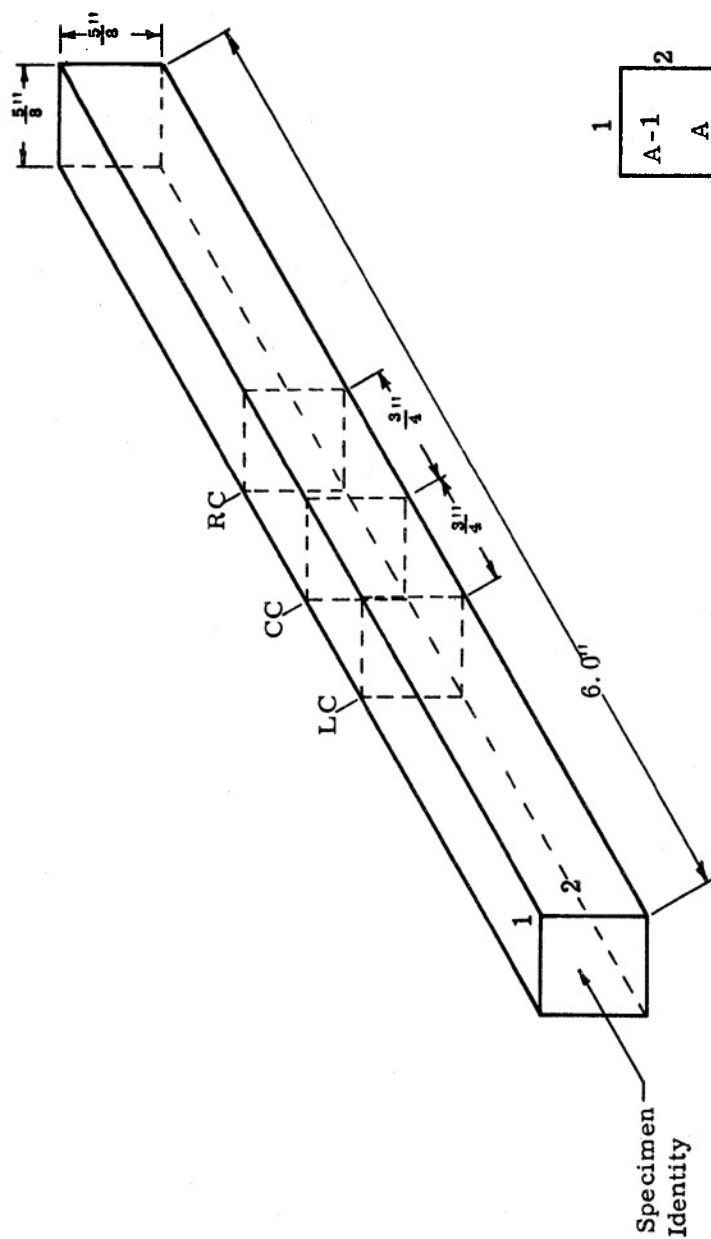
## Avco Ultrasonic Inspection Results for ATJ-S Graphite Billet L-1-8

### Explanation of Symbols:

1. Refer to Figure G1 for the significance and relationships of the numbers "1" and "2" as located on the left-hand ends of the tensile blank lay-outs.
2. The lay-outs represent two surfaces or faces of each tensile blank, even though ultrasonic testing was performed on all four faces of each specimen.
3. Circled areas designate detected discontinuities; solid circles indicating anomalies detected from sides # 1 and # 2, dotted circles indicating those anomalies detected from the opposite sides (i. e. those sides located 180° from sides # 1 and # 2).
4. The figures beside each indicated suspect area are the depths below surface at which the discontinuity may be found.
5. The letter designations refer to relative size of discontinuity thus:
  - S - Small, according to the level of test sensitivity this signal amplitude was observed just above noise level.
  - M - Medium, signal amplitude significantly above noise level.
  - L - Large, signal amplitude readily observed above noise level.
  - VL - Very large indication with high signal amplitude.
  - BE - Attenuation of back-echo amplitude.
  - VC - Velocity change.
6. Plotted discontinuity indications which are located outside the gauge length are included as supplementary information.
7. Solid line indicates fracture location.

Typical Identity  
of Radial Specimens

1	2
A-7	
W	



Typical Identity  
of Axial Specimens

1	2
A-1	
A	

Figure G1. Avco Sketch of Tensile Blank Specimen Describing Ultrasonic Inspection Symbols and Nomenclature



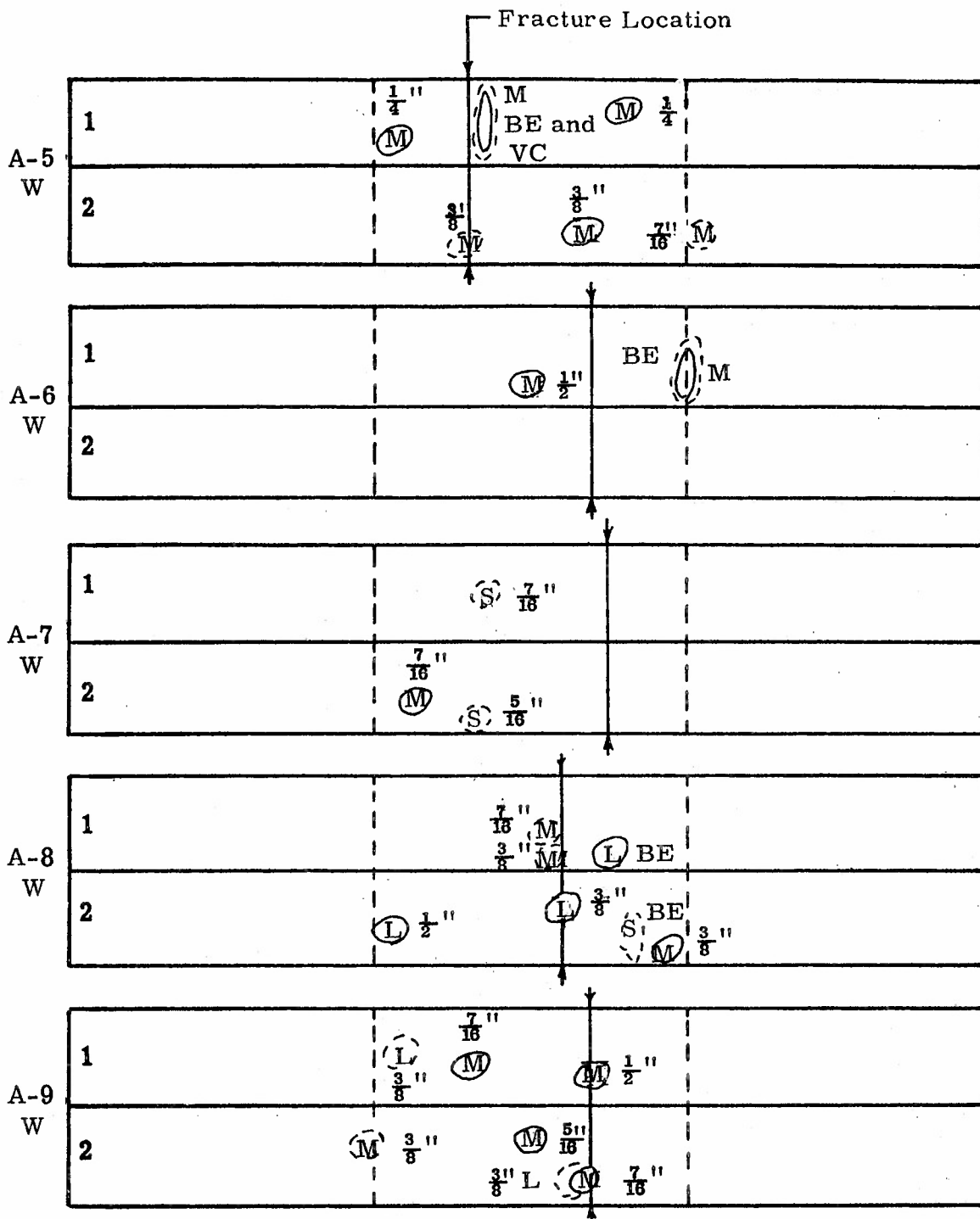


Figure G 2

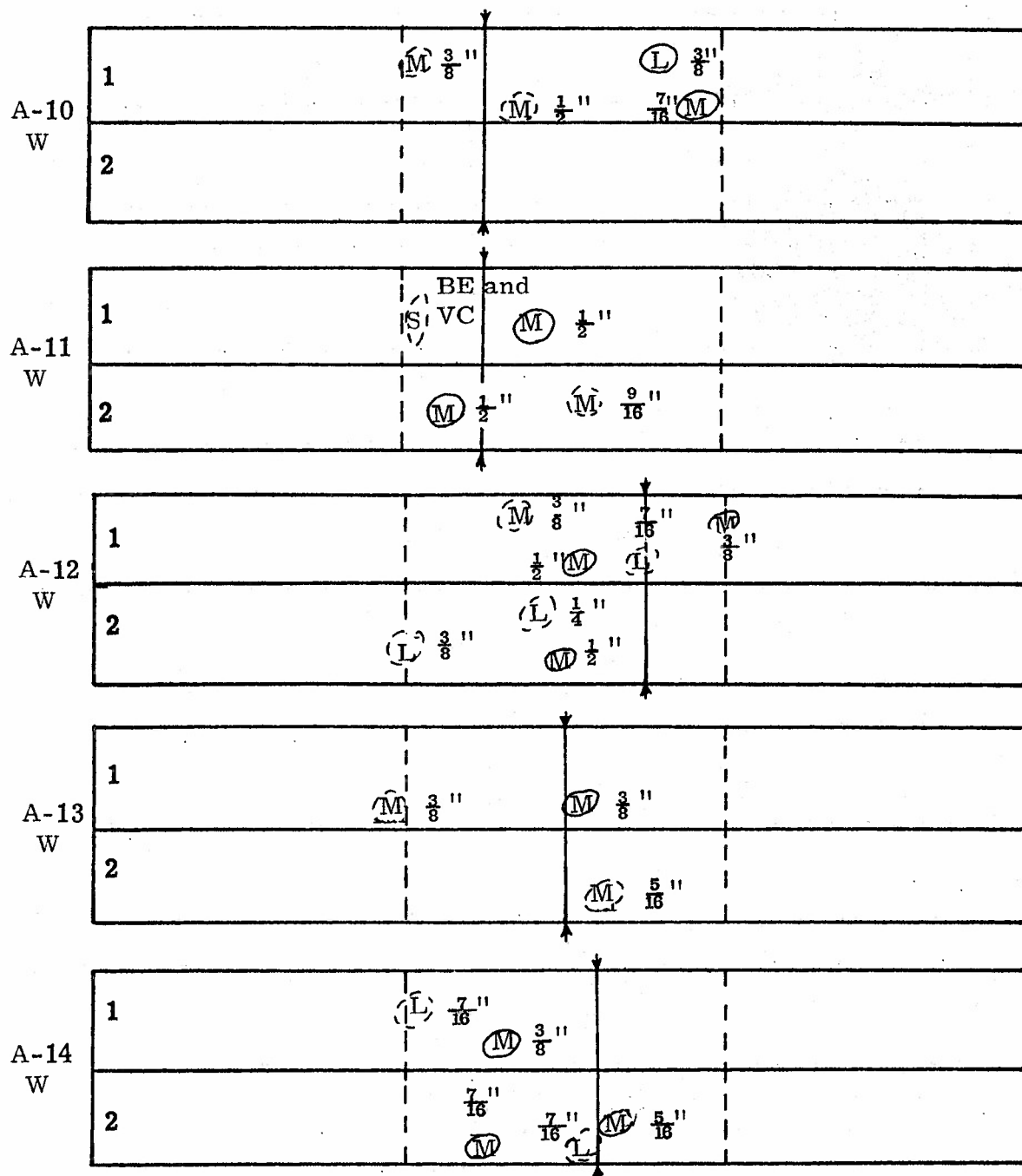


Figure G3

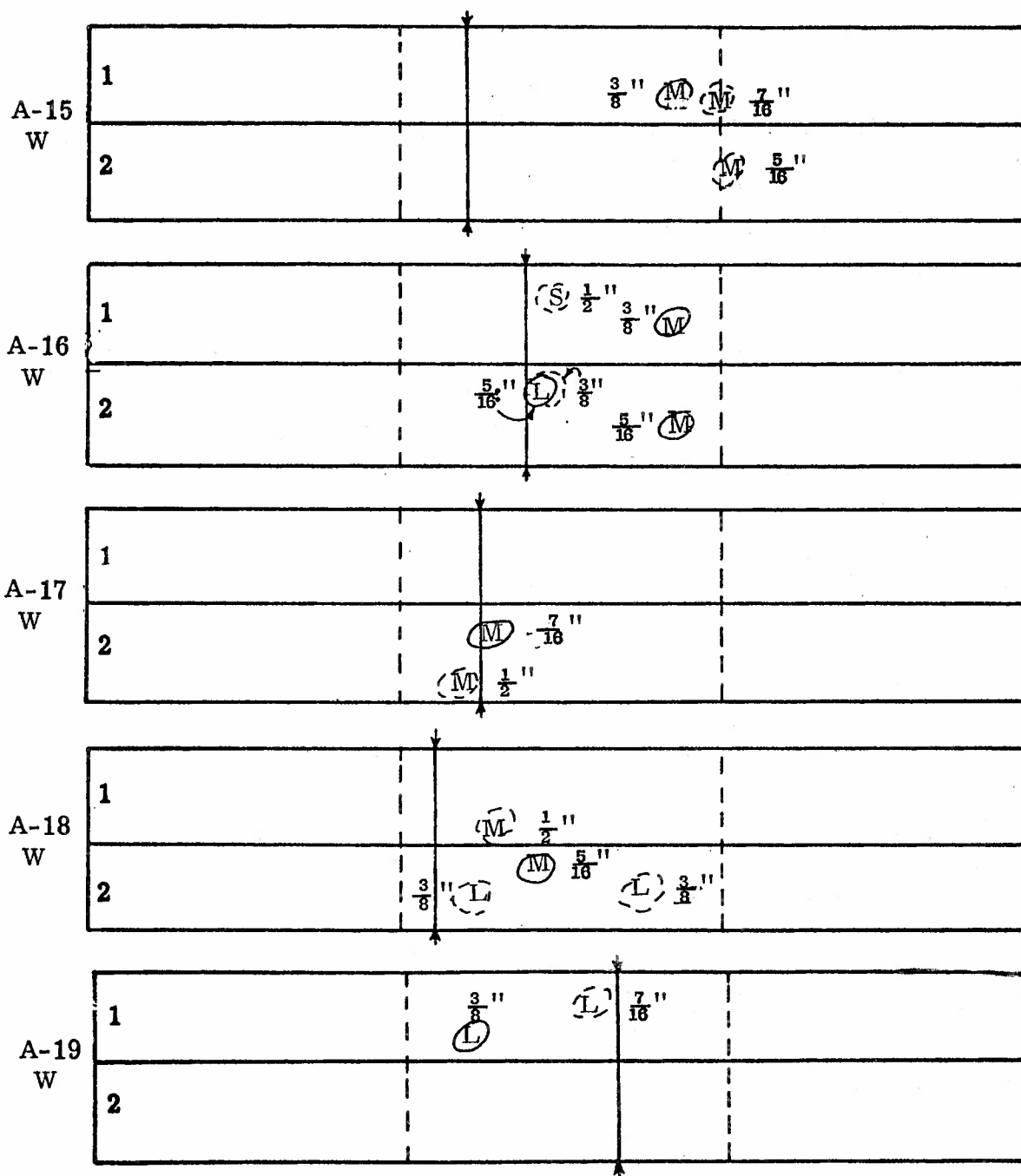


Figure G4

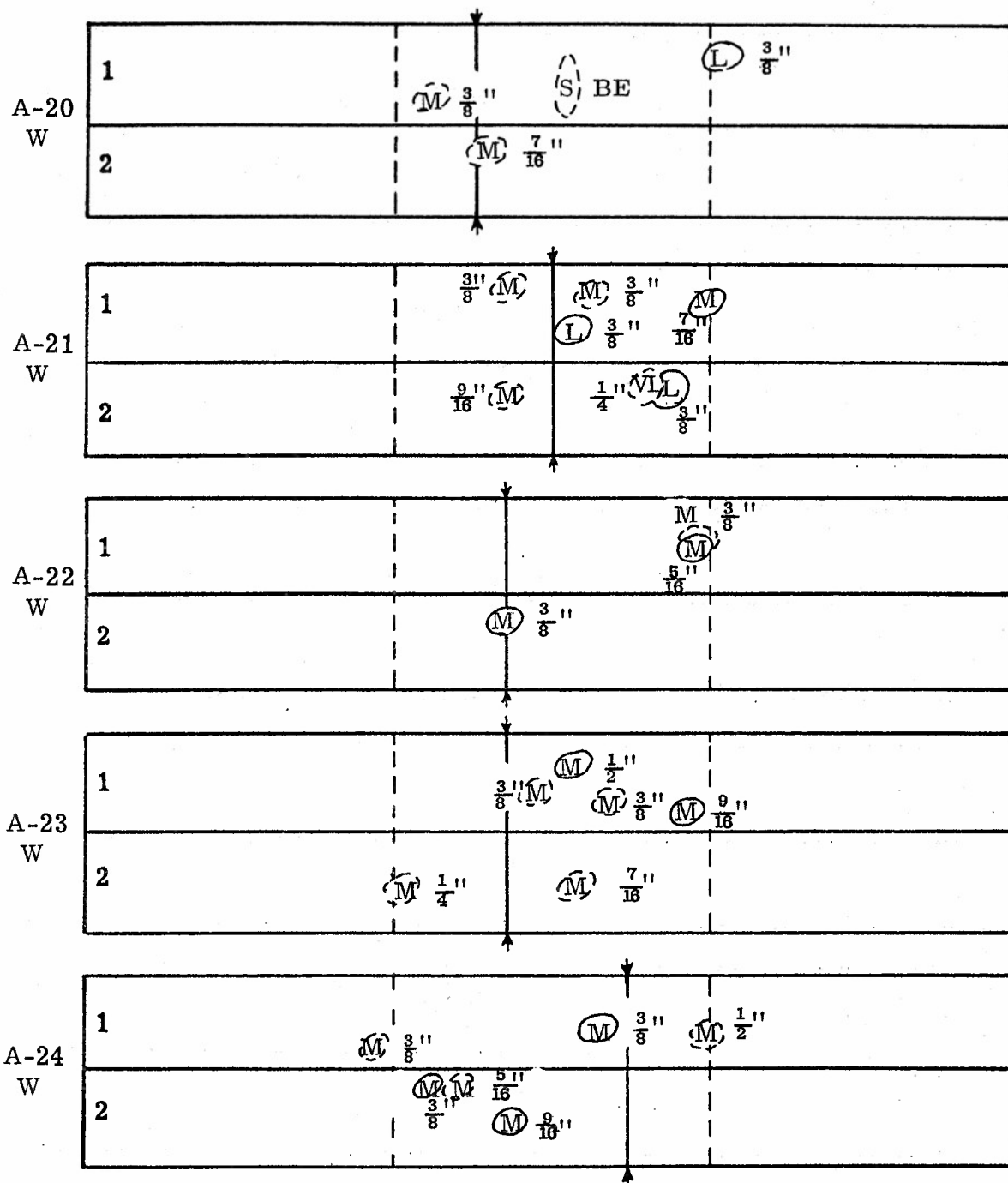


Figure G5

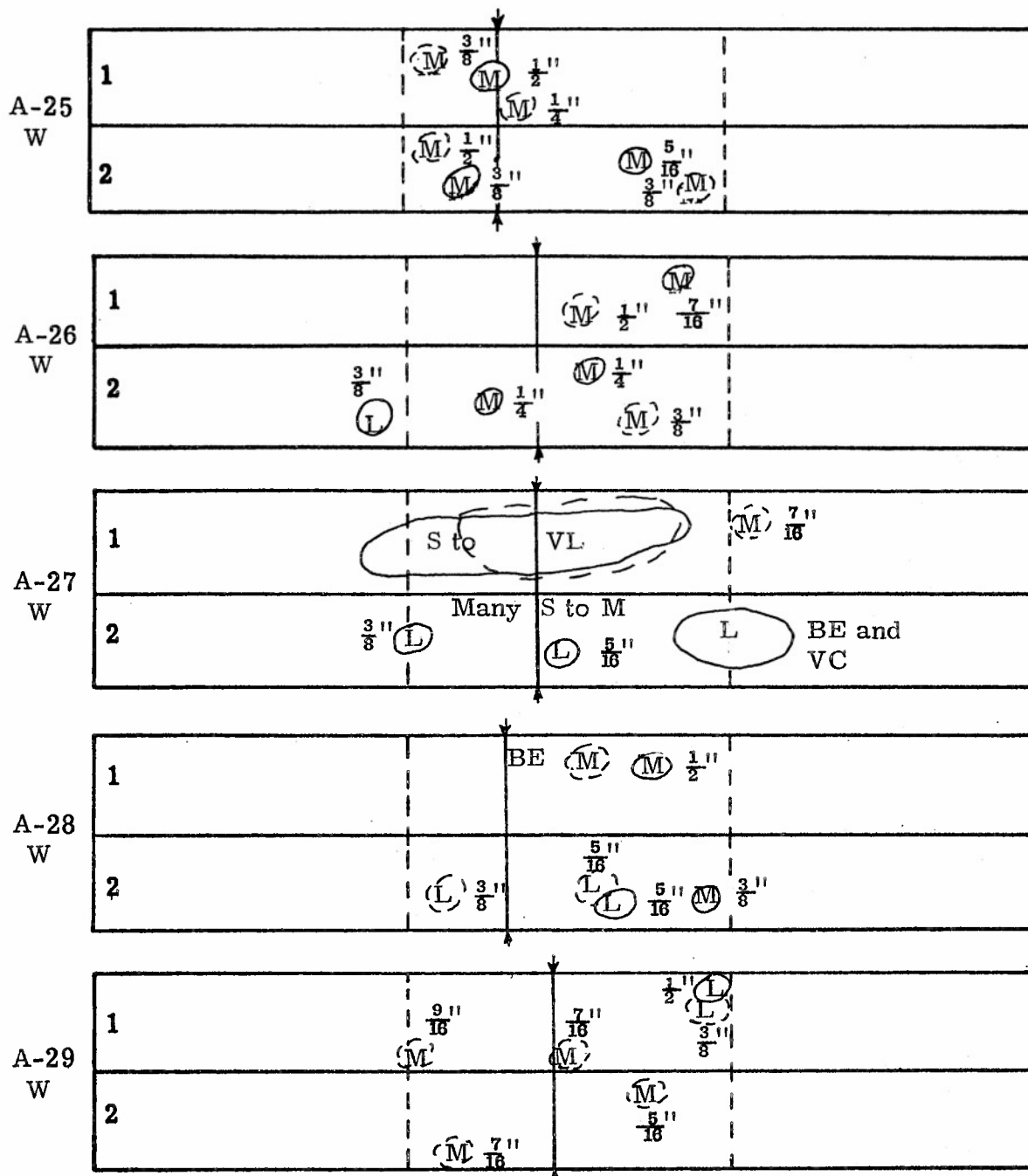


Figure G6

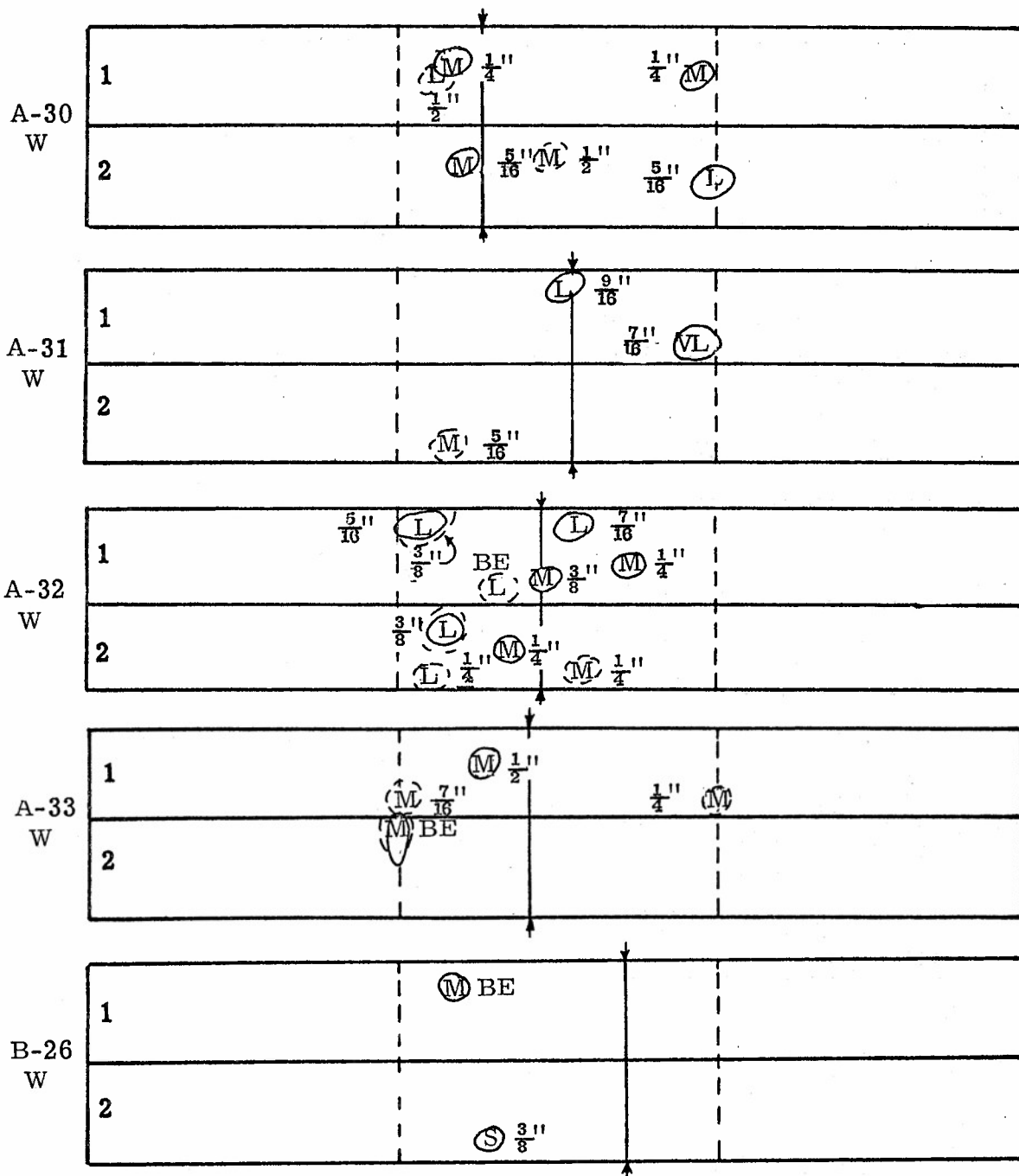


Figure G7

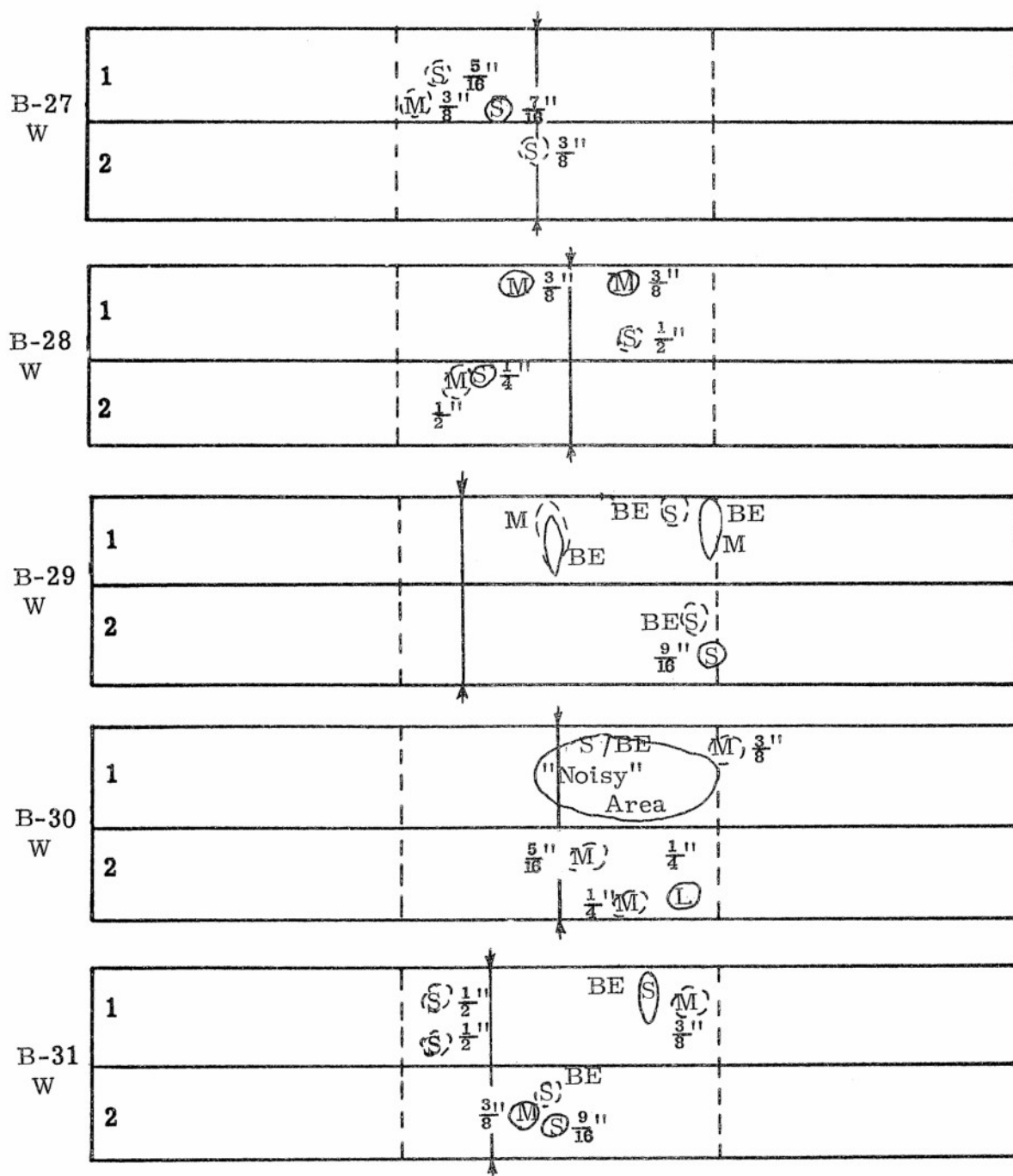


Figure G8

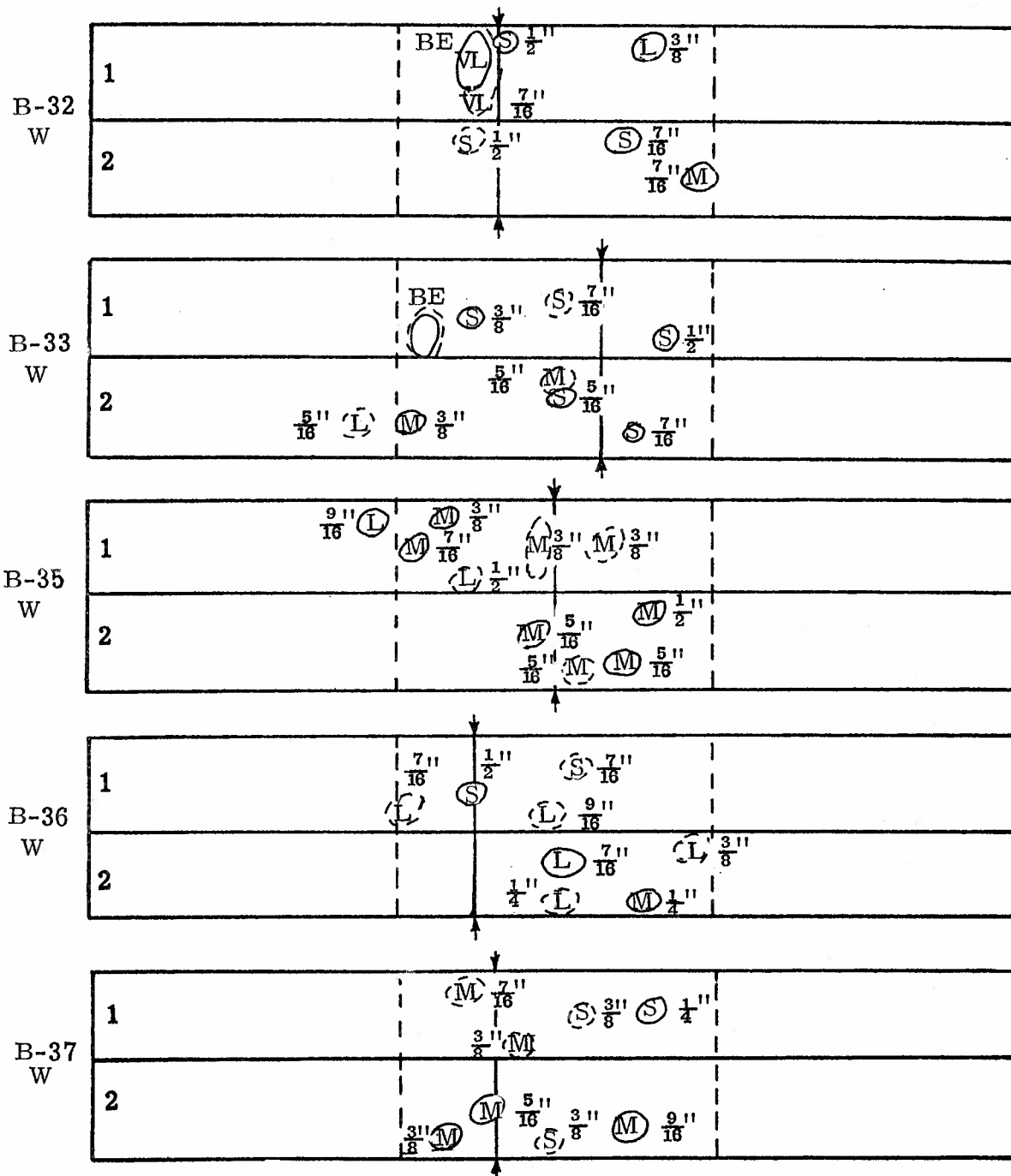


Figure G9



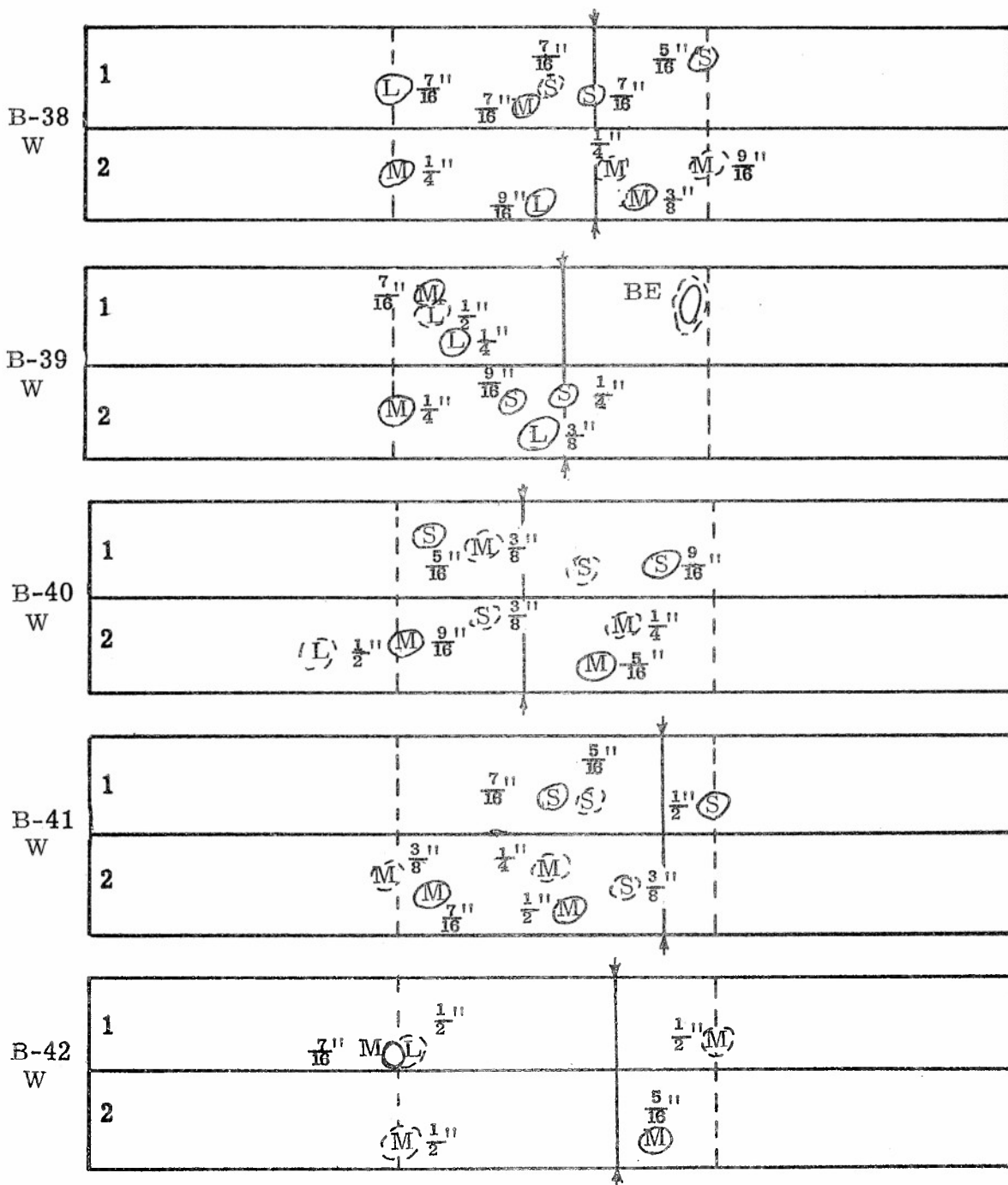


Figure G10

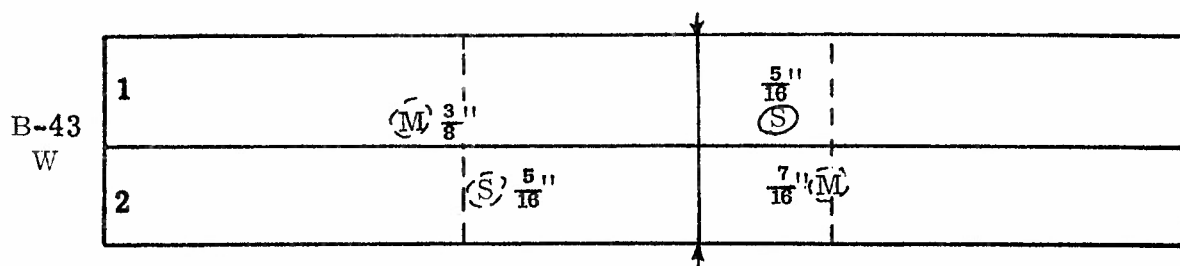


Figure G11

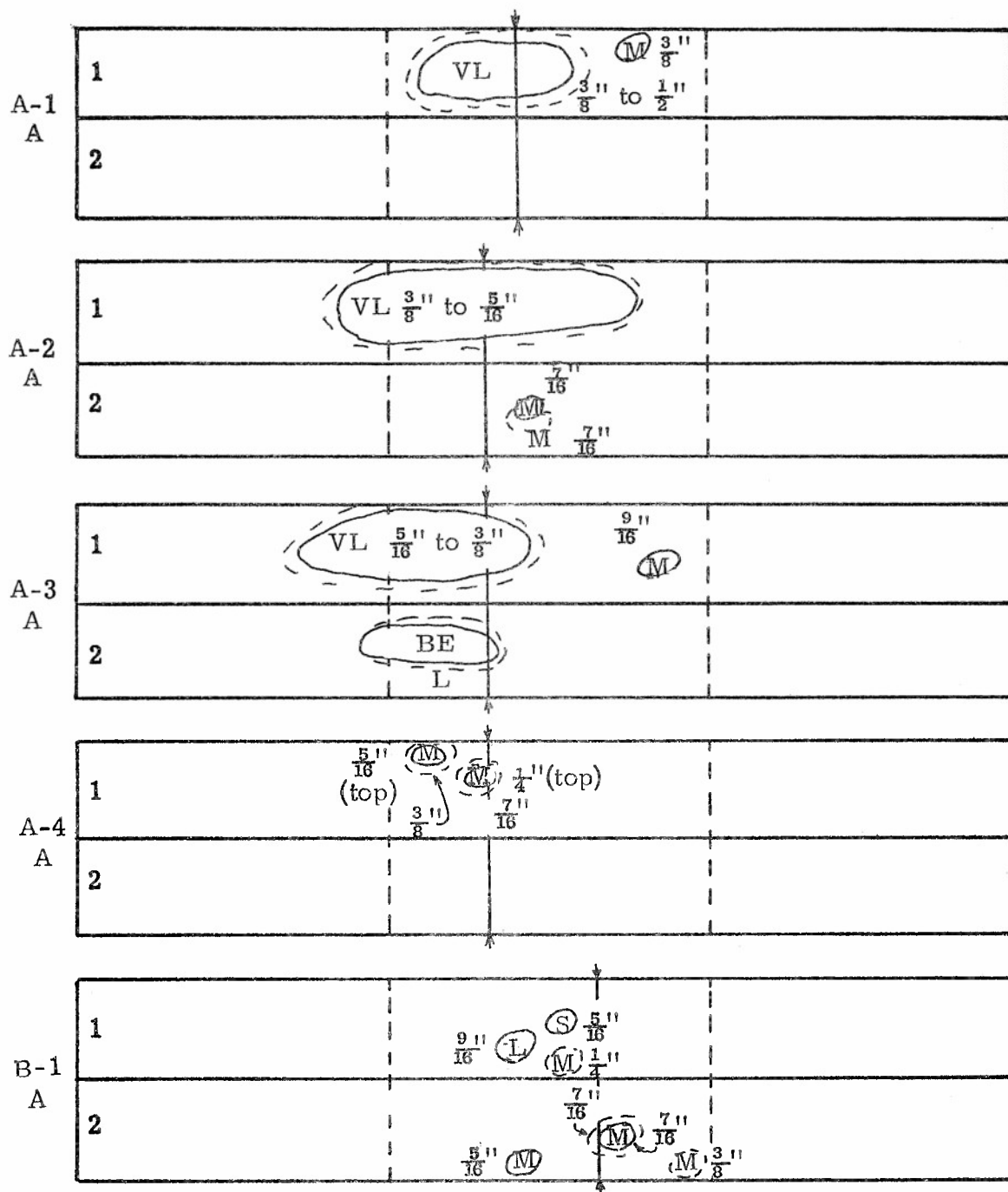


Figure G 12

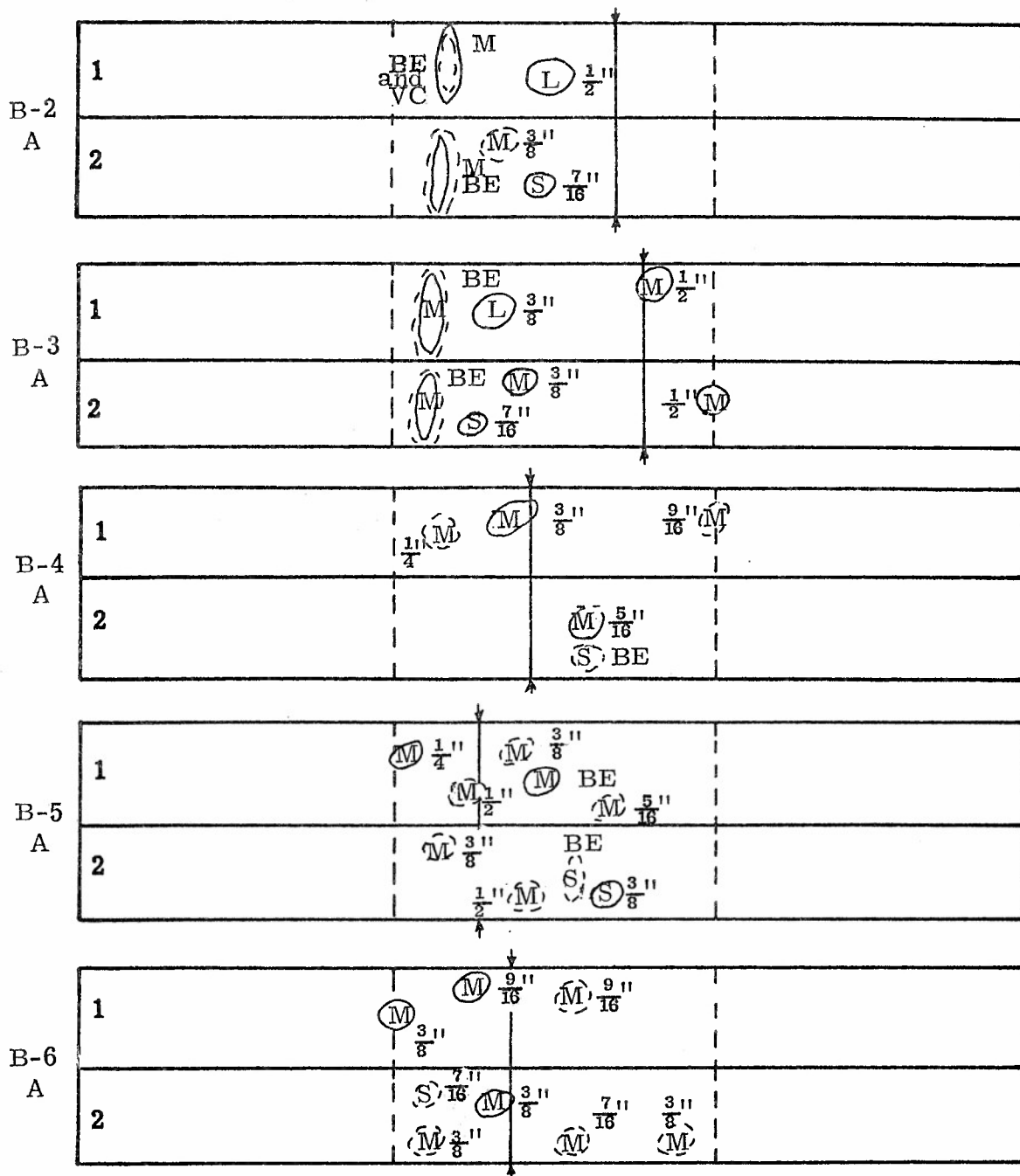


Figure G13

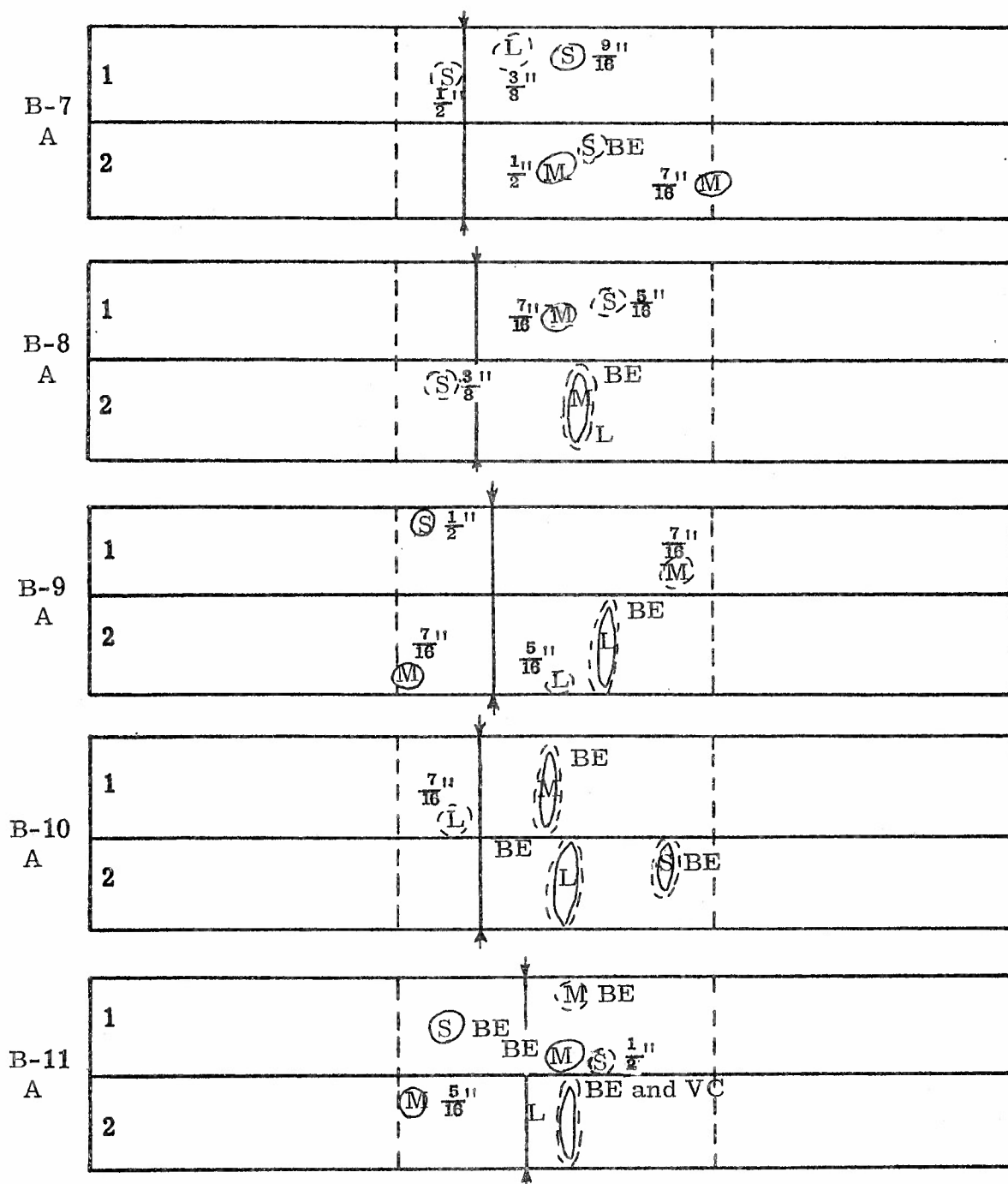


Figure G14

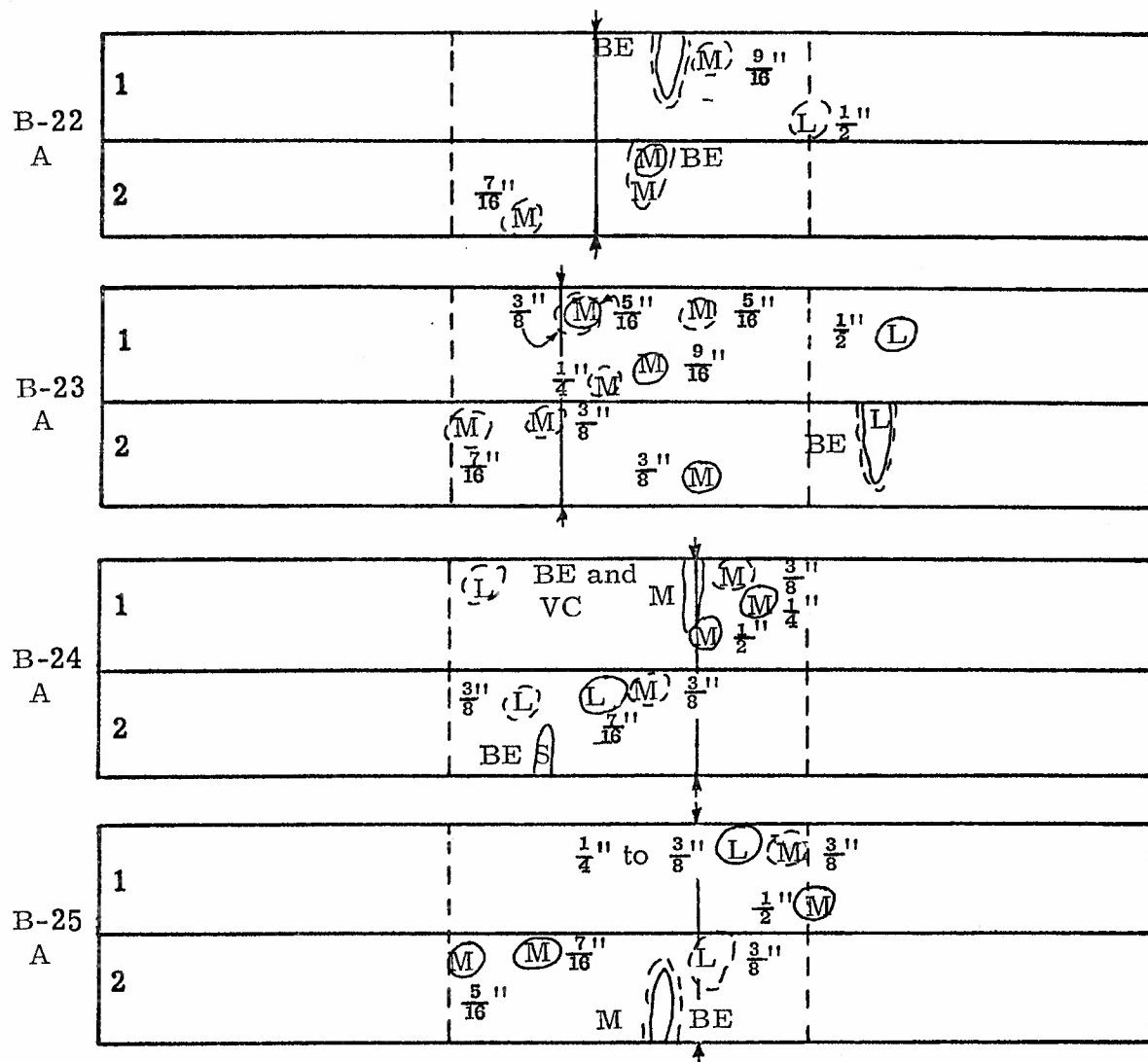


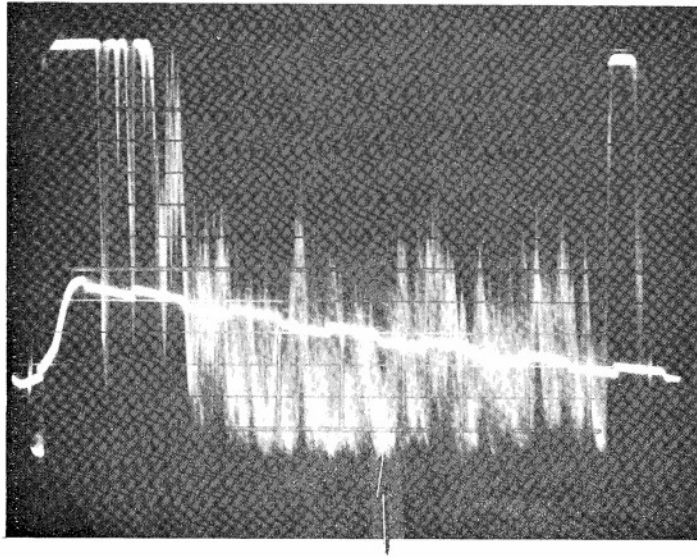
Figure G17

## APPENDIX H

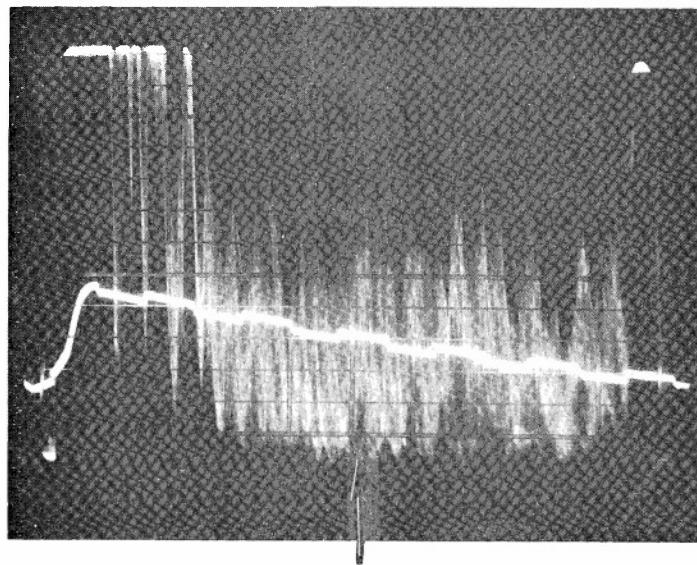
Southern's Multiple Traces (Smears) of Pulse-Echo Signals from  
Referenced End of Tensile Specimen Blanks from ATJ-S Billet  
L-1-8 With Grain only







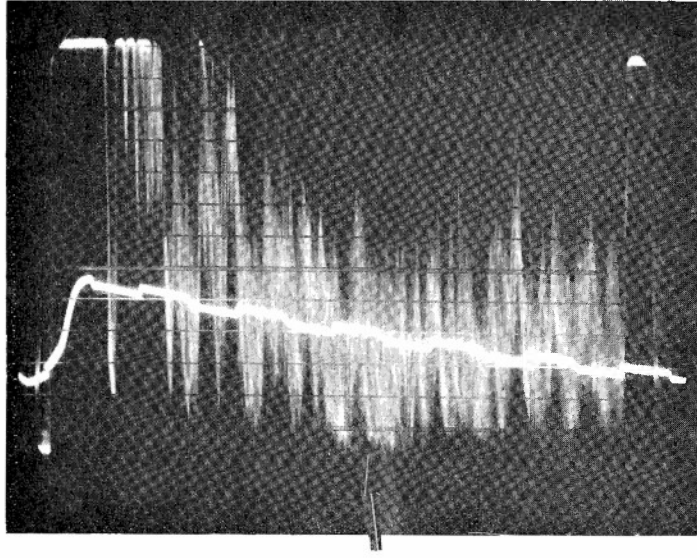
A7W



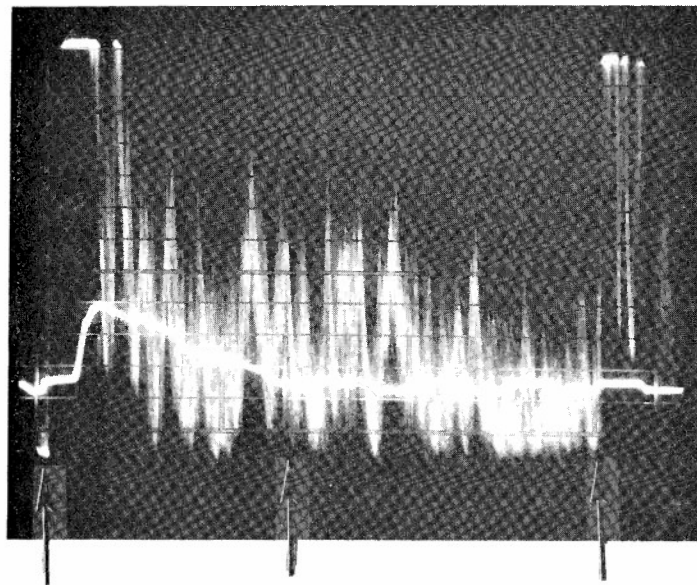
A8W

Figure H2





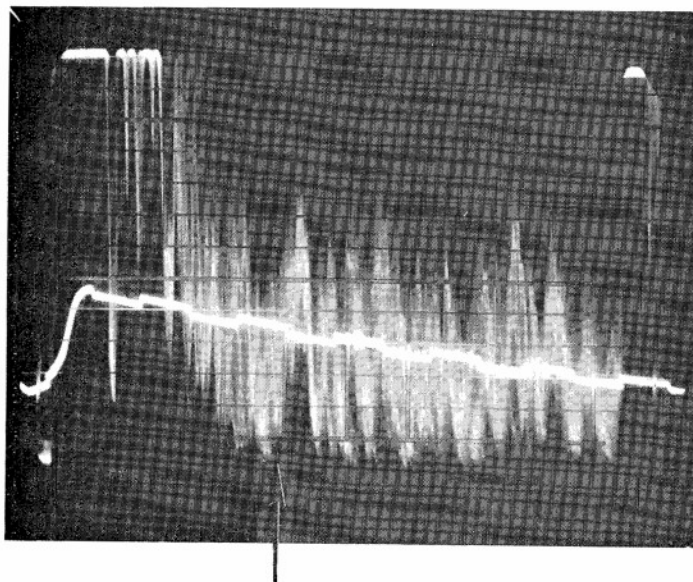
A9W



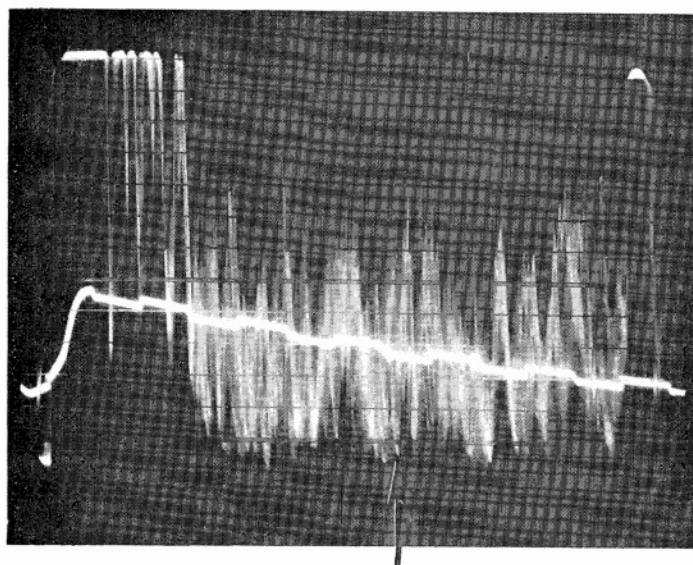
A10W

Figure H3



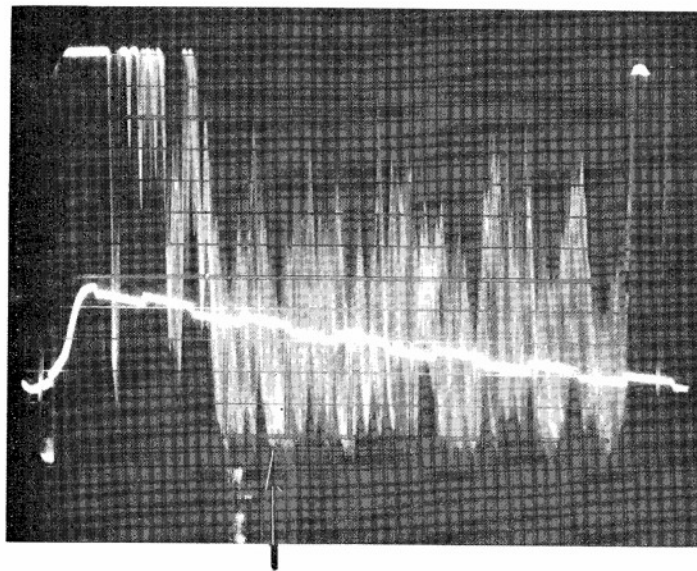


A11W

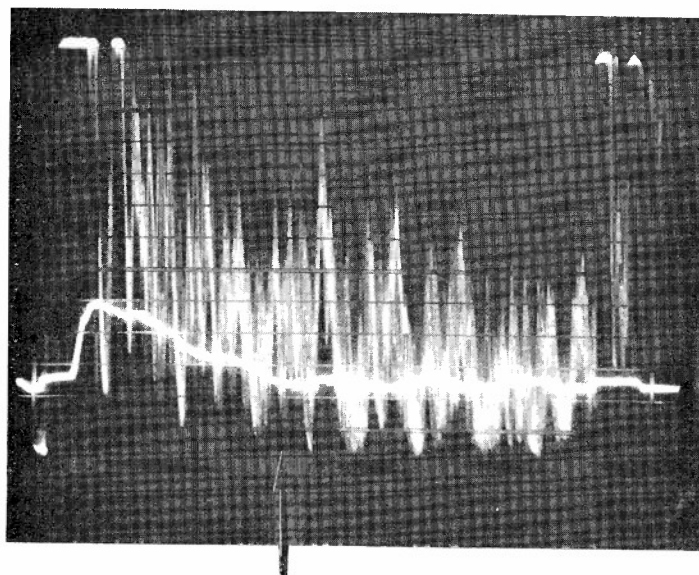


A12W





A13W

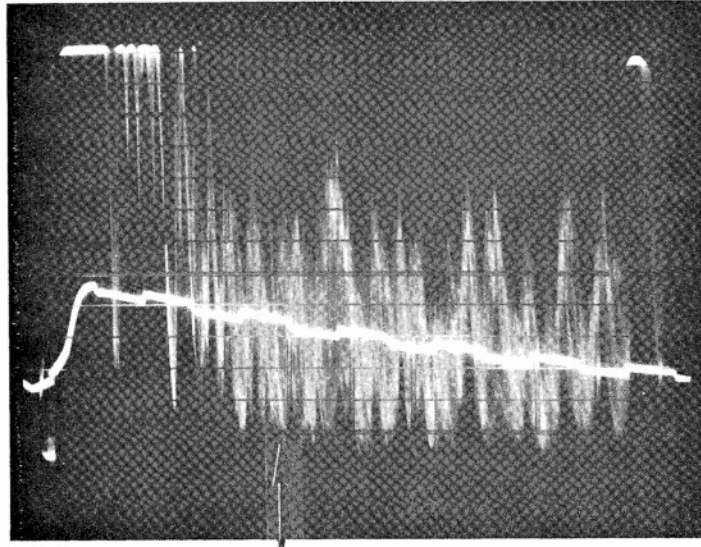


A14W

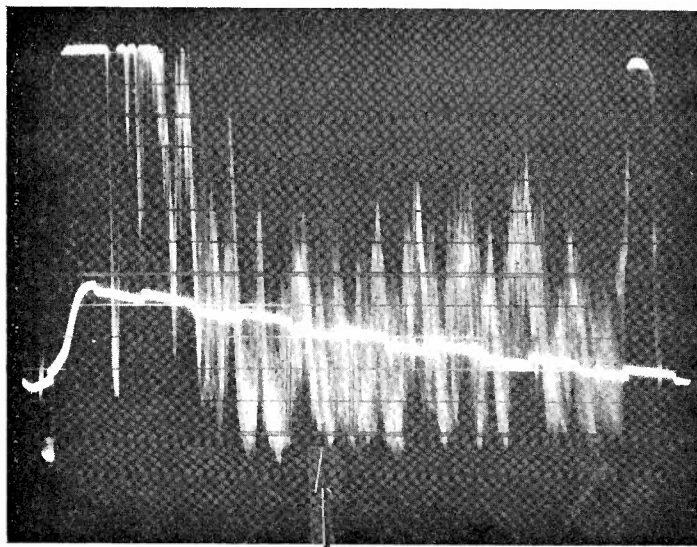
Figure H5







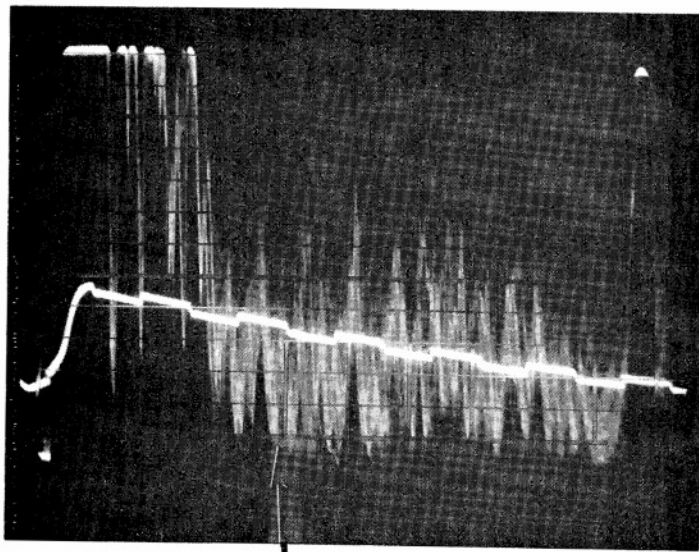
A15W



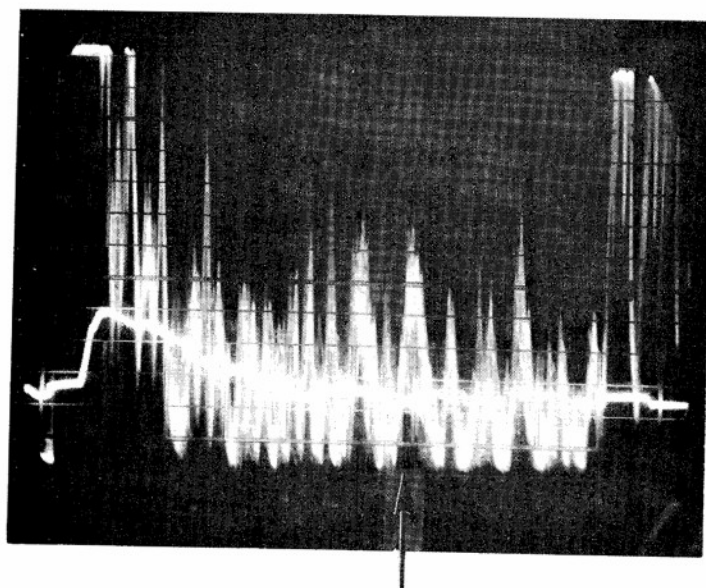
A16W

Figure H6





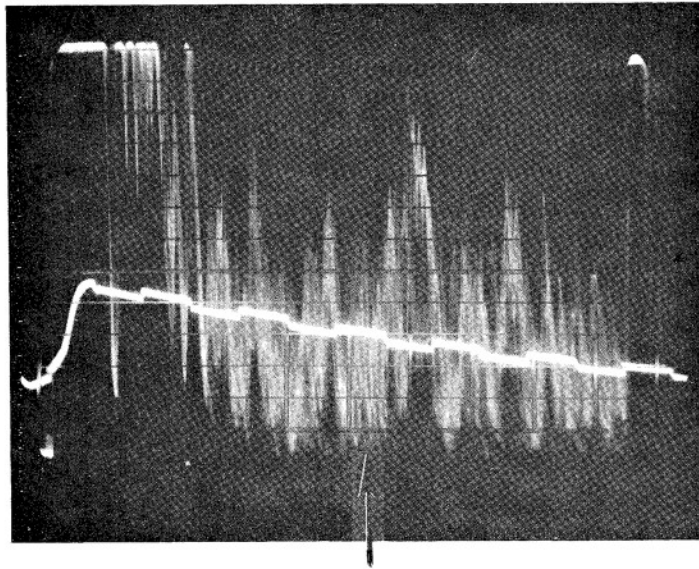
A17W



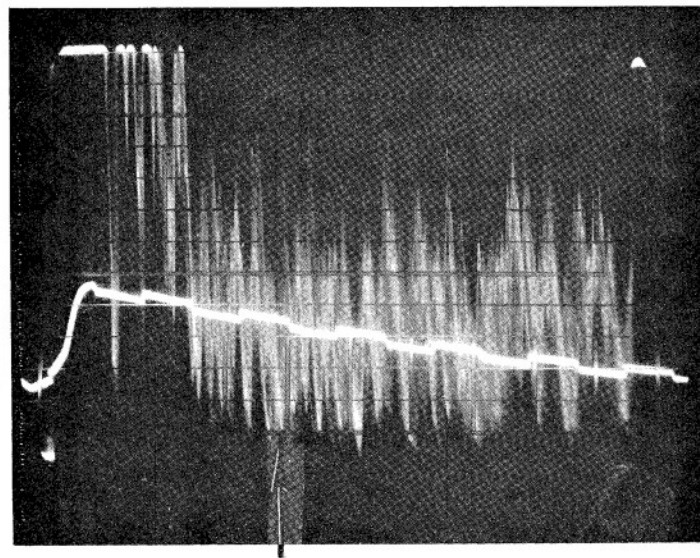
A18W

Figure H7





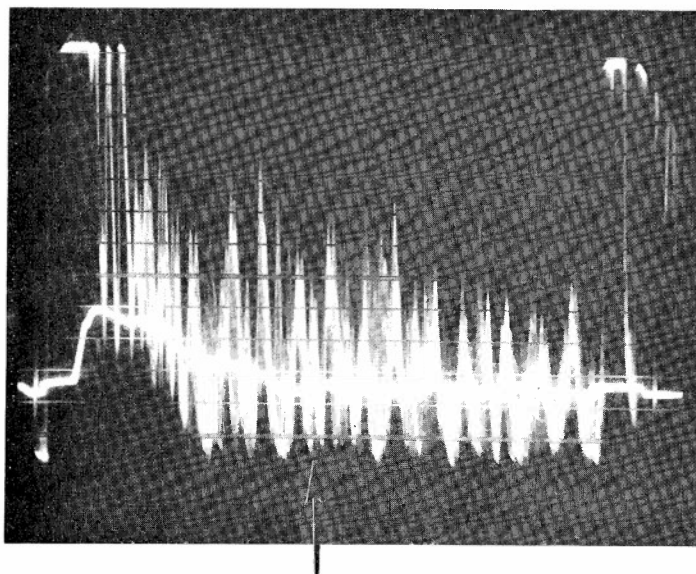
A19W



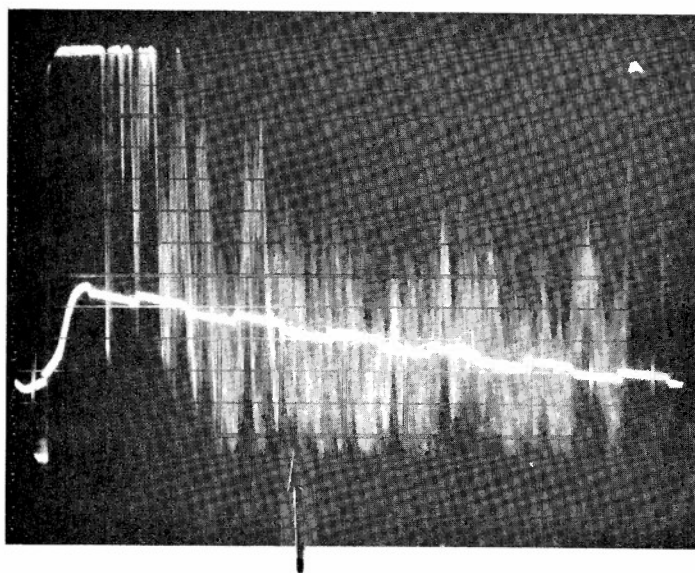
A20W

Figure H8





A21W

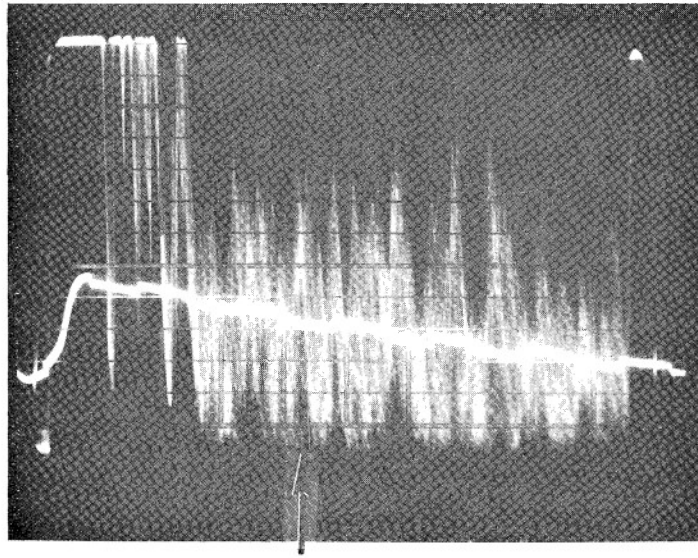


A22W

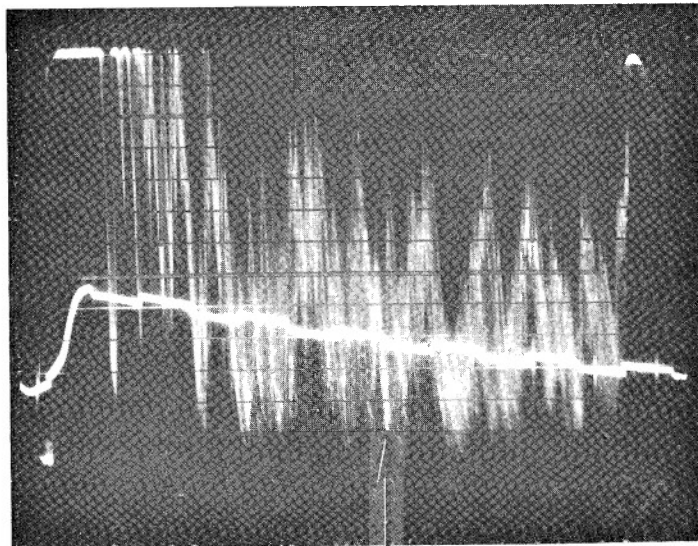
Figure H9





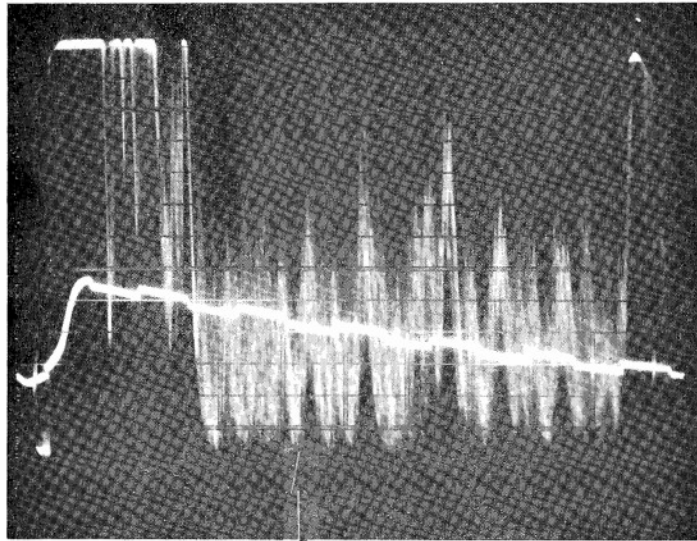


A23W

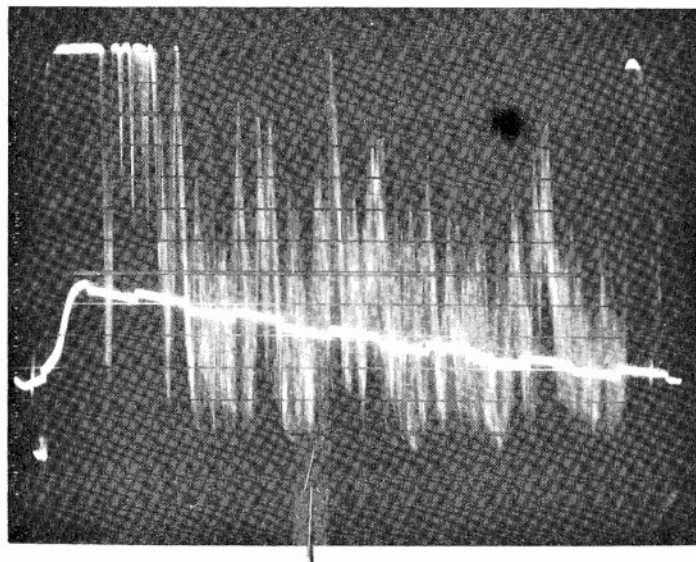


A24W  
Figure H10





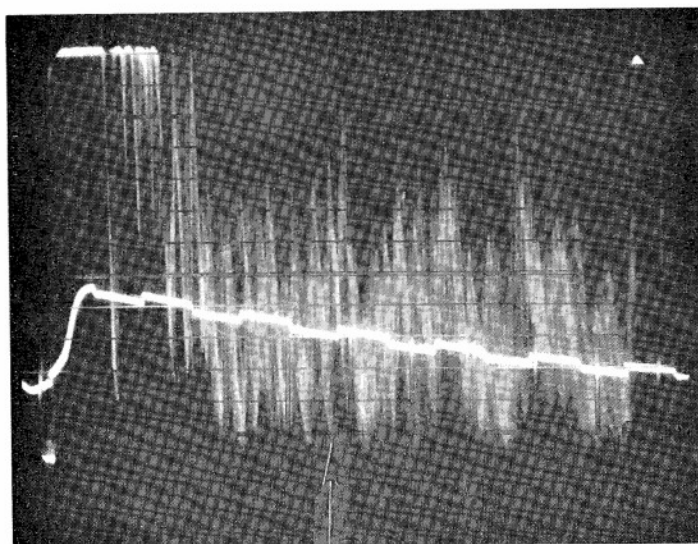
A25W



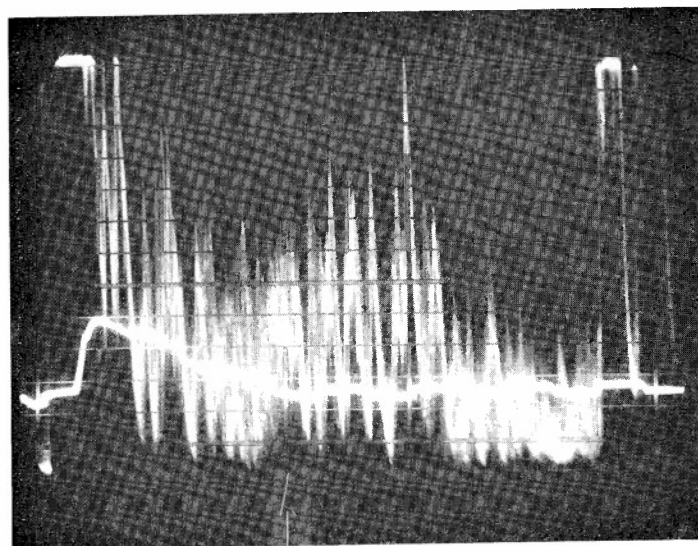
A26W

Figure H11





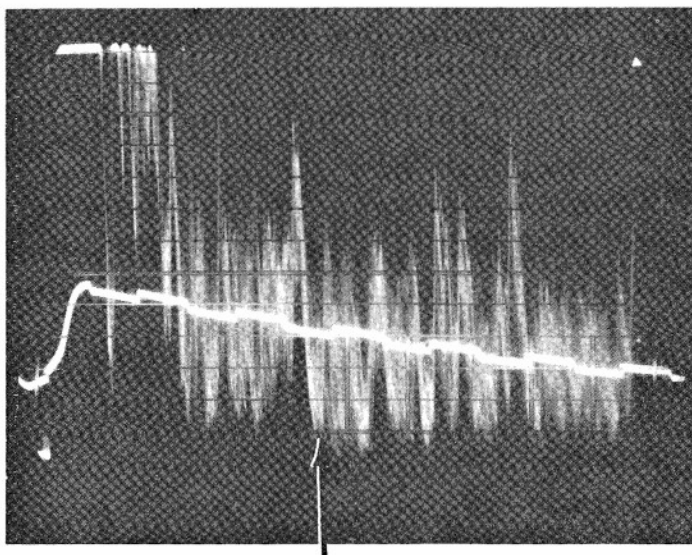
A27W



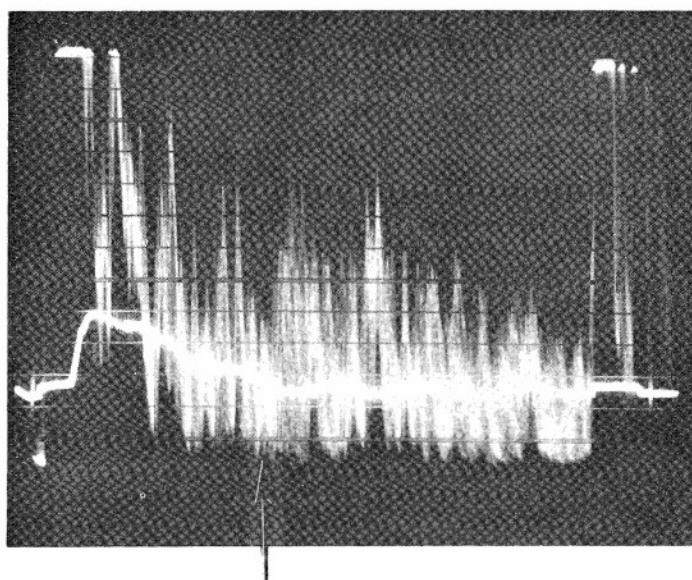
A28W

Figure H12





A29W

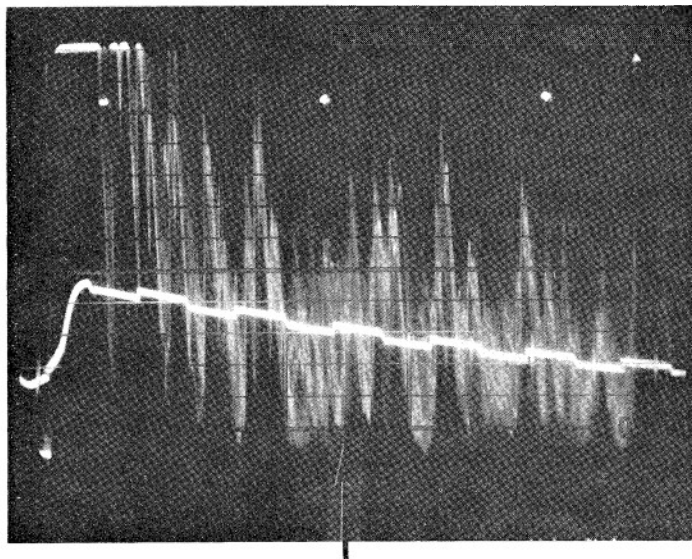


A30W

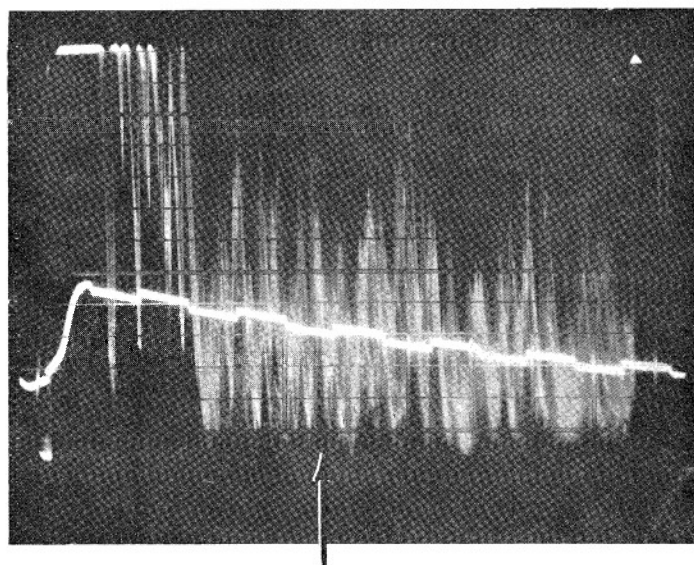
Figure H13







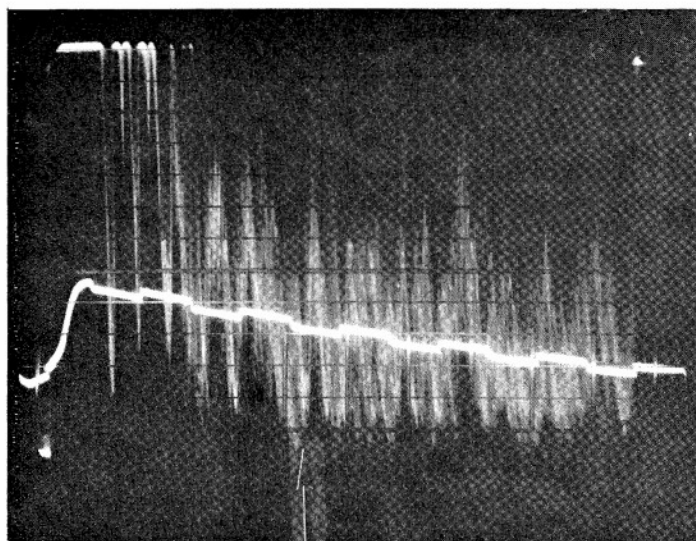
A31W



A32W

Figure H14

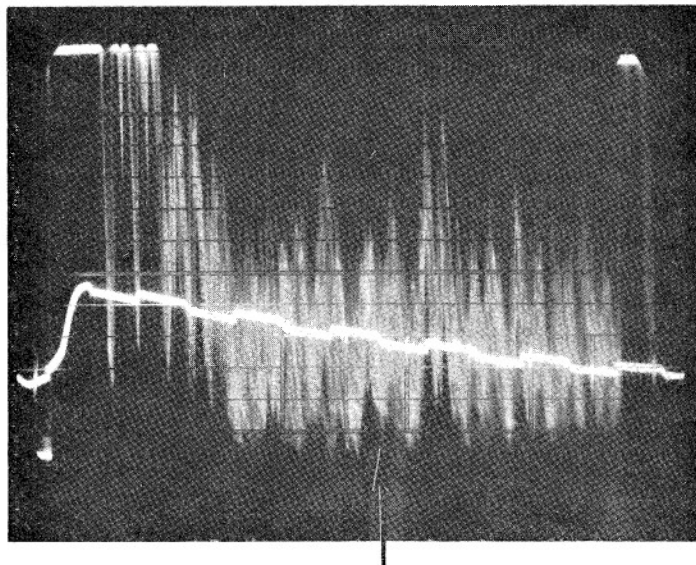




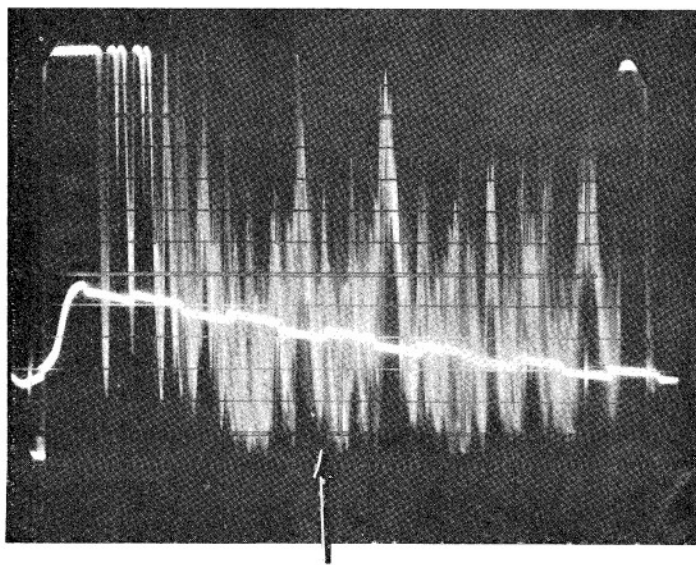
A33W

Figure H15





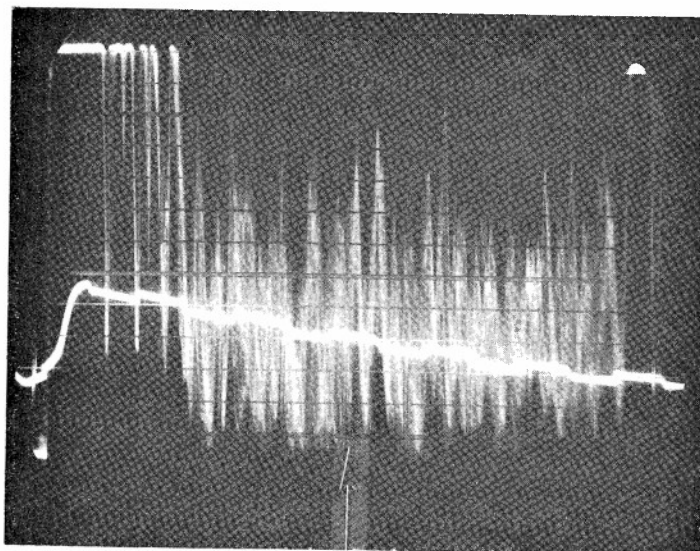
B26W



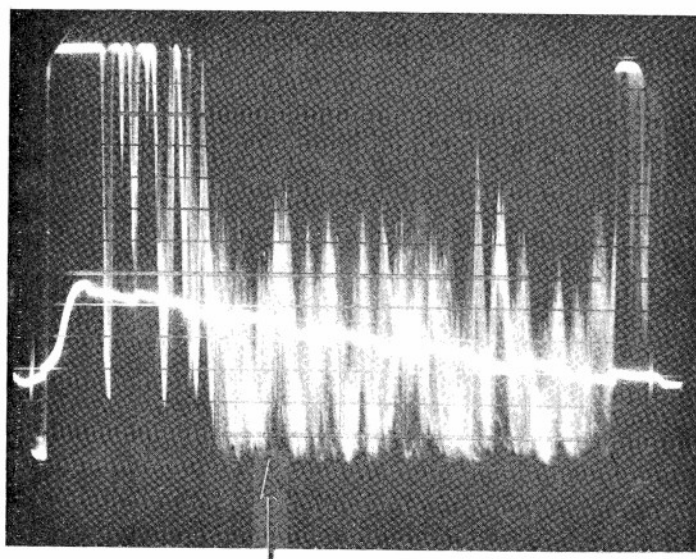
B27W

Figure H16





B28W

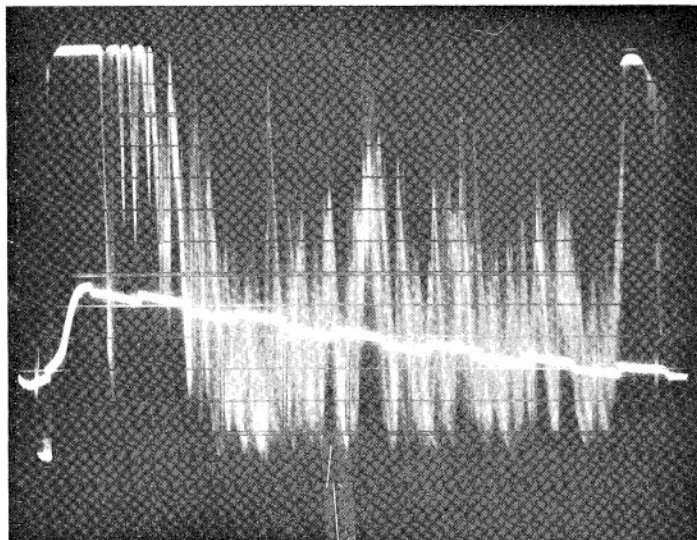


B29W

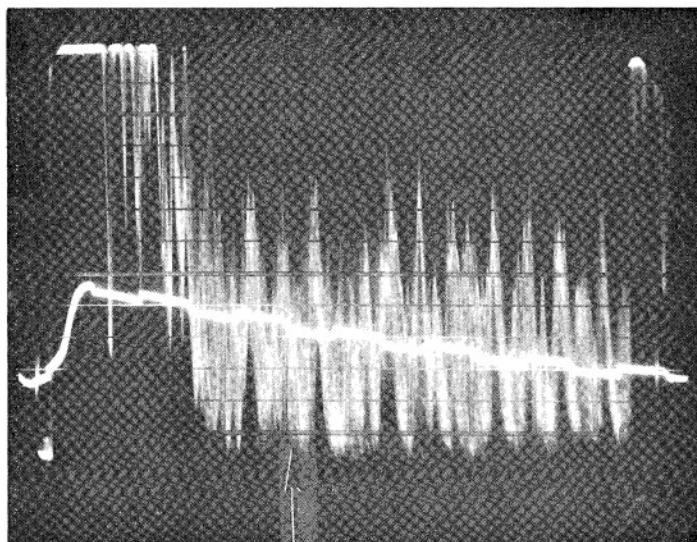
Figure H17







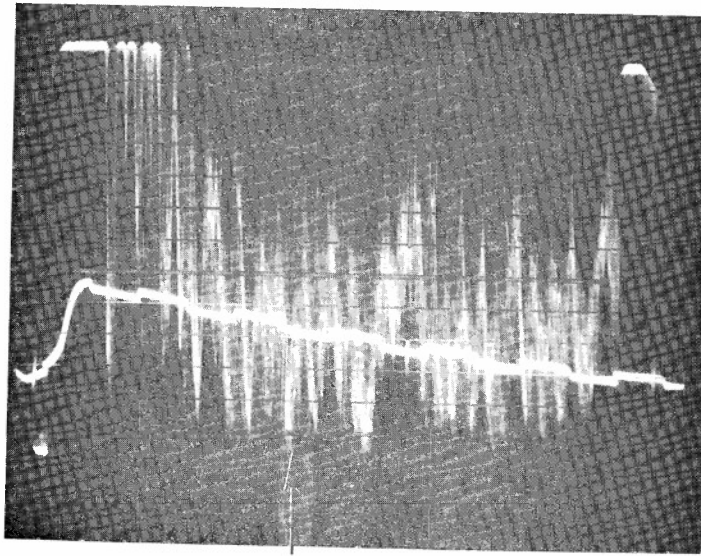
B30W



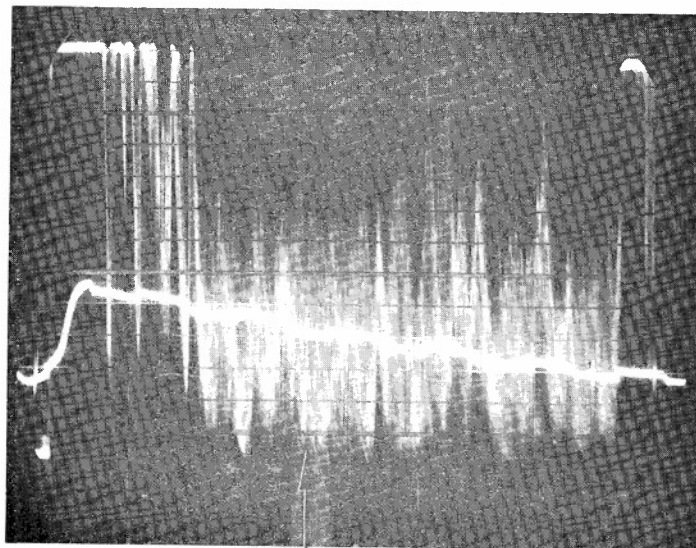
B31W

Figure H18





B32W



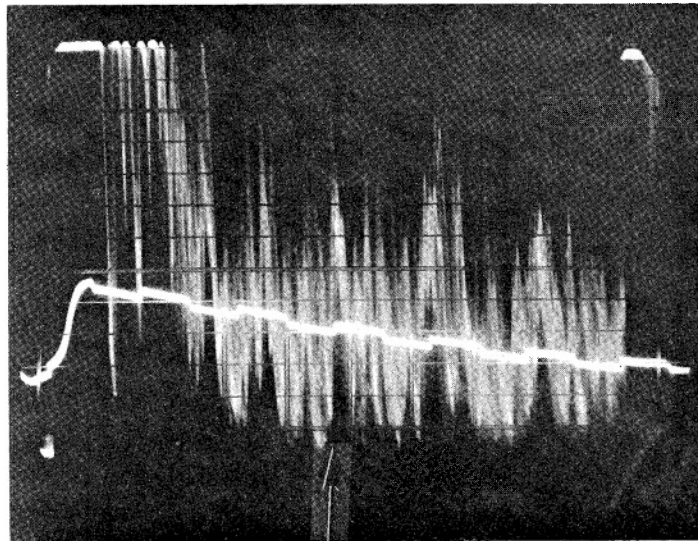
B33W

Figure H19  
605



No Specimen

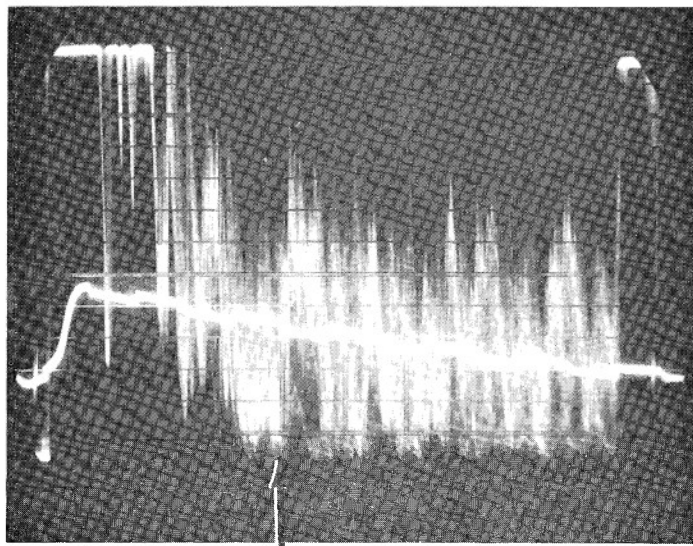
B34W



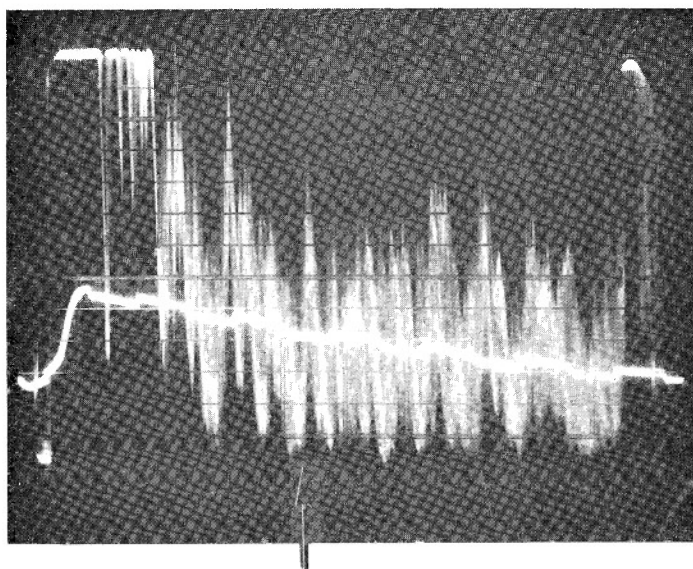
B35W

Figure H20  
606





B36W



B37W

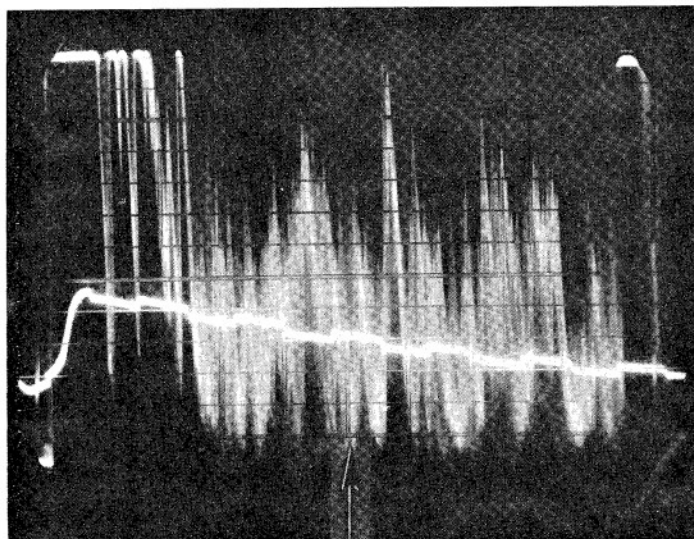
Figure H21





See Figure 94

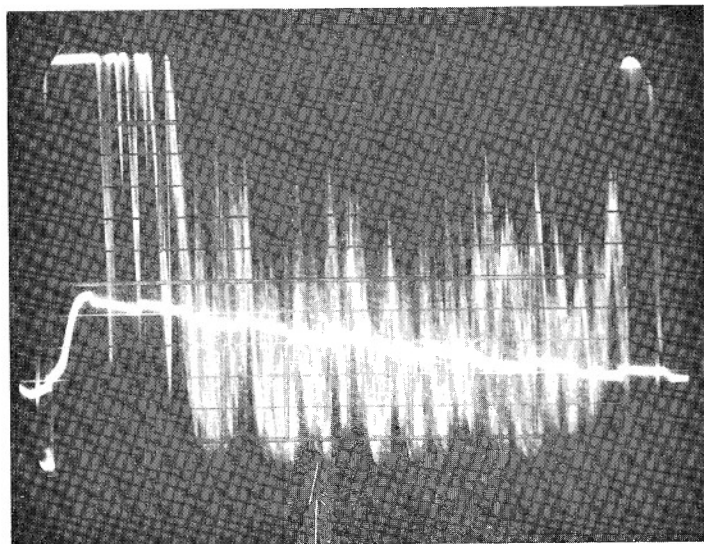
B38W



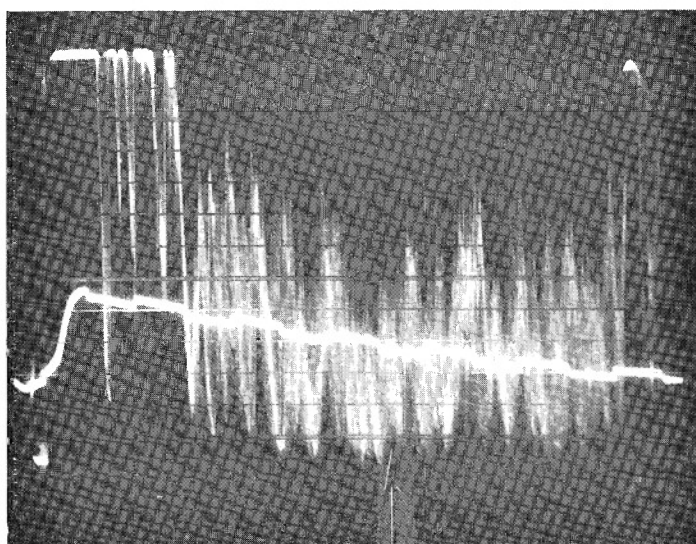
B39W

Figure H22





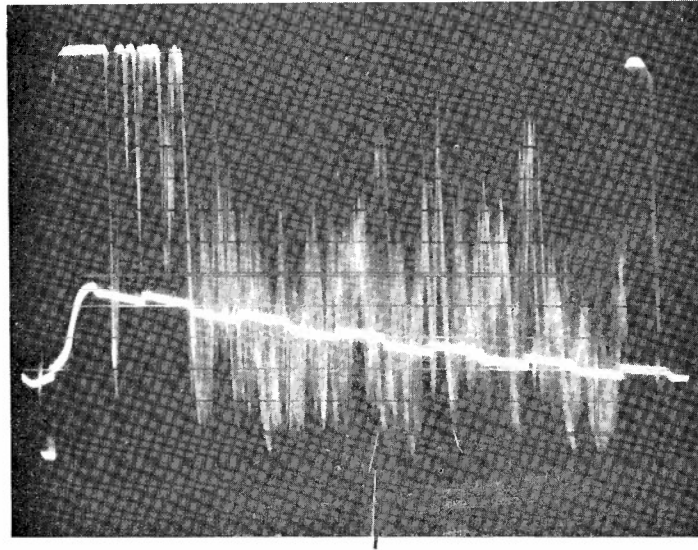
B40W



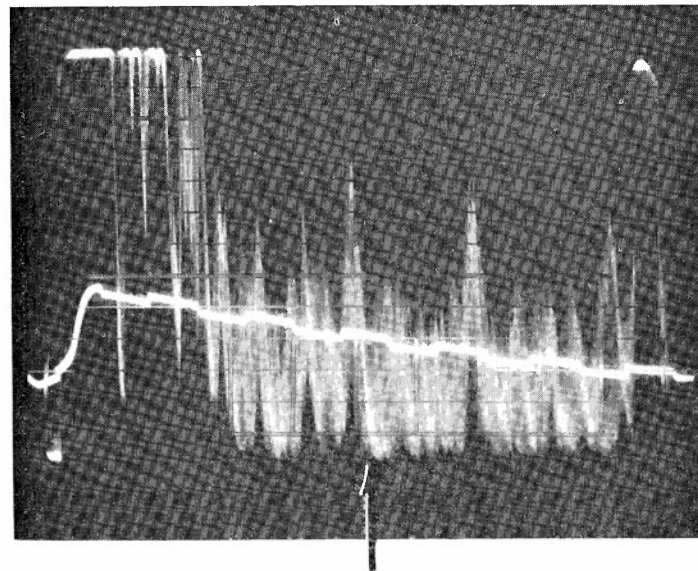
B41W

Figure H23





B42W



B43W

Figure H24



## APPENDIX I

Original Stress-Strain Curves for ATJ-S Billet L-1-8 With  
Grain and Across Grain at 70°F





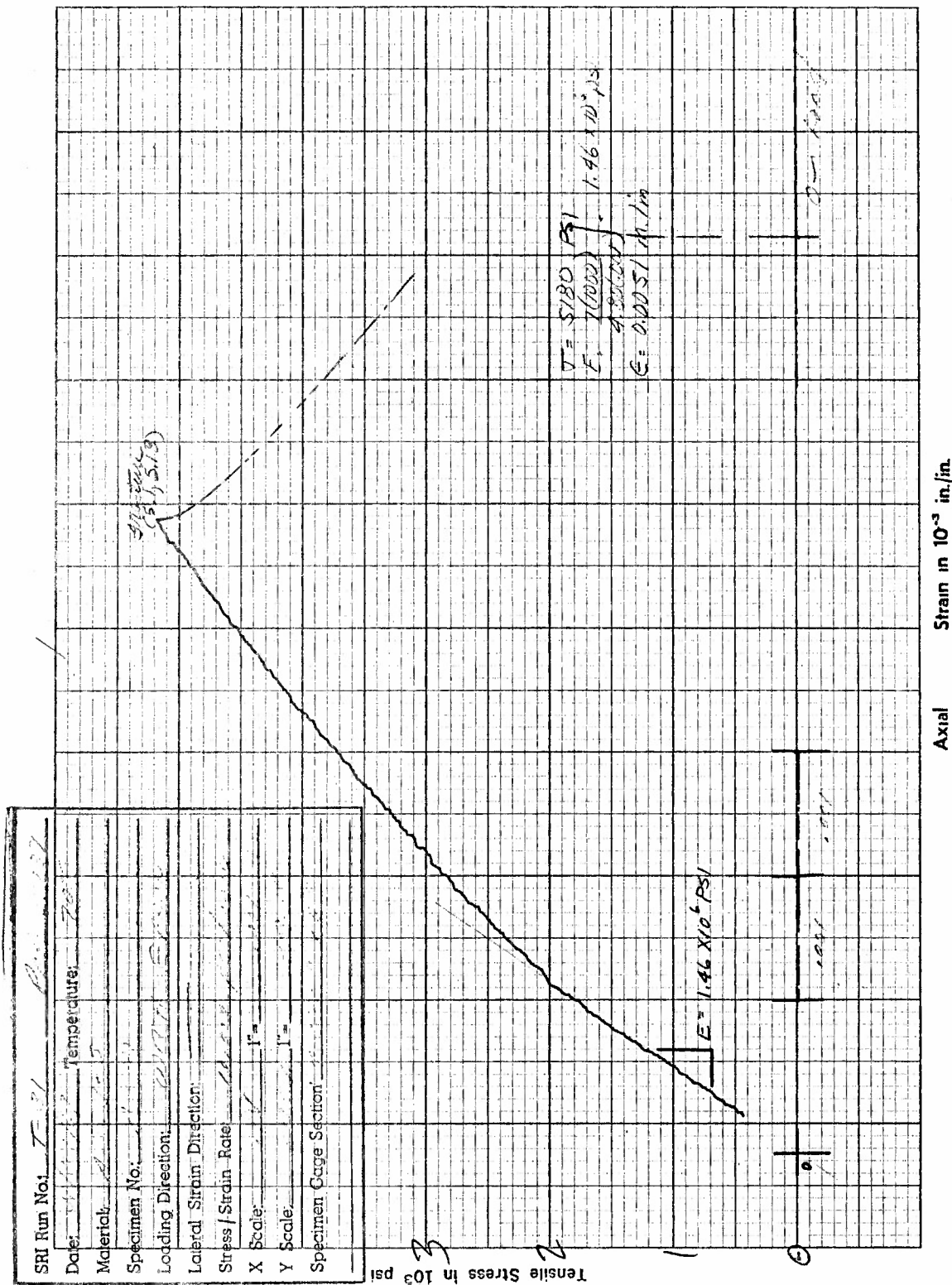


Figure I1. Tensile Stress versus Axial Strain for Specimen A5W of ATJ-S Graphite at 70°F

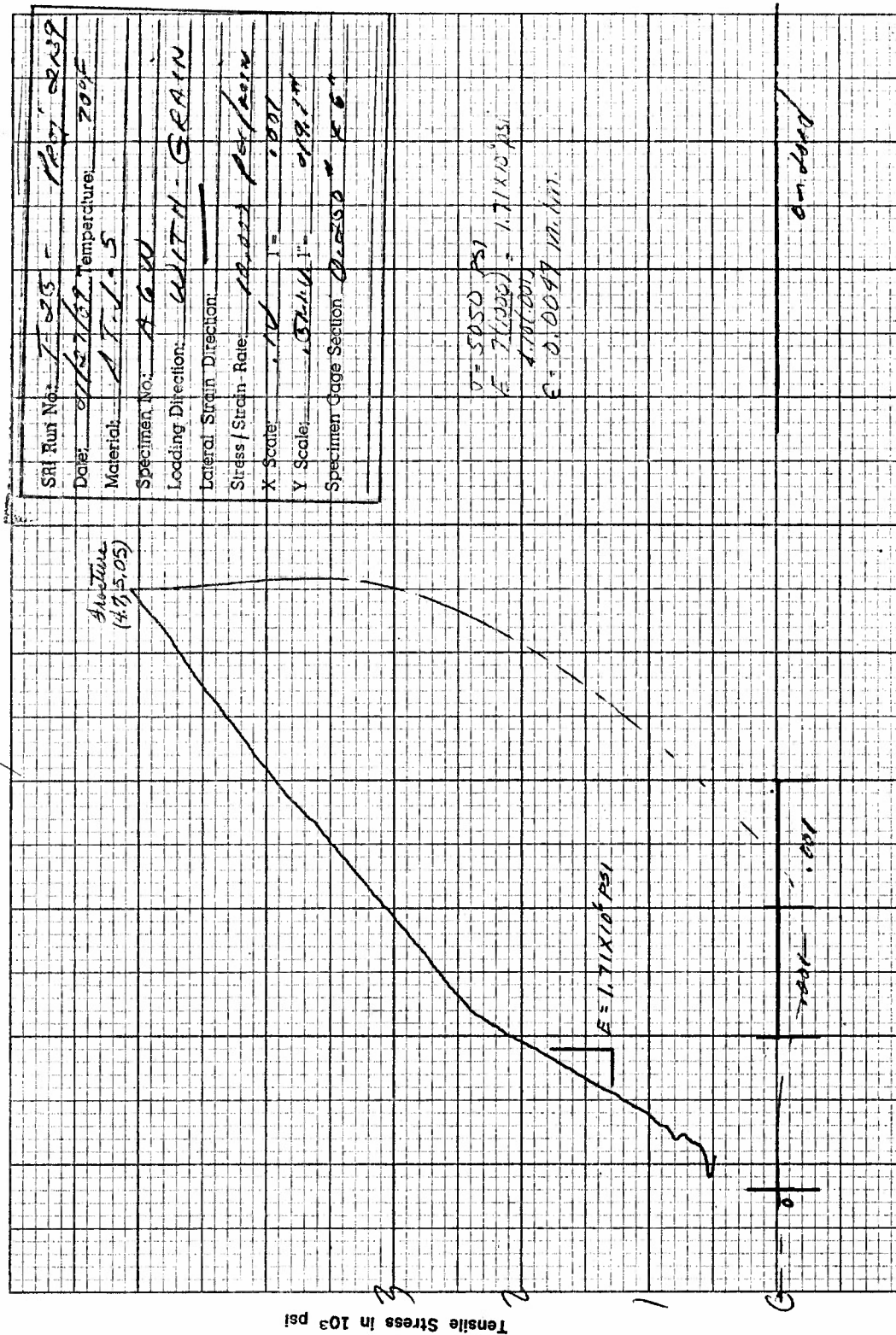


Figure I2. Tensile Stress versus Axial Strain for Specimen A6W of ATJ-S Graphite at 70°F

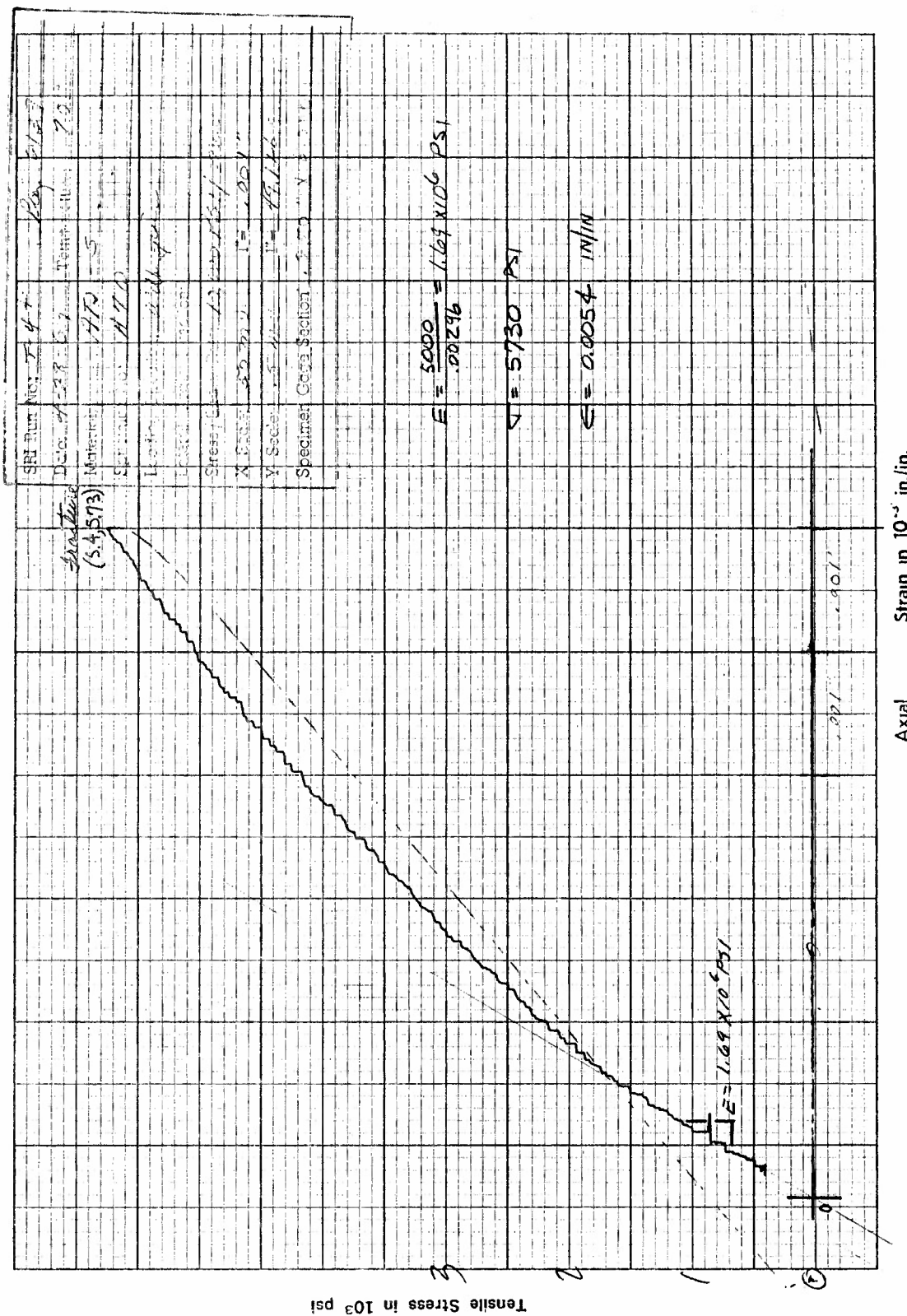


Figure I3. Tensile Stress versus Axial Strain for Specimen A7W of ATJ-S Graphite at 70°F



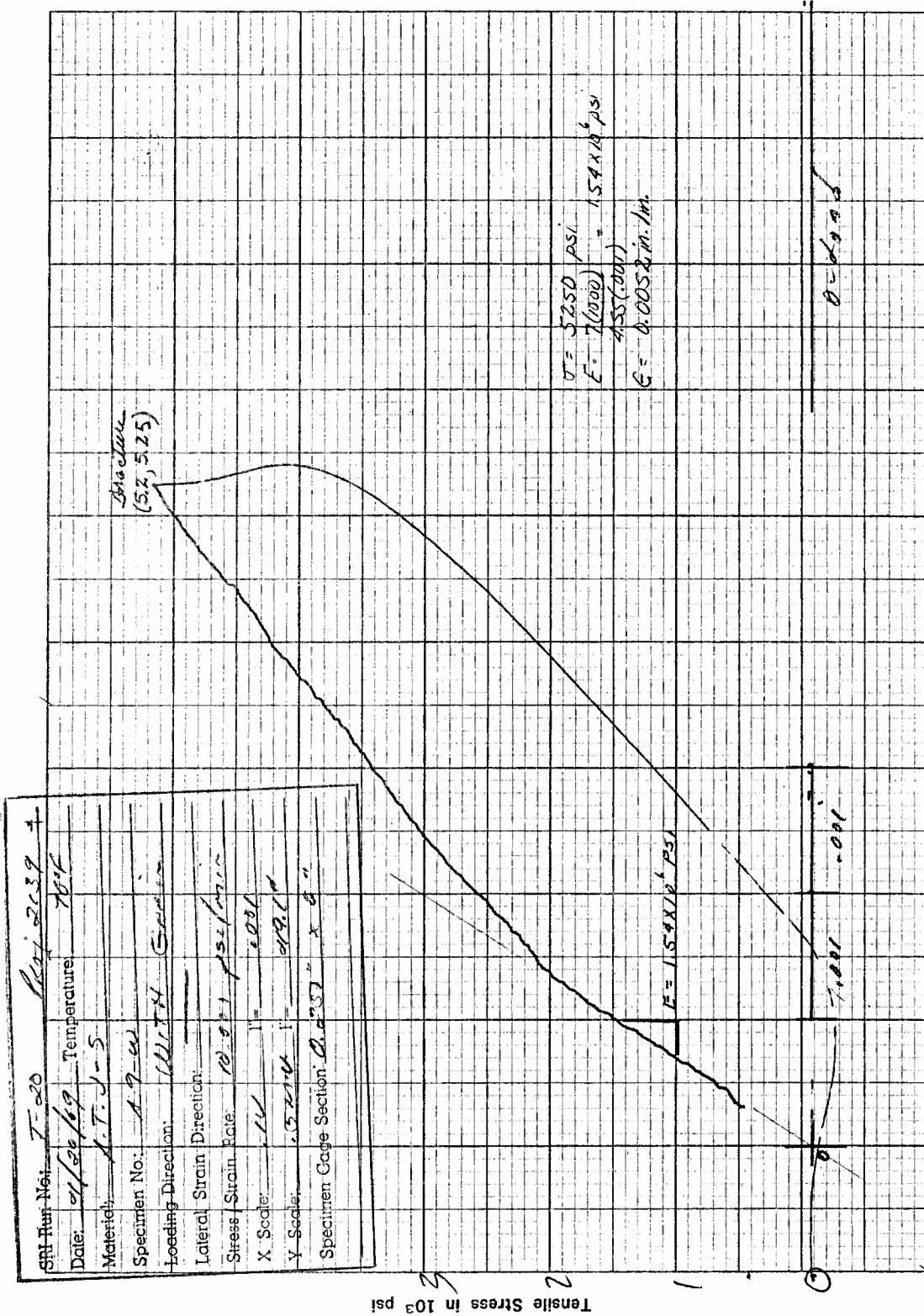


Figure I5, Tensile Stress versus Axial Strain for Specimen A9W of ATJ-S Graphite at 70°F



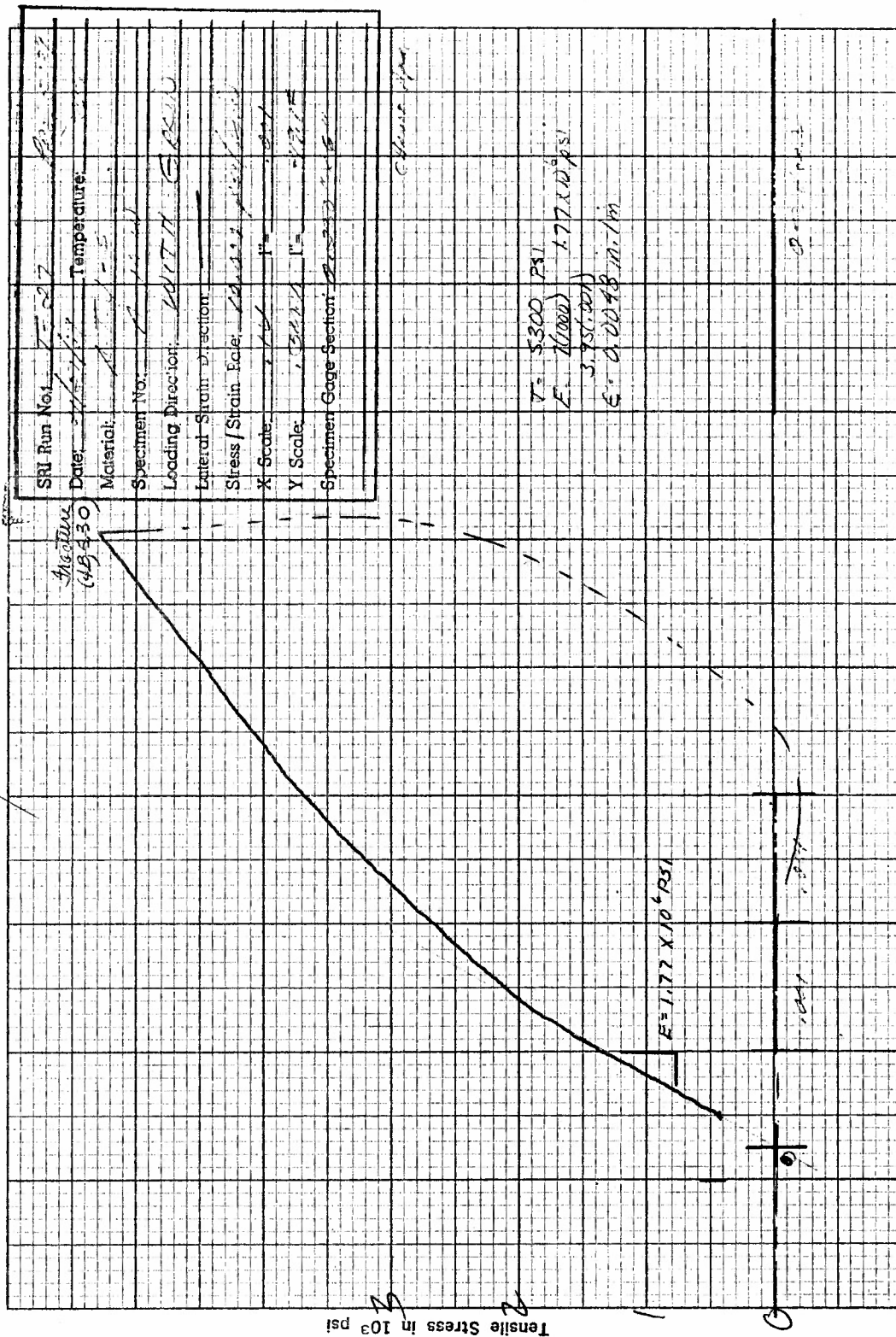


Figure I6. Tensile Stress versus Axial Strain for Specimen A10W of ATJ-S Graphite at 70°F

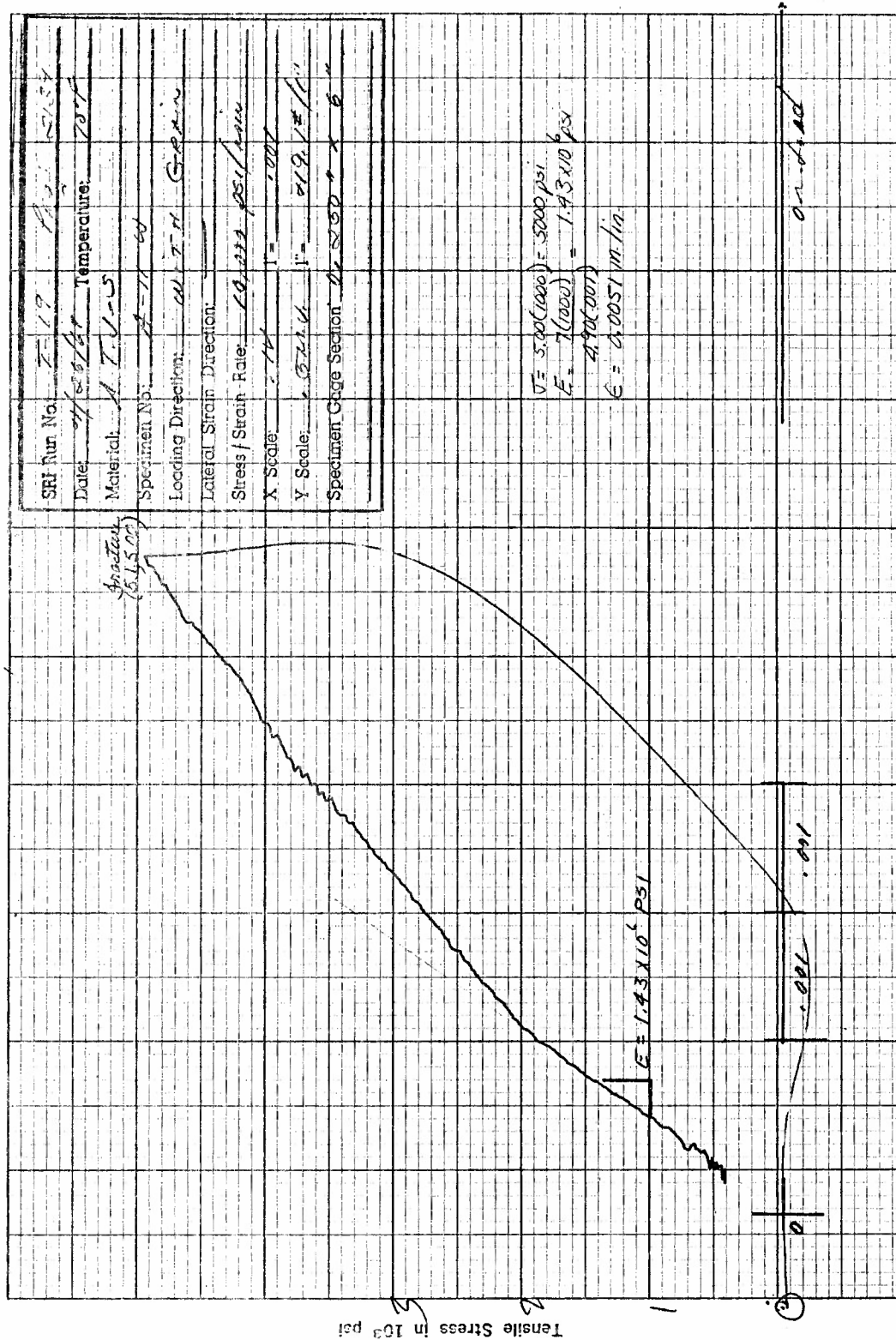


Figure I7. Tensile Stress versus Axial Strain for Specimen A11W of ATJ-S Graphite at 70°F

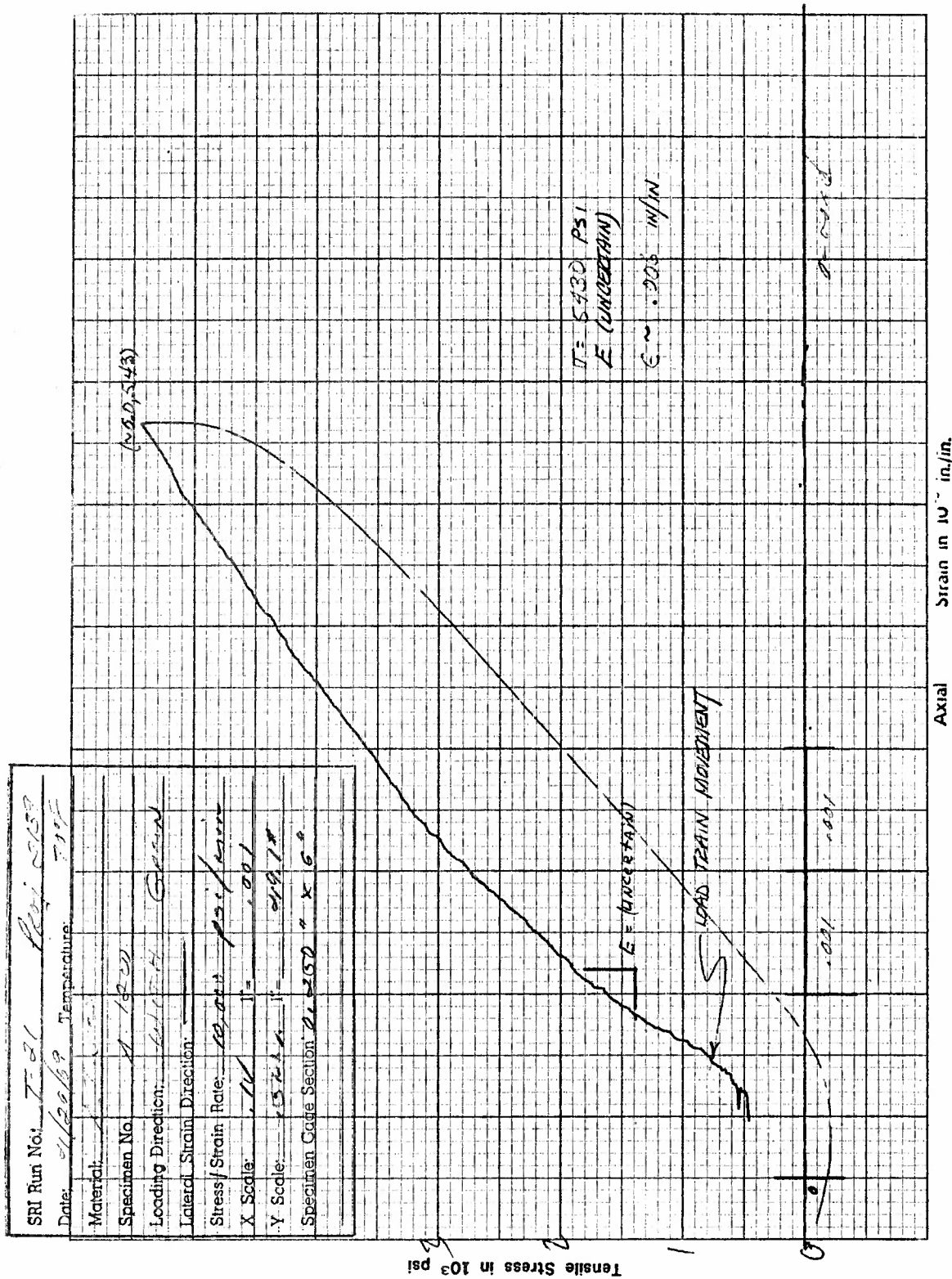


Figure I8. Tensile Stress versus Axial Strain for Specimen A12W of ATJ-S Graphite at 70°F



SRI Run No.	7-43	Rev.	2139
Date:	7-16-61	Temperature:	70°F
Material:	A-5-S		
Specimen No.:	A13W		
Loading Direction:	CRUTN	Specimen	
Lateral Strain Direction:			
Stress/Strain Rate:	14,000 psi/min		
X Scale:	0.10 in		
Y Scale:	5000 psi		
Specimen Gage Section:	0.750" x 0.125"		

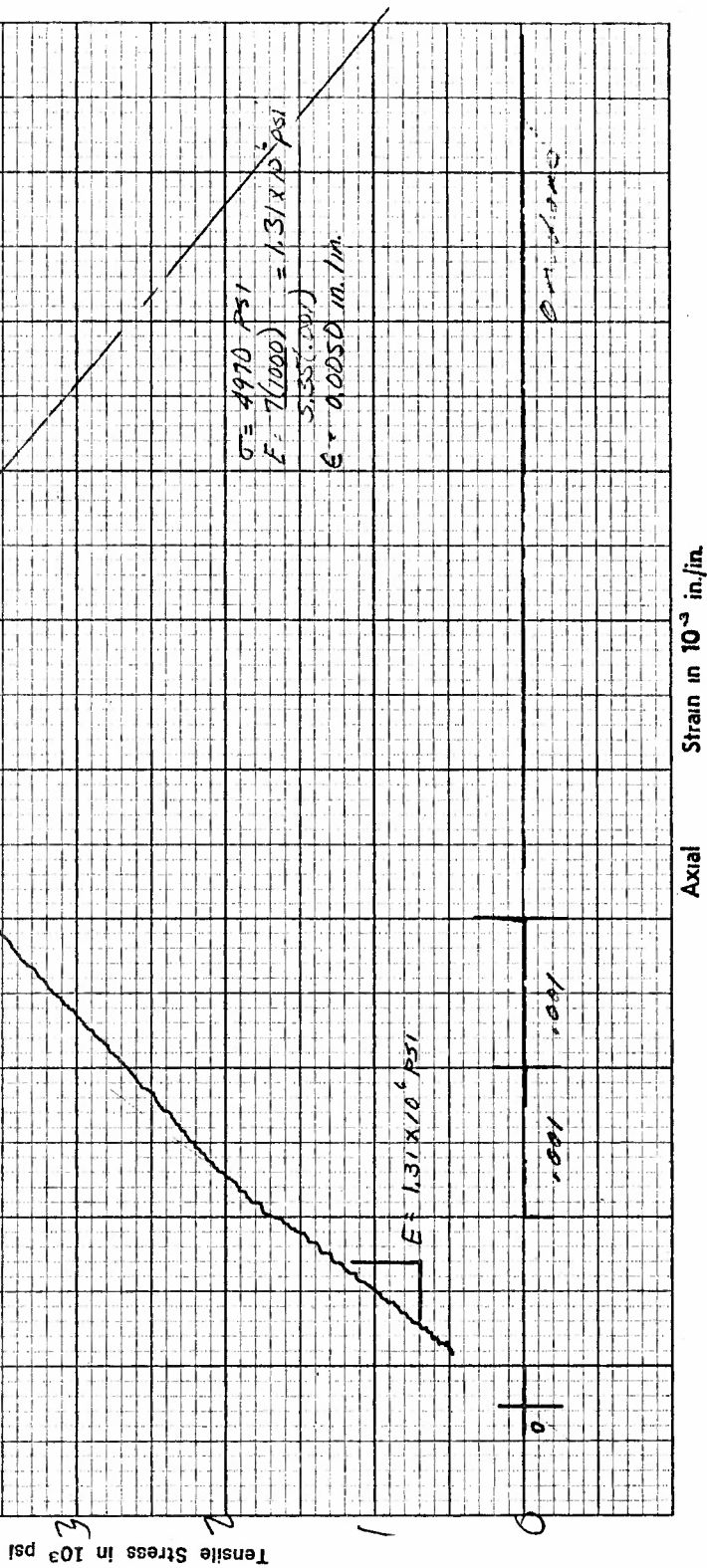


Figure I9. Tensile Stress versus Axial Strain for Specimen A13W of ATJ-S Graphite at 70°F

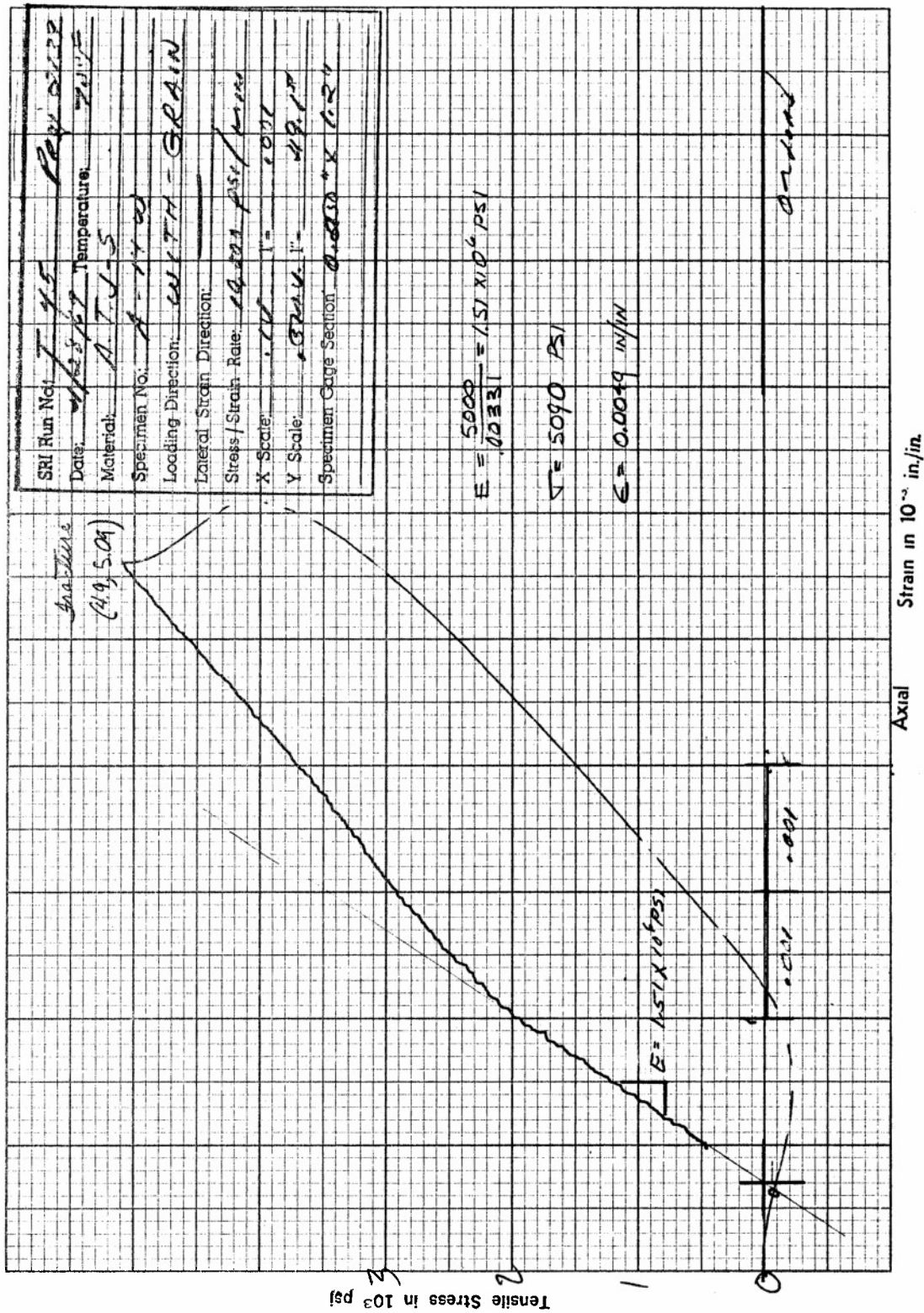
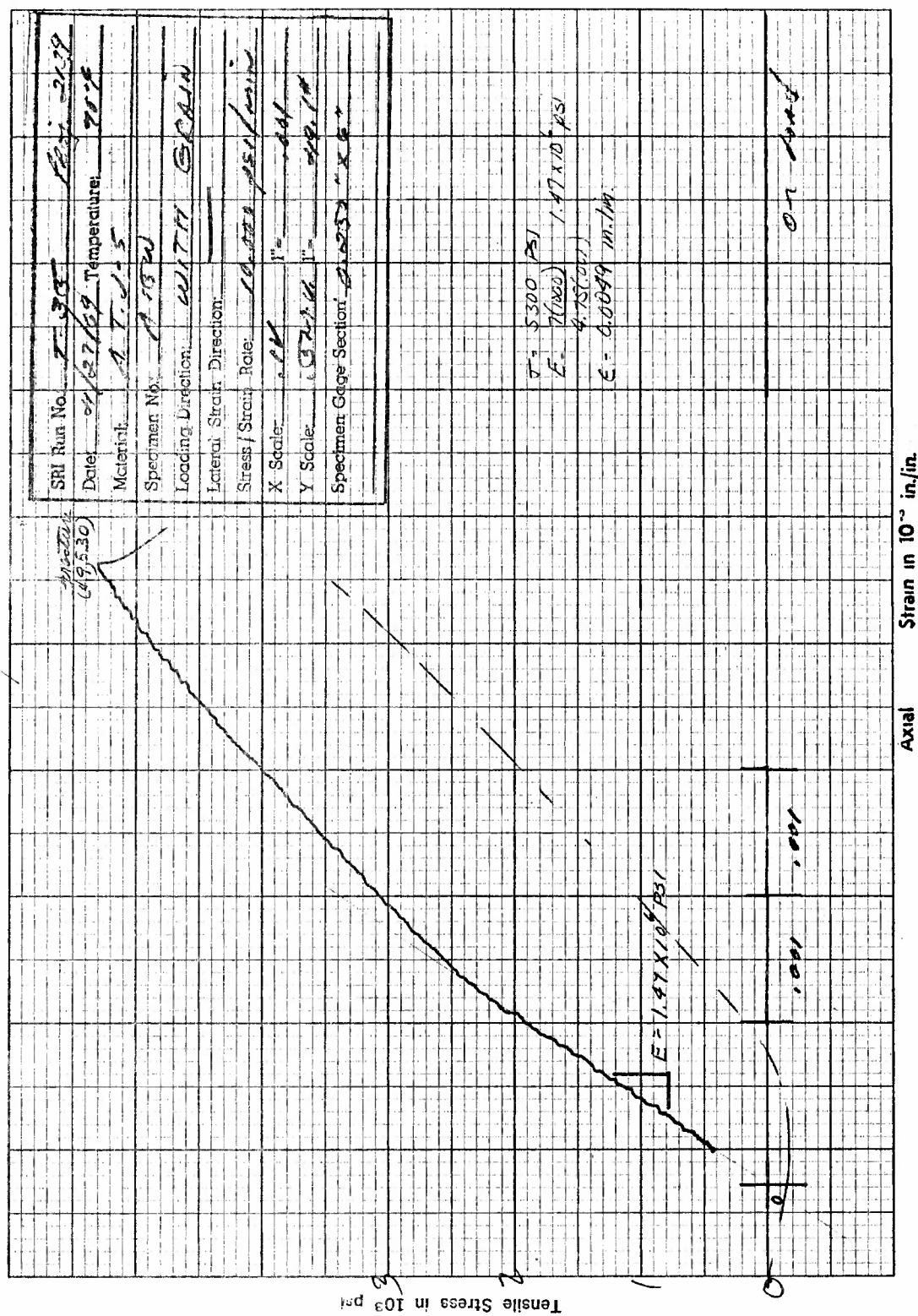


Figure I10. Tensile Stress versus Axial Strain for Specimen A14W of ATJ-S Graphite at 70°F



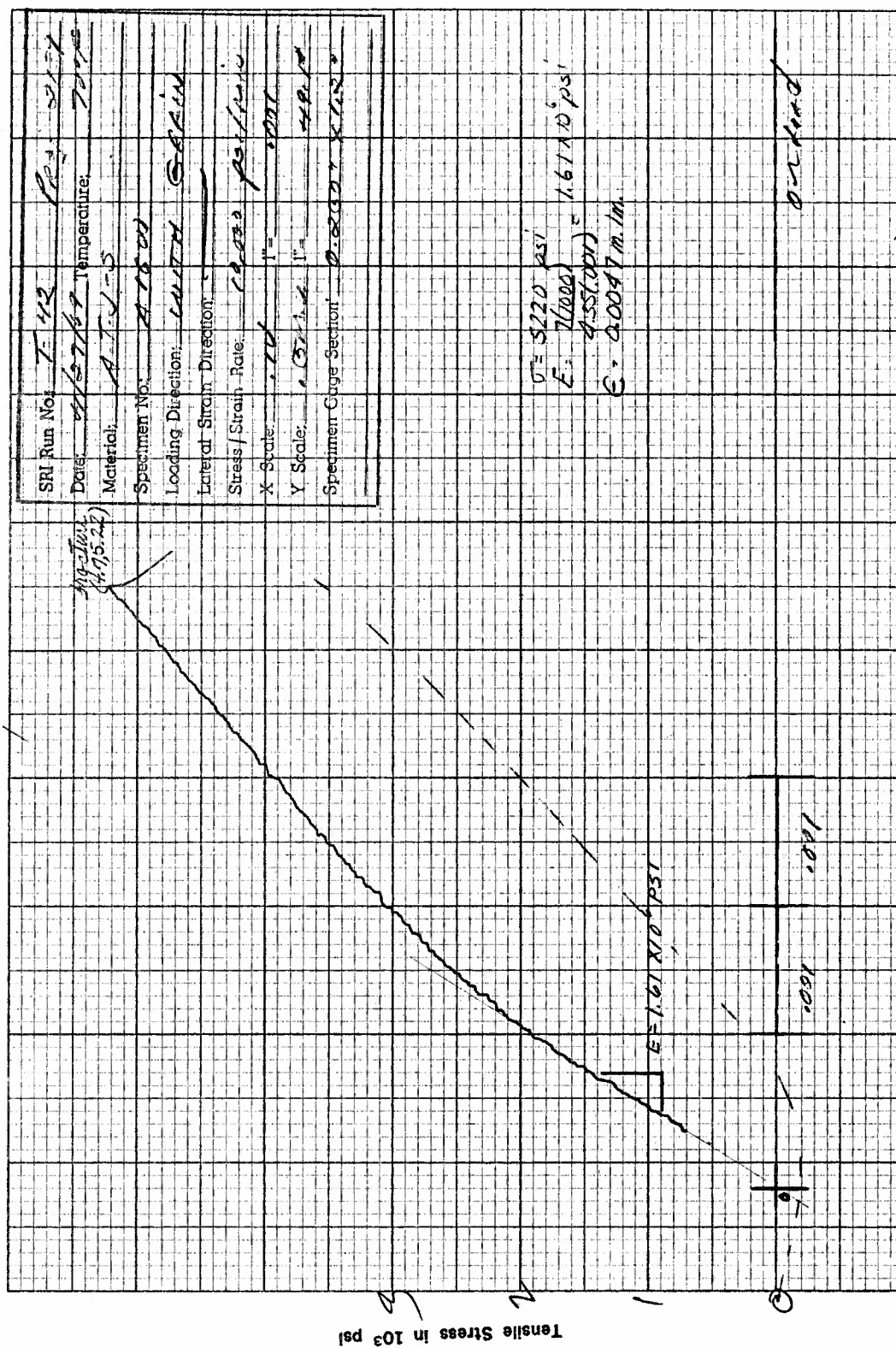


Figure I12. Tensile Stress versus Axial Strain for Specimen A16W of ATJ-S Graphite at 70°F

SRI Run No.	7-46	App: 2039
Date:	4/27/68	Temperature: 70°F
Material:	A.T.J-S	
Specimen No:	A17W	
Loading Direction:	WITH GRAIN	
Lateral Strain Direction:		
Stress/Strain Rate:	20,000 PSI/MIN	
X Scale:	1" = 1001	
Y Scale:	1" = 49,147	
Specimen Gage Section:	0.252" x 0.125"	

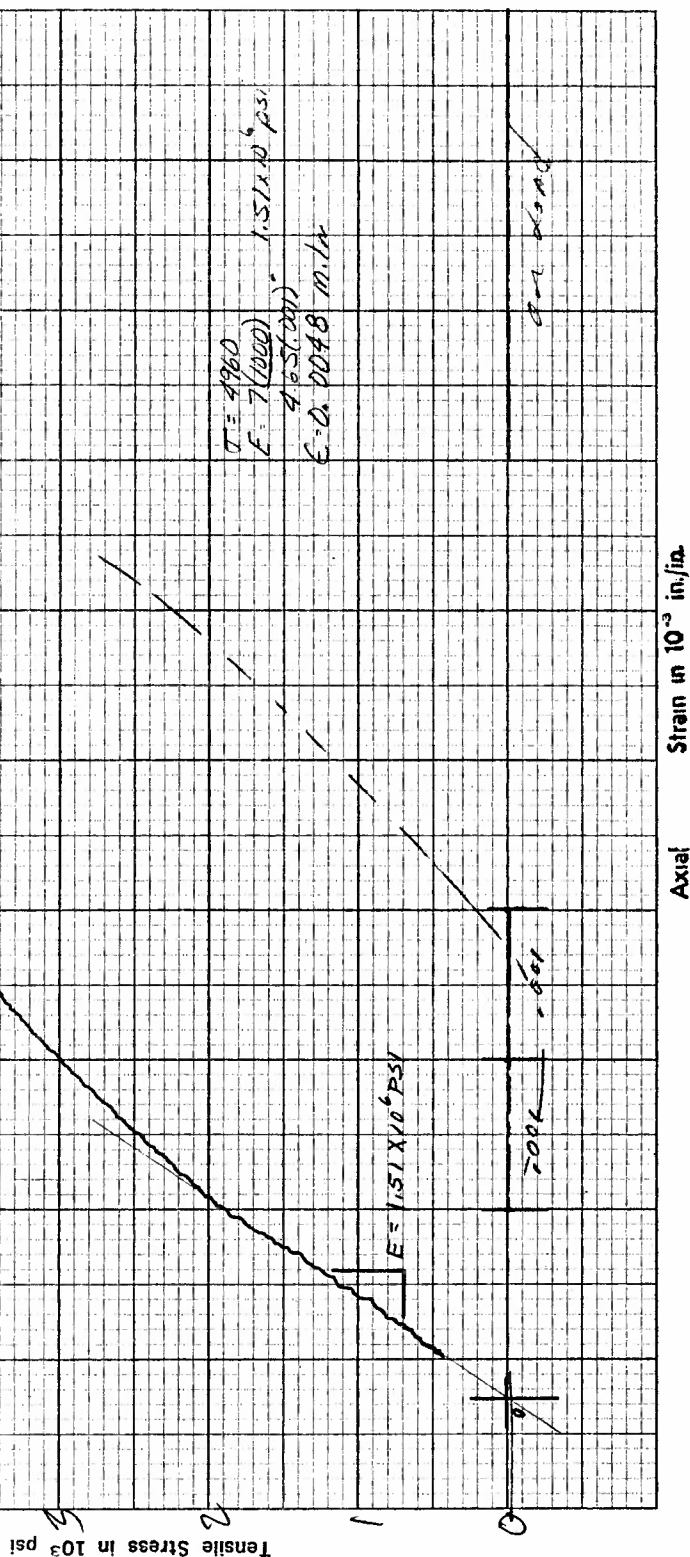


Figure I13, Tensile Stress versus Axial Strain for Specimen A17W of ATJ-S Graphite at 70°F



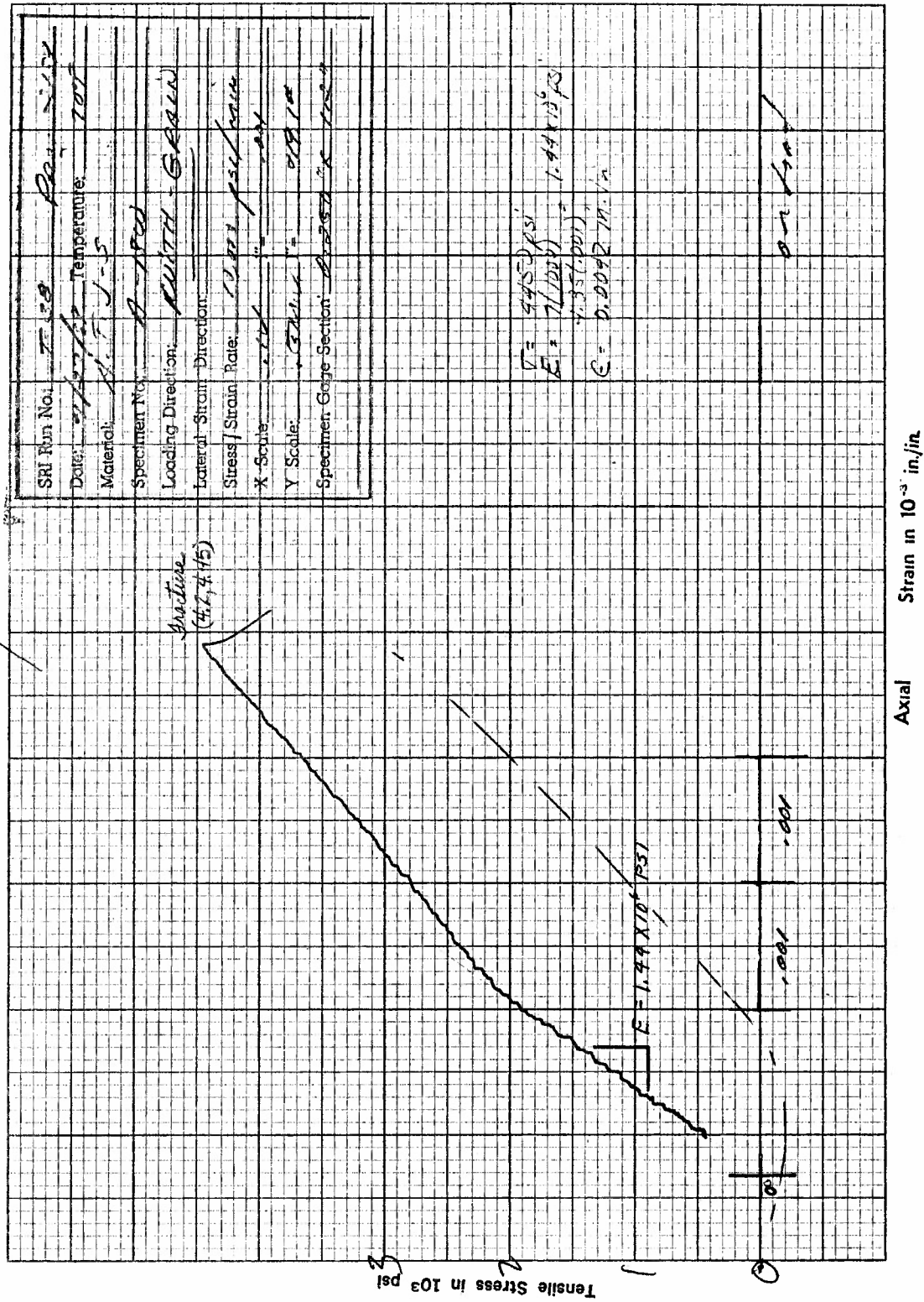


Figure 114. Tensile Stress versus Axial Strain for Specimen A18W of ATJ-S Graphite at 70°F

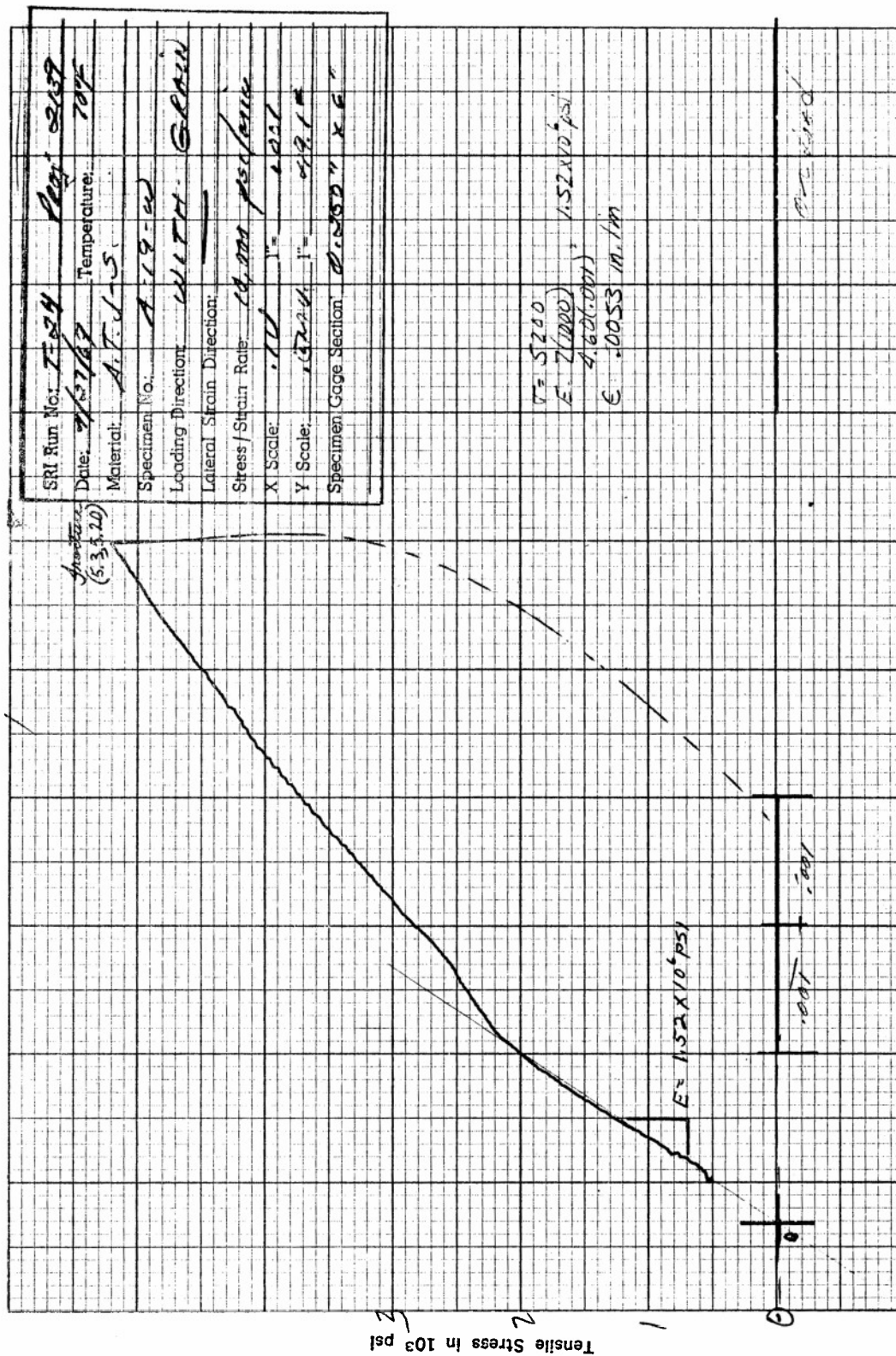


Figure 115. Tensile Stress versus Axial Strain for Specimen A19W of ATJ-S Graphite at 70°F

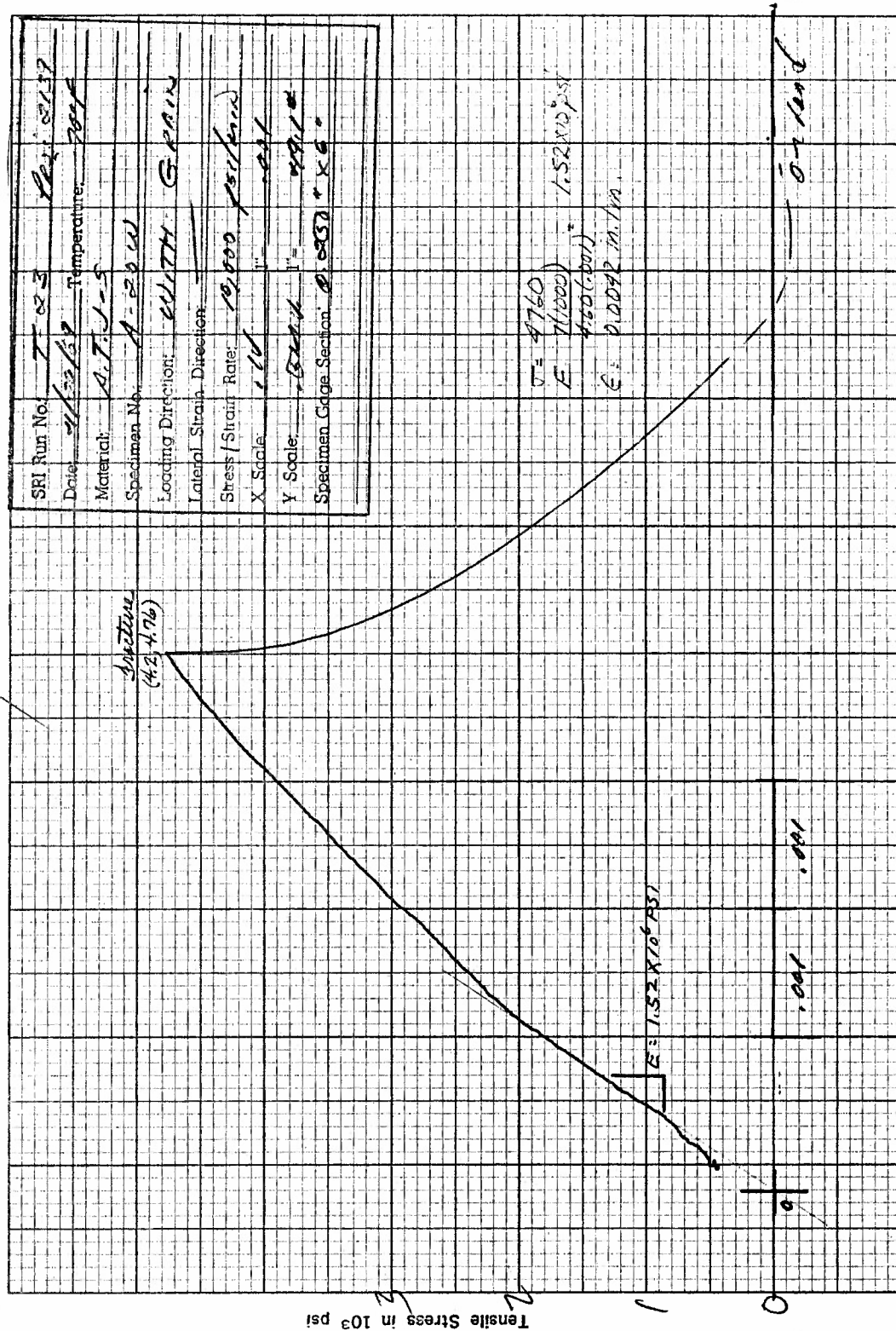


Figure I16. Tensile Stress versus Axial Strain for Specimen A20W of ATJ-S Graphite at 70°F



SRI Run No.	T-24	Proj.	2139
Date:	11/27/63	Temperature:	70°F
Material:	A.T.V.-5		
Specimen No.:	A-2144		
Loading Direction:	WITH GRAIN		
Lateral Strain Direction:			
Stress / Strain Rate:	12,000 psi/min		
X Scale:	1" = 100		
Y Scale:	1.34161" = 100		
Specimen Gage Section:	0.250" x 0.125"		

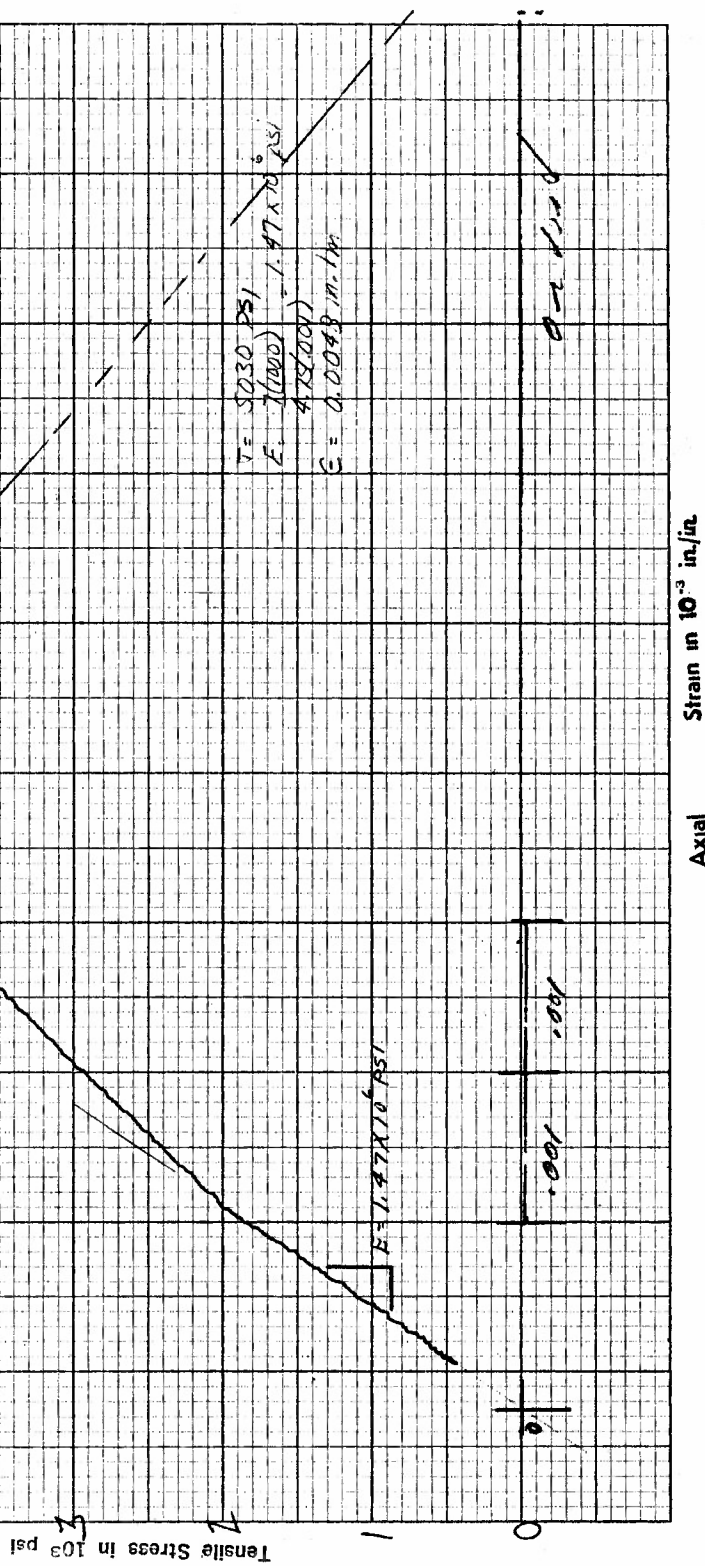
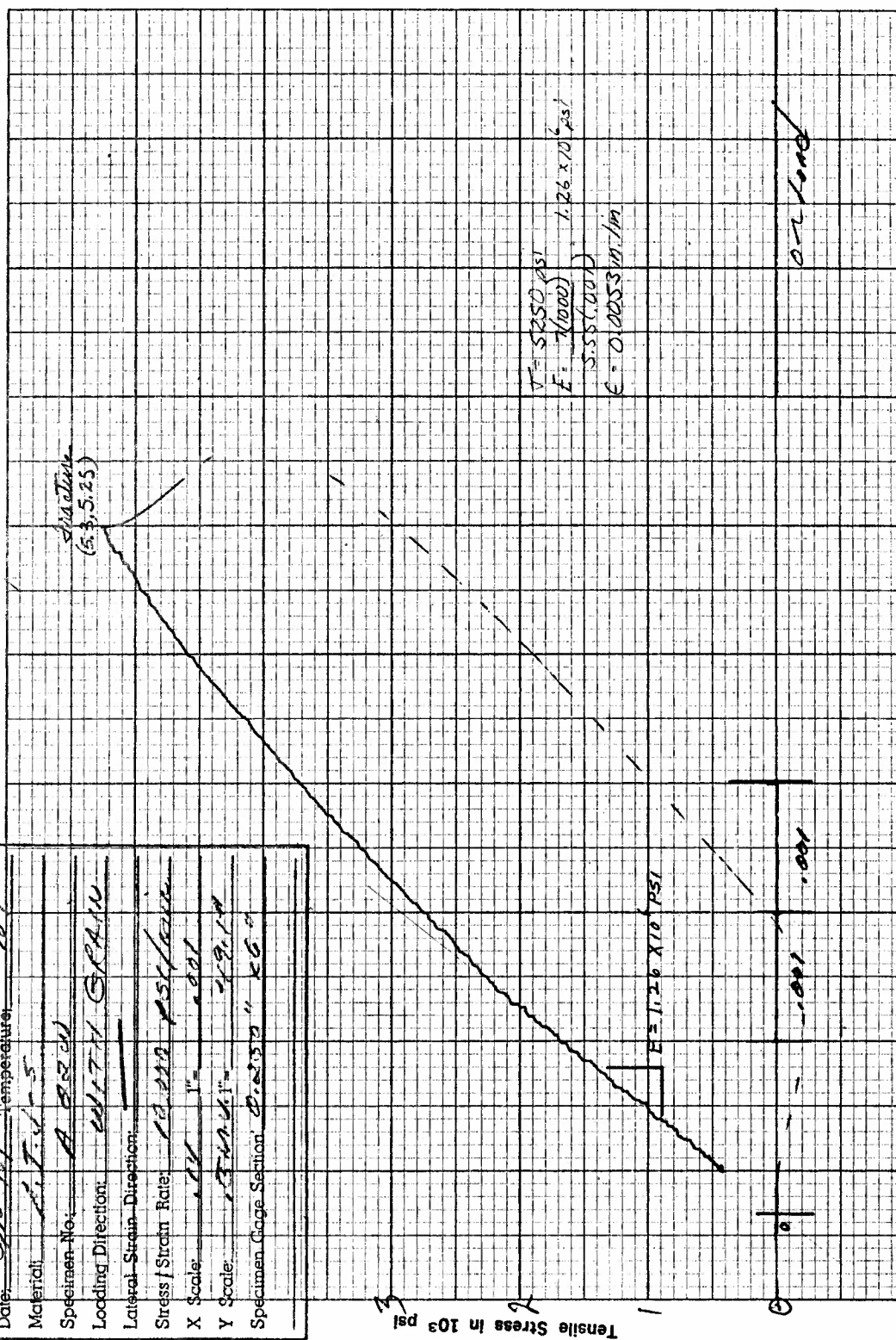


Figure I17. Tensile Stress versus Axial Strain for Specimen A21W of ATJ-S Graphite at 70°F

SRI Run No:	T-36	Proj.	3039
Date:	8-16-69	Temperature:	70°F
Material:	A.T. 6-5		
Specimen No:	A 8820		
Loading Direction:	WITH GRAIN		
Lateral Strain Direction:			
Stress / Strain Rate:	10,000 PSI/min		
X Scale:	1" = 1001		
Y Scale:	13,000 PSI = 1001		
Specimen Gage Section:	0.250" x 0.5"		



Axial Strain in  $10^{-3}$  in./in.

Figure I18. Tensile Stress versus Axial Strain for Specimen A22W of ATJ-S Graphite at 70°F



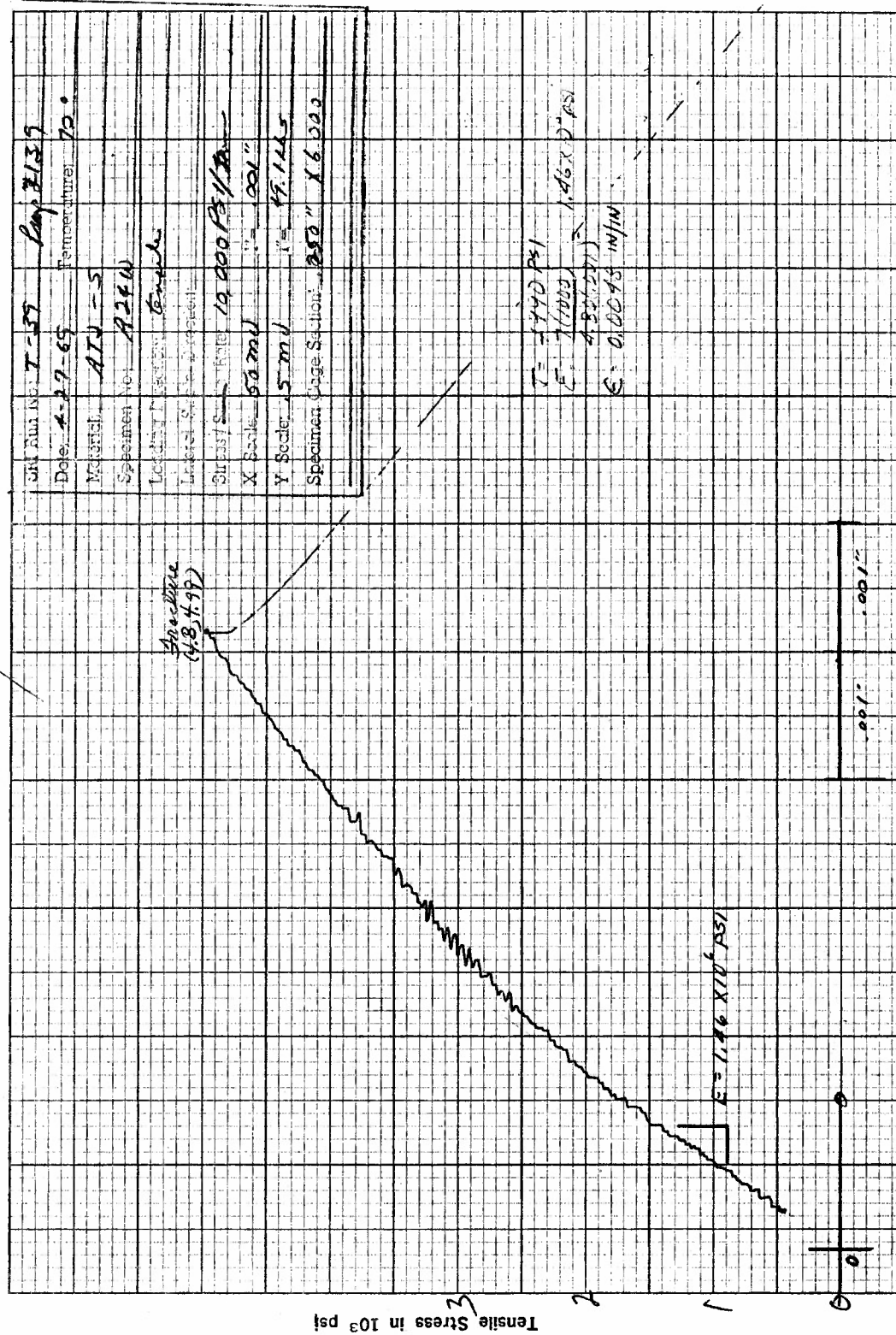


Figure I20. Tensile Stress versus Axial Strain for Specimen A24W of ATJ-S Graphite at 70°F

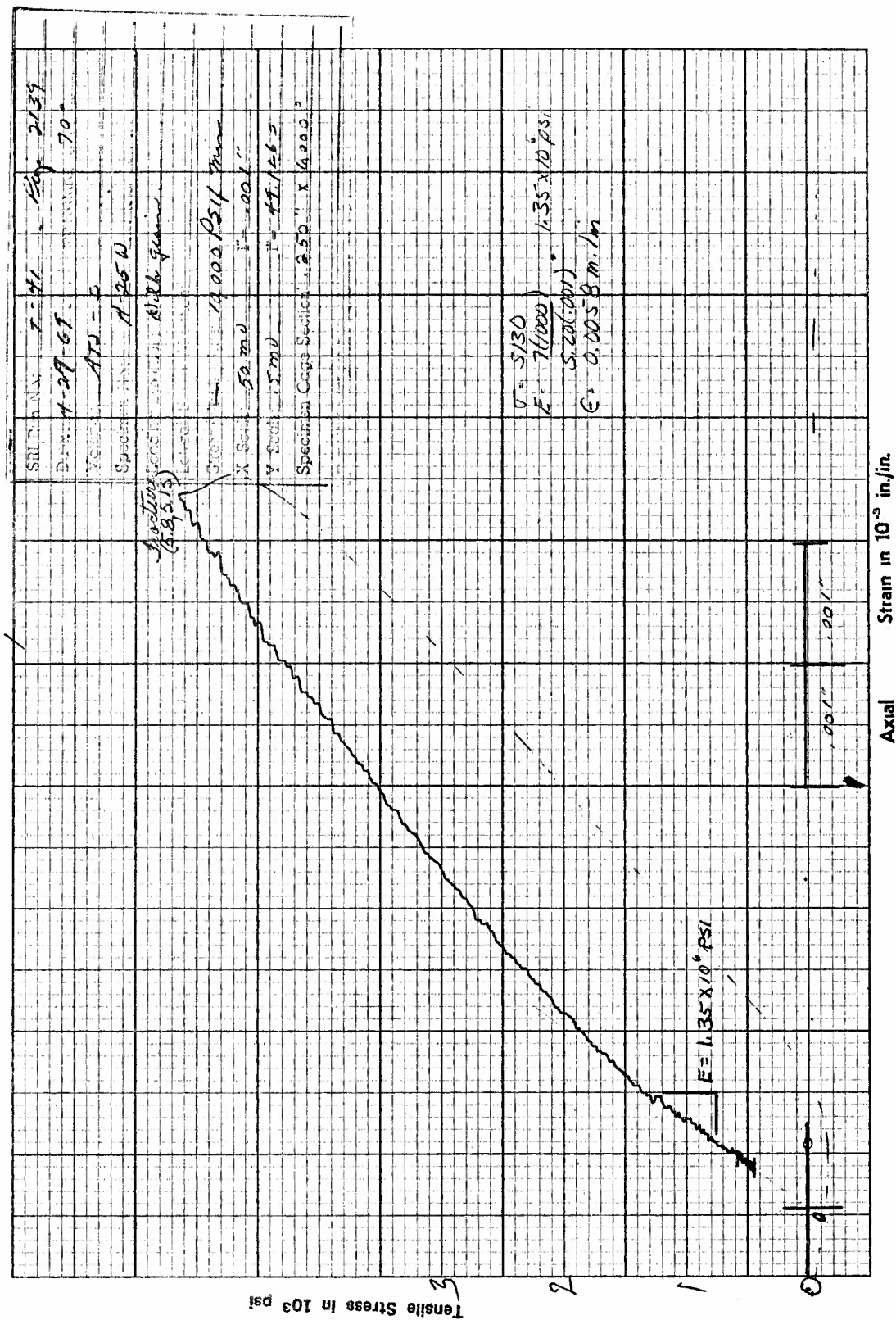


Figure I21. Tensile Stress versus Axial Strain for Specimen A25W of ATJ-S Graphite at 70°F



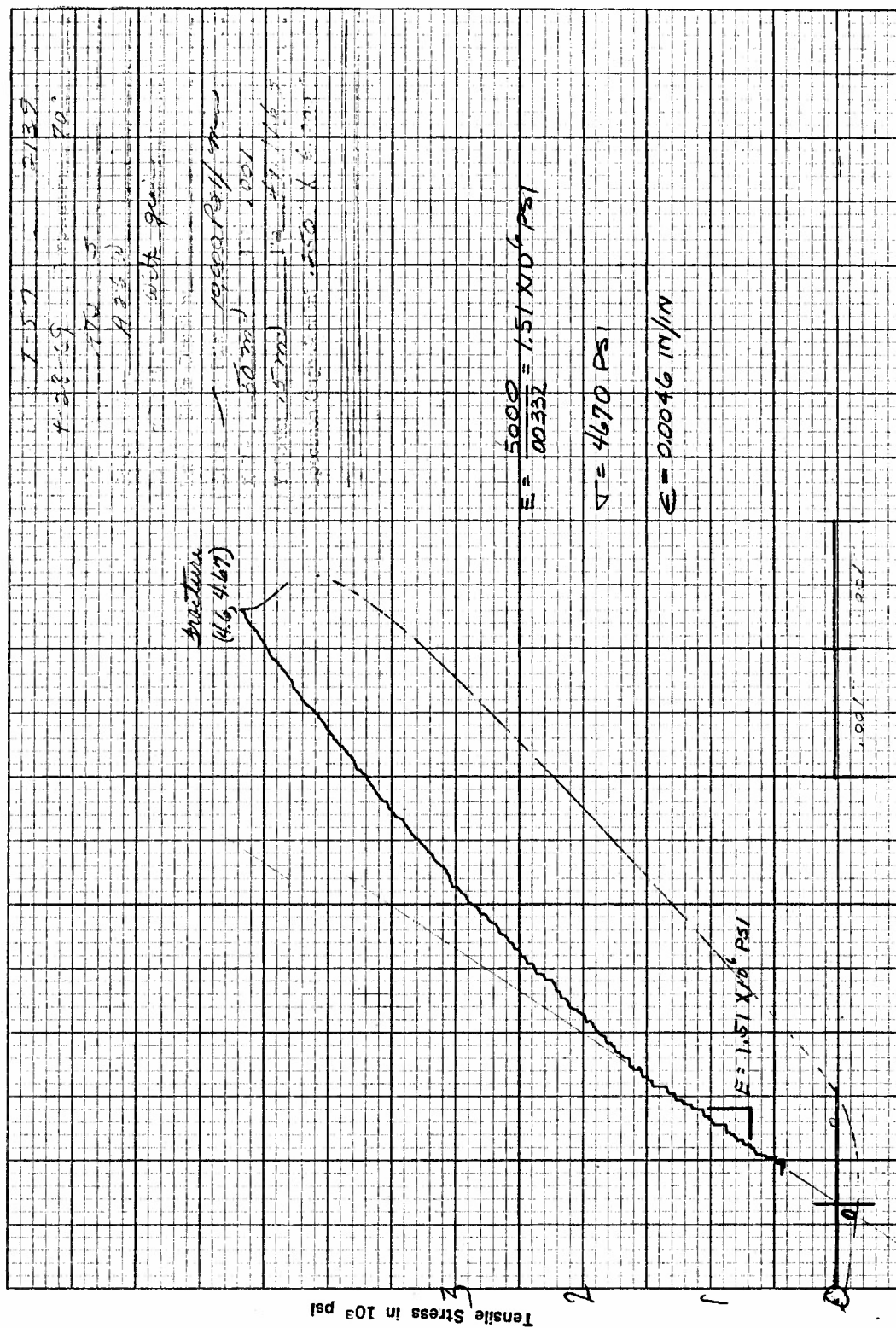


Figure 122. Tensile Stress versus Axial Strain for Specimen A26W of ATJ-S Graphite at 70°F

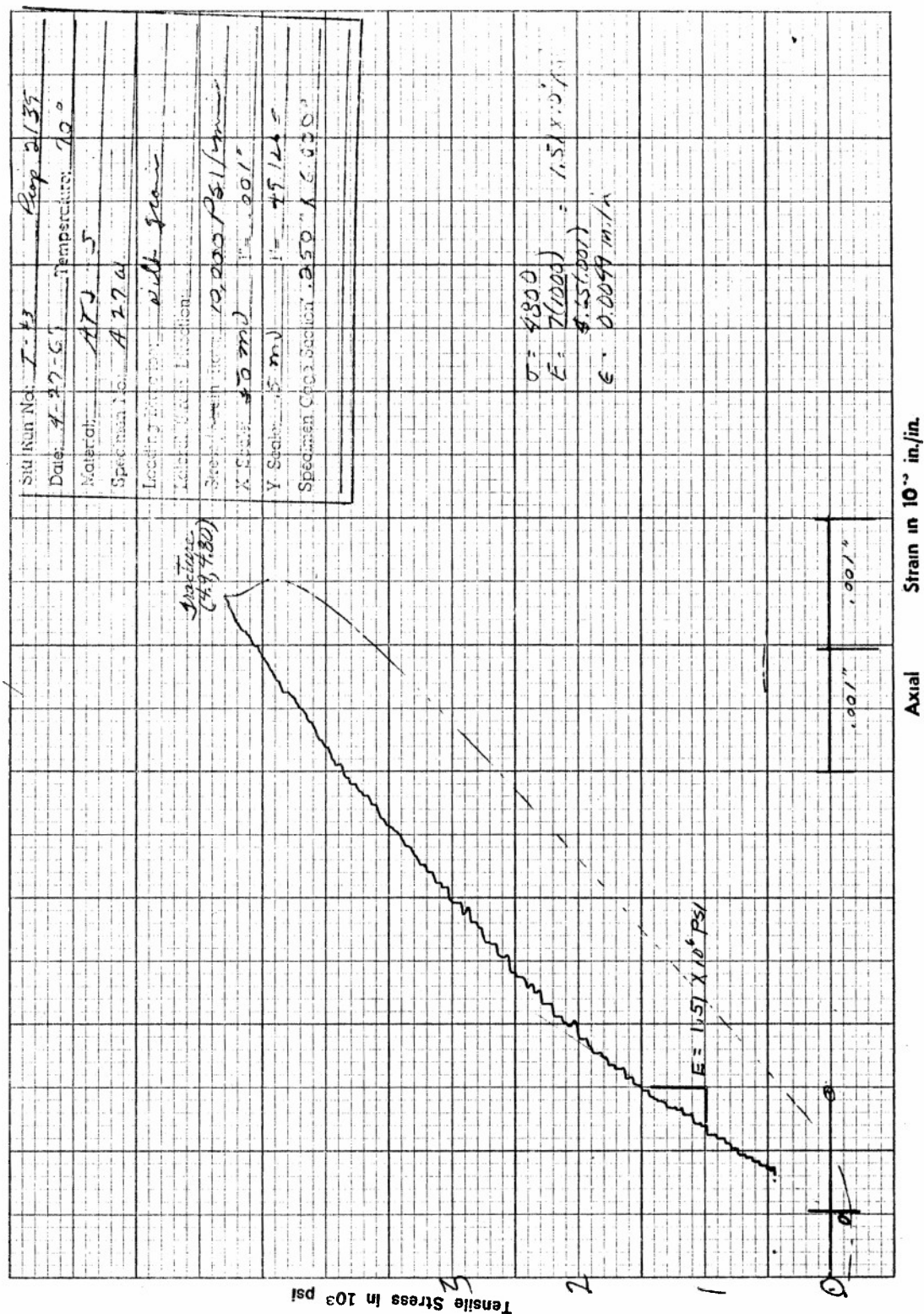


Figure I23. Tensile Stress versus Axial Strain for Specimen A27W of ATJ-S Graphite at 70°F

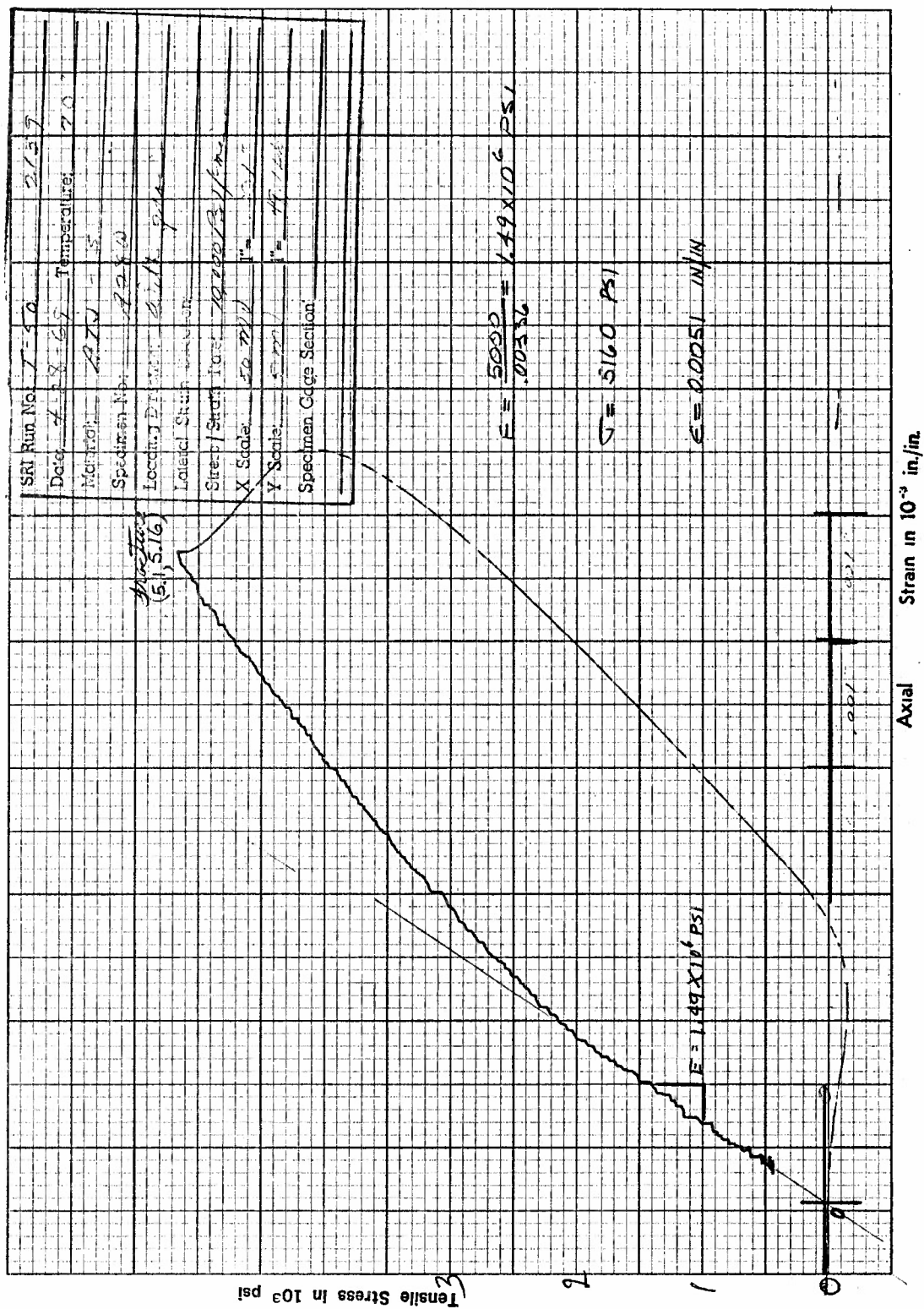


Figure I24. Tensile Stress versus Axial Strain for Specimen A28W of ATJ-S Graphite at 70°F



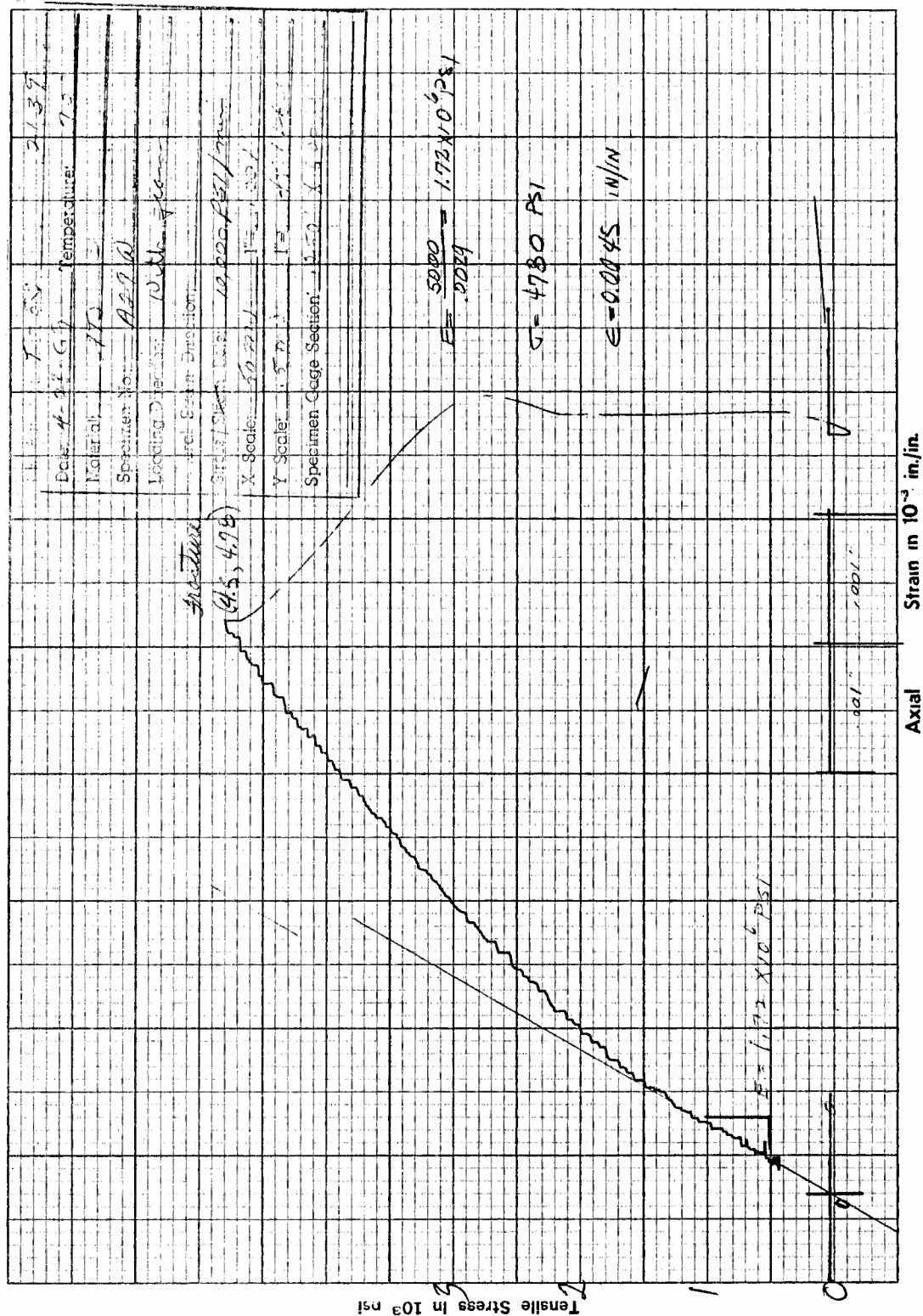


Figure I25. Tensile Stress versus Axial Strain for Specimen A29W of ATJ-S Graphite at 70°F

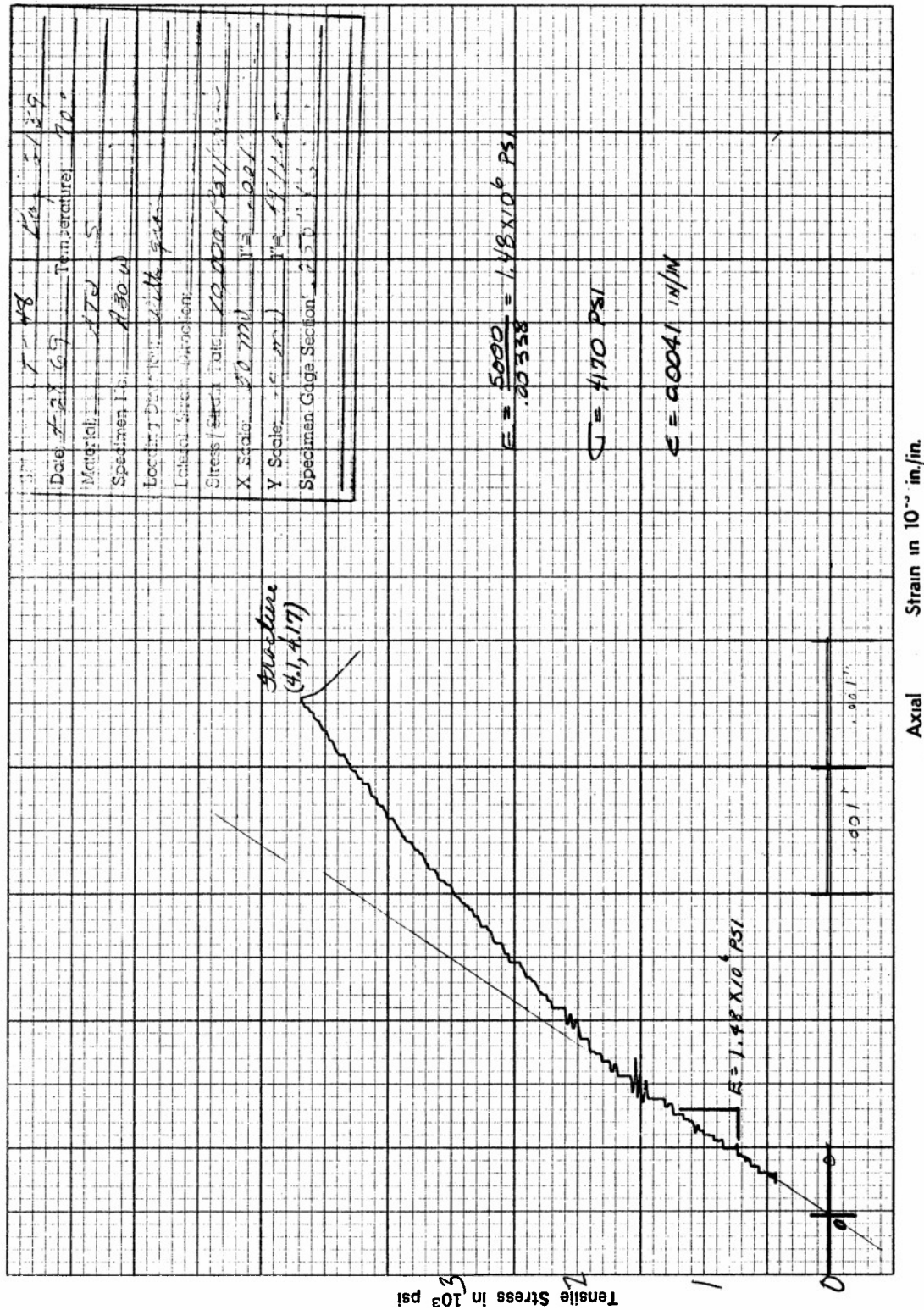
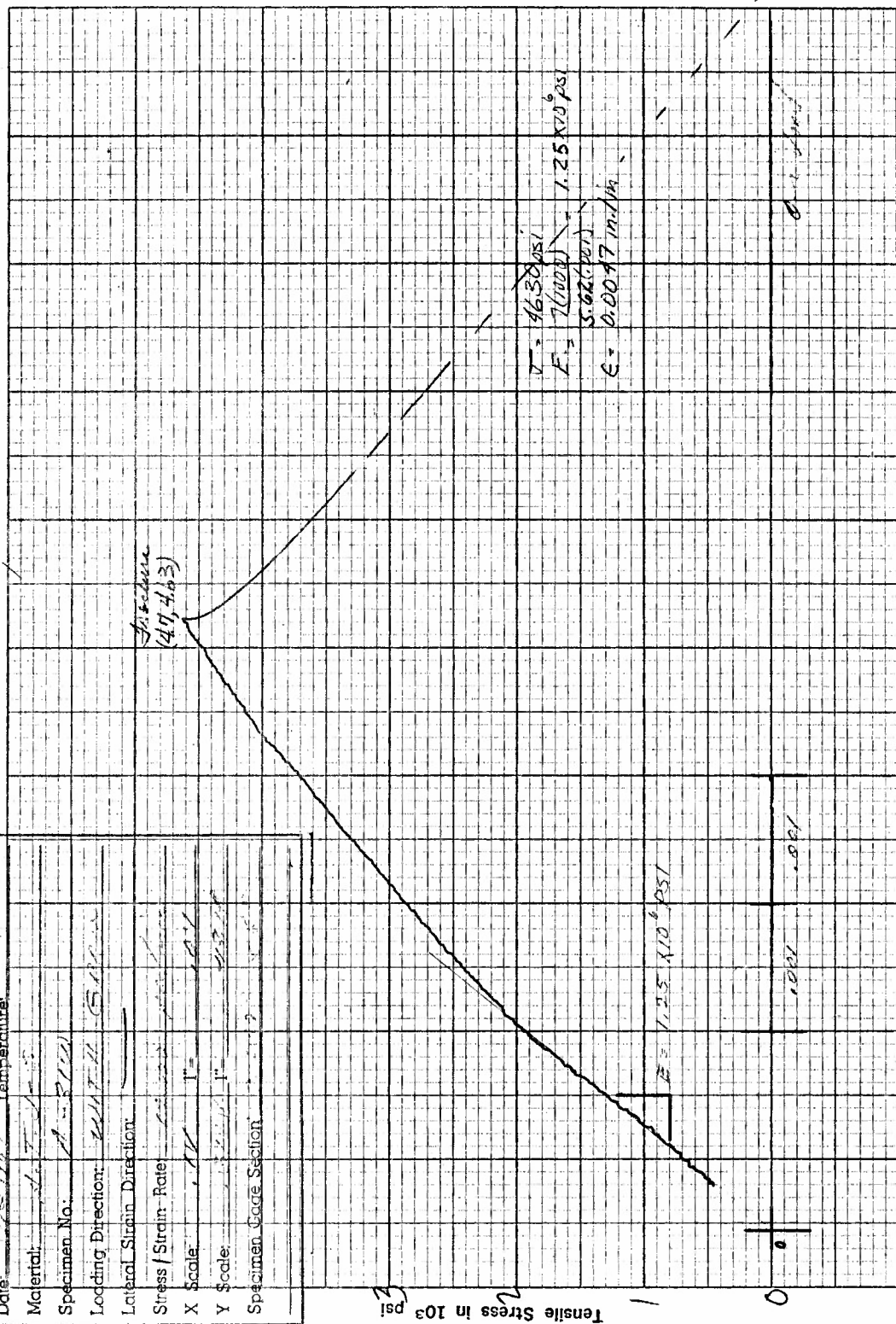


Figure I26. Tensile Stress versus Axial Strain for Specimen A30W of ATJ-S Graphite at 70°F

SRI Run No: T-35 6-10-67

Date: 6-10-67 Temperature: 70°F

Material:	<u>ATJ-S</u>
Specimen No:	<u>8111</u>
Loading Direction:	<u>5011</u>
Lateral Strain Direction:	<u>—</u>
Stress / Strain Rate:	<u>1000</u>
X Scale:	<u>100</u>
Y Scale:	<u>1000</u>
Specimen Code Section:	<u>—</u>



Axial Strain in  $10^{-3}$  in./in.

Figure I27. Tensile Stress versus Axial Strain for Specimen A31W of ATJ-S Graphite at 70°F

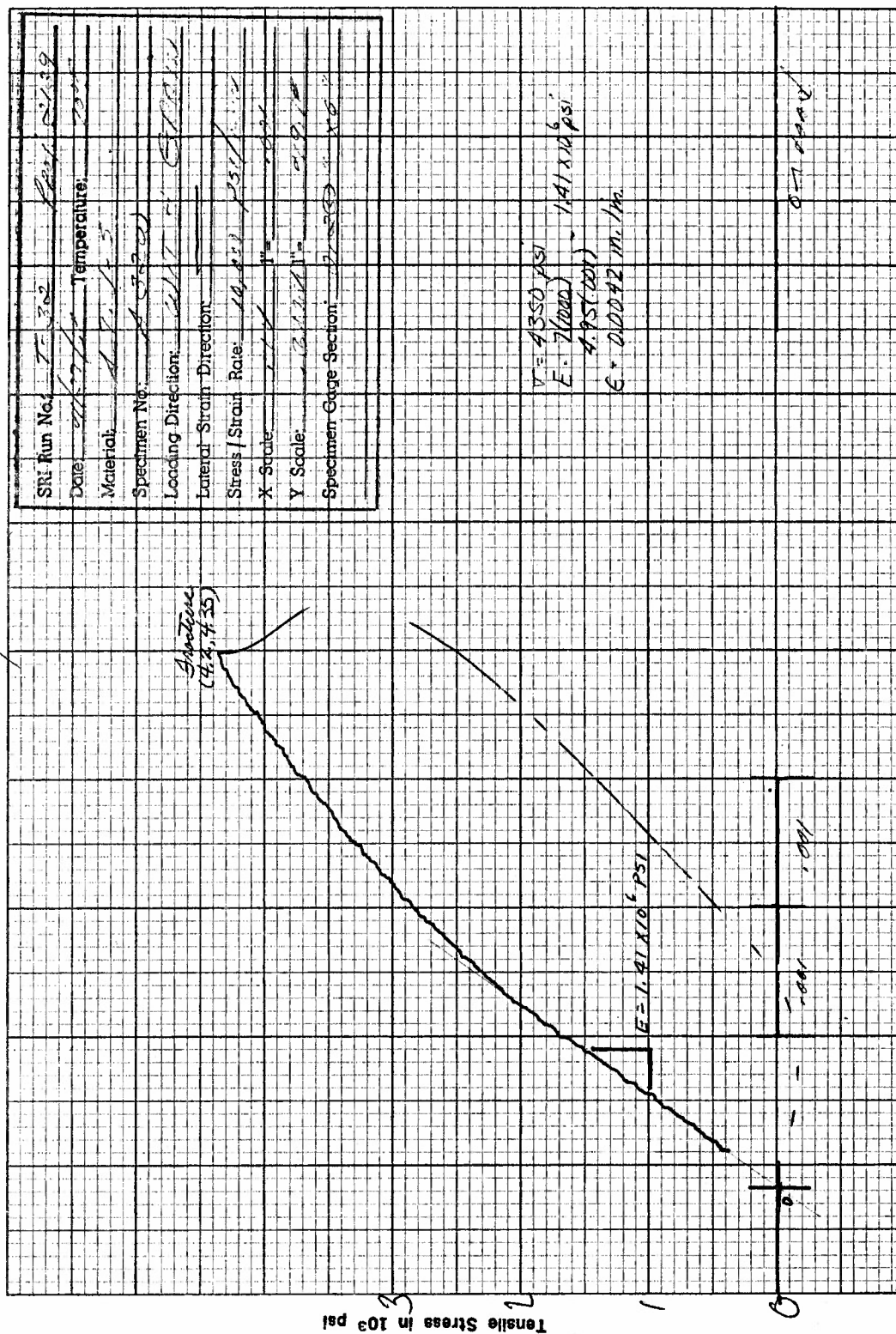


Figure 128. Tensile Stress versus Axial Strain for Specimen A32W of ATJ-S Graphite at 70°F



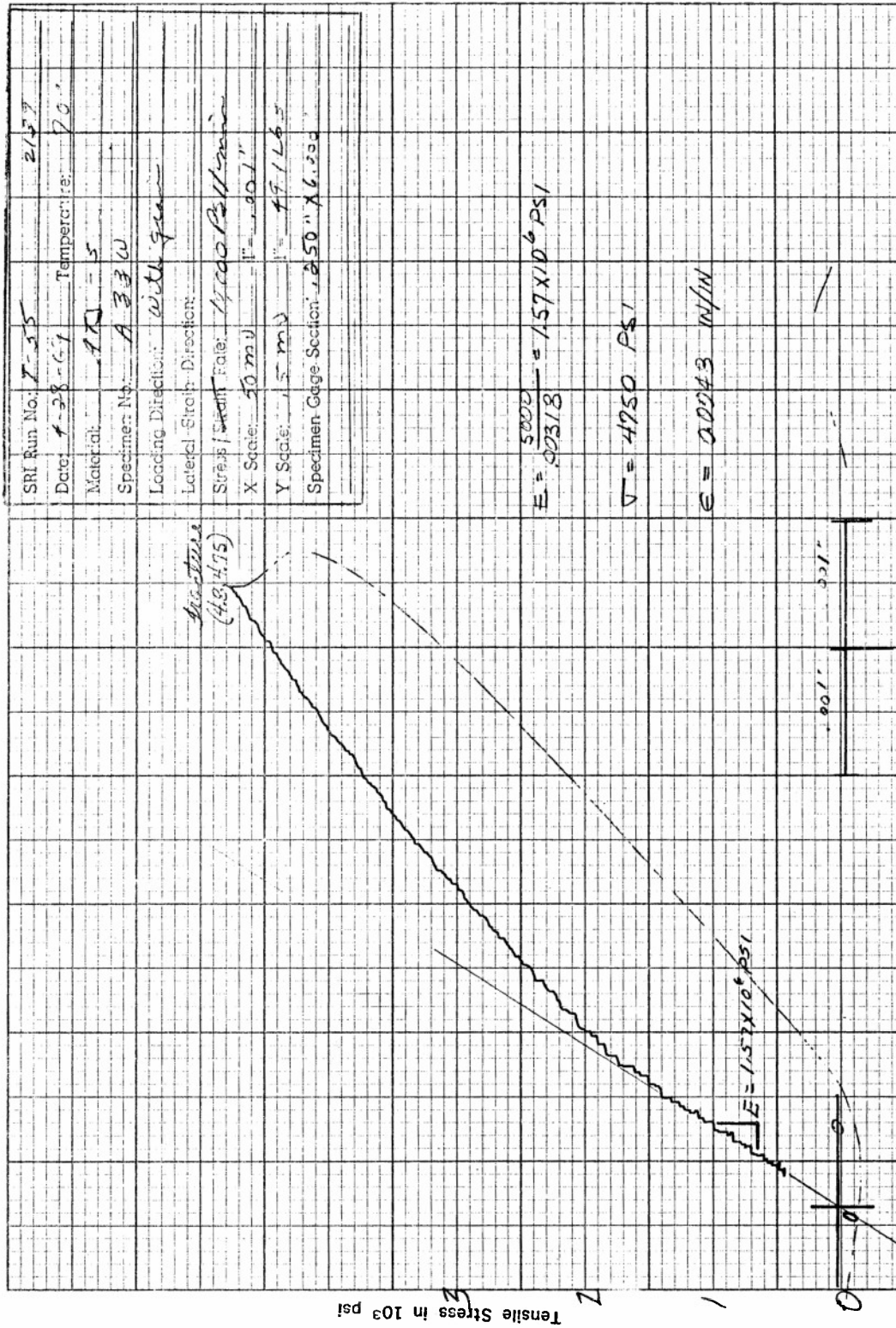


Figure I29. Tensile Stress versus Axial Strain for Specimen A33W of ATJ-S Graphite at 70°F

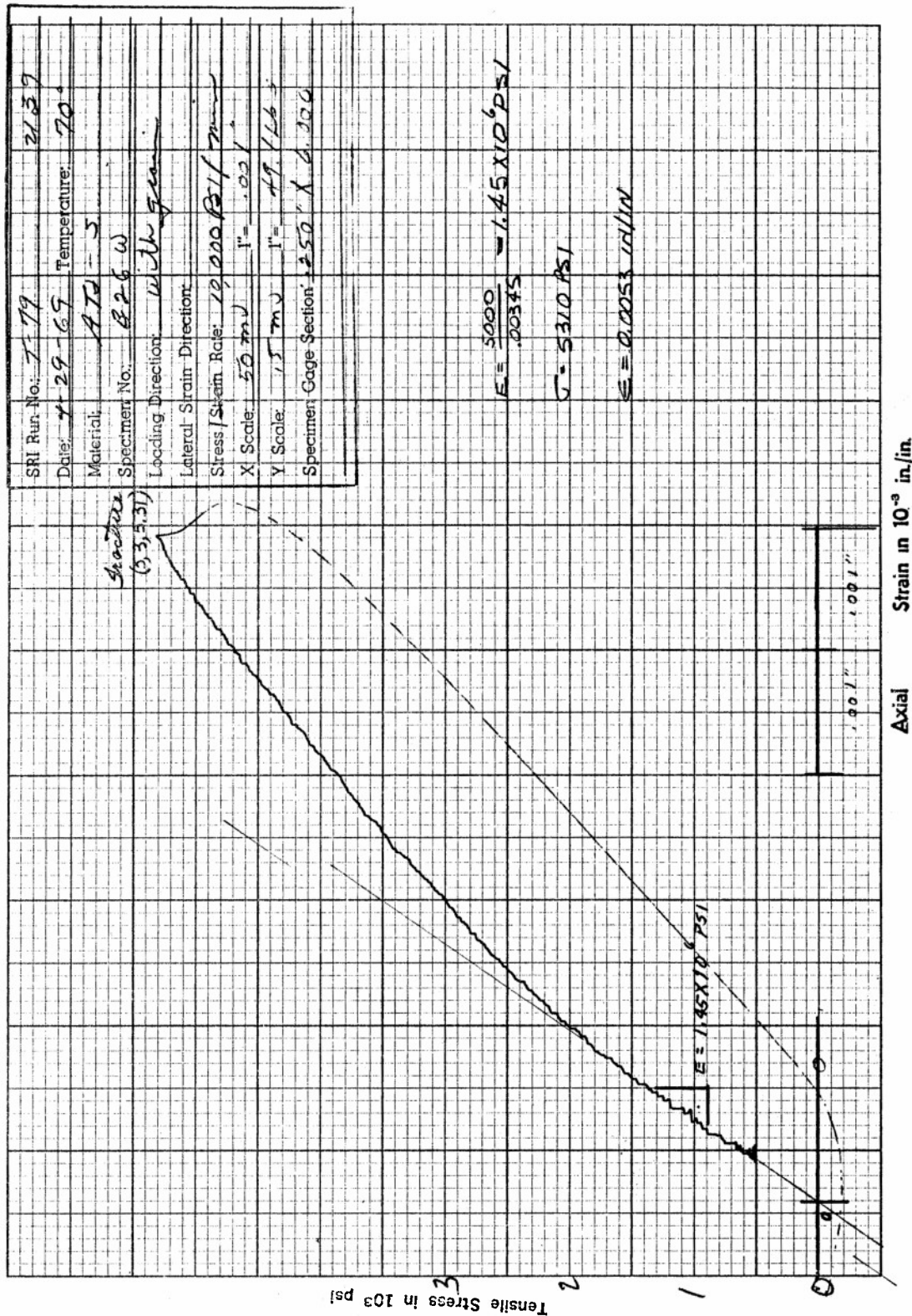


Figure I30. Tensile Stress versus Axial Strain for Specimen B26W of ATJ-S Graphite at 70°F

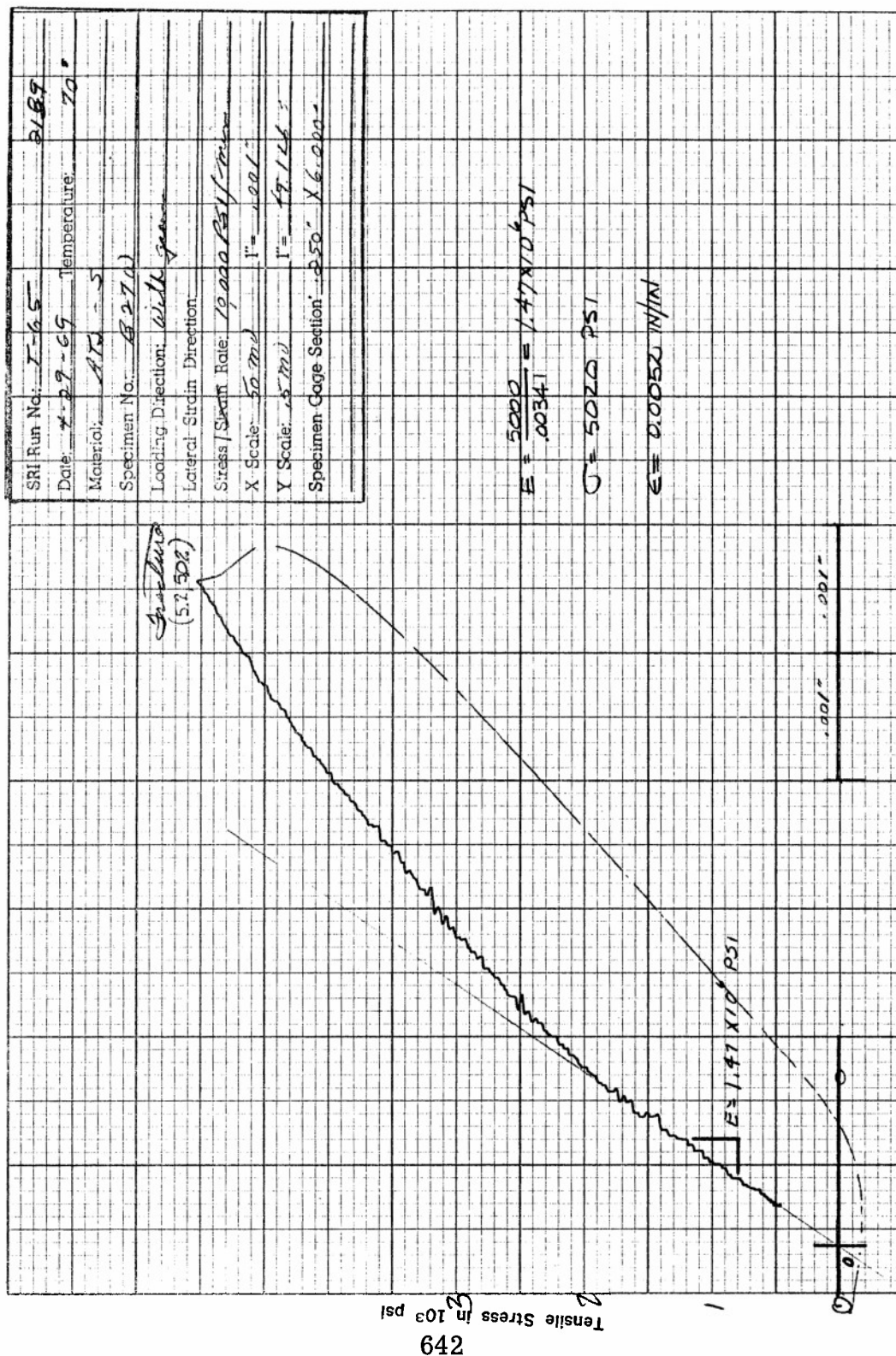


Figure I31. Tensile Stress versus Axial Strain for Specimen B27W of ATJ-S Graphite at 70°F

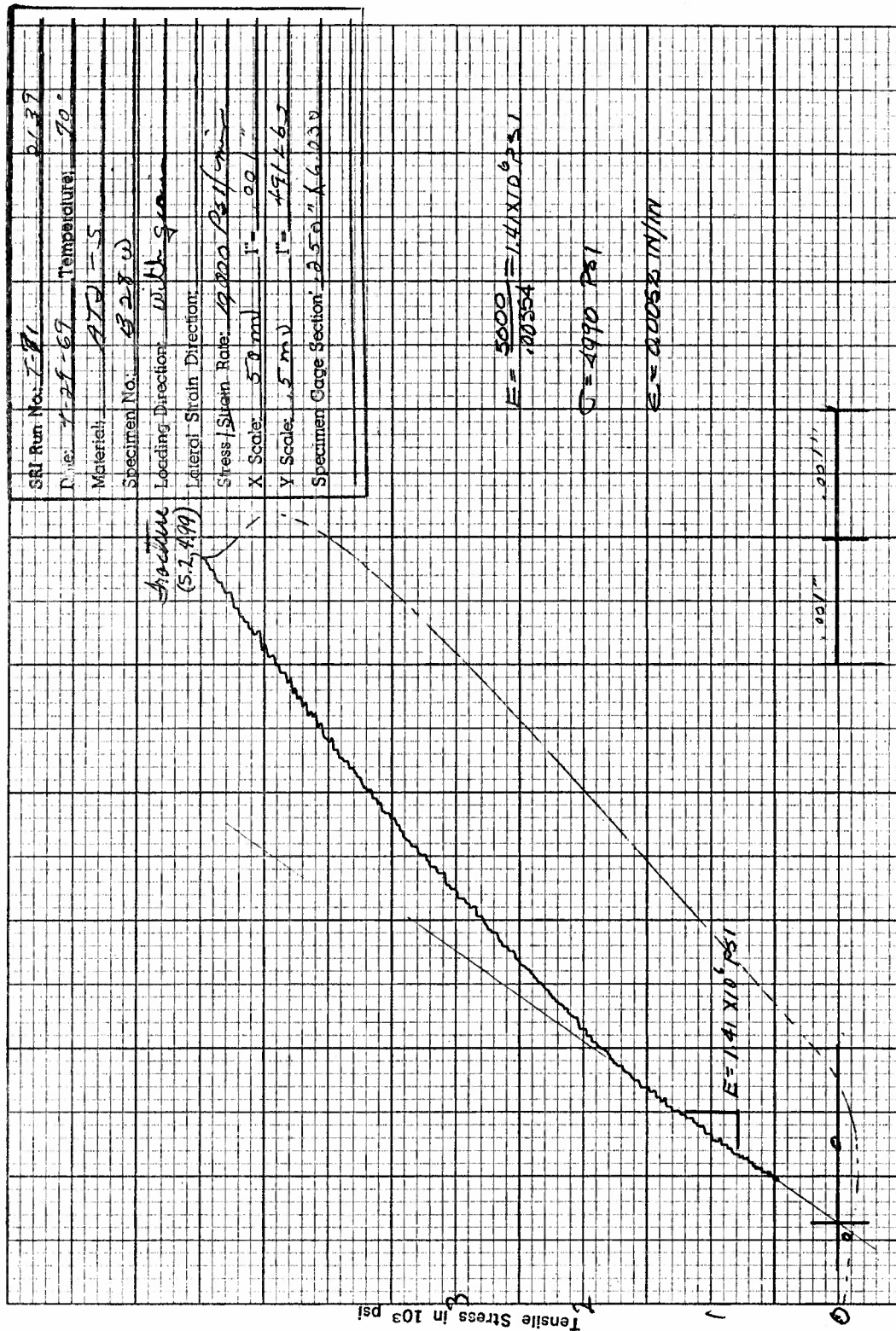


Figure I32. Tensile Stress versus Axial Strain for Specimen B28W of ATJ-S Graphite at 70°F





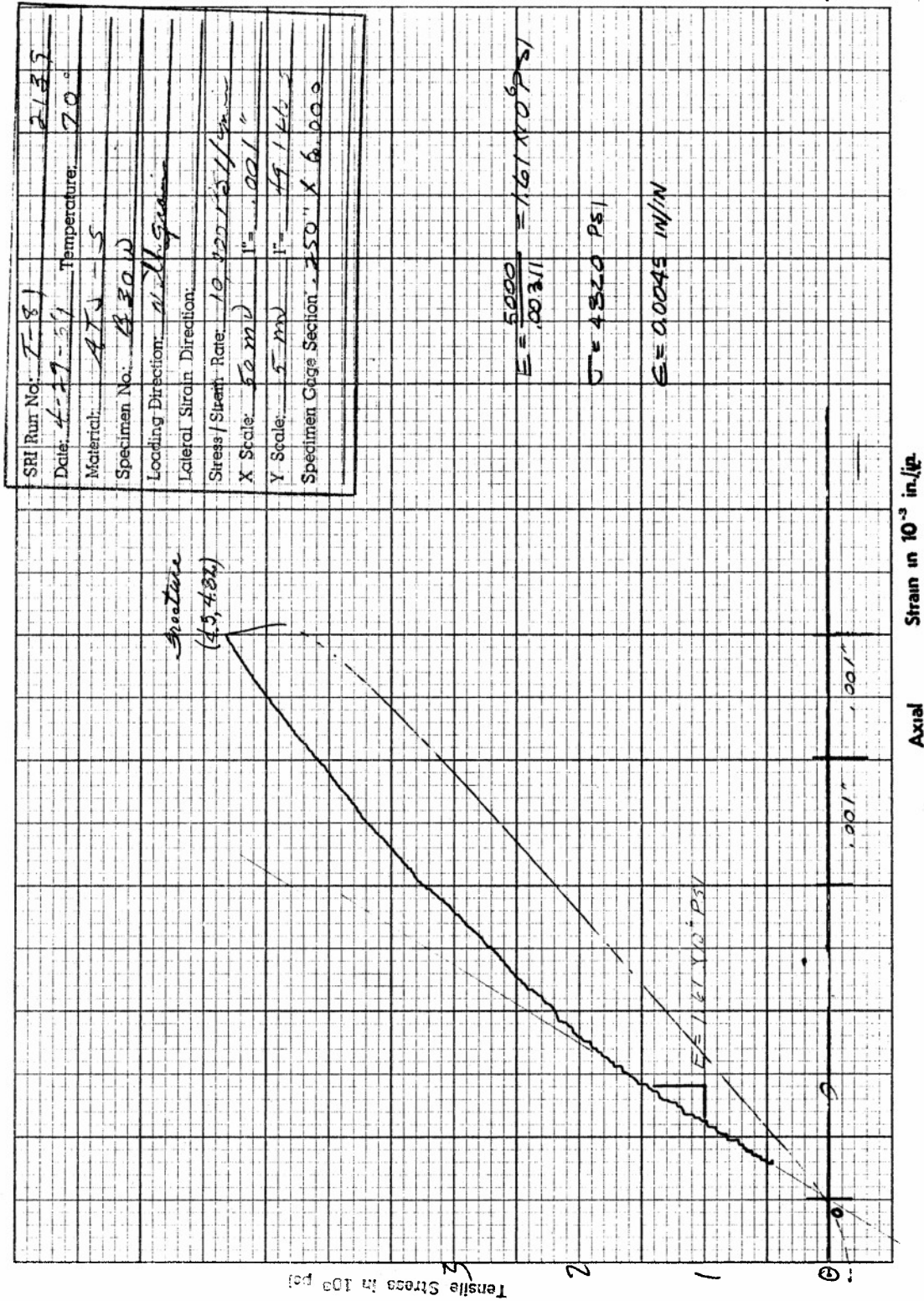


Figure I34. Tensile Stress versus Axial Strain for Specimen B30W of ATJ-S Graphite at 70°F

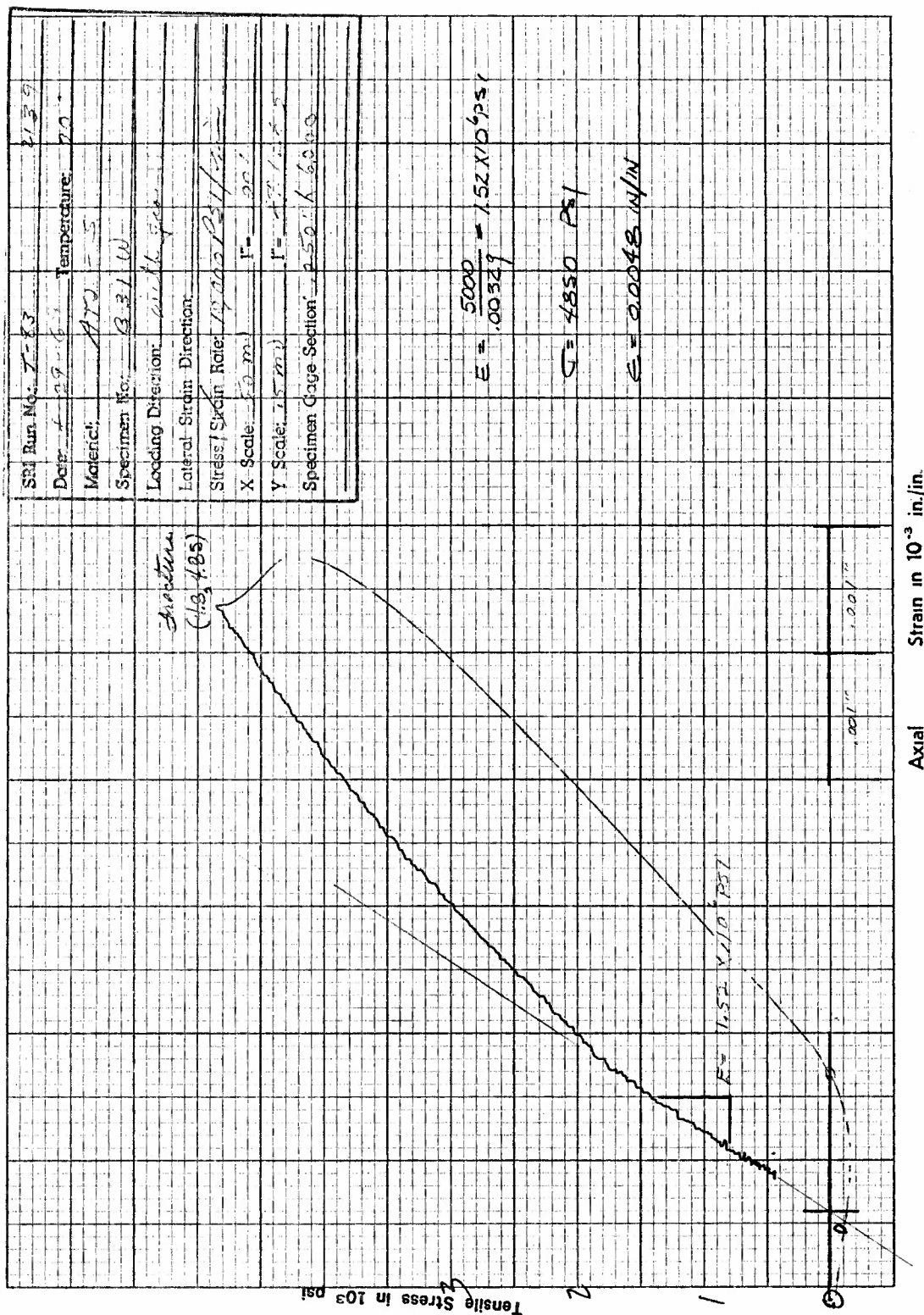
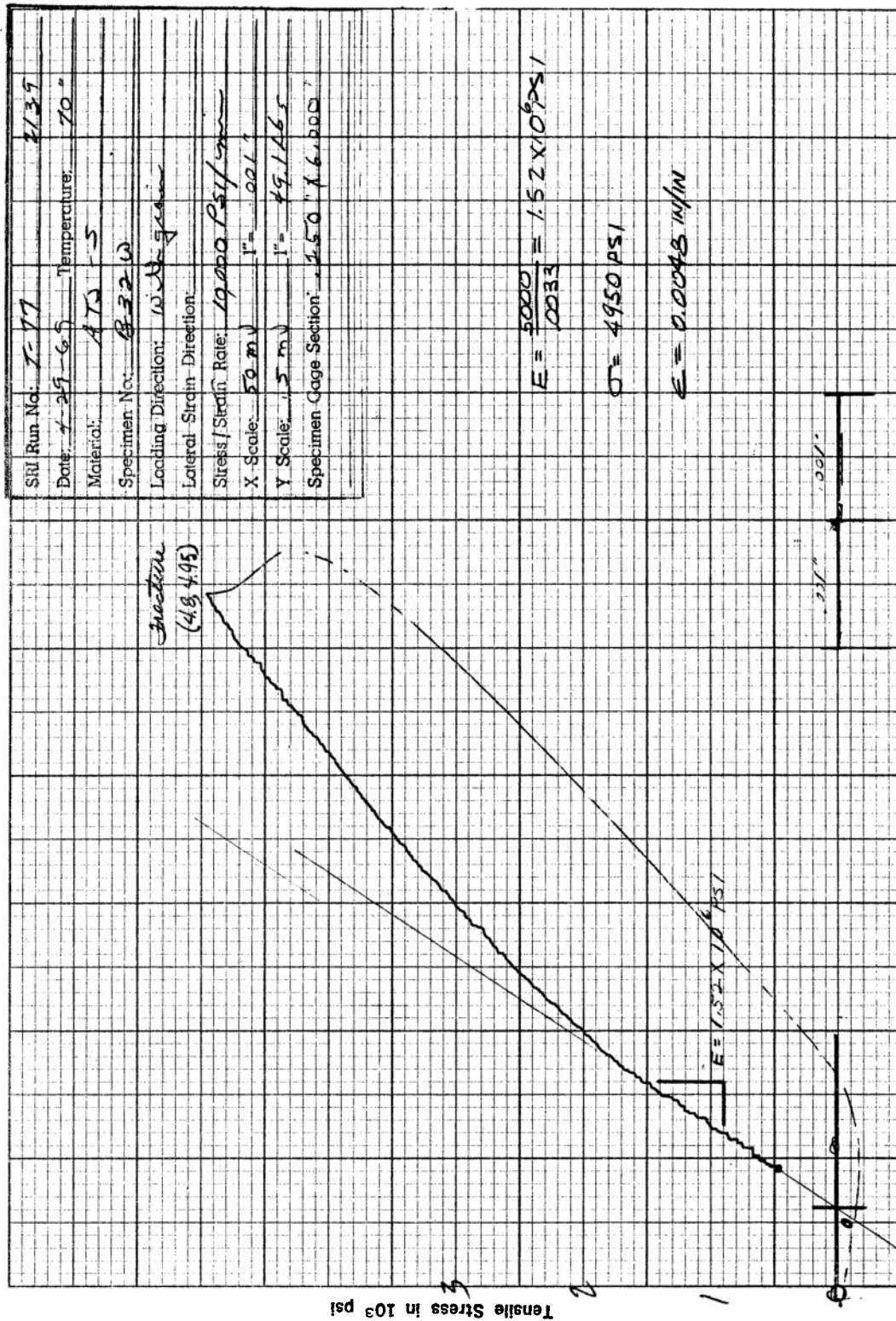


Figure I35. Tensile Stress versus Axial Strain for Specimen B31W of ATJ-S Graphite at 70°F



Axial Strain in  $10^{-3}$  in./in.

Figure I36. Tensile Stress versus Axial Strain for Specimen B32W of ATJ-S Graphite at 70°F



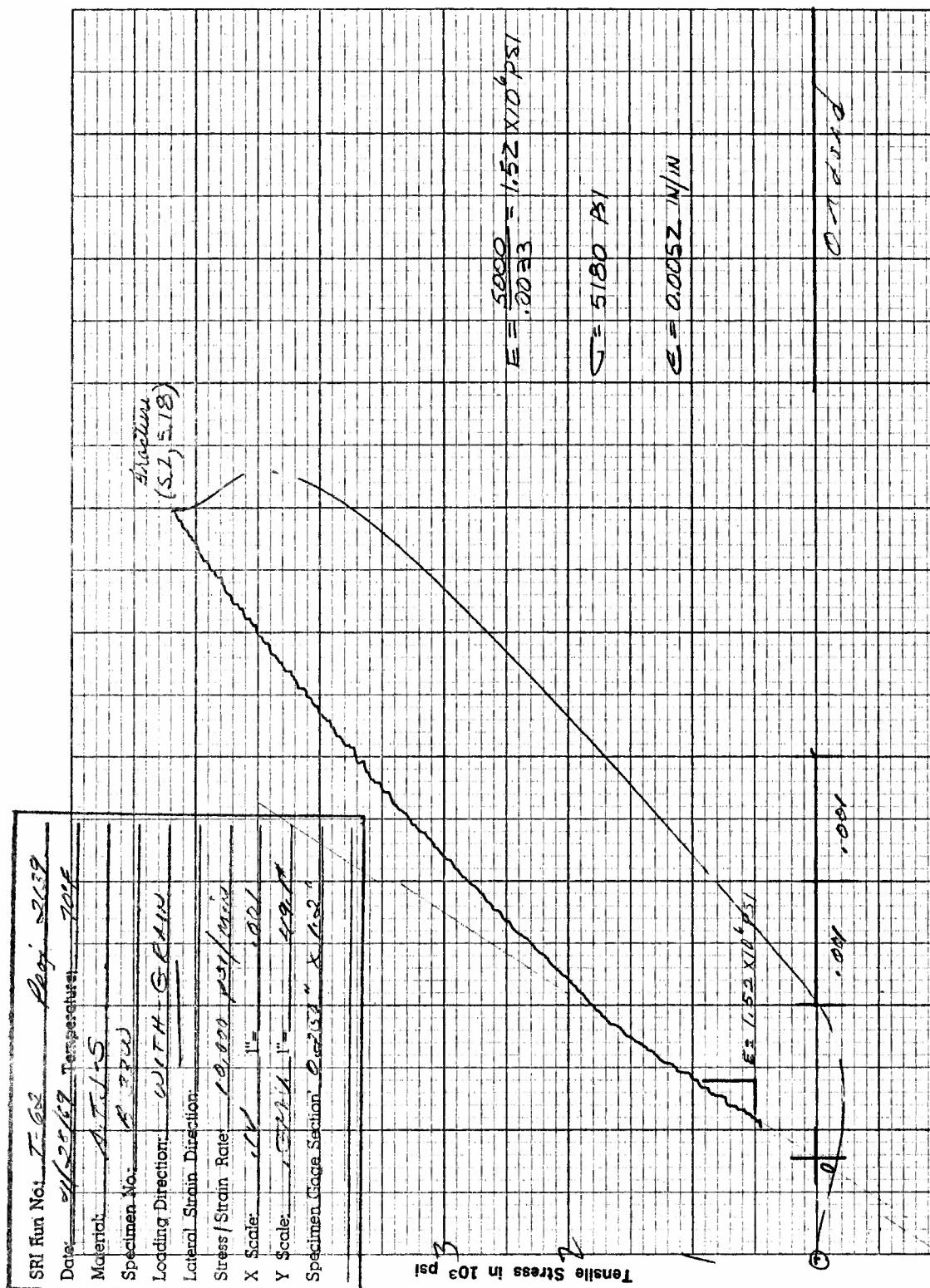


Figure I37. Tensile Stress versus Axial Strain for Specimen B33W of ATJ-S Graphite at 70°F

SRI Run No: 7-67 Specimen

Date: 4-22-67 Temperature: 70°F

Material: ATJ-S

Specimen No: 015-20

Loading Direction: WITH GRAIN

Lateral Strain Direction: PERPENDICULAR

Stress/Strain Rate: 1000 psi/min

X Scale: 1" = 2000

Y Scale: 1" = 4000

Specimen Gauge Section: 0.250 x 1.000

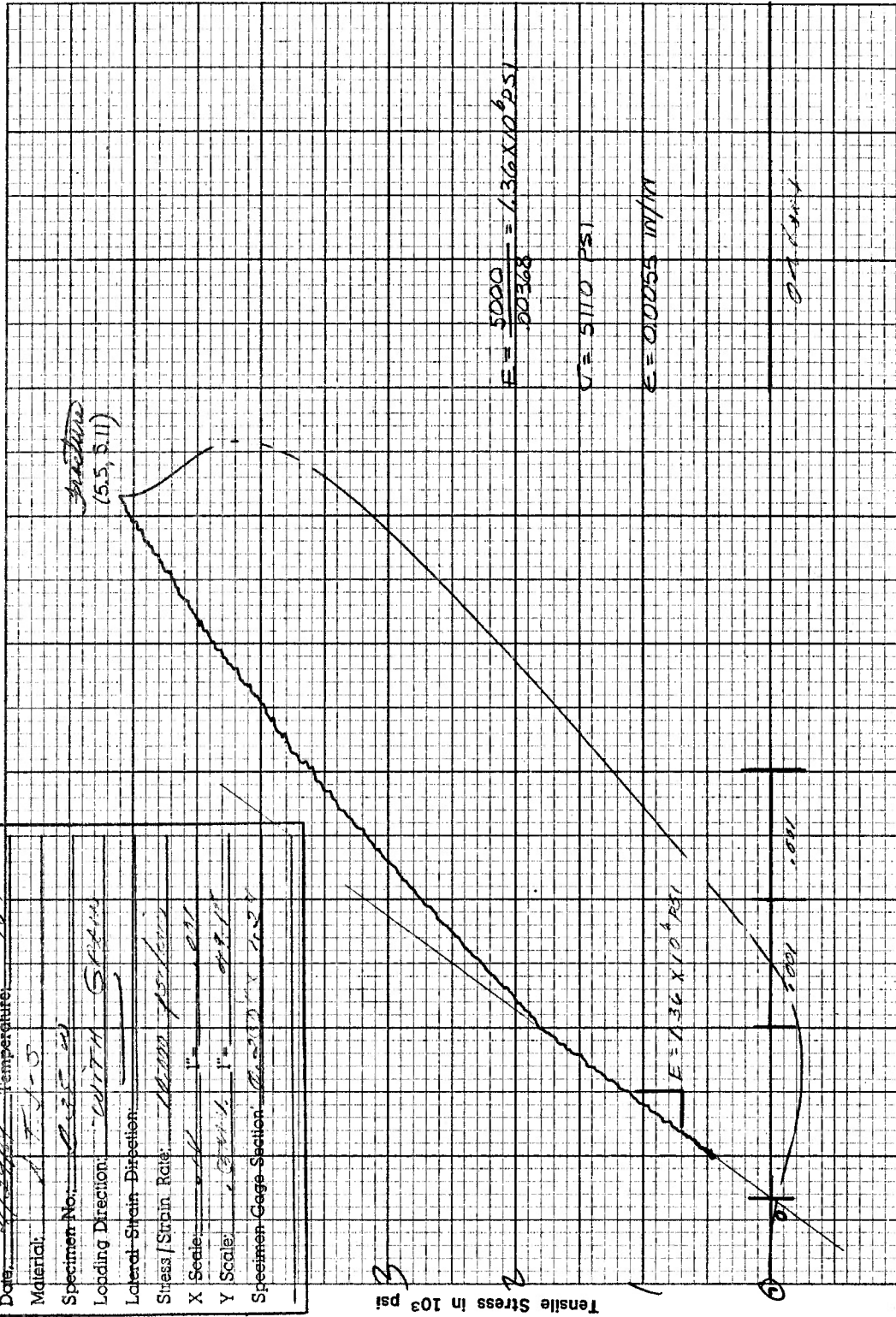


Figure I38. Tensile Stress versus Axial Strain for Specimen B35W of ATJ-S Graphite at 70°F

SRI Run No: T-70 Rev. 12/77

Date: 11/10/77 Temperature: 70°F

Material: ATJ-S

Specimen No.: 0-2337

Loading Direction: 22.5°

Lateral Strain Direction: 10.0°

Stress / Strain Rate: 10.0 / 1.0

X Scale: 1.0 1.001

Y Scale: 1.0 1.001

Specimen Gage Section: 0.2337

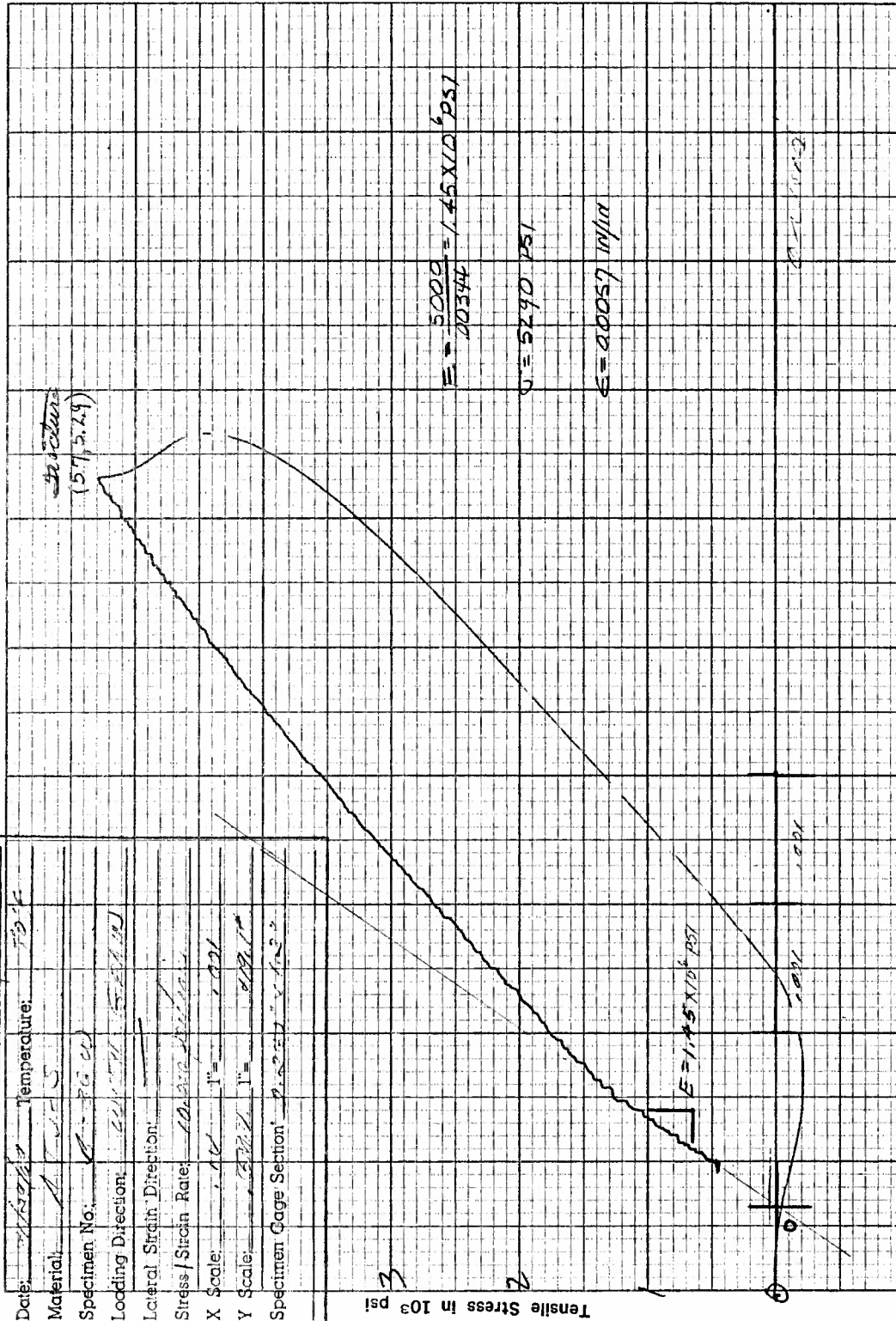


Figure I39. Tensile Stress versus Axial Strain for Specimen B36W of ATJ-S Graphite at 70°F

SRI Run No.: T-66		Proj: 2139	
Date:	4/22/61	Temperature:	70°F
Material:	A.T.-J-S		
Specimen No.:	A.3700		
Loading Direction:	WITH GRAIN		
Lateral Strain Direction:			
Stress/Strain Rate:	1000 psi/min		
X Scale:	1" = 100		
Y Scale:	1" = 1000		
Specimen Cage Section:	0.25" x 1.25"		

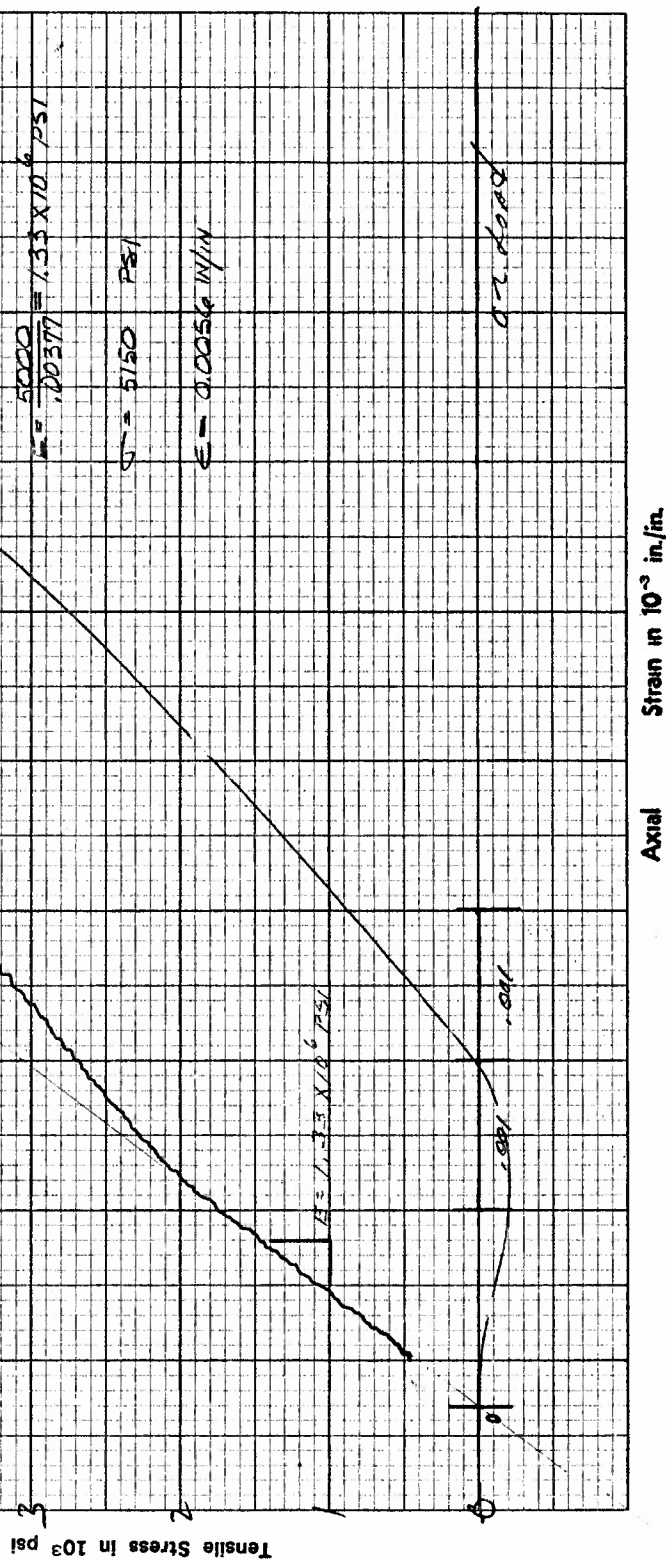


Figure I40. Tensile Stress versus Axial Strain for Specimen B37W of ATJ-S Graphite at 70°F



SRI Run No:	T-73	Specimen No:	B-380
Date:	11/1/59	Material:	ATJ-S Graphite
Temperature:	70°F	Lading Direction:	LONGITUDINAL
Specimen No.:	B-380	Lateral Strain Direction:	
Lading Direction:	LONGITUDINAL	Stress / Strain Rate:	1000 PSI / MIN
Lateral Strain Direction:		X Scale:	1" = 1000 PSI
Stress / Strain Rate:	1000 PSI / MIN	Y Scale:	1" = 1000 PSI
X Scale:	1" = 1000 PSI	Specimen Cage Section:	
Y Scale:	1" = 1000 PSI		

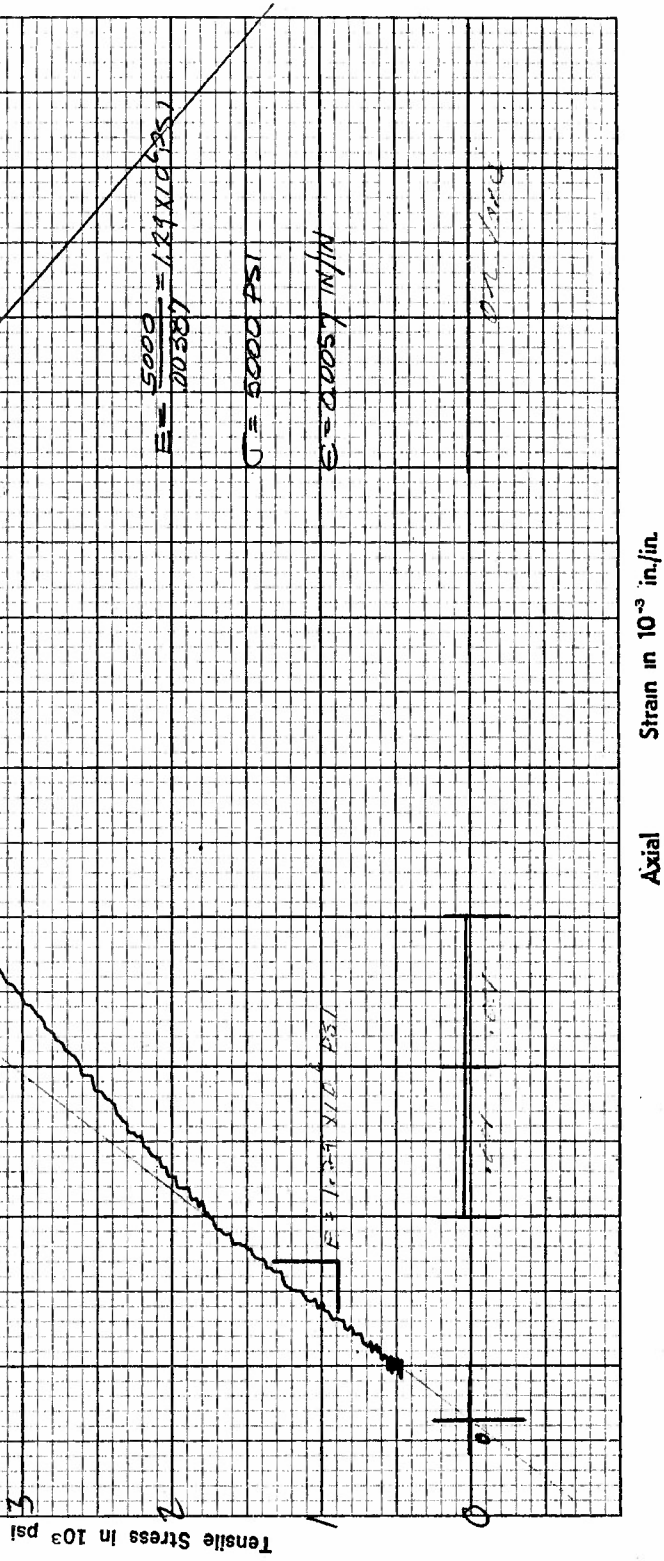


Figure I41. Tensile Stress versus Axial Strain for Specimen B38W of ATJ-S Graphite at 70°F

SRI Run No. <u>7-8</u> Rev. <u>2139</u>	
Date: <u>4/29/69</u>	Temperature: <u>70°F</u>
Material: <u>ATJ-S</u>	
Specimen No.: <u>8390</u>	
Loading Direction: <u>WITH GRAIN</u>	
Lateral Strain Direction: <u>---</u>	
Stress/Strain Rate: <u>12000 psi/min</u>	
X Scale: <u>1" = 1000</u>	
Y Scale: <u>1" = 10000</u>	
Specimen Gage Section: <u>0.250" K1.2 V</u>	

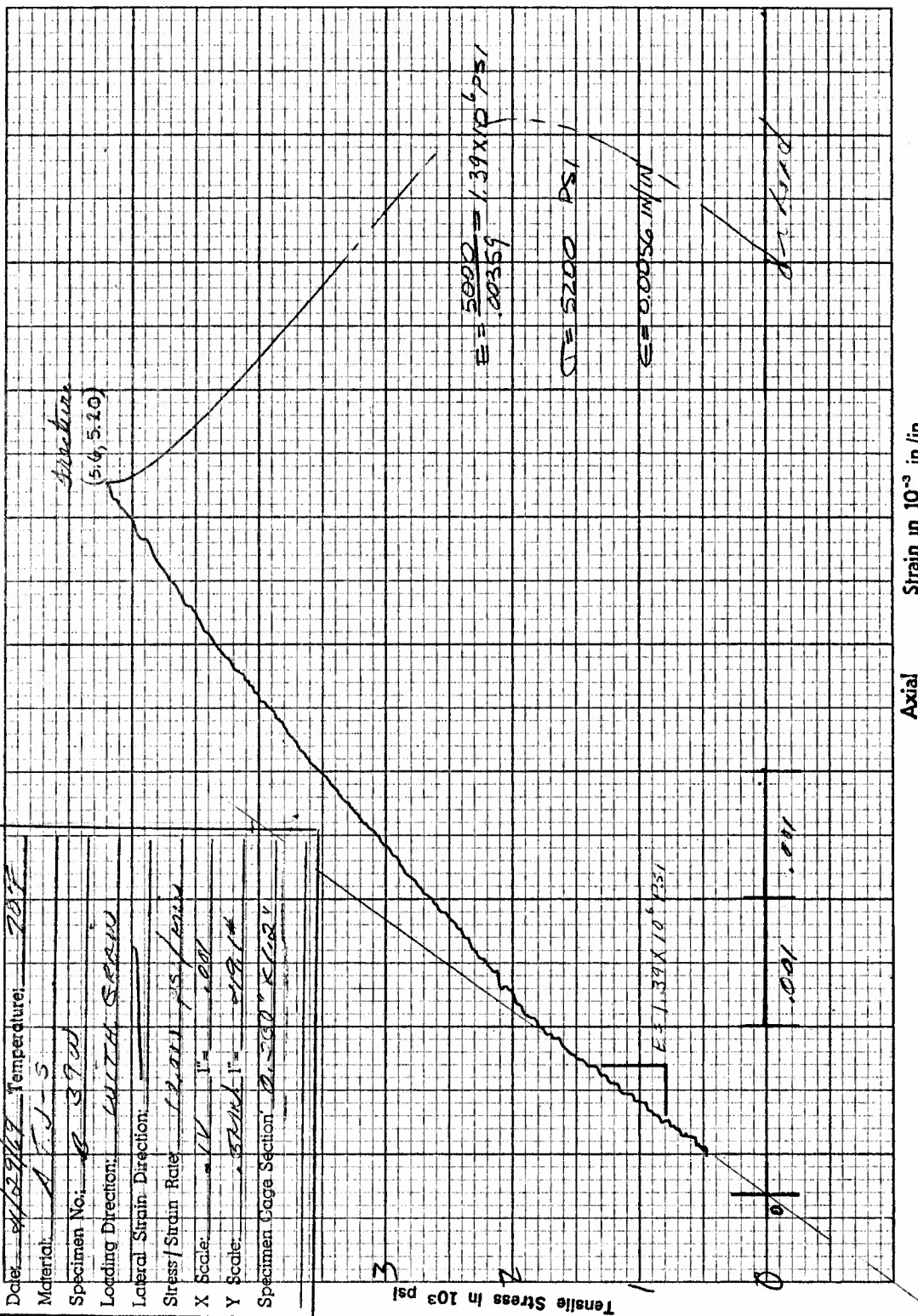


Figure I42. Tensile Stress versus Axial Strain for Specimen B39W of ATJ-S Graphite at 70°F

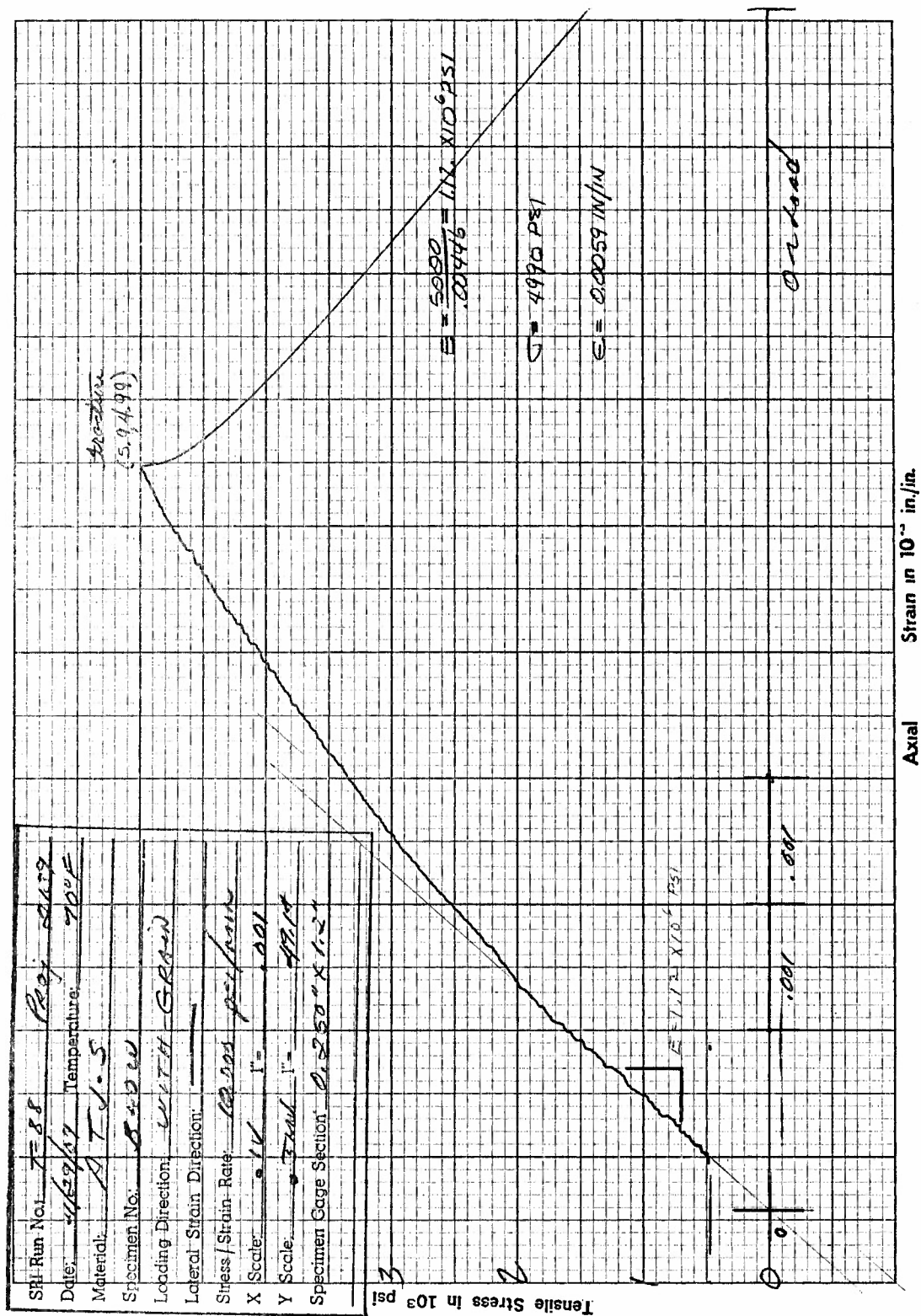


Figure I43. Tensile Stress versus Axial Strain for Specimen B40W of ATJ-S Graphite at 70°F

SRI Run No. <u>T-90 Per 2139</u>	
Date: <u>4/24/69</u>	Temperature: <u>70°F</u>
Material: <u>A.T.J-S</u>	
Specimen No.: <u>B41W</u>	
Loading Direction: <u>WITH GRAIN</u>	
Lateral Strain Direction: _____	
Stress/Strain Rate: <u>10,000 psi/min</u>	
X Scale: <u>1" = .001</u>	
Y Scale: <u>1" = 19.12</u>	
Specimen Gage Section: <u>0.250" x 1.2"</u>	

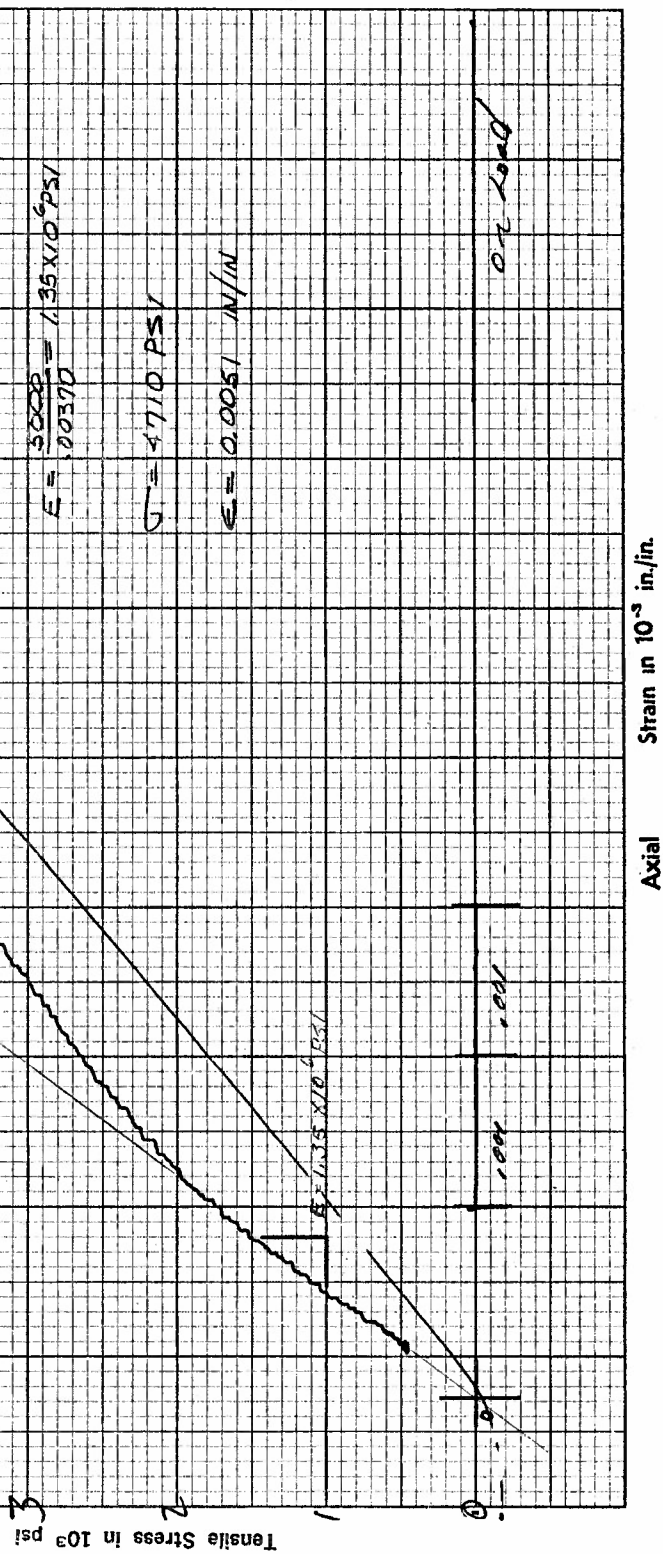


Figure I44. Tensile Stress versus Axial Strain for Specimen B41W of ATJ-S Graphite at 70°F

SRI Run No.	T-82	Page	2139
Date	4/24/77	Temperature	71°F
Material	A.T.J-5		
Specimen No.	B.1120		
Loading Direction	WITH - GRAIN		
Lateral Strain Direction			
Stress / Strain Rate	10.000 psi/min		
X Scale	1" = 0.001		
Y Scale	0.0250" = 0.001"		
Specimen Gage Section	0.250" x 1.02"		

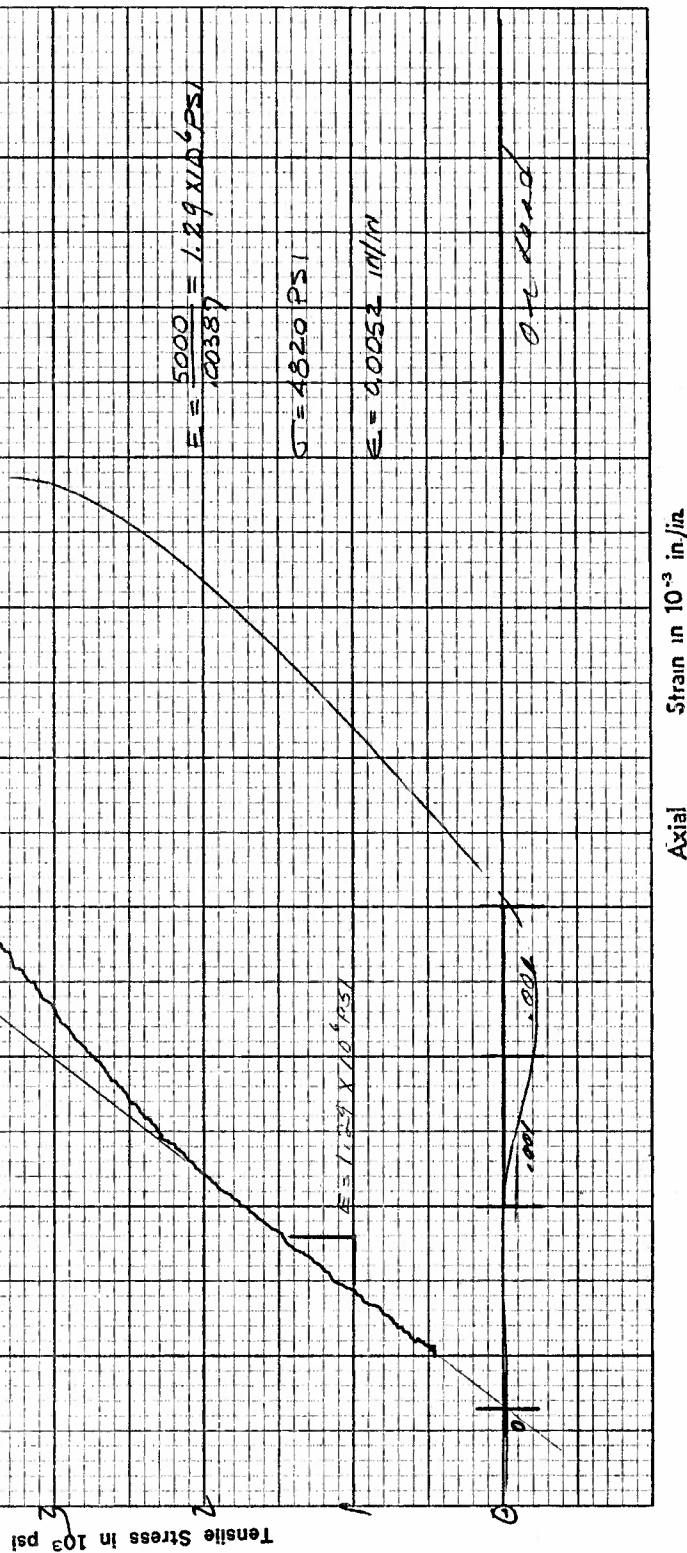


Figure I45. Tensile Stress versus Axial Strain for Specimen B42W of ATJ-S Graphite at 70°F



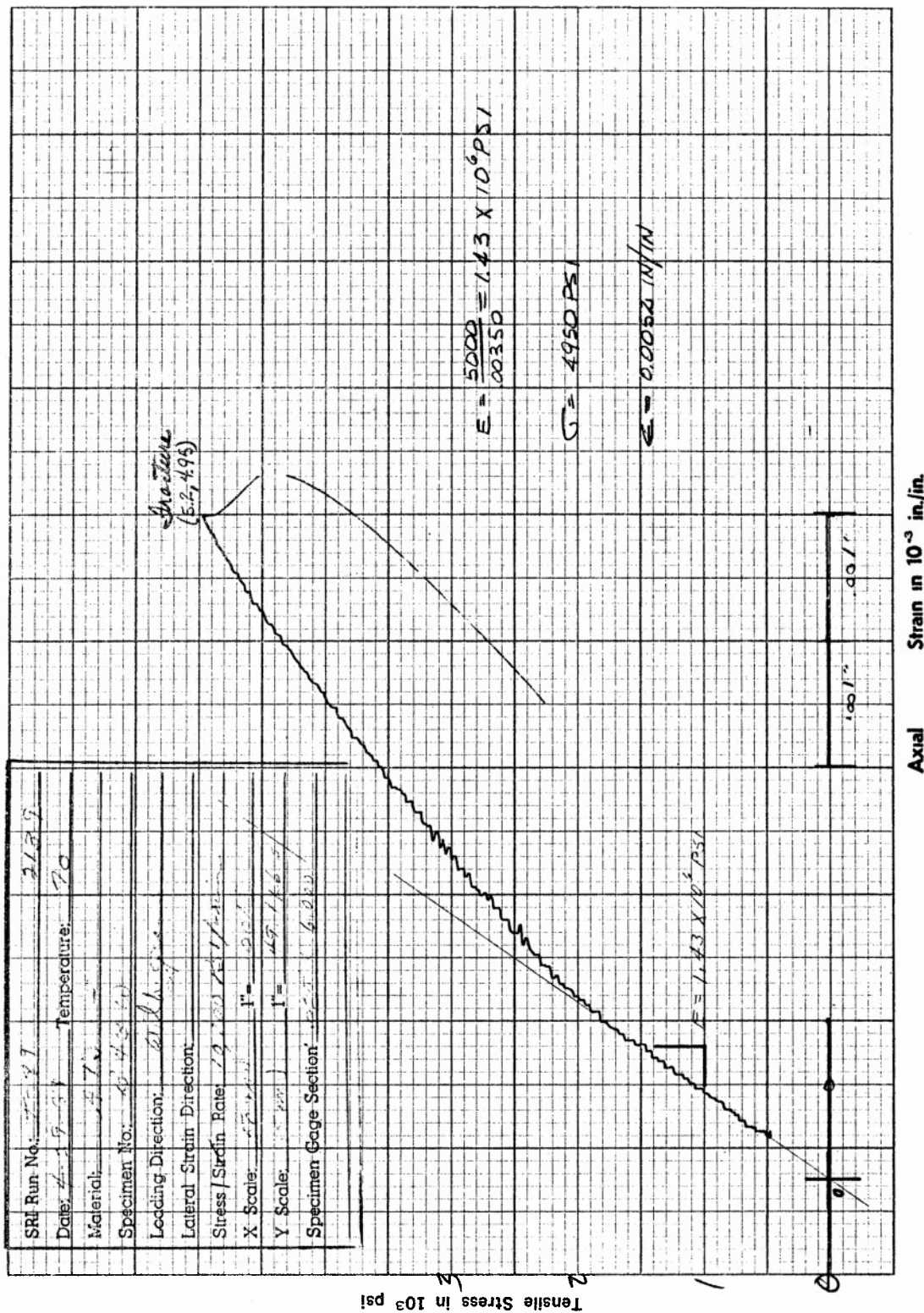


Figure 146. Tensile Stress versus Axial Strain for Specimen B43W of ATJ-S Graphite at 70°F

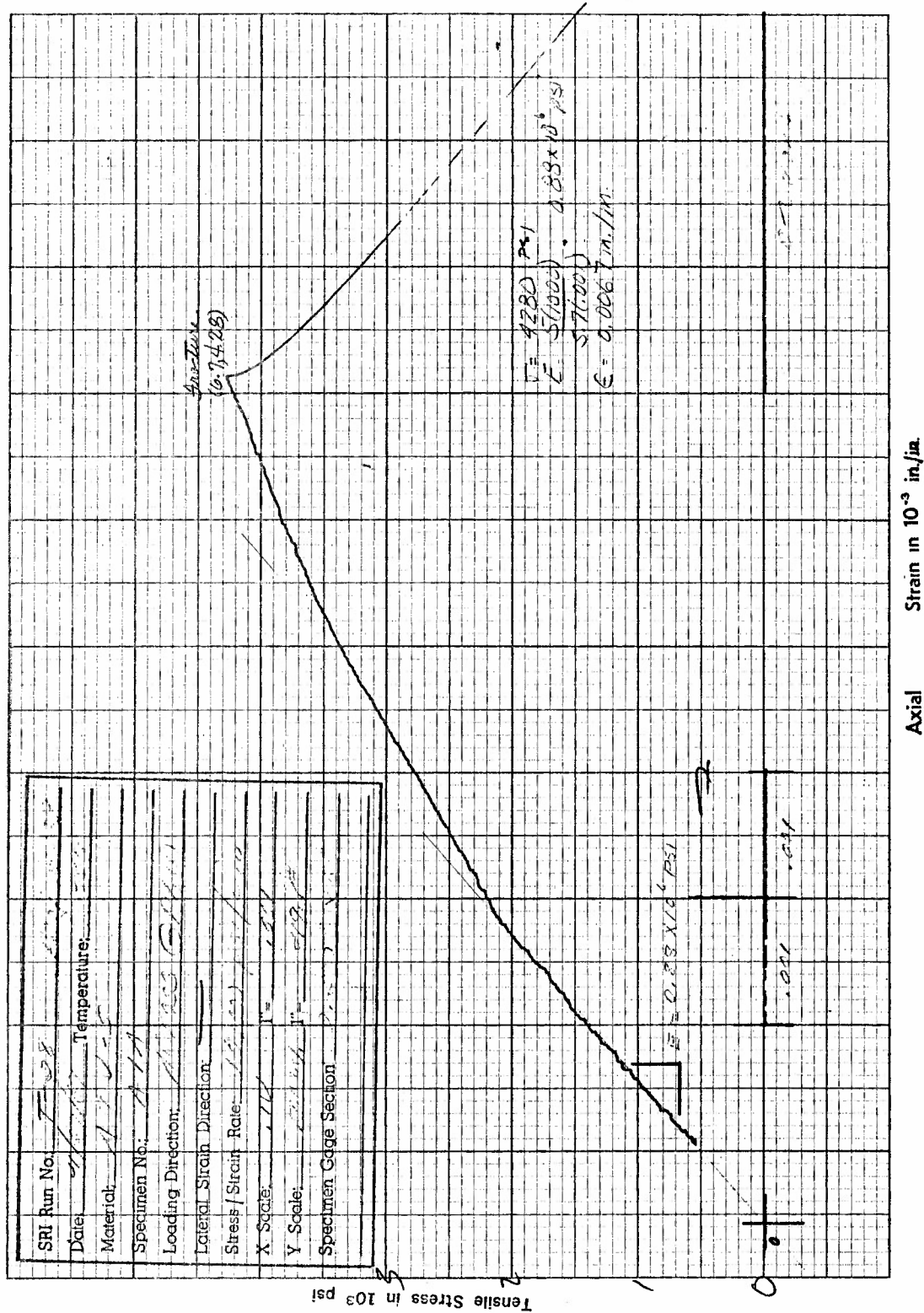


Figure I47. Tensile Stress versus Axial Strain for Specimen A1A of ATJ-S Graphite at 70°F

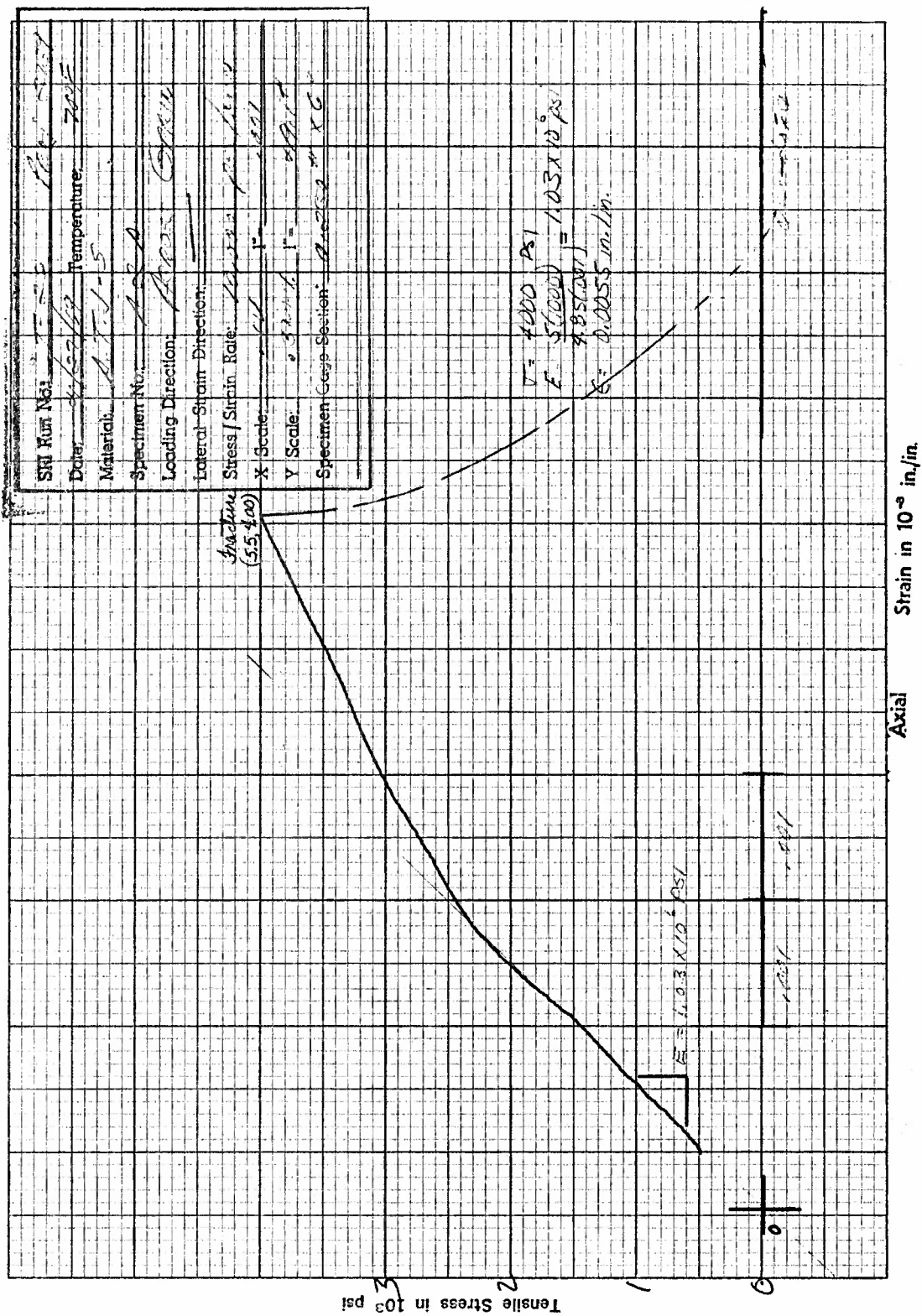


Figure I48. Tensile Stress versus Axial Strain for Specimen A2A of ATJ-S Graphite at 70°F



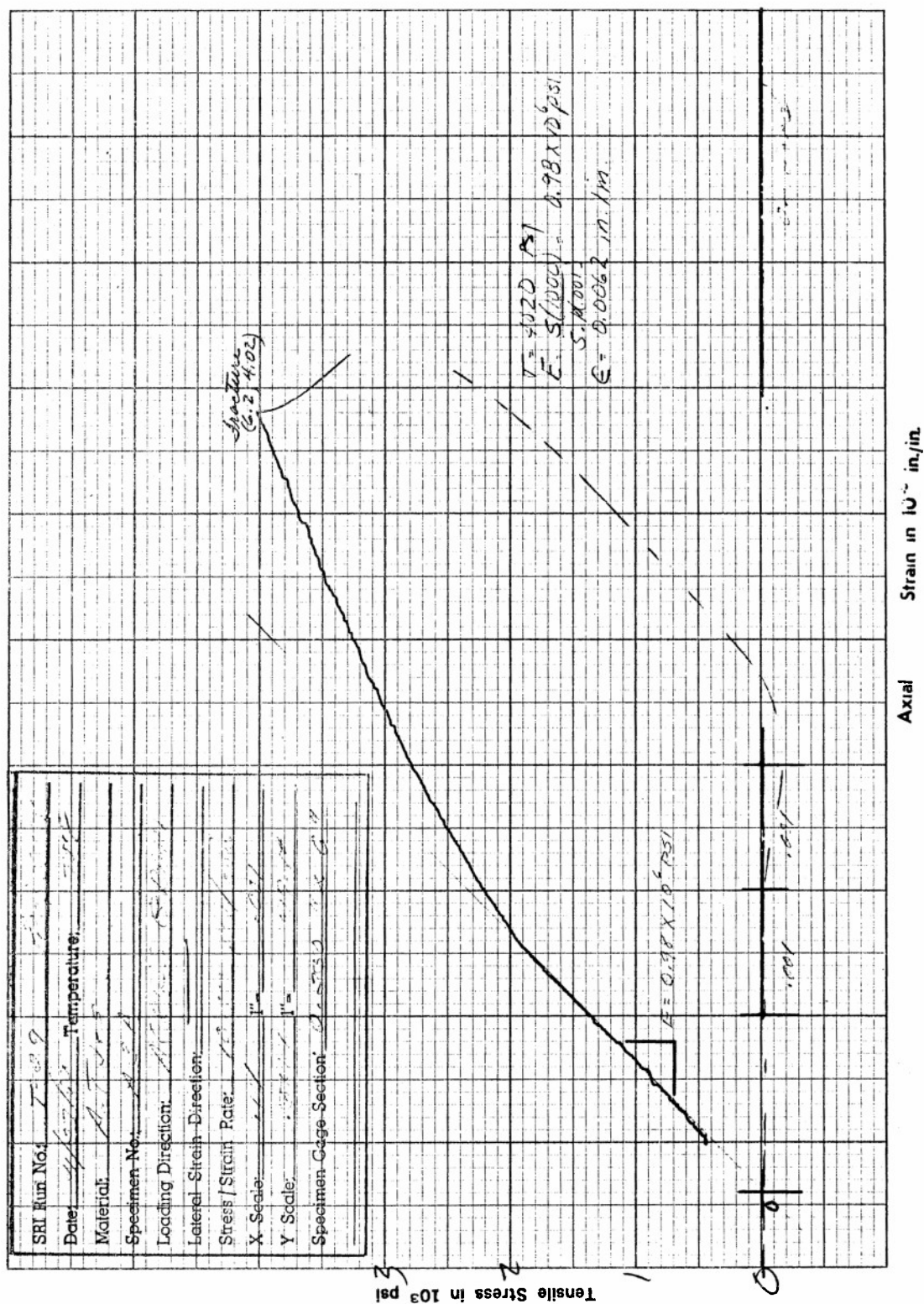


Figure I49. Tensile Stress versus Axial Strain for Specimen A3A of ATJ-S Graphite at 70°F

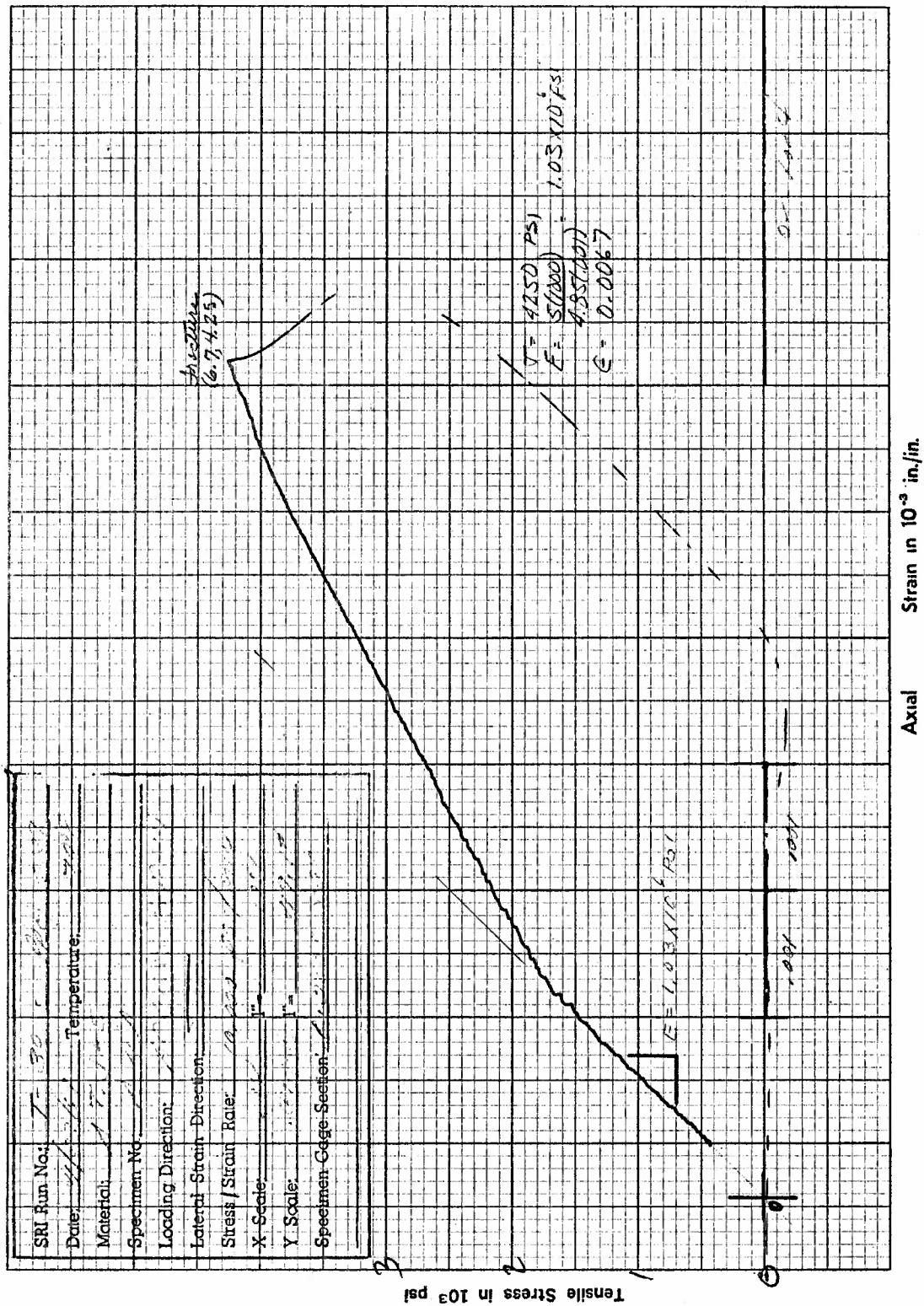


Figure I50. Tensile Stress versus Axial Strain for Specimen A4A of ATJ-S Graphite at 70°F

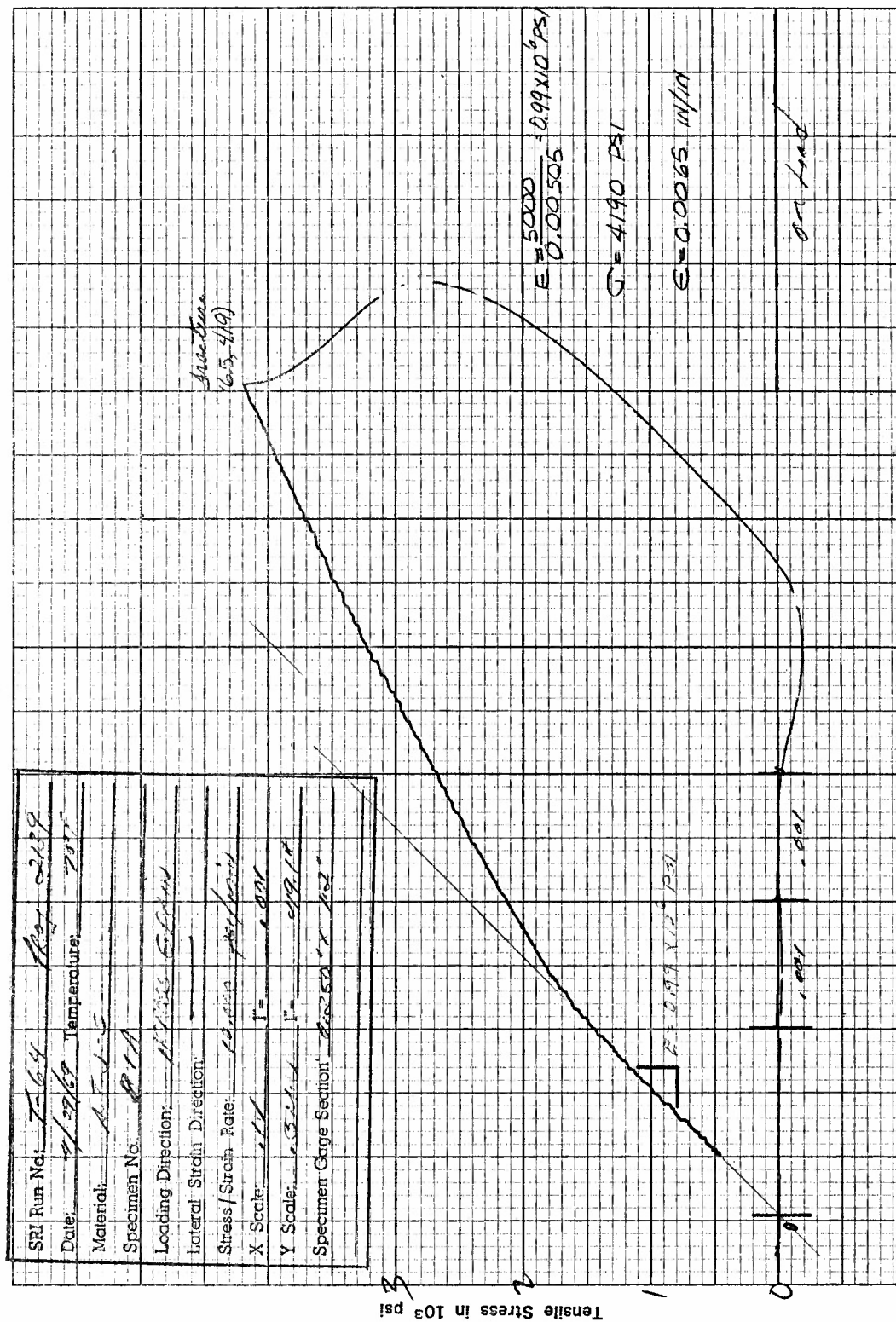


Figure I51. Tensile Stress versus Axial Strain for Specimen B1A of ATJ-S Graphite at 70°F

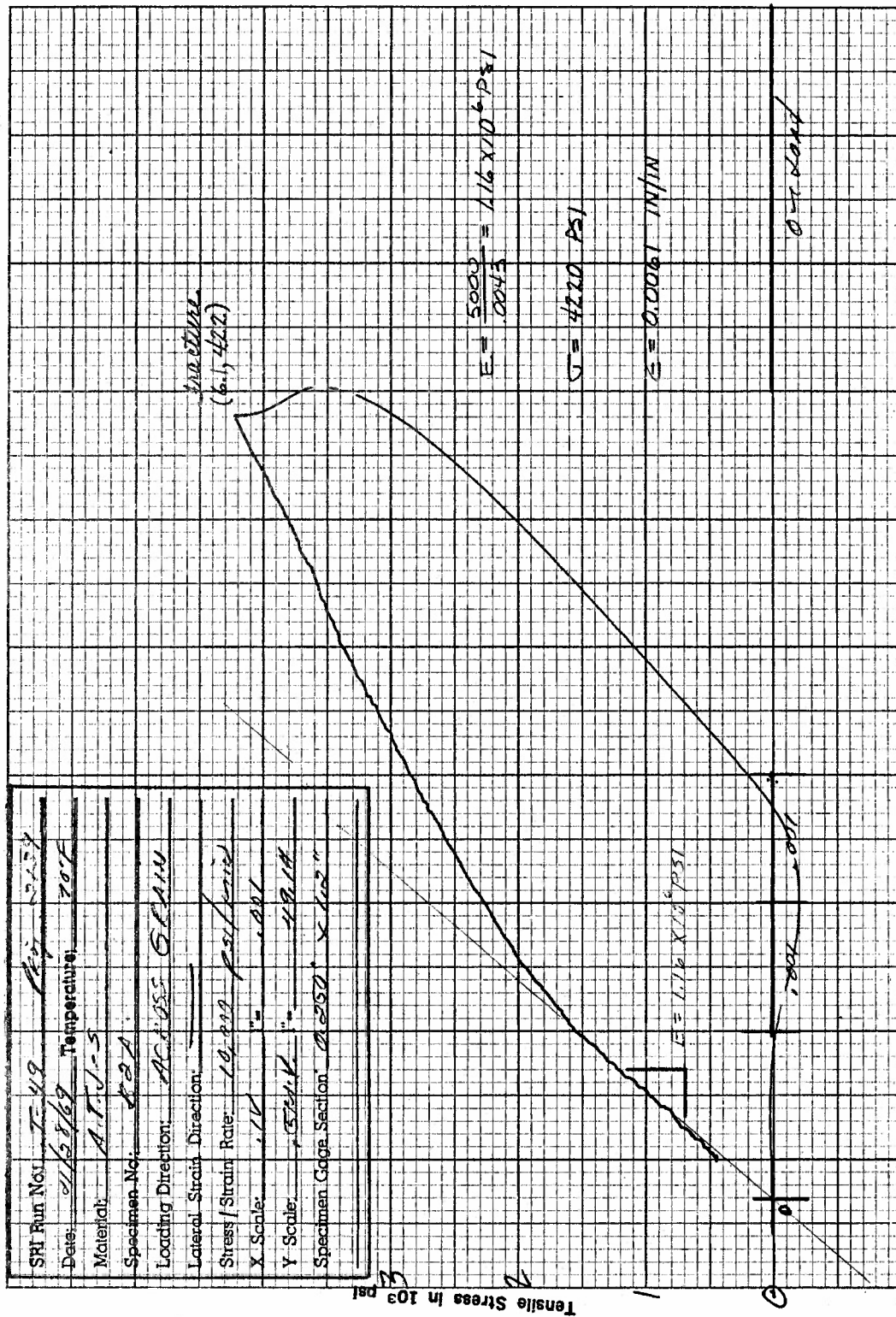


Figure I52. Tensile Stress versus Axial Strain for Specimen B2A of ATJ-S Graphite at 70°F

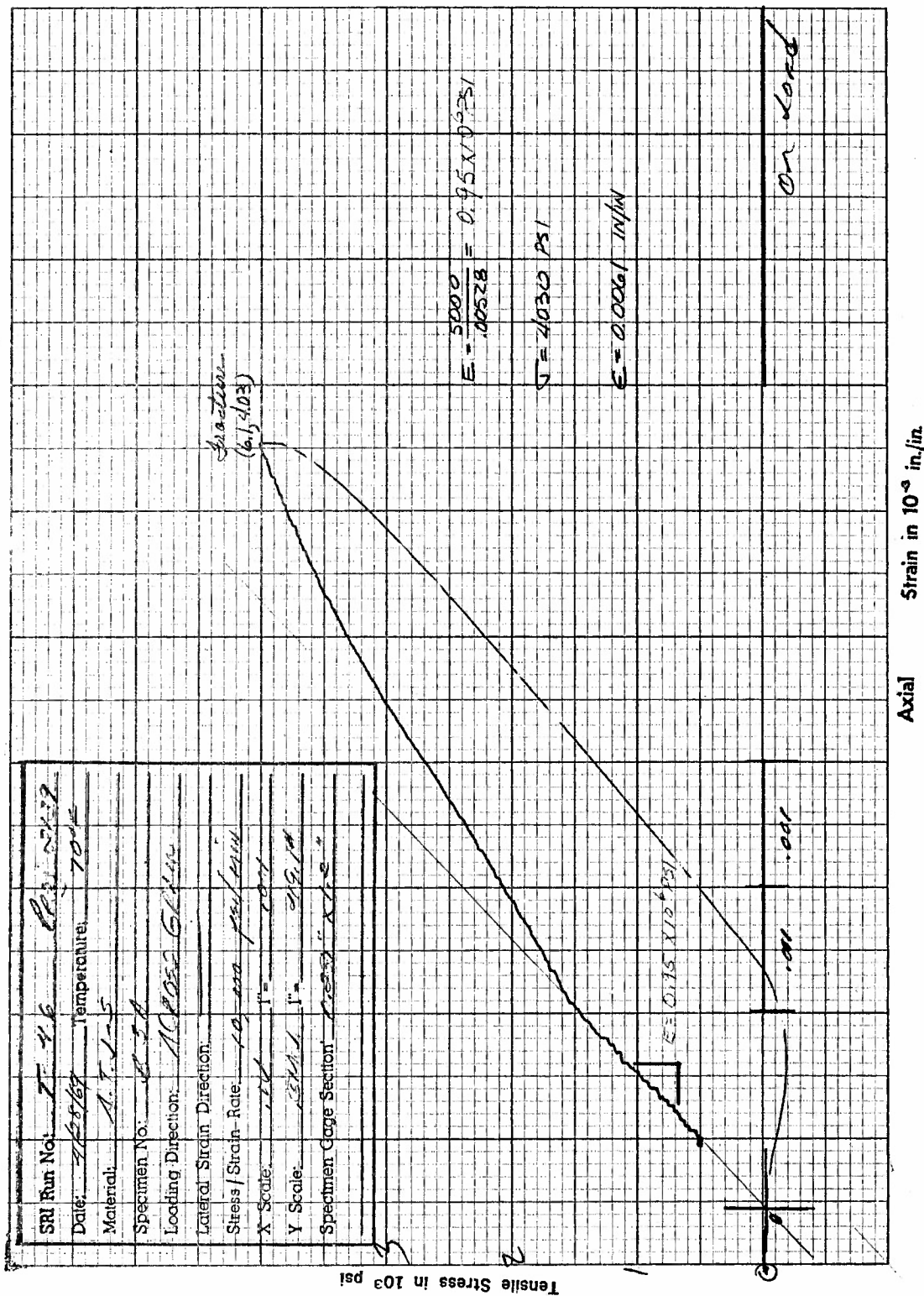


Figure I53. Tensile Stress versus Axial Strain for Specimen B3A of ATJ-S Graphite at 70°F



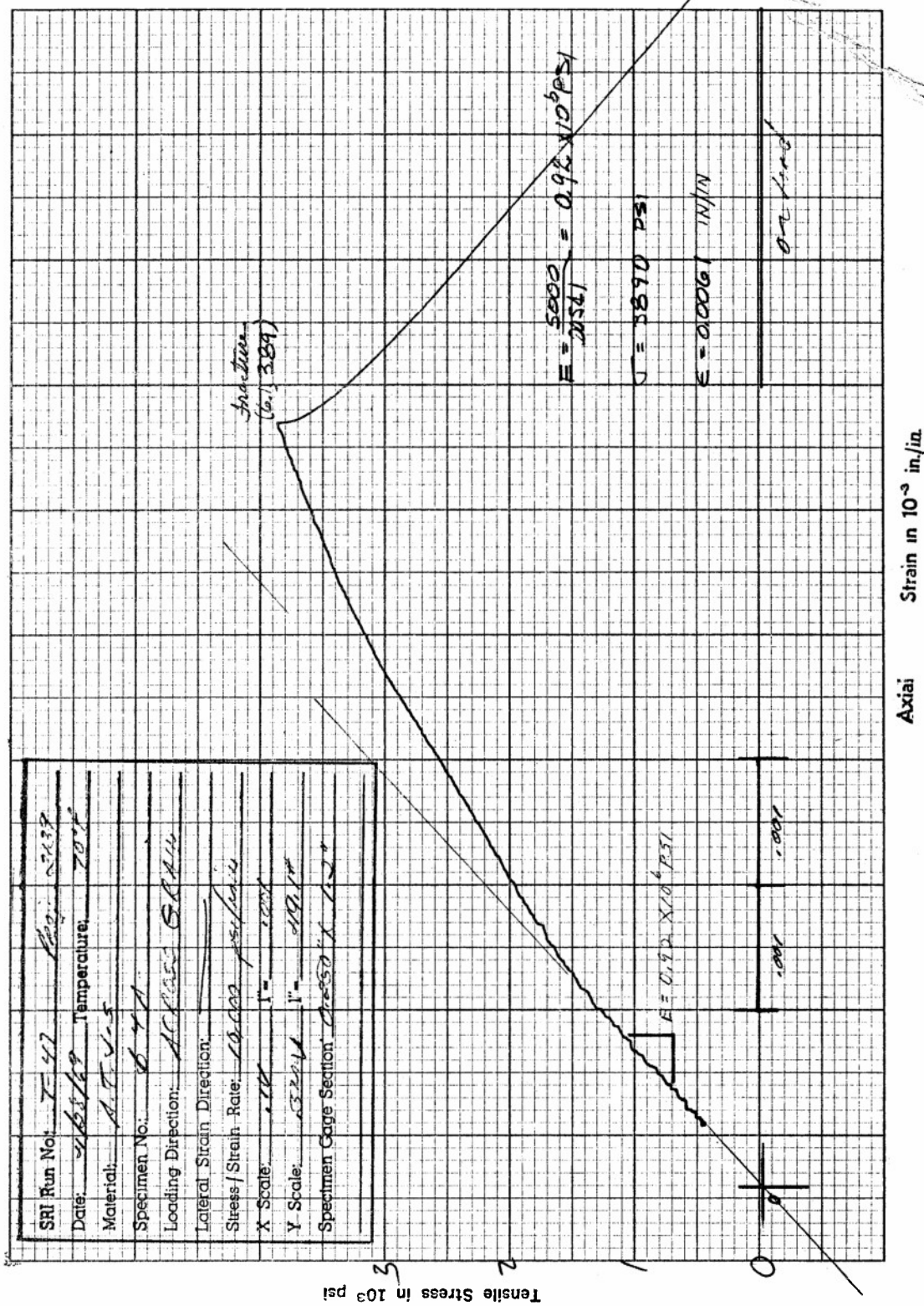


Figure I54. Tensile Stress versus Axial Strain for Specimen B4A of ATJ-S Graphite at 70°F



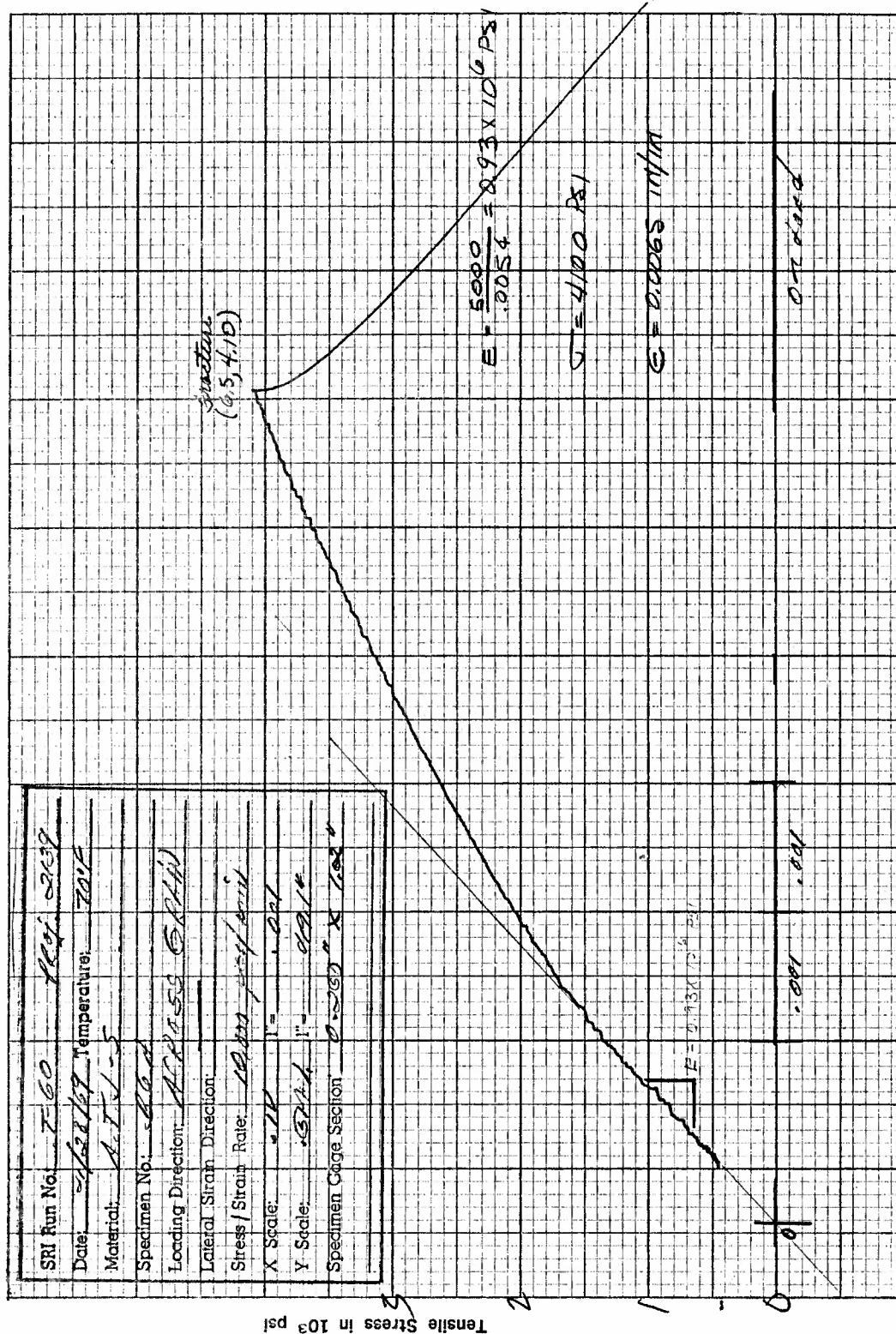


Figure I56. Tensile Stress versus Axial Strain for Specimen B6A of ATJ-S Graphite at 70°F



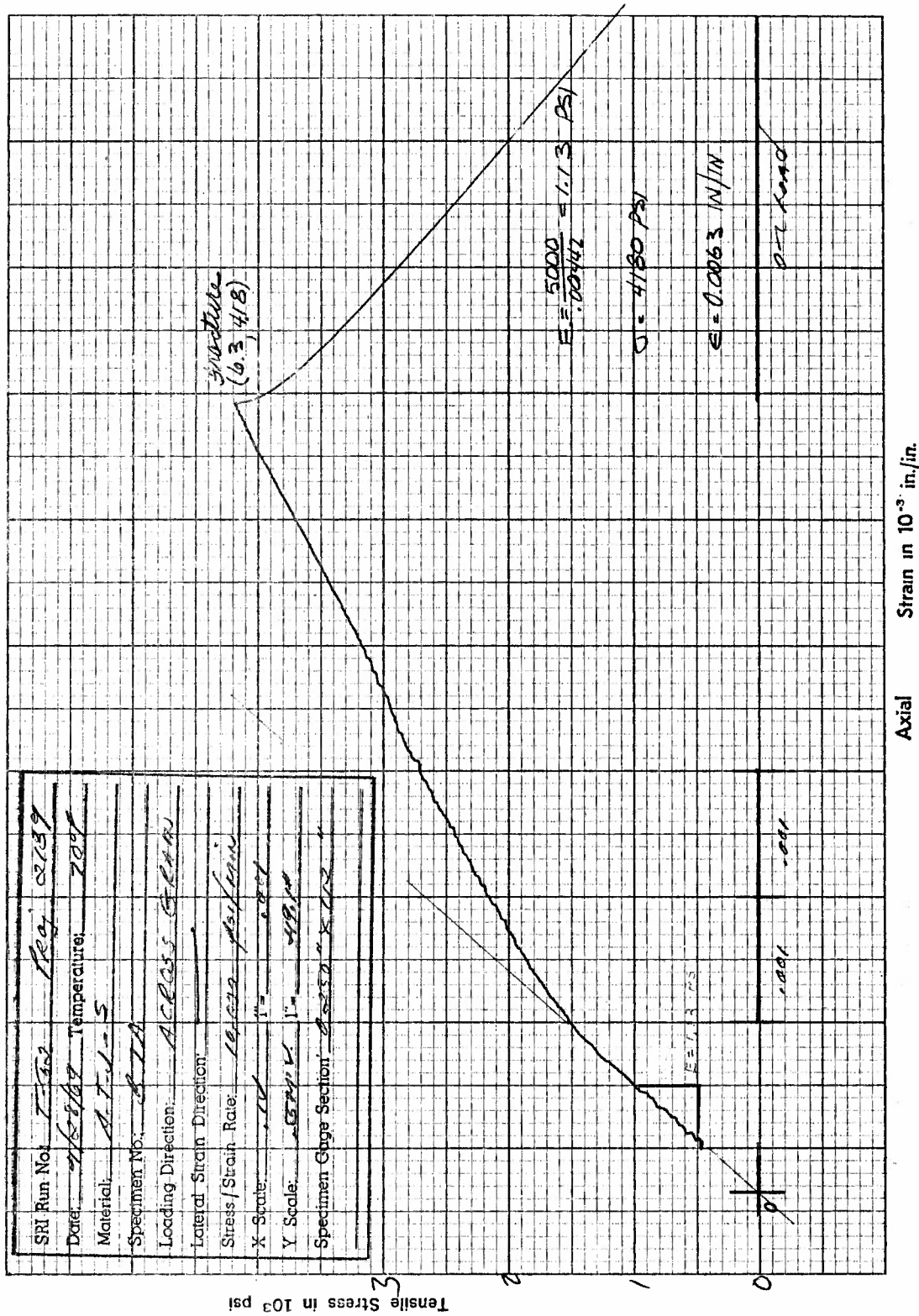


Figure I57. Tensile Stress versus Axial Strain for Specimen B7A of ATJ-S Graphite at 70°F

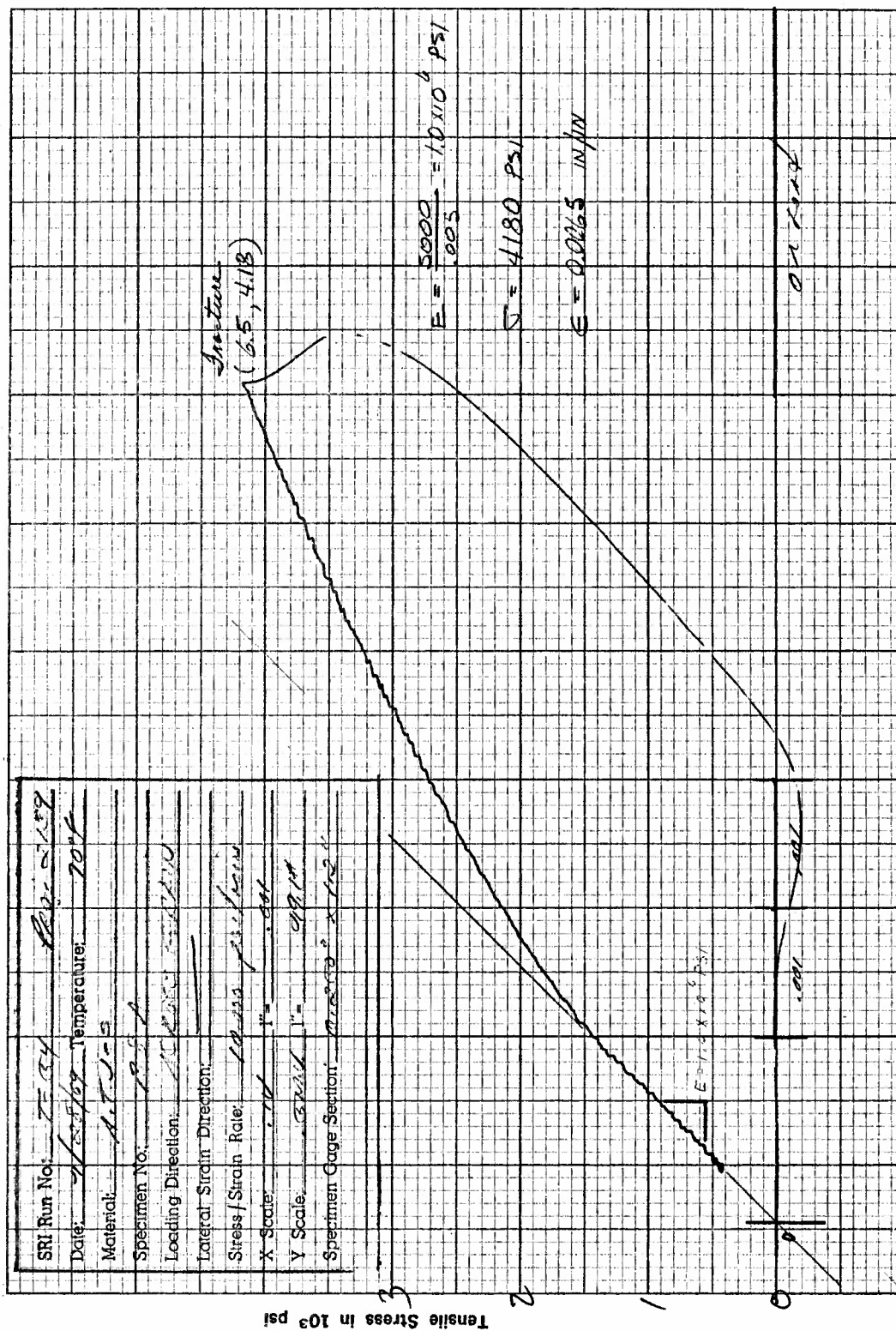


Figure I58. Tensile Stress versus Axial Strain for Specimen B8A of ATJ-S Graphite at 70°F



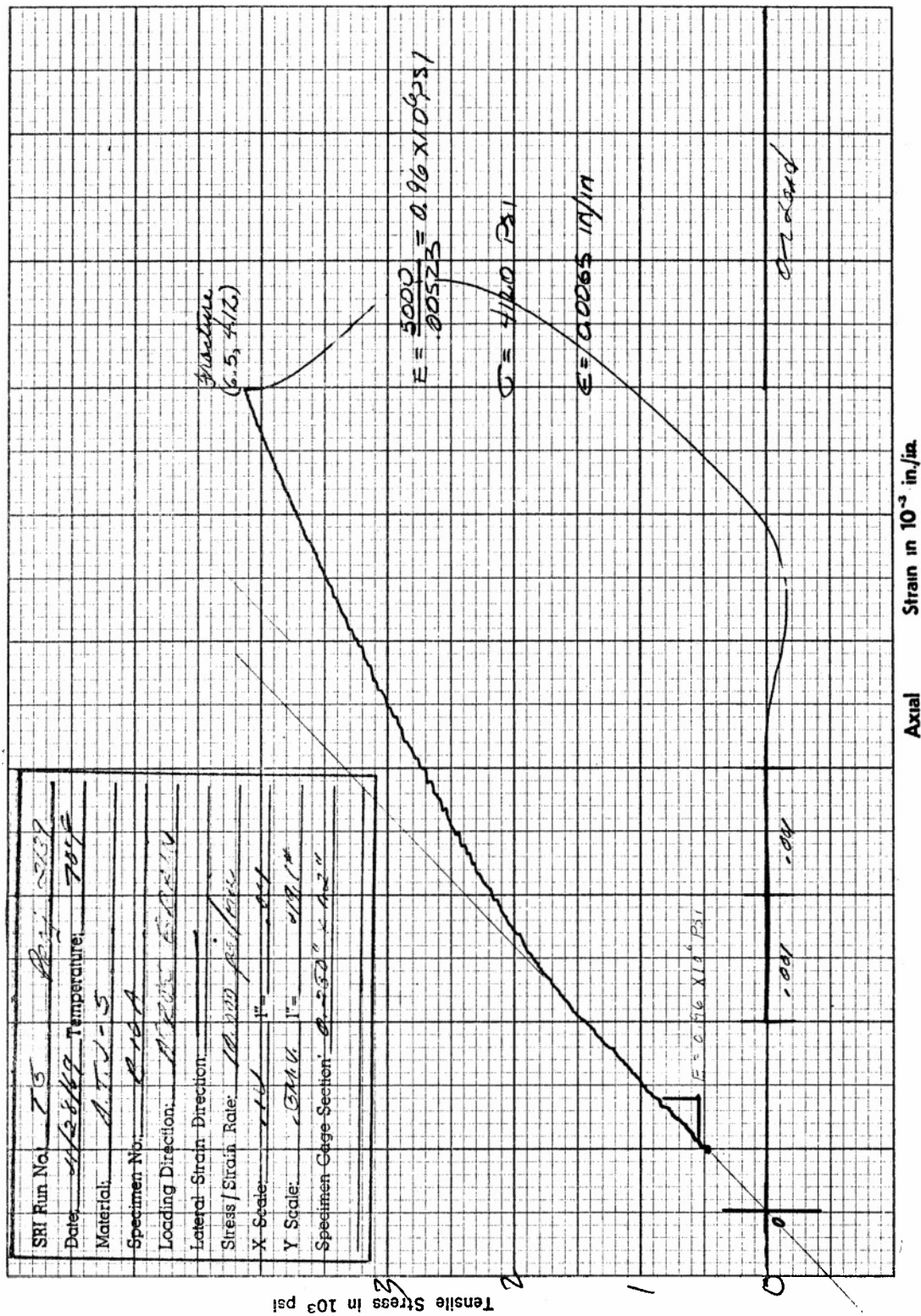


Figure I60. Tensile Stress versus Axial Strain for Specimen B10A of ATJ-S Graphite at 70°F

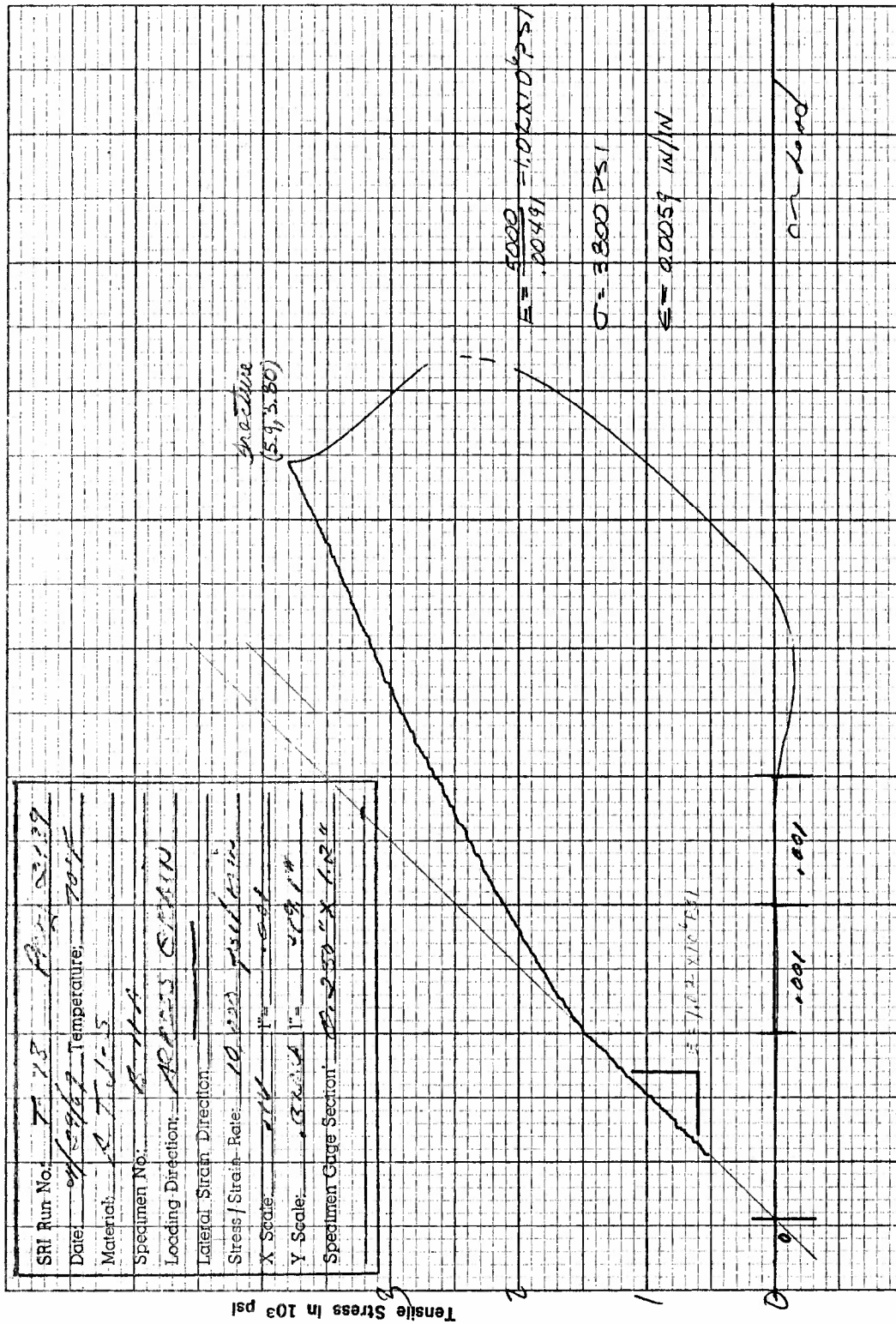


Figure I61. Tensile Stress versus Axial Strain for Specimen B11A of ATJ-S Graphite at 70°F



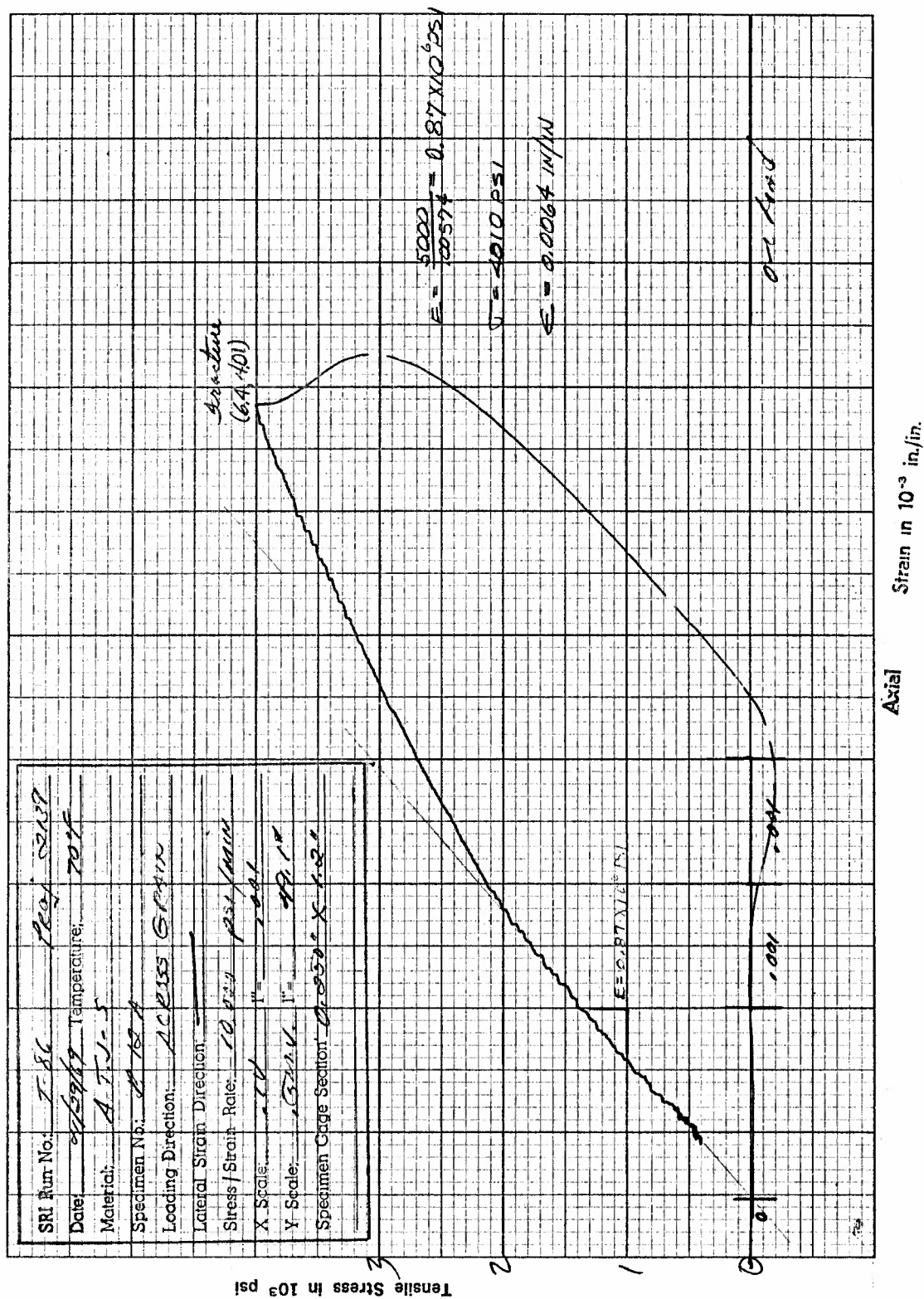
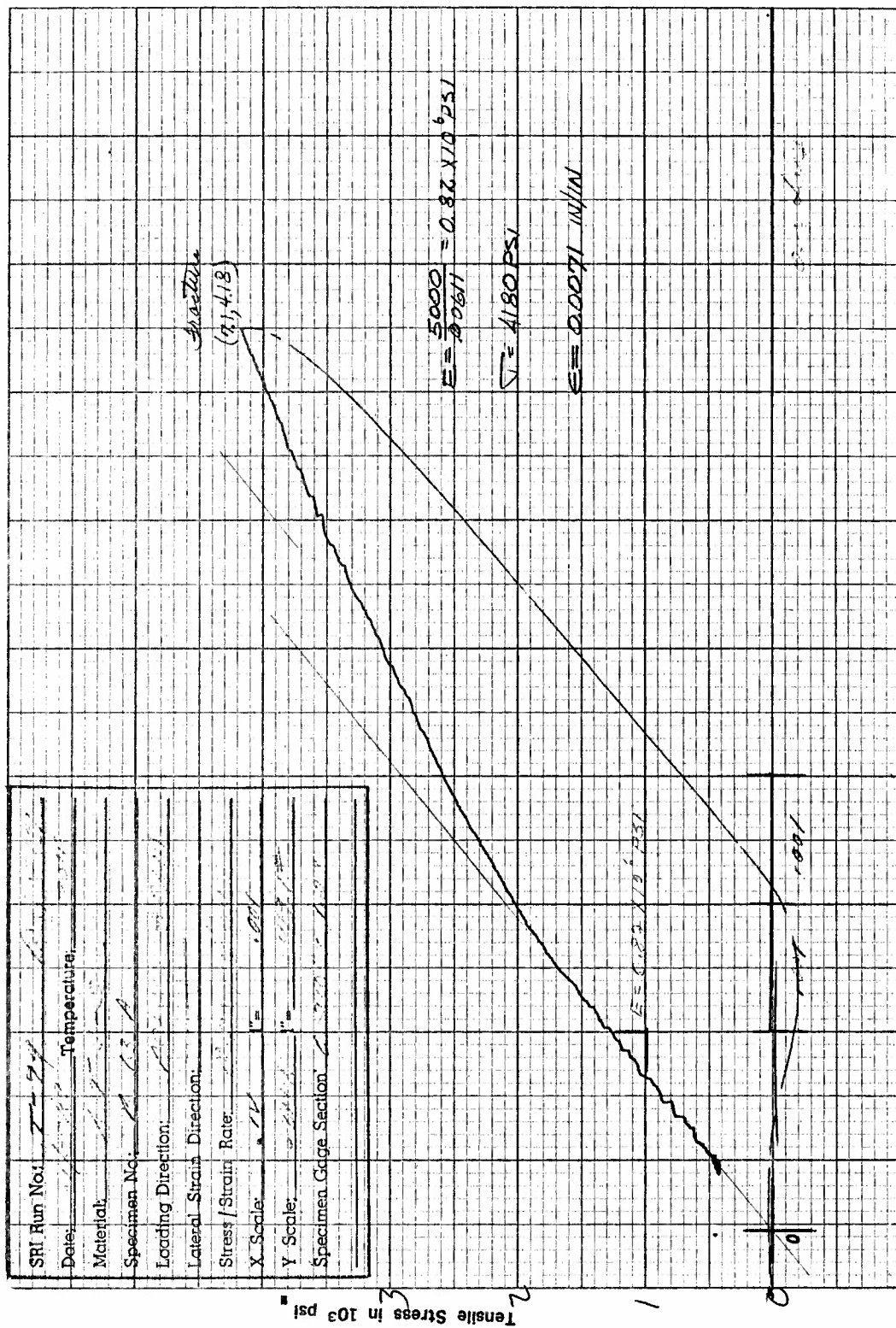


Figure I62. Tensile Stress versus Axial Strain for Specimen B12A of ATJ-S Graphite at 70°F



Axial Strain in  $10^{-3}$  in./in.

Figure I63. Tensile Stress versus Axial Strain for Specimen B13A of ATJ-S Graphite at 70°F

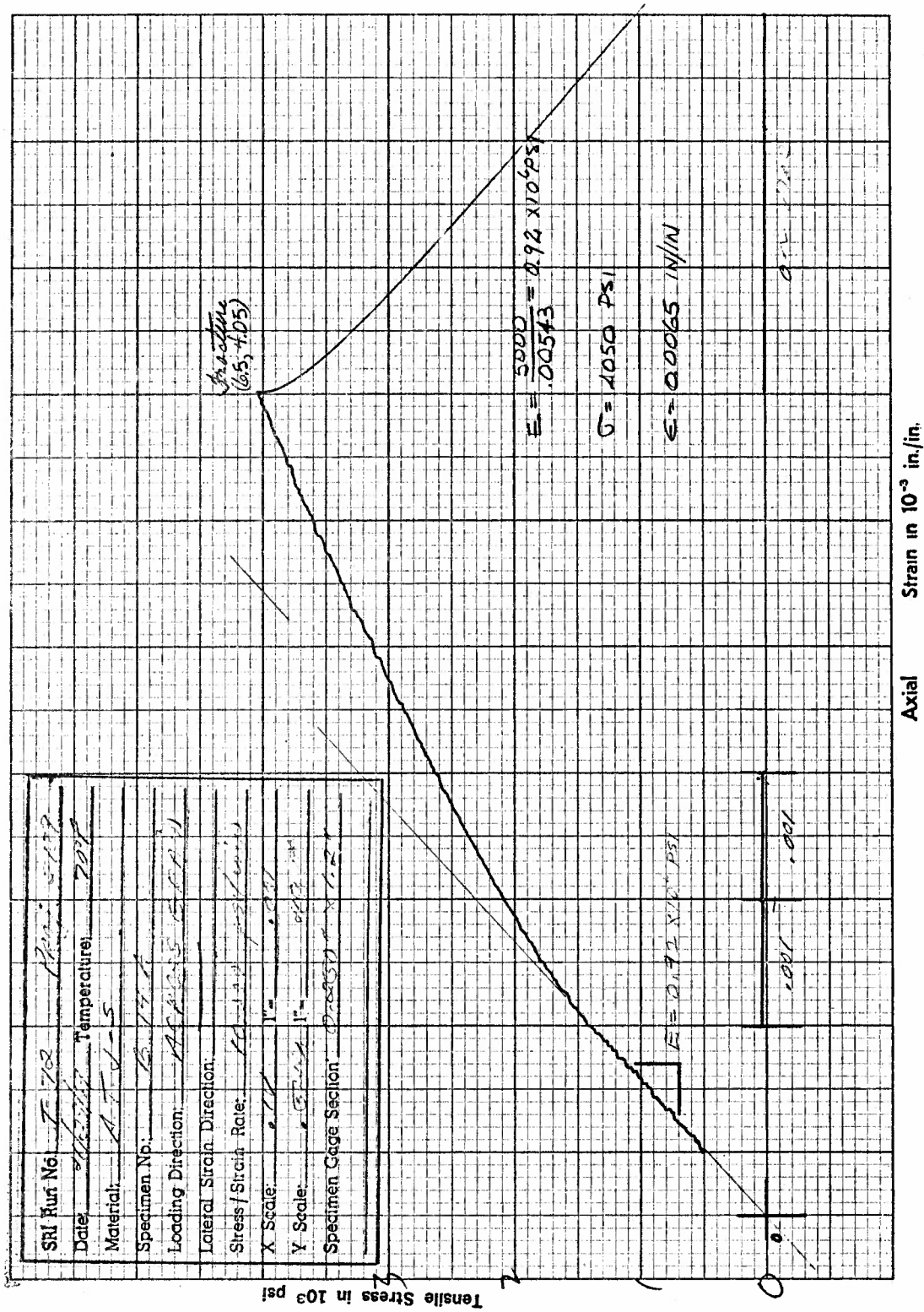


Figure I64. Tensile Stress versus Axial Strain for Specimen B14A of ATJ-S Graphite at 70°F



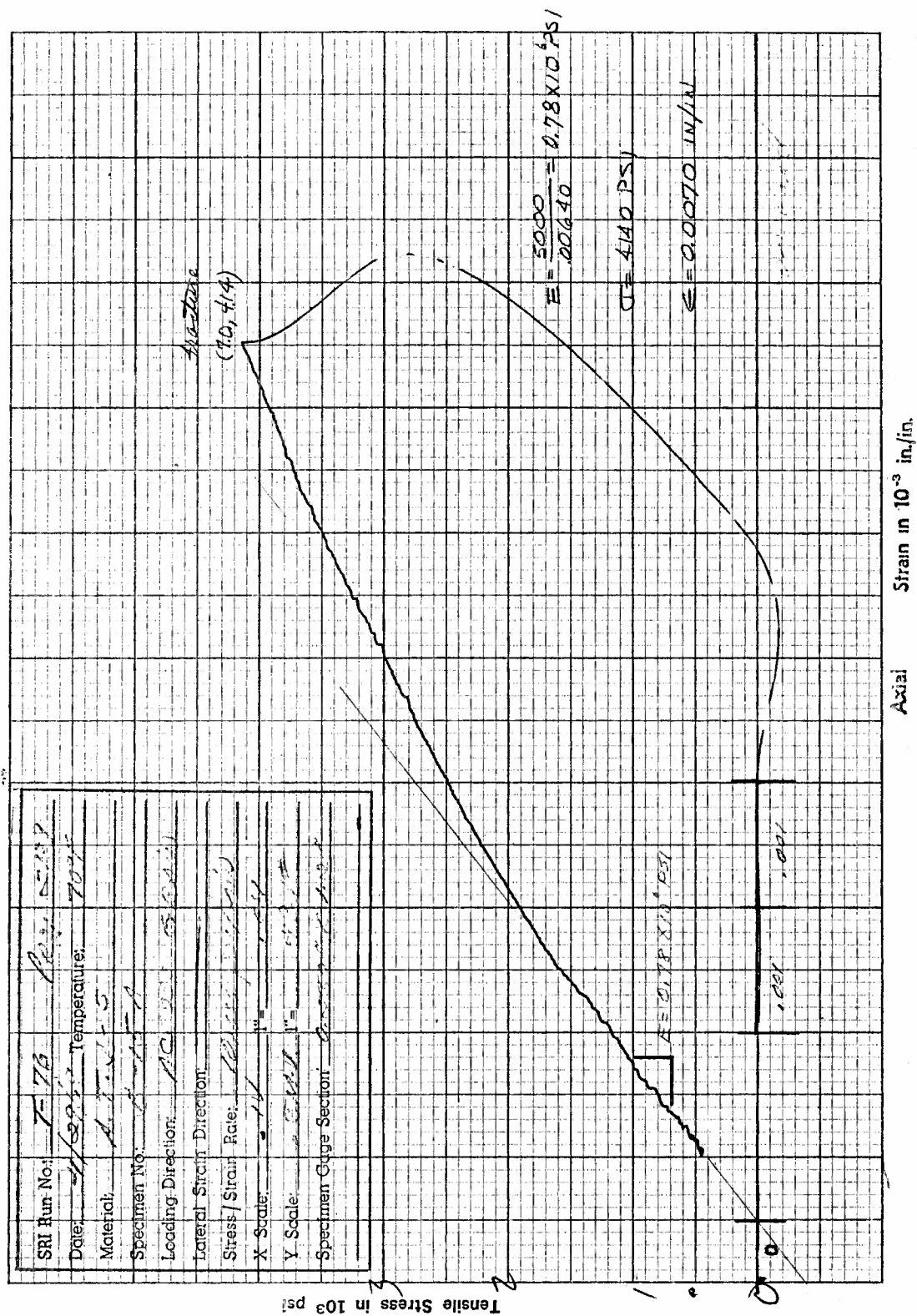


Figure I65. Tensile Stress versus Axial Strain for Specimen B15A of ATJ-S Graphite at 70°F

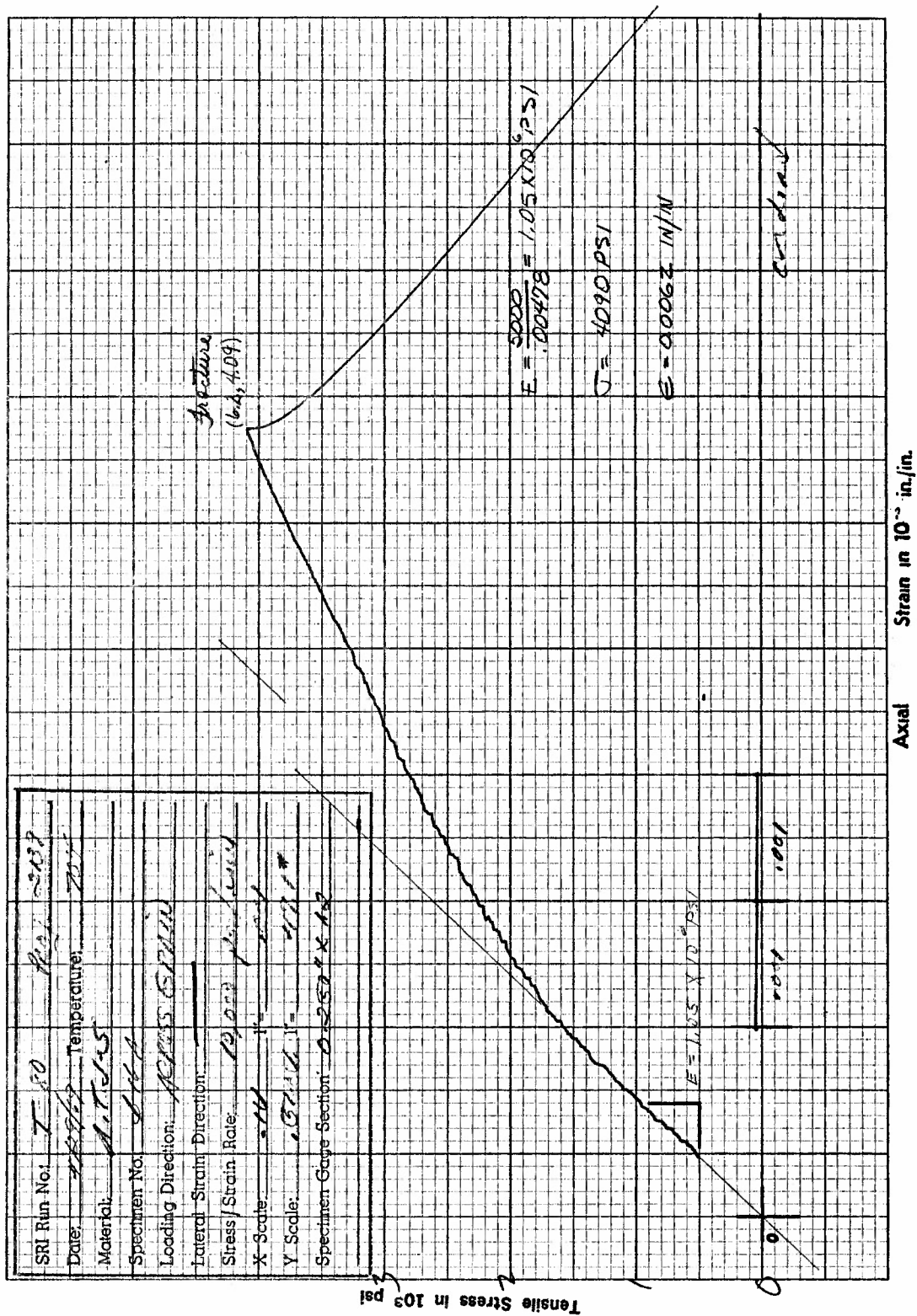


Figure I66. Tensile Stress versus Axial Strain for Specimen B16A of ATJ-S Graphite at 70°F

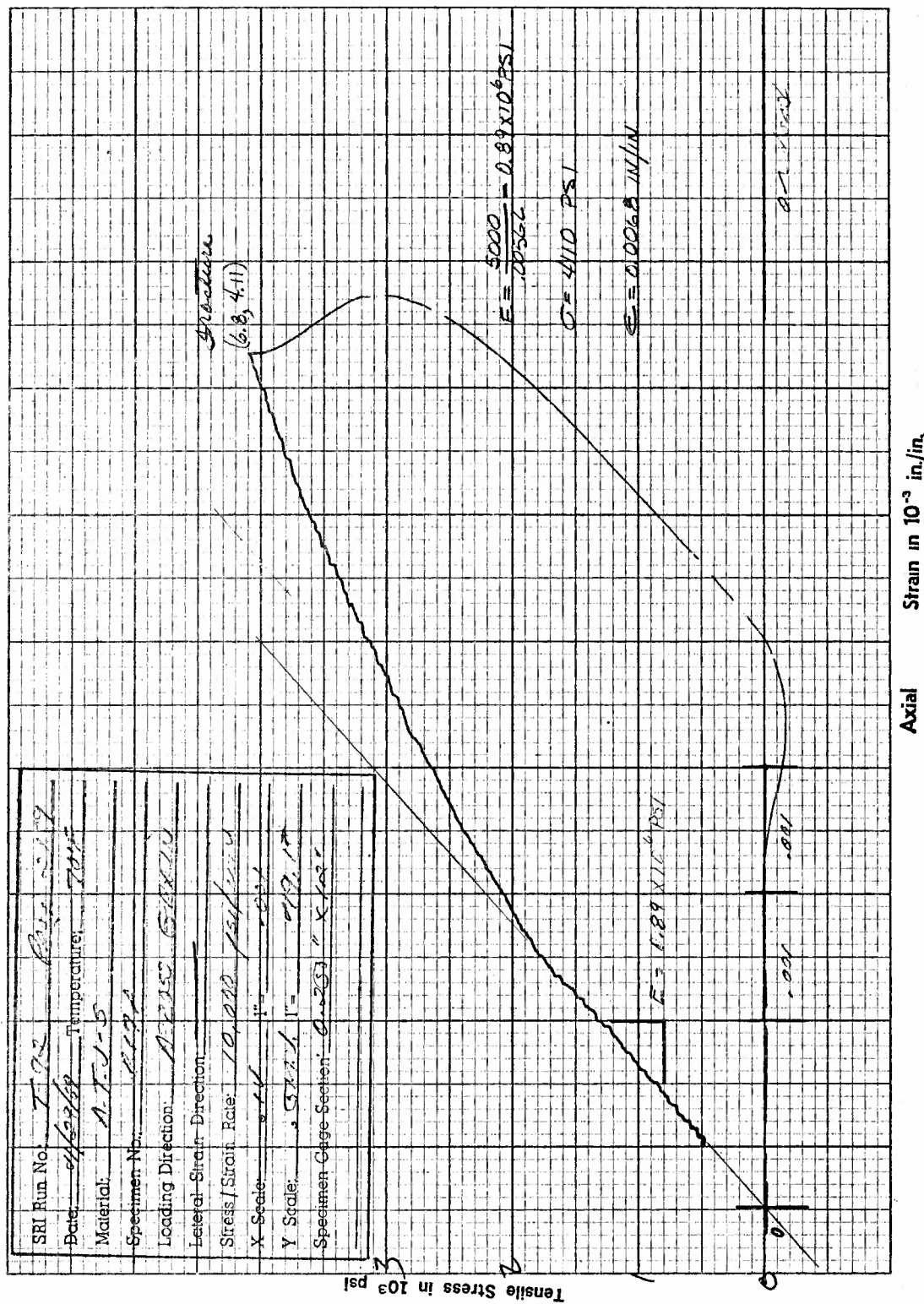


Figure I67. Tensile Stress versus Axial Strain for Specimen B17A of ATJ-S Graphite at 70°F

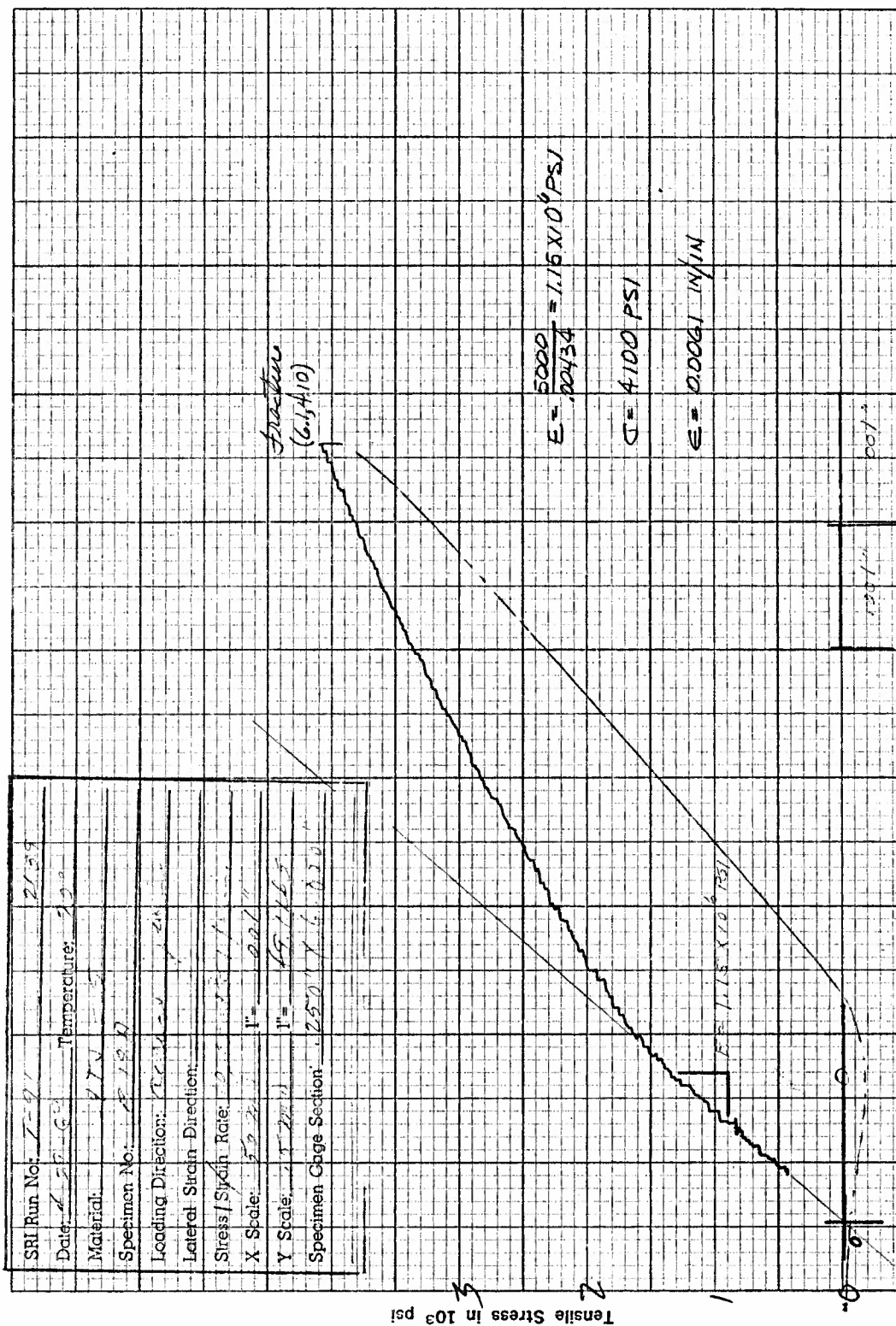


Figure I68. Tensile Stress versus Axial Strain for Specimen B18A of ATJ-S Graphite at 70°F

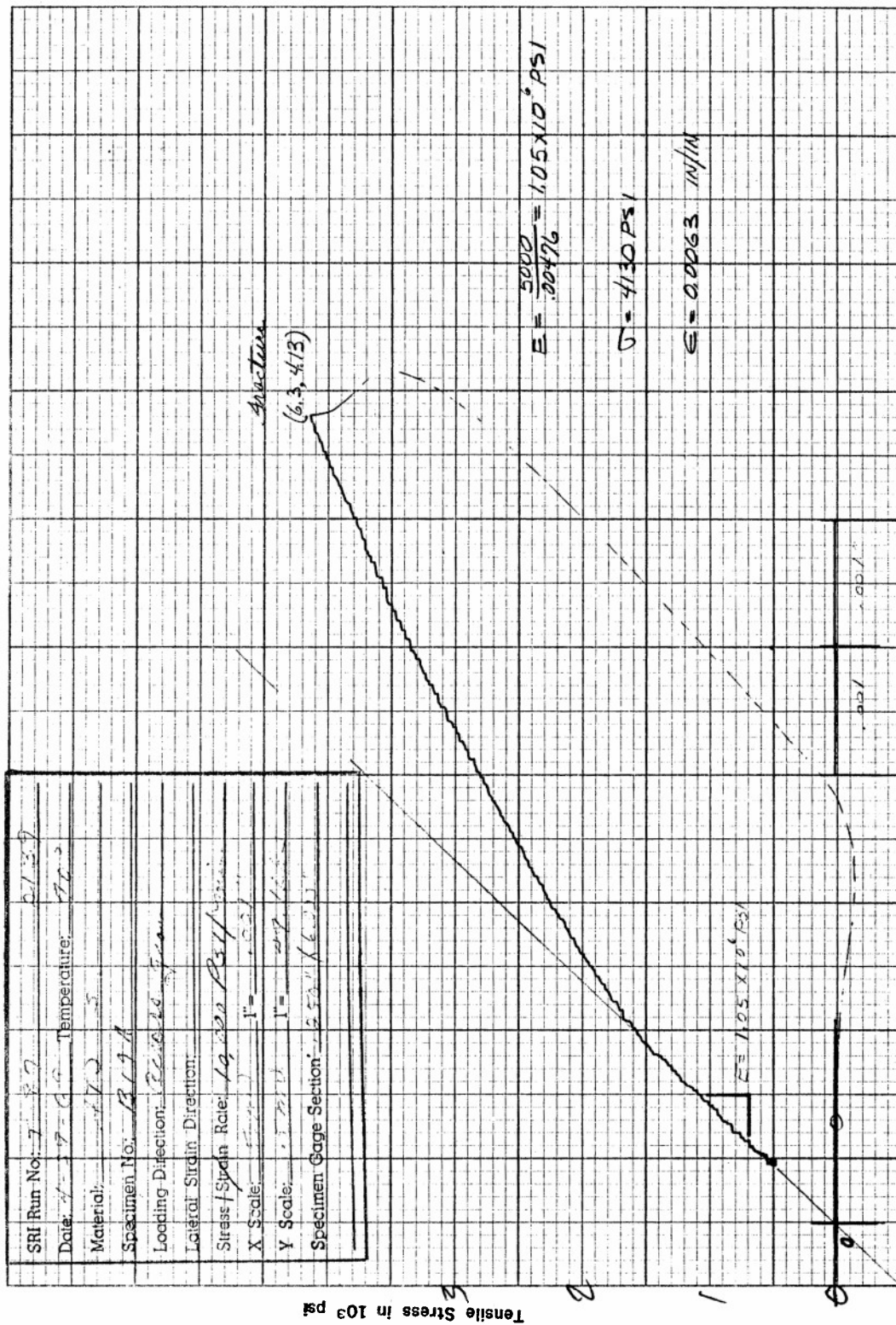


Figure 169. Tensile Stress versus Axial Strain for Specimen B19A of ATJ-S Graphite at 70°F



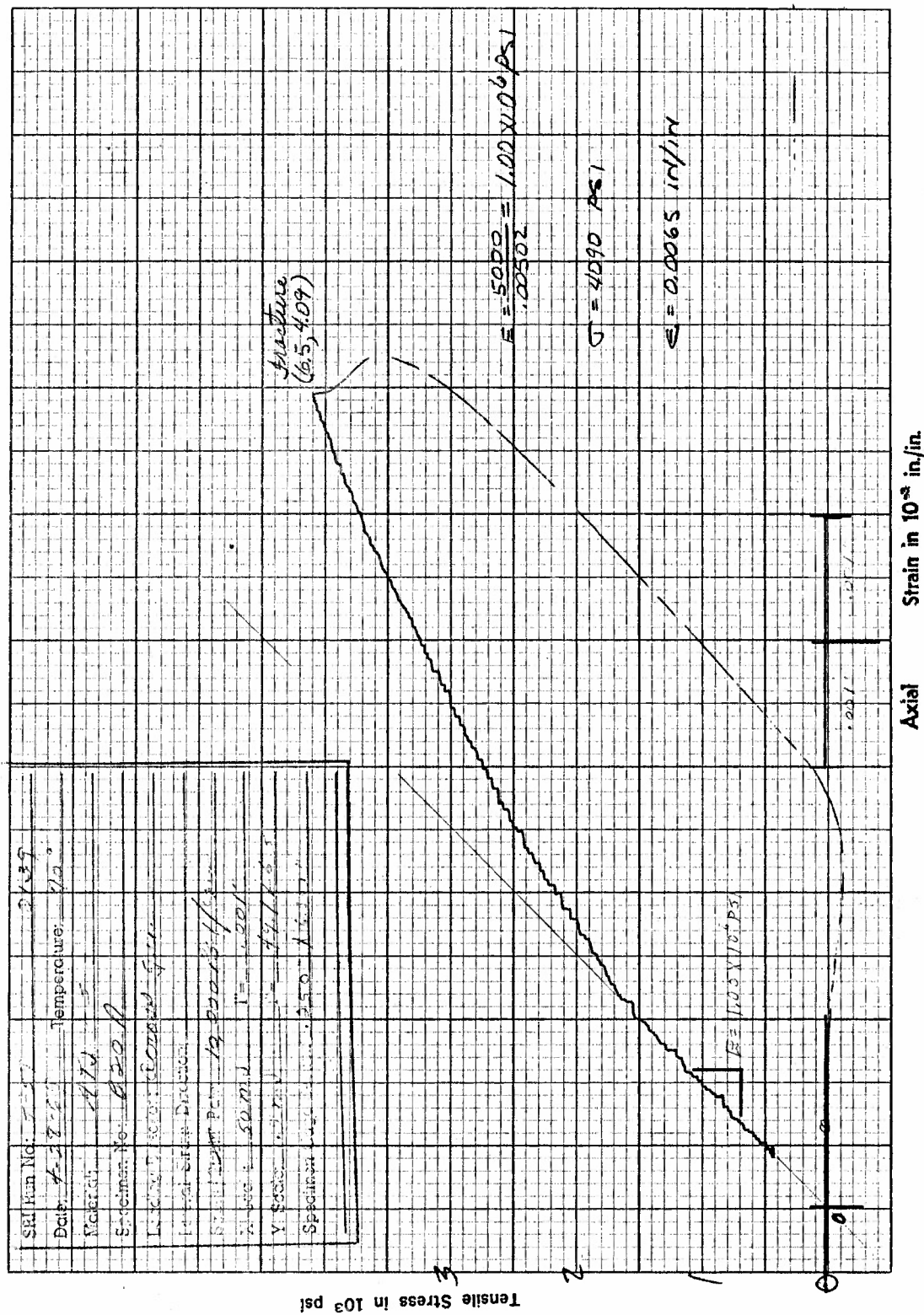


Figure I70. Tensile Stress versus Axial Strain for Specimen B20A of ATJ-S Graphite at 70°F

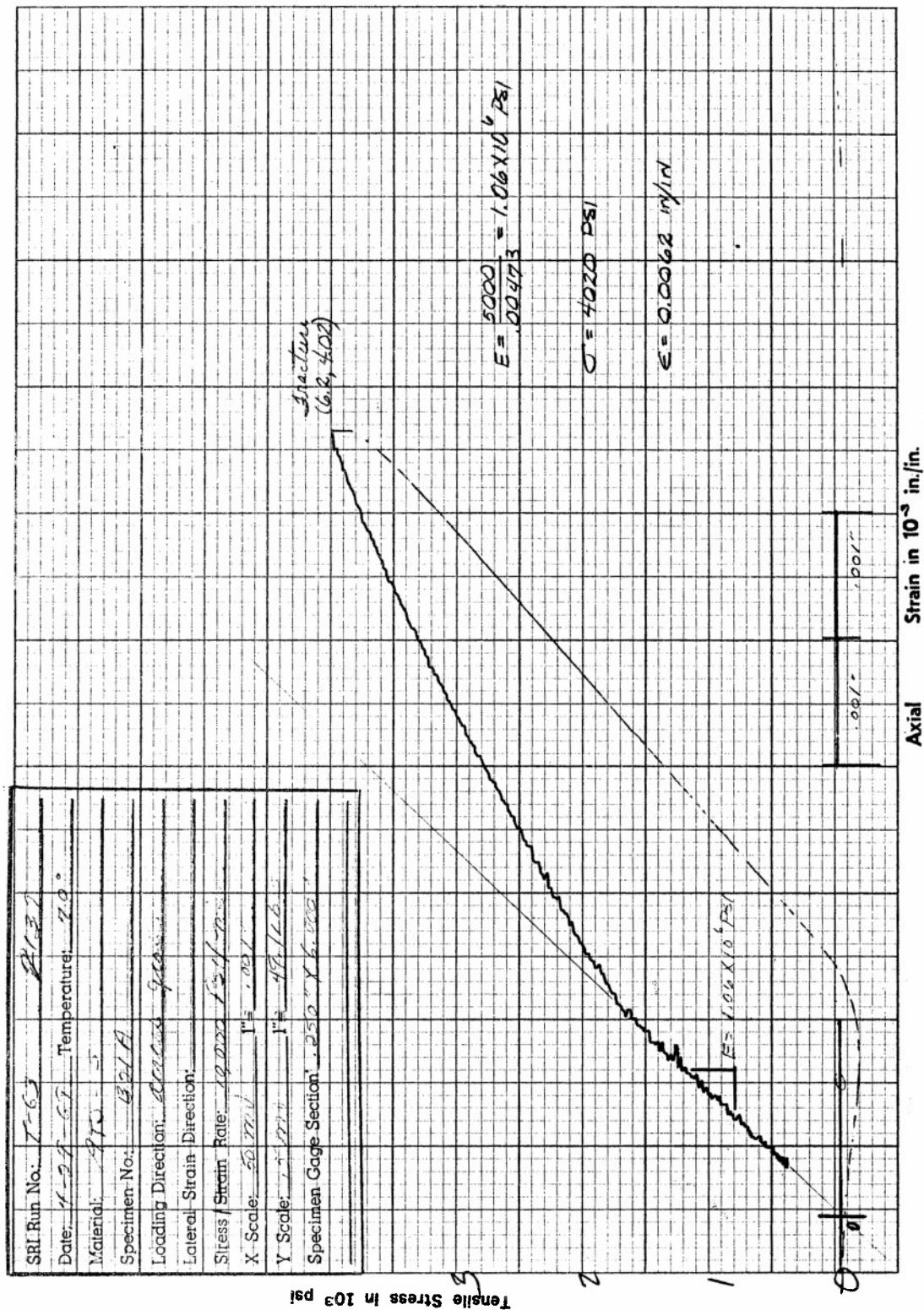


Figure I71. Tensile Stress versus Axial Strain for Specimen B21A of ATJ-S Graphite at 70°F

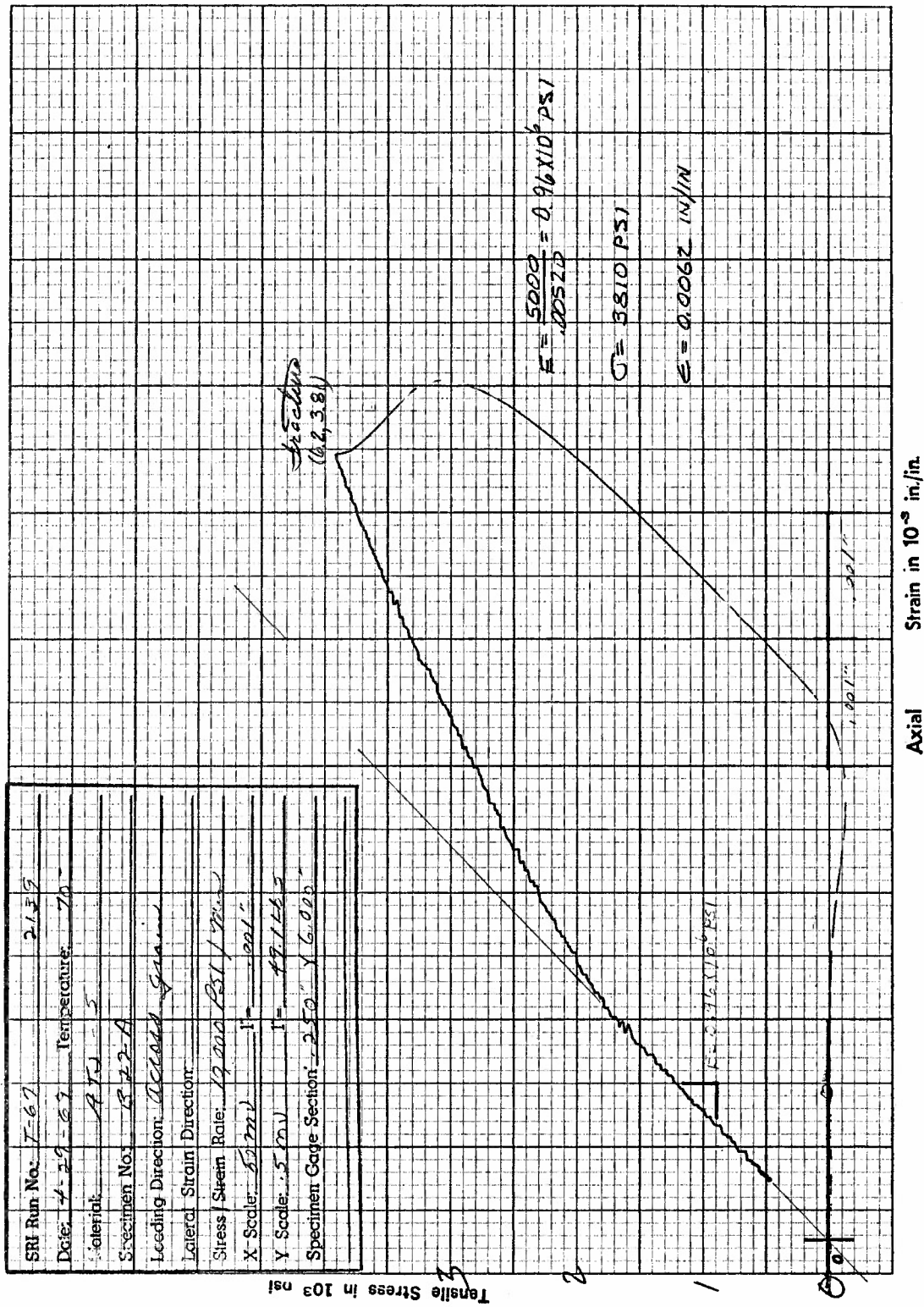


Figure I72. Tensile Stress versus Axial Strain for Specimen B22A of ATJ-S Graphite at 70°F



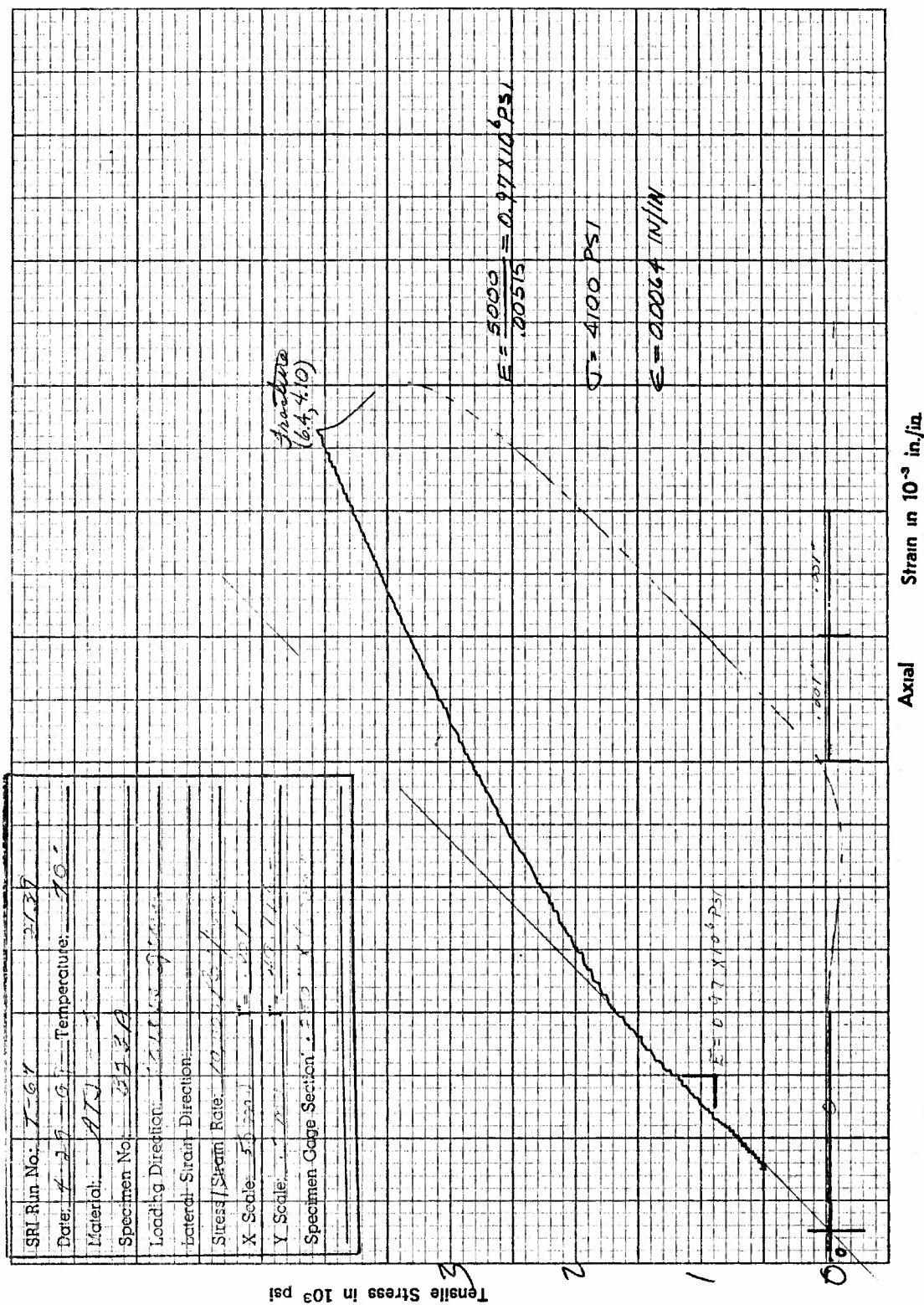


Figure I73. Tensile Stress versus Axial Strain for Specimen B23A of ATJ-S Graphite at 70°F

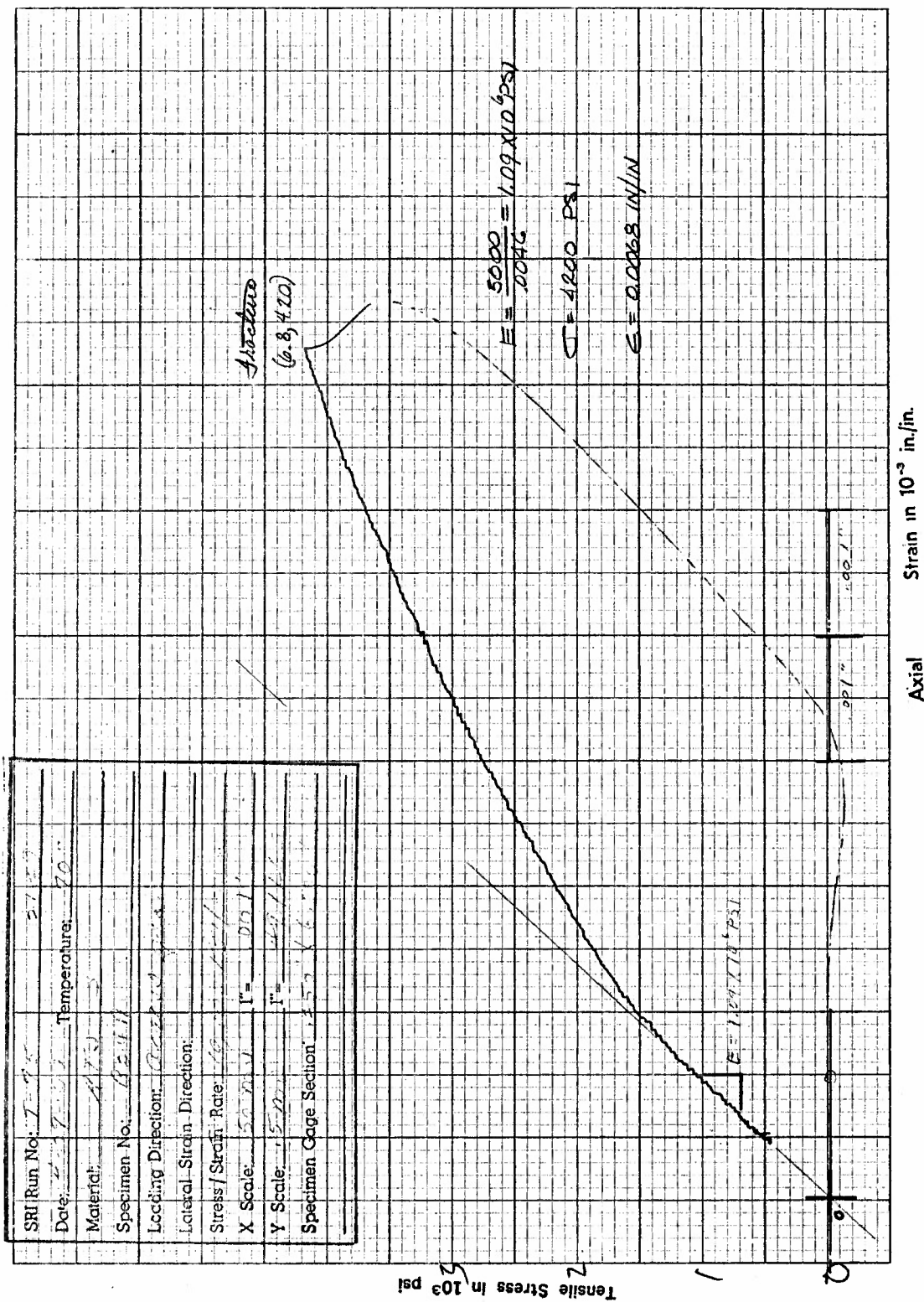


Figure I74. Tensile Stress versus Axial Strain for Specimen B24A of ATJ-S Graphite at 70°F

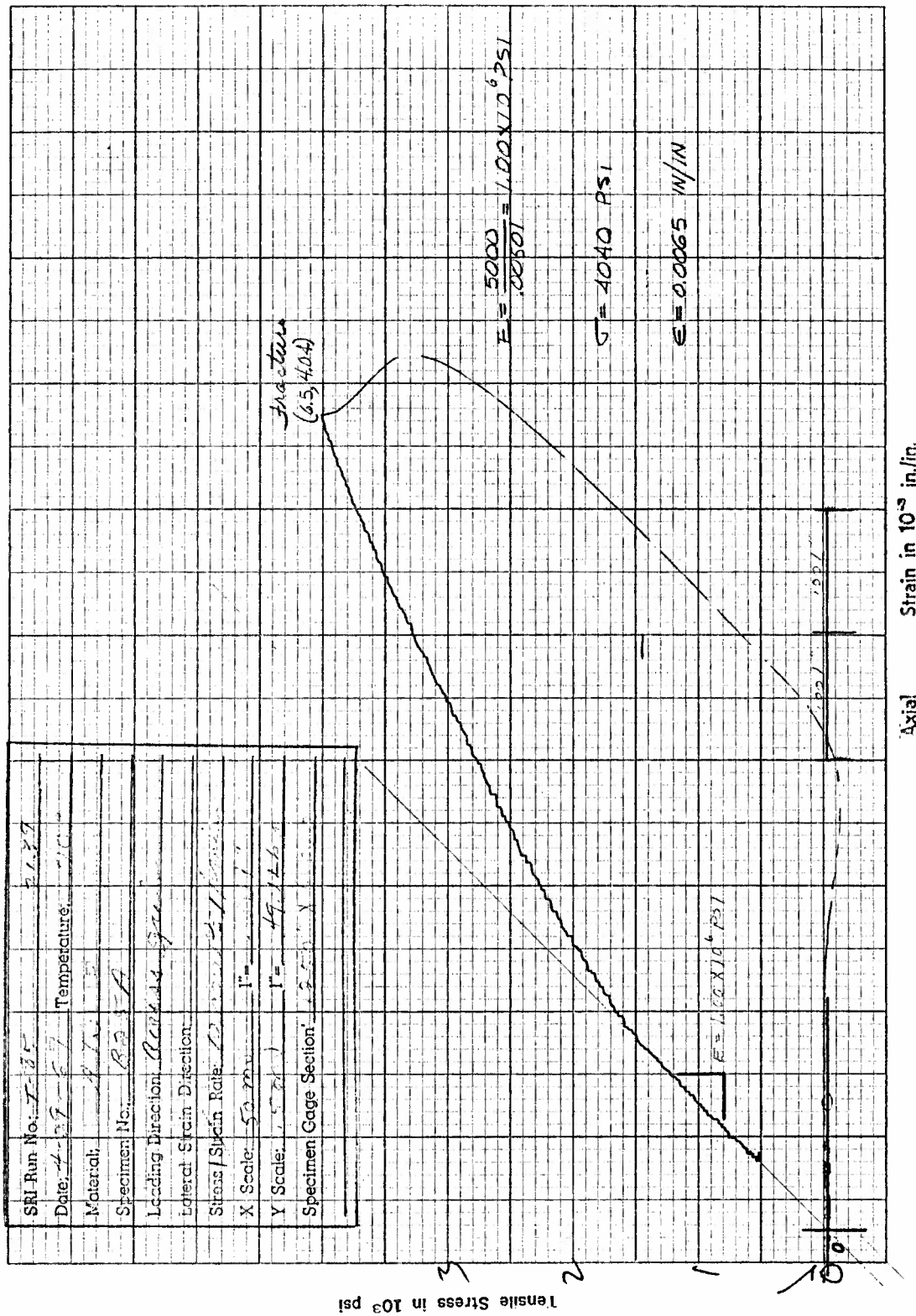


Figure I75. Tensile Stress versus Axial Strain for Specimen B25A of ATJ-S Graphite at 70°F



## APPENDIX J

Results of Avco Ultrasonic Inspection and Alcohol Penetrant  
Test of Specimens from ATJ-S Billet L-6-3



Avco Ultrasonic Inspection Symbols and  
Nomenclature Used for ATJ-S Billet L-6-3

1. The sizes represented by the following symbols placed by a discontinuity were determined by comparison with flat-bottomed holes in graphite referenced standards:

A =  $\frac{1}{64}$ " Diameter discontinuity  
B =  $\frac{1}{64}$ " to  $\frac{1}{32}$ " Diameter discontinuity  
C =  $\frac{1}{32}$ " Diameter discontinuity  
D = Slightly larger than  $\frac{1}{32}$ " diameter discontinuity  
X = Attenuation of back-echo and change in velocity

2. All fractional sizes located by discontinuity represents depth of discontinuity from top (A and B) and bottom surfaces of sketches.
3. Solid line across specimen with arrowheads at both ends denotes fracture location.

# RESULTS OF ULTRASONIC FLAW INSPECTION

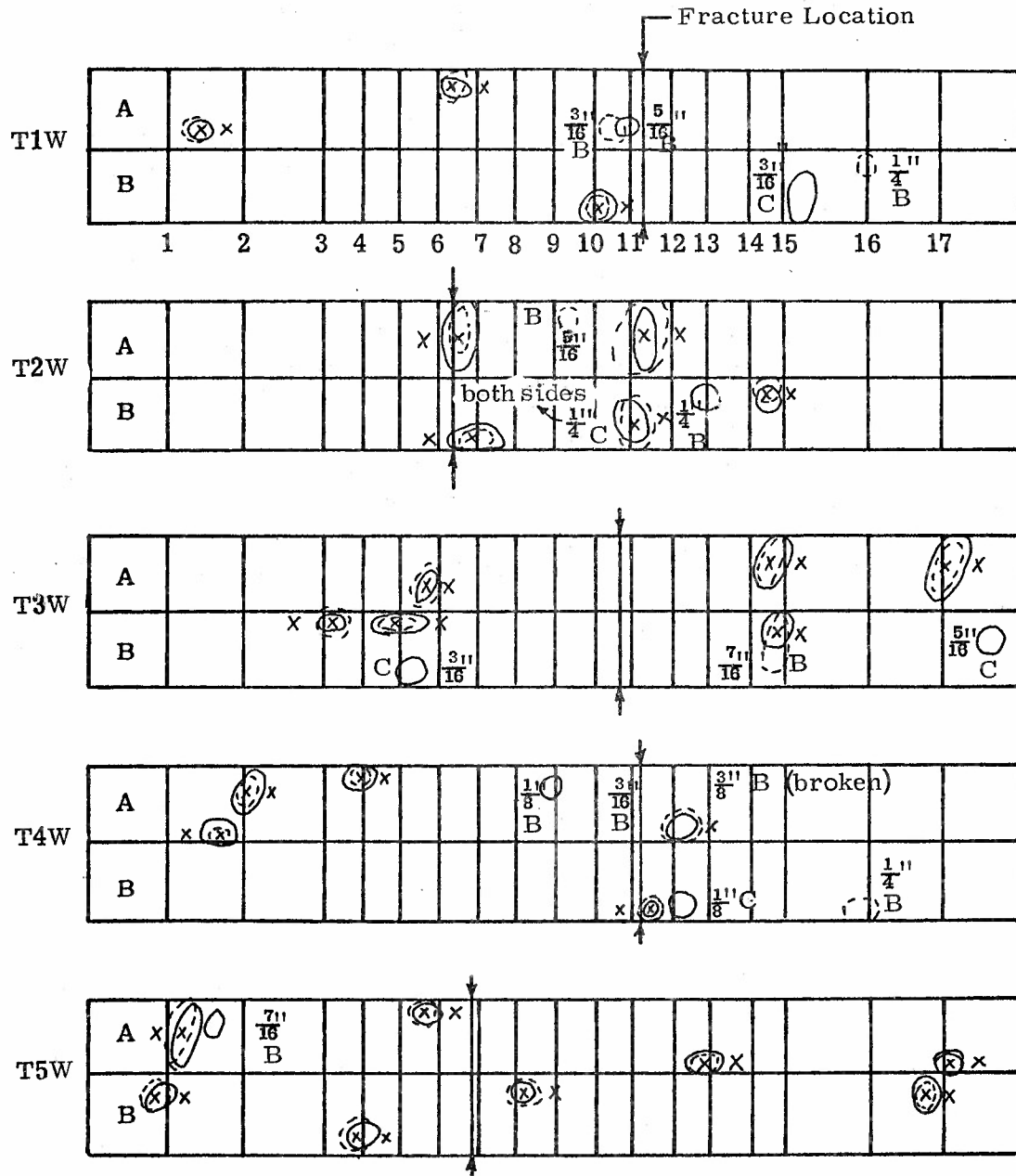


Figure J1



# RESULTS OF ULTRASONIC FLAW INSPECTION

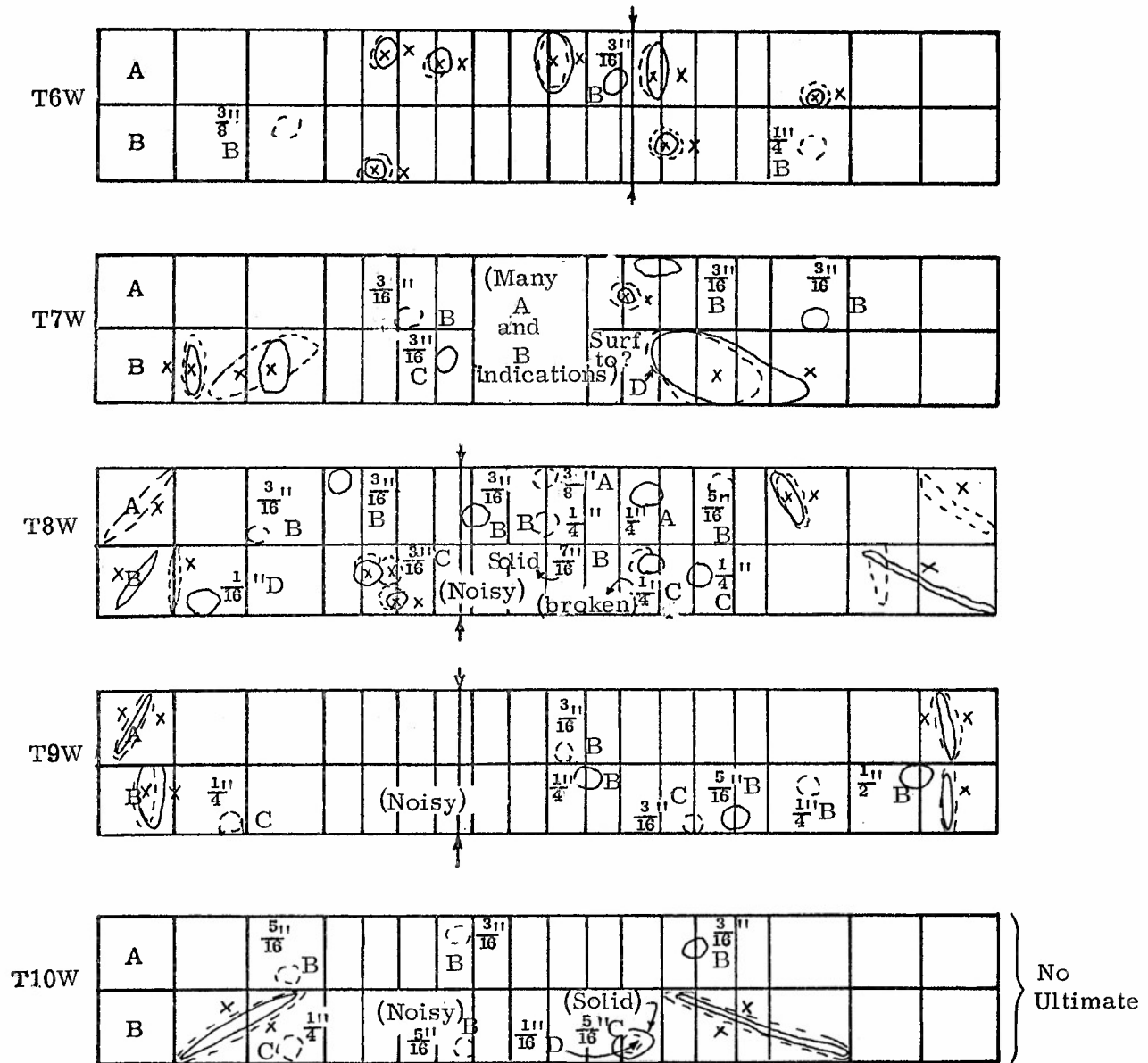


Figure J2

691

# RESULTS OF ULTRASONIC FLAW INSPECTION

T16W

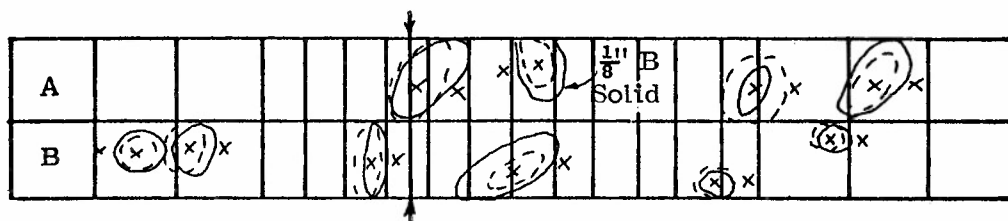


Figure J4

# RESULTS OF ULTRASONIC FLAW INSPECTION

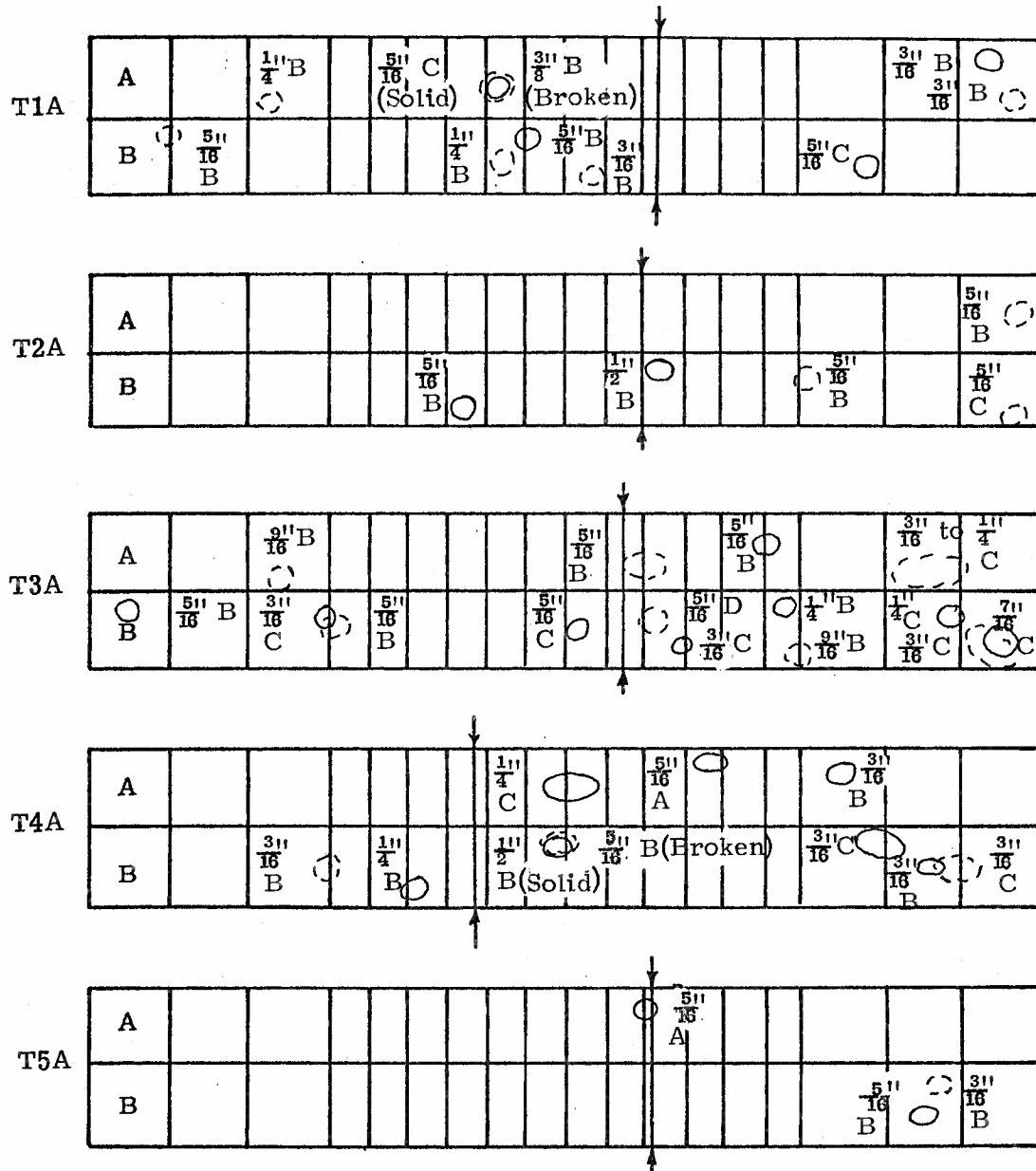


Figure J5

# RESULTS OF ULTRASONIC FLAW INSPECTION

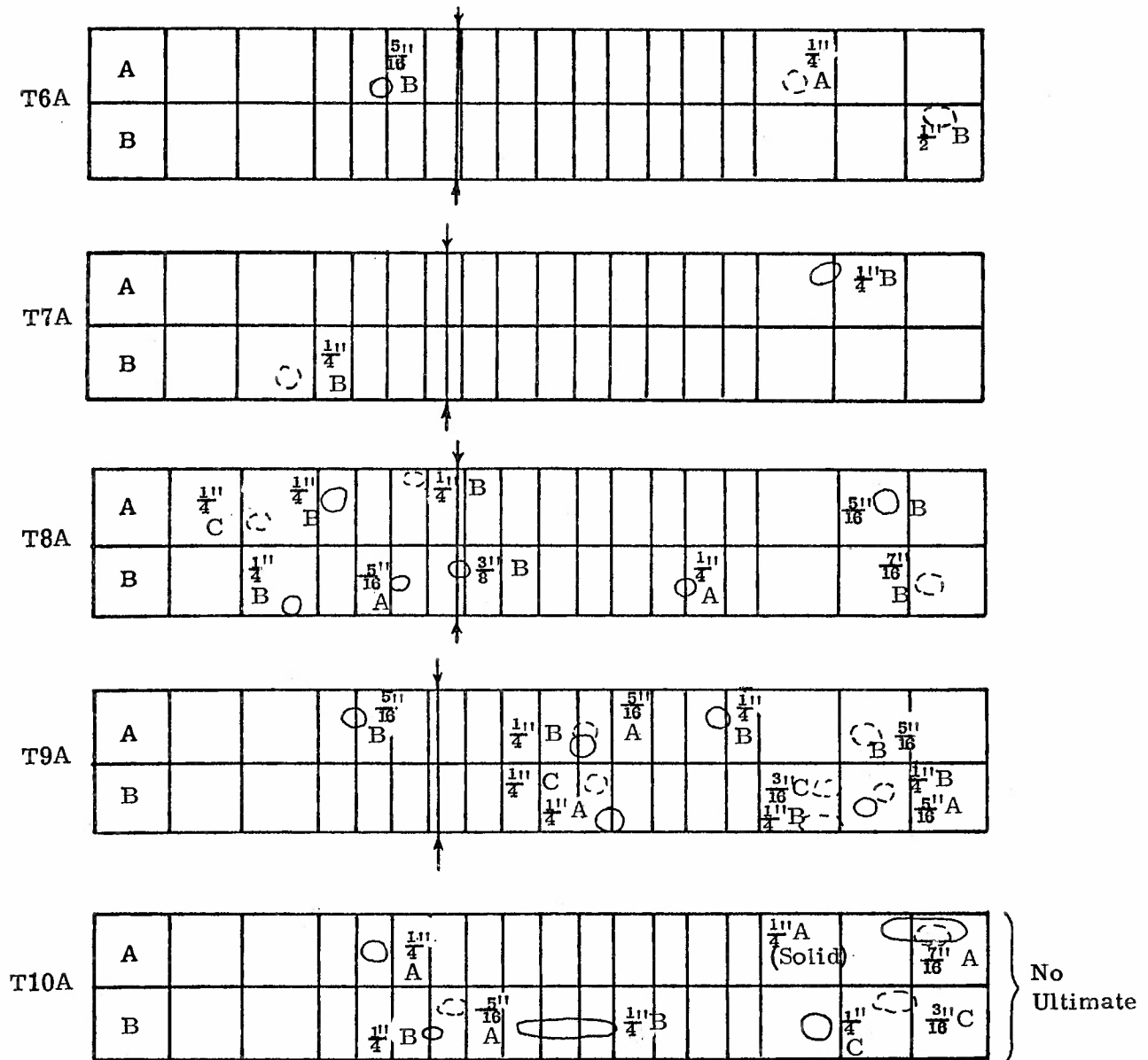


Figure J6

# RESULTS OF ULTRASONIC FLAW INSPECTION

T11A	A																		} No Ultimate
	B																		
T12A	A													○ $\frac{3}{16}$ "	B				} No Ultimate
	B																		
T13A	A	○ $\frac{3}{16}$ "															$\frac{1}{4}$ "	○	
	B																○ $\frac{1}{4}$ "	○ $\frac{1}{4}$ "	
T14A	A																$\frac{1}{8}$ " to $\frac{1}{4}$ "	○	
	B																$\frac{5}{16}$ "	○	
T15A	A																$\frac{3}{16}$ "	○	
	B	$\frac{3}{16}$ "	○														$\frac{1}{4}$ "	○	

Figure J7

RESULTS OF ULTRASONIC FLAW INSPECTION

T16A

A																	$\frac{11}{4}$ B	○
B														○	$\frac{11}{4}$ A		$\frac{511}{18}$ B	○

Figure J8

# RESULTS OF ALCOHOL PENETRANT

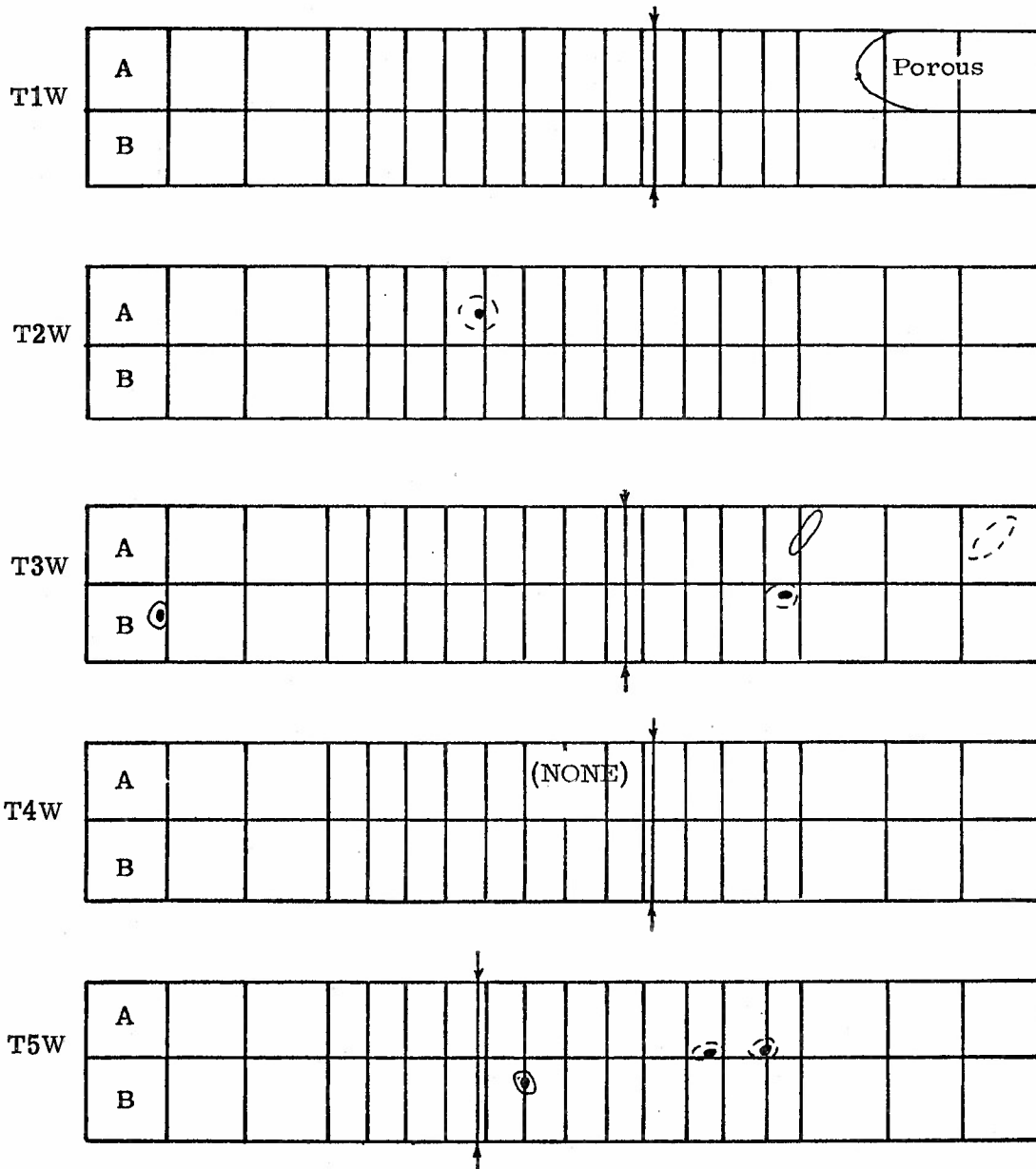


Figure J9



# RESULTS OF ALCOHOL PENETRANT

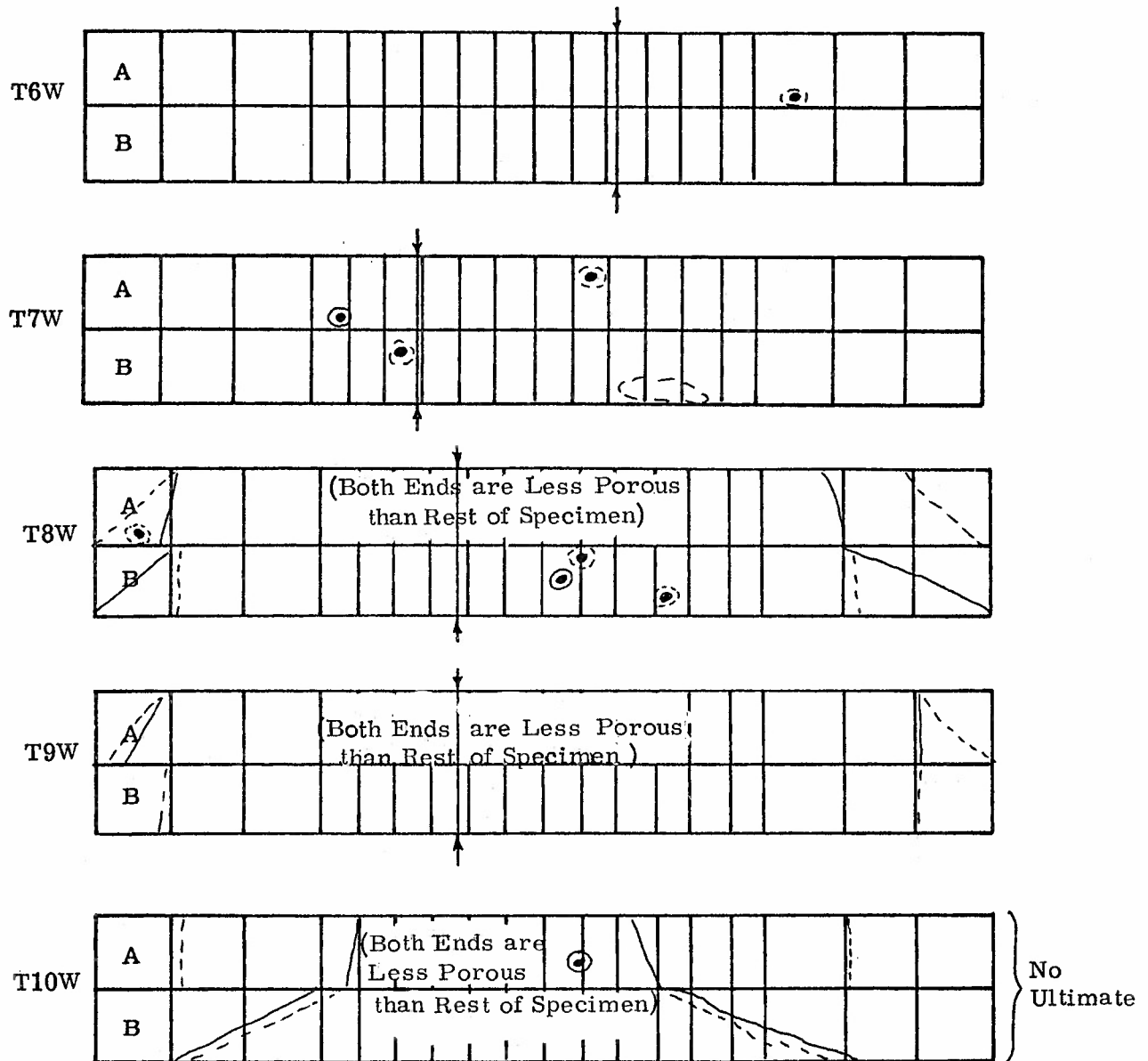


Figure J10

# RESULTS OF ALCOHOL PENETRANT

T11W	A			●															
	B																●		

No  
Ultimate

T12W	A						●												
	B						●												

No  
Ultimate

T13W	A																		
	B																		

Thin  
Line

T14W	A																		
	B	●																	

T15W	A						(NONE)												
	B																		

Figure J11

# RESULTS OF ALCOHOL PENETRANT

T16W

A	○																
B																	

Figure J12

# RESULTS OF ALCOHOL PENETRANT

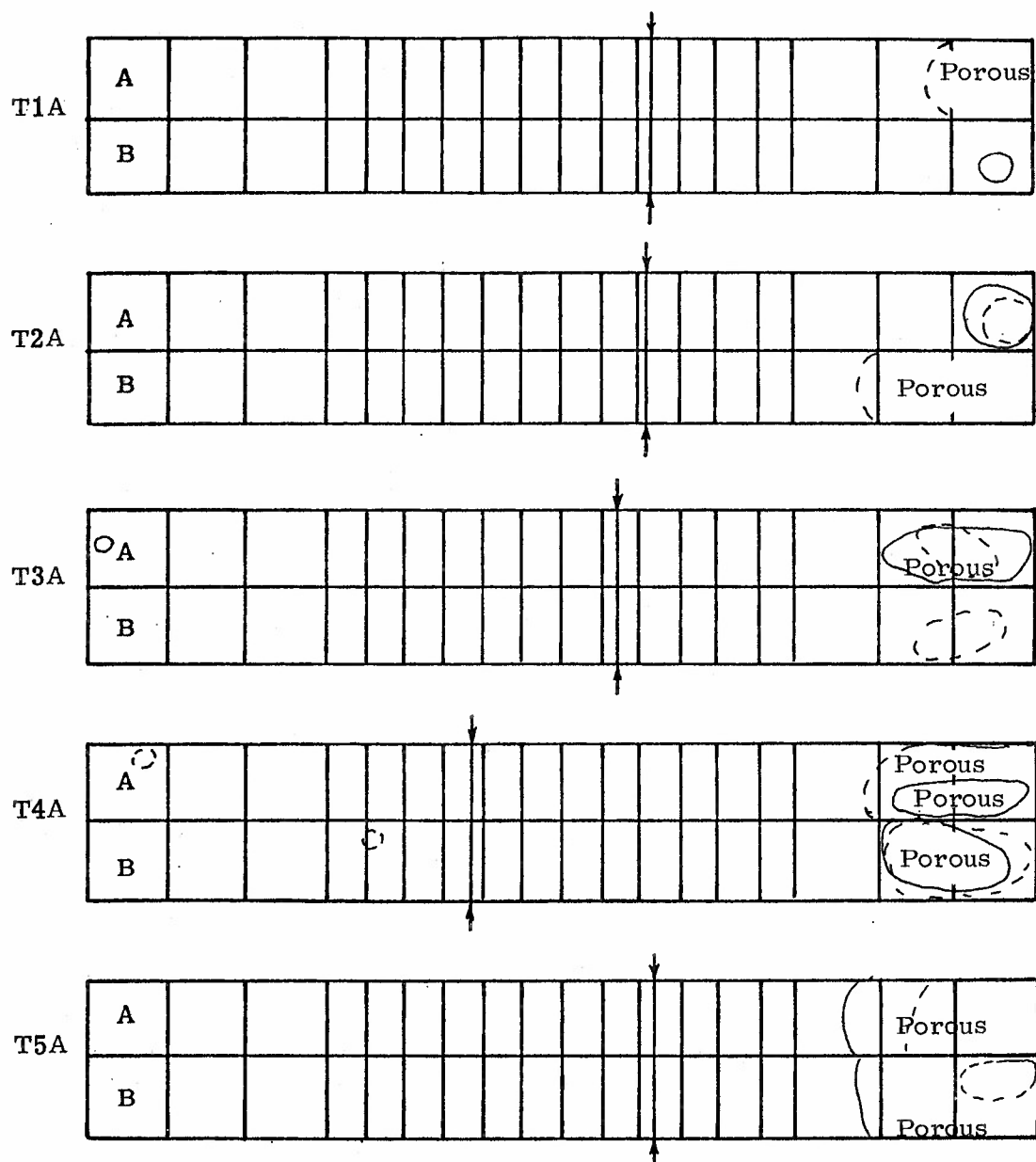


Figure J13

# RESULTS OF ALCOHOL PENETRANT

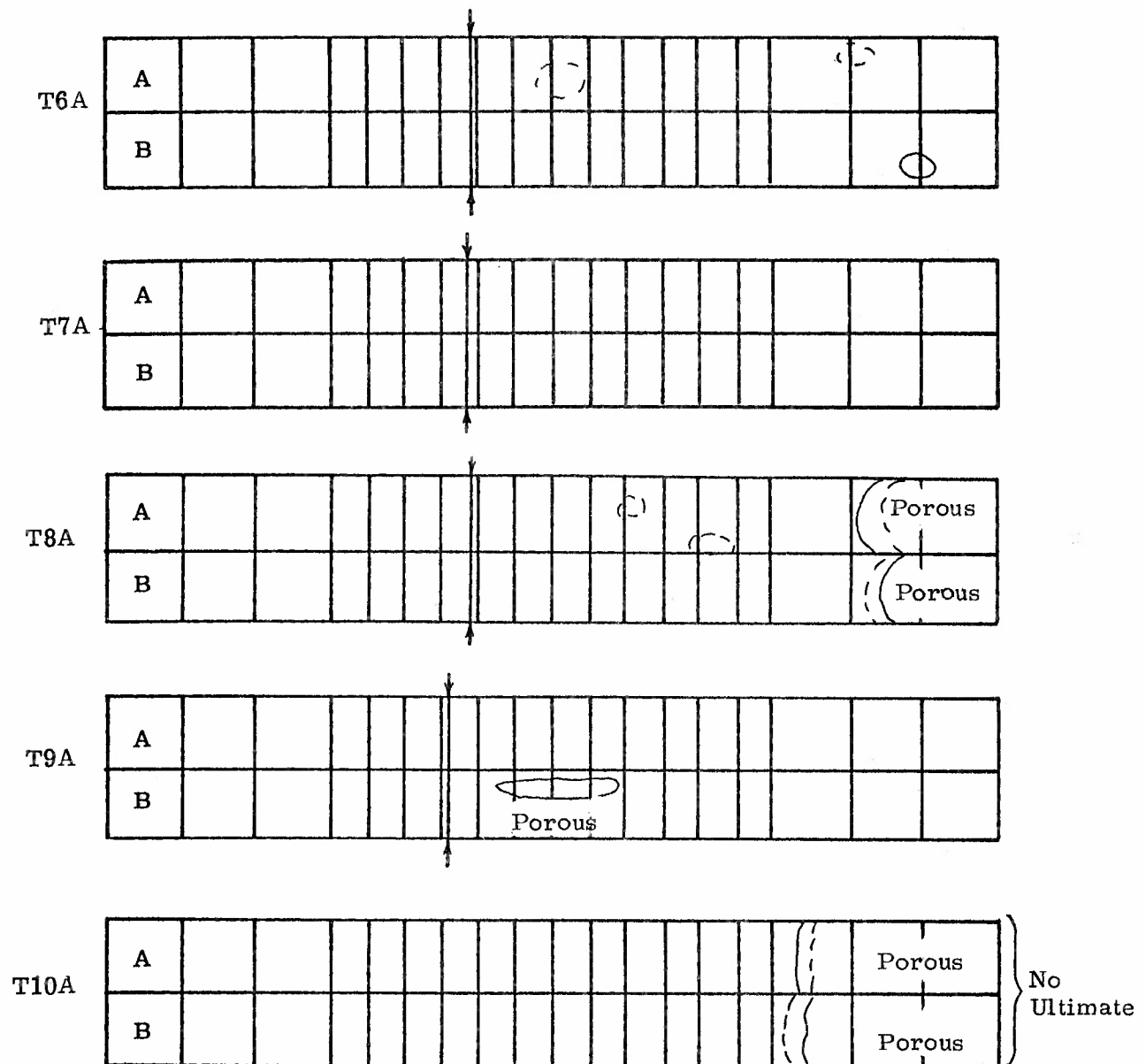


Figure J14

[illegible]

703

**T16A**

[illegible]

704

